

materialstoday
Connecting the materials community

Transfer Printing Technologies and Applications

Edited by Changhong Cao and Yu Sun



Transfer Printing Technologies and Applications

This page intentionally left blank

Materials Today Series

Transfer Printing Technologies and Applications

Edited by

CHANGHONG CAO

Department of Mechanical Engineering, McGill University, Montreal,
QC, Canada

YU SUN

Department of Mechanical and Industrial Engineering, University
of Toronto, Toronto, ON, Canada



Elsevier

Radarweg 29, PO Box 211, 1000 AE Amsterdam, Netherlands
125 London Wall, London EC2Y 5AS, United Kingdom
50 Hampshire Street, 5th Floor, Cambridge, MA 02139, United States

Copyright © 2024 Elsevier Inc. All rights are reserved, including those for text and data mining, AI training, and similar technologies.

No part of this publication may be reproduced or transmitted in any form or by any means, electronic or mechanical, including photocopying, recording, or any information storage and retrieval system, without permission in writing from the publisher. Details on how to seek permission, further information about the Publisher's permissions policies and our arrangements with organizations such as the Copyright Clearance Center and the Copyright Licensing Agency, can be found at our website: www.elsevier.com/permissions.

This book and the individual contributions contained in it are protected under copyright by the Publisher (other than as may be noted herein).

Notices

Knowledge and best practice in this field are constantly changing. As new research and experience broaden our understanding, changes in research methods, professional practices, or medical treatment may become necessary.

Practitioners and researchers must always rely on their own experience and knowledge in evaluating and using any information, methods, compounds, or experiments described herein. In using such information or methods they should be mindful of their own safety and the safety of others, including parties for whom they have a professional responsibility.

To the fullest extent of the law, neither the Publisher nor the authors, contributors, or editors, assume any liability for any injury and/or damage to persons or property as a matter of products liability, negligence or otherwise, or from any use or operation of any methods, products, instructions, or ideas contained in the material herein.

ISBN: 978-0-443-18845-9

For Information on all Elsevier publications
visit our website at <https://www.elsevier.com/books-and-journals>

Publisher: Matthew Deans

Acquisitions Editor: Ana Claudia Garcia

Editorial Project Manager: Rafael Guilherme Trombaco

Production Project Manager: Fizza Fathima

Cover Designer: Miles Hitchen

Typeset by MPS Limited, Chennai, India



Contents

<i>List of contributors</i>	<i>xi</i>
<i>About the editors</i>	<i>xv</i>
<i>Introduction</i>	<i>xvii</i>

Part I Transfer printing methods and fundamentals **1**

1. Mechanics, structure, and materials science of transfer printing **3**

Honglei Zhou, Ankan Dutta and Huanyu Cheng

1.1 Introduction	3
1.2 Mechanics of transfer printing	5
1.3 Structure for transfer printing	17
1.4 Materials science of transfer printing	24
1.5 Conclusions	32
References	32

2. Transfer printing by kinetic control of adhesion **37**

Guorui Wang

2.1 Introduction	37
2.2 Working principle	38
2.3 Mechanics theory	39
2.4 Modulation strategy	42
2.5 Rate-dependent mechanical transfer of graphene	50
2.6 Conclusions and prospects	57
References	58

3. Thermal release tape–enabled transfer printing techniques **63**

Yuan Lin and Zhenlong Huang

3.1 Introduction	63
3.2 Mechanisms of thermal release transfer printing	64
3.3 Mechanism of thermally expandable microspheres-based thermal release tape stamp for large adhesion switchability	67
3.4 Thermal treatment with laser for programmable transfer printing	68
3.5 Shape-conformal thermal release tape stamp for curve electronics	70
3.6 Thermal release tape stamp–enabled roll-to-roll processing for large-scale transfer printing	71

3.7	Conclusions and future outlook	74
	References	74
4.	Laser-driven noncontact transfer printing technique	79
	Rui Li and Dongqi An	
4.1	Introduction	79
4.2	Transient heat conduction	82
4.3	Interfacial delamination	85
4.4	Size effect of the ink	89
4.5	Stamp modification design	91
	References	93
5.	Magnetic-assisted transfer printing techniques	97
	Chenglong Li, Suhao Wang, Shun Zhang and Jizhou Song	
5.1	Introduction	97
5.2	Latest development of magnetic-assisted transfer printing techniques	98
5.3	Conclusion	113
	References	114
6.	Transfer printing techniques enabled by advanced carbon nanomaterials	117
	Seong Jae Kim and Sanha Kim	
6.1	Working principles	117
6.2	Process physics	123
6.3	Future works	135
	References	137
7.	Water-assisted transfer printing techniques	145
	Hongyu Hou, Lingzhi Zhang, Zi Xin Zhang and Changhong Cao	
7.1	Water-assisted transfer printing with self-assembled monolayer-based release layer	145
7.2	Water-assisted transfer printing with sacrificial layer	147
	References	151
8.	Novel nontraditional transfer printing technologies	153
	Seok Kim and Hohyun Keum	
8.1	Transfer printing using unusual manipulator—shape memory polymer	153
8.2	Transfer printing involving photoresist thin film	164
8.3	Transfer printing of elastic membrane for pattern generation	168

8.4 Epoxy-based subtractive transfer printing	170
References	170

Part II State-of-the-art applications enabled by transfer printing **175**

9. Microtransfer printing techniques for optical applications **177**

Bongjoong Kim, Woohyun Park, Jehwan Hwang and Chi Hwan Lee

9.1 Introduction	177
9.2 Transfer printing techniques	180
9.3 Optical applications	187
9.4 Conclusions	197
Acknowledgment	198
References	198

10. Flexible sensors enabled by transfer printing techniques **207**

Xinghao Huang, Liangshu Liu, Jaemin Seo, Qinai Zhao and Hangbo Zhao

10.1 Strain sensors	207
10.2 Pressure sensors	214
10.3 Thermal sensors	217
10.4 Electrophysiology sensors	221
10.5 Chemical sensors	226
References	230

11. Construction of flexible transistors enabled by transfer printing **235**

Han Eol Lee

11.1 Introduction	235
11.2 Flexible Si thin-film transistors	238
11.3 Compound semiconductor-based flexible transistors	240
11.4 Flexible transistors with carbon materials	244
11.5 Ion gel-based flexible transistors	246
11.6 Flexible oxide transistors	249
11.7 Flexible transistors with other materials	252
11.8 Flexible Si transistors with novel transfer methods	255
11.9 Transistors on various flexible substrates	260
11.10 Conclusion	262
Acknowledgments	262
References	262

12. Transfer-printed devices for biomedical applications	279
Changbo Liu and Xing Sheng	
12.1 Introduction	279
12.2 Materials	281
12.3 Functional devices	303
12.4 Conclusion	316
References	316
13. Laser-driven transfer printing techniques for micro-LED display	325
Hongyu Luo, Chengjun Wang, Shun Zhang and Jizhou Song	
13.1 Introduction to micro-light-emitting diode display	325
13.2 Laser-driven transfer printing techniques for micro-light-emitting diode display	327
13.3 Contact laser-driven transfer printing techniques	330
13.4 Noncontact laser-driven transfer printing techniques	339
13.5 Conclusion	347
References	347
14. Energy systems fabricated by transfer printing technologies	353
Yijia Wang and Yang Zhao	
14.1 Introduction	353
14.2 Rechargeable batteries	353
14.3 Supercapacitors	356
14.4 Fuel cells	359
14.5 Water splitting	360
14.6 Solar cells	362
14.7 Conclusion	364
References	365
15. Transfer printing of metal films	369
Kaihao Zhang	
15.1 Preparation of metal films	369
15.2 Metal transfer principles	379
15.3 Transfer printing processes for metal films	384
15.4 Environmentally-assisted bonding and debonding of the metal/substrate interfaces	401
15.5 Electromechanical behaviors of ultrathin metal films bonded on a substrate	404
References	411

16. Stacking of two-dimensional materials	419
Wenhao Li, Jichuang Shen, Huaze Zhu, Han Chen and Wei Kong	
16.1 Introduction	419
16.2 Process	420
16.3 Characterization	442
16.4 Performance	456
16.5 Conclusion	463
References	463
17. 2D materials—based electronics enabled by transfer printing technologies	475
Sangmoon Han, Zhihao Xu, Yuan Meng and Sang-Hoon Bae	
17.1 Overview	475
17.2 2D layer—based logic devices	475
17.3 2D layer—based optoelectronics	480
17.4 2D layer—based memory devices	484
17.5 Conclusion and outlook	489
References	489
18. Outlooks	495
Changyong (Chase) Cao	
18.1 Introduction	495
18.2 Major challenges	495
18.3 Future research directions	496
18.4 Possible breakthroughs in future transfer printing	501
18.5 Conclusion	501
References	502
<i>Index</i>	505

This page intentionally left blank

List of contributors

Dongqi An

Department of Engineering Mechanics, Dalian University of Technology, Dalian, P.R. China

Sang-Hoon Bae

Department of Mechanical Engineering & Materials Science, Washington University in St. Louis, Saint Louis, MO, United States; The Institution of Materials Science and Engineering, Washington University in St. Louis, Saint Louis, MO, United States

Changhong Cao

Department of Mechanical Engineering, McGill University, Montreal, QC, Canada

Changyong (Chase) Cao

Department of Mechanical and Aerospace Engineering, Case Western Reserve University, Cleveland, OH, United States; Department of Electrical, Computer, and Systems Engineering, Case Western Reserve University, Cleveland, OH, United States; Advanced Platform Technology (APT) Center, Louis Stokes Cleveland VA Medical Center, Cleveland, OH, United States

Han Chen

School of Engineering, Westlake University, Hangzhou, P.R. China

Huanyu Cheng

Department of Engineering Science and Mechanics, The Pennsylvania State University, University Park, PA, United States

Ankan Dutta

Department of Engineering Science and Mechanics, The Pennsylvania State University, University Park, PA, United States; Center for Neural Engineering, The Pennsylvania State University, University Park, PA, United States

Sangmoon Han

Department of Mechanical Engineering & Materials Science, Washington University in St. Louis, Saint Louis, MO, United States

Hongyu Hou

Department of Mechanical Engineering, McGill University, Montreal, QC, Canada

Xinghao Huang

Department of Aerospace and Mechanical Engineering, University of Southern California, Los Angeles, CA, United States

Zhenlong Huang

School of Materials and Energy, University of Electronic Science and Technology of China, Chengdu, P.R. China

Jehwan Hwang

Weldon School of Biomedical Engineering, Purdue University, West Lafayette, IN, United States

Hohyun Keum

Korea Institute of Industrial Technology, Digital Healthcare, Cheonan, South Korea

Bongjoong Kim

Department of Mechanical and System Design Engineering, Hongik University, Seoul, South Korea

Sanha Kim

Department of Mechanical Engineering, Korea Advanced Institute of Science and Technology (KAIST), Daejeon, South Korea

Seok Kim

Pohang University of Science and Technology, Mechanical Engineering, Pohang, South Korea

Seong Jae Kim

Department of Mechanical Engineering, Korea Advanced Institute of Science and Technology (KAIST), Daejeon, South Korea

Wei Kong

School of Engineering, Westlake University, Hangzhou, P.R. China

Chi Hwan Lee

Biomedical Engineering, Mechanical Engineering and Materials Engineering, Purdue University, West Lafayette, IN, United States

Han Eol Lee

Division of Advanced Materials Engineering, Jeonbuk National University, Jeonju, South Korea; Department of Electronic Engineering, Jeonbuk National University, Jeonju, South Korea; Department of JBNU-KIST Industry-Academia Convergence Research, Jeonbuk National University, Jeonju, South Korea

Chenglong Li

Department of Engineering Mechanics, Soft Matter Research Center, and Key Laboratory of Soft Machines and Smart Devices of Zhejiang Province, Zhejiang University, Hangzhou, P.R. China

Rui Li

Department of Engineering Mechanics, Dalian University of Technology, Dalian, P.R. China

Wenhao Li

School of Engineering, Westlake University, Hangzhou, P.R. China

Yuan Lin

School of Materials and Energy, University of Electronic Science and Technology of China, Chengdu, P.R. China

Changbo Liu

School of Materials Science and Engineering, Beihang University, Beijing, P.R. China; Hangzhou Innovation Institute, Beihang University, Hangzhou, P.R. China

Liangshu Liu

Department of Aerospace and Mechanical Engineering, University of Southern California, Los Angeles, CA, United States

Hongyu Luo

Department of Engineering Mechanics, Soft Matter Research Center, and Key Laboratory of Soft Machines and Smart Devices of Zhejiang Province, Zhejiang University, Hangzhou, P.R. China

Yuan Meng

Department of Mechanical Engineering & Materials Science, Washington University in St. Louis, Saint Louis, MO, United States; The Institution of Materials Science and Engineering, Washington University in St. Louis, Saint Louis, MO, United States

Woohyun Park

School of Mechanical Engineering, Purdue University, West Lafayette, IN, United States

Jaemin Seo

Department of Aerospace and Mechanical Engineering, University of Southern California, Los Angeles, CA, United States

Jichuang Shen

School of Engineering, Westlake University, Hangzhou, P.R. China

Xing Sheng

Department of Electronic Engineering, Tsinghua University, Beijing, P.R. China

Jizhou Song

Department of Engineering Mechanics, Soft Matter Research Center, and Key Laboratory of Soft Machines and Smart Devices of Zhejiang Province, Zhejiang University, Hangzhou, P.R. China; Department of Rehabilitation Medicine, The First Affiliated Hospital, Zhejiang University, Hangzhou, P.R. China; The State Key Lab of Brain-Machine Intelligence, Zhejiang University, Hangzhou, P.R. China

Chengjun Wang

International Research Center for Information Science and Electronic Engineering, Zhejiang University, Haining, P.R. China

Guorui Wang

CAS Key Laboratory of Mechanical Behavior and Design of Materials, Department of Modern Mechanics, University of Science and Technology of China, Hefei, P.R. China

Suhao Wang

Department of Engineering Mechanics, Soft Matter Research Center, and Key Laboratory of Soft Machines and Smart Devices of Zhejiang Province, Zhejiang University, Hangzhou, P.R. China

Yijia Wang

Department of Mechanical and Materials Engineering, Western University, London, ON, Canada

Zhihao Xu

Department of Mechanical Engineering & Materials Science, Washington University in St. Louis, Saint Louis, MO, United States; The Institution of Materials Science and Engineering, Washington University in St. Louis, Saint Louis, MO, United States

Kaihao Zhang

Smart Manufacturing Thrust, Systems Hub, The Hong Kong University of Science and Technology, Guangzhou, P.R. China

Lingzhi Zhang

Department of Mechanical Engineering, McGill University, Montreal, QC, Canada

Shun Zhang

International Research Center for Information Science and Electronic Engineering, Zhejiang University, Haining, P.R. China; College of Information Science & Electronic Engineering, Zhejiang University, Hangzhou, P.R. China

Zi Xin Zhang

Department of Mechanical Engineering, McGill University, Montreal, QC, Canada

Hangbo Zhao

Department of Aerospace and Mechanical Engineering, University of Southern California, Los Angeles, CA, United States; Alfred E. Mann Department of Biomedical Engineering, University of Southern California, Los Angeles, CA, United States

Qinai Zhao

Department of Aerospace and Mechanical Engineering, University of Southern California, Los Angeles, CA, United States

Yang Zhao

Department of Mechanical and Materials Engineering, Western University, London, ON, Canada

Honglei Zhou

Department of Engineering Science and Mechanics, The Pennsylvania State University, University Park, PA, United States; Department of Engineering Mechanics, Tsinghua University, Beijing, P.R. China; Institute of Flexible Electronics Technology of THU, Zhejiang, Jiaxing, P.R. China

Huaze Zhu

School of Engineering, Westlake University, Hangzhou, P.R. China

About the editors

Changhong Cao is the director of McGill Nanofactory and an assistant professor in the Department of Mechanical Engineering at the McGill University. His research group focuses on the development of printing technologies (2D and 3D), mechano-electrochemical studies of energy storage materials, as well as synthesis, assembly, and multiscale characterizations of low-dimensional materials. He was a recipient of the Microsystem and Nanoengineering Outstanding Young Researcher Award, has authored a number of publications in premium journals such as *Science Advances*, *Nano Letters*, and *ACS Nano*, and has been sponsored by multiple national and international funding agencies and companies.



international funding

Yu Sun is a member of two national academies of Canada (Canadian Academy of Engineering; Academy of Science of the Royal Society of Canada). He is a Tier I Canada Research Chair and the director of the University of Toronto Robotics Institute. His Advanced Micro and Nanosystems Laboratory specializes in developing innovative technologies and instruments for manipulating and characterizing cells, molecules, and nanomaterials. He was an elected fellow of ASME (American Society of Mechanical Engineers), IEEE (Institute of Electrical and Electronics Engineers), AAAS (American Association for the Advancement of Science), NAI (US National Academy of Inventors), and AIMBE (American Institute of Medicine and Biomedical Engineering) for his work on micro-nano devices and robotic systems.



This page intentionally left blank

Introduction

Transfer printing (TP) is a class of techniques for the deterministic assembly of disparate micro/nanomaterials into functional devices. TP has become an emerging suite of technologies for micro/nano fabrication. Systems enabled by TP range from complex molecular scale materials (e.g., DNA, graphene), to high-performance hard materials (e.g., metals, oxide films), and to fully integrated devices (e.g., Light Emitting Diode, Complementary Metal-Oxide-Semiconductor). A variety of subtechniques for different purposes have boomed in the last decade (e.g., kinetically controlled, water-assisted, magnetic-assisted, etc.), which led to nonconventional electronics, optoelectronics, photovoltaics, and photonics and enabled the development of nonplanar and flexible electronics.

As TP is a highly versatile class of technologies, it can be overwhelming and time-consuming to identify proper techniques for certain applications. This will be the first book providing a comprehensive introduction to TP. The overview and detailed breakdown of this class of technologies in this book aim to provide a clear path to help nonexpert and expert researchers to understand where the technology stands today and where it is going. This book will provide the audience with a comprehensive introduction to major TP technologies and their state-of-the-art applications.

Three key features of this book will be most valuable to the readers:

- Comprehensive coverage of TP technologies and their specific features for different applications
- Highlight of breakthrough results and systems enabled by novel TP techniques
- Insightful outlook and perspectives on future directions and trends in each chapter that covers a subarea of TP

This page intentionally left blank

PART I

Transfer printing methods and fundamentals

This page intentionally left blank

CHAPTER 1

Mechanics, structure, and materials science of transfer printing

Honglei Zhou^{1,2,3,*}, Ankan Dutta^{1,4,*} and Huanyu Cheng^{1,**}

¹Department of Engineering Science and Mechanics, The Pennsylvania State University, University Park, PA, United States

²Department of Engineering Mechanics, Tsinghua University, Beijing, P.R. China

³Institute of Flexible Electronics Technology of THU, Zhejiang, Jiaxing, P.R. China

⁴Center for Neural Engineering, The Pennsylvania State University, University Park, PA, United States

1.1 Introduction

Conventional micro- or nanofabrication techniques facilitate the fabrication of stretchable inorganic devices on conventional substrates such as silicon wafers. However, further processes are necessary for robust substrate handling and embedding the fabricated functional materials and devices onto a flexible or stretchable substrate conformal to human skin performing biomedical applications. Transferring the fabricated device from the original growth substrate to the target substrate is often termed transfer printing. Micro- and nanomaterials can be deterministically and functionally assembled and organized on a large scale through transfer printing (Carlson, et al., 2012a; Feng et al., 2007; Meitl et al., 2004; Park et al., 2009). The conventional transfer printing process generally includes two essential stages: picking up and printing (Fig. 1.1A). For the picking-up process, a stamp is controlled to pick up the prefabricated functional devices such as nano/micro-membrane or nanowires from the donor substrate. During the printing phase, the stamp loaded with a prefabricated device is then transferred to the receiver substrate and contacted with the substrate surface. After removing the stamp, the desired devices are precisely printed onto the target substrate (receiver). A critical role is played by the stamp in successfully implementing the whole transfer printing process with sufficient controllability and fidelity (Feng et al., 2007; Yi et al., 2018). The fracture at the interface between the stamp and device competes with that at the interface between the device and substrate, which determines the success of the transfer printing process. In the printing step, the stamp/device fracture appears, whereas in the picking-up step, the device/donor substrate interface fractures (Feng et al., 2007; Meitl et al., 2006). The stamp/device's adhesion strength should be greater than the device/donor interface for successful

* These authors contributed equally.

** Huanyu Cheng led the preparation of the manuscript and contributed to editorial modifications of the overall text.

Transfer Printing Technologies and Applications

DOI: <https://doi.org/10.1016/B978-0-443-18845-9.00001-6>

© 2024 Elsevier Inc. All rights are reserved, including those for text and data mining, AI training, and similar technologies.

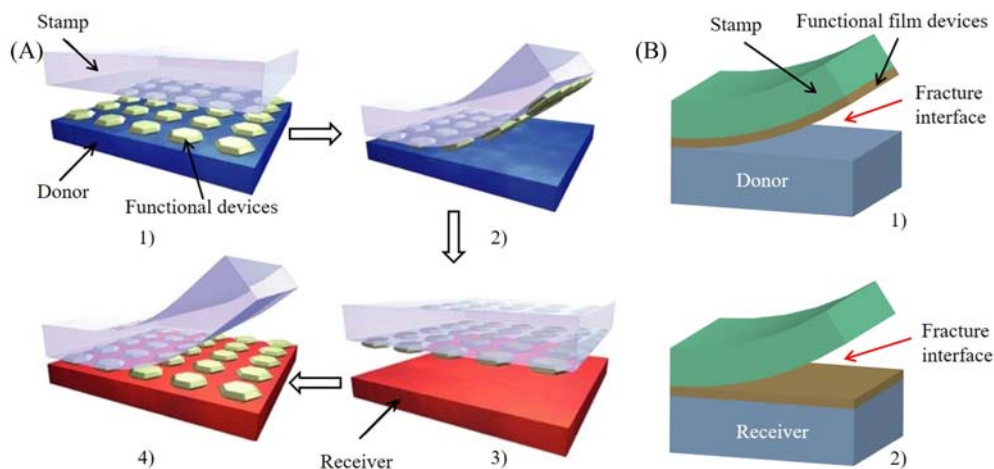


Figure 1.1 Schematic diagram of the transfer printing process and the involved interface fracture. (A) (1) Pressing the stamp on the growth substrate with prefabricated functional components; (2) detaching the stamp to pick up the devices to be transferred from the growth substrate; (3) bringing the stamp loaded with the device into contact with the receiver; (4) detaching the stamp to complete the printing process with the devices printed onto the receiving substrate. (B) (1) The interface fracture occurred at the device/donor interface for the picking-up step; (2) the interface delamination between the device and stamp occurred during the printing step. (A) Reprinted with permission from Meitl, M.A., Zhu, Z.T., Kumar, V., Lee, K.J., Feng, X., Huang, Y.Y., Adesida, I., Nuzzo, R.G., & Rogers, J.A. (2006). *Transfer printing by kinetic control of adhesion to an elastomeric stamp*. *Nature Materials*, 5(1), 33–38. <https://doi.org/10.1038/nmat1532>; Copyright 2006, Nature Publishing Group. (B) With permission from Nature Publishing Group.

picking up, leading to device/donor delamination and enabling the elastomeric stamp to pick up the functional devices [Fig. 1.1B(1)]. On the other hand, in the printing step, the stamp/device adhesion is weaker than that at the device/receiver interface. Therefore, peeling off the stamp enables the delamination between the stamp and devices, which allows the printing of the desired devices onto the receiver [Fig. 1.1B(2)]. The development of transfer printing technology, including mechanical theory, structure, and material science, has been applied to promote more efficient transfer printing methods and provide a solid theoretical basis for optimizing the transfer printing technology (Bian et al., 2019; Carlson et al., 2012b; Liang et al., 2021; Linghu et al., 2018; Luo, Wang, et al., 2021; Park et al., 2020; Sim et al., 2015; Zhang et al., 2019b). Several methods proposed based on mechanics, structure, and material science have been used for modulating the adhesion strength of the target interface on demand. Among the various techniques, the strategies based on dynamic adhesion control (Feng et al., 2007, 2013; Kim, Carlson et al., 2009; Meitl et al., 2006), dynamics of change in the contact area between device and stamp regulating interface adhesion strength, and other active methods are essential to be analyzed and optimized following the theory of mechanics. The surface/interface

properties can also be modulated using novel structures [e.g., bulging structures (Carlson et al., 2012b; Guo et al., 2022; Li, Luo et al., 2021; Linghu, Wang, et al., 2019; Luo et al., 2020)] and new functional materials [e.g., shape memory polymer, SMP (Eisenhaure, Rhee et al., 2014; Kim, Lakshmanan, et al., 2022; Kim, Liu, et al., 2022; Luo, Li, et al., 2021)] to optimize the stamp's unique surface/interface properties. In most cases, the interface fracture often depends on the synergetic effect of mechanics, structures, and materials. In this chapter, the mechanics, structure, and materials science involved in transfer printing are comprehensively analyzed, and transfer printing methods with high efficiency developed from these principles are systematically introduced.

1.2 Mechanics of transfer printing

Understanding the underlying mechanical principles of modulating interface adhesion strength of different types of transfer printing technology is imperative. Therefore, several typical transfer printing methods and their implied mechanical mechanism are introduced in this section.

1.2.1 Kinetically controlled transfer printing

For this kinetically controlled transfer printing method, modulating the stamp/device interface adhesion strength based on the characteristics of kinetic dependence of the viscoelastic stamp is essential (Feng et al. 2007, 2013; Meitl et al., 2006), which can be controlled by leveraging the stamp retraction speed. In this mode, van der Waals forces have sufficient strength in the absence of the adhesive layer. The critical energy release rate ($G_{crit}^{film/substrate}$) remains unchanged at the thin-film device/substrate interface during the process of transfer printing when the substrate and thin-film devices are assumed to be elastic. However, the critical energy release rate ($G_{crit}^{stamp/substrate}$) at the interface between the thin-film device and stamp is rate-sensitive and closely related to the peeling velocity because of the viscoelastic nature of the stamp. Using a viscoelastic model, the pull-off force is found to increase monotonically with the increasing peeling velocity, which is supported by finite element simulations and experimental results (Cheng, Li et al., 2013). The critical energy release rate ($G_{crit}^{stamp/substrate}$) related to the peeling velocity ν (Fig. 1.2) can be written as

$$G_{crit}^{stamp/film}(\nu) = G_0 \left[1 + \left(\frac{\nu}{\nu_0} \right)^n \right] \quad (1.1)$$

where G_0 is the critical energy release rate for zero peeling velocity, ν_0 is the reference peeling velocity corresponding to $2G_0$, and n as a scaling exponent can be obtained from experiments.

The interface adhesion strength between the device and stamp can be easily regulated by changing the peeling velocity to realize controlled delamination: the thin-film

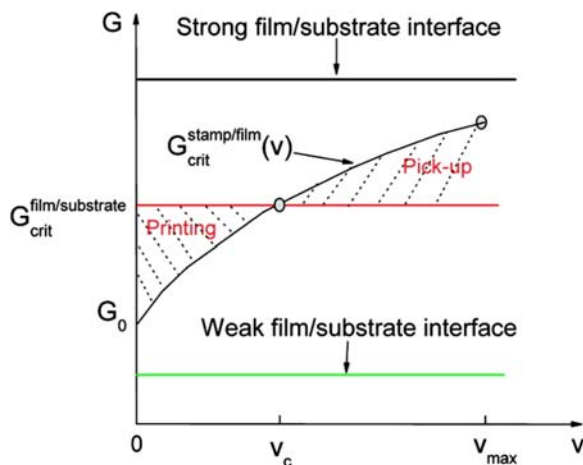


Figure 1.2 Schematic illustration of critical energy release rates related to peeling velocity at the thin-film device/stamp and thin-film device/substrate interfaces during picking-up and printing steps. In the picking-up step, the more significant critical energy release rate at the device/stamp interface leads to the propagation of crack at the interface of thin-film/substrate by peeling the stamp to pick up the device. During the printing stage, the lower critical energy release rate at the thin-film device/stamp interface allows interface cracking between the device and stamp to peel off the thin-film device onto the receiver. Reprinted with permission from Feng, X., Meitl, M.A., Bowen, A.M., Huang, Y., Nuzzo, R.G., & Rogers, J.A. (2007). *Competing fracture in kinetically controlled transfer printing*. *Langmuir: the ACS Journal of Surfaces and Colloids*, 23(25), 12555–12560. <https://doi.org/10.1021/la701555n>; Copyright 2007, American Chemical Society. With permission from American Chemical Society.

devices can be picked up at a sufficiently high velocity [Figs. 1.1B(1)] and then printed onto the receiver at a suitable low velocity [Fig. 1.1B(2)]. Through this practical and easy-to-operate kinetically controlled transfer printing method, different functional thin-film devices can be successfully assembled onto several flexible substrates, but the peeling speed limits the range of modulation. Moreover, this transfer printing method is not applicable to a viscoelastic receiver, which restricts its application to receiving substrate prepared from certain viscoelastic materials.

1.2.2 Shear-enhanced transfer printing

The shear-enhanced transfer printing uses a rectangular stamp of the exact lateral dimensions of the device and mounts to a thick backing layer. In the picking-up step, the viscoelastic stamp is retracted with a high peeling velocity, maximizing adhesion strength at the device/stamp interface to pick up the microdevice. During printing, a shear load is applied to the viscoelastic inked stamp in contact with the receiving substrate to reduce the interface adhesive force between the stamp and device, facilitating printing the device on the receiving substrate (Fig. 1.3) (Carlson et al., 2011; Cheng, Wu et al., 2012; Yang et al., 2012). The applied shear load adding the normal adhesion force produces a mixed loading mode at the

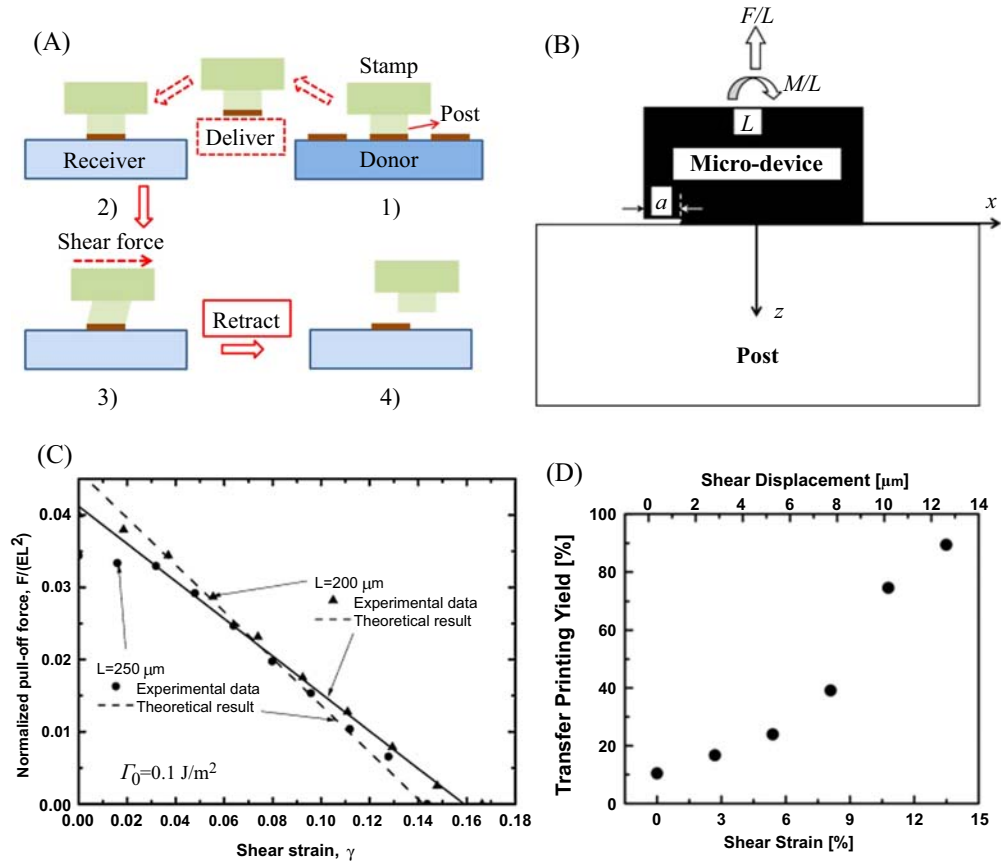


Figure 1.3 (A) Schematic diagram of the shear-enhanced transfer printing: (1) the device is picked up successfully through the rapid retraction of the stamp; (2) the inked stamp is kept in contact with the receiver, and (3) the interface pull-off force between the device and stamp is reduced by applying a shear force; (4) the device is printed onto the receiver after a slow retraction of the stamp. (B) Schematic diagram of the fracture mechanics model loaded by vertical pull-off force and applied shear load for illustrating the mechanism of shear-enhanced transfer printing. (C) The relation curves between normalized pull-off force and shear strain with a good agreement between experimental results (symbols) and theoretical results (lines). (D) The relation curve between transfer printing yield and shear strain and displacement. (A)–(C) Reprinted with permission from Cheng, H., Wu, J., Yu, Q., Kim-Lee, H.J., Carlson, A., Turner, K.T., Hwang, K.C., Huang, Y., & Rogers, J.A. (2012). *An analytical model for shear-enhanced adhesiveless transfer printing*. *Mechanics Research Communications*, 43, 46–49. <https://www.sciencedirect.com/science/article/pii/S0093641312000407>, <https://doi.org/10.1016/j.mechrescom.2012.02.011>; Copyright 2012, Elsevier. (D) Reprinted with permission from Carlson, A., Kim-Lee, H.J., Wu, J., Elvikis, P., Cheng, H., Kovalsky, A., Elgan, S., Yu, Q., Ferreira, P.M., Huang, Y., Turner, K.T., & Rogers, J.A. (2011). *Shear-enhanced adhesiveless transfer printing for use in deterministic materials assembly*. *Applied Physics Letters*, 98(26), 264104. <https://doi.org/10.1063/1.3605558>; Copyright 2011, American Institute of Physics. With permission from Elsevier and American Institute of Physics.

stamp/device interface, thus changing its fracture behaviors. Therefore, the applied shear load can reduce the interface adhesion and improve the printing efficiency. An analytical model was established to explain the mechanism of this shear-enhanced transfer printing and critical parameters for the shear-enhanced interface fracture mode were identified. Assuming an edge crack with the length of a at the microdevice/postinterface, the post is subjected to a shear strain γ and pull-off force F and can be approximately affected by the combined effect of uniform tension F/L and uniform moment M/L (Fig. 1.3B). The interface fracture mode is considered a mixture of mode I and mode II cracks, from which the interface energy release rate G can be expressed as:

$$G = \pi EL \left[0.0417 \left(\frac{F}{EL^2} \right)^2 + 0.0701 \left(\frac{\gamma h}{L} \right)^2 + 0.108 \frac{F}{EL^2} \frac{\gamma h}{L} \right] \quad (1.2)$$

where E is Young's modulus and L and h are the width and height of the rectangular post.

When the interface fracture toughness (Γ_0) reaches the interface energy release rate (G), the relational expression between dimensionless peeling force and shear strain is written as

$$\frac{F}{EL^2} = \sqrt{24.0 \frac{\Gamma_0}{\pi EL} - 1.72 \times 10^{-3} \left(\frac{\gamma h}{L} \right)^2} - 1.30 \frac{\gamma h}{L} \quad (1.3)$$

As the second term can be ignored compared to the first term, Eq. (1.3) can be simplified as

$$\frac{F}{EL^2} + \frac{13\gamma h}{10L} \approx 2\sqrt{\frac{6\Gamma_0}{\pi EL}} \quad (1.4)$$

The linear relationship between dimensionless peel force and shear stress Eq. (1.4) agrees reasonably well with the experimental data (Fig. 1.3C). The results show that the shear strain can efficiently regulate the adhesion strength of the stamp/device interface by decreasing the peeling force, and thereby realizing efficient printing (Fig. 1.3D). The shear-enhanced transfer printing technology is an effective transfer method, but the precise regulation for the applied shear strain increases the complexity of the printing process. To achieve ideal results, a larger shear strain must be applied to the stamp, causing damage to the stamp or affecting the accurate alignment of the location for the microdevice to be printed.

1.2.3 Laser-driven noncontact transfer printing

Laser-driven noncontact transfer printing was developed based on the large thermal mismatch between soft stamps (e.g., PDMS) and stiff devices (e.g., silicon). The laser-induced heat induces different deformations of the stamp and device and initiates

separation at the adhesive surface, as shown in Fig. 1.4A (Li, Li, Lü, Song, Saeidpourazar, et al., 2012b; Saeidpourazar, Li, et al., 2012; Saeidpourazar, Sangid, et al., 2012). The modulation of the laser pulse in the printing step determines the efficiency of this transfer printing method. To start, the inks are picked up from a donor substrate by the retraction of the PDMS stamp [Fig. 1.4A(1 and 2)], and the “inked” stamp is then pulled to the position above the receiving substrate and close to its upper surface [Fig. 1.4A(3)]. After applying a pulsed laser beam, the significant thermal mismatch causes the interface delamination between the device and stamp,

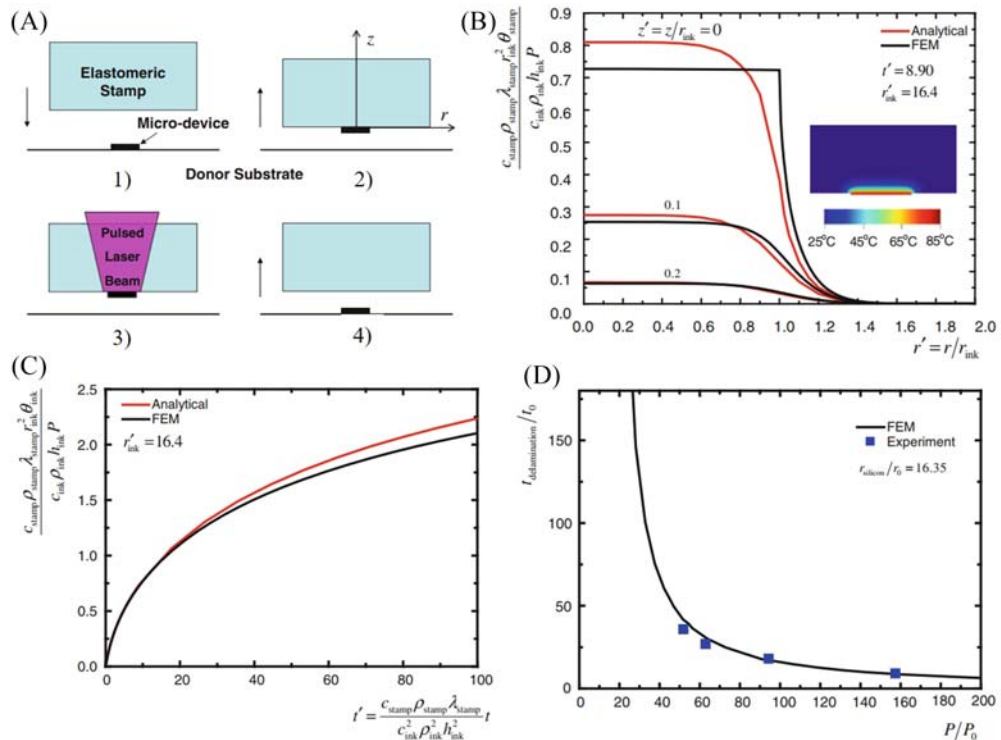


Figure 1.4 (A) Schematic diagram of the whole transfer printing process using laser-driven non-contact transfer printing technology: (1) the stamp is arranged above the donor substrate and (2) the microdevice is picked up from the donor substrate; (3) a laser pulse is applied to heat microdevice/stamp interface after the stamp is positioned above the stamp; and (4) the microdevice is released onto the surface of receiving substrate. Distribution of normalized temperature increase inside the (B) stamp and (C) microdevice. (D) Scaling law for interface delamination between stamp and microdevice and the interfacial energy release rate at the crack tip for different absorbed laser powers. Reprinted with permission from Li, R., Li, Y., Lü, C., Song, J., Saeidpouraza, R., Fang, B., Zhong, Y., Ferreira, P.M., Rogers, J.A., & Huang, Y. (2012a). Thermo-mechanical modeling of laser-driven non-contact transfer printing: Two-dimensional analysis. *Soft Matter*, 8(27), 7122–7127. <http://doi.org/10.1039/C2SM25339A>; Copyright 2012, Springer. With permission from Springer.

thereby actively releasing the devices from the stamp to land on the receiver [Fig. 1.4A(4)]. The noncontact laser-assisted transfer printing eliminates the restriction on the receiving substrate because there is no direct contact between the devices loaded on the stamp and the target receiver. The mechanism of the laser-induced interface delamination with the energy release rate related to temperature distribution was revealed by experiments and finite element analysis (Al-okaily & Ferreira, 2015; Al-okaily, Rogers et al., 2014; Gao et al., 2017; Li, Li, Lü, Song, Saeidpouraza, et al., 2012a; Li, Li, Lü, Song, Saeidpourazar, et al., 2012b), and the device-dependent temperature distribution from the laser pulse was analyzed.

A thermo-mechanical axisymmetric model was deduced to identify the interface delamination due to material thermal mismatch between the stamp and device. In addition, a scaling law was proposed to illustrate a single nondimensional combined parameter composed of material parameters and geometric parameters that dominates laser-driven noncontact transfer printing. The transient heat conduction equation inside the stamp is written as

$$\frac{\partial^2 \theta_{stamp}}{\partial r^2} + \frac{1}{r} \frac{\partial \theta_{stamp}}{\partial r} + \frac{\partial^2 \theta_{stamp}}{\partial z^2} - \frac{c_{stamp} \rho_{stamp}}{\lambda_{stamp}} \frac{\partial \theta_{stamp}}{\partial t} = 0 \quad (1.5)$$

where (r, z) represents the cylindrical coordinates, t is time, θ_{stamp} is the temperature increase relative to room temperature and its value is zero for initial condition ($t = 0$), and ρ_{stamp} , c_{stamp} , and λ_{stamp} are the specific mass density, heat density, and thermal conductivity, respectively.

The obtained expression of the temperature increase inside the stamp is given as

$$\theta_{stamp}(r, z, t) = \frac{c_{ink} \rho_{ink} h_{ink}}{c_{stamp} \rho_{stamp} \lambda_{stamp} \sqrt{\pi^3} r_{ink}^2} \times \left\{ \int_0^{t'} \frac{1 - \exp(t' - \tau) \operatorname{erfc} \sqrt{t' - \tau}}{\sqrt{\tau}} \exp \left[\frac{-z'^2 (r'_{ink})^2}{4\tau} \right] d\tau \right. \\ \left. \times \int_0^\infty J_0(r' \eta) J_1(\eta) \exp \left[\frac{-\tau \eta^2}{(r'_{ink})^2} \right] d\eta \right\} \quad (1.6)$$

where $r' = r/r_{ink}$ and $z' = z/z_{ink}$ represent normalized cylindrical coordinates, $t' = t/t_0$ and $r'_{ink} = (c_{stamp} \rho_{stamp} r_{ink}) / (c_{ink} \rho_{ink} h_{ink})$ are normalized time and normalized ink radius.

There has a nearly uniform distribution of temperature increase inside the device because of its good thermal conductivity, and the expression was obtained analytically as follows:

$$\theta_{ink}(t) = \frac{c_{ink} \rho_{ink} h_{ink}}{c_{stamp} \rho_{stamp} \lambda_{stamp} \sqrt{\pi^3} r_{ink}^2} \times \int_0^{t'} \frac{1 - \exp(t' - \tau) \operatorname{erfc} \sqrt{t' - \tau}}{\sqrt{\tau}} dt \times \int_0^\infty \frac{J_1^2(\eta)}{\eta} \exp \left[\frac{-\tau \eta^2}{(r'_{ink})^2} \right] d\eta \quad (1.7)$$

As shown in Fig. 1.4B and C, the normalized temperature increase inside the stamp and device from theoretical predictions can agree well with numerical results obtained by finite element analysis.

The interfacial energy release rate at the crack tip (G) is obtained as follows:

$$G = \frac{c_{stamp}\rho_{stamp}\mu_{stamp}\alpha_{stamp}^2 P^2}{8c_{ink}\rho_{ink}h_{ink}\lambda_{stamp}^2} \cdot \left| \bar{K}\left(\frac{t}{t_0}, r'_{ink}\right) \right|^2$$

$$K = \mu_{stamp}\alpha_{stamp}\sqrt{\pi^3 r_{ink}^{-5}/2} \int_0^\infty \int_{r=0}^\infty \theta_{stamp}(r, z, t) f\left(\frac{r}{r_{ink}}, \frac{z}{r_{ink}}\right) r dr dz$$

$$= \sqrt{\frac{c_{stamp}\rho_{stamp}}{c_{ink}\rho_{ink}h_{ink}}} \frac{\mu_{stamp}\alpha_{stamp}P}{\lambda_{stamp}} \cdot \bar{K}\left(\frac{t}{t_0}, r'_{ink}\right) \quad (1.8)$$

where K is the stress intensity factor, \bar{K} is a nondimensional function related to normalized time and ink radius.

When the interfacial energy release rate at the crack tip shown in Eq. (1.8) reaches the work of interface adhesion force (λ), the interface between the device and stamp will delaminate and release the device on the receiving substrate. From the expression $G = \lambda$, the critical time of interfacial delamination can be obtained as follows:

$$\frac{t_{delamination}}{t_0} = \bar{t}\left(\frac{P}{P_0}, \frac{r_{ink}}{r_0}\right) P_0 = \frac{\lambda_{PDMS}}{\alpha_{PDMS}} \sqrt{\frac{\gamma c_{silicon}\rho_{silicon}h_{silicon}}{c_{PDMS}\rho_{PDMS}\mu_{PDMS}}} r_0 = \frac{c_{silicon}\rho_{silicon}h_{silicon}}{c_{PDMS}\rho_{PDMS}} \quad (1.9)$$

Eq. (1.9) shows that the normalized critical time of delamination is only related to the two parameters of normalized absorbed laser power and device radius. The comparison between experimental and simulation results of the interfacial energy release rate at the crack tip for different absorbed laser powers is shown in Fig. 1.4D with a good agreement.

Thermal and mechanical properties of the stamp and device are two leading factors determining the transfer efficiency of laser-driven noncontact transfer printing. This method eliminates the restrictions of the receiving substrate on transfer printing, transferring devices to three-dimensional surfaces, liquid surfaces, and many others. However, the significantly high temperature increase of the stamp/ink interface caused by laser heating may damage the stamp surface or devices. Furthermore, the laser pulse intensity and irradiation time are needed to be controlled precisely for laser-assisted transfer printing, which requires relatively expensive equipment to successfully complete the transfer printing process.

1.2.4 Magnetic-assisted transfer printing

The transfer printing can also be triggered by the external magnetic field. Magnetic-assisted transfer printing method was developed based on an elastic magnetic-responsive thin film

(Yu, Chen et al., 2018, Yu, Yu et al., 2019; Yu, Li et al., 2021) with embedded magnetic particles (Linghu, Wang, et al., 2019), with deformation driven by an external magnetic field. A structurally designed stamp was exploited, in which a chamber filled with incompressible liquid is stacked on top of a gas chamber formed by contact between stamp and device to be transfer printed. The top and bottom of the liquid cavity are magnetic-response thin film and PDMS thin film, respectively (Fig. 1.5A). In the picking-up step, the external magnetic field actuates the top magnetic-responsive thin film to deform upward, transferring the motion to the bottom PDMS thin film and then reducing the pressure inside the bottom gas chamber. The reduced pressure creates an adsorption force to adsorb the device to the stamp (Fig. 1.5B). On the other hand, the magnetic-responsive thin film is driven to deform downward through the reverse external magnetic field in the printing step. As a result, the bottom PDMS thin film moves downward to narrow the volume of the bottom gas chamber, which produces an increased pressure in the gas chamber to push the device downward and prints it on the receiving substrate (Fig. 1.5C). As the pressure change inside the gas chamber is the dominant factor for modulating the interfacial adhesion, an analytical model illustrating the magnitude of pressure change inside the gas chamber related to the displacement profile of the top thin film of the gas chamber upon magnetic actuation was established. The relational expression between volume-induced pressure change (ΔP_c) inside the bottom gas chamber and the displacement profile of the bottom PDMS thin film is obtained as

$$\Delta P_c = \frac{\Delta V_c P_c^0}{V_c^0 + \alpha \Delta V_c} = \frac{w_{bot}^{max}}{3h_c + \alpha w_{bot}^{max}} P_c^0 \quad (1.10)$$

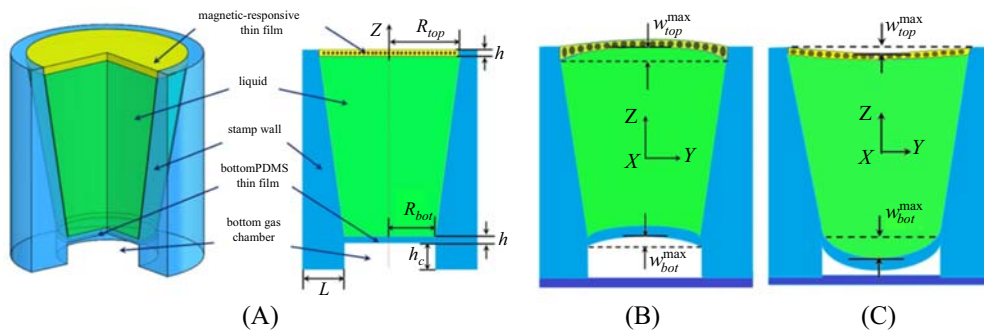


Figure 1.5 Schematic diagram of the magnetic-assisted stamp consisting of a chamber filled with an incompressible liquid, thin magnetic-response elastic film, and thin PDMS film on either side of the liquid chamber for magnetic-assisted transfer printing. (A) Three-dimensional representation and cross-sectional views of the stamp structure with the stamp deformations driven by an external magnetic field in the (B) picking-up and (C) printing steps. *Reprinted with permission from Yu, Q., Chen, F., Zhou, H., Yu, X., Cheng, H., & Wu, H. (2018). Design and analysis of magnetic-assisted transfer printing. Journal of Applied Mechanics, 85(10). <https://doi.org/10.1115/1.4040599>; Copyright 2018, ASME. With permission from ASME.*

where ΔV_c , V_c^0 and P_c^0 are the volume change, initial volume and pressure of the bottom gas chamber, respectively, h_c is the gas chamber height, and α is a constant.

The established analytical model provides theoretical guidance for the design and optimization of magnetic-assisted transfer printing.

1.2.5 Thermal release transfer printing

Thin and flexible thermal release tape (TRT) is easy to control and is extensively utilized in transfer printing. Based on TRT, thermal release transfer printing was proposed and a fracture mechanics model was established for theoretical analysis (Yan et al., 2017). This method depends on the large irreversible adhesion strength changes of TRT upon heating above the transition temperature (i.e., 100°C) (Fig. 1.6). The energy release rate at the functional membrane/TRT interface ($G_{TRT/membrane}$) depends on the temperature and peeling velocity, which is expressed as:

$$G_{TRT/membrane}(v, T) = \begin{cases} [-e^{\lambda(T-T_r)+\ln(G_0-G_r)} + G_0] \left[1 + \left(\frac{v}{v_0}\right)^n\right], & T \leq T_r \\ G_0 \left[1 + \left(\frac{v}{v_0}\right)^n\right], & T > T_r \end{cases} \quad (1.11)$$

where T is the temperature, G_0 and G_r are the critical energy release rates under the near zero peeling velocity condition and with deactivated adhesive on TRT, e is the Euler's constant, v_0 is the reference peeling velocity corresponding to $2G_0$, v is peeling velocity, γ is a material parameter, the exponent (n) is a scaling parameter obtained from experiments, and T_r is the transition temperature. Compared with only kinetic controlled transfer printing, the strong-to-weak adhesion ratio becomes larger for thermal release transfer printing with the additional control by changing temperature.

The nearly unchanged critical energy release rate ($G_{TRT/membrane}$) at the temperature below 70°C (Fig. 1.6B) is much larger than that for the interface between the membrane and donor substrate ($G_{membrane/donorsubstrate}$). Therefore, the membrane devices could be effortlessly picked up because the interface delamination occurs at the donor substrate/device interface. Upon heating above 80°C, the critical energy release rate ($G_{TRT/membrane}$) of the TRT/membrane interface significantly decreases to be much smaller than that at the interface between the membrane device and receiver ($G_{receiver/donorsubstrate}$). The crack will propagate at the TRT/membrane interface after peeling off the TRT, and the membrane devices can be printed onto the receiving substrate. Since the critical energy release rate at the interface between TRT and membrane devices ($G_{TRT/membrane}$) can be modulated over a large range by changing the peeling velocity and temperature (Fig. 1.6D and E), thermal release transfer printing shows its unique advantages for device integration.

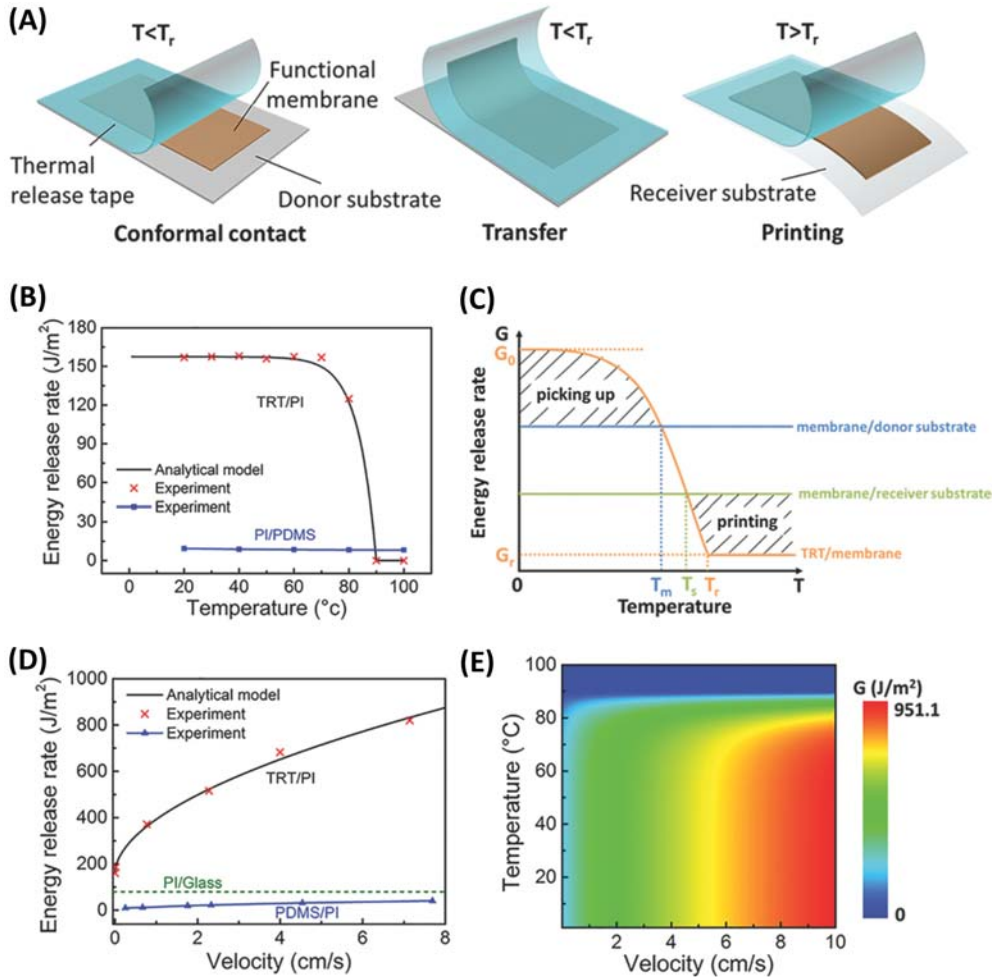


Figure 1.6 (A) Schematic diagram of thermal release transfer printing using thermal release tape. The interface energy release rate as a function of (B) temperature and (D) peeling velocity. (C) The variation of energy release rate with temperature during the picking-up and printing processes. (E) A contour profile illustrates the relationship of energy release rate at the TRT/PI interface between peeling velocity and temperature. Reprinted with permission from Yan, Z., Pan, T., Xue, M., Chen, C., Cui, Y., Yao, G., Huang, L., Liao, F., Jing, W., Zhang, H., Gao, M., Guo, D., Xia, Y., & Lin, Y. (2017). Thermal release transfer printing for stretchable conformal bioelectronics. *Advanced Science*, 4(11), 1700251. <https://doi.org/10.1002/adv.201700251>; Copyright 2016, John Wiley and Sons. With permission from John Wiley and Sons.

1.2.6 Magnet-controlled transfer printing

The magnet-controlled transfer printing leverages the fast response of the magnetic particles under a magnetic field and changes the interfacial adhesion induced through the interface contact area between the stamp and device (Linghu, Wang, et al., 2019;

Linghu, Zhu, et al., 2019). As shown in Fig. 1.7A, the elastomer stamp is a cylindrical cavity structure filled with magnetic particles, enclosed by an upper glass backing plate, elastomer, and bottom soft thin film. In the picking-up step, the bottom soft thin film

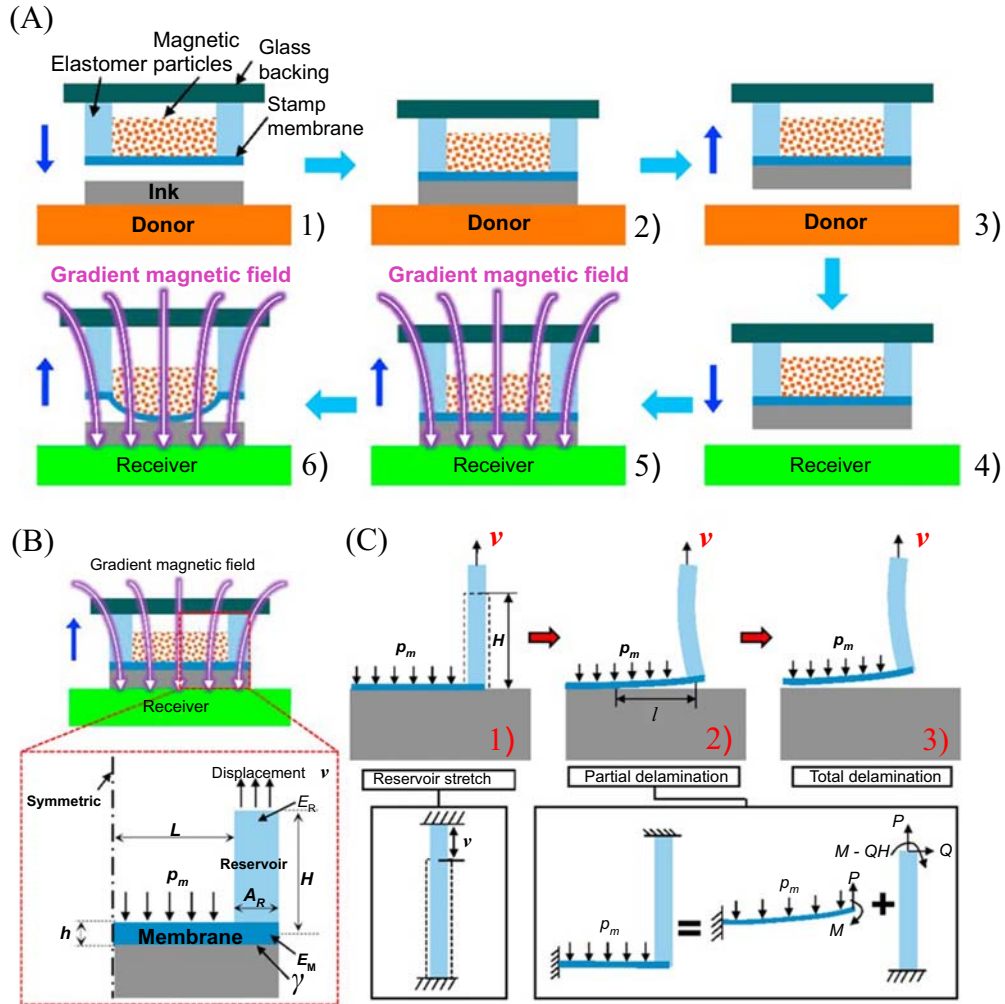


Figure 1.7 Schematic illustration of the magnet-controlled transfer printing process. (A) The device is first picked up through rapid retraction with conformal contact at the stamp/device interface (1–3). Next, the magnetic force pushes the bottom thin film to bulge around the interface, releasing the device on the receiving substrate (4–6). (B) Cross-section diagram of the magnet-controlled stamp. (C) Simplified force diagram for illustrating stretch configuration, partial and total delamination between stamp and receiver during the printing process. Reprinted with permission from Linghu, C., Zhu, H., Zhu, J., Li, C., & Song, J. (2019). *Mechanics of magnet-controlled transfer printing*. *Extreme Mechanics Letters*, 27, 76–82. <https://www.sciencedirect.com/science/article/pii/S2352431618302578>, <https://doi.org/10.1016/j.eml.2019.01.006>; Copyright 2019, Elsevier. With permission from Elsevier.

remains a flat state with a conformal contact between the stamp and the device to be transferred [Fig. 1.7A(2)]. Rapid retraction of the stamp can produce enough interface adhesion between the stamp and the device for picking up the device from the donor substrate [Fig. 1.7A(3)]. A gradient magnetic field covering the entire stamp is applied after the inked stamp is moved to a position above the receiver [Fig. 1.7A(5)]. As a result, the magnetic particles inside the cavity are driven to push the bottom thin film bulge downward around the interface for releasing the elastomer from the substrate. The thin film starts to peel at the outer perimeter and gradually propagates to the center as the release continues, which decreases the contact area between the stamp and device, thereby reducing the interfacial adhesion and facilitating the interfacial delamination. Therefore, the device is released from the stamp and printed on the receiving substrate. The reduced interfacial adhesion induced by deformations of the bottom thin film driven by the magnetic field is critical for the printing step. Therefore, an analytical model is essential to reveal the underlying mechanism, predicting the interfacial delamination between the device and stamp for magnet-controlled transfer printing.

The symmetric cross-sectional illustration with the magnet-controlled stamp's stress state during the magnetic field's retraction process is shown in Fig. 1.7B. The corresponding simplified mechanics model for different delamination conditions is shown in Fig. 1.7C, where L and H are the radius and height of the cylindrical cavity, A_R is the elastomer thickness, h is the bottom thin-film thickness, P_m is the uniform magnetic pressure, v represents the displacement of stamp deformation, E_R and E_M are Young's modulus of elastic stamp and the bottom membrane, and γ represents interfacial adhesion. The interfacial adhesion between the device and stamp can prevent interfacial delamination under a small displacement (v). The elastic stamp is only in the uniaxial tension state [Fig. 1.7B(1)]. The total potential energy equals the strain energy of the stretched stamp at this condition, which is expressed as

$$\Pi_1 = \frac{E_R A_R H}{2} \left(\frac{v}{H} \right)^2 \quad (1.12)$$

With the increase of applied displacement, the delamination begins at the interface between the bottom thin film of the stamp and device, and the delamination length (l) gradually becomes larger [Fig. 1.7C(2)] until the occurrence of total delamination [Fig. 1.7C(3)]. In this partial delamination case, the stamp can be considered a double-clamped beam loaded by magnetic pressure (P_m) and displacement (v). This is a statically indeterminate system, which can be analyzed by the superposition of the solutions of the following two simple problems: (1) a horizontal cantilever beam loaded by a uniformly distributed pressure (P_m) at the top surface, a moment (M) and a concentrated force (P) at the right end; (2) a vertical cantilever beam clamped at one end and loaded by a concentrated force (P), a moment ($M - Q \times H$) and a lateral

load (Q) at the other end [Fig. 1.7C(2)]. The expression of the potential energy for the whole system is written as

$$\begin{aligned} \Pi_2 = & \frac{Pw|_{x=l}}{2} + \frac{P^2H}{2E_RA_R} + \frac{1}{2} \int_0^l P_m w dx + \gamma l = \frac{P}{2E_M I_M} \left(\frac{Pl^3}{3} - \frac{Ml^2}{2} - \frac{P_m l^4}{8} \right) \\ & + \frac{P^2H}{2E_RA_R} - \frac{P_m^2}{48E_M I_M} \left(\frac{6l^5}{5} - \frac{3Pl^4}{P_m} + \frac{4Ml^3}{P_m} \right) + \gamma l \end{aligned} \quad (1.13)$$

where w and I_M are the deflection and moment of inertia for the bottom membrane.

The difference between the two energies ($\Pi_R = \Pi_2 - \Pi_1$) is an essential criterion to determine the interface state. The condition $\Pi_R > 0$ indicates an energetically favorable state and smaller potential energy under the stretched configuration. The situation $\Pi_R < 0$ implies energetically favorable partial delamination and that the potential energy under partial delamination is smaller. Furthermore, the delamination length (l) can be deduced from the energy minimization ($\partial\Pi_R/\partial l = 0$).

The pull force under the condition of stretch configuration increases with the increasing applied displacement in the printing step and can be analytically predicted [Fig. 1.7C(1)]. The stamp begins to delaminate from the device after the applied displacement reaches the critical value (v_{crit}), and the value of pull force will reach a peak (pull-off force), which can be obtained from the equilibrium of the stamp as

$$F_{pull-off} = 4E_R \frac{v_{crit}}{H} A_R (L + A_R) - \pi P_m L^2 \quad (1.14)$$

The interface adhesion strength can be calculated by dividing the pull-off force by the adhesion area as

$$P_a = \frac{v_{crit}}{H} \frac{E_R A_R}{(L + A_R)} - \frac{\pi P_m L^2}{4(L + A_R)^2} \quad (1.15)$$

The established analytical model reveals the configuration evolution of stamps during printing. The delamination between the stamp and device and its adhesion strength can be predicted. The proposed mechanics model explains the effects of geometric and material parameters on the adhesion strength, and determines the critical magnetic pressure for printing, providing design guidelines for optimizing the magnet-controlled transfer printing technology.

1.3 Structure for transfer printing

The van der Waals interaction dominated interfacial adhesion strength depends on the interface contact area. Based on the structural changes for changing the contact area,

various novel structural designs of the stamp were developed to regulate the interfacial adhesion strength according to the change of interface contact area. Several typical stamp structures that endow transfer printing with the advantages of simplicity and high efficiency are introduced in this section.

1.3.1 Surface relief structures

Using a flat, soft stamp designed with surface relief structures [e.g., pyramidal microtips (Kim, Wu et al., 2010), patterned pillars (Chen, Feng, & Huang, Huang, et al., 2013), grating-like reliefs (Chen, Feng, & Chen, 2013; Jeong et al., 2014), and angled microflaps (et al., 2014)] can change the interface contact area through structural collapses, thus regulating the interface adhesion strength. For the stamp designed with microstructures of pyramidal microtips on its bottom surface (Fig. 1.8A) (Kim, Wu et al., 2010), a compressive pressure needs to be applied to collapse the pyramidal microtips in the picking-up step [Fig. 1.8A(2)]. The contact area increases when the pyramidal microtips collapse under compression, thus enhancing the interface adhesion between the device and stamp. Therefore, the rapid stamp retraction can pick up the device successfully [Fig. 1.8A(3)]. During the printing stage, removal of the applied pressure will make the collapsed pyramidal microtips recover to their original shape [Fig. 1.8A(4 and 5)], which significantly reduces the interface contact area and minimizes the adhesion strength between stamp and device to release the device on the receiver [Fig. 1.8A(6)]. It should be noted that there will have a better result of transfer printing when this method is combined with kinetically controlled transfer printing through rapid peeling and slow retraction in the picking-up and printing step, respectively. The important parameters are the height and width of the microtips and the stamp width in the structural design of the stamp with pyramidal surface microtips. The stamp with tall microtips will cause a large elastic restoring force and may result in a failure for picking up the device from the donor substrate. However, the stamp with short microtips makes its elastic restoring force too small to recover to its original shape with a large adhesion strength between the stamp and device such that the device cannot be peeled from the stamp and printed onto the receiving substrate. For this reason, two-dimensional and three-dimensional mechanics models used to determine the optimal range of the height and width of microtips are established (Wu et al., 2011), and the analytical models provide useful guidelines for the design and optimization of the stamp with pyramidal surface microtips.

Another stamp with the angled microflaps on its surface can realize the simultaneous transfer printing of multiple devices with reversible adhesion. Based on the combination of viscoelastic material properties and structural shapes, this stamp can produce higher and lower adhesion strength for picking up and printing, respectively, as shown in Fig. 1.8B (Yoo et al., 2014). Firstly, the angled microflap stamp is

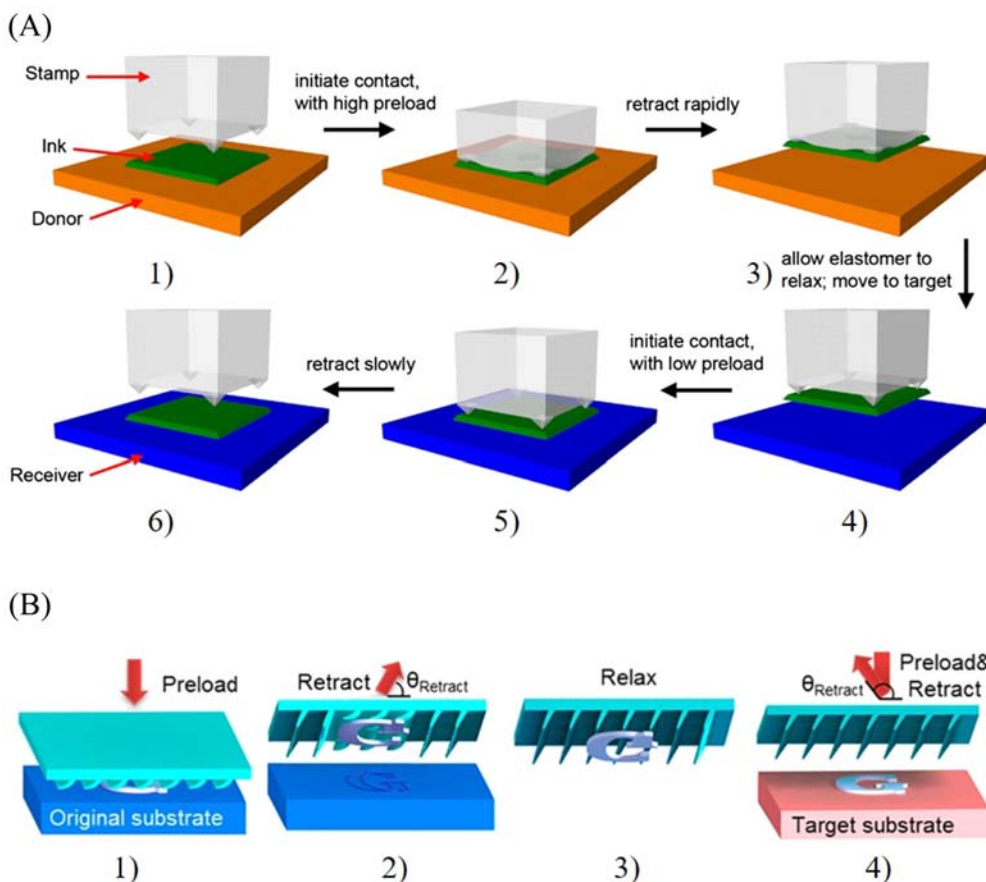


Figure 1.8 (A) Schematic diagram of surface relief structure-assisted transfer printing. (1) Using four pyramidal microtips, the stamp is first placed above the donor substrate and (2) an external pressure is applied to collapse the microtips for conformal contact between the stamp and device; (3) the device is picked up successfully onto the stamp through a rapid retraction of the stamp; (4) the stamp is quickly moved to the receiving substrate to (5) release the device onto the receiver after the microtips recover to their original shape; (6) the device is printed onto the receiver after a slow retraction of the stamp. (B) Schematic diagrams of the whole transfer printing process using the angled microflap stamp. (1) the stamp is preloaded to make the large area contact between the angled microflap array and the device on the original substrate; (2) the collapsed microflaps enhance the interface adhesion to pick up the device with a rapid retraction; (3) the resulting minimal interface adhesion due to small area contact between the stamp and device after the angled microflap array recovers to its original shape promotes; (4) the release of the device onto the target substrate after retracting the angled microflap stamp slowly. (A) Reprinted with permission from Kim, S., Wu, J., Carlson, A., Jin, S.H., Kovalsky, A., Glass, P., Liu, Z., Ahmed, N., Elgan, S.L., Chen, W., Ferreira, P.M., Sitti, M., Huang, Y., Rogers, J.A. (2010). Microstructured elastomeric surfaces with reversible adhesion and examples of their use in deterministic assembly by transfer printing. *Proceedings of the National Academy of Sciences*, 107(40), 17095–17100 <https://doi.org/10.1073/pnas.1005828107>; Copyright 2010, National Academy of Sciences. (B) Reprinted with permission from Yoo, B., Cho, S., Seo, S., Lee, J. (2014). Elastomeric angled microflaps with reversible adhesion for transfer printing semiconductor membranes onto dry surfaces. *ACS Applied Material Interfaces*, 6(21), 19247–19253. <https://doi.org/10.1021/am505286b>; Copyright 2014, American Chemical Society. With permissions from National Academy of Science and American Chemical Society.

preloaded to collapse angled microflaps to contact laterally with the device to be transferred (Fig. 1.81). The larger contact area enhances the adhesion strength at the stamp/device interface, such that the device can be then easily picked up by a rapid retracting of the angled microflap stamp [Fig. 1.8B(2)]. Due to the viscoelasticity of the elastomer stamp, the deformed angled microflaps will return to their original shape within 2 seconds [Fig. 1.8B(3)], which results in only the tip contact between the device and stamp to minimize the adhesion strength. Finally, the device can be placed on the receiving substrate after a slow retraction of the inked angled microflap stamp [Fig. 1.8B(4)].

1.3.2 Bulging structures

Stamps based on the bulged thin film provide some novel and effective transfer printing methods, and the bulging behaviors of the thin films contacted with the device to be transfer printed can modulate the adhesion strength by changing the stamp/device contact area. As described in Section 1.2.5, the stamp bottom thin film will form a bulge under the downward pressure caused by magnetic particles exposed in a gradient magnetic field (Figs. 1.7A and 1.9A) (Linghu, Wang, et al., 2019). Under the action of this pressure, the thin-film device starts to peel from the outer perimeter and gradually propagates to the center until the interfacial delamination between the stamp and device happens. Based on this stamp structure, a laser-driven transfer printing method was proposed as shown in Fig. 1.9B (Luo et al., 2020). The stamp has circular cavities filled with air, and the bottom surfaces of these cavities are sealed by a thin film with micropatterned surface structures. The metal layer as the laser absorbing layer is deposited on the inner-cavity surfaces [Fig. 1.9B(1)]. For this method, the picking-up step is realized by the rapid retraction of the stamp with a conformal contact because of collapsed microtips between the stamp and the devices to maximize the interface adhesion [Fig. 1.9B(2)]. A laser beam is applied to the target cavity after moving the inked stamp to a close position above the receiver [Fig. 1.9B(3)]. The metal layer will absorb the laser energy to heat the air inside the cavity quickly to produce pressure on the stamp bottom thin film. The induced pressure pushes the thin film to bend downward and form a bulge [Fig. 1.9B(4)], which will reduce the contact area between and device, and thereby weak adhesion strength. As a result, the device can be successfully printed onto the receiver without contact with the receiver surface [Fig. 1.9B(5)]. This method can realize the programmable printing of devices onto the receiver through selective emission of the laser beam, the devices adhered to heated regions can be printed onto the target substrate while those adhered to unheated regions remain on the stamp without bending deformations of the thin film. Compared with the flat bottom thin film of the stamp, the thin film with micropatterned surface structures has a better regulation ability for interface adhesion strength with a greater change in the interface contact area.

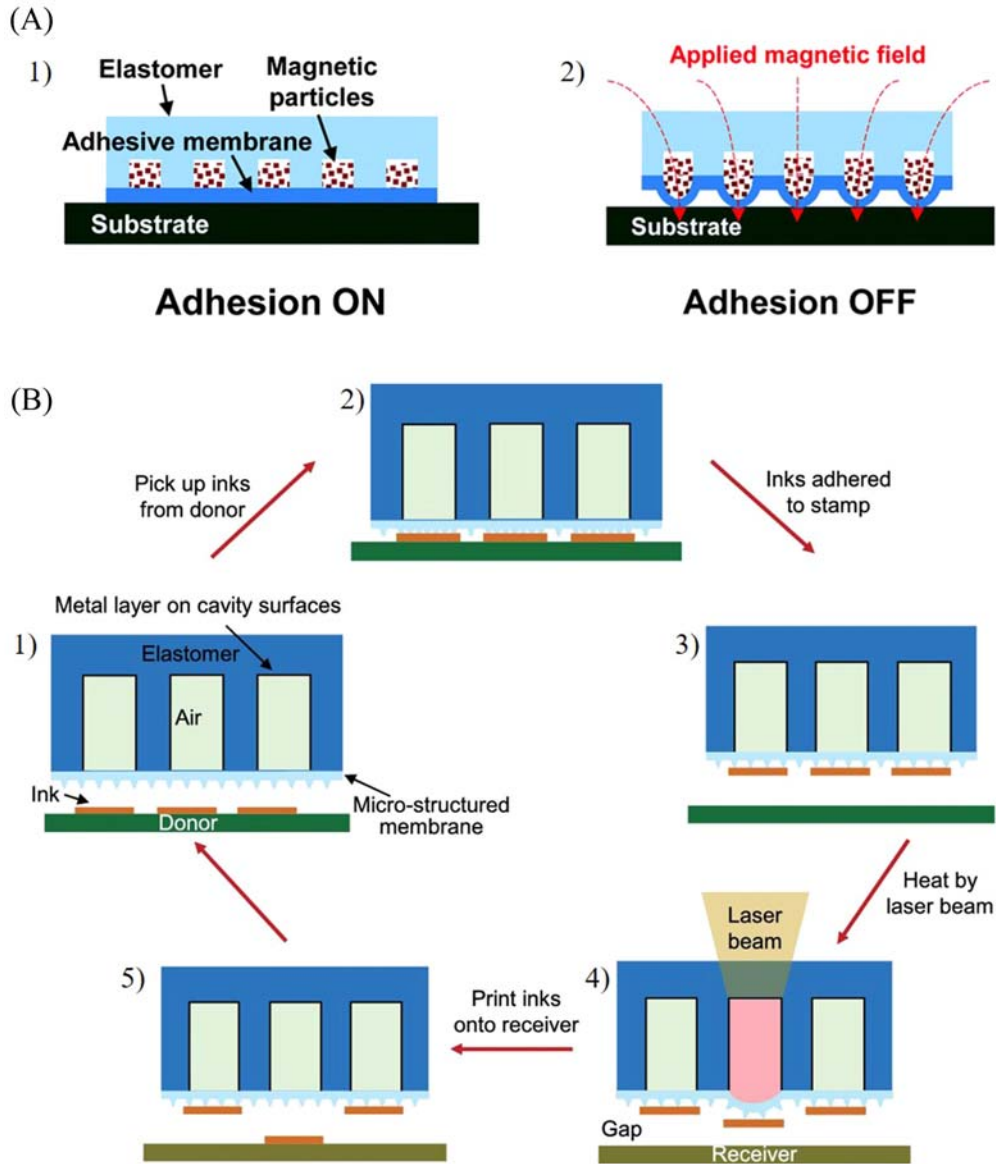


Figure 1.9 (A) Schematic illustration of the interface adhesion regulated by bulging structure: (1) strong adhesion state with conformal contact between the stamp bottom thin film and device in the picking-up step, (2) weak adhesion contact state with minimum contact area because of bulging of the thin film caused by magnetic field-induced pressure. (B) Schematic diagram of the laser-driven programmable noncontact transfer printing process based on the bulging of the thin film. (1) The stamp is placed above the donor and (2) contacted with the device with collapsed surface microtips caused by a light pressure; (3) the desired device is picked up by a rapid retraction of the

(Continued)

1.3.3 Biomimetic structures

The success in the picking-up and printing steps for a complete transfer printing process depends on the controllability of demanded delamination at various interfaces. Artificially controllable adhesives inspired by animals are a promising strategy to optimize the delamination process, improving the efficacy and robustness of the transfer printing process. Nature provides some impressive examples that possess excellent adhesion properties based on nano- and microstructured systems. As representative examples, the gecko's foot has amazing dry adhesion ability, whereas the byssal thread of mussels and feet of tree frogs and insects have the outstanding wet adhesive capability. Furthermore, these biological adhesive systems can actively control and switch their strong adhesion strength on demand for locomotion. As a bio-inspired transfer printing example, the adhesive layer on the gecko's foot has been mimicked in the design of the stamp for the transfer printing (Autumn et al., 2000) (Fig. 1.10A). The deformation of surface microstructures induced by compressive pressure can control the contact area, thus modulating the interfacial adhesion. In view of this, an array of surface microtip structures is introduced (Kim, Wu et al., 2010) for a bio-inspired stamp [Fig. 1.10A(V)]. The microtips collapse under compressive pressure and enlarge the contact area to increase the interface adhesion strength between the stamp and the device for picking up the device. The stamp/ink adhesion is then reduced drastically by the recovery of deformed viscoelastic microtips. Another gecko-inspired method was proposed to realize directional adhesion by using directional loading used in shear-assisted transfer printing and directional structure used in angled-stamp transfer printing [Fig. 1.10A(VI)] (Murphy et al., 2009). Octopus-inspired stamp as smart adhesive pads is proposed for transfer printing, in which the adhesion strength is modulated by actuating temperature-responsive hydrogel muscles to reversibly change the (Fig. 10B) internal pressure (Lee, Um et al., 2016). As the adhesion mechanism of octopus shown in Fig. 1.10B(II), the pressure inside the sucker cavity is the same as the outside at its original state. Through the contraction of the radial muscle, the wall of the sucker becomes thin, and the volume of the inside cavity increases to result in

-
- ◀ stamp; (4) the heating from the laser beam produces bulging deformation of the micropatterned bottom thin film, which releases the device from the stamp; (5) the device on the heated region is released onto the receiver while the devices on the unheated region remain on the stamp. (A) Reprinted with permission from Linghu, C., Wang, C., Cen, N., Wu, J., Lai, Z., & Song, J. (2019). Rapidly tunable and highly reversible bio-inspired dry adhesion for transfer printing in air and a vacuum. *Soft Matter*, 15(1), 30–37. <http://doi.org/10.1039/C8SM01996G>; Copyright 2019, The Royal Society of Chemistry. (B) Reprinted with permission from Luo, H., Wang, C., Linghu, C., Yu, K., Wang, C., & Song, J. (2020). Laser-driven programmable non-contact transfer printing of objects onto arbitrary receivers via an active elastomeric microstructured stamp. *National Science Review*, 7(2), 296–304. <https://doi.org/10.1093/nsr/nwz109>; Copyright 2020, Oxford University Press. With permissions from The Royal Society of Chemistry and Oxford University Press.

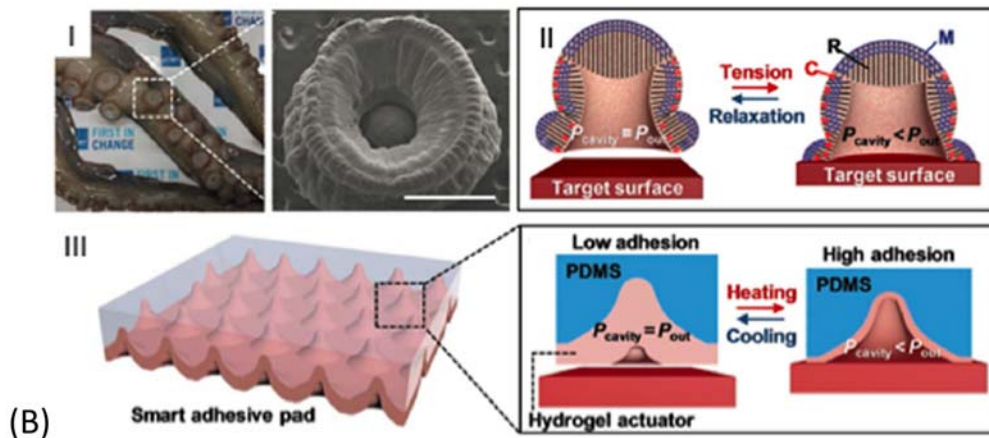
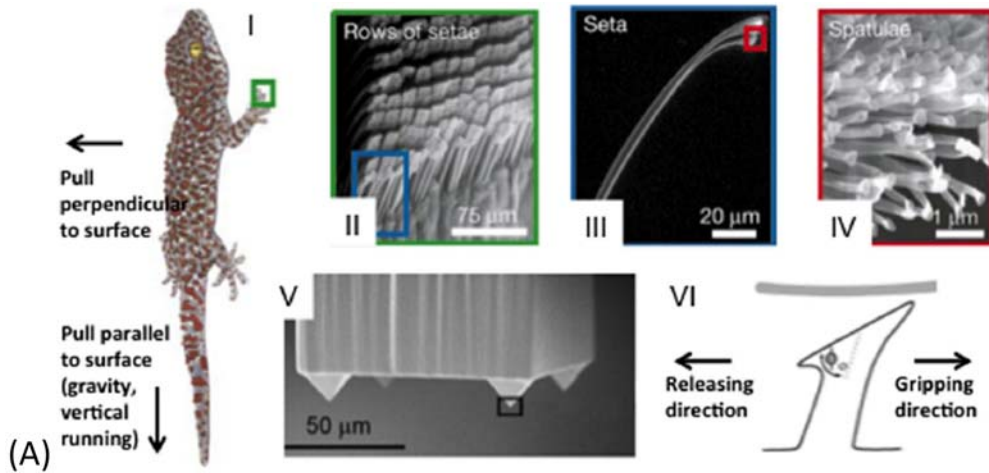


Figure 1.10 Biomimetic structures for transfer printing. (A) Hierarchical microstructure of gecko setae for transfer printing. (I) Schematic diagram of a tokay gecko (*Gekko gekko*). (II–IV) SEMs of rows of setae from (II) toe, (III) seta, and spatulae (IV). (V) SEM image of the elastomeric stamp with microtips. (VI) Directional dependent adhesion for gripping and releasing. (B) Smart adhesive pad inspired by octopus (I, scale bar of 1 mm) with the adhesion switched by reversibly changing the pressure inside the sucker cavity (II), via the actuation of temperature-responsive hydrogel muscles. (A) (I)–(IV) Reprinted with permission from Autumn, K., Liang, Y.A., Hsieh, S.T., Zesch, W., Chan, W.P., Kenny, T.W., Fearing, R., & Full, R.J. (2008). Adhesive force of a single gecko foot-hair. *Nature*, 405 (6787), 681–685. <https://doi.org/10.1038/35015073>; Copyright 2000, Nature Publishing Group. (V) Reprinted with permission from Kim, S., Wu, J., Carlson, A., Jin, S.H., Kovalsky, A., Glass, P., Liu, Z., Ahmed, N., Elgan, S.L., Chen, W., Ferreira, P.M., Sitti, M., Huang, Y., & Rogers, J.A. (2010). Microstructured elastomeric surfaces with reversible adhesion and examples of their use in deterministic assembly by transfer printing. *Proceedings of the National Academy of Sciences*, 107(40), (Continued)

the reduction of pressure inside the sucker cavity, thus facilitating sucker adherence. For detaching its sucker, the circular muscles contract to thicken the walls of the sucker, thereby increasing the cavity pressure and lowering the adhesion strength [Fig. 1.10B(III)].

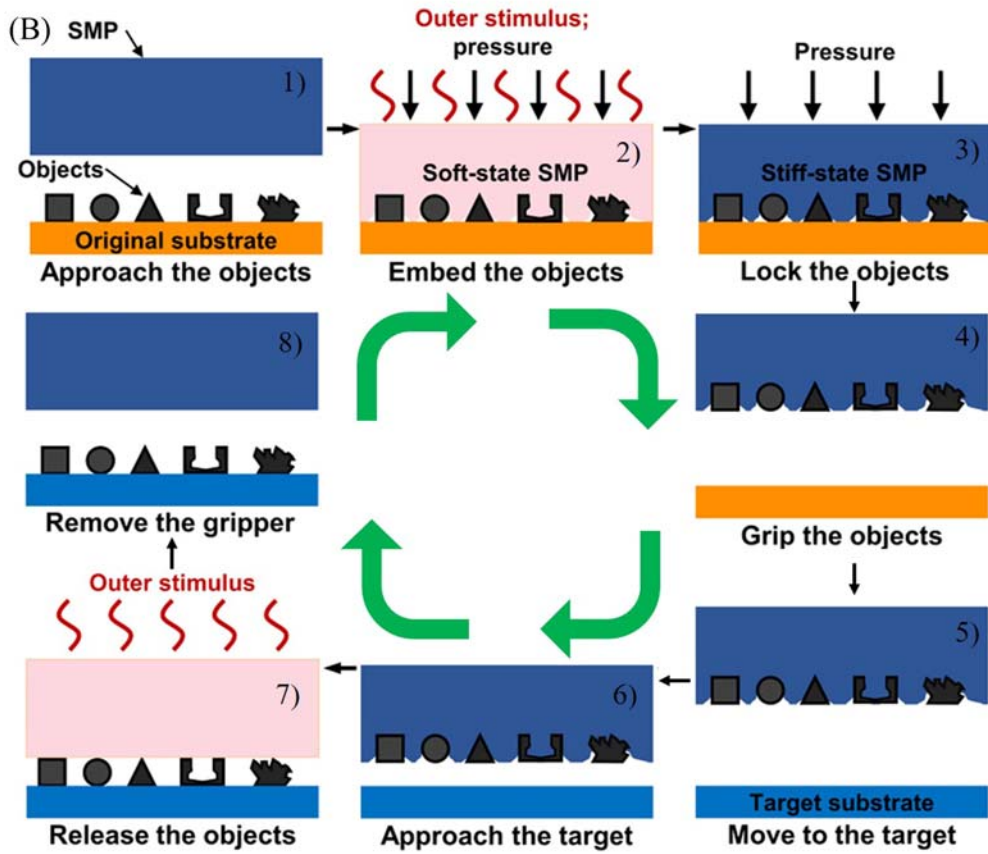
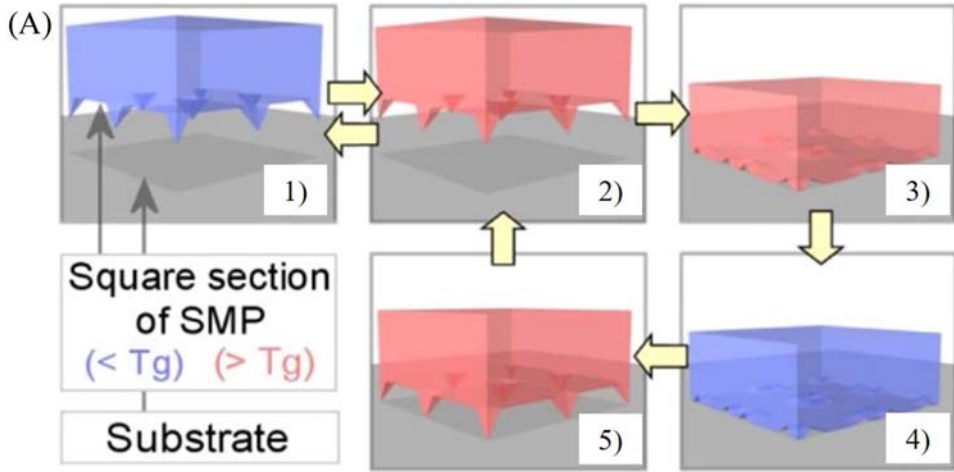
1.4 Materials science of transfer printing

The controlled interface delamination is critical for a successful transfer printing method. Except for structural designs, functional materials with some special properties also play a crucial role in regulating the interfacial adhesion strength. In this section, some functional materials used for the fabrication of stamps or the regulation of the interface adhesion are introduced.

1.4.1 Shape memory polymer

Shape memory polymer (SMP) is a specially formed polymer that has a memory function: the temporary shape formed by various external preloads can be memorized. After applying external stimuli such as heat, electricity, or others, SMP will recover its permanent shape (Koerner et al., 2004; Liu et al., 2007; Yu, Ge et al., 2014). When a strain is applied to deform SMP at a high temperature above its glass transition temperature (T_g), the strained SMP will remain the deformed shape when it is cooled to a temperature below T_g . Upon reheating over the temperature of T_g , the deformed SMP will return to its initial shape. Based on this switching capability, SMP shows attractive characteristics for the fabrication of stamps compared with conventional PDMS stamps in transfer printing (Eisenhaure, Rhee et al., 2014). There are two advantages of the SMP stamp: (1) it can realize a dramatic increase of adhesion to pick up the device at a temperature below T_g ; (2) the adhesion strength can be controlled through external stimulus and is no longer time-sensitive. In a representative use as shown in Fig. 1.11A, the SMP stamp having the microtips of permanent shape can be pressed to form a temporary collapsed shape at a high temperature above T_g [Fig. 1.11A(3)] (Eisenhaure et al., 2013). There has a large contact area in the temporary collapsed state of microtips, which produces a large interfacial adhesion force to

◀ 17095–17100. <https://doi.org/10.1073/pnas.1005828107>; Copyright 2010, National Academy of Sciences. (VII) Reprinted with permission from Murphy, M.P., Aksak, B., & Sitti, M. (2009). Gecko-inspired directional and controllable adhesion. *Small (Weinheim an der Bergstrasse, Germany)*, 5(2), 170–175. <https://doi.org/10.1002/sml.200801161>; Copyright 2009, John Wiley and Sons. (B) Reprinted with permission from Lee, H., Um, D.S., Lee, Y., Lim, S., Kim, H.J., & Ko, H. (2016). Octopus-inspired smart adhesive pads for transfer printing of semiconducting nanomembranes. *Advanced Materials*, 28(34), 7457–7465. <https://doi.org/10.1002/adma.201601407>; Copyright 2016, John Wiley and Sons. With permissions from Nature Publishing Group, National Academy of Sciences and John Wiley and Sons.



(Continued)

pick up the device [Fig. 1.11A(3 and 4)]. The SMP stamp recuperates to its initial shape to substantially reduce the contact area and thus the interfacial adhesion strength, thereby releasing the device onto the target substrate [Fig. 1.11A(5)]. Furthermore, for improving the results of this temperature-controlled transfer printing based on an SMP stamp, an analytical model was established to optimize surface relief structures (Xue et al., 2015).

Transfer printing of devices with various sizes ranging from macroscale (> 1 mm) down to mesoscale (100–1 mm) and even microscale (10–100 nm) and diverse shapes of planar, spherical, or even arbitrarily shaped is a great challenge. In order to address this challenge, a universal gripper (also called a stamp) based on a simple SMP block is designed and fabricated to manipulate multiscale and arbitrarily shaped objects in individual, deterministic, massive, and selective ways (Fig. 1.11B) (Linghu et al., 2020). In a similar way to the above method, the initial stiff SMP block with a high modulus (2.53 GPa) at the temperature of 25°C is actuated to be a very soft block with a low modulus of about 2.5 MPa by heating to 60°C (above the glass transition temperature). The applied compressive pressure presses the soft block as a gripper to contact intimately with arbitrarily shaped objects on the original substrate, and the

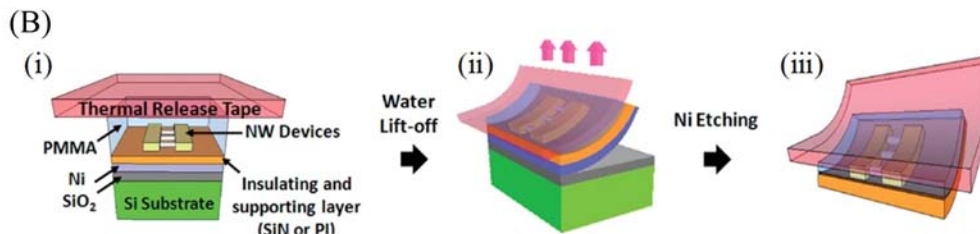
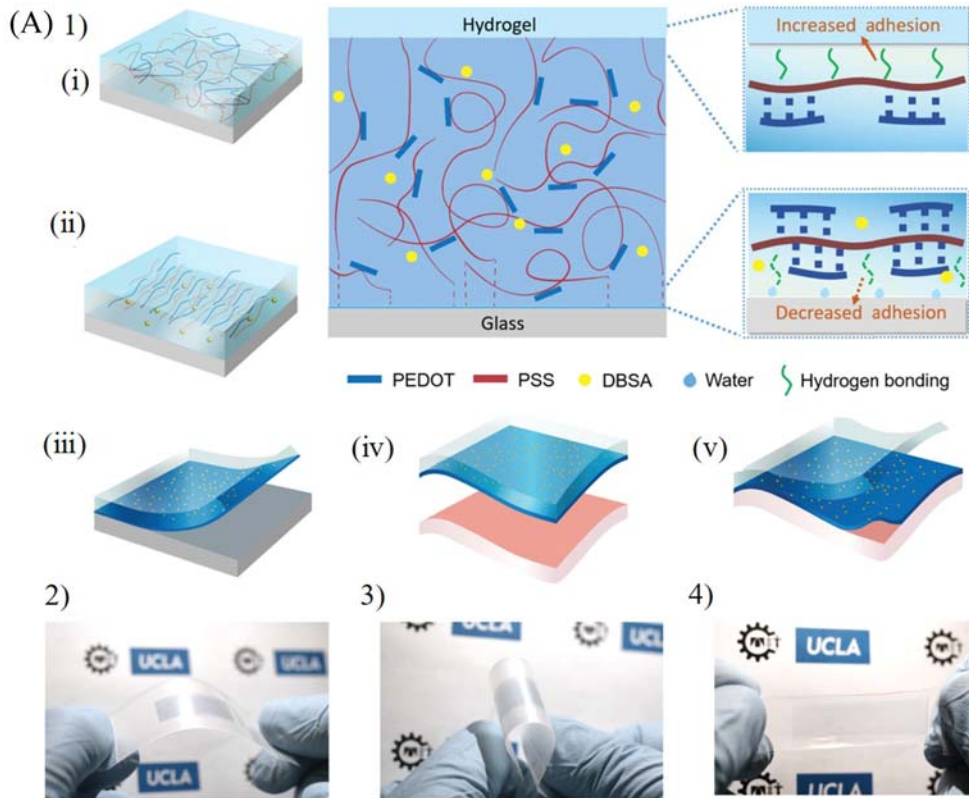
-
- ◀ **Figure 1.11** (A) Schematic diagram of transfer printing mechanism using the shape memory polymer (SMP) stamp with surface relief structure made of shape memory polymers. The initial state of stamp (1) below and (2) above the transition temperature; (3) the microtips are collapsed by an applied pressure for increasing adhesion strength at the interface of the device and donor substrate, increasing the contact area; (4) cooling the SMP stamp down lower than the transition temperature picks up the device with the programmed temporary shape; (5) The SMP stamp is heated above the transition temperature to recover its permanent shape to release the ink onto the receiving substrate. (B) Schematic illustration of gripping and releasing devices using the universal SMP gripper. (1) The SMP gripper is arranged close to the objects on the original substrate; (2) after heating above the glass transition temperature, the SMP stamp transforms into a soft state, and the objects are embedded into the soft SMP gripper under the action of compressive pressure; (3) the SMP gripper is then actuated back to the stiff state by cooling to lock the embedded objects; (4) the objects are gripped from the original substrate and will not fall off from the gripper due to reliable locking during the process of (5) moving gripper and (6) approaching the receiving substrate; (7) the gripper is activated by reheating to enable the shape recovery of the gripper and release the objects; (8) the objects are released onto the target substrate successfully after removing the gripper. (A) Reprinted with permission from Eisenhaure, J.D., Xie, T., Varghese, S., & Kim, S. (2013). *Microstructured shape memory polymer surfaces with reversible dry adhesion*. *ACS Applied Material Interfaces*, 5(16), 7714–7717. <https://doi.org/10.1021/am402479f>; Copyright 2013, American Chemical Society. (B) Reprinted with permission from Linghu, C., Zhang, S., Wang, C., Yu, K., Li, C., Zeng, Y., Zhu, H., Jin, X., You, Z., & Song, J. (2020). *Universal SMP gripper with massive and selective capabilities for multiscaled, arbitrarily shaped objects*. *Science Advances*, 6(7). <https://doi.org/10.1126/sciadv.aay5120>; Copyright 2020, American Association for the Advancement of Science. With permission from American Chemical society and American Association for the Advancement of Science.

objects are embedded conformally into the block [Fig. 1.11B(2)]. After cooling to 25°C and removing the pressure, the SMP gripper becomes a rigid gripper with a temporary shape to lock the target objects tightly by a large grip force produced from interlocking, suction, and friction effects [Fig. 1.11B(3)]. The retraction of the gripper can grip the target objects from the original substrate [Fig. 1.11B(4)]. During the process of moving the gripper to and approaching the target substrate, the embedded objects will not fall off the gripper [Fig. 1.11B(5 and 6)]. Upon reheating to 60°C, the deformed SMP gripper recovers to its initial permanent shape with a flat bottom surface, which enables the release of embedded objects onto the target substrate after removing the gripper. For this method, the arbitrarily shaped objects can be easily embedded conformally into the soft SMP gripper due to its compliant characteristic at a temperature above the glass transition temperature. The fixed temporary shape of the deformed SMP gripper enables solid locking with a large grip force for objects of arbitrary shapes with smooth or roughed surfaces. The recovery of the permanent shape of the SMP gripper because of the shape memory function allows the smooth release of target objects. This simple design of a block-structured gripper based on embedding mode is applicable to objects with both planar and complex three-dimensional surfaces that are challenging with the adhesion-based scheme. It can also be easily scaled for gripping objects ranging from tens of millimeters to tens of micrometers. As a transfer printing stamp, this SMP gripper realized reliable transfer printings of a 7×7 array of steel spheres (diameter: 1 mm) and a 10×10 array of steel spheres (diameter: 200 nm and 300 nm) onto the PDMS substrate without disrupting the original sphere order. Furthermore, both selective printings and patterned printings of LED chips were realized through local shape recovery of the SMP gripper induced by local heating. The capabilities of selective releasing and printing on demand permit successful printing of any desired pattern of the device onto the target substrate, which can provide a powerful tool for the large-scale assembly of functional devices such as the mass transfer for the fabrication of micro-LED.

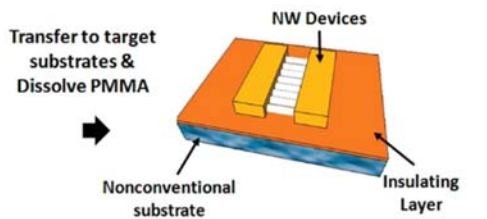
1.4.2 Hydrophilic material

The hydrophilic layer at the bottom of the stamp can significantly enhance the water affinity and facilitate water diffusion to the stamp/device interface, which forms a water boundary layer to decrease the adhesion strength at the interface. Therefore, the device can be printed onto various substrates. Based on this mechanism, some hydrophilic materials are used for versatile transfer printing methods (Kim, Kang et al., 2015; Zhang et al., 2020).

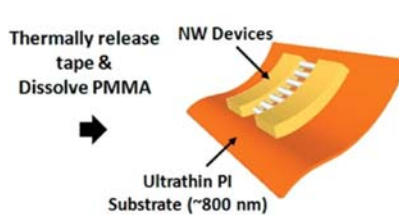
For a proposed method of hydrogel-enabled transfer printing, conductive PEDOT:PSS (poly(3,4-ethylenedioxythiophene) polystyrene sulfonate) thin films on glass substrates can be successfully transferred to soft substrates when it is mixed with a hydrophilic surfactant of dodecylbenzene sulfonic acid (DBSA) (Fig. 1.12A) (Zhang et al.,



1) Water lift-off process for NW devices



2) NW devices on nonconventional substrate



3) NW devices on ultrathin substrate

(Continued)

2020). PEDOT:PSS suspension is first mixed with DBSA and then spin-coated and patterned on a glass substrate followed by thermal annealing to form a PEDOT:PSS thin film. A water-soluble PVA (poly(lactic acid)) hydrogel carrier is then placed on the top surface of the fabricated PEDOT:PSS thin film [Fig. 1.12A(1-i and ii)]. The hydrogel containing a large amount of water will swell the PEDOT:PSS thin film when it is arranged to contact with the PEDOT:PSS thin film, forming a strong hydrogen bonding with PSS at the interface between the hydrogel carrier and PEDOT:PSS thin film. On the other hand, the addition of DBSA reduces the adhesion strength of the interface between PEDOT:PSS thin film and glass substrate. The reason is that the molecules of the surfactant of DBSA contain hydrophilic SO_3^- tails as a wettability enhancer, which can greatly enhance the water affinity of the resultant PEDOT:PSS thin film as shown in the zoomed diagram. Since there has a stronger adhesion force between the hydrogel carrier and PEDOT:PSS thin film compared with that between the glass substrate and PEDOT:PSS thin film, the PEDOT:PSS thin film can be seamlessly transferred without any residues left on the glass substrate after detaching the hydrogel carrier [Fig. 11A(1-iii)].

In the printing step, the hydrogel carried PEDOT:PSS thin film is first gently placed on the position of the target substrates [Fig. 1.12A(1-iv)] and a compressive pressure is applied to increase the adhesion strength between the PEDOT:PSS thin film and the target substrate. Finally, the soluble PVA hydrogel carrier is dissolved

-
- ◀ **Figure 1.12** (A) Schematic image of the process for the hydrogel-enabled transfer printing of PEDOT:PSS thin film mixed with DBSA onto target substrates: (1) PEDOT:PSS suspension is (i) spin-coated and (ii) baked on a glass substrate; PEDOT:PSS thin film is (iii) peeled with a hydrogel carrier and (iv) placed onto a target soft substrate; (v) PEDOT:PSS thin film is printed onto a target substrate by removing the hydrogel carrier. Zoomed-in diagram shows the strong hydrogen bonding between the hydrogel and PEDOT:PSS (green), and the weak adhesion force between glass and DBSA-treated PEDOT:PSS (dotted green); PEDOT:PSS thin film is transfer printed onto a (2 and 3) plastic substrate and (4) a PDMS substrate. (B) Schematic diagram of water-assisted transfer printing (1) (i) on a supporting insulating layer (SiN or PI): the nanowire (NW) devices are prefabricated covering the thin Ni layer deposited on the Si wafer with SiO_2 coating; (ii) a lift-off in a room temperature water bath is used to pick up the Ni layer and the nanowire device onto the thermal release tape; (iii) The devices with an insulating layer are reproduced using (2) a nonconventional substrate or (3) a Ni layer etched ultrathin polyimide substrate. (A) Reprinted with permission from Zhang, S., Ling, H., Chen, Y., Cui, Q., Ni, J., Wang, X., Hartel, M.C., Meng, X., Lee, K.J., Lee, J., Sun, W., Lin, H., Emaminejad, S., Ahadian, S., Ashammakhi, N., Dokmeci, M.R., & Khademhosseini, A. (2020). *Hydrogel-enabled transfer printing of conducting polymer films for soft organic bioelectronics. Advanced Functional Materials*, 30(6), 1906016. <https://doi.org/10.1002/adfm.201906016>; Copyright 2020, John Wiley and Sons. (B) Reprinted with permission from Lee, C.H., Kim, D.R., & Zheng, X. (2011). *Fabrication of nanowire electronics on nonconventional substrates by water-assisted transfer printing method. Nano Letters*, 11(8), 3435–3439. <https://doi.org/10.1021/nl201901z>; Copyright 2011, American Chemical Society. With permissions from John Wiley and Sons and American Chemical Society.

when the whole sample is immersed in water, thereby printing the PEDOT:PSS thin film onto the target substrate [Fig. 1.12A(1-v)]. This hydrogel-enabled transfer printing method is proven to be an effective technology from the successful examples of transferring prepatterned PEDOT:PSS thin film from glass substrates to different soft substrates including plastics [Fig. 1.12A(2)], elastomers [Fig. 1.12A(3)], and human skin [Fig. 1.12A(4)]. In addition, the PEDOT:PSS thin films can be patterned on glass substrates through advanced micropatterning technologies. This method can, therefore, realize facile and rapid patterning of PEDOT:PSS thin films on various soft substrates.

Using a thin Ni layer deposited on the donor substrate (e.g., Si wafer coated with SiO₂), a developed water-assisted transfer printing (WTP) method was used to transfer print nanowires (NWs)-based electronic devices fabricated on the Ni layer onto different substrates (Fig. 1.12B) (Lee, Kim et al., 2011; Lee, Kim et al., 2014; Zhao et al., 2016). Peeling off with a TRT in a water bath at room temperature can pick up the device with the supporting Ni layer onto the TRT. The device can be moved to print onto various nonconventional substrates without any defects by etching the Ni layer.

For the WTP method, the water-assisted interfacial fracture between the Ni layer and SiO₂ layer is the key to successful transfer printing. Nickel silicate or nickel oxide is formed during the Ni layer deposition on a thin film SiO₂-coated Si wafer, producing Ni hydroxide when immersed in the water. Due to the hydrophilicity of Ni hydroxide and SiO₂, penetration of water is enhanced at the interface, separating the Ni layer from the SiO₂ layer after immersing the whole system in the water. The device accompanied by the Ni layer can be easily picked up for the next printing process. The whole lift-off process is operated at room temperature, and it will, therefore, bring no possible thermal damage caused by high temperatures. The detailed mechanism of the interfacial debonding process is also comprehensively analyzed with theory, finite simulations, and experiments (Wie et al., 2018; Zhang et al., 2019a).

1.4.3 Thermoplastic polymer

In a developed programmable and scalable transfer printing method, the thermoplastic polymer is used to fabricate an expandable microsphere, which consists of a thermoplastic polymer shell and hydrocarbons encapsulated inside the shell (Wang et al., 2020). Expandable microspheres are embedded uniformly and randomly inside the adhesive layer (TRT) of a thin bilayer sheet made up of an adhesive stamp layer and a polymeric backing layer, conforming to the shape [Fig. 1.13A(1)]. Initially, flat tomography is ensured by the small size microspheres which have limited impact on the adhesive layer for picking up devices. When the stamp is treated by external thermal stimuli with a temperature of 90°C, hydrocarbons inside the shell initiate the liquid-vapor transition, which leads to softening of thermoplastic polymer shells resulting in an increased diameter of microspheres (~10–45 μm) without any gas bubbles generated [Fig. 1.13A(2)]. The large

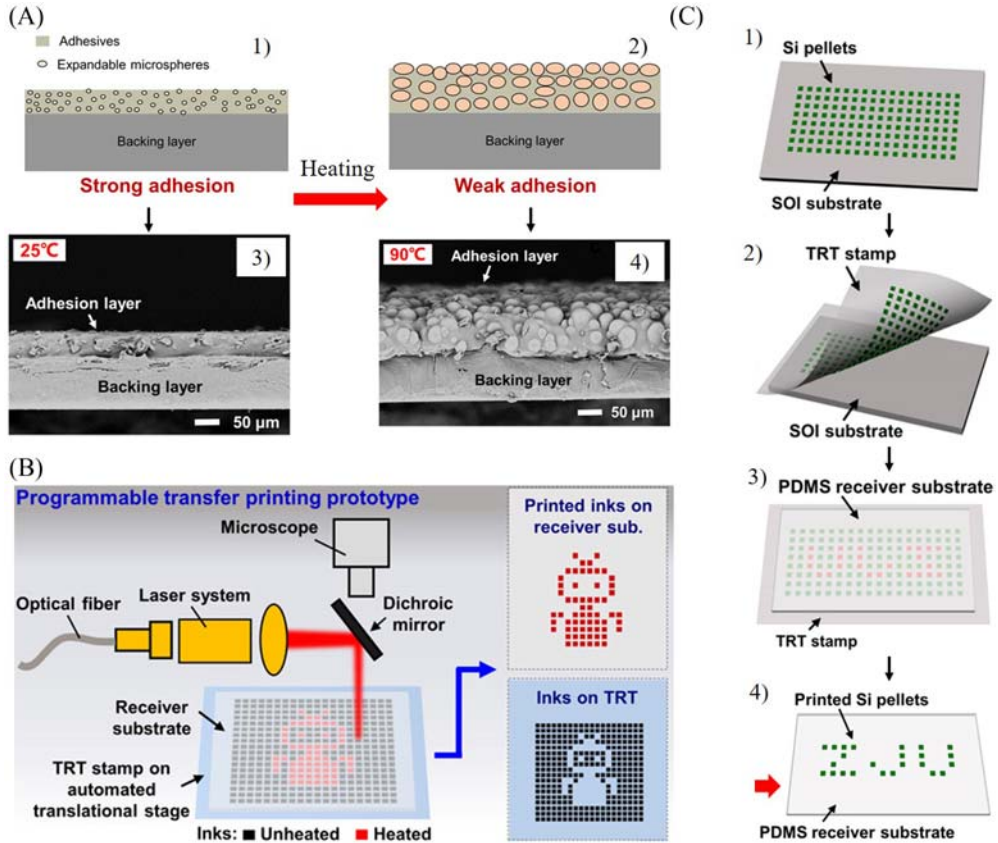


Figure 1.13 (A) Schematic illustration of the shape-conformal stamp embedded with expandable microspheres: (1) initial state with strong adhesion before microsphere expansion; (2) rough state with weak adhesion after microsphere expansion actuated by heating; SEM images of the adhesive layer (3) before and (4) after expansion of microspheres. (B) Schematic model of the programmable laser-assisted transfer printing system with its automated translational mode. (C) Schematic illustration of the transfer printing process with programmable capabilities: (1) Si pellets are prepared on an SOI substrate, (2) Si pellets are pulled out by the TRT stamp, (3) the stamp is heated programmatically and (4) Si pellets are selectively printed onto PDMS substrate at desired positions. Reprinted with permission from Wang, C., Linghu, C., Nie, S., Li, C., Lei, Q., Tao, X., Zeng, Y., Du, Y., Zhang, S., Yu, K., Jin, H., Chen, W., & Song, J. (2020). Programmable and scalable transfer printing with high reliability and efficiency for flexible inorganic electronics. *Science Advances*, 6(25), eabb2393. <https://doi.org/10.1126/sciadv.abb2393>. Copyright 2020, American Association for the Advancement of Science.

temperature-mediated microsphere volume expansion produces hierarchical microstructures rapidly on the adhesive layer, thus decreasing the adhesion strength because of the decreased stamp/device contact area. Therefore, the attached device on the stamp can be released and printed onto various receiver substrates.

The rapid switchability of adhesion strength can be achieved by the expansion of microspheres actuated by external thermal stimuli. A scalable, programmable transfer printing method was developed leveraging the weak adhesion of the TRT stamp which is induced by instant localized heat transport through a controllable laser system and the precise alignment controlled by an automated translational stage (Fig. 1.13B). As a result, the TRT stamp can initially pick up the prefabricated array of functional devices on the source substrate and then print selectively onto various customized receiving substrates by irradiating locally to decrease the adhesion strength of the TRT stamp where individual devices to be transferred printed are located (Fig. 1.13C).

1.5 Conclusions

In this chapter, transfer printing technologies and involved mechanics, structure, and material science are introduced for the fabrication and large-scale assembly of inorganic flexible and stretchable electronics. Various established analytical mechanical models used to characterize the interfacial adhesion strength for kinetically controlled transfer printing technique, shear-enhanced transfer technique, laser-driven noncontact transfer printing technique, magnetic-assisted transfer printing technique, thermal release transfer printing technique, and magnet-controlled transfer printing technique are summarized. Furthermore, novel structures (e.g., surface relief structures, bulging structures, and bio-inspired structures) and functional materials (e.g., SMPs, hydrophilic materials, and thermoplastic polymers) for greatly regulating the interface adhesion strength are also discussed. The basic concepts for existing typical transfer printing techniques are overviewed to illustrate the key roles of mechanics, structure, and material science in the development of transfer printing techniques. It can be known that a successful transfer printing technique with rapid adhesion switchability is usually achieved by the synergy of two or three designs in mechanics, structure, and material science.

References

- Al-okaily, A. M., & Ferreira, P. M. (2015). Multi-physics modeling for laser micro-transfer printing delamination. *Special Section: NAMRC, 20(2014)*, 414–424. Available from <https://doi.org/10.1016/j.jmapro.2014.07.006>, <https://www.sciencedirect.com/science/article/pii/S152661251400067X>.
- Al-okaily, A. M., Rogers, J. A., & Ferreira, P. M. (2014). Characterization of delamination in laser micro-transfer printing. *Journal of Micro and Nano-Manufacturing*, 2(1). Available from <https://doi.org/10.1115/1.4026238>.
- Autumn, K., Liang, Y. A., Hsieh, S. T., Zesch, W., Chan, W. P., Kenny, T. W., Fearing, R., & Full, R. J. (2000). Adhesive force of a single gecko foot-hair. *Nature*, 405(6787), 681–685. Available from <https://doi.org/10.1038/35015073>.
- Bian, J., Zhou, L., Wan, X., Zhu, C., Yang, B., & Huang, Y. A. (2019). Laser transfer, printing, and assembly techniques for flexible electronics. *Advanced Electronic Materials*, 5(7)1800900. Available from <https://doi.org/10.1002/aelm.201800900>.

- Carlson, A., Bowen, A. M., Huang, Y., Nuzzo, R. G., & Rogers, J. A. (2012a). Transfer printing techniques for materials assembly and micro/nanodevice fabrication. *Advanced Materials*, 24(39), 5284–5318. Available from <https://doi.org/10.1002/adma.201201386>.
- Carlson, A., Kim-Lee, H. J., Wu, J., Elvikis, P., Cheng, H., Kovalsky, A., Elgan, S., Yu, Q., Ferreira, P. M., Huang, Y., Turner, K. T., & Rogers, J. A. (2011). Shear-enhanced adhesiveless transfer printing for use in deterministic materials assembly. *Applied Physics Letters*, 98(26)264104. Available from <https://doi.org/10.1063/1.3605558>.
- Carlson, A., Wang, S., Elvikis, P., Ferreira, P. M., Huang, Y., & Rogers, J. A. (2012b). Active, programmable elastomeric surfaces with tunable adhesion for deterministic assembly by transfer printing. *Advanced Functional Materials*, 22(21), 4476–4484. Available from <https://doi.org/10.1002/adfm.201201023>.
- Cheng, H., Li, M., Wu, J., Carlson, A., Kim, S., Huang, Y., Kang, Z., Hwang, K.-C., & Rogers, J. A. (2013). A Viscoelastic model for the rate effect in transfer printing. *Journal of Applied Mechanics*, 88(4). Available from <https://doi.org/10.1115/1.4007851>.
- Cheng, H., Wu, J., Yu, Q., Kim-Lee, H. J., Carlson, A., Turner, K. T., Hwang, K. C., Huang, Y., & Rogers, J. A. (2012). An analytical model for shear-enhanced adhesiveless transfer printing. *Mechanics Research Communications*, 43, 46–49. Available from <https://doi.org/10.1016/j.mechrescom.2012.02.011>, <https://www.sciencedirect.com/science/article/pii/S0093641312000407>.
- Chen, H., Feng, X., & Chen, Y. (2013). Directionally controlled transfer printing using micropatterned stamps. *Applied Physics Letters*, 103(15)151607. Available from <https://doi.org/10.1063/1.4824976>.
- Chen, H., Feng, X., Huang, Y., Huang, Y., & Rogers, J. A. (2013). Experiments and viscoelastic analysis of peel test with patterned strips for applications to transfer printing. *Journal of the Mechanics and Physics of Solids*, 61(8), 1737–1752. Available from <https://doi.org/10.1016/j.jmps.2013.04.001>, <https://www.sciencedirect.com/science/article/pii/S0022509613000720>.
- Eisenhaure, J. D., Rhee, S. I., Al-Okaily, A. M., Carlson, A., Ferreira, P. M., & Kim, S. (2014). The use of shape memory polymers for microassembly by transfer printing. *Journal of Microelectromechanical Systems*, 23(5), 1012–1014. Available from <https://doi.org/10.1109/JMEMS.2014.2345274>.
- Eisenhaure, J. D., Xie, T., Varghese, S., & Kim, S. (2013). Microstructured shape memory polymer surfaces with reversible dry adhesion. *ACS Appl. Mater. Interfaces*, 5(16), 7714–7717. Available from <https://doi.org/10.1021/am402479f>.
- Feng, X., Cheng, H., Bowen, A. M., Carlson, A. W., Nuzzo, R. G., & Rogers, J. A. (2013). A finite-deformation mechanics theory for kinetically controlled transfer printing. *Journal of Applied Mechanics*, 80(6). Available from <https://doi.org/10.1115/1.4023963>.
- Feng, X., Meitl, M. A., Bowen, A. M., Huang, Y., Nuzzo, R. G., & Rogers, J. A. (2007). Competing fracture in kinetically controlled transfer printing. *Langmuir: the ACS Journal of Surfaces and Colloids*, 23(25), 12555–12560. Available from <https://doi.org/10.1021/la701555n>.
- Gao, Y., Li, Y., Li, R., & Song, J. (2017). An accurate thermomechanical model for laser-driven micro-transfer printing. *Journal of Applied Mechanics*, 84(6). Available from <https://doi.org/10.1115/1.4036257>.
- Guo, D., Li, Y., Zhao, Q., Liu, P., Che, L., Kang, Z., Li, M., & Luo, Y. (2022). Stiffness modulation-driven transfer printing and strain isolation in stretchable electronics. *Materials & Design*, 217110602. Available from <https://doi.org/10.1016/j.matdes.2022.110602>, <https://www.sciencedirect.com/science/article/pii/S0264127522002234>.
- Jeong, J., Kim, J., Song, K., Autumn, K., & Lee, J. (2014). Geckoprinting: Assembly of microelectronic devices on unconventional surfaces by transfer printing with isolated gecko setal arrays. *Journal of The Royal Society Interface*, 11(99)20140627. Available from <https://doi.org/10.1098/rsif.2014.0627>.
- Kim, T. H., Carlson, A., Ahn, J. H., Won, S. M., Wang, S., Huang, Y., & Rogers, J. A. (2009). Kinetically controlled, adhesiveless transfer printing using microstructured stamps. *Applied Physics Letters*, 94(11)113502. Available from <https://doi.org/10.1063/1.3099052>.
- Kim, N., Kang, H., Lee, J. H., Kee, S., Lee, S. H., & Lee, K. (2015). Highly conductive all-plastic electrodes fabricated using a novel chemically controlled transfer-printing method. *Advanced Materials* (14), 2317–2323. Available from <https://doi.org/10.1002/adma.201500078>.

- Kim, S., Lakshmanan, S., Li, J., Anthamatten, M., Lambropoulos, J., & Shestopalov, A. A. (2022). Modulation of interfacial adhesion using semicrystalline shape-memory polymers. *Langmuir: the ACS Journal of Surfaces and Colloids* (11), 3607–3616. Available from <https://doi.org/10.1021/acs.langmuir.2c00291>.
- Kim, S., Liu, N., & Shestopalov, A. A. (2022). Contact printing of multilayered thin films with shape memory polymers. *ACS Nano*, 16(4), 6134–6144. Available from <https://doi.org/10.1021/acsnano.1c11607>.
- Kim, S., Wu, J., Carlson, A., Jin, S. H., Kovalsky, A., Glass, P., Liu, Z., Ahmed, N., Elgan, S. L., Chen, W., Ferreira, P. M., Sitti, M., Huang, Y., & Rogers, J. A. (2010). Microstructured elastomeric surfaces with reversible adhesion and examples of their use in deterministic assembly by transfer printing. *Proceedings of the National Academy of Sciences*, 107(40), 17095–17100. Available from <https://doi.org/10.1073/pnas.1005828107>.
- Koerner, H., Price, G., Pearce, N. A., Alexander, M., & Vaia, R. A. (2004). Remotely actuated polymer nanocomposites—stress-recovery of carbon-nanotube-filled thermoplastic elastomers. *Nature Materials*, 3(2), 115–120. Available from <https://doi.org/10.1038/nmat1059>.
- Lee, C. H., Kim, D. R., & Zheng, X. (2011). Fabrication of nanowire electronics on nonconventional substrates by water-assisted transfer printing method. *Nano Letters*, 11(8), 3435–3439. Available from <https://doi.org/10.1021/nl201901z>.
- Lee, C. H., Kim, D. R., & Zheng, X. (2014). Transfer printing methods for flexible thin film solar cells: basic concepts and working principles. *ACS Nano*, 8(9), 8746–8756. Available from <https://doi.org/10.1021/nn5037587>.
- Lee, H., Um, D. S., Lee, Y., Lim, S., Kim, H. J., & Ko, H. (2016). Octopus-inspired smart adhesive pads for transfer printing of semiconducting nanomembranes. *Advanced Materials*, 28(34), 7457–7465. Available from <https://doi.org/10.1002/adma.201601407>.
- Liang, C., Wang, F., Huo, Z., Shi, B., Tian, Y., & Zhang, D. (2021). Adhesion performance study of a novel microstructured stamp for micro-transfer printing. *Soft Matter*, 17(19), 4989–4997. Available from <https://doi.org/10.1039/D0SM02161J>.
- Linghu, C., Wang, C., Cen, N., Wu, J., Lai, Z., & Song, J. (2019). Rapidly tunable and highly reversible bio-inspired dry adhesion for transfer printing in air and a vacuum. *Soft Matter*, 15(1), 30–37. Available from <https://doi.org/10.1039/C8SM01996G>.
- Linghu, C., Zhu, H., Zhu, J., Li, C., & Song, J. (2019). Mechanics of magnet-controlled transfer printing. *Extreme Mechanics Letters*, 27, 76–82. Available from <https://doi.org/10.1016/j.eml.2019.01.006>, <https://www.sciencedirect.com/science/article/pii/S2352431618302578>.
- Linghu, C., Zhang, S., Wang, C., & Song, J. (2018). Transfer printing techniques for flexible and stretchable inorganic electronics. *NPJ Flexible Electronics*, 2(1), 26. Available from <https://doi.org/10.1038/s41528-018-0037-x>.
- Linghu, C., Zhang, S., Wang, C., Yu, K., Li, C., Zeng, Y., Zhu, H., Jin, X., You, Z., & Song, J. (2020). Universal SMP gripper with massive and selective capabilities for multiscaled, arbitrarily shaped objects. *Science Advances*, 6(7). Available from <https://doi.org/10.1126/sciadv.aay5120>.
- Liu, C., Qin, H., & Mather, P. T. (2007). Review of progress in shape-memory polymers. *Journal of Materials Chemistry*, 17(16), 1543–1558. Available from <https://doi.org/10.1039/B615954K>.
- Li, R., Li, Y., Lü, C., Song, J., Saeidpourazar, R., Fang, B., Zhong, Y., Ferreira, P. M., Rogers, J. A., & Huang, Y. (2012b). Axisymmetric thermo-mechanical analysis of laser-driven non-contact transfer printing. *International Journal of Fracture*, 176(2), 189–194. Available from <https://doi.org/10.1007/s10704-012-9744-9>.
- Li, R., Li, Y., Lü, C., Song, J., Saeidpouraza, R., Fang, B., Zhong, Y., Ferreira, P. M., Rogers, J. A., & Huang, Y. (2012a). Thermo-mechanical modeling of laser-driven non-contact transfer printing: Two-dimensional analysis. *Soft Matter*, 8(27), 7122–7127. Available from <https://doi.org/10.1039/C2SM25339A>.
- Li, C., Luo, H., & Song, J. (2021). Magnetically driven non-contact transfer printing based on a bi-stable elastomeric stamp. *Advanced Materials Technologies*, 6(11)2100335. Available from <https://doi.org/10.1002/admt.202100335>.

- Luo, H., Li, C., Shi, C., Nie, S., & Song, J. (2021). Switchable dry adhesive based on shape memory polymer with hemispherical indenters for transfer printing. *Theoretical and Applied Mechanics Letters*, 11(6)100308. Available from <https://doi.org/10.1016/j.taml.2021.100308>, <https://www.sciencedirect.com/science/article/pii/S209503492100115X>.
- Luo, H., Wang, C., Linghu, C., Yu, K., Wang, C., & Song, J. (2020). Laser-driven programmable non-contact transfer printing of objects onto arbitrary receivers via an active elastomeric microstructured stamp. *National Science Review*, 7(2), 296–304. Available from <https://doi.org/10.1093/nsr/nwz109>.
- Luo, H., Wang, S., Wang, C., Linghu, C., & Song, J. (2021). Thermal controlled tunable adhesive for deterministic assembly by transfer printing. *Advanced Functional Materials*, 31(16)2010297. Available from <https://doi.org/10.1002/adfm.202010297>.
- Meitl, M. A., Zhou, Y., Gaur, A., Jeon, S., Usrey, M. L., Strano, M. S., & Rogers, J. A. (2004). Solution casting and transfer printing single-walled carbon nanotube films. *Nano Letters*, 4(9), 1643–1647. Available from <https://doi.org/10.1021/nl0491935>.
- Meitl, M. A., Zhu, Z. T., Kumar, V., Lee, K. J., Feng, X., Huang, Y. Y., Adesida, I., Nuzzo, R. G., & Rogers, J. A. (2006). Transfer printing by kinetic control of adhesion to an elastomeric stamp. *Nature Materials*, 5(1), 33–38. Available from <https://doi.org/10.1038/nmat1532>.
- Murphy, M. P., Aksak, B., & Sitti, M. (2009). Gecko-inspired directional and controllable adhesion. *Small (Weinheim an der Bergstrasse, Germany)*, 5(2), 170–175. Available from <https://doi.org/10.1002/sml.200801161>.
- Park, J., Lee, Y., Lee, H., & Ko, H. (2020). Transfer printing of electronic functions on arbitrary complex surfaces. *ACS Nano*, 14(1), 12–20. Available from <https://doi.org/10.1021/acsnano.9b09846>.
- Park, S. L., Xiong, Y., Kim, R. H., Elvikis, P., Meitl, M., Kim, D. H., Wu, J., Yoon, J., Yu, C. J., Liu, Z., Huang, Y., Hwang, K. C., Ferreira, P., Li, X., Choquette, K., & Rogers, J. A. (2009). Printed assemblies of inorganic light-emitting diodes for deformable and semitransparent displays. *Science (New York, N.Y.)*, 325(5943), 977–981. Available from <https://doi.org/10.1126/science.1175690>.
- Saeidpourazar, R., Li, R., Li, Y., Sangid, M. D., Lu, C., Huang, Y., Rogers, J. A., & Ferreira, P. M. (2012). Laser-driven micro transfer placement of prefabricated microstructures. *Journal of Microelectromechanical Systems*, 21(5), 1049–1058. Available from <https://doi.org/10.1109/JMEMS.2012.2203097>.
- Saeidpourazar, R., Sangid, M. D., Rogers, J. A., & Ferreira, P. M. (2012). A prototype printer for laser driven micro-transfer printing. *Advanced Manufacturing Processes*, 14(4), 416–424. Available from <https://doi.org/10.1016/j.jmapro.2012.09.014>, <https://www.sciencedirect.com/science/article/pii/S152661251200076X>.
- Sim, K., Chen, S., Li, Y., Kammoun, M., Peng, Y., Xu, M., Gao, Y., Song, J., Zhang, Y., Ardebili, H., & Yu, C. (2015). High fidelity tape transfer printing based on chemically induced adhesive strength modulation. *Scientific Reports*, 5(1), 16133. Available from <https://doi.org/10.1038/srep16133>.
- Wang, C., Linghu, C., Nie, S., Li, C., Lei, Q., Tao, X., Zeng, Y., Du, Y., Zhang, S., Yu, K., Jin, H., Chen, W., & Song, J. (2020). Programmable and scalable transfer printing with high reliability and efficiency for flexible inorganic electronics. *Science Advances*, 6(25), eabb2393. Available from <https://doi.org/10.1126/sciadv.abb2393>.
- Wie, D. S., Zhang, Y., Kim, M. K., Kim, B., Park, S., Kim, Y. J., Irazoqui, P. P., Zheng, X., Xu, B., Chi, H., & Lee. (2018). Wafer-recyclable, environment-friendly transfer printing for large-scale thin-film nanoelectronics. *Proceedings of the National Academy of Sciences*, 115(31), E7236–E7244. Available from <https://doi.org/10.1073/pnas.1806640115>.
- Wu, J., Kim, S., Chen, W., Carlson, A., Hwang, K. C., Huang, Y., & Rogers, J. A. (2011). Mechanics of reversible adhesion. *Soft Matter*, 7(18), 8657–8662. Available from <https://doi.org/10.1039/C1SM05915G>.
- Xue, Y., Zhang, Y., Feng, X., Kim, S., Rogers, J. A., & Huang, Y. (2015). A theoretical model of reversible adhesion in shape memory surface relief structures and its application in transfer printing. *Journal of the Mechanics and Physics of Solids*, 77, 27–42. Available from <https://doi.org/10.1016/j.jmps.2015.01.001>, <https://www.sciencedirect.com/science/article/pii/S0022509615000022>.
- Yang, S. Y., Carlson, A., Cheng, H., Yu, Q., Ahmed, N., Wu, J., Kim, S., Sitti, M., Ferreira, P. M., Huang, Y., & Rogers, J. A. (2012). Elastomer surfaces with directionally dependent adhesion strength and their use in transfer printing with continuous roll-to-roll applications. *Advanced Materials*, 24(16), 2117–2122. Available from <https://doi.org/10.1002/adma.201104975>.

- Yan, Z., Pan, T., Xue, M., Chen, C., Cui, Y., Yao, G., Huang, L., Liao, F., Jing, W., Zhang, H., Gao, M., Guo, D., Xia, Y., & Lin, Y. (2017). Thermal release transfer printing for stretchable conformal bioelectronics. *Advanced Science*, 4(11)1700251. Available from <https://doi.org/10.1002/adv.201700251>.
- Yi, H., Seong, M., Sun, K., Hwang, I., Lee, K., Cha, C., Kim, T., & Jeong, H. E. (2018). Wet-responsive, reconfigurable, and biocompatible hydrogel adhesive films for transfer printing of nano-membranes. *Advanced Functional Materials*, 28(18)1706498. Available from <https://doi.org/10.1002/adfm.201706498>.
- Yoo, B., Cho, S., Seo, S., & Lee, J. (2014). Elastomeric angled microflaps with reversible adhesion for transfer-printing semiconductor membranes onto dry surfaces. *ACS Appl. Mater. Interfaces*, 6(21), 19247–19253. Available from <https://doi.org/10.1021/am505286b>.
- Yu, Q., Chen, F., Zhou, H., Yu, X., Cheng, H., & Wu, H. (2018). Design and analysis of magnetic-assisted transfer printing. *Journal of Applied Mechanics*, 85(10). Available from <https://doi.org/10.1115/1.4040599>.
- Yu, K., Ge, Q., & Qi, H. J. (2014). Reduced time as a unified parameter determining fixity and free recovery of shape memory polymers. *Nature Communications*, 5(1), 3066. Available from <https://doi.org/10.1038/ncomms4066>.
- Yu, Q., Li, A., Yu, X., Zhou, H., & Cheng, H. (2021). Design of the magnetic stamp film for electromagnetic-assisted transfer printing. *Journal of Applied Mechanics*, 88(7). Available from <https://doi.org/10.1115/1.4050536>.
- Yu, Q., Yu, X., Zhou, H., Chen, F., Cheng, H., & Wu, H. (2019). Effects of material properties and geometric parameters on electromagnetic-assisted transfer printing. *Journal of Physics D: Applied Physics*, 52(25)255302. Available from <https://doi.org/10.1088/1361-6463/ab10b0>.
- Zhang, Y., Kim, B., Gao, Y., Wie, D. S., Lee, C. H., & Xu, B. (2019a). Chemomechanics of transfer printing of thin films in a liquid environment. *International Journal of Solids and Structures*, 180–181, 30–44. Available from <https://doi.org/10.1016/j.ijsolstr.2019.07.011>, <https://www.sciencedirect.com/science/article/pii/S0020768319303221>.
- Zhang, Y., Lu, B., Wang, T., Feng, X., & Xu, H. (2019b). A photochemical approach toward high-fidelity programmable transfer printing. *Advanced Materials Technologies*, 4(9)1900163. Available from <https://doi.org/10.1002/admt.201900163>.
- Zhang, S., Ling, H., Chen, Y., Cui, Q., Ni, J., Wang, X., Hartel, M. C., Meng, X., Lee, K. J., Lee, J., Sun, W., Lin, H., Emaminejad, S., Ahadian, S., Ashammakhi, N., Dokmeci, M. R., & Khademhosseini, A. (2020). Hydrogel-enabled transfer-printing of conducting polymer films for soft organic bioelectronics. *Advanced Functional Materials*, 30(6)1906016. Available from <https://doi.org/10.1002/adfm.201906016>.
- Zhao, J., Guo, Y., Cai, L., Li, H., Wang, K. X., Cho, I. S., Lee, C. H., Fan, S., & Zheng, X. (2016). High-performance ultrathin BiVO₄ photoanode on textured polydimethylsiloxane substrates for solar water splitting. *ACS Energy Lett.*, 1, 68–75. Available from <https://doi.org/10.1021/acsenergylett.6b00032>.

CHAPTER 2

Transfer printing by kinetic control of adhesion

Guorui Wang

CAS Key Laboratory of Mechanical Behavior and Design of Materials, Department of Modern Mechanics, University of Science and Technology of China, Hefei, P.R. China

2.1 Introduction

Stretchable and flexible electronics have gained tremendous attention and indicated a mainstream direction in modern electronics. In striking contrast to conventional rigid electronic devices, they can be integrated comfortably and compliantly into the dynamically deformable human body (Kim et al., 2015; Nathan et al., 2012; Qi et al., 2020; Rogers et al., 2010). So far, flexible electronics in a myriad of forms have underpinned much of the technological innovation in various societal sectors, including health care, displays, sensors, human–machine interfaces, energy conversion, and computing platforms (Nathan et al., 2012).

The multifunctionality and multimodality of flexible electronics originate from layer-by-layer configurations (Wang et al., 2022). The most straightforward approach to constructing flexible electronics is to directly fabricate featured structures and devices on polymer substrates, which is however technically challenging and limited by its universality and cost-effectiveness. In this context, transfer printing offers an alternative solution through transferring prefabricated devices on hard donor substrates to soft acceptor substrates in a high-yield manner (Park et al., 2020). Furthermore, by separating the electronic device fabrication from the integration process, transfer printing circumvents the incompatibility issue between polymer substrates and traditional fabrication technologies, thus accelerating the commercialization of flexible and stretchable electronics.

Typically, transfer printing requires electronic devices with high tolerances to mechanical deformation and conformal adhesion to target surfaces. Among the various transfer printing techniques, kinetically controlled transfer printing that leverages peeling velocity to modulate the adhesion strength at the stamp and the functional material interface is one of the most common and earliest methods for soft electronics (Fig. 2.1). It has been successfully employed to print objects with a broad range of sizes and shapes, including single-crystal silicon and gallium nitride (GaN), mica, highly ordered pyrolytic graphite, silica and so forth, onto various substrates (Meitl et al., 2005). In this chapter,

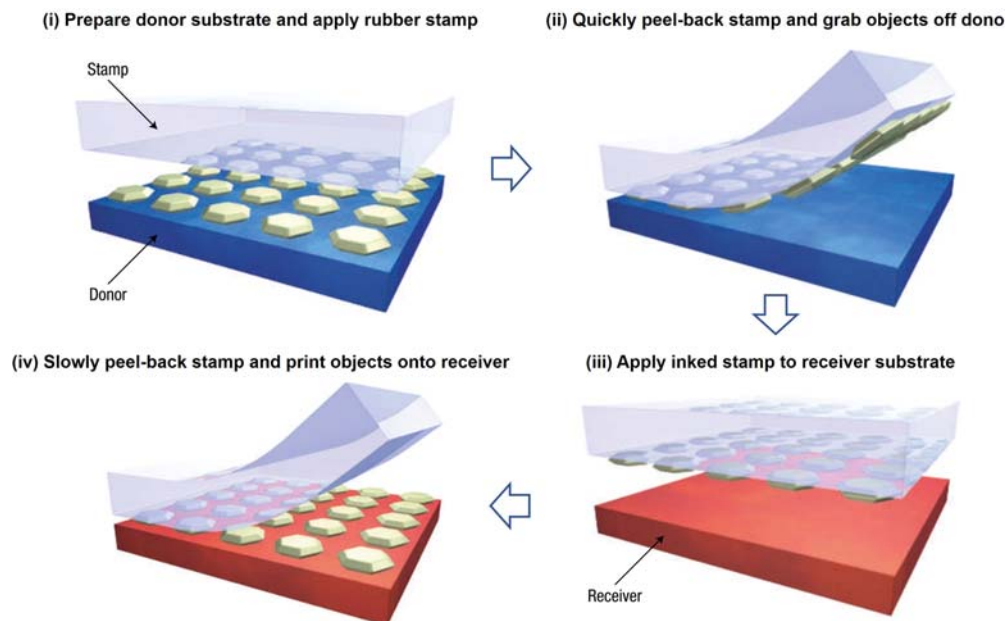


Figure 2.1 Schematic illustration of the kinetically controlled transfer printing process. Adapted from Meitl, M. A., Zhu, Z.-T., Kumar, V., Lee, K. J., Feng, X., Huang, Y. Y., Adesida, I., Nuzzo, R. G., & Rogers, J. A. (2005). *Transfer printing by kinetic control of adhesion to an elastomeric stamp*. *Nature Materials*, 5(1), 33–38.

we will introduce such a transfer printing technique by describing in detail the working principle, mechanics theory, and modulation strategy. A similar rate-dependent transfer strategy that is extended to emerging two-dimensional (2D) materials is also discussed. The conclusion and outlook will also be presented finally to guide the implementation of kinetically controlled transfer printing in flexible and electronic applications.

2.2 Working principle

To explore the full potential of kinetically controlled transfer printing techniques, it is important to understand the working mechanism. In fact, the underlying physics governing the kinetic dependence of the adhesion process originated from the viscoelastic effect of the elastomer stamp such as polydimethylsiloxane (PDMS). In particular, the critical energy release rate tends to increase monotonically with the elevated separation speed. This allows for a tunable adhesion between the stamp and target materials by controlling the peeling speed.

The viscoelastic response of PDMS has been demonstrated early in the last century. For example, Roberts (1979) and Barquins (1992) successively carried out rolling experiments where a ball or a cylinder rolled upon an inclined rubber surface and

gravity worked to separate the steel from the rubber track at the trailing edge of the contact region. The rolling resistance acted as a measure of peeling energy and the loss of gravitational potential was taken as the adhesion energy hysteresis. Since the energy contributed to the advancing contact area at the front of the rolling ball/cylinder was small (She et al., 1998), the adhesion energy hysteresis was considered as the energy release rate (G) (Shull et al., 1998). The experimental results showed that G was altered by more than one order of magnitude during the rolling speed range from 0.02 to 4.8 cm/s. Similar rolling tests were performed for glass rods on PDMS slabs as shown in Fig. 2.2A, where the adhesion energy is almost tripled as the rolling speed increases from 1 to 8 mm/s (Cho et al., 2016).

The rate-dependent adhesion of PDMS was also reported by pull-off force measurements during the unloading stage of indentation tests (Petroli et al., 2022). In the experiments, the PDMS can serve as either the stamp or the substrate layer. Note that, in the latter case, a spherical colloidal probe rather than a sharp tip is necessary as the larger radius of curvature allows the sample to relax; instead, a sharp AFM tip may easily penetrate into the soft PDMS, making it undergo irreversible plastic deformation (Charitidis, 2011; Wang et al., 2022b). For instance, an adhesion test apparatus was developed by Jang et al. (2011) to characterize the adhesion between a spherical PDMS stamp and a silicon substrate. The Johnson–Kendall–Roberts (JKR) contact mechanics model was adopted to analyze the experimental data and the energy release rate could be estimated according to the measured pull-off force and contact radius. It was shown that the pull-off force was greatly enhanced with increasing unloading velocity, corresponding to an elevated adhesion. Based on such a kinetically controlled switch of adhesion, they attempted to detach the silicon membrane from the silicon-on-insulator wafer and found that the transfer process was nearly perfect for an unloading velocity $>50 \mu\text{m/s}$, while failure probability increased dramatically under an unloading velocity of less than $20 \mu\text{m/s}$. Alternatively, Kim et al. conducted an inverse indentation test by pressing the PDMS/SiO₂ samples to fused silica lenses (Kim et al., 2017). It is documented that the pull-off force of the PDMS layer strongly relies on the critical contact area which expands with increasing separation velocity (Fig. 2.2B). Specifically, the energy release rate rises from approximately 0.3 to approximately 5.1 J/m^2 as the separation velocity increased from 2 to $500 \mu\text{m/s}$. By adjusting the adhesion strength of the elastomeric layer via changing separation velocity, the array of silicon chips could be picked up and placed onto flexible substrates, and hence easily rearranged as desired (Fig. 2.2C).

2.3 Mechanics theory

From the mechanics' perspective, the transfer process is deemed as the competing fracture of two interfaces. Considering a stamp subjected to a peel force F detaches from

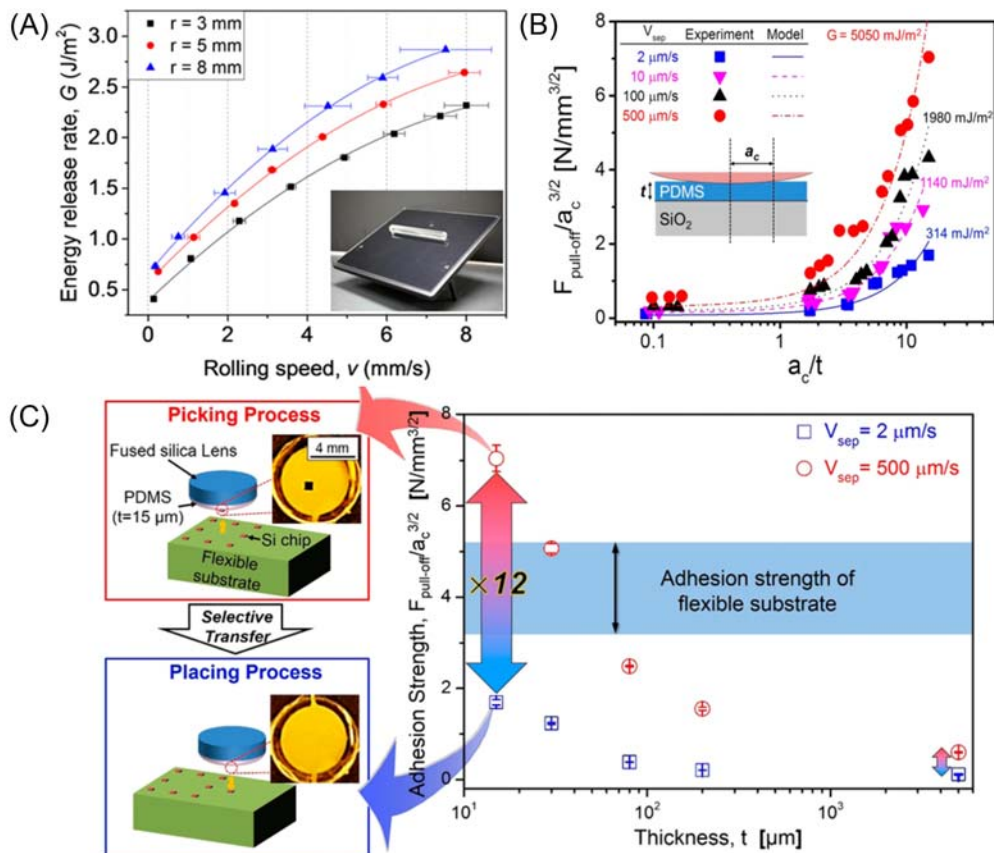


Figure 2.2 (A) Measurements of energy release rates for glass rods with different radii with increasing rolling speed. The inset is the schematic of rolling tests where glass rods roll on inclined polydimethylsiloxane (PDMS) slabs to quantify energy release rates. (B) Normalized pull-off force of the PDMS film as a function of confinement ratio for different separation velocities. (C) Controllable range of the adhesion strength of the PDMS layer for different thicknesses and a flexible substrate when the separation velocity was changed from 2 to 500 $\mu\text{m}/\text{s}$, guiding the design strategy for an elastomeric stamp to realize the reversible transfer of silicon chips onto a flexible substrate. Adapted from (A) Cho, S., Kim, N., Song, K., & Lee, J. (2016) Adhesiveless transfer printing of ultrathin microscale semiconductor materials by controlling the bending radius of an elastomeric stamp. *Langmuir* 32(31), 7951–7957. (B and C) Kim, C., Yoon, M. A., Jang, B., Kim, J. H., Lee, H. J., & Kim, K. S. (2017). Ultimate control of rate-dependent adhesion for reversible transfer process via a thin elastomeric layer. *ACS Applied Material Interfaces*, 9(14), 12886–12892.

the substrate at a constant velocity v , the energy release rate G for steady-state crack propagation at the interface is given by

$$G = F/w \quad (2.1)$$

where w is the width of the stamp in the out-of-plane direction. According to the Griffith theory of fracture (Anderson, 2017), the interfacial crack propagates steadily once G reaches the critical energy release rate. For simplicity, the transfer printing system can be modeled as a trilayer configuration, containing an elastic substrate, an elastic continuous thin film, and a viscoelastic stamp (Feng et al., 2007). As the thin film is peeled apart, either the interface between the substrate and thin film fails or the interface between the thin film and the stamp fails. Therefore, there exists a critical separation velocity above which separation occurs between the film and the substrate that leads to the pickup behavior; on the contrary, the printing will be allowed when the separation velocity is below the critical value so that the separation occurs between the film and the stamp.

This criterion for pickup and printing is illustrated in Fig. 2.3A. As the film and the substrate are both elastic, the critical energy release rate for the film/substrate interface (G_c^{fs}) as an intrinsic material property is independent of the separation velocity, as indicated by the horizontal red line. In contrast, given the viscoelastic nature of the stamp, the critical energy release rate for the stamp/film interface (G_c^{sf}) rests on the peeling speed, which typically follows a power law (Fig. 2.3A):

$$G_c^{sf} = G_0 [1 + (v/v_0)^n] \quad (2.2)$$

where G_0 is the critical energy release rate associated with $v \rightarrow 0$, v_0 is the reference peeling speed at which the critical energy release rate doubles to G_0 , and the exponent n is a

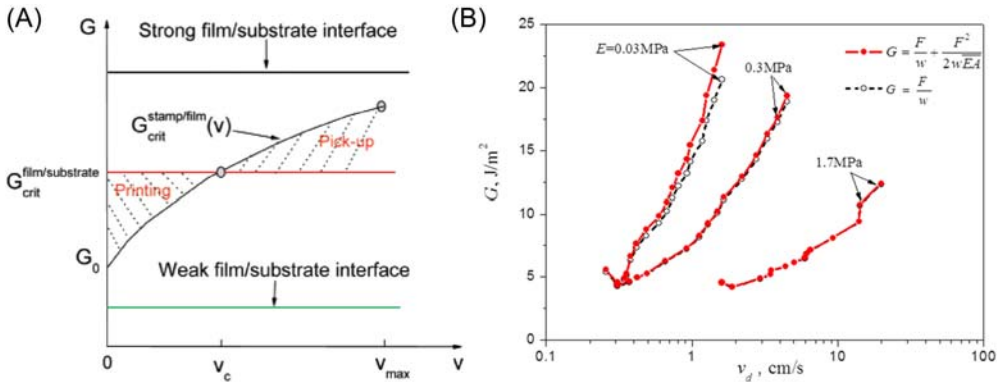


Figure 2.3 (A) Schematic diagram of critical energy release rates for the film/substrate interface and for the stamp/film interface. (B) Comparison of the energy release rates calculated from Eqs. (2.1) and (2.3) for different separation velocities. Adapted from (A) Feng, X., Meitl, M.A., Bowen, A.M., Huang, Y., Nuzzo, R.G., & Rogers, J.A. (2007). *Competing fracture in kinetically controlled transfer printing*. *Langmuir* 23(25),12555–12560. (B) Feng, X., Cheng, H., Bowen, A.M., Carlson, A.W., Nuzzo, R. G., Rogers, J.A. (2013). *A finite-deformation mechanics theory for kinetically controlled transfer printing*. *Journal of Applied Mechanics*, 80(6), 061023.

scaling parameter determined during the experiment. Obviously, increasing the separation velocity would improve G_c^{sf} to exceed G_c^s , thus allowing for a transition from printing to pick up. One thing should be noted that, if the film/substrate interface is quite strong (e.g., chemically bonded) or weak (e.g., high surface roughness) beyond the tunable range, the kinetically controlled transfer printing strategy would be disabled.

Although Eq. (2.1) can well account for the peeling process in most implementations, it suffers two assumptions that limit its application in the highly compliant stamp-based system. On one hand, the model assumes that peeling velocity equals the separation velocity at the film/substrate interface; on the other hand, the incremental elastic energy in the detached stamp is considered negligible compared to the dissipation energy at the film/substrate interface. These two assumptions lead to $Eh \gg G/2$ that only holds for stiff PDMS stamps (e.g., $E \sim 1.7$ MPa) (Kim & Aravas, 1988; Kim & Kim, 1988), where E is Young's modulus of the stamp, h is the stamp thickness.

To this end, Feng et al. (2013) developed a new analytical expression for the steady-state energy release rate for a soft PDMS stamp with $E < 1$ MPa. It is found that G is also dependent on the stiffness of the detached part of the stamp, where the axial stretching becomes significant for a compliant stamp:

$$G = \frac{F}{w} \left(1 + \frac{F}{2EA} \right) \quad (2.3)$$

where A is the cross-sectional area of the stamp. Fig. 2.3B makes a comparison between Eqs. (2.1) and (2.3) to describe the energy release rate as a function of the separation velocity for a PDMS stamp with varying modulus. Clearly, the prediction results from Eqs. (2.1) and (2.3) are highly overlapped for relatively stiff PDMS stamps of 1.7 and 0.3 MPa, while a discrepancy is observed for relatively compliant PDMS stamps of only 0.03 MPa especially at higher separation velocity (> 1 cm/s).

2.4 Modulation strategy

Kinetic approaches to switching adhesion are effective and useful, however, the controllable range of adhesion is limited to a narrow range, thereby restricting the utility of transfer printing for certain cases. In this scenario, extensive research endeavors have been made towards complementary or synergetic strategies for optimization of the transfer capability and efficiency. Several factors that influence adhesion performance are discussed in this section, such as stamp stiffness, stamp thickness, surface patterning, and temperature.

2.4.1 Stamp stiffness

An elementary fracture mechanics analysis shows that the effective failure strength of an adhered contact scales with the critical energy release rate and Young's modulus of

the stamp (Anderson, 2017). As stated in the section above, when the stamp is considerably soft ($E < 1$ MPa), the contribution of axial stretching of the peeled stamp to the energy release rate cannot be neglected. Such a so-called finite deformation effect is anticipated to cause the shift of the critical separation velocity.

As presented in Fig. 2.4A, with increasing tensile stiffness of the stamp, the critical peeling force keeps unvaried because of the constant energy release rate at the film/substrate interface. In contrast, the critical separation velocity for stamps with different moduli displays obvious discrepancy up to two orders of magnitude, as shown in Fig. 2.4B. It can be seen that the critical velocity decreases as the stamp modulus degrades, indicating that film retrieval can be achieved at a lower peeling velocity for softer stamps. This may be beneficial for the transfer printing of inks that are impossible to retrieve with a traditional stiff PDMS stamp ($E \sim 1.7$ MPa).

In addition, it should be noted that a plateau of critical velocity is visible for a certain modulus as shown in Fig. 2.4B. Below the threshold of the stiffness (~ 100 N/m), the critical velocity shows a sluggish increase for thinner stamps. This phenomenon is observed for stamps with different elastic moduli, indicating that thickness plays an important role in the adhesion performance. Besides that, a recent study reported a strain rateredependence of elastic modulus of ultrathin polymer films (Yiu et al., 2020). This may deserve extra attention if the stamp thickness is downscaled to nanometers in the future. These thickness effects will be discussed in detail in the next section.

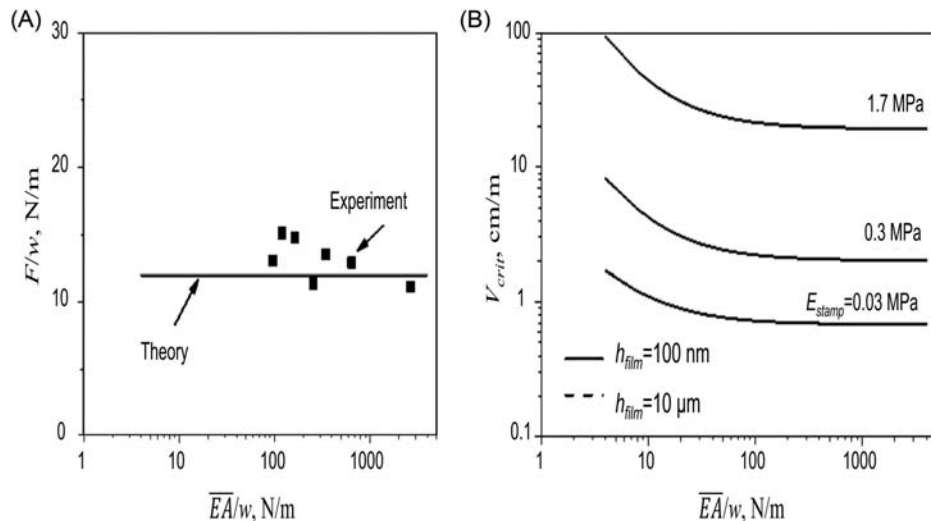


Figure 2.4 (A) The critical peeling force and (B) the critical separation velocity as functions of the tensile stiffness of the stamp for Young's modulus of stamps of 1.7, 0.3, and 0.03 MPa and the thickness of gold films of 100 nm and 10 μ m, respectively. Adapted from Feng, X., Cheng, H., Bowen, A.M., Carlson, A.W., Nuzzo, R.G., & Rogers, J.A. (2013) A finite-deformation mechanics theory for kinetically controlled transfer printing. *Journal of Applied Mechanics*, 80(6), 061023.

2.4.2 Stamp thickness

Both experimental and theoretical works demonstrated that the stamp thickness affects the stress distribution at the interfaces, thus determining the delamination path between two interfaces during the transfer printing process (Bartlett & Crosby, 2014; Luo & Turner, 2020; Shull et al., 2000). Generally, the stress prefers concentrating on the contact edges for thicker substrates, whereas for ultrathin substrates the maximum stress occurs at the center of contact (Fig. 2.5A). Based on the mechanical analysis and

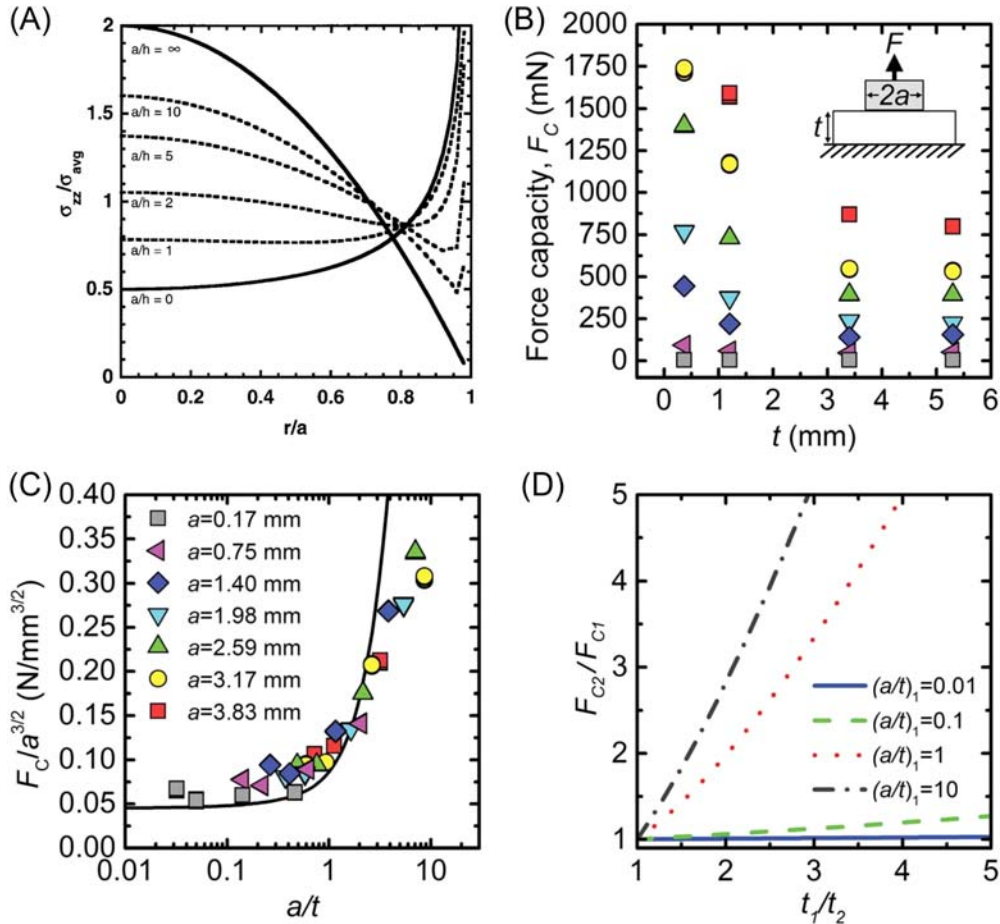


Figure 2.5 (A) Normal stress distribution for a flat, cylindrical punch loaded to a thin elastomeric layer for different thicknesses. (B) Force capacity (i.e., pull-off force) versus film thickness for a range of probe radii. (C) The data plotted in (B) on a linear-log plot of normalized force capacity versus the confinement of the interface. (D) The driving force to transfer an object versus the relative thickness ratio. Adapted from (A) Shull, K.R., Flanigan, C.M., & Crosby, A.J. (2000). Fingering instabilities of confined elastic layers in tension. *Physics Review Letters* 84(14), 3057. (B–D) Bartlett, M.D., & Crosby, A.J. (2014) Material transfer controlled by elastomeric layer thickness. *Material Horizons*, 1(5), 104066.

finite element modeling, Luo and Turner (2020) found that tailoring the stress distribution at the stamp/chip interface would also alter the stress distribution at the chip/substrate interface. Only when the stamp thickness is comparable or lower than that of the chip, can the crack path selection be engineered in the transfer printing process.

In addition to the stress distribution, the stamp thickness also brings the geometric confinement of the interface that was analyzed using contact mechanics in previous research (Ganghoffer & Gent, 1995). As the confinement of the interface increases, the thinner elastomeric layer tends to minimize the strain energy relative to the thicker one. The driving force for separation, namely the strain energy release rate for interfacial failure at the thinner stamp interface, is less than that for the thicker substrate (Crosby & Shull, 1999). On the other hand, the confinement effect may change the mechanical properties of polymers (including Young's modulus) as proven by previous studies using different methods (Vogt, 2018). In this case, the effect of stamp thickness on the transfer printing performance is similar to that of stamp stiffness.

Bartlett and Crosby (2014) performed contact adhesion experiments to quantitatively probe the stamp thickness dependence of the pull-off force. In the experiments, a probe was brought in contact with an elastomeric substrate and then retracted normally to the surface. The maximum force F_c is reached until the interface separates. As depicted in Fig. 2.5B, for a constant punch radius, the measured adhesive force capacity (i.e., pull-off force) gradually increases as the substrate thickness decreases. They further established the relation between the pull-off force and specific geometric parameters of the stamp (Fig. 2.5C), given by (Bartlett & Crosby, 2013)

$$\frac{F_c}{a^{3/2}} \sim \sqrt{G_c E} \sqrt{1 + 1.33 \frac{a}{t} + 1.33 \left(\frac{a}{t}\right)^3} \quad (2.4)$$

where G_c is the critical strain energy release rate of the interface, A is the contact area, C is the compliance in the loading direction, a is the contact radius, and t is the stamp thickness. Apparently, the pull-off force can be modulated by the geometric confinement ratio (a/t) of the interface. As the geometric confinement ratio is enhanced from 0.6 to 8.7, the pull-off force shows a 320% increase for the probe with a contact radius of 3.17 mm. It can be therefore envisaged that, by lowering the compliant stamp thickness, the transfer and release of an object to progressively thinner compliant substrates are enabled. Furthermore, the driving force for the transfer process was defined by the force capacity ratio of the “receiver” compliant substrate (F_{c2}) to the “inked” compliant substrate (F_{c1}). This governing parameter (F_{c2}/F_{c1}) plotted in Fig. 2.5D provides a more clear picture of the stamp thickness modulation mechanism.

Similar stamp thickness-controlled adhesion was observed in another work by Kim et al. (2017), where the confinement effect was introduced to combine with rate-dependent effects. As the confinement ratio increases, the adhesion strength of thin

elastomeric layers could be extended up to 12 times that of the bulk, as presented in Fig. 2.2C. On the basis of an adhesion test, a reversible transfer of silicon-based devices onto the flexible substrate was successfully demonstrated. Since the adhesion of the elastomeric stamp can be tailored by thickness at the millimeter scale, this methodology can be well fit for roll-to-roll transfer of electronic devices in the high-yield fabrication of flexible electronics.

2.4.3 Surface patterning

The interfacial adhesion strength dominated by van der Waals interaction is directly related to the contact area at the interface. Specifically, the delicate design of surface patterns helps alter the contact area and tailor the interfacial adhesion (Chen, Feng, & Huang, Huang, et al., 2013; Kim et al., 2010; Wu et al., 2011; Yoon et al., 2012). In particular, for picking and printing processes, pressure-modulated switchable adhesion was demonstrated in which the contact area between the stamp with microtips and devices was switched by the contact pressure, as shown in Fig. 2.6A (Kim et al., 2010). In this approach, the applied preloads collapse the regions between the microtips and enhance the overall contact area with the chip during the retrieval process, giving rise to a high adhesion between the stamp and chip (upper inset in Fig. 2.6A). Additionally, leveraging the viscoelastic response of the stamp, quick retrieval would maximize the adhesion of the chip to the stamp. Note that, once the stamp is

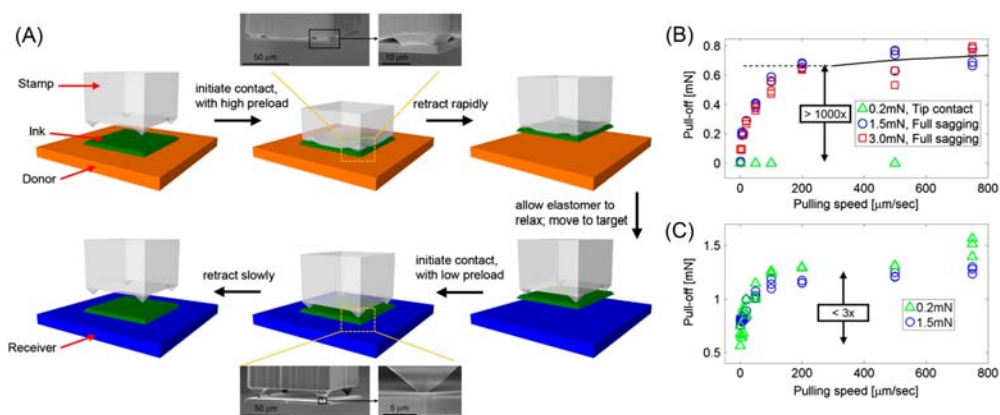


Figure 2.6 (A) Implementation of elastomeric, microtip adhesive surface in a stamp for deterministic assembly by transfer printing. The insets are magnified scanning electron microscopy images of representative elastomeric stamps showing one of the microtips deforming during the transfer process. Plots of force required to remove (B) a microtip surface and (C) a corresponding flat surface from the silicon substrate, as a function of retraction speed for three different preload cases. Adapted from Kim, S., Wu, J., Carlson, A., Jin, S.H., Kovalsky, A., Glass, P., et al. (2010). Microstructured elastomeric surfaces with reversible adhesion and examples of their use in deterministic assembly by transfer printing. *Proceedings of National Academy of Sciences USA*, 107(40), 17095–17100.

retracted, the geometry of microtips would recover under elastic restoring forces, leaving contact only at the sharp points of microtips. In the printing step, the preloads are controlled at a relatively low level to avoid the collapse of microtips and maintain low adhesive surfaces. The slow retrieval further minimizes the adhesion strength, enabling the release and printing of chips.

The underlying mechanics principles can be understood more straightforwardly from Fig. 2.6B, where the tip contact corresponds to a negligible pull-off force (i.e., adhesion) regardless of pulling speed, while increasing preloads causes dramatically enhanced adhesion that can be further tailored by pulling speed. According to the change in contact area captured by SEM images, increasing from approximately 0.07% for the uncollapsed states to approximately 80% for collapsed states, the adhesion strength is expected to improve by up to three orders of magnitude. Such a tunable adhesion range for a surface patterned stamp is much larger than that for a flat one, as presented in Fig. 2.6C.

Another issue of scrutiny is the geometry of the microtip. Not surprisingly, the first key parameter is the radius of curvature of the microtip which is directly correlated to the contact area. The mechanical analysis indicated that the contact radius decreases with microtip radius, reaching an asymptotic value when the microtip radius approaches zero, giving a minimal value ($R_{\text{contact}}^{\text{min}}$):

$$R_{\text{contact}}^{\text{min}} = \frac{32\gamma}{\pi\bar{E}} \tan^2 \frac{\theta}{2} \quad (2.5)$$

where γ is the adhesion energy between the stamp and contacting surface, $\bar{E} = E/(1 - \nu^2)$ is the plane-strain modulus of the stamp, ν is Poisson's ratio, and θ is the angle between two opposite edges of the pyramid. It is evident that existing techniques for fabricating elastomer surfaces (e.g., PDMS) can already achieve the microtip radius well below the value required to realize minimal contact area. In addition to the microtip radius of the patterned stamp, the microtip height and pattern spacing also play a critical role in the transfer efficiency. Specifically, there exists an optimized range for the selection of microtip heights, based on the balance between the strain energy in the stamp with microtips and the adhesion energy between the contacting surfaces. Theoretical analysis also pointed out that, the energy release rate for patterned strips initially decreases and becomes smaller than that of a flat stamp as the pattern spacing increases (Chen, Feng, & Huang, Huang, et al., 2013). Once the spacing reaches a critical value, the microtips self-collapse onto the substrate and enhance the contact area as well as the adhesion strength.

By modifying the density of surface relief structures, Kim et al. investigated in detail the relation between the surface patterning altered contact area and the adhesion strength (Kim et al., 2009). As shown in Fig. 2.7A, reducing the contact area leads to

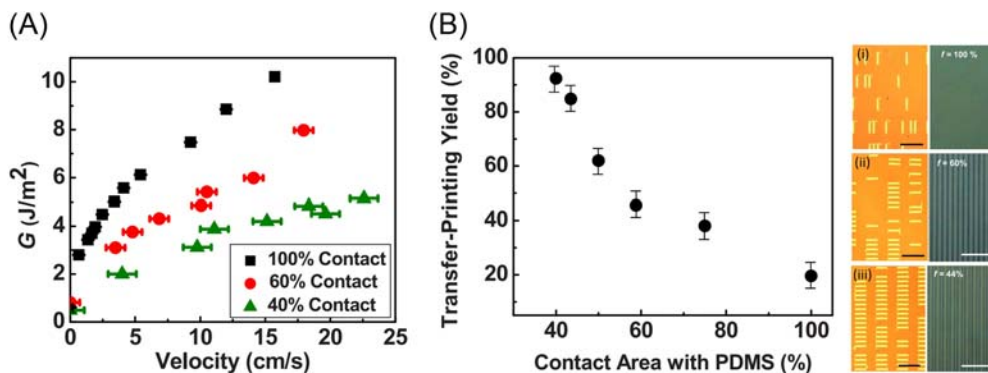


Figure 2.7 (A) Velocity-dependent adhesive strength of structured polydimethylsiloxane (PDMS) stamps with different contact areas. (B) Printing yield as a function of the contact area between structured PDMS stamps and silicon ribbons. Adapted from Kim, T-H., Carlson, A., Ahn, J-H., Won, S. M., Wang, S., Huang, Y., et al. (2009). Kinetically controlled, adhesiveless transfer printing using micro-structured stamps. *Applied Physics Letters*, 94(11), 113502.

a decrease in the adhesive strength. For instance, at a peeling speed of around 10 cm/s , the adhesion for structured stamps having 40% contact area is only half of that for a flat stamp (100% contact). As a result, the transfer printing yield is also affected by the contact area as seen in Fig. 2.7B. While a full contact case leads to a yield of only 20%, the patterned surface enhances the value up to 85% at a 40% contact since the lower adhesion allows a more efficient release and printing.

Directional peeling also offers an alternative way to modulate the contact area (Carlson et al., 2012; Chen, Feng, & Chen, 2013; Yoo et al., 2014). Generally, the degree of shear loading controls the initiation of cracks at the edges of the contact area. The higher loadings yield weaker adhesion. Yang et al. introduced angled surface relief features on PDMS stamps that provide adhesion-switching capability by control of the direction of retraction (Yang et al., 2012). In light of the tilt microtip with $\theta_a < \theta_b$ (Fig. 2.8A) the interfacial crack between the stamp and substrate tends to propagate from the corner at θ_a . Therefore, retracting the stamp along a direction opposite to the orientation of the angle could accelerate the crack propagation from the corner θ_a , thereby leading to a reduced pull-off force. By comparison, if the loading direction goes along the other orientation, the crack propagation would be retarded, yielding an increased pull-off force. As depicted in Fig. 2.8A, the maximum pull-off force is generated at a positive shear strain for an angled microtip, featuring an overall asymmetric distribution. This allows us to tune the pull-off force by simply controlling the direction of the applied separation loads. Namely, higher adhesion can be achieved by applying optimum shear strain along directions that inhibit crack propagation, whereas lower adhesion occurs for shear strains along the direction that accelerates crack propagation, as shown in Fig. 2.8B.

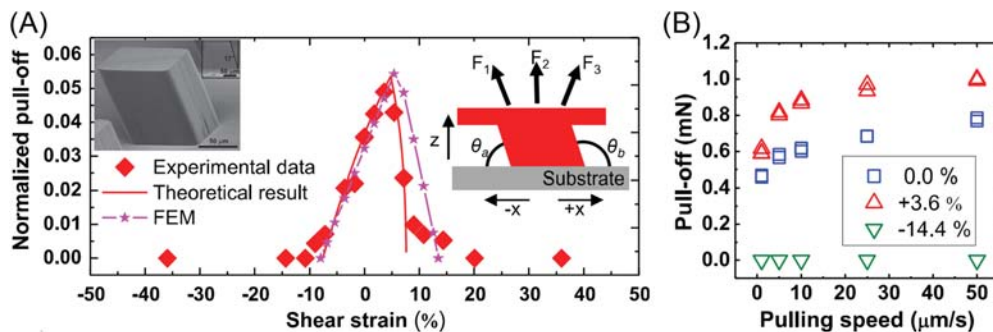


Figure 2.8 (A) Normalized pull-off force for an angled post as a function of shear strain. (B) Measured pull-off forces for an angled post as a function of pulling speed for three different shear strains. Adapted from Yang, S.Y., Carlson, A., Cheng, H., Yu, Q., Ahmed, N., Wu, J., et al. (2012). *Elastomer surfaces with directionally dependent adhesion strength and their use in transfer printing with continuous roll-to-roll applications*. *Advanced Materials*, 24(16), 2117–2122.

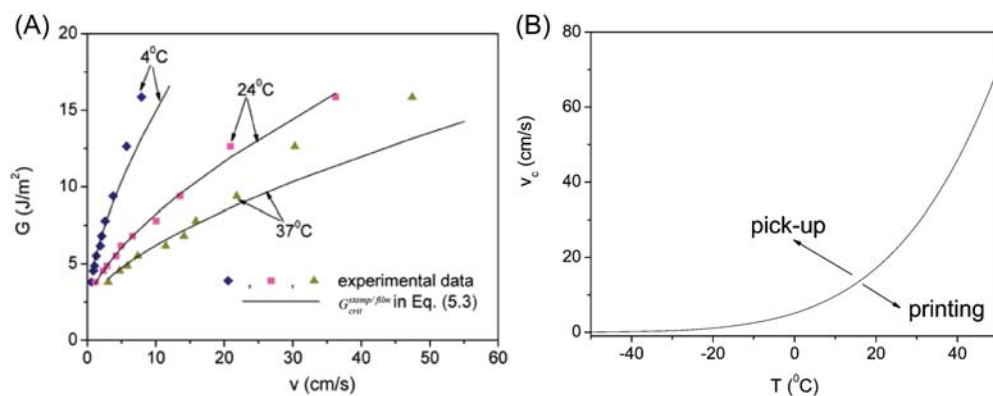


Figure 2.9 (A) Rate-temperature equivalence of the critical energy release rate for the stamp/film interfaces at different temperatures. (B) Critical velocity separating pickup from printing versus temperature. Adapted from Feng, X., Meitl, M.A., Bowen, A.M., Huang, Y., Nuzzo, R. G., & Rogers, J.A. (2007). *Competing fracture in kinetically controlled transfer printing*. *Langmuir*, 23(25), 12555–12560.

2.4.4 Temperature

As viscoelastic properties are highly temperature-dependent, the additional control of the temperature enables a flexible adjustment of adhesion. This was confirmed by Feng et al. who measured the adhesion energy between the stamp and the gold film over a variable temperature range, as shown in Fig. 2.9A. In particular, low temperatures correspond to higher adhesion at the same separation velocity and hence favor the extraction of the target materials, while high temperatures instead favor printing. As expected, the dependence of the critical energy release rate on separation velocity

still follows the theoretical prediction by Eq. (2.2), where a temperature shift factor (a_T) needs to be introduced, as expressed by

$$G_c^{sf} = G_0 [1 + (a_T \nu / \nu_0)^n] \quad (2.6)$$

Empirically, for most polymers within 50 K of the glass transition temperature (T_g), the temperature shift factor can be approximated as

$$\log_{10} a_T = -17.6 \frac{(T - T_g)}{52 + T - T_g} \quad (2.7)$$

Taking the temperature effect into account, the critical separation velocity tends to increase with the temperature as shown in Fig. 2.9B. Consequently, it can be concluded that, it is advantageous for pickup at low temperatures and printing at high temperatures during the kinetically controlled transfer.

Recently, some studies exploited a laser pulse to create local heating at the interface and initiate separation by forces arising from the thermal expansion mismatch between the stamp and adhered materials (Li, Li, Lü, Song, Saeidpouraza, et al., 2012b; Li, Li, Lü, Song, Saeidpourazar, et al., 2012b; Saeidpourazar et al., 2012). Such a thermal effect may also bring forth an additional viscoelastic response of the elastomeric stamp during the transfer printing process.

2.5 Rate-dependent mechanical transfer of graphene

To fulfill the unique demands of next-generation flexible electronics technologies, new materials that go beyond the limit of traditional semiconductors are urgently required. 2D materials, a class of atomically thin materials pioneered by Nobel Laureates Geim and Novoselov following their discovery of graphene in 2004, have emerged as promising building blocks for novel nanoelectronics, providing a full range of material types including insulators, semiconductors and semimetals (Liu et al., 2016; Novoselov, 2005).

There is no doubt that the transfer of 2D materials from the growth substrates to target substrates with large-area, clean, and low defect surfaces is the first step to the realization of 2D material-based devices for practical applications. With the advantages of high compatibility of nano/microstructure patterns, transfer printing technology as discussed above can be a good option for the assembly of various nanomaterials and structures. Therein, the adhesion properties of 2D materials play a central role in the transfer efficiency and yield. So far, numerous studies have reported adhesion measurements of 2D materials interacting with different substrates by a variety of testing methods, including blister/bulging test (Cao et al., 2014; Koenig et al., 2011; Sanchez et al., 2018; Wang, Ma, et al., 2022), indentation test (Fang et al., 2022; Suk et al.,

2016), double cantilever beam (DCB) fracture tests (Na et al., 2017; Na, Suk, Ruoff et al., 2014; Walker et al., 2016; Yoon et al., 2012), buckling instability measurement (Brennan et al., 2015; Dai et al., 2016; Deng et al., 2017; Wang, Gau et al., 2017), etc. The collected data of adhesion energy for various 2D materials have been summarized in reviews (Dai et al., 2020; Megra & Suk, 2019; Wang, Hou et al., 2023), which lay a solid foundation for the understanding and design of the transfer printing process.

However, the atomic thinness of 2D materials renders them prone to mechanical damage during the transfer process and to degradation of their superior electrical and mechanical properties. Hence, in order to transfer large-area 2D materials directly on flexible polymer substrates and reduce the occurrence of breaks, tears, and damages, various strategies have been proposed [e.g., stamp thickness control (Kim, Yoon, Jang, Kim, Kim et al., 2021), interfacial engineering (Tavakoli et al., 2020), etc.], among which the rate dependence of mechanical transfer is one promising approach to address the issue. This is also in reminiscence of the kinetic controlled transfer printing technique that leverages the switchable adhesion, demonstrating the massive transfer of a wide range of materials and devices, including silicon integrated circuits, GaAs lasers, GaN LEDs, etc. (Meitl et al., 2005).

Recently, the kinetic control of adhesion has been extended to the transfer of chemical vapor deposition (CVD) graphene films. Different decohesion modes are identified at different separation speeds during the DCB fracture tests. Liechti and co-workers demonstrated for the first time how graphene can be mechanically delaminated from the copper foil and dry transferred to a target substrate (Na, Suk et al., 2015). By sandwiching the graphene/copper between two silicon strips with epoxy and separating the assembly over a wide range of peeling rates, they were able to control when the graphene/copper or graphene/epoxy interface delaminates. As shown in Fig. 2.10A, the highest displacement rate of 254.0 $\mu\text{m/s}$ allows for a complete separation of graphene from the copper foil, accounting for a successful transfer to the target silicon substrate. When the applied displacement rate was an order of magnitude lower (25.4 $\mu\text{m/s}$), the graphene is prone to delaminate from the epoxy surface instead. Through the experimental measurements and fracture mechanics analysis, the adhesion energy between graphene and its seed copper foil (6.0 J/m^2) and between graphene and the epoxy (3.4 J/m^2) were estimated at the respective loading rates. Such a rate-dependent adhesion, therefore, affords a controllable mechanism for selective transfer of graphene in future nanofabrication systems such as roll-to-roll transfer.

Kang et al. further explored the role of crack deflection in the rate-dependent mechanical transfer of graphene films (Kang et al., 2019). Similar conclusions were drawn based on the DCB fracture experiments that the transfer yield of multilayer graphene increases at a higher loading rate. The rate dependency was well explicable by the degree of crack deflection, which was due to the elastic mismatch between the

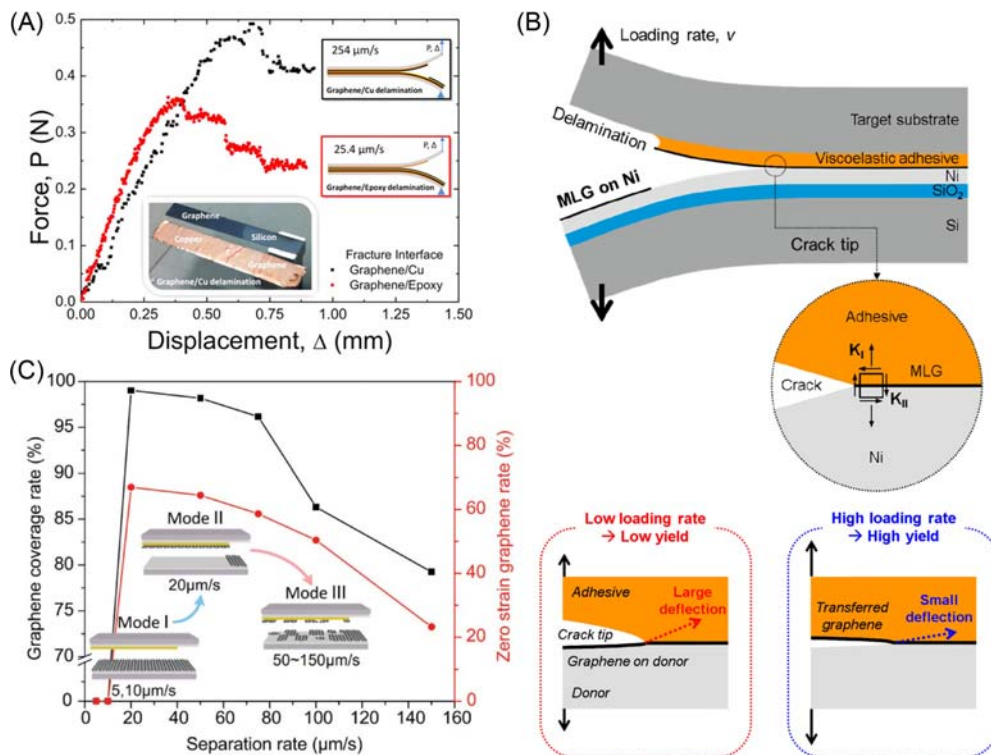


Figure 2.10 (A) Force–displacement responses of double cantilever beam (DCB) fracture experiment at different applied separation rates, giving rise to different fracture interfaces. (B) Schematic diagram of the loading rate controlled DCB fracture test and mode mixity at the crack tip. A large crack deflection occurs at a low loading rate due to a highly mismatched elastic modulus between the nickel and adhesive layers, while the degree of elastic mismatch is mitigated at a high loading rate due to the viscoelastic property of the adhesive, leading to a relatively small crack deflection. (C) Coverage rate and zero strain graphene rate of the transferred graphene as a function of the separation rate. Insets show the schematics of three decohesion modes at varied separation rates. Adapted from (A) Na, S.R., Suk, J.W., Tao, L., Akinwande, D., Ruoff, R.S., Huang, R., et al. (2015). Selective mechanical transfer of graphene from seed copper foil using rate effects. *ACS Nano*, 9(2), 1325–1335. (B) Kang, S., Yoon, T., Kim, S., Kim, T-S. (2019). Role of crack deflection on rate dependent mechanical transfer of multilayer graphene and its application to transparent electrodes. *ACS Applied Nano Materials*, 2(4), 1980–1985. (C) Xu, C., Yang, T., Kang, Y., Li, Q., Xue, T., Liechti, K.M., et al. (2019). Rate-dependent decohesion modes in graphene-sandwiched interfaces. *Advanced Material Interfaces*, 6(23), 1901217.

nickel substrate and the adhesive. Particularly, at a low separation rate, a highly mismatched elastic modulus causes a large deflection at the crack tip because a mode II stress intensity factor is introduced to influence the crack trajectory as illustrated in Fig. 2.10B. By contrast, a high separation rate could increase the elastic modulus of the viscoelastic adhesive and mitigate the degree of elastic mismatch, thereby

decreasing the deflection angle of the crack and enabling more graphene to be detached from the nickel substrate.

Different from earlier reports where a higher separation rate facilitates the dry transfer of graphene with better integrity, a more recent study by Xu et al. (2019) discovered a new decohesion mode, where the transferred graphene was locally fractured and damaged containing a significant level of residual tensile strain as the separation rate was continuously increased (mode III in Fig. 2.10C). In addition, due to the extra energy dissipation by the local fracture and the residual straining, the rate dependence of measured apparent adhesion energy appears more significant and cannot reflect the intrinsic property of the interface. This implies that a moderate separation rate should be adopted to properly measure the adhesion energy and optimize the dry transfer efficiency of graphene with minimum damage and residual strain.

DCB studies have important implications for nanomanufacturing processes such as roll-to-roll transfer, where loading rates can be controlled so as to produce delamination at the desired interface. As illustrated in Fig. 2.11A, Hong et al. have developed a new roll-to-roll system for the dry transfer of large-scale graphene with simultaneous control of peeling tension and speed (Hong et al., 2022). The whole transfer process consists of the lamination, peeling and loading in sequence (Fig. 2.11B). Due to the strain rate effect of the polymer carrier layer, the peeling speed greatly affects the coverage rate and integrity of transferred graphene, as reflected by the sheet's electrical resistance. Fig. 2.11C depicts a Pareto Frontier chart of the peeling conditions which

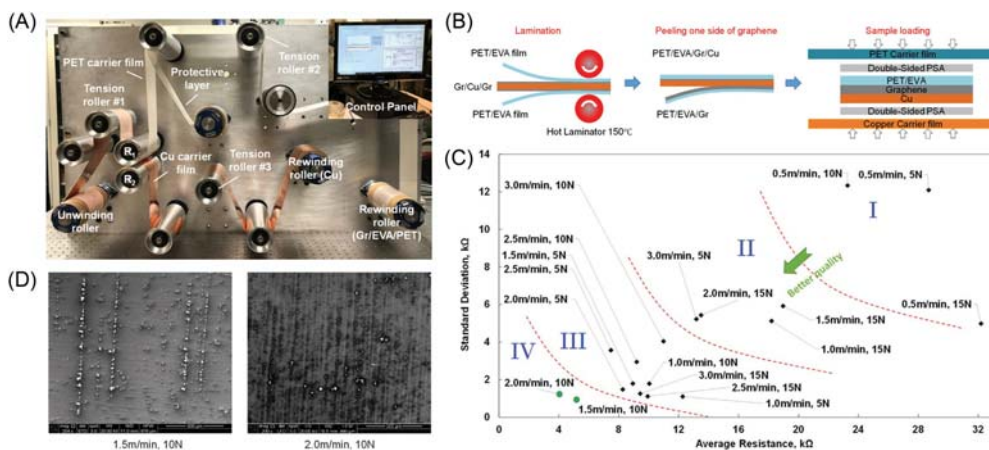


Figure 2.11 (A) Front view of the roll-to-roll graphene transfer system with the control panel. (B) Sample preparation procedure including lamination, peeling and loading. (C) A Pareto Frontier plot of the roll-to-roll dry transfer process of graphene. (D) Scanning electron microscopy images of transferred graphene on polyethylene terephthalate/ethylene vinyl acetate (PET/EVA) under the two identified peeling conditions. Adapted from Hong, N., Kireev, D., Zhao, Q., Chen, D., Akinwande, D., & Li, W. (2022). Roll-to-roll dry transfer of large-scale graphene. *Advanced Materials*, 34(3), e2106615.

is divided into four regions. From Region I to Region II, it is clear that increasing the peeling speed at a given peeling tension can reduce the average resistance and improve the quality of graphene. Leveraging the synergetic effect of moderate peeling tension and speed, the quality of transferred graphene is further improved as seen in Region III. Note that, cracks tend to form at grain boundaries of CVD graphene under considerably high peeling tension, which induces more randomness and higher electrical resistance in the transferred graphene. Therefore, the most desirable conditions are realized for the peeling force of 10 N at a peeling speed of 2 m/min in Region IV, and a lower speed of 1.5 m/min gives rise to a comparable efficacy. Fig. 2.11D displays the SEM images of transferred graphene within Region IV. It is apparent that transferred graphene almost completely covers the substrate for both samples. These results are consistent with the finding from another study, where the peeling speed is regarded as the dominant factor on the graphene coverage at higher speeds, whereas avoiding cracks by choosing a large guiding roller diameter (lower peeling tension) is vital to successful graphene transfer at lower speeds (Xin et al., 2018).

The effect of stamp stiffness was also investigated in a recent study, which is the first demonstration of the rate-dependent transfer printing of graphene using PDMS stamp (Seo et al., 2018). Therein, a unique direct transfer method was proposed using copper instead of the polymeric layer as carrier material. By tuning the mixing ratios of base polymer to curing agent and curing conditions, PDMS stamps of various moduli can be fabricated. Fig. 2.12A plots the graphene transfer yield as a function of the storage modulus of the PDMS stamp at two different peeling rates. As expected, at the same storage modulus values, such as 1.5 MPa, the transfer yield at a low peeling rate

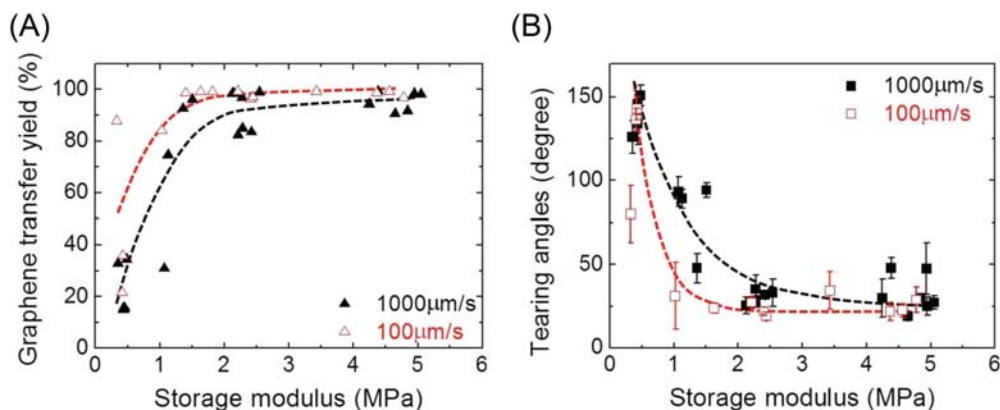


Figure 2.12 (A) Graphene transfer yield versus storage moduli of polydimethylsiloxane stamps. (B) Tearing angles of transferred trilayer graphene by storage moduli. Adapted from Seo, J., Kim, C., Ma, B.S., Lee, T.-I., Bong, J.H., Oh, J.G., et al. (2018). Direct graphene transfer and its application to transfer printing using mechanically controlled, large area graphene/copper freestanding layer. *Advanced Functional Materials*, 28(26), 1707102.

(100 $\mu\text{m/s}$) appears higher than that of the high rate (1000 $\mu\text{m/s}$), which can be interpreted by the rate dependency of adhesion as discussed above. More importantly, it is found that the graphene transfer yield presents an increasing tendency with the growing storage moduli irrespective of peeling rates. There exists a threshold value of storage modulus beyond which a plateau for the transfer yield is observed, implying that the transfer yield in this stage has little relationship with the storage modulus. However, below the threshold modulus is approximately 1.5 MPa for 100 $\mu\text{m/s}$ and approximately 2.0 MPa for 1000 $\mu\text{m/s}$, the transfer yield in this range is closely linked to the storage modulus. Similar relevancy is observed for tearing angles as shown in Fig. 2.12B. In fact, the tearing angle is also associated with the adhesion difference between the graphene and substrates. Buehler and co-workers combined experiments and atomistic simulations to conclude that, small tearing angles (6–8 degrees) hold for low adhesion with SiO_2/Si substrate while PMMA substrates with high adhesion yield large tearing angles (22–30 degrees) (Sen et al., 2010). Consequently, a large tearing angle with high peelings rate in Fig. 2.13B can be explained by the high adhesion to the PDMS stamp.

By tuning the PDMS layer thickness, two common damage mechanisms caused by instability and tensile strain can be suppressed so as to allow large-area damage-free transfer of graphene films using the roll-to-roll transfer machine (Fig. 2.13A). Through in situ observation using optical microscopy, the interfacial crack front can be monitored in real time. As can be seen in Fig. 2.13A(i–iii), the shape and evolution of the interfacial crack front appear quite distinct relying on the stamp thickness. Specifically, for the stamp thickness of 400 μm , the interfacial crack front looks straight and smooth; whereas as the stamp thickness is reduced below 100 μm , it turns into a complex shape resembling fingers and ripples. This discrepancy originated from the adhesion-induced instability of a confined thin film (Ghatak et al., 2000). Typically, if the shear modulus of the polymer layer is lower than 10 MPa, thinner layers are more inclined to deform laterally than thicker ones during the peeling process, hence promoting instability to release the strain energy stored in the film as shown in Fig. 2.13B (Ghatak & Chaudhury, 2003; Shenoy & Sharma, 2001). After the complete removal of transfer films, interestingly, only the transfer process with a 100- μm thick PDMS layer yields no structural damage in the view. By contrast, using a higher (400 μm) or lower (25 μm) stamp thickness would make the transferred graphene severely cracked and torn [Fig. 2.13A(ii and iii)].

To quantify the instability, an instability ratio is defined as the overall length (L) of the interfacial crack front divided by the reference length (L_0). As plotted in Fig. 2.13C, the instability ratio rises as the stamp thickness decreases especially below approximately 50 μm , regardless of mixing ratio and surface treatment of PDMS. The real-time optical imaging further validates that the interfacial crack front at the end of the fingers propagated much faster to spread damages for thinner stamps. Fig. 2.13D

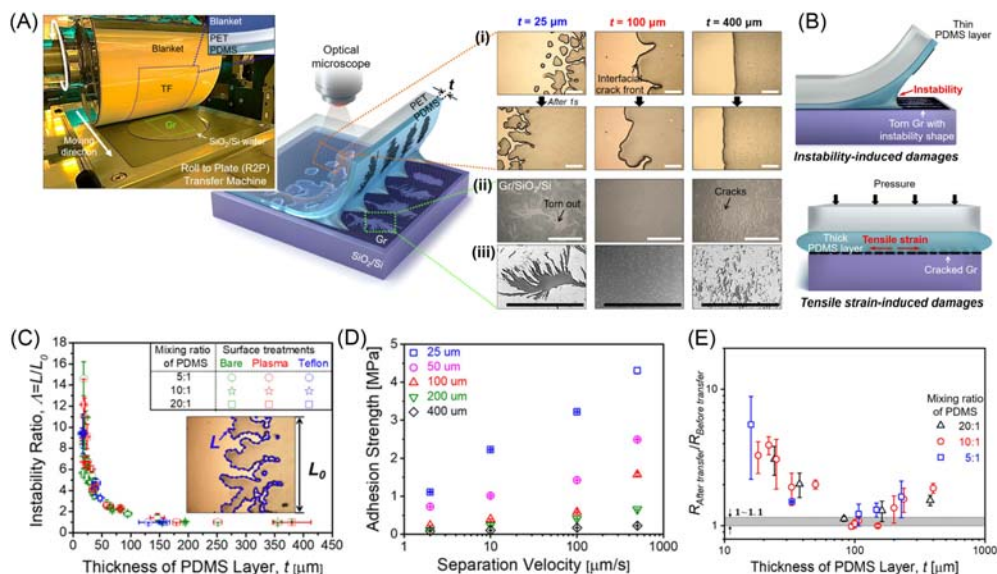


Figure 2.13 (A) Photograph of the roll-to-roll transfer machine and schematic illustration showing the transfer of large-area graphene onto the SiO₂/Si substrate using the transfer films, where the interfacial crack front is observed in real time using optical microscopy. (B) Schematic illustration showing the structural damage mechanism occurring during the transfer process and the role of the polydimethylsiloxane (PDMS) layer thickness. (C) Instability ratio as a function of the PDMS layer thickness, PDMS mixing ratio, and SiO₂/Si substrate surface treatment. (D) Rate-dependent adhesion characteristics of the PDMS layer for different PDMS layer thicknesses. (E) Sheet resistance changes of the transferred graphene before and after the transfer process as a function of the PDMS layer thickness. When the thickness of the PDMS layer was approximately 100 μm , the change in sheet resistance was minimal due to the reduced structural damage irrespective of the PDMS mixing ratio. Adapted from Kim, C., Yoon, M-A., Jang, B., Kim, H-D., Kim, J-H., Hoang, A.T., et al. (2021). *Damage-free transfer mechanics of 2-dimensional materials: Competition between adhesion instability and tensile strain*. NPG Asia Materials, 13(1), 44.

shows the relationship between the separation velocity and adhesion strength, which is aligned with previous studies. Note that, the enhancement in adhesion strength was more substantial for thinner PDMS stamps ($<100 \mu\text{m}$), corresponding to the propagation shape of the instability.

As the stamp thickness increases, the adhesion instability is found to disappear; however, higher thickness endows the stamp with a high stiffness so that the tensile strain in the layer along the circumferential direction of the roller due to contact pressure may exceed the failure strain of graphene and result in the formation of cracks. In this case, it can be envisioned that an optimal layer thickness should be selected to minimize both of these two damage mechanisms and achieve a damage-free transfer. As shown in Fig. 2.13E, according to the change in the electrical resistance of graphene before and after the transfer, the optimal PDMS thickness is set as approximately 100 μm .

2.6 Conclusions and prospects

As an emerging micromanufacturing and assembly technology for flexible electronics, microtransfer printing has generated increasing interest over the last decade due to its unique capability of deterministically integrating diverse heterogeneous materials into various structures and layouts. It creates a vast number of new applications and industrialization opportunities for next-generation flexible and stretchable electronics, which are impossible by conventional pick-and-place techniques. Basically, the successful transfer printing process hinges on the modulation of the interfacial adhesion at different material/structural interfaces. To this end, substantial efforts have been dedicated to exploring feasible methods for the modulation of adhesion strength. Compared with other transfer printing methods (e.g., surface chemistry- and solvent-assisted transfer printing, laser-driven noncontact transfer printing, gecko-inspired transfer printing), the kinetically controlled transfer printing technique provides the most versatile and convenient scheme.

In this review, recent advancements in transfer printing by kinetically controlled adhesion are overviewed. Detailed discussions are provided from basic working principles to state-of-the-art demonstrations. Despite the achieved progress, there is a continuing need for further development before it becomes reliable manufacturing candidate for the industrialized manufacturing of flexible electronics. Currently, the kinetically controlled transfer printing technique still suffers some limitations.

Firstly, the adhesion modulation range is limited at a certain peeling velocity and the adhesion switchability is relatively low. One potential solution is to combine a kinetically controlled adhesion mechanism with other modulation strategies to create a synergistic effect, for example, through the design of surface relief structures as discussed above. In addition, some new materials and technologies are urgent to be introduced. For instance, the stamp properties and geometries can be effectively modified by using shape memory polymers, whose elastic modulus can be changed by approximately 1000 times under external stimuli such as heat (Wang & Urban, 2020). In fact, several studies have demonstrated the use of shape memory polymer stamps for high-yield microtransfer printing. On the other hand, three-dimensional printing technology allows for the delicate design and precise fabrication of stamps with desired properties and structures, even with gradient features (Zhou et al., 2020). This could tremendously improve the tunability and broaden the adhesion strength range.

Secondly, graphene and the plethora of other two-dimensional materials are demonstrated as promising candidates for next-generation flexible electronics. Their huge specific surface area makes surface forces likely to be dominant when integrated into electronic devices as well as in micro/nanoelectromechanical systems. This may induce some novel deformation and failure mechanisms, such as spontaneous self-tearing and peeling (Annett & Cross, 2016). However, a lack of theoretical guidance, which helps

estimate their mechanical robustness and adhesion properties in a device under complex deformation and build the ideal device layout for designated applications, becomes the current bottleneck. Thus, a further in-depth experimental mechanics study of two-dimensional materials is necessary. The essential relationship between the process parameters and interface interactions (e.g., interfacial shear strength/friction, adhesion strength, fracture mechanics, etc.) can undoubtedly provide quantitative guidance for the high reliability of transfer. Computationally, through a richer database of the physical properties of materials and a more mature model between micromechanical performance of devices and materials, can three-dimensional printing and artificial intelligence be incorporated to develop high-performance flexible electronics.

Lastly, the additional instrument for precise control of velocity is required which increases the complexity and post challenges in its integration into assembly line production. Even though small-area transfer schemes have been extensively validated at a lab scale, a further improvement in the reliability, accuracy, and efficiency of industrial-scale transfer techniques is still an area to be developed. These challenges can probably be overcome by further optimization of the structural design and manufacturing processes of transfer heads. Obviously, as a multidisciplinary problem, transfer printing represents an interesting combination of fracture mechanics, material science, chemistry, microfabrication/processing, and electronics, which not only necessitates more endeavors and inputs from different research fields but also requires more concerted efforts and deeper cooperations from academia and industry.

References

- Anderson, T. L. (2017). *Fracture mechanics: Fundamentals and applications*. CRC press.
- Annett, J., & Cross, G. L. (2016). Self-assembly of graphene ribbons by spontaneous self-tearing and peeling from a substrate. *Nature*, 535(7611), 271–275. Available from <https://doi.org/10.1038/nature18304>, <http://www.ncbi.nlm.nih.gov/pubmed/27411633>.
- Barquins, M. (1992). Adherence, friction and wear of rubber-like materials. *Wear*, 158(1–2), 87–117.
- Bartlett, M. D., & Crosby, A. J. (2014). Material transfer controlled by elastomeric layer thickness. *Materials Horizons*, 1(5), 507–512.
- Bartlett, M. D., & Crosby, A. J. (2013). Scaling normal adhesion force capacity with a generalized parameter. *Langmuir: the ACS Journal of Surfaces and Colloids*, 29(35), 11022–11027.
- Brennan, C. J., Nguyen, J., Yu, E. T., & Lu, N. S. (2015). Interface adhesion between 2D materials and elastomers measured by buckle delaminations. *Advanced Materials Interfaces*, 2(16), 1500176, <http://<Go to ISI>://WOS:000368224600002>. Artn 1500176.
- Cao, Z., Wang, P., Gao, W., Tao, L., Suk, J. W., Ruoff, R. S., Akinwande, D., Huang, R., & Liechti, K. M. (2014). A blister test for interfacial adhesion of large-scale transferred graphene. *Carbon*, 69, 390–400. Available from <https://doi.org/10.1016/j.carbon.2013.12.041>.
- Carlson, A., Wang, S., Elvikis, P., Ferreira, P. M., Huang, Y., & Rogers, J. A. (2012). Active, programmable elastomeric surfaces with tunable adhesion for deterministic assembly by transfer printing. *Advanced Functional Materials*, 22(21), 4476–4484. Available from <https://doi.org/10.1002/adfm.201201023>.
- Charitidis, C. (2011). Nanoscale deformation and nanomechanical properties of soft matter study cases: Polydimethylsiloxane, cells and tissues. *International Scholarly Research Notices*, 2011, 1–13.

- Chen, H., Feng, X., & Chen, Y. (2013). Directionally controlled transfer printing using micropatterned stamps. *Applied Physics Letters*, 103(15), 151607. Available from <https://doi.org/10.1063/1.4824976>.
- Chen, H., Feng, X., Huang, Y., Huang, Y., & Rogers, J. A. (2013). Experiments and viscoelastic analysis of peel test with patterned strips for applications to transfer printing. *Journal of the Mechanics and Physics of Solids*, 61(8), 1737–1752. Available from <https://doi.org/10.1016/j.jmps.2013.04.001>.
- Cho, S., Kim, N., Song, K., & Lee, J. (2016). Adhesiveless transfer printing of ultrathin microscale semiconductor materials by controlling the bending radius of an elastomeric stamp. *Langmuir: the ACS Journal of Surfaces and Colloids*, 32(31), 7951–7957. Available from <https://doi.org/10.1021/acs.langmuir.6b01880>, <https://www.ncbi.nlm.nih.gov/pubmed/27458878>.
- Crosby, A. J., & Shull, K. R. (1999). Adhesive failure analysis of pressure-sensitive adhesives. *Journal of Polymer Science Part B: Polymer Physics*, 37(24), 3455–3472.
- Dai, Z., Lu, N., Liechti, K. M., & Huang, R. (2020). Mechanics at the interfaces of 2D materials: Challenges and opportunities. *Current Opinion in Solid State and Materials Science*, 24(4), 100837. Available from <https://doi.org/10.1016/j.cossms.2020.100837>.
- Deng, S., Gao, E., Xu, Z., & Berry, V. (2017). Adhesion energy of MoS₂ thin films on silicon-based substrates determined via the attributes of a single MoS₂ wrinkle. *ACS Applied Material Interfaces*, 9(8), 7812–7818. Available from <https://www.ncbi.nlm.nih.gov/pubmed/28124892>.
- Dai, Z., Wang, G., Liu, L., Hou, Y., Wei, Y., & Zhang, Z. (2016). Mechanical behavior and properties of hydrogen bonded graphene/polymer nano-interfaces. *Composites Science and Technology*, 136, 1–9. Available from <https://doi.org/10.1016/j.compscitech.2016.09.005>.
- Fang, Z., Dai, Z., Wang, B., Tian, Z., Yu, C., Chen, Q., & Wei, X. (2022). Pull-to-peel of two-dimensional materials for the simultaneous determination of elasticity and adhesion. *Nano Letters*. Available from <https://doi.org/10.1021/acs.nanolett.2c03145>, <https://www.ncbi.nlm.nih.gov/pubmed/36472369>.
- Feng, X., Cheng, H., Bowen, A. M., Carlson, A. W., Nuzzo, R. G., & Rogers, J. A. (2013). A finite-deformation mechanics theory for kinetically controlled transfer printing. *Journal of Applied Mechanics*, 80(6), 061023. Available from <https://doi.org/10.1115/1.4023963>.
- Feng, X., Meitl, M. A., Bowen, A. M., Huang, Y., Nuzzo, R. G., & Rogers, J. A. (2007). Competing fracture in kinetically controlled transfer printing. *Langmuir: the ACS Journal of Surfaces and Colloids*, 23(25), 12555–12560. Available from <https://doi.org/10.1021/la701555n>, <https://www.ncbi.nlm.nih.gov/pubmed/17990898>.
- Ganghoffer, J. F., & Gent, A. N. (1995). Adhesion of a rigid punch to a thin elastic layer. *The Journal of Adhesion*, 6(1–4), 75–84.
- Ghatak, A., & Chaudhury, M. K. (2003). Adhesion-induced instability patterns in thin confined elastic film. *Langmuir: the ACS Journal of Surfaces and Colloids*, 19(7), 2621–2631.
- Ghatak, A., Chaudhury, M. K., Shenoy, V., & Sharma, A. (2000). Meniscus instability in a thin elastic film. *Physical Review Letters*, 85(20), 4329.
- Hong, N., Kireev, D., Zhao, Q., Chen, D., Akinwande, D., & Li, W. (2022). Roll-to-roll dry transfer of large-scale graphene. *Advanced Materials*, 34(3), e2106615. Available from <https://doi.org/10.1002/adma.202106615>, <https://www.ncbi.nlm.nih.gov/pubmed/34751484>.
- Jang, B., Kim, K. S., Kim, J. H., Choi, H. J., Park, H. S., & Lee, H. J. (2011). Rate-dependent adhesion between a spherical pdms stamp and silicon substrate for a transfer-assembly process. *The Journal of Adhesion*, 87(7–8), 744–754. Available from <https://doi.org/10.1080/00218464.2011.597302>.
- Kang, S., Yoon, T., Kim, S., & Kim, T. S. (2019). Role of crack deflection on rate dependent mechanical transfer of multilayer graphene and its application to transparent electrodes. *ACS Applied Nano Materials*, 2(4), 1980–1985. Available from <https://doi.org/10.1021/acsanm.9b00014>.
- Kim, K. S., & Aravas, N. (1988). Elastoplastic analysis of the peel test. *International Journal of Solids and Structures*, 24(4), 417–435.
- Kim, T. H., Carlson, A., Ahn, J. H., Won, S. M., Wang, S., Huang, Y., & Rogers, J. A. (2009). Kinetically controlled, adhesiveless transfer printing using microstructured stamps. *Applied Physics Letters*, 94(11), 113502.
- Kim, S. J., Choi, K., Lee, B., Kim, Y., & Hong, B. H. (2015). Materials for flexible, stretchable electronics: Graphene and 2D materials. *Annual Review of Materials Research*, 45(1), 63–84. Available from <https://doi.org/10.1146/annurev-matsci-070214-020901>.

- Kim, K. S., & Kim, J. (1988). Elasto-plastic analysis of the peel test for thin film adhesion. *Journal of Engineering Material Technology*, 110(3), 266–273.
- Kim, S., Wu, J., Carlson, A., Jin, S. H., Kovalsky, A., Glass, P., Liu, Z., Ahmed, N., Elgan, S. L., Chen, W., Ferreira, P. M., Sitti, M., Huang, Y., & Rogers, J. A. (2010). Microstructured elastomeric surfaces with reversible adhesion and examples of their use in deterministic assembly by transfer printing. *Proceedings of National Academy of Science United States of America*, 107(40), 17095–17100. Available from <https://doi.org/10.1073/pnas.1005828107>, <https://www.ncbi.nlm.nih.gov/pubmed/20858729>.
- Kim, C., Yoon, M. A., Jang, B., Kim, H. D., Kim, J. H., Hoang, A. T., Ahn, J. H., Jung, H. J., Lee, H. J., & Kim, K. S. (2021). Damage-free transfer mechanics of 2-dimensional materials: Competition between adhesion instability and tensile strain. *NPG Asia Materials*, 13(1), 44. Available from <https://doi.org/10.1038/s41427-021-00311-1>.
- Kim, C., Yoon, M. A., Jang, B., Kim, J. H., Lee, H. J., & Kim, K. S. (2017). Ultimate control of rate-dependent adhesion for reversible transfer process via a thin elastomeric layer. *ACS Applied Material Interfaces*, 9(14), 12886–12892. Available from <https://doi.org/10.1021/acsami.7b02214>, <https://www.ncbi.nlm.nih.gov/pubmed/28338313>.
- Koenig, S. P., Boddeti, N. G., Dunn, M. L., & Bunch, J. S. (2011). Ultrastrong adhesion of graphene membranes. *Nature and Nanotechnology*, 6(9), 543–546. Available from <https://doi.org/10.1038/nnano.2011.123>, <http://www.ncbi.nlm.nih.gov/pubmed/21841794>.
- Liu, Y., Weiss, N. O., Duan, X., Cheng, H. C., Huang, Y., & Duan, X. (2016). Van der Waals heterostructures and devices. *Nature Reviews Materials*, 1(9), 16042. Available from <https://doi.org/10.1038/natrevmats.2016.42>.
- Li, R., Li, Y., Lü, C., Song, J., Saeidpourazar, R., Fang, B., Zhong, Y., Ferreira, P. M., Rogers, J. A., & Huang, Y. (2012b). Axisymmetric thermo-mechanical analysis of laser-driven non-contact transfer printing. *International Journal of Fracture*, 176, 189–194.
- Li, R., Li, Y., Lü, C., Song, J., Saeidpouraza, R., Fang, B., Zhong, Y., Ferreira, P. M., Rogers, J. A., & Huang, Y. (2012b). Thermo-mechanical modeling of laser-driven non-contact transfer printing: Two-dimensional analysis. *Soft Matter*, 8(27), 7122–7127.
- Luo, A., & Turner, K. T. (2020). Mechanics of crack path selection in microtransfer printing: Challenges and opportunities for process control. *Journal of the Mechanics and Physics of Solids*, 143, 104066.
- Megra, Y. T., & Suk, J. W. (2019). Adhesion properties of 2D materials. *Journal of Physics D: Applied Physics*, 52(36), 364002. Available from <https://doi.org/10.1088/1361-6463/ab27ad>.
- Meitl, M. A., Zhu, Z. T., Kumar, V., Lee, K. J., Feng, X., Huang, Y. Y., Adesida, I., Nuzzo, R. G., & Rogers, J. A. (2005). Transfer printing by kinetic control of adhesion to an elastomeric stamp. *Nature Materials*, 5(1), 33–38. Available from <https://doi.org/10.1038/nmat1532>.
- Nathan, A., Ahnood, A., Cole, M.T., Lee, S., Suzuki, Y., Hiralal, P., Bonaccorso, F., Hasan, T., Garcia-Gancedo, L., Dyadyusha, A., Haque, S., Andrew, P., Hofmann, S., Moultrie, J., Chu, D.P., Flewitt, A.J., Ferrari, A.C., Kelly, M.J., Robertson, J., ... Milne, W.I. (2012). Flexible electronics: The next ubiquitous platform. *Proceedings of the IEEE*, 2012 1486–1517 <http://<Go to ISI>://WOS:000309838000036>. Available from <https://doi.org/10.1109/Jproc.2012.2190168>.
- Na, S. R., Kim, Y., Lee, C., Liechti, K. M., & Suk, J. W. (2017). Adhesion and self-healing between monolayer molybdenum disulfide and silicon oxide. *Scientific Reports*, 7(1), 14740. Available from <https://doi.org/10.1038/s41598-017-14921-9>, <https://www.ncbi.nlm.nih.gov/pubmed/29116198>.
- Na, S. R., Suk, J. W., Ruoff, R. S., Huang, R., & Liechti, K. M. (2014). Ultra long-range interactions between large area graphene and silicon. *ACS Nano*, 8(11), 11234–11242.
- Na, S. R., Suk, J. W., Tao, L., Akinwande, D., Ruoff, R. S., Huang, R., & Liechti, K. M. (2015). Selective mechanical transfer of graphene from seed copper foil using rate effects. *ACS Nano*, 9(2), 1325–1335. Available from <https://doi.org/10.1021/nn505178g>, <http://<GotoISI>://WOS:000349940500029>.
- Novoselov, K. S. (2005). Two-dimensional atomic crystals. *Proceedings of the National Academy of Sciences*, 102(30), 10451–10453.
- Park, J., Lee, Y., Lee, H., & Ko, H. (2020). Transfer printing of electronic functions on arbitrary complex surfaces. *ACS Nano*, 14(1), 12–20. Available from <https://doi.org/10.1021/acsnano.9b09846>, <https://www.ncbi.nlm.nih.gov/pubmed/31913600>.

- Petroli, A., Petroli, M., Romagnoli, M., & Geoghegan, M. (2022). Determination of the rate-dependent adhesion of polydimethylsiloxane using an atomic force microscope. *Polymer*, *262*, 125445. Available from <https://doi.org/10.1016/j.polymer.2022.125445>.
- Qi, D., Zhang, K., Tian, G., Jiang, B., & Huang, Y. (2020). Stretchable electronics based on PDMS substrates. *Advanced Material*, e2003155. Available from <https://doi.org/10.1002/adma.202003155>, <https://www.ncbi.nlm.nih.gov/pubmed/32830370>.
- Roberts, A. D. (1979). Looking at rubber adhesion. *Rubber Chemistry and Technology*, *52*(1), 23–42.
- Rogers, J. A., Someya, T., & Huang, Y. (2010). Materials and mechanics for stretchable electronics. *Science (New York, N.Y.)*, *327*(5973), 1603–1607. Available from <https://doi.org/10.1126/science.1182383>, <http://www.ncbi.nlm.nih.gov/pubmed/20339064>.
- Saeidpourazar, R., Li, R., Li, Y., Sangid, M. D., Lu, C., Huang, Y., Rogers, J. A., & Ferreira, P. M. (2012). Laser-driven micro transfer placement of prefabricated microstructures. *Journal of Microelectromechanical Systems*, *21*(5), 1049–1058.
- Sanchez, D. A., Dai, Z., Wang, P., Cantu-Chavez, A., Brennan, C. J., Huang, R., & Lu, N. (2018). Mechanics of spontaneously formed nanoblisters trapped by transferred 2D crystals. *Proceedings of the National Academy of Science USA*, *115*(31), 7884–7889. Available from <https://doi.org/10.1073/pnas.1801551115>, <https://www.ncbi.nlm.nih.gov/pubmed/30006468>.
- Sen, D., Novoselov, K. S., Reis, P. M., & Buehler, M. J. (2010). Tearing graphene sheets from adhesive substrates produces tapered nanoribbons. *Small (Weinheim an der Bergstrasse, Germany)*, *6*(10), 1108–1116. Available from <https://doi.org/10.1002/sml.201000097>, <http://www.ncbi.nlm.nih.gov/pubmed/20449852>.
- Seo, J., Kim, C., Ma, B. S., Lee, T. I., Bong, J. H., Oh, J. G., Cho, B. J., & Kim, T. S. (2018). Direct graphene transfer and its application to transfer printing using mechanically controlled, large area graphene/copper freestanding layer. *Advanced Functional Materials*, *28*(26), 1707102. Available from <https://doi.org/10.1002/adfm.201707102>.
- Shenoy, V., & Sharma, A. (2001). Pattern formation in a thin solid film with interactions. *Physical Review Letters*, *86*(1), 119.
- She, H., Malotky, D., & Chaudhury, M. K. (1998). Estimation of adhesion hysteresis at polymer/oxide interfaces using rolling contact mechanics. *Langmuir: the ACS Journal of Surfaces and Colloids*, *14*(11), 3090–3100.
- Shull, K. R., Ahn, D., Chen, W. L., Flanigan, C. M., & Crosby, A. J. (1998). Axisymmetric adhesion tests of soft materials. *Macromolecular Chemistry and Physics*, *199*(4), 489–511.
- Shull, K. R., Flanigan, C. M., & Crosby, A. J. (2000). Fingering instabilities of confined elastic layers in tension. *Physical Review Letters*, *84*(14), 3057.
- Suk, J. W., Na, S. R., Stromberg, R. J., Stauffer, D., Lee, J., Ruoff, R. S., & Liechti, K. M. (2016). Probing the adhesion interactions of graphene on silicon oxide by nanoindentation. *Carbon*, *103*, 63–72. Available from <https://doi.org/10.1016/j.carbon.2016.02.079>.
- Tavakoli, M. M., Azzellino, G., Hempel, M., Lu, A. Y., Martin-Martinez, F. J., Zhao, J., Yeo, J., Palacios, T., Buehler, M. J., & Kong, J. (2020). Synergistic roll-to-roll transfer and doping of CVD-graphene using parylene for ambient-stable and ultra-lightweight photovoltaics. *Advanced Functional Materials*, *30*(31), 2001924. Available from <https://doi.org/10.1002/adfm.202001924>.
- Vogt, B. D. (2018). Mechanical and viscoelastic properties of confined amorphous polymers. *Journal of Polymer Science Part B: Polymer Physics*, *56*(1), 9–30. Available from <https://doi.org/10.1002/polb.24529>.
- Walker, E. S., Na, S. R., Jung, D., March, S. D., Kim, J. S., Trivedi, T., Li, W., Tao, L., Lee, M. L., Liechti, K. M., Akinwande, D., & Bank, S. R. (2016). Large-area dry transfer of single-crystalline epitaxial bismuth thin films. *Nano Letters*, *16*(11), 6931–6938. Available from <https://doi.org/10.1021/acs.nanolett.6b02931>, <http://www.ncbi.nlm.nih.gov/pubmed/27775368>.
- Wang, G., Gao, E., Dai, Z., Liu, L., Xu, Z., & Zhang, Z. (2017). Degradation and recovery of graphene/polymer interfaces under cyclic mechanical loading. *Composites of Science Technology*, *149*(8), 220–227. Available from <https://doi.org/10.1016/j.compscitech.2017.06.004>.
- Wang, G., Hou, H., Yan, Y., Jagatramka, R., Shirsalimian, A., Wang, Y., Li, B., Daly, M., & Cao, C. (2023). Recent advances in the mechanics of 2D materials. *International Journal of Extreme Manufacturing*, *5*, 032002.

- Wang, W., Ma, X., Dai, Z., Zhang, S., Hou, Y., Wang, G., Li, Q., Zhang, Z., Wei, Y., & Liu, L. (2022a). Mechanical behavior of blisters spontaneously formed by multilayer 2D materials. *Advanced Materials Interfaces*. Available from <https://doi.org/10.1002/admi.202101939>.
- Wang, G., Najafi, F., Ho, K., Hamidinejad, M., Cui, T., Walker, G. C., Singh, C. V., & Filleter, T. (2022b). Mechanical size effect of freestanding nanoconfined polymer films. *Macromolecules*, *55*(4), 1248–1259. Available from <https://doi.org/10.1021/acs.macromol.1c02270>.
- Wang, S., & Urban, M. W. (2020). Self-healing polymers. *Nature Review Materials*., *5*(8), 562–583. Available from <https://doi.org/10.1038/s41578-020-0202-4>.
- Wang, Y., Xu, C., Yu, X., Zhang, H., & Han, M. (2022). Multilayer flexible electronics: Manufacturing approaches and applications. *Materials Today Physics*, *23*, 100647. Available from <https://doi.org/10.1016/j.mtphys.2022.100647>.
- Wu, J., Kim, S., Chen, W., Carlson, A., Hwang, K. C., Huang, Y., & Rogers, J. A. (2011). Mechanics of reversible adhesion. *Soft Matter*, *7*(18), 8657–8662.
- Xin, H., Zhao, Q., Chen, D., & Li, W. (2018). Roll-to-roll mechanical peeling for dry transfer of chemical vapor deposition graphene. *Journal of Micro and Nano-Manufacturing*, *6*(3), 031004. Available from <https://doi.org/10.1115/1.4040449>.
- Xu, C., Yang, T., Kang, Y., Li, Q., Xue, T., Liechti, K. M., Huang, R., & Qiu, W. (2019). Rate-dependent decohesion modes in graphene-sandwiched interfaces. *Advanced Materials Interfaces*, *6*(23), 1901217. Available from <https://doi.org/10.1002/admi.201901217>.
- Yang, S. Y., Carlson, A., Cheng, H., Yu, Q., Ahmed, N., Wu, J., Kim, S., Sitti, M., Ferreira, P. M., Huang, Y., & Rogers, J. A. (2012). Elastomer surfaces with directionally dependent adhesion strength and their use in transfer printing with continuous roll-to-roll applications. *Advanced Materials*, *24*(16), 2117–2122. Available from <https://doi.org/10.1002/adma.201104975>, <https://www.ncbi.nlm.nih.gov/pubmed/22431430>.
- Yiu, P. M., Yuan, H., Gu, Q., Gao, P., & Tsui, O. K. C. (2020). Strain rate and thickness dependences of elastic modulus of free-standing polymer nanometer films. *ACS Macro Letters*., *9*(11), 1521–1526. Available from <https://doi.org/10.1021/acsmacrolett.0c00471>.
- Yoon, T., Shin, W. C., Kim, T. Y., Mun, J. H., Kim, T. S., & Cho, B. J. (2012). Direct measurement of adhesion energy of monolayer graphene as-grown on copper and its application to renewable transfer process. *Nano Letters*, *12*(3), 1448–1452. Available from <https://doi.org/10.1021/nl204123h>, <http://www.ncbi.nlm.nih.gov/pubmed/22335825>.
- Yoo, B., Cho, S., Seo, S., & Lee, J. (2014). Elastomeric angled microflaps with reversible adhesion for transfer-printing semiconductor membranes onto dry surfaces. *ACS Applied Material Interfaces*, *6*(21), 19247–19253. Available from <https://doi.org/10.1021/am505286b>, <https://www.ncbi.nlm.nih.gov/pubmed/25330816>.
- Zhou, L. Y., Fu, J., & He, Y. (2020). A review of 3D printing technologies for soft polymer materials. *Advanced Functional Materials*. Available from <https://doi.org/10.1002/adfm.202000187>.

CHAPTER 3

Thermal release tape—enabled transfer printing techniques

Yuan Lin and Zhenlong Huang

School of Materials and Energy, University of Electronic Science and Technology of China, Chengdu, P.R. China

3.1 Introduction

Soft electronics are of great interest in the area of healthcare (Gao et al., 2016; Lee, Moon, et al., 2020; Niu et al., 2019), human–machine interface (Huang et al., 2018; Wang, Lin, et al., 2018), bio-integrated electronics (Chen et al., 2020; Sang et al., 2022), transient electronics (Choi et al., 2022; Han et al., 2020), and flexible display (Park et al., 2017; Zou et al., 2020), owing to their capabilities of dynamic nonplanar surface integration. The most intuitive approach is to extend soft electronic materials for the device construction (Wang, Wang, et al., 2018). Organic materials, which are intrinsically flexible or stretchable, solution process-compatible, and low cost, have been widely studied for soft electronics (Gao et al., 2022; Matsuhisa et al., 2021; Park, Heo et al., 2018; Tan et al., 2022). Yet, compared with inorganic electronic materials, organic materials have poor electrical performance, such as low conductivity and charge carrier mobility. Transfer printing, which enables prefabricate devices on rigid substrates with inorganic materials and prints these devices onto soft substrates, is one of the most widely used microfabrication and nanofabrication techniques for soft electronics (Carlson et al., 2012; Huang & Lin, 2022; Linghu et al., 2018; Zhou et al., 2019). This technique is compatible with the conventional microfabrication process and can assemble a wide range of inorganic materials for high-performance soft electronics. Based on the feasible approaches for the modulation of stamp adhesion, lots of transfer printing techniques have been studied, such as kinetic adhesion control (Feng et al., 2007; Meitl et al., 2006), surface relief structure-assisted methods (Kim et al., 2010; Xue et al., 2015), solvent-assisted adhesion control approaches (Jeong et al., 2014; Yang et al., 2008), laser-assisted methods (Eisenhaure & Kim, 2016; Luo et al., 2020), and thermal release tape (TRT) enabled techniques (Wie et al., 2018; Yan et al., 2017). Among the various transfer printing techniques, the adhesion switchability (max/min adhesion), applicable inks, substrates, and cost are different, which have to be considered in the selection of methods.

TRT is a unique tape, whose adhesion can be modulated upon thermal treatment. It has a strong adhesion at room temperature and can be easily released after heating, indicating the large adhesion switchability, which allows the easy picking up and printing of inks by the control of temperature. TRT is constructed with a cheap polymer adhesive matrix and thermally expandable microspheres (Wang et al., 2020). It doesn't need complex microstructure design and complicated manufacturing process. Thus, TRT is low cost, ultrathin, and flexible, which makes TRT the ideal stamp for reliable, efficient, and high-production transfer printing.

In this chapter, we summarize the implementation strategies of TRT-enabled transfer printing techniques, including the working mechanisms of this technique, the working principle of thermally expandable microspheres-based TRT stamp, laser thermal treatment for programmable transfer printing, conformal TRT stamp for curve electronics, and roll-to-roll processing for large-scale transfer printing. At last, we give a brief discussion on the potential challenges of TRT-enabled transfer printing techniques.

3.2 Mechanisms of thermal release transfer printing

The purpose of transfer printing is to assemble ink (functional membrane) from the donor substrate to the receiver substrate with the help of a stamp. This process involves the competing fracture at the stamp/functional membrane interface and the functional membrane/donor or receiver substrate interface. TRT is kind of widely used stamp, which is flexible, ultrathin, and commercially available. It adheres tightly at room temperature and can be peeled off effortlessly by necessary heating. Fig. 3.1 shows the transfer printing process with TRT (Yan et al., 2017). First, the TRT is attached to the surface of the functional membrane, which is originally placed on the donor substrate. After uniformly pressing, the TRT is peeled off. Due to the strong adhesion force of TRT, the functional membrane will be peeled away from the donor substrate. The TRT/functional membrane is then transferred onto the receiver substrate and is heated above the transition temperature (T_r) of the TRT, which will greatly reduce the

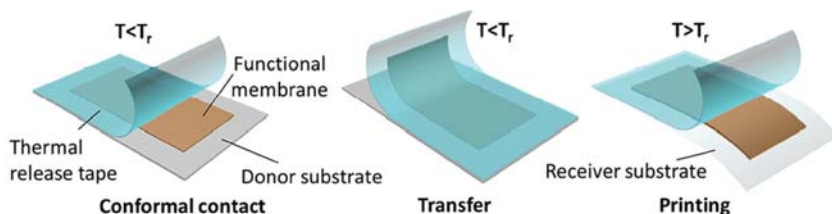


Figure 3.1 Schematic illustration of transfer printing process with thermal release tape. From Yan, Z., Pan, T., Xue, M., Chen, C., Cui, Y., Yao, G., Huang, L., Liao, F., Jing, W., Zhang, H., Gao, M., Guo, D., Xia, Y. & Lin, Y. (2017). Thermal release transfer printing for stretchable conformal bioelectronics. *Advanced Science*, 4(11), 1700251. <https://doi.org/10.1002/adv.201700251>.

interfacial adhesion between the TRT and functional membrane. Finally, the TRT is peeled off with a functional membrane left on the receiver substrate.

The key to successful transfer printing is the ability to adjust the energy release rates (G) of the interface between the stamp and functional membrane or functional membrane and substrate (donor or receiver). The energy release rate G for steady-state crack propagation can be determined:

$$G = \frac{F}{w}$$

where F is the peeling force and W is the interface width. The parameter G describes both the energy of interfacial bond breaking and adhesion dissipation around the crack tip. Based on the Griffith criterion in fracture mechanics, the crack propagates steadily once the critical energy release rate reaches the critical G value. The critical G value for the interface of TRT/membrane, membrane/donor substrate, and membrane/receiver substrate can be described as $G_{\text{TRT/membrane}}$, $G_{\text{membrane/donor substrate}}$, and $G_{\text{membrane/receiver substrate}}$, respectively. For the pick-up process, the $G_{\text{TRT/membrane}}$ should be larger than $G_{\text{membrane/donor substrate}}$. For the print process, the $G_{\text{TRT/membrane}}$ should be smaller than $G_{\text{membrane/receiver substrate}}$. As the $G_{\text{membrane/donor substrate}}$ and $G_{\text{membrane/receiver substrate}}$ are relatively stable, the key technology for TRT-enabled transfer printing is the modulation of $G_{\text{TRT/membrane}}$. The adhesion force of TRT is highly influenced by temperature and the relationship between $G_{\text{TRT/membrane}}$ and temperature can be expressed as

$$G_{\text{TRT/membrane}}(T) = \begin{cases} -e^{\gamma(T-T_r)+\ln(G_0-G_r)} + G_0 & T \leq T_r \\ G_r & T > T_r \end{cases}$$

where T is the temperature of the TRT/membrane interface, G_0 is the critical energy release rate when the temperature approaches zero degrees centigrade, G_r is the critical energy release rate when the adhesion force of TRT decreases rapidly at a temperature above the transition temperature T_r , γ is a constant parameter which is relevant to the interface materials. The relationship between $G_{\text{TRT/membrane}}$ and T is shown in Fig. 3.2A, which is well-fitted with the experimental data (polyimide (PI) as the membrane and polydimethylsiloxane (PDMS) as the receiver substrate). The critical energy release rate of membrane/substrate (donor or receiver) is relatively stable with temperature (PI/PDMS substrate for example shown in Fig. 3.2A). When the temperature is much lower than the transition temperature T_r , $G_{\text{TRT/membrane}}$ is larger than $G_{\text{membrane/donor substrate}}$, indicating that the membrane can be easily picked up from the donor substrate together with TRT. When the temperature is higher than T_r , $G_{\text{TRT/membrane}}$ decays rapidly and is much smaller than $G_{\text{membrane/receiver substrate}}$, which makes it easy for the membrane to print onto the receiver substrate (Fig. 3.2B).

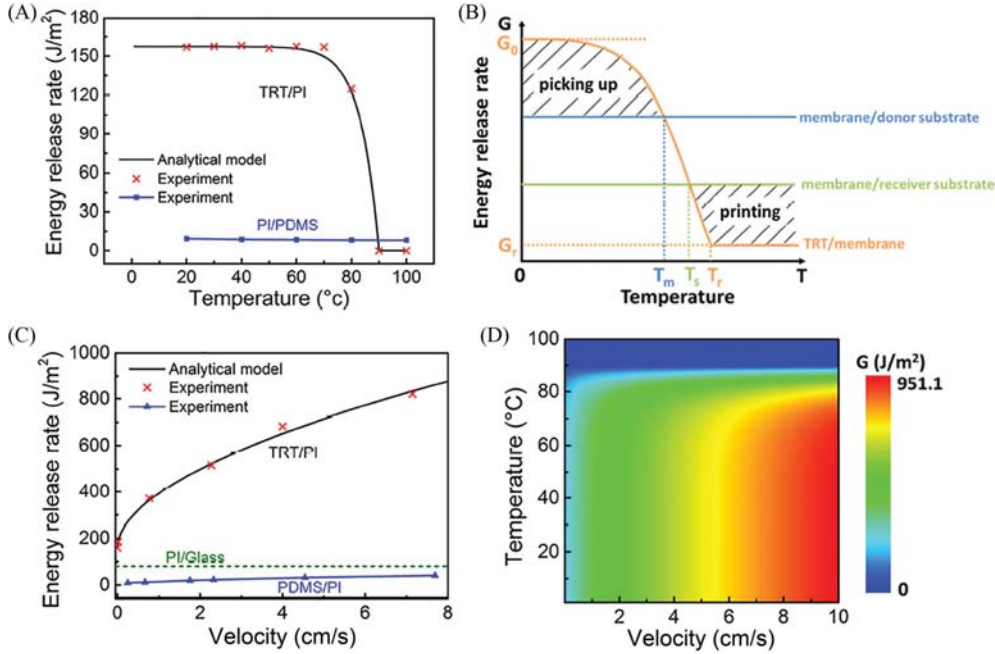


Figure 3.2 Mechanisms of thermal release transfer printing (A) The experimental and theoretical critical energy release rate at the interface of thermal release tape (TRT)/PI and PI/PDMS as a function of temperature. (B) Schematic illustration showing the relationship between energy release rate and temperature for picking up and printing. (C) The experimental and theoretical critical energy release rate at the TRT/PI and PI/PDMS interface as a function of peeling velocity. (D) The contour map shows the energy release rate of the TRT/PI interface as a function of both temperature and peeling velocity. From Yan, Z., Pan, T., Xue, M., Chen, C., Cui, Y., Yao, G., Huang, L., Liao, F., Jing, W., Zhang, H., Gao, M., Guo, D., Xia, Y. & Lin, Y. (2017). Thermal release transfer printing for stretchable conformal bioelectronics. *Advanced Science*, 4(11), 1700251. <https://doi.org/10.1002/adv.201700251>.

Compared with other approaches to transfer printing, TRT-enabled transfer printing has very high adhesion switchability (max/min adhesion > 1000). For example, kinetic control transfer printing, which is one of the most popular methods and uses peel velocity to modulate the critical energy release rate of stamp/membrane interface, can only achieve adhesion switchability of less than 10. Considering the influence of peel velocity, the critical energy rate $G_{\text{TRT/membrane}}$ can be further expressed as

$$G_{\text{TRT/membrane}}(\nu, T) = \begin{cases} \left[-e^{\gamma(T-T_r)+\ln(G_0-G_r)} + G_0 \right] \left[1 + \left(\frac{\nu}{\nu_0} \right)^n \right] & T \leq T_r \\ G_r \left[1 + \left(\frac{\nu}{\nu_0} \right)^n \right] & T > T_r \end{cases}$$

where v is the peeling velocity of the TRT, v_0 is the reference peeling velocity at which the critical energy release rate equals to $2Gr$, and n is the scaling parameter that can be determined by experimental data. As shown in Fig. 3.2C and D, the critical energy release rate of the TRT/membrane interface can be modulated by both temperature and peeling velocity over a large range, indicating the better controllability and repeatability of TRT-enabled transfer printing.

3.3 Mechanism of thermally expandable microspheres-based thermal release stamp for large adhesion switchability

The TRT, which is constructed by the backing layer and adhesive layer, has a strong adhesion at room temperature and the adhesion will decline by application of heat. The adhesive layer of such tapes typically contains an adhesive matrix and thermal expandable microspheres to serve as a stamp for transfer printing (Nestler et al., 2016; Wang et al., 2020). Preferred adhesives include acrylic, polyurethane, polyvinyl alcohol, ethylene-vinyl acetate, and polyvinyl acetate. Thermally expandable microspheres are made up of a thermoplastic shell filled with liquid or hydrogel particles, which have large volume changes of liquid-vapor transition (Gadhavé & Gadhavé, 2022; Jonsson et al., 2006; Schmid et al., 2009). Typically, the microspheres are constructed with polymer as the shell and a low boiling point liquid hydrocarbon as the core. On heating the microspheres up to the glass transition temperature of the polymer, the shell softens and the liquid hydrocarbon boils simultaneously. The shell will expand with the increased pressure from the large volume change of the core for the liquid-vapor transition. As a result, the size of microspheres expands many times (about 3–10 times their diameter) than the original state (Fig. 3.3) (Gadhavé & Gadhavé, 2022). The microspheres have a critical temperature at which they start to expand and a second temperature at which they expand to the max volume. By regulating the material composition of the core

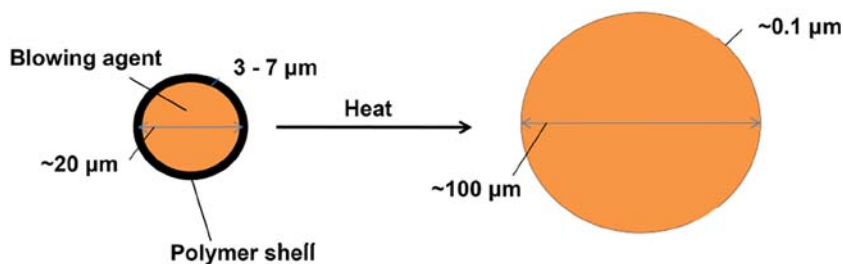


Figure 3.3 The schematic showing the expansion of thermally expandable microspheres upon heating. From Gadhavé, R. V. I. & Gadhavé, C. R. (2022). *Application of thermally expandable microspheres in adhesives: Review*. *Open Journal of Polymer Chemistry*, 12(02), 80–92. <https://doi.org/10.4236/ojpcem.2022.122005>.

and shell, the critical and second temperatures can be tuned on a wide range. Usually, the microspheres have a critical temperature of around 35°C–110°C and have a second temperature of around 50°C–150°C. Thermally expandable microspheres were originally invented by Dow Chemical Co. and are worldwide commercialized by the companies of Expancel Nobel Industries, Matsumoto Yushi Seiyaku, and Nishiyama. Owing to their unique performance, they have been proven to be a very useful product in the industry for diverse applications, such as printing ink (Safajou-Jahankhanemlou *et al.*, 2016; Urbas & Elesini, 2015), thermally sensitive paper board (Banea *et al.*, 2018), and automotive impact coatings.

Due to the unique heat-expandable properties, the thermally expandable microspheres are also widely used in the application of disbondable adhesive, TRT for example. At room temperature, the microspheres remain in the shape of small size and the surface of the adhesive layer is flat, which enables strong adhesion. During heating, the microspheres get expanded and the contact area between the tape and functional inks decreases, which rapidly induces the interfacial adhesion and allows the tape to be released (Fig. 3.4A) (Chengjun Wang *et al.*, 2020). The researchers illustrated the working principle with the commercially available TRT (no. 3195, Nitto). The adhesive layer was constructed with hydrocarbon microspheres encapsulated inside thermoplastic polymer shells. Due to the liquid–vapor transition of hydrocarbons, the diameter of inner microspheres expanded from around 10 to 45 μm , which increased the thickness and roughness of the adhesive layer (Fig. 3.4B–D). The energy release rate of the TRT stamp with glass significantly decreased from 22.68 J/m^2 at 25°C to less than 0.2 J/m^2 at 90°C, indicating the large adhesion switchability (Fig. 3.4E). Due to its high reliability and efficiency, the TRT is very suitable for the transfer printing of tiny, ultrathin, and large-area devices. For demonstration, an inorganic μ -LED (285 μm by 285 μm \times 4.6 μm) was transferred on the thermally released tape stamp. The SEM images give the surface topography comparison of μ -LED on the TRT before and after thermal treatment (Fig. 3.4F), which clearly shows the surface roughness modulation of TRT upon heating.

3.4 Thermal treatment with laser for programmable transfer printing

The adhesion of the TRT stamp can be modulated with temperature. The hotplate or oven is one of the most popular choices for thermal treatment with good uniformity, high efficiency, and low cost. Yet, the heating from the hotplate or oven is not spatially selective and all the functional ink will be released onto the receiver substrate at the same time. In this way, the pattern of functional ink has to be preprocessed with microfabrication techniques such as photolithography, dry/wet etching (Xu *et al.*, 2015), two-dimensional/three-dimensional printing (Valentine *et al.*, 2017; Yuk *et al.*, 2020), and mechanical/laser cutting (Huang *et al.*, 2018; Wang, Li, *et al.*, 2018). Laser with

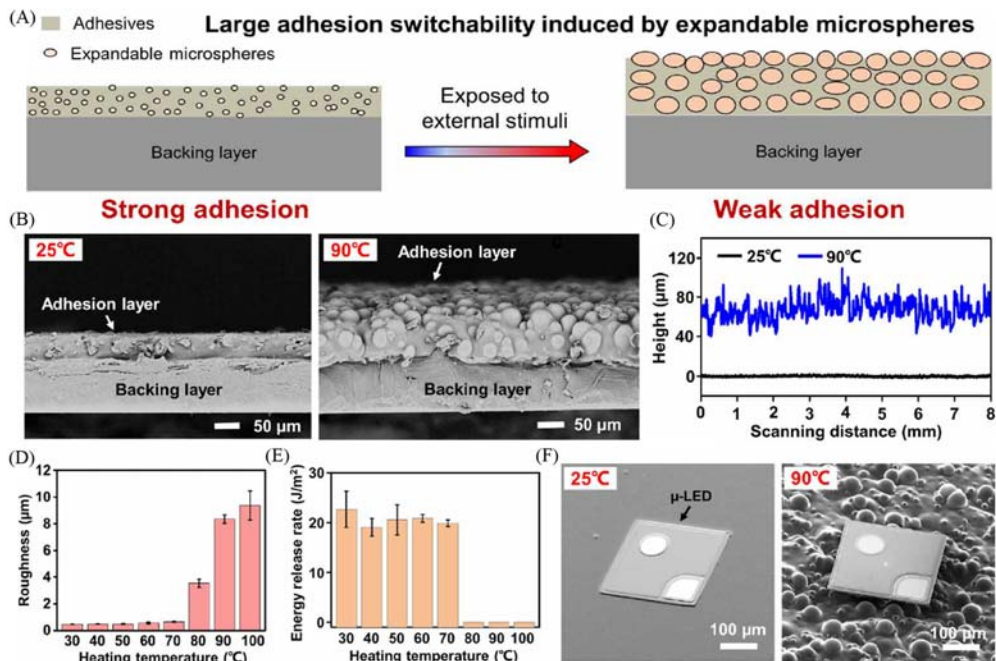


Figure 3.4 The mechanism of thermally expandable microspheres-based thermal release tape (TRT) stamp for large adhesion switchability. (A) Schematic illustration of the working principle of TRT stamp. (B) The surface topography of the TRT stamp before and after heating. (C) The surface height of the TRT stamp before and after expansion upon heating. (D) and (E) The TRT surface roughness and energy release rate with glass slide at a temperature from 30°C to 100°C. (F) The SEM images of the μ -LED attached by TRT stamp before and after heating treatment. From Wang, C., Linghu, C., Nie, S., Li, C., Lei, Q., Tao, X., Zeng, Y., Du, Y., Zhang, S., Yu, K., Jin, H., Chen, W. & Song, J. (2020). Programmable and scalable transfer printing with high reliability and efficiency for flexible inorganic electronics. *Science Advances*, 6(25). <https://doi.org/10.1126/sciadv.abb2393>.

near-infrared (NIR) or infrared (IR) wavelength can be absorbed by multiple materials and cause a thermal reaction. Due to the ultra-high machining accuracy and excellent controllability, NIR or IR laser is widely used in surface microstructure modification or localized thermal treatment without affecting the entire device. Thus, with the advantages of a layer thermal treatment system, TRT stamp can be used for programmable transfer printing, which allows localized modulation of stamp adhesion and pattern of the functional inks.

Chengjun Wang et al. developed a platform for programmable transfer printing, which consists of a laser-generation system for precise heating, a displacement control system for device alignment, and an optical microscope system for sample observation (Fig. 3.5A) (Wang et al., 2020). A laser beam with 808 nm wavelength and 350 μ m diameter passed through the transparent PDMS receiver substrate and was focused on the functional inks for the localized heating. With laser power adjustment, the temperature

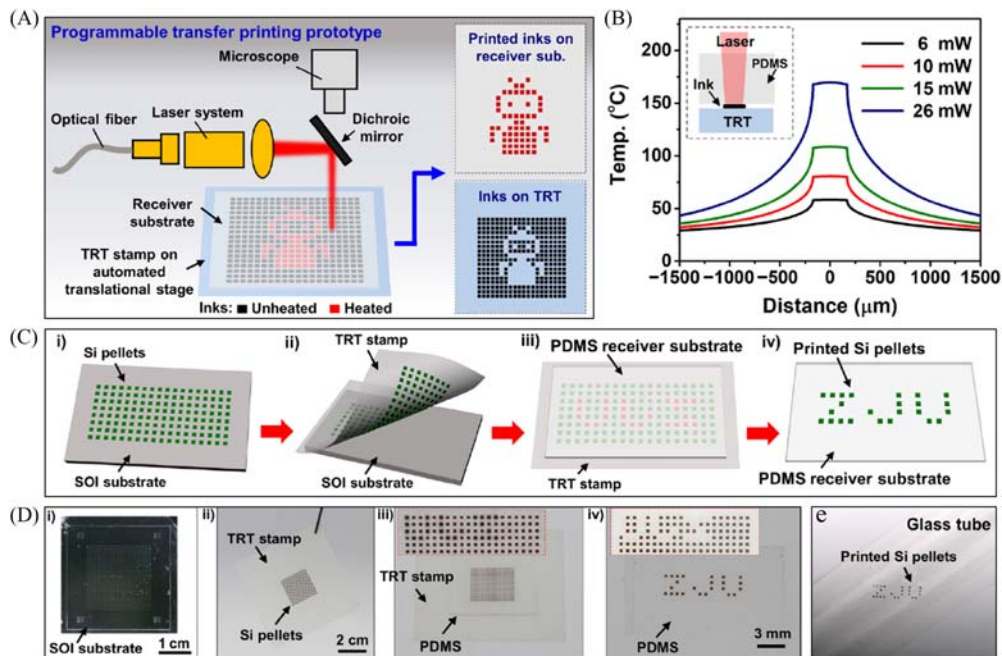


Figure 3.5 Thermal treatment with laser for programmable transfer printing. (A) Schematic illustration of the programmable transfer printing system. (B) The temperature distribution of the ink-thermal release tape interface with different laser power. (C) Schematic illustration of the programmable transfer printing. (D) Photographs showing the fabrication process. (E) The patterned silicon pellets on an ecoflex-coated glass tube. From Wang, C., Linghu, C., Nie, S., Li, C., Lei, Q., Tao, X., Zeng, Y., Du, Y., Zhang, S., Yu, K., Jin, H., Chen, W. & Song, J. (2020). Programmable and scalable transfer printing with high reliability and efficiency for flexible inorganic electronics. *Science Advances*, 6(25). <https://doi.org/10.1126/sciadv.abb2393>.

of the ink-TRT interface could be controlled precisely (Fig. 3.5B), which allows the precise adhesion modulation of TRT. For demonstration, programmable transfer printing of silicon pellets was realized. Schematic and photograph recordings of the transfer process were shown in Fig. 3.5C and D, respectively. The selective laser irradiation could heat the TRT/silicon pellets interface and separate the silicon from the TRT with predefined patterns. Finally, these pre-designed silicon pellets could be transferred to the target substrate (Fig. 3.5E).

3.5 Shape-conformal thermal release tape stamp for curve electronics

Curvy electronics that assemble devices on three-dimensional surfaces can achieve unique performance in applications of curve imagers (Kim et al., 2020; Song et al., 2013), smart contact lenses (Kim et al., 2021; Ku et al., 2020; Park, Kim et al., 2018), nonplanar

antennae (Kucukdeger et al., 2021), and flying perception (Xiong et al., 2021). Conventional electronics are typically fabricated on flat surfaces due to the hardness and two-dimensional nature of the wafer. Some manufacturing technologies have been studied to fabricate curvy electronics including deterministic folding (Xu et al., 2017), three-dimensional printing (Mohammed & Kramer, 2017; Skylar-Scott et al., 2019), thermal pressure-forming (Sun et al., 2013), controlled growth of nanostructures (Kim et al., 2016), and shape memory polymer-assisted method (Luo et al., 2021), but they can only achieve devices with certain materials. For example, three-dimensional printing is a kind of technique that directly constructs devices into three-dimensional shapes with curable inks. Yet, the functional inks for electronics are usually made of inorganic nanomaterials or organic semiconductors, whose electrical performance and stability are still relatively poor compared with wafer-based components. Transfer printing, which allows fabrication of the devices on a two-dimensional plane with a traditional process and delivery of these devices on a three-dimensional surface, can achieve curve electronics with performance comparable to wafer-based electronics. TRT stamp is a kind of film composed of polymer and liquid hydrocarbon. It is ultrathin and flexible, which makes it can be deformed into various structures to have good contact with the curve surface. Eun Kwang Lee et al. reported a fractal web design of hemispherical photodetector arrays with organic-dye-sensitized graphene hybrid composites for three-dimensional imaging (Lee, Baruah, et al., 2020). The photodetector arrays were first fabricated on a planar silicon wafer coated with thin films of nickel and polyimide as the separation layer (Fig. 3.6A). Then the TRT was used to peel the device from the silicon wafer in distilled water at room temperature. With 80°C thermal treatment, the TRT was easily removed and the device was printed on a transparent hemispherical dome (Fig. 3.6B). Due to the conformability of the TRT stamp and fractal web structure design, the device had good contact with the curve surface and could tolerate various external loads. With 48-pixel photodetectors integrated at the cross-junctions of the spiral and radial thread (Fig. 3.6C and D), the hemispherical device enabled excellent optoelectronic functionality for simultaneous detection of the light intensity and direction. As a demonstration, the laser beam was focused on the hemispherical photodetectors and the representative photocurrent was measured (Fig. 3.6E and F). The photodetector was semitransparent and had three-dimensional architecture, which meant the device could sense two locations upon the stimulation of the laser. Thus, the incidence angle of the laser beam could be calculated.

3.6 Thermal release tape stamp-enabled roll-to-roll processing for large-scale transfer printing

Roll-to-roll (R2R) processing also known as web processing or reel-to-reel processing, is a fabrication method used in manufacturing electronic devices on a rolled substrate (Greener et al., 2018). It allows the coating or deposition of varying materials

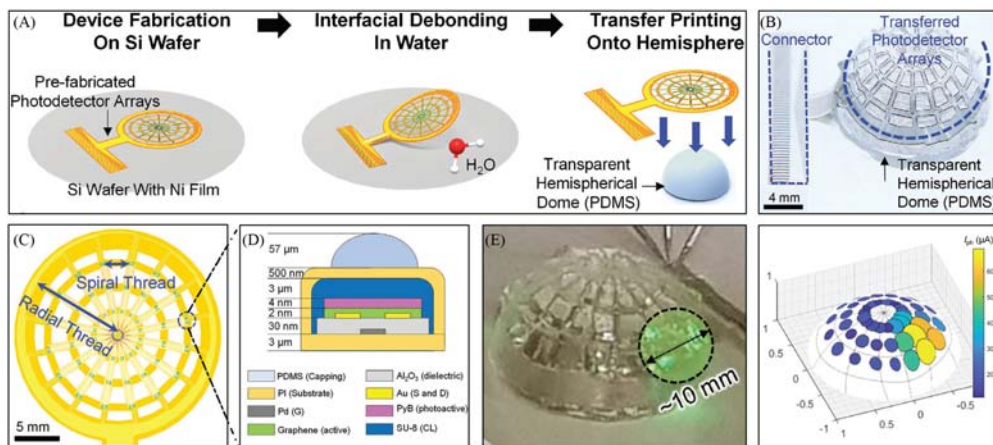


Figure 3.6 Shape-conformal TRT stamp for curve electronics. (A) Schematic illustration of the fabrication process for the hemispherical photodetector arrays. (B) The photograph of the photodetector arrays integrated on the surface of the hemispherical dome. (C) Schematic illustration of the fractal web design. (D) The side view of the single-pixel photodetector. (E) The photograph of the hemispherical photodetector arrays upon the stimulation of the laser spot. (F) The photocurrent mapping of the hemispherical photodetector. From Lee, E. K., Baruah, R. K., Leem, J. W., Park, W., Kim, B. H., Urbas, A., Ku, Z., Kim, Y. L., Alam, M. A. & Lee, C. H. (2020). Fractal web design of a hemispherical photodetector array with organic-dye-sensitized graphene hybrid composites. *Advanced Materials*, 32(46), 2004456. <https://doi.org/10.1002/adma.202004456>.

from one roller to another continuously, offering the advantages of large-scale, low-cost, time-saving, and high-output manufacturing methods. The R2R processing is compatible with most of the printing techniques, such as screen printing, gravure printing, and transfer printing, which can print functional inks on a soft substrate and are very efficient for the fabrication of flexible electronics (A. M. et al., 2022; Koo et al., 2015). TRT is flexible, ultrathin, and highly reliable, which makes it a good stamp for large-scale transfer printing with R2R processing. Yan Wang et al. demonstrated the TRT stamp-enabled R2R approach for the wafer-scale transfer of silicon nanowire (SiNW) arrays (Wang et al., 2014). The remarkable uniformity of printed SiNW arrays indicated the excellent ability of this processing for one-dimensional materials transfer. Two-dimensional materials such as graphene, hexagonal boron nitride, transition metal dichalcogenides, phosphorene, and xenes, exhibit varying electrical and thermological properties. Due to the flat nano/micro surface, two-dimensional materials have good contact with the TRT stamp. And lots of studies have reported the transfer of two-dimensional materials with R2R processing. Graphene, the most prominent member of two-dimensional materials, have extremely high carrier mobility, good thermal conductivity, superelastic mechanical behavior,

and excellent optical transmittance. These remarkable properties allow it a compelling material to be used in the applications of logic chips, sensors, energy devices, and flexible displays (Novoselov et al., 2012; Zhang et al., 2013). With the advanced chemical vapor deposition method, the graphene can be grown on a copper substrate on a large scale. In the early stage, methyl methacrylate (PMMA) was used as the support layer for graphene transfer and then dissolved in an organic solvent after transfer. However, it is not suitable for large-scale manufacture in the industry. Sukang Bae et al. first demonstrated the large-scale graphene transfer with TRT stamp-enabled R2R processing (Fig. 3.7A) (Bae et al., 2010). Three steps were involved in the graphene transfer: the adhesion of TRT as the polymer support layer, wet etching of the copper substrate, and thermal treatment for the release of the TRT stamp (Fig. 3.7B). Finally, 30-inch graphene was transferred on the flexible polyethylene terephthalate film (Fig. 3.7C) and a touch-screen panel was demonstrated with the transparent and conductive film (Fig. 3.7D).

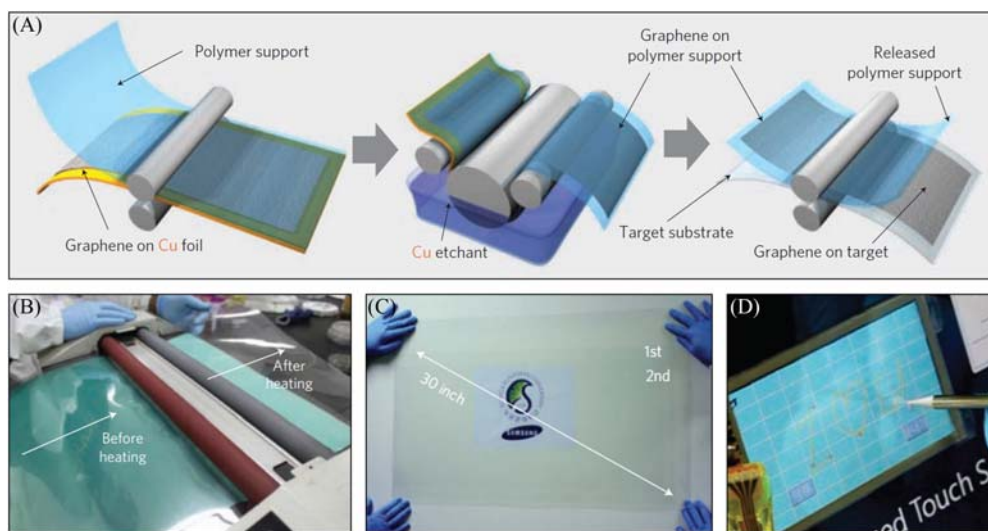


Figure 3.7 Thermal release tape (TRT) stamp enabled roll-to-roll (R2R) processing for larger-scale transfer printing. (A) Schematic illustration of the three steps for R2R-based large-scale graphene transfer. TRT was attached with graphene as the polymer support in the first step and was released with thermal treatment in the third step. (B) The photograph shows the R2R transfer of graphene with TRT before and after heating. (C) The photograph of 30-inch transparent graphene film integrated with PET sheet. (D) The demonstration of the transparent and conductive graphene film-based touch-screen panel. From Bae, S., Kim, H., Lee, Y., Xu, X., Park, J.-S., Zheng, Y., Balakrishnan, J., Lei, T., Ri Kim, H., Song, Y. I., Kim, Y.-J., Kim, K. S., Özyilmaz, B., Ahn, J.-H., Hong, B. H. & Iijima, S. (2010). Roll-to-roll production of 30-inch graphene films for transparent electrodes. *Nature Nanotechnology*, 5 (8), 574–578. <https://doi.org/10.1038/nnano.2010.132>.

3.7 Conclusions and future outlook

This chapter presents a brief discussion of TRT-enabled transfer printing techniques. Due to the unique heat-expandable properties of the microspheres within TRT, the interface adhesion between tape and inks can be precisely adjusted over a wide range upon heating, thus allowing extremely high adhesion switchability for reliable and programmable transfer printing. Without complex microstructure, the TRT can be ultrathin and flexible. Thus, the tape can be deformed into various shapes for the transfer printing of curve electronics. For high reliability and low-cost, TRT-enabled transfer printing is also suitable for large-scale fabrication with roll-to-roll processing. Although there are many advances of TRT-enabled transfer printing techniques, several challenges still exist for future development. One opportunity may lie in the study of low-temperature working, residue-free, and recyclable TRT stamps. TRT requires a high processing temperature close to the glass transition temperature of the polymer shell, which results in considerable thermal stress on the inks. Thermal-stress deformation of the tape and inks will highly influence the transfer printing precision and service life of the stamp. And the tape residue will be left on the receiver substrate. The adhesive of the tape needs to be extensively studied to fabricate devices in the nano-scale with better printing precision, greater integration, and longer service life. Second, shape-conformal TRT stamp shall be further developed for curve electronics. At present, TRT is unstretchable and can transfer inks onto developable surfaces, such as cylindrical and conical surfaces. With mesh design, the TRT can construct curve electronics with limited nondevelopable surfaces (such as hemispherical surfaces). But the contact between TRT and the curve receiver surface is unsatisfactory. Advanced TRT stamp should be extended to satisfy more complex surfaces for biological applications and others.

References

- A. M., T., Moon, H., Cho, G., & Lee, J. (2022). Fully roll-to-roll gravure printed electronics: Challenges and the way to integrating logic gates. *Japanese Journal of Applied Physics (SE)*. Available from <https://doi.org/10.35848/1347-4065/ac575e>, SE0802.
- Bae, S., Kim, H., Lee, Y., Xu, X., Park, J.-S., Zheng, Y., Balakrishnan, J., Lei, T., Ri Kim, H., Song, Y. I. L., Kim, Y.-J., Kim, K. S., Özyilmaz, B., Ahn, J.-H., Hong, B. H., & Iijima, S. (2010). Roll-to-roll production of 30-inch graphene films for transparent electrodes. *Nature Nanotechnology*, 8, 574–578. Available from <https://doi.org/10.1038/nnano.2010.132>.
- Banea, M. D., da Silva, L. F. M., Carbas, R. J. C., Barbosa, A. Q., de Barros, S., & Viana, G. (2018). Effect of water on the behaviour of adhesives modified with thermally expandable particles. *International Journal of Adhesion and Adhesives*, 250–256. Available from <https://doi.org/10.1016/j.ijadhadh.2018.04.002>.
- Carlson, A., Bowen, A. M., Huang, Y., Nuzzo, R. G., & Rogers, J. A. (2012). Transfer printing techniques for materials assembly and micro/nanodevice fabrication. *Advanced Materials*, 39, 5284–5318. Available from <https://doi.org/10.1002/adma.201201386>.

- Chen, S., Sun, L., Zhou, X., Guo, Y., Song, J., Qian, S., Liu, Z., Guan, Q., Meade Jeffries, E., Liu, W., Wang, Y., He, C., & You, Z. (2020). Mechanically and biologically skin-like elastomers for bio-integrated electronics. *Nature Communications*, 1. Available from <https://doi.org/10.1038/s41467-020-14446-2>.
- Choi, Y. S., Jeong, H., Yin, R. T., Avila, R., Pfenninger, A., Yoo, J., Lee, J. Y., Tzavelis, A., Lee, Y. J., Chen, S. W., Knight, H. S., Kim, S., Ahn, H.-Y., Wickerson, G., Vázquez-Guardado, A., Higbee-Dempsey, E., Russo, B. A., Napolitano, M. A., Holleran, T. J., . . . Rogers, J. A. (2022). A transient, closed-loop network of wireless, body-integrated devices for autonomous electrotherapy. *Science*, 6596, 1006–1012. Available from <https://doi.org/10.1126/science.abm1703>.
- Eisenhaure, J., & Kim, S. (2016). Laser-driven shape memory effect for transfer printing combining parallelism with individual object control. *Advanced Materials Technologies*, 7. Available from <https://doi.org/10.1002/admt.201600098>, [http://onlinelibrary.wiley.com/journal/10.1002/\(ISSN\)2365-709X](http://onlinelibrary.wiley.com/journal/10.1002/(ISSN)2365-709X).
- Feng, X., Meitl, M. A., Bowen, A. M., Huang, Y., Nuzzo, R. G., & Rogers, J. A. (2007). Competing fracture in kinetically controlled transfer printing. *Langmuir*, 25, 12555–12560. Available from <https://doi.org/10.1021/la701555n>.
- Gadhav, R. V. I., & Gadhave, C. R. (2022). Application of thermally expandable microspheres in adhesives: review. *Open Journal of Polymer Chemistry*, 02, 80–92. Available from <https://doi.org/10.4236/ojchem.2022.122005>.
- Gao, W., Emaminejad, S., Nyein, H. Y. Y., Challa, S., Chen, K., Peck, A., Fahad, H. M., Ota, H., Shiraki, H., Kiriya, D., Lien, D. H., Brooks, G. A., Davis, R. W., & Javey, A. (2016). Fully integrated wearable sensor arrays for multiplexed in situ perspiration analysis. *Nature*, 538, 509–514. Available from <https://doi.org/10.1038/nature16521>, <http://www.nature.com/nature/index.html>.
- Gao, D., Lv, J., & Lee, P. S. (2022). Natural polymer in soft electronics: opportunities, challenges, and future prospects. *Advanced Materials*, 252105020. Available from <https://doi.org/10.1002/adma.202105020>.
- Greener, J., Pearson, G., & Cakmak, M. (2018). *Roll-to-Roll Manufacturing: Process Elements and Recent Advances Roll-to-Roll Manufacturing: Process Elements and Recent Advances* (pp. 1–408). United States: Wiley. Available from <http://onlinelibrary.wiley.com/book/10.1002/9781119163824>, [10.1002/9781119163824](https://doi.org/10.1002/9781119163824).
- Han, W. B., Lee, J. H., Shin, J. -W., & Hwang, S. -W. (2020). Advanced materials and systems for bio-degradable, transient electronics. *Advanced Materials*, 512002211. Available from <https://doi.org/10.1002/adma.202002211>.
- Huang, Z., Hao, Y., Li, Y., Hu, H., Wang, C., Nomoto, A., Pan, T., Gu, Y., Chen, Y., Zhang, T., Li, W., Lei, Y., Kim, N., Wang, C., Zhang, L., Ward, J. W., Maralani, A., Li, X., Durstock, M. F., . . . Xu, S. (2018). Three-dimensional integrated stretchable electronics. *Nature Electronics*, 8, 473–480. Available from <https://doi.org/10.1038/s41928-018-0116-y>.
- Huang, Z., & Lin, Y. (2022). Transfer printing technologies for soft electronics. *Nanoscale*, 45, 16749–16760. Available from <https://doi.org/10.1039/d2nr04283e>.
- Jeong, J. W., Yang, S. R., Hur, Y. H., Kim, S. W., Baek, K. M., Yim, S., Jang, H.-I., Park, J. H., Lee, S. Y., Park, C.-O., & Jung, Y. S. (2014). High-resolution nanotransfer printing applicable to diverse surfaces via interface-targeted adhesion switching. *Nature Communications*, 1. Available from <https://doi.org/10.1038/ncomms6387>.
- Jonsson, M., Nordin, O., Malmström, E., & Hammer, C. (2006). Suspension polymerization of thermally expandable core/shell particles. *Polymer*, 10, 3315–3324. Available from <https://doi.org/10.1016/j.polymer.2006.03.013>.
- Kim, M., Lee, G. J., Choi, C., Kim, M. S., Lee, M., Liu, S., Cho, K. W., Kim, H. M., Cho, H., Choi, M. K., Lu, N., Song, Y. M., & Kim, D.-H. (2020). An aquatic-vision-inspired camera based on a monocentric lens and a silicon nanorod photodiode array. *Nature Electronics*, 9, 546–553. Available from <https://doi.org/10.1038/s41928-020-0429-5>.
- Kim, W.-H., Minaye Hashemi, F. S., Mackus, A. J. M., Singh, J., Kim, Y., Bobb-Semple, D., Fan, Y., Kaufman-Osborn, T., Godet, L., & Bent, S. F. (2016). A process for topographically selective deposition on 3d nanostructures by ion implantation. *ACS Nano*, 4, 4451–4458. Available from <https://doi.org/10.1021/acsnano.6b00094>.

- Kim, J., Park, J., Park, Y.-G., Cha, E., Ku, M., An, H. S., Lee, K.-P., Huh, M.-I., Kim, J., Kim, T.-S., Kim, D. W., Kim, H. K., & Park, J.-U. (2021). A soft and transparent contact lens for the wireless quantitative monitoring of intraocular pressure. *Nature Biomedical Engineering*, 7, 772–782. Available from <https://doi.org/10.1038/s41551-021-00719-8>.
- Kim, S., Wu, J., Carlson, A., Jin, S. H., Kovalsky, A., Glass, P., Liu, Z., Ahmed, N., Elgan, S. L., Chen, W., Ferreira, P. M., Sitti, M., Huang, Y., & Rogers, J. A. (2010). Microstructured elastomeric surfaces with reversible adhesion and examples of their use in deterministic assembly by transfer printing. *Proceedings of the National Academy of Sciences*, 40, 17095–17100. Available from <https://doi.org/10.1073/pnas.1005828107>.
- Koo, H., Lee, W., Choi, Y., Sun, J., Bak, J., Noh, J., Subramanian, V., Azuma, Y., Majima, Y., & Cho, G. (2015). Scalability of carbon-nanotube-based thin film transistors for flexible electronic devices manufactured using an all roll-to-roll gravure printing system. *Scientific Reports*, 1. Available from <https://doi.org/10.1038/srep14459>.
- Kucukdeger, E., Tong, Y., Singh, M., Zhang, J., Harding, L. K., Salado, A., Ellingson, S. W., & Johnson, B. N. (2021). Conformal 3D printing of non-planar antennas on wrinkled and folded kapton films using point cloud data. *Flexible and Printed Electronics*, 4044002. Available from <https://doi.org/10.1088/2058-8585/ac28f1>.
- Ku, M., Kim, J., Won, J.-E., Kang, W., Park, Y.-G., Park, J., Lee, J.-H., Cheon, J., Lee, H. H., & Park, J.-U. (2020). Smart, soft contact lens for wireless immunosensing of cortisol. *Science Advances*, 28. Available from <https://doi.org/10.1126/sciadv.abb2891>.
- Lee, E. K., Baruah, R. K., Leem, J. W., Park, W., Kim, B. H., Urbas, A., Ku, Z., Kim, Y. L., Alam, M. A., & Lee, C. H. (2020). Fractal web design of a hemispherical photodetector array with organic-dye-sensitized graphene hybrid composites. *Advanced Materials*, 462004456. Available from <https://doi.org/10.1002/adma.202004456>.
- Lee, G. H., Moon, H., Kim, H., Lee, G. H., Kwon, W., Yoo, S., Myung, D., Yun, S. H., Bao, Z., & Hahn, S. K. (2020). Multifunctional materials for implantable and wearable photonic healthcare devices. *Nature Reviews Materials*, 2, 149–165. Available from <https://doi.org/10.1038/s41578-019-0167-3>, <http://www.nature.com/natrevmats/>.
- Linghu, C., Zhang, S., Wang, C., & Song, J. (2018). Transfer printing techniques for flexible and stretchable inorganic electronics. *NPJ Flexible Electronics*, 1. Available from <https://doi.org/10.1038/s41528-018-0037-x>.
- Luo, H., Li, C., Shi, C., Nie, S., & Song, J. (2021). Switchable dry adhesive based on shape memory polymer with hemispherical indenters for transfer printing. *Theoretical and Applied Mechanics Letters*, 6100308. Available from <https://doi.org/10.1016/j.taml.2021.100308>.
- Luo, H., Wang, C., Linghu, C., Yu, K., Wang, C., & Song, J. (2020). Laser-driven programmable non-contact transfer printing of objects onto arbitrary receivers via an active elastomeric microstructured stamp. *National Science Review*, 2, 296–304. Available from <https://doi.org/10.1093/nsr/nwz109>.
- Matsuhisa, N., Niu, S., O'Neill, S. J. K., Kang, J., Ochiai, Y., Katsumata, T., Wu, H.-C., Ashizawa, M., Wang, G.-J. N., Zhong, D., Wang, X., Gong, X., Ning, R., Gong, H., You, I., Zheng, Y., Zhang, Z., Tok, J. B.-H., Chen, X., & Bao, Z. (2021). High-frequency and intrinsically stretchable polymer diodes. *Nature*, 7888, 246–252. Available from <https://doi.org/10.1038/s41586-021-04053-6>.
- Meitl, M. A., Zhu, Z.-T., Kumar, V., Lee, K. J., Feng, X., Huang, Y. Y., Adesida, I., Nuzzo, R. G., & Rogers, J. A. (2006). Transfer printing by kinetic control of adhesion to an elastomeric stamp. *Nature Materials*, 1, 33–38. Available from <https://doi.org/10.1038/nmat1532>.
- Mohammed, M. G., & Kramer, R. (2017). All-printed flexible and stretchable electronics. *Advanced Materials*, 19. Available from <https://doi.org/10.1002/adma.201604965>, <http://www3.interscience.wiley.com/journal/119030556/issue>.
- Nestler, J., Haber, N., Stiehl, C., Otto, T., & Gessner, T. (2016). Germany Liquid reagent storage in self-pumping lab-on-a-chip systems for quick assay and biosensor integration. *IEEE 11th annual international conference on nano/micro engineered and molecular systems*. Institute of Electrical and Electronics Engineers Inc., NEMS 2016, pp. 139–143. 10.1109/NEMS.2016.7758217 9781509019472.
- Niu, S., Matsuhisa, N., Beker, L., Li, J., Wang, S., Wang, J., Jiang, Y., Yan, X., Yun, Y., Burnett, W., Poon, A. S. Y., Tok, J. B. H., Chen, X., & Bao, Z. (2019). A wireless body area sensor network based on stretchable passive tags. *Nature Electronics*, 8, 361–368. Available from <https://doi.org/10.1038/s41928-019-0286-2>, <https://www.nature.com/natelectron/>.

- Novoselov, K. S., Fal'Ko, V. I., Colombo, L., Gellert, P. R., Schwab, M. G., & Kim, K. (2012). A roadmap for graphene. *Nature.*, *7419*, 192–200. Available from <https://doi.org/10.1038/nature11458>.
- Park, S., Heo, S. W., Lee, W., Inoue, D., Jiang, Z., Yu, K., Jinno, H., Hashizume, D., Sekino, M., Yokota, T., Fukuda, K., Tajima, K., & Someya, T. (2018). Self-powered ultra-flexible electronics via nano-grating-patterned organic photovoltaics. *Nature*, *7724*, 516–521. Available from <https://doi.org/10.1038/s41586-018-0536-x>.
- Park, J., Heo, S., Park, K., Song, M. H., Kim, J.-Y., Kyung, G., Ruoff, R. S., Park, J.-U., & Bien, F. (2017). Research on flexible display at Ulsan National Institute of Science and Technology. *NPJ Flexible Electronics*, *1*. Available from <https://doi.org/10.1038/s41528-017-0006-9>.
- Park, J., Kim, J., Kim, S.-Y., Cheong, W. H., Jang, J., Park, Y.-G., Na, K., Kim, Y.-T., Heo, J. H., Lee, C. Y., Lee, J. H., Bien, F., & Park, J.-U. (2018). Soft, smart contact lenses with integrations of wireless circuits, glucose sensors, and displays. *Science Advances*, *1*. Available from <https://doi.org/10.1126/sciadv.aap9841>.
- Safajou-Jahankhanemlou, M., Abbasi, F., & Salami-Kalajahi, M. (2016). Synthesis and characterization of thermally expandable PMMA-based microcapsules with different cross-linking density. *Colloid and Polymer Science*, *6*, 1055–1064. Available from <https://doi.org/10.1007/s00396-016-3862-2>.
- Sang, M., Kim, K., Shin, J., & Yu, K. J. (2022). Ultra-thin flexible encapsulating materials for soft bio-integrated electronics. *Advanced Science.*, *30*. Available from <https://doi.org/10.1002/advs.202202980>, [http://onlinelibrary.wiley.com/journal/10.1002/\(ISSN\)2198-3844](http://onlinelibrary.wiley.com/journal/10.1002/(ISSN)2198-3844).
- Schmid, A., Sutton, L. R., Armes, S. P., Bain, P. S., & Manfrè, G. (2009). Synthesis and evaluation of polypyrrole-coated thermally-expandable microspheres: An improved approach to reversible adhesion. *Soft Matters.*, *2*, 407–412. Available from <https://doi.org/10.1039/B811246K>.
- Skylar-Scott, M. A., Mueller, J., Visser, C. W., & Lewis, J. A. (2019). Voxellated soft matter via multimaterial multinozzle 3D printing. *Nature*, *7782*, 330–335. Available from <https://doi.org/10.1038/s41586-019-1736-8>.
- Song, Y. M., Xie, Y., Malyarchuk, V., Xiao, J., Jung, I., Choi, K.-J., Liu, Z., Park, H., Lu, C., Kim, R.-H., Li, R., Crozier, K. B., Huang, Y., & Rogers, J. A. (2013). Digital cameras with designs inspired by the arthropod eye. *Nature.*, *7447*, 95–99. Available from <https://doi.org/10.1038/nature12083>.
- Sun, D.-M., Timmermans, M. Y., Kaskela, A., Nasibulin, A. G., Kishimoto, S., Mizutani, T., Kauppinen, E. I., & Ohno, Y. (2013). Mouldable all-carbon integrated circuits. *Nature Communications.*, *1*. Available from <https://doi.org/10.1038/ncomms3302>.
- Tan, P., Wang, H., Xiao, F., Lu, X., Shang, W., Deng, X., Song, H., Xu, Z., Cao, J., Gan, T., Wang, B., & Zhou, X. (2022). Solution-processable, soft, self-adhesive, and conductive polymer composites for soft electronics. *Nature Communications*, *1*. Available from <https://doi.org/10.1038/s41467-022-28027-y>.
- Urbas, R., & Elesini, U. S. (2015). Color differences and perceptive properties of prints made with microcapsules. *Journal of Graphic Engineering and Design*, 15–21.
- Valentine, A. D., Busbee, T. A., Boley, J. W., Raney, J. R., Chortos, A., Kotikian, A., Berrigan, J. D., Durstock, M. F., & Lewis, J. A. (2017). Hybrid 3D printing of soft electronics. *Advanced Materials*, *401703817*. Available from <https://doi.org/10.1002/adma.201703817>.
- Wang, C., Linghu, C., Nie, S., Li, C., Lei, Q., Tao, X., Zeng, Y., Du, Y., Zhang, S., Yu, K., Jin, H., Chen, W., & Song, J. (2020). Programmable and scalable transfer printing with high reliability and efficiency for flexible inorganic electronics. *Science Advances*, *25*. Available from <https://doi.org/10.1126/sciadv.abb2393>.
- Wang, J., Lin, M. F., Park, S., & Lee, P. S. (2018). Deformable conductors for human-machine interface. *Materials Today*, *5*, 508–526. Available from <https://doi.org/10.1016/j.mattod.2017.12.006>, <http://www.journals.elsevier.com/materials-today/>.
- Wang, C., Li, X., Hu, H., Zhang, L., Huang, Z., Lin, M., Zhang, Z., Yin, Z., Huang, B., Gong, H., Bhaskaran, S., Gu, Y., Makihata, M., Guo, Y., Lei, Y., Chen, Y., Wang, C., Li, Y., Zhang, T., . . . Xu, S. (2018). Monitoring of the central blood pressure waveform via a conformal ultrasonic device. *Nature Biomedical Engineering*, *9*, 687–695. Available from <https://doi.org/10.1038/s41551-018-0287-x>.

- Wang, C., Wang, C., Huang, Z., & Xu, S. (2018). Materials and structures toward soft electronics. *Advanced Materials*, 501801368. Available from <https://doi.org/10.1002/adma.201801368>.
- Wang, Y., Zhang, X., Gao, P., Shao, Z., Zhang, X., Han, Y., & Jie, J. (2014). Air heating approach for multilayer etching and roll-to-roll transfer of silicon nanowire arrays as SERS substrates for high sensitivity molecule detection. *ACS Applied Materials & Interfaces*, 2, 977–984. Available from <https://doi.org/10.1021/am4043883>.
- Wie, D. S., Zhang, Y., Kim, M. K., Kim, B., Park, S., Kim, Y.-J., Irazoqui, P. P., Zheng, X., Xu, B., & Lee, C. H. (2018). Wafer-recyclable, environment-friendly transfer printing for large-scale thin-film nanoelectronics. *Proceedings of the National Academy of Sciences*, 31. Available from <https://doi.org/10.1073/pnas.1806640115>.
- Xiong, W., Zhu, C., Guo, D., Hou, C., Yang, Z., Xu, Z., Qiu, L., Yang, H., Li, K., & Huang, Y. (2021). Bio-inspired, intelligent flexible sensing skin for multifunctional flying perception. *Nano Energy*106550. Available from <https://doi.org/10.1016/j.nanoen.2021.106550>.
- Xue, Y., Zhang, Y., Feng, X., Kim, S., Rogers, J. A., & Huang, Y. (2015). A theoretical model of reversible adhesion in shape memory surface relief structures and its application in transfer printing. *Journal of the Mechanics and Physics of Solids*, 27–42. Available from <https://doi.org/10.1016/j.jmps.2015.01.001>.
- Xu, W., Qin, Z., Chen, C.-T., Kwag, H. R., Ma, Q., Sarkar, A., Buehler, M. J., & Gracias, D. H. (2017). Ultrathin thermoresponsive self-folding 3D graphene. *Science Advances*, 10. Available from <https://doi.org/10.1126/sciadv.1701084>.
- Xu, S., Yan, Z., Jang, K.-I., Huang, W., Fu, H., Kim, J., Wei, Z., Flavin, M., McCracken, J., Wang, R., Badea, A., Liu, Y., Xiao, D., Zhou, G., Lee, J., Chung, H. U., Cheng, H., Ren, W., Banks, A., ... Rogers, J. A. (2015). Assembly of micro/nanomaterials into complex, three-dimensional architectures by compressive buckling. *Science*, 6218, 154–159. Available from <https://doi.org/10.1126/science.1260960>.
- Yang, H., Wang, P., Wang, H., Wang, X., Zhang, F., Li, B., & Li, H. (2008). Organic solvent-assisted transfer printing on hydrophobic polymer substrate with high efficiency. *Surface Review and Letters*, 6, 763–768. Available from <https://doi.org/10.1142/S0218625X08012153>.
- Yan, Z., Pan, T., Xue, M., Chen, C., Cui, Y., Yao, G., Huang, L., Liao, F., Jing, W., Zhang, H., Gao, M., Guo, D., Xia, Y., & Lin, Y. (2017). Thermal release transfer printing for stretchable conformal bioelectronics. *Advanced Science*, 111700251. Available from <https://doi.org/10.1002/adv.201700251>.
- Yuk, H., Lu, B., Lin, S., Qu, K., Xu, J., Luo, J., & Zhao, X. (2020). 3D printing of conducting polymers. *Nature Communications*, 1. Available from <https://doi.org/10.1038/s41467-020-15316-7>.
- Zhang, Y., Zhang, L., & Zhou, C. (2013). Review of chemical vapor deposition of graphene and related applications. *Accounts of Chemical Research*, 10, 2329–2339. Available from <https://doi.org/10.1021/ar300203n>.
- Zhou, H., Qin, W., Yu, Q., Cheng, H., Yu, X., & Wu, H. (2019). Transfer printing and its applications in flexible electronic devices. *Nanomaterials*, 2, 283. Available from <https://doi.org/10.3390/nano9020283>.
- Zou, S.-J., Shen, Y., Xie, F.-M., Chen, J.-D., Li, Y.-Q., & Tang, J.-X. (2020). Recent advances in organic light-emitting diodes: toward smart lighting and displays. *Materials Chemistry Frontiers*, 3, 788–820. Available from <https://doi.org/10.1039/c9qm00716d>.

CHAPTER 4

Laser-driven noncontact transfer printing technique

Rui Li and Dongqi An

Department of Engineering Mechanics, Dalian University of Technology, Dalian, P.R. China

4.1 Introduction

The laser-induced forward transfer (LIFT) technique was first reported in 1986 (Bohandy et al., 1986). The LIFT process has been associated with transferring prefabricated microstructures, which has found applications for batch assembly in microelectromechanical systems fabrication (Holmes & Saidam, 1998). Conventional LIFT variants usually involve laser ablation of a sacrificial layer at the interface of the transfer tool (i.e., stamp) and the chiplet (i.e., ink) to achieve the transfer (Huang et al., 2016; Saeidpourazar, Li, et al., 2012). By contrast, the laser-driven noncontact transfer printing (LNTP) technique does not use laser ablation to drive the delamination of the ink from the stamp. Instead, it exploits a mismatched thermomechanical response of the ink and the stamp to a laser pulse incident on the stamp/ink interface to cause the delamination of the ink from the stamp and its transfer to the functional receiver substrate. With relatively lower temperatures produced in the LNTP process, the damage to both the stamp and functional inks can be effectively avoided, which enables a safe and repeatable pick-and-place cycle. Meanwhile, the stamp is made of an elastomeric material [e.g., polydimethylsiloxane (PDMS)], which enables a direct selective transfer of the ink from the growth/fabrication (i.e., donor) substrate to the stamp by adopting well-established pick-up techniques (Linghu et al., 2018; Loo et al., 2003; Meitl et al., 2004; Menard et al., 2004; Sun & Rogers, 2004; Zaumseil et al., 2003). Therefore, the LNTP combines the facile elegance of the transfer printing processes in transferring microstructures directly from their donor substrates into receiver substrates with the flexibility of the noncontact LIFT processes that are relatively independent of the surface properties and preparation of the receiver substrates onto which the microstructures are transferred (Saeidpourazar, Li, et al., 2012; Saeidpourazar, Sangid, et al., 2012).

As illustrated in Fig. 4.1, the LNTP employs an elastomeric stamp to transfer microstructures as “ink” from the donor substrate onto a receiver substrate (Saeidpourazar, Li, et al., 2012). A laser pulse initiates separation at the adhesive surface due to a large thermal mismatch between the stamp and the ink. The process starts with the retrieval of

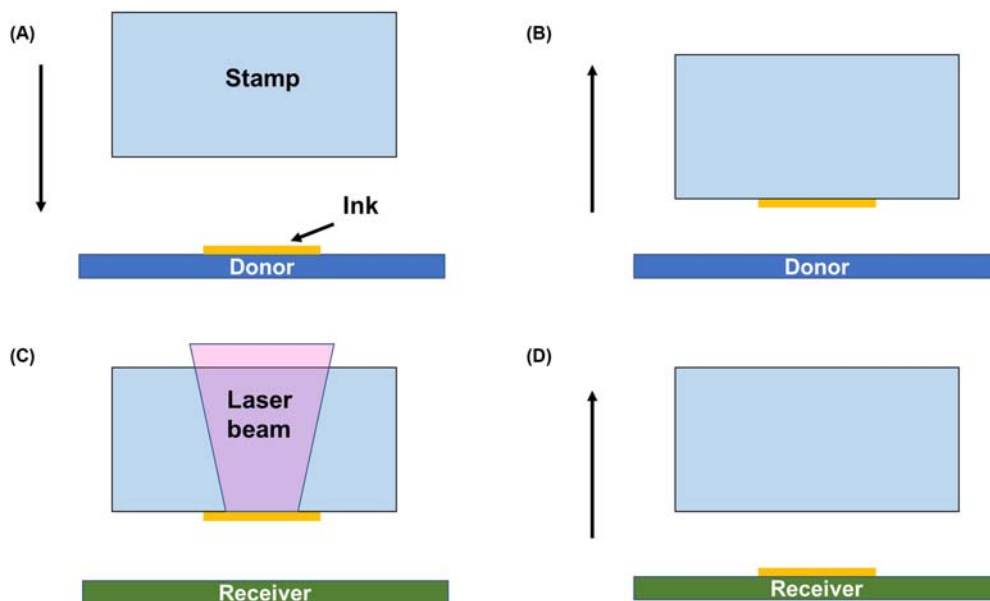


Figure 4.1 Schematic illustration of the laser-driven noncontact transfer printing process. (A) The stamp is moved to a donor substrate to retrieve the ink; (B) the ink is lifted onto the surface of the stamp; (C) the stamp is moved to a receiver substrate and a pulsed laser beam is used to deliver heat to the interface between the ink and the stamp; and (D) the ink is transferred to the receiver substrate and the stamp is withdrawn for the next printing cycle.

inks from a donor substrate Fig. 4.1A and B with an elastomeric stamp. The “inked” stamp is then brought close (a few micrometers) to the receiver substrate Fig. 4.1C. A pulsed laser beam, focusing on the stamp/ink interface, causes the active ejection of the inks from the stamp such that they land on the receiver substrate Fig. 4.1D. The wavelength of the laser is chosen so that the stamp material is transparent, while the ink is more absorbing it.

To realize this process (Fig. 4.2), an LNTP print head is created by using an electronically pulsed 30 W 805 nm laser diode with a minimum pulse width of 1 ms. The laser is coupled into the system through a 250 μm core optical fiber. At the end of the fiber are a diameter collimator and a focusing lens with a focal distance to focus the laser beam on a circular area with a diameter of approximately 400–800 μm . Fig. 4.2 shows a schematic and photograph of the LNTP print head. The laser beam is brought in through the side of the print head, bent through 90 degrees by a dichroic mirror, and focused onto the surface of a post (typically, 200 \times 200 μm , 100 μm tall) patterned on the PDMS stamp. An objective directly above the stamp along with a CCD camera and suitable optics allows observation of the process with a pixel resolution of 1 μm .

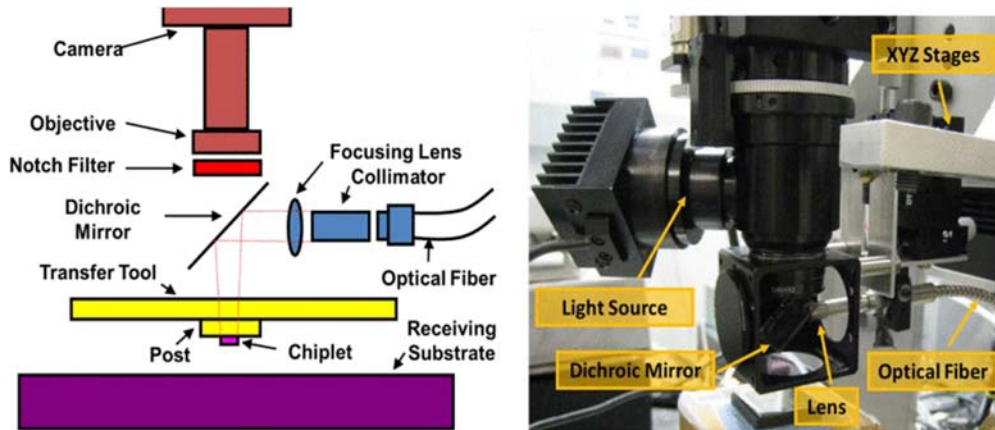


Figure 4.2 A schematic depiction and photograph of the laser-driven noncontact transfer printing print head. The laser beam is brought into the print head by an optical fiber, bent, and focused on the stamp/ink interface. A dichroic mirror allows for monitoring the process with a high-speed camera positioned above the stamp. From Saeidpourazar, R., Li, R., Li, Y., Sangid, M. D., Lu, C., Huang, Y., Rogers, J. A. & Ferreira, P. M. (2012). *Journal of Microelectromechanical Systems*, 21(5), 1049–1058. <https://doi.org/10.1109/JMEMS.2012.2203097>.

Several feasibility tests were conducted. As shown in Fig. 4.3A, the chips were printed as an array above an RC1 cleaned, patterned Si substrate with 50-micron gold traces. The second test, shown in Fig. 4.3B, demonstrates the construction of three-dimensional assemblies using the LNTP. A 3-layer pyramid is constructed of the same $100 \times 100 \times 3 \mu\text{m}$ Si squares. In a third test (Fig. 4.3C), simulating the printing of microstructures into other functional structures, the same square Si chip is printed onto an atomic force microscope cantilever, something that would be difficult to achieve with the other process. Finally, Fig. 4.3D shows a 320-nm-thick Si chip placed onto the structured surface. This verifies the claim that the LNTP process is independent of the properties of the receiver substrate and demonstrates the ability of the process to place ultrathin microstructures.

The ejection of the ink is the key process and the distinctive feature of the LNTP, which involves a complex thermomechanical behavior. To realize the optimal design of a stamp for transfer printing of prefabricated inks, the establishment of a theoretical model that can identify the mechanism and quantitatively reveal the relationships among key quantities becomes indispensable.

In the following, a thermomechanical model is established to analytically obtain the temperature field and the energy release rate for delamination at the interface between the stamp and the ink in the form of a rigid plate. The nondimensional critical laser pulse time for interfacial delamination depends only on the nondimensional total heat flux at the interface and the nondimensional width of the ink. A further

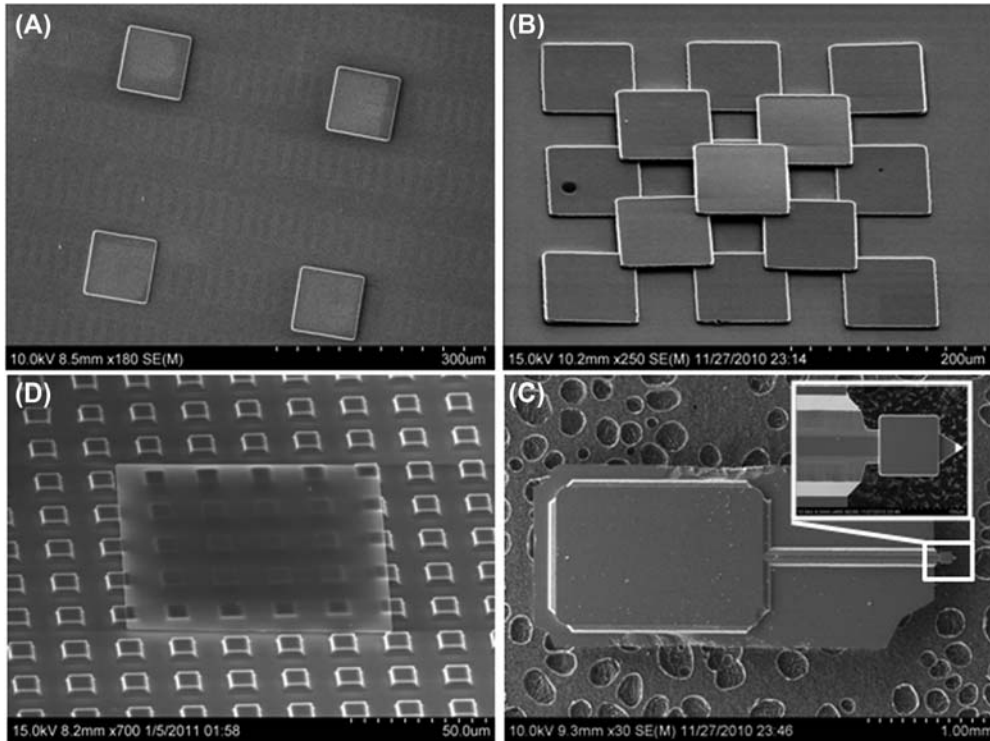


Figure 4.3 Micrographs of examples of printing using the laser-driven noncontact transfer printing process. (A) $100 \times 100 \times 3 \mu\text{m}$ Si squares printed on a Si wafer; (B) a three-dimensional pyramid printed with the same Si squares; (C) a Si square printed on a Si cantilever; and (D) $100 \times 100 \times 0.32 \mu\text{m}$ ultrathin Si square printed onto a structured substrate. From Saeidpourazar, R., Li, R., Li, Y., Sangid, M. D., Lu, C., Huang, Y., Rogers, J. A. & Ferreira, P. M. (2012). *Journal of Microelectromechanical Systems*, 21(5), 1049–1058. <https://doi.org/10.1109/JMEMS.2012.2203097>.

refined interfacial fracture mechanics model accounting for the size effect of a Si chip ink is also presented. Stamp modification designs to tackle the problems encountered in actual production are introduced at the end of the chapter.

4.2 Transient heat conduction

The laser beam penetrates the stamp, which is transparent to the laser, and provides heat to the ink, and thus to the stamp/ink interface, in a very short time in the LNTP process illustrated in Fig. 4.1C.

As shown in Fig. 4.4, a transient heat conduction model is first established. As the stamp is much larger than the ink, it is modeled as a semiinfinite solid. For simplicity, the analysis here is two-dimensional (Li, Li, Lü, Song, Saeidpouraza, et al., 2012).

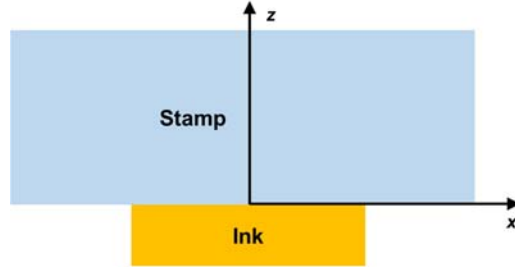


Figure 4.4 Two-dimensional model for transient heat conduction in the laser-driven noncontact transfer printing.

The origin of the Cartesian coordinate system (x, z) is at the center of the stamp/ink interface, with x running along the interface and z pointing into the stamp.

The governing equation for two-dimensional transient heat conduction in the stamp as shown in Fig. 4.4 is

$$\frac{\partial^2 \theta_{\text{stamp}}}{\partial x^2} + \frac{\partial^2 \theta_{\text{stamp}}}{\partial z^2} - \frac{c_{\text{stamp}} \rho_{\text{stamp}}}{\lambda_{\text{stamp}}} \frac{\partial \theta_{\text{stamp}}}{\partial t} = 0 \quad (4.1)$$

where θ_{stamp} is the temperature difference from the ambient temperature, t is time, c_{stamp} , ρ_{stamp} and λ_{stamp} are respectively the specific heat, mass density and thermal conductivity of the stamp.

The initial ambient temperature condition gives

$$\theta_{\text{stamp}}|_{t=0} = 0 \quad (4.2)$$

Since the laser beam duration is very short, the natural convection of heat on the stamp surface is negligible. Therefore, the heat insulation boundary condition yields

$$-\lambda_{\text{stamp}} \frac{\partial \theta_{\text{stamp}}}{\partial z} \Big|_{z=0} = \begin{cases} q(t) & \text{for } |x| \leq \frac{L_{\text{ink}}}{2} \text{ (in ink region)} \\ 0 & \text{for } |x| > \frac{L_{\text{ink}}}{2} \text{ (otherwise)} \end{cases} \quad (4.3)$$

Here, L_{ink} is the width of the ink, $q(t)$ is the heat flux into the stamp, which can be approximately obtained from a simplified transient heat conduction analysis through the thickness direction of the stamp, incorporating the uniform temperature distribution in the ink and the temperature continuity across the stamp/ink interface (Li, Li, Lü, Song, Saaidpouraza, et al., 2012):

$$q(t) = q_{\text{total}} \left[1 - \exp\left(\frac{t}{t_0}\right) \operatorname{erfc}\left(\sqrt{\frac{t}{t_0}}\right) \right] \quad (4.4)$$

where $q_{\text{total}} = P/A$ is the total heat flux to the stamp/ink interface (Li, Li, Lü, Song, Saeidpouraza, et al., 2012), which is equal to the absorbed laser power by the stamp/ink system, P , divided by the area of the ink, A , erfc denotes the complementary error function (Fettis et al., 1973), and

$$t_0 = \frac{c_{\text{ink}}^2 \rho_{\text{ink}}^2 h_{\text{ink}}^2}{c_{\text{stamp}} \rho_{\text{stamp}} \lambda_{\text{stamp}}} \quad (4.5)$$

represents the characteristic time in the LNTP.

Eq. (4.1) is analytically solved with the Fourier transform method, which gives the temperature increase in the stamp:

$$\theta_{\text{stamp}}(x, z, t) = \frac{c_{\text{ink}} \rho_{\text{ink}} h_{\text{ink}}}{c_{\text{stamp}} \rho_{\text{stamp}} \lambda_{\text{stamp}}} \frac{q_{\text{total}}}{2\sqrt{\pi}} \times \int_0^{\bar{t}} \left\{ \frac{1 - \exp(\bar{t} - \tau) \text{erfc}(\sqrt{\bar{t} - \tau})}{\sqrt{\tau}} \exp\left(-\frac{\bar{z}^2 \bar{L}_{\text{ink}}^2}{4\tau}\right) \right. \\ \left. \left[\text{erf}\left(\frac{2\bar{x} + 1}{4\sqrt{\tau}} \bar{L}_{\text{ink}}\right) - \text{erf}\left(\frac{2\bar{x} - 1}{4\sqrt{\tau}} \bar{L}_{\text{ink}}\right) \right] \right\} d\tau \quad (4.6)$$

where $\bar{x} = x/L_{\text{ink}}$ and $\bar{z} = z/L_{\text{ink}}$ are the nondimensional coordinates, $\bar{t} = t/t_0$ is the nondimensional time,

$$\bar{L}_{\text{ink}} = \frac{c_{\text{stamp}} \rho_{\text{stamp}} L_{\text{ink}}}{c_{\text{ink}} \rho_{\text{ink}} h_{\text{ink}}} \quad (4.7)$$

is the nondimensional width of the ink, and erf is the error function (Fettis et al., 1973).

As shown in Fig. 4.5, the temperature increase of the PDMS stamp in Eq. (4.6), normalized by $c_{\text{ink}} \rho_{\text{ink}} h_{\text{ink}} q_{\text{total}} / (c_{\text{stamp}} \rho_{\text{stamp}} \lambda_{\text{stamp}})$, versus \bar{x} agrees well with that obtained by FEM for $\bar{z} = 0, 0.1$ and 0.2 , and the normalized time $\bar{t} = 8.90$ and $\bar{L}_{\text{ink}} = 29.0$, which corresponds to $c_{\text{ink}} = 708 \text{ J/kg/K}$, $\rho_{\text{ink}} = 2.30 \times 10^3 \text{ kg/m}^3$ (Campbell, 2000), $c_{\text{stamp}} = 1.46 \text{ kJ/kg/K}$, $\rho_{\text{stamp}} = 970 \text{ kg/m}^3$ (Mark, 1999), $L_{\text{ink}} = 100 \mu\text{m}$, and $h_{\text{ink}} = 3 \mu\text{m}$ in the experiment (Saeidpourazar, Li, et al., 2012).

Using the continuity condition across the stamp/ink interface (Li, Li, Lü, Song, Saeidpouraza, et al., 2012), the temperature increase in the ink is obtained as

$$\theta_{\text{ink}}(t) = \frac{c_{\text{ink}} \rho_{\text{ink}} h_{\text{ink}}}{c_{\text{stamp}} \rho_{\text{stamp}} \lambda_{\text{stamp}}} \frac{q_{\text{total}}}{\sqrt{\pi} \bar{L}_{\text{ink}}} \times \int_0^{\bar{t}} \left[1 - \exp(\bar{t} - \tau) \text{erfc}(\sqrt{\bar{t} - \tau}) \right] \left\{ \frac{\bar{L}_{\text{ink}}}{\sqrt{\tau}} \text{erf}\left(\frac{\bar{L}_{\text{ink}}}{2\sqrt{\tau}}\right) \right. \\ \left. - \frac{2}{\sqrt{\pi}} \left[1 - \exp\left(-\frac{(\bar{L}_{\text{ink}})^2}{4\tau}\right) \right] \right\} d\tau \quad (4.8)$$

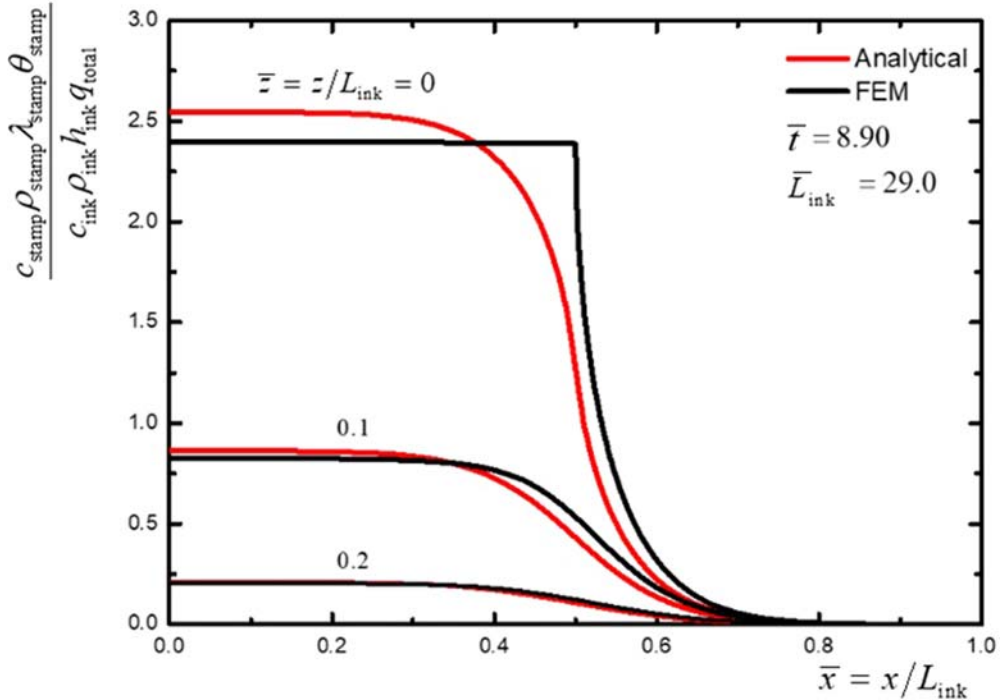


Figure 4.5 The distribution of the increase in normalized temperature of the stamp.

From Li, R., Li, Y., Lü, C., Song, J., Saeidpouraza, R., Fang, B., Zhong, Y., Ferreira, P. M., Rogers, J. A. & Huang, Y. (2012). *Soft Matter*, 8(27), 7122–7127. <https://doi.org/10.1039/C2SM25339A>.

The normalized temperature increase in the ink (Si chip), $\frac{c_{stamp}\rho_{stamp}\lambda_{stamp}\theta_{stamp}}{c_{ink}\rho_{ink}h_{ink}q_{total}}$ depends only on the normalized time \bar{t} and a single combination of stamp and ink properties $\bar{L}_{ink} = \frac{c_{stamp}\rho_{stamp}L_{ink}}{c_{ink}\rho_{ink}h_{ink}}$. This is shown in Fig. 4.6 for $\bar{L}_{ink} = 29.0$, which agrees well with the results obtained by FEM.

4.3 Interfacial delamination

In the LNTP process, both the stamp and the ink are expanded due to heat. However, the coefficient of the thermal expansion (CTE) of the rigid ink is much smaller than that of the soft stamp. Accordingly, the thermal strain in ink is negligible in the analysis of stamp/ink interfacial delamination (Al-Okaily & Ferreira, 2015; Li et al., 2012). For the present plane-strain problem, the in-plane thermal strain in the stamp is $(1 + \nu_{stamp})\alpha_{stamp}\theta_{stamp}$, where ν_{stamp} and α_{stamp} are the Poisson's ratio and the CTE of the stamp, respectively.

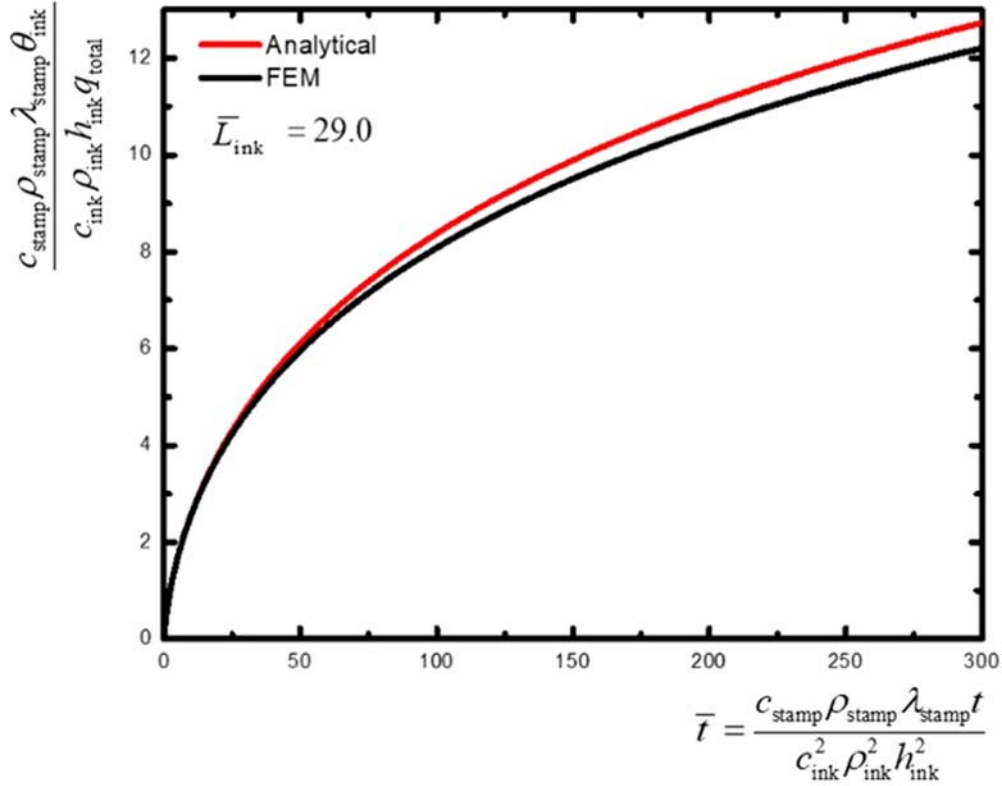


Figure 4.6 The normalized temperature increase in the ink.

From Li, R., Li, Y., Lü, C., Song, J., Saeidpouraza, R., Fang, B., Zhong, Y., Ferreira, P. M., Rogers, J. A. & Huang, Y. (2012). *Soft Matter*, 8(27), 7122–7127. <https://doi.org/10.1039/C2SM25339A>.

The complex stress intensity factor of an interfacial crack with the tip at $(x_0, 0)$ induced by a uniform transformation strain in a circular region of radius R in the stamp is (Suo & Hutchinson, 1989)

$$K^* = R^2 \sqrt{2\pi} \mu_{\text{stamp}} (\varepsilon_{xx}^T + \varepsilon_{zz}^T) (x - x_0 - iz)^{-\frac{3}{2}} \quad (4.9)$$

where μ_{stamp} is the shear modulus of the stamp, ε_{xx}^T and ε_{zz}^T are the transformation strains, and i is the imaginary unit. The stress intensity factor due to a point dilatation is thus

$$K = \sqrt{\frac{2}{\pi}} \mu_{\text{stamp}} (\varepsilon_{xx}^T + \varepsilon_{zz}^T) (x - x_0 - iz)^{-\frac{3}{2}} \quad (4.10)$$

Under the thermal transformation strains $\varepsilon_{xx}^T = \varepsilon_{zz}^T = (1 + \nu_{\text{stamp}})\alpha_{\text{stamp}}\theta_{\text{stamp}}$, the stress intensity factor at the crack tip $(-L_{\text{stamp}}/2, 0)$ is thus

$$K = 2\sqrt{\frac{2}{\pi}}(1 + \nu_{\text{stamp}})\mu_{\text{stamp}}\alpha_{\text{stamp}} \int_{z=0}^{\infty} \int_{x=-\infty}^{\infty} \theta_{\text{stamp}}(x, z, t) \left(x + \frac{L_{\text{stamp}}}{2} - iz\right)^{-\frac{3}{2}} dx dz \quad (4.11)$$

Substituting Eq. (4.6) into Eq. (4.11),

$$K = \frac{4(1 + \nu_{\text{stamp}})\mu_{\text{stamp}}\alpha_{\text{stamp}}}{\lambda_{\text{stamp}}} \sqrt{\frac{2L_{\text{ink}}^3}{\pi^3} q_{\text{total}}} \int_0^{\bar{t}} \frac{\exp(\bar{t} - \tau) \operatorname{erfc}(\sqrt{\bar{t} - \tau}) - 1}{\tau} d\tau \\ \times \int_0^{\infty} \exp\left[\frac{-\eta^2(\bar{L}_{\text{ink}})^2}{4\tau}\right] d\eta \int_{-\infty}^{\infty} (\xi - i\eta)^{-\frac{1}{2}} \exp\left[-\frac{(2\xi - 1)^2 + 1}{16\tau} (\bar{L}_{\text{ink}})^2\right] \sinh\left[\frac{2\xi - 1}{8\tau} (\bar{L}_{\text{ink}})^2\right] d\xi \quad (4.12)$$

The interfacial crack tip energy release rate $G = |K|^2/(8\mu_{\text{stamp}})$ is further given by

$$G = 6(1 + \nu_{\text{stamp}})\mu_{\text{stamp}} \left(\frac{\alpha_{\text{stamp}}}{\lambda_{\text{stamp}}}\right)^2 \left(\frac{c_{\text{ink}}\rho_{\text{ink}}h_{\text{ink}}}{\pi c_{\text{stamp}}\rho_{\text{stamp}}}\right)^3 q_{\text{total}}^2 (\bar{L}_{\text{ink}})^3 \quad (4.13) \\ \times \left| \int_0^{\bar{t}} \frac{\exp(\bar{t} - \tau) \operatorname{erfc}(\sqrt{\bar{t} - \tau}) - 1}{\tau} d\tau \int_0^{\infty} \exp\left[\frac{-\eta^2(\bar{L}_{\text{ink}})^2}{4\tau}\right] d\eta \times \right. \\ \left. \int_{-\infty}^{\infty} (\xi - i\eta)^{-\frac{1}{2}} \exp\left[-\frac{(2\xi - 1)^2 + 1}{16\tau} (\bar{L}_{\text{ink}})^2\right] \sinh\left[\frac{2\xi - 1}{8\tau} (\bar{L}_{\text{ink}})^2\right] d\xi \right|^2$$

The stamp/ink interface delaminates when the interfacial crack tip energy release rate G reaches the work of adhesion γ of the interface, i.e.,

$$G = \gamma \quad (4.14)$$

To determine the critical action time of the laser beam for successful delamination, $t_{\text{delamination}}$, substituting Eq. (4.13) into Eq. (4.14) gives

$$\frac{t_{\text{delamination}}}{t_0} = f\left(\frac{L_{\text{ink}}}{L_0}, \frac{q_{\text{total}}}{q_0}\right) \quad (4.15)$$

where q_0 and L_0 are given by

$$L_0 = \frac{c_{\text{ink}}\rho_{\text{ink}}h_{\text{ink}}}{c_{\text{stamp}}\rho_{\text{stamp}}} q_0 = \frac{\lambda_{\text{stamp}}}{\alpha_{\text{stamp}}} \sqrt{\frac{\gamma}{\mu_{\text{stamp}} L_0^3}} \quad (4.16)$$

The normalized delamination time $t_{\text{delamination}}/t_0$ depends only on two parameters: the normalized total heat flux q_{total}/q_0 and the normalized width of Si chip L_{ink}/L_0 . Fig. 4.7 shows the scaling law in Eq. (4.15), $t_{\text{delamination}}/t_0$ versus q_{total}/q_0 , for $L_{\text{ink}}/L_0 = 3, 5, 10,$ and 29.0 . The laser pulse time of 1, 2, 3, and 4 ms in the experiment correspond to absorbed laser power by the ink ($100 \times 100 \times 3 \mu\text{m}$ polished single-crystal Si squares) 0.0672, 0.0403, 0.0269, and 0.0222 W, respectively, which give the total heat flux $6.72 \times 10^6, 4.03 \times 10^6, 2.69 \times 10^6,$ and $2.22 \times 10^6 \text{ W/m}^2$. The results from experiments and FEM, shown in Fig. 4.7 for $L_{\text{ink}}/L_0 = 29.0$, agree very well with the analytical model.

The LNTP involves up to nine properties of the stamp, the ink, and their interface: the specific heat c_{stamp} and c_{ink} , the mass density ρ_{stamp} and ρ_{ink} , the thermal conductivity λ_{stamp} , the CTE α_{stamp} , the shear modulus μ_{stamp} , the Poisson's ratio ν_{stamp} and the work of adhesion γ of the interface. It also depends on the thickness h_{ink} and the width L_{ink} of the transferred ink, and the total heat flux to the stamp/ink interface

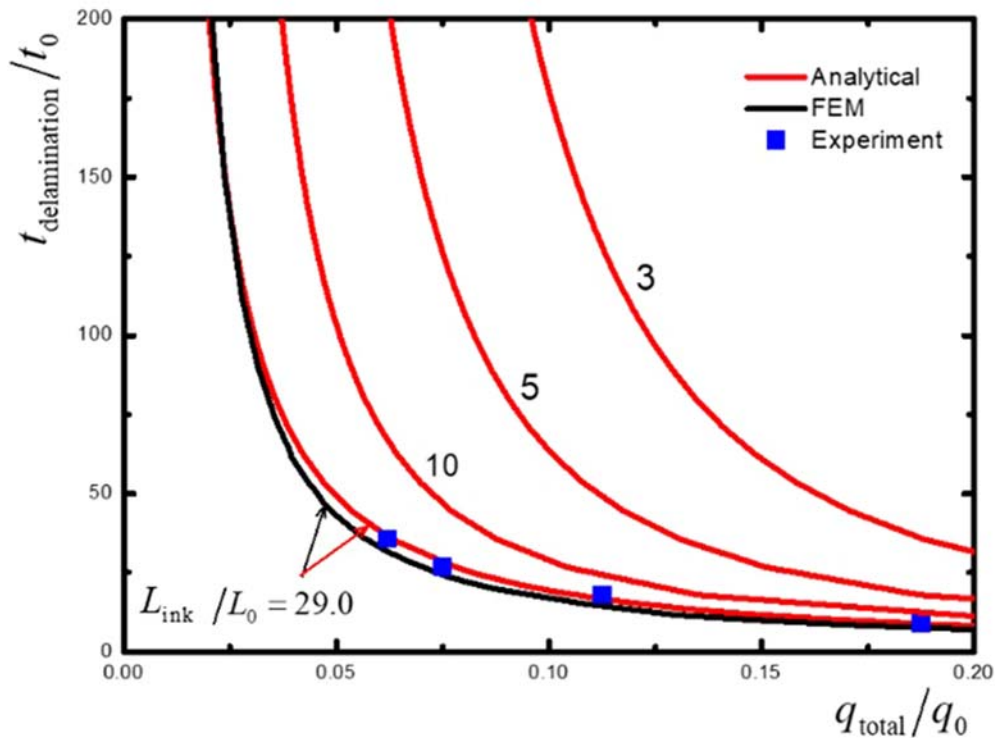


Figure 4.7 The scaling law for delamination of the stamp/ink interface.

From Li, R., Li, Y., Lü, C., Song, J., Saeidpouraza, R., Fang, B., Zhong, Y., Ferreira, P. M., Rogers, J. A. & Huang, Y. (2012). *Soft Matter*, 8(27), 7122–7127. <https://doi.org/10.1039/C2SM25339A>.

q_{total} from the pulsed laser beam. However, the scaling law shown in Eq. (4.15) indicates that the nondimensional delamination time depends only on the nondimensional ink width and the nondimensional total heat flux.

4.4 Size effect of the ink

The previous analysis provides reliable predictions of the temperature distribution and the energy release rate for interfacial delamination, which have been well validated by the finite element analysis and experiments for a Si chip ink with a width of $100 \mu\text{m}$ transferred by a PDMS stamp (Li, Li, Lü, Song, Saeidpouraza, et al., 2012). However, for inks of much smaller widths, the size effect should be investigated in the interfacial delamination analysis.

Taking PDMS/Si as the stamp/ink system, the original problem under consideration is illustrated in Fig. 4.8A. Since the modulus of Si is much larger than that of PDMS, the Si chip is approximated by a large Si solid bonded with the PDMS stamp, as shown in Fig. 4.8B, with the width of the bonded region being L_{Si} . The approximated problem can be decomposed into two problems, as shown in Fig. 4.8C and D, respectively. In the first problem, the stamp is well bonded with the ink, with a uniform transformation strain prescribed in a circular region of radius R in the stamp. The second problem corresponds to an interfacial crack with prescribed tractions to negate those from problem I on the faces $x \geq -L_{\text{Si}}/2$ and $x \leq L_{\text{Si}}/2$ under $z = 0$.

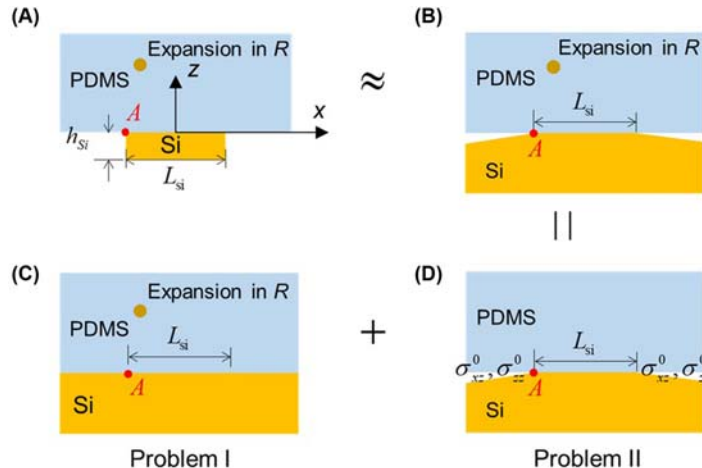


Figure 4.8 The approximate superposition mechanical model to obtain the interfacial stress intensity factor at the crack tip (point A as shown in the figure). (A) Schematic diagram of the previous analytical model; (B) an approximate model for (A); (C) a well-bonded stamp/ink interface with uniform transformation strain; and (D) interfacial crack with tractions prescribed on the faces.

The stress intensity factor at the crack tip $A (-L_{Si}/2, 0)$ is (Gao et al., 2017)

$$K^* = K_I^* + iK_{II}^* = \begin{cases} \frac{iB\sqrt{\pi\frac{L_{Si}}{2}}}{s\sqrt{s(s-L_{Si})}} + \frac{2B\sqrt{2\pi}\text{Im}[(L_{Si}-2\bar{s})\sqrt{s(s-L_{Si})}]}{L_{Si}\sqrt{L_{Si}}|s(s-L_{Si})|} & \text{Re}(s) \leq 0 \\ -\frac{iB\sqrt{\pi\frac{L_{Si}}{2}}}{s\sqrt{s(s-L_{Si})}} - \frac{2B\sqrt{2\pi}\text{Im}[(L_{Si}-2\bar{s})\sqrt{s(s-L_{Si})}]}{L_{Si}\sqrt{L_{Si}}|s(s-L_{Si})|} & \text{Re}(s) > 0 \end{cases} \quad (4.17)$$

where $B = 6\mu_{PDMS}\alpha_{PDMS}\theta_{PDMS}R^2$, and s is the location of the center of the circular region. Under the thermal strains $\varepsilon_{xx}^T = \varepsilon_{zz}^T = (1 + \nu_{PDMS})\alpha_{PDMS}\theta_{PDMS} = 3\alpha_{PDMS}\theta_{PDMS}/2$, where $\nu_{PDMS} = 0.5$ because PDMS is nearly incompressible (Gao et al., 2017), the stress intensity factor is obtained via the integration of K^* over the PDMS domain, yielding

$$K = \int_{y=-\infty}^0 \int_{x=-\infty}^{\infty} \frac{K^*}{R^2} dx dy = \sqrt{\frac{c_{PDMS}\rho_{PDMS}}{c_{Si}\rho_{Si}h_{Si}} \frac{\mu_{PDMS}\alpha_{PDMS}q_{total}}{\lambda_{PDMS}}} \bar{K}(\bar{t}, \bar{L}_{Si}) \quad (4.18)$$

where $\bar{K}(\bar{t}, \bar{L}_{Si})$ is a nondimensional function depending only on the nondimensional time and the nondimensional width of the Si.

The interfacial crack tip energy release rate G is given by

$$G = \frac{c_{stamp}\rho_{stamp}\mu_{stamp}\alpha_{stamp}^2 q_{total}^2}{8c_{ink}\rho_{ink}h_{ink}\lambda_{stamp}^2} |\bar{K}(\bar{t}, \bar{L}_{ink})|^2 \quad (4.19)$$

Substituting Eq. (4.19) into Eq. (4.14) gives the scaling law of the critical delamination time $t_{delamination}$. It has the same forms as Eq. (4.15), but they have different expressions of $f(L_{ink}/L_0, q_{total}/q_0)$.

Fig. 4.9 demonstrates the predicted nondimensional delamination time versus the nondimensional total heat flux q_{total}/q_0 for $\bar{L}_{Si} = 29, 5.8, \text{ and } 2.9$, which correspond to the width of Si chip of 100, 25, and 10 μm , respectively. Overall, the nondimensional delamination time decreases with the increases in the total heat flux and the width of Si chip. The predictions based on the stress intensity factor K from Eq. (4.18) are denoted by the solid lines, and agree well with the finite element analysis for all sizes of Si chip. The results based on Eq. (4.11) without accounting for the size effect of Si chip in the derivation of the energy release rate are shown by the dashed lines. When the width of Si chip is large (e.g., 100 μm), the model based on Eq. (4.11) yields a good prediction. However, as the width of Si chip becomes smaller (e.g., 25, and 10 μm), it gives a large discrepancy from the finite element analysis. Therefore, it is essential to account for the size effect of Si chip in interfacial fracture mechanics modeling.

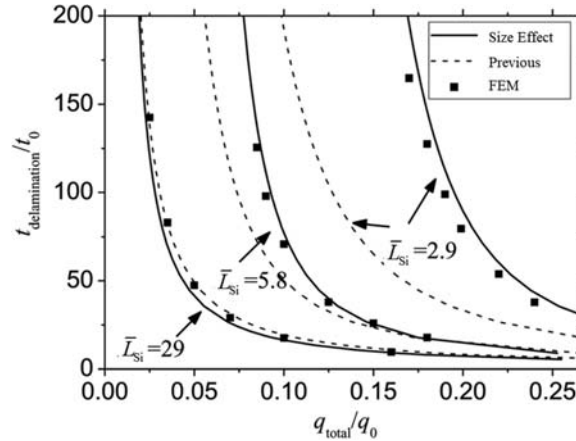


Figure 4.9 The scaling law for the delamination time at the PDMS/Si chip interface. From Gao, Y., Li, Y., Li, R. & Song, J. (2017). *Journal of Applied Mechanics*, Transactions ASME, 84(6). <https://doi.org/10.1115/1.4036257>.

4.5 Stamp modification design

Modification on the stamp is necessary for reliable and programmable noncontact transfer printing. The LNTP technique realizes noncontact transfer printing, eliminating the restriction of the receiver substrate on transfer printing, and thus can transfer the device to the three-dimensional surface, liquid surface, etc. However, due to the high-temperature rise at the interface caused by laser heating, the stamp interface or device may be damaged in the process.

A stamp with cavities filled with air encapsulated by a micropatterned surface membrane could provide tunable adhesive properties (Luo et al., 2020). The active elastomeric microstructured stamp, as shown in Fig. 4.10, incorporates three critical components: (i) the cavities filled with air and embedded under the contacting surface, (ii) the micropatterned membrane that encapsulates the air cavities and serves as the tunable adhesive, and (iii) the metal layer on the inner-cavity surfaces that serves as the laser-absorbing layer. The air in the cavities expands and provides pressure on the surface membrane when heated by the laser beam. The deformation of the membrane ejects the ink on the receiver substrate in a lower temperature increase.

The maximum membrane deflection, d , is given by

$$d = \left(\frac{cR^4 \Delta P}{2Et} \right)^{\frac{1}{3}} \left(1 + \frac{1}{4}c + \frac{5}{36}c^2 \right) \quad (4.20)$$

where c is a nondimensional parameter depending on the Poisson's ratio (Sun et al., 2013), R is the radius of the circular cavity, E and t are Young's modulus and

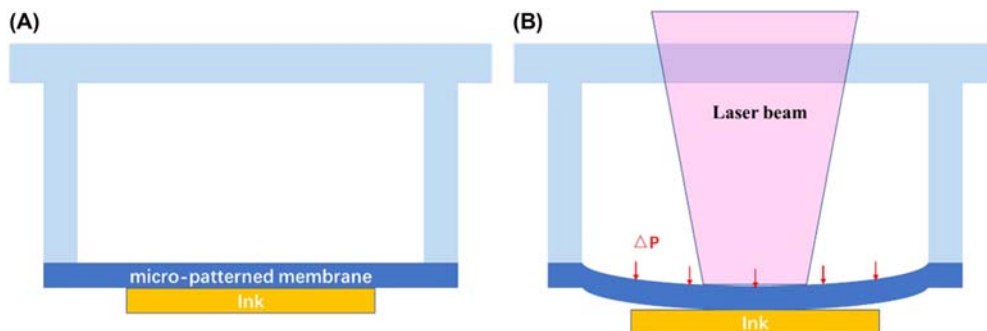


Figure 4.10 The active elastomeric microstructured stamp with a macro-scale cavity (A) before and (B) after pulsed laser beam projection.

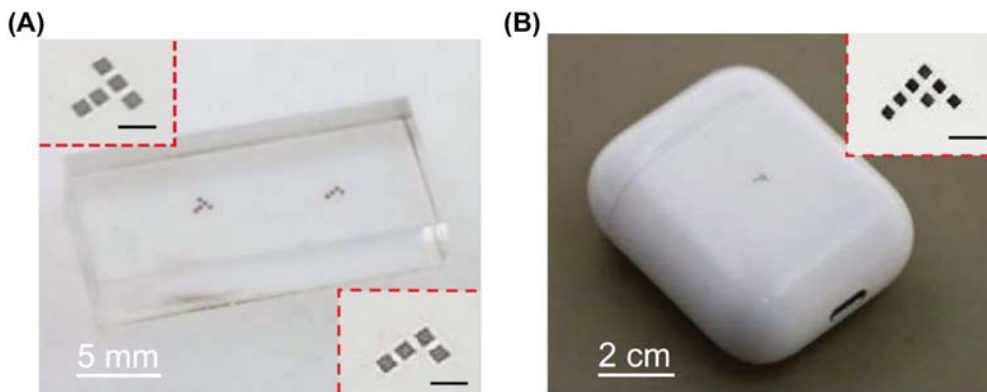


Figure 4.11 Demonstrations of the microstructured stamp printing Si platelets onto (A) acrylic to form a letter “T” and letter “L” and (B) the cover of Apple AirPods to form a letter “F”.

From Luo, H., Wang, C., Linghu, C., Yu, K., Wang, C. & Song, J. (2020). National Science Review, 7(2), 296–304. <https://doi.org/10.1093/NSR/NWZ109>.

thickness of the membrane, respectively, and ΔP is the inflation pressure caused by laser heating effect.

The system has a large switchability of more than three orders of magnitude at a temperature increase below 100°C. Therefore, the components that cannot withstand high heat can be transferred. Fig. 4.11 demonstrates Si platelets printed onto acrylic to form the letters “T” and “L” and the cover of Apple AirPods to form a letter “F”, respectively, which shows the unusual ability of programmable printing microscale inks onto smooth surfaces with ultra-low adhesion.

Another way to avoid heat damage to the ink is employing shape memory polymer (SMP). A stamp with carbon black particles embedded within the stamp surface near to stamp/ink interface was designed (Eisenhaure & Kim, 2016). An epoxy-based

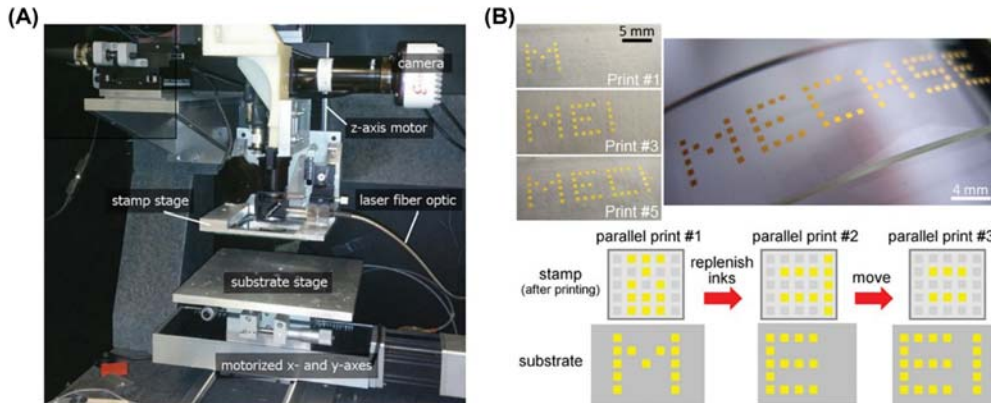


Figure 4.12 (A) The photograph of the automated laser-driven printer using SMP stamp. (B) A 5×5 array of SMP stamps is used to print "MECHSE" on a polydimethylsiloxane (PDMS) substrate with gold-coated Si inks using multiple parallel printing steps. The PDMS substrate is conformed to a curved surface.

From Eisenhaure, J. & Kim, S. (2016). *Advanced Materials Technologies*, 1(7), 1600098-1600098. <https://doi.org/10.1002/ADMT.201600098>.

SMP was used. It has optical transparency, good shape fixity, and recovery factors, suitable glass transition temperature, and a large storage modulus ratio between glassy and rubbery states (Xie & Rousseau, 2009).

By embedding laser-absorbing particles, carbon black composite, within the SMP matrix, the speed and localization of heat delivery are greatly enhanced. SMP stamps are locally heated using near-infrared (NIR) laser illumination to provide the necessary heat to trigger the SMP fixing/recovery cycle.

Fig. 4.12A shows the laser-driven transfer printing system using the SMP stamp with carbon black composite. Fig. 4.12B demonstrates printing gold-coated Si inks on a flexible PDMS substrate which is placed on a curved glass surface. The gold coating is ≈ 100 nm in thickness and causes near total reflection of the NIR laser, thus providing an example of a printing task with a nonabsorbing ink. This method conserves inks when compared to a purely parallel print method where unused inks are discarded. Significant time savings are also realized by reducing the number of pickup steps since a significant portion of a typical process cycle is used to transition between pickup and printing of the ink arrays. This method greatly reduces the required power input of the laser and the risk of thermal damage.

References

Al-Okaily, A. M., & Ferreira, P. M. (2015). Multi-physics modeling for laser micro-transfer printing delamination. *Journal of Manufacturing Processes*, 20, 414–424. Available from <https://doi.org/10.1016/J.JMAPRO.2014.07.006>.

- Bohandy, J., Kim, B. F., & Adrian, F. J. (1986). Metal deposition from a supported metal film using an excimer laser. *Journal of Applied Physics*, 4, 1538–1539. Available from <https://doi.org/10.1063/1.337287>.
- Campbell, S. A. (2000). The science and engineering of microelectronic fabrication. *Industrial Robot*, 27. Available from <https://doi.org/10.1108/ir.2000.04927bae.002>, <https://www.emerald.com/insight/content/doi/10.1108/ir.2000.04927bae.002/full/html>.
- Eisenhaure, J., & Kim, S. (2016). Laser-driven shape memory effect for transfer printing combining parallelism with individual object control. *Advanced Materials Technologies*, 1(7), 1600098. Available from <https://doi.org/10.1002/ADMT.201600098>, <https://onlinelibrary.wiley.com/doi/10.1002/admt.201600098>.
- Fettis, H. E., Caslin, J. C., & Cramer, K. R. (1973). Complex zeros of the error function and of the complementary error function. *Mathematics of Computation*, 27, 401–407. Available from <https://doi.org/10.1090/S0025-5718-1973-0326991-7>, <https://www.ams.org/mcom/1973-27-122/S0025-5718-1973-0326991-7/>.
- Gao, Y., Li, Y., Li, R., & Song, J. (2017). An accurate thermomechanical model for laser-driven micro-transfer printing. *Journal of Applied Mechanics, Transactions ASME*, 84(6), 064501. Available from <https://doi.org/10.1115/1.4036257>, <https://asmédigitalcollection.asme.org/appliedmechanics/article/84/6/064501/384418/An-Accurate-Thermomechanical-Model-for-Laser>.
- Holmes, A. S., & Saidam, S. M. (1998). Sacrificial layer process with laser-driven release for batch assembly operations. *Journal of Microelectromechanical Systems*, 7, 416–422. Available from <https://doi.org/10.1109/84.735350>, <http://ieeexplore.ieee.org/document/735350/>.
- Huang, Y., Zheng, N., Cheng, Z., Chen, Y., Lu, B., Xie, T., & Feng, X. (2016). Direct laser writing-based programmable transfer printing via bioinspired shape memory reversible adhesive. *ACS Applied Materials and Interfaces*, 8(51), 35628–35633. Available from <https://doi.org/10.1021/acsami.6b11696>.
- Linghu, C., Zhang, S., Wang, C., & Song, J. (2018). Transfer printing techniques for flexible and stretchable inorganic electronics. *NPJ Flexible Electronics*, 2(1), 26. Available from <https://doi.org/10.1038/S41528-018-0037-X>.
- Li, R., Li, Y., Lü, C., Song, J., Saeidpourazar, R., Fang, B., Zhong, Y., Ferreira, P. M., Rogers, J. A., & Huang, Y. (2012). Axisymmetric thermo-mechanical analysis of laser-driven non-contact transfer printing. *International Journal of Fracture*, 176, 189–194. Available from <https://doi.org/10.1007/s10704-012-9744-9>, <http://link.springer.com/10.1007/s10704-012-9744-9>.
- Li, R., Li, Y., Lü, C., Song, J., Saeidpouraza, R., Fang, B., Zhong, Y., Ferreira, P. M., Rogers, J. A., & Huang, Y. (2012). Thermo-mechanical modeling of laser-driven non-contact transfer printing: two-dimensional analysis. *Soft Matter*, 8, 7122–7127. Available from <https://doi.org/10.1039/C2SM25339A>, <https://pubs.rsc.org/en/content/articlelanding/2012/sm/c2sm25339a>.
- Loo, Y.-L., Lang, D. V., Rogers, J. A., & Hsu, J. W. P. (2003). Electrical contacts to molecular layers by nanotransfer printing. *Nano Letters*, 3, 913–917. Available from <https://doi.org/10.1021/nl034207c>, <https://pubs.acs.org/doi/10.1021/nl034207c>.
- Luo, H., Wang, C., Linghu, C., Yu, K., Wang, C., & Song, J. (2020). Laser-driven programmable non-contact transfer printing of objects onto arbitrary receivers via an active elastomeric microstructured stamp. *National Science Review*, 7, 296–304. Available from <https://doi.org/10.1093/NSR/NWZ109>, <https://academic.oup.com/nsr/article/7/2/296/5544002>.
- Mark, J. E. (1999). *Polymer data handbook*. Oxford University press.
- Meitl, M. A., Zhou, Y., Gaur, A., Jeon, S., Usrey, M. L., Strano, M. S., & Rogers, J. A. (2004). Solution casting and transfer printing single-walled carbon nanotube films. *Nano Letters*, 4, 1643–1647. Available from <https://doi.org/10.1021/nl0491935>, <https://pubs.acs.org/doi/10.1021/nl0491935>.
- Menard, E., Billhaut, L., Zaumseil, J., & Rogers, J. A. (2004). Improved surface chemistries, thin film deposition techniques, and stamp designs for nanotransfer printing. *Langmuir: the ACS Journal of Surfaces and Colloids*, 20, 6871–6878. Available from <https://doi.org/10.1021/la048827k>, <https://pubs.acs.org/doi/10.1021/la048827k>.
- Saeidpourazar, R., Li, R., Li, Y., Sangid, M. D., Lu, C., Huang, Y., Rogers, J. A., & Ferreira, P. M. (2012). Laser-driven micro transfer placement of prefabricated microstructures. *Journal of Microelectromechanical Systems*, 21, 1049–1058. Available from <https://doi.org/10.1109/JMEMS.2012.2203097>, <http://ieeexplore.ieee.org/document/6232424/>.

- Saeidpourazar, R., Sangid, M. D., Rogers, J. A., & Ferreira, P. M. (2012). A prototype printer for laser driven micro-transfer printing. *Journal of Manufacturing Processes*, *14*(4), 416–424. Available from <https://doi.org/10.1016/J.JMAPRO.2012.09.014>.
- Sun, Y., & Rogers, J. A. (2004). Fabricating semiconductor nano/microwires and transfer printing ordered arrays of them onto plastic substrates. *Nano Letters*, *4*, 1953–1959. Available from <https://doi.org/10.1021/nl048835l>, <https://pubs.acs.org/doi/10.1021/nl048835l>.
- Sun, J., Rong, Y., He, X., Gao, X., & Zheng, Z. (2013). Power series solution of circular membrane under uniformly distributed loads: Investigation into Hencky transformation. *Structural Engineering and Mechanics*, *45*, 631–641. Available from <https://doi.org/10.12989/sem.2013.45.5.631>, <http://koreascience.or.kr/journal/view.jsp?kj=KJKHB9&py=2013&vnc=v45n5&sp=631>.
- Suo, Z., & Hutchinson, J. W. (1989). Steady-state cracking in brittle substrates beneath adherent films. *International Journal of Solids and Structures*, *25*, 1337–1353. Available from [https://doi.org/10.1016/0020-7683\(89\)90096-6](https://doi.org/10.1016/0020-7683(89)90096-6), <https://linkinghub.elsevier.com/retrieve/pii/0020768389900966>.
- Xie, T., & Rousseau, I. A. (2009). Facile tailoring of thermal transition temperatures of epoxy shape memory polymers. *Polymer*, *50*, 1852–1856. Available from <https://doi.org/10.1016/j.polymer.2009.02.035>.
- Zaumseil, J., Meitl, M. A., Hsu, J. W. P., Acharya, B. R., Baldwin, K. W., Loo, Y.-L., & Rogers, J. A. (2003). Three-dimensional and multilayer nanostructures formed by nanotransfer printing. *Nano Letters*, *3*, 1223–1227. Available from <https://doi.org/10.1021/nl0344007>, <https://pubs.acs.org/doi/10.1021/nl0344007>.

This page intentionally left blank

CHAPTER 5

Magnetic-assisted transfer printing techniques

Chenglong Li¹, Suhao Wang¹, Shun Zhang² and Jizhou Song^{1,3,4}

¹Department of Engineering Mechanics, Soft Matter Research Center, and Key Laboratory of Soft Machines and Smart Devices of Zhejiang Province, Zhejiang University, Hangzhou, P.R. China

²College of Information Science & Electronic Engineering, Zhejiang University, Hangzhou, P.R. China

³Department of Rehabilitation Medicine, The First Affiliated Hospital, Zhejiang University, Hangzhou, P.R. China

⁴The State Key Lab of Brain-Machine Intelligence, Zhejiang University, Hangzhou, P.R. China

5.1 Introduction

As a material assembly technique, the transfer printing technique enables the heterogeneous material integration in desired two-dimensional (2D) or three-dimensional (3D) layouts and has been widely used in developing novel electronic devices such as stretchable electronics (Cui et al., 2022; Wang, Cai, et al., 2021; Zhou et al., 2020), flexible electronics (Cai et al., 2021; Ma et al., 2020; Xiao et al., 2022) and micro LED displays (Chen, Yan, et al., 2021; Ho et al., 2020; Huang, Hsiang, et al., 2020). The typical process of transfer printing is to use an elastomeric stamp to pick up the target materials (i.e., inks) from the donor substrate and then print them onto the receiving substrate (Linghu et al., 2018). Thus, successful transfer printing critically relies on the switchability of the stamp/ink interfacial adhesion between a strong state for reliable pick-up and a weak state for easy printing.

The switchability between strong adhesion and weak adhesion are usually achieved by applying various stimuli to the designed adhesive, which yields many advanced transfer printing techniques. Typical examples are light-assisted transfer printing techniques (Guo et al., 2022; Tan et al., 2019; Zhang et al., 2019), heat-assisted transfer printing techniques (Linghu et al., 2020; Luo, Wang, Linghu, et al., 2020; Luo, Wang, Wang, et al., 2021), electric-assisted transfer printing techniques (Chopra et al., 2020; Kim et al., 2019; Li, Tian, et al., 2020), magnetic-assisted transfer printing techniques (Linghu, Wang, et al., 2019; Wang, Luo, et al., 2021; Wang, Wang, Liang, et al., 2020), etc. All these transfer printing techniques are very promising and have attracted much attention from academia and industry. This chapter will overview the latest development of magnetic-assisted transfer printing techniques, which possess the unique advantages of fast response, no interface damage, simple fabrication process and remote control.

5.2 Latest development of magnetic-assisted transfer printing techniques

In a typical magnetic-assisted transfer printing cycle, a magnetic field is used to enhance and/or weaken the adhesion strength of a stamp to achieve the transfer of ink from the fabricated substrate (i.e., donor) onto a receiving substrate (i.e., receiver), as shown in Fig. 5.1. The transfer printing process starts by placing the stamp above the donor (Fig. 5.1A). The intimate contact of the stamp with the ink to be transferred followed by a retrieval completes the pick-up process (Fig. 5.1B and C). The inked stamp is then moved above the receiver (Fig. 5.1D). When the stamp is exposed to a magnetic field (Fig. 5.1E), the stamp/ink interfacial adhesion strength decreases and promotes the release of the ink from the stamp onto the receiver. The stamp then leaves the receiver for another transfer printing cycle (Fig. 5.1F). It should be noted that although the magnetic field is only adopted to weaken the stamp/ink interfacial adhesion strength during the printing process in Fig. 5.1, it can also be adopted to enhance the adhesion strength during the pick-up process. Based on the adhesion modulation principles of the stamp/ink interface under a magnetic field, the magnetic-assisted transfer printing techniques can be classified into two categories: the magnetic-assisted transfer printing techniques based on van der Waals force control and the magnetic-assisted transfer printing techniques based on gas pressure control.

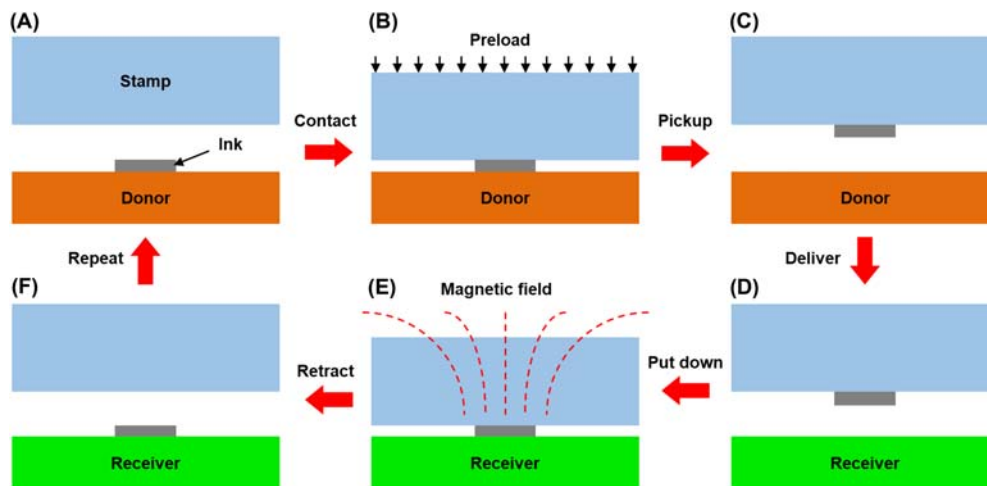


Figure 5.1 Schematic illustration of a typical process of magnetic-assisted transfer printing (A) The stamp is placed above the donor. (B) The stamp is moved down to intimately contact with the ink by a preload. (C) The retraction of stamp picks up the ink. (D) The inked stamp is moved above the receiver. (E) The adhesion strength of the stamp decreases under a magnetic field, causing the ink to be released onto the receiver. (F) The stamp then leaves the receiver for another transfer printing cycle.

5.2.1 Magnetic-assisted transfer printing techniques based on van der Waals force control

Van der Waals forces arise spontaneously when any two surfaces come into contact with each other (Eisenhaure & Kim, 2017). They are suitable to develop tunable adhesives with high reversibility since the interfacial adhesion strength could be easily modulated by changing the contact area (Carlson et al., 2012; Huang, 2020; Zhang et al., 2021), modulus (Krahn et al., 2011; Linghu et al., 2020; Ye et al., 2016), critical energy release rate (Carlson et al., 2011; Chen et al., 2013; Meitl et al., 2006), etc. As a fast responsive stimulus, the magnetic field offers desired capabilities of remote control without introducing interface damage and has been widely used to develop tunable adhesive (i.e., stamp) for magnetic-assisted transfer printing techniques. Some representative magnetic-assisted transfer printing techniques based on van der Waals force control will be overviewed in this section.

5.2.1.1 Magnetic-assisted transfer printing technique based on an aphid-inspired stamp

Linghu, Wang, et al. (2019), Linghu, Zhu, et al. (2019) developed a high-efficient magnetic-assisted transfer printing technique based on an aphid-inspired, magnetic-controlled stamp (i.e., adhesive) (Fig. 5.2). The stamp features open reservoirs in an elastomer body filled with iron particles and sealed with a surface membrane, which can be deformed in a controlled manner via the magnetic field to modulate the interfacial adhesion strength. The combination of rate-dependent effect and magnetic actuation of the surface membrane provides a good tool to develop the high-efficient magnetic-assisted transfer printing technique with the typical process illustrated in Fig. 5.2A. During the pick-up process, the magnetic field is off and the stamp membrane remains flat to ensure a large interfacial contact area and thus a strong adhesion between the stamp and the ink. Rapid retraction of the stamp can further enhance the adhesion due to the rate-dependent effect to enable a reliable pick-up of the ink. During the printing process with a slow retraction of the stamp, a magnetic field is applied to drive the magnetic particles downward to induce a magnetic pressure (i.e., the magnetic force over the surface area of the stamp membrane), which bulges the membrane and promotes the delamination of the ink from the stamp.

The pull-off tests (Fig. 5.2B) show that the adhesion strength of the aphid-inspired stamp is highly sensitive to the retraction speed of the stamp and the magnetic pressure. The adhesion strength is continuously tunable and can be modulated to a specific value by controlling the magnetic pressure and the retraction speed. The adhesion switchability, defined as the ratio of maximal adhesion strength to the minimum adhesion strength, can reach as high as 104 within the measurement capabilities of experiments. Moreover, under certain conditions (such as large magnetic pressure and slow retraction speed), the adhesion between the ink and the stamp may disappear, which

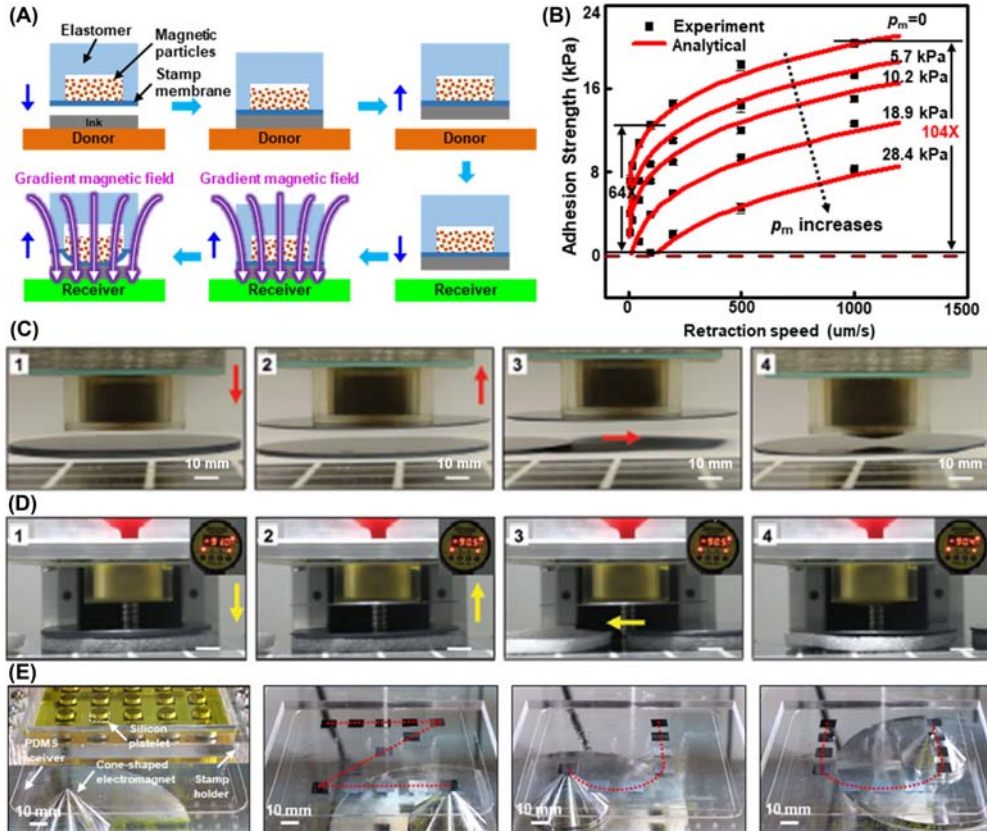


Figure 5.2 Magnetic-assisted transfer printing technique based on an aphid-inspired stamp. (A) Schematic illustration of the typical process of the aphid-inspired magnetic-assisted transfer printing. (B) Measured adhesion strength between the stamp and the flat glass substrate under different magnetic pressures as a function of retraction speed. (C) Noncontact transfer printing process in air and (D) Noncontact transfer printing process of a silicon wafer (4 inches in diameter, 1 mm in thickness) in a vacuum. (E) Pattern printing by the scanning of a localized magnetic field. From Linghu, C., Wang, C., Cen, N., Wu, J., Lai, Z., & Song, J. (2019). Rapidly tunable and highly reversible bio-inspired dry adhesion for transfer printing in air and a vacuum. *Soft Matter*, 15(1), 30–37. <https://doi.org/10.1039/C8SM01996G>.

enables the noncontact printing of inks (Luo et al., 2020) (i.e., the inks remain non-contacted with the receiver during the printing process). Due to the fast response of magnetic particles to the magnetic field, the printing process is quick (~ 100 ms), thus enhancing the efficiency of transfer printing. The superior capabilities of the magnetic-assisted transfer printing were demonstrated by the noncontact transfer printing of a silicon wafer in an atmospheric environment (Fig. 5.2C) and a vacuum with a vacuum degree of 92 kPa (Fig. 5.2D), and by patterned printing of silicon chips onto a PDMS (polydimethylsiloxane) substrate (Fig. 5.2E).

5.2.1.2 Magnetic-assisted transfer printing technique based on a cantilever-shaped stamp

Zhao et al. (2022) developed a magnetic-assisted transfer printing technique based on a cantilever-shaped stamp (Fig. 5.3). The structure of the stamp and the transfer printing process are schematically shown in Fig. 5.3A. The surface morphology of the stamp features an array of cantilever-shaped units, which consists of a tip (i.e., the cantilever beam) and stalk with the tip on one side of the stalk, on a backing layer. The tip is made of a composite material of PDMS and magnetic hard particles (NdFeB).

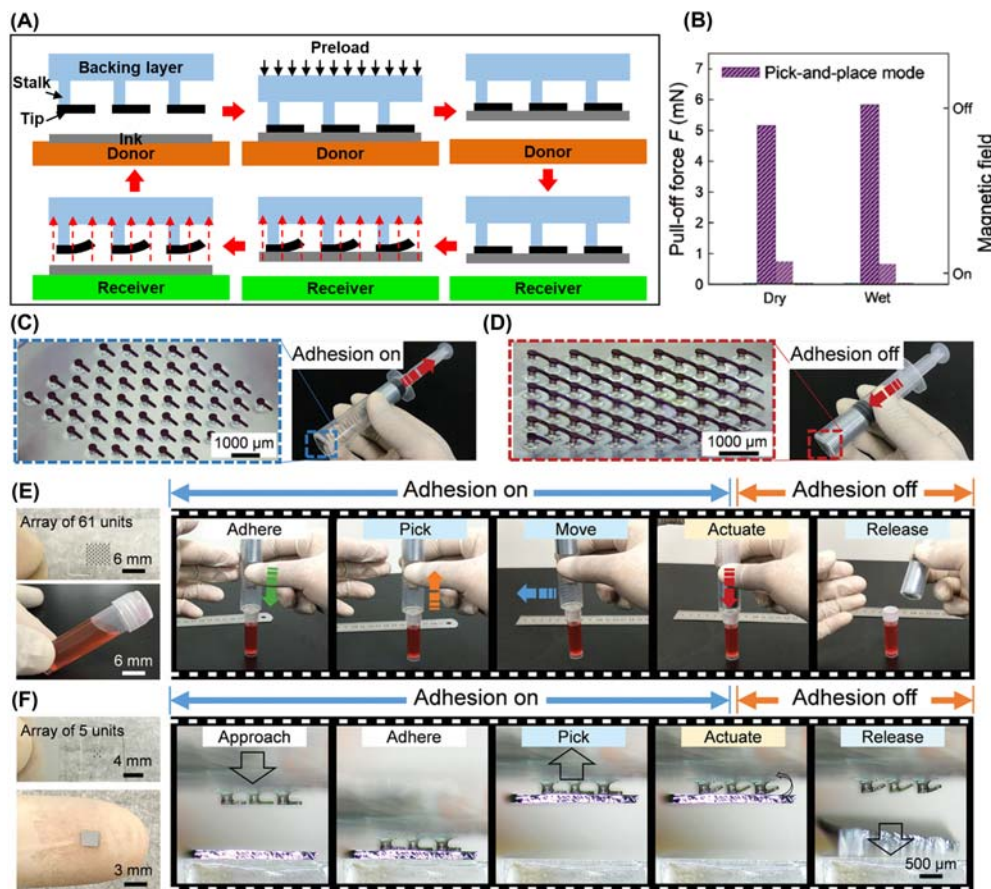


Figure 5.3 Magnetic-assisted transfer printing technique based on a cantilever-shaped stamp. (A) Schematic illustration of the stamp structure and the transfer printing process. (B) Pull-off force of the stamp in dry and wet conditions under different magnetic field state. The handheld pickup device with the adhesion (C) turned on and (D) turned off. (E) Transfer printing process snapshots for a reagent bottle full of red water. (F) A silicon wafer is picked and released by an array of five units. From Zhao, J., Li, X., Tan, Y., Liu, X., Lu, T., & Shi, M. (2022). *Smart Adhesives via Magnetic Actuation*. *Advanced Materials*, 34(8), 2107748. <https://doi.org/10.1002/adma.202107748>.

The stalk and backing layer is made of PDMS only. At the pick-up stage, the contact between flattened tips and the ink followed by a preload provides a large contact area and high compliance between the stamp and ink, resulting in a strong adhesion for pick-up. While printing, a magnetic field is applied to cause the upward bending of tips and drive the generation of an initial crack at the edge of the tip/ink interface, which further leads to a sharp decrease in the adhesion for the release of ink.

The pull-off forces of the cantilever-shaped stamp with and without the magnetic field, as shown in Fig. 5.3B, indicate that the adhesive is magnetically switchable with an adhesion switchability of more than 5 in the dry or wet conditions. To illustrate the capability of the adhesive for transfer printing, the authors developed a handheld pick-up device to realize the manipulation of objects, as shown in Fig. 5.3C–E. The device consists of an injector, a magnet fixed on the pushrod inside the injector, and a cantilever-shaped stamp with an array of 61 units attached to the top of the injector. The distance between the stamp surface and the magnet can be adjusted by the pushrod. When the magnet is away from the stamp surface (Fig. 5.3C), the tips have no deformations and the adhesion is on. When the magnet approaches the stamp surface (Fig. 5.3D), the tips bend upward and the adhesion is off. As a demonstration, the handheld pick-up device is used to pick and place a reagent bottle full of red water (Fig. 5.3E). During the pick-up and move processes, the adhesion is on, enabling the bonding of the reagent bottle to the adhesive. Upon completion of the transfer of the reagent bottle to the target location, the release of the bottle occurs under an activated magnetic field. In addition to the manual manipulation of a large object, an automated pick-and-place of a thin and brittle silicon wafer (2.5 mm × 2.5 mm) by a stamp with five units further illustrate the superior potential of the cantilever-shaped stamp for transfer printing (Fig. 5.3F). When the stamp is actuated by an external magnetic field, the tips all bend upward and the silicon wafer is released from the stamp.

5.2.1.3 Magnetic-assisted transfer printing technique based on a mechanical property changing stamp

Pang et al. (2020) developed a magnetic-assisted transfer printing technique based on a mechanical property changing stamp (Fig. 5.4). The stamp features a magnetorheological polymer gel (MRPG) core inside a PDMS shell and is close to the PDMS surface. The mechanical properties of MRPG are sensitive to the magnetic field with the modulus and yield stress increasing with the magnetic field, which can be adapted to modulate the interfacial adhesion strength, thus developing a magnetic-assisted transfer printing technique with the typical process illustrated in Fig. 5.4A. During the pick-up process, the stamp with a soft MRPG core firstly approaches and touches the ink on the donor with the magnetic field off. Then a magnetic field is on, which yields a hard MRPG core to enhance the interfacial adhesion strength for a reliable pick-up of

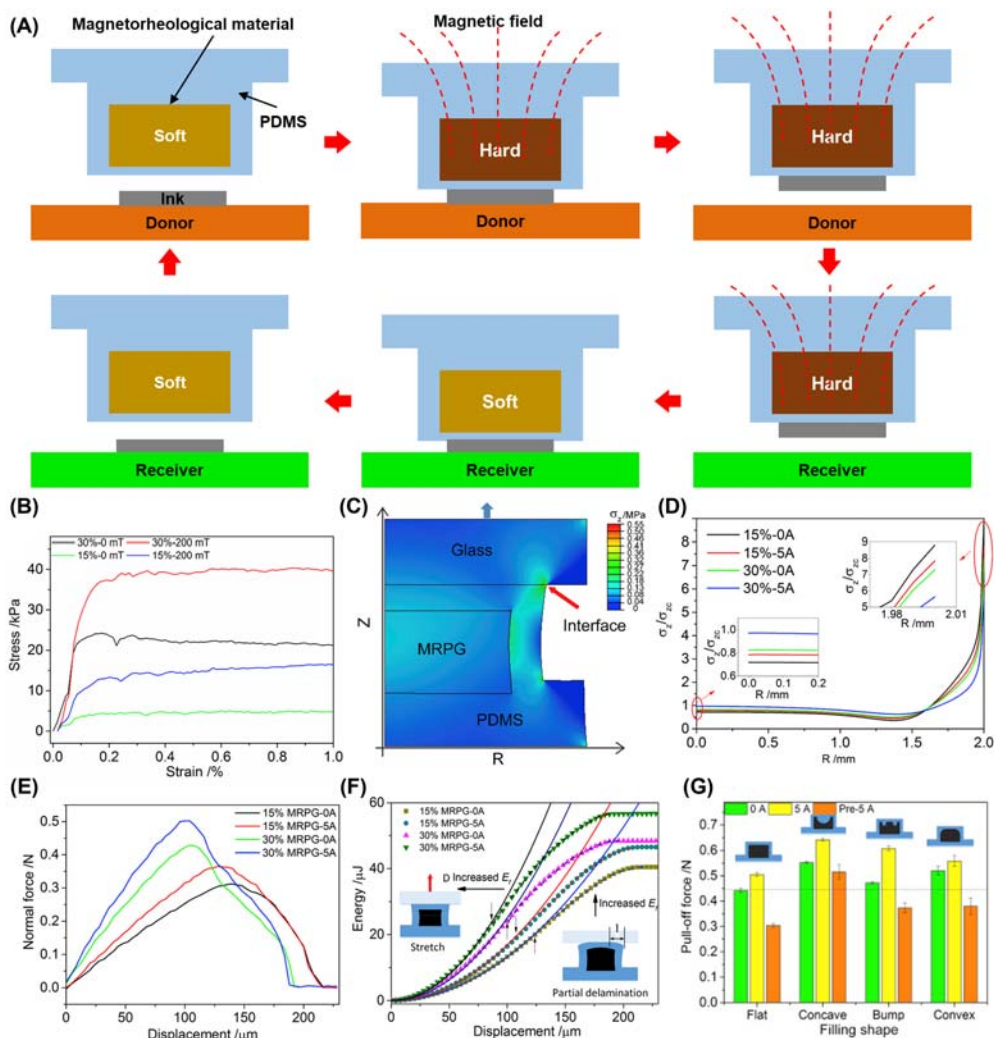


Figure 5.4 Magnetic-assisted transfer printing technique based on a mechanical property changing stamp. (A) Schematic illustration of the typical process of the mechanical property changing transfer printing. (B) Stress–strain curves under different CIP volume fractions and magnetic fields. (C) Stress distribution from finite element analysis. (D) The normalized normal stress σ_z/σ_{zc} distribution from finite element analysis at the contact interface of the mechanical property changing stamp with different cores under different magnetic fields. (E) Normal force–displacement curves during the pull-off process. (F) Energy change during the pull-off process. The arrow indicates the position of the inflection point with the slope corresponding to the pull-off force. (G) Pull-off forces of mechanical changing stamp with different core shapes under different magnetic fields. From Pang, H., Pei, L., Xu, J., Cao, S., Wang, Y., & Gong, X. (2020). Magnetically tunable adhesion of composite pads with magnetorheological polymer gel cores. *Composites Science and Technology*, 192, 108115. <https://doi.org/10.1016/j.compscitech.2020.108115>.

the ink from the donor. As the inked stamp moves onto the receiver, the reduction in interfacial adhesion strength due to the removal of the magnetic field causes the release of ink from the stamp onto the receiver.

The MRPG is prepared by dispersing carbonyl iron particles (CIPs) into a home-made polyurethane gel. Different ratios of CIPs will result in stamps with diverse adhesion characteristics. Fig. 5.4B shows the stress-strain curves of MRPG with CIP volume fractions of 15% and 30% under different magnetic fields. These curves suggest that the increase in the volume fraction of CIPs and the presence of a magnetic field may increase the modulus and yield stress of MRPG. An axisymmetric finite element model was developed to explore the normal stress distribution at the interface for explaining the adhesion change under the magnetic fields. The MRPG is regarded as an ideal plastic material. Fig. 5.4C shows the contour plot of the normal stress distribution for the case with Young's modulus of 2 MPa and yield stress of 4 kPa for MRPG-15%-0 A. Fig. 5.4D shows the normalized normal stress distribution, which is defined as the local stress σ_z divided by the average stress σ_{zc} , at the contact interface of the adhesive with different CIP volume fractions under different magnetic fields. The normalized stress increases with the distance to the center of the adhesive and reaches the maximum at the edge, which indicates that the crack first appears at the edge. Fig. 5.4E shows the normal force-displacement curves in the pull-tests with the highest point of each curve corresponding to the pull-off force (i.e., adhesive force) of the adhesive.

The combination of Fig. 5.4B–E shows that with the increasing yield stress of MRPG core, the normalized stress at the edge decreases and the pull-off force increases. The smaller the edge stress is, the more uniform the stress distribution is, so the contact interface can bear more tension. In addition, the pull-off force changes can also be seen from the energy change in Fig. 5.4F. The separation process of the contact interface can be divided into two stages. First, as the displacement increases, the adhesive remains in full contact with the substrate surface. The adhesive is just stretched and the energy curve is a parabola. As the displacement further increases, the stress at the edge exceeds the critical value and cracks may initiate to cause the interface delamination. The arrow in Fig. 5.4F indicates that the slope of the inflection point of the two stages corresponds to the pull-off force. As the modulus of the filler MRPG increases, the energy required for the same deformation increases and the slope at the inflection point increases, that is, adhesion increases. To sum up, the pull-off force depends on the yield stress and modulus of MRPG. It should be noted that the pull-off force also depends on the core shape (e.g., flat, concave, bump, and convex) and the working mode of the magnetic field as illustrated in Fig. 5.4G. Here, “5 A” means the magnetic field is only on by applying a 5 A current in the coil during the pull-off process while “Pre-5 A” means the magnetic field is only on during the approach and contact processes but off during the pull-off process. These results show that the pad-concave core yields the largest pull-off force no matter how the magnetic field is applied.

Similarly using the magnetorheological material as a part of the stamp, Wang et al. (2022) reported a double-layer stamp consisting of PDMS as the top layer and magnetorheological elastomer (MRE, composed of CIPs and PDMS) as the bottom contact layer to achieve controllable and switchable adhesion. The influences of the magnetic field and magnetic particle size on the adhesion strength were investigated experimentally. These results indicate that when the weight ratio of magnetic particles remains unchanged, a moderate increase in particle size contributes to the improvement of adhesion under the action of high magnetic field intensity. More simply, Testa et al. (2020) directly utilized the magnetorheological elastomer (fabricated by dispersing a magneto-rheological fluid into liquid silicone) as a gripper, where the ink was embedded to achieve a reliable pick-up. The adhesion tests show that a high indentation depth is conducive to the enhancement of pick-up force under the magnetic field.

5.2.1.4 Magnetic-assisted transfer printing technique based on a bi-stable stamp

Li et al. (2021) reported a magnetic-assisted transfer printing technique with high reliability and efficiency based on a bi-stable elastomeric stamp. Fig. 5.5A schematically illustrates the construct of the stamp and the typical process of the magnetic-assisted transfer printing technique. The bi-stable stamp features three components: (1) adhesive blocks responsible for the pick-up of the ink through the peel-rate dependent effect of material, (2) a buckled magnetic-response film that can be actively actuated under a magnetic field to induce a rapid snap-through to facilitate the printing of inks, and (3) a cavity providing the deformation space for the snap-through of buckled magnetic-response film. These three components yield a rapidly switchable adhesive, which allows for a rapid snap-through of the magnetic-response film from one stable buckled configuration (i.e., buckling inward) to the other (i.e., buckling outward) under a magnetic field. A high-speed camera was used to record the release process of ink from the stamp (Fig. 5.5B), which indicates that the snap-through of the film is very fast (~ 100 ms). The quick snap-through process is due to the fast response of the magnetic-response film to the applied magnetic field, which is the key to yield a rapidly switchable adhesion and thus to enhance the efficiency of transfer printing.

The front view of the stamp is shown in Fig. 5.5C with key dimensions labeled including the cavity length L , the magnetic-response film thickness t , the adhesive block thickness d , and the distributed magnetic force acting on the film F_m/bL with F_m representing the total magnetic force and b representing the width of stamp. When the magnetic force exceeds some critical value, the snap-through of the film occurs and introduces a thrust force F_t on the ink, which delaminates the ink from the stamp. Experiments and finite element analysis were performed to investigate the effect of the magnetic force F_m and the adhesive thickness d on the thrust force F_t as shown in Fig. 5.5D and E. Fig. 5.5D shows that the configurations of the magnetic-response film differ at different adhesive block thicknesses, resulting in increasing and then

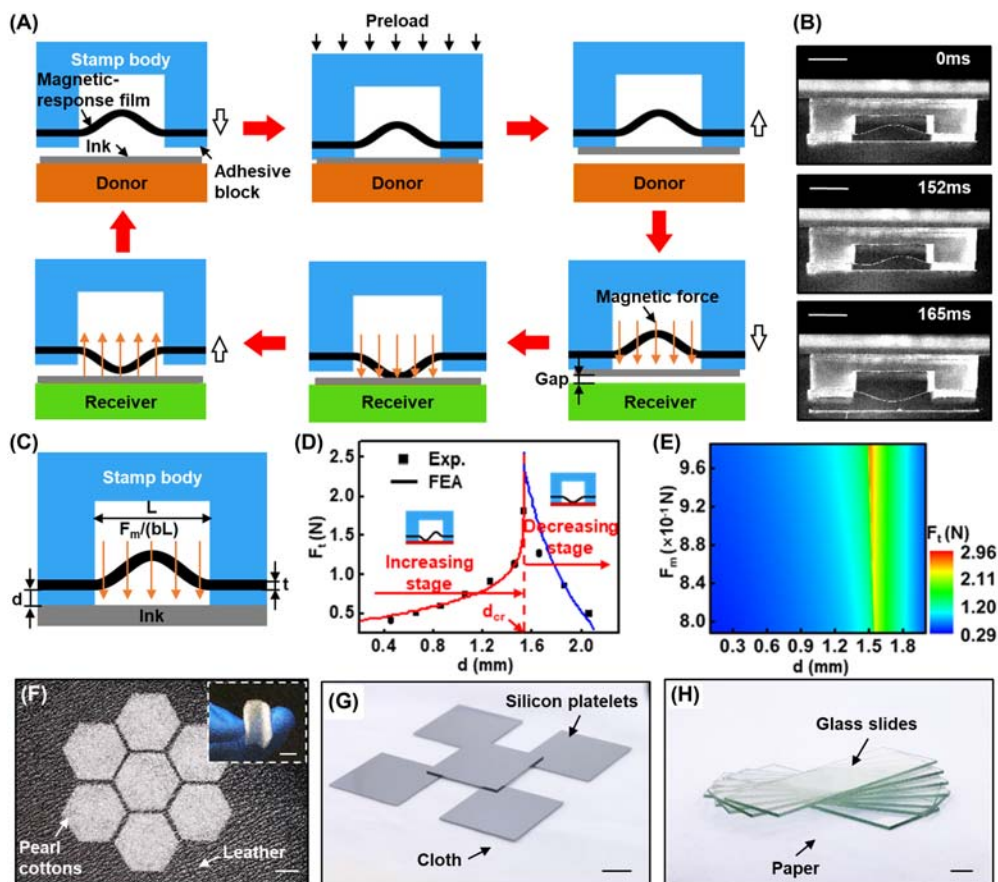


Figure 5.5 *Magnetic-assisted transfer printing technique based on a bi-stable stamp.* (A) Schematic illustration of the transfer printing based on a bi-stable stamp. (B) The snapshots of the release process of an acrylic sheet. (C) Schematic diagram of the front view of stamp with key dimensions labeled. (D) Influences of adhesive block thickness and configurations of magnetic-response film on the thrust force. (E) Influences of adhesive block thickness and magnetic force on the thrust force. (F) A hexagon layout of soft hexagon-shaped pearl cotton printed onto a roughed leather substrate. (G) Four silicon platelets capped with one platelet in the center onto a rough and soft cloth. (H) Multilayer configurations of rigid glass printed onto a paper substrate. The scale bar in the figure is 10 mm. From Li, C., Luo, H., & Song, J. (2021). *Magnetically driven non-contact transfer printing based on a bi-stable elastomeric stamp.* *Advanced Materials Technologies*, 6(11). <https://doi.org/10.1002/admt.202100335>.

decreasing thrust force with the increase of block thickness. These results indicate that a critical adhesive block thickness d_{cr} may be desired to maximize the thrust force for reliable printing. Fig. 5.5E shows the influences of the magnetic force F_m and the adhesive thickness d on the thrust force F_t calculated from finite element analysis. As expected, the thrust force increases with adhesive block thickness when d is smaller

than d_{cr} while decreasing when d is larger than d_{cr} . The maximum thrust force obtained at the critical adhesive block thickness d_{cr} increases with increasing magnetic force. Therefore, a sufficiently large magnetic force and a suitable adhesive thickness will generate a proper thrust force for the reliable release of the ink. The versatility and utility of the bi-stable stamp were demonstrated in Fig. 5.5F–H by noncontact transfer printing of various inks including pearl cottons, silicon platelets and glass slides onto different receivers (such as leather, cloth and paper) in 2D and 3D layouts.

5.2.1.5 Magnetic-assisted transfer printing technique based on a micropillar-shaped stamp

Micropillars are typical surface microstructures to develop tunable adhesives (Kim et al., 2009; Mi et al., 2022; Song & Sitti, 2014; Yang et al., 2012). In order to achieve the highly-controlled bending actuation of micropillars by the magnetic field, Wang, Wang, Liang, et al. (2020), Wang, Wang, and Tang (2020) reported a novel design of heterogeneous magnetic micropillars, which can be used as magnetic micro-tweezers for the transfer printing of objects. As illustrated in Fig. 5.6A, the heterogeneous magnetic micropillars with different distributions of the magnetic nanoparticles are fabricated by concentrating the magnetic nanoparticles at either the tip or the base region of the micropillars, resulting in the magnetic-induced bending deformations of the pillars being highly variable. Under the same magnetic field, the magnetic forces applied to the nanoparticles inside the micropillars dominate the actuations and the bending responses. The deformation degrees of micropillars will be different due to the varied spatial distributions of the magnetic nanoparticle concentration along the different micropillars, which can classify pillars into small deformation pillars (SDPs) with the nanoparticles concentrated at the base and large deformation pillars (LDPs) with the nanoparticles concentrated at the tip.

A hybrid pair of micropillars consisting of one SDP and one LDP can offer a magnetic-controlled micro-tweezer behavior, which can serve as the base for developing a magnetic-assisted transfer printing technique. Fig. 5.6B schematically shows the pick and place process through the magnetic micro-tweezers that could smartly grip and release microscale objects. The microtweezer is controlled to approach and contact with a microparticle using two adjacent LDP and SDP. The magnetic field is then on and the LDP bends along the field direction significantly while the SDP keeps small deformed, which enable an effective grip of the microparticle due to the clamping effect. The captured particle can thus be lifted up from the donor and moved onto the receiver. After the particle is reattached to the receiver, the magnetic field is switched off. Immediately, the bending deformations of the LDP and the SDP disappear and the particle is released from the hybrid pillars to the receiver. The micro-tweezer is finally withdrawn from the receiver for the next cycle. The corresponding snapshots of the hybrid micropillars applied as a microscale magnetic microtweezer to

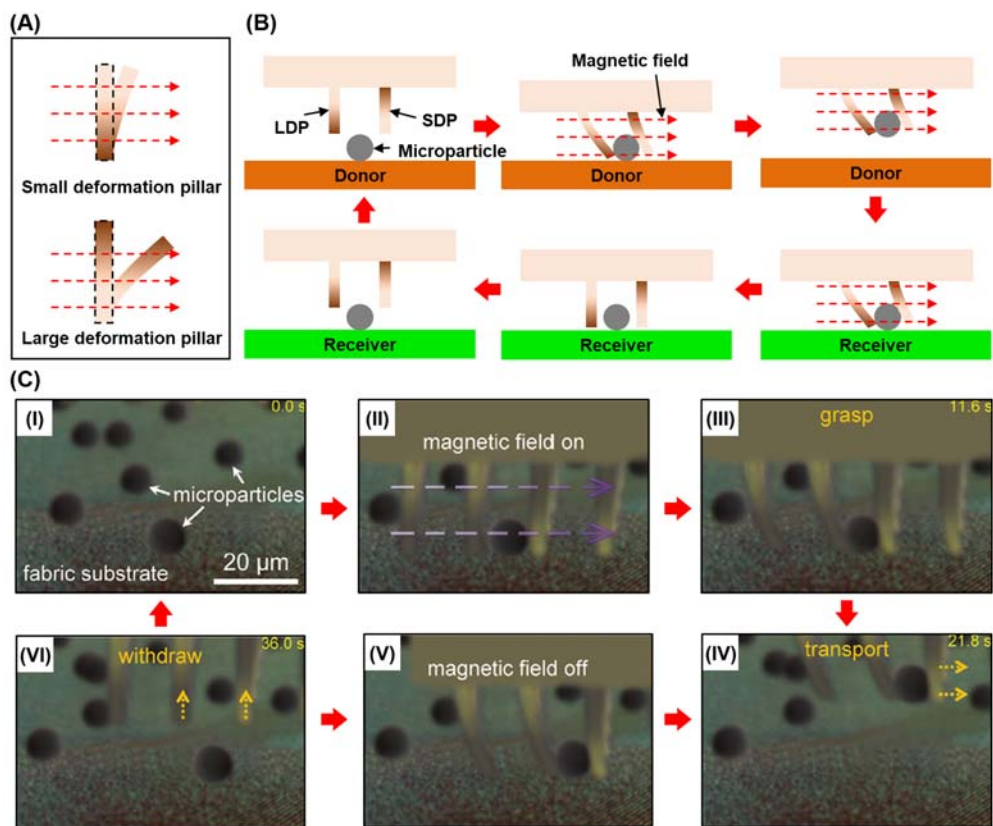


Figure 5.6 *Magnetic-assisted transfer printing technique based on a micropillar-shaped stamp.* (A) Schematic illustration of the bending for the two different micropillars, where the color gradients indicate the variations in the local nanoparticle concentration inside the pillars and the bending amplitude of the pillars under the same magnetic field correlates with the concentration distribution. (B) Schematic illustration and (C) snapshots of the hybrid micropillars applied as a microscale magnetic micro-tweezer to pick and place a microparticle. *From Wang, Z., Wang, K., Liang, D., Yan, L., Ni, K., Huang, H., Li, B., Guo, Z., Wang, J., Ma, X., Tang, X., & Chen, L. (2020). Hybrid magnetic micropillar arrays for programmable actuation. Advanced Materials, 32(25), 2001879. <https://doi.org/10.1002/adma.202001879>.*

transfer a microparticle are shown in Fig. 5.6C, which illustrate the great potential to provide a universal tool for deterministic assembly of 3D objects.

5.2.2 Magnetic-assisted transfer printing techniques based on gas pressure control

As a typical bio-inspired adhesive design, the octopus's sucker has aroused much attention due to its remarkable adhesion performance against all smooth nonporous surfaces in both dry and wet environments. Through muscle contraction and relaxation, the

octopus can easily control the gas pressure inside the sucker to generate reversible and switchable adhesion strengths on surfaces. The adhesion features of the octopus's sucker result from its unique morphology, which consists of the exposed disc-like infundibulum and the embedded hollow acetabulum. The softness of the infundibular portion ensures conformal contact to surfaces of various roughnesses, thus forming a watertight seal. The volume of the acetabular cavity can be changed by utilizing the complex musculature, thus adjusting the cavity pressure and controlling the adhesion. Some representative magnetic-assisted transfer printing techniques based on gas pressure control from the octopus-inspired stamp will be overviewed in this section.

Wang, Luo, et al. (2021) reported a novel design of an octopus-inspired stamp that provides a rapidly switchable and highly reversible adhesion strength by mimicking both the morphology and the muscle actuation of an octopus's sucker. As shown in Fig. 5.7A and B, the stamp features two cavities separated by an elastic membrane with the upper cavity filled with magnetic particles while the lower one empty. This construct enables the reproduction of the adhesion and release strategies of an octopus's sucker in which the deformation of the elastic membrane is actively controlled by an external magnetic field in a fashion analogous to that of acetabular roof. In order to improve the conformability of the stamp to outside surfaces, a stiffness gradient design with a stamp surface layer (i.e., green part) much softer than other parts is introduced. The elastic energy storage strategy is adopted to produce an energy-efficient stamp (Fig. 5.5C–E). Prior to attachment, a magnetic field is applied and induces a magnetic pressure P_{m0} (i.e., the magnetic force over the area of the stamp membrane) on the stamp membrane, which acts as the preload to deform the membrane downward to decrease the cavity volume and store the elastic energy (Fig. 5.7C). At this initial state, the maximum membrane deflection is denoted by w_0 and the cavity pressure is the same as the atmosphere (i.e., $P_{cavity} = P_{atm}$). Upon attachment, the magnetic field is removed after the lower cavity is sealed with the target surface. The stored elastic energy tends to pull the membrane upward, thus producing a high adhesion state due to the negative pressure difference ($\Delta P_1 = P_{cavity} - P_{atm}$) between the cavity and atmosphere (Fig. 5.7D). At this high adhesion state, $P_{cavity} < P_{atm}$ with the maximum membrane deflection $w_1 < w_0$, which enables a reliable pick-up of inks from the donor substrate. When applying a magnetic field (Fig. 5.7E), which induces an equal or larger applied magnetic pressure P_{m2} than the preload P_{m0} , to the membrane again, the pressure difference ($\Delta P_2 = P_{cavity} - P_{atm}$) vanishes or becomes positive, thus leading to a low adhesion state. At this low adhesion state, $P_{cavity} \geq P_{atm}$ with the maximum membrane deflection $w_2 \geq w_0$, which enables a successful release of inks from the stamp to the receiver.

Fig. 5.7F and G show the air pressure differences as functions of the magnetic pressures. These results indicate that by adjusting the magnetic pressure, the stamp can change the absolute pressure in the cavity and control its interfacial adhesion strength

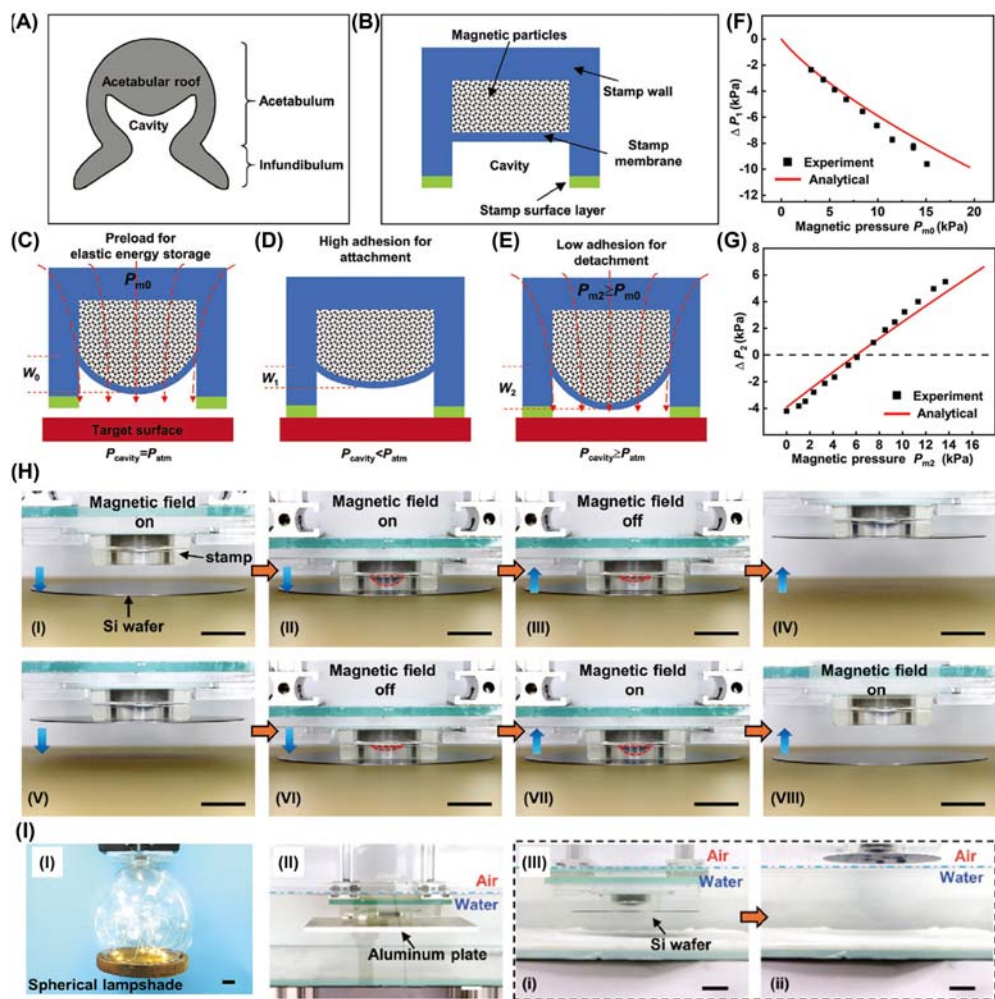


Figure 5.7 *Magnetic-assisted transfer printing technique based on an octopus-inspired stamp.* (A) Schematic illustration of the octopus's sucker. (B) Schematic illustration of the magnetically-actuated, octopus-inspired stamp. (C) A magnetic pressure serves as the preload to the stamp membrane to store elastic energy. (D) A high adhesion state is due to the negative pressure difference between the cavity and atmosphere when the magnetic pressure is removed. (E) A low adhesion state is due to the positive pressure difference between the cavity and atmosphere when the magnetic pressure is added. (F) The pressure difference between the cavity and atmosphere ΔP_1 at the high adhesion stage plotted against the magnetic pressure P_{m0} . (G) The pressure difference between the cavity and atmosphere ΔP_2 at the low adhesion stage plotted against the magnetic pressure P_{m2} . (H) Snapshots of the transfer printing process of a silicon wafer with a diameter of 4 in. in air. (I) Demonstrations of the pickup of (I) spherical lampshade, (II) aluminum plate and (III) silicon wafer in wet conditions. Scale bars: 2 cm. From Wang, S., Luo, H., Linghu, C., & Song, J. (2021). *Elastic energy storage enabled magnetically actuated, octopus-inspired smart adhesive*. *Advanced Functional Materials*, 31(9). <https://doi.org/10.1002/adfm.202009217>.

to realize the pick-up/release of inks under negative/positive pressures. Fig. 5.7H shows the snapshots of the transfer printing process of a Si wafer. First, the stamp is moved downward to approach and contact the Si wafer under which an electromagnet is placed and turned on [Fig. 5.7H(I)]. The stamp membrane bulges during the approaching process and reaches the maximum deflection when the stamp contacts the wafer [Fig. 5.7H(II)]. The stamp is then pressed slightly to ensure an air-tight seal. The electromagnet is then turned off and the stamp membrane relaxes instantaneously to generate a negative pressure inside the lower cavity, leading to a high adhesion strength for a successful pick-up of Si wafer [Fig. 5.7H(III and IV)]. The lifted wafer is then brought back to contact with the substrate [Fig. 5.7H(V and VI)]. The electromagnet is then turned on again to deform the stamp membrane, yielding the same (or a larger) magnetic pressure for a successful release of Si wafer [Fig. 5.7H(VII and VIII)]. The stiffness gradient design of the stamp enhances the sealing capability and enables its applicability to manipulate various objects with diverse shapes and materials (such as spherical lampshade, aluminum plate, and Si wafer) in both dry and wet conditions as illustrated in Fig. 5.7I.

Similarly, Yu et al. (2018) proposed a magnetic-assisted stamp design (Fig. 5.8A), consisting of a lower open cavity, an upper closed cavity filled with incompressible liquid, a top magnetic-response film prepared by adding magnetic particles to a silicone elastomer, and a bottom elastic film prepared by the silicon elastomer. The top magnetic-response film in the stamp can be driven by the external magnetic field to deform either upward or downward, which transmits the deformation to the bottom film and changes the pressure in the lower cavity. The schematic of the magnetic-assisted transfer printing process is shown in Fig. 5.8A. In the pick-up step, the lower cavity of the stamp is brought into contact with an ink followed by a tight seal formed at the interface. The external magnetic field deflects the top magnetic-response film upward and transmits the deformation to the bottom film. The volume increase induced by the bottom film deformation in the lower cavity results in a negative pressure difference between the inside and outside of the cavity, leading to a successful retraction of the ink. In the printing step, after the transfer of the inked stamp from the donor onto the receiver, the direction of the magnetic field is reversed to induce a downward deformation of the top magnetic-response film. The increased pressure in the lower cavity drives the separation of the ink from the stamp onto the receiver. After removing the magnetic field, the retracted stamp is ready for the next cycle.

Analytical and finite element models were established to study the deflection of the bottom film and the pressure change in the lower cavity upon magnetic actuation. The front view of the stamp is shown in Fig. 5.8 with key parameters labeled including the cavity height h_c , the magnetic-response film thickness h and radius R_{top} , the same bottom film thickness h and radius R_{bot} , relatively uniform magnetic pressure Δp , air pressure p_c in the cavity, atmosphere pressure p_c^0 , and the maximum deflection $w_{\text{bot}}^{\text{max}}$. Fig. 5.8B and C

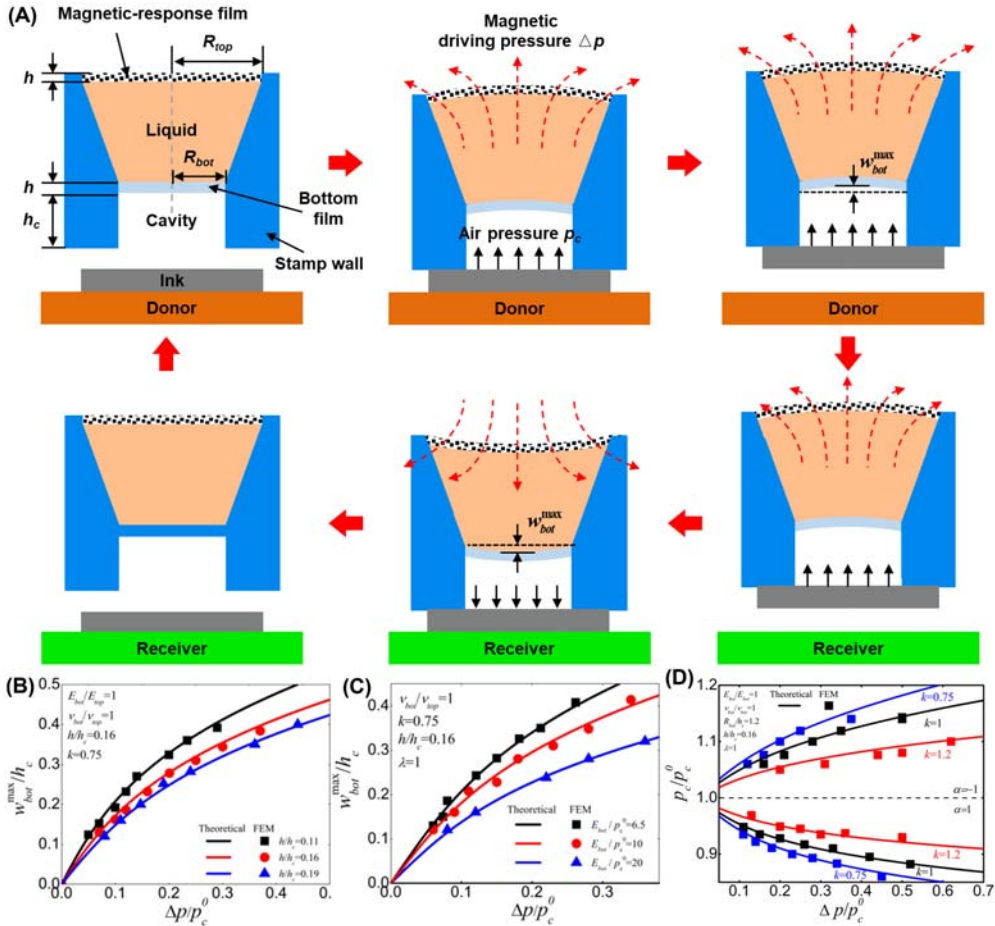


Figure 5.8 Magnetic-assisted transfer printing technique based on an air pressure-controlled stamp similar to the octopus-inspired stamp. (A) Illustration of the structure and transfer process of the air pressure-controlled transfer printing with a liquid chamber. The normalized maximum displacement of the bottom film with (B) three thicknesses or (C) three moduli as a function of the normalized magnetic driving pressure during the pickup step. (D) The effect of the normalized magnetic driving pressure on the normalized pressure in the cavity during the pick-up step ($\alpha = 1$) and the printing step ($\alpha = -1$) for different radius ratios k of the bottom film to the top magnetic-response film. From Yu, Q., Chen, F., Zhou, H., Yu, X., Cheng, H., & Wu, H. (2018). Design and analysis of magnetic-assisted transfer printing. Journal of Applied Mechanics, 85(10). <https://doi.org/10.1115/1.4040599>.

show that the normalized maximum deflection of the bottom film increases during the pick-up step with the increasing normalized magnetic pressure but decreases with increasing thickness h and the modulus E_{bot} . The air pressure in the cavity is obtained from the analytical model as $p_c = \left(1 - \frac{\alpha W_{bot}^{max}}{3h_c + \alpha W_{bot}^{max}}\right) p_c^0$ with $\alpha = 1$ (or $\alpha = -1$) for the pick-up (or printing)

step, which establishes a connection between $u_{\text{bot}}^{\text{max}}$ and p_c , thus gives the dependence of the air pressure on the magnetic pressure. Fig. 5.8D shows that the air pressure in the cavity decreases during the pick-up step ($\alpha = 1$) and increases during the printing step ($\alpha = -1$) with the increasing normalized magnetic pressure, but the trend changes inversely with the increasing radius ratio $k = R_{\text{bot}}/R_{\text{top}}$ of the bottom film to the top magnetic-response film. Therefore, a large pressure difference between the inner and outer of the cavity is associated with a small radius ratio, a low modulus and a thin thickness of the bottom film.

In a simplified version, Li, Xiao, et al. (2020) removed the cavity between the top and bottom films and used only a magnetic film with sucker-like microcavities as a magnetic-assisted stamp for air pressure control. The stamp features a magnetic film evenly dotted with many micro suckers composed of two parts: micro acetabulum (That is, the margin around the sucker for sealing) and infundibulum groove (i.e., the protruding part in the middle of the sucker for air pressure regulation). The two parts of the sucker are made of the same material and their respective magnetization orientations are opposite, resulting in opposing deformations when exposed to an external magnetic field, which facilitates a tight seal. Theoretical and numerical investigations show that the higher the magnetic field strength and the higher the content of filled NdFeB particles before reaching saturation content, the larger deformation of the film and stronger adhesion during the pick-up step. Hu et al. (2021) presented an acarid-inspired, magnetically-actuated stamp consisting of a flat magnetic film and a porous substrate with suction cups. When the suction cup on one side of the porous substrate forms a seal with the ink, the deformed magnetic film on the other side of the porous substrate under the magnetic field changes the air pressure inside the porous substrate and suction cups, realizing the pick-up and release of the ink.

5.3 Conclusion

This chapter presents a brief review on the latest development of magnetic-assisted transfer printing techniques based on two types of adhesion control methods: van der Waals force control and gas pressure control. Van der Waals force control methods mainly control the adhesion strength of the stamp/ink interface by changing the characteristics of the contact surface. The principles and performances of several magnetic-assisted transfer printing techniques based on van der Waals force control, ranging from aphid-inspired transfer printing, cantilever-shaped transfer printing, mechanical property changing transfer printing, bi-stable transfer printing, and micropillar-shaped transfer printing are summarized and overviewed. Gas pressure control methods, mainly inspired by octopus's suckers, introduce air pressure control as an approach to adjust the adhesion of the stamp/ink, thus expanding the range of adhesion strength. The principles and performances of several magnetic-assisted octopus-inspired transfer

printing techniques based on gas pressure control are summarized and overviewed. Demonstrations of the magnetic-assisted transfer printing techniques with advantages of fast response, no interface damage, simple fabrication process and remote control illustrate their robust capabilities in manipulation of a wide range of nonmagnetic materials, thereby creating engineering opportunities in applications requiring the heterogeneous integration of diverse materials.

References

- Cai, M., Jiao, Z., Nie, S., Wang, C., Zou, J., & Song, J. (2021). A multifunctional electronic skin based on patterned metal films for tactile sensing with a broad linear response range. *Science Advances*, 7(52). Available from <https://doi.org/10.1126/sciadv.abl8313>, <https://www.science.org/doi/10.1126/sciadv.abl8313>.
- Carlson, A., Kim-Lee, H. J., Wu, J., Elvikis, P., Cheng, H., Kovalsky, A., Elgan, S., Yu, Q., Ferreira, P. M., Huang, Y., Turner, K. T., & Rogers, J. A. (2011). Shear-enhanced adhesiveless transfer printing for use in deterministic materials assembly. *Applied Physics Letters*, 98(26). Available from <https://doi.org/10.1063/1.3605558>.
- Carlson, A., Wang, S., Elvikis, P., Ferreira, P. M., Huang, Y., & Rogers, J. A. (2012). Active, programmable elastomeric surfaces with tunable adhesion for deterministic assembly by transfer printing. *Advanced Functional Materials*, 22(21), 4476–4484. Available from <https://doi.org/10.1002/adfm.201201023>.
- Chen, H., Feng, X., & Chen, Y. (2013). Directionally controlled transfer printing using micropatterned stamps. *Applied Physics Letters*, 103(15), 151607. Available from <https://doi.org/10.1063/1.4824976>.
- Chen, Z., Yan, S., & Danesh, C. (2021). MicroLED technologies and applications: Characteristics, fabrication, progress, and challenges. *Journal of Physics D: Applied Physics*, 54(12). Available from <https://doi.org/10.1088/1361-6463/abcfe4>, <https://iopscience.iop.org/article/10.1088/1361-6463/abcfe4>.
- Chopra, V., Chopra, V., Chudak, M., Hensel, R., Darhuber, A. A., Arzt, E., & Arzt, E. (2020). Enhancing dry adhesion of polymeric micropatterns by electric fields. *ACS Applied Materials and Interfaces*, 12(24), 27708–27716. Available from <https://doi.org/10.1021/acsami.0c05077>, <http://pubs.acs.org/journal/aamick>.
- Cui, Z., Wang, W., Xia, H., Wang, C., Tu, J., Ji, S., Tan, J. M. R., Liu, Z., Zhang, F., Li, W., Lv, Z., Li, Z., Guo, W., Koh, N. Y., Ng, K. B., Feng, X., Zheng, Y., & Chen, X. (2022). Freestanding and scalable force-softness bimodal sensor arrays for haptic body-feature identification. *Advanced Materials*, 34(47). Available from <https://doi.org/10.1002/adma.202207016>, [http://onlinelibrary.wiley.com/journal/10.1002/\(ISSN\)1521-4095](http://onlinelibrary.wiley.com/journal/10.1002/(ISSN)1521-4095).
- Eisenhaure, J., & Kim, S. (2017). A review of the state of dry adhesives: Biomimetic structures and the alternative designs they inspire. *Micromachines*, 8(4), 125. Available from <https://doi.org/10.3390/mi8040125>.
- Guo, C., Pan, Z., Li, C., Zou, S., Pang, C., Wang, J., Hu, J., & Gong, Z. (2022). Large-scale programmable assembly of functional micro-components for advanced electronics via light-regulated adhesion and polymer growth. *NPJ Flexible Electronics*, 6(1). Available from <https://doi.org/10.1038/s41528-022-00180-w>, <http://nature.com/npjflexelectron/>.
- Ho, S. J., Hsu, H. C., Yeh, C. W., & Chen, H. S. (2020). Inkjet-printed salt-encapsulated quantum dot film for UV-based RGB color-converted micro-light emitting diode displays. *ACS Applied Materials and Interfaces*, 12(29), 33346–33351. Available from <https://doi.org/10.1021/acsami.0c05646>, <http://pubs.acs.org/journal/aamick>.
- Huang, Y. (2020). Highly switchable and reversible dry adhesion for transfer printing. *National Science Review*, 7(3), 558–559. Available from <https://doi.org/10.1093/nsr/nwz134>, <http://nsr.oxfordjournals.org/>.
- Huang, Y., Hsiang, E. L., Deng, M. Y., & Wu, S. T. (2020). Mini-LED, micro-LED and OLED displays: present status and future perspectives. *Light: Science and Applications*, 9(1). Available from <https://doi.org/10.1038/s41377-020-0341-9>, <http://www.nature.com/lsa/>.

- Hu, X., Fu, Y., Liu, Y., Liu, B., & Qu, S. (2021). Acarid suction cup-inspired rapid and tunable magnetic adhesion. *Advanced Materials Technologies*, 6(8). Available from <https://doi.org/10.1002/admt.202100004>, [http://onlinelibrary.wiley.com/journal/10.1002/\(ISSN\)2365-709X](http://onlinelibrary.wiley.com/journal/10.1002/(ISSN)2365-709X).
- Kim, S., Jiang, Y., Towell, K. L. T., Boutilier, M. S. H., Nayakanti, N., Cao, C., Chen, C., Jacob, C., Zhao, H., Turner, K. T., & Hart, A. J. (2019). Soft nanocomposite electroadhesives for digital micro- and nanotransfer printing. *Science Advances*, 5(10). Available from <https://doi.org/10.1126/sciadv.aax4790>, <https://advances.sciencemag.org/content/5/10/eaax4790/tab-pdf>.
- Kim, S., Sitti, M., Xie, T., & Xiao, X. (2009). Reversible dry micro-fibrillar adhesives with thermally controllable adhesion. *Soft Matter*, 5(19), 3689–3693. Available from <https://doi.org/10.1039/b909885b>.
- Krahn, J., Sameoto, D., & Menon, C. (2011). Controllable biomimetic adhesion using embedded phase change material. *Smart Materials and Structures*, 20(1). Available from <https://doi.org/10.1088/0964-1726/20/1/015014Canada>, http://iopscience.iop.org/0964-1726/20/1/015014/pdf/0964-1726_20_1_015014.pdf.
- Linghu, C., Wang, C., Cen, N., Wu, J., Lai, Z., & Song, J. (2019). Rapidly tunable and highly reversible bio-inspired dry adhesion for transfer printing in air and a vacuum. *Soft Matter*, 15(1), 30–37. Available from <https://doi.org/10.1039/C8SM01996G>, <http://pubs.rsc.org/en/journals/journal/sm>.
- Linghu, C., Zhang, S., Wang, C., & Song, J. (2018). Transfer printing techniques for flexible and stretchable inorganic electronics. *NPJ Flexible Electronics*, 2(1). Available from <https://doi.org/10.1038/s41528-018-0037-x>, <http://nature.com/npjflexelectron/>.
- Linghu, C., Zhang, S., Wang, C., Yu, K., Li, C., Zeng, Y., Zhu, H., Jin, X., You, Z., & Song, J. (2020). Universal SMP gripper with massive and selective capabilities for multiscaled, arbitrarily shaped objects. *Science Advances*, 6(7). Available from <https://doi.org/10.1126/sciadv.aay5120>, <https://advances.sciencemag.org/content/6/7/eaay5120/tab-pdf>.
- Linghu, C., Zhu, H., Zhu, J., Li, C., & Song, J. (2019). Mechanics of magnet-controlled transfer printing. *Extreme Mechanics Letters*, 27, 76–82. Available from <https://doi.org/10.1016/j.eml.2019.01.006>, <https://www.sciencedirect.com/science/article/pii/S2352431618302578>.
- Li, C., Luo, H., & Song, J. (2021). Magnetically driven non-contact transfer printing based on a bi-stable elastomeric stamp. *Advanced Materials Technologies*, 6(11). Available from <https://doi.org/10.1002/admt.202100335>, [http://onlinelibrary.wiley.com/journal/10.1002/\(ISSN\)2365-709X](http://onlinelibrary.wiley.com/journal/10.1002/(ISSN)2365-709X).
- Li, S., Tian, H., Shao, J., Liu, H., Wang, D., & Zhang, W. (2020). Switchable adhesion for nonflat surfaces mimicking geckos' adhesive structures and toe muscles. *ACS Applied Materials and Interfaces*, 12(35), 39745–39755. Available from <https://doi.org/10.1021/acsami.0c08686>, <http://pubs.acs.org/journal/aamick>.
- Li, R., Xiao, Q., Yang, P., Wang, H., & Liu, L. (2020). Magnet-induced deformation enhanced adhesion based on magneto-responsive polymer: Theoretical analysis and experimental verification. *Materials & Design*, 194, 108905. Available from <https://doi.org/10.1016/j.matdes.2020.108905>.
- Luo, H., Wang, C., Linghu, C., Yu, K., Wang, C., & Song, J. (2020). Laser-driven programmable non-contact transfer printing of objects onto arbitrary receivers via an active elastomeric microstructured stamp. *National Science Review*, 7(2), 296–304. Available from <https://doi.org/10.1093/nsr/nwz109>, <http://nsr.oxfordjournals.org/>.
- Luo, H., Wang, S., Wang, C., Linghu, C., & Song, J. (2021). Thermal controlled tunable adhesive for deterministic assembly by transfer printing. *Advanced Functional Materials*, 22(16). Available from <https://doi.org/10.1002/adfm.202010297>, [http://onlinelibrary.wiley.com/journal/10.1002/\(ISSN\)1616-3028](http://onlinelibrary.wiley.com/journal/10.1002/(ISSN)1616-3028).
- Ma, Y., Zhang, Y., Cai, S., Han, Z., Liu, X., Wang, F., Cao, Y., Wang, Z., Li, H., Chen, Y., & Feng, X. (2020). Flexible hybrid electronics for digital healthcare. *Advanced Materials*, 32(15). Available from <https://doi.org/10.1002/adma.201902062>, [http://onlinelibrary.wiley.com/journal/10.1002/\(ISSN\)1521-4095](http://onlinelibrary.wiley.com/journal/10.1002/(ISSN)1521-4095).
- Meitl, M. A., Zhu, Z. T., Kumar, V., Lee, K. J., Feng, X., Huang, Y. Y., Adesida, I., Nuzzo, R. G., & Rogers, J. A. (2006). Transfer printing by kinetic control of adhesion to an elastomeric stamp. *Nature Materials*, 5(1), 33–38. Available from <https://doi.org/10.1038/nmat1532>, <http://www.nature.com/nmat/>.
- Mi, Y., Niu, Y., Ni, H., Zhang, Y., Wang, L., Liu, Y., Ramos, M. A., Hu, T. S., & Xu, Q. (2022). Gecko inspired reversible adhesion via quantum dots enabled photo-detachment. *Chemical Engineering Journal*, 431. Available from <https://doi.org/10.1016/j.cej.2021.134081>, <http://www.elsevier.com/inca/publications/store/6/0/1/2/7/3/index.ht>.

- Pang, H., Pei, L., Xu, J., Cao, S., Wang, Y., & Gong, X. (2020). Magnetically tunable adhesion of composite pads with magnetorheological polymer gel cores. *Composites Science and Technology*, 192, 108115. Available from <https://doi.org/10.1016/j.compscitech.2020.108115>.
- Song, S., & Sitti, M. (2014). Soft grippers using micro-fibrillar adhesives for transfer printing. *Advanced Materials*, 26(28), 4901–4906. Available from <https://doi.org/10.1002/adma.201400630>, <http://www3.interscience.wiley.com/journal/119030556/issue>.
- Tan, D., Wang, X., Liu, Q., Shi, K., Yang, B., Liu, S., Wu, Z. S., & Xue, L. (2019). Switchable adhesion of micropillar adhesive on rough surfaces. *Small (Weinheim an der Bergstrasse, Germany)*, 15(50), 1904248. Available from <https://doi.org/10.1002/smll.201904248>.
- Testa, P., Chappuis, B., Kistler, S., Style, R. W., Heyderman, L. J., & Dufresne, E. R. (2020). Switchable adhesion of soft composites induced by a magnetic field. *Soft Matter*, 16(25), 5806–5811. Available from <https://doi.org/10.1039/d0sm00626b>, <http://pubs.rsc.org/en/journals/journal/sm>.
- Wang, C., Cai, M., Hao, Z., Nie, S., Liu, C., Du, H., Wang, J., Chen, W., & Song, J. (2021). Stretchable, multifunctional epidermal sensor patch for surface electromyography and strain measurements. *Advanced Intelligent Systems*, 3(11), 2100031. Available from <https://doi.org/10.1002/aisy.202100031>.
- Wang, S., Luo, H., Linghu, C., & Song, J. (2021). Elastic energy storage enabled magnetically actuated, octopus-inspired smart adhesive. *Advanced Functional Materials*, 31(9). Available from <https://doi.org/10.1002/adfm.202009217>, [http://onlinelibrary.wiley.com/journal/10.1002/\(ISSN\)1616-3028](http://onlinelibrary.wiley.com/journal/10.1002/(ISSN)1616-3028).
- Wang, Z., Wang, K., Liang, D., Yan, L., Ni, K., Huang, H., Li, B., Guo, Z., Wang, J., Ma, X., Tang, X., & Chen, L. Q. (2020). Hybrid magnetic micropillar arrays for programmable actuation. *Advanced Materials*, 32(25), 2001879. Available from <https://doi.org/10.1002/adma.202001879>.
- Wang, Z., Wang, K., & Tang, X. (2020). Heterogeneous magnetic micropillars for regulated bending actuation. *Extreme Mechanics Letters*, 38, 100734. Available from <https://doi.org/10.1016/j.eml.2020.100734>.
- Wang, T., Zhang, P., Yang, X., Zhang, Y., Zhang, J., He, X., Gu, P., Gong, X., & Zhao, Y. (2022). Rapidly switchable double-layered adhesive modified by magnetic field. *Chemical Engineering Journal*, 438, 135441. Available from <https://doi.org/10.1016/j.cej.2022.135441>.
- Xiao, X., Mu, B., Cao, G., Yang, Y., & Wang, M. (2022). Flexible battery-free wireless electronic system for food monitoring. *Journal of Science: Advanced Materials and Devices*, 7(2). Available from <https://doi.org/10.1016/j.jsamd.2022.10043>, <http://www.journals.elsevier.com/journal-of-science-advanced-materials-and-devices>.
- Yang, S. Y., Carlson, A., Cheng, H., Yu, Q., Ahmed, N., Wu, J., Kim, S., Sitti, M., Ferreira, P. M., Huang, Y., & Rogers, J. A. (2012). Elastomer surfaces with directionally dependent adhesion strength and their use in transfer printing with continuous roll-to-roll applications. *Advanced Materials*, 24(16), 2117–2122. Available from <https://doi.org/10.1002/adma.201104975>.
- Ye, Z., Lum, G. Z., Song, S., Rich, S., & Sitti, M. (2016). Phase change of gallium enables highly reversible and switchable adhesion. *Advanced Materials*, 28(25), 5088–5092. Available from <https://doi.org/10.1002/adma.201505754>, <http://www3.interscience.wiley.com/journal/119030556/issue>.
- Yu, Q., Chen, F., Zhou, H., Yu, X., Cheng, H., & Wu, H. (2018). Design and analysis of magnetic-assisted transfer printing. *Journal of Applied Mechanics*, 85(10), 10.1115/1.4040599.
- Zhang, S., Luo, H., Wang, S., Chen, Z., Nie, S., Liu, C., & Song, J. (2021). A thermal actuated switchable dry adhesive with high reversibility for transfer printing. *International Journal of Extreme Manufacturing*, 3(3). Available from <https://doi.org/10.1088/2631-7990/abff69>, <https://iopscience.iop.org/article/10.1088/2631-7990/abff69>.
- Zhang, Y., Lu, B., Wang, T., Feng, X., & Xu, H. (2019). A photochemical approach toward high-fidelity programmable transfer printing. *Advanced Materials Technologies*, 4(9), 1900163. Available from <https://doi.org/10.1002/admt.201900163>.
- Zhao, J., Li, X., Tan, Y., Liu, X., Lu, T., & Shi, M. (2022). Smart adhesives via magnetic actuation. *Advanced Materials*, 34(8), 2107748. Available from <https://doi.org/10.1002/adma.202107748>.
- Zhou, H., Zhang, Y., Qiu, Y., Wu, H., Qin, W., Liao, Y., Yu, Q., & Cheng, H. (2020). Stretchable piezoelectric energy harvesters and self-powered sensors for wearable and implantable devices. *Biosensors and Bioelectronics*, 168. Available from <https://doi.org/10.1016/j.bios.2020.112569>, <http://www.elsevier.com/locate/bios>.

CHAPTER 6

Transfer printing techniques enabled by advanced carbon nanomaterials

Seong Jae Kim and Sanha Kim

Department of Mechanical Engineering, Korea Advanced Institute of Science and Technology (KAIST), Daejeon, South Korea

6.1 Working principles

6.1.1 Large contrast in surface adhesion

Transfer printing processes comprise picking and placing operations. For objects in micro and nanoscale, means to control the surface adhesion of the transfer printing tool is necessary where the strong adhesion picks up the object from the donor substrate while the weak adhesion places the object onto a target surface. Such capability of manipulating surface adhesion from strong to weak or vice versa becomes extremely important on the micro/nanometer scale, as the surface forces strongly dominate over gravitational force. In general practices, we can easily experience that small particles or thin sheets stick on other surfaces like our own fingers and do not fall by their weight (Hattori et al., 2013). Such surface stiction issues between micro components and robotic gripping tools are critical in automated manufacturing (Šafarič & Lukman, 2014). To overcome the adhesion-driven failure of the transfer printing in small-scale picking and placing, different working principles to achieve strong and weak adhesion should be suggested along with the strategy to switch them reversibly. Herein, we introduce the tunable adhesion using a nanoporous composite material that has intrinsically low surface adhesion yet can modulate the adhesion to become 100-fold stronger via electrostatic attraction against small objects.

6.1.1.1 Low surface adhesion via nanoscale porosity

Although a great adhesion is preferable for reaching the high picking throughput, an excess adhesion of a stamp often degrades the throughput of the transfer printing due to incomplete placement. To realize surfaces with low intrinsic adhesion, we may modify the surfaces with chemical treatments which can lower the surface energy (Chen et al., 2012) or design the surface geometry and mechanical properties to alter the contact area with the target object (Kim et al., 2019). Their approaches can be solely or synergetically introduced to the stamp to modulate the surface adhesion.

In contrast to chemical approaches, the geometrical alteration does not depend on the interfacial composition, thereby being considered a more universal approach.

Intensive studies have been conducted to explain the role of contact geometry in dry adhesion strength (Persson & Scaraggi, 2014). In light of the strong distance-dependent nature of intermolecular forces (Alam & Bailey, 2011), the interfacial adhesion strength is governed by real contact area rather than nominal contact area. Different types of attractive intermolecular potentials which rapidly diminish as increasing distance can be listed as follows (Alam & Bailey, 2011):

$$V_{\text{polar}}(r) = - \frac{2\mu_1^2\mu_2^2/3(4\pi\epsilon_0)^2kT}{r^6} \quad (6.1)$$

$$V_{\text{dipole-induceddipole}}(r) = - \frac{\alpha'_2\mu_1^2/4\pi\epsilon_0}{r^6} \quad (6.2)$$

$$V_{\text{dispersive}}(r) = - \frac{3/2\{\alpha'_1\alpha'_2I_1I_2/(I_1 + I_2)\}}{r^6} \quad (6.3)$$

where μ is the dipole moment, ϵ_0 is the vacuum permittivity, k is the Boltzmann constant, T is the temperature, r is the intermolecular distance, α' is the polarizability, and I is the ionization energy. Therefore, low adhesion can be achieved when the surface can induce a small real area of contact.

Experimental validations showed that surface adhesion can be minimized by nano-scale surface geometry (Fleming & Zou, 2018). Low adhesive strengths were reported using nanostructured materials, including self-assembled crystals (Bhushan et al., 2008), nanopatterned polymer (Burton & Bhushan, 2005), metal nanodots (Zou, Wang, et al., 2006), colloidal silica (Zou, Cai, et al., 2006), and nanoporous materials, such as vertically-aligned nanocomposite tubes (Kim et al., 2019). In particular, vertically-aligned carbon nanotubes (CNTs) having approximately 10 nm in diameter coated with a nanometer-thick Al_2O_3 layer could achieve 40-fold less adhesion compared to the Al_2O_3 -coated flat surface (Kim et al., 2019). The relative adhesive strengths of other nanoengineered surfaces are listed in Table 6.1.

6.1.1.2 Strong adhesion and reversible adhesion modulation via electrostatic force

In addition to the low intrinsic adhesion, transfer printing requires means to actively tune the surface adhesion to be sufficiently large to enable the picking process. On a submicrometer scale, capillary forces are known to be the strongest due to the linear length scale dependency (Fan et al., 2015). Different techniques can be suggested to reversely alter the capillary adhesion, such as meniscus shearing (Lambert et al., 2006), inertial release (Fan et al., 2015), gas injection (Bark et al., 1998), electrowetting

Table 6.1 Previous reports on nanostructure-induced low adhesion strength.

Materials	Relative adhesion to the flat surface	Indenter diameter	References
Self-assembled crystals	~30%	30 μm	Bhushan et al. (2008)
Nanopatterned polymer	~50% (PMMA)	30 μm	Burton and Bhushan (2005)
Metal nanodots	10%–20% (compared with Si flat surface)	100 μm	Zou, Wang, et al. (2006)
Colloidal silica	2%–5% (compared with Si flat surface)	100 μm	Zou, Cai, et al. (2006)
Vertically-aligned nanotubes	~2.5%	4 μm	Kim et al. (2019)

(Vasudev et al., 2009), mechanical deformation of the stamp surface (Fantoni et al., 2013), and evaporation (Uran et al., 2017). However, the interfacial stiction of the liquid-containing nozzle remains the challenge (Fantoni et al., 2013). Pneumatic force can be utilized as an alternative (Fantoni et al., 2014; Lee et al., 2016). Nevertheless, preload requirement (Lee et al., 2016), less compatibility with porous target surface (Fantoni et al., 2014), and stiction on the microscale operation (Kim et al., 2019) hinder their use for reliable applications. Magnetic force can often be used for specific active materials in the semiconductor (Ashdown et al., 2011) and display (Linghu et al., 2021) manufacturing, yet the complex head design requires increased cost and limited packing density of the module (Linghu et al., 2021).

Electrostatic forces can alter the attractive interaction at the contact interface via the electrical potential difference between two contacting surfaces. One advantage of electrostatic adhesives is the simple and cost-effective apparatus, as a single voltage source is enough to realize the mechanism. In virtue of facile implementation, copious electroadhesives have been demonstrated by many researchers (Guo et al., 2020). To date, diverse applications regarding semiconductor industries (Wardly, 1973), textile industries (Taylor et al., 1989), and intelligent robotics (Rajagopalan et al., 2022) have been reported. Also, its rapid and digital modulation enables ultrafast processing for the massive manufacturing process. The maximum transfer rate of 1 million/hour was reported in the previous work (Anwar et al., 2022; Bibl et al., 2013). The electroadhesive mechanism can pick both conductive and insulating materials. For conductive materials, which have sufficient electron mobility, attracted charges on the surface allow electrostatic attraction with the electrically charged tool surface. In the case of dielectrics, polarization can be induced which supports the interfacial force. For both cases, thin dielectric materials should be introduced between the transfer tool and the object to prevent charge neutralization and dielectric breakdown (Guo et al., 2020). The electrostatic force intensity in a two bodies

configuration comprising a spherical particle and cylindrical fiber for the case of the charged-driven force (F_c) against conductive objects and for the case of the polarization-driven force (F_p) against nonconductive objects can be estimated respectively as (Wang, 2001)

$$F_c = \frac{qQ}{2\pi\epsilon_0 r} \quad (6.4)$$

$$F_p = \frac{d_p^3}{8\pi\epsilon_0} \left(\frac{\epsilon_p - 1}{\epsilon_p + 2} \right) \frac{Q^2}{r^3} \quad (6.5)$$

where q is the net charge on a particle, Q is the net charge on the unit length of a fiber, ϵ_0 is the permittivity of free space, ϵ_p is the dielectric constant of a particle, r is the radial distance between two bodies, and d_p is the particle diameter. Metallic electrodes covered by dielectric material are widely used for electroadhesives (Guo et al., 2020), and 8.4 kPa of adhesive strength can be achieved with a voltage of 2 kV (Choi et al., 2019). Compared to other pneumatic, capillary, and magnetic forces, electrostatic attraction has wide potential applications, broad compatible materials, simple equipment, low energy consumption, and low working pressure (Guo et al., 2020).

6.1.2 Vertically-aligned carbon nanotube for soft nanocomposite electrodes

To synergetically integrate the two strategies for transfer printing, weak intrinsic adhesion realized via nanoporous surface and strong adhesion with tunability produced via electrostatic force, a vertically-aligned CNT (VACNT) can be selected as the great material. VACNT is a collective assembly of individual CNTs, where a CNT is an allotrope of carbon formed in a cylindrical manner (Fig. 6.1A–C). The structure can be spontaneously constructed by mechanical interlocking and van der Waals forces during the chemical vapor deposition (CVD) process. VACNT has a number of beneficial properties for stamp materials such as high surface porosity (De et al., 2011), excellent mechanical properties (Jia et al., 2011), and low surface modulus (Kim et al., 2016; Maschmann et al., 2014). Furthermore, its high electrical conductivity (Chang & Liu, 2011) allows the efficient charge accumulation on the stamp to electrostatically attract the target materials. Since direct contact between two conductive surfaces may produce an intensive current and dissipate the charges, an ultrathin conformal insulation layer (~ 1 nm of Al_2O_3) should be deposited onto each nanotube, Fig. 6.1D (Kim et al., 2019). The selected thickness was sufficient for preventing an electrical short circuit, yet maintaining high surface porosity.

The operation principle of transfer printing using Al_2O_3 -coated VACNTs was suggested by Kim et al. (2019) as illustrated in Fig. 6.1E–F. During the picking stage, the voltage was exerted on the surface via a conductive layer to cumulate charges. Subsequently,

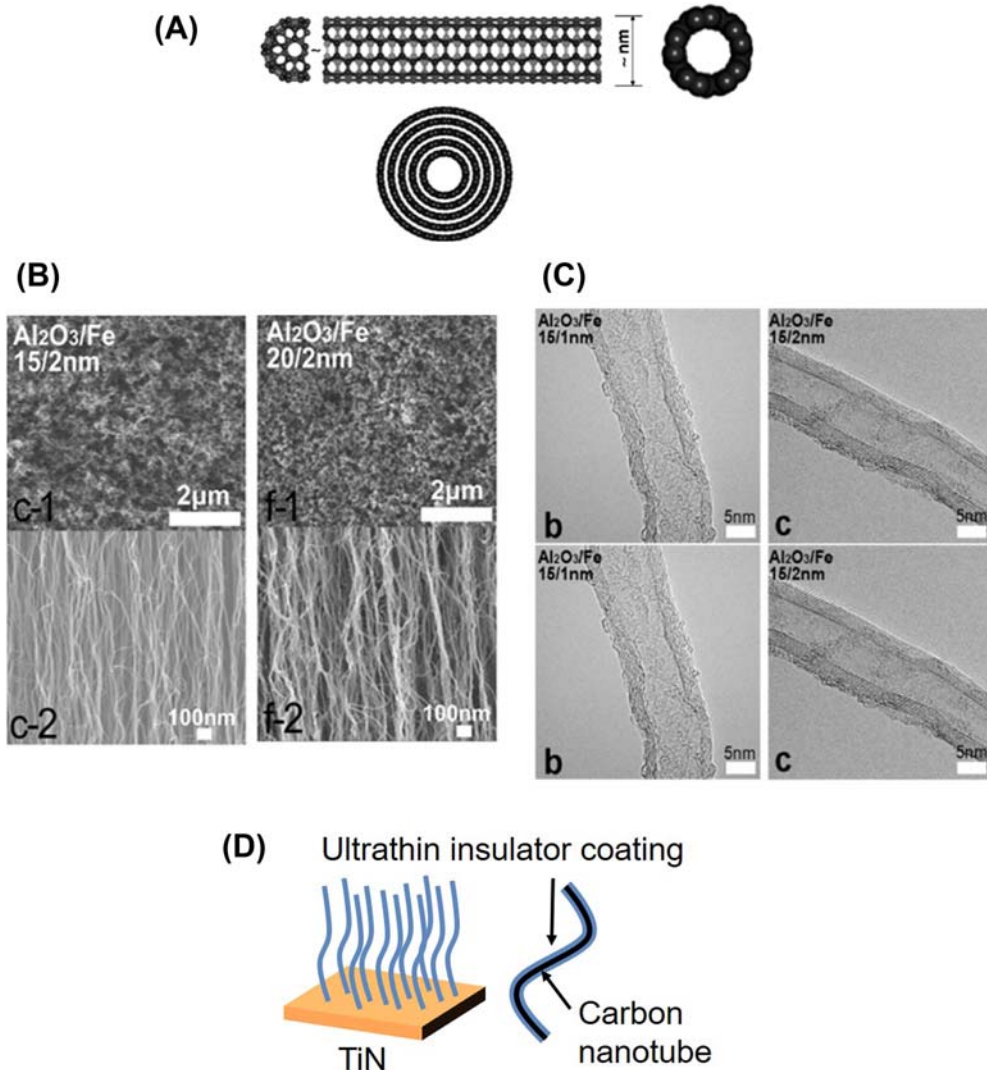


Figure 6.1 *Transfer printing using Al_2O_3 -coated vertically-aligned carbon nanotubes (VACNTs).* (A) Schematic of an ideal, defect-free molecular structure of a multiwalled carbon nanotube (Koziol et al., 2010). (B) and (C) Electron microscopic images of as-grown CNTs from chemical vapor deposition (Ji et al., 2018). (D) Schematic of a stamp made of ceramic-coated vertically-aligned CNTs for transfer printing. (E) Schematic of a pick-and-place procedure using electrostatic adhesion tuning of vertically-aligned-CNTs-based stamp. (F) Electron microscopic image of ceramic-coated vertically-aligned CNTs for transfer printing. (G) Demonstration of pick-and-place using ceramic-coated vertically-aligned CNTs.

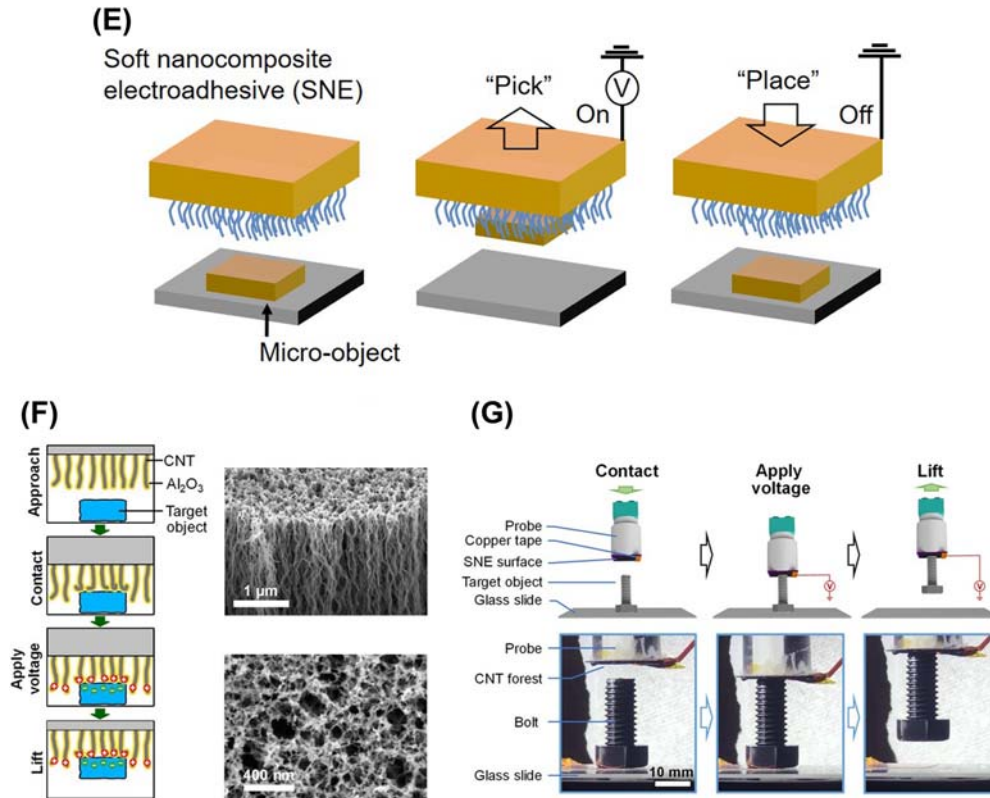


Figure 6.1 (Continued)

the electroadhesive was brought into contact with the target surface to delaminate the microobject. For placement, the voltage source was turned off to lower the adhesion. Quantitative analysis by atomic force microscopy with colloidal probes showed that a pull-off force of a charged nanoporous surface resulted in a 100-fold higher value than an uncharged case. The general flat electrostatic electrodes only exhibited a sevenfold higher value than a case without voltage. The extreme adhesion contrast evidently supported the role of the nanoporosity, which produced a smaller real contact area, thereby reducing the intermolecular interactions. The distinct adhesion contrast between the “on” state and the “off” state induced the facile picking and placing on the receiver, which had identical surface chemistry with the donor surface (Fig. 6.1G). In virtue of its great on/off ratio of adhesion (> 100 for 30 V of the applied voltage), this technique can be adapted to the microscopic regime, where the gravitation force is nearly neglected. Kim et al. (2019) also showed some exemplary demonstrations to validate the capability of picking and placing micro- and nanoobjects. Currently, microchips such as μ -LED components create a demand for reliable microtransfer processes (Anwar et al., 2022). Accordingly, a transfer

printing application of a micro-LED chip (a width of 170 μm) using VACNT electroadhesive was demonstrated.

6.2 Process physics

6.2.1 Introduction of carbon nanotubes

Carbon is a distinctive element that can generate bonds between adjacent carbon atoms, thereby constructing long chains themselves. Despite their unlimited potential to form numerous variants, only two classical allotropes—diamond and graphite—were experimentally found until 1985 (Delgado et al., 2008). After the historical discovery of the third allotropes, fullerenes (Kroto et al., 1985), other allotropic forms were actively explored. Among them, CNT, of which Iijima first discovered its single-walled form in 1991 (Chen et al., 2021; Iijima & Ichihashi, 1993), is one of the most widely used nanomaterials. Depending on the number of walls, it can be classified as single-walled CNT (SWCNT) and multi-walled CNT (MWCNT), Fig. 6.2A. The earlier form of CNT

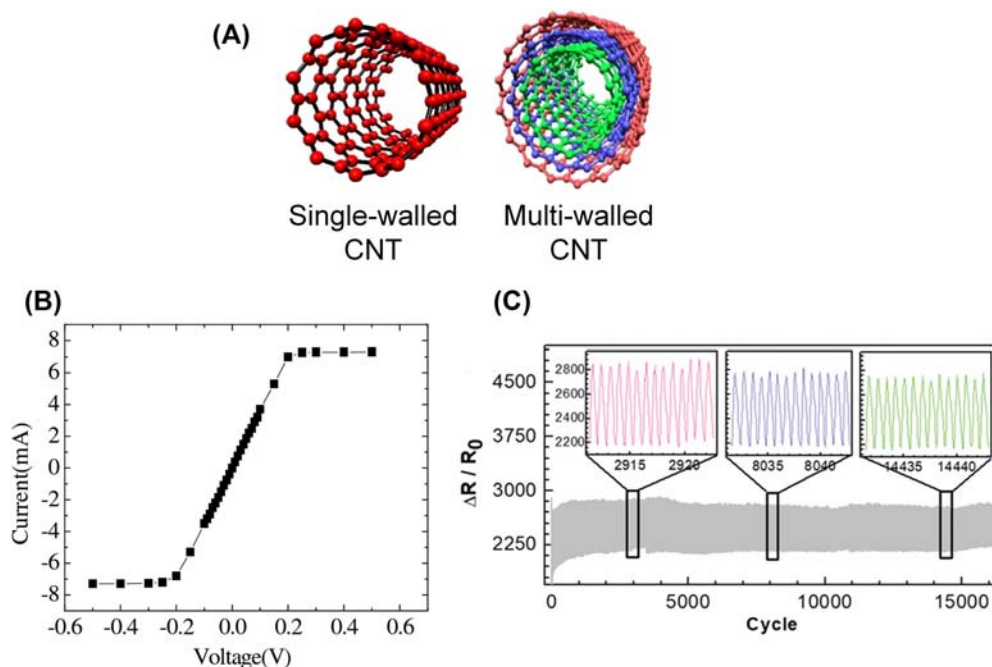


Figure 6.2 Outstanding physical properties of carbon nanotubes (CNTs). (A) Schematics of a single-walled CNT and a multi-walled CNT (MWCNT) (Rathinavel et al., 2021). (B) I – V characteristic curve from an isolated MWCNT (Li et al., 2005). (C) Long-cycle fatigue test result from a CNT-based piezoresistive strain sensor (Lin et al., 2020).

(White & Mintmire, 2005), MWCNT, is more frequently introduced for mechanical applications than pure SWCNTs due to their convenient synthesis.

The superior mechanical properties of CNT were repeatedly emphasized throughout the literature (Coleman et al., 2006). Even though they have a density as low as approximately 1.3 g/cm^3 , the highest experimental strength reached 63 GPa (Yu et al., 2000), which was far apart from that of carbon nanofibers ($\sim 3 \text{ GPa}$) (Callister & Rethwisch, 2018). However, it is also important to remark that its mechanical properties are highly sensitive to its defect density. Aside from the arc discharge method, which produces fewer defect sites than CVD, CVD resulted in a strength of 12–50 GPa for MWCNTs (Salvetat et al., 1999). CNTs also have a high carrier mobility and phonon conductivity. The electric conductivity of pure CNTs can be as high as 10^6 – 10^7 S/m , which is even close to that of copper ($5.96 \times 10^7 \text{ S/m}$) (Wang & Weng, 2017). Also, the theory predicted that the thermal conductivity can be up to $6000 \text{ W/m} \cdot \text{K}$ (Che et al., 2000). For both SWCNTs (Brady et al., 2016) and MWCNTs (Li et al., 2005), quasiballistic carrier transports were observed which enable impressively efficient charge conduction (Fig. 6.2B). The exact electronic behaviors of CNTs highly rely on their chirality represented via a chiral vector (Yang et al., 2020) and the resulting bandgap energies span from metallic to semiconducting regime. Achiral CNTs are considered metallic materials, the rest of CNTs are otherwise small or moderate band gap semiconductors. MWCNTs, the popular form of CNTs, are normally zero-gap metals (Barnett et al., 2020).

In virtue of its outstanding properties, its applications not only span composite materials but also encompass coating technologies, microelectronics, energy devices, and biotechnologies (De Volder et al., 2013). Since transfer printing technologies require intensive repetition of stress applications, CNTs are highly beneficial as stamp materials. The robustness of CNTs against fatigue cycles has been indirectly proved by many literatures regarding piezoresistive CNT-based strain sensors (Wang, 2022), which showed their long-term stability during thousands of loading-unloading cycles. In these studies, 15,000 cycles of operation were performed without noticeable failure (Fig. 6.2C) (Lin et al., 2020).

6.2.2 Synthesis of vertically-aligned carbon nanotubes

The very early method to synthesize CNTs was an arc discharge method suggested by Iijima (Fig. 6.3A) (Iijima, 1991). The graphical illustration in Fig. 6.3B shows the apparatus for synthesis (Arora & Sharma, 2014). When two electrodes are located with a small gap during the voltage application, the arc is generated and simultaneously causes a surge of temperature near the surface. Typically, the anode contains the carbon precursor powder, while the cathode is solely composed of graphite. By the introduction of extreme heat (4000–6000 K), carbon precursor can be vaporized via plasma inside the chamber. As the temperature gradient in the chamber, vapor-state precursor gas can be

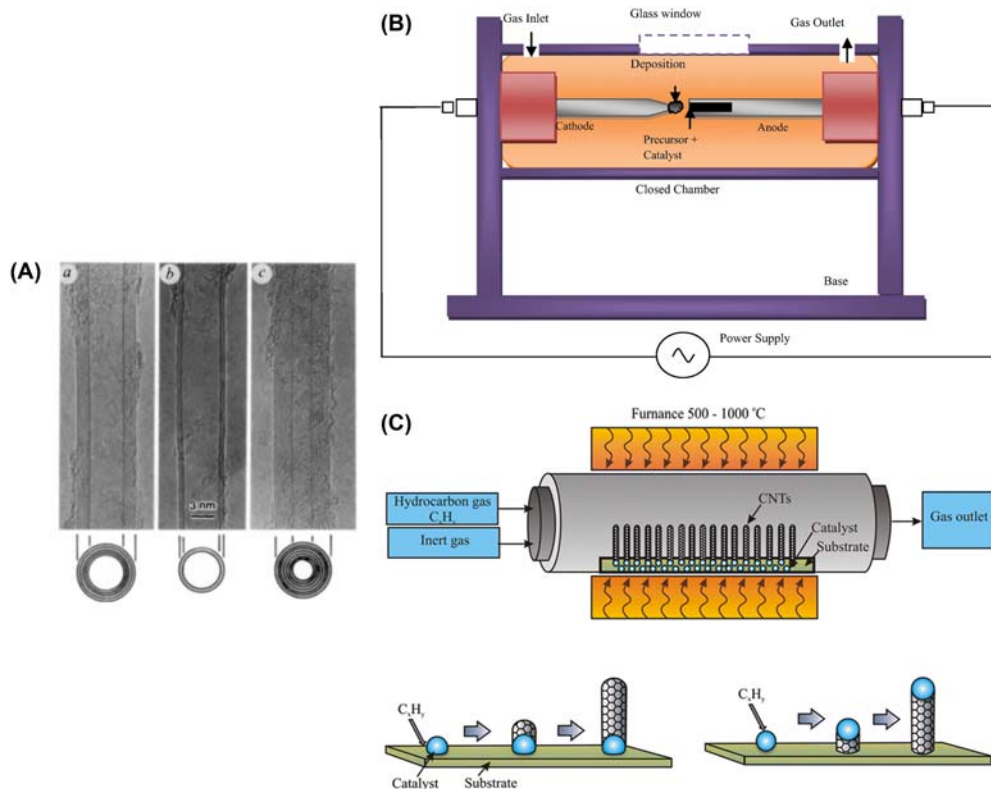


Figure 6.3 *Synthesis methods for carbon nanotubes (CNTs).* (A) Electron microscopic images of multi-walled CNTs from arc discharge method (Iijima, 1991). (B) Schematic of apparatus for arc discharge method (Arora et al., 2014). (C) Schematic of apparatus for chemical vapor deposition method and two different growth configurations: base-growth and tip-growth (Zaytseva et al., 2016).

deposited on the cathode to form CNTs (Arora & Sharma, 2014). The laser ablation method is similar to the arc discharge method, yet the energy source is laser, not arc discharge (Guo et al., 1995). In addition to these commonly used methods, hydro-thermal synthesis (Gogotsi et al., 2000), electrolysis (Bai et al., 2002), and ball milling methods (Pierard et al., 2001) have been applied to synthesize CNTs.

Although the arc discharge method can provide high-quality, low-defect MWCNTs (Cadek et al., 2002), the CVD method first suggested by Li et al. (1996), is the commonly used approach for mass production (Coleman et al., 2006). In contrast to other methods, CVD has plenty of advantages: high surface density (10^9 – $10^{13}/\text{cm}^2$) (Lee et al., 2019), extremely high aspect-ratio reaching the centimeter height (~ 14 cm) (Hata et al., 2004; Sugime et al., 2021), and self-alignment along the vertical direction (Herman's orientation factor of ~ 0.99) (Fan et al., 1999; Goh et al., 2019). While the consensus on the CVD-based growth mechanism is still ongoing, the

vapor–liquid–solid (VLS) mechanism is generally accepted. The first step of CVD is heating a tube to a high temperature (700°C–1000°C), in which a catalyst-nanoparticle-deposited wafer is loaded (Fig. 6.3C) (Zaytseva & Neumann, 2016). For catalyst particles, transition metals (Fe, Co, and Ni) have been widely used. Once the chamber reaches the target temperature, a gas-phase hydrocarbon source such as ethylene (C₂H₄) is flown through the tube and this subsequently dissolves into the catalyst particles. Soon afterward, the saturated carbon-catalyst alloy initiates CNT nucleation from the surface and continues to grow until termination (Liu et al., 2021).

The self-assembly of a VACNT “forest” has been explained via the collective growth dynamics of individual CNTs. Bedewy et al. summarized the overall stages of CNT forest growth, in which catalyst nanoparticles are first prepared by dewetting Fig. 6.4 (Bedewy et al., 2011). Spontaneous solid-state dewetting can provide a facile method to produce nanoparticles spanning large areas. Upon the basic principle of surface free energy minimization, surface diffusion at high temperature reshapes the thin film into nanoclusters (Thompson, 2012). Thereafter gas-phase hydrocarbon is blown along the chamber, the catalyst particles meanwhile maintain their size (Meshot et al., 2012). Once CNT nucleation occurs and continuous growth is initiated, CNTs crowd on the surface. This strong mechanical interlocking is a key to fixing the uppermost region of the individual CNTs during continuous growth. Thanks to the self-supporting roof, CNTs are collectively vertically-aligned through the growth stage. Finally, the growth is terminated along with density decay and diameter widening likely due to proposed limiting mechanisms (Bedewy et al., 2011): Ostwald ripening and subsequent sub-surface diffusion (Kim et al., 2010), catalyst poisoning (Poretzky et al., 2005), and accumulation of the amorphous carbon patches (Stadermann et al., 2009).

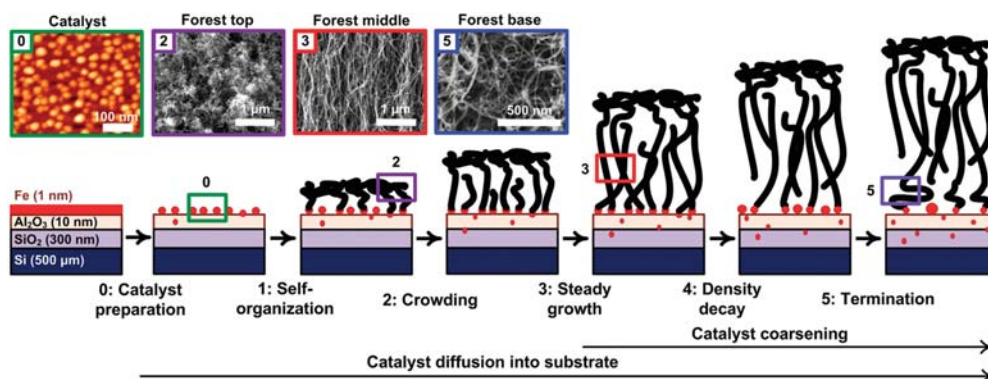


Figure 6.4 Mechanism of vertically-aligned carbon nanotube growth via chemical vapor deposition. From Bedewy, M., Meshot, E.R., Reinker, M.J., & Hart, A.J. (2011). Population growth dynamics of carbon nanotubes. *ACS Nano*, 5(11), 8974–8989. <https://doi.org/10.1021/nn203144f>.

To realize reproducible and uniform synthesis of CNTs and use for the transfer printing stamp, we should understand the process parameter in CVD growth. According to molecular dynamics study, optimization of the process temperature is essential to produce the nucleation of the CNTs successfully (Ding et al., 2004). The simulation results supported that iron-carbide nanoparticles can grow SWCNTs at 800–1400 K, while graphite encapsulation hinders the growth at a temperature below 600 K. With the even higher temperature at >1600 K, soot-like structures containing a large number of defects are formed rather than well-defined nanotubes. In addition, the extent of alignment and the number of walls highly rely on the morphological distributions of catalytic nanoparticles. An empirical study demonstrated a discrete transition between SWCNT growth and MWCNT growth regime regarding the catalyst diameter (Chen et al., 2016). Toward the smaller diameter of CNTs, which likely allows the transfer printing of extremely small objects, alumina capping (Chen et al., 2013; Zhong et al., 2005) or copper-anchored cobalt catalysts (Cui et al., 2016) can be introduced. A summary of various catalyst preparation methods is presented in the previous publication (Chen et al., 2016). For reaching enhanced synthesis quality, Al₂O₃ is the common supporting layer for catalyst nanoclusters, which has a crucial role to prevent the aggregation of nanoparticles (Kaneko et al., 2012). In addition, a slight addition of water vapor (Hata et al., 2004) and carbon species (Dee et al., 2019) can enhance the catalytic activity or density, thereby increasing the density and extent of alignment.

6.2.3 Surface modification of vertically-aligned carbon nanotubes

Surface modification approaches are necessary to adjust the adhesion energy of VACNTs to match the purposes of transfer printing. First, inconsistent mechanical properties can be observed at the top surface of the CVD-grown VACNTs due to the randomly entangled CNTs on the top (Kim et al., 2016). Removal of the “crust” layer on the top surface can effectively suppress the adverse irregularities. One of the most versatile methods is using Ar/O₂ plasma etching (Fig. 6.5A and B) (Seo et al., 2021). The mechanism of surface etching encompasses both ion bombardment and oxygen-driven chemical reactions. By applying high voltage inside the working chamber, excited ions are generated and collide with the surface. When Ar gas, which is chemically inert, is solely applied as the feed gas, the surface is physically etched by the excited gas atoms accompanying the anisotropic nature of an etching profile. In contrast, when chemically active gas such as oxygen is blown into the chamber, the etching phenomenon incorporating both physical and chemical mechanisms results in more isotropic etching behavior. In addition, the O₂ plasma treatment activates the CNT surfaces with oxygen-containing surface groups enhancing the surface energy (Wang et al., 2003). This likely counteracts our initial purpose to reduce the adhesion strength. Furthermore, the extent

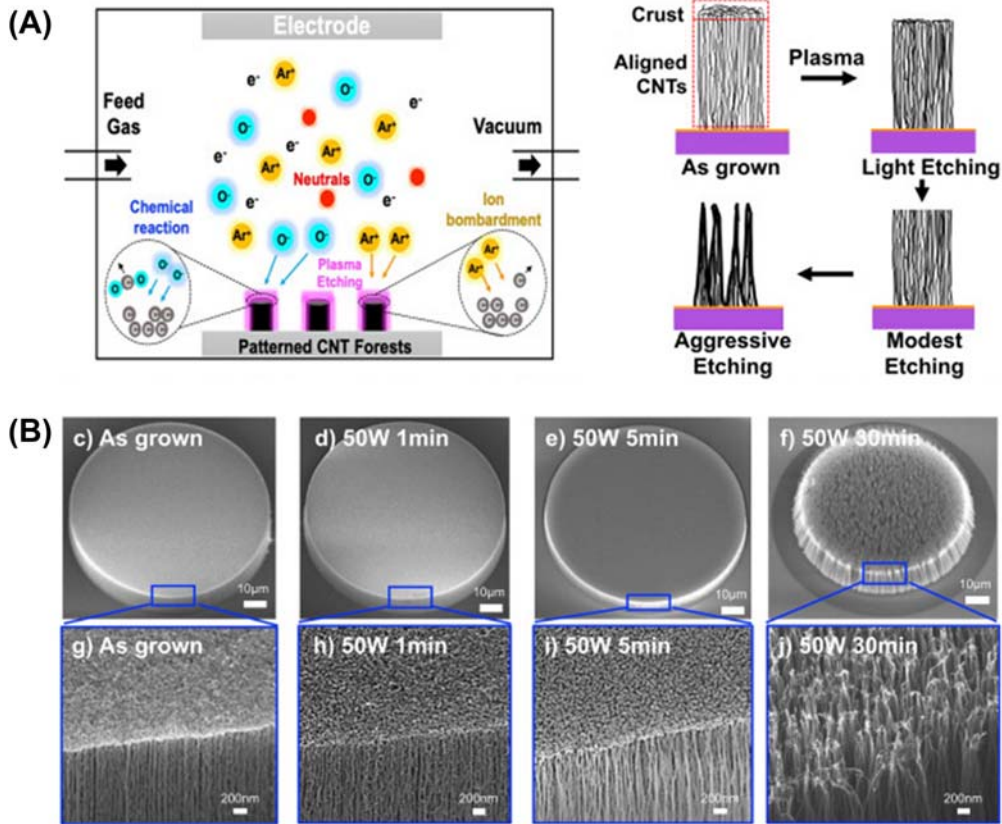


Figure 6.5 Surface modification of vertically-aligned carbon nanotube (VACNT). (A) Schematic of Ar/O₂ etching process and the resulting change in CNT top surface (Seo et al., 2021). (B) Electron microscopic images of Ar/O₂-plasma-treated CNTs according to different exposure time (8 sccm of Ar and 2 sccm of O₂ were supplied) (Seo et al., 2021). (C) Polymer-coated VACNTs using initiated chemical vapor deposition (iCVD) (Sojoudi et al., 2017). (D) Electron microscopic images of Al₂O₃-coated CNTs using atomic layer deposition (ALD) (Verma et al., 2020). (E) Nanoindentation test results showing the enhancement of mechanical properties after ALD coating (Verma et al., 2020).

of plasma treatment highly alters the surface geometries (Seo et al., 2021). While moderate etching resulted in almost identical microstructures as an initial state, aggressive etching with relatively long exposure time highly distorts both the surfaces and microstructures in accordance with aggregations of adjacent CNTs (Chen et al., 2011).

While the plasma alters the surface energy via a subtractive approach, conformal coating technologies can be used as an additive method. Ultrathin polymeric and ceramic materials can be coated on individual CNTs via initiated CVD (iCVD)

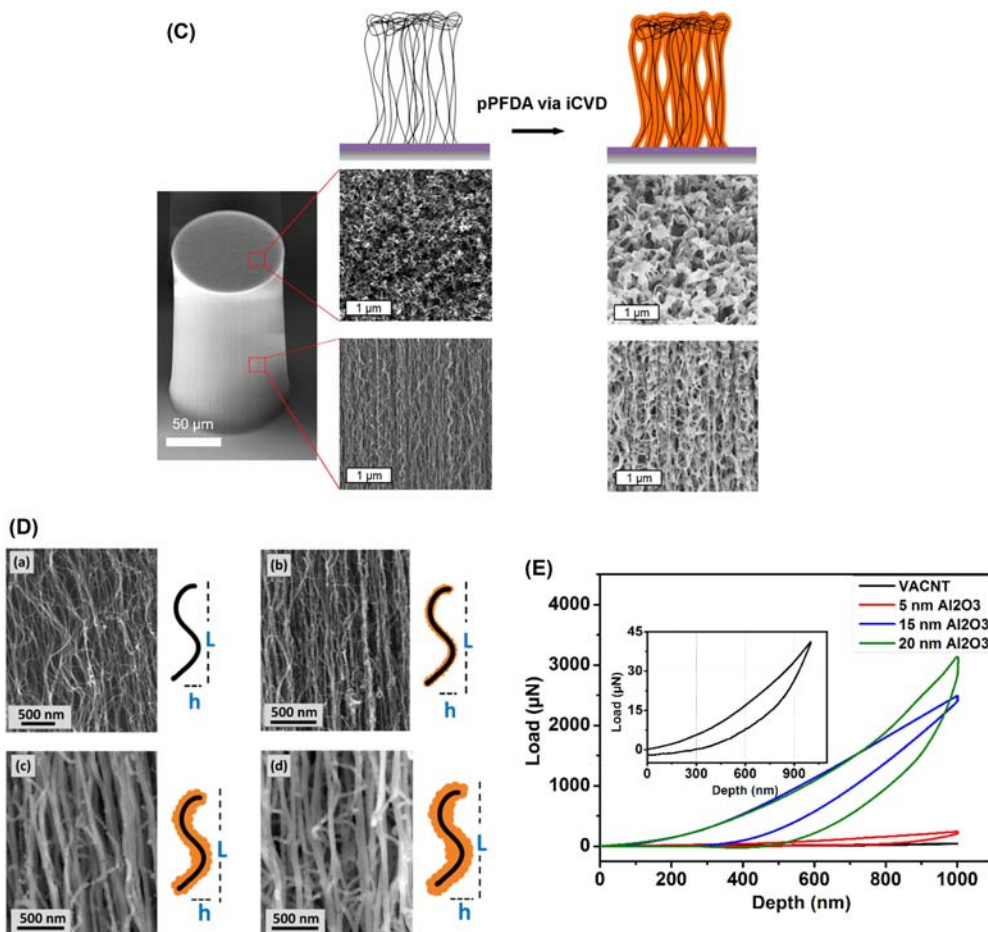


Figure 6.5 (Continued)

(Sojoudi et al., 2017) and atomic layer deposition (ALD), respectively (Verma et al., 2020) (Fig. 6.5C and D). Table 6.2 lists a few representative works of conformally coated VACNTs using these methods. Such modification contributes to enhancing the mechanical stability through nanobridges linking the adjacent tubes, thus it prevents elastocapillary collapse during solvent evaporation (Kim et al., 2016). Likewise, ALD of Al₂O₃ produced armored porous networks wherein its Young's modulus can be largely tuned, which can be enhanced 135-fold in maximum compared to a bare sample (Fig. 6.5E) (Verma et al., 2020). Importantly, they can also act as a dielectric barrier to remove any unintended charge conduction from the contact amidst the operation of CNT electroadhesive (Kim et al., 2019).

Table 6.2 List of conformal surface coating methods for carbon nanotubes.

Categories	Materials	Method	References
Metal	Au	E-beam deposition and thermal annealing	Lee et al. (2012)
Ceramics	Al ₂ O ₃	ALD	Kim et al. (2019), Verma et al. (2020), Brieland-Shoultz et al. (2014)
	ZnO	ALD	Li et al. (2010)
Polymers or organic materials	HfO ₂	ALD	Kong et al. (2018)
	pPFDA	iCVD	Kim et al. (2016), Sojoudi et al. (2017)
	PTFE	iCVD	Lau et al. (2003)
	Carbon fluorine films	Plasma polymerization	He et al. (2005)

6.2.4 Contact mechanics of vertically-aligned carbon nanotubes

The optimal printing for an electrostatic nanoporous stamp is the condition that realizes the minimum adhesion force with conformal contact. Generally, adhesion strength is a function of real contact area, which is determined by applied pressure and surface roughness. Instead of a random selection of fabrication and operation parameters, the contact mechanical model can give a strategic method to determine them. To discuss the mechanical behavior of VACNTs at the contact interface, we need to first understand their overall responses under compression. Once we know the collective load–displacement behavior of the VACNT forest, we can directly predict the local pressure distribution of the stamp protrusions using the height profiles and determine the appropriate pressure preventing the irreversible failure of the structure (Fig. 6.6A).

VACNT is a spatially heterogeneous nanowire network, having a characteristic cluster on the uppermost surface, and this complicates the modeling of the mechanical properties. In addition, the nonuniform growth kinetics of VACNTs results in a non-linear CNT number density across the thickness (Bedewy et al., 2011). At a glance with lower magnification, VACNT may look ordered and vertically-aligned, yet their realistic nanostructure is a highly tortuous network, making them nearly foam-like structures (Hutchens et al., 2010; Hutchens & Pathak, 2012). In the early research, distinct compressibility of VACNT was reported; zig-zag-like buckles of CNTs (porosity of ~87%) enabled them to nearly recoil their original length against the repeated stress

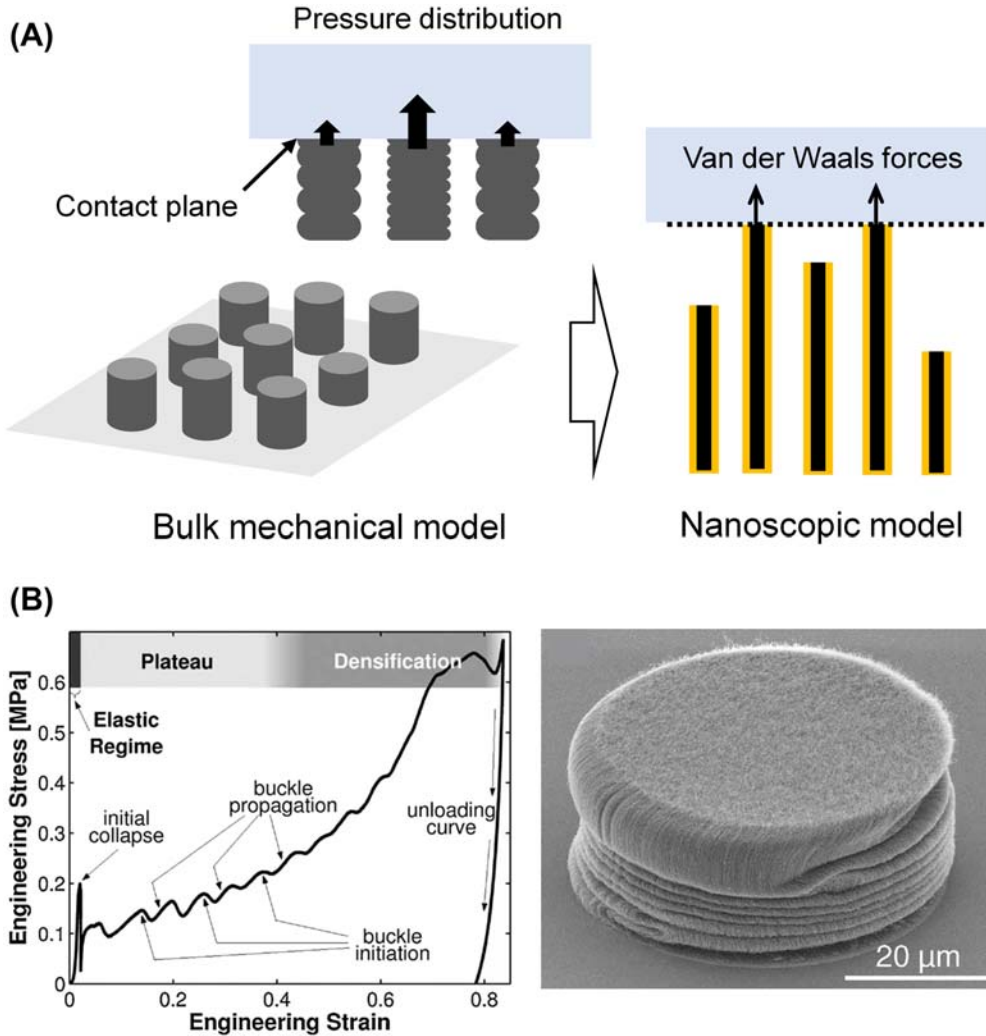


Figure 6.6 Contact mechanics of a vertically-aligned carbon nanotube (VACNT) surface. (A) Schematic of the bulk mechanical and nanoscopic contact model. (B) Typical compression behavior of a single VACNT column (left) and electron microscopic image of an as-compressed VACNT cylinder (right) (Hutchens et al., 2010).

cycles. Only <20% of permanent reduction in thickness was observed after 10,000 cycles (Cao et al., 2005).

To shed light on their mechanical behaviors, in situ mechanical testing was given. The typical compression behavior of VACNTs, which is analogous to foam-like

materials, is characterized by three stages: (1) short elastic region, (2) quasi-plateau region, and (3) stiffening region (Hutchens et al., 2010). The plateau-like region corresponds to repeated buckling nucleation-propagation cycles, which was proven by resulting postmortem morphologies and in situ videography (Fig. 6.6B). During this plateau, the applied stress gradually increases rather than producing a constant level of stress, as the buckle nucleation site shifts toward stiffer and denser regions.

As well as the qualitative description, the modeling approaches were provided to explain the behavior. The early model describing the collective behavior of VACNTs assumed two ideal stages, where the first stage is fully elastic yet the latter reflects the densification of the nanofoam as

$$\sigma = E\varepsilon \quad (6.6)$$

$$\frac{d\sigma}{d\varepsilon} = \frac{E}{(\varepsilon - \varepsilon_f)} \quad (6.7)$$

where σ is the applied stress, E is Young's modulus, ε is the strain, and ε_f is the strain to full compression (Cao et al., 2005). Despite its simplicity, the experiment well accords with the model. On the other hand, the buckling criteria were introduced to elucidate the behavior of VACNTs. The initiation of buckling can be also estimated from Euler's beam theory as (Zbib et al., 2008)

$$\frac{\mu}{\sigma_{\text{instable}}} \approx \frac{1 - h_1/h}{h_1/h} \quad (6.8)$$

where μ is the effective shear modulus of the upper part of a CNT forest, σ_{instable} is the first-order instability stress, h is the total length of a CNT forest, and h_1 is the vertical position of bulking, respectively. According to this formulation, VACNTs with higher pillar height result in lower instability stress with a fixed vertical position of buckling. The buckling behavior after the first instability can be analyzed using numerical methods (Hutchens et al., 2011).

From now on, we explain the adhesion change considering the nanoscopic contacts, which cause Van der Waals interaction (Fig. 6.6A). When VACNTs are compressed by physical contact, the mechanical deformation and contact behavior are in part similar to general compression yet can be different depending on the geometry at the top surface. For example, the top of CVD-grown VACNT is in general not ideally aligned (Bedewy et al., 2011), forming highly random networks with many interlocked tubes. With the existence of such a "crust" layer, the deformation at the contact interface is much more rigid than the compressive foam beneath (Kim et al., 2016). However, an idealized surface, where CNTs are normally aligned with respect to the uppermost surface, can be produced by gentle dry etching (Seo et al., 2021). The excited gas atoms by plasma can effectively remove the top crust, and therefore the number density and the degree of alignment at the top surface become similar to those of overall VACNTs

(Kim et al., 2016). With a hypothesis of a normal distribution of heights for dry etched VACNTs, we can attain the real contact area as (Kim et al., 2016)

$$A_{\text{real}}(d) = \bar{A}_{\text{cnt}} N_{\text{CNT}} \int_d^{\infty} \varphi(l_{\text{CNT}}) dl = \frac{1}{2} \bar{A}_{\text{cnt}} N_{\text{CNT}} \left\{ 1 - \operatorname{erf} \frac{d}{\sqrt{2}\sigma_l} \right\} \quad (6.9)$$

where A_{real} is the real contact area, A_{CNT} is the mean cross-sectional area of CNTs, N_{CNT} is the total number of CNT, φ is the probability density, d is the surface-to-surface separation distance, and σ_l is the standard deviation of the heights, respectively.

We now consider the total adhesion force as a summation of isolated CNT-to-object contacts. Two well-accepted classical models for adhesion at the contact points are the Johnson, Kendall, and Roberts (JKR) theory (Johnson et al., 1971) and Derjaguin, Muller, and Toporov (DMT) theory (Derjaguin et al., 1975). While the JKR theory is based on the attractive interaction balanced between the elastically stored energy and surface energy, the DMT coincides with the intermolecular forces outside the contact (Xu et al., 2007). It has been believed that the DMT model is useful for small and rigid asperities with low surface energy, yet the JKR model is applicable for soft and large asperities with high surface energy (Prokopovich & Pemi, 2011). Rigorously, the JKR and DMT theory are only extremes of adhesion phenomena, and the transition rule was investigated (Johnson & Greenwood, 1997; Tabor, 1977). Although approaches were given to explain the intermediate regime (Maugis, 1992; Muller et al., 1980), a simple DMT approach can still be used for the sake of simplicity (Kim et al., 2019). Upon the DMT-based model, the pull-off force at a single asperity, P_i , can be modeled as (Kim et al., 2019):

$$P_i = 2\pi\Delta\gamma R_i \quad (6.10)$$

where $\Delta\gamma$ is the adhesion work per unit area, R is the single asperity radius, and $\Delta\gamma$ is the material property determined by interfacial chemistry which can be expressed with interfacial energies as

$$\Delta\gamma = \gamma_A + \gamma_B - \gamma_{AB} \quad (6.11)$$

wherein two solid surfaces, A and B, bring into ideal contact. According to Eq. (6.9), contact ratio (η), which is the ratio of contacted CNTs with respect to total CNTs, can be derived from the probability density function ($\int_d^{\infty} \varphi(l_{\text{CNT}}) dl$). Then, the total pull-off force is directly represented as

$$P = 2\pi\Delta\gamma\bar{R}\eta N = 2\pi\Delta\gamma\bar{R}N \int_d^{\infty} \varphi(l_{\text{CNT}}) dl \quad (6.12)$$

where N is the total number of CNTs, and \bar{R} is the average radius of CNTs. Finally, we have the most important relationship between geometry and adhesion force. In light of Eq. (6.12), the nanoscopic height profile and surface roughness, have a major role in the pull-off force. The total pull-off force may be minimized when the surface is extremely rough, in which the height profile shows vastly high variance. This condition can be produced by introducing optimal dry etching (Seo et al., 2021), which forms needle-like surface morphologies.

6.2.5 Electrostatic adhesion of vertically-aligned carbon nanotubes

The active modulation of electrostatic adhesion provides an extreme contrast on the interfacial adhesion, having a great advantage for transfer printing. To precisely understand and reproduce the adhesion modulation, researchers have suggested models describing the electrostatic force (Rajagopalan et al., 2022). The most simplified model is based on a parallel plate capacitor given as (Boutilier et al., 2021)

$$F_{\text{plate}} = \frac{\varepsilon_0 \varepsilon_r A}{2} \left(\frac{V_0}{h} \right)^2 \quad (6.13)$$

where F_{plate} is the normal electrostatic force, ε_0 is the vacuum permittivity, ε_r is the relative permittivity, A is the area of plates, V_0 is the potential difference, and h is the separation distance.

Boutilier et al. (2021) discussed the mechanisms and scaling of electrostatically-controlled adhesion of VACNTs and confirmed the voltage-squared relation before the dielectric breakdown of the VACNT surface. A simple addition of the intrinsic adhesion enabled the prediction of up to approximately 175 V for conductive materials (Fig. 6.7A). The authors used gold, acrylic, and silica tips as target materials, and all of those resembled the model well. In addition to the voltage dependence, the separation distance has an h^{-2} relation, which was also observed by the force measurement (Fig. 6.7B). Additionally, it is important to note that the preload effect was suppressed by the creating mechanical enhancement by coating. For more accurate prediction, finite element analysis was used for solving the electrostatic partial differential equation. The simulation was produced by altering the relative gap distance between the CNT tip and the target surface, where the dielectric breakdown was neglected. As a result, field distribution was computed for each case (Fig. 6.7C). When the CNT tip is close to the surface, the field localizes near the gap between two surfaces, while the field is mostly distributed at the intervals of CNTs for the large separation distance.

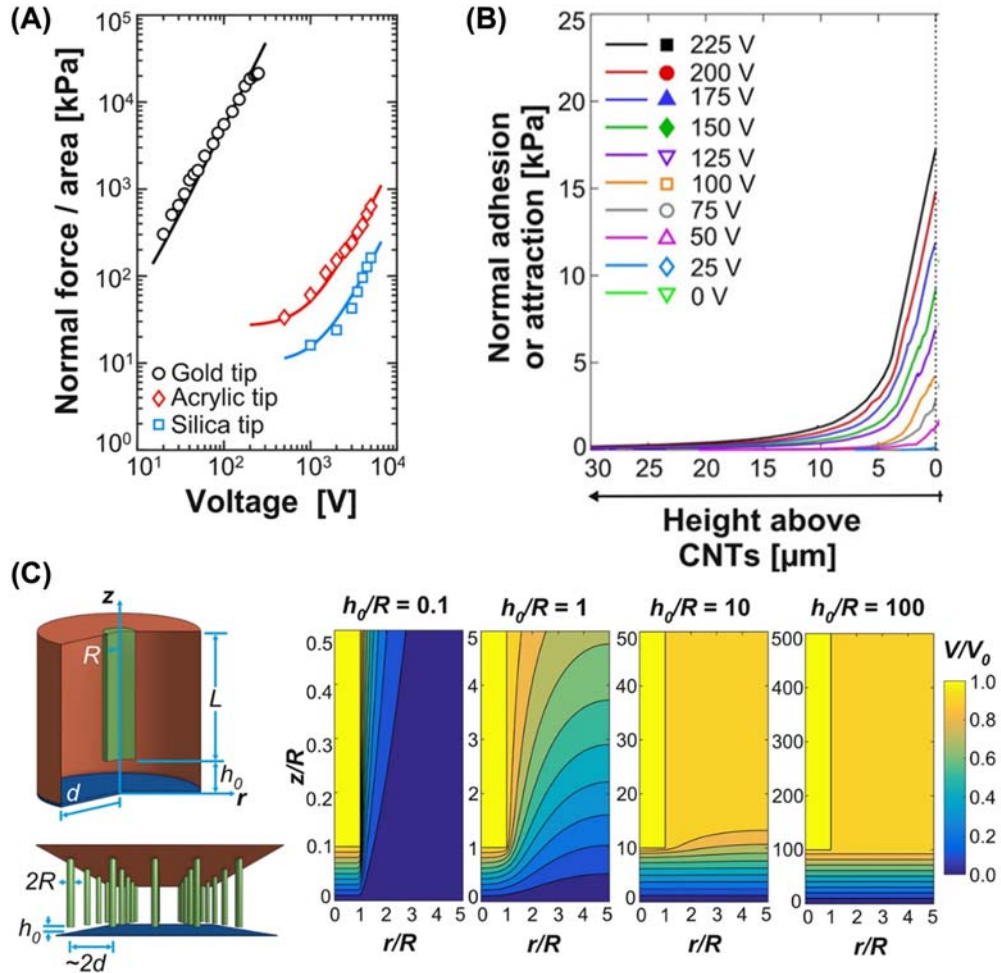


Figure 6.7 Models for electroadhesion. (A) Voltage dependence of the electroadhesion. (B) Distance dependence of the electroadhesion. (C) Finite element simulation of the field profiles with different relative gap distances, where h_0 is the gap distance and R is the radius of a carbon nanotube (Boutillier et al., 2021).

6.3 Future works

With the rise of novel state-of-the-art materials, new strategies for transfer printing have been suggested. Nanoporous materials are beneficial over bulk materials within various perspectives: surface compliances, conformal contacts, and high adhesion contrast. This can be directly applied to industrial areas which require high throughput such as micro-LED display fabrication (Bibl et al., 2013). Moreover, the digitalized controllability of the electrostatic adhesion provides a way to realize the accelerated

processing speed matching the practical needs. Thanks to the great adhesion enhancement, this may also be applied to pads of miniaturized climbing robots. The adhesive strength of the stamp can reach approximately 20 kPa at 225 V, which is comparable to planar electroadhesives at >5 kV (Kim et al., 2019).

However, further development is necessary to expand their use. For example, large-area process capability is a key to matching industrial demands, yet the fabrication of the large-area nanoporous stamp is not fully matured. Irregularities in CNT synthesis (Piwko et al., 2015) hinder industrial practices, which require a high standard of reproducibility, therefore recent efforts have been introduced to improve the consistency in process quality via autonomous and cost-effective manner (Oliver et al., 2013). Quality control along with the capability of large-area synthesis of VACNTs is the key prerequisite for VACNT-based transfer printing.

Another limitation of VACNT-based electroadhesive is in the length scale. A simple planar capacitor model predicts that electrostatic force has a L^2 scaling of the strength with respect to its length. Thus, this limits the use of VACNT-based adhesion in macroscale applications. To realize the gripping on the large scale over a millimeter or greater, we should increase the electric field at the contact interface. However, once the field intensity exceeds the dielectric strength, the leaking current may occur

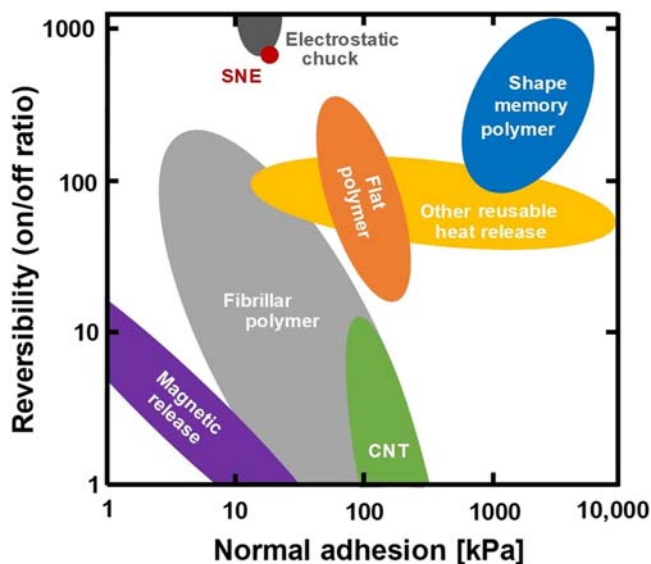


Figure 6.8 Reversibility and adhesion strength of the electrostatic nanoporous stamp (SNE in the figure). From Boutilier, M. S. H., Cao, C., Nayakanti, N., Kim, S., Taheri-Mousavi, S. M., & Hart, A. J. (2021). Limiting mechanisms and scaling of electrostatically controlled adhesion of soft nanocomposite surfaces for robotic gripping. *ACS Applied Materials and Interfaces*, 13(1), 1192–1203. <https://doi.org/10.1021/acsaami.0c17096>.

and cause irreversible damage to the target materials. For the dielectric-layer-coated nanotubes with nanometers thick dielectric, a small leaking current was observed beyond 175 V (Boutilier et al., 2021). The criteria for breakdown (dielectric strength) were determined by the electric field inside, which is a function of both voltage (V) and distance (h). The capability of the electrostatic method reached the centimeter scale with approximately 20 kPa of attractive pressure (Fig. 6.8), which remains less compared to other means. To realize the multiscale operation of the electrostatic transfer, a hybrid mechanism, combining the electrostatic attraction with other adhesion approaches, can be a possible solution (Kim et al., 2022).

Nanoscale transfer printing, manipulating a few tens of nanometer objects or less, is also challenging due to the intrinsic roughness of the stamp surface. To enable the reliable printing of the nanoscopic materials, the bump size on the stamp surface should be small enough compared to the length scale of the target materials. The issue may be alleviated by replacing multiwalled CNTs with single-walled CNTs can have an extremely small diameter approaching a nanometer or even less (Diaz et al., 2019).

References

- Alam, M. O., & Bailey, C. (2011). *Advanced adhesives in electronics: Materials, properties and applications*. Elsevier.
- Anwar, A. R., Sajjad, M. T., Johar, M. A., Hernández-Gutiérrez, C. A., Usman, M., & èpkowski, S. P. (2022). Recent progress in micro-LED-based display technologies. *Laser and Photonics Reviews*, 16(6). Available from <https://doi.org/10.1002/lpor.202100427>, [http://onlinelibrary.wiley.com/journal/10.1002/\(ISSN\)1863-8899](http://onlinelibrary.wiley.com/journal/10.1002/(ISSN)1863-8899).
- Arora, N., & Sharma, N. N. (2014). Arc discharge synthesis of carbon nanotubes: Comprehensive review. *Diamond and Related Materials*, 50, 135–150. Available from <https://doi.org/10.1016/j.diamond.2014.10.001>.
- Ashdown, I., Speier, I., Sheen, C. W., & Schick, P. M. (2011). *Method and magnetic transfer stamp for transferring semiconductor dice using magnetic transfer printing techniques*, U.S. Patent Application No. 12/966,997.
- Bai, J. B., Hamon, A. L., Marraud, A., Jouffrey, B., & Zymly, V. (2002). Synthesis of SWNTs and MWNTs by a molten salt (NcCl) method. *Chemical Physics Letters*, 365(1–2), 184–188. Available from [https://doi.org/10.1016/S0009-2614\(02\)01447-1](https://doi.org/10.1016/S0009-2614(02)01447-1).
- Bark, C., Binnenboese, T., Voegelé, G., Weisener, T., & Widmann, M. (1998). IEEE Germany Gripping with low viscosity fluids. *Proceedings of the IEEE Micro Electro Mechanical Systems (MEMS)*, pp. 301–305.
- Barnett, C. J., McCormack, J. E., Deemer, E. M., Evans, C. R., Evans, J. E., White, A. O., Dunstan, P. R., Chianelli, R. R., Cobley, R. J., & Barron, A. R. (2020). Enhancement of multiwalled carbon nanotubes' electrical conductivity using metal nanoscale copper contacts and its implications for carbon nanotube-enhanced copper conductivity. *Journal of Physical Chemistry C*, 124(34), 18777–18783. Available from <https://doi.org/10.1021/acs.jpcc.0c05000>, <http://pubs.acs.org/journal/jpccck>.
- Bedewy, M., Meshot, E. R., Reinker, M. J., & Hart, A. J. (2011). Population growth dynamics of carbon nanotubes. *ACS Nano*, 5(11), 8974–8989. Available from <https://doi.org/10.1021/nn203144f>.
- Bhushan, B., Koch, K., & Jung, Y. C. (2008). Nanostructures for superhydrophobicity and low adhesion. *Soft Matter*, 4(9), 1799–1804. Available from <https://doi.org/10.1039/b808146h>.
- Bibl, A., Higginson, J. A., Hu, H.-H., & Law, H.-F. S. (2013). *Method of transferring and bonding an array of micro devices*, U.S. Patent No. 9,773,750.
- Boutilier, M. S. H., Cao, C., Nayakanti, N., Kim, S., Taheri-Mousavi, S. M., & Hart, A. J. (2021). Limiting mechanisms and scaling of electrostatically controlled adhesion of soft nanocomposite

- surfaces for robotic gripping. *ACS Applied Materials and Interfaces*, 13(1), 1192–1203. Available from <https://doi.org/10.1021/acsami.0c17096>, <http://pubs.acs.org/journal/aamick>.
- Brady, G. J., Way, A. J., Safron, N. S., Evensen, H. T., Gopalan, P., & Arnold, M. S. (2016). Quasi-ballistic carbon nanotube array transistors with current density exceeding Si and GaAs. *Science Advances*, 2(9). Available from <https://doi.org/10.1126/sciadv.1601240>, <http://advances.sciencemag.org/content/advances/2/9/e1601240.full.pdf>.
- Brieland-Shoultz, A., Tawfick, S., Park, S. J., Bedewy, M., Maschmann, M. R., Baur, J. W., & Hart, A. J. (2014). Scaling the stiffness, strength, and toughness of ceramic-coated nanotube foams into the structural regime. *Advanced Functional Materials*, 24(36), 5728–5735. Available from <https://doi.org/10.1002/adfm.201400851>, [http://onlinelibrary.wiley.com/journal/10.1002/\(ISSN\)1616-3028](http://onlinelibrary.wiley.com/journal/10.1002/(ISSN)1616-3028).
- Burton, Z., & Bhushan, B. (2005). Hydrophobicity, adhesion, and friction properties of nanopatterned polymers and scale dependence for micro- and nanoelectromechanical systems. *Nano Letters*, 5(8), 1607–1613. Available from <https://doi.org/10.1021/nl050861b>.
- Cadek, M., Murphy, R., McCarthy, B., Drury, A., Lahr, B., Barklie, R. C., In Het Panhuis, M., Coleman, J. N., & Blau, W. J. (2002). Optimisation of the arc-discharge production of multi-walled carbon nanotubes. *Carbon*, 40(6), 923–928. Available from [https://doi.org/10.1016/S0008-6223\(01\)00221-4](https://doi.org/10.1016/S0008-6223(01)00221-4).
- Callister, W. D., & Rethwisch, D. G. (2018). *Materials science and engineering: an introduction*. Wiley.
- Cao, A., Dickrell, P. L., Sawyer, W. G., Ghasemi-Nejhad, M. N., & Ajayan, P. M. (2005). Super-compressible foamlike carbon nanotube films. *Science (New York, N.Y.)*, 310(5752), 1307–1310. Available from <https://doi.org/10.1126/science.1118957>.
- Chang, C. M., & Liu, Y. L. (2011). Electrical conductivity enhancement of polymer/multiwalled carbon nanotube (MWCNT) composites by thermally-induced defunctionalization of MWCNTs. *ACS Applied Materials and Interfaces*, 3(7), 2204–2208. Available from <https://doi.org/10.1021/am200558f>.
- Che, J., Çağın, T., & Goddard, W. A. (2000). Thermal conductivity of carbon nanotubes. *Nanotechnology*, 11(2), 65–69. Available from <https://doi.org/10.1088/0957-4484/11/2/305>.
- Chen, C., Ogino, A., Wang, X., & Nagatsu, M. (2011). Oxygen functionalization of multiwall carbon nanotubes by Ar/H₂O plasma treatment. *Diamond and Related Materials*, 20(2), 153–156. Available from <https://doi.org/10.1016/j.diamond.2010.11.018>.
- Chen, G., Davis, R. C., Futaba, D. N., Sakurai, S., Kobashi, K., Yumura, M., & Hata, K. (2016). A sweet spot for highly efficient growth of vertically aligned single-walled carbon nanotube forests enabling their unique structures and properties. *Nanoscale*, 8(1), 162–171. Available from <https://doi.org/10.1039/c5nr05537g>, <http://www.rsc.org/publishing/journals/NR/Index.asp>.
- Chen, G., Futaba, D. N., Kimura, H., Sakurai, S., Yumura, M., & Hata, K. (2013). Absence of an ideal single-walled carbon nanotube forest structure for thermal and electrical conductivities. *ACS Nano*, 7(11), 10218–10224. Available from <https://doi.org/10.1021/nm404504f>.
- Chen, J., Wei, S., & Xie, H. (2021). A brief introduction of carbon nanotubes: history, synthesis, and properties. *Journal of Physics: Conference Series*, 1948(1). Available from <https://doi.org/10.1088/1742-6596/1948/1/012184>, IOP Publishing Ltd United States, <http://iopscience.iop.org/journal/1742-6596>.
- Chen, Q., Martin, C., & Cumming, D. R. S. (2012). Transfer printing of nanoplasmonic devices onto flexible polymer substrates from a rigid stamp. *Plasmonics*, 7(4), 755–761. Available from <https://doi.org/10.1007/s11468-012-9370-4>.
- Choi, K., Chan Kim, Y., Sun, H., Kim, S. H., Yoo, J. W., Park, I. K., Lee, P. C., Choi, H. J., Choi, H. R., Kim, T., Suh, J., Lee, Y. K., & Nam, J. D. (2019). Quantitative electrode design modeling of an electroadhesive lifting device based on the localized charge distribution and interfacial polarization of different objects. *ACS Omega*, 4(5), 7994–8000. Available from <https://doi.org/10.1021/acsomega.9b00071>, <http://pubs.acs.org/journal/acsofd>.
- Coleman, J. N., Khan, U., Blau, W. J., & Gun'ko, Y. K. (2006). Small but strong: A review of the mechanical properties of carbon nanotube-polymer composites. *Carbon*, 44(9), 1624–1652. Available from <https://doi.org/10.1016/j.carbon.2006.02.038>.
- Cui, K., Kumamoto, A., Xiang, R., An, H., Wang, B., Inoue, T., Chiashi, S., Ikuhara, Y., & Maruyama, S. (2016). Synthesis of subnanometer-diameter vertically aligned single-walled carbon nanotubes with

- copper-anchored cobalt catalysts. *Nanoscale.*, 8(3), 1608–1617. Available from <https://doi.org/10.1039/c5nr06007a>, <http://www.rsc.org/publishing/journals/NR/Index.asp>.
- De, M. F. L., Volder, S. J., Park, S. H., Tawfick, D. O., Vidaud, A. J., & Hart. (2011). Fabrication and electrical integration of robust carbon nanotube micropillars by self-directed elastocapillary densification. *Journal of Micromechanics Microengineering*, 21.
- De Volder, M. F. L., Tawfick, S. H., Baughman, R. H., & Hart, A. J. (2013). Carbon nanotubes: Present and future commercial applications. *Science (New York, N.Y.)*, 339(6119), 535–539. Available from <https://doi.org/10.1126/science.1222453>, <http://www.sciencemag.org/content/339/6119/535.full.pdf>.
- Dee, N. T., Li, J., Orbaek White, A., Jacob, C., Shi, W., Kidambi, P. R., Cui, K., Zakharov, D. N., Janković, N. Z., Bedewy, M., Chazot, C. A. C., Carpena-Núñez, J., Maruyama, B., Stach, E. A., Plata, D. L., & Hart, A. J. (2019). Carbon-assisted catalyst pretreatment enables straightforward synthesis of high-density carbon nanotube forests. *Carbon*, 153, 196–205. Available from <https://doi.org/10.1016/j.carbon.2019.06.083>, <http://www.journals.elsevier.com/carbon/>.
- Delgado, J. L., Herranz, M. A., & Martín, N. (2008). The nano-forms of carbon. *Journal of Materials Chemistry*, 18(13), 1417–1426. Available from <https://doi.org/10.1039/b717218d>.
- Derjaguin, B. V., Muller, V. M., & Toporov, Yu. P. (1975). Effect of contact deformations on the adhesion of particles. *Journal of Colloid and Interface Science*, 53(2), 314–326. Available from [https://doi.org/10.1016/0021-9797\(75\)90018-1](https://doi.org/10.1016/0021-9797(75)90018-1).
- Diaz, M. C., Jiang, H., Kauppinen, E., Sharma, R., & Balbuena, P. B. (2019). Can single-walled carbon nanotube diameter be defined by catalyst particle diameter? *Journal of Physical Chemistry C*, 123(50), 30305–30317. Available from <https://doi.org/10.1021/acs.jpcc.9b07724>, <http://pubs.acs.org/journal/jpccck>.
- Ding, F., Bolton, K., & Rosén, A. (2004). Nucleation and growth of single-walled carbon nanotubes: A molecular dynamics study. *Journal of Physical Chemistry B*, 108(45), 17369–17377. Available from <https://doi.org/10.1021/jp046645>.
- Fan, S., Chapline, M. G., Franklin, N. R., Tomblor, T. W., Cassell, A. M., & Dai, H. (1999). Self-oriented regular arrays of carbon nanotubes and their field emission properties. *Science (New York, N.Y.)*, 283(5401), 512–514. Available from <https://doi.org/10.1126/science.283.5401.512>.
- Fan, Z., Rong, W., Wang, L., & Sun, L. (2015). A single-probe capillary microgripper induced by dropwise condensation and inertial release. *Journal of Micromechanics and Microengineering*, 25(11). Available from <https://doi.org/10.1088/0960-1317/25/11/115011>, http://iopscience.iop.org/0960-1317/25/11/115011/pdf/0960-1317_25_11_115011.pdf.
- Fantoni, G., Hansen, H. N., & Santochi, M. (2013). A new capillary gripper for mini and micro parts. *CIRP Annals - Manufacturing Technology*, 62(1), 17–20. Available from <https://doi.org/10.1016/j.cirp.2013.03.005>.
- Fantoni, G., Santochi, M., Dini, G., Tracht, K., Scholz-Reiter, B., Fleischer, J., Kristoffer Lien, T., Seliger, G., Reinhart, G., Franke, J., Nørgaard Hansen, H., & Verl, A. (2014). Grasping devices and methods in automated production processes. *CIRP Annals - Manufacturing Technology*, 63(2), 679–701. Available from <https://doi.org/10.1016/j.cirp.2014.05.006>, http://www.elsevier.com/wps/find/journaldescription.cws_home/709764/description#description.
- Fleming, R. A., & Zou, M. (2018). Nanostructure-textured surfaces with low friction and high deformation resistance. *Tribology Transactions*, 61(1), 80–87. Available from <https://doi.org/10.1080/10402004.2016.1274066>, <http://www.tandf.co.uk/journals/titles/10402004.asp>.
- Gogotsi, Y., Libera, J. A., & Yoshimura, M. (2000). Hydrothermal synthesis of multiwall carbon nanotubes. *Journal of Materials Research*, 15(12), 2591–2594. Available from <https://doi.org/10.1557/JMR.2000.0370>.
- Goh, G. L., Agarwala, S., & Yeong, W. Y. (2019). Directed and on-demand alignment of carbon nanotube: a review toward 3D printing of electronics. *Advanced Materials Interfaces*, 6(4). Available from <https://doi.org/10.1002/admi.201801318>, [http://onlinelibrary.wiley.com/journal/10.1002/\(ISSN\)2196-7350](http://onlinelibrary.wiley.com/journal/10.1002/(ISSN)2196-7350).
- Guo, J., Leng, J., & Rossiter, J. (2020). Electroadhesion technologies for robotics: A comprehensive review. *IEEE Transactions on Robotics*, 36(2), 313–327. Available from <https://doi.org/10.1109/TRO.2019.2956869>, <http://ieeexplore.ieee.org/xpl/RecentIssue.jsp?punumber=8860>.

- Guo, T., Nikolaev, P., Thess, A., Colbert, D. T., & Smalley, R. E. (1995). Catalytic growth of single-walled nanotubes by laser vaporization. *Chemical Physics Letters*, 243(1–2), 49–54. Available from [https://doi.org/10.1016/0009-2614\(95\)00825-O](https://doi.org/10.1016/0009-2614(95)00825-O).
- Hata, K., Futaba, D. N., Mizuno, K., Namai, T., Yumura, M., & Iijima, S. (2004). Water-assisted highly efficient synthesis of impurity-free single-walled carbon nanotubes. *Science (New York, N.Y.)*, 306(5700), 1362–1364. Available from <https://doi.org/10.1126/science.1104962>.
- Hattori, T., Heusler, S., Webb, J. P., & Hattori, T. (2013). *Ultraclean surface processing of silicon wafers: Secrets of VLSI manufacturing*. Springer Science & Business Media.
- He, P., Shi, D., Lian, J., Wang, L. M., Ewing, R. C., Van Ooij, W., Li, N. Z., & Ren, Z. F. (2005). Plasma deposition of thin carbonfluorine films on aligned carbon nanotube. *Applied Physics Letters*, 86(4), 1–43107. Available from <https://doi.org/10.1063/1.1846957>.
- Hutchens, S. B., Hall, L. J., & Greer, J. R. (2010). In situ mechanical testing reveals periodic buckle nucleation and propagation in carbon nanotube bundles. *Advanced Functional Materials*, 20(14), 2338–2346. Available from <https://doi.org/10.1002/adfm.201000305>, <http://www3.interscience.wiley.com/cgi-bin/fulltext/123430443/PDFSTART>.
- Hutchens, S. B., Needleman, A., & Greer, J. R. (2011). Analysis of uniaxial compression of vertically aligned carbon nanotubes. *Journal of the Mechanics and Physics of Solids*, 59(10), 2227–2237. Available from <https://doi.org/10.1016/j.jmps.2011.05.002>.
- Hutchens, S. B., & Pathak, S. (2012). Vertically aligned carbon nanotubes. *Collective Mechanical Behavior* (pp. 2809–2818). Springer Science and Business Media LLC. Available from https://doi.org/10.1007/978-90-481-9751-4_387.
- Iijima, S. (1991). Helical microtubules of graphitic carbon. *Nature*, 354(6348), 56–58. Available from <https://doi.org/10.1038/354056a0>.
- Iijima, S., & Ichihashi, T. (1993). Single-shell carbon nanotubes of 1-nm diameter. *Nature*, 363(6430), 603–605. Available from <https://doi.org/10.1038/363603a0>.
- Jia, J., Zhao, J., Xu, G., Di, J., Yong, Z., Tao, Y., Fang, C., Zhang, Z., Zhang, X., Zheng, L., & Li, Q. (2011). A comparison of the mechanical properties of fibers spun from different carbon nanotubes. *Carbon*, 49(4), 1333–1339. Available from <https://doi.org/10.1016/j.carbon.2010.11.054>.
- Johnson, K. L., & Greenwood, J. A. (1997). An adhesion map for the contact of elastic spheres. *Journal of Colloid and Interface Science*, 192(2), 326–333. Available from <https://doi.org/10.1006/jcis.1997.4984>, <http://www.elsevier.com/inca/publications/store/6/2/2/8/6/1/index.htm>.
- Johnson, K. L., Kendall, K., & Roberts, A. D. (1971). Surface energy and the contact of elastic solids. *Proceedings of the Royal Society of London. A. Mathematical and Physical Sciences*, 324(1558), 301–313. Available from <https://doi.org/10.1098/rspa.1971.0141>.
- Kaneko, A., Yamada, K., Kumahara, R., Kato, H., & Homma, Y. (2012). Comparative study of catalytic activity of iron and cobalt for growing carbon nanotubes on alumina and silicon oxide. *Journal of Physical Chemistry C*, 116(49), 26060–26065. Available from <https://doi.org/10.1021/jp309232w>.
- Kim, D. G., Je, H., Hart, A. J., & Kim, S. (2022). Additive manufacturing of flexible 3D surface electrodes for electrostatic adhesion control and smart robotic gripping. *Friction*.
- Kim, S., Jiang, Y., Towell, K. L. T., Boutilier, M. S. H., Nayakanti, N., Cao, C., Chen, C., Jacob, C., Zhao, H., Turner, K. T., & Hart, A. J. (2019). Soft nanocomposite electroadhesives for digital micro-And nanotransfer printing. *Science Advances*, 5(10). Available from <https://doi.org/10.1126/sciadv.aax4790>, <https://advances.sciencemag.org/content/5/10/eaax4790/tab-pdf>.
- Kim, S., Sojoudi, H., Zhao, H., Mariappan, D., McKinley, G. H., Gleason, K. K., & Hart, A. J. (2016). Ultrathin high-resolution flexographic printing using nanoporous stamps. *Science Advances*, 2(12). Available from <https://doi.org/10.1126/sciadv.1601660>, <http://advances.sciencemag.org/content/advances/2/12/e1601660.full.pdf>.
- Kim, S. M., Pint, C. L., Amama, P. B., Zakharov, D. N., Hauge, R. H., Maruyama, B., & Stach, E. A. (2010). Evolution in catalyst morphology leads to carbon nanotube growth termination. *The Journal of Physical Chemistry Letters*, 1(6), 918–922. Available from <https://doi.org/10.1021/jz9004762>.

- Kong, W., Wang, D., Yan, L., Luo, Y., Jiang, K., Li, Q., Zhang, L., Lu, S., Fan, S., Li, J., & Wang, J. (2018). Ultrathin HfO_2 -modified carbon nanotube films as efficient polysulfide barriers for Li-S batteries. *Carbon*, 139, 896–905. Available from <https://doi.org/10.1016/j.carbon.2018.07.063>, <http://www.journals.elsevier.com/carbon/>.
- Kroto, H. W., Heath, J. R., O'Brien, S. C., Curl, R. F., & Smalley, R. E. (1985). C60: Buckminsterfullerene. *Nature*, 318(6042), 162–163. Available from <https://doi.org/10.1038/318162a0>.
- Lambert, P., Seigneur, F., Koelemeijer, S., & Jacot, J. (2006). A case study of surface tension gripping: The watch bearing. *Journal of Micromechanics and Microengineering*, 16(7), 1267–1276. Available from <https://doi.org/10.1088/0960-1317/16/7/021>.
- Lau, K. K. S., Bico, J., Teo, K. B. K., Chhowalla, M., Amaratunga, G. A. J., Milne, W. I., McKinley, G. H., & Gleason, K. K. (2003). Superhydrophobic carbon nanotube forests. *Nano Letters*, 3(12), 1701–1705. Available from <https://doi.org/10.1021/nl034704t>.
- Lee, C. H., Lee, J., Park, J., Lee, E., Kim, S. M., & Lee, K. H. (2019). Rationally designed catalyst layer toward “immortal” growth of carbon nanotube forest: Fe ion implanted substrates. *Carbon*, 152, 482–488. Available from <https://doi.org/10.1016/j.carbon.2019.06.030>, <http://www.journals.elsevier.com/carbon/>.
- Lee, H., Um, D. S., Lee, Y., Lim, S., Kim, H. J., & Ko, H. (2016). Octopus-inspired smart adhesive pads for transfer printing of semiconducting nanomembranes. *Advanced Materials*, 28(34), 7457–7465. Available from <https://doi.org/10.1002/adma.201601407>, <http://www3.interscience.wiley.com/journal/119030556/issue>.
- Lee, S., Hahm, M. G., Vajtai, R., Hashim, D. P., Thurakitseree, T., Chipara, A. C., Ajayan, P. M., & Hafner, J. H. (2012). Utilizing 3D SERS active volumes in aligned carbon nanotube scaffold substrates. *Advanced Materials*, 24(38), 5261–5266. Available from <https://doi.org/10.1002/adma.201200645>.
- Li, H. J., Lu, W. G., Li, J. J., Bai, X. D., & Gu, C. Z. (2005). Multichannel ballistic transport in multiwall carbon nanotubes. *Physical Review Letters*, 95(8). Available from <https://doi.org/10.1103/PhysRevLett.95.086601China>, http://oai.aps.org/oai/?verb=ListRecords&metadataPrefix=oai_apsmeta_2&set=journal:PRL:95.
- Li, W. Z., Xie, S. S., Qian, L. X., Chang, B. H., Zou, B. S., Zhou, W. Y., Zhao, R. A., & Wang, G. (1996). Large-scale synthesis of aligned carbon nanotubes. *Science (New York, N.Y.)*, 274(5293), 1701–1703. Available from <https://doi.org/10.1126/science.274.5293.1701>.
- Li, X. L., Li, C., Zhang, Y., Chu, D. P., Milne, W. I., & Fan, H. J. (2010). Atomic layer deposition of ZnO on multi-walled carbon nanotubes and its Use for synthesis of CNT-ZnO heterostructures. *Nanoscale Research Letters*, 5(11), 1836–1840. Available from <https://doi.org/10.1007/s11671-010-9721-z>.
- Lin, W., He, C., Huang, H., Zhao, W., Qiu, Y., Guan, X., Zhang, Q., Wang, Z., & Peng, Z. (2020). Simultaneously achieving ultrahigh sensitivity and wide detection range for stretchable strain sensors with an interface-locking strategy. *Advanced Materials Technologies*, 5(5). Available from <https://doi.org/10.1002/admt.202000008>, [http://onlinelibrary.wiley.com/journal/10.1002/\(ISSN\)2365-709X](http://onlinelibrary.wiley.com/journal/10.1002/(ISSN)2365-709X).
- Linghu, C., Zhang, S., Wang, C., Luo, H., & Song, J. (2021). Mass transfer for Micro-LED display: Transfer printing techniques. *Semiconductors and Semimetals*, 106, 253–280. Available from <https://doi.org/10.1016/bs.semsem.2020.12.002>, <http://books.elsevier.com/uk/bookscat/search/results.asp?country=United+Kingdom&ref=&community=engineering&cmscssid=JP3B2U2KMCVJ9PGWXL1UUNX0PRW62H1A>.
- Liu, Q., Shi, X., Jiang, Q., Li, R., Zhong, S., & Zhang, R. (2021). Growth mechanism and kinetics of vertically aligned carbon nanotube arrays. *EcoMat*, 3(4). Available from <https://doi.org/10.1002/eom2.12118>.
- Maschmann, M. R., Ehlert, G. J., Tawfick, S., Hart, A. J., & Baur, J. W. (2014). Continuum analysis of carbon nanotube array buckling enabled by anisotropic elastic measurements and modeling. *Carbon*, 377–386. Available from <https://doi.org/10.1016/j.carbon.2013.09.013>.
- Maugis, D. (1992). Adhesion of spheres: The JKR-DMT transition using a Dugdale model. *Journal of Colloid and Interface Science*, 150(1), 243–269. Available from [https://doi.org/10.1016/0021-9797\(92\)90285-T](https://doi.org/10.1016/0021-9797(92)90285-T).
- Meshot, E. R., Verploegen, E., Bedewy, M., Tawfick, S., Woll, A. R., Green, K. S., Hromalik, M., Koerner, L. J., Philipp, H. T., Tate, M. W., Gruner, S. M., & Hart, A. J. (2012). High-speed in situ

- X-ray scattering of carbon nanotube film nucleation and self-organization. *ACS Nano*, 6(6), 5091–5101. Available from <https://doi.org/10.1021/nn300758f>.
- Muller, V. M., Yushchenko, V. S., & Derjaguin, B. V. (1980). On the influence of molecular forces on the deformation of an elastic sphere and its sticking to a rigid plane. *Journal of Colloid and Interface Science*, 77(1), 91–101. Available from [https://doi.org/10.1016/0021-9797\(80\)90419-1](https://doi.org/10.1016/0021-9797(80)90419-1).
- Oliver, C. R., Westrick, W., Koehler, J., Brieland-Shoultz, A., Anagnostopoulos-Politis, I., Cruz-Gonzalez, T., & Hart, A. J. (2013). Robofurnace: A semi-automated laboratory chemical vapor deposition system for high-throughput nanomaterial synthesis and process discovery. *Review of Scientific Instruments*, 84(11). Available from <https://doi.org/10.1063/1.4826275>.
- Persson, B. N. J., & Scaraggi, M. (2014). Theory of adhesion: Role of surface roughness. *The Journal of Chemical Physics*, 141(12), 124701. Available from <https://doi.org/10.1063/1.4895789>.
- Pierard, N., Fonseca, A., Konya, Z., Willems, I., Van Tendeloo, G., & Nagy, J. B. (2001). Production of short carbon nanotubes with open tips by ball milling. *Chemical Physics Letters*, 335(1–2), 1–8. Available from [https://doi.org/10.1016/S0009-2614\(01\)00004-5](https://doi.org/10.1016/S0009-2614(01)00004-5).
- Piwko, M., Althues, H., Schumm, B., & Kaskel, S. (2015). Confocal microscopy for process monitoring and wide-area height determination of vertically-aligned carbon nanotube forests. *Coatings*, 5(3), 477–487. Available from <https://doi.org/10.3390/coatings5030477>, <https://www.mdpi.com/2079-6412/5/3/477/pdf>.
- Prokopovich, P., & Perni, S. (2011). Comparison of JKR- and DMT-based multi-asperity adhesion model: Theory and experiment. *Colloids and Surfaces A: Physicochemical and Engineering Aspects*, 383(1–3), 95–101. Available from <https://doi.org/10.1016/j.colsurfa.2011.01.011>, <http://www.elsevier.com/locate/colsurfa>.
- Puretzky, A. A., Geohegan, D. B., Jesse, S., Ivanov, I. N., & Eres, G. (2005). In situ measurements and modeling of carbon nanotube array growth kinetics during chemical vapor deposition. *Applied Physics A: Materials Science and Processing*, 81(2), 223–240. Available from <https://doi.org/10.1007/s00339-005-3256-7>.
- Rajagopalan, P., Muthu, M., Liu, Y., Luo, J., Wang, X., & Wan, C. (2022). Advancement of electroadhesion technology for intelligent and self-reliant robotic applications. *Advanced Intelligent Systems*, 4(7), 2200064. Available from <https://doi.org/10.1002/aisy.202200064>.
- Šafarić, R., & Lukman, D. (2014). One-finger gripper based on the variable van der Waals force used for a single nano/micro-sized object. *Journal of Micromechanics and Microengineering*, 24(8). Available from <https://doi.org/10.1088/0960-1317/24/8/085012>, http://iopscience.iop.org/0960-1317/24/8/085012/pdf/0960-1317_24_8_085012.pdf.
- Salvetat, J. P., Kulik, A. J., Bonard, J. M., Briggs, G. A. D., Stöckli, T., Méténier, K., Bonnamy, S., Béguin, F., Burnham, N. A., & Forró, L. (1999). Elastic modulus of ordered and disordered multi-walled carbon nanotubes. *Advanced Materials*, 11(2), 161–165. Available from <http://www3.interscience.wiley.com/journal/119030556/issue>, [https://doi.org/10.1002/\(SICI\)1521-4095\(199902\)11:2<161::AID-ADMA161>3.0.CO;2-J](https://doi.org/10.1002/(SICI)1521-4095(199902)11:2<161::AID-ADMA161>3.0.CO;2-J).
- Seo, S., Kim, S., Yamamoto, S., Cui, K., Kodama, T., Shiomi, J., Inoue, T., Chiashi, S., Maruyama, S., & Hart, A. J. (2021). Tailoring the surface morphology of carbon nanotube forests by plasma etching: A parametric study. *Carbon*, 180, 204–214. Available from <https://doi.org/10.1016/j.carbon.2021.04.066>, <http://www.journals.elsevier.com/carbon/>.
- Sojoudi, H., Kim, S., Zhao, H., Annarapu, R. K., Mariappan, D., Hart, A. J., McKinley, G. H., & Gleason, K. K. (2017). Stable wettability control of nanoporous microstructures by ICVD coating of carbon nanotubes. *ACS Applied Materials and Interfaces*, 9(49), 43287–43299. Available from <https://doi.org/10.1021/acsami.7b13713>, <http://pubs.acs.org/journal/aamick>.
- Stadermann, M., Sherlock, S. P., In, J. B., Fornasiero, F., Park, H. G., Artyukhin, A. B., Wang, Y., De Yoreo, J. J., Grigoropoulos, C. P., Bakajin, O., Chernov, A. A., & Noy, A. (2009). Mechanism and kinetics of growth termination in controlled chemical vapor deposition growth of multiwall carbon nanotube arrays. *Nano Letters*, 9(2), 738–744. Available from <https://doi.org/10.1021/nl803277g>, <http://pubs.acs.org/doi/pdfplus/10.1021/nl803277g>, United States.

- Sugime, H., Sato, T., Nakagawa, R., Hayashi, T., Inoue, Y., & Noda, S. (2021). Ultra-long carbon nanotube forest via in situ supplements of iron and aluminum vapor sources. *Carbon*, 172, 772–780. Available from <https://doi.org/10.1016/j.carbon.2020.10.066>, <http://www.journals.elsevier.com/carbon/>.
- Tabor, D. (1977). Surface forces and surface interactions. *Journal of Colloid and Interface Science*, 58(1). Available from <https://doi.org/10.1016/b978-0-12-404501-9.50009-2>.
- Taylor, P. M., Monkman, G. J., & Farnworth, G. J. F. (1989). Principles of electroadhesion in clothing robotics. *International Journal of Clothing Science and Technology*, 1(3), 14–20. Available from <https://doi.org/10.1108/eb002951>.
- Thompson, C. V. (2012). Solid-state dewetting of thin films. *Annual Review of Materials Research*, 42, 399–434. Available from <https://doi.org/10.1146/annurev-matsci-070511-155048>.
- Uran, S., Šafarič, R., & Bratina, B. (2017). Reliable and accurate release of micro-sized objects with a gripper that uses the capillary-force method. *Micromachines*, 8(6). Available from <https://doi.org/10.3390/mi8060182>, <http://www.mdpi.com/2072-666X/8/6/182/pdf>.
- Vasudev, A., Jagtiani, A., Du, L., & Zhe, J. (2009). A low-voltage droplet microgripper for micro-object manipulation. *Journal of Micromechanics and Microengineering*, 19(7). Available from <https://doi.org/10.1088/0960-1317/19/7/075005>.
- Verma, D., Avasthi, P., & Balakrishnan, V. (2020). Upscaling mechanical properties of Al₂O₃ coated VACNT forest architecture under compression. *Materials Characterization*, 170. Available from <https://doi.org/10.1016/j.matchar.2020.110687>, <https://www.journals.elsevier.com/materials-characterization>.
- Wang, C. S. (2001). Electrostatic forces in fibrous filters - A review. *Powder Technology*, 118(1–2), 166–170. Available from [https://doi.org/10.1016/S0032-5910\(01\)00307-2](https://doi.org/10.1016/S0032-5910(01)00307-2), <http://www.elsevier.com/locate/powtec>.
- Wang, J., Kawde, A. N., & Musameh, M. (2003). Carbon-nanotube-modified glassy carbon electrodes for amplified label-free electrochemical detection of DNA hybridization. *Analyst*, 128(7), 912–916. Available from <https://doi.org/10.1039/b303282e>, <http://pubs.rsc.org/en/journals/journal/an>.
- Wang, R. (2022). Carbon nanotube-based strain sensors: structures, fabrication, and applications. *Adv. Materials Technology*.
- Wang, Y., & Weng, G. J. (2017). Electrical conductivity of carbon nanotube and graphene-based nanocomposites. *Micromechanics and nanomechanics of composite solids* (pp. 123–156). United States: Springer International Publishing. Available from <http://doi.org/10.1007/978-3-319-52794-9>.
- Wardly, G. A. (1973). Electrostatic wafer chuck for electron beam microfabrication. *Review of Scientific Instruments*, 44(10), 1506–1509. Available from <https://doi.org/10.1063/1.1685985>.
- White, C. T., & Mintmire, J. W. (2005). Fundamental properties of single-wall carbon nanotubes. *Journal of Physical Chemistry B*, 109(1), 52–65. Available from <https://doi.org/10.1021/jp047416>.
- Xu, D., Liechti, K. M., & Ravi-Chandar, K. (2007). On the modified Tabor parameter for the JKR–DMT transition in the presence of a liquid meniscus. *Journal of Colloid and Interface Science*, 315(2), 772–785. Available from <https://doi.org/10.1016/j.jcis.2007.07.048>.
- Yang, F., Wang, M., Zhang, D., Yang, J., Zheng, M., & Li, Y. (2020). Chirality pure carbon nanotubes: growth, sorting, and characterization. *Chemical Reviews*, 120(5), 2693–2758. Available from <https://doi.org/10.1021/acs.chemrev.9b00835>, <http://pubs.acs.org/journal/chreay>.
- Yu, M. F., Lourie, O., Dyer, M. J., Moloni, K., Kelly, T. F., & Ruoff, R. S. (2000). Strength and breaking mechanism of multiwalled carbon nanotubes under tensile load. *Science (New York, N.Y.)*, 287(5453), 637–640. Available from <https://doi.org/10.1126/science.287.5453.637>.
- Zaytseva, O., & Neumann, G. (2016). Carbon nanomaterials: Production, impact on plant development, agricultural and environmental applications. *Chemical and Biological Technologies in Agriculture*, 3(1). Available from <https://doi.org/10.1186/s40538-016-0070-8>, <http://chembioagro.springeropen.com/>.
- Zbib, A. A., Mesarovic, S. D., Lilleodden, E. T., McClain, D., Jiao, J., & Bahr, D. F. (2008). The coordinated buckling of carbon nanotube turfs under uniform compression. *Nanotechnology*, 19(17). Available from <https://doi.org/10.1088/0957-4484/19/17/175704>.
- Zhong, G., Iwasaki, T., Honda, K., Furukawa, Y., Ohdomari, I., & Kwarada, H. (2005). Low temperature synthesis of extremely dense and vertically aligned single-walled carbon nanotubes. *Japanese Journal of Applied Physics, Part 1: Regular Papers and Short Notes and Review Papers*, 44(4 A), 1558–1561. Available from <https://doi.org/10.1143/JJAP.44.1558>.

- Zou, M., Cai, L., & Wang, H. (2006). Adhesion and friction studies of a nano-textured surface produced by spin coating of colloidal silica nanoparticle solution. *Tribology Letters*, 21(1), 25–30. Available from <https://doi.org/10.1007/s11249-005-9004-5>.
- Zou, M., Wang, H., Larson, P. R., Hobbs, K. L., Johnson, M. B., & Awitor, O. K. (2006). Ni nanodot-patterned surfaces for adhesion and friction reduction. *Tribology Letters*, 24(2), 137–142. Available from <https://doi.org/10.1007/s11249-006-9157-x>.

CHAPTER 7

Water-assisted transfer printing techniques

Hongyu Hou, Lingzhi Zhang, Zi Xin Zhang and Changhong Cao

Department of Mechanical Engineering, McGill University, Montreal, QC, Canada

Water-assisted transfer printing (WTP) method has been developed to integrate electronic devices onto various backplanes by using water as a medium to transfer devices (i.e., inks) from the donor substrate to a receiver substrate. It leverages a release or a sacrificial layer to promote the separation between inks and the donor substrate with the aid of water at room temperature. When a release layer is used, in the “picking” process, water serves as an adhesive layer to form covalent bonds at the ink/receiver interface; in the “placing” process, the weak adhesion between the release layer [e.g., self-assembled monolayer (SAM) (Lee et al., 2007)] and the ink results in the detachment of the ink from the donor substrate to the receiver substrate. An alternative is to use a sacrificial layer [e.g., a nickel (Ni) layer (Lee et al., 2011)] in WTP. It is introduced at the ink/donor substrate interface and will be dissolved after ink detachment with water-assisted interfacial fractures at the ink/donor substrate. WTP is a straightforward and cost-effective approach and has been widely leveraged for the transfer printing of metal thin films (Oh et al., 2009), flexible electronics (Zhou et al., 2019), nanomaterials-based patterns (Aghajamali et al., 2018), and two-dimensional materials (Shivayogimath et al., 2019). This chapter introduces WTP and discusses its general steps, benefits, and drawbacks.

7.1 Water-assisted transfer printing with self-assembled monolayer-based release layer

SAMs, formed by the spontaneous absorption of molecules on a surface, play a crucial role in WTP by serving as a release layer between the ink and the donor substrate. In WTP, a SAM is typically composed of a functional group that can bind to a target surface (i.e., ink/donor substrate interface), as well as provide a smooth surface for the transfer process.

Lee et al. (2007) reported a water-mediated nanotransfer process to deposit patterned Al thin films to Si substrates using either Si stamps manufactured through laser interference lithography, or polydimethylsiloxane (PDMS) stamps fabricated through

casting and curing. As indicated in Fig. 7.1A, the transfer process starts with coating an octadecylsiloxane SAM layer by contact-inking method (Libioule et al., 1999) onto a Si or PDMS stamp cleaned under ozone exposure. Subsequently, an Al thin film layer is uniformly deposited onto the stamp by electron-beam evaporation, forming a weak

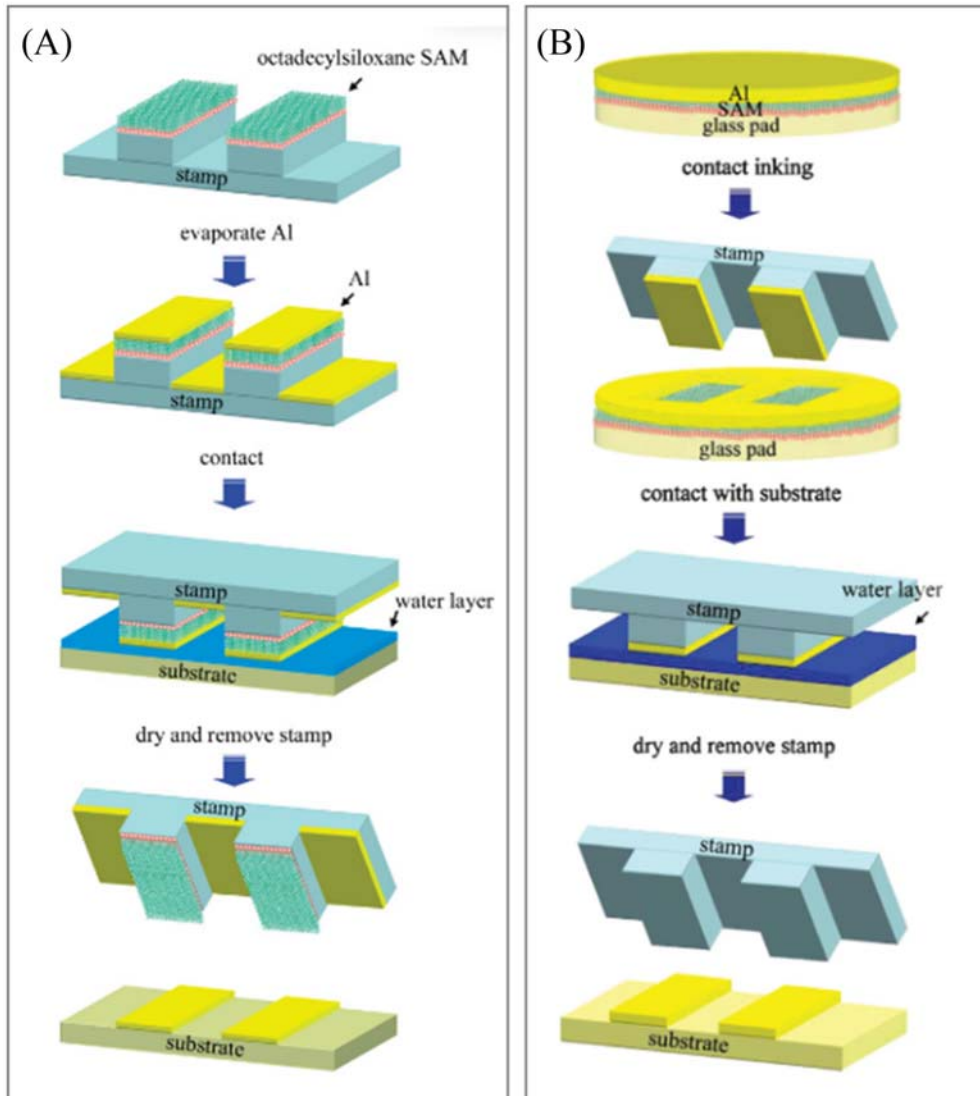


Figure 7.1 Schematic of WTP with self-assembled monolayer-based release layer. (A) Schematic of the procedure to fabricate patterned Al by using water-mediated nanotransfer printing process. (B) Schematic of the procedure to fabricate patterned Al by using water-mediated transfer printing process with contact inking.

adhesion with the SAM release layer. The stamp laminated with SAM and Al ink is then brought into contact with a Si receiver substrate covered by a 100 μm thick water layer. After evaporating the water layer at room temperature, the adhesion at the Al/Si interface is stronger than that at the Al/SAM interfaces such that Al can be easily detached from the stamp and adhered to the Si substrate.

In this method, the water layer promotes a conformal contact between the Al ink and the substrate through attractive capillary force. During the drying process, oxidation occurs on both the Al and Si surfaces, forming a 5-nm/2-nm thin oxide layer, respectively. Materials from the oxidized surfaces precipitate and further enhance the adhesion between the Al thin film and the Si substrate through the formation of covalent bonds. However, the presence of an oxide layer increases the resistivity of Al thin film. For an Al thin film with a thickness smaller than 20 nm, this effect is not trivial. As the film thickness increases, its resistivity rapidly decreases, and gradually levels off to approximately 1.4 times the resistivity of bulk Al at 50 nm. Using this method, the author successfully transferred lines of Al patterns with 95 nm width, 30 nm thickness, and 108 nm spacing onto SiO_2/Si substrate as hard masks for dry etching.

Similarly, Sung and co-workers (Oh et al., 2009) transferred Al thin film from a glass pad onto a Si substrate with a PDMS stamp. As shown in Fig. 7.1B, an Al thin film layer is uniformly evaporated onto a SAM-coated glass pad instead. Then, a patterned PDMS stamp picks up the Al thin film from the pad with a gentle touch. Subsequently, the stamp inked with the Al thin film is brought into contact with a water-coated Si substrate. After drying, the stamp is removed to complete the transfer process. Compared to the method reported by Lee et al., the PDMS stamp in this method can be used repeatedly because its elastomeric property allows it to recover to its original shape without any treatment.

The SAM-based method is limited in applications because SAMs can be sensitive to chemical and thermal environments, which can limit their use in certain applications; it also requires careful deposition methods, which can be time-consuming and challenging to achieve a uniform and stable monolayer. However, the Al-Si bonding connection inspired the development of metal layer-based WTP.

7.2 Water-assisted transfer printing with sacrificial layer

The WTP method with a sacrificial layer relies on water to seep into the interface between the sacrificial layer and the donor substrate to lift off the sacrificial layer. Generally, two types of sacrificial layers are used: a metal layer or a water-soluble organic layer. Metal layers [i.e., Ni (Lee et al., 2011)] can form hydroxides on the metal surface in water and water-soluble organic compounds [i.e., poly(vinyl alcohol) (PVA) (Zhao et al., 2016)] can be dissolved in water directly. In this section, sacrificial layer-based WTP is discussed.

7.2.1 Water-assisted transfer printing with nickel-based sacrificial layer

Lee et al. (2011) demonstrated a WTP method using nickel as a sacrificial layer to transfer nanowire (NW)-based electronics from SiO_2/Si wafer onto nonconventional substrates. The general steps are as follows (Fig. 7.2A): first, a thin layer of Ni followed by an insulation layer [i.e., polyimide (PI), silicon nitride (SiN)] are deposited on SiO_2/Si substrate. The deposited Ni forms nickel silicate or nickel oxide at the SiO_2/Ni interference. Second, the NW device layer is fabricated via lithography on top of the insulation layer. Third, a thermal release tape (TRT) coated with a layer of PMMA (to avoid direct contact between the glue on TRT and the NW device layer) is attached atop the NW device layer [Fig. 7.2A(i)]. Subsequently, the entire laminated structure is placed into deionized water at room temperature [Fig. 7.2A(ii)] such that the nickel silicate or nickel oxides turns to nickel hydroxide which will weaken the adhesion between the Ni layer and the SiO_2/Si substrate and eventually lead to interfacial fracture at the Ni/ SiO_2 interface. Finally, the Ni layer is etched away and the device structures carried by TRT are then pasted onto receiver substrates; the TRT will be released by heating and

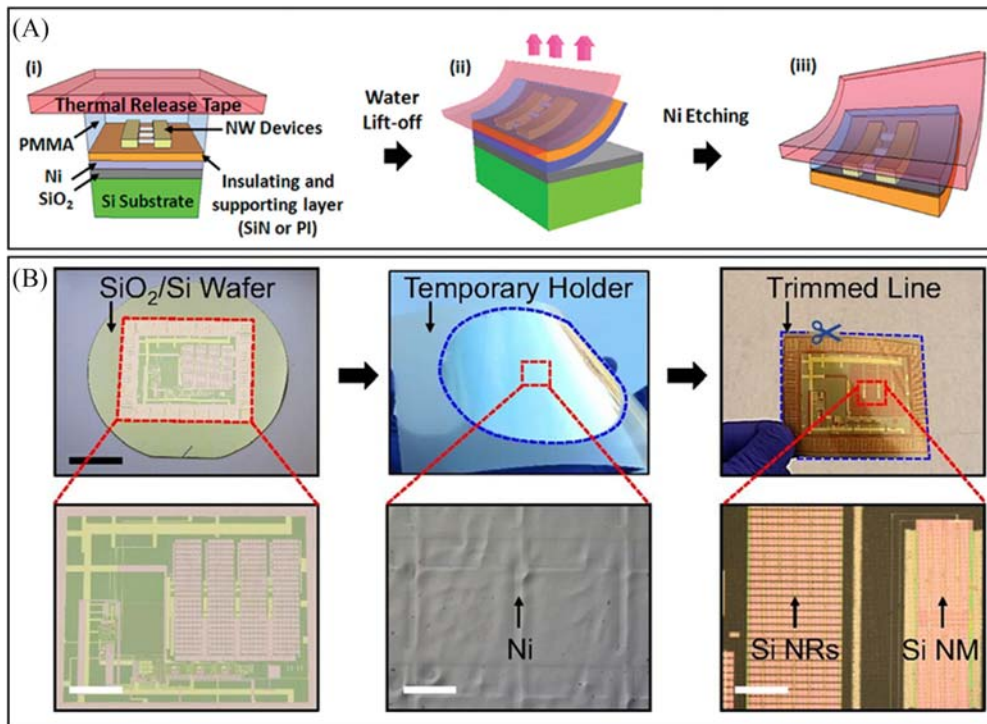


Figure 7.2 Schematic of water-assisted transfer printing with nickel-based sacrificial layer. (A) WTP with a nickel-based sacrificial layer. (B) optical images of the thin-film nanoelectronics on the SiO_2/Si wafer (Left), peeled with a thermally releasable tape (Middle), and then trimmed neatly (Right).

the PMMA layer will be dissolved. With this method, NW-based devices have been successfully transferred onto nonconventional substrates, such as paper, plastics, glass, tapes, PDMS, ultrathin PI substrates, etc.

With a similar process in Lee's work, [Wie et al. \(2018\)](#) successfully transferred wafer-scale thin-film nanoelectronics (i.e., two-dimensional Si nanomembranes, molybdenum disulfide monolayer, silver NWs, etc.) from SiO₂/Si wafer onto a temporary holder and finally to various receiver substrate (i.e., silicone glues, spray adhesives, etc.) as shown in [Fig. 7.2B](#). The method facilitates defect-free interfacial delamination of thin-film nanoelectronics from their original substrate at wafer-scale through a controlled fracturing process at room temperature in water environment. In this process, any excessive areas, such as corner spaces or alignment marks for the delaminated layers, could be trimmed with commercial scissors. The subsequent structure could be adhered to the desired location of interest using commercially available adhesives such as silicone glues, adhesive spray, or tapes. It was reported that the yield rate for defect-free interfacial debonding was 98.26% among more than 200 test bed specimens.

Overall, the Ni layer serves as a sacrificial layer because it can be selectively etched away during the transfer process, leaving the transferred pattern intact on the receiver substrate. It also provides a flat and smooth surface for the device layer, enabling the precise transfer of patterns onto receiver substrates. Meanwhile, Ni is compatible with a wide range of inks and materials used in the transfer film, making it a versatile material for WTP. However, Ni is toxic and can be harmful if not handled properly. Moreover, Ni is a nonrenewable resource, and the manufacturing and disposal of Ni layers can contribute to environmental pollution and waste.

7.2.2 Water-assisted transfer printing with polyvinyl alcohol-based sacrificial layer

[Zhao et al. \(2016\)](#) developed a modified WTP process by replacing Ni layer with a water-soluble PVA layer to transfer ultrathin bismuth vanadate (BiVO₄) photoanode film onto textured PDMS substrates. As indicated in [Fig. 7.3A](#), the process started with the deposition of a 300-nm thick Au film onto a SiO₂/Si wafer using electron beam evaporation. Thin films of SiO₂ and BiVO₄ with an approximate thickness of 10 and 80 nm, respectively, were then deposited on the top surface of the Au film by spin coating. Next, a thin layer of water-soluble PVA was spin-coated onto BiVO₄. A TRT was further applied on top of the PVA to act as a temporary transfer handle layer. Then, the entire structure (TRT/PVA/BiVO₄/SnO₂/Au) was peeled from the SiO₂/Si substrate and immersed in the water bath at room temperature for a few hours to dissolve the PVA layer completely. The PVA dissolution leads to the detachment between TRT and the BiVO₄/SnO₂/Au structure. The remaining BiVO₄/SnO₂/Au film floats on the water surface and can be scooped out using the patterned PDMS

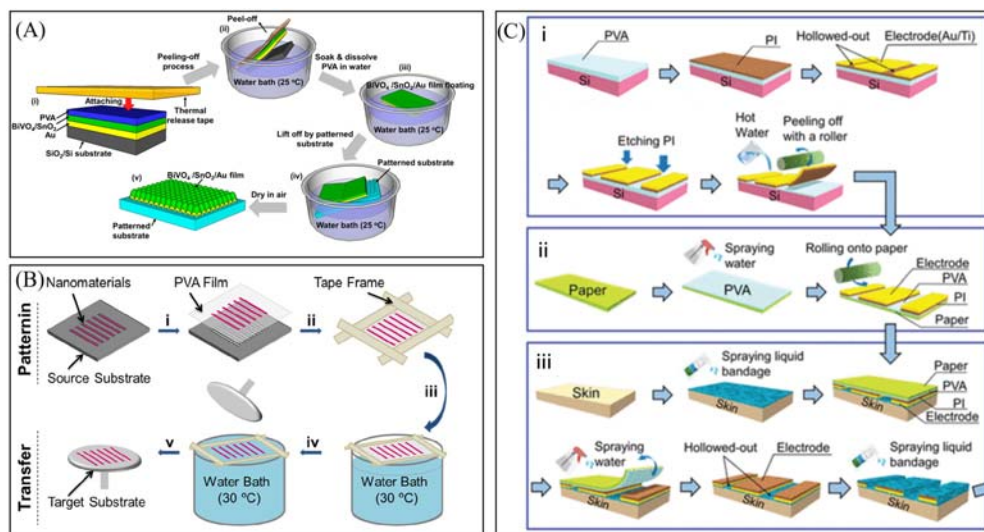


Figure 7.3 Schematic of water-assisted transfer printing with PVA-based sacrificial layer. (A) Transfer process of ultrathin bismuth vanadate (BiVO₄) photoanode film on textured PDMS substrates. (B) Illustration of water-assisted transfer patterning of nanomaterials. (C) Paper-assisted WTP of tattoo electrode from Si substrate to human skin.

substrate. Finally, the transferred structure was air-dried and the BiVO₄/SnO₂/Au film conformed to the textured PDMS substrates by capillary force as a result of water evaporation. With this method, photoelectrochemical (PEC) devices with high photocurrent densities and low onset potentials were fabricated on textured substrates, providing an approach to improve PEC performance. Others also (Shivayogimath et al., 2019; Van Ngoc et al., 2016; Whelan et al., 2017; Yang et al., 2015) successfully transferred graphene using similar PVA-based WTP process from their growth substrate [i.e., Cu (Yang et al., 2015)] to target substrates [i.e., SiO₂/Si wafers (Shivayogimath et al., 2019)].

Maryam et al. (Aghajamali et al., 2018) applied the PVA-based WTP method to transfer hydrophobic silicon nanocrystal and gold nanoparticle patterns from a patterned source substrate onto a receiver substrate. As shown in Fig. 7.3B, the patterned nanomaterials are peeled off by PVA film from the donor substrate. The film edge is then framed with standard Scotch Tape and attached to a partially water-filled vessel with the nanomaterial side on the top. Later, more water is added to the vessel until the PVA film is in contact with water. After the PVA film is dissolved, nanomaterial patterns will be afloat on the water surface. Finally, the receiver substrate is immersed in the water to scoop up the nanomaterials. PVA film makes the transfer printing process more cost-effective and leaves off the adhesion energy control problems. However, it was found that NM patterns expand slightly after transfer, which is more evident in small features.

The authors attribute this phenomenon to PVA film dissolution, which involves shrinking and expanding the film. In addition, the dissolution of PVA may alter the viscosity of the water solution, thereby impacting the integrity of the pattern.

Inspired by the previous PVA-based water-assisted method, Wang et al. (2022) further proposed a paper-assisted strategy to fabricate a tattoo electrocardiogram (ECG) electrode, which allows for conformable deformation with skin. In the beginning, similar to the structure in work (Lee et al., 2011), PVA layer replaced Ni layer embedded between the silicone substrate and PI layer and helped transfer electrode patterns from the initial silicon substrate onto a roller [Fig. 7.3C(i)]. The roller then pressed the rolled electrode sheet onto a paper, which is also spray-coated with a thin PVA layer [Fig. 7.3C(ii)]. At the same time, the skin surface was sprayed with a layer of liquid bandage so that the paper-based electrode sheets could be attached to the skin tightly. In a moment, water soaks into the paper and dissolves the PVA layer below and finally separates electrodes and paper [Fig. 7.3C(iii)]. The transferred electrode has high mechanical stability, low contact impedance and excellent ECG signals under both relax and exercise conditions. In this paper-assisted method, the roll-to-roll procedure makes interfacial force control more easily and promotes large-area fabrication.

Overall, compared to other sacrificial layers, PVA not only is a cost-effective option but also provides mechanical support to inks, preventing them from breaking or tearing during the transfer process, making it the most popular candidate in WTP processes. However, the dissolution of PVA requires several hours, and PVA is not very durable and can degrade over time, which potentially can affect the quality of the transferred inks.

In summary, WTP offers several advantages over other transfer printing methods, including the ability to transfer complex designs onto irregular surfaces, low cost and high throughput. However, the wet transfer process has limited applications in the transfer printing industry. It is still challenging to transfer high-quality patterns onto various substrates. Also, WTP is currently limited to small-scale manufacturing due to many factors, including unwanted defects/wrinkles introduced when to-be-transferred inks are large, stabilizing large water surfaces, etc.

References

- Aghajamali, M., Cheong, I. T., & Veinot, J. G. C. (2018). Water-assisted transfer patterning of nanomaterials. *Langmuir: the ACS Journal of Surfaces and Colloids*, *34*(32), 9418–9423. Available from <https://doi.org/10.1021/acs.langmuir.8b00694>.
- Lee, B. H., Cho, Y. H., Lee, H., Lee, K.-D., Kim, S. H., & Sung, M. M. (2007). High-resolution patterning of aluminum thin films with a water-mediated transfer process. *Advanced Materials*, *19*(13), 1714–1718. Available from <https://doi.org/10.1002/adma.200601884>.
- Lee, C. H., Kim, D. R., & Zheng, X. (2011). Fabrication of nanowire electronics on nonconventional substrates by water-assisted transfer printing method. *Nano Letters*, *11*(8), 3435–3439. Available from <https://doi.org/10.1021/nl201901z>.

- Libioulle, L., Bietsch, A., Schmid, H., Michel, B., & Delamarche, E. (1999). Contact-inking stamps for microcontact printing of alkanethiols on gold. *Langmuir: the ACS Journal of Surfaces and Colloids*, 15(2), 300–304. Available from <https://doi.org/10.1021/la980978y>.
- Oh, K., Lee, B. H., Hwang, J. K., Lee, H., Im, S., & Sung, M. M. (2009). Water-mediated Al metal transfer printing with contact inking for fabrication of thin-film transistors. *Small (Weinheim an der Bergstrasse, Germany)*, 5(5), 558–561. Available from <https://doi.org/10.1002/sml.200801108>.
- Shivayogimath, A., Whelan, P. R., Mackenzie, David M. A., Luo, B., Huang, D., Luo, D., Wang, M., Gammelgaard, L., Shi, H., Ruoff, R. S., Bøggild, P., & Booth, T. J. (2019). Do-it-yourself transfer of large-area graphene using an office laminator and water. *Chemistry of Materials: a Publication of the American Chemical Society*, 31(7), 2328–2336. Available from <https://doi.org/10.1021/acs.chemmater.8b04196>.
- Van Ngoc, H., Qian, Y., Han, S. K., & Kang, D. J. (2016). PMMA-etching-free transfer of wafer-scale chemical vapor deposition two-dimensional atomic crystal by a water soluble polyvinyl alcohol polymer method. *Scientific Reports*, 6(1), 33096. Available from <https://doi.org/10.1038/srep33096>.
- Wang, H., Wang, J., Chen, D., Ge, S., Liu, Y., Wang, Z., Zhang, X., Guo, Q., & Yang, J. (2022). Robust Tattoo Electrode Prepared by Paper-Assisted Water Transfer Printing for Wearable Health Monitoring. *IEEE Sensors Journal*, 22(5), 3817–3827. Available from <https://ieeexplore.ieee.org/document/9674934/authors>.
- Whelan, P. R., Jessen, B. S., Wang, R., Luo, B., Stoot, A. C., Mackenzie, D. M. A., Braeuninger-Weimer, P., Jouvray, A., Prager, L., Camilli, L., Hofmann, S., Bøggild, P., & Booth, T. J. (2017). Raman spectral indicators of catalyst decoupling for transfer of CVD grown 2D materials. *Carbon*, 117, 75–81. Available from <https://doi.org/10.1016/j.carbon.2017.02.028>, <https://www.sciencedirect.com/science/article/pii/S0008622317301562>.
- Wie, D. S., Zhang, Y., Kim, M. K., Kim, B., Park, S., Kim, Y.-J., Irazoqui, P. P., Zheng, X., Xu, B., & Lee, C. H. (2018). Wafer-recyclable, environment-friendly transfer printing for large-scale thin-film nanoelectronics. *Proceedings of the National Academy of Sciences*, 115(31), E7236–E7244. Available from <https://doi.org/10.1073/pnas.1806640115>.
- Yang, S. Y., Oh, J. G., Jung, D. Y., Choi, H. K., Yu, C. H., Shin, J., Choi, C.-G., Cho, B. J., & Choi, S.-Y. (2015). Metal-etching-free direct delamination and transfer of single-layer graphene with a high degree of freedom. *Small (Weinheim an der Bergstrasse, Germany)*, 11(2), 175–181. Available from <https://doi.org/10.1002/sml.201401196>.
- Zhao, J., Guo, Y., Cai, L., Li, H., Wang, K. X., Cho, I. S., Lee, C. H., Fan, S., & Zheng, X. (2016). High-performance ultrathin BiVO₄ photoanode on textured polydimethylsiloxane substrates for solar water splitting. *ACS Energy Letters*, 1(1), 68–75. Available from <https://doi.org/10.1021/acsenerylett.6b00032>.
- Zhou, H., Qin, W., Yu, Q., Cheng, H., Yu, X., & Wu, H. (2019). Transfer printing and its applications in flexible electronic devices. *Nanomaterials*, 9(2). Available from <https://doi.org/10.3390/nano9020283>.

CHAPTER 8

Novel nontraditional transfer printing technologies

Seok Kim¹ and Hohyun Keum²

¹Pohang University of Science and Technology, Mechanical Engineering, Pohang, South Korea

²Korea Institute of Industrial Technology, Digital Healthcare, Cheonan, South Korea

8.1 Transfer printing using unusual manipulator—shape memory polymer

8.1.1 Background of shape memory polymer

Shape memory polymer (SMP) is an emerging class of smart polymer that exhibits the property of shape reconfiguration between predefined shapes and programmed shapes upon external stimulus. SMPs display at least two different phases, that is, stable phase and switch phase (often referred as soft phase). Stable network of SMP is responsible for retaining its original (permanent) shape by the introduction of strong bonds between different chemical chains such as chemical crosslinks, crystalline phase or interpenetrating networks (Behl et al., 2010; Hu et al., 2012; Julich-Gruner et al., 2013) while switch phase temporarily fixes the temporary shape by crystallization, a glass transition, state change between liquid to solid phase, reversible bonds activated by an external stimulus such as heat (Zhang et al., 2016), light (Toshikj et al., 2021), electric field (Zhang et al., 2016), magnetic field (Testa et al., 2019), pH (Meng et al., 2015), and distinct solvent (Chen et al., 2009), etc. The two distinct phases in SMPs indicate the material's distinct shape memory effect is not a material intrinsic property, meaning that conventional molding merely empowers the polymer with permanent configuration and the following temporal fixation process called polymer programming is compulsory to explore the reversible shape memory effect (Shahi et al., 2021).

Thermally activated SMP, amid vastly distinct stimulation mechanisms, is repeatedly exploited for transfer printing applications owing to its simplicity in fabrication, large stiffness change and insignificant volumetric change between rubbery and glassy states (Eisenhaure et al., 2014, 2015; Kim et al., 2022). In order to exhibit the shape-memory effect, the polymer network obligatorily establishes a deformed state under environmental conditions, which is authorized by switching segments while net points determine permanent configuration.

Fig. 8.1 briefly describes the operation mechanism of thermally activated SMPs where T_{trans} or T_g represents thermal or glass transition temperature, and shape A and shape B

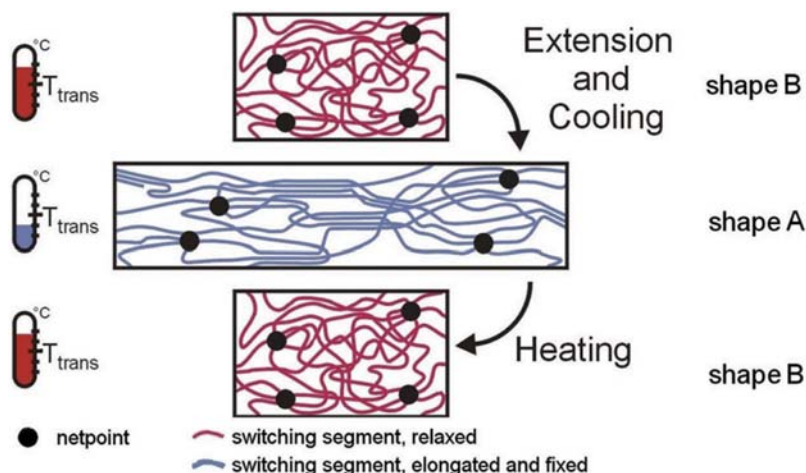


Figure 8.1 Molecular mechanism of thermally induced shape-memory effect with thermal or glass transition temperature (T_{trans} or T_g) (Behl & Lendlein, 2007).

represent temporal and permanent configurations respectively (Behl & Lendlein, 2007). Upon heating thermally activated SMPs above T_g , switching segments become compliant and susceptible to deformation by external stress (i.e., elongation in Fig. 8.1). While undergoing deformation, the SMP is cooled below T_g to fix at temporal state, which returns to its permanent shape when exposed to a temperature above T_g without external stress. In the realm of micro/nanoscale where volumetric effects such as gravity are negligible, an SMP that displays the ability to adjust adhesion by altering contacting surface area is an appealing candidate as a manipulator.

In comparison with polydimethylsiloxane (PDMS) reversible dry adhesive, which exploits viscoelastic intrinsic material property, thermally activated SMP requires the incorporation of a heat source for adhesion control. Quadrini has demonstrated SMP composite with an embedded heater, which is made of a flexible microheater encapsulated between two polyimide (PI) films (Quadrini et al., 2021). Additionally, the flexible heater is located at the neutral plane of the shape memory polymer composite (SMPC) to minimize stress-induced when the SMPC is bent. Another approach to incorporating a heating source into SMP is to use carbon black (CB) as a dopant during SMP fabrication (Eisenhaure & Kim, 2014). The authors varied CB weight percent blend with SMP and successfully demonstrated utilization of the shape memory effect by applying sufficient current respectively. Albeit of a distinctive approach to embody a heat source with SMP, externally induced thermal energy via oven, and joule heater made of indium tin oxide (ITO) is much practiced for simplicity.

8.1.2 Mechanics of shape memory polymer for deterministic transfer printing

To understand the mechanics of SMP dry adhesion for the purpose of transfer printing, Eisenhaure and his colleagues considered an SMP stamp with a flat surface as shown in Fig. 8.2A (Eisenhaure et al., 2015). SMP formulation can be chosen according to its desirable properties; high shape fixity and recovery factors, large rigidity change near T_g , convenient and narrow T_g range (40°C–60°C), and optical transparency. Using test procedures similar to those used previously for similar PDMS stamps (Keum et al., 2016; Kim et al., 2010), the adhesion between the SMP stamp and a silicon substrate may be measured. Fully utilizing the shape-memory properties of SMP requires the retraction step to occur at a temperature below the glass transition zone, corresponding to a stamp rigidity greater than 3 GPa, occurring when the SMP temperature is below 40°C. However, in order to investigate the role of the stamp's rigidity on its adhesive performance, it is necessary to test the stamp at intermediate temperatures within its glass transition zone. The essential steps of the testing procedure are illustrated in Fig. 8.2A, showing how a bond is formed and adhesion is tested for SMP stamps at varied retraction temperatures, and thus at varying values of stamp rigidity or storage modulus.

As an approximation to predict the effect of stamp rigidity on adhesive performance, linear elastic fracture theory which does not take polymeric viscoelasticity into account is employed. The energy release rate G for a propagating crack in a homogeneous isotropic material for plane stress conditions is given as

$$G = K_I^2/E \quad (8.1)$$

where K_I is the mode-I stress intensity factor and E is the material's elastic modulus, for which storage modulus may be substituted for analysis of SMP. In the case of fracture between the stamp-substrate interface, the mismatch between the elastic moduli of the two materials must be accounted for. Recognizing that the elastic modulus of SMP is very small compared with that of the silicon substrate, it is sufficient to treat the bimaterial interface as a homogeneous interface with double the elastic modulus of the SMP. In this case, the energy release rate becomes

$$G = K_I^2/2E_{\text{SMP}} \quad (8.2)$$

The mode-I stress intensity factor for an edge crack of length a in a semiinfinite material subject to an evenly distributed stress σ is given by (Eisenhaure et al., 2015)

$$K_I = 1.1215\sigma\sqrt{\pi a} \quad (8.3)$$

To derive the expected pull-off force, it is assumed that the crack will begin to propagate when the energy release rate reaches the SMP-substrate work of adhesion γ_0 . It is further assumed that an initial crack length of 1 μm exists at the edge of the

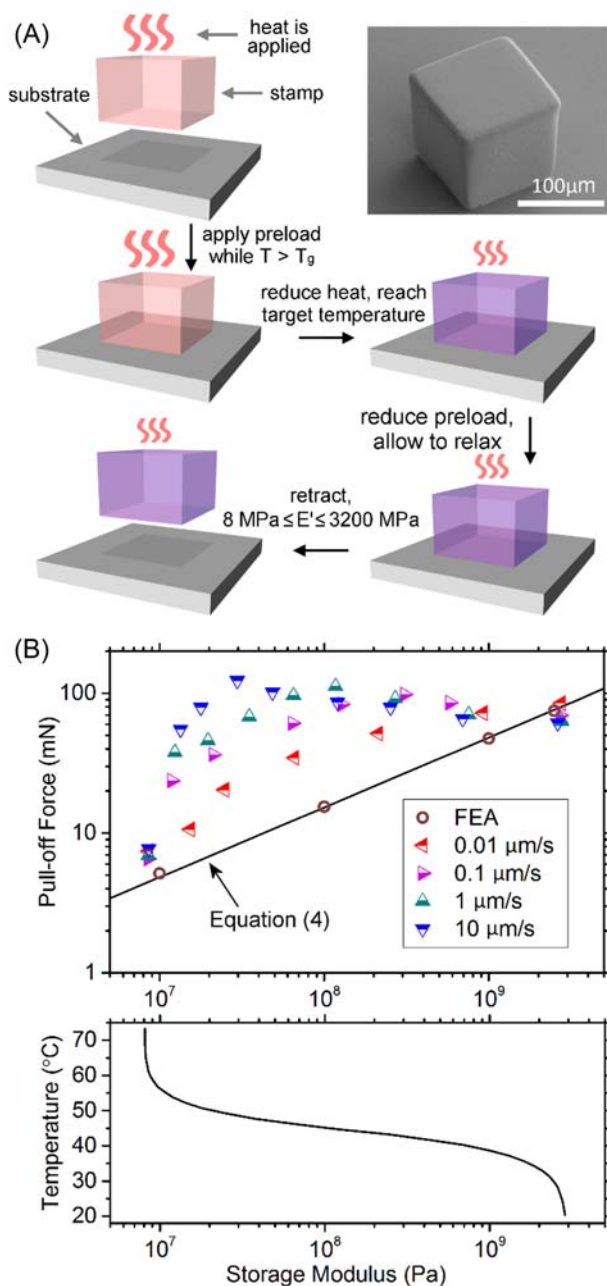


Figure 8.2 (A) An adhesion test schematic for a flat SMP stamp, showing the steps for testing with varying stamp storage modulus. (B) Pull-off force versus storage modulus for a $100 \mu\text{m} \times 100 \mu\text{m}$ flat poststamp for various retraction speeds. The analytical solution of Eq. (8.1) and linear elastic finite element results are compared. The temperature corresponding to each value of storage modulus, spanning the shape memory polymer glass transition zone, is shown (Eisenhaure et al., 2015).

interface, giving an a/L ratio of 0.01 for the square stamps of $100\ \mu\text{m}$ width under investigation, where L is the width of the stamp. Inserting Eq. (8.3) into Eq. (8.2) and rearranging, recognizing that $\sigma = F/A = F/L2$, yields

$$F_{\text{pulloff}} = \sqrt{25.31\gamma_0(2E_{\text{SMP}})L^3} \quad (8.4)$$

Eq. (8.4) is plotted in Fig. 8.2B for an SMP-silicon work of adhesion estimated to be $46\ \text{mJ/m}^2$ (Eisenhaure et al., 2013). An Abaqus finite element analysis (FEA) was performed using analogous assumptions as an additional check for the validity of the analytical solution. The axisymmetric model evaluates the energy release rate as a function of the uniformly distributed stress, applied on the substrate normal to the interface, using the J-integral method (Eisenhaure et al., 2015). A fixed boundary condition is used to restrict the stamp end displacement, as shown in Fig. 8.3. The uniform stress at which the energy release rate reaches the work of adhesion of the stamp-substrate interface is considered to be the critical stress required to delaminate the stamp. The force corresponding to this critical stress was evaluated for several values of stamp rigidity. The results are plotted in Fig. 8.2B to compare with Eq. (8.4).

Adhesion data was collected for a range of temperatures and retraction speeds using a $100\ \mu\text{m} \times 100\ \mu\text{m}$ flat SMP stamp. When compared to the linear elasticity-based analysis, the adhesion data show much more complex behavior. The adhesive strength of the interface is highly dependent upon retraction speed, indicating a strong viscoelastic effect within the glass transition zone. The effect of polymeric viscoelasticity on adhesion has previously been studied. The adhesive strength of polymers may be more thoroughly described by accounting for viscoelasticity using an equation of the form given in (Eisenhaure et al., 2015),

$$\gamma_{\text{eff}}(\nu, T) = \gamma_0 [1 + f(\nu, T)] \quad (8.5)$$

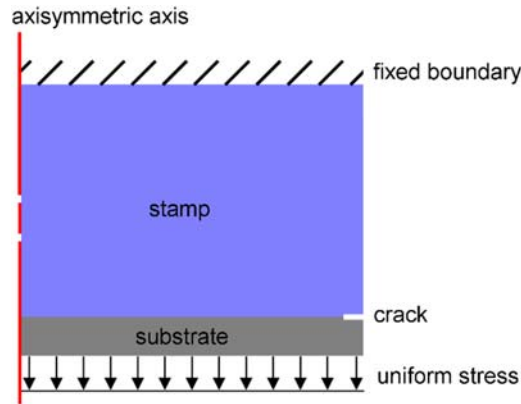


Figure 8.3 A schematic of the finite element analysis model used to predict the critical normal force required to delaminate the stamp from the substrate (Eisenhaure et al., 2015).

where γ_{eff} is the amount of energy required to advance the crack tip by one unit area, γ_0 is the energy required to break the interfacial polymer-substrate bonds at extremely low crack velocities, and $f(\nu, T)$ describes the bulk viscoelastic energy dissipation in front of the crack tip as a function of crack tip velocity and temperature. The viscoelastic dissipation term vanishes as crack tip velocity approaches zero.

The collected adhesion data in Fig. 8.2B is in agreement with this expectation, with adhesion increasing as retraction velocity is increased. The effect of velocity is greatest near to the “center” of the glass transition zone where the loss modulus, a measure of viscous dissipation within the polymer, reaches a maximum. At the tail ends of the glass transition region, where the loss modulus is very small compared with the elastic modulus, the adhesion is relatively unaffected by retraction velocity. As the retraction speed is reduced, the adhesion approaches the linear elastic result predicted by Eq. (8.4) due to the diminishing contribution from viscous dissipation. Since the typical operation of the SMP stamp requires that pickup and print events occur below and above the glass transition zone, respectively, to take advantage of the shape memory effect, the stamps are relatively insensitive to the retraction speed in practice. Since a polymer’s work of adhesion is not significantly affected by small temperature variations, it is concluded that the primary factor affecting the change in adhesion between the hot ($T > T_g$) and cold ($T < T_g$) states of the SMP stamps is the change in storage modulus. The SMP at room temperature is three orders of magnitude more rigid than PDMS, corresponding to a factor of 30 expected increase in maximum adhesion assuming similar surface energies.

8.1.3 Application of shape memory polymer for deterministic transfer printing

Transfer printing of microobjects prepared by conventional photolithography is an emerging additive manufacturing technique that enables heterogeneous material integration in highly systematic arrangement, construction of unusual three-dimensional form factors in microscale to stretch conventional micromanufacturing technique to widely diverse applications (Eisenhaure et al., 2013; Keum et al., 2012, 2016; Kim, Brueckner, et al., 2011; Kim et al., 2012). The principal operation procedure of the transfer printing is reversible adhesion of a manipulator often referred as a stamp that significant adhesion on/off ratio for successful retrieval and printing processes. Advanced forms of stamps are developed ranging from engineered structures (Kim et al., 2012; Mengüç et al., 2012; Yang et al., 2012), magnetic (Yu et al., 2018), laser (Luo et al., 2020; Oh et al., 2011), pressure driven stamps (Carlson, Wang, et al., 2012). Individuals are recommended to develop suitable stamps for specific applications, but deliberately engineered stamp designs with explicit structures in conjunction with the shape memory effect of SMP demonstrate sufficient efficacy for transfer printing of microobjects.

Eisenhaure and his colleagues first demonstrated the utilization of SMP as a reconfigurable dry adhesive incorporating shape memory effects with a micropatterned surface design inspired by Kim's previous work (Kim et al., 2010). The authors constructed epoxy-based SMP with microscale pyramids (often referred as microtip) features on the surface by molding, which adjusts its Young's modulus from 2.5 GPa to 10 MPa below and above the glass transition temperature (T_g) (Eisenhaure et al., 2013). The reversible dry adhesion utilizing the microscale pyramid feature on SMP is described in Fig. 8.4. The principal mechanism of reversible dry adhesion is governed by regulating the contact area between the SMP and opposing surface, through which the authors demonstrated as high as 184 N/cm^2 when compared with a low adhesion state at $3 \times 10^{-3} \text{ N/cm}^2$.

The pattern shown in Fig. 8.4 was also used for the purpose of microscale assembly where the interplay of time-insensitive shape fixing of the SMP and extreme adhesion reduction possible through microstructuring shows its true value (Eisenhaure et al., 2015). The particular microscale pattern was chosen for the convenience of demonstrating this interplay, as its manufacturing method is well-developed to create microscale stamps (Eisenhaure et al., 2015). Alternative patterns, including those incorporating heterogeneous materials, are also available with one example included in Fig. 8.5.

8.1.4 Microassembly of unusual three-dimensional microstructures using shape memory polymer stamp

Microtip stamps made of PDMS had demonstrated exceeding 1000:1 ratio of adhesion on/off ratio, through which construction of multiple unusual complex three-dimensional microassemblies had been demonstrated. Kinetically modulated PDMS stamp that fully exploits viscoelastic material intrinsic property along with enhanced

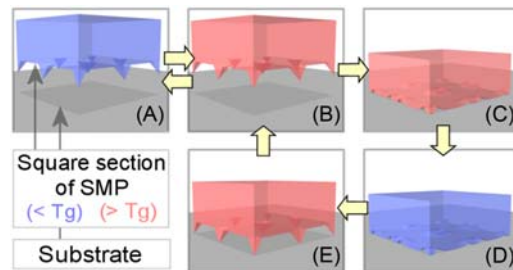


Figure 8.4 Schematic illustration of the bonding/debonding between a shape memory polymer (SMP) surface and a substrate. (A) The SMP with a microscale pyramid permanent shape is prepared ($<T_g$). (B) The SMP is heated above T_g . (C) SMP is pressed against the substrate while heated ($>T_g$). (D) The SMP is cooled below T_g to fix a large contacting temporal shape for higher adhesion. (E) SMP is heated above T_g with stress relieved to restore to permanent shape and exhibit contact against substrate only at the tip of the microscale pyramid for lower adhesion (Eisenhaure et al., 2013).

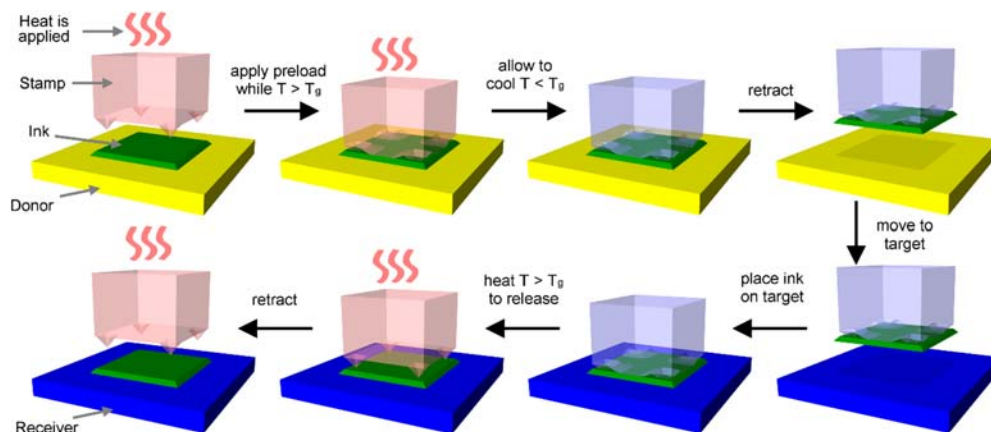


Figure 8.5 Implementation of shape memory polymer microtip surface in a stamp for deterministic assembly by transfer printing (Eisenhaure et al., 2014, 2015).

ink release prefabrication are two key aspects of successful transfer printing. The maximum adhesion attainable with a PDMS stamp is relatively low (~ 0.1 MPa), which requires intensive attention for ink (target microobjects transfer printed) preparation procedure to minimize adhesion with substrate prior to the retrieval process.

Additionally, complex three-dimensional structured inks are strenuous since conformal contact throughout the transfer printing process is impervious. To overcome the aforementioned challenges with the PDMS stamp, Eisenhaure demonstrated a microstructured (pyramid tip and silica-sphere embedded) SMP stamp and characterized (Eisenhaure et al., 2014). Fig. 8.6 shows pull-off force versus retraction speed for three different SMP stamp designs along with scanning electron microscopy (SEM) images of microtip stamp adhesion off and on the state (Fig. 8.6B and C) as well as silica-sphere embedded adhesion off and on the state (Fig. 8.6D and E). Owing to the temporal shape fixation characteristics of SMP, the adhesion off and on states are irreversible without external stimuli, making the pull-off force independent from the retraction speed of the stamp. Employing these structured SMP stamp, the authors successfully demonstrated the microassembly of three-dimensional complex individual inks in the letter (Eisenhaure et al., 2014, 2015).

8.1.5 Multilayered thin film contact printing with shape memory polymer

Temporal fixation of an arbitrarily deformed shape and recovery to the originally configured structure through external stimuli enables microscale individually patterned multilayered thin film inks in a large and parallel manner (Kim, Liu, et al., 2022). To facilitate convenient retrieval of patterned thin film inks, the authors first developed a mushroom-shaped platform where the surface is coated with gold (Au) thin film

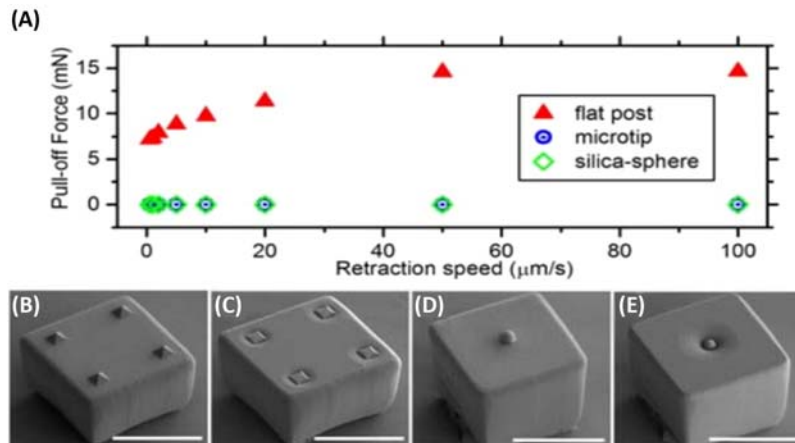


Figure 8.6 (A) Pull-off force versus retraction speed for three shape memory polymer (SMP) stamp designs during adhesion off state, (B) pyramid SMP stamp at adhesion off state, (C) pyramid SMP stamp at adhesion on state, (D) silica-sphere embedded SMP stamp at adhesion off state, (E) silica-sphere embedded SMP stamp at adhesion on state. All scale bars are 100 μm (Eisenhaure et al., 2014, 2015).

followed by a self-assembled monolayer (SAM) to reduce surface energy while maintaining low roughness. This modulation of surface energy at the donor platform enables the retrieval of thin film inks at the engineered interface.

Highly efficient printing of the transferred ink from SMP stamp to receiver substrate requires additional careful surface treatment to match the interfacial energy. The authors exploited thermomechanical characteristics of SMP through which stored elastic energy is transformed to facilitate the printing process as demonstrated elsewhere (Eisenhaure & Kim, 2016; Kim, Lakshmanan, et al., 2022). Nonetheless, the work sufficiently supports the use of SMP as a manipulator in transfer printing of microscale objects on a considerable scale in a systematic parallel manner, which possesses the potential to effectively complement traditional photolithography.

8.1.6 Selective printing combined cooperatively with parallelism in transfer printing

Batch process characteristics of transfer printing are principal merits that empower the use of transfer printing in conjunction with the conventional micromanufacturing process. Two modes of transfer printing technique are often exercised, parallel transfer printing and serial transfer printing. Parallel print mode involves a collectively preprocessed array of inks that are retrieved and printed collectively whereas serial transfer printing describes each ink as individually manipulated as specified by applications. Parallel transfer print mode merits from expedited process time, which is best suited

for large-scale manufacturing, but suffers from intolerance of defects that may have been caused by flaws in ink or misalignment in the large array transfer printing process. On the other hand, serial transfer printing mode empowered by high precision alignment and defect scrutiny mitigates the drawbacks of parallel transfer printing, while undergoing impediments in overall tact time.

A solution for such a dilemma is proposed referred to as “selective print,” which attempts to complement parallel and serial transfer printing techniques by retrieving inks in an array format as a parallel transfer printing process followed by selective printing on demand similar to serial transfer printing (Eisenhaure & Kim, 2016) as depicted in Fig. 8.7. The authors used SMP as the functional stamp material in conjunction with near-infrared (NIR, peak 807 nm wavelength) laser illumination to selectively activate individual posts in the ink array for the printing process. The stamp is prepared by a commonly practiced molding process with the addition of carbon black (CB) particles embedded on the SMP surface to absorb external stimulus by NIR laser. Such prepared carbon black-SMP (CBSMP) is fundamentally distinct from other previously demonstrated laser-assisted PDMS-based serial printing systems, such that previous work requires high-intensity ($3\text{--}30\text{ W/mm}^2$) for the ink to absorb laser energy whereas CBSMP requires relatively low energy for operation. Furthermore, the CBSMP stamp absorbs the external triggering energy, which yields a wide range of candidate material for ink when compared with laser-assisted PDMS serial printing system (Al-okaily & Ferreira, 2015; Saeidpourazar, Li, et al., 2012; Saeidpourazar, Sangid, et al., 2012).

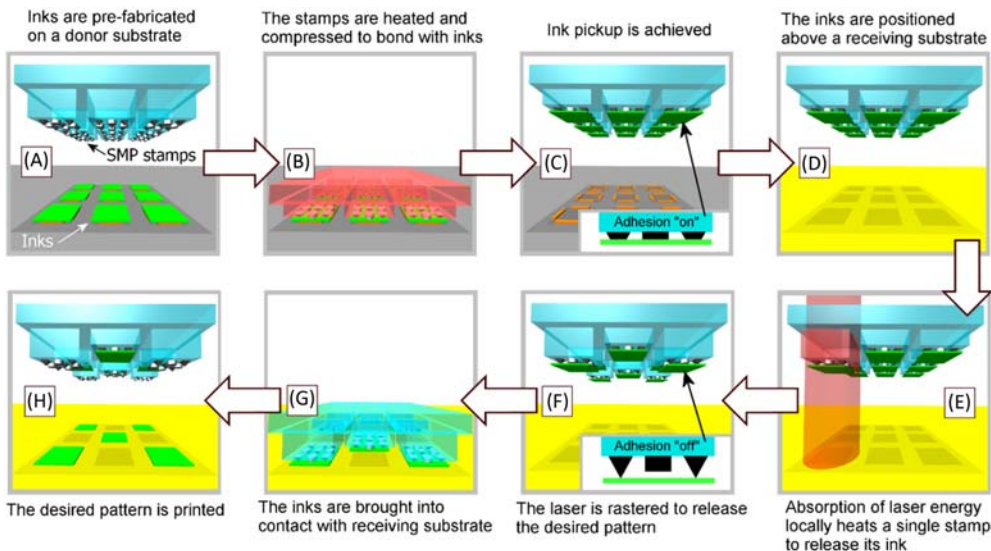


Figure 8.7 The operation of the laser-driven carbon black shape memory polymer transfer printing process is depicted. (Eisenhaure and Kim, 2016).

In order to accomplish CBSMP, the authors first prepared a negative mold made of PDMS, at which a thin layer of CB particles is coated on micro features on the surface. In the presented work, the features are an array of microtips and an array of cylinders where each array corresponds to effectively reducing adhesion during printing and providing a flat adhesive surface to firmly bond the ink during adhesion on the state. After CB coating, SMP is poured over the mold and cured to accomplish the CBSMP stamp. The proposed work is promising for micro-LED-based display manufacturing industry where each individual red, green and blue LEDs are required to be heterogeneously integrated onto a TFT backplane in a particularly organized array on large scale.

8.1.7 Application of shape memory polymer for subtractive transfer Printing of colloids

Subtractive transfer printing, which selectively removes and pattern active material or etch mask requires cohesive fracture at the interface between inks and the substrate (Gargas et al., 2006; Li et al., 2005; Sirbuluy et al., 2003). In order to achieve cohesive fracture to remove material at undesirable regions, diverse stamp materials had been explored, (i.e. PDMS (Carlson, Bowen, et al., 2012), PMMA (Nakamatsu et al., 2006), PUA (Suh et al., 2005)), but the higher surface energy and ability to make conformal contact with an opposing surface make SMP a strong candidate for subtractive transfer printing.

Colloids are a mixture of insoluble micro/nanoparticles suspended and dispersed in a medium, which found applications in a wide range of industries such as sensing, optics, composite materials, electronics, and others. To create specific patterns, self-assembly using external energy such as meniscus, electrostatic, magnetic and surface energy modifications or direct writing methods have been explored intensively. In this scenario, subtractive transfer printing, which removes unwanted regions from a sheet of thin coated substrate may suggest another tool to achieve microscopically patterned colloids in a much uncomplicated manner.

Transfer printing of colloidal quantum dot (c-QD) to prepare a display have been proposed owing to color tunability, narrow emission spectra, high quantum yield and photo/air stability, printability, high photoluminescence and thin self-light emitting active layer nature (Keum et al., 2017; Kim, Cho, et al., 2011; Yang et al., 2021). Inspired by intaglio technique, intaglio-based transfer printing using PDMS stamp has successfully demonstrated 2460 p.p.i. red, green, blue pixels over 7 cm × 7 cm area, which greatly improved from their previous work that suffered from nonuniform stress distribution of PDMS stamp due to utilization of unreliable viscoelastic property to control adhesion.

Keum and his colleagues explored the SMP tool to negative transfer print (or microscopically pattern) QD film (Keum et al., 2017). The authors explored three different scenarios of negative transfer printing qualities, where the SMP stamp is

made contact and separated while keeping at below T_g and above T_g , as well as exploiting thermomechanical switching characteristics where stamp and QD film are brought to contact at above T_g , followed with separation after sufficiently cooling the SMP. $200\ \mu\text{m}$ by $200\ \mu\text{m}^2$ QD fine pattern was achievable via thermomechanical technique and the photoluminescence (PL) intensity test shows compatibility with pristine QD.

8.2 Transfer printing involving photoresist thin film

8.2.1 Detachment lithography—photoresist thin film patterning and transfer printing

Access to shorter wavelength optical source together with smaller critical dimension (CD) resists empowered photolithography to grow into a dominant micromanufacturing technique for the past several decades, through which unprecedented computing power in small form factor becomes feasible. The processing power of these microchips have emerged to the level where general consumers are insensitive to mere upgrades in performance, rather they look for diverse form factor for better utilization. In this aspect, photolithography, which solely rely on two-dimensional rigid substrate such as silicon (Si), possesses inherent problems owing to reliance on projection optics and the limited depth of focus.

Microcontact printing (μCP) is a low-cost soft lithography process that allows transferring microscopic patterns onto a curvilinear substrate, which had demonstrated its effectiveness by printing functional ink materials such as alkanethiol SAM on gold surface, organic molecules, and various types of nanomaterials (Jackman et al., 1995; Kumar & Whitesides, 1993; Xia & Whitesides, 1998; Xia et al., 1999). However, relatively thin and agglomerative micro/nanoscale material with low cohesive energy bounds the process transformation to wider employment in diversified industries. Hence forward, a technique termed detachment lithography (DL) based on mCP had developed (Yeom & Shannon, 2010).

Interfacial energy between thin film and mold ($G_{\text{film-mold}}$) and thin film and stamp ($G_{\text{film-stamp}}$) as well as cohesive bonding energy of the photoresist thin film ($G_{\text{film-film}}$) all play role in DL where three possible outcomes (no transfer, (NT), detachment transfer (DT), and blanket transfer (BT)) are suggested by the authors as below.

$$\begin{aligned} F/N &= b \cdot G_{\text{film-mold}}(NT) \\ F/N &= b \cdot G_{\text{stamp-film}} + t \cdot G_{\text{film-film}}(DT) \\ F/N &= (a + b) \cdot G_{\text{stamp-film}}(BT) \end{aligned} \quad (8.6)$$

As Eq. (8.6) suggests, DL, DT, and BT can all be successfully modulated by the careful modulation of the interfacial energy as well as microscopic features such as width b , spacing a , and thickness of the film t (Yeom & Shannon, 2010).

The DL process fully exploits the characteristics of viscoelastic PDMS material, which alters adhesion depending on separation velocity and temperature (Feng et al., 2007; Gent, 1996). Numerous research groups had explored transfer printing using viscoelastic materials (dominantly PDMS due to its chemically inert nature) by modulating adhesion through separation velocity. Yeom demonstrated the DL technique to transfer photoresist thin film by manipulating temperature in conjunction with separation velocity (Yeom & Shannon, 2010). Fig. 8.8 shows the process flow of DL where Si mold is photolithographically patterned to manifest positive mold and a photoresist thin layer is coated on a PDMS stamp (Fig. 8.8A). The two elements in DL are brought to contact and thermally treated to elevate the arranged system temperature to 50°C (Fig. 8.8B). Once the system is sufficiently treated with a raised temperature, the system is brought to a low temperature (4°C) to increase the adhesion of PDMS and photoresist interface and rapidly separated (Fig. 8.8C). Upon separation, regions of the photoresist layer

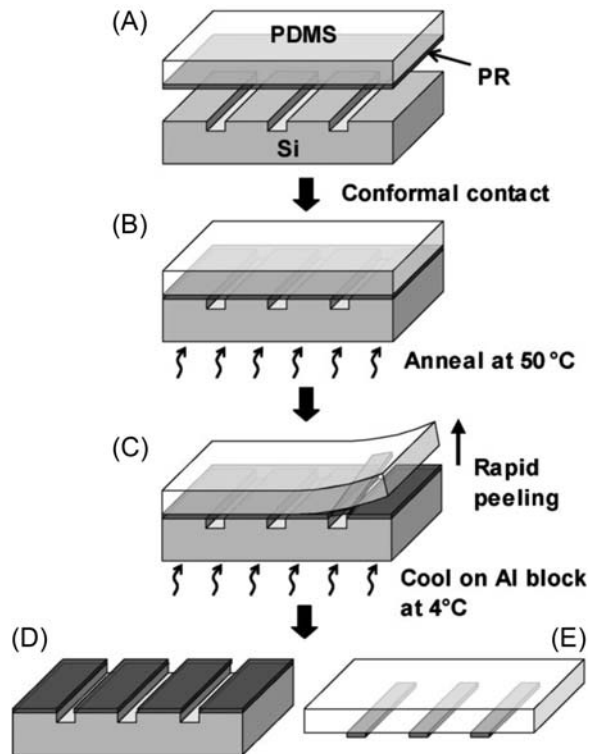


Figure 8.8 Process flow of detachment lithography. (A) Photoresist coated polydimethylsiloxane (PDMS) is brought to contact with prepatterned Si mold. (B) While in contact, PDMS and Si mold temperature is elevated to 50°C. (C) The whole structure is brought to low temperature (4°C) and rapidly separate, (D) and (E) show results of DL where cohesively coated photoresist is transferred onto extruded regions of Si mold and rest remains on PDMS.⁵²

making contact with Si mold remains on the mold while the rest adheres to PDMS with a cohesive fracture at the photoresist interface (Fig. 8.8D and E).

Through DL, the authors demonstrated an array of micropatterned photoresist pattern transfer onto flat and curvilinear surfaces as well as making complex three-dimensional patterns using DL technique. In order to guarantee the successful transfer, modulating G values at different interfaces is prerequisite, which can be adjusted by modulating the thermodynamic work of adhesion values (W_a). In this aspect, effective surface treatments such as 1 H,1 H,2 H,2H-perfluorodecyltrichlorosilane (FDTS) coating on silicon dioxide surface (SiO_2) to reduce $G_{\text{film-mold}}$ or to induce thiol interaction to increase $G_{\text{film-substrate}}$ is recommended.

8.2.2 Quantum dot patterning via photoresist transfer printing

Colloidal quantum dot is advantageous when compared with other Si based micro-electronics manifested by micro/nanomanufacturing processes by virtue of a solution-based process that does not require high-cost vacuum-based industrial equipment. For example, deposition of a thin film onto a substrate requires a high vacuum environment (approximate vacuum pressure of 10^{-7} millitorr, mTorr) achieved by either cryopump or turbopump to guarantee uniformity and quality, while c-QD thin film deposition is often simply formed by mere spin casting onto a substrate.

Adverse to the benefits in the simplicity of the deposition process, patterning of the deposited material, which is imperative to construct any devices, is obscure since the solvents suspend QD are often not compatible with other frequently accessed materials involved in photolithography. Tailoring the QD surface by ionization to display hydrophilic properties implements layer-by-layer deposition that can withstand photolithography process or by incorporating photoactive ionic molecule ligands onto c-QD authorizes direct optical patterning of the c-QD layer (Park et al., 2016; Wang et al., 2017). However, such fine-tuning of the c-QD may inhibit the chemical structures of the QDs, which otherwise can be functionalized varyingly to best suit each individual application.

The cohesive bonding energy of a c-QD film-formed spin casting is at a moderate level that often yields to externally applied mechanical separation energy. Inspired by soft lithography and transfer printing techniques, bountiful manufacturing techniques like intaglio transfer printing, mechanical transfer printing using PDMS (Kim, Cho, et al., 2011; Yang et al., 2021), and subtractive QD film patterning using SMP (Keum et al., 2017) that facilitate micropatterning and integration of QDs using PDMS and SMP had been demonstrated. In addition to PDMS and SMP, photoresist contact patterning technique delivers photoresist on elastomer (referred as PR stamp) as a tool for patterning c-QD layer (Jackman et al., 1999). The patterning resolution of an optically patterned PR stamp is inherently high while giving versatility to different designs since

the pattern on the PR stamp is generated through a conventional optical photolithography process. Additionally, the manuscript discusses transferring patterned photoresist layer onto c-QD film similarly to DL, which is further utilized as a lift-off masking layer for subsequent metal electrical contact deposition.

Fig. 8.9 schematically describes the PR contact patterning process. As with other transfer printing techniques, controlling interfacial surface energy is the fundamental aspect of photoresist contact patterning process. To ensure flawless exfoliation of c-QD layer, octadecyltrichlorosilane (ODTS) SAM is coated onto Si substrate in order to minimize the adhesion between c-QD film and the substrate (Fig. 8.9A). Independently, photolithographically patterned photoresist pattern is prepared on a PDMS stamp to manifest the PR stamp and brought to contact with c-QD coated substrate (Fig. 8.9B). Facilitating velocity dependency of viscoelastic material, high-speed separation of the two constituents (Fig. 8.9C) results in a QD pattern on the substrate (Fig. 8.9D). An embodiment of photoresist in PR contact printing process not only enables microscopic patterning of c-QD film that mirrors photoresist pattern formed via comparatively simple and genuine manner but also the enhanced interfacial adhesion between c-QD film and photoresist guarantees subtractive transfer printing. Through the PR contact patterning process, the authors manifest microscopically patterned QD in a large array arrangement, which could be subsequently transfer printed with a higher yield.

Besides, the DL process is adopted to transfer the thin photoresist pattern from the PR stamp onto c-QD by lowering interfacial adhesion at the interface between the photoresist and the PDMS backing layer for posterior utilization is demonstrated in

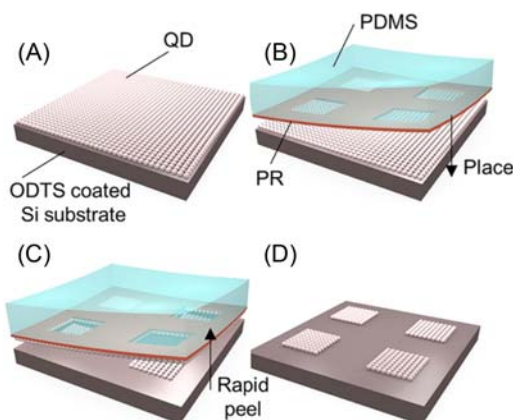


Figure 8.9 Schematic process flow of PR contact patterning of a quantum dot (QD) film. (A) c-QD film coated on ODTS-treated Si substrate. (B) PDMS with a photoresist pattern (PR stamp) is brought to contact with the QD substrate. (C) PR stamp is rapidly separated. (D) QD pattern remains on the substrate.⁵⁷

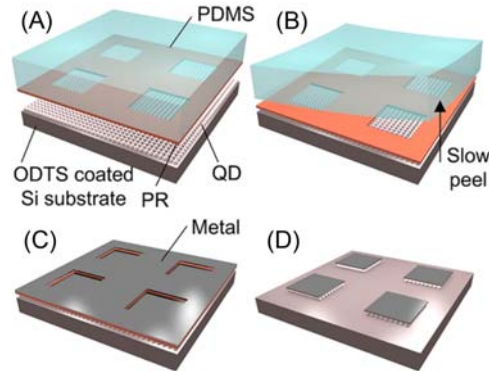


Figure 8.10 Schematic process flow of DL to construct c-QD with metal electrode composite ink. (A) PR stamp is brought to contact with c-QD coated ODTs Si substrate. (B) slow peeling at elevated temperature results in the transferred photoresist film. (C) The subsequent metal electrode is deposited via conventional physical vapor deposition. (D) Removing photoresist masking layer results in c-QD pattern with electrode pattern on the substrate.

the same manuscript as described in Fig. 8.10. At elevated process temperature ($\sim 65^\circ\text{C}$) in conjunction with low separation velocity, work of adhesion at the photoresist—PDMS interface is drastically reduced to yield photoresist layer onto c-QD substrate, which serves as lift off masking layer to establish a composite metal electrode and c-QD functional material. Such DL-incorporated PR contact patterning process minimizes potential problems with liquid-based process compatibility of high solubility c-QD materials.

8.3 Transfer printing of elastic membrane for pattern generation

8.3.1 Transfer of elastomeric membrane for lift-off mask

The lift-off procedure represents an associative measure in which vapor phase deposition of material onto a substrate with patterned photoresist and only the material deposited on the photoresist is lifted off and removed along with the photoresist by an appropriate solvent. While the lift-off procedure prevails in micromanufacturing industries, the nature of the solution process restricts other industries that involve organic entities, c-QDs, etc. where the deposited material is not compatible with the solution. The transfer printing process, which transfers patterns contoured in advance, is an exclusively dry measure that effectively overcome the aforementioned issue. Accordingly, PDMS with its chemically inert ability to make conformal contact with diverse surfaces reversibly possesses favorable material characteristics of PDMS for the purpose of dry lift-off masks to transfer patterns.

Jackman first demonstrated utilization of PDMS elastomeric membrane as a lift-off mask in 1998 (Jackman et al., 1999). Since PDMS is difficult to pattern with reactive

ion etching (RIE) or chemical etching techniques, geometrically arranged discrete patterns of PDMS membrane are first prepared using molding technique. The master mold is made by photolithographically patterning of 5–50 mm thick photoresist on Si substrate. To ensure the PDMS membrane is thinner than the photoresist features, PDMS prepolymer is spin-coated on the master mold followed by curing at elevated temperature. To provide adequate structure rigidity, additional overcoating at the edge of the thin PDMS membrane is administered. The freestanding PDMS membrane is subsequently registered and exploited as a masking layer for wet-chemical etching, dry etching, electrodeposition, sol-gel process, hydrogel surface coating, lift-off mask for metal and organometallic compound evaporation, biological material patterning and chemical vapor deposition of polymer precursors (Jackman et al., 1999). Such proposed methodology is seemingly applicable for discrete patterns (e.g., microwells), but the authors also claim that registration of multiple elastomeric membranes can prior to deposition of the target material also result in continuous and complex geometry.

8.3.2 Transfer of elastomeric membrane to pattern photoluminescent material for display application

Employment of elastic membrane as a dry lift-off mask is further enlarged by successful patterning of a hole transporting layer, *N,N'*-diphenyl-*N,N'*-bis(3-methylphenyl)-1-1'-biphenyl-4,4'-diamine (TPD) and a light emitting layer, tris(8-hydroxyquinoline) aluminum (Alq₃), which are closely associated with display industry (Duffy et al., 1999). The detailed methodology of patterning a TPD or an Alq₃ layer is unambiguous and hence not discussed in detail in this manuscript. However, the authors also additionally demonstrated patterning of red, green and blue (RGB) multicolor patterning on a substrate using two separate elastomeric membranes. The bottom masking membrane is configured with openings at all regions where all RGB photoluminescent (PL) would be positioned while the second elastomeric masking layer exhibits an array of openings where single color PL is deposited. The elastomeric lift-off mask with all the openings is first registered on a substrate tightly sealing the interface between the elastomeric mask and the substrate. The second mask is aligned and positioned on top of the first layer such that single color PL is deposited and the remaining openings on the first mask are covered. Once the composite mask is precisely situated, the first PL is deposited by the physical vapor deposition process. To deposit the second PL material, only the second mask is peeled and shifted to expose the second array openings on the first masking layer and the PL is deposited. The identical second masking layer shift is conducted to generate a third PL array.

The elastomeric membrane pattern transfer technique grants the ability to pattern not only two-dimensional planar surfaces but also curvilinear surfaces owing to the flexible property of elastomer. Additionally, the dry pattern generation process is

comparably inexpensive when compared with the conventional lithography-based patterning process since photoresist patterning and removal measures are not involved. Lastly, while the manuscript describes measures to deposit PL array, materials with different classes can also be patterned so long as the deposition process operates under the thermal degradation temperature of the elastomer.

8.4 Epoxy-based subtractive transfer printing

8.4.1 Pattern generation through epoxy stamp with temperature control

Microcrystalline organic semiconducting materials such as copper phthalocyanine (CuPc), metal-free phthalocyanine (H_2Pc), N,N' -di(naphtalen-1-yl)- N,N' -diphenylbenzidine (NPB) and tris(8-quinolinolato)aluminum (AlQ_3) are often patterned by using rigid shadow mask deposition procedure. When two contacting surfaces are rigid, the microscopic interfacial gap is inevitable, which sets limit of pattern resolution. Elastomeric membrane to transfer pattern is an alternative method to configure small molecule organic semiconducting materials. Another uncomplicated approach is proposed by Wang where a partially cured epoxy stamp is used as a subtractive stamp to remove materials at undesired regions (hot lift-off technique) (Wang et al., 2003).

Process flow of epoxy-based subtractive transfer printing is as follows: A thin film of microcrystalline organic semiconducting material is deposited on a substrate and epoxy stamps with protruded regions are prepared separately. Subsequently, the two are brought together with high preload (10 kg/cm^2) for approximately 30 seconds, and the external pressure is reduced to 2 kg/cm^2 while heating to $80^\circ\text{C} - 120^\circ\text{C}$. The system is brought to room temperature and separated to remove unwanted regions of the microcrystalline film.

The process is only possible by low cohesive energy of microcrystalline material property in conjunction with high work of adhesion of epoxy stamp surface. Additionally, a high level of external pressure is required to make conformal contact between the epoxy stamp and the film. Lastly, the authors also experimentally determined that elevating temperature increases surface energy hence aiding the subtractive transfer printing procedure. It is important to note that depending on the thin film deposition parameters, intergranular properties can be altered and affect the hot lift-off process accordingly.

References

- Al-okaily, A., & Ferreira, P. M. (2015). Multi-physics modeling for laser micro-transfer printing delamination. *Journal of Manufacturing Processes*, 20, 414–424. Available from <https://doi.org/10.1016/j.jmapro.2014.07.006>.
- Behl, M., & Lendlein, A. (2007). Shape-memory polymers. *Materials Today*, 10(4), 20–28. Available from <https://www.sciencedirect.com/science/article/pii/S1369702107700470>.

- Behl, M., Razaq, M. Y., & Lendlein, A. (2010). Multifunctional shape-memory polymers. *Advanced Materials*, 22(31), 3388–3410. Available from <https://doi.org/10.1002/adma.200904447>.
- Carlson, A., Bowen, A. M., Huang, Y., Nuzzo, R. G., & Rogers, J. A. (2012). Transfer printing techniques for materials assembly and micro/nanodevice fabrication. *Advanced Materials*, 24(39), 5284–5318. Available from <https://doi.org/10.1002/adma.201201386>.
- Carlson, A., Wang, S., Elvikis, P., Ferreira, P. M., Huang, Y., & Rogers, J. A. (2012). Active, programmable elastomeric surfaces with tunable adhesion for deterministic assembly by transfer printing. *Advanced Functional Materials*, 22(21), 4476–4484. Available from <https://doi.org/10.1002/adfm.201201023>.
- Chen, S., Hu, J., Yuen, C.-w., & Chan, L. (2009). Novel moisture-sensitive shape memory polyurethanes containing pyridine moieties. *Polymer*, 50(19), 4424–4428. Available from <https://doi.org/10.1016/j.polymer.2009.07.031>.
- Duffy, D. C., Jackman, R. J., Vaeth, K. M., Jensen, K. F., & Whitesides, G. M. (1999). Electroluminescent materials with feature sizes as small as 5 μm using elastomeric membranes as masks for dry lift-off. *Advanced Materials*, 11(7), 546–552. Available from [https://doi.org/10.1002/\(SICI\)1521-4095\(199905\)11:7<546::AID-ADMA546>3.3.CO;2-5](https://doi.org/10.1002/(SICI)1521-4095(199905)11:7<546::AID-ADMA546>3.3.CO;2-5).
- Eisenhaure, J. D., Rhee, S. I., Al-Okaily, A., Carlson, A., Ferreira, P. M., & Kim, S. (2014). The use of shape memory polymers for microassembly by transfer printing. *Journal of Microelectromechanical Systems*, 23(5), 1012–1014. Available from <https://doi.org/10.1109/JMEMS.2014.2345274>.
- Eisenhaure, J. D., Rhee, S. I., Al-Okaily, A., Carlson, A., Ferreira, P. M., & Kim, S. (2015). The use of shape memory polymers for MEMS assembly. *Journal of Microelectromechanical Systems*, 25(1), 69–77. Available from <https://doi.org/10.1109/jmems.2015.2482361>.
- Eisenhaure, J. D., Xie, T., Varghese, S., & Kim, S. (2013). Microstructured shape memory polymer surfaces with reversible dry adhesion. *ACS Applied Materials & Interfaces*, 5(16), 7714–7717. Available from <https://doi.org/10.1021/am402479f>.
- Eisenhaure, J., & Kim, S. (2014). An internally heated shape memory polymer dry adhesive. *Polymers*, 6(8), 2274–2286. Available from <https://doi.org/10.3390/polym6082274>.
- Eisenhaure, J., & Kim, S. (2016). Laser-driven shape memory effect for transfer printing combining parallelism with individual object control. *Advanced Materials Technologies*, 1(7). Available from <https://doi.org/10.1002/admt.201600098>, [http://onlinelibrary.wiley.com/journal/10.1002/\(ISSN\)2365-709X](http://onlinelibrary.wiley.com/journal/10.1002/(ISSN)2365-709X).
- Feng, X., Meitl, M. A., Bowen, A. M., Huang, Y., Nuzzo, R. G., & Rogers, J. A. (2007). Competing fracture in kinetically controlled transfer printing. *Langmuir: the ACS Journal of Surfaces and Colloids*, 23(25), 12555–12560. Available from <https://doi.org/10.1021/la701555n>.
- Gargas, D. J., Muresan, O., Sirbulu, D. J., & Buratto, S. K. (2006). Micropatterned porous-silicon bragg mirrors by dry-removal soft lithography. *Advanced Materials*, 18(23), 3164–3168. Available from <https://doi.org/10.1002/adma.200601354>.
- Gent, A. N. (1996). Adhesion and strength of viscoelastic solids. Is there a relationship between adhesion and bulk properties? *Langmuir: the ACS Journal of Surfaces and Colloids*, 12(19), 4492–4496. Available from <https://doi.org/10.1021/la950887q>.
- Hu, J., Zhu, Y., Huang, H., & Lu, J. (2012). Recent advances in shape-memory polymers: structure, mechanism, functionality, modeling and applications. *Progress in Polymer Science*, 37(12), 1720–1763. Available from <https://doi.org/10.1016/j.progpolymsci.2012.06.001>.
- Jackman, R. J., Duffy, D. C., Cherniavskaya, O., & Whitesides, G. M. (1999). Using elastomeric membranes as dry resists and for dry lift-off. *Langmuir: the ACS Journal of Surfaces and Colloids*, 15(8), 2973–2984. Available from <https://doi.org/10.1021/la981591y>.
- Jackman, R. J., Wilbur, J. L., & Whitesides, G. M. (1995). Fabrication of submicrometer features on curved substrates by microcontact printing. *Science (New York, N.Y.)*, 269(5224), 664–666. Available from <https://doi.org/10.1126/science.7624795>.
- Julich-Gruner, K. K., Löwenberg, C., Neffe, A. T., Behl, M., & Lendlein, A. (2013). Recent trends in the chemistry of shape-memory polymers. *Macromolecular Chemistry and Physics*, 214(5), 527–536. Available from <https://doi.org/10.1002/macp.201200607>.
- Keum, H., Carlson, A., Ning, H., Mihi, A., Eisenhaure, J. D., Braun, P. V., Rogers, J. A., & Kim, S. (2012). Silicon micro-masonry using elastomeric stamps for three-dimensional microfabrication.

- Journal of Micromechanics and Microengineering*, 22(5)055018. Available from <https://doi.org/10.1088/0960-1317/22/5/055018>.
- Keum, H., Jiang, Y., Park, J., Flanagan, J., Shim, M., & Kim, S. (2017). Solvent-free patterning of colloidal quantum dot films utilizing shape memory polymers. *Micromachines.*, 8(1), 18. Available from <https://doi.org/10.3390/mi8010018>.
- Keum, H., Yang, Z., Han, K., Handler, D. E., Nguyen, T. N., Schutt-Aine, J., Bahl, G., & Kim, S. (2016). Microassembly of heterogeneous materials using transfer printing and thermal processing. *Scientific Reports*, 6(1), 1–9. Available from <https://doi.org/10.1038/srep29925>.
- Kim, H.-s, Brueckner, E., Song, J., Li, Y., Kim, S., Lu, C., Sulkin, J., Choquette, K., Huang, Y., Nuzzo, R. G., & Rogers, J. A. (2011). Unusual strategies for using indium gallium nitride grown on silicon (111) for solid-state lighting. *Proceedings of the National Academy of Sciences*, 108(25), 10072–10077. Available from <https://doi.org/10.1073/pnas.1102650108>.
- Kim, S., Carlson, A., Cheng, H., Lee, S., Park, J.-K., Huang, Y., & Rogers, J. A. (2012). Enhanced adhesion with pedestal-shaped elastomeric stamps for transfer printing. *Applied Physics Letters*, 100(17) 171909. Available from <https://doi.org/10.1063/1.4706257>.
- Kim, S., Lakshmanan, S., Li, J., Anthamatten, M., Lambropoulos, J., & Shestopalov, A. A. (2022). Modulation of interfacial adhesion using semicrystalline shape-memory polymers. *Langmuir: the ACS Journal of Surfaces and Colloids*, 38(11), 3607–3616. Available from <https://doi.org/10.1021/acs.langmuir.2c00291>.
- Kim, S., Liu, N., & Shestopalov, A. A. (2022). Contact printing of multilayered thin films with shape memory polymers. *ACS Nano*, 16(4), 6134–6144. Available from <https://doi.org/10.1021/acsnano.1c11607>.
- Kim, S., Wu, J., Carlson, A., Jin, S. H., Kovalsky, A., Glass, P., Liu, Z., Ahmed, N., Elgan, S. L., Chen, W., Ferreira, P. M., Sitti, M., Huang, Y., & Rogers, J. A. (2010). Microstructured elastomeric surfaces with reversible adhesion and examples of their use in deterministic assembly by transfer printing. *Proceedings of the National Academy of Sciences*, 107(40), 17095–17100. Available from <https://doi.org/10.1073/pnas.1005828107>.
- Kim, T.-H., Cho, K.-S., Lee, E. K., Lee, S. J., Chae, J., Kim, J. W., Kim, D. H., Kwon, J.-Y., Amaratunga, G., Lee, S. Y., Choi, B. L., Kuk, Y., Kim, J. M., & Kim, K. (2011). Full-colour quantum dot displays fabricated by transfer printing. *Nature Photonics*, 5(3), 176–182. Available from <https://doi.org/10.1038/nphoton.2011.12>.
- Kumar, A., & Whitesides, G. M. (1993). Features of gold having micrometer to centimeter dimensions can be formed through a combination of stamping with an elastomeric stamp and an alkanethiol “ink” followed by chemical etching. *Applied Physics Letters*, 63(14), 2002–2004. Available from <https://doi.org/10.1063/1.110628>.
- Li, Y. Y., Kim, P., & Sailor, M. J. (2005). Painting a rainbow on silicon - A simple method to generate a porous silicon band filter gradient. *Physica Status Solidi (a)*, 202(8), 1616–1618. Available from <https://doi.org/10.1002/pssa.200461200>.
- Luo, H., Wang, C., Linghu, C., Yu, K., Wang, C., & Song, J. (2020). Laser-driven programmable non-contact transfer printing of objects onto arbitrary receivers via an active elastomeric microstructured stamp. *National Science Review*, 7(2), 296–304. Available from <https://doi.org/10.1093/nsr/nwz109>.
- Meng, H., Zheng, J., Wen, X. F., Cai, Z. Q., Zhang, J. W., & Chen, T. (2015). PH- and sugar-induced shape memory hydrogel based on reversible phenylboronic acid-diol ester bonds. *Macromolecular Rapid Communications*, 36(6), 533–537. Available from <https://doi.org/10.1002/marc.201400648>, <http://www3.interscience.wiley.com/journal/117932056/grouphome>.
- Mengüç, Y., Yang, S. Y., Kim, S., Rogers, J. A., & Sitti, M. (2012). Gecko-inspired controllable adhesive structures applied to micromanipulation. *Advanced Functional Materials*, 22(6), 1246–1254. Available from <https://doi.org/10.1002/adfm.201101783>.
- Nakamatsu, K.-i, Tone, K., Namatsu, H., & Matsui, S. (2006). Room-temperature nanocontact printing using soft template. *Journal of Vacuum Science & Technology B: Microelectronics and Nanometer Structures Processing, Measurement, and Phenomena*, 24(1), 195–199. Available from <https://doi.org/10.1116/1.2151913>.

- Oh, D.-W., Kim, S., Rogers, J. A., Cahill, D. G., & Sinha, S. (2011). Interfacial thermal conductance of transfer-printed metal films. *Advanced Materials*, 23(43), 5028–5033. Available from <https://doi.org/10.1002/adma.201102994>.
- Park, J.-S., Kyhm, J., Kim, H. H., Jeong, S., Kang, J., Lee, S.-e, Lee, K.-T., Park, K., Barange, N., Han, J., Song, J. D., Choi, W. K., & Han, I. K. (2016). Alternative patterning process for realization of large-area, full-color, active quantum dot display. *Nano Letters*, 16(11), 6946–6953. Available from <https://doi.org/10.1021/acs.nanolett.6b03007>.
- Quadrini, F., Iorio, L., Bellisario, D., & Santo, L. (2021). Shape memory polymer composite unit with embedded heater. *Smart Materials and Structures*, 30(7)075009. Available from <https://doi.org/10.1088/1361-665x/ac00cb>.
- Saeidpourazar, R., Li, R., Li, Y., Sangid, M. D., Lu, C., Huang, Y., Rogers, J. A., & Ferreira, P. M. (2012). Laser-driven micro transfer placement of prefabricated microstructures. *Journal of Microelectromechanical Systems*, 21(5), 1049–1058. Available from <https://doi.org/10.1109/JMEMS.2012.2203097>.
- Saeidpourazar, R., Sangid, M. D., Rogers, J. A., & Ferreira, P. M. (2012). A prototype printer for laser driven micro-transfer printing. *Journal of Manufacturing Processes*, 14(4), 416–424. Available from <https://doi.org/10.1016/j.jmapro.2012.09.014>, 15266125 United States.
- Shahi, K., Boomurugan, R., & Velmurugan, R. (2021). Cold programming of epoxy-based shape memory polymer. *Structures*, 29, 2082–2093. Available from <https://doi.org/10.1016/j.istruc.2020.05.023>, Elsevier.
- Sirbulu, D. J., Lowman, G. M., Scott, B., Stucky, G. D., & Buratto, S. K. (2003). Patterned microstructures of porous silicon by dry-removal soft lithography. *Advanced Materials*, 15(2), 149–152. Available from <https://doi.org/10.1002/adma.200390031>.
- Suh, D., Choi, S.-J., & Lee, H. H. (2005). Rigidflex lithography for nanostructure transfer. *Advanced Materials*, 17(12), 1554–1560. Available from <https://doi.org/10.1002/adma.200402010>.
- Testa, P., Style, R. W., Cui, J., Donnelly, C., Borisova, E., Derlet, P. M., Dufresne, E. R., & Heyderman, L. J. (2019). Magnetically addressable shape-memory and stiffening in a composite elastomer. *Advanced Materials*, 31(29)1900561. Available from <https://doi.org/10.1002/adma.201900561>, [http://onlinelibrary.wiley.com/journal/10.1002/\(ISSN\)1521-4095](http://onlinelibrary.wiley.com/journal/10.1002/(ISSN)1521-4095).
- Toshikj, N., Robin, J.-J., Ramonda, M., Catrouillet, S., & Blanquer, S. (2021). Photo-cross-linked poly(trimethylene carbonate)/poly(ϵ -caprolactone) triblock copolymers with controlled architectures: From phase-separated structures to shape-memory materials. *ACS Applied Polymer Materials*, 3(10), 4966–4976. Available from <https://doi.org/10.1021/acsapm.1c00721>.
- Wang, Y., Fedin, I., Zhang, H., & Talapin, D. V. (2017). Direct optical lithography of functional inorganic nanomaterials. *Science (New York, N.Y.)*, 357(6349), 385–388. Available from <https://doi.org/10.1126/science.aan2958>.
- Wang, Z., Zhang, J., Xing, R., Yuan, J., Yan, D., & Han, Y. (2003). Micropatterning of organic semiconductor microcrystalline materials and ofet fabrication by hot lift off. *Journal of the American Chemical Society*, 125(50), 15278–15279. Available from <https://doi.org/10.1021/ja036581k>.
- Xia, Y., Rogers, J. A., Paul, K. E., & Whitesides, G. M. (1999). Unconventional methods for fabricating and patterning nanostructures. *Chemical Reviews*, 99(7), 1823–1848. Available from <https://doi.org/10.1021/cr980002q>.
- Xia, Y., & Whitesides, G. M. (1998). Soft lithography. *Angewandte Chemie International Edition*, 37(5), 550–575. Available from [https://doi.org/10.1002/\(SICI\)1521-3773\(19980316\)37:5<550::AID-ANIE550>3.3.CO;2-7](https://doi.org/10.1002/(SICI)1521-3773(19980316)37:5<550::AID-ANIE550>3.3.CO;2-7).
- Yang, J., Choi, M. K., Yang, U. J., Kim, S. Y., Kim, Y. S., Kim, J. H., Kim, D.-H., & Hyeon, T. (2021). Toward full-color electroluminescent quantum dot displays. *Nano Letters*, 21(1), 26–33. Available from <https://doi.org/10.1021/acs.nanolett.0c03939>.
- Yang, S. Y., Carlson, A., Cheng, H., Yu, Q., Ahmed, N., Wu, J., Kim, S., Sitti, M., Ferreira, P. M., Huang, Y., & Rogers, J. A. (2012). Elastomer surfaces with directionally dependent adhesion strength and their use in transfer printing with continuous roll-to-roll applications. *Advanced Materials*, 24(16), 2117–2122. Available from <https://doi.org/10.1002/adma.201104975>.
- Yeom, J., & Shannon, M. A. (2010). Detachment lithography of photosensitive polymers: A route to fabricating three-dimensional structures. *Advanced Functional Materials*, 20(2), 289–295. Available from <https://doi.org/10.1002/adfm.200900686>.

- Yu, Q., Chen, F., Zhou, H., Yu, X., Cheng, H., & Wu, H. (2018). Design and analysis of magnetic-assisted transfer printing. *Journal of Applied Mechanics*, *85*(10)101009. Available from <https://doi.org/10.1115/1.4040599>.
- Zhang, Q., Wei, H., Liu, Y., Leng, J., & Du, S. (2016). Triple-shape memory effects of bismaleimide based thermosetting polymer networks prepared via heterogeneous crosslinking structures. *RSC Advances*, *6*(13), 10233–10241. Available from <https://doi.org/10.1039/C5RA24247A>.

PART II

State-of-the-art applications enabled by transfer printing

This page intentionally left blank

CHAPTER 9

Microtransfer printing techniques for optical applications

Bongjoong Kim¹, Woohyun Park², Jehwan Hwang³ and Chi Hwan Lee⁴

¹Department of Mechanical and System Design Engineering, Hongik University, Seoul, South Korea

²School of Mechanical Engineering, Purdue University, West Lafayette, IN, United States

³Weldon School of Biomedical Engineering, Purdue University, West Lafayette, IN, United States

⁴Biomedical Engineering, Mechanical Engineering and Materials Engineering, Purdue University, West Lafayette, IN, United States

9.1 Introduction

Transfer printing techniques are widely used for assembling materials and manufacturing devices, allowing for scalable and cost-effective production in many applications. These techniques involve repeatedly transferring functional “inks” or complete devices from donor to receiver substrates. The functional inks consist of a wide range of material classes, geometries and configurations, which can be integrated into precise architectures for various devices. The materials vary from high-performance hard materials [e.g., semiconductors (Baca et al., 2008; Lee et al., 2005; Menard et al., 2004; Park et al., 2021), metals (Wang et al., 2018; Zhao et al., 2022; Zheng et al., 2019), and oxide thin films (Kim et al., 2008; Liu, Peng, et al., 2022)] to complex molecular scale materials [e.g., monolayers (Rogers & Nuzzo, 2005), nanotubes (Cao & Rogers, 2009; Liang et al., 2019), and graphene (Sollami Delekta et al., 2019; Suk et al., 2016)]. They can be fully integrated into device-grade structures such as thin film transistors (Chen et al., 2020; Sharma et al., 2013; Tong et al., 2018), light-emitting diodes (LEDs) (Bower et al., 2017; Choi et al., 2015; Li et al., 2021; Park et al., 2021), semiconductor circuits (Webb et al., 2013; Yoon et al., 2010), sensing arrays (Shi et al., 2016; Webb et al., 2013; Yamashita et al., 2015), and solar cells (Kang et al., 2010; Koo et al., 2012; Lee et al., 2012).

Among those, the transfer printing of metamaterials has attracted significant attention in optical applications due to its potential to alter the properties of electromagnetic waves in various ways. These metamaterials have been used to demonstrate unusual optical features such as phase discontinuity control, invisible cloaking, and superlens that are not seen in nature (Cheben et al., 2018; Naldoni et al., 2017; Stockman et al., 2018; Yang et al., 2012). This research has also led to the development of usual optical devices in both industrial and military sectors, such as light-driven sensors and actuators like lasers, imagers, antennas, and biosensors (Franklin et al., 2017; Huang et al., 2016; Ni et al., 2015; Safaie et al., 2018; Stewart et al., 2006; Vázquez-Guardado et al., 2016; Zhang et al., 2014).

Integrating metamaterials and their devices into two-dimensional (2D) or three-dimensional (3D) configurations is typically achieved through the use of monolithic fabrication methods, which involve a combination of techniques such as photolithographic patterning, physical and chemical deposition, and wet or dry etching. However, integrating metamaterials into devices can be challenging due to limitations such as the risk of thermal or chemical damage to substrates, complex and time-consuming fabrication procedures, and poor quality and scope of 3D devices. Transfer printing techniques have been explored as a solution to overcome these limitations by efficiently and robustly incorporating metamaterials into 2D or 3D configurations on various substrates or materials (Chanda et al., 2011; Dong et al., 2016; Kim Jeon et al., 2019; Kim et al., 2021; Wang et al., 2018; Yoo et al., 2015; Zheng et al., 2019).

Optoelectronic devices are electronic transmitters that convert electrical signals into optical signals or vice versa, using the principles of both optics and electronics to generate, detect, and control light. These devices include light-emitting devices (e.g., LED and laser diodes) (Li et al., 2018; Liu et al., 2018; Olle & Viršile, 2013), photoelectric devices (e.g., photodiodes, phototransistors, and photomultipliers) (Ouyang et al., 2019; Saliba et al., 2016; Teng et al., 2018; Zhang et al., 2016), as well as photoconductive devices (e.g., photoresistors, photoconductive camera tubes) (Liu, Liang, et al., 2016; Witkowski et al., 2017) which have been widely used for a variety of applications such as optical fiber communications (Kikuchi, 2016; Willner et al., 2015), precision measurement tools (Berger & Wendel, 2018; Leopardi et al., 2017; Lyons et al., 2016), healthcare (Pogue, 2019; Zhang, Yang, et al., 2015), and power sources (Cao et al., 2015; Im et al., 2015; Lan et al., 2016; Liu, Chen, et al., 2016). Despite their high performance, traditional optoelectronic devices made of inorganic materials with active layer structures have limitations, such as the need to be grown on rigid, bulky, and heat-resistant intrinsic wafers. Recent advancements in transfer printing techniques have made it possible to create flexible and stretchable optoelectronic devices. These techniques have enabled the integration of optoelectronic components and devices onto a wide range of substrates, including glass, plastic, and even soft materials such as rubber and silicone, without compromising device performance. Examples of transfer-printed optoelectronics include functional arrays of red (AlInGaP) and blue (InGaN) LEDs, visible and near-infrared (IR) photodetectors, and high-performance solar cells on flexible and stretchable substrates (Hornig et al., 2018, 2019).

In this review, we focus on recent advancements in transfer printing techniques and their applications in metamaterial assembly and integration into optoelectronic devices. We specifically examine the mechanisms behind these techniques and how they work to achieve integration. This review provides examples of the optical applications of transfer printing techniques, as well as an overview of the structures, functions, and principles involved. We also delve into the fundamental components and device designs utilizing metamaterials and examine the optical effects resulting from their use. Fig. 9.1 illustrates various material

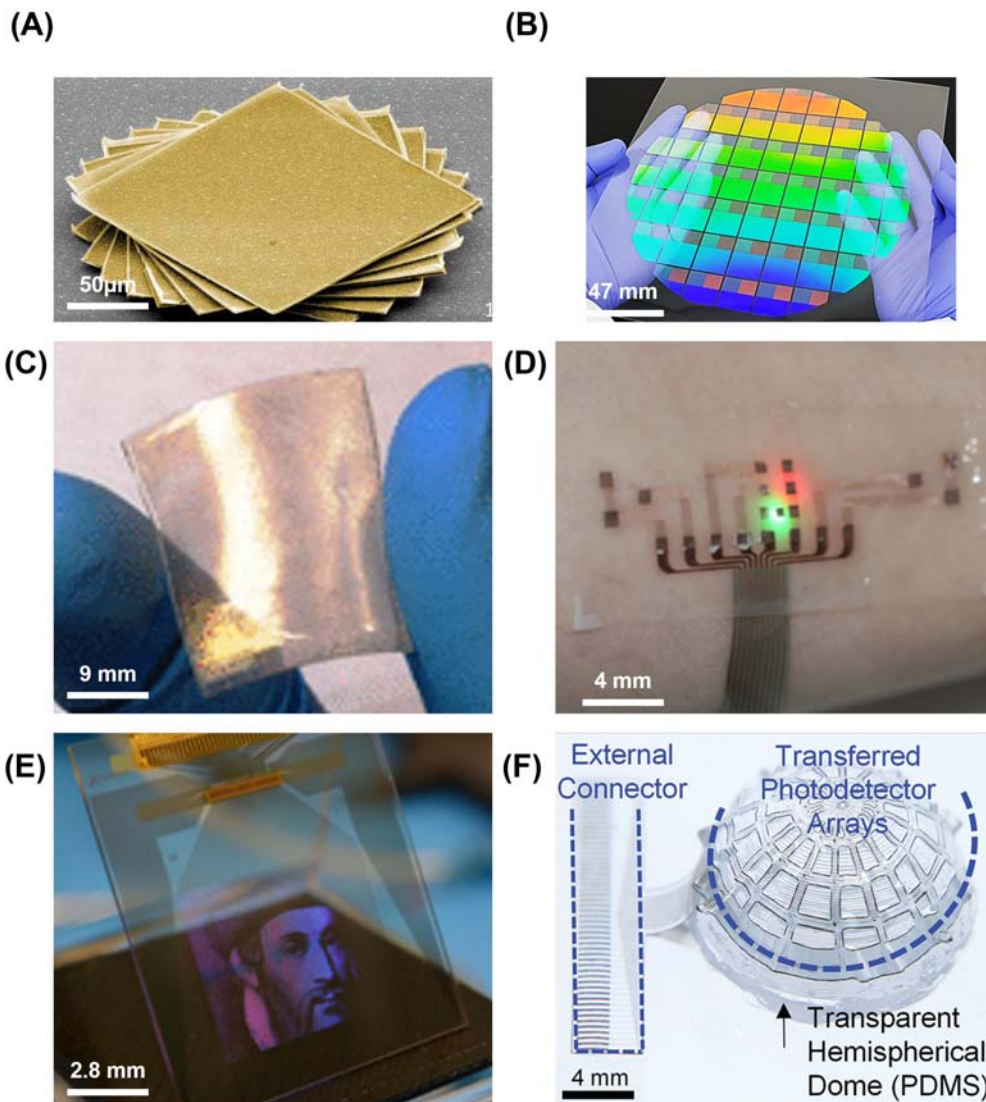


Figure 9.1 *Representative illustrations of novel structures, gadgets, and integrated systems made possible by transfer printing techniques.* (A) a colored scanning electron microscope image of assembled Au (yellow color)/Si platelets with rotations, (B) a large area of a transferred pattern comprised of alternating layers of Au and PMMA in a nanoscale pattern printed on a transparent and flexible PET substrate, (C) a 1 in. \times 1 in. flexible PDMS film fully covered with Au pyramids, (D) a skin-like optoelectronics for blood pressure monitoring conformally laminated onto the skin's surface with light-emitting diodes (LEDs) and photodetectors fabricated by transfer printing, (E) a blue 10 mm \times 10 mm \times 10 mm, 254 PPI, passive-matrix display, and (F) the device placed on a transparent hemispherical dome (PDMS) with a base diameter of 15 mm.

constructions and devices created using transfer printing techniques. These examples showcase how metamaterials and geometries discussed in this chapter can be integrated in a functional manner. Additionally, these methods open up possibilities for advanced fabrication technologies, multidimensional assembly of nanostructured metamaterials, and the production of optical devices with lightweight, flexible, and curved forms.

9.2 Transfer printing techniques

Transfer printing techniques are a versatile manufacturing method for creating flexible and stretchable electronic materials and devices. These techniques enable the assembly of micro- and nanomaterials into 2D and 3D structures in a precise, spatially controlled manner. This section covers various examples of transfer printing techniques that utilize mechanical, chemical, thermo-mechanical, and chemo-mechanical mechanisms. These methods are powerful due to their compatibility with high-performance semiconductor materials such as Si, GaN, and GaAs in micro- or nanostructured forms (Baca et al., 2008; Meitl et al., 2006; Menard et al., 2004; Sun & Rogers, 2007; Sun et al., 2005). These materials can be assembled onto a wide range of receiver substrates at room temperature with high precision, yield, and speed. Repeatedly carrying out this procedure results in a high-resolution, large-area assembly with the ability to create 2D or 3D layouts and integrate them into heterogeneous systems.

9.2.1 Mechanical transfer printing

9.2.1.1 *Pick and place*

One of the commonly used transfer printing techniques involves picking up functional materials, such as micro-/nanomembranes, ribbons, nanowires, and nanotubes, from their original substrates (e.g., wafers) using an elastomeric stamp and transferring them onto a desired receiver substrate (Fig. 9.2) (Feng et al., 2007; Tong et al., 2018; Yi et al., 2018). This pick-and-place step allows for the stacking of multiple layers, enabling the heterogeneous assembly of functional devices over large areas (Liu et al., 2012; Thanh et al., 2012; Winters et al., 2012). The use of an elastomeric stamp in transfer printing techniques allows for precise control over the adhesion between the stamp and the devices or components at the two interfaces (elastomeric stamp/film and film/substrates) (Yi et al., 2018). The viscoelastic property of the stamp enables the peeling speed to dominate the adhesion strength, which is sufficient to maintain van der Waals forces between the stamp and the devices (Feng et al., 2007, 2013; Meitl et al., 2006). This results in a constant critical energy release rate at the device/substrate interface during the pickup step and a rate-sensitive critical energy release rate at the stamp/device interface, which leads to an increased pull-off force with a higher peeling rate. This approach has been applied to various materials in various configurations including 0D dots (Hoshino et al., 2008; Kim et al., 2011), 1D wires

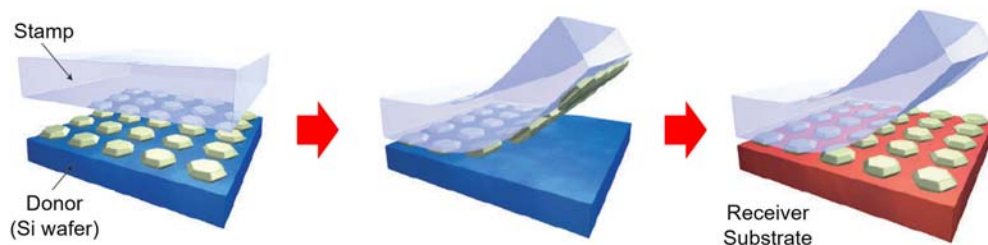


Figure 9.2 Schematic illustrations showing the process of pick-and-place transfer printing technique. A donor substrate containing prefabricated micro or nanostructures is brought into contact with a stamp. When the stamp is removed, the chosen structures from the donor substrate are transferred. The printing process is complete when the structures are printed onto the receiving substrate.

and ribbons (Lee et al., 2010; Nam et al., 2009; Rizzo et al., 2008), 2D membranes (Baca et al., 2010; Park et al., 2009; Yang et al., 2011), and 3D architectures (Lee et al., 2016; Xu et al., 2015; Yan, Zhang, Liu, et al., 2016; Yan, Zhang, Wang, et al., 2016; Zhang, Yan, et al., 2015).

The strength of the interface between the functional devices or components and the elastomeric stamp during transfer printing is primarily determined by the van der Waals interactions, which are directly influenced by the contact area between them (Hsia et al., 2005; Huang et al., 2005). A bio-inspired transfer printing method has been developed to improve control over interfacial adhesion strength (Kim et al., 2010). This method utilizes an elastomeric stamp with pyramidal micro-points that simulate reversible dry adhesion. The stamp's microtips collapse under applied pressure, increasing the contact area and adhesion at the stamp/device interface during the pickup step. However, when pressure is released, the microtips recover, reducing the contact area and adhesion strength at the stamp/device interface.

Choi et al. reported an intaglio transfer printing method for integrating high-definition full-color red, green, and blue (RGB) quantum dot light emitting diode (QLED) arrays, regardless of pixel size, shape, and layout (Choi et al., 2015). The process begins by picking up the quantum dot (QD) layer on the mother substrate with a flat polydimethylsiloxane (PDMS) stamp. The stamp is then lightly contacted onto an intaglio trench under a pressure of less than $50 \text{ g}\cdot\text{cm}^{-2}$. The stamp is then slowly detached at a rate of less than 1 mm/s , leaving only the non-contacted part on the stamp. The QD layer is then transferred to the target substrate. This process can be repeated multiple times to precisely integrate additional quantum dot layers without altering their shape, resulting in high-resolution aligned RGB pixels of various sizes. A similar approach has been also applied to create heterostructure devices using multiple stacked 2D materials, such as graphene, MoS_2 , and graphene. An example includes

successively transferring single-layer graphene films, a 6 nm thick MoS₂ flake, and a second single-layer graphene film from their donor substrates onto prepatterned electrodes to create active areas. However, this method can be challenging, particularly when high printing strength is needed to correct substrate and stamp misalignments. This can lead to a risk of stamp collapse and potential damage to the donor and receiver substrates.

9.2.1.2 Crack-driven transfer printing

Fig. 9.3A illustrates examples of transfer printing methods that utilize controlled cracking to physically separate 3D materials and devices from their fabrication substrate (Kim et al., 2020). For instance, arrays of Si nanowires (2 μm height and 60–110 nm diameters) were fabricated using a traditional Si nanofabrication technique. The thermal oxidation process and wet etching treatments using hydrofluoric acid were then employed to control the diameter of the Si nanowires. After that, the Si nanowires were coated with PDMS (5:1 ratio of base elastomer and cross-linking agent) and thermally annealed at 230°C for 2 hours. The Si nanowires embedded within PDMS

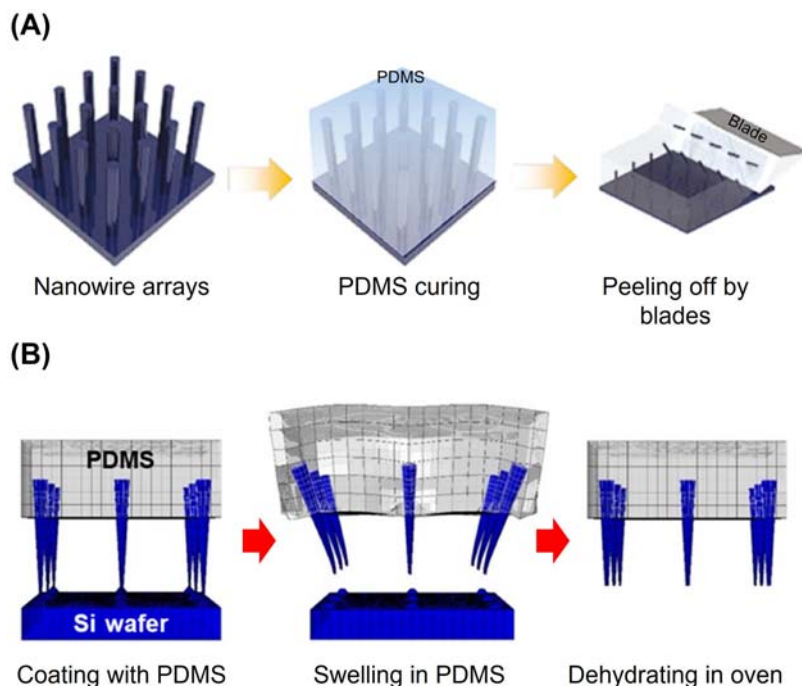


Figure 9.3 Schematic illustrations of crack-driven transfer printing technique. (A) Transfer using a blade to generate cracks in undercut areas of silicon nanowires, causing fracture of the nanowire array. (B) Transfer using the swelling phenomenon of PDMS in a solvent solution, resulting in volumetric changes and mechanical deformations such as bending and twisting through the substrate.

were then physically separated from the fabrication wafer using a blade to complete the process. Alternatively, the PDMS could be swollen to $>230\%$ of its volume by immersing it in a solvent such as hexane. This led to the concentration of mechanical stress at the bottom root of each Si nanowire beyond its fracture limit (Fig. 9.3B) (Kim et al., 2018). As a result, the Si nanowires were physically separated from the fabrication wafer with uniform height. The vertically arranged Si nanowires that are partly embedded in an elastomeric substrate (i.e., PDMS) offer both mechanical flexibility and optical transparency simultaneously.

9.2.2 Chemical transfer printing (self-delamination-based transfer)

Fig. 9.4 shows the process of transferring a thin silicon membrane from a substrate using controllable self-delamination. This method, called chemical transfer printing, begins with conventional micro/nanolithography on a silicon-on-insulator (SOI) donor wafer using etchant-compatible materials (Park et al., 2021). The device layer is then attached to the donor wafer after the silicon dioxide layer is removed using hydrofluoric acid. To separate the device layer from the substrate, the entire structure is immersed in a bath of acetone, which triggers the controlled self-delamination of the device layer. This is achieved by manipulating the interfacial forces, resulting in a deterministic and controlled separation of the silicon devices. Considering a quasistatic delamination process, the energy balance (ΔW^F) between the work done by peeling force can be expressed as follows:

$$\Delta W^F = \Delta E_{\text{surface}} = F\Delta l \quad (9.1)$$

where F is the steady-state peeling force of thin film of width b at a 90 degrees peeling angle with a small peeling distance Δl in a liquid environment model; $\Delta E_{\text{surface}} (= (G_{ts} - \gamma_1(\cos\theta_{tl} + \cos\theta_{sl})\Delta l(1 - \rho)b))$ is the change of associated surface energy, where γ_1 is liquid surface tension, ρ is the porosity of the film, and θ_{tl}, θ_{sl} are the contact angle of the liquid on the thin film and the substrate, respectively

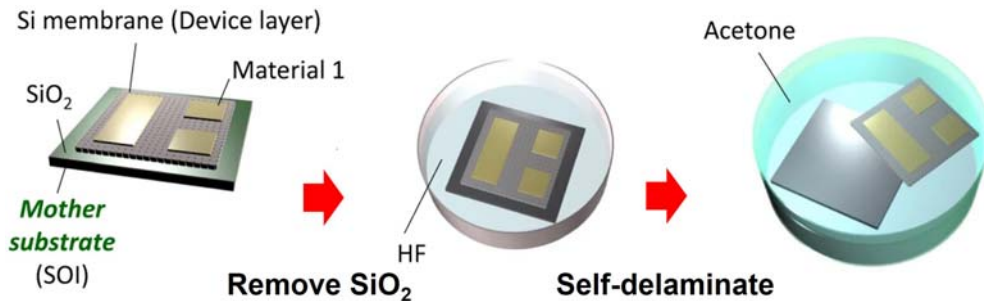


Figure 9.4 Controllable self-delamination-based pattern transfer. The outcome depends on precise control of the interfacial force between contacting surfaces in liquid settings.

(Zhang et al., 2017, 2020). Also, $G_{ts} (= \gamma_t + \gamma_s - \gamma_{ts})$ is the interfacial adhesion energy between the thin film and substrate in a dry air condition, where γ_t and γ_s are the surface tension of the thin component and the substrate, and γ_{ts} is the interfacial tension between the thin component and the substrate, respectively. The success of this technique is dependent on factors such as the required peeling force per unit width, the wettability of the film, the interfacial adhesion energy, and the porosity of the film. This technique allows for the integration of thin membranes on intermediary substrates and the ability to assemble them into functional systems with specific designs. However, it is important to note that the device layer must have a certain level of chemical resistance to withstand postfabrication conditions.

9.2.2.1 Thermo-mechanical transfer printing

Fig. 9.5A shows the process of transferring 3D zinc oxide (ZnO) nanorods from a donor substrate (GaN/Sapphire) to a receiver substrate (polycarbonate) for use in a flexible color filter (Liu, Peng, et al., 2022). This process begins with the synthesis of ZnO nanorods on an e-beam resist pattern, followed by the application of a polymer

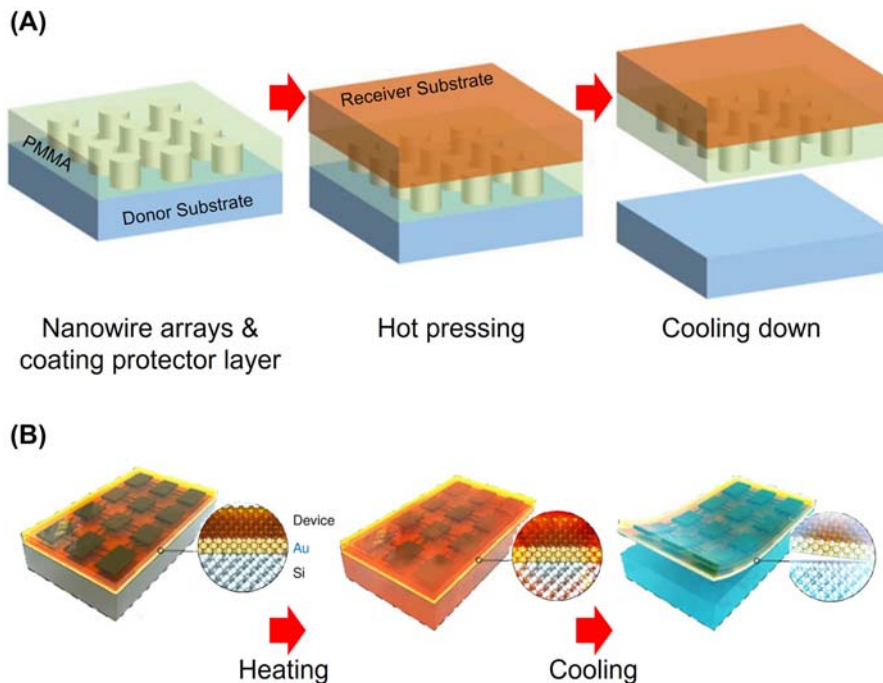


Figure 9.5 Schematic illustrations of thermo-mechanical transfer printing technique. (A) Transfer through thermal pressing that adheres to receiver substrate. (B) Transfer through thermal expansion mismatch between adjacent materials. Heating and cooling cycles create repeated thermal stresses at the interface, leading to an increased likelihood of delamination.

resist (PMMA, $\sim 1 \mu\text{m}$ thick) to protect the grown nanorods. The nanorods are then bonded to a flexible polycarbonate substrate (0.175 mm thick) through thermal pressing at 180°C with a pressure of 400 MPa for 15 minutes, ensuring a strong bond and eliminating any air gaps between the substrates. Finally, the PMMA layer is removed using an inductively coupled plasma etching process utilizing O_2 gas at a flow rate of 30 sccm under RF plasma power and bias RF power of 100 and 20 W, respectively. Advantages of this technique include the ability to reuse the template substrate, control the morphologies of the ZnO nanorods, increase surface roughness, homogenize the height of the ZnO nanorods, and achieve a high level of precision and productivity. The resulting ZnO nanorods on the flexible substrate can be used as effective color filters with a vibrant color pattern.

Fig. 9.5B illustrates a thermo-mechanical transfer printing technique that utilizes the thermal expansion mismatch between materials (Heo et al., 2021). The process begins by applying a thin metal layer with a thermal expansion coefficient (CTE) higher than the substrate, such as a Si wafer or glass. Conventional surface machining is then used to define the microstructures of the device layer (left image). By applying heat at 100°C – 300°C for 3 seconds, followed by rapid cooling of the device, thermal stress is generated at the junction of the device layer and the underlying substrate. This stress results in the propagation of interfacial cracks, enabling physical delamination. This method is performed in dry conditions without the use of wet chemicals, making it a versatile, high-throughput, and efficient transfer printing technique.

9.2.2.2 Chemo-mechanical transfer printing

Alternative transfer printing techniques have been developed for transferring components or devices from a donor substrate without sacrificing the donor wafer. These methods, known as chemo-mechanical transfer printing techniques, physically separate the components or devices through chemical and mechanical reactions at the interface, providing precise control over the interfacial adhesion for defect-free delamination (Kim Jeon et al., 2019; Kim et al., 2021; Lee et al., 2012, 2013, 2014; Lee et al., 2020; Wie et al., 2018). This allows for the recycling of the donor substrate, unlike other transfer printing techniques that rely on chemical etching or mechanical fracture. Wie et al. demonstrated the use of this technique for the transfer printing of 4-inch wafer-scale thin-film devices (Wie et al., 2018). The process involves depositing layers of Ni (300 nm thick) and polyimide (300 nm thick) on a donor substrate, patterning the layers using photolithography, and attaching a thermally releasable tape for temporary handling. The tape is then gently peeled in a bath of water, causing the bottom Ni film to delaminate from the donor substrate (i.e., Si wafer). The delaminated devices are then trimmed and placed on receiver substrates, endowing the surfaces with electronic functionalities. Fig. 9.6A shows

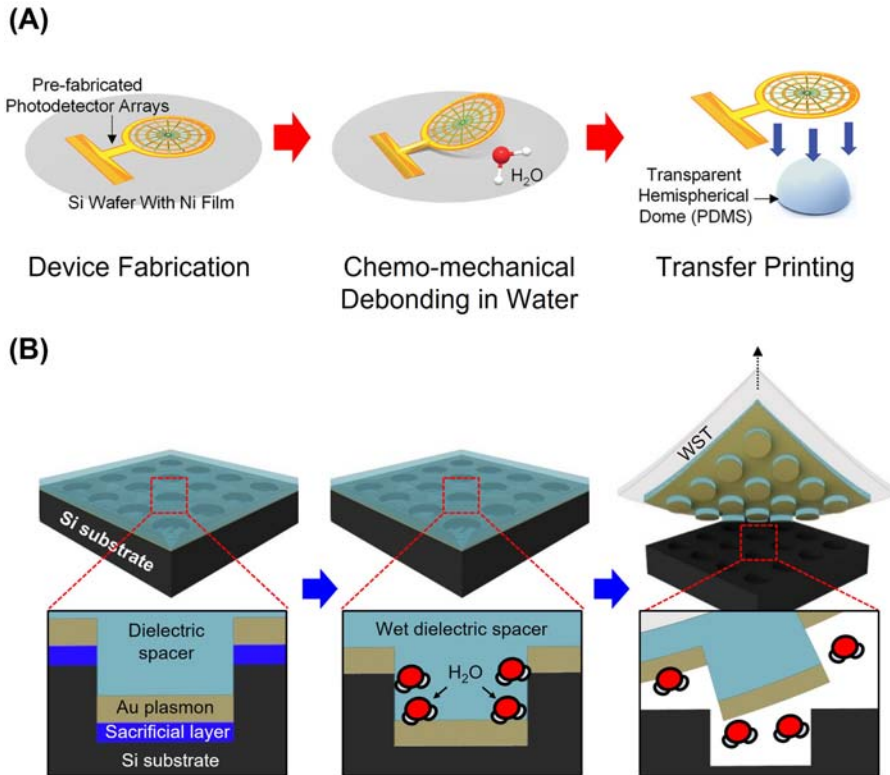
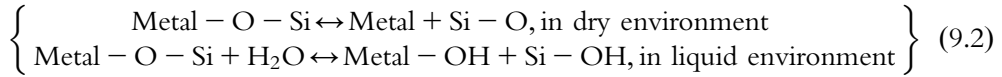


Figure 9.6 Schematic illustrations of chemo-mechanical transfer printing technique. (A) Transfer of hemispherical photodetector arrays. The photodetector array was manufactured using a sequential deposition and patterning procedure. The device architecture was then transferred to a clear hemispherical dome made of PDMS by first detaching it from the Si wafer with a thermal release tape, followed by immersing it in DI water at room temperature, and then applying heat to remove the thermal release tape. (B) Transfer of 3D plasmonic nanoarrays by the identical mechanism described in Fig. 9.6A.

another example of this technique to assemble a hemispherical photodetector array (Lee et al., 2020). The array is first fabricated on top of a polyimide layer on a Si wafer. The entire structure is then submerged in distilled water and separated from the Si wafer using a thermal release tape. This separation is caused by electrostatic interactions with water molecules at the debonding interface and the deformation of adhering thin films. Finally, heat is applied at 80°C for 3 minutes to remove the thermal release tape, leaving the device architecture in a hemispherical dome. This technique has been also applied to transfer quasi-3D metaarrays from their fabrication Si wafer to receiver substrates of interest (Fig. 9.6B) (Kim et al., 2019). This approach is impactful as it can produce heterogeneous quasi-3D metaarrays without

chemical, thermal, or mechanical treatments, which typically have been required for the conventional manufacturing of these arrays.

The fundamental mechanism of defect-free interfacial debonding is based on a chemical reaction of water molecules at the debonding tip. When the metal/SiO₂ interfacial delamination occurs, the related bonding fracture process becomes



where the metal is the Ni. As a result, interfacial adhesion energy G was obtained (0.74 J/m² in dry condition and 0.22 J/m² in liquid water condition). It proves that the applied peeling load and chemical reaction dominantly affect the interfacial fracture, which initiates and propagates during the peeling process.

9.3 Optical applications

9.3.1 Optical filters

Plasmonic metamaterials at the nanoscale exhibit unique electrical and optical properties when interacting with light, leading to the emergence of a field called plasmonics. The strong confinement of electromagnetic fields at subwavelength scales in these materials offers numerous opportunities for controlling and enhancing light-matter interactions (Barnes et al., 2003; Gramotnev & Bozhevolnyi, 2010; Gu et al., 2023; Koenderink et al., 2015; Meng et al., 2021). Advances in physics and nanofabrication technology have driven research on plasmonic metamaterials in recent years. The development of nanofabrication and characterization techniques has also provided opportunities to design efficient nanostructured plasmonic metamaterials capable of controlling light. These materials can have tunable physical and chemical properties, such as optical, mechanical, electrical and magnetic, by adjusting factors like chemical composition, atomic arrangement, and size. When light comes into contact with the free electrons at nanostructured surfaces, it excites the oscillation of these electrons in the form of surface plasmon (SP) waves. During the coupling of surface plasmon polaritons (SPPs), the nanostructured surfaces act as antennas that convert light into localized electrical fields at subwavelength dimensions. This localization of light below the diffraction limit results in a strong enhancement of the confined near-field electromagnetic field.

Plasmon modes can be broadly classified into two types: SPPs and localized surface plasmon resonance (LSPR). (i) SPP happens when light is localized at a metal-dielectric interface as radio waves propagate and (ii) LSPR occurs when light-matter coupling is enhanced within a nanostructure. The structural tuning of plasmonic metamaterials, including periodical structural patterns, dimensions, composition, and spatial

arrangement, can alter SPP and LSPR modes. This interaction allows the modification of light properties such as controlled scattering at specific wavelengths and sensitive polarization beyond the diffraction limit at subwavelength spatial resolution (Liu, Wu, et al., 2022; Martínez, 2018). This section provides an overview of recent developments in optical filters enabled by micro/nanotransfer printing techniques.

9.3.1.1 Two-dimensional metamaterials for tuning optical properties

The 2D metamaterials made up of periodically arranged nanopatterns on a substrate offer tunable coupling properties by adjusting the nanopatterns' period, diameter, size, and shape (Kasani et al., 2019). As a result, the coupling properties of nanopatterns are limited to the horizontal direction, and LSPR and SPP modes can be obtained depending on the nanopatterns. Different nanopattern shapes, including nanowires, nanodisks, nanorods, nanorings, and nanoholes, have been demonstrated to produce tunable plasmon resonance properties (Conteduca et al., 2021; Haddadnezhad et al., 2020; Han & Ye, 2020; Smirnov et al., 2021). Among the various nanopatterns, subwavelength gratings are widely used in 2D metamaterials and exhibit different optical properties based on the polarization state of light. Ko et al. created smart contact lenses with unique optical characteristics by using a nanotransfer printing method based on water bridge formation in hyaluronic acid (HA) (Fig. 9.7A) (Ko et al., 2021; Smirnov et al., 2021). To optimize the polarizer design, finite-difference time-domain simulations were performed to determine the pattern size and material, resulting in an Al nanoline array on a HA film. The nanoline array patterns on the contact lens displayed a polarization extinction ratio (TM/TE) of approximately 38 at 670 nm. Binocular parallax-induced stereoscopy was implemented by utilizing the transmission/blocking of visible light produced by the proposed structure, a periodic Al nanoline array.

Another type of optical filter based on LSPR with metallic nanoparticle arrays has been extensively studied in recent years. The alignment of metallic nanoparticles in a specific pattern allows for greater control over the LSPR mode, making it more tunable. Fig. 9.7B shows the optical properties of a microstructure made up of a 2D periodic array of metallic disks (Wang et al., 2014). Three different types of plasmonic microstructures were created using Au disks, rings, and crescents through a combination of colloidal lithography and the pick-and-place transfer printing technique. A PDMS stamp coated with Au was compressed onto a Si wafer in a specific pressure range from 3.0 to 75.0 kPa. The contact area between the PDMS stamp and the Si wafer was affected by pressure. The shape and diameter of the Au disks were precisely controlled by adjusting the pressure applied during the printing process. The resulting structure exhibited LSPR optical properties dependent on the diameter of the Au disks in the infrared (IR) range. The variation of the peak position and full width at half maximum was also investigated by adjusting the diameter of the Au disks.

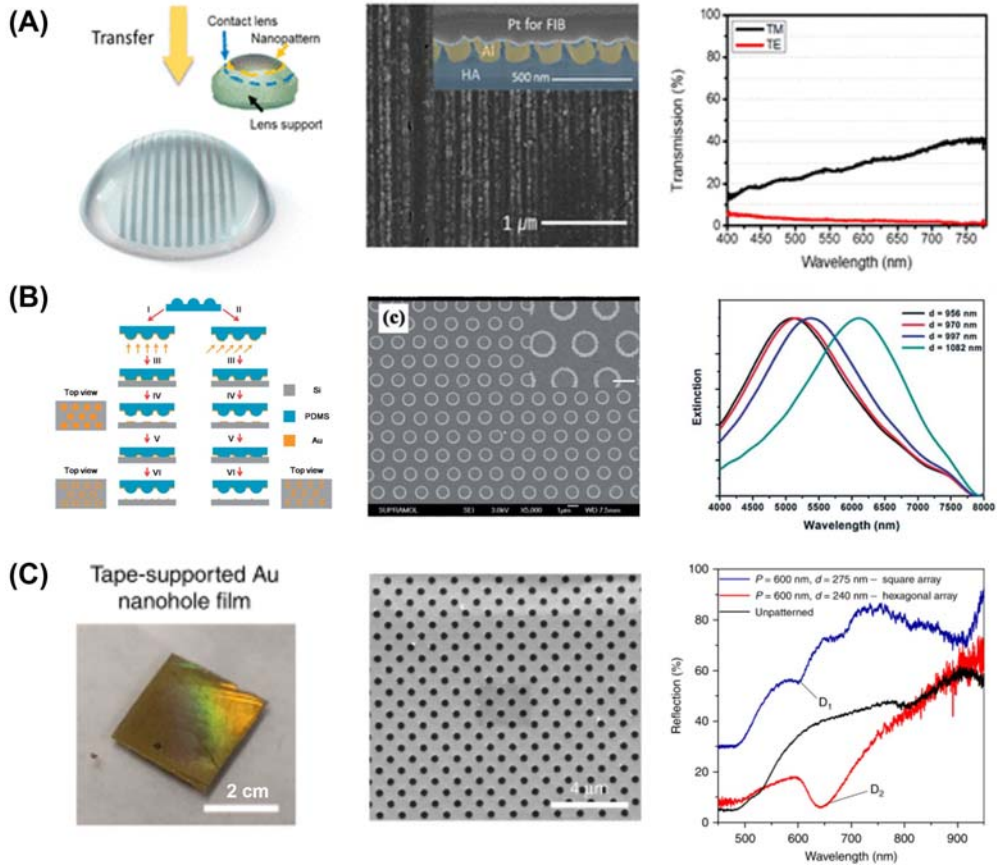


Figure 9.7 SEM images and optical properties of two-dimensional metamaterial for optical filter. (A) Nanopatterned contact lens obtained by hyaluronic acid film transfer. SEM image of the nanopatterned contact lens and the transmission spectra for TM- and TE-modes. The line width and spacing of the Al nanopatterned HA film were 100 and 100 nm, respectively. (B) A schematic illustration and SEM image of the micromolding procedure with Au ring arrays. Inner diameter of gold rings with Au ring arrays ranges from 87 to 931 nm. Calculated extinction spectra depending on the change in the diameter of the Au ring. (C) Digital and SEM image of single-layer Au nanohole array on a tape. Experimental reflection spectra with periods of $P = 600$ nm.

Wang et al. reported metallo-dielectric nanostructures using nanolithography and pick-and-place transfer printing (Fig. 9.7C) (Wang et al., 2018). The fabrication process of plasmonic metal nanostructures was simplified by using an elastomeric donor substrate, such as PDMS, to create the desired nanopatterns. These patterns were then transferred to an adhesive tape surface, eliminating the need for additional nanopatterning techniques. In this specific example, the plasmonic metal nanostructures were designed as single-layer arrays of Au nanoholes. The reflection spectra of square and hexagonally spaced Au nanoholes were measured and optical resonances of 600 and

637 nm wavelengths were observed. The resonance occurred at the metal–dielectric interface through SPP mode. The method was versatile, as the optical properties of the nanoholes could be adjusted through changes in geometry. The sensitivity to refractive index, angle dependence, and flexibility of F–P resonators in tape-based plasmonic Au nanoholes were also studied. Transfer printing techniques for optical filters based on 2D metamaterials were reviewed and classified. This method is simple and cost-effective, allowing for the precise implementation of nanoscale metamaterials for specific optical filter purposes.

9.3.1.2 Three-dimensional metamaterials for tuning optical properties

The 2D metamaterials have shown potential in optical applications, but their optical tunability is limited by structural constraints. To overcome this, researchers have developed a range of 3D metamaterials by stacking patterns or films with a spacer layer in between (Chanda et al., 2011). These 3D nanopatterns can also be created in a hybrid mode, which combines both surface plasmon resonance (SPR) and LSPR modes in horizontal and vertical nanostructures. The additional dimension of 3D metamaterials allows for greater structural flexibility and tunability of the nanopattern arrays, resulting in improved optical and electronic properties.

Dong et al. designed reconfigurable metamolecules comprising an extensive array of Au nanowires with features of U-shaped cross-sections (Fig. 9.8A) (Dong et al., 2016). The metamolecules were made of Au nanowires with a vertical U-shaped cross-section, which allowed the optical properties to be dynamically changed by combining optical and mechanical resonances. They were fabricated using the pick-and-place technique, where a metal layer was deposited on two opposite sides of a soft mold using evaporation deposition and then transferred onto a receiver substrate (e.g., glass). The pick-and-place transfer printing method with an elastomeric stamp (i.e., PDMS) provided high resolution (width of 160 nm and rabbit-ear height of 75 nm) 3D nanostructures on the receiver substrate. The optical transmission spectra of the fabricated metamolecules were observed at a wavelength of 805 nm in TM polarization.

Yoo et al. developed nonplanar 3D metamaterials, such as Au pyramids, using template stripping for mechanical adjustment (Fig. 9.8B) (Yoo et al., 2015). The template stripping technique, which is based on the pick-and-place process, enables the recycling of Si templates and the transfer of high-quality patterned metamaterials onto flexible substrates of interest. This method allows for the modulation of the extraordinary optical transmission (EOT) spectrum via the wavelength of light resonantly scattered at the tip of the Au pyramids. The resonance peak occurs at a wavelength of 545 nm and shifts to 682 nm when the Au pyramids are stretched. As the Au pyramids on PDMS are stretched, the angle between the pyramid face and the incident light decreases, resulting in a shift in their peak wavelength.

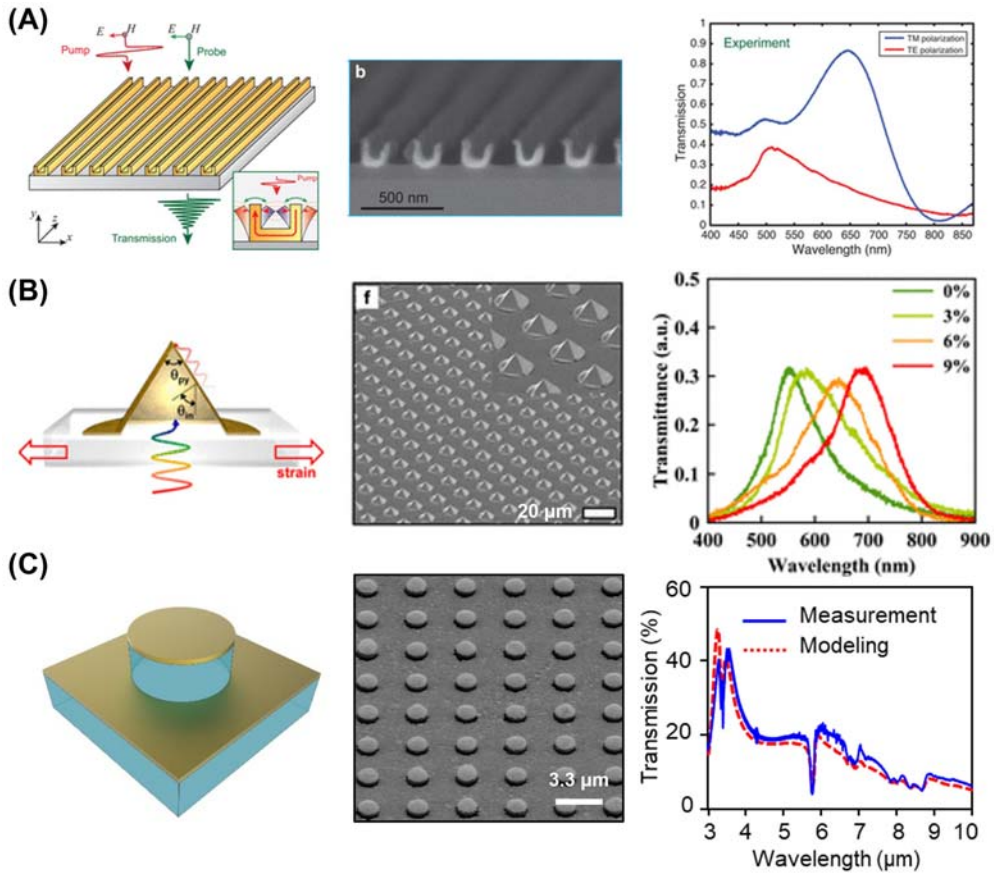


Figure 9.8 SEM images and optical properties of three-dimensional metamaterial for optical filter. (A) All-optical modulation with U-shaped Au nanowires along with measured transmission spectra under TM and TE polarization, (B) stretched metallic pyramids on PDMS along with measured transmittance spectra with applied force increases, and (C) quasi-3D plasmonic nanoarrays with nano-posts along with simulated and measured transmission spectra in the infrared range.

Recent studies have revealed that quasi-3D plasmonic nanostructures can enable controlled and enhanced light scattering at specific wavelengths and polarizations. Kim et al. developed a unique 3D nanoassembly technique that allows for the precise integration of quasi-3D plasmonic nanostructures, as shown in Fig. 9.8 (Kim et al., 2019). The nanostructures were physically and chemically separated from the donor Si wafer using a transfer printing method that involved chemically etching a sacrificial layer (such as Ni). A sacrificial layer and plasmonic Au patterns were deposited on a Si mold made up of periodic circular patterns with a dielectric layer coated over the surface. Then, the entire structure was immersed in an etchant solution to remove the sacrificial layer and physically separate the plasmonic Au patterns from the Si mold.

Different types of quasi-3D plasmonic patterns, including nanoposts, nanoholes, bilayer nanowire gratings, and ring-shaped disks, were fabricated and measured. The resonance wavelength of the quasi-3D nanoposts was generated in a hybrid mode that combines SPP and LSPR.

In addition to transferring the completed 3D metamaterials, a method to stack multiple layers of identical metamaterials vertically has also been reported. Kim et al. created flexible and stretchable optical filters using polymer-embedded Si nanowires (Kim et al., 2020). They were able to adjust the filters' resonance properties by controlling the size and spacing of the nanowires, and created a new type of filter by layering two different filters. Zheng et al. created polarization rotators that operate in the IR range using a transfer printing technique (Zheng et al., 2019). They built the rotators using ultralong, fully aligned nanowires that were stacked with gold gratings. The process involved assembling 3D nanostructures in multiple layers using two steps. An Au patterned layer on a PMMA film was separated from a PDMS substrate using a water-soluble poly(acrylic acid) (PAA) film. The patterned layer was then stacked in multiple layers by applying pressure and heat for conformal contact. The researchers also were able to demonstrate a polarization rotator that provides various rotation angles by adjusting the angle of the adjacent gratings.

Zhao et al. used a nanoimprinting method to create a nanogap between the upper and lower layers of the substrate (Zhao et al., 2021). The size of this gap was able to be adjusted to a range of 1–40 nm by adjusting the pressure, heating time, and temperature during the process. However, the steps of layering nanowires have limitations in achieving precise alignment across multiple layers. Alternatively, Liu et al. developed a metal-assisted transfer method to fabricate structurally flexible 2D (e.g., bowtie, disks, bull's eye, and circular grooves) and 3D (e.g., golden bridges, 3D square, and triangle dimers) nano-/microstructures on PDMS substrates (Liu et al., 2019). An Ag film was inserted as an auxiliary layer between Au nanostructures and a Si substrate to aid in the transfer process. The entire layer of the Au nanostructures and Ag film was easily transferred to PDMS due to the weak adhesion between the Ag film and the Si substrate. Additionally, the prestrain of the PDMS was controlled to adjust the gap between the Au nanostructures. By releasing the uniaxial deformation of the PDMS, the team was able to demonstrate the creation of various 3D microstructures such as golden bridges, 3D square dimers, and 3D triangle dimers using the Au-assisted transfer layer.

9.3.1.3 Metamaterials tailored for plasmonic color filters

Color filters are mainly made by using the optical scattering and absorption properties of metamaterials (De Proft et al., 2022; Dong et al., 2022; King et al., 2015; Sun et al., 2017). The colorful appearance of some types of butterflies, squids, and chameleons is a result of naturally occurring photonic metamaterials that are created by the combination of thin-film/multilayer interference, photonic crystals, diffraction

gratings, and light scattering. Structural engineering of metamaterials is an effective way to modify optical properties for new color filters. To achieve this, there has been extensive research on designing and developing various metal-dielectric metamaterials due to their ability to manipulate light's optical properties. By manipulating the structural dimensions and refractive index of these metamaterials, the optical properties such as reflection, absorption, and transmission can be controlled to produce a wide range of colors. Plasmonic metamaterials on a subwavelength scale can make the pixels of color imaging substantially small, resulting in an improvement in resolution up to the diffraction limit. The SPs and LSPRs of these nanoantennas can be manipulated by adjusting the geometry and dimensions of the plasmonic structure, which allows for the desired reflection, absorption, and transmission spectra to be achieved, resulting in the creation of plasmonic color filters (PCFs).

Liu et al. demonstrated metasurface color filters using a facile thermal transfer printing technique for solution-processed high-quality ZnO nanostructures (Fig. 9.9A) (Liu, Peng, et al., 2022). The 3D ZnO nanostructure was formed on a GaN epitaxy/Sapphire-c substrate, followed by a PMMA coating to protect the nanostructure. Then, thermal compression was applied between the PMMA layer and the polymer film to form a strong bond. The 3D ZnO nanostructure embedded in the PMMA

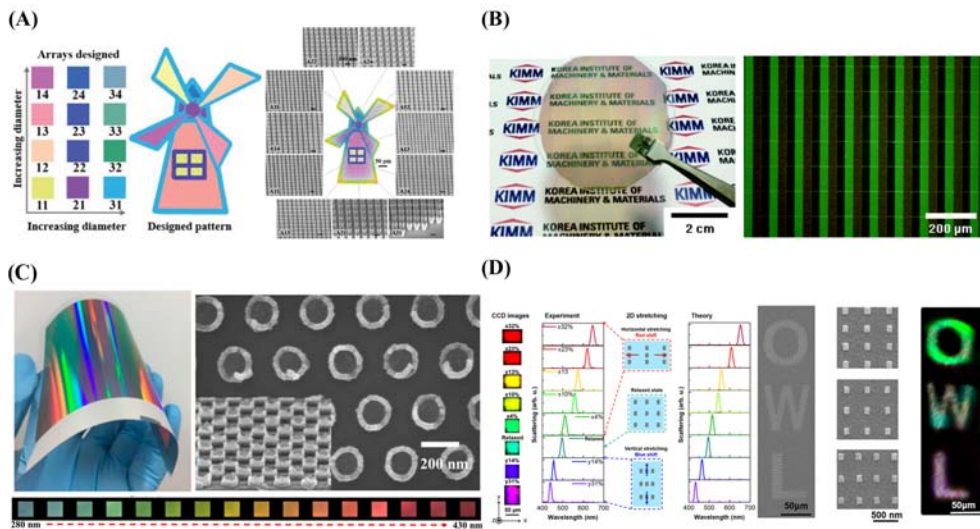


Figure 9.9 Optical spectrum and color palettes of plasmonic color filters (PCFs). (A) Designed "windmill" pattern image and various color palette. Scanning electron microscopic (SEM) image corresponding to the color position on the "windmill" pattern. (B) Digital and optical microscopy of the fabricated PCFs with Ag nanohole array on glass. (C) Optical and SEM image of the Al hexagonal arrays. Various color images varying between 280 and 430 nm pattern periods. (D) Charge-coupled device (CCD) images and scattering spectra of the square array of Al nanostructures onto an elastomeric substrate.

layer was uniformly exfoliated from the substrate. Nanorods with varying geometric parameters were arranged in a windmill pattern to form a metasurface color filter. The nanorod diameter affected the resonance wavelength, allowing for full-color tunability. The windmill pattern had a uniform color distribution.

Hwang et al. designed a PCF made of an array of Ag nanoholes on a glass wafer (Fig. 9.9B) (Hwang et al., 2019). A novel transfer printing method that utilizes the oxidation of various metals and generation of covalent bonds was employed to fabricate Ag nanohole arrays. At 150°C, natural oxidation formed a strong covalent bond between the Ag layers with the nanopattern and the adhesive-coated Si wafers, resulting in a fast and effortless transfer of the Ag layers onto the Si substrate without additional postprocessing. This solid covalent bond at the interface between the Ag layer and the Si substrate provided improved color resolution due to the EOT phenomenon, which was not affected by the polarization of the light source, unlike general nanograting structures.

Hwang et al. showed the results of the transfer printing technique used to pattern Al nanodots and nanohole for creating large-area transmission-type flexible PCFs (Fig. 9.9C) (Hwang et al., 2017). A PET film substrate was flattened with a material of low surface roughness to enable uniform transfer of the dot-type PCFs. A layer of Al was then deposited onto a replica mold with dot pattern arrays, before being transferred onto the flattened PET film. By controlling the thickness and structure of the Al film, the light transmittance and various colors were designed and achieved through the EOT phenomenon. As the pattern periods of hole-type PCFs increased to 280 and 430 nm, the color of the transmitted light changed due to the shift in resonance frequency.

Tseng et al. presented a PCF composed of an array of Al metamaterials embedded in an elastomeric substrate that could continuously tune the entire visible spectrum (Fig. 9.9D) (Tseng et al., 2017). The color of the Al metamaterials was altered across the entire visible spectrum due to changes in period and scattering when the substrate was subjected to 2D stretching. Specifically, the scattering peak of the Al nanostructures was red-shifted from 495 to 645 nm when the strain was less than 35%.

9.3.2 Optoelectronics

9.3.2.1 Photodetector

Transfer printing is a versatile technique that can be used to incorporate a range of micro/nanomaterials into a heterogeneous structure of photodetectors for a variety of applications such as automated systems, remote controls, and fiber optic equipment. Wie et al. demonstrated a hybrid photodiode system in which a p-doped Si membrane (~ 1 cm wide and ~ 200 nm thick) was vertically stacked on an n-doped MoS₂ monolayer (~ 5 mm wide and ~ 4 nm thick) using the chemo-mechanical transfer printing (Wie et al., 2018). To address the issues of a lack of p–n junction and low-

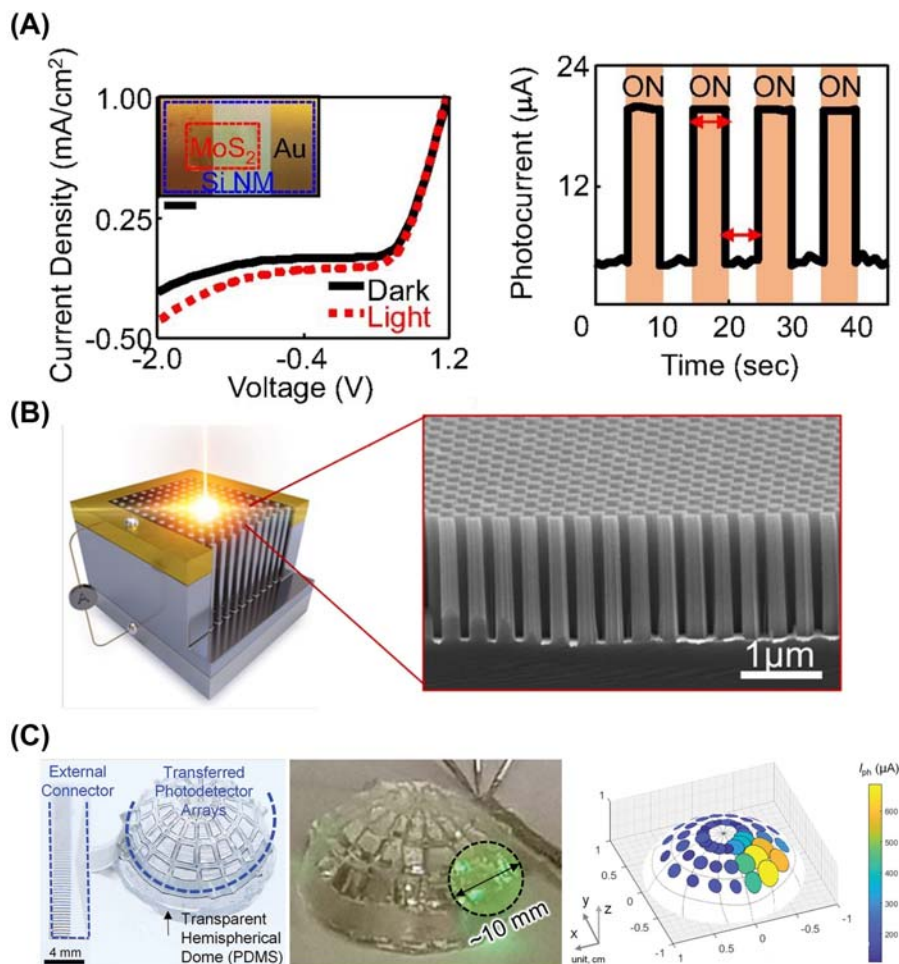


Figure 9.10 Transferred photodetectors. (A) hybrid photodiode system where in p-doped Si nano-membrane (~ 1 cm wide and ~ 200 nm thick) is vertically stacked on an n-doped MoS₂ monolayer (~ 5 mm wide and ~ 4 nm thick). (B) Schottky-type photodetectors in three-dimensional (3D) layout transferred onto a Si substrate. (C) 3D photodetectors transferred onto a transparent hemispherical dome (PDMS).

light absorption, the MoS₂ monolayer was transferred to a piece of glass. Fig. 9.10A (left image) shows the current density–voltage (J – V) curves under two lighting conditions: darkness (black lines) and illumination (red dotted lines) from a 540 nm laser with a light intensity of 3 W/cm². The inset optical image indicates the sample of the hybrid photodetector used for testing. The results of the experiments and finite element analysis simulations indicate that there is no significant difference in the electrical characteristics of the transferred hybrid photodetector and control samples made on a

SiO₂/Si wafer. Furthermore, the photoresponse of the hybrid photodiode is demonstrated in the right image, which reveals an abrupt rise and fall in photocurrent when a 540 nm laser was used. These findings suggest no difference between the current densities for dark and illuminated conditions at forward bias, yet a notable difference at reverse bias at approximately 33 μA . Consequently, the photodetector devices can be fabricated on arbitrary substrates such as glass windows, commercial flowerpots and toy blocks.

Fig. 9.10B shows an example of Schottky-type photodetectors that were fabricated in a vertically stacked layout by transfer printing of Au nanodisks from polymer mold onto a Si wafer to serve as masks, in detail as follows (Zhao et al., 2022). First, a polymer mold (RM-311 resin/PET film) created by nanoimprinting was used to replicate a Si master mold. Then, a layer of Au film was deposited onto the mold to form a well-organized nanomesh. Next, the resulting Au nanohole arrays were transfer-printed onto a Si wafer by inducing chemisorption between the Au and Si substrates for 5 minutes at 5 bars and 160°C. After that, an etching process was used to generate uniform Si nanowires with different diameters and pitches (200 nm diameter and 340, 380, 420, and 500 nm pitch), as seen in the accompanying image. The increased surface area of the vertical Schottky-type photodetectors provided superior device performance (Oh et al., 2012), while the Si nanowires served as an antireflection layer to disperse the incident photons (Kim, Yoon et al., 2019). This prolonged the duration of optical absorption, resulting in improved device performance. The proposed approach addresses scalability, uniformity, controllability, and reproducibility issues, making it a viable platform technology for commercial manufacturing and scientific research.

Another example includes 3D photodetectors transferred onto a transparent dome (PDMS) using the chemo-mechanical transfer method (Fig. 9.10C) (Lee et al., 2020). The fractal web design contained 48-pixel photodetectors with a photocurrent of $591.1 \pm 5.5 \mu\text{A}$ and a dark current of $120.4 \pm 9.4 \mu\text{A}$. The accuracy of the laser beam's position improved with a smaller spot size. This photodetector array was heterogeneously integrated with a hemispherical PDMS dome and doped with PyB-doped graphene, which provided robustness, functionality, and resilience. The graphene also had a photoresponsivity of $>1000 \text{ A/W}$, making it a viable alternative to silicon for a flexible and effective photoactive component. This process opens up new possibilities for the development of electronic and optical devices, as it enables the deployment of 2D deformable functional materials within 3D device architectures.

9.3.2.2 Displays

The human-computer interface's display is a critical component, but traditional screens remain bulky and rigid. On the other hand, flexible screens are a fairly recent technology which is lightweight and delicate. Transfer printing techniques, which are

currently being explored as an essential manufacturing process for flexible displays, have enabled the systematic assembly of different functional components, such as emissive or transport layers, into a device stack (Koo et al., 2018). One example involves transferring miniaturized crystalline Si circuitry (chipllets) from their source wafers (e.g., SOI) onto active-matrix OLED displays (Bower et al., 2011; Lakatos, 2000). This approach requires photolithographic processing of their source wafers to create an array of identical integrated circuits. The chipllets, which can be up to 500- μm long, 75- μm broad and 8- to 20- μm thick, are connected to an anchor region nearby with tethers. Once a shielding layer is applied, the chipllet is undercut and connected to a PDMS stamp. Van der Waals forces then push the chipllets to the base of a single post, which is then pressed against a target substrate coated with a thin adhesive. After the stamp is removed, the chipllets are connected to the OLED display, resulting in flexible and functional OLED panels. The intaglio transfer printing method discussed in Section 2.1 can be also utilized to create an ultra-high resolution, full-color, deformable QLED arrays (Choi et al., 2015). Even after being laminated on human skin or crumpled Al foil, these QLEDs maintained their impressive electroluminescence efficiency. An array of RGB diodes were precisely aligned with a variety of printing procedures to create a high-resolution display (ranging from 441 to 2460 p.p.i.).

9.4 Conclusions

Advances in transfer printing techniques have enabled the versatile assembly of functional nanomaterials into 2D or 3D optical devices. In this chapter, the broad and rapid changes in several representative transfer printing techniques are discussed with their underlying working principles outlined as well. These malleable techniques permit the successful transfer of different micro/nanomaterials or device components, such as nanomembranes, nanowires, and nanoribbons, from donor substrates to receiver substrates with desired device performance. As each transfer printing procedure has its own distinct characteristics, it is essential to choose the appropriate technique for the corresponding application, especially in the burgeoning fields of metamaterials/devices and optoelectronics. Consequently, future research would focus on developing new processes and further optimizing current transfer printing techniques for specific applications.

The design and enhancement of active, programmable elastomeric stamps could revolutionize transfer printing techniques that rely on the pick-and-place process, enabling the effective assembly of complex patterns and devices. The various crack-driven, thermo-mechanical, and chemo-mechanical transfer printing techniques discussed in this chapter are low-cost, quick, and reliable. Additionally, further research into the geometrical and material characteristics that can affect the interfacial adhesion of these techniques is necessary to gain a better understanding.

In summary, these transfer printing techniques have been powerful and practical for the integration of micro/nanoscale functional materials or complete devices, as well as the fabrication of brittle photonic materials in flexible, stretchable, and/or transparent forms.

Acknowledgment

Lee Chi Hwan acknowledges the support from the National Science Foundation (NSF) Civil, Mechanical, and Manufacturing Innovation (CMMI) (1928784), as well as the Leslie A. Geddes Endowment from Purdue University.

References

- Baca, A. J., Ahn, J. H., Sun, Y., Meitl, M. A., Menard, E., Kim, H. S., Choi, W. M., Kim, D. H., Huang, Y., & Rogers, J. A. (2008). Semiconductor wires and ribbons for high-performance flexible electronics. *Angewandte Chemie - International Edition*, 47(30), 5524–5542. Available from <https://doi.org/10.1002/anie.200703238>, <http://www3.interscience.wiley.com/cgi-bin/fulltext/120749216/PDFSTART>.
- Baca, A. J., Yu, K. J., Xiao, J., Wang, S., Yoon, J., Ryu, J. H., Stevenson, D., Nuzzo, R. G., Rockett, A. A., Huang, Y., & Rogers, J. A. (2010). Compact monocrystalline silicon solar modules with high voltage outputs and mechanically flexible designs. *Energy and Environmental Science*, 3(2), 208–211. Available from <https://doi.org/10.1039/b920862c>.
- Barnes, W. L., Dereux, A., & Ebbesen, T. W. (2003). Surface plasmon subwavelength optics. *Nature*, 424(6950), 824–830. Available from <https://doi.org/10.1038/nature01937>.
- Berger, G., & Wendel, M. (2018). Optical metrology of freeforms and complex lenses. *Optik & Photonik*, 13(1), 40–43. Available from <https://doi.org/10.1002/opph.201800007>.
- Bower, C. A., Meitl, M. A., Raymond, B., Radauscher, E., Cok, R., Bonafede, S., Gomez, D., Moore, T., Pevatte, C., Fisher, B., Rotzoll, R., Melnik, G. A., Fecioru, A., & Trindade, A. J. (2017). Emissive displays with transfer-printed assemblies of $8\ \mu\text{m} \times 15\ \mu\text{m}$ inorganic light-emitting diodes. *Photonics Research*, 5(2), A23–A29. Available from <https://doi.org/10.1364/PRJ.5.000A23>, <https://www.osapublishing.org/prj/viewmedia.cfm?uri=prj-5-2-A23&seq=0>.
- Bower, C. A., Menard, E., Bonafede, S., Hamer, J. W., & Cok, R. S. (2011). Transfer-printed microscale integrated circuits for high performance display backplanes. *IEEE Transactions on Components, Packaging and Manufacturing Technology*, 1(12), 1916–1922. Available from <https://doi.org/10.1109/TCPMT.2011.2128324>, United States. 21563950.
- Cao, Q., & Rogers, J. A. (2009). Ultrathin films of single-walled carbon nanotubes for electronics and sensors: A review of fundamental and applied aspects. *Advanced Materials*, 21(1), 29–53. Available from <https://doi.org/10.1002/adma.200801995>, <http://www3.interscience.wiley.com/cgi-bin/fulltext/121548772/PDFSTART>, United States.
- Cao, D. H., Stoumpos, C. C., Farha, O. K., Hupp, J. T., & Kanatzidis, M. G. (2015). 2D homologous perovskites as light-absorbing materials for solar cell applications. *Journal of the American Chemical Society*, 137(24), 7843–7850. Available from <https://doi.org/10.1021/jacs.5b03796>, <http://pubs.acs.org/journal/jacsat>.
- Chanda, D., Shigeta, K., Gupta, S., Cain, T., Carlson, A., Mihi, A., Baca, A. J., Bogart, G. R., Braun, P., & Rogers, J. A. (2011). Large-area flexible 3D optical negative index metamaterial formed by nano-transfer printing. *Nature Nanotechnology*, 6(7), 402–407. Available from <https://doi.org/10.1038/nnano.2011.82>, <http://www.nature.com/nnano/index.html>.
- Cheben, P., Halir, R., Schmid, J. H., Atwater, H. A., & Smith, D. R. (2018). Subwavelength integrated photonics. *Nature*, 560(7720), 565–572. Available from <https://doi.org/10.1038/s41586-018-0421-7>, <http://www.nature.com/nature/index.html>.

- Chen, Y., Shu, Z., Feng, Z., Kong, L., Liu, Y., & Duan, H. (2020). Reliable patterning, transfer printing and post-assembly of multiscale adhesion-free metallic structures for nanogap device applications. *Advanced Functional Materials*, 30(32), 2002549. Available from <https://doi.org/10.1002/adfm.202002549>.
- Choi, M. K., Yang, J., Kang, K., Kim, D. C., Choi, C., Park, C., Kim, S. J., Chae, S. I., Kim, T.-H., Kim, J. H., Hyeon, T., & Kim, D.-H. (2015). Wearable red–green–blue quantum dot light-emitting diode array using high-resolution intaglio transfer printing. *Nature Communications*, 6(1). Available from <https://doi.org/10.1038/ncomms8149>.
- Conteduca, D., Barth, I., Pitruzzello, G., Reardon, C. P., Martins, E. R., & Krauss, T. F. (2021). Dielectric nanohole array metasurface for high-resolution near-field sensing and imaging. *Nature Communications*, 12(1). Available from <https://doi.org/10.1038/s41467-021-23357-9>, <http://www.nature.com/ncomms/index.html>.
- De Prof, A., Lodewijks, K., Figeys, B., Kouznetsov, D., Verellen, N., Pham, N. P., Vereecke, B., Sabuncuoglu Tezcan, D., Jansen, R., Van Dorpe, P., & Rottenberg, X. (2022). Highly selective color filters based on hybrid plasmonic-dielectric nanostructures. *ACS Photonics*, 9(4), 1349–1357. Available from <https://doi.org/10.1021/acsp Photonics.1c01983>, <http://pubs.acs.org/journal/apchd5>.
- Dong, B., Chen, X., Zhou, F., Wang, C., Zhang, H. F., & Sun, C. (2016). Gigahertz all-optical modulation using reconfigurable nanophotonic metamolecules. *Nano Letters*, 12, 7690–7695. Available from <https://doi.org/10.1021/acs.nanolett.6b03760>, <http://pubs.acs.org/journal/nalefd>.
- Dong, Z., Jin, L., Rezaei, S. D., Wang, H., Chen, Y., Tjiptoharsono, F., Ho, J., Gorelik, S., Hong Ng, R. J., Ruan, Q., Qiu, C. W., & Yang, J. K. W. (2022). Schrödinger's red pixel by quasi-bound-states-in-the-continuum. *Science Advances*, 8(8). Available from <https://doi.org/10.1126/sciadv.abm4512>, <https://www.science.org/doi/10.1126/sciadv.abm4512>.
- Feng, X., Cheng, H., Bowen, A. M., Carlson, A. W., Nuzzo, R. G., & Rogers, J. A. (2013). A finite-deformation mechanics theory for kinetically controlled transfer printing. *Journal of Applied Mechanics, Transactions ASME*, 80(6). Available from <https://doi.org/10.1115/1.4023963>.
- Feng, X., Meitl, M. A., Bowen, A. M., Huang, Y., Nuzzo, R. G., & Rogers, J. A. (2007). Competing fracture in kinetically controlled transfer printing. *Langmuir: the ACS Journal of Surfaces and Colloids*, 25, 12555–12560. Available from <https://doi.org/10.1021/la701555n>.
- Franklin, D., Frank, R., Wu, S. T., & Chanda, D. (2017). Actively addressed single pixel full-colour plasmonic display. *Nature Communications*, 8. Available from <https://doi.org/10.1038/ncomms15209>, <http://www.nature.com/ncomms/index.html>.
- Gramotnev, D. K., & Bozhevolnyi, S. I. (2010). Plasmonics beyond the diffraction limit. *Nature Photonics*, 4(2), 83–91. Available from <https://doi.org/10.1038/nphoton.2009.282>.
- Gu, T., Kim, H. J., Rivero-Baleine, C., & Hu, J. (2023). Reconfigurable metasurfaces towards commercial success. *Nature Photonics*, 17(1), 48–58. Available from <https://doi.org/10.1038/s41566-022-01099-4>, <https://www.nature.com/nphoton/>.
- Haddadnezhad, M., Yoo, S., Kim, J., Kim, J. M., Son, J., Jeong, H. S., Park, D., Nam, J. M., & Park, S. (2020). Synthesis and surface plasmonic characterization of asymmetric Au split nanorings. *Nano Letters*, 24(10), 7774–7782. Available from <https://doi.org/10.1021/acs.nanolett.0c03385>, <http://pubs.acs.org/journal/nalefd>.
- Han, C., & Ye, J. (2020). Polarized resonant emission of monolayer WS₂ coupled with plasmonic sawtooth nanoslit array. *Nature Communications*, 11(1). Available from <https://doi.org/10.1038/s41467-020-14597-2>, <http://www.nature.com/ncomms/index.html>.
- Heo, S., Ha, J., Son, S. J., Choi, I. S., Lee, H., Oh, S., Jekal, J., Kang, M. H., Lee, G. J., Jung, H. H., Yea, J., Lee, T., Lee, Y., Choi, J. W., Xu, S., Choi, J. H., Jeong, J. W., Song, Y. M., Rah, J. C., ... Jang, K. I. (2021). Instant, multiscale dry transfer printing by atomic diffusion control at heterogeneous interfaces. *Science Advances*, 7(28). Available from <https://doi.org/10.1126/sciadv.abh0040>, <https://advances.sciencemag.org/content/7/28/eabh0040>.
- Hornig, R. H., Chien, H. Y., Chen, K. Y., Tseng, W. Y., Tsai, Y. T., & Tarntair, F. G. (2018). Development and fabrication of AlGaInP-based flip-chip micro-LEDs. *IEEE Journal of the Electron Devices Society*, 6, 475–479. Available from <https://doi.org/10.1109/JEDS.2018.2823981>, <http://ieeexplore.ieee.org/servlet/opac?punumber=6245494>.

- Hong, R. H., Sinha, S., Lee, C. P., Feng, H. A., Chung, C. Y., & Tu, C. W. (2019). Composite metal substrate for thin film AlGaInP LED applications. *Optics Express*, 27(8), A397–A403. Available from <https://doi.org/10.1364/OE.27.00A397>, <https://www.osapublishing.org/oe/abstract.cfm?uri=oe-27-8-A397>.
- Hoshino, K., Turner, T. C., Kim, S., Gopal, A., & Zhang, X. (2008). Single molecular stamping of a sub-10-nm colloidal quantum dot array. *Langmuir: the ACS Journal of Surfaces and Colloids*, 24(23), 13804–13808. Available from <https://doi.org/10.1021/la802936h>, <http://pubs.acs.org/doi/pdfplus/10.1021/la802936h>, United States.
- Hsia, K. J., Huang, Y., Menard, E., Park, J. U., Zhou, W., Rogers, J., & Fulton, J. M. (2005). Collapse of stamps for soft lithography due to interfacial adhesion. *Applied Physics Letters*, 86(15), 1–3. Available from <https://doi.org/10.1063/1.1900303>.
- Huang, Q., Peh, J., Hergenrother, P. J., & Cunningham, B. T. (2016). Porous photonic crystal external cavity laser biosensor. *Applied Physics Letters*, 109(7), 071103. Available from <https://doi.org/10.1063/1.4961107>.
- Huang, Y. Y., Zhou, W., Hsia, K. J., Menard, E., Park, J. U., Rogers, J. A., & Alleyne, A. G. (2005). Stamp collapse in soft lithography. *Langmuir: the ACS Journal of Surfaces and Colloids*, 21(17), 8058–8068. Available from <https://doi.org/10.1021/la0502185>.
- Hwang, B., Shin, S.-H., Hwang, S.-H., Jung, J.-Y., Choi, J.-H., Ju, B.-K., & Jeong, J.-H. (2017). Flexible plasmonic color filters fabricated via nanotransfer printing with nanoimprint-based planarization. *ACS Applied Materials & Interfaces*, 9(33), 27351–27356. Available from <https://doi.org/10.1021/acsami.7b06228>.
- Hwang, S. H., Zhao, Z. J., Jeon, S., Kang, H., Ahn, J., & Jeong, J. H. (2019). Repeatable and metal-independent nanotransfer printing based on metal oxidation for plasmonic color filters. *Nanoscale*, 11(23), 11128–11137. Available from <https://doi.org/10.1039/c9nr00176j>, <http://pubs.rsc.org/en/journals/journal/nr>.
- Im, J. H., Luo, J., Franckevičius, M., Pellet, N., Gao, P., Moehl, T., Zakeeruddin, S. M., Nazeeruddin, M. K., Grätzel, M., & Park, N. G. (2015). Nanowire perovskite solar cell. *Nano Letters*, 15(3), 2120–2126. Available from <https://doi.org/10.1021/acs.nanolett.5b00046>, <http://pubs.acs.org/journal/nalefd>.
- Kang, M. G., Joon Park, H., Hyun Ahn, S., & Jay Guo, L. (2010). Transparent Cu nanowire mesh electrode on flexible substrates fabricated by transfer printing and its application in organic solar cells. *Solar Energy Materials and Solar Cells*, 94(6), 1179–1184. Available from <https://doi.org/10.1016/j.solmat.2010.02.039>.
- Kasani, S., Curtin, K., & Wu, N. (2019). A review of 2D and 3D plasmonic nanostructure array patterns: fabrication, light management and sensing applications. *Nanophotonics*, 8(12), 2065–2089. Available from <https://doi.org/10.1515/nanoph-2019-0158>.
- Kikuchi, K. (2016). Fundamentals of coherent optical fiber communications. *Journal of Lightwave Technology*, 34(1), 157–179. Available from <https://doi.org/10.1109/JLT.2015.2463719>.
- Kim, T. H., Choi, W. M., Kim, D. H., Meitl, M. A., Menard, E., Jiang, H., Carlisle, J. A., & Rogers, J. A. (2008). Printable, flexible, and stretchable forms of ultrananocrystalline diamond with applications in thermal management. *Advanced Materials*, 20(11), 2171–2176. Available from <https://doi.org/10.1002/adma.200702434>, <http://www3.interscience.wiley.com/cgi-bin/fulltext/119030542/PDFSTART>, United States.
- Kim, T. H., Cho, K. S., Lee, E. K., Lee, S. J., Chae, J., Kim, J. W., Kim, D. H., Kwon, J. Y., Amarutunga, G., Lee, S. Y., Choi, B. L., Kuk, Y., Kim, J. M., & Kim, K. (2011). Full-colour quantum dot displays fabricated by transfer printing. *Nature Photonics*, 5(3), 176–182. Available from <https://doi.org/10.1038/nphoton.2011.12>.
- Kim, B., Hwang, J., Yi, J., Kim, D. R., Urbas, A., Ku, Z., & Lee, C. H. (2021). Replicable quasi-three-dimensional plasmonic nanoantennas for infrared bandpass filtering. *ACS Applied Materials and Interfaces*, 13(20), 24024–24031. Available from <https://doi.org/10.1021/acsami.1c03932>, <http://pubs.acs.org/journal/aamick>.
- Kim, H., Jang, H., Kim, B., Kim, M. K., Wie, D. S., Lee, H. S., Kim, D. R., & Lee, C. H. (2018). Flexible elastomer patch with vertical silicon nanoneedles for intracellular and intratissue nanoinjection of biomolecules. *Science Advances*, 4(11). Available from <https://doi.org/10.1126/sciadv.aau6972>, <http://advances.sciencemag.org/content/4/11/eaau6972/tab-pdf>.

- Kim, B., Jeon, J., Zhang, Y., Wie, D. S., Hwang, J., Lee, S. J., Walker, D. E., Abeysinghe, D. C., Urbas, A., Xu, B., Ku, Z., & Lee, C. H. (2019). Deterministic nanoassembly of quasi-three-dimensional plasmonic nanoarrays with arbitrary substrate materials and structures. *Nano Letters*, *19*(8), 5796–5805. Available from <https://doi.org/10.1021/acs.nanolett.9b02598>, <http://pubs.acs.org/journal/nalefd>.
- Kim, S., Wu, J., Carlson, A., Jin, S. H., Kovalsky, A., Glass, P., Liu, Z., Ahmed, N., Elgan, S. L., Chen, W., Ferreira, P. M., Sitti, M., Huang, Y., & Rogers, J. A. (2010). Microstructured elastomeric surfaces with reversible adhesion and examples of their use in deterministic assembly by transfer printing. *Proceedings of the National Academy of Sciences of the United States of America*, *107*(40), 17095–17100. Available from <https://doi.org/10.1073/pnas.1005828107>, <http://www.pnas.org/content/107/40/17095.full.pdf+html>, United States.
- Kim, K., Yoon, S., Seo, M., Lee, S., Cho, H., Meyyappan, M., & Baek, C. K. (2019). Whispering gallery modes enhance the near-infrared photoresponse of hourglass-shaped silicon nanowire photo-diodes. *Nature Electronics*, *2*(12), 572–579. Available from <https://doi.org/10.1038/s41928-019-0317-z>, <https://www.nature.com/natelectron/>.
- Kim, Y. J., Yoo, Y. J., Kang, M. H., Ko, J. H., Park, M. R., Yoo, D. E., Lee, D. W., Kim, K., Kang, I. S., & Song, Y. M. (2020). Mechanotunable optical filters based on stretchable silicon nanowire arrays. *Nanophotonics*, *9*(10), 3287–3293. Available from <https://doi.org/10.1515/nanoph-2020-0062>, <http://www.degruyter.com/view/j/nanoph?rskey=PZEKdQ&result=1&q=Nanophotonics>.
- King, N. S., Liu, L., Yang, X., Cerjan, B., Everitt, H. O., Nordlander, P., & Halas, N. J. (2015). Fano resonant aluminum nanoclusters for plasmonic colorimetric sensing. *ACS Nano*, *9*(11), 10628–10636. Available from <https://doi.org/10.1021/acsnano.5b04864>, <http://pubs.acs.org/journal/ancac3>.
- Koenderink, A. F., Alù, A., & Polman, A. (2015). Nanophotonics: Shrinking light-based technology. *Science (New York, N.Y.)*, *348*(6234), 516–521. Available from <https://doi.org/10.1126/science.1261243>, <http://www.sciencemag.org/content/348/6234/516.full.pdf>.
- Koo, J. H., Kim, D. C., Shim, H. J., Kim, T. H., & Kim, D. H. (2018). Flexible and stretchable smart display: materials, fabrication, device design, and system integration. *Advanced Functional Materials*, *28*(35). Available from <https://doi.org/10.1002/adfm.201801834>, [http://onlinelibrary.wiley.com/journal/10.1002/\(ISSN\)1616-3028](http://onlinelibrary.wiley.com/journal/10.1002/(ISSN)1616-3028).
- Koo, M., Park, K. I., Lee, S. H., Suh, M., Jeon, D. Y., Choi, J. W., Kang, K., & Lee, K. J. (2012). Bendable inorganic thin-film battery for fully flexible electronic systems. *Nano Letters*, *12*(9), 4810–4816. Available from <https://doi.org/10.1021/nl302254v>.
- Ko, J., Kang, H. J., Ahn, J., Zhao, Z. J., Jeong, Y., Hwang, S. H., Bok, M., Jeon, S., Gu, J., Ha, J. H., Rho, J., Jeong, J. H., & Park, I. (2021). Biocompatible nanotransfer printing based on water bridge formation in hyaluronic acid and its application to smart contact lenses. *ACS Applied Materials and Interfaces*, *13*(29), 35069–35078. Available from <https://doi.org/10.1021/acsmi.1c06225>, <http://pubs.acs.org/journal/aamick>.
- Lakatos, A. I. (2000). Introduction. *Journal of the Society for Information Display*, *8*(1), 1. Available from <https://doi.org/10.1889/1.1828693>.
- Lan, X., Voznyy, O., Kiani, A., García De Arquer, F. P., Abbas, A. S., Kim, G. H., Liu, M., Yang, Z., Walters, G., Xu, J., Yuan, M., Ning, Z., Fan, F., Kanjanaboos, P., Kramer, I., Zhitomirsky, D., Lee, P., Perelgut, A., Hoogland, S., & Sargent, E. H. (2016). Passivation using molecular halides increases quantum dot solar cell performance. *Advanced Materials*, *28*(2), 299–304. Available from <https://doi.org/10.1002/adma.201503657>, <http://www3.interscience.wiley.com/journal/119030556/issue>.
- Lee, E. K., Baruah, R. K., Leem, J. W., Park, W., Kim, B. H., Urbas, A., Ku, Z., Kim, Y. L., Alam, M. A., & Lee, C. H. (2020). Fractal web design of a hemispherical photodetector array with organic-dye-sensitized graphene hybrid composites. *Advanced Materials*, *32*(46). Available from <https://doi.org/10.1002/adma.202004456>, [http://onlinelibrary.wiley.com/journal/10.1002/\(ISSN\)1521-4095](http://onlinelibrary.wiley.com/journal/10.1002/(ISSN)1521-4095).
- Lee, S., Kang, B., Keum, H., Ahmed, N., Rogers, J. A., Ferreira, P. M., Kim, S., & Min, B. (2016). Heterogeneously assembled metamaterials and metadevices via 3D modular transfer printing. *Scientific Reports*, *6*(1). Available from <https://doi.org/10.1038/srep27621>.

- Lee, C. H., Kim, D. R., Cho, I. S., William, N., Wang, Q., & Zheng, X. (2012). Peel-and-stick: Fabricating thin film solar cell on universal substrates. *Scientific Reports*, 2. Available from <https://doi.org/10.1038/srep01000>.
- Lee, C. H., Kim, D. R., & Zheng, X. (2014). Transfer printing methods for flexible thin film solar cells: Basic concepts and working principles. *ACS Nano*, 23(9), 8746–8756. Available from <https://doi.org/10.1021/nn5037587>, <http://pubs.acs.org/journal/ancac3>.
- Lee, C. H., Kim, D. R., & Zheng, X. (2010). Fabricating nanowire devices on diverse substrates by simple transfer-printing methods. *Proceedings of the National Academy of Sciences of the United States of America*, 107(22), 9950–9955. Available from <https://doi.org/10.1073/pnas.0914031107>, <http://www.pnas.org/content/107/22/9950.full.pdf>, United States.
- Lee, C. H., Kim, J. H., Zou, C., Cho, I. S., Weisse, J. M., Nemeth, W., Wang, Q., Van Duijn, A. C. T., Kim, T. S., & Zheng, X. (2013). Peel-And-stick: Mechanism study for efficient fabrication of flexible/ transparent thin-film electronics. *Scientific Reports*, 3. Available from <https://doi.org/10.1038/srep02917>, <http://www.nature.com/srep/index.html>.
- Lee, K. J., Lee, J., Hwang, H., Reitmeier, Z. J., Davis, R. F., Rogers, J. A., & Nuzzo, R. G. (2005). A printable form of single-crystalline gallium nitride for flexible optoelectronic systems. *Small (Weinheim an der Bergstrasse, Germany)*, 1(12), 1164–1168. Available from <https://doi.org/10.1002/sml.200500166>.
- Leopardi, H., Davila-Rodriguez, J., Quinlan, F., Olson, J., Sherman, J. A., Diddams, S. A., & Fortier, T. M. (2017). Single-branch Er: fiber frequency comb for precision optical metrology with $10^4 - 18$ fractional instability. *Optica*, 4(8), 879. Available from <https://doi.org/10.1364/optica.4.000879>.
- Liang, B., Zhang, Z., Chen, W., Lu, D., Yang, L., Yang, R., Zhu, H., Tang, Z., & Gui, X. (2019). Direct Patterning of carbon nanotube via stamp contact printing process for stretchable and sensitive sensing devices. *Nano-Micro Letters*, 11(1). Available from <https://doi.org/10.1007/s40820-019-0323-8>, <http://www.springer.com/engineering/journal/40820>.
- Liu, J., Chen, S., Qian, D., Gautam, B., Yang, G., Zhao, J., Bergqvist, J., Zhang, F., Ma, W., Ade, H., Inganäs, O., Gundogdu, K., Gao, F., & Yan, H. (2016). Fast charge separation in a non-fullerene organic solar cell with a small driving force. *Nature Energy*, 1(7). Available from <https://doi.org/10.1038/nenergy.2016.89>, <http://www.nature.com/nenergy/>.
- Liu, J., Liang, Y., Wang, L., Wang, B., Zhang, T., & Yi, F. (2016). Fabrication and photosensitivity of CdS photoresistor on silica nanopillars substrate. *Materials Science in Semiconductor Processing*, 56, 217–221. Available from <https://doi.org/10.1016/j.mssp.2016.08.024>.
- Liu, Y., Li, C., Ren, Z., Yan, S., & Bryce, M. R. (2018). All-organic thermally activated delayed fluorescence materials for organic light-emitting diodes. *Nature Reviews Materials*, 3. Available from <https://doi.org/10.1038/natrevmats.2018.20>, <http://www.nature.com/natrevmats/>.
- Liu, X., Long, Y.-Z., Liao, L., Duan, X., & Fan, Z. (2012). Large-scale integration of semiconductor nanowires for high-performance flexible electronics. *ACS Nano*, 6(3), 1888–1900. Available from <https://doi.org/10.1021/nn204848r>.
- Liu, H., Peng, H., Li, K., Lu, L., Deng, J., Liu, Y., Qiu, C., Li, G., & Cheng, X. (2022). Transfer printing of solution-processed 3D ZnO nanostructures with ultra-high yield for flexible metasurface color filter. *Advanced Materials Interfaces*, 9(21), 2101963. Available from <https://doi.org/10.1002/admi.202101963>.
- Liu, Z., Wu, J., Cai, C., Yang, B., & Qi, Zm (2022). Flexible hyperspectral surface plasmon resonance microscopy. *Nature Communications*, 13(1). Available from <https://doi.org/10.1038/s41467-022-34196-7>, <https://www.nature.com/ncomms/>.
- Liu, W., Zou, Q., Zheng, C., & Jin, C. (2019). Metal-assisted transfer strategy for construction of 2D and 3D nanostructures on an elastic substrate. *ACS Nano*, 13(1), 440–448. Available from <https://doi.org/10.1021/acsnano.8b06623>, <http://pubs.acs.org/journal/ancac3>.
- Li, H., Wang, Z., Cao, Y., Chen, Y., & Feng, X. (2021). High-efficiency transfer printing using droplet stamps for robust hybrid integration of flexible devices. *ACS Applied Materials and Interfaces*, 13(1), 1612–1619. Available from <https://doi.org/10.1021/acami.0c19837>, <http://pubs.acs.org/journal/aamick>.
- Li, X., Zhao, Y.-B., Fan, F., Levina, L., Liu, M., Quintero-Bermudez, R., Gong, X., Quan, L. N., Fan, J., Yang, Z., Hoogland, S., Voznyy, O., Lu, Z.-H., & Sargent, E. H. (2018). Bright colloidal

- quantum dot light-emitting diodes enabled by efficient chlorination. *Nature Photonics*, 12(3), 159–164. Available from <https://doi.org/10.1038/s41566-018-0105-8>.
- Lyons, K., Pang, S., Kwiat, P. G., & Jordan, A. N. (2016). Precision optical displacement measurements using biphotons. *Physical Review A*, 93(4). Available from <https://doi.org/10.1103/PhysRevA.93.043841>, <http://harvest.aps.org/bagit/articles/10.1103/PhysRevA.93.043841/apsxml>.
- Martínez, A. (2018). Polarimetry enabled by nanophotonics. *Science (New York, N.Y.)*, 362(6416), 750–751. Available from <https://doi.org/10.1126/science.aau7494>, <http://science.sciencemag.org/content/362/6416/750/tab-pdf>.
- Meitl, M. A., Zhu, Z. T., Kumar, V., Lee, K. J., Feng, X., Huang, Y. Y., Adesida, I., Nuzzo, R. G., & Rogers, J. A. (2006). Transfer printing by kinetic control of adhesion to an elastomeric stamp. *Nature Materials*, 5(1), 33–38. Available from <https://doi.org/10.1038/nmat1532>, <http://www.nature.com/nmat/>.
- Menard, E., Lee, K. J., Khang, D. Y., Nuzzo, R. G., & Rogers, J. A. (2004). A printable form of silicon for high performance thin film transistors on plastic substrates. *Applied Physics Letters*, 84(26), 5398–5400. Available from <https://doi.org/10.1063/1.1767591>.
- Meng, Y., Chen, Y., Lu, L., Ding, Y., Cusano, A., Fan, J. A., Hu, Q., Wang, K., Xie, Z., Liu, Z., Yang, Y., Liu, Q., Gong, M., Xiao, Q., Sun, S., Zhang, M., Yuan, X., & Ni, X. (2021). Optical meta-waveguides for integrated photonics and beyond. *Light: Science and Applications*, 10(1). Available from <https://doi.org/10.1038/s41377-021-00655-x>, <http://www.nature.com/lsa/>.
- Naldoni, A., Shalae, V. M., & Brongersma, M. L. (2017). Applying plasmonics to a sustainable future. *Science (New York, N.Y.)*, 356(6341), 908–909. Available from <https://doi.org/10.1126/science.aan5802>.
- Nam, S., Jiang, X., Xiong, Q., Ham, D., & Lieber, C. M. (2009). Vertically integrated, three-dimensional nanowire complementary metal-oxide-semiconductor circuits. *Proceedings of the National Academy of Sciences of the United States of America*, 106(50), 21035–21038. Available from <https://doi.org/10.1073/pnas.0911713106>, <http://www.pnas.org/content/106/50/21035.full.pdf>, United States.
- Ni, X., Wong, Z. J., Mrejen, M., Wang, Y., & Zhang, X. (2015). An ultrathin invisibility skin cloak for visible light. *Science (New York, N.Y.)*, 349(6254), 1310–1314. Available from <https://doi.org/10.1126/science.aac9411>, <http://www.sciencemag.org/content/349/6254/1310.full.pdf>.
- Oh, J., Yuan, H. C., & Branz, H. M. (2012). An 18.2%-efficient black-silicon solar cell achieved through control of carrier recombination in nanostructures. *Nature Nanotechnology*, 7(11), 743–748. Available from <https://doi.org/10.1038/nnano.2012.166>, <http://www.nature.com/nnano/index.html>.
- Olle, M., & Viršile, A. (2013). The effects of light-emitting diode lighting on greenhouse plant growth and quality. *Agricultural and Food Science*, 22(2), 223–234. Available from <https://doi.org/10.23986/afsci.7897>, <http://ojs.tsv.fi/index.php/AFS/article/view/7897/6303>.
- Ouyang, W., Teng, F., He, H., Jr, & Fang, X. (2019). Enhancing the photoelectric performance of photodetectors based on metal oxide semiconductors by charge-carrier engineering. *Advanced Functional Materials*, 29(9), 1807672. Available from <https://doi.org/10.1002/adfm.201807672>.
- Park, S. I., Xiong, Y., Kim, R. H., Elvikis, P., Meitl, M., Kim, D. H., Wu, J., Yoon, J., Chang-Jae, Y., Liu, Z., Huang, Y., Hwang, K. C., Ferreira, P., Xiuling, L., Choquette, K., & Rogers, J. A. (2009). Printed assemblies of inorganic light-emitting diodes for deformable and semitransparent displays. *Science (New York, N.Y.)*, 325(5943), 977–981. Available from <https://doi.org/10.1126/science.1175690>.
- Park, J. K., Zhang, Y., Xu, B., & Kim, S. (2021). Pattern transfer of large-scale thin membranes with controllable self-delamination interface for integrated functional systems. *Nature Communications*, 12(1). Available from <https://doi.org/10.1038/s41467-021-27208-5>, <http://www.nature.com/ncomms/index.html>.
- Pogue, B. W. (2019). Biomedical engineering or biomedical optics: Will the real discipline please stand up? *Journal of Biomedical Optics*, 24(4), 1. Available from <https://doi.org/10.1117/1.jbo.24.4.040101>.
- Rizzo, A., Mazzeo, M., Palumbo, M., Lerario, G., D'Amone, S., Cingolani, R., & Gigli, G. (2008). Hybrid light-emitting diodes from microcontact-printing double-transfer of colloidal semiconductor CdSe/ZnS quantum dots onto organic layers. *Advanced Materials*, 20(10), 1886–1891. Available from <https://doi.org/10.1002/adma.200701480Italy>, <http://www3.interscience.wiley.com/cgi-bin/full-text/119139589/PDFSTART>.

- Rogers, J. A., & Nuzzo, R. G. (2005). Recent progress in soft lithography. *Materials Today*, 8(2), 50–56. Available from [https://doi.org/10.1016/S1369-7021\(05\)00702-9](https://doi.org/10.1016/S1369-7021(05)00702-9), <http://www.journals.elsevier.com/materials-today/>.
- Safaei, A., Modak, S., Lee, J., Chandra, S., Franklin, D., Vázquez-Guardado, A., & Chanda, D. (2018). Multi-spectral frequency selective mid-infrared microbolometers. *Optics Express*, 26(25), 32931. Available from <https://doi.org/10.1364/oe.26.032931>.
- Saliba, M., Matsui, T., Domanski, K., Seo, J. Y., Ummadisingu, A., Zakeeruddin, S. M., Correa-Baena, J. P., Tress, W. R., Abate, A., Hagfeldt, A., & Grätzel, M. (2016). Incorporation of rubidium cations into perovskite solar cells improves photovoltaic performance. *Science (New York, N.Y.)*, 354(6309), 206–209. Available from <https://doi.org/10.1126/science.aah5557>, <http://science.sciencemag.org/content/sci/354/6309/206.full.pdf>.
- Sharma, B. K., Jang, B., Lee, J. E., Bae, S. H., Kim, T. W., Lee, H. J., Kim, J. H., & Ahn, J. H. (2013). Load-controlled roll transfer of oxide transistors for stretchable electronics. *Advanced Functional Materials*, 23(16), 2024–2032. Available from <https://doi.org/10.1002/adfm.201202519>.
- Shi, J., Li, X., Cheng, H., Liu, Z., Zhao, L., Yang, T., Dai, Z., Cheng, Z., Shi, E., Yang, L., Zhang, Z., Cao, A., Zhu, H., & Fang, Y. (2016). Graphene reinforced carbon nanotube networks for wearable strain sensors. *Advanced Functional Materials*, 26(13), 2078–2084. Available from <https://doi.org/10.1002/adfm.201504804>, [http://onlinelibrary.wiley.com/journal/10.1002/\(ISSN\)1616-3028](http://onlinelibrary.wiley.com/journal/10.1002/(ISSN)1616-3028).
- Smirnov, V., Stephan, S., Westphal, M., Emmrich, D., Beyer, A., Götzhäuser, A., Lienau, C., & Silies, M. (2021). Transmitting surface plasmon polaritons across nanometer-sized gaps by optical near-field coupling. *ACS Photonics*, 8(3), 832–840. Available from <https://doi.org/10.1021/acsp Photonics.0c01797>, <http://pubs.acs.org/journal/apchd5>.
- Sollami Deleka, S., Östling, M., & Li, J. (2019). Wet transfer of inkjet printed graphene for microsuper-capacitors on arbitrary substrates. *ACS Applied Energy Materials*, 2(1), 158–163. Available from <https://doi.org/10.1021/acsaem.8b01225>, <http://pubs.acs.org/journal/aeemcq>.
- Stewart, M. E., Mack, N. H., Malyarchuk, V., Soares, J. A. N. T., Lee, T. W., Gray, S. K., Nuzzo, R. G., & Rogers, J. A. (2006). Quantitative multispectral biosensing and 1D imaging using quasi-3D plasmonic crystals. *Proceedings of the National Academy of Sciences of the United States of America*, 103(46), 17143–17148. Available from <https://doi.org/10.1073/pnas.0606216103>.
- Stockman, M. I., Kneipp, K., Bozhevolnyi, S. I., Saha, S., Dutta, A., Ndukaife, J., Kinsey, N., Reddy, H., Guler, U., Shalae, V. M., Boltasheva, A., Gholipour, B., Krishnamoorthy, H. N. S., MacDonald, K. F., Soci, C., Zheludev, N. I., Savinov, V., Singh, R., Groß, P., . . . Kling, M. F. (2018). Roadmap on plasmonics. *Journal of Optics*, 20(4), 043001. Available from <https://doi.org/10.1088/2040-8986/aaa114>.
- Suk, J. W., Na, S. R., Stromberg, R. J., Stauffer, D., Lee, J., Ruoff, R. S., & Liechti, K. M. (2016). Probing the adhesion interactions of graphene on silicon oxide by nanoindentation. *Carbon*, 103, 63–72. Available from <https://doi.org/10.1016/j.carbon.2016.02.079>, <http://www.journals.elsevier.com/carbon/>.
- Sun, Y., Kim, S., Adesida, I., & Rogers, J. A. (2005). Bendable GaAs metal-semiconductor field-effect transistors formed with printed GaAs wire arrays on plastic substrates. *Applied Physics Letters*, 87(8), 083501. Available from <https://doi.org/10.1063/1.2032609>.
- Sun, Y., & Rogers, J. A. (2007). Inorganic semiconductors for flexible electronics. *Advanced Materials*, 19(15), 1897–1916. Available from <https://doi.org/10.1002/adma.200602223>.
- Sun, S., Zhou, Z., Zhang, C., Gao, Y., Duan, Z., Xiao, S., & Song, Q. (2017). All-dielectric full-color printing with TiO₂ metasurfaces. *ACS Nano*, 11(5), 4445–4452. Available from <https://doi.org/10.1021/acsnano.7b00415>, <http://pubs.acs.org/journal/ancac3>.
- Teng, F., Hu, K., Ouyang, W., & Fang, X. (2018). Photoelectric detectors based on inorganic p-type semiconductor materials. *Advanced Materials*, 30(35), 1706262. Available from <https://doi.org/10.1002/adma.201706262>.
- Thanh, Q. N., Jeong, H., Kim, J., Kevek, J. W., Ahn, Y. H., Lee, S., Minot, E. D., & Park, J. Y. (2012). Transfer-printing of as-fabricated carbon nanotube devices onto various substrates. *Advanced Materials*, 24(33), 4499–4504. Available from <https://doi.org/10.1002/adma.201201794>.
- Tong, S., Sun, J., & Yang, J. (2018). Printed thin-film transistors: Research from China. *ACS Applied Materials and Interfaces*, 10(31), 25902–25924. Available from <https://doi.org/10.1021/acsaami.7b16413>, <http://pubs.acs.org/journal/aamick>.

- Tseng, M. L., Yang, J., Semmlinger, M., Zhang, C., Nordlander, P., & Halas, N. J. (2017). Two-dimensional active tuning of an aluminum plasmonic array for full-spectrum response. *Nano Letters*, 17(10), 6034–6039. Available from <https://doi.org/10.1021/acs.nanolett.7b02350>, <http://pubs.acs.org/journal/nalefd>.
- Vázquez-Guardado, A., Smith, A., Wilson, W., Ortega, J., Perez, J. M., & Chanda, D. (2016). Hybrid cavity-coupled plasmonic biosensors for low concentration, label-free and selective biomolecular detection. *Optics Express*, 22, 25785. Available from <https://doi.org/10.1364/oe.24.025785>.
- Wang, Q., Han, W., Wang, Y., Lu, M., & Dong, L. (2018). Tape nanolithography: a rapid and simple method for fabricating flexible, wearable nanophotonic devices. *Microsystems and Nanoengineering*, 4(1). Available from <https://doi.org/10.1038/s41378-018-0031-4>, <http://www.nature.com/micronano/>.
- Wang, T., Zhang, J., Xue, P., Chen, H., Ye, S., Wang, S., Yu, Y., & Yang, B. (2014). Nanotransfer printing of gold disk, ring and crescent arrays and their IR range optical properties. *Journal of Materials Chemistry C*, 2(13), 2333. Available from <https://doi.org/10.1039/c3tc31338g>.
- Webb, R. C., Bonifas, A. P., Behnaz, A., Zhang, Y., Yu, K. J., Cheng, H., Shi, M., Bian, Z., Liu, Z., Kim, Y.-S., Yeo, W.-H., Park, J. S., Song, J., Li, Y., Huang, Y., Gorbach, A. M., & Rogers, J. A. (2013). Ultrathin conformal devices for precise and continuous thermal characterization of human skin. *Nature Materials*, 12(10), 938–944. Available from <https://doi.org/10.1038/nmat3755>.
- Wie, D. S., Zhang, Y., Kim, M. K., Kim, B., Park, S., Kim, Y. J., Irazoqui, P. P., Zheng, X., Xu, B., & Lee, C. H. (2018). Wafer-recyclable, environment-friendly transfer printing for large-scale thin-film nanoelectronics. *Proceedings of the National Academy of Sciences of the United States of America*, 115(31), E7236–E7244. Available from <https://doi.org/10.1073/pnas.1806640115>, <http://www.pnas.org/content/pnas/115/31/E7236.pdf>.
- Willner, A. E., Huang, H., Yan, Y., Ren, Y., Ahmed, N., Xie, G., Bao, C., Li, L., Cao, Y., Zhao, Z., Wang, J., Lavery, M. P. J., Tur, M., Ramachandran, S., Molisch, A. F., Ashrafi, N., & Ashrafi, S. (2015). Optical communications using orbital angular momentum beams. *Advances in Optics and Photonics*, 7(1), 66–106. Available from <https://doi.org/10.1364/AOP.7.000066>, http://www.optic-sinfobase.org/DirectPDFAccess/9FEA734D-D699-EB1B-BC66992F4C332BE3_314298/aop-7-1-66.pdf?da=1&id=314298&seq=0&mobile=no.
- Winters, S., Hallam, T., Nolan, H., & Duesberg, G. S. (2012). Production of 3D-shaped graphene via transfer printing. *Physica Status Solidi (b)*, 249(12), 2515–2518. Available from <https://doi.org/10.1002/pssb.201200157>.
- Witkowski, B. S., Pietruszka, R., Gieraltowska, S., Wachnicki, L., Przybylinska, H., & Godlewski, M. (2017). Photoresistor based on ZnO nanorods grown on a p-type silicon substrate. *Opto-Electronics Review*, 25(1), 15–18. Available from <https://doi.org/10.1016/j.opelre.2017.02.001>, <http://journals.pan.pl/opusre>.
- Xu, S., Yan, Z., Jang, K. I., Huang, W., Fu, H., Kim, J., Wei, Z., Flavin, M., McCracken, J., Wang, R., Badea, A., Liu, Y., Xiao, D., Zhou, G., Lee, J., Chung, H. U., Cheng, H., Ren, W., Banks, A., . . . Rogers, J. A. (2015). Assembly of micro/nanomaterials into complex, three-dimensional architectures by compressive buckling. *Science (New York, N.Y.)*, 347(6218), 154–159. Available from <https://doi.org/10.1126/science.1260960>, <http://www.sciencemag.org/content/347/6218/154.full.pdf>.
- Yamashita, T., Okada, H., Itoh, T., & Kobayashi, T. (2015). Manufacturing process for piezoelectric strain sensor sheet involving transfer printing methods. *Japanese Journal of Applied Physics*, 54(10S), 10ND08. Available from <https://doi.org/10.7567/jjap.54.10nd08>.
- Yang, Y., Hwang, Y., Cho, H. A., Song, J. H., Park, S. J., Rogers, J. A., & Ko, H. C. (2011). Arrays of silicon micro/nanostructures formed in suspended configurations for deterministic assembly using flat and roller-type stamps. *Small (Weinheim an der Bergstrasse, Germany)*, 7(4), 484–491. Available from <https://doi.org/10.1002/sml.201001633>.
- Yang, X., Yao, J., Rho, J., Yin, X., & Zhang, X. (2012). Experimental realization of three-dimensional indefinite cavities at the nanoscale with anomalous scaling laws. *Nature Photonics*, 6(7), 450–454. Available from <https://doi.org/10.1038/nphoton.2012.124>.
- Yan, Z., Zhang, F., Liu, F., Han, M., Ou, D., Liu, Y., Lin, Q., Guo, X., Fu, H., Xie, Z., Gao, M., Huang, Y., Kim, J. H., Qiu, Y., Nan, K., Kim, J., Gutruf, P., Luo, H., Zhao, A., . . . Rogers, J. A. (2016). Mechanical assembly of complex, 3D mesostructures from releasable multilayers of advanced

- materials. *Science Advances*, 2(9). Available from <https://doi.org/10.1126/sciadv.1601014>, <http://advances.sciencemag.org/content/advances/2/9/e1601014.full.pdf>.
- Yan, Z., Zhang, F., Wang, J., Liu, F., Guo, X., Nan, K., Lin, Q., Gao, M., Xiao, D., Shi, Y., Qiu, Y., Luan, H., Kim, J. H., Wang, Y., Luo, H., Han, M., Huang, Y., Zhang, Y., & Rogers, J. A. (2016). Controlled mechanical buckling for origami-inspired construction of 3D microstructures in advanced materials. *Advanced Functional Materials*, 26(16), 2629–2639. Available from <https://doi.org/10.1002/adfm.201504901>, [http://onlinelibrary.wiley.com/journal/10.1002/\(ISSN\)1616-3028](http://onlinelibrary.wiley.com/journal/10.1002/(ISSN)1616-3028).
- Yi, H., Seong, M., Sun, K., Hwang, I., Lee, K., Cha, C., Kim, T., & Jeong, H. E. (2018). Wet-responsive, reconfigurable, and biocompatible hydrogel adhesive films for transfer printing of nano-membranes. *Advanced Functional Materials*, 28(18), 1706498. Available from <https://doi.org/10.1002/adfm.201706498>.
- Yoon, J., Jo, S., Chun, I. S., Jung, I., Kim, H.-S., Meitl, M., Menard, E., Li, X., Coleman, J. J., Paik, U., & Rogers, J. A. (2010). GaAs photovoltaics and optoelectronics using releasable multilayer epitaxial assemblies. *Nature*, 465(7296), 329–333. Available from <https://doi.org/10.1038/nature09054>.
- Yoo, D., Johnson, T. W., Cherukulappurath, S., Norris, D. J., & Oh, S. H. (2015). Template-stripped tunable plasmonic devices on stretchable and rollable substrates. *ACS Nano*, 9(11), 10647–10654. Available from <https://doi.org/10.1021/acs.nano.5b05279>, <http://pubs.acs.org/journal/ancac3>.
- Zhang, Y., Liu, Q., & Xu, B. (2017). Liquid-assisted, etching-free, mechanical peeling of 2D materials. *Extreme Mechanics Letters*, 16, 33–40. Available from <https://doi.org/10.1016/j.eml.2017.08.005>.
- Zhang, M., Lu, M., Ge, C., & Cunningham, B. T. (2014). Plasmonic external cavity laser refractometric sensor. *Optics Express*, 22(17), 20347. Available from <https://doi.org/10.1364/oe.22.020347>.
- Zhang, K., Wang, S., & Yang, Y. (2016). A one-structure-based piezo-tribo-pyro-photoelectric effects coupled nanogenerator for simultaneously scavenging mechanical, thermal, and solar energies. *Advanced Energy Materials*, 7(6), 1601852. Available from <https://doi.org/10.1002/aenm.201601852>.
- Zhang, J., Yang, Q., Saito, K., Nozato, K., Williams, D. R., & Rossi, E. A. (2015). An adaptive optics imaging system designed for clinical use. *Biomedical Optics Express*, 6(6), 2120. Available from <https://doi.org/10.1364/boe.6.002120>.
- Zhang, Y., Yan, Z., Nan, K., Xiao, D., Liu, Y., Luan, H., Fu, H., Wang, X., Yang, Q., Wang, J., Ren, W., Si, H., Liu, F., Yang, L., Li, H., Wang, J., Guo, X., Luo, H., Wang, L., ... Rogers, J. A. (2015). A mechanically driven form of Kirigami as a route to 3D mesostructures in micro/nanomembranes. *Proceedings of the National Academy of Sciences of the United States of America*, 112(38), 11757–11764. Available from <https://doi.org/10.1073/pnas.1515602112>, <http://www.pnas.org/content/112/38/11757.full.pdf>.
- Zhang, Y., Yin, M., Baek, Y., Lee, K., Zangari, G., Cai, L., & Xu, B. (2020). Capillary transfer of soft films. *Proceedings of the National Academy of Sciences*, 117(10), 5210–5216. Available from <https://doi.org/10.1073/pnas.200034011>.
- Zhao, Z. J., Ahn, J., Hwang, S. H., Ko, J., Jeong, Y., Bok, M., Kang, H. J., Choi, J., Jeon, S., Park, I., & Jeong, J. H. (2021). Large-area nanogap-controlled 3D nanoarchitectures fabricated via layer-by-layer nanoimprint. *ACS Nano*, 15(1), 503–514. Available from <https://doi.org/10.1021/acs.nano.0c05290>, <http://pubs.acs.org/journal/ancac3>.
- Zhao, Z. J., Shin, S. H., Lee, S. Y., Son, B., Liao, Y., Hwang, S., Jeon, S., Kang, H., Kim, M., & Jeong, J. H. (2022). Direct chemisorption-assisted nanotransfer printing with wafer-scale uniformity and controllability. *ACS Nano*, 16(1), 378–385. Available from <https://doi.org/10.1021/acsnano.1c06781>, <http://pubs.acs.org/journal/ancac3>.
- Zheng, C., Shen, Y., Liu, M., Liu, W., Wu, S., & Jin, C. (2019). Layer-by-layer assembly of three-dimensional optical functional nanostructures. *ACS Nano*, 13(5), 5583–5590. Available from <https://doi.org/10.1021/acs.nano.9b00549>, <http://pubs.acs.org/journal/ancac3>.

CHAPTER 10

Flexible sensors enabled by transfer printing techniques

Xinghao Huang¹, Liangshu Liu¹, Jaemin Seo¹, Qinai Zhao¹ and Hangbo Zhao^{1,2}

¹Department of Aerospace and Mechanical Engineering, University of Southern California, Los Angeles, CA, United States

²Alfred E. Mann Department of Biomedical Engineering, University of Southern California, Los Angeles, CA, United States

10.1 Strain sensors

Strain sensors transduce mechanical deformations into changes in the electrical or optical properties of the sensing elements. Currently, there are various types of strain sensors, including piezoresistive, piezoelectric, capacitive, optical, and triboelectric strain sensors (Souri et al., 2020). Among all these types, piezoresistive and capacitive strain sensors are most commonly used due to their simple measurement interfaces. Conventional piezoresistive strain sensors, or strain gauges, usually consist of metallic units that are sensitive to mechanical strains. Deformations such as stretching, compressing, twisting, and bending can change the sensor's geometry or resistivity, resulting in an overall change in the resistance. Similarly, capacitive strain sensors rely on strain-induced changes in geometry or dielectric property. Electric potentials applied on structures such as parallel plates and interdigitated electrodes generate capacitance, which can change when the structures deform due to applied strain. Strain sensors have been widely used in industry to measure accurate deformations, vibrations, and various mechanical properties.

Recent developments in wearable technologies and soft robotics have increased the demand for flexible and stretchable electronics. Since it is challenging to measure strain and motions on soft surfaces with large, complex deformations, strain sensors that have conformal contact with target objects, generate high sensitivity, and sustain large deformation without fracture or hysteresis are becoming increasingly desirable. To fulfill these requirements, flexible and soft materials such as polymer thin films, elastomers, and hydrogels provide highly stretchable platforms. In addition, advances in material science and microfabrication have led to high-performance sensing elements, such as nanomaterials, conductive polymers, and doped silicon, as well as innovative sensing structures like serpentines, origami- and kirigami-inspired structures, which can be integrated with flexible/stretchable substrates to create high-performance strain sensors. However, assembling such sensing elements or structures on flexible/stretchable substrates can be challenging because they require chemical

processes or microscale patterning on rigid, planar substrates, such as silicon wafers or glasses. Traditional top-down and bottom-up fabrication methods are able to create these sensing elements and structures, but it is difficult to incorporate soft or flexible materials (Zhao et al., 2020).

Transfer printing provides a pathway for transferring the sensing elements to flexible or stretchable substrates. The process usually requires a soft, elastomeric stamp to pick up brittle sensing elements from planar substrates, then release them on target substrates. The transfer printing process allows more complicated fabrication to take place before and after transferring the sensing elements, which can enable strain sensors to achieve higher functionality with better sensing performances. Since flexible and stretchable strain sensors are the two main categories in current strain sensor research, the required transfer printing processes are different. This section will specifically discuss how transfer printing is utilized and adapted to fabricate flexible and stretchable strain sensors.

Flexible strain sensors usually utilize substrate materials that have excellent mechanical flexibility, electrical insulation, and optical transparency. Polymer materials such as polyimide (PI), polyethylene terephthalate (PET), polyvinyl alcohol (PVA), and polyethylene (PE) are commonly used as flexible substrates (Zhou et al., 2021). By designing the sensors to be structurally flexible, the sensor structures can have low bending stiffness and are able to bend, twist, and conform to different shapes without fracturing. Common sensing elements in flexible strain sensors include inorganic, rigid materials, and conductive nanomaterials, which are usually fabricated or grown on planar substrates. For instance, metal and doped silicon are strain sensitive but have small fracture limit, which is usually below 5% (Souri et al., 2020). Transfer printing offers a reliable way to transfer these fragile elements from rigid substrates to flexible substrates. For example, a small vacuum collet can act as a stamp to pick up piezoelectric strain sensor arrays made of lead zirconate titanate (PZT) from wafers and print them on PI films (Yamashita et al., 2018) (Fig. 10.1A). Coating a layer of ultraviolet (UV)-curable resin can then fix the sensor arrays in place. The completed sensor array can detect the oscillatory bending strains on a stainless-steel cantilever with microstrain-level sensitivity. Another commonly used stamp material is polydimethylsiloxane (PDMS), which has good adhesion and conformability. For example, a recent work uses PDMS slabs to pick up freestanding SiC nanomembranes from silicon wafers and release them on PI layers (Phan et al., 2019) (Fig. 10.1B). Depositing metals on SiC membranes forms electrodes and coating an extra PI layer completes the device encapsulation. Such a SiC-based flexible platform can utilize its piezoresistive and thermoresistive properties to enable high sensitivity in both strain and temperature sensing. Transfer printing can also be used to fabricate flexible strain sensors that use conductive nanoparticles. In a representative work (Ketelsen et al., 2018), a cross-linked gold nanoparticles film is created by a layer-by-layer spin-coating method. Since the process requires a

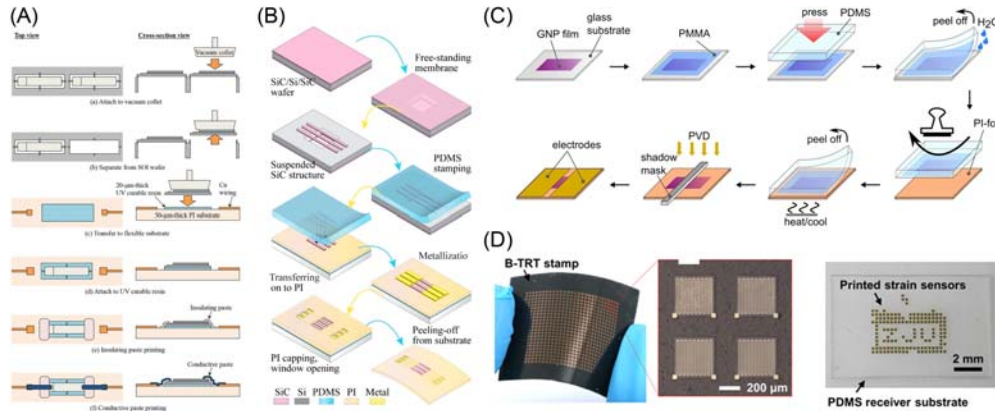


Figure 10.1 Examples of flexible strain sensors fabricated using transfer printing techniques.

(A) Transfer printing of PZT strain sensors using a vacuum collet. (B) Transfer printing of SiC components using PDMS stamps. (C) Contact printing of cross-linked gold nanoparticle films on PI substrates. (D) Programmable transfer printing of strain sensors using a laser scanner and thermal release tapes. (A) Adapted from Yamashita, T., Takamatsu, S., Okada, H., Itoh, T., & Kobayashi, T. (2018). Development of flexible piezoelectric strain sensor array. *Electrical Engineering in Japan*, 204(1), 52–58 <https://doi.org/10.1002/eej.23084>. (B) Reprinted with permission from Phan, H.P., Zhong, Y., Nguyen, T.K., Park, Y., Dinh, T., Song, E., Vadivelu, R.K., Masud, M.K., Li, J., Shiddiky, M.J.A., Dao, D., Yamauchi, Y., Rogers, J.A., & Nguyen, N.T. (2019). Long-lived, transferred crystalline silicon carbide nanomembranes for implantable flexible electronics. *ACS Nano*, 13(10), 11572–11581: <http://pubs.acs.org/journal/ancac3.1021/acs.nano.9b05168>. Copyright 2019 American Chemical Society. (C) Reprinted with permission from Ketelsen, B., Yesilmen, M., Schlicke, H., Noei, H., Su, C.H., Liao, Y.C., & Vossmeier, T. (2018). Fabrication of strain gauges via contact printing: A simple route to healthcare sensors based on cross-linked gold nanoparticles. *ACS Applied Materials and Interfaces*, 43, 37374–37385. <http://pubs.acs.org/journal/aamick.1021/acsami.8b12057>. Copyright 2018 American Chemical Society. (D) Adapted from Wang, C., Linghu, C., Nie, S., Li, C., Lei, Q., Tao, X., Zeng, Y., Du, Y., Zhang, S., Yu, K., Jin, H., Chen, W., & Song, J. (2020). Programmable and scalable transfer printing with high reliability and efficiency for flexible inorganic electronics. *Science Advances*, 6(25). <https://advances.sciencemag.org/content/advances/6/25/EABB2393.full.pdf.1126/sciadv.abb2393>.

chemically robust substrate, the films are fabricated on glass substrates first and transferred to PI film via a PDMS stamp and a heating/cooling process (Fig. 10.1C). The resulting resistive strain sensors have high gauge factors ($GF = \frac{\Delta R/R_0}{\epsilon} = 14\text{--}26$), excellent durability (10,000 cycles of strain-relaxation), and a strain range of 1.2%. However, selectively transferring small-size flexible strain sensors can be difficult for the methods mentioned above because all materials attached to the stamp are printed. One recent work achieves programmable transfer printing by using external thermal stimuli (Wang et al., 2020). In this work, a thermal release tape attached to a stamp contains thermally expandable microspheres, which initially remain in flat surface topography with strong adhesion to pick up samples. When exposed to external thermal stimuli at 90°C, the microspheres expand and form surface hierarchical

microstructures, which weakens the adhesion to release samples. To achieve programmable and scalable printing with high throughput, a scanning laser system is used to apply precise, localized heating at fast scanning speeds. This method is used to successfully transfer wafer-scale, ultrathin strain sensors (Fig. 10.1D), surface acoustic wave sensors, and micro-light-emitting diodes (LEDs) from silicon-based substrates to PI and PDMS substrates at spatially organized patterns.

Compared to flexible strain sensors, stretchable strain sensors with intrinsically stretchable materials can achieve higher stretchability, which is usually above 50% for wearable applications (Souri et al., 2020). Commonly used stretchable materials include silicone elastomers, rubbers, thermoplastic polymers, or natural fibers (Khalid & Chang, 2022; Souri et al., 2020). They serve as stretchable platforms to support sensing materials such as conductive nanomaterials or conductive polymers, which act as stretchable electrodes and interconnects for strain sensing. One typical method to combine conductive materials and stretchable platforms is to form conductive composites, in which nanomaterials are dispensed into polymer matrices as fillers to form conductive paths (Khalid & Chang, 2022). Transfer printing can help increase the production rate for such stretchable conductive composites. A rapid fabrication process from a recent work achieves massive production of capacitive strain sensors made of off-the-shelf insulating and conductive acrylic tapes (Bartlett et al., 2016). Both types of tapes are laser-cut into desired shapes and transferred onto each other to form parallel-plate capacitors (Fig. 10.2A). With a gauge factor of 0.9, the sensors can be stretched over 100% strain and remain functional over 25,000 cycles of loading, showing low hysteresis and creep. Transfer printing can also introduce prestretch on stretchable conductive polymer. In a representative work, a self-healable semiconducting polymer film is first developed on a wafer and picked up by a PDMS stamp (Oh et al., 2019). To show the film material is highly strain sensitive, the PDMS is stretched 100% strain and attached the film to another doped Si substrate for depositing gold electrodes (Fig. 10.2B). The results show that the semiconducting polymer film has a gauge factor of 5.75×10^5 at 100% strain.

On the other hand, transfer printing can deposit conductive materials directly onto the stretchable materials' surfaces instead of mixing them. Fabrication processes that utilize direct printing/coating stretchable sensing materials can allow more customization. A representative method to make soft strain sensors uses aerosol jet printing to directly print silver nanowire (AgNW) and PI to form desired sensor patterns on glass (Herbert et al., 2020), followed by transfer printing the pattern onto a silicone elastomer using water-soluble tapes (Fig. 10.2C). The final soft strain sensor can stretch up to 200% with a resistive gauge factor of up to 13. It can also be attached firmly to surfaces like skin or valves to perform different functions. In some cases, the stamp itself can become a part of the sensor's stretchable substrate. For example, this method enables a representative resistive strain sensor made by overlapped carbon nanotubes (CNTs) (Lee et al., 2019). During the fabrication process shown in Fig. 10.2D, the

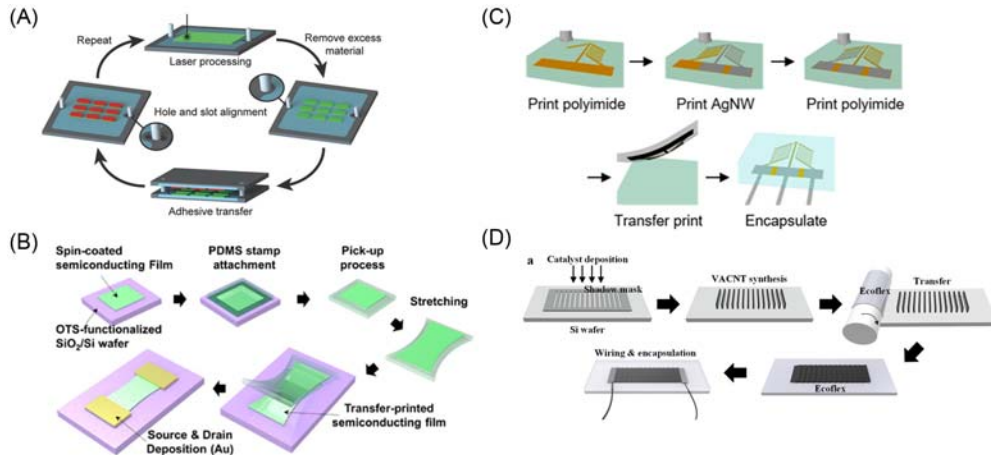


Figure 10.2 Schematic illustrations of fabricating stretchable strain sensors using transfer printing techniques. (A) Rapid transfer printing of capacitive strain sensors using conductive tapes. (B) Transfer printing of strain-sensitive semiconducting polymers. (C) Fabrication processes of AgNW-based stretchable strain sensors. (D) Fabrication processes of strain sensors made of overlapped carbon nanotubes. (A) Reprinted with permission from Bartlett, M.D., Markvicka, E.J., & Majidi, C. (2016). Rapid fabrication of soft, multilayered electronics for wearable biomonitoring. *Advanced Functional Materials*, 26(46), 8496–8504: [http://onlinelibrary.wiley.com/journal/10.1002/\(ISSN\)1616-3028](http://onlinelibrary.wiley.com/journal/10.1002/(ISSN)1616-3028). 1002/adfm.201602733. (B) Adapted from Oh, J.Y., Son, D., Katsumata, T., Lee, Y., Kim, Y., Lopez, J., Wu, H.C., Kang, J., Park, J., Gu, X., Mun, J., Wang, N.G.J., Yin, Y., Cai, W., Yun, Y., Tok, J.B.H., & Bao, Z. (2019). Stretchable self-healable semiconducting polymer film for active-matrix strain-sensing array. *Science Advances*, 5(11). <https://advances.sciencemag.org/content/5/11/eaav3097/tab-pdf.1126/sciadv.aav3097>. (C) Adapted from Herbert, R., Lim, H.R., Yeo, W.H., Yeo, W.H., Yeo, & W.H. (2020). Printed, soft, nanostructured strain sensors for monitoring of structural health and human physiology. *ACS Applied Materials and Interfaces*, 12(22), 25020–25030: <http://pubs.acs.org/journal/aamick.1021/acsami.0c04857>. (D) Adapted from Lee, J., Pyo, S., Kwon, D-S., Jo, E., Kim, W., Kim, & J. (2019). Ultrasensitive strain sensor based on separation of overlapped carbon nanotubes. *Small* (Weinheim an der Bergstrasse, Germany), 15(12), 1805120 <https://doi.org/10.1002/sml.201805120>. Copyright 2020 American Chemical Society.

line-patterned vertically aligned carbon nanotube (VACNT) bundles are synthesized on silicon wafers. A silicone (Ecoflex) substrate attached on a custom roller then pushes down and picks up VACNTs from wafers. This process changes the CNT direction from vertical to horizontal, overlapping each other to form conductive networks with varying resistance. Similarly, this method can also lead to capacitive strain sensors. In a recent work, VACNTs in interdigitated patterns are first encapsulated by PDMS on a wafer (Wang et al., 2022). The PDMS with VACNTs is then peeled off to apply another PDMS layer on its backside, creating a thin, repeatable, and pressure-insensitive strain sensor.

Another route to creating stretchable strain sensors is to use stretchable structures, which can accommodate large mechanical deformations through bending and twisting.

Stretchable structures can be fully attached to stretchable substrates, which remain in two-dimensional (2D) and measure plane strains. They can also be partially attached to stretchable substrates, leading to 3D structures for both in-plane and out-of-plane strain sensing. Since microfabrication is usually necessary to pattern stretchable structures on 2D substrates (referred to as 2D precursors), transfer printing provides a way to pick them up, apply backside modification, and bond them on soft substrates. In a recent work, transfer printing enables a wearable silent speech interface using 2D stretchable serpentine structures (Kim et al., 2022). The strain sensor array utilizes serpentine and mesh structures with ultrathin PI bilayers and a silicon nanomembrane to achieve biaxial strain sensing. After fabricating the silicon nanomembranes on wafers, a PDMS stamp with photoresist adhesive is used to pick up the silicon nanomembranes from the wafers and press them on a soft-baked PI layer (Fig. 10.3A). Dissolving the resist after fully baking PI removes the stamp. The completed strain sensor arrays are picked up by water-soluble tapes to form tattoos and then attached to specific locations on a subject's face to capture facial strains. Another type of 2D stretchable structure is wrinkled thin films, which can form stretchable parallel-plate capacitive strain sensors (Nur et al., 2018). As shown in Fig. 10.3B, a PDMS sheet first picks up fabricated parylene/Au films and then transfers them to both sides of a prestretched adhesive elastomer. After the relaxation of the elastomer, both films form compressive wrinkled structures on the surface. This novel design not only increases the strain range but also increases the gauge factor of the conventional parallel plate capacitive strain sensor from 1 to 3.

Recently, mechanically guided assembly of 3D mesostructures and transfer printing have enabled a new platform for 3D stretchable electronics. Water-soluble tapes first pick up 2D precursors and allow material deposition and chemical treatment at the bonding sites. Next, laminating the 2D precursor on an elastomer substrate creates strong covalent bonding at the bonding sites (Fig. 10.3C). The elastomer substrate can be either stretched after bonding (Guo et al., 2018) or prestretched before bonding (Zhao, et al., 2019), so the displacement of the bonding sites can transform 2D precursors to 3D stretchable structures through mechanical buckling. Such mechanically guided assembly method enables many novel 3D strain sensors. For example, a 3D strain sensor fabricated by two spiral copper ribbons on a silicone elastomer can detect large strains using an LED indicator (Guo et al., 2018). Treating the bonding sites with silicon dioxide (SiO_2) followed by UV-ozone treatment of both the bonding sites and the elastomer creates strong covalent bonding on the elastomer. By applying tensile strain on the elastomer, the spiral patterns can be transformed into 3D configurations through tensile buckling. At a critical strain, the two 3D ribbons touch each other, creating a closed-loop circuit to turn on an LED (Fig. 10.3B). An array of 3D strain sensors with programmed, varying, critical strains can sequentially light up LEDs to indicate applied strain levels from 0% to 50%. Another application of 3D

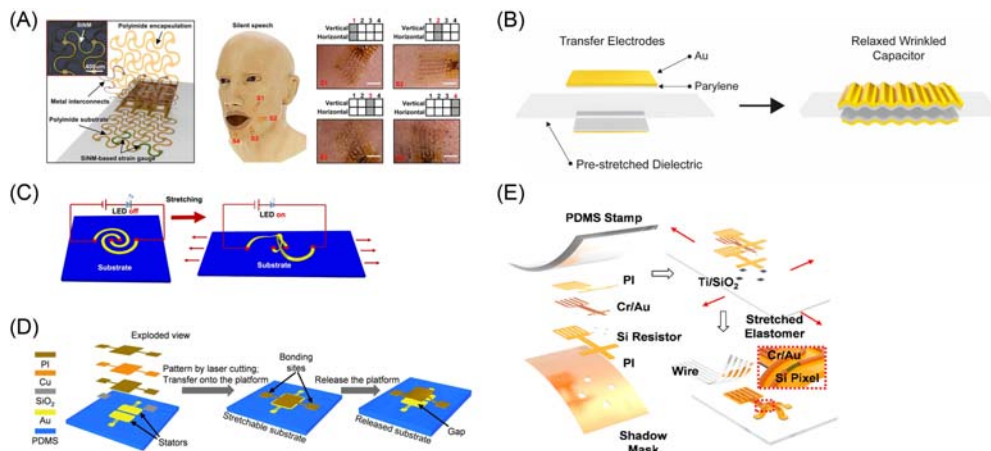


Figure 10.3 Schematic illustrations of fabricating mechanically buckled three-dimensional (3D) electronics. (A) Transfer printing of single-crystalline silicon nanomembrane-based strain sensors for facial strain mapping. (B) Capacitive strain sensors using wrinkled gold films. (C) 3D strain sensor using LED indicators. (D) Fabrication processes for a tunable seesaw-like 3D capacitive sensor. (E) Multimodal sensing using 3D piezoresistive structures. (A) Adapted from Kim, T., Shin, Y., Kang, K., Kim, K., Kim, G., Byeon, Y., Kim, H., Gao, Y., Lee, J.R., Son, G., Kim, T., Jun, Y., Kim, J., Lee, J., Um, S., Kwon, Y., Son, B.G., Cho, M., Sang, M., ... & Yu, K.J. (2022). Ultrathin crystalline-silicon-based strain gauges with deep learning algorithms for silent speech interfaces. *Nature Communications*, 13(1). <http://www.nature.com/ncomms/index.html.1038/s41467-022-33457-9>. (B) Reprinted with permission from Nur, R., Matsuhisa, N., Jiang, Z., Nayeem, M.O.G., Yokota, T., & Someya, T. (2018). A highly sensitive capacitive-type strain sensor using wrinkled ultrathin gold films. *Nano Letters*, 18(9) 5610–5617: <http://pubs.acs.org/journal/nalefd.1021/acs.nanolett.8b02088>. Copyright 2018 American Chemical Society. (C) Adapted from Guo, X., Wang, X., Ou, D., Ye J., Pang, W., Huang, Y., Rogers, J.A., & Zhang, Y. (2018). Controlled mechanical assembly of complex 3D mesostructures and strain sensors by tensile buckling. *NPJ Flexible Electronics*, 2(1). <http://nature.com/npjflexelectron/.1038/s41528-018-0028-y>. (D) Adapted from Ye J., Zhang F., Shen Z., Cao S., Jin T., Guo X., Li Z., Lin L., Zhang Y. (2021). Tunable seesaw-like 3D capacitive sensor for force and acceleration sensing. *NPJ Flexible Electronics*, 5, 28. (E) Reprinted with permission from Won, S.M., Wang, H., Kim, B.H., Lee K., Jang, H., Kwon, K., Han, M., Crawford, K.E., Li, H., Lee, Y., Yuan, X., Kim, S.B., Oh, Y.S., Jang W.J., Lee J.Y., Han, S., Kim, J., Wang, X., Xie, Z., ... & Rogers, J.A. (2019). Multimodal sensing with a three-dimensional piezoresistive structure. *ACS Nano*, 13(10), 10972–10979. <http://pubs.acs.org/journal/ancac3.1021/acs.nano.9b02030>. Copyright 2019 American Chemical Society.

mesostructures is measuring motions. In a representative work, the mechanical guided assembly method leads to a seesaw-like 3D capacitive sensor (Ye et al., 2021). The sensor layer is prepared on a water-soluble tape and then transferred to a stretched PDMS substrate (Fig. 10.3C). The buckled 3D structure can measure forces at 5.22 nN resolution and acceleration at sensitivity ranging from 5.59×10^{-3} to 0.197 pF/g. In addition, the mechanically guided assembly method also transforms many conventional strain sensors made of metal or silicon strain elements with

polymer bilayers into 3D configurations. Biaxially buckled 3D strain sensor systems can detect small contractions in muscle tissue, which outperforms the traditional microscopy methods (Zhao, et al., 2021). A similar 3D system can also detect compressive and shear strain (Won et al., 2019), which enables multimodal and multidirectional force sensing. Fig. 10.3D shows a representative 3D system that involves a 2D precursor made of PI layers and four silicon-based piezoresistive elements. After being picked up by a PDMS stamp followed by bonding site deposition, the 2D precursor is bonded to a prestretched Ecoflex substrate and then buckled to its 3D configuration. The resulting structures can sense multidirectional strain generated by the normal force, shear force, and bending.

In summary, transfer printing allows high-performance sensing materials and complex structures to be integrated into flexible and stretchable strain sensors. Although transfer printing for strain sensors is mostly manually controlled, strain sensors reported in current research show high sensitivity, high stretchability, and good conformability, and can measure multidirectional strain. These features enable strain sensing applications in wearable healthcare, soft robotics, and human–machine interfaces.

10.2 Pressure sensors

Mechanisms used for pressure sensing include piezoelectricity, piezoresistivity, triboelectricity, and many others. To enhance measurement accuracy and enlarge measuring range, miniaturization and flexibility of pressure sensors have become increasingly important. In biomedical engineering, the conformability of pressure sensors is also a significant requirement for wearable and implantable devices. For these purposes, sensors usually need to be relatively small in size but sensitive to load variations and highly tolerable with large deformations. Although elastomers possess excellent stretchability and conformability, the pressure-sensing elements composed of materials such as metals, graphene polyvinylidene difluoride (PVDF, a piezoelectric polymer), and nanoparticles are relatively stiff, where the mismatching of stiffness may lead to structural failure under large deformations and limit the performance of the sensors. To overcome this mechanical mismatch, the sensing elements usually need to be patterned into complex stretchable shapes at small scale, such as serpentine and kirigami-inspired structures using microfabrication methods including lithography, laser cutting, and 3D printing. As an emerging technique, transfer printing allows the transfer of patterned modules composed of relatively stiff materials onto soft substrates such as silicone rubbers. Therefore, it has been applied to the fabrication of a wide variety of force, pressure, and tactile sensors. In this section, recent progress in these sensors enabled by transfer printing is discussed based on the type of signals measured by the sensors, including voltage, resistance, and capacitance.

To sense passive voltage change induced by pressure changes, piezoelectric, triboelectric materials, and field effect transistors (FETs) are often employed. A tactile sensor based on

graphene FET and piezoelectric capacitance is presented in [Yogeswaran et al. \(2018\)](#), where the graphene array in the top gate of the FET is transferred to the substrate via transfer printing. The pressure variation on piezoelectric capacitance will result in voltage and current change in FET. The sensor shows improved sensitivity to pressure and durability against cyclic loads. In another representative study, a patterned PDMS array is bonded to an electrode array composed of liquid metal as a dielectric layer to develop a pressure-sensing artificial skin with capacitance mode and triboelectric mode ([Zhang, Liu, et al., 2019](#)). The capacitance mode can sense either proximity or pressure, while the triboelectric can measure both contact pressure and location with higher sensitivity in the low-pressure range. A wireless blood pressure sensor can sense the voltage output of a piezoelectric PVDF film to reflect the blood pressure change ([Dong et al., 2017](#)). The stretchable serpentine structure of the sensor is processed separately and transferred to a PDMS substrate via transfer printing ([Fig. 10.4A](#)).

Pressure sensing is also achievable by measuring resistance changes of conductors caused by changes in the geometries of conductors. For flexibility, the sensing elements and circuits are usually designed in curvy shapes or other stretchable formats. In a recent work, a transfer printing method using hydrogel as a template stamp is used to transfer conductive nanonetwork patterns onto surfaces with complex morphology ([Kang et al., 2019](#)). With this approach, a planar serpentine-shaped strain sensor and a pressure sensor are successfully developed to monitor finger motion and arterial pulses, respectively ([Fig. 10.4B](#)). Furthermore, a pressure sensor with a buckled CNT film is reported by [Kim et al. \(2019\)](#). The film is transferred to a swollen elastomer substrate and buckled during de-swelling. Another use of buckled 3D structures can be found in [Zhao et al. \(2021\)](#), where planar strain sensors are mechanically buckled to form a 3D framework. The integrated system can measure muscle contractile displacements and forces. In addition, the piezoresistive effects of semiconductors can also be employed in force and pressure sensing. A typical example involves the use of a piezoresistive silicone nanomembrane which is assembled into a 3D table-like shape after a transfer printing process and a mechanically guided assembly process ([Won et al., 2019](#)). The sensor can measure and separate multiple stress modes including normal pressure, bending, shearing, and temperature-related stimuli. Another example of piezoresistive pressure sensor integrated with a flexible actuator appears in [Ozioko et al. \(2021\)](#). The piezoresistive sensing element is fabricated using graphite paste encapsulated in an elastomer and the key element of the actuator is a gold spiral coil fabricated through lithography and assembled via transfer printing. The system can be applied to robotic fingertips for pressure mapping with potential to generate controlled vibration with feedback.

Capacitance changes can be employed to measure force or pressure as well since the distance between the plates of capacitance or their effective area can vary with external forces. [Fig. 10.4C](#) shows a highly sensitive pressure sensor capable of either normal or shear force sensing and insensitive to mechanical damage such as cuts and

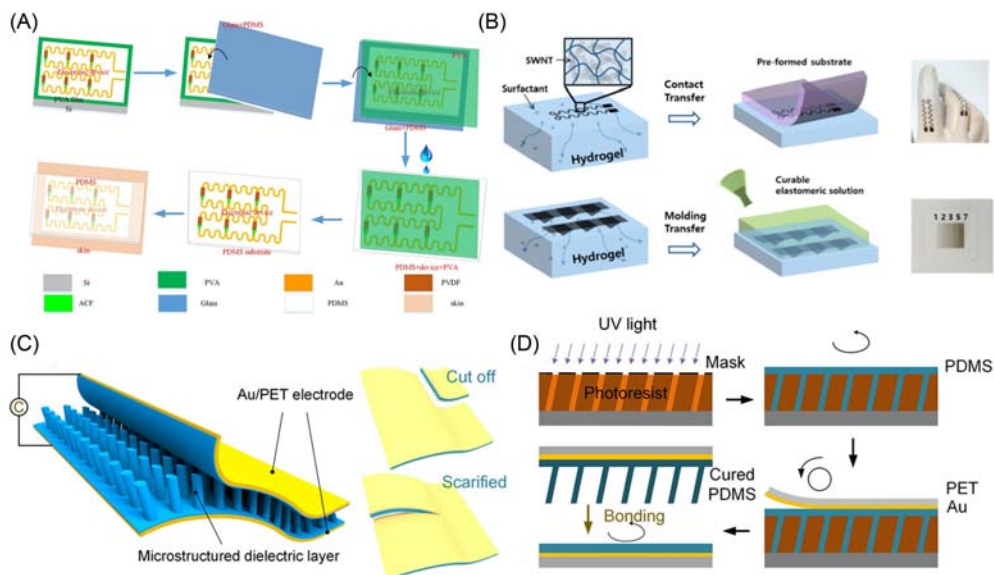


Figure 10.4 Examples of pressure sensors enabled by transfer printing. (A) Schematic illustration of the fabrication process of a piezoelectric pressure sensor. (B) The schematic diagram of transfer printing process using hydrogel as the template to fabricate resistive strain and pressure sensors. (C) The schematic diagram of the design of a capacitive pressure sensor insensitive to mechanical damage. (D) The fabrication schematic diagram of the sensor shown in (C). (A) Adapted from Dong, W., Xiao, L., Hu, W., Zhu, C., Huang, Y., & Yin, Z. (2017). Wearable human-machine interface based on PVDF piezoelectric sensor. *Transactions of the Institute of Measurement and Control*, 39(4), 398–403. <https://journals.sagepub.com/home/TIM.1177/0142331216672918>. (B) Adapted from Kang, T.H., Chang, H., Choi, D., Kim, S., Moon J., Lim, J.A., Lee, K.Y., & Yi, H. (2019). Hydrogel-templated transfer-printing of conductive nanonetworks for wearable sensors on topographic flexible substrates. *Nano Letters*, 19(6), 3684–3691. <http://pubs.acs.org/journal/nalefd.1021/acs.nanolett.9b00764>. (C) Adapted from Luo, Y., Shao, J., Chen, S., Chen, X., Tian, H., Li, X., Wang, L., Wang, D., & Lu, B. (2019). Flexible capacitive pressure sensor enhanced by tilted micropillar arrays. *ACS Applied Materials and Interfaces*, 11(19), 17796–17803. <http://pubs.acs.org/journal/aamick.1021/acsami.9b03718>.

scratches (Luo et al., 2019). The key sensing element is the microstructured dielectric layer which is placed and further cured on the electrode via transfer printing. In a more recent study (Luo et al., 2021), a microstructured dielectric layer and patterned electrode are assembled together to improve sensitivity and resolution. A framework to conduct the parametric study is also proposed to optimize the design. More research on capacitive pressure sensors can be found in a review paper (Mishra et al., 2021).

In summary, miniaturization and flexibility are critical in sensing pressure applied to soft and dynamic target objects. Transfer printing, as an advanced microfabrication technique, enables the creation of mechanically compliant pressure sensors that can have intimate contact with the target and closely follow their deformations. Currently, the patterns of most sensing elements are planar structures and relatively simple, which may

have limited sensitivity. Future research in this area may focus on more complex patterns to be integrated into novel sensor designs via transfer printing, and new soft materials may also be used as substrates to reduce sensor hysteresis caused by the viscoelasticity of elastomers.

10.3 Thermal sensors

Temperature or thermal sensors have been used in a broad range of applications such as manufacturing, environmental monitoring, and healthcare. Several sensing mechanisms are used in temperature sensors. Various physical factors, including resistance, volumetric expansion, vapor pressure, and spectral properties, exhibit temperature dependence. As a result, these physical stimuli have been utilized in the development of temperature-sensing devices. The temperature values obtained from such devices are derived from a measurement model that utilizes a mathematical relationship between the measurement data. Thermocouples, resistance temperature detectors (RTDs), and thermistors are some of the most frequently used types of temperature sensors (Kuzubasoglu & Bahadir, 2020).

Thermocouples rely on the Seebeck effect, which states that when a closed circuit is formed by joining two dissimilar metals at junctions, a voltage is generated across the junction, which is proportional to the temperature difference: $V = \alpha(T_2 - T_1)$. Here, V is the output voltage, α is the thermoelectric sensitivity of the thermocouple, T_1 and T_2 are the temperatures of the two junctions. The voltage generated by the thermocouple can be measured and used to calculate the temperature difference (Childs et al., 2000).

RTDs use the temperature dependence of a material's electrical resistance to determine the temperature. RTDs typically have high accuracy, linearity, and quick response, making them a more attractive temperature sensing option than thermocouples. Additionally, thin-film RTDs are available, which typically consists of a thin layer of conductor deposited on a substrate. For analyzing the temperature sensitivity of materials in RTDs, the temperature coefficient of resistance (TCR) is a critical parameter: $TCR = (R_2 - R_1) / R_1(T_2 - T_1)$, where R_2 and R_1 are the resistances at temperatures T_2 and T_1 , respectively (Childs et al., 2000). The most frequently used materials for temperature sensing applications are copper, gold, nickel, platinum, and silver. In addition to these metals, conductive polymers and carbon-based materials are also widely employed for temperature-sensing purposes. The TCR for a resistor is determined by measuring the resistances values over an appropriate temperature range. After the TCR is experimentally determined, the temperature change of the sensor can be calibrated with resistance change (Nag et al., 2022). Thermistors are temperature-sensing devices that are similar to RTDs but use semiconductor-based resistors. As semiconductors exhibit a significant change in electrical resistivity with temperature, thermistors are more sensitive to temperature changes than RTDs.

Temperature sensing for the human body has attracted considerable attention in recent years as temperature can provide critical information about body functions for disease diagnosis. The normal human body temperature ranges between 37°C and 37.5°C (Chen et al., 2015; Ring, 1998). Temperature sensors for the human body typically need sufficient sensing resolution for small temperature changes ($\pm 0.1^\circ\text{C}$). For high-precision temperature measurements, direct contact with the human body is preferred. However, traditional rigid temperature detectors cannot achieve conformal contact with curvilinear surfaces, which can cause inaccurate temperature measurements, or even significant discomfort and skin irritation. Therefore, soft, biocompatible, lightweight, and durable temperature sensors are highly desirable for wearable applications (Kuzubasoglu & Bahadir, 2020).

Most inorganic semiconductors or metal materials cannot be directly fabricated on flexible polymeric substrates using conventional fabrication techniques because these flexible polymeric substrates are not able to withstand extreme processing conditions such as high temperature or chemical etching (Linghu et al., 2018). Transfer printing offers a viable solution for transferring these functional sensing elements to flexible or stretchable substrates. By using the transfer printing method, temperature-sensing materials are printed onto a flexible, stretchable substrate or even nonplanar surfaces (Chen et al., 2015; Liao et al., 2017; Linghu et al., 2018; Sim et al., 2019). This creates highly conformal and flexible temperature sensors that can be integrated into a variety of devices and systems in applications where rigid temperature sensors may not be suitable.

The materials commonly used as substrates in flexible temperature sensors include PI, PDMS, polyurethane (PU), PET-based films, papers, and fabrics. PI provides strong adhesion to metal coatings and can withstand a temperature range of -269°C to 400°C , making it suitable for deposition techniques such as sputtering and electron beam evaporation. PDMS is a popular choice due to its flexibility and high thermal expansion coefficient, which contributes to the responses of temperature sensors. The melting temperature of PET is around 160°C and it is compatible with widely used substrates (Htwe & Mariatti, 2022; Yuan et al., 2022).

Schematic images for fabricating flexible, biocompatible, and wearable temperature sensors appear in Fig. 10.5A and D, respectively (Chen et al., 2015; Liao et al., 2017). Specifically, Fig. 10.5A shows a temperature sensor consisting of VO_2 as the sensing material and Au as interconnects. The sensing material, VO_2 , is synthesized and patterned on a SiO_2/Si substrate while the interconnection material, Au, is patterned on a PET film using a lift-off process. Subsequently, HF solution is used to etch the SiO_2 layer underneath the VO_2 and a piece of 1-mm-thick PDMS film is pressed on the surface of the VO_2 . With the help of van der Waals forces, the VO_2 can be easily peeled off from the Si substrate and transferred onto a prepatterned Au film to form a temperature sensor (Liao et al., 2017). Transfer printing of a thin film layer with

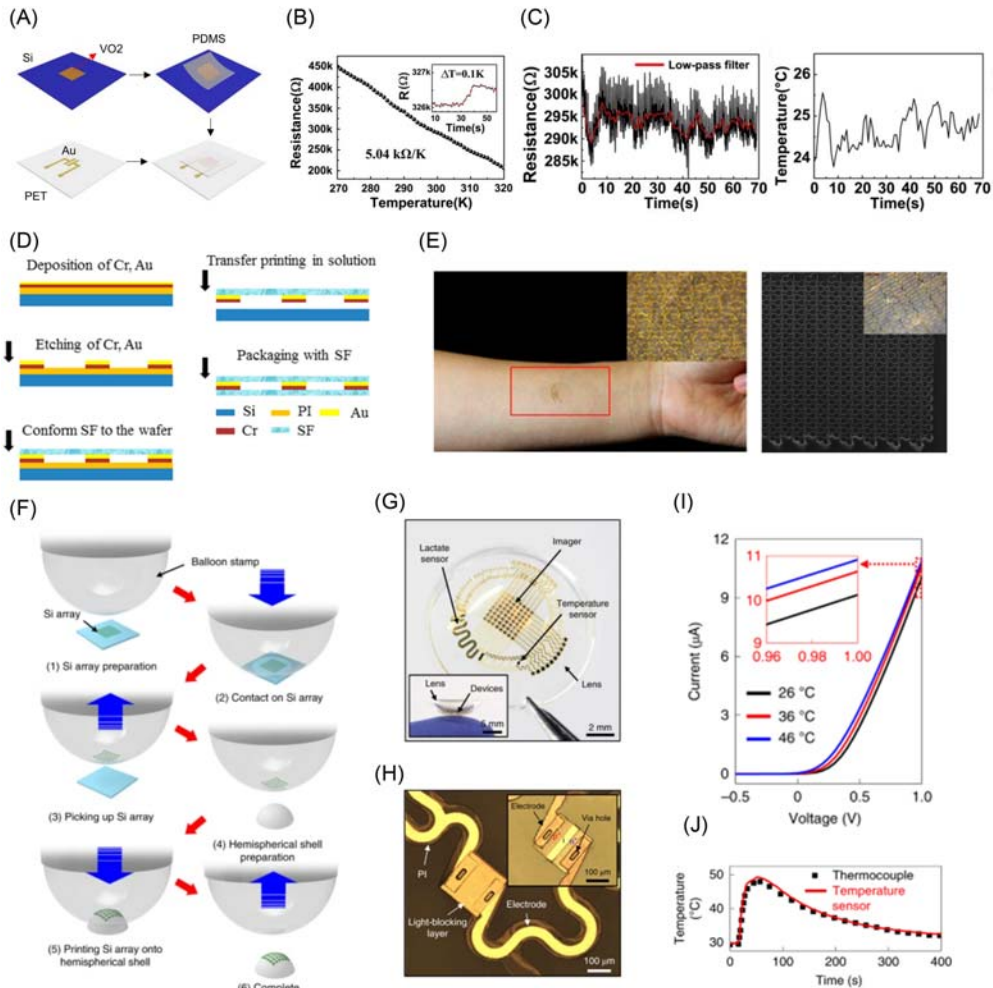


Figure 10.5 Examples of temperature sensors fabricated by transfer printing. (A) Schematic illustration of the fabrication process of a temperature sensor consisting of PET, Au pattern, inorganic vanadium dioxide (VO_2) material, and PDMS from the bottom layer, respectively. (B) Measured TCR for the temperature sensing material (VO_2). (C) Measured resistance change from the temperature sensor while real-time monitoring of the body's (wrist) temperature (left), and the measured temperature signal converted from resistance change (right). (D) Schematic illustration of the fabrication process of a temperature sensor consisting of semipermeable film, Au pattern, and SF from the bottom layer, respectively. (E) Optical images of the demonstration of attaching the device to the forearm (left) and the SEM image of the sensor. The inset shows the optical microscopy image of the sensor (right). (F) Process of the fabrication method for smart contact lens by using conformal additive stamp printing. (G) Optical image of the contact lens electronics. Inset: side view of the lens electronics. (H) Optical microscope image of the Si temperature sensor. Inset: device before the formation of the light-blocking layer. (I) Characteristics of the temperature sensor at different representative temperatures. (J) Plots of temperature sensing by using a commercially available thermocouple (black squares) and the printed temperature sensor (red line). (Continued)

complicated patterns may be challenging for a dry stamp-based process because fracture or wrinkling may occur in the thin films. Therefore, transfer printing in solution is introduced (Fig. 10.5D). After patterning Au on the PI film, transferring the whole device to a semipermeable film as a soft substrate completes the device fabrication (Chen et al., 2015).

After fabrication, the temperature sensor's TCR is calculated as the slope of the relative resistance change over temperature change (Fig. 10.5B). The temperature sensor has a negative TCR of $-1.12 \times 10^{-2}/\text{K}$. After conversion from electrical resistance to temperature, real-time monitoring of body surface temperature is demonstrated on the wrist (Fig. 10.5E) and the body surface temperature is measured and shown in Fig. 10.5C (Liao et al., 2017).

Furthermore, transfer printing enables the transfer of components and sensors to complex and nonplanar surfaces by using a method referred to as conformal additive stamp (CAS) printing (Fig. 10.5F) (Sim et al., 2019). CAS printing uses a pneumatically inflated elastomeric balloon as a medium to pick up prefabricated electronic devices in 2D geometries created using microfabrication and then to deliver them onto arbitrary curvilinear 3D surfaces, such as the surface of a lens (Fig. 10.5G). The temperature sensor for ocular surface temperature monitoring is based on a Si p-i-n diode, which changes its electrical resistance in response to temperature changes (Fig. 10.5H). A light-blocking layer of metal is used to eliminate any photo response. Fig. 10.5I shows the $I-V$ curves of the diode temperature sensor under different temperatures (26°C, 36°C, and 46°C). A clear temperature dependency on the forward bias current is shown. Furthermore, Fig. 10.5J shows continuous temperature sensing based on the diode sensor.

Transfer printing technologies are widely used in the fabrication of various temperature sensors due to their numerous advantages discussed above. One of the key advantages is the ability to achieve high-precision temperature sensing through conformal contact with the target surface. This enables accurate and reliable temperature measurements, which is critical for many applications.

◀ available thermocouple and the Si-based temperature sensor. (A)–(C) Adapted from Liao, F., Lu, C., Yao, G., Yan, Z., Gao, M., Pan, T., Zhang, Y., Feng, X., & Lin, Y. (2017). *Ultrasensitive flexible temperature-mechanical dual-parameter sensor based on vanadium dioxide films*. *IEEE Electron Device Letters*, 38(8), 1128–1131. <https://doi.org/10.1109/LED.2017.2714260>. (D) and (E) Adapted from Chen, Y., Lu, B., Chen, Y. & Feng, X. (2015). *Breathable and stretchable temperature sensors inspired by skin*. *Scientific Reports*, 5(1). <https://doi.org/10.1038/srep11505>. (F)–(J) Adapted from Sim, K., Chen, S., Li, Z., Rao, Z., Liu, J., Lu, Y., Jang, S., Ershad, F., Chen, J., Xiao, J., & Yu, C. (2019). *Three-dimensional curvy electronics created using conformal additive stamp printing*. *Nature Electronics*, 2(10), 471–479. <https://www.nature.com/natelectron/1038/s41928-019-0304-4>.

10.4 Electrophysiology sensors

Electrophysiology is a branch of physiology that studies the electrical properties of biological cells, tissues, or organs in the body. It involves the use of techniques that measure the electrical activity of cells, such as voltage and current changes, to investigate the functions of the nervous, muscular, and cardiac systems. By measuring electrophysiological signals, it is possible to gain insights into the functional states of cells, tissues, and organs, and use this information for diagnosis and therapeutics. Therefore, the main purpose of using electrophysiology sensors is to accurately detect the electrical signals generated by cells and tissues.

Examples of electrophysiology sensors include the following: electromyography (EMG) sensors which measure electrical activities of muscles; electrooculography (EOG) sensors detecting the electrical potential difference between the cornea and retina of the eye; electrocardiography (ECG) sensors that measure electrical activities of the heart; electroencephalography (EEG) sensors, used to measure electrical activities of the brain from electrodes placed on the scalp; electrocorticography (ECoG) sensors, which measure electrical activities of the brain through electrodes placed directly on the surface of the brain.

Electrophysiological signals are typically measured using electrodes placed on or near the cells of interest. The electrodes are typically made of conductive materials, such as silver, gold, and platinum. These metals are selected for their excellent electrical conductivity, chemical stability and biocompatibility. Low electrical conductivity, or equivalently, high impedance, can introduce signal distortion, noise, and other artifacts, compromising the accuracy and reliability of the measurements. To reduce electrode impedance, several materials can be coated onto the electrode surfaces, increasing the effective surface area and decreasing the electrical impedance without increasing the geometrical dimensions of the electrodes (Sharafkhani et al., 2022). Commonly used materials for this purpose include Poly(3,4-ethylenedioxythiophene) polystyrene sulfonate (PEDOT:PSS), platinum black, iridium oxide (IrO_x) (Sharafkhani et al., 2022), poly(3,4-ethylenedioxythiophene) (PEDOT) (Wang et al., 2021), and CNTs (Foremny, 2021).

As mentioned above, reducing the impedance of sensor electrodes can improve the sensitivity and quality of the measured electrophysiology signals. However, for the fabrication of sensors intended for high-precision measurements, it is essential to use flexible and biocompatible materials. These materials ensure direct contact with the human body while minimizing discomfort and irritation. Consequently, transfer printing becomes an effective method to meet these requirements, allowing the transfer of sensing parts to biocompatible adhesives, polymers or shape memory polymers (SMPs) (Fig. 10.6) (Namkoong et al., 2022; Park, 2017; Yan et al., 2017; Zhang, Zheng, et al., 2019).

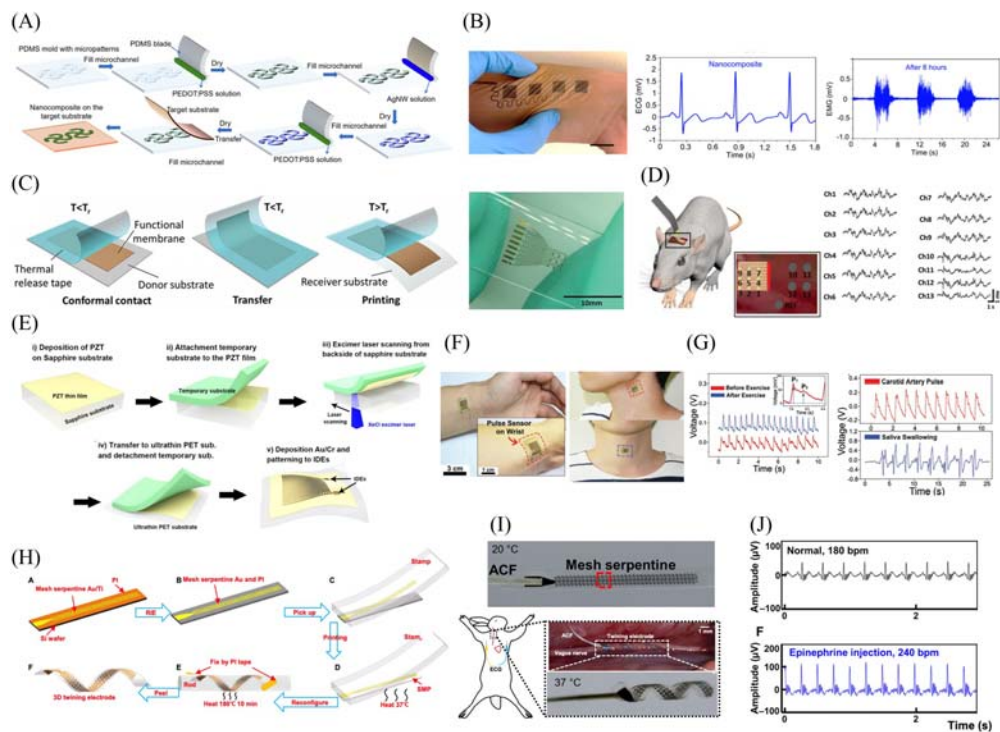


Figure 10.6 Examples of transfer printing techniques employed in various flexible materials for electrophysiological sensors to form conformal contact with target surfaces. (A) Schematic illustration of the fabrication process for an electrophysiological sensor using nanocomposites as electrode materials. (B) Photograph of a nanocomposite electrode array transferred onto a medical adhesive and laminated on the forearm (left, scale bar: 2 cm) and measured ECG and EMG signals (right). (C) Schematic illustration of the thermal release transfer printing method (left) and the electrode array for neural sensing printed on the PDMS after transfer printing (right). (D) Schematic illustration of the anatomy and locations of the nine channels of a stretchable neural electrode array (left). Representative ECoG signals recorded by a stretchable neural electrode array (channels 1–9) and stainless-steel screw electrodes (channels 10–13) (right). (E) Detailed fabrication steps of a self-powered piezoelectric pressure sensor on an ultrathin PET substrate via an inorganic-based laser lift-off process. (F) Photograph of a piezoelectric pulse sensor conformally attached to a human wrist (left) and to the carotid artery position (right, top) and the middle of the throat (right, bottom) using a biocompatible liquid bandage. (G) Radial artery pulse signals detected by the self-powered pulse sensor, which show different heart rates and generated output voltages before and after physical exercise (left). The generated output voltage in response to carotid arterial pressure (right, top) and saliva swallowing actions (right, bottom). (H) Schematic illustrations of the detailed fabrication process of the twining electrode on shape memory polymer. (I) Images of an implanted twining electrode on the vagus nerve. (J) Recorded ECG signals of the anesthetized rabbit before (top) after (bottom) epinephrine injection. (A) and (B) Adapted from Namkoong, M., Guo, H., Rahman, M.S., Wang, D., Pfeil, C.J., Hager S., & Tian, L. (2022). Moldable and transferrable conductive nanocomposites for epidermal electronics. *NPJ Flexible Electronics*, 6(1). <http://nature.com/npjflexelectron/.1038/s41528-022-00170-y>. (C) and (D) Adapted from Yan, Z., Pan, T., Xue, M., Chen, C., Cui, Y., Yao, G., (Continued)

As shown in Fig. 10.6A, a sandwich composite of PEDOT:PSS/AgNW/PEDOT:PSS is preshaped in a PDMS mold and then transfer printed onto various adhesives to create an electrophysiological sensor. The nanocomposite electrodes can provide robust and clear ECG and EMG recordings due to the conformal contact between the adhesive and the tissues (Fig. 10.6B) (Namkoong et al., 2022).

By using thermal release-assisted transfer printing processes, a flexible neural recording electrode array consisting of nine channels on a 50- μm -thick PDMS is fabricated. The sensor is placed on the visual cortical surface of the left hemisphere of a rat and an ECoG signal is recorded (Fig. 10.6D). All channels of the PDMS neural electrodes are in conformal contact with the curved surface of the rat's brain (Yan et al., 2017). In addition to PDMS, PET is also a good candidate for ultrathin polymeric substrate materials. Fig. 10.6E shows an example in which a XeCl excimer laser exfoliates a thin film from a rigid substrate for fabricating a self-powered flexible pressure sensor. The sensing components are transferred to an ultrathin PET substrate, which enables the sensor to detect physiological signs including arterial pulses and respiration rates. Fig. 10.6F and G show a piezoelectric pulse sensor conformally attached to a human wrist and neck for measuring radial artery pulses and carotid artery pulses (Park, 2017).

Strategies for creating conformal contact with target organs can be enhanced by using SMPs to make climbing-inspired twining electrodes for peripheral nerve recording (Fig. 10.6H). The transfer printing method offers a solution to print on various polymeric substrates. After releasing the mesh serpentine structure onto the SMP, the initial 2D planar SMP assembly undergoes the shape memory process under controlled temperature. As a demonstration of applications, *in vivo* vagus nerve stimulation experiments are conducted on a rabbit for ECG recording (Fig. 10.6I). The heart rates of the anesthetized rabbit after the injection of epinephrine are successfully recorded (Fig. 10.6J) (Zhang, Zheng, et al., 2019).

Transfer printing techniques offer a significant advantage by enabling convenient manufacturing of complex, multifunctional devices. This is because transfer printing allows for the transferring of functional components that have complex forms and shapes and ensures high precision in the placement of electronic components and sensors on the substrate. Therefore, transfer printing not only supports the production of

-
- ◀ Huang, L., Liao, F., Jing, W., Zhang, H., Gao, M., Guo, D., Xia, Y., & Lin, Y. (2017). Thermal release transfer printing for stretchable conformal bioelectronics. *Advanced Science*, 4(11), 1700251. <https://doi.org/10.1002/advs.201700251>. (E)–(G) Adapted from Park, D.Y. (2017). Self-powered real-time arterial pulse monitoring using ultrathin epidermal piezoelectric sensors. *Advanced Materials*, 29(37). (H)–(J) Adapted from Zhang, Y., Zheng, N., Cao, Y., Wang, F., Wang, P., Ma, Y., Lu, B., Hou, G., Fang, Z., Liang, Z., Yue, M., Li, Y., Chen, Y., Fu, J., Wu, J., Xie, T., & Feng, X. (2019). Climbing-inspired twining electrodes using shape memory for peripheral nerve stimulation and recording. *Science Advances*, 5(4). <https://advances.sciencemag.org/content/5/4/eaaw1066/tab-pdf.1126/sciadv.aaw1066>.

large volumes of sensors cost-effectively but also enables the transfer of multiple types of sensors simultaneously or in multilayered configurations (Han et al., 2020; Ji et al., 2020; Song et al., 2019).

As Fig. 10.7A illustrates, electronics distributed over large areas can be fabricated using transfer printing. By using prepatterned PDMS, a large number of prefabricated functional electrodes can be retrieved from a wafer. Retrieval of specific sets of electrodes is facilitated using PDMS stamps with relief features and spacings that align with the dimensions and arrangements of the electrodes. Fig. 10.7B shows PDMS with

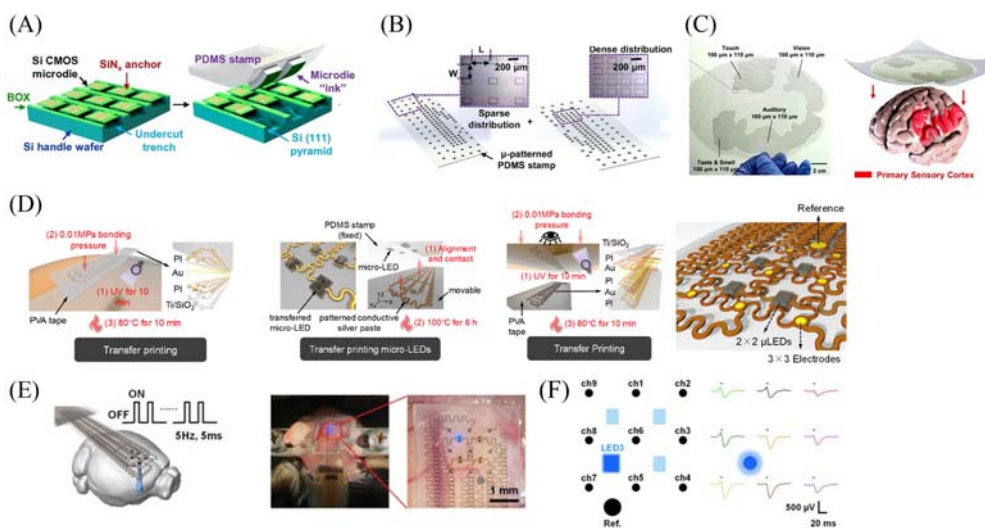


Figure 10.7 Examples of transfer printing used for creating large-area, multilayered, and micropatterned electrophysiological sensors. (A) Processing schemes for the transfer printing of prefabricated silicon microdies using a PDMS stamp. (B) Schematic illustration of magnified views of micropatterned PDMS stamps in different distribution densities. (C) Photograph of approximately 32,000 microelectrodes printed onto a thin, flexible sheet of PET and cut into the approximate outline shape of an adult brain model. (D) Schematic diagram of the fabrication process using 3 transfer printing methods (left) and the flexible optoelectronic device, integrated with micro-LEDs and recording microelectrodes (right). (E) Illustration (left) and an image (right) of a sensor array on the cortical surface of a mouse with optical stimulation. (F) In vivo recording of ECoG signals with optogenetics stimulation and comparison of ECoG signals recorded from all 9 channels with a single light pulse optical stimulation at LED3 location. (A)–(C) Adapted from Song, E., Chiang, C-H., Li, R., Jin, X., Zhao, J., Hill, M., Xia, Y., Li, L., Huang, Y., Won, S.M., Yu, K.J., Sheng, X., Fang, H., Alam, M.A., Huang, Y., Viventi, J., J-K. Chang, J-K., & Rogers, J.A. (2019). Flexible electronic/optoelectronic microsystems with scalable designs for chronic biointegration. *Proceedings of the National Academy of Sciences*, 116(31), 15398–15406. <https://doi.org/10.1073/pnas.1907697116>. <https://www.pnas.org/doi/10.1073/pnas.1907697116>. (D)–(F) Adapted from Ji, B., Ge, C., Guo, Z., Wang, L., Wang, M., Xie, Z., Xu, Y., Li, H., Yang, B., Wang, X., Li, C., & Liu, J. (2020). Flexible and stretchable opto-electric neural interface for low-noise electrocorticogram recordings and neuromodulation in vivo. *Biosensors and Bioelectronics*, 153, 112009. <https://doi.org/10.1016/j.bios.2020.112009>.

different densities of relief features at microscale. Printing the retrieved electrodes as “inks” onto a target substrate results in heterogeneously integrated systems. This transfer printing technique for numerous electrodes in diverse densities enables high spatial resolution in electrical mapping or stimulation of different sensory functions in the brain (Fig. 10.7C). Specifically, the regions of dense electrode distribution ($100 \times 110 \mu\text{m}^2$ in electrode size) correlate with the locations of the primary sensory cortex for visual, auditory, somatic, gustation, and olfactory sensory functions (Song et al., 2019).

Transfer printing also enables the creation of multilayer soft electronics, with different electrophysiological sensors in each layer, ensuring high precision and accuracy in the placement of each sensor layers on the substrate. Fig. 10.7D shows a structure of 3×3 microelectrode sites ($100 \mu\text{m}$ in diameter) for ECoG recording, 2×2 micro-LEDs for optical stimulation, and one large reference electrode, all fabricated using transfer printing methods. This multilayered sensor can be constructed in a compact size, allowing it to make conformal contact with the surface of a rat’s brain (Fig. 10.7E). The measured ECoG during optical stimulation is shown in Fig. 10.7F (Ji et al., 2020).

By utilizing all the advantages presented above, fully integrated sensor systems that possess different functions for electrophysiological recording, electrical stimulation, temperature sensor arrays, and pressure sensor arrays can be easily transferred to nonplanar surfaces (Fig. 10.8). Each sensor modality is first fabricated on silicon wafers as temporary substrates, and then stacked using transfer printing. This approach is possible because transfer printing offers high precision in placing the electronic components and sensors on the substrate. The fully integrated sensor system is transferred onto the surface of balloon catheter-based systems, which serve as minimally invasive medical tools. Fig. 10.8A and B show a representative balloon catheter instrumented with an electrode array when the catheter is deflated and inflated. Furthermore, experiments on Langendorff rabbit heart models validate the diagnostic functions of the instrumented balloon catheters. Temperature distribution and voltage maps for electrograms are measured on the left posterior ventricular surface of the rabbit heart using a balloon catheter (Fig. 10.8C). Temperature distribution is measured with the temperature sensor array while radiofrequency ablation with electrode arrays is performed simultaneously. Moreover, electrograms and corresponding voltage maps, recorded from the epicardial surface of a rabbit heart using the electrode array during both paced activation patterns and arrhythmia, demonstrate the capability to detect atrial excitation (P wave), ventricular excitation (QRS wave), and ventricular relaxation (T wave). Voltage maps for selected time points are also presented (Fig. 10.8D) (Han et al., 2020).

In conclusion, transfer printing is a promising method for fabricating flexible sensors due to its numerous advantages. One of the key advantages is the ability to transfer a variety of materials and components with high precision, allowing for the creation of complex, multifunctional, integrated devices. Transfer printing can also enable the transfer of sensors and other components to various materials and nonplanar

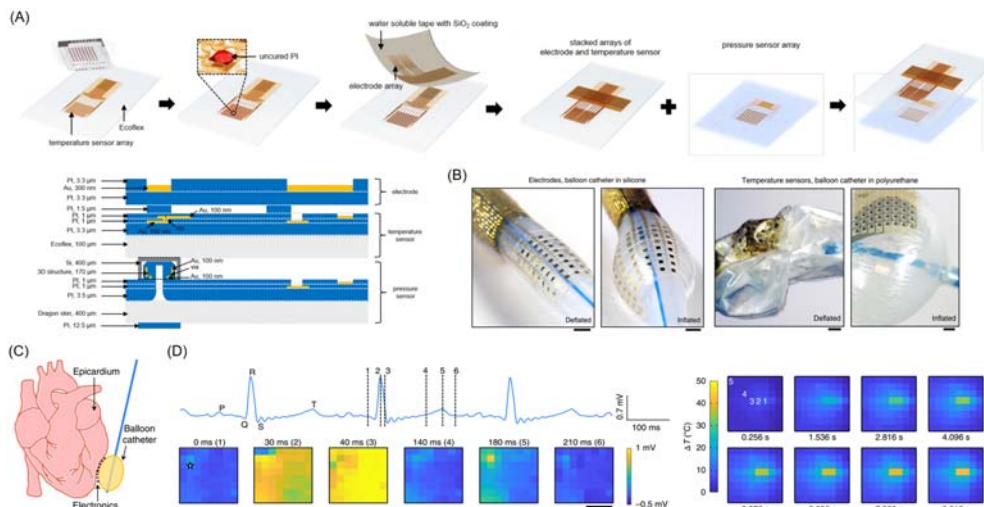


Figure 10.8 Examples of transfer printing used for creating an integrated sensor system by stacking and transferring onto a nonplanar surface. (A) Schematic illustration of the fabrication procedures for stacking multilayers of multiplexed electronics. (B) Images of the array of electrodes transferred onto a balloon catheter made of silicone (top) and PU (bottom). Scale bars, 2 mm. (C) Schematic of the test setup showing the balloon catheter in contact with the surface of a rabbit heart. (D) A single trace electrogram measured from the electrode array under pacing at 200 beats per min (left). Spatiotemporal temperature mapping during bipolar radiofrequency ablation on a rabbit heart, measured from the temperature sensor array (right). Adapted from Han, M., Chen, L., Aras, K., Liang, C., Chen, X., Zhao, H., Li, K., Faye, N.R., Sun, B., Kim, J.H., Bai, W., Yang, Q., Ma, Y., Lu, W., Song, E., Baek, J.M., Lee, Y., Liu, C., Model, J.B., ... & Rogers, J.A. (2020). Catheter-integrated soft multilayer electronic arrays for multiplexed sensing and actuation during cardiac surgery. *Nature Biomedical Engineering*, 4(10), 997–1009. <http://www.nature.com/natbiomedeng/1038/s41551-020-00604-w>.

surfaces, which can significantly expand the range of applications. In addition, transfer printing is a scalable and cost-effective technique that can be used to produce both high-density and multifunctional sensors and other functional devices.

10.5 Chemical sensors

Chemical sensors are devices designed to detect the presence and concentration of target substances. Common chemical sensing mechanisms include the following:

- 1. Optical sensors:** Identify changes in optical properties such as absorption, fluorescence, and reflectance upon interaction with the target analyte.
- 2. Electrochemical sensors:** Measure changes in electrical signals, including current, potential, or impedance, resulting from redox reactions of the analyte at an electrode surface. Techniques include amperometry, potentiometry, voltammetry, and impedance spectroscopy.

3. **Mass-based sensors:** Detect changes in mass or mechanical properties of the sensing material upon analyte adsorption, for example, quartz crystal microbalance sensors and cantilever-based sensors.
4. **Gas sensors:** Identify changes in properties like conductivity, capacitance, or mass upon interaction with gas molecules, such as metal oxide semiconductor gas sensors and chemiresistive sensors.
5. **Biosensors:** Leverage biological recognition elements to selectively bind to the target analyte and generate a measurable signal, for instance, enzyme-based sensors, immunosensors, and DNA sensors.

Common materials used in chemical sensors include sensing materials (e.g., metal nanoparticles, carbon-based materials, conductive polymers, and metal oxides), recognition elements (e.g., enzymes, antibodies, and aptamers), transduction elements (e.g., electrodes, optical fibers, and piezoelectric crystals), substrates and supports (e.g., glass, silicon, and polymers), as well as coatings and membranes (e.g., ion-selective membranes and enzyme immobilization matrices).

Transfer printing presents distinct advantages in the development and integration of sensing elements with a variety of substrates and devices. This technique addresses material compatibility challenges, enables seamless heterogeneous integration, and streamlines the fabrication of flexible, stretchable sensors for wearable and implantable applications. Moreover, transfer printing offers precise control and high resolution, which is crucial for miniaturized sensors, while also providing cost-effective, scalable fabrication for disposable sensors employed in point-of-care diagnostics and environmental monitoring applications.

Transfer printing has been utilized in the development of wearable sensors for health monitoring. These sensors can detect a broad range of analytes, such as glucose, lactate, and pH, while also monitoring various physiological parameters, including heart rate, respiration rate, and body temperature. For instance, sweat sensors are wearable devices designed to analyze the chemical composition of sweat for numerous biomarkers like electrolytes, metabolites, and proteins. These sensors offer valuable insights into an individual's health and physiological status. Sweat sensors' sensing mechanisms can be broadly classified into electrochemical and optical sensing techniques. Transfer printing is crucial for fabricating sweat sensors because it enables the deposition and integration of various materials and structures onto flexible, stretchable, and wearable substrates. Essential components for sweat sensors include sensing materials, recognition elements, electrodes and transducers, flexible and stretchable substrates, and protective coatings and barriers.

Transfer printing has been used for the fabrication of a wearable sensor capable of detecting glucose levels in sweat (Lee et al., 2016). The device comprises graphene and gold sensors transfer-printed onto a silicone patch and selectively electrochemically functionalized. The glucose sensor employs hydrogen peroxide reduction to measure glucose concentration, while the pH sensor corrects for pH-dependent deviations

(Fig. 10.9). Another study employs transfer printing to create a wearable sensor for monitoring lactate levels in sweat (Huang et al., 2022). This stretchable, self-powered biosensor features an epidermal electronic format that facilitates in situ detection of lactate and glucose concentrations in sweat. Enzymatic biofuel cells function as self-powered sensing modules, allowing the sweat sensor to exhibit a determination coefficient (R^2) of 0.98 with a sensitivity of 2.48 mV/mM for lactate detection and an R^2 of 0.96 with a sensitivity of 0.11 mV/ μ M for glucose detection. The ultra-thin, soft, flexible PDMS layer's microfluidic channels enable not only effective sweat collection but also excellent mechanical properties with stable performance output, even under 30% stretching. These soft sweat sensors can be integrated on the skin for continuous monitoring of lactate and glucose changes during everyday activities, such as exercise. These sensors could be employed for continuous monitoring of glucose and lactate levels in patients with diabetes or other metabolic disorders. They can accommodate the deformations of skin, providing a more comfortable user experience. Additionally, they can be integrated into wearable devices that continuously and noninvasively monitor an individual's health.

One of the primary advantages of transfer printing technology is its ability to create thin and flexible electrochemical sensors. These sensors are widely employed for detecting and analyzing various chemical and biological species. Electrochemical sensor mechanisms depend on the interaction between an analyte and an electrode, resulting in a change in electrical signals such as current, potential, or impedance. Common materials in electrochemical sensors include electrode materials, membranes, coatings, redox mediators, recognition elements, and supporting electrolytes. These sensors can be seamlessly integrated into wearable devices, enabling real-time monitoring of the chemical environment.

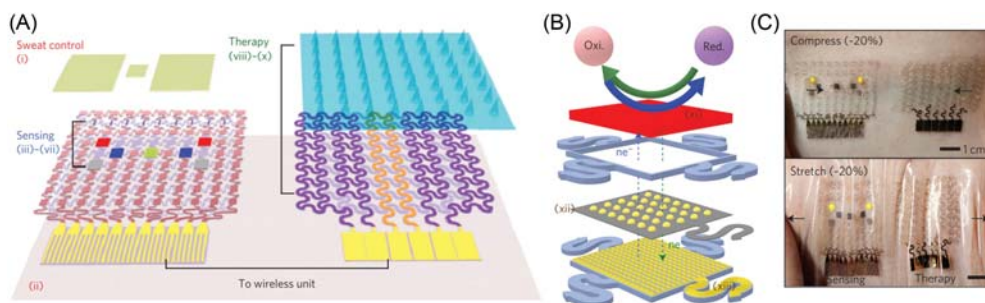


Figure 10.9 Schematic drawings and corresponding optical images of the diabetes patch. (A) Schematic drawings of the diabetes patch. (B) Schematic of the graphene-hybrid electrochemical unit. (C) Optical images of the diabetes patch laminated on human skin under mechanical deformations. Adapted from Lee, H., Choi, T.K., Lee, Y.B., Cho, H.R., Ghaffari, R., Wang, L., Choi, H.J., Chung, T.D., Lu, N., Hyeon, T., Choi, S.H., & Kim, D.H. (2016). A graphene-based electrochemical device with thermoresponsive microneedles for diabetes monitoring and therapy. *Nature Nanotechnology*, 11(6), 566–572. <https://www.nature.com/articles/nnano.2016.38>.

For instance, conductive CNT electrodes have been fabricated using transfer printing (Lee & Lee, 2018). This process involves printing CNT ink on an overhead projector film and transferring the pattern to a flexible PDMS film. The transferred CNT electrode is then used as a working electrode for selective dopamine detection using cyclic voltammetry. Moreover, wax transfer printing is utilized on fabrics to create electrochemical devices (Downs et al., 2018) (Fig. 10.10A). A hot laminator enhances wax transfer, resulting in leak-proof barriers. Stencil-printed electrodes are added to the fabric substrate, and a glucose-sensing device is developed, featuring a sensitivity of $0.076 \pm 0.01 \mu\text{A}/\text{mM}$ and a linear range of 0.1–30 mM. These results demonstrate the promising potential of fabric-based electrochemical devices for wearable sensing applications.

Additionally, transfer printing is employed to create a wearable potentiometric sodium ion sensor (Kimura et al., 2020). The sensor's accuracy remains unaffected by the irregularity of the electrode surface on the textile. The sensor is evaluated as a potassium ion sensor and exhibits high selectivity for potassium ions over sodium and ammonium ions commonly present in human sweat.

Transfer printing technology also enables the creation of chemical sensors with high specific surface area, which can be used for environmental monitoring and other applications. For example, a chemical sensor based on tin dioxide (SnO_2) nanowires is fabricated by transfer printing (Sosada-Ludwikowska et al., 2019). The SnO_2

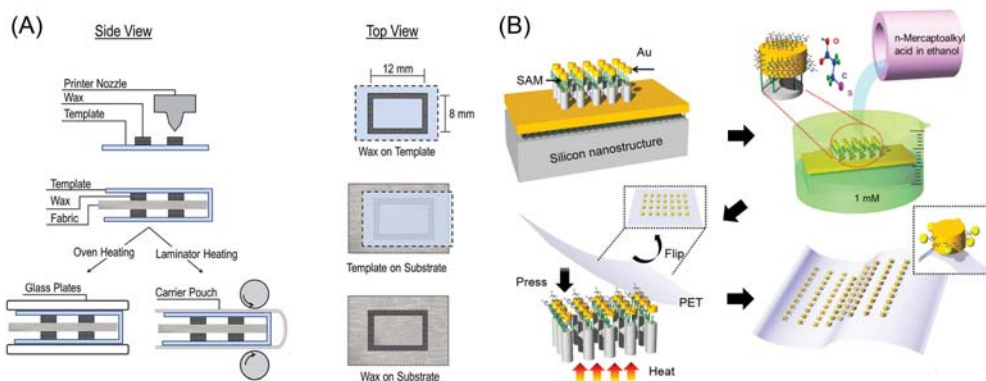


Figure 10.10 Schematic drawings of transfer printing processes used in the fabrication of two different electrochemical sensors. (A) Schematic drawings of the wax transfer printing processes to create hydrophobic barriers in fabric. (B) Schematic illustration of fabrication processes for the side edge prefunctionalized nanostructure arrays. (A) Adapted from Downs C., Nejely, A., & Fu, E. (2018). Disposable fabric-based electrochemical sensors fabricated from wax-transfer-printed fluidic cells and stencil-printed electrodes. *Analytical Methods*, 10(29), 3696–3703. <https://pubs.rsc.org/en/content/articlelanding/2018/ay/c8ay01028e>. (B) Adapted from Lee, J., Park, J., Lee, J.-Y., Yeo, & J.-S. (2015). Contact transfer printing of side edge prefunctionalized nanoplasmonic arrays for flexible microRNA biosensor. *Advanced Science*, 2(9), 1500121. <https://doi.org/10.1002/adv.201500121>.

nanowires are grown using a two-step technology, including spray pyrolysis deposition and a thermal annealing process in the presence of a Cu catalyst. The SnO₂ NWs are then transfer printed by a PDMS stamp onto Si-substrates with gold interdigital electrode structures, creating a multi-NW chemical sensing device. Transfer printing technology offers a fast, reproducible, and cost-effective method to integrate nanowires into gas sensing devices. The “dry” transfer printing technology avoids potential contamination of the gas-sensitive material by organic residuals, which might be detrimental to sensor performance. The transfer printing technology enables fast, easy, and affordable fabrication of NW-based sensor devices with good reproducibility. Additionally, a humidity sensor is developed using transfer printing (Aziz et al., 2016). The device consists of silver interdigital transducers printed on a sensing layer and then transferred to a PDMS substrate. The nanocomposite film has a thickness of 150 nm and a porous structure, making it favorable for humidity sensing. The humidity sensing response is tested and shows fast response time and high sensitivity to relative humidity changes. Moreover, a flexible nano-plasmonic biosensing platform is developed using transfer printing of self-assembled protein film nanostructures onto a flexible substrate (Lee et al., 2015) (Fig. 10.10B). The platform demonstrates ultrasensitive detection of miRNA-21 with a detection limit of 10×10^{-15} M. The platform has the potential for use in various applications, including sensitive strain gauges, functional molecular devices, and functionalized particle-based photoconductance.

In conclusion, transfer printing technology has the potential to revolutionize the field of chemical and electrochemical sensors. It provides a solution to the limitations of traditional chemical and electrochemical sensors and enables the creation of thin, flexible, and cost-effective devices. As this technology continues to advance, it is likely that transfer printing technology will play a significant role in the development of next-generation chemical and electrochemical sensors. Its versatility, adaptability, and cost-effectiveness make it an ideal choice for various chemical sensing applications, including wearable health monitoring devices and environmental monitoring systems.

References

- Aziz, S., Bum, K. G., Yang, Y. J., Yang, B. S., Kang, C. U., Doh, Y. H., Choi, K. H., & Kim, H. C. (2016). Fabrication of ZnSnO₃ based humidity sensor onto arbitrary substrates by micro-nano scale transfer printing. *Sensors and Actuators, A: Physical*, 246, 1–8. Available from <https://doi.org/10.1016/j.sna.2016.04.059>.
- Bartlett, M. D., Markvicka, E. J., & Majidi, C. (2016). Rapid fabrication of soft, multilayered electronics for wearable biomonitoring. *Advanced Functional Materials*, 26(46), 8496–8504. Available from <https://doi.org/10.1002/adfm.201602733>, [http://onlinelibrary.wiley.com/journal/10.1002/\(ISSN\)1616-3028](http://onlinelibrary.wiley.com/journal/10.1002/(ISSN)1616-3028).
- Chen, Y., Lu, B., Chen, Y., & Feng, X. (2015). Breathable and stretchable temperature sensors inspired by skin. *Scientific Reports*, 5(1), 11505. Available from <https://doi.org/10.1038/srep11505>.
- Childs, P. R. N., Greenwood, J. R., & Long, C. A. (2000). Review of temperature measurement. *Review of Scientific Instruments*, 71(8), 2959–2978. Available from <https://doi.org/10.1063/1.1305516>, <http://scitation.aip.org/content/aip/journal/rsi>.

- Dong, W., Xiao, L., Hu, W., Zhu, C., Huang, Y., & Yin, Z. (2017). Wearable human-machine interface based on PVDF piezoelectric sensor. *Transactions of the Institute of Measurement and Control*, 39(4), 398–403. Available from <https://doi.org/10.1177/0142331216672918>, <https://journals.sagepub.com/home/TIM>.
- Downs, C., Nejely, A., & Fu, E. (2018). Disposable fabric-based electrochemical sensors fabricated from wax-transfer-printed fluidic cells and stencil-printed electrodes. *Analytical Methods*, 10(29), 3696–3703. Available from <https://doi.org/10.1039/c8ay01028e>, <http://pubs.rsc.org/en/journals/journal/ay>.
- Foremny, K. (2021). Carbon-nanotube-coated surface electrodes for cortical recordings in vivo. *Nanomaterials*, 11(4), 1029. Available from <https://doi.org/10.3390/nano11041029>.
- Guo, X., Wang, X., Ou, D., Ye, J., Pang, W., Huang, Y., Rogers, J. A., & Zhang, Y. (2018). Controlled mechanical assembly of complex 3D mesostructures and strain sensors by tensile buckling. *NPJ Flexible Electronics*, 2(1). Available from <https://doi.org/10.1038/s41528-018-0028-y>, <http://nature.com/npjflexelectron/>.
- Han, M., Chen, L., Aras, K., Liang, C., Chen, X., Zhao, H., Li, K., Faye, N. R., Sun, B., Kim, J. H., Bai, W., Yang, Q., Ma, Y., Lu, W., Song, E., Baek, J. M., Lee, Y., Liu, C., Model, J. B., . . . Rogers, J. A. (2020). Catheter-integrated soft multilayer electronic arrays for multiplexed sensing and actuation during cardiac surgery. *Nature Biomedical Engineering*, 4(10), 997–1009. Available from <https://doi.org/10.1038/s41551-020-00604-w>, <http://www.nature.com/natbiomedeng/>.
- Herbert, R., Lim, H. R., Yeo, W. H., Yeo, W. H., & Yeo, W. H. (2020). Printed, soft, nanostructured strain sensors for monitoring of structural health and human physiology. *ACS Applied Materials and Interfaces*, 12(22), 25020–25030. Available from <https://doi.org/10.1021/acsami.0c04857>, <http://pubs.acs.org/journal/aamick>.
- Htwe, Y. Z. N., & Mariatti, M. (2022). Printed graphene and hybrid conductive inks for flexible, stretchable, and wearable electronics: Progress, opportunities, and challenges. *Journal of Science: Advanced Materials and Devices*, 7(2), 100435. Available from <https://doi.org/10.1016/j.jsamd.2022.100435>.
- Huang, X., Li, J., Liu, Y., Wong, T., Su, J., Yao, K., Zhou, J., Huang, Y., Li, H., Li, D., Wu, M., Song, E., Han, S., & Yu, X. (2022). Epidermal self-powered sweat sensors for glucose and lactate monitoring. *Bio-Design and Manufacturing*, 5(1), 201–209. Available from <https://doi.org/10.1007/s42242-021-00156-1>, <https://link.springer.com/journal/volumesAndIssues/42242>.
- Ji, B., Ge, C., Guo, Z., Wang, L., Wang, M., Xie, Z., Xu, Y., Li, H., Yang, B., Wang, X., Li, C., & Liu, J. (2020). Flexible and stretchable opto-electric neural interface for low-noise electrocorticogram recordings and neuromodulation in vivo. *Biosensors and Bioelectronics*, 153, 112009. Available from <https://doi.org/10.1016/j.bios.2020.112009>.
- Kang, T. H., Chang, H., Choi, D., Kim, S., Moon, J., Lim, J. A., Lee, K. Y., & Yi, H. (2019). Hydrogel-templated transfer-printing of conductive nanonetworks for wearable sensors on topographic flexible substrates. *Nano Letters*, 19(6), 3684–3691. Available from <https://doi.org/10.1021/acs.nanolett.9b00764>, <http://pubs.acs.org/journal/nalefd>.
- Ketelsen, B., Yesilmen, M., Schlicke, H., Noei, H., Su, C. H., Liao, Y. C., & Vossmeier, T. (2018). Fabrication of strain gauges via contact printing: A simple route to healthcare sensors based on cross-linked gold nanoparticles. *ACS Applied Materials and Interfaces*, 43, 37374–37385. Available from <https://doi.org/10.1021/acsami.8b12057>, <http://pubs.acs.org/journal/aamick>.
- Khalid, M. A. U., & Chang, S. H. (2022). Flexible strain sensors for wearable applications fabricated using novel functional nanocomposites: A review. *Composite Structures*, 284. Available from <https://doi.org/10.1016/j.compstruct.2022.115214>, <http://www.elsevier.com/inca/publications/store/4/0/5/9/2/8>.
- Kim, H., Choi, E., Jung, M., Sul, O., & Lee, S.-B. (2019). Buckled carbon nanotube network thin-film fabricated using chemically swelled elastomer substrates. *Nanotechnology*, 30(28), 285501. Available from <https://doi.org/10.1088/1361-6528/ab1363>.
- Kim, T., Shin, Y., Kang, K., Kim, K., Kim, G., Byeon, Y., Kim, H., Gao, Y., Lee, J. R., Son, G., Kim, T., Jun, Y., Kim, J., Lee, J., Um, S., Kwon, Y., Son, B. G., Cho, M., Sang, M., . . . Yu, K. J. (2022). Ultrathin crystalline-silicon-based strain gauges with deep learning algorithms for silent speech interfaces. *Nature Communications*, 13(1). Available from <https://doi.org/10.1038/s41467-022-33457-9>, <http://www.nature.com/ncomms/index.html>.

- Kimura, R., Hoshi, Y., Watanabe, H., Shitanda, I., & Itagaki, M. (2020). Evaluation of wearable potassium ion sensor fabricated by heat transfer printing. *ECS Meeting Abstracts, MA2020-02*, 3687. Available from <https://iopscience.iop.org/article/10.1149/MA2020-02683687mtgabs>.
- Kuzubasoglu, B. A., & Bahadir, S. K. (2020). Flexible temperature sensors: A review. *Sensors and Actuators A: Physical*, *315*, 112282. Available from <https://doi.org/10.1016/j.sna.2020.112282>.
- Lee, H., Choi, T. K., Lee, Y. B., Cho, H. R., Ghaffari, R., Wang, L., Choi, H. J., Chung, T. D., Lu, N., Hyeon, T., Choi, S. H., & Kim, D. H. (2016). A graphene-based electrochemical device with thermo-responsive microneedles for diabetes monitoring and therapy. *Nature Nanotechnology*, *11*(6), 566–572. Available from <https://doi.org/10.1038/nnano.2016.38>, <http://www.nature.com/nnano/index.html>.
- Lee, H., & Lee, S. Y. (2018). Simple fabrication method of flexible carbon nanotube electrodes using inkjet and transfer printing methods for dopamine detection. *Journal of the Taiwan Institute of Chemical Engineers*, *92*, 63–71. Available from <https://doi.org/10.1016/j.jtice.2018.03.031>, http://www.elsevier.com/wps/find/journaldescription.cws_home/715607/description#description.
- Lee, J., Park, J., Lee, J.-Y., & Yeo, J.-S. (2015). Contact transfer printing of side edge prefunctionalized nanoplasmonic arrays for flexible microRNA biosensor. *Advanced Science*, *2*(9), 1500121. Available from <https://doi.org/10.1002/advs.201500121>.
- Lee, J., Pyo, S., Kwon, D.-S., Jo, E., Kim, W., & Kim, J. (2019). Ultrasensitive strain sensor based on separation of overlapped carbon nanotubes. *Small (Weinheim an der Bergstrasse, Germany)*, *15*(12), 1805120. Available from <https://doi.org/10.1002/sml.201805120>.
- Liao, F., Lu, C., Yao, G., Yan, Z., Gao, M., Pan, T., Zhang, Y., Feng, X., & Lin, Y. (2017). Ultrasensitive temperature-mechanical dual-parameter sensor based on vanadium dioxide films. *IEEE Electron Device Letters*, *38*(8), 1128–1131. Available from <https://doi.org/10.1109/LED.2017.2714260>.
- Linghu, C., Zhang, S., Wang, C., & Song, J. (2018). Transfer printing techniques for flexible and stretchable inorganic electronics. *NPJ Flexible Electronics*, *2*(1). Available from <https://doi.org/10.1038/s41528-018-0037-x>, <http://nature.com/npjflexelectron/>.
- Luo, Z., Chen, J., Zhu, Z., Li, L., Su, Y., Tang, W., Omisore, O. M., Wang, L., & Li, H. (2021). High-resolution and high-sensitivity flexible capacitive pressure sensors enhanced by a transferable electrode array and a micropillar-PVDF film. *ACS Applied Materials and Interfaces*, *13*(6), 7635–7649. Available from <https://doi.org/10.1021/acsami.0c23042>, <http://pubs.acs.org/journal/aamick>.
- Luo, Y., Shao, J., Chen, S., Chen, X., Tian, H., Li, X., Wang, L., Wang, D., & Lu, B. (2019). Flexible capacitive pressure sensor enhanced by tilted micropillar arrays. *ACS Applied Materials and Interfaces*, *11*(19), 17796–17803. Available from <https://doi.org/10.1021/acsami.9b03718>, <http://pubs.acs.org/journal/aamick>.
- Mishra, R. B., El-Atab, N., Hussain, A. M., & Hussain, M. M. (2021). Recent progress on flexible capacitive pressure sensors: from design and materials to applications. *Advanced Materials Technologies*, *6*(4), 2001023. Available from <https://doi.org/10.1002/admt.202001023>.
- Nag, A., Simorangkir, R. B. V. B., Gawade, D. R., Nuthalapati, S., Buckley, J. L., O'Flynn, B., Altinsoy, M. E., & Mukhopadhyay, S. C. (2022). Graphene-based wearable temperature sensors: A review. *Materials & Design*, *221*, 110971. Available from <https://doi.org/10.1016/j.matdes.2022.110971>.
- Namkoong, M., Guo, H., Rahman, M. S., Wang, D., Pfeil, C. J., Hager, S., & Tian, L. (2022). Moldable and transferrable conductive nanocomposites for epidermal electronics. *NPJ Flexible Electronics*, *6*(1). Available from <https://doi.org/10.1038/s41528-022-00170-y>, <http://nature.com/npjflexelectron/>.
- Nur, R., Matsuhisa, N., Jiang, Z., Nayeem, M. O. G., Yokota, T., & Someya, T. (2018). A highly sensitive capacitive-type strain sensor using wrinkled ultrathin gold films. *Nano Letters*, *18*(9), 5610–5617. Available from <https://doi.org/10.1021/acs.nanolett.8b02088>, <http://pubs.acs.org/journal/nalefd>.
- Oh, J. Y., Son, D., Katsumata, T., Lee, Y., Kim, Y., Lopez, J., Wu, H. C., Kang, J., Park, J., Gu, X., Mun, J., Wang, N. G. J., Yin, Y., Cai, W., Yun, Y., Tok, J. B. H., & Bao, Z. (2019). Stretchable self-healable semiconducting polymer film for active-matrix strain-sensing array. *Science Advances*, *5*(11). Available from <https://doi.org/10.1126/sciadv.aav3097>, <https://advances.sciencemag.org/content/5/11/eaav3097/tab-pdf>.
- Ozioko, O., Karipoth, P., Escobedo, P., Ntagios, M., Pullanchiyodan, A., & Dahiya, R. (2021). SensAct: The soft and squishy tactile sensor with integrated flexible actuator. *Advanced Intelligent Systems*, *3*(3), 1900145. Available from <https://doi.org/10.1002/aisy.201900145>.
- Park, D. Y. (2017). Self-powered real-time arterial pulse monitoring using ultrathin epidermal piezoelectric sensors. *Advanced Materials*, *29*(37), 1702308.

- Phan, H. P., Zhong, Y., Nguyen, T. K., Park, Y., Dinh, T., Song, E., Vadivelu, R. K., Masud, M. K., Li, J., Shiddiky, M. J. A., Dao, D., Yamauchi, Y., Rogers, J. A., & Nguyen, N. T. (2019). Long-lived, transferred crystalline silicon carbide nanomembranes for implantable flexible electronics. *ACS Nano*, *13*(10), 11572–11581. Available from <http://pubs.acs.org/journal/ancac3.1021/acsnano.9b05168>.
- Ring, E. F. J. (1998). Progress in the measurement of human body temperature. *IEEE Engineering in Medicine and Biology Magazine*, *17*(4), 19–24. Available from <https://doi.org/10.1109/51.687959>.
- Sharafkhani, N., Kouzani, A. Z., Adams, S. D., Long, J. M., Lissorgues, G., Rousseau, L., & Orwa, J. O. (2022). Neural tissue–microelectrode interaction: Brain micromotion, electrical impedance, and flexible microelectrode insertion. *Journal of Neuroscience Methods*, *365*, 109388. Available from <https://doi.org/10.1016/j.jneumeth.2021.109388>.
- Sim, K., Chen, S., Li, Z., Rao, Z., Liu, J., Lu, Y., Jang, S., Ershad, F., Chen, J., Xiao, J., & Yu, C. (2019). Three-dimensional curvy electronics created using conformal additive stamp printing. *Nature Electronics*, *2*(10), 471–479. Available from <https://doi.org/10.1038/s41928-019-0304-4>, <https://www.nature.com/natelectron/>.
- Song, E., Chiang, C.-H., Li, R., Jin, X., Zhao, J., Hill, M., Xia, Y., Li, L., Huang, Y., Won, S. M., Yu, K. J., Sheng, X., Fang, H., Alam, M. A., Huang, Y., Viventi, J., Chang, J.-K., & Rogers, J. A. (2019). Flexible electronic/optoelectronic microsystems with scalable designs for chronic biointegration. *Proceedings of the National Academy of Sciences*, *116*(31), 15398–15406. Available from <https://doi.org/10.1073/pnas.1907697116>.
- Sosada-Ludwikowska, F., Wimmer-Teubenbacher, R., Sagmeister, M., & Köck, A. (2019). Transfer printing technology as a straightforward method to fabricate chemical sensors based on tin dioxide nanowires. *Sensors*, *19*(14), 3049. Available from <https://doi.org/10.3390/s19143049>.
- Souri, H., Banerjee, H., Jusufi, A., Radacsi, N., Stokes, A. A., Park, I., Sitti, M., & Amjadi, M. (2020). Wearable and stretchable strain sensors materials, sensing mechanisms, and applications. *Advanced Intelligent Systems*, *2*, 2000039. Available from <https://doi.org/10.1002/aisy.202000039>.
- Wang, X., Deng, Y., Jiang, P., Chen, X., & Yu, H. (2022). Low-hysteresis, pressure-insensitive, and transparent capacitive strain sensor for human activity monitoring. *Microsystems and Nanoengineering*, *8*(1). Available from <https://doi.org/10.1038/s41378-022-00450-7>, <http://www.nature.com/micronano/>.
- Wang, A., Jung, D., Lee, D., & Wang, H. (2021). Impedance characterization and modeling of subcellular to micro-sized electrodes with varying materials and PEDOT:PSS coating for bioelectrical interfaces. *ACS Applied Electronic Materials*, *3*(12), 5226–5239. Available from <https://doi.org/10.1021/acsaem.1c00687>, <http://pubs.acs.org/journal/aeembp>.
- Wang, C., Linghu, C., Nie, S., Li, C., Lei, Q., Tao, X., Zeng, Y., Du, Y., Zhang, S., Yu, K., Jin, H., Chen, W., & Song, J. (2020). Programmable and scalable transfer printing with high reliability and efficiency for flexible inorganic electronics. *Science Advances*, *6*(25). Available from <https://doi.org/10.1126/sciadv.abb2393>, <https://advances.sciencemag.org/content/advances/6/25/EABB2393.full.pdf>.
- Won, S. M., Wang, H., Kim, B. H., Lee, K., Jang, H., Kwon, K., Han, M., Crawford, K. E., Li, H., Lee, Y., Yuan, X., Kim, S. B., Oh, Y. S., Jang, W. J., Lee, J. Y., Han, S., Kim, J., Wang, X., Xie, Z., ... Rogers, J. A. (2019). Multimodal sensing with a three-dimensional piezoresistive structure. *ACS Nano*, *13*(10), 10972–10979. Available from <https://doi.org/10.1021/acsnano.9b02030>, <http://pubs.acs.org/journal/ancac3>.
- Yamashita, T., Takamatsu, S., Okada, H., Itoh, T., & Kobayashi, T. (2018). Development of flexible piezoelectric strain sensor array. *Electrical Engineering in Japan*, *204*(1), 52–58. Available from <https://doi.org/10.1002/ej.23084>.
- Yan, Z., Pan, T., Xue, M., Chen, C., Cui, Y., Yao, G., Huang, L., Liao, F., Jing, W., Zhang, H., Gao, M., Guo, D., Xia, Y., & Lin, Y. (2017). Thermal release transfer printing for stretchable conformal bioelectronics. *Advanced Science*, *4*(11), 1700251. Available from <https://doi.org/10.1002/advs.201700251>.
- Ye, J., Zhang, F., Shen, Z., Cao, S., Jin, T., Guo, X., Li, Z., Lin, L., & Zhang, Y. (2021). Tunable seesaw-like 3D capacitive sensor for force and acceleration sensing. *NPJ Flexible Electronics*, *5*(1). Available from <https://doi.org/10.1038/s41528-021-00125-9>, <http://nature.com/npjflexelectron/>.

- Yogeswaran, N., Navaraj, W. T., Gupta, S., Liu, F., Vinciguerra, V., Lorenzelli, L., & Dahiya, R. (2018). Piezoelectric graphene field effect transistor pressure sensors for tactile sensing. *Applied Physics Letters*, *113*(1), 014102. Available from <https://doi.org/10.1063/1.5030545>.
- Yuan, Y., Liu, B., Li, H., Li, M., Song, Y., Wang, R., Wang, T., & Zhang, H. (2022). *Flexible Wearable Sensors in Medical Monitoring*, *12*(12), 1069. Available from <https://doi.org/10.3390/bios12121069>.
- Zhang, C., Liu, S., Huang, X., Guo, W., Li, Y., & Wu, H. (2019). A stretchable dual-mode sensor array for multifunctional robotic electronic skin. *Nano Energy*, *62*, 164–170. Available from <https://doi.org/10.1016/j.nanoen.2019.05.046>, <http://www.journals.elsevier.com/nano-energy/>.
- Zhang, Y., Zheng, N., Cao, Y., Wang, F., Wang, P., Ma, Y., Lu, B., Hou, G., Fang, Z., Liang, Z., Yue, M., Li, Y., Chen, Y., Fu, J., Wu, J., Xie, T., & Feng, X. (2019). Climbing-inspired twining electrodes using shape memory for peripheral nerve stimulation and recording. *Science Advances*, *5*(4). Available from <https://doi.org/10.1126/sciadv.aaw1066>, <https://advances.sciencemag.org/content/5/4/eaaw1066/tab-pdf>.
- Zhao, H., Kim, Y., Wang, H., Ning, X., Xu, C., Suh, J., Han, M., Pagan-Diaz, G. J., Lu, W., Li, H., Bai, W., Aydin, O., Park, Y., Wang, J., Yao, Y., He, Y., Saif, M. T. A., Huang, Y., Bashir, R., & Rogers, J. A. (2021). Compliant 3D frameworks instrumented with strain sensors for characterization of millimeter-scale engineered muscle tissues. *Proceedings of the National Academy of Sciences*, *118*(19), e2100077118. Available from <https://doi.org/10.1073/pnas.2100077118>.
- Zhao, H., Lee, Y., Han, M., Sharma, B. K., Chen, X., Ahn, J.-H., & Rogers, J. A. (2020). Nanofabrication approaches for functional three-dimensional architectures. *Nano Today*, *30*, 100825. Available from <https://doi.org/10.1016/j.nantod.2019.100825>.
- Zhao, H., Li, K., Han, M., Zhu, F., Vázquez-Guardado, A., Guo, P., Xie, Z., Park, Y., Chen, L., Wang, X., Luan, H., Yang, Y., Wang, H., Liang, C., Xue, Y., Schaller, R. D., Chanda, D., Huang, Y., Zhang, Y., & Rogers, J. A. (2019). Buckling and twisting of advanced materials into morphable 3D mesostructures. *Proceedings of the National Academy of Sciences of the United States of America*, *116*(27), 13239–13248. Available from <https://doi.org/10.1073/pnas.1901193116>, <https://www.pnas.org/content/pnas/116/27/13239.full.pdf>.
- Zhou, Z., Zhang, H., Liu, J., & Huang, W. (2021). Flexible electronics from intrinsically soft materials. *Giant*, *6*, 100051. Available from <https://doi.org/10.1016/j.giant.2021.100051>.

CHAPTER 11

Construction of flexible transistors enabled by transfer printing

Han Eol Lee^{1,2,3}

¹Division of Advanced Materials Engineering, Jeonbuk National University, Jeonju, South Korea

²Department of Electronic Engineering, Jeonbuk National University, Jeonju, South Korea

³Department of JBNU-KIST Industry-Academia Convergence Research, Jeonbuk National University, Jeonju, South Korea

11.1 Introduction

Since the development of thin-film transistors (TFTs) in 1925, TFTs have been suggested as field effect transistors (FETs) for applying integrated circuits (ICs) (Arns, 1998; Kuo, 2008, 2013, 2018; Zhang et al., 2011). However, because the industry of single crystal silicon (sc-Si) with high-performance was widely extended in the IC field, it was difficult to realize the TFT-based IC circuits. Therefore, new TFT applications had been spotlighted such as active-matrix (AM) displays, power devices, and various types of sensors (Jayathilaka et al., 2019; Kwon & Pode, 2013; Lee, Shin, Park et al., 2019; Park et al., 2017). Especially, AM liquid crystal display (AMLCD) was a representative application of the TFT using the sputtered compound semiconductors (e.g., CdS and CdSe) at room temperature (RT) (Badano et al., 2003; Pavlicek et al., 2000; Petrov, 1995; Sheraw et al., 2002). Because the AM for operating the display was composed of large-sized one transistor/one capacitor (1T-1C) or two transistor/one capacitor (2T-1C), the TFT was a best-fit strategy to realize the driving circuit due to their simple fabrication processes, low-cost materials, and excellent repeatability (Chen et al., 2016; Duan et al., 2003; Sun et al., 2016; Zhu et al., 2020). After the first demonstration of AMLCD in 1973, most researchers had been concentrated to investigate the AM circuits and enhance the process reliability, device uniformity, and repeatability (Heikenfeld et al., 2011; Kamiya et al., 2009; Pribat et al., 2011; Reuss et al., 2005).

These issues had been gradually solved by a realization of hydrogenated amorphous silicon (a-Si:H)-based TFTs. The a-Si:H TFT was successfully accomplished by the plasma-enhanced chemical vapor deposition (PECVD) method in 1979, enabling to establish large array of TFTs and storage capacitors on a glass substrate at low temperature (Kuo, 2013; Shim et al., 2020; Wu, 1994). In a word, it was the right technology to reduce manufacturing costs and ensure repeatable production for LCD mass production. However, the a-Si with the disorderly arrangement of silicon had a critical disadvantage of low electron mobility during the TFT operation (Kamiya & Hosono,

2010; Kamiya et al., 2016; Shim et al., 2020; Siringhaus, 2014). By considering that the TFT controlled the current flow to adjust the brightness of each pixel in the display screen, the a-Si TFTs with slow signal transmission speed could be only utilized to low-resolution LCDs, but not complex high-resolution displays (Arias et al., 2010; Guo et al., 2017; Heikenfeld et al., 2011; Menard et al., 2007).

Recently, low-temperature poly-silicon (LTPS) TFT was proposed to alternate the a-Si TFTs by recrystallizing the highly disordered atoms in amorphous silicon with a laser to the orderly poly-crystalline silicon (poly-Si), accomplishing hundreds of times faster electron mobility than the a-Si TFT (Gao et al., 2015; Lin & Chen, 2007; Lin et al., 2011; Lin et al., 2012; Wager, 2020; Yoneda et al., 2001). Furthermore, the smaller-sized poly-Si TFT than the a-Si TFT could achieve sufficient drive current and the increased effective area, enabling high-resolution displays due to the improved aperture opening ratio (Boyce & Mei, 2000). Because the LTPS TFTs were directly integrated into the glass, they could be applied to small or medium-sized LCDs for realizing low-cost, efficient power consuming, and ultrathin displays (Lee & Souk, 2018; Werner, 1975; Wu, Chen et al., 2005). These effective advances in mass production in the TFT field have opened a new era of the LCD industry for several global companies.

By entering the internet of things (IoT) era, a form-factor, which means a structured form, has been emerging as a significant factor in the electronics field (Khan, Thielens et al., 2020; Kim et al., 2013). This form factor innovation has been expected to be developed for improving flexibility to overcome the limitation of the rigid form of the displays in the future (Hou et al., 2019; Koo et al., 2018). Form factor innovation has been important in the display industry because it is necessary to secure new growth momentum as the LCDs, which have led technology development and market growth for the past decades, are maturing (Jeong et al., 2014; Kang et al., 2021; Lee et al., 2023; Lee, 2021; Lee, Choi, et al., 2018; Lee, Lee et al., 2019; Lee, Shin, Lee et al., 2019). Another factor is the desire for a form factor that can be utilized freely and conveniently regardless of usage environment conditions, away from typical form factors customized for specific usage environments in the past due to increased mobility of consumers, convergence between devices, and rapid progress in smartization (Bock et al., 2014; Hou et al., 2019). Form factor innovation will be a big wave in the display industry in the future in terms of the inconvenience users feel about their current displays and the potential to differentiate themselves from LCDs. Therefore, considering the usage of flexible electronics that repeat the deformation process indefinitely, such as 'folding and unfolding' and 'rolling and unrolling', flexible displays need to satisfy technical requirements such as flexibility, durability, and mass production (Sun et al., 2020; Wang et al., 2019; Zhang, Huang et al., 2020). First, there should be flexibility which can withstand repeated external mechanical stress and restore their

initial structure. Second, despite periodic changes, the durability of the displays is important to maintain their performance, lifespan, and quality. Third, new processes which can simultaneously achieve mass production and decline in production cost, are also essential requirements. In order to accomplish these technical requirements, technological innovations such as substrates, light sources, TFT-based circuits, and process technology should be supported (Chang et al., 2012; Geffroy et al., 2006; Giannouli et al., 2015; Keum et al., 2020; Martinez et al., 2012; Mujahid et al., 2020). The emerged first flexible device was a flexible organic thin film field effect transistor (f-OTFT). As conducting polymers were discovered in the 1970s, organic electronics had been rapidly developed in the past two decades (Fukuda et al., 2014; Gong et al., 2018; Li et al., 2012; Lucas et al., 2009; Minamiki et al., 2021). These organic electronics have many advantages such as low cost, low temperature, light weight, flexibility, and large-area fabrication. The first OTFT was demonstrated by using polythiophene as an active layer in 1986, subsequently achieving great progresses over the last two decades (Chang et al., 2006; Torsi et al., 2003; Wu, Liu et al., 2005). In particular, p-type OTFTs have already caught up with a-Si TFT in mobility and replaced their position in the display industry. Solution-processed fabrication technologies of f-OTFTs (e.g., spin-coating, dipping, and inkjet printing) have overcome the limitations of traditional photolithography process such as high-temperature, expensive, toxic, time-consuming procedure, showing a suitability to flexible electronics (Lee et al., 2008; Xie et al., 2020). However, there are still intrinsic critical issues of organic materials including water/heat instability, bad durability, and short lifetime.

In order to solve these problems of organic materials, flexible inorganic material-based TFTs are required to be realized with thermal/mechanical/humidity stability and a long lifetime (Kwon et al., 2019; Xiang & Tress, 2019; Zhang & Rogers, 2019). Although these inorganic TFTs should be accompanied by a high-temperature thermal annealing process to obtain the desired performances, flexible plastic substrates cannot endure high-temperature processes over 300°C (Liu et al., 2019; Mitzi, 2004; Ni et al., 2015; Zhai et al., 2012). Therefore, a transfer printing technique has been proposed in which inorganic TFTs or circuits are fabricated onto rigid substrates such as Si, GaAs, and glass, and transferred to flexible plastic substrates (Baeg & Lee, 2020; Choi et al., 2017; Dahiya et al., 2020; Sun & Rogers, 2007).

In this chapter, major progress of TFT transfer printing techniques and key advancements are introduced in terms of transferred materials (e.g., carbon, ion gel, polymer, oxide, compound semiconductor, and Si), novel transfer methodologies (e.g., dry transfer, laser lift-off, mechanical delamination, roll-to-roll printing, and wet transfer), and flexible applications including photodetector, complementary inverter, gas sensor, AM circuit, and glucose sensor. Furthermore, the possible future developments are also examined and discussed to overcome challenges that several researchers have faced in this flexible TFT field.

11.2 Flexible Si thin-film transistors

Research about single-crystal Si semiconductors, the most excellent material in terms of electrical performance, heat/water stability, and material cost, have recently begun to apply to flexible electronic devices (Lee et al., 2010; Menard et al., 2005; Qin et al., 2009; Shou et al., 2019; Yuan et al., 2009). Although typical single-crystal Si is brittle by external mechanical stresses, low-dimension Si including in the form of micro/nanosized wires, ribbons, plates, and thin films can be printable to flexible plastic substrates due to its enhanced mechanical flexibility (Baca et al., 2007, 2008; Mack et al., 2006; Park, Lee, Wi et al., 2016; Yoon et al., 2008). A representative transfer printing technique is known as a top-down method of extracting a micro/nanosized Si structures from a mother wafer through a wet-etching process. This process has the important advantage of process versatility such as advanced complementary metal-oxide-semiconductor (CMOS) technology and a high-temperature annealing process (Hussain & Hussain, 2016; Park et al., 2020; Seo et al., 2017; Wang, Al-Jawhari et al., 2015; Zhang & Zhang, 2014).

Flexible Si transistors for large-area radio-frequency (RF) applications were realized with a nanotrench structure onto a flexible polyethylene terephthalate (PET) film by using dry transfer printing (Seo et al., 2016). In general, RF transistors have some advantages that apply flexible electronic devices to wireless data/power transmission and operating circuits with low power consumption due to their excellent signal processability (Sarpeshkar et al., 2008; Sawan et al., 2005). However, the major challenges in implementing flexible RF TFTs were a lack of flexible materials with sufficient carrier mobility and a difficulty in forming a ultrasmall channel by the existing CMOS processes (Khan, Tareen et al., 2020; Parbrook et al., 2021). Although flexible single-crystal semiconductor nanomembranes (NMs) adequately satisfied first requirements, deep submicron features were hard to pattern on the NMs on flexible substrate. These challenges related to conventional transistor structures and their fabrication processes become the most important factor when the device dimensions are reduced, restricting the electrical performance of flexible electronic devices (Devoret & Schoelkopf, 2000; Heo et al., 2018; Martins et al., 2013; Zeng et al., 2014). Currently, the smallest channel length of the flexible NM-based transistor formed on the plastic is just approximately 1 μm . In order to solve this critical problem and produce large-scale, high-performance flexible RF transistors, Si NMs were patterned by a nanoimprinting lithography (NIL) technology to make a three-dimensional nanotrench structure (sub-100 nm channel length), and transferred onto PET substrate by dry transfer printing (Seo et al., 2016). Fig. 11.1A and B illustrate a procedure comparison between the proposed three-dimensional nanotrench Si NM-based flexible TFT and the conventional Si TFT. The NM of silicon-on-insulator (SOI) wafer was utilized to make RF TFTs with high-mobility. Prior to NIL process, phosphorous implantation was fulfilled to form n^{++} doping layer at p -Si NM. Then, sub-

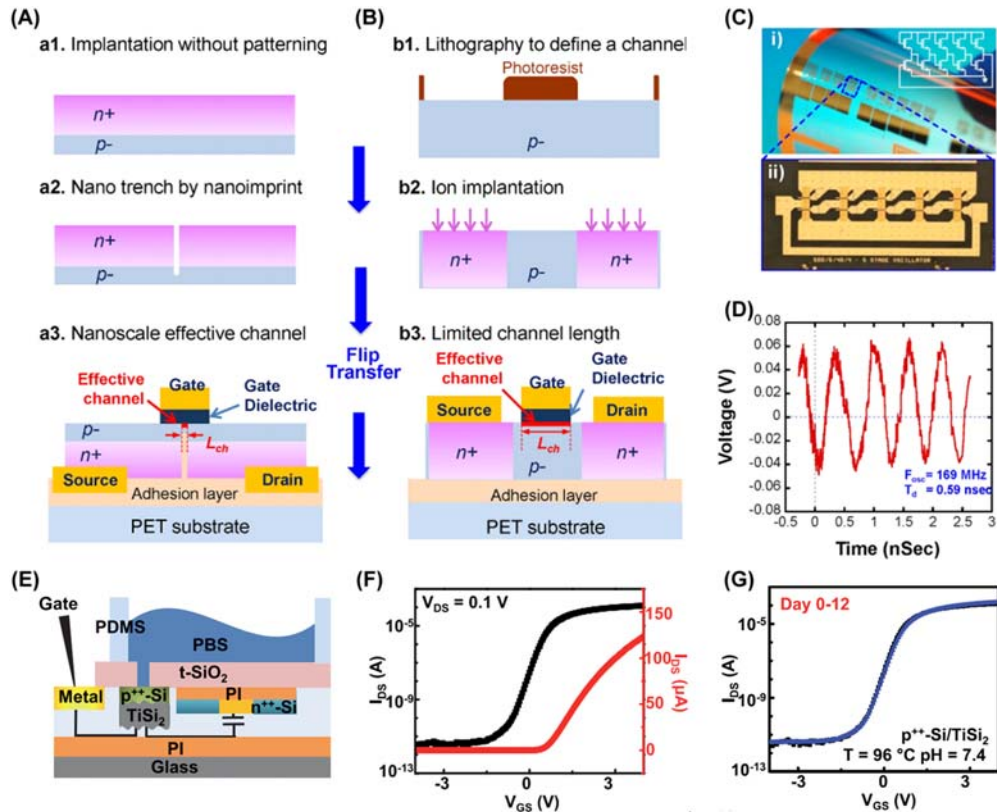


Figure 11.1 Flexible Si thin-film transistors. Fabrication process of (A) a flexible radio frequency TRT with three-dimensional trench Si NM, and (B) a conventional flexible thin-film transistor (TFT). (C) Optical images of flexible TFTs and ring oscillators on a single flexible substrate. (D) Voltage–time curve of flexible five-stage ring oscillator. (E) Schematic illustration of a NMOS transistor during PBS soaking test. Transfer curve of (F) flexible NMOS transistor as fabricated, and (G) after 12-day soaking tests. From Seo, J. H., Ling, T., Gong, S., Zhou, W., Ma, A. L., Guo, L. J., & Ma, Z. (2016). Fast Flexible Transistors with a Nanotrench Structure. *Scientific Reports*, 6. <https://doi.org/10.1038/srep24771>, and Li, J., Li, R., Du, H., Zhong, Y., Chen, Y., Nan, K., Won, S. M., Zhang, J., Huang, Y., & Rogers, J. A. (2019). Ultrathin, transferred layers of metal silicide as faradaic electrical interfaces and biofluid barriers for flexible bioelectronic implants. *ACS Nano*, 13(1), 660–670. <https://doi.org/10.1021/acsnano.8b07806>.

100 nm deep trench was created by NIL and anisotropic dry etching processes. Since the effective channel length (L_{ch}) of the NIL-induced TFT is absolutely independent of the doping region unlike that of the conventional TFT, the proposed TFT can obtain sub-micron channel without the influence of gate length. After depositing Au thin-films as source/drain electrodes, the film was detached from the SOI wafer by SiO_2 wet etching, and then attached to the PET film with a flipped state. The flexible TFT was completed by forming Al_2O_3 gate dielectric and Au gate electrode onto the p-Si surface. For

optimizing the trench depth and width which is closely related to L_{ch} , semiconductor simulations were carried out, proving that the TFTs with narrow and shallow trenches have a large amount of leakage current and field effect controllability. The TFT was applied to a flexible 5-stage ring oscillator, as shown in Fig. 11.1C. Flexible ring oscillator had a 169 MHz oscillation frequency and 0.59 ns delay time at 2 V of V_{DD} (Fig. 11.1D).

TiSi₂-based flexible n-channel metal oxide semiconductors (NMOS) transistors were realized to be high-performance implantable devices with the increased lifetime in the human body (Li et al., 2019). TiSi₂ was made as follows. SOI wafer was doped by boron at 1000°C for 15 minutes for making p⁺⁺-Si layer (doping concentration: 10²⁰/cm³). After depositing Ti thin-film, 850°C thermal annealing was fulfilled to form TiSi₂/p⁺⁺-Si/SiO₂ structure. Then, n-type Si transistor was transfer-printed by polydimethylsiloxane (PDMS) and laterally interconnected with TiSi₂/p⁺⁺-Si layers for forming a Faradaic biointerface. By soaking tests of p⁺⁺-Si, Ti, P⁺⁺-Si/Ti, and Ti/p⁺⁺-Si in phosphate-buffered saline (PBS) solution, Ti-coated p⁺⁺-Si showed 2-times increased lifetime compared to bare p⁺⁺-Si, owing to the slow diffusion of water from the surface to Si. Fig. 11.1E displayed a soaking test diagram of flexible n-type MOSFET (20 μm channel length and 400 μm channel width) interconnected with p⁺⁺-Si/TiSi₂. According to the transfer curve in Fig. 11.1F and G, the device had approximately 300 cm²/V/s mobility, approximately 10³ I_{on}/I_{off} ratio, and approximately 200 mV/dec subthreshold swing (SS), maintaining its performance until 12 days in 96°C PBS solution. These flexible Si TFTs with long lifetime provide a significant potential for high-performance electrophysiological devices in biomedical fields. Future studies should contain that the suggested concepts need to be applied to active multiplatform systems with various scales.

11.3 Compound semiconductor-based flexible transistors

Compound semiconductors mean semiconductor materials with two or more types of elements (III–V or III–N series), unlike a single-element semiconductor (Si or Ge) (Detchprohm et al., 2019; Ferguson et al., 2001; Kim et al., 2022; Kum et al., 2019; Peng et al., 2019; Yuan et al., 2021). In the past few decades, single-element semiconductors have accomplished swift technological progress by achieving high-density device integration, but RC delay and heat generation problems have been discovered in the semiconductor devices with sub-10 nm line width/pitch (Chen et al., 2015; Choi et al., 2022; Reddy et al., 2012; Vidya et al., 2018). In order to resolve these obstacles in the semiconductor industry, researches about compound semiconductors have been actively implemented as next-generation materials (Decoutere et al., 2010; Jeong et al., 2022; Zhang et al., 2018). In particular, compound semiconductors have significant merit in that the element combination can be diversified to make a specialized semiconductor with specific properties such as high speed (5–10 times of Si mobility), high voltage (~2 times of Si), low power consumption (1/8–1/10 of Si),

high frequency (10 MHz to 100 GHz), and high-temperature applications (Pillarisetty, 2011; Riel et al., 2014; Subash et al., 2014). These compound semiconductors are mainly utilized for nonmemory devices, consisting of system semiconductors, optical devices, and power devices. Furthermore, with the development of various technologies such as defense industry, 5G communication networks, electric vehicles, and renewable energy, the need for flexible devices with free form-factor is increasing, nowadays (Flamini et al., 2022; Kim et al., 2016, 2017; Lee, Lee et al., 2020; Park et al., 2022; Subramanyam et al., 2013).

Micro-structured semiconductors ($\mu\text{s-Sc}$) of compound semiconductors have been also easily manufactured by using a wafer with interlayer structures such as GaAs/AlAs/SiGaAs or AlGaN/GaN/Si (Baca et al., 2008). The producing process is the same as the Si NM transfer method from the SOI substrate which was mentioned in the above section. First, by patterning a photoresist (PR) on a wafer surface and wet-etching a specific sacrificial layer under the semiconductor (e.g., SiO_2 in SOI, AlAs in GaAs/AlAs/SiGaAs, and Si in AlGaN/Si), the ribbons, rods, wires, and thin-films with specific sizes can be easily delaminated by the PDMS elastomeric stamp from the mother wafer (Geiger et al., 2020; Kim et al., 2020; Namdari et al., 2020). This simple transfer printing has been applied to single crystalline GaAs, InP, and GaN materials, developing various types of high-performance flexible electronic devices.

Sun et al. developed flexible metal-semiconductor FET (MESFET) using high-performance GaAs wire with ohmic contacts (Sun et al., 2006). The main process was on the basis of top-down process using a bulk GaAs wafer with single crystallinity. After forming ohmic contacts between n-type GaAs and AuGe/Ni/Au metal thin-film, the patterned GaAs wires became the freestanding state by conducting wet-etching of the sacrificial layer (Ti/SiO_2). The freestanding wires were attached to the PDMS stamp, and then released onto the polyurethane (PU) adhesive-coated PET film. By forming the gate and source/drain electrodes on the transferred wires, the flexible MESFET array was completely finished. In accordance with transfer curves, flexible GaAs MESFET showed $I_{\text{on}}/I_{\text{off}}$ ratio of approximately 10^6 , and a maximum transconductance of approximately $880 \mu\text{S}$. The GaAs wire-based MESFET had some advantages of no parasitic capacitance, high intrinsic mobility over $8000 \text{ cm}^2/\text{V/s}$, a simple fabrication process without gate dielectric layer unlike MOSFET, and high-speed operation on a flexible substrate. These high-performance flexible MESFETs could be complexly combined in parallel or series for demonstrating NOR or NAND gates. Despite of high-cost GaAs material, $\mu\text{s-Sc}$ transfer printing with high yield compensated for the demerit by enabling to build of high-performance transistors and logic circuits on the flexible substrate. Not only low-dimension $\mu\text{s-Sc}$ but also thin-film compound semiconductors were also utilized for flexible transistors (Lerner et al., 2018). After fabricating a GaN-based high electron mobility transistor (HEMT) on $\langle 111 \rangle$ Si wafer, the device was passivated by a silicon nitride layer, and tethered by

polymer anchors. By etching the bottom Si using KOH, the device was in a freestanding state, and detached from the wafer through PDMS stamp. The device attached to the stamp surface could be transferred onto a CMOS circuit or flexible substrate for the purpose. According to thermal simulations and experimental analyses, Si CMOS or flexible substrate can electrically isolate the vertically-stacked GaN HEMT without any vertical leakage current and influence of thermal resistance.

Flexible microwave integrated circuits (f-MIC), which have been considered as a potential candidate for flexible wireless communication system, was demonstrated to transfer AlGaIn/GaN HEMT onto wood-derived cellulose nanofibril (CNF) substrate (Zhang, Li et al., 2020). Heterogeneously-integrated monolithic f-MIC (f-MMIC) was produced by the following procedure. The high-density array of AlGaIn/GaN HEMT was fabricated on a 1 mm-thick Si wafer, and selectively transfer printed on a carrier substrate. After making passive microwave components based on the HEMT, they were simultaneously printed onto a flexible CNF substrate. Fig. 11.2A and B depict microscopic images of AlGaIn/GaN HEMT-based f-MIC amplifier and the active HEMT region, respectively. The f-MIC amplifier was composed of III-N HEMT, input (2.5-turn spiral inductor)/output (1.5-turn spiral inductor) impedance matching networks and SiO₂-based capacitor (30 × 40 μm size). The devices showed the increasing peak-gain value and the decreasing peak-gain frequency when the gate bias (V_{GS}) was increased, as shown in Fig. 11.2C. This degradation was come from the impedance mismatching between the HEMT and the input/output impedance due to the slightly bent amplifier device, which was also confirmed by simulations. Because the device was transfer printed onto the biodegradable wood-based flexible substrate, it could be burned and easily disposed by fungi (Fig. 11.2D). On the basis of these results, this f-MIC was first realized to enable to make 10 mW output power with > 5 GHz, indicating the possibility of future green electronics with biodegradability.

Zhang et al. demonstrated flexible AlGaIn/GaN HEMT using an insulator removal-based transfer printing technique (Zhang et al., 2022). Heterogeneous structure with AlGaIn and GaN was grown on Si (111) wafer and then bonded onto SiO₂-deposited Si (100) wafer. After removing Si (111) by chemical/mechanical grinding, Si (100)/AlGaIn/GaN was bonded onto SiO₂/SiN/SiO₂-deposited Si (111) wafer, again. After these twice flipping/bonding processes, the AlGaIn/GaN substrate was completely fabricated by wet-etching Si (100). By removing SiO₂ and SiN layers, the AlGaIn/GaN HEMTs, which were formed onto the AlGaIn/GaN substrate, was transfer printed through PDMS onto a flexible SU8-coated PET film. In the output curves of rigid and flexible HEMT devices, the maximum saturated drain current density ($I_{DS,max}$) of flexible HEMT was 110 mA/mm which decreased value compared to rigid one (226.7 mA/mm). According to finite element method (FEM) simulations, the AlGaIn layer dissipated the heat that was self-generated during the device operation due to its extremely high mobility. However, this degradation of

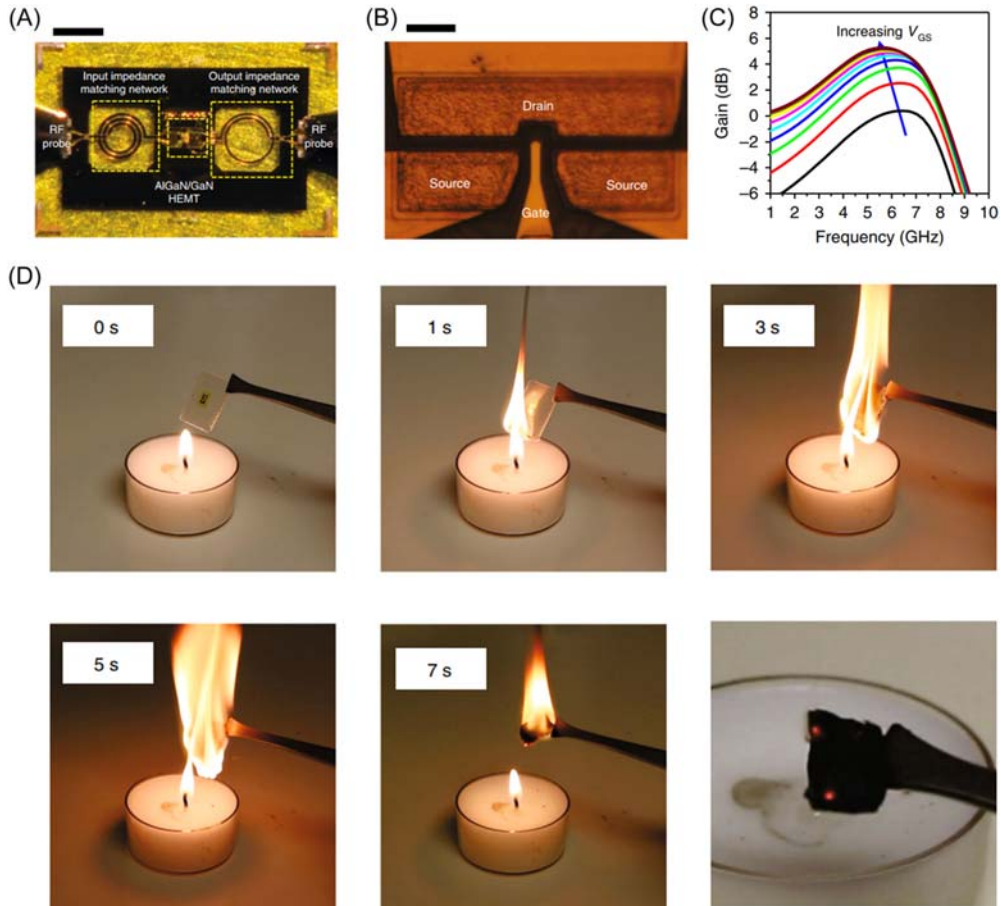


Figure 11.2 Compound semiconductor-based flexible transistors. (A) Optical image of AlGaIn/GaN HEMT-based flexible amplifier. (B) Magnified microscopic image of the HEMT in flexible amplifier. (C) Gain value of flexible amplified as a function of frequency under 28.5 mm bent condition. (D) Incineration photographs of flexible amplifier with time. From Zhang, H., Li, J., Liu, D., Min, S., Chang, T. H., Xiong, K., Park, S. H., Kim, J., Jung, Y. H., Park, J., Lee, J., Han, J., Katehi, L., Cai, Z., Gong, S. & Ma, Z. (2020). Heterogeneously integrated flexible microwave amplifiers on a cellulose nanofibril substrate. *Nature Communications*, 11(1). <https://doi.org/10.1038/s41467-020-16957-4>.

electrical property is attributed to the self-heating effect of flexible HEMT on the flexible substrate with low thermal conductivity. The $I_{DS,max}$ of flexible HEMT was affected by stress conditions. When the $I_{DS,max}$ at flat state (stress = 0 MPa) was set as a reference point, the $I_{DS,max}$ was increased in tensile stress and decreased in compressive stress due to piezoelectric charge accumulation at the junction interface of the heterogeneous structure. According to the bending fatigue test results of flexible AlGaIn/GaN HEMT at 88 MPa tensile strain during periodic 50 cycles, the device maintained

its $I_{DS,max}$ value with only 5% property degradation, which resulted from the strain-free structure of the fabricated flexible HEMT. Consequently, the AlGaIn layer in the heterostructure took important roles of the dislocation-suppressing buffer layer in the epitaxy, and the heat dissipation layer during the device operation, which was achieved by the developed insulator removal-based transfer method.

11.4 Flexible transistors with carbon materials

Carbon-based materials including graphite, carbon nanotube (CNT), and graphene have been suggested for applying to flexible TFTs owing to their significant performance metrics of intrinsic flexibility, superior electrical properties (e.g., fast operating speed, high power efficiency, and excellent mobility), and transparency (Baek et al., 2017; Kim, Im et al., 2019; Wang et al., 2020). Especially, although the CNTs have strengths for flexible devices including low material cost, and chirality of conducting/semiconducting, large-scale array fabrication of CNT-based devices, has been an important obstacle to their commercialization. Ishikawa et al. solved this scalability issue of CNT-based flexible TFT array by using the transfer printing technique (Ishikawa et al., 2009). They grew the aligned single-wall CNT (SWCNT) on a quartz wafer by using the chemical vapor deposition (CVD) method and then transferred the SWCNTs onto the target substrate through a 120°C-thermal releasing tape. This material transfer to the target area was carried out at low temperatures, which is an essential factor for realizing flexible TFTs. Fig. 11.3A shows a scanning electron microscopy (SEM) image of the transferred SWCNTs on a SU8-coated glass substrate. Large amounts of the transferred SWCNTs (length: >50 μm , diameter: 1–2 nm, and CNT density: 1–2 tubes/ μm) were fabricated to TFTs with various channel widths from 8 to 100 μm , as shown in Fig. 11.3B. The highly-aligned SWCNTs were utilized as an active material of the TFTs, composed of ITO, SU8, and Au/ITO layers as gate, gate dielectric (GI), and source/drain contacts (the inset SEM image of Fig. 11.3B). The fabricated TFTs on the glass substrate exhibited excellent effective mobility of approximately 1300 $\text{cm}^2/\text{V}\cdot\text{s}$ (Fig. 11.3C) and high on/off ratio of 3×10^4 (Fig. 11.3D). Furthermore, flexible and fully-transparent SWCNT TFTs were demonstrated with ITO gate, 2 μm -thick SU8 GI, and ITO source/drain on the PET substrate. Flexible TFTs maintained their electrical properties even at 120 degrees bending angle, presenting superior flexibility, as shown in Fig. 11.3E. The developed TFTs were applied to logic gates and a driving circuit of light sources. Fig. 11.3F is an optical image of a flexible PMOS inverter on the PET film using only one SWCNT. The flexible inverter had a approximately 0.38 gain at the input voltage of approximately 12 V. The light intensity of a GaN-based light-emitting diode (LED) was stably modulated by the electrically connected SWCNT TFT. According to these

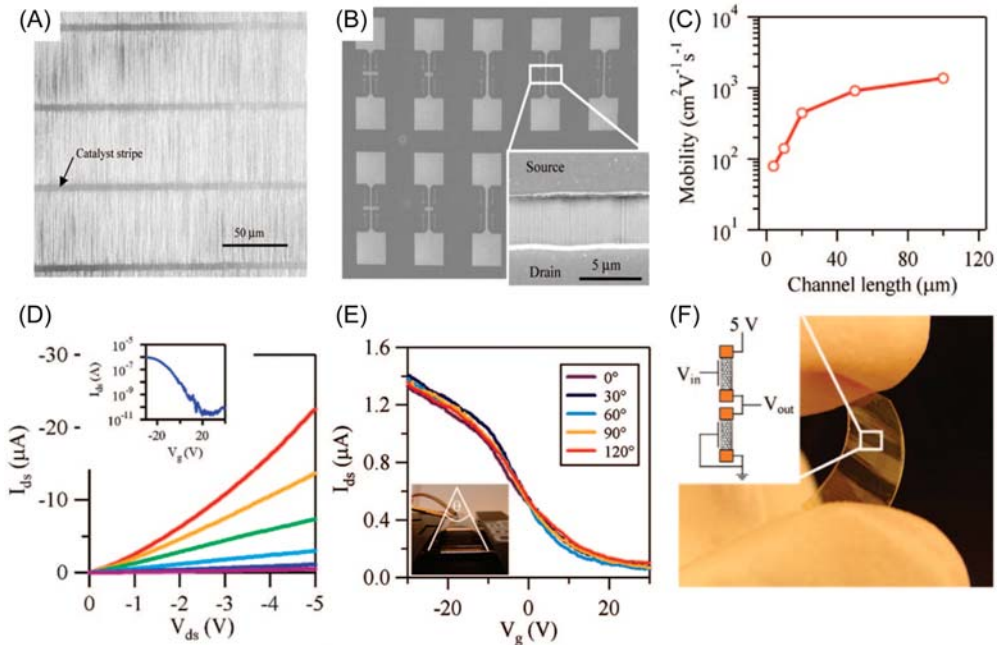


Figure 11.3 Flexible transistors with carbon materials. (A) Scanning electron microscopy (SEM) image of the transferred single-wall carbon nanotubes (SWCNTs) with excellent alignment. (b) SEM image of the SWCNT-based transistors. (C) Mobility of the SWCNT transistors according to channel length. (D) Output curve of the fabricated SWCNT-transistor. The inset shows transfer curve of the device. (E) Transfer curve of the device under various bent condition. (F) Optical image of flexible transparent SWCNT inverter, and its circuit diagram. From Ishikawa, F. N., Chang, H. K., Ryu, K., Chen, P. C., Badmaev, A., De Arco, L. G., Shen, G. & Zhou, C. (2009). Transparent electronics based on transfer printed aligned carbon nanotubes on rigid and flexible substrates. *ACS Nano*, 3(1), 73–79. <https://doi.org/10.1021/nn800434d>.

results, the suggested transfer printing method of massive SWCNTs has a significant potential to realize high-performance, transparent and flexible TFT devices for several optoelectronic applications.

Tseng et al. suggested a new dry transfer method of SWCNT, which solved limitations of the existing dry/wet transfer techniques such as a clumsy dry stamp and material damage during wet transfer (Tseng & Tai, 2009). The developed printing method has significant advantages including the strong adherence between SWCNTs and flexible polycarbonate (PC) substrate and the maintenance of a dense SWCNT network with excellent electrical properties. The randomly distributed SWCNTs, which were grown on SiO₂/Si wafer by using CVD, were attached to 160°C-heating PC substrate and were partially embedded into a slightly viscous polymer due to the conglutinating effect of PC. After spin-coating of polymethylmethacrylate (PMMA) as a dielectric

layer, second SWNT transfer was performed onto 70°C-heating PMMA for making a conducting channel of the TFT. Then, 20 nm-thick Au film was deposited as source/drain electrodes. The transferred SWCNT layer maintained its intrinsic conductivity of 5–6 k Ω /sq and transparency of approximately 80%. The FET had a typical p-type behavior of approximately 10⁻⁴A current. The TFT with the bottom gate exhibited a regular I - V curve at 0.5 V drain voltage, performing 10⁻⁷A on-current, which is approximately 1000 times lower than that of the FET, because of the embedding and density decrease of the SWCNTs during the transfer process. According to the increase of the device channel length, flexible TFT had an increased electron mobility of 23.4 cm²/V/s and a decreased $I_{\text{on}}/I_{\text{off}}$ ratio of approximately 10³. Furthermore, in spite of the bent state of flexible TFT with 6 mm bending curvature radius, the drain current showed a negligible decrease of 7%, and recovered at the released state. Wang et al. proposed a simple transfer printing method of the CNT layer with a simple manufacturing pathway (Wang et al., 2020). In order to fabricate the flexible substrate of all CNT-based TFT, polyimide film (PI) was dip-coated by multiwall CNT (MWCNT) suspension, and then spin-coated by SU-8/PU layers as a dielectric layer). On the PU, SWCNT, and MWCNT layers were successively dry-transferred as electrodes of the TFT by using PDMS. By the analyses of the electrical properties, the all CNT-based flexible TFT had 6.39 cm²/V/s mobility and approximately 10⁵ $I_{\text{on}}/I_{\text{off}}$ ratio, which was higher than other printed all-CNT transistors despite low dielectric constant of SU-8/PU layer. According to these results, the directed transfer printing of the carbon material was realized to demonstrate various types of flexible TFT without any high-vacuum and high-temperature annealing processes. The proposed transfer technique could be repeatedly used to stack carbon-based layers, showing a major advantage in terms of a manufacturing viewpoint.

11.5 Ion gel-based flexible transistors

Ion gel materials have been newly proposed as insulating materials with high-capacity for flexible electronics such as low-voltage TFTs, capacitors, and sensors (Claro et al., 2021; Fahlman et al., 2019; Lee, Cho et al., 2019; Nguyen & Nguyen, 2016). Particularly, the ion gels have an insulating characteristic in a specific voltage range determined by the electrochemical ion stability, simultaneously maintaining their ionically conducting property (Deka & Kumar, 2010; Khan et al., 2019; Maleki Kheimeh Sari & Li, 2019; Shi et al., 2018). In order to use the ion gel in practical applications, the ion gel thin-film has to be patterned to specific shapes as necessary. In accordance with the previously reported papers, the spin-coating or aerosol jet printing methods were dominantly applied to realized ion gel-based TFTs, but they have a critical limitation of the limited processing option with low throughput (Garlapati et al., 2018; Li et al., 2018). A dry printing technique using PDMS was proposed to transfer the

patterned ion gel materials to various flexible substrates (Nketia-Yawson & Noh, 2018). Lee et al. developed an ion gel transfer-printing technique using the patterned PDMS stamp (Lee et al., 2013). Fig. 11.4A depicts optical microscopic images of hexagon, square, and triangle-patterned ion gel arrays on PI film. The spin-coated ion gel on the PDMS, which was composed of poly(styrene-*b*-ethylene oxide-*b*-styrene) [SOS], and ethyl-3-methylimidazolium *bis*(trifluoromethyl sulfonyl)amide [EMI] [TFSA], was attached to the target substrate, and heated at 100°C for gelation of the ion gel. After slow detachment of the stamp, the ion gel was cooled at RT for a few seconds. In particular, these processes could be reliably repeated to multiple stages with the same PDMS stamp, maintaining a high capacitance value ($> 1 \mu\text{F}/\text{cm}^2$) of the ion gel layers before and after the transfer process. An electrolyte-gated TFT (EGT) was demonstrated to investigate the electronic function of the transferred ion gel, as shown in Fig. 11.4B. All layers were stacked by using the suggested transfer method to make the top-gate flexible TFT, composed of a semiconductor layer (poly(3-hexylthiophene); P3HT and ion-gel), gate electrode (poly(3,4-ethylene dioxythiophene):poly(styrene sulfonate); PEDOT:PSS), and source/drain electrodes (Au thin-film). Fig. 11.4C shows I_D-V_D characteristics of the EGT devices, displaying the typical p-type device behavior with low operating voltage under 1 V and high output current over 1 mA. The developed flexible EGT exhibited superior reproducibility of the printing technique, providing a possibility in the transfer printing to pattern ion gels for flexible electronics.

Song et al. demonstrated flexible EGT through a printing transfer based on a selective dewetting effect of the graphene ink in a robust Si mold (Song et al., 2017). The graphene ink, which was composed of graphene flakes and terpeneol/cyclohexanone-mixed solvent, had a low viscosity of about $150 \text{ mPa} \cdot \text{s}$, satisfying the selective dewetting from Si mold ($\leq 500 \text{ mPa} \cdot \text{s}$) and dry transfer condition. After 1 hour annealing at 250°C, the graphene ink was selectively filled in Cytop-coated Si mold due to its higher surface energy (γ) of approximately $33 \text{ mJ}/\text{m}^2$ than that of top Cytop layer ($\sim 19 \text{ mJ}/\text{m}^2$). The graphene lines in the mold were transferred onto flexible PET film through UV-curable polymer (Fig. 11.4D). According to various analyses, the transferred graphene patterns had flat surfaces with a root-mean-square roughness (rms) of 9 nm, and low sheet resistance of approximately $35 \Omega/\text{sq}$, achieving high-resolution patterns with $3.2 \mu\text{m}$ line width and $2.7 \mu\text{m}$ line spacing. A p-type EGT was realized using the transferred graphene electrode (source/drain), P3HT layer (semiconductor), ion gel (dielectric), and PEDOT:PSS (gate). As displayed in Fig. 11.4E, other layers except the graphene electrode were simply printed by aerosol jetting. The device had a stable transfer curve with imperceptible hysteresis of the drain current and mechanical reliability in 1000 cycles at 1% tensile strain (Fig. 11.4F). The proposed transfer method could be applied to roll-to-roll processing due to the possibility of flexible mold, providing a considerable potential for realizing large-scale and high-resolution ink patterning.

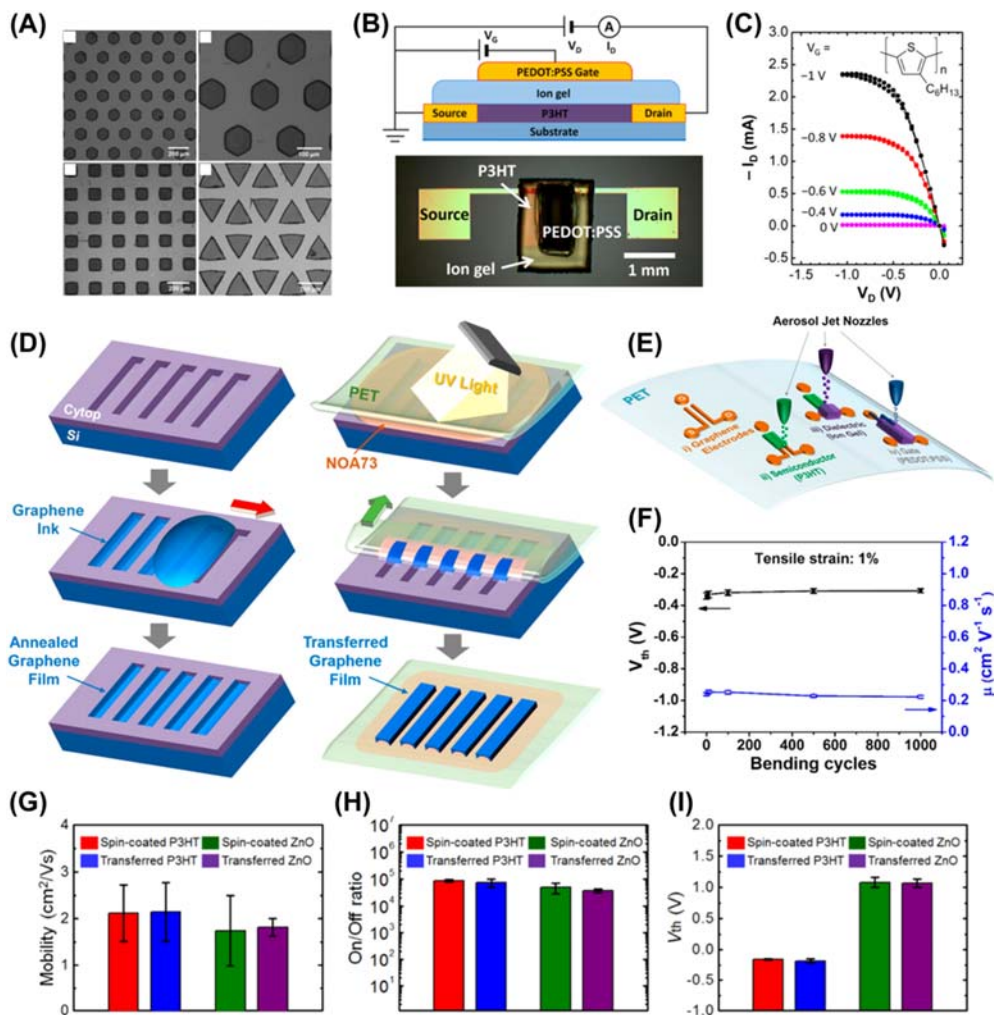


Figure 11.4 Ion gel-based flexible transistors. (A) Magnified microscopic images of the transferred ion gel patterns. (B) Schematic illustration of flexible electrolyte gated thin-film transistor (EGT). (C) Quasi-output curves of an EGT. (D) Three-dimensional schematics of a printing process for transfer the patterned graphene film. (E) EGT fabrication process using a dewetting-based film transfer and aerosol jet printing. (F) Fatigue test results of flexible EGT during 1000 bending cycles. Electrical properties of flexible P3HT and ZnO-based EGTs including (G) mobility, (H) I_{ON}/I_{OFF} ratio, and (I) threshold voltage. From Lee, K. H., Zhang, S., Gu, Y., Lodge, T. P., & Frisbie, C. D. (2013). Transfer printing of thermoreversible ion gels for flexible electronics. *ACS Applied Materials and Interfaces*, 5(19), 9522–9527. <https://doi.org/10.1021/am402200n>, Song, D., Mahajan, A., Secor, E. B., Hersam, M. C., Francis, L. F., & Frisbie, C. D. (2017). High-resolution transfer printing of graphene lines for fully printed, flexible electronics. *ACS Nano*, 11(7), 7431–7439. <https://doi.org/10.1021/acsnano.7b03795>, and Cho, K. G., Kim, H. J., Yang, H. M., Seol, K. H., Lee, S. J., & Lee, K. H. (2018). Sub-2 V, Transfer-stamped organic/inorganic complementary inverters based on electrolyte-gated transistors. *ACS Applied Materials and Interfaces*, 10(47), 40672–40680. <https://doi.org/10.1021/acsami.8b13140>.

Cho et al. reported about EGT-based organic/inorganic hybrid inverters using a dry transfer method (Cho et al., 2018). For fabricating the EGT, the poly(vinylidene fluoride) (PVDF)-based ion gel layer for a dielectric and PEDOT:PSS for a gate electrode were dry-printed onto the semiconductor-stacked Au source/drain electrode by using PDMS stamp. In order to the performance comparison between spin-coated and transferred devices, the four different flexible TFTs were fabricated with the same conditions, including a spin-coated P3HT, a transferred P3HT, a spin-coated ZnO, and a transferred ZnO-based flexible EGTs (Fig. 11.4G–I). In terms of hole/electron mobility, $I_{\text{on}}/I_{\text{off}}$ ratio, and threshold voltage (V_T), the printed devices showed similar values with the spin-coated devices, presenting higher values in p-type P3HT EGTs than n-type ZnO devices. The EGTs with high mobility over $1 \text{ cm}^2/\text{V}\cdot\text{s}$ could be operated at small voltages, and the n- and p-type devices were integrated in series for realizing organic/inorganic complementary inverters. The developed inverter proved appropriate logic inversion with a high gain value ($\partial V_{\text{out}}/\partial V_{\text{in}}$) of approximately 18, deriving supply voltage (V_{DD}) at small input voltage (V_{in}) and 0 V at high V_{in} . Based on these results, the transfer printings for ion gel-based flexible TFTs are implying to offer a simple/easy method for realizing high-performance and large-scale logic circuits.

11.6 Flexible oxide transistors

Since amorphous In-Ga-Zn-O (a-IGZO)-based TFTs were developed in late 2004, oxide TFTs have been actively investigated in industry/academic researches for applying to the backplane of LCDs, organic LED (OLED) displays, and electronic papers (Chen et al., 2021; He et al., 2018; Kamiya et al., 2009; Zhu et al., 2021). In particular, because the oxide TFTs with ultrathin structure can be produced with high electrical mobility, negligible leakage, and high optical transparency, they have received a lot of attention as switching/driving units in flexible OLED displays (Cho et al., 2022; Zhu et al., 2020). Dahiya et al. developed flexible ZnO nanowire (NW) FETs and UV photodetectors for biodegradable applications, which were realized by an in-tandem contact-transfer printing method (Dahiya, Christou, et al., 2022). Fig. 11.5A illustrates process schematics of the reported in-tandem dry transfer. Vertically-aligned NWs on a mother wafer or uniformly-dispersed NWs in solution were laterally assembled onto the surface of an intermediate substrate, and then selectively attached by the patterned PDMS stamp. The attached NWs were transferred onto the target location from the sticky elastomeric stamp. This printing method has some significant merits including highly-aligned unidirectional nanomaterials, a one-step process, low fabrication cost, and negligible contamination of nanomaterials during the transfer process. The Ti/Au electrodes were deposited onto the transferred ZnO NWs on SiO_2/Si wafer, making simple NW-FET (Fig. 11.5B). In the FET device, the Ti/Au, ZnO NW, SiO_2 , and $\text{p}^{++}\text{-Si}$ were used as source/drain electrodes, active material, gate

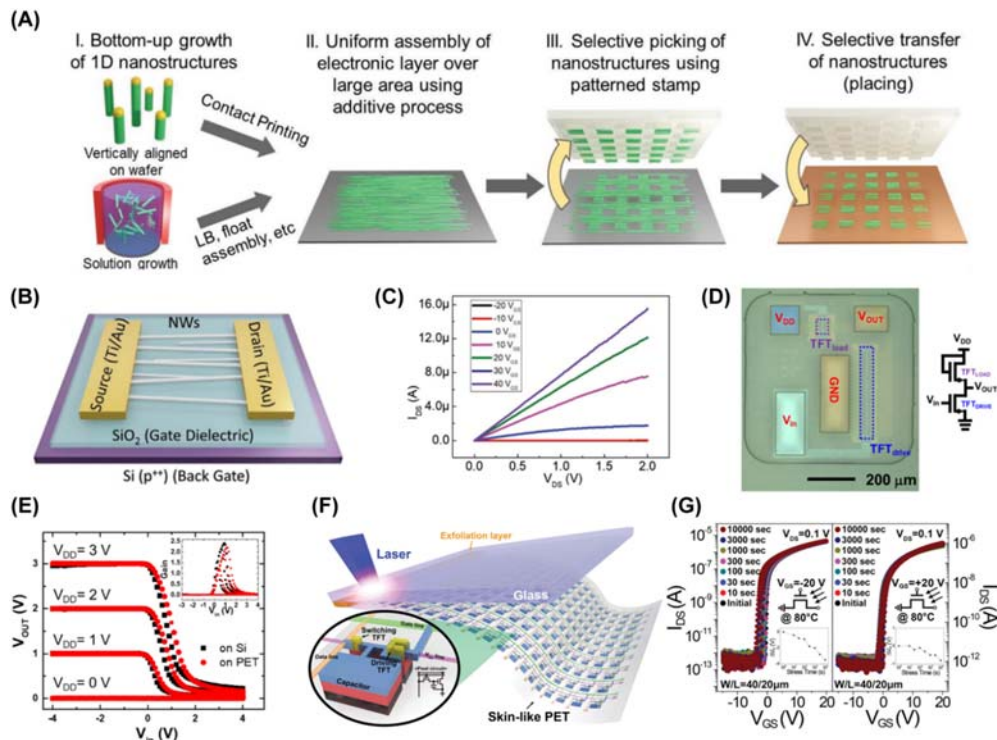


Figure 11.5 Flexible oxide transistors. (A) Schematic illustration of in-tandem contact-transfer printing of the nanostructured materials. (B) Three-dimensional image and (C) output curve of ZnO nanowire-based field-effect transistors (FETs). (D) Optical microscopic image of flexible IGZO inverter and its circuit diagram. (E) Output characteristics of the inverter on the rigid substrate (black) and PET film (red). (F) Laser-induced transfer process for realizing the IZO TFT-based flexible display backplane. (G) Transfer characteristics of flexible IZO thin-film transistor during 10,000 s NBTIS and PBTIS tests. From Dahiya, A. S., Christou, A., Neto, J., Zumeit, A., Shakhiveli, D., & Dahiya, R. (2022). *In tandem contact-transfer printing for high-performance transient electronics. Advanced Electronic Materials*, 8(9), 2200170. <https://doi.org/10.1002/aelm.202200170>, Yoo, J. I., Jang, H. S., Jang, J., Yoon, J., Kwon, O. Y., Park, J. J., Kang, S. M., Yoo, T. J., Kim, S. H., Lee, B. H., Cho, S. H., & Ko, H. C. (2018). *Reliable peripheral anchor-assisted transfer printing of ultrathin SiO₂ for a transparent and flexible IGZO-based inverter. Microelectronic Engineering*, 197, 15–22. <https://doi.org/10.1016/j.mee.2018.05.003>, and Lee, H. E., Kim, S., Ko, J., Yeom, H. I., Byun, C. W., Lee, S. H., Joe, D. J., Im, T. H., Park, S. H. K., & Lee, K. J. (2016). *Skin-like oxide thin-film transistors for transparent displays. Advanced Functional Materials*, 26(34), 6170–6178. <https://doi.org/10.1002/adfm.201601296>.

dielectric, and back gate layer, respectively. The NW-FET exhibited approximately $50 \text{ cm}^2/\text{V}\cdot\text{s}$ of effective mobility, $> 10^3$ of $I_{\text{on}}/I_{\text{off}}$ ratio, and -13 V of V_T . As displayed in Fig. 11.5C, the device showed stable output characteristics in various gate voltage from 40 to -20 V owing to the clearly-transferred NWs without any contamination and the ohmic contact between Ti metal and ZnO NWs. The printed NWs onto Mg foil were demonstrated to transient and flexible UV monitoring sensor,

showing excellent photo sensitivity over 10^7 A/W, superior UV detectivity of approximately 10^{17} jones, and high external quantum efficiency (EQE) of $2.5 \times 10^{10}\%$ at $0.1 \mu\text{W}/\text{cm}^2$ UV radiation. According to the soaking test, the printed flexible device except Au electrodes was successfully dissolved in 27°C deionized water (DI water) in 240 days, opening new era of flexible and transient electronics with high-performance and sustainability.

Yoo et al. demonstrated flexible and transparent IGZO inverters on PET film by using common Si fabrication processes and an anchor-induced dry transfer (Yoo et al., 2018). The IGZO TFTs or inverters, which consisted of ITO gate, HfO_2 dielectric, IGZO active layer, and ITO source/drain electrodes, were fabricated onto 150 nm-thick GeO_x /600 nm-thick SiO_2 on Si wafer. After device isolation by reactive ion etching (RIE), SU-8 anchors were formed onto the device for partially adhering the device to SiO_2 during wet etching of the sacrificial GeO_x layer. After warm water-based wet etching of GeO_x , the device array was detached by PDMS stamp, and transmitted to the PET film. The fabricated fully-transparent flexible TFT had 84.7% transparency in 400–700 nm wavelength. Fig. 11.5D depicts a magnified optical image and circuit diagram of a flexible IGZO inverter. As shown in Fig. 11.5E, the device presented a typical switching performance of an oxide inverter before and after transfer printing, showing a small V_T shift due to the water-induced electron donation during the GeO_x removing stage. In accordance with bending tests, the flexible inverter maintained its electrical performance even at 8.6 mm bending radius, and 500 cycles of bending/unbending periodic motions.

Over the past few decades, various approaches have been proposed to transfer high-temperature annealed thin-film devices to flexible substrates, which were fully fabricated on a rigid substrate (Hwang et al., 2015; Hyeon & Park, 2019; Leppäniemi et al., 2015; Yoon et al., 2020). Several methods such as wafer thinning, epitaxial layer transfer, and stress-modulated delamination have been studied to accomplish high performance, and flexible device with multifunctionality (Chowdhury et al., 2022; Gao, 2017; Min et al., 2021; Shen et al., 2017; Shi et al., 2017). However, these processes still have critical problems including as complex processes, limited applicability, and high fabrication cost. In order to solve these issues, laser-induced thin-film lift-off (ILLO) was established to delaminate only thin-film devices on a sacrificial layer by laser-material interactions (e.g., melting, gas formation, and material dissociation) (Han et al., 2019; Im et al., 2017; Im et al., 2021; Joe et al., 2017; Jung et al., 2019; Park et al., 2018; Shin et al., 2021; Wang et al., 2021). Lee et al. realized transparent and ultrathin oxide TFTs for flexible displays by ILLO process (Fig. 11.5F) (Lee et al., 2016). The IZO TFTs fabricated on a-Si:H sacrificial layer/glass substrate were transferred to 4 μm -thick ultrathin PET substrate, keeping their $>80\%$ transparency, $38.5 \text{ cm}^2/\text{V}/\text{s}$ mobility, 168 mV/dec SS, and $8 \times 10^7 I_{\text{on}}/I_{\text{off}}$ ratio values. When the TFT backplane is actually used in a transparent display, heating, light irradiating, and biasing are continuously applied to the TFT by driving the display, and mechanical

stress is applied in the case of a flexible device. Therefore, to confirm the application validity of oxide TFT to transparent/flexible display, various stability tests during 10^4 seconds were fulfilled in mechanical (bending radius from 30 to 7.5 mm, and 10^4 periodic bending cycles), positive/negative bias (+20 and -20 V), temperature (80°C) and illumination stresses (500 cd/m^2), as displayed in Fig. 11.5G. As a result, the device exhibited negligible optical/electrical degradation in the negative bias-temperature stress (NBTS) test, positive bias-temperature stress (PBTS) test, and mechanical fatigue test, only showing a small V_T shift of -4 V in extremely harsh negative bias-temperature-illumination stress (NBTIS) test. On the basis of these reports, it is conspicuous that flexible oxide TFTs printed by various transfer methods can be novel approaches for developing wearable/flexible displays in upcoming IoT era.

11.7 Flexible transistors with other materials

With the upcoming hyperconnected era in which a large amount of information is circulated, recent researches on electronics have been actively conducted to realize multifunctionality in a single device, not simple flexible electronics (Seo et al., 2019). Therefore, transfer printings of novel materials were fulfilled to add new function (e.g., stretchability, wearability, and gas sensing) to flexible transistors. Flexible and stretchable nanofiber (NF)-based FET was demonstrated by transferring the stacked layers of the wavy AgNFs and a polystyrene-block-poly(ethylene butadiene)-block-polystyrene (SEBS) (Kim et al., 2021). Fig. 11.6A is a three-dimensional schematic illustration of highly-integrated all-stretchable/flexible transparent NF-FET arrays. The wave-structured Ag NFs with $50\text{ }\mu\text{m}$ gap could be directly printed onto PDMS substrate by using electrohydrodynamic (EHD) printing, displaying biaxial stretchability, and excellent transparency of approximately 97%. Mechanical stabilities of the printed NF arrays were theoretically analyzed by FEM simulation, and experimentally verified by uniaxial/biaxial stretching tests and durability test. Finally, this method was adopted to fabricate all-stretchable/flexible NF-FETs, consisting of the Ag NFs, the SEBS layer, the patterned organic semiconductor (OSC) NFs, and Au NFs as gate electrodes, a dielectric layer, channels, and source/drain electrodes, respectively. The fabricated NF-FETs of 6250 units (areal density of $10\text{ FETs}\cdot\text{mm}^{-2}$) showed uniform electrical properties of $1.0\text{--}1.3\text{ cm}^2/\text{V}\cdot\text{s}$ mobility and $1.85\text{--}1.88\times 10^5$ $I_{\text{on}}/I_{\text{off}}$ ratio (Fig. 11.6B). Especially, the devices maintained their optical/electrical properties even in 87% uniaxial stretching, and 90% biaxial stretching. As shown in Fig. 11.6C, various mechanical deformations including 3000 periodic uniaxial stretching, biaxial stretching, poking, and twisting could not degrade the electron mobility and $I_{\text{on}}/I_{\text{off}}$ ratio value of the fabricated devices.

FET-based ultrasensitive flexible NO_2 gas sensor was accomplished by multiple printing and three-dimensional integration of porous polymer films (Gao et al., 2022).

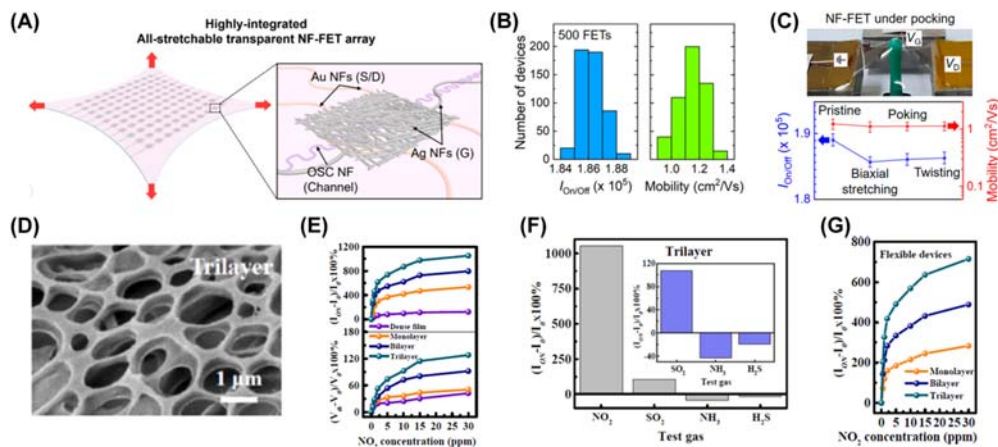


Figure 11.6 Flexible transistors with other materials. (A) Three-dimensional image of stretchable and transparent NF-field-effect transistor (FET) array, realized by the transfer printing process. (B) Mobility and I_{ON}/I_{OFF} ratio distribution of the 500 NF-FETs. (C) Mechanical stress tests of the NF-FETs. (D) SEM image of the three-times transferred OSC film. (E) NO_2 responsivity and (F) selectivity of multilayer porous OFETs. (G) NO_2 responsivity of flexible OFETs. From Kim, D. W., Kwon, J., Kim, H. S., & Jeong, U. (2021). Printed stretchable single-nanofiber interconnections for individually-addressable highly-integrated transparent stretchable field effect transistor array. *Nano Letters*, 21(13), 5819–5827. <https://doi.org/10.1021/acs.nanolett.1c01744>, and Gao, L., Liu, C., Peng, Y., Deng, J., Hou, S., Cheng, Y., Huang, W., & Yu, J. (2022). Ultrasensitive flexible NO_2 gas sensors via multilayer porous polymer film. *Sensors and Actuators B: Chemical*, 368, 132113. <https://doi.org/10.1016/j.snb.2022.132113>.

P3HT:SEBS-based porous OSC layer was formed on polyvinyl alcohol (PVA)-coated glass substrate by using the breath figure method (Fig. 11.6D). By dissolving the PVA layer, the porous OSC was transferred onto dielectric (PMMA)-formed flexible conductive substrate (ITO/PET). This transfer process was conducted three times for making three-dimensional-stacked OSC multilayers, and Au source/drain layer was deposited onto the multi-OSC layer for fabricating flexible and porous organic FETs (OFETs). The NO_2 sensitivity of FET-based gas sensor was enhanced by increasing the number of the stacked OSC layer, as depicted in Fig. 11.6E. This result was come from the extended gas absorbing sites and easy charge carrier generation due to the porous structure of the OSCs. Multilayer porous OFET had approximately 100 times superior NO_2 gas responsivity and excellent selectivity compared to SO_2 , NH_3 , and H_2S gases (Fig. 11.6F). As presented in Fig. 11.6G, the flexible multilayered gas sensors also successfully detected NO_2 gas, enduring 500 bending/unbending cycles and a bending curvature radius of 1 mm. Based on these results, the developed flexible OFET showed high gas sensing properties even at an ultralow gas concentration of approximately 2.3 ppb, proving that the multilayer transfer of semiconductor layers become a common approach for attaining flexible and wearable electronic devices.

Chen et al. demonstrated a stretchable and flexible two-dimensional material-based nanogap transistor by using a transfer printing of multiscale metallic structures without any adhesive (Chen et al., 2020). The fabrication process of flexible nanogap transistors using MoS₂ flakes is as follows. First, e-beam-based sketch and peel lithography (SPL) were implemented to form the outline of the multiscale metallic structure onto negative-tone hydrogen silsequioxane (HSQ) polymer. After making a gold film on the patterned HSQ, only Au patterns were selectively transferred to the MoS₂ flake-coated PDMS substrate. This adhesion-free transfer method could be applied to various multiscale Au structures with 100% transfer yield including the interdigitated nanogap, circle, microscale jigsaw, and bowtie patterns. Furthermore, the Au electrodes with 70 nm gap were appropriately transferred onto micron-scaled single MoS₂ flake, showing n-type transistor behavior with a high $I_{\text{on}}/I_{\text{off}}$ ratio of approximately 10^7 . In accordance with these results, the suggested patterning and transfer processes can be a potential approach for developing advanced nanoplasmonic and nonelectronic devices.

Wearable organic electrochemical transistors (OECTs), integrated with a portable Bluetooth readout system, were reported by Zhang et al. for applying skin-attachable glucose sensors (Zhang, Ling et al., 2019). Although PEDOT:PSS has been considered as a promising solution-processable conductive polymer, its patterning difficulty on flexible/stretchable substrates has a critical challenge which has hindered to apply various flexible devices (Khan et al., 2016; Liu et al., 2021; Wen & Xu, 2017). Since the PEDOT:PSS transfer could be a potential solution to these obstacles, a hydrogel-based printing technique was utilized to fabricate wearable OECT (Wang et al., 2022). The prepatterned PEDOT:PSS layer on the glass was transferred to various soft substrates (e.g., plastic films, elastomers, and real human skin surface) through a water-soluble PVA hydrogel. The pressed hydrogel enhanced the interfacial adhesion between PEDOTSS and hydrogel, then transmitted to the target area by decreasing the adhesion force through the hydrogel dissolution in the water. The transferred polymer presented similar conductivity compared to before the transfer. Wearable OECT was accomplished by transferring the patterned PEDOT:PSS onto Au source/drain electrodes on a tattoo paper, enabling it to be ultraconformally attached to the human skin surface. The large-sized device (width: 10 mm, 1 mm) had typical output and transfer characteristics of PEDOT:PSS OECTs with 1.5 mS transconductance, and approximately 50 $I_{\text{on}}/I_{\text{off}}$ ratio. For confirming the usability of the wearable OECT to biosensing applications, a Bluetooth-based wireless data communication system was integrated with the developed device. In order to detect glucose levels which is important to diabetic patients, GO_x-deposited Pt was used to gate electrode. The GO_x catalyst in the gate was reduced with the reduction of glucose to glucono-1,5-lactone, and made hydrogen peroxide (H₂O₂). The formed H₂O₂ was decomposed by Pt for occurring an electrochemical reaction in the system. In electrolytes with various glucose concentrations, the device displayed

superior detectivity of glucose level of about 1×10^{-6} M. According to various methodologies for transferring novel materials, it is noteworthy that the previously reported techniques can be an ideal platform to realize next-generation transistors for wearable and biomedical applications.

11.8 Flexible Si transistors with novel transfer methods

Flexible and large-area electronic devices have been developed to implement new applications in a variety of areas including wearable systems, soft robotics, bendable displays, and biomedical devices (Jeong et al., 2020; Lee et al., 2022; Lee, Kim et al., 2018; Lee, Lee et al., 2018; Lee, Park et al., 2020; Park, Lee, Lee et al., 2016). After the form-factor revolution, fast computing and info-communication have been required in high-performance flexible devices for enabling numerous human-machine interactions (HMIs). For example, single-crystalline Si thin-film, which is the most commonly used semiconductor material, has been demonstrate to flexible transistor forms, but they have some limitations of high process cost and the difficulty of an increasing device density (Asadirad et al., 2016; Ishihara et al., 2012; Qin et al., 2011). Therefore, it is necessary to develop flexible electronic devices/circuits using nano-structured silicon materials (e.g., NW, nanorod, and nanoribbon), new film delaminating method and transfer method for large-area (Yao et al., 2019). This section will introduce novel strategies for flexible Si transistor which can improve the yield and reliability of the process and further expand the transfer printing capacity.

Zumeit et al. developed flexible Si nanoribbon (NR)-based FET (f-NRFET) with extremely excellent electron mobility ($\sim 656 \text{ cm}^2/\text{V/s}$) and $I_{\text{on}}/I_{\text{off}}$ ratio ($> 10^6$) using a RT-deposited dielectric layer (Zumeit et al., 2020). In general, the existing transfer printing methods of the fully-fabricated FETs have the advantage of high-temperature annealing on a rigid substrate, but they cause an increasing in the process complexity and cost. Another method for high-performance flexible transistors is the use of a metal foil-based flexible substrate that can withstand high-temperature fabrication processes (Balasingam et al., 2013; Fan et al., 2010; Wang, Li et al., 2015). Since the flexible device on the metal foil requires an additional manufacturing stage (e.g., the deposition of the insulating layer), thin-films through low-temperature processes are preferred to realize flexible electronics with excellent properties. Fig. 11.7A depicts the fabrication processes of f-NRFET which were completely fulfilled at RT. After making NR arrays (dimension of $5 \times 60 \mu\text{m}$) on the SOI wafer, the selective n+ doping was implemented by the spin-on doping of phosphorous for making source/drain region. Then, the NR arrays were transfer printed onto PI film. For forming a gate dielectric layer of SiN_x , inductively coupled plasma CVD (ICP-CVD) was used at RT, which can make high-quality dielectric materials without any problems such as high growth temperature over 250°C (atomic layer deposition and low-pressure

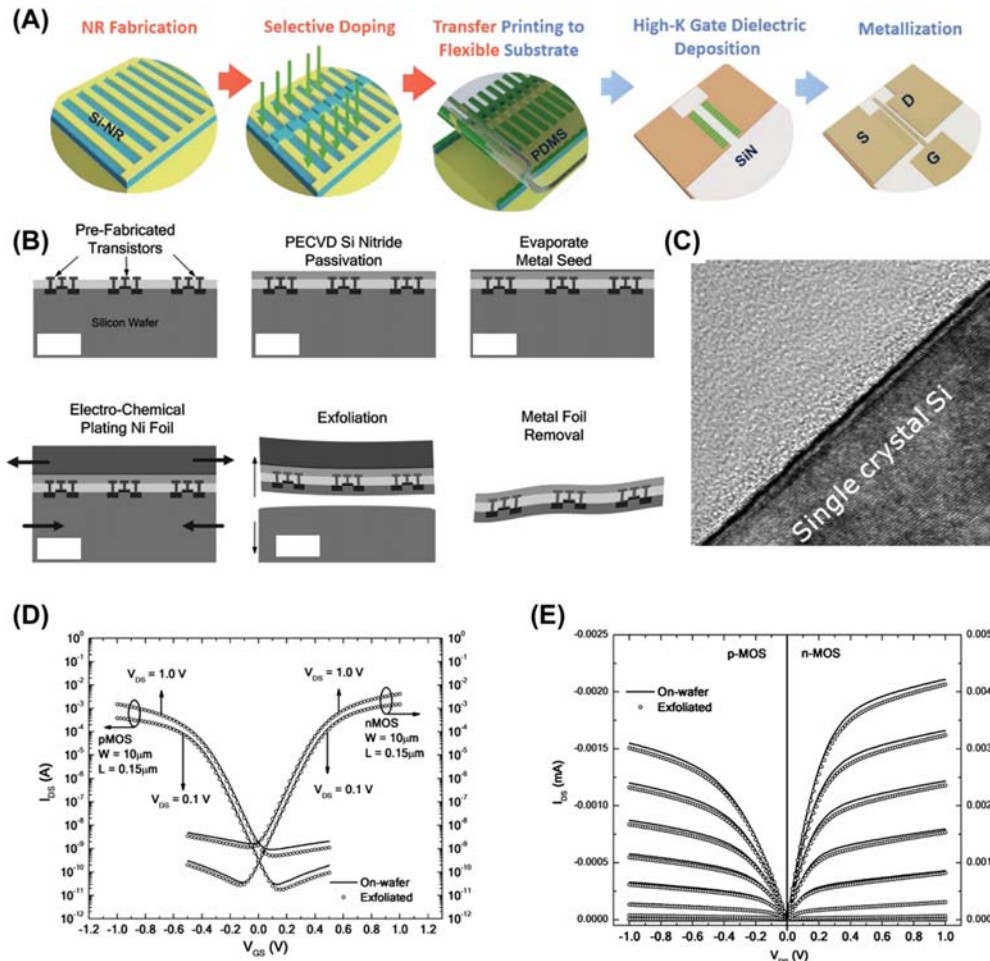


Figure 11.7 *New Si exfoliation techniques for flexible transistors*. (A) Fabrication processes of NR-based flexible transistor at room temperature. (B) Mechanical delamination process by using Ni stressor. (C) Transmission electron microscopy (TEM) image of the exfoliated single crystal Si. (D) Transfer curves and (E) output characteristics of n- and p-MOSFET before and after the device exfoliation. From Zumeit, A., Navaraj, W. T., Shakthivel, D., & Dahiya, R. (2020). Nanoribbon-based flexible high-performance transistors fabricated at room temperature. *Advanced Electronic Materials*, 6(4), 1901023. <https://doi.org/10.1002/aelm.201901023>, and Zhai, Y., Mathew, L., Rao, R., Xu, D., & Banerjee, S. K. (2012). High-performance flexible thin-film transistors exfoliated from bulk wafer. *Nano Letters*, 12(11), 5609–5615. <https://doi.org/10.1021/nl302735f>.

CVD) and plasma-induced charge trapping/material degradation/defect formation (PECVD). By depositing Ti/Au layers as metal contacts, f-NRFET array with high-k dielectric layer was finally fabricated. Based on the transfer curve, the device had the effective surface mobility of 656, 679, and 637 $\text{cm}^2/\text{V}\cdot\text{s}$ at flat, convexly bent, and

concavely bent state, respectively, which were confirmed by experimental bending tests and simulations. The mechanical durability of the device was also investigated by performing 100 tensile and compression bending cycles. The high-quality SiN_x, deposited by ICP-CVD, induced the improvement of the electrical performance compared to other RT-deposited materials.

Mechanical stress-induced Si film delamination was developed by Zhai et al. for fast and easy thin-film transfer (Zhai et al., 2012). Because of the slow/complex transfer (extremely long wet-etching time of the sacrificial layer between the mother wafer and the semiconductor materials), previously-reported PDMS-based transfer printing was only executed in the nanostructured features and the sub-cm sized thin-film devices, restricting the increase of the device density (Kim, Lee et al., 2019; Yeon et al., 2021). As shown in Fig. 11.7B, transistors were fabricated onto a bulk Si wafer through conventional CMOS process, and then passivated by PECVD-grown SiN_x layer. After making Ni seed layer by e-beam evaporation, the 10–100 μm-thick Ni stressor with high-tensile stress was electro-plated onto the seed layer. Because the Ni film and the Si wafer simultaneously received the tensile and the compressive stress, respectively, the formed crack was rapidly propagated to the crystal direction of the Si (Fig. 11.7C). This crack-induced thin-film exfoliation could be conducted in 8-inch Si wafer for a few seconds, and repeatedly applied to the same reusable wafer, swiftly reducing the production cost. The peeled-off Si thin-film had a thickness of 20–30 μm, maintaining its single crystallinity according to the material analyses. Fig. 11.7D showed transfer curves of n-/p-MOSFET before and after delamination. The flexible n-MOS device had mobility of 2526 cm²/Vs and I_{on}/I_{off} ratio of approximately 10⁶, showing negligible degradation compared to the device on the rigid Si wafer. According to the output characteristics in Fig. 11.7E, the device was successfully and stably operated in various V_{DS} from 0 to 10 V regardless of the device exfoliation. Based on the results, it is noted that the suggested mechanical stress-induced semiconductor printing can be the most potential transfer method for flexible semiconductor devices due to its simple/fast process, wafer reusability, and compatibility with high-tech semiconductor technology.

Heretofore, the transfer printing of the semiconductor materials was performed by using typical transfer media of the sticky PDMS, thermal release tape (TRT), or water-soluble tape (WST). However, they have some obstacles to commercialization such as low transfer efficacy, and the kinetic control difficulty of the stamp (Béraud et al., 2021; Jeong et al., 2017; Yu et al., 2022). In order to solve these issues of transfer printing, the new stamp of an acetone soluble tape was offered by Zhang, Wu et al. (2019) The AST-based transfer printing similarly proceeded with the conventional one: (1) Micro or nano-scaled transistors were fabricated with polymer anchors onto Si wafer. (2) After picking the devices by the AST, they were transmitted to the target flexible substrate. (3) The AST was removed by soaking in acetone.

Through this technique, the Si transistor array could be transferred onto AlGaN/GaN/sapphire, Ge, fluorine-doped tin oxide, Ga₂O₃ and the curved glass cylinder substrate, proving the possibility of heterogeneous integration of various thin-film materials. Based on the experimental results, contrastive plot was made for comparing four transfer printing methods (AST, TFT, WST, and PDMS-based printing) in terms of five crucial parameters including the transfer printing efficiency (E_{tp}), the transfer yield (Y_{tp}), the cleanliness (C), the simplicity of the process (S_p) and the reciprocal of process cost (D_{1c}), as shown in Fig. 11.8A. E_{tp} (97.37%), D_{1c} (0.01) and S_p (0.25) values were highest in the AST transfer compared to other techniques. C of the AST transfer was the second highest after that of the PDMS method because of the dissolvable tape residual created in the releasing procedure. Since the thickness of the AST was thinner than other stamps, it kept semiconductor materials less than others, reducing the transfer yield. Despite this critical limitation of the AST, Y_{tp} of the AST printing was 90.54%, similar to the PDMS (90.63%). Considering these factors overall, it was confirmed that the AST is a mostly promising stamp for transfer printing. Fig. 11.8B displayed Si TFT array on a sapphire substrate, showing stable operations with typical I–V characteristics (Fig. 11.8C). Because the inelastic AST was completely dissolved in acetone, transfer printing efficiency could be maximized without any misalignments of the semiconductor devices.

Printed flexible electronics conventionally mean the production of electrical components or modules through the transfer printing, locating specific conductive, semiconductive or functional features onto flexible substrates such as plastic, paper, or clothes with the desired functions (Espera et al., 2019; Reuss et al., 2015; Wu, 2017; Yu et al., 2017). The representative advantage of the printed flexible electronics is the scalability to fabricate large-area device integration and high-speed mass production using a roll-to-roll (R2R)-based transfer process which can transmit the features from the mother wafer to flexible substrate using a stamp-coated rotating roll (Geiger et al., 2020; Morrison et al., 2015; Torres Sevilla & Hussain, 2017). This process can simultaneously conduct the device transfer and bonding, reducing the fabrication cost by a tenth of the existing normal transfer printing. Simple and cost-effective R2R transfer with a transfer yield of $\sim 95\%$ was demonstrated to make f-NRFET array on the PI film (Zumeit et al., 2021). As illustrated in Fig. 11.8D, the roll, which was wrapped by the semicured PI-coated flexible film, was directly rolled with the pressure on the Si NRs/SOI wafer. According to this simple rolling, the Si NR array was easily transferred onto flexible film, then fulfilled by conventional transistor fabrication processes. As an easy-to-understand advantage, direct roll printing reduced process steps, complexity, printing time, and production costs compared to the conventional PDMS or other stamp-based transfer printing methods. Fig. 11.8E presents the cross-sectional illustration (upper) and the magnified microscopic image (lower) of f-NRFET on the PI film, realized by the R2R-based printing. The mobility and I_{on}/I_{off} ratio of the flexible device was over $630 \text{ cm}^2/\text{V/s}$ and approximately

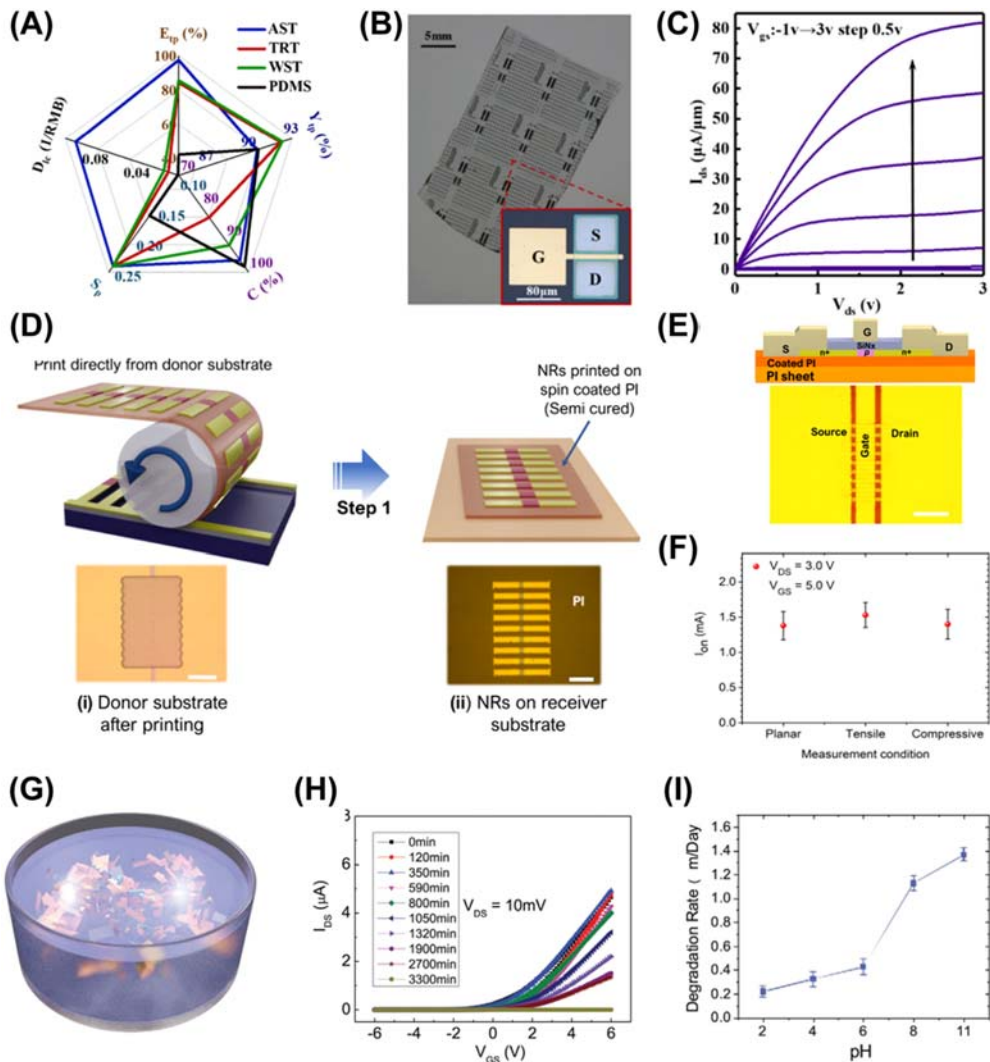


Figure 11.8 Flexible Si transistors with novel transfer methods. (A) Comparison of four different transfer methods. (B) Photograph of Si thin-film transistor (TFT) array, transferred onto sapphire through AST-based printing. (C) Output curves of the transferred Si TFTs. (D) Schematic illustrations of direct roll printing method for realizing NR-based flexible field-effect transistors (FETs). (E) Cross-sectional image of an NR-based flexible FET. (F) On-current comparison of flexible NRFET at flat, convex bending, and concave bending states. (G) Schematic image of biodegradation of flexible n-channel transistors on Mg foil. (H) Transfer characteristics of flexible transistors on Mg for PBS soaking tests. (I) Biodegradation rate of the device as a function of pH level. From Zhang, J., Wu, Y., Li, Z., Zhang, Y., Peng, Y., Chen, D., Zhu, W., Xu, S., Zhang, C., & Hao, Y. (2019). High-performance acetone soluble tape transfer printing method for heterogeneous integration. *Scientific Reports*, 9(1). <https://doi.org/10.1038/s41598-019-52235-0>, Zumeit, A., Dahiya, A. S., Christou, A., Shakhiviel, D., & Dahiya, R. (2021). Direct roll transfer printed silicon nanoribbon arrays based high-performance flexible electronics. *NPJ Flexible Electronics*, 5(1). <https://doi.org/10.1038/s41528-021-00116-w>, and Dahiya, A. S., Zumeit, A., Christou, A., & Dahiya, R. (2022). High-performance n-channel printed transistors on biodegradable substrate for transient electronics. *Advanced Electronic Materials*, 8(9), 2200098. <https://doi.org/10.1002/aelm.202200098>.

10^6 , showing a similar value to the previously reported Si f-NRFETs. On the other hand, as explained in Fig. 11.8F, types of strain (0, tensile, and compressive strain) influenced the band structure of Si NR on a flexible substrate, occurring the effective mass/mobility change of the charge carriers. However, the change of the on-state current was too small to dynamically reverse the driving characteristics of f-NRFET. Excellent mechanical reliability was verified by the fatigue test with periodic 100 bending/unbending cycles. Furthermore, the developed direct R2R printing was applied to biodegradable f-NRFET on Mg foil which was a well-known material with superior chemical/thermal/mechanical stability, hygroscopicity and biodegradability (Dahiya, Zumeit, et al., 2022). The device was fabricated by using the aforementioned R2R printing process, only supplementing the inelastic Mg foil by coating the semicured PI in order to enhance the transfer yield. The n-Si NRFET on the Mg foil showed $I_{\text{on}}/I_{\text{off}}$ ratio over 10^4 and effective mobility over $60 \text{ cm}^2/\text{V}/\text{s}$, stably withstanding the repeated bias stresses (10 mV) over 3000 cycles in a day and the thermal stresses (5°C – 50°C), as shown in Fig. 11.8G and H. Finally, biodegradable property of f-NRFET was confirmed by the device dissolving tests in various pH solutions at 37°C which is a mimicking condition of the internal human body (Fig. 11.8I). In pH 8 solution, the device on the Mg foil lost its operating performance of the transistor after 55 hours of soaking. Based on these results, it is conspicuous that the R2R-induced large-scale flexible transistors can be applied to various green and sustainable electronic systems, reducing the electronic waste that is considered as the most serious future environmental issue.

11.9 Transistors on various flexible substrates

In the future, the development of novel high-performance electric systems with extraordinary flexibility, stretchability, and wearability will be the most important standard for actualizing the veritable Internet of Everything which is a superordinate concept over the IoT (Lee, Park et al., 2018; Park et al., 2019). In particular, the flexibility/stretchability of the next-generation devices is seriously considered as a game changer and a critical factor to combine the devices onto the subject with the curved, uneven, and conjugated surface. In recent decades, several researchers have made efforts to deliver high-performance inorganic thin-films onto just flexible films (plastics, metal foils and wood-based substrates) for demonstrating displays, energy harvesters, logic circuits, and bioelectronics. The mechanical flexibility of these inorganic materials could be obtained by making ultrathin forms, enabling to realize remarkable performance and high-density integrated devices. Although these approaches are regarded as attractive methods for free form-factor devices, there are still some bottlenecks for integrating the device to various material substrates with nonplanar, micro/nanoscale, and asymmetric structures.

Rojas et al. realized a heterogeneous integration of single-crystalline n-MOSFET and FinFET, which is a mostly advanced FET structure for ultrahigh device density, on a single flexible substrate (Rojas et al., 2015). Fig. 11.9A schematically illustrates the fabrication process of the double-transfer for realizing flexible Si devices. Prior to the device production, the periodic 45 μm -trenches were made onto the 8-inch Si wafer. The Si devices, fabricated onto p-type Si (100) wafer, were peeled-off by isotropic etching of the wafer. The exfoliated Si devices were flipped over, and attached to the uncured

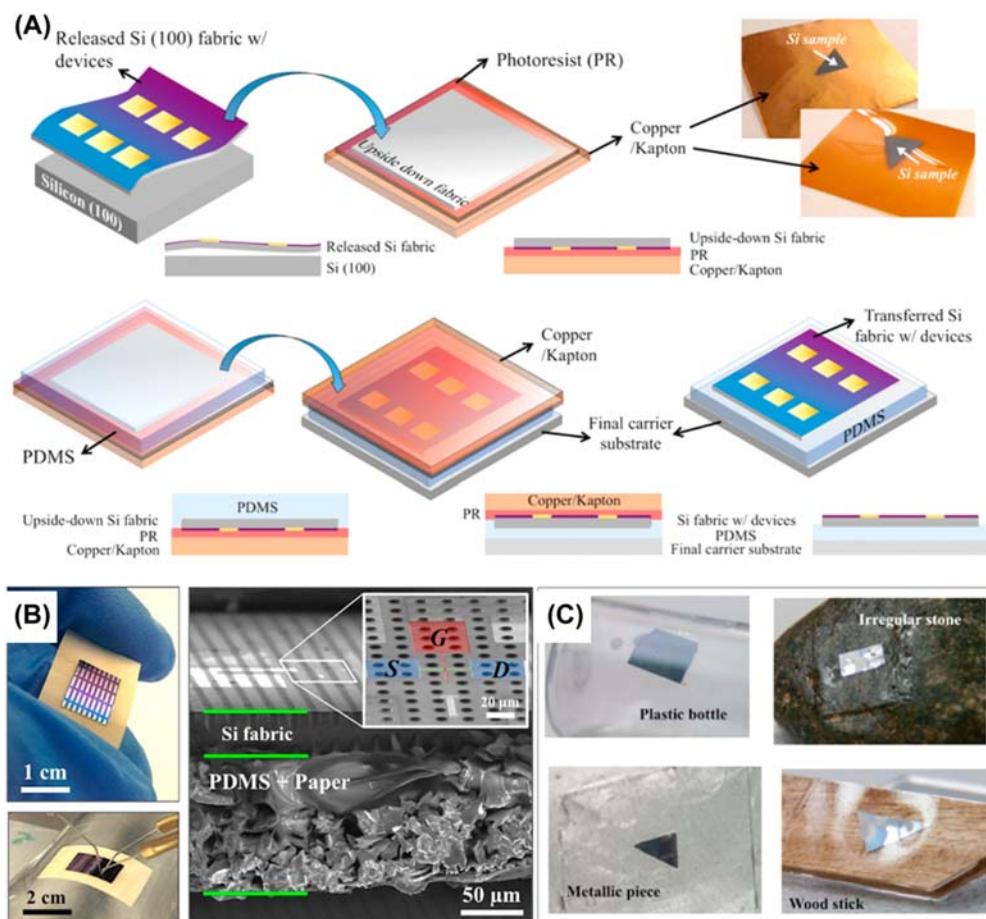


Figure 11.9 Transistors on various flexible substrates. (A) Process flow of the Si double-transfer for transmitting the devices onto various substrates. (B) Optical and SEM images of n-MOSFET array on a paper substrate. (C) Photographs of the release Si thin-film, transferred onto plastic bottle, stone with irregular surface, metal, and wood stick. From Rojas, J. P., Torres Sevilla, G. A., Alfaraj, N., Ghoneim, M. T., Kutbee, A. T., Sridharan, A. & Hussain, M. M. (2015). Nonplanar nanoscale fin field effect transistors on textile, paper, wood, stone, and vinyl via soft material-enabled double-transfer printing. *ACS Nano*, 9(5), 5255–5263. <https://doi.org/10.1021/acs.nano.5b00686>.

PR-coated Cu/PI which is a temporary handling wafer, as shown in the inset photographs of Fig. 11.9A. After spin-coating PDMS on the Si, the layers were bonded with the target substrate. The final flexible device was completed after removing the PR layer through the acetone soaking process. Fig. 11.9B displayed images of flexible n-MOSFET in a flat and bent state (left), and a cross-sectional SEM image of the n-MOSFETs on a paper substrate. The fabricated flexible 20 nm-FinFET and flexible n-MOSFET showed negligible changes of SS , V_T , I_{on}/I_{off} ratio, and effective mobility compared to the device on the rigid Si wafer. Finally, this double-transfer printing method was applied to transmit the Si device onto the curved plastic bottle, the stone with irregular surface, the metal piece, and the wood stick, indicating that the suggested technique overcomes material/surface limitations of the target substrate (Fig. 11.9C).

11.10 Conclusion

This chapter introduced and discussed the recent approaches of transfer printing techniques to realize flexible transistors and their novel applications. Fundamentally, although high-temperature processes are essential to produce materials with excellent electrical performances, these thermal issues have restricted to commercialize of flexible electronic systems. Implementation of high-performance flexible transistors has dynamically advanced the device technologies in terms of materials, device structures, transfer processes, and applications. Flexible transistors were demonstrated by elastomer-based stamping, printing by using sticky tapes, laser-induced transfer, and R2R process. Of course, a traditional semiconductor material of single-crystal Si was flexibilized to high-performance devices with NW, NR, and thin-film forms for making the freestanding micro/nanofeatures. The compound semiconductor-based flexible devices including III-V and III-N materials were demonstrated for power devices, and logic circuits. Oxide and other materials were utilized to apply flexible transparent displays/circuits and gas/strain sensors, respectively. In the upcoming Internet of Everything era, these perspectives for next-generation transistors with free form-factor will become a mainstream trend for developing fully flexible heterogeneous-integrated systems, opening new paradigm shifts for future computing methodologies.

Acknowledgments

H.E. Lee was supported by National University Development Project at Jeonbuk National University in 2022.

References

- Arias, A. C., MacKenzie, J. D., McCulloch, I., Rivnay, J., & Salleo, A. (2010). Materials and applications for large area electronics: Solution-based approaches. *Chemical Reviews*, 110(1), 3–24. Available from <https://doi.org/10.1021/cr900150b>, <http://pubs.acs.org/doi/pdfplus/10.1021/cr900150b>, United States.

- Arns, R. G. (1998). The other transistor: Early history of the metal-oxide-semiconductor field-effect transistor. *Engineering Science and Education Journal*, 7(5), 233–240. Available from <https://doi.org/10.1049/esej:19980509>.
- Asadirad, M., Gao, Y., Dutta, P., Shervin, S., Sun, S., Ravipati, S., Kim, S. H., Yao, Y., Lee, K. H., Litvinchuk, A. P., Selvamanickam, V., & Ryou, J. H. (2016). High-performance flexible thin-film transistors based on single-crystal-like germanium on glass. *Advanced Electronic Materials*, 2(8)1600041. Available from <https://doi.org/10.1002/aelm.201600041>.
- Baca, A. J., Ahn, J. H., Sun, Y., Meitl, M. A., Menard, E., Kim, H. S., Choi, W. M., Kim, D. H., Huang, Y., & Rogers, J. A. (2008). Semiconductor wires and ribbons for high-performance flexible electronics. *Angewandte Chemie - International Edition*, 47(30), 5524–5542. Available from <https://doi.org/10.1002/anie.200703238>, <http://www3.interscience.wiley.com/cgi-bin/fulltext/120749216/PDFSTART>.
- Baca, A. J., Meitl, M. A., Ko, H. C., Mack, S., Kim, H. S., Dong, J., Ferreira, P. M., & Rogers, J. A. (2007). Printable single-crystal silicon micro/nanoscale ribbons, platelets and bars generated from bulk wafers. *Advanced Functional Materials*, 17(16), 3051–3062. Available from <https://doi.org/10.1002/adfm.200601161>.
- Badano, A., Flynn, M. J., Martin, S., & Kanicki, J. (2003). Angular dependence of the luminance and contrast in medical monochrome liquid crystal displays. *Medical Physics*, 30(10), 2602–2613. Available from <https://doi.org/10.1118/1.1606449>, [http://aapm.onlinelibrary.wiley.com/hub/journal/10.1002/\(ISSN\)2473-4209/issues/](http://aapm.onlinelibrary.wiley.com/hub/journal/10.1002/(ISSN)2473-4209/issues/).
- Baeg, K. J., & Lee, J. (2020). Flexible electronic systems on plastic substrates and textiles for smart wearable technologies. *Advanced Materials Technologies*, 5(7)2000071. Available from <https://doi.org/10.1002/admt.202000071>.
- Baek, C., Wang, J. E., Ryu, S., Kim, J. H., Jeong, C. K., Park, K. I., & Kim, D. K. (2017). Facile hydrothermal synthesis of BaZrxTi1-xO3 nanoparticles and their application to a lead-free nanocomposite generator. *RSC Advances*, 7(5), 2851–2856. Available from <https://doi.org/10.1039/c6ra26285f>, <http://pubs.rsc.org/en/journals/journalissues>.
- Balasingam, S. K., Kang, M. G., & Jun, Y. (2013). Metal substrate based electrodes for flexible dye-sensitized solar cells: fabrication methods, progress and challenges. *Chemical Communications*, 49(98), 11457. Available from <https://doi.org/10.1039/c3cc46224b>.
- Bock, K., Yacoub-George, E., Hell, W., Drost, A., Wolf, H., Bollmann, D., Landesberger, C., Klink, G., Gieser, H., & Kutter, C. (2014). Multifunctional system integration in flexible substrates. Proceedings - Electronic Components and Technology Conference. Institute of Electrical and Electronics Engineers Inc., Germany, pp. 1482–1487. 9781479924073. Available from <https://doi.org/10.1109/ECTC.2014.6897489>.
- Boyce, J. B., & Mei, P. (2000). *Laser crystallization for polycrystalline silicon device applications* (pp. 94–146). Springer Science and Business Media LLC. Available from https://doi.org/10.1007/978-3-662-04141-3_3.
- Béraud, A., Sauvage, M., Bazán, C. M., Tie, M., Bencherif, A., & Bouilly, D. (2021). Graphene field-effect transistors as bioanalytical sensors: Design, operation and performance. *Analyst*, 146(2), 403–428. Available from <https://doi.org/10.1039/d0an01661f>, <http://pubs.rsc.org/en/journals/journal/an>.
- Chang, M. H., Das, D., Varde, P. V., & Pecht, M. (2012). Light emitting diodes reliability review. *Microelectronics Reliability*, 52(5), 762–782. Available from <https://doi.org/10.1016/j.microrel.2011.07.063>.
- Chang, J. B., Liu, V., Subramanian, V., Sivula, K., Luscombe, C., Murphy, A., Liu, J., & Fréchet, J. M. J. (2006). Printable polythiophene gas sensor array for low-cost electronic noses. *Journal of Applied Physics*, 100(1)014506. Available from <https://doi.org/10.1063/1.2208743>.
- Chen, K., Gao, W., Emaminejad, S., Kiriya, D., Ota, H., Nyein, H. Y. Y., Takei, K., & Javey, A. (2016). Printed carbon nanotube electronics and sensor systems. *Advanced Materials*, 28(22), 4397–4414. Available from <https://doi.org/10.1002/adma.201504958>, [http://onlinelibrary.wiley.com/journal/10.1002/\(ISSN\)1521-4095](http://onlinelibrary.wiley.com/journal/10.1002/(ISSN)1521-4095).
- Chen, W., Huang, J. J., Chen, Y., Qian, Y., Ruan, S., Su, C. Y., & Tseng, C. Y. (2021). P-1.3: Development of an 11.6-inch 144Hz LCD utilizing an IGZO TFT backplane. *SID Symposium Digest of Technical Papers*, 52(S1), 420–422. Available from <https://doi.org/10.1002/sdtp.14507>.
- Chen, A., Hutchby, J., Zhirnov, V. V., & Bourianoff, G. (2015). Emerging nanoelectronic devices. *Emerging Nanoelectronic Devices*. Available from <https://doi.org/10.1002/9781118958254>, <http://www.wiley.com/remtitle.cgi?isbn = 1118447743>.

- Chen, Y., Shu, Z., Feng, Z., Kong, L., Liu, Y., & Duan, H. (2020). Reliable patterning, transfer printing and post-assembly of multiscale adhesion-free metallic structures for nanogap device applications. *Advanced Functional Materials*, 30(32)2002549. Available from <https://doi.org/10.1002/adfm.202002549>.
- Choi, M., Jang, B., Lee, W., Lee, S., Kim, T. W., Lee, H.-J., Kim, J. H., & Ahn, J. H. (2017). Stretchable active matrix inorganic light-emitting diode display enabled by overlay-aligned roll-transfer printing. *Advanced Functional Materials*, 27(11)1606005. Available from <https://doi.org/10.1002/adfm.201606005>.
- Choi, C., Kim, H., Kang, J. H., Song, M. K., Yeon, H., Chang, C. S., Suh, J. M., Shin, J., Lu, K., Park, B. I., Kim, Y., Lee, H. E., Lee, D., Lee, J., Jang, I., Pang, S., Ryu, K., Bae, S. H., Nie, Y., . . . Kim, J. (2022). Reconfigurable heterogeneous integration using stackable chips with embedded artificial intelligence. *Nature Electronics*, 5(6), 386–393. Available from <https://doi.org/10.1038/s41928-022-00778-y>, <https://www.nature.com/natelectron/>.
- Chowdhury, S. A., Inzani, K., Peña, T., Dey, A., Wu, S. M., Griffin, S. M., & Askari, H. (2022). Mechanical properties and strain transfer behavior of molybdenum ditelluride (MoTe₂) thin films. *Journal of Engineering Materials and Technology*, 144(1). Available from <https://doi.org/10.1115/1.4051306>.
- Cho, M. H., Choi, C. H., & Jeong, J. K. (2022). Comparative study of atomic layer deposited indium-based oxide transistors with a fermi energy level-engineered heterojunction structure channel through a cation combinatorial approach. *ACS Applied Materials and Interfaces*, 14(16), 18646–18661. Available from <https://doi.org/10.1021/acsami.1c23889>, <http://pubs.acs.org/journal/aamick>.
- Cho, K. G., Kim, H. J., Yang, H. M., Seol, K. H., Lee, S. J., & Lee, K. H. (2018). Sub-2 V, transfer-stamped organic/inorganic complementary inverters based on electrolyte-gated transistors. *ACS Applied Materials and Interfaces*, 10(47), 40672–40680. Available from <https://doi.org/10.1021/acsami.8b13140>, <http://pubs.acs.org/journal/aamick>.
- Claro, P. I. C., Cunha, I., Paschoalin, R. T., Gaspar, D., Miranda, K., Oliveira, O. N., Martins, R., Pereira, L., Marconcini, J. M., Fortunato, E., & Mattoso, L. H. C. (2021). Ionic conductive cellulose mats by solution blow spinning as substrate and a dielectric interstrate layer for flexible electronics. *ACS Applied Materials and Interfaces*, 13(22), 26237–26246. Available from <https://doi.org/10.1021/acsami.1c06274>, <http://pubs.acs.org/journal/aamick>.
- Dahiya, A. S., Christou, A., Neto, J., Zumeit, A., Shakthivel, D., & Dahiya, R. (2022). In tandem contact-transfer printing for high-performance transient electronics. *Advanced Electronic Materials*, 8(9) 2200170. Available from <https://doi.org/10.1002/aelm.202200170>.
- Dahiya, A. S., Shakthivel, D., Kumaresan, Y., Zumeit, A., Christou, A., & Dahiya, R. (2020). High-performance printed electronics based on inorganic semiconducting nano to chip scale structures. *Nano Convergence*, 7(1). Available from <https://doi.org/10.1186/s40580-020-00243-6>, <https://link.springer.com/journal/40580>.
- Dahiya, A. S., Zumeit, A., Christou, A., & Dahiya, R. (2022). High-performance n-channel printed transistors on biodegradable substrate for transient electronics. *Advanced Electronic Materials*, 8(9)2200098. Available from <https://doi.org/10.1002/aelm.202200098>.
- Decoutere, S., Osman, H., Dekoster, J., Dutta, B., Biesemans, S. (2010). GaN-on-Si: A scalable material system to realize cost effective next-generation solid state lighting and power devices. Digest of Technical Papers - Symposium on VLSI Technology, Belgium. 151–152. 07431562. Available from <https://doi.org/10.1109/VLSIT.2010.5556207>.
- Deka, M., & Kumar, A. (2010). Enhanced electrical and electrochemical properties of PMMA-clay nanocomposite gel polymer electrolytes. *Electrochimica Acta*, 55(5), 1836–1842. Available from <https://doi.org/10.1016/j.electacta.2009.10.076>.
- Detchprohm, T., Ryou, J., Li, X., & Dupuis, R. D. (2019). *Future aspects of MOCVD technology for epitaxial growth of semiconductors metalorganic vapor phase epitaxy (MOVPE)* (pp. 507–548). Wiley. Available from [10.1002/9781119313021.ch14](https://doi.org/10.1002/9781119313021.ch14).
- Devoret, M. H., & Schoelkopf, R. J. (2000). Amplifying quantum signals with the single-electron transistor. *Nature*, 406(6799), 1039–1046. Available from <https://doi.org/10.1038/35023253>.
- Duan, X., Niu, C., Sahi, V., Chen, J., Parce, J. W., Empedocles, S., & Goldman, J. L. (2003). High-performance thin-film transistors using semiconductor nanowires and nanoribbons. *Nature*, 425 (6955), 274–278. Available from <https://doi.org/10.1038/nature01996>.

- Espera, A. H., Dizon, J. R. C., Chen, Q., & Advincula, R. C. (2019). 3D-printing and advanced manufacturing for electronics. *Progress in Additive Manufacturing*, 4(3), 245–267. Available from <https://doi.org/10.1007/s40964-019-00077-7>, <https://link.springer.com/journal/40964>.
- Fahlman, M., Fabiano, S., Gueskine, V., Simon, D., Berggren, M., & Crispin, X. (2019). Interfaces in organic electronics. *Nature Reviews Materials*, 4(10), 627–650. Available from <https://doi.org/10.1038/s41578-019-0127-y>, <http://www.nature.com/natrevmats/>.
- Fan, K., Peng, T., Chai, B., Chen, J., & Dai, K. (2010). Fabrication and photoelectrochemical properties of TiO₂ films on Ti substrate for flexible dye-sensitized solar cells. *Electrochimica Acta*, 55(18), 5239–5244. Available from <https://doi.org/10.1016/j.electacta.2010.04.051>.
- Ferguson, I. T., Thompson, A. G., Barnett, S. A., Long, F. H., & Feng, Z. C. (2001). Epitaxial film growth and characterization. *Thin Films*, 28(C), 1–69. Available from [https://doi.org/10.1016/S1079-4050\(01\)80017-X](https://doi.org/10.1016/S1079-4050(01)80017-X).
- Flamini, R., De Donno, D., Gambini, J., Giuppi, F., Mazzucco, C., Milani, A., & Resteghini, L. (2022). Toward a heterogeneous smart electromagnetic environment for millimeter-wave communications: An industrial viewpoint. *IEEE Transactions on Antennas and Propagation*, 70(10), 8898–8910. Available from <https://doi.org/10.1109/TAP.2022.3151978>, <https://ieeexplore.ieee.org/servlet/opac?punumber=8>.
- Fukuda, K., Takeda, Y., Mizukami, M., Kumaki, D., & Tokito, S. (2014). Fully solution-processed flexible organic thin film transistor arrays with high mobility and exceptional uniformity. *Scientific Reports*, 4(1). Available from <https://doi.org/10.1038/srep03947>.
- Gao, L. (2017). Flexible device applications of 2D semiconductors. *Small (Weinheim an der Bergstrasse, Germany)*, 13(35), 1603994. Available from <https://doi.org/10.1002/smll.201603994>.
- Gao, X., Lin, L., Liu, Y., & Huang, X. (2015). LTPS TFT process on polyimide substrate for flexible AMOLED. *IEEE/OSA. Journal of Display Technology*, 11(8), 666–669. Available from <https://doi.org/10.1109/JDT.2015.2419656>, <http://ieeexplore.ieee.org/xpl/RecentIssue.jsp?punumber=9425>.
- Gao, L., Liu, C., Peng, Y., Deng, J., Hou, S., Cheng, Y., Huang, W., & Yu, J. (2022). Ultrasensitive flexible NO₂ gas sensors via multilayer porous polymer film. *Sensors and Actuators B: Chemical*, 368132113. Available from <https://doi.org/10.1016/j.snb.2022.132113>.
- Garlapati, S. K., Divya, M., Breitung, B., Kruk, R., Hahn, H., & Dasgupta, S. (2018). Printed electronics based on inorganic semiconductors: From processes and materials to devices. *Advanced Materials*, 30(40), 1707600. Available from <https://doi.org/10.1002/adma.201707600>.
- Geffroy, B., Le Roy, P., & Prat, C. (2006). Organic light-emitting diode (OLED) technology: Materials, devices and display technologies. *Polymer International*, 55(6), 572–582. Available from <https://doi.org/10.1002/pi.1974>.
- Geiger, S., Michon, J., Liu, S., Qin, J., Ni, J., Hu, J., Gu, T., & Lu, N. (2020). Flexible and stretchable photonics: The next stretch of opportunities. *ACS Photonics*, 7(10), 2618–2635. Available from <https://doi.org/10.1021/acsp Photonics.0c00983>, <http://pubs.acs.org/journal/apchd5>.
- Giannouli, M., Drakonakis, V. M., Savva, A., Eleftheriou, P., Florides, G., & Choulis, S. A. (2015). Methods for improving the lifetime performance of organic photovoltaics with low-costing encapsulation. *Chem Phys Chem*, 16(6), 1134–1154. Available from <https://doi.org/10.1002/cphc.201402749>, [http://onlinelibrary.wiley.com/journal/10.1002/\(ISSN\)1439-7641](http://onlinelibrary.wiley.com/journal/10.1002/(ISSN)1439-7641).
- Gong, Y., Zhao, K., He, H., Cai, W., Tang, N., Ning, H., Wu, S., Gao, J., Zhou, G., Lu, X., & Liu, J.-M. (2018). Solution processable high quality ZrO₂ dielectric films for low operation voltage and flexible organic thin film transistor applications. *Journal of Physics D: Applied Physics*, 51(11), 115105. Available from <https://doi.org/10.1088/1361-6463/aaac1b>.
- Guo, X., Xu, Y., Ogier, S., Ng, T. N., Caironi, M., Perinot, A., Li, L., Zhao, J., Tang, W., Sporea, R. A., Nejjim, A., Carrabina, J., Cain, P., & Yan, F. (2017). Current status and opportunities of organic thin-film transistor technologies. *IEEE Transactions on Electron Devices*, 64(5), 1906–1921. Available from <https://doi.org/10.1109/TED.2017.2677086>.
- Han, J., Park, K. I., & Jeong, C. (2019). Dual-structured flexible piezoelectric film energy harvesters for effectively integrated performance. *Sensors*, 19(6), 1444. Available from <https://doi.org/10.3390/s19061444>.
- Heikenfeld, J., Drzaic, P., Yeo, J.-S., & Koch, T. (2011). Review paper: A critical review of the present and future prospects for electronic paper. *Journal of the Society for Information Display*, 19(2), 129. Available from <https://doi.org/10.1889/jsid19.2.129>.

- Heo, J. S., Eom, J., Kim, Y. H., & Park, S. K. (2018). Recent progress of textile-based wearable electronics: A comprehensive review of materials, devices, and applications. *Small (Weinheim an der Bergstrasse, Germany)*, 14(3). Available from <https://doi.org/10.1002/smll.201703034>, [http://onlinelibrary.wiley.com/journal/10.1002/\(ISSN\)1613-6829](http://onlinelibrary.wiley.com/journal/10.1002/(ISSN)1613-6829).
- He, Y., Wang, X., Gao, Y., Hou, Y., & Wan, Q. (2018). Oxide-based thin film transistors for flexible electronics. *Journal of Semiconductors*, 39(1), 011005. Available from <https://doi.org/10.1088/1674-4926/39/1/011005>.
- Hou, R., Gund, G. S., Qi, K., Nakhnivej, P., Liu, H., Li, F., Xia, B. Y., & Park, H. S. (2019). Hybridization design of materials and devices for flexible electrochemical energy storage. *Energy Storage Materials*, 19, 212–241. Available from <https://doi.org/10.1016/j.ensm.2019.03.002>, <http://www.journals.elsevier.com/energy-storage-materials/>.
- Hussain, A. M., & Hussain, M. M. (2016). CMOS-technology-enabled flexible and stretchable electronics for internet of everything applications. *Advanced Materials*, 28(22), 4219–4249. Available from <https://doi.org/10.1002/adma.201504236>, <http://www3.interscience.wiley.com/journal/119030556/issue>.
- Hwang, G. T., Byun, M., Jeong, C. K., & Lee, K. J. (2015). Flexible piezoelectric thin-film energy harvesters and nanosensors for biomedical applications. *Advanced Healthcare Materials*, 4(5), 646–658. Available from <https://doi.org/10.1002/adhm.201400642>, [http://onlinelibrary.wiley.com/journal/10.1002/\(ISSN\)2192-2659](http://onlinelibrary.wiley.com/journal/10.1002/(ISSN)2192-2659).
- Hyeon, D. Y., & Park, K. I. (2019). Piezoelectric flexible energy harvester based on BaTiO₃ thin film enabled by exfoliating the mica substrate. *Energy Technology*, 7(10), 1900638. Available from <https://doi.org/10.1002/ente.201900638>.
- Im, T. H., Lee, C. H., Kim, J. C., Kim, S., Kim, M., Park, C. M., Lee, H. E., Park, J. H., Jang, M. S., Lee, D. C., Choi, S. Y., Wang, H. S., Jeong, H. Y., Jeon, D. Y., & Lee, K. J. (2021). Metastable quantum dot for photoelectric devices via flash-induced one-step sequential self-formation. *Nano Energy*, 84. Available from <https://doi.org/10.1016/j.nanoen.2021.105889>, <http://www.journals.elsevier.com/nano-energy/>.
- Im, T. H., Park, D. Y., Lee, H. K., Park, J. H., Jeong, C. K., Joe, D. J., & Lee, K. J. (2017). Xenon flash lamp-induced ultrafast multilayer graphene growth. *Particle & Particle Systems Characterization*, 34(9), 1600429. Available from <https://doi.org/10.1002/ppsc.201600429>.
- Ishihara, R., Derakhshandeh, J., Tajari Mofrad, M. R., Chen, T., Golshani, N., & Beenakker, C. I. M. (2012). Netherlands monolithic 3D-ICs with single grain Si thin film transistors. *Solid-State Electronics*, 71, 80–87. Available from <https://doi.org/10.1016/j.sse.2011.10.025>, 00381101.
- Ishikawa, F. N., Chang, H. K., Ryu, K., Chen, P. C., Badmaev, A., De Arco, L. G., Shen, G., & Zhou, C. (2009). Transparent electronics based on transfer printed aligned carbon nanotubes on rigid and flexible substrates. *ACS Nano*, 3(1), 73–79. Available from <https://doi.org/10.1021/nn800434d>.
- Jayathilaka, W. A. D. M., Qi, K., Qin, Y., Chinnappan, A., Serrano-García, W., Baskar, C., Wang, H., He, J., Cui, S., Thomas, S. W., & Ramakrishna, S. (2019). Significance of nanomaterials in wearables: A review on wearable actuators and sensors. *Advanced Materials*, 31(7), 1805921. Available from <https://doi.org/10.1002/adma.201805921>.
- Jeong, H., Ha, T., Kuang, I., Shen, L., Dai, Z., Sun, N., & Lu, N. (2017). NFC-enabled, tattoo-like stretchable biosensor manufactured by 'cut-and-paste' method. *Proceedings of the annual international conference of the IEEE engineering in medicine and biology society, EMBS*. Institute of Electrical and Electronics Engineers Inc. United States, pp. 4094–4097. [10.1109/EMBC.2017.8037756](https://doi.org/10.1109/EMBC.2017.8037756). 9781509028092.
- Jeong, J., Kim, S. K., Kim, J., Geum, D. M., Kim, D., Jo, E., Jeong, H., Park, J., Jang, J. H., Choi, S., Kwon, I., & Kim, S. (2022). Heterogeneous and monolithic 3D integration of III-V-based radio frequency devices on Si CMOS circuits. *ACS Nano*, 16(6), 9031–9040. Available from <https://doi.org/10.1021/acsnano.2c00334>, <http://pubs.acs.org/journal/ancac3>.
- Jeong, Y. C., Lee, H. E., Shin, A., Kim, D. G., Lee, K. J., & Kim, D. (2020). Progress in brain-compatible interfaces with soft nanomaterials. *Advanced Materials*, 32(35), 1907522. Available from <https://doi.org/10.1002/adma.201907522>.

- Jeong, C. K., Park, K. I., Son, J. H., Hwang, G. T., Lee, S. H., Park, D. Y., Lee, H. E., Lee, H. K., Byun, M., & Lee, K. J. (2014). Self-powered fully-flexible light-emitting system enabled by flexible energy harvester. *Energy Environmental Science*, 7(12), 4035–4043. Available from <https://doi.org/10.1039/C4EE02435D>.
- Joe, D. J., Kim, S., Park, J. H., Park, D. Y., Lee, H. E., Im, T. H., Choi, I., Ruoff, R. S., & Lee, K. J. (2017). Laser-material interactions for flexible applications. *Advanced Materials*, 29(26), 1606586. Available from <https://doi.org/10.1002/adma.201606586>.
- Jung, D. H., Park, J. H., Lee, H. E., Byun, J., Im, T. H., Lee, G. Y., Seok, J. Y., Yun, T., Lee, K. J., & Kim, S. O. (2019). Flash-induced ultrafast recrystallization of perovskite for flexible light-emitting diodes. *Nano Energy*, 61, 236–244. Available from <https://doi.org/10.1016/j.nanoen.2019.04.061>, <http://www.journals.elsevier.com/nano-energy/>.
- Kamiya, T., & Hosono, H. (2010). Material characteristics and applications of transparent amorphous oxide semiconductors. *NPG Asia Materials*, 2(1), 15–22. Available from <https://doi.org/10.1038/asiamat.2010.5>.
- Kamiya, T., Nomura, K., & Hosono, H. (2009). Origins of high mobility and low operation voltage of amorphous oxide TFTs: Electronic structure, electron transport, defects and doping. *Journal of Display Technology*, 5(12), 468–483. Available from <https://doi.org/10.1109/jdt.2009.2034559>.
- Kamiya, T., Nomura, K., & Hosono, H. (2016). Present status of amorphous In–Ga–Zn–O thin-film transistors. *Science and Technology of Advanced Materials*, 11(4), 044305. Available from <https://doi.org/10.1088/1468-6996/11/4/044305>.
- Kang, S. M., Lee, H. E., Wang, H. S., Shin, J. H., Jo, W., Lee, Y., Lee, H., Lee, D., Kim, Y. H., Kim, T. S., Lee, K. J., & Bae, B. S. (2021). Self-powered flexible full-color display via dielectric-tuned hybri-mer triboelectric nanogenerators. *ACS Energy Letters*, 6(11), 4097–4107. Available from <https://doi.org/10.1021/acscenergylett.1c01729>, <http://pubs.acs.org/journal/aelccp>.
- Keum, K., Kim, J. W., Hong, S. Y., Son, J. G., Lee, S. S., & Ha, J. S. (2020). Flexible/stretchable supercapacitors with novel functionality for wearable electronics. *Advanced Materials*, 32(51). Available from <https://doi.org/10.1002/adma.202002180>, [http://onlinelibrary.wiley.com/journal/10.1002/\(ISSN\)1521-4095](http://onlinelibrary.wiley.com/journal/10.1002/(ISSN)1521-4095).
- Khan, Y., Ostfeld, A. E., Lochner, C. M., Pierre, A., & Arias, A. C. (2016). Monitoring of vital signs with flexible and wearable medical devices. *Advanced Materials*, 28(22), 4373–4395. Available from <https://doi.org/10.1002/adma.201504366>, [http://onlinelibrary.wiley.com/journal/10.1002/\(ISSN\)1521-4095](http://onlinelibrary.wiley.com/journal/10.1002/(ISSN)1521-4095).
- Khan, K., Tareen, A. K., Aslam, M., Wang, R., Zhang, Y., Mahmood, A., Ouyang, Z., Zhang, H., & Guo, Z. (2020). Recent developments in emerging two-dimensional materials and their applications. *Journal of Materials Chemistry C*, 8(2), 387–440. Available from <https://doi.org/10.1039/c9tc04187g>, <http://pubs.rsc.org/en/journals/journal/tc>.
- Khan, Y., Thielens, A., Muin, S., Ting, J., Baumbauer, C., & Arias, A. C. (2020). A new frontier of printed electronics: flexible hybrid electronics. *Advanced Materials*, 32(15), 1905279. Available from <https://doi.org/10.1002/adma.201905279>.
- Khan, K., Tu, Z., Zhao, Q., Zhao, C., & Archer, L. A. (2019). Synthesis and properties of poly-ether/ethylene carbonate electrolytes with high oxidative stability. *Chemistry of Materials*, 31(20), 8466–8472. Available from <https://doi.org/10.1021/acs.chemmater.9b02823>, <http://pubs.acs.org/journal/cmater>.
- Kim, S. J., Choi, H., Kim, Y., We, J. H., Shin, J. S., Lee, H. E., Oh, M. W., Lee, K. J., & Cho, B. J. (2017). Post ionized defect engineering of the screen-printed Bi₂Te_{2.7}Se_{0.3} thick film for high performance flexible thermoelectric generator. *Nano Energy*, 31, 258–263. Available from <https://doi.org/10.1016/j.nanoen.2016.11.034>, <http://www.journals.elsevier.com/nano-energy/>.
- Kim, I. H., Im, T. H., Lee, H. E., Jang, J. S., Wang, H. S., Lee, G. Y., Kim, I. D., Lee, K. J., & Kim, S. O. (2019). Janus graphene liquid crystalline fiber with tunable properties enabled by ultrafast flash reduction. *Small (Weinheim an der Bergstrasse, Germany)*, 15(48). Available from <https://doi.org/10.1002/smll.201901529>, [http://onlinelibrary.wiley.com/journal/10.1002/\(ISSN\)1613-6829](http://onlinelibrary.wiley.com/journal/10.1002/(ISSN)1613-6829).
- Kim, B. G., Jeong, E. J., Chung, J. W., Seo, S., Koo, B., & Kim, J. (2013). A molecular design principle of lyotropic liquid-crystalline conjugated polymers with directed alignment capability for plastic electronics. *Nature Materials*, 12(7), 659–664. Available from <https://doi.org/10.1038/nmat3595>.

- Kim, K., Kim, B., & Lee, C. H. (2020). Printing flexible and hybrid electronics for human skin and eye-interfaced health monitoring systems. *Advanced Materials*, 32(15)1902051. Available from <https://doi.org/10.1002/adma.201902051>.
- Kim, D. W., Kwon, J., Kim, H. S., & Jeong, U. (2021). Printed stretchable single-nanofiber interconnections for individually-addressable highly-integrated transparent stretchable field effect transistor array. *Nano Letters*, 21(13), 5819–5827. Available from <https://doi.org/10.1021/acs.nanolett.1c01744>, <http://pubs.acs.org/journal/nalefd>.
- Kim, S. J., Lee, H. E., Choi, H., Kim, Y., We, J. H., Shin, J. S., Lee, K. J., & Cho, B. J. (2016). High-performance flexible thermoelectric power generator using laser multiscanning lift-off process. *ACS Nano*, 10(12), 10851–10857. Available from <https://doi.org/10.1021/acsnano.6b05004>, <http://pubs.acs.org/journal/ancac3>.
- Kim, D. H., Lee, H. E., You, B. K., Cho, S. B., Mishra, R., Kang, I. S., & Lee, K. J. (2019). Flexible crossbar-structured phase change memory array via mo-based interfacial physical lift-off. *Advanced Functional Materials*, 29(6). Available from <https://doi.org/10.1002/adfm.201806338>, [http://onlinelibrary.wiley.com/journal/10.1002/\(ISSN\)1616-3028](http://onlinelibrary.wiley.com/journal/10.1002/(ISSN)1616-3028).
- Kim, Y., Suh, J. M., Shin, J., Liu, Y., Yeon, H., Qiao, K., Kum, H. S., Kim, C., Lee, H. E., Choi, C., Kim, H., Lee, D., Lee, J., Kang, J. H., Park, B. I., Kang, S., Kim, J., Kim, S., Perozek, J. A., ... Kim, J. (2022). Chip-less wireless electronic skins by remote epitaxial freestanding compound semiconductors. *Science (New York, N.Y.)*, 377(6608), 859–864. Available from <https://doi.org/10.1126/science.abn7325>.
- Koo, J. H., Kim, D. C., Shim, H. J., Kim, T. H., & Kim, D. H. (2018). Flexible and stretchable smart display: Materials, fabrication, device design, and system integration. *Advanced Functional Materials*, 28(35). Available from <https://doi.org/10.1002/adfm.201801834>, [http://onlinelibrary.wiley.com/journal/10.1002/\(ISSN\)1616-3028](http://onlinelibrary.wiley.com/journal/10.1002/(ISSN)1616-3028).
- Kum, H., Lee, D., Kong, W., Kim, H., Park, Y., Kim, Y., Baek, Y., Bae, S. H., Lee, K., & Kim, J. (2019). Epitaxial growth and layer-transfer techniques for heterogeneous integration of materials for electronic and photonic devices. *Nature Electronics*, 2(10), 439–450. Available from <https://doi.org/10.1038/s41928-019-0314-2>, <https://www.nature.com/natelectron/>.
- Kuo, Y. (2013). Thin film transistor technology—Past, present, and future. *Electrochemical Society Interface*, 22(1), 55–61. Available from <https://doi.org/10.1149/2.F06131if>, http://www.electrochem.org/dl/interface/if_prev_iss.htm.
- Kuo, Y. (2008). Thin-film transistor and ultra-large scale integrated circuit: Competition or collaboration. *Japanese Journal of Applied Physics*, 47(3), 1845–1852. Available from <https://doi.org/10.1143/JJAP.47.1845>, <http://ijap.ipap.jp/link?JJAP/47/1845/pdf>, United States.
- Kuo, Y. (2018). Progress of thin film transistor technology. In *14th IEEE international conference on solid-state and integrated circuit technology, ICSICT 2018 – Proceedings*. Institute of Electrical and Electronics Engineers Inc., United States. 9781538644409. <http://ieeexplore.ieee.org/xpl/mostRecentIssue.jsp?punumber=8540788>. 10.1109/ICSICT.2018.8565738.
- Kwon, J. H., Jeong, E. G., Jeon, Y., Kim, D. G., Lee, S., & Choi, K. C. (2019). Design of highly water resistant, impermeable, and flexible thin-film encapsulation based on inorganic/organic hybrid layers. *ACS Applied Materials and Interfaces*, 11(3), 3251–3261. Available from <https://doi.org/10.1021/acsaami.8b11930>, <http://pubs.acs.org/journal/aamick>.
- Kwon, J.H., Pode, M. (2013). Applications of organic and printed electronics. 10.1007/978-1-4614-3160-2.
- Lee, J. H., Ahn, Y., Lee, H. E., Jang, Y. N., Park, A. Y., Kim, S., Jung, Y. H., Sung, S. H., Shin, J. H., Lee, S. H., Park, S. H., Kim, K. S., Jang, M. S., Kim, B. J., Oh, S. H., & Lee, K. J. (2023). wearable surface-lighting micro-light-emitting diode patch for melanogenesis inhibition. *Advanced healthcare. Materials*, 12(1), 2201796. Available from <https://doi.org/10.1002/adhm.202201796>.
- Lee, H. E., Choi, J. H., Lee, S. H., Jeong, M., Shin, J. H., Joe, D. J., Kim, D. H., Kim, C. W., Park, J. H., Lee, J. H., Kim, D., Shin, C. S., & Lee, K. J. (2018). Monolithic flexible vertical GaN light-emitting diodes for a transparent wireless brain optical stimulator. *Advanced Materials*, 30(28), 1521–4095. Available from <https://doi.org/10.1002/adma.201800649>, [http://onlinelibrary.wiley.com/journal/10.1002/\(ISSN\)](http://onlinelibrary.wiley.com/journal/10.1002/(ISSN)).

- Lee, D., Cho, K. G., Seol, K. H., Lee, S., Choi, S. H., & Lee, K. H. (2019). Low voltage, high gain electrolyte-gated complementary inverters based on transfer-printed block copolymer ion gels. *Organic Electronics*, 71, 266–271. Available from <https://doi.org/10.1016/j.orgel.2019.05.026>, <http://www.elsevier.com/locate/orgel>.
- Lee, Y. L., Hsu, H. L., Chen, S. Y., & Yew, T. R. (2008). Solution-processed naphthalene diimide derivatives as n-type semiconductor materials. *Journal of Physical Chemistry C*, 112(5), 1694–1699. Available from <https://doi.org/10.1021/jp076278w>.
- Lee, S. K., Jang, H., Hasan, M., Koo, J. B., & Ahn, J. H. (2010). Mechanically flexible thin film transistors and logic gates on plastic substrates by use of single-crystal silicon wafers from bulk wafers. *Applied Physics Letters*, 96(17). Available from <https://doi.org/10.1063/1.3409475>.
- Lee, H. E., Kim, S., Ko, J., Yeom, H. I., Byun, C. W., Lee, S. H., Joe, D. J., Im, T. H., Park, S. H. K., & Lee, K. J. (2016). Skin-like oxide thin-film transistors for transparent displays. *Advanced Functional Materials*, 26(34), 6170–6178. Available from <https://doi.org/10.1002/adfm.201601296>, [http://onlinelibrary.wiley.com/journal/10.1002/\(ISSN\)1616-3028](http://onlinelibrary.wiley.com/journal/10.1002/(ISSN)1616-3028).
- Lee, S. H., Kim, J., Shin, J. H., Lee, H. E., Kang, I. S., Gwak, K., Kim, D. S., Kim, D., & Lee, K. J. (2018). Optogenetic control of body movements via flexible vertical light-emitting diodes on brain surface. *Nano Energy*, 44, 447–455. Available from <https://doi.org/10.1016/j.nanoen.2017.12.011>, <http://www.journals.elsevier.com/nano-energy/>.
- Lee, H. E., Lee, S. H., Jeong, M., Shin, J. H., Ahn, Y., Kim, D., Oh, S. H., Yun, S. H., & Lee, K. J. (2018). Trichogenic photostimulation using monolithic flexible vertical AlGaInP light-emitting diodes. *ACS Nano*, 12(9), 9587–9595. Available from <https://doi.org/10.1021/acsnano.8b05568>, <http://pubs.acs.org/journal/ancac3>.
- Lee, H. E., Lee, D., Lee, T. I., Jang, J., Jang, J., Lim, Y. W., Shin, J. H., Kang, S. M., Choi, G. M., Joe, D. J., Kim, J. H., Lee, S. H., Park, S. H., Park, C. B., Kim, T. S., Lee, K. J., & Bae, B. S. (2022). Siloxane hybrid material-encapsulated highly robust flexible μ LEDs for biocompatible lighting applications. *ACS Applied Materials and Interfaces*, 14(24), 28258–28269. Available from <https://doi.org/10.1021/acsam.2c03922>, <http://pubs.acs.org/journal/aamick>.
- Lee, H. E., Lee, D., Lee, T. I., Shin, J. H., Choi, G. M., Kim, C., Lee, S. H., Lee, J. H., Kim, Y. H., Kang, S. M., Park, S. H., Kang, I. S., Kim, T. S., Bae, B. S., & Lee, K. J. (2019). Wireless powered wearable micro light-emitting diodes. *Nano Energy*, 55, 454–462. Available from <https://doi.org/10.1016/j.nanoen.2018.11.017>, <http://www.journals.elsevier.com/nano-energy/>.
- Lee, H., Lee, H. E., Wang, H. S., Kang, S. M., Lee, D., Kim, Y. H., Shin, J. H., Lim, Y. W., Lee, K. J., & Bae, B. S. (2020). Hierarchically surface-textured ultrastable hybrid film for large-scale triboelectric nanogenerators. *Advanced Functional Materials*, 30(49)2005610. Available from <https://doi.org/10.1002/adfm.202005610>.
- Lee, H. E., Park, J. H., Jang, D., Shin, J. H., Im, T. H., Lee, J. H., Hong, S. K., Wang, H. S., Kwak, M. S., Peddigari, M., Jeong, C. K., Min, Y., Park, C. H., Choi, J. J., Ryu, J., Yoon, W. H., Kim, D., Lee, K. J., & Hwang, G. T. (2020). Optogenetic brain neuromodulation by stray magnetic field via flash-enhanced magneto-mechano-triboelectric nanogenerator. *Nano Energy*, 75, 104951. Available from <https://doi.org/10.1016/j.nanoen.2020.104951>.
- Lee, H. E., Park, J. H., Kim, T. J., Im, D., Shin, J. H., Kim, D. H., Mohammad, B., Kang, I. S., & Lee, K. J. (2018). Novel electronics for flexible and neuromorphic computing. *Advanced Functional Materials*, 28(32), 1801690. Available from <https://doi.org/10.1002/adfm.201801690>.
- Lee, H. E., Shin, J. H., Lee, S. H., Lee, J. H., Park, S. H., & Lee, K. J. (2019). SPIE South Korea flexible micro light-emitting diodes for wearable applications. *Proceedings of SPIE - The international society for optical engineering*, 10940. Available from <https://doi.org/10.1117/12.2506926>, <http://spie.org/x1848.xml>, 1996756X.
- Lee, H. E., Shin, J. H., Park, J. H., Hong, S. K., Park, S. H., Lee, S. H., Lee, J. H., Kang, I. S., & Lee, K. J. (2019). Micro light-emitting diodes for display and flexible biomedical applications. *Advanced Functional Materials*, 29(24). Available from <https://doi.org/10.1002/adfm.201808075>, [http://onlinelibrary.wiley.com/journal/10.1002/\(ISSN\)1616-3028](http://onlinelibrary.wiley.com/journal/10.1002/(ISSN)1616-3028).
- Lee, H. E. (2021). Novel bio-optoelectronics enabled by flexible micro light-emitting diodes. *Electronics*, 10(21), 2644. Available from <https://doi.org/10.3390/electronics10212644>.

- Lee, W., & Souk, J. (2018). *Flexible OLED manufacturing* (pp. 173–191). Wiley. Available from [10.1002/9781119161387.ch10](https://doi.org/10.1002/9781119161387.ch10).
- Lee, K. H., Zhang, S., Gu, Y., Lodge, T. P., & Frisbie, C. D. (2013). Transfer printing of thermoreversible ion gels for flexible electronics. *ACS Applied Materials and Interfaces*, 5(19), 9522–9527. Available from <https://doi.org/10.1021/am402200n>, <http://pubs.acs.org/journal/aamick>.
- Leppänen, J., Huttunen, O. H., Majumdar, H., & Alastalo, A. (2015). Flexography-printed In₂O₃ semiconductor layers for high-mobility thin-film transistors on flexible plastic substrate. *Advanced Materials*, 27(44), 7168–7175. Available from <https://doi.org/10.1002/adma.201502569>.
- Lerner, R., Eisenbrandt, S., Fischer, F., Fecioru, A., Trindade, A. J., Bonafede, S., Bower, C., Waltereit, P., Reiner, R., & Czap, H. (2018). Flexible and scalable heterogeneous integration of GaN HEMTs on Si-CMOS by micro-transfer-printing. *Physica Status Solidi (A)*, 215(8), 1700556. Available from <https://doi.org/10.1002/pssa.201700556>.
- Lin, C. L., Chang, W. Y., Hung, C. C., & Tu, C. D. (2012). LTPS-TFT pixel circuit to compensate for OLED luminance degradation in three-dimensional AMOLED display. *IEEE Electron Device Letters*, 33(5), 700–702. Available from <https://doi.org/10.1109/LED.2012.2188270>.
- Lin, C. S., Chen, Y. C., Chang, T. C., Jian, F. Y., Hsu, W. C., Kuo, Y. J., Dai, C. H., Chen, T. C., Lo, W. H., Hsieh, T. Y., & Shih, J. M. (2011). NBTI degradation in LTPS TFTs under mechanical tensile strain. *IEEE Electron Device Letters*, 32(7), 907–909. Available from <https://doi.org/10.1109/LED.2011.2144953>.
- Lin, C. L., & Chen, Y. C. (2007). A novel LTPS-TFT pixel circuit compensating for TFT threshold-voltage shift and OLED degradation for AMOLED. *IEEE Electron Device Letters*, 28(2), 129–131. Available from <https://doi.org/10.1109/LED.2006.889523>.
- Liu, Q., Tian, B., Liang, J., & Wu, W. (2021). Recent advances in printed flexible heaters for portable and wearable thermal management. *Materials Horizons*, 8(6), 1634–1656. Available from <https://doi.org/10.1039/d0mh01950j>, <http://pubs.rsc.org/en/journals/journal/mh>.
- Liu, C., Zhang, L., Zhou, X., Gao, J., Chen, W., Wang, X., & Xu, B. (2019). Hydrothermally treated SnO₂ as the electron transport layer in high-efficiency flexible perovskite solar cells with a certificated efficiency of 17.3%. *Advanced Functional Materials*, 29(47), 1807604. Available from <https://doi.org/10.1002/adfm.201807604>.
- Li, J., Liu, D., Miao, Q., & Yan, F. (2012). The application of a high-k polymer in flexible low-voltage organic thin-film transistors. *Journal of Materials Chemistry*, 22(31), 15998. Available from <https://doi.org/10.1039/c2jm32177g>.
- Li, J., Li, R., Du, H., Zhong, Y., Chen, Y., Nan, K., Won, S. M., Zhang, J., Huang, Y., & Rogers, J. A. (2019). Ultrathin, transferred layers of metal silicide as faradaic electrical interfaces and biofluid barriers for flexible bioelectronic implants. *ACS Nano*, 13(1), 660–670. Available from <https://doi.org/10.1021/acsnano.8b07806>, <http://pubs.acs.org/journal/ancac3>.
- Li, J., Tang, W., Wang, Q., Sun, W., Zhang, Q., Guo, X., Wang, X., & Yan, F. (2018). Solution-processable organic and hybrid gate dielectrics for printed electronics. *Materials Science and Engineering R: Reports*, 127, 1–36. Available from <https://doi.org/10.1016/j.mser.2018.02.004>.
- Lucas, B., El Amrani, A., Chakaroun, M., Ratier, B., Antony, R., & Moliton, A. (2009). Ultraviolet light effect on electrical properties of a flexible organic thin film transistor. *Thin Solid Films*, 517(23), 6280–6282. Available from <https://doi.org/10.1016/j.tsf.2009.02.065>.
- Mack, S., Meitl, M. A., Baca, A. J., Zhu, Z.-T., & Rogers, J. A. (2006). Mechanically flexible thin-film transistors that use ultrathin ribbons of silicon derived from bulk wafers. *Applied Physics Letters*, 88(21), 213101. Available from <https://doi.org/10.1063/1.2206688>.
- Maleki Kheimeh Sari, H., & Li, X. (2019). Controllable cathode–electrolyte interface of Li[Ni 0.8 Co 0.1 Mn 0.1]O₂ for lithium ion batteries: A review. *Advanced Energy Materials*, 9(39)1901597. Available from <https://doi.org/10.1002/aenm.201901597>.
- Martinez, R. V., Fish, C. R., Chen, X., & Whitesides, G. M. (2012). Elastomeric origami: Programmable paper–elastomer composites as pneumatic actuators. *Advanced Functional Materials*, 22(7), 1376–1384. Available from <https://doi.org/10.1002/adfm.201102978>.

- Martins, R. F. P., Ahnood, A., Correia, N., Pereira, L. M. N. P., Barros, R., Barquinha, P. M. C. B., Costa, R., Ferreira, I. M. M., Nathan, A., & Fortunato, E. E. M. C. (2013). Recyclable, flexible, low-power oxide electronics. *Advanced Functional Materials*, 23(17), 2153–2161. Available from <https://doi.org/10.1002/adfm.201202907>.
- Menard, E., Meitl, M. A., Sun, Y., Park, J. U., Shir, D. J. L., Nam, Y. S., Jeon, S., & Rogers, J. A. (2007). Micro- and nanopatterning techniques for organic electronic and optoelectronic systems. *Chemical Reviews*, 107(4), 1117–1160. Available from <https://doi.org/10.1021/cr050139y>.
- Menard, E., Nuzzo, R. G., & Rogers, J. A. (2005). Bendable single crystal silicon thin film transistors formed by printing on plastic substrates. *Applied Physics Letters*, 86(9), 1–3. Available from <https://doi.org/10.1063/1.1866637>.
- Minamiki, T., Minami, T., Chen, Y. P., Mano, T., Takeda, Y., Fukuda, K., & Tokito, S. (2021). Flexible organic thin-film transistor immunosensor printed on a one-micron-thick film. *Communications Materials*, 2(1). Available from <https://doi.org/10.1038/s43246-020-00112-z>, <https://www.nature.com/commsmat/>.
- Min, J. H., Li, K. H., Kim, Y. H., Min, J. W., Kang, C. H., Kim, K. H., Lee, J. S., Lee, K. J., Jeong, S. M., Lee, D. S., Bae, S. Y., Ng, T. K., & Ooi, B. S. (2021). Toward large-scale Ga₂O₃ membranes via quasi-van der Waals epitaxy on epitaxial graphene layers. *ACS Applied Materials and Interfaces*, 13(11), 13410–13418. Available from <https://doi.org/10.1021/acsmi.1c01042>, <http://pubs.acs.org/journal/aamick>.
- Mitzi, D. B. (2004). Solution-processed inorganic semiconductors. *Journal of Materials Chemistry*, 14(15), 2355. Available from <https://doi.org/10.1039/b403482a>.
- Morrison, N. A., Stolley, T., Hermanns, U., Reus, A., Deppisch, T., Bolandi, H., Melnik, Y., Singh, V., & Griffith Cruz, J. (2015). An overview of process and product requirements for next generation thin film electronics, Advanced touch panel devices, and ultra high barriers. *Proceedings of the IEEE*, 103(4), 518–534. Available from <https://doi.org/10.1109/JPROC.2015.2408052>, <http://ieeexplore.ieee.org/xpl/RecentIssue.jsp?punumber=5>.
- Mujahid, M., Chen, C., Hu, W., Wang, Z. K., & Duan, Y. (2020). Progress of high-throughput and low-cost flexible perovskite solar cells. *Solar RRL*, 4(8). Available from <https://doi.org/10.1002/solr.201900556>, <https://onlinelibrary.wiley.com/journal/2367198x>.
- Namdari, N., Mohammadian, B., Jafari, P., Mohammadi, R., Sojoudi, H., Ghasemi, H., & Rizvi, R. (2020). Advanced functional surfaces through controlled damage and instabilities. *Materials Horizons*, 7(2), 366–396. Available from <https://doi.org/10.1039/c9mh01516g>, <http://pubs.rsc.org/en/journals/journal/mh>.
- Nguyen, B. H., & Nguyen, V. H. (2016). Promising applications of graphene and graphene-based nanostructures. *Advances in Natural Sciences: Nanoscience and Nanotechnology*, 7(2), 023002. Available from <https://doi.org/10.1088/2043-6262/7/2/023002>.
- Ni, H. J., Liu, J. G., Wang, Z. H., & Yang, S. Y. (2015). A review on colorless and optically transparent polyimide films: Chemistry, process and engineering applications. *Journal of Industrial and Engineering Chemistry*, 28, 16–27. Available from <https://doi.org/10.1016/j.jiec.2015.03.013>, <http://www.sciencedirect.com/science/journal/1226086X>.
- Nketia-Yawson, B., & Noh, Y. Y. (2018). Recent progress on high-capacitance polymer gate dielectrics for flexible low-voltage transistors. *Advanced Functional Materials*, 28(42), 1802201. Available from <https://doi.org/10.1002/adfm.201802201>.
- Parbrook, P. J., Corbett, B., Han, J., Seong, T. Y., & Amano, H. (2021). Micro-light emitting diode: From chips to applications. *Laser & Photonics Reviews*, 15(5), 2000133. Available from <https://doi.org/10.1002/lpor.202000133>.
- Park, J., Heo, S., Park, K., Song, M. H., Kim, J. Y., Kyung, G., Ruoff, R. S., Park, J. U., & Bien, F. (2017). Research on flexible display at Ulsan National Institute of Science and Technology. *NPJ Flexible Electronics*, 1(1). Available from <https://doi.org/10.1038/s41528-017-0006-9>, <http://nature.com/npjflexelectron/>.
- Park, J. W., Kang, B. H., & Kim, H. J. (2020). A review of low-temperature solution-processed metal oxide thin-film transistors for flexible electronics. *Advanced Functional Materials*, 30(20), 1904632. Available from <https://doi.org/10.1002/adfm.201904632>.

- Park, J. H., Lee, H. E., Jeong, C. K., Kim, D. H., Hong, S. K., Park, K. I., & Lee, K. J. (2019). Self-powered flexible electronics beyond thermal limits. *Nano Energy*, *56*, 531–546. Available from <https://doi.org/10.1016/j.nanoen.2018.11.077>, <http://www.journals.elsevier.com/nano-energy/>.
- Park, A. H., Lee, S. H., Lee, C., Kim, J., Lee, H. E., Paik, S. B., Lee, K. J., & Kim, D. (2016). Optogenetic mapping of functional connectivity in freely moving mice via insertable wrapping electrode array beneath the skull. *ACS Nano*, *10*(2), 2791–2802. Available from <https://doi.org/10.1021/acsnano.5b07889>, <http://pubs.acs.org/journal/ancac3>.
- Park, S., Lee, Y. H., Wi, J. S., & Oh, J. (2016). A semitransparent and flexible single crystal Si thin film: Silicon on nothing (SON) revisited. *ACS Applied Materials and Interfaces*, *8*(29), 18962–18968. Available from <https://doi.org/10.1021/acsami.6b05261>, <http://pubs.acs.org/journal/aamick>.
- Park, J., Lim, Y. W., Cho, S. Y., Byun, M., Park, K. I., Lee, H. E., Bu, S. D., Lee, K. T., Wang, Q., & Jeong, C. K. (2022). Ferroelectric polymer nanofibers reminiscent of morphotropic phase boundary behavior for improved piezoelectric energy harvesting. *Small (Weinheim an der Bergstrasse, Germany)*, *18*(15), 2104472. Available from <https://doi.org/10.1002/smll.202104472>.
- Park, J. H., Seo, J., Kim, C., Joe, D. J., Lee, H. E., Im, T. H., Seok, J. Y., Jeong, C. K., Ma, B. S., Park, H. K., Kim, T. S., & Lee, K. J. (2018). Flash-induced stretchable Cu conductor via multiscale-interfacial couplings. *Advanced Science*, *5*(11), 1801146. Available from <https://doi.org/10.1002/advs.201801146>.
- Pavlicek, W., Owen, J. M., & Peter, M. B. (2000). Active matrix liquid crystal displays for clinical imaging: Comparison with cathode ray tube displays. *Journal of Digital Imaging*, *13*(2), 155–161. Available from <https://doi.org/10.1007/bf03167650>.
- Peng, Y., Que, M., Lee, H. E., Bao, R., Wang, X., Lu, J., Yuan, Z., Li, X., Tao, J., Sun, J., Zhai, J., Lee, K. J., & Pan, C. (2019). Achieving high-resolution pressure mapping via flexible GaN/ ZnO nanowire LEDs array by piezo-phototronic effect. *Nano Energy*, *58*, 633–640. Available from <https://doi.org/10.1016/j.nanoen.2019.01.076>, <http://www.journals.elsevier.com/nano-energy/>.
- Petrov, V. F. (1995). Liquid crystals for AMLCD and TFT-PDLC applications. *Liquid Crystals*, *19*(6), 729–741. Available from <https://doi.org/10.1080/02678299508031092>.
- Pillarisetty, R. (2011). Academic and industry research progress in germanium nanodevices. *Nature*, *479* (7373), 324–328. Available from <https://doi.org/10.1038/nature10678>.
- Pribat, D., Plais, F., Legagneux, P., & Reita, C. (2011). *Thin films for large area electronics* (pp. 293–359). World Scientific Pub Co Pte Lt. Available from [10.1142/9789814261425_0010](https://doi.org/10.1142/9789814261425_0010).
- Qin, G., Yuan, H. C., Celler, G. K., Zhou, W., Ma, J., & Ma, Z. (2011). RF model of flexible microwave single-crystalline silicon nanomembrane PIN diodes on plastic substrate. *Microelectronics Journal*, *42*(3), 509–514. Available from <https://doi.org/10.1016/j.mejo.2010.10.012>.
- Qin, G., Yuan, H. C., Celler, G. K., Zhou, W., & Ma, Z. (2009). Flexible microwave PIN diodes and switches employing transferrable single-crystal Si nanomembranes on plastic substrates. *Journal of Physics D: Applied Physics*, *42*(23), 234006. Available from <https://doi.org/10.1088/0022-3727/42/23/234006>.
- Reddy, D., Register, L. F., Carpenter, G. D., & Banerjee, S. K. (2012). Graphene field-effect transistors. *Journal of Physics D: Applied Physics*, *45*(1), 019501. Available from <https://doi.org/10.1088/0022-3727/45/1/019501>.
- Reuss, R.H., Chalamala, B.R., Moussessian, A., Kane, M.G., Kumar, A., Zhang, D.C., Rogers, J.A., Hatalis, M., Temple, D., Moddel, G., Eliasson, B.J., Estes, M.J., Kunze, J., Handy, E.S., Harmon E. S., Salzman, D.B., Woodall, J.M., Alam, M.A., Murthy, J.Y., ... & Snow, E. (2005). Macroelectronics: Perspectives on technology and applications. *Proceedings of the IEEE Institute of Electrical and Electronics Engineers Inc., United States*, *93*(7) 1239–1256. 00189219. <http://ieeexplore.ieee.org/xpl/RecentIssue.jsp?punumber=5>. 10.1109/JPROC.2005.851237.
- Reuss, R. H., Raupp, G. B., & Gnade, B. E. (2015). Special issue on advanced flexible electronics for sensing applications [Scanning the Issue]. *Proceedings of the IEEE*, *103*(4), 491–496. Available from <https://doi.org/10.1109/JPROC.2015.2414486>, <http://ieeexplore.ieee.org/xpl/RecentIssue.jsp?punumber=5>.
- Riel, H., Wernersson, L. E., Hong, M., & del Alamo, J. A. (2014). III–V compound semiconductor transistors—From planar to nanowire structures. *MRS Bulletin*, *39*(8), 668–677. Available from <https://doi.org/10.1557/mrs.2014.137>.

- Rojas, J. P., Torres Sevilla, G. A., Alfaraj, N., Ghoneim, M. T., Kutbee, A. T., Sridharan, A., & Hussain, M. M. (2015). Nonplanar nanoscale fin field effect transistors on textile, paper, wood, stone, and vinyl via soft material-enabled double-transfer printing. *ACS Nano*, 9(5), 5255–5263. Available from <https://doi.org/10.1021/acsnano.5b00686>, <http://pubs.acs.org/journal/ancac3>.
- Sarpeshkar, R., Wattanapanitch, W., Arfin, S. K., Rapoport, B. I., Mandal, S., Baker, M. W., Fee, M. S., Musallam, S., & Andersen, R. A. (2008). Low-power circuits for brain-machine interfaces. *IEEE Transactions on Biomedical Circuits and Systems*, 2(3), 173–183. Available from <https://doi.org/10.1109/TBCAS.2008.2003198>, 19324545.
- Sawan, M., Hu, Y., & Coulombe, J. (2005). Wireless smart implants dedicated to multichannel monitoring and microstimulation. *IEEE Circuits and Systems Magazine*, 5(1), 21–39. Available from <https://doi.org/10.1109/MCAS.2005.1405898>.
- Seo, J., Kim, Y., Park, W. Y., Son, J. Y., Jeong, C. K., Kim, H., & Kim, W. H. (2019). Out-of-plane piezoresponse of monolayer MoS₂ on plastic substrates enabled by highly uniform and layer-controllable CVD. *Applied Surface Science*, 487, 1356–1361. Available from <https://doi.org/10.1016/j.apsusc.2019.05.140>, <http://www.journals.elsevier.com/applied-surface-science/>.
- Seo, J. H., Ling, T., Gong, S., Zhou, W., Ma, A. L., Guo, L. J., & Ma, Z. (2016). Fast flexible transistors with a nanotrench structure. *Scientific Reports*, 6. Available from <https://doi.org/10.1038/srep24771>, <http://www.nature.com/srep/index.html>.
- Seo, J. H., Zhang, K., Kim, M., Zhou, W., & Ma, Z. (2017). High-performance flexible BiCMOS electronics based on single-crystal Si nanomembrane. *NPJ Flexible Electronics*, 1(1). Available from <https://doi.org/10.1038/s41528-017-0001-1>, <http://nature.com/npjflexelectron/>.
- Shen, L., Wu, L., Sheng, Q., Ma, C., Zhang, Y., Lu, L., Ma, J., Ma, J., Bian, J., Yang, Y., Chen, A., Lu, X., Liu, M., Wang, H., & Jia, C.-L. (2017). Epitaxial lift-off of centimeter-scaled spinel ferrite oxide thin films for flexible electronics. *Advanced Materials*, 29(33), 1702411. Available from <https://doi.org/10.1002/adma.201702411>.
- Sheraf, C. D., Zhou, L., Huang, J. R., Gundlach, D. J., Jackson, T. N., Kane, M. G., Hill, I. G., Hammond, M. S., Campi, J., Greening, B. K., Francl, J., & West, J. (2002). Organic thin-film transistor-driven polymer-dispersed liquid crystal displays on flexible polymeric substrates. *Applied Physics Letters*, 80(6), 1088–1090. Available from <https://doi.org/10.1063/1.1448659>.
- Shim, G. W., Hong, W., Cha, J. H., Park, J. H., Lee, K. J., & Choi, S. Y. (2020). TFT channel materials for display applications: From amorphous silicon to transition metal dichalcogenides. *Advanced Materials*, 32(35), 1907166. Available from <https://doi.org/10.1002/adma.201907166>.
- Shin, J. H., Park, J. H., Seo, J., Im, T. H., Kim, J. C., Lee, H. E., Kim, D. H., Woo, K. Y., Jeong, H. Y., Cho, Y. H., Kim, T. S., Kang, I. S., Lee, K. J., & Flash-Induced, A. (2021). Robust Cu electrode on glass substrates and its application for thin-film μ LEDs. *Advanced Materials*, 33(13), 2007186. Available from <https://doi.org/10.1002/adma.202007186>.
- Shi, Z., Gao, X., Yuan, J., Zhang, S., Jiang, Y., Zhang, F., Jiang, Y., Zhu, H., & Wang, Y. (2017). Transferrable monolithic III-nitride photonic circuit for multifunctional optoelectronics. *Applied Physics Letters*, 111(24), 241104. Available from <https://doi.org/10.1063/1.5010892>.
- Shi, L., Zhu, T., Gao, G., Zhang, X., Wei, W., Liu, W., & Ding, S. (2018). Highly stretchable and transparent ionic conducting elastomers. *Nature Communications*, 9(1). Available from <https://doi.org/10.1038/s41467-018-05165-w>, <http://www.nature.com/ncomms/index.html>.
- Shou, W., Ludwig, B., Wang, L., Gong, X., Yu, X., Grigoropoulos, C. P., & Pan, H. (2019). Feasibility study of single-crystal Si island manufacturing by microscale printing of nanoparticles and laser crystallization. *ACS Applied Materials and Interfaces*, 11(37), 34416–34423. Available from <https://doi.org/10.1021/acsmi.9b09577>, <http://pubs.acs.org/journal/aamick>.
- Sirringhaus, H. (2014). 25th anniversary article: Organic field-effect transistors: The path beyond amorphous silicon. *Advanced Materials*, 26(9), 1319–1335. Available from <https://doi.org/10.1002/adma.201304346>.
- Song, D., Mahajan, A., Secor, E. B., Hersam, M. C., Francis, L. F., & Frisbie, C. D. (2017). High-resolution transfer printing of graphene lines for fully printed, flexible electronics. *ACS Nano*, 11(7), 7431–7439. Available from <https://doi.org/10.1021/acsnano.7b03795>, <http://pubs.acs.org/journal/ancac3>.

- Subash, T. D., Gnanasekaran, T., Nirmal, D., & Johnson, A. (2014). Modelling and investigation of III-V compound semiconductor based HEMT's for high performance applications. In *Proceedings of the IEEE international caracas conference on devices, circuits and systems, ICCDCS*. Institute of Electrical and Electronics Engineers Inc., India. 9781479913565. [10.1109/ICDCSyst.2014.6926123](https://doi.org/10.1109/ICDCSyst.2014.6926123).
- Subramanyam, G., Cole, M. W., Sun, N. X., Kalkur, T. S., Sbrockey, N. M., Tompa, G. S., Guo, X., Chen, C., Alpay, S. P., Rossetti, G. A., Dayal, K., Chen, L. Q., & Schlom, D. G. (2013). Challenges and opportunities for multi-functional oxide thin films for voltage tunable radio frequency/microwave components. *Journal of Applied Physics*, 114(19). Available from <https://doi.org/10.1063/1.4827019>.
- Sun, N., Jiang, C., Li, Q., Tan, D., Bi, S., & Song, J. (2020). Performance of OLED under mechanical strain: a review. *Journal of Materials Science: Materials in Electronics*, 31(23), 20688–20729. Available from <https://doi.org/10.1007/s10854-020-04652-5>, <https://rd.springer.com/journal/10854>.
- Sun, Y., Kim, H. S., Menard, E., Kim, S., Adesida, I., & Rogers, J. A. (2006). Printed arrays of aligned GaAs wires for flexible transistors, diodes, and circuits on plastic substrates. *Small*, 2(11), 1330–1334. Available from <https://doi.org/10.1002/sml.200500528>, 16136829.
- Sun, D. M., Liu, C., Ren, W. C., & Cheng, H. M. (2016). All-carbon thin-film transistors as a step towards flexible and transparent electronics. *Advanced Electronic Materials*, 2(11), 1600229. Available from <https://doi.org/10.1002/aelm.201600229>.
- Sun, Y., & Rogers, J. A. (2007). Inorganic semiconductors for flexible electronics. *Advanced Materials*, 19(15), 1897–1916. Available from <https://doi.org/10.1002/adma.200602223>.
- Torres Sevilla, G. A., & Hussain, M. M. (2017). Printed organic and inorganic electronics: Devices to systems. *IEEE Journal on Emerging and Selected Topics in Circuits and Systems*, 7(1), 147–160. Available from <https://doi.org/10.1109/JETCAS.2016.2619979>.
- Torsi, L., Tafuri, A., Cioffi, N., Gallazzi, M. C., Sassella, A., Sabbatini, L., & Zambonin, P. G. (2003). Regioregular polythiophene field-effect transistors employed as chemical sensors. *Sensors and Actuators, B: Chemical*, 93(1–3), 257–262, Italy. Available from [https://doi.org/10.1016/S0925-4005\(03\)00172-2](https://doi.org/10.1016/S0925-4005(03)00172-2).
- Tseng, S. H., & Tai, N. H. (2009). Fabrication of a transparent and flexible thin film transistor based on single-walled carbon nanotubes using the direct transfer method. *Applied Physics Letters*, 95(20), 204104. Available from <https://doi.org/10.1063/1.3264970>.
- Vidya, S., Khan, A.R., Kamat, S.V., & Venkatesh, V. (2018). 3D FinFET for next generation nano devices. In *Proceedings of the 2018 international conference on current trends towards converging technologies, ICCTCT 2018*. Institute of Electrical and Electronics Engineers Inc. India. 9781538637012. Available from <https://doi.org/10.1109/ICCTCT.2018.8550967>, <http://ieeexplore.ieee.org/xpl/mostRecentIssue.jsp?punumber=8536362>.
- Wager, J. F. (2020). TFT technology: Advancements and opportunities for improvement. *Information Display*, 36(2), 9–13. Available from <https://doi.org/10.1002/msid.1098>.
- Wang, W. H., Abbasi, S. A., Chai, Z., Jeong, H., & Busnaina, A. (2020). Solution processed all-carbon transistors via directed assembly and transfer printing of CNT channel and electrodes. *Applied Physics Letters*, 117(13)133101. Available from <https://doi.org/10.1063/5.0010945>.
- Wang, Z., Al-Jawhari, H. A., Nayak, P. K., Caraveo-Frescas, J. A., Wei, N., Hedhili, M. N., & Alshareef, H. N. (2015). Low temperature processed complementary metal oxide semiconductor (CMOS) device by oxidation effect from capping layer. *Scientific Reports*, 5(1). Available from <https://doi.org/10.1038/srep09617>.
- Wang, H. S., Im, T. H., Kim, Y. B., Sung, S. H., Min, S., Park, S. H., Lee, H. E., Jeong, C. K., Park, J. H., & Lee, K. J. (2021). Flash-welded ultraflat silver nanowire network for flexible organic light-emitting diode and triboelectric tactile sensor. *APL Materials*, 9(6). Available from <https://doi.org/10.1063/5.0051431>, <http://scitation.aip.org/content/aip/journal/aplmater>.
- Wang, W., Li, Z., Li, M., Fang, L., Chen, F., Han, S., Lan, L., Chen, J., Chen, Q., Wang, H., Liu, C., Yang, Y., Yue, W., & Xie, Z. (2022). High-transconductance, highly elastic, durable and recyclable all-polymer electrochemical transistors with 3D micro-engineered interfaces. *Nano-Micro Letters*, 14(1). Available from <https://doi.org/10.1007/s40820-022-00930-5>, <http://www.springer.com/engineering/journal/40820>.

- Wang, X., Li, Z., Xu, W., Kulkarni, S. A., Batabyal, S. K., Zhang, S., Cao, A., & Wong, L. H. (2015). TiO₂ nanotube arrays based flexible perovskite solar cells with transparent carbon nanotube electrode. *Nano Energy*, 11, 728–735. Available from <https://doi.org/10.1016/j.nanoen.2014.11.042>, <http://www.journals.elsevier.com/nano-energy/>.
- Wang, C., Xia, K., Wang, H., Liang, X., Yin, Z., & Zhang, Y. (2019). Advanced carbon for flexible and wearable electronics. *Advanced Materials*, 31(9), 1801072. Available from <https://doi.org/10.1002/adma.201801072>.
- Wen, Y., & Xu, J. (2017). Scientific importance of water-processable PEDOT–PSS and preparation, challenge and new application in sensors of its film electrode: A review. *Journal of Polymer Science, Part A: Polymer Chemistry*, 55(7), 1121–1150. Available from <https://doi.org/10.1002/pola.28482>, [http://onlinelibrary.wiley.com/journal/10.1002/\(ISSN\)1099-0518](http://onlinelibrary.wiley.com/journal/10.1002/(ISSN)1099-0518).
- Werner, K. (1975). Display materials and processes. *Inf Disp*, 31. Available from <https://doi.org/10.1002/j.2637-496X.2015.tb00841.x>.
- Wu, C.-C., Chen, C.-W., Lin, C.-L., & Yang, C.-J. (2005). Advanced organic light-emitting devices for enhancing display performances. *Journal of Display Technology*, 1(2), 248–266. Available from <https://doi.org/10.1109/JDT.2005.858942>.
- Wu, Y., Liu, P., Ong, B. S., Srikumar, T., Zhao, N., Botton, G., & Zhu, S. (2005). Controlled orientation of liquid-crystalline polythiophene semiconductors for high-performance organic thin-film transistors. *Applied Physics Letters*, 86(14), 142102. Available from <https://doi.org/10.1063/1.1894597>.
- Wu, W. (2017). Inorganic nanomaterials for printed electronics: A review. *Nanoscale*, 9(22), 7342–7372. Available from <https://doi.org/10.1039/c7nr01604b>, <http://pubs.rsc.org/en/journals/journal/nr>.
- Wu, I. - (1994). High-definition displays and technology trends in TFT-LCDs. *Journal of the Society for Information Display*, 2(1), 1–14. Available from <https://doi.org/10.1889/1.1984902>.
- Xiang, W., & Tress, W. (2019). Review on recent progress of all-inorganic metal halide perovskites and solar cells. *Advanced Materials*, 31(44), 1902851. Available from <https://doi.org/10.1002/adma.201902851>.
- Xie, P., Liu, T., Sun, J., Jiang, J., Yuan, Y., Gao, Y., Zhou, J., & Yang, J. (2020). Solution-processed ultra-flexible C8-BTBT organic thin-film transistors with the corrected mobility over 18 cm²/(V s). *Science Bulletin*, 65(10), 791–795. Available from <https://doi.org/10.1016/j.scib.2020.03.013>, <http://link.springer.com/journal/11434>.
- Yao, Y., Zhang, L., Orgiu, E., & Samorì, P. (2019). Unconventional nanofabrication for supramolecular electronics. *Advanced Materials*, 31(23), 1900599. Available from <https://doi.org/10.1002/adma.201900599>.
- Yeon, H., Lee, H., Kim, Y., Lee, D., Lee, Y., Lee, J. S., Shin, J., Choi, C., Kang, J. H., Suh, J. M., Kim, H., Kum, H. S., Lee, J., Kim, D., Ko, K., Ma, B. S., Lin, P., Han, S., Kim, S., . . . Kim, J. (2021). Long-term reliable physical health monitoring by sweat pore-inspired perforated electronic skins. *Science Advances*, 7(27). Available from <https://doi.org/10.1126/sciadv.abg8459>, <https://advances.sciencemag.org/content/7/27/eabg8459>.
- Yoneda, K., Yokoyama, R., & Yamada, T. (2001). Development trends of LTPS TFT LCDs for mobile applications. In *IEEE symposium on VLSI circuits*, Digest of Technical Papers, Japan, pp. 85–90.
- Yoon, J., Baca, A. J., Park, S. I., Elvikis, P., Geddes, J. B., Li, L., Kim, R. H., Xiao, J., Wang, S., Kim, T. H., Motala, M. J., Ahn, B. Y., Duoss, E. B., Lewis, J. A., Nuzzo, R. G., Ferreira, P. M., Huang, Y., Rockett, A., & Rogers, J. A. (2008). Ultrathin silicon solar microcells for semitransparent, mechanically flexible and microconcentrator module designs. *Nature Materials*, 7(11), 907–915. Available from <https://doi.org/10.1038/nmat2287>, <http://www.nature.com/nmat/>.
- Yoon, J., Bae, G. Y., Yoo, S., Yoo, J., You, N. H., Hong, W.-K., & Ko, H. C. (2020). Deep-ultraviolet sensing characteristics of transparent and flexible IGZO thin film transistors. *Journal of Alloys and Compounds*, 817, 152788. Available from <https://doi.org/10.1016/j.jallcom.2019.152788>.
- Yoo, J. I., Jang, H. S., Jang, J., Yoon, J., Kwon, O. Y., Park, J. J., Kang, S. M., Yoo, T. J., Kim, S. H., Lee, B. H., Choa, S. H., & Ko, H. C. (2018). Reliable peripheral anchor-assisted transfer printing of ultrathin SiO₂ for a transparent and flexible IGZO-based inverter. *Microelectronic Engineering*, 197, 15–22. Available from <https://doi.org/10.1016/j.mee.2018.05.003>, <http://www.journals.elsevier.com/microelectronic-engineering/>.
- Yuan, X., Pan, D., Zhou, Y., Zhang, X., Peng, K., Zhao, B., Deng, M., He, J., Tan, H. H., & Jagadish, C. (2021). Selective area epitaxy of III–V nanostructure arrays and networks: Growth, applications, and future directions. *Applied Physics Reviews*, 8(2), 021302. Available from <https://doi.org/10.1063/5.0044706>.

- Yuan, H. C., Qin, G., Celler, G. K., & Ma, Z. (2009). Bendable high-frequency microwave switches formed with single-crystal silicon nanomembranes on plastic substrates. *Applied Physics Letters*, *95*(4), 043109. Available from <https://doi.org/10.1063/1.3176407>.
- Yu, W., Gong, K., Li, Y., Ding, B., Li, L., Xu, Y., Wang, R., Li, L., Zhang, G., & Lin, S. (2022). Flexible 2D materials beyond graphene: Synthesis, properties, and applications. *Small (Weinheim an der Bergstrasse, Germany)*, *18*(14), 2105383. Available from <https://doi.org/10.1002/sml.202105383>.
- Yu, K. J., Yan, Z., Han, M., & Rogers, J. A. (2017). Inorganic semiconducting materials for flexible and stretchable electronics. *NPJ Flexible Electronics*, *1*(1). Available from <https://doi.org/10.1038/s41528-017-0003-z>, <http://nature.com/npjflexelectron/>.
- Zeng, W., Shu, L., Li, Q., Chen, S., Wang, F., & Tao, X. M. (2014). Fiber-based wearable electronics: A review of materials, fabrication, devices, and applications. *Advanced Materials*, *26*(31), 5310–5336. Available from <https://doi.org/10.1002/adma.201400633>, <http://www3.interscience.wiley.com/journal/119030556/issue>.
- Zhai, Y., Mathew, L., Rao, R., Xu, D., & Banerjee, S. K. (2012). High-performance flexible thin-film transistors exfoliated from bulk wafer. *Nano Letters*, *12*(11), 5609–5615. Available from <https://doi.org/10.1021/nl302735f>, <http://pubs.acs.org/journal/nalefd>.
- Zhang, Y. Y., An, S., Zheng, Y., Lai, J., Seo, J. H., Lee, K. H., & Kim, M. (2022). Releasable AlGaIn/GaN 2D electron gas heterostructure membranes for flexible wide-bandgap electronics. *Advanced Electronic Materials*, *8*(2), 2100652. Available from <https://doi.org/10.1002/aelm.202100652>.
- Zhang, D., Huang, T., & Duan, L. (2020). Emerging self-emissive technologies for flexible displays. *Advanced Materials*, *32*(15), 1902391. Available from <https://doi.org/10.1002/adma.201902391>.
- Zhang, S., Ling, H., Chen, Y., Cui, Q., Ni, J., Wang, X., Hartel, M. C., Meng, X., Lee, K., Lee, J., Sun, W., Lin, H., Emaminejad, S., Ahadian, S., Ashammakhi, N., Dokmeci, M. R., & Khademhosseini, A. (2019). Hydrogel-enabled transfer-printing of conducting polymer films for soft organic bioelectronics. *Advanced Functional Materials*, *30*(6), 1906016. Available from <https://doi.org/10.1002/adfm.201906016>.
- Zhang, H., Li, J., Liu, D., Min, S., Chang, T. H., Xiong, K., Park, S. H., Kim, J., Jung, Y. H., Park, J., Lee, J., Han, J., Katehi, L., Cai, Z., Gong, S., & Ma, Z. (2020). Heterogeneously integrated flexible microwave amplifiers on a cellulose nanofibril substrate. *Nature Communications*, *11*(1). Available from <https://doi.org/10.1038/s41467-020-16957-4>, <http://www.nature.com/ncomms/index.html>.
- Zhang, L., Ou, F., Chong, W. C., Chen, Y., & Li, Q. (2018). Wafer-scale monolithic hybrid integration of Si-based IC and III–V epi-layers—A mass manufacturable approach for active matrix micro-LED micro-displays. *Journal of the Society for Information Display*, *26*(3), 137–145. Available from <https://doi.org/10.1002/jsid.649>, [http://onlinelibrary.wiley.com/journal/10.1002/\(ISSN\)1938-3657](http://onlinelibrary.wiley.com/journal/10.1002/(ISSN)1938-3657).
- Zhang, H., & Rogers, J. A. (2019). Recent advances in flexible inorganic light emitting diodes: From materials design to integrated optoelectronic platforms. *Advanced Optical Materials*, *7*(2), 1800936. Available from <https://doi.org/10.1002/adom.201800936>.
- Zhang, J., Wang, C., Fu, Y., Che, Y., & Zhou, C. (2011). Air-stable conversion of separated carbon nanotube thin-film transistors from p-type to n-type using atomic layer deposition of high- κ oxide and its application in CMOS logic circuits. *ACS Nano*, *5*(4), 3284–3292. Available from <https://doi.org/10.1021/nn2004298>.
- Zhang, J., Wu, Y., Li, Z., Zhang, Y., Peng, Y., Chen, D., Zhu, W., Xu, S., Zhang, C., & Hao, Y. (2019). High-performance acetone soluble tape transfer printing method for heterogeneous integration. *Scientific Reports*, *9*(1). Available from <https://doi.org/10.1038/s41598-019-52235-0>.
- Zhang, S.-L., & Zhang, Z. (2014). *Metal silicides in advanced complementary metal-oxide-semiconductor (CMOS) technology* (pp. 244–301). Elsevier BV. Available from [10.1533/9780857096296.1.244](https://doi.org/10.1533/9780857096296.1.244).
- Zhu, Y., He, Y., Jiang, S., Zhu, L., Chen, C., & Wan, Q. (2021). Indium–gallium–zinc–oxide thin-film transistors: Materials, devices, and applications. *Journal of Semiconductors*, *42*(3), 031101. Available from <https://doi.org/10.1088/1674-4926/42/3/031101>.
- Zhu, H., Shin, E. S., Liu, A., Ji, D., Xu, Y., & Noh, Y. Y. (2020). Printable semiconductors for back-plane TFTs of flexible OLED displays. *Advanced Functional Materials*, *30*(20), 1904588. Available from <https://doi.org/10.1002/adfm.201904588>.

- Zumeit, A., Dahiya, A. S., Christou, A., Shakthivel, D., & Dahiya, R. (2021). Direct roll transfer printed silicon nanoribbon arrays based high-performance flexible electronics. *NPJ Flexible Electronics*, 5(1). Available from <https://doi.org/10.1038/s41528-021-00116-w>, <http://nature.com/npjflexelectron/>.
- Zumeit, A., Navaraj, W. T., Shakthivel, D., & Dahiya, R. (2020). Nanoribbon-based flexible high-performance transistors fabricated at room temperature. *Advanced Electronic Materials*, 6(4), 1901023. Available from <https://doi.org/10.1002/aelm.201901023>.

This page intentionally left blank

CHAPTER 12

Transfer-printed devices for biomedical applications

Changbo Liu^{1,2} and Xing Sheng³

¹School of Materials Science and Engineering, Beihang University, Beijing, P.R. China

²Hangzhou Innovation Institute, Beihang University, Hangzhou, P.R. China

³Department of Electronic Engineering, Tsinghua University, Beijing, P.R. China

12.1 Introduction

As an emerging manufacturing technique, the “transfer printing” method provides opportunities for the integration of brittle inorganic electronic materials and organic flexible/stretchable substrates. Transfer printing processes provide versatile routes to high-performance, heterogeneously integrated functional systems, including those in flexible electronics, three-dimensional (3D) and/or curvilinear optoelectronics, and biointegrated sensing and therapeutic devices (Carlson et al., 2012). This method can integrate brittle inorganic electronic materials and devices onto nearly any type of substrate including but not limited to rubber, plastic, and fabric (Khang et al., 2006). The most appealing feature of this approach is that the majority of the manufacturing process involves conventional fabrication technology, which already has a mature, established commercial infrastructure, thereby accelerating time toward commercialization and practical applications (Rogers et al., 2016).

Recent advances in material sciences and microfabrication technologies have enabled the creation of flexible and stretchable inorganic electronics, which are fabricated based on microfabrication including film deposition, lithography, and most importantly transfer printing technology (Chen et al., 2020). The performance of flexible electronic devices is almost the same as that of their conventional counterparts, which is attributed to the fact that transfer printing is relatively benign, and it conserves the performance metrics of the source materials. This not only preserves the high-performance characteristics but also makes the devices flexible or stretchable depending on the material of the target substrate. Compared with traditional Si-based electronics, flexible inorganic electronics offer several advantages: they are soft, deformable, foldable, lightweight, portable, and can be manufactured using less expensive methods (Mostafalu et al., 2016). These unique characteristics make them excellent for applications that require smaller footprints or possess surfaces with curvilinear and irregular morphology. Flexible electronics can be bent, twisted, and wrapped

around irregularly shaped objects without losing their functionalities, which provides an array of opportunities for application in the biomedical field, such as controlling disease conditions, improving surgical procedures, continuous health monitoring, and so on. The electronic devices, which are transferred onto the flexible substrate, can conformal to the curved biotissue surface and dynamically adapt to the tissue's deformation, the signal-to-noise ratio (SNR) and spatial resolution have been much improved compared with the conventional counterparts. One of the promising applications of flexible electronics that could not be addressed with conventional technology includes advanced wireless biomedical devices, especially implantable and wearable medical electronics. We can collect, and analysis of biological signals related to the physiological health status by wrapping (or implanting into) the brain with them or putting them on the skin to achieve an intimate interface with the body.

In the past decade, flexible inorganic electronics have received and continuously attracted attention from academia and industry due to their wide potential applications in the biomedical area. Many emerging bioelectronics systems have become increasingly popular due to exciting characteristics, such as wearable electronics, flexible implantable electronics, electronic tattoos, and electronic skin. With the rapid development of flexible electronics, the transfer printing technique has also been greatly improved, including the range of materials for patterning the and scope of applications enabled. At present, transfer printing has developed into a sophisticated approach to materials assembly and device fabrication creates opportunities for a wide range of device platforms over conventional manufacturing or growth techniques. Transfer printing has broad substrate applicability and materials versatility. Essentially any class of material or device can be integrated onto the foreign substrate using transfer printing-based fabrication schemes: from two-dimensional (2D) materials (carbon nanotubes, graphene, Maxene, etc.) high-performance hard materials (metals, oxide thin films, single-crystalline/noncrystalline inorganic semiconductors, etc.), to biomaterials (DNA, protein, viruses, cell, etc.), to fully integrated device structures [thin film transistors (TFTs), light emitting diodes (LEDs), photodetector (PD), complementary metal oxide semiconductor (CMOS) circuits, sensing arrays, solar cells, energy-harvesting devices, etc.]. Additionally, transfer printing enables the cointegration of dissimilar materials: single-crystalline materials with various lattice constants and noncrystalline materials; those with high and low thermal stability; those with high and low moduli, and so on (Yoon et al., 2015).

In this chapter, we introduce the recent advance in heterogeneously integrated materials and integrated inorganic devices for biomedical applications. The first part of the chapter describes materials including metals, oxides, silicon, wide bandgap semiconductors, 2D materials, and biomaterials. The second part of the chapter describes functional devices including LEDs, PD, energy-harvesting devices, and bioresorbable materials and devices. This chapter introduces different fabrication methods for flexible bioelectronics and discusses their working mechanism.

12.2 Materials

12.2.1 Metals

Metal materials have been in use as biomaterials for a long time due to their excellent yield strength and biocompatibility. In recent years, with the development of transfer printing technology, metal materials are also widely integrated with flexible substrates to form flexible bioelectronic devices, which have unique performance over traditional brittle metal devices. Metal materials are considered superior candidates for preparing electrodes, electrical interconnection wires, antennas, and stress-sensor due to excellent conductivity, electrical stability, and mature preparation technology. Metal films can be transferred onto flexible substrates to get bendable, stretchable, twistable electrodes or antenna structures for electrical stimulation, electrophysiological signal collection, or wireless transmission.

Flexible electrodes provide a perfect contact interface for electrophysiological monitoring. The Au film is chosen as the electrode material in most flexible electronics for its biocompatibility, chemical inertness, as well as ductility. As shown in Fig. 12.1A, *left* photo, a stretchable neural electrocorticography (ECoG) electrode array, which consists of nine channels with a three-layered serpentine-like interconnect structure, is fabricated by transferring Au conductive layer onto the polydimethylsiloxane (PDMS) substrate (Yan et al., 2017). The transferred Au conductive layer includes three parts: the output part, the serpentine interconnector, and signal collection. Nine small circles, serving as signal collect parts, are connected to the output part (nine parallel square pads to connect to the ECoG recorder) via the serpentine interconnectors. To improve the mechanical stability of the ECoG electrode array during deformation, the Au conductive layer is located at the neutral mechanical plane of the two PI films. The ability of the stretchable electrode array to conform to different curved surfaces is confirmed by the experiment. The right figure shows an optical image of a stretchable neural electrode array placed on the visual cortical surface of the left hemisphere of a rat. The surgeries in a rat have demonstrated that the stretchable electrode array maintained perfect contact against the curved surface of the brain in the rat, and high-quality ECoG signals from anesthetized rats are collected. The application of the stretchable electrode array on the detection of steady-state visual evoked potentials (SSVEPs) response has also been demonstrated by in vivo experiments, the results indicated that SSVEP responses recorded by the stretchable neural electrode array are more obvious than those detected by traditional stainless-steel screw electrodes (Yan et al., 2017). In addition, Au film can also be integrated with the ultra-thin flexible substrate to get epidermal electronic systems (EESs), which are ultra-thin and ultra-soft electronics, sensors, and actuators, whose physical properties (modulus, thickness, and areal mass density) match well with those of human epidermis (Kim et al., 2011; Wang et al., 2018; Yeo et al., 2013). Fig. 12.1B shows a representative EES based on

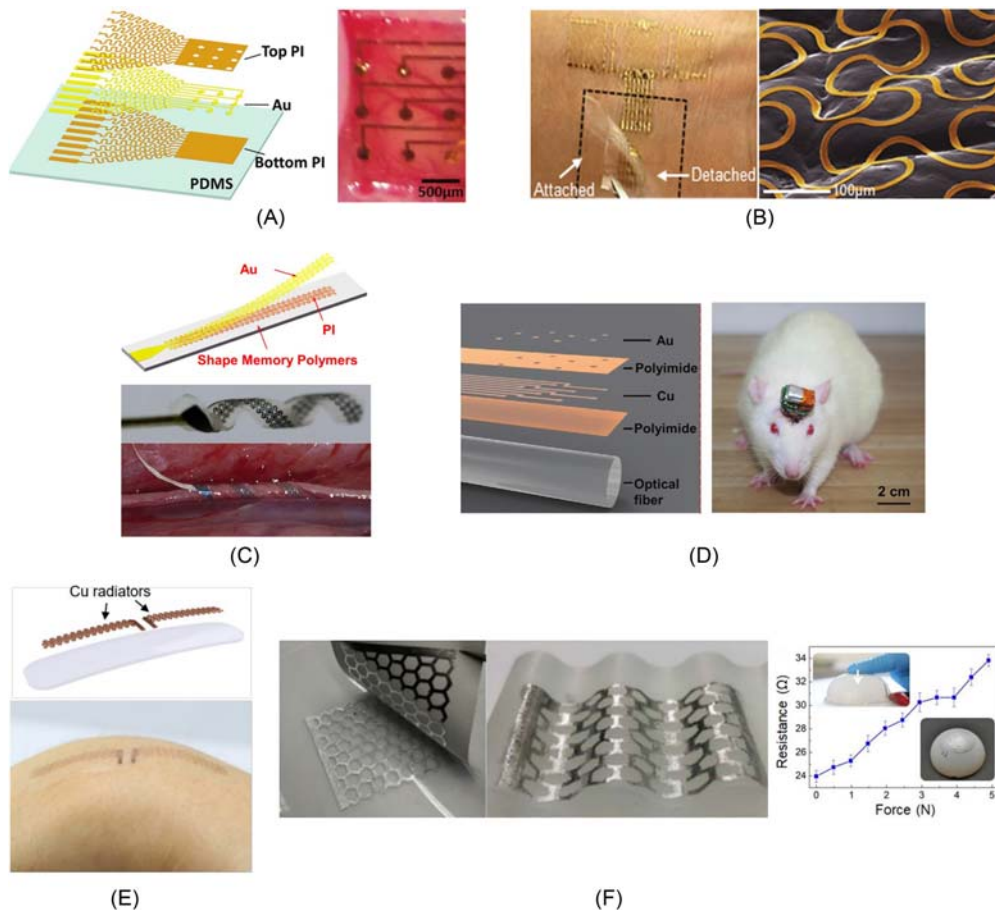


Figure 12.1 Metal materials: (A) Transfer Au film onto elastomer substrate for in vivo ECoG measurement (*Left*: exploded view schematic diagram of the electrode array layout; *Right*: Optical image of a neural electrode array placed on the visual cortical surface of the left hemisphere of a rat). (B) The electronic tattoo sensors based on transferred Au film (*Left*: image of an epidermal electronic systems (EES) on skin; *Right*: colorized SEM image of an EESs mounted on the skin replica). (C) A 3D twining electrode by integrating stretchable mesh serpentine Au wires onto a flexible shape memory substrate (*Upper* and *middle*: the exploded view and optical image of the twining electrode; *Bottom*: the image of an implanted twining electrode). (D) Transfer Cu/Au microelectrode array onto the optical fibers for implantable neurological stimulation and monitoring (*Left*: the exploded view of the device; *Right*: a rat implanted with the device). (E) The wearable compliant antennas based on transferred Cu films (*Upper*: illustration showing multilayered structures for the antenna; *Bottom*: direct integration of an antenna on the wrist). (F) The transfer printing method of liquid metal for 3D wiring in flexible electronics (*Left* and *middle*: liquid-metal on planar and wavy soft substrates; *Right*: the liquid-metal stress-sensor and Resistance-Force curve). (A) *Reproduced with permission; Copyright © 2017 The Authors. Published by WILEY-VCH Verlag GmbH & Co. KGaA, Weinheim;* (B) *Reproduced with permission; Copyright © 2013 WILEY-VCH Verlag GmbH & Co. KGaA, Weinheim;* (C) *Reproduced with permission; Copyright © 2019 The Authors, some rights reserved; exclusive licensee American Association for the Advancement of Science;* (D) *Reproduced with permission; Copyright © 2020 Wiley-VCH GmbH;* (E) *Reproduced with permission; Copyright © 2020, American Chemical Society;* (F) *Reproduced with permission; Copyright © 2020, American Chemical Society.*

transferred Au film for monitoring electrophysiological signals (Yeo et al., 2013). The EES consists of an interconnected collection of thin, filamentary serpentine conductive traces and electrophysiological sensors, all in an open mesh layout with exposed metal (Au) that contacts the skin directly. The total thickness of the EES is only approximately 0.8 μm , in its thickest region. The top and bottom layers of PI (each 0.3 μm thick) placed the Au-based active sensing components in the neutral mechanical plane. Such designs provide the EES with extremely low effective elastic moduli and large deformability. These characters allow the EES to follow the contoured surfaces and time-dynamic motions of the skin in a natural way, which can minimize interfacial slippage and as a result, motion artifacts. Putting the EES on the skin can get conformal contact and adequate adhesion based on van der Waals interactions alone, in a manner that is without mechanical constraints for the user. As shown in Fig. 12.1B, right, the EES layout follows the topography of the skin including the deepest creases and pits. This conformal coverage on the skin not only seriously improves the mechanical robustness of integration, but also enlarges the contact area between the EES and the skin, which can minimize contact impedances and enables precision measurements for the case of electrophysiological.

Au film can also be integrated with new smart materials by transfer printing method and get exciting performance. Zhang et al. develop a 3D twining electrode for peripheral nerve stimulation and recording, which are fabricated by integrating stretchable mesh serpentine wires (Au) onto a flexible shape memory substrate (Zhang, Zheng, et al., 2019). The key substrate materials are shape memory polymers (SMPs), which have the dual-shape capability and can change their shape in a predefined way from shape A to shape B when exposed to an appropriate stimulus (Behl & Lendlein, 2007). Based on this feature, a 3D electronic system can be fabricated by traditional 2D planar processing and transfer printing technology. The layout of the 3D twining electrode is shown in Fig. 12.1C. The thermo-responsive SMP with a transition temperature of approximately 37°C is chosen to be the substrate. Au film with mesh serpentine structure is transferred onto the SMP substrate. After the transfer printing process, heating up and deforming the initial 2D planar assembly leads to the reconfiguration of the permanent shape to the desired 3D helical shape to match the 3D peripheral nerves. Before surgical implantation, the twining electrodes are temporarily flattened to a 2D planar state. Driven by 37°C, the temporarily flattened electrode can automatically climb onto the nerve to restore its permanent spiral structure and form 3D flexible neural interfaces. Conformal contact can lead to lower interfacial impedance, and stimulation efficiency and the recorded SNR will be improved. Additionally, no additional surgical fixation is required in the whole installation process, which can greatly reduce the nerve injury associated with the mechanical and geometrical mismatches and the surgical implantation. This twining electrode has great potential in both clinical practice and basic neuroscience research.

Transfer printing technology can integrate functional materials and devices onto nearly any type of substrate with different material properties and different surfaces. Compared with traditional electronics manufacturing techniques, the Transfer printing method makes it easy for electronics to be integrated onto complex 3D surfaces, which will greatly expand the functions and applications of electronic devices. As shown in Fig. 12.1D (Yu et al., 2021). A multichannel flexible optoelectronic fiber, which consists of flexible fibers and Cu/Au microelectrode array, is reported for implantable neurological stimulation and monitoring. The Cu/Au microelectrode array located at the neutral mechanical plane of the two PI films is transferred and printed onto the curved surface of the optical fibers by elastomer stamps and gets conformal contact with the optical fiber. The flexible optoelectronic fiber device offers multiple stimulations and sensing channels, allowing optical stimulation in selective wavelengths guided by the optical fibers while conducting distributed, high-throughput biopotential sensing using the flexible microelectrode arrays. Animal experiments have confirmed the capability of the optoelectronic fiber to conduct closed-loop neuromodulation. Using the same transfer printing method, various flexible electronic devices with complex functions can be integrated with optical fibers, and optoelectronic fibers with more advanced and sophisticated functions can be fabricated in the future.

In the biomedical field, metal materials are not only used as electrodes but also ideal materials for fabricating antennas due to their excellent conductivity. Antennas play an important role in wireless communication and remote sensing. There are huge demands for various types of antennas for bioelectronics, the internet of things, and smart healthcare. Flexible antennas have been considered a feasible solution for emerging on- and intra-body wearable bioelectronics to establish remote data transfer. Fig. 12.1E shows a stretchable dipole antenna fabricated by transfer printing technology (Kim et al., 2020). The key functional component is Cu film with 2D serpentine patterns, which is transferred onto elastomer substrates. The stretchable dipole antenna shows highly compliant mechanical characteristics and has a conformal coverage on challenging locations, such as wrists, elbows, and knees. Benefiting from excellent mechanical stretchability and low effective moduli, the dipole antenna on the wrist (bottom photo) shows no delamination with repetitive flexion. The electromagnetic properties of the stretchable antennas are characterized by both simulation and experiment to verify the stable functionalities of the antenna even in the stretched state. These stretchable antennas can be integrated with various wearable devices for long-range wireless data communication.

Liquid metal is a liquid-state metallic material with a low melting point at or around room temperature. Liquid metal is investigated as a highly desirable candidate in biosensors due to its high electrical conductivity, low toxicity, and superior fluidity. The liquid metal can achieve stable electrical signal transmission under deformation of approximately

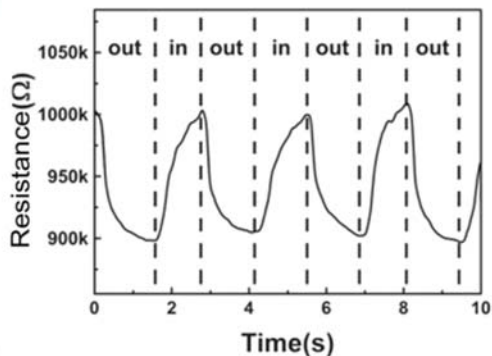
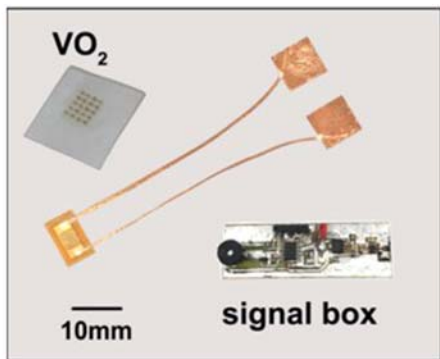
700% (Zhang, Wang, et al., 2020). Additionally, their self-healing quality enables liquid metal with stronger durability and robustness which are essential for biosensors. As illustrated in Fig. 12.1F, A liquid–metal honeycomb circuit is fabricated on soft paper, and then transferred onto Ecoflex substrates with planar (left) and wavy surface (middle) (Zhao et al., 2020). The liquid–metal circuit on Ecoflex substrates possesses high stability and good conductivity. A piezoresistive stress sensor is fabricated by transferring a liquid metal circuit onto a flexible model with an uneven surface (spherical) to form a conformal 3D circuit (right), which benefits from the cross-section of liquid metal lines can be reduced when pressed leading to a rise in resistance. The resistance–force curve shows a good relationship between resistance and stress.

12.2.2 Oxides

The broad spectrum of physical and chemical properties in oxide materials has attracted intensive research interest in recent years. Various solid-state oxide materials have been investigated for flexible bioelectronics, such as VO_2 , TiO_2 , MgO , ZnO , SiO_2 , and so on. Most high-performance oxide materials are prepared at high temperatures, which is incompatible with the flexible substrate. Fortunately, transfer printing technology can solve this problem, and then emerging various flexible electronics based on oxides (Fig. 12.2).

Vanadium dioxide (VO_2)-based flexible breath sensor is reported, which can conformal coverage on the skin under different curvatures and temperatures through day and night (shown in Fig. 12.2A) (Liao et al., 2017). VO_2 film is fabricated on SiO_2/Si substrate, and then transferred onto PI substrate and encapsulated with PDMS. This structure enables the sensor with robust electrical characteristics for body movements. The PDMS layer facilitated nonirritation skin bonding, and the PI layer enable isolation of the VO_2 material from applied tensile strain introduced from body movements. The breath sensor shows high sensitivity and ultrafast response time benefits from the high-temperature coefficient of resistance of VO_2 film. The results of real-time breath monitoring demonstrated that the VO_2 -based flexible breath sensor is feasible for the flexible sensitive device in the apnea detection field.

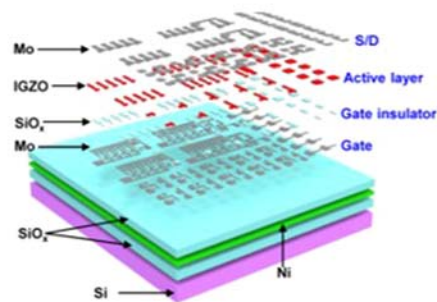
Titanium dioxide (TiO_2) has remarkable properties involving chemical stability, negligible protein denaturation, and biocompatibility, and is an excellent candidate for biosensing. Lee et al. report a technology that can transfer electrospinning TiO_2 nanofibers to any target surface using a thin PDMS adhesive layer. Fig. 12.2B shows the TiO_2 -based sensor for protein detection from whole blood (Lee et al., 2015). The sensor is fabricated by integrating TiO_2 nanofibers with a PC disk and affords a significant improvement in sensitivity with a broad dynamic range. The detection limits are approximately 300-fold lower than the conventional detection technique. With this transfer-printing technology, we can fully utilize the excellent properties of TiO_2 in flexible bioelectronics.



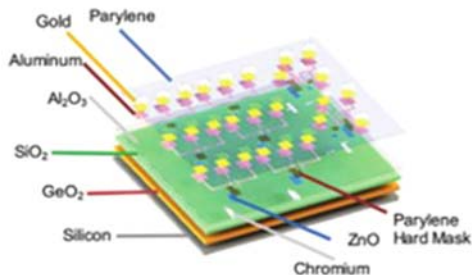
(A)



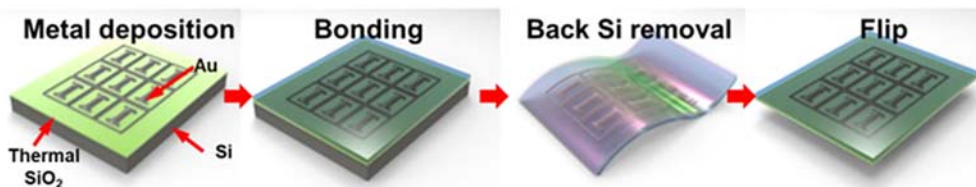
(B)



(C)



(D)



(E)

Figure 12.2 Oxides. (A) The flexible breath sensor based on vanadium dioxide (*Left*: the photograph of the VO₂ film-based breath sensor; *Right*: the resistance change of breath sensor during exhaling and inhaling). (B) Transferred TiO₂-nanofibers for protein detection from whole blood. (Continued)

Memristors have been considered promising candidates for next-generation memory and neuromorphic computing due to their remarkable advantages, such as simple structure, fast switching speed, and high energy efficiency. Cao et al. report Mg/MgO-based memristors with remarkable threshold switching behaviors and fully dissolvable characteristics and named physically transient memristors (Cao et al., 2022). Memristors are fabricated on a silicon substrate and then transferred onto the biocompatible and biodegradable PVA substrate to acquire the fully transient system. Memristor devices demonstrated the critical synaptic functions including paired-pulse facilitation, paired-pulse depression, and the transition from short-term to long-term plasticity. These functions can be attributed to the drift and diffusion of Mg^{2+} ions in the MgO resistive switching layer. Memristor could be degraded and dissolved in deionized water at room temperature, showing transient behaviors. We can conclude that physically transient memristors can be potentially applied in biodegradable or biointegrated neuromorphic computing systems, secure electronic devices, and green electronics.

A thin-film transistor (TFT) as a special type of field-effect transistor (FET) is thin relative to the conventional bulk metal oxide field effect transistor, which makes TFT to be an ideal candidate for fabricating flexible electronics. The fabrication of TFTs on flexible substrates is a key technique to realizing flexible electronics. It has attracted intensive research interest in recent years to fabricate TFT by using a-IGZO (amorphous indium-gallium-zinc oxide) as the key semiconductor. Compared to traditional amorphous silicon (a-Si), a-IGZO offers several attractive properties including optical transparency, high mobility, low-temperature deposition, and operational stability. Fig. 12.2C shows a schematic illustration of a-IGZO TFT and circuits formed on a Si wafer with a sacrificial Ni film (Jin et al., 2015). The a-IGZO TFT can be picked up by immersion in water and then transferred onto a flexible substrate for obtaining the flexible TFT. The electrical performances of flexible TFT, including field effect mobilities, on/off ratios, sub-threshold slopes, and Ohmic contact properties, are all comparable to otherwise similar devices constructed in conventional ways. These characters show application possibilities in bioelectronics. Additionally, compared with synthetic polymers, biopolymers have ideal biocompatibility and similar mechanical properties to biotissue and are attractive bioelectronics substrate candidates. Collagen is one of the most extensively studied biopolymers. Collagen is an important component of the extracellular matrix and is found

(C) Thin film transistors and circuits based on amorphous indium – gallium – zinc oxide. (D) Fabricate the Zinc Oxide transistors on mammalian collagen. (E) Transferred silicon dioxide layers as biofluid barriers for biointegrated flexible electronic systems. (A) Reproduced with permission; Copyright © 2007 IOP Publishing, Ltd; (B) Reproduced with permission; Copyright © 2015 The Royal Society of Chemistry Reproduced with permission; (C) Reproduced with permission; Copyright © 2015, American Chemical Society; (D) Reproduced with permission; Copyright © 2020 WILEY-VCH Verlag GmbH & Co. KGaA, Weinheim; (E) Copyright © 2016 National Academy of Sciences.

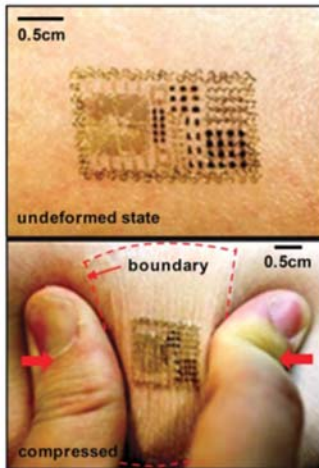
in all tissues, particularly in connective tissues such as skin, tendons, corneas, and bone. However, denaturation temperature and swelling in water/vacuum have been fundamental barriers to the electronic fabrication of collagen. These problems can be avoided by transfer printing technology. As shown in Fig. 12.2D, flexible ZnO-based TFTs are fabricated on a carrier wafer (Si) using a sacrificial layer of germanium oxide and then transferred onto collagen (Moreno et al., 2020). The mobility and threshold voltage of the TFT on collagen shows only $\approx 41\%$ and $\approx 22\%$ drop compared to the ones on a rigid silicon substrate, which can be attributed to stresses experienced during the transfer, which may affect the gate/dielectric interface. These changes can be further reduced by optimizing the transfer process. Due to their high degree of biocompatibility, TFTs can be used for long-term implants.

Encapsulation materials are essential to the development of bioelectronics, especially for chronic electron implants. The encapsulation schemes for conventional electronic implants rely on thick (millimeter-scale), rigid enclosures constructed using bulk metal or ceramic parts, which is incompatible with the types of flexible bioelectronics. A challenge is in the development of materials that can serve as long-lived, perfect barriers to biofluids. This material should encapsulate the entire surfaces of the electronics, to prevent biofluid penetration across any exposed interfaces. Meanwhile, an encapsulation scheme is required to form high-quality sensing/actuating interfaces and compliant mechanical interfaces. Fig. 12.2E illustrates an encapsulation scheme: ultrathin, transferred layers of thermally grown silicon dioxide are used as biofluid barriers for flexible bioelectronic (Fang et al., 2016). The process begins with the thermal oxidation of a silicon wafer to form an ultrathin SiO_2 layer, and then high-quality functional electronics can be fabricated on this layer of oxide. The transfer process consists of bonding the top surface of this substrate onto a temporary supporting substrate. The silicon is removed by dry etching in a way that terminates at the bottom surface of the SiO_2 . Peeling the device from the temporary support and yield a piece of flexible electronics encapsulated across its entire front surface with a layer of thermal SiO_2 as a barrier to biofluids. Similar growth and transfer processes can deliver a layer of SiO_2 to the bottom of the flexible substrate to prevent biofluid penetration from the back side. Accelerated lifetime tests suggest robust barrier characteristics on timescales that approach many decades, in layers that are sufficiently thin (less than $1\ \mu\text{m}$) to provide the compliant mechanical interface. Additionally, the bilayer barrier can offer more excellent capabilities to prevent water and ion permeation, such as $\text{HfO}_2/\text{SiO}_2$ barrier. Song et al. report that a 100/100-nm-thick bilayer of $\text{HfO}_2/\text{SiO}_2$ barrier has a lifetime ≈ 10 times longer than that of an isolated 100-nm-thick layer of thermal SiO_2 barrier. A bilayer of $\text{HfO}_2/\text{SiO}_2$ barrier offers a projected lifetime of over 40 years at 37°C PBS (pH of 7.4) due to the enhanced ion-barrier properties, which shows the potential advantages for wide applications in chronic biointegrated devices.

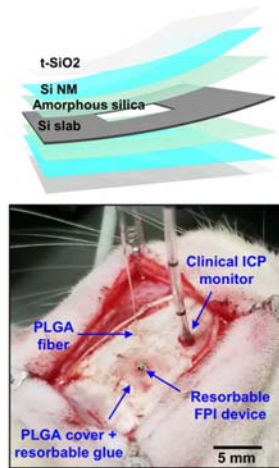
12.2.3 Silicon

As a very important semiconductor material, Silicon (Si) plays a crucial role in our everyday lives. Silicon has broad applications in both electronic and photonic technologies and can be found in almost all electronic devices, including but not limited to laptops, smartphones, tablets, microwaves, and bioelectronics. The present microelectronics technology is based on silicon materials. They are also expected to play a more significant role in the next generation, such as flexible electronics. For conventional semiconductor materials and devices, there is a tradeoff between device performance and growth temperature, which is unreal for fabricating inorganic semiconductor materials on a flexible substrate due to poor thermo-chemical stability. The realization of electronics with performance equal to established technologies that use rigid semiconductor wafers, but in lightweight, foldable, and stretchable formats would enable many new applications (Fig. 12.3).

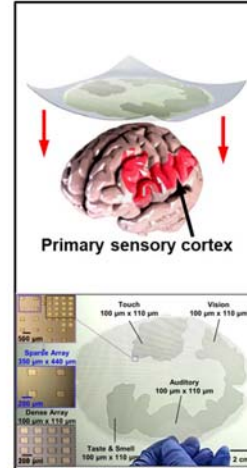
Various Si-based sensors are manufactured and integrated with flexible substrates, which have potential applications in the biomedical field. Kim et al. report an EES (Kim et al., 2011), which is achieve thicknesses, effective elastic moduli, bending stiffnesses, and areal mass densities matched to the epidermis, and thus is mechanically invisible to the user. By transferring printing technology, several classes of Si-based devices are integrated onto tattoo paper including Silicon MOSFET, silicon feedback resistor, Si solar cells, Si-based strain gauges, and Si PIN diode. EES is integrated with a collection of multifunctional sensors (such as temperature, strain, and electrophysiological), active/passive circuit elements (such as transistors, diodes, and resistors), wireless power coils, and devices for radio frequency (RF) communications (such as high-frequency inductors, capacitors, oscillators, and antennae). A key capability of EES is in monitoring electrical activity produced by the heart, brain, and skeletal muscles. As shown in Fig. 12.3A (Kim et al., 2011), the skin deforms freely and reversibly, without any apparent constraints in motion due to the EES. ECG recordings from the chest and EMG measured on the leg reveal high-quality signals. The measurements agree remarkably well with signals simultaneously collected using commercial, bulk tin electrodes, that require conductive gels, mounted with tapes at the same location. EES has potential applications in the biomedical field including physiological status monitoring, wound measurement/treatment, biological/chemical sensing, human-machine interfaces, covert communications, and others. Shin et al. report an optical pressure and temperature sensor that uses a Fabry-Pérotinterferometer (FPI) design (Shin et al., 2019). Fig. 12.3B upper photo shows a schematic illustration of an FPI pressure and temperature sensor composed of a thermally grown silicon dioxide ($t\text{-SiO}_2$) encapsulation layer, silicon nanomembranes (Si NMs), amorphous silica adhesion layer, and a slab of silicon with a square cavity. The layers of $t\text{-SiO}_2$ and Si NM serve as pressure-sensitive diaphragms that seal an air chamber formed by bonding with a silicon slab



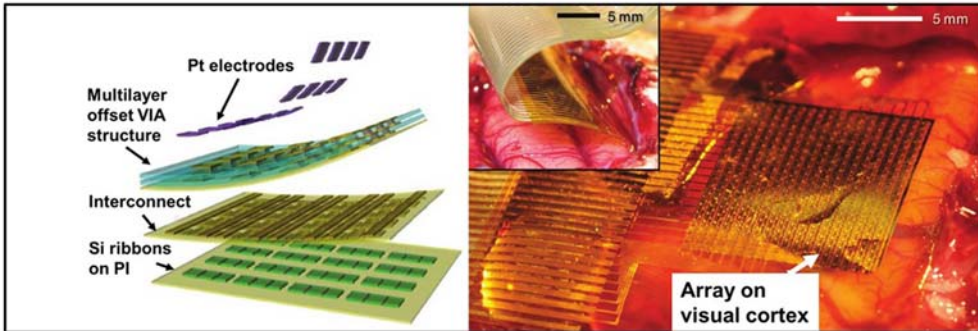
(A)



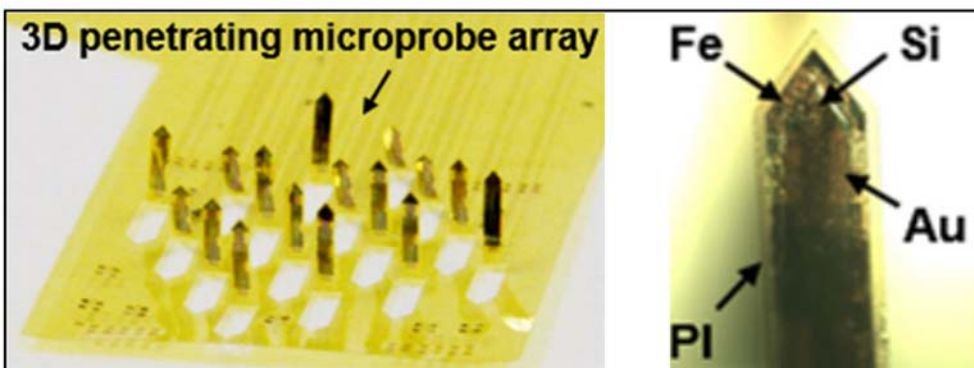
(B)



(C)



(D)



(E)

(Continued)

with a cavity. Optical fibers connected to a tunable laser and PD couple light in and out of the device to enable measurement of pressure and temperature via changes in measured reflection spectra. Sensors rely on pressure-induced deflections of Si NM diaphragms and the resulting changes in the thickness of an air cavity, which cause shifts in resonant peak positions in the reflection spectra. In vivo monitoring of intracranial pressure (ICP) and intracranial temperature (ICT) in rats demonstrates the potential clinical utility of these systems.

The transistor is the basic semiconductor device which uses for regulating the current and voltage in small electronic circuits. Transistors represent the fundamental device building blocks for microelectronics and are used in a wide variety of electronic devices. TFTs are well-compatible with flexible electronic systems due to compliant mechanical characteristics. As the most common active thin film devices, TFTs are significant building blocks for flexible platforms. Conventional Si-based TFTs are widely used in microelectronics. Flexible Si-based TFTs have been investigated for various amazing and unique applications. Viventi et al. report a class of mechanically flexible silicon electronics composed of 2016 silicon nanomembrane transistors for multiplexed measurement of signals in an intimate, conformal integrated mode on the dynamic, 3D surfaces of living biological tissues (Viventi et al., 2010). Benefiting from transfer printing technology, transistors integrated with flexible substrates show high performance. In vivo experiments are performed in male Yorkshire pigs. The flexible silicon electronics system is placed on the heart of an adult pig and conformed to the epicardial surface, including epicardial coronary vessels. The spread of spontaneous and paced ventricular depolarization with high temporal and spatial resolution is mapped using this electronic system. Large-scale electronic platforms that support intimate,

←

Figure 12.3 Si-based devices for wearable and implantable systems. (A) The multifunctional epidermal electronics based on Si-based electronics. (B) The Fabry-Pérot interferometer sensors for monitoring intracranial pressure and temperature (*Upper*: schematic illustration of an FPI pressure and temperature sensor; *Bottom*: the photograph of an FPI sensor implanted in the intracranial space of a rat). (C) Printed silicon microdie arrays with variable density for chronic biointegration (*Upper*: Schematic illustration of contact of the system on the surface of a brain model; *Bottom*: heterogeneous integration of Si microelectronics). (D) The flexible, high-density electrode array for mapping brain activity (*Left*: the schematic exploded view of each layer; *Right*: a flexible, high-density active electrode array was placed on the visual cortex). (E) The ultra-thin transfer printed Si optoelectronic microprobe arrays (*Left*: the optical image of microprobe array on a curved surface; *Right*: the optical microscopic image of a single microprobe). (A) *Reproduced with permission; Copyright* © 2011, *The American Association for the Advancement of Science*; (B) *Reproduced with permission; Copyright* © 2019 *The Authors, some rights reserved; exclusive licensee American Association for the Advancement of Science*; (C) *Reproduced with permission; Copyright* © 2019 *National Academy of Sciences*; (D) *Reproduced with permission; Copyright* © 2011, *Nature Publishing Group, a division of Macmillan Publishers Limited. All Rights Reserved*; (E) *Reproduced with permission; Copyright* © 2018, *The Author (s)*.

functional biointerfaces offer important capabilities in monitoring and/or stimulation of living tissues. This platform can be potentially applied in neural recording. Fig. 12.3D left photo shows an electronic system that integrates ultrathin silicon nano-membrane transistors into the electrode array, enabling new dense arrays of thousands of amplified and multiplexed sensors that are connected using fewer wires (Viventi et al., 2011). This system is used to map neural activity at high resolution on the surface of the visual cortex of ten cats in vivo (as shown in Fig. 12.3D right photo). The electronic system can either sample broad regions of the brain at low spatial resolution or small regions of the brain at high spatial resolution. The electronic system can offer a spatial scale 400-fold finer than that used clinically (Viventi et al., 2011). The increases in spatial and temporal resolution would allow a more detailed characterization of brain networks. Song et al. establish a scalable approach for building combined electronic–optoelectronic microsystems that served as functional interfaces to soft tissues. As demonstrations, as many as tens of thousands ($> 32,000$) of thin, microscale functional elements (including a pair of n-channel metal-oxide-semiconductor transistors) derived from source wafers are integrated with the flexible substrate by transferring printing method, as interconnected networks across areas that approach those of the human brain (as shown in Fig. 12.3C) (Song et al., 2019). The scalable approach may herald a new generation of diagnostic and therapeutic brain-machine interface devices.

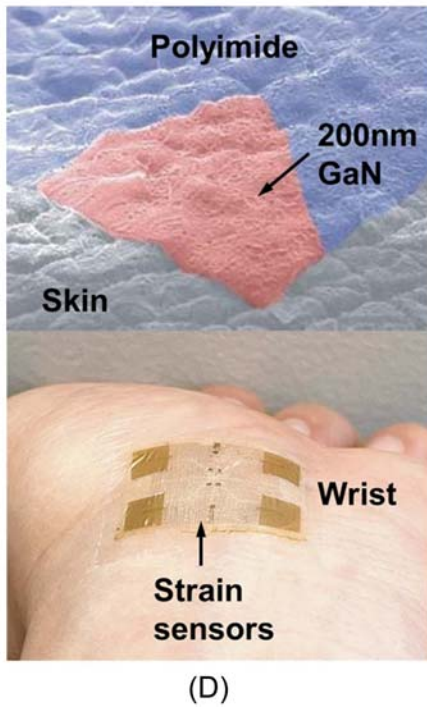
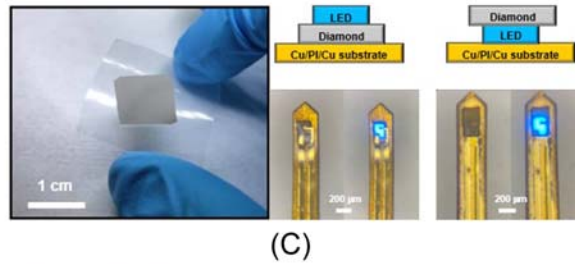
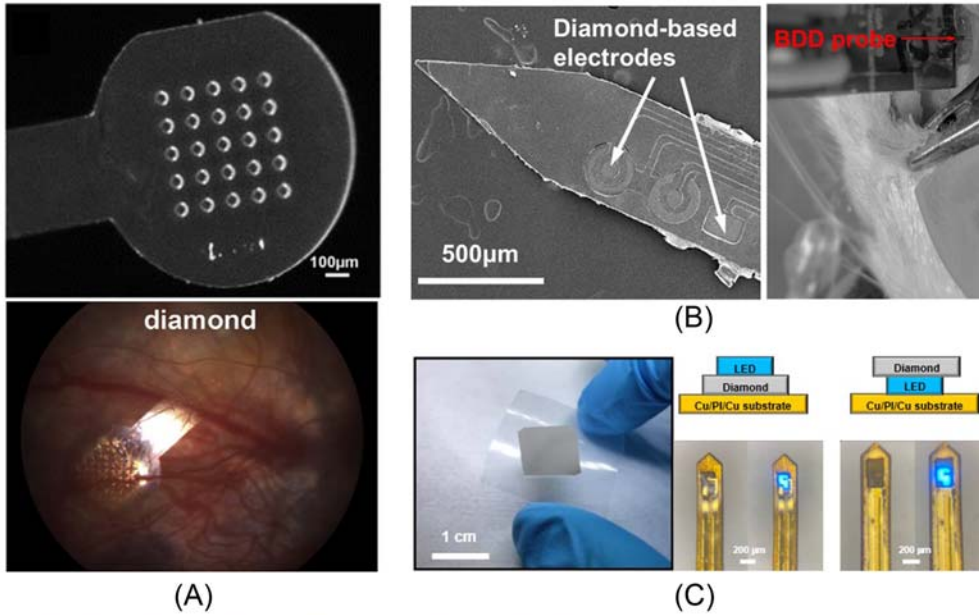
With the rapid development of optogenetics, which optogenetics involves injecting light into the brain to stimulate or control neurons, the optical neural probe has attracted intensive research interest in recent years. Detecting the light intensity in spatial positions can facilitate the understanding of the biological consequences. Sim et al. report a penetrating microprobe array can serve this purpose. The 3D penetrating microprobe array is formed in a thin and flexible format, which can attach and conform to curved surfaces and whose function is enabled by transfer printed ultrathin Si PDs (Sim et al., 2018). The PD employs two n–p Si diodes configured in a back-to-back (n–p–p–n) fashion. Fig. 12.3E shows an optical image of a 3D penetrating microprobe array on a curved surface (left photo) and an optical microscopic image of a single microprobe (right photo) (Sim et al., 2018). The capability of mapping the photo intensity in space is verified in a brain model. This type of penetrating microprobe array can find potential and broad utilities in a wide range of biointegrated applications, such as optogenetics, deep brain stimulation, cortex mapping, etc.

12.2.4 Wide bandgap semiconductors

Si semiconductor technology is approaching the theoretical limits of the Si material. To overcome this limitation and fabricate high-performance devices, new semiconductor materials are needed. Wide bandgap semiconductors like silicon carbide (SiC),

gallium nitride (GaN), and diamond, due to their superior electrical characters are likely candidates to replace Si shortly for high power, or high frequency, and short wavelength optoelectronic devices. Among these, diamond is an attractive material due to its exceptional physical characteristics, including the hardest materials, high density, the highest thermal conductivity, optical transparency that extends from the far infrared to the deep ultraviolet, low coefficient of thermal expansion, chemically inert, and excellent biological compatibility. Using the transfer printing method, many flexible diamond-based devices emerge for application in the biomedical field. Hess et al. report a chemical release transfer method to integrate microcrystalline diamond film onto a mechanically flexible polymer substrate (Hess et al., 2011). The high-temperature diamond growth process is performed on a temperature-tolerant substrate (Si wafer) using a thin SiO₂ film as a sacrificial layer, and then the diamond film is released from the wafer by dissolving the SiO₂ sacrificial layer in HF, thus transferring the diamond film from the Si/SiO₂ wafer to the flexible polymer substrate. The flexibility of the diamond-on-polymer structure is confirmed by wrapping the dogbone-shaped test structure around a cylindrical object with a radius of 650 μm without resulting in diamond delamination or cracking. The diamond-on-polymer structures can withstand a high degree of bending around small radii of curvature and will be able to conform well to curved biological structures (Fig. 12.4).

In addition to electrical and mechanical properties, biocompatibility is essential for bioelectronic devices, especially for implantable devices. Critical to the success of bioelectronics is reducing the immune response of an organism to the external device. Ideally, an implant is biologically inert and does not activate an immunological response but allows target cells to integrate with the bioelectronic application. If the bioelectronic device elicits an immunological response, the device may become encapsulated within a fibrous tissue, compromising or seriously disrupting the interface between the device and neural tissue (Feron et al., 2018). Bendali et al. develop a procedure for depositing diamond onto flexible 3D retinal implants (shown in Fig. 12.4A upper photo) and investigate the biocompatibility of diamond as an electrode (Bendali et al., 2015). In vitro experiment shows diamond electrode displays biocompatibility with embryonic cortical neurons and stem cells and even retinal neurons. For investigation of the biocompatibility of diamond in vivo, soft polyimide implants with diamond are inserted into the subretinal space of P23H rats (shown in Fig. 12.4A bottom photo). The absence of a massive inflammatory reaction and the presence of many bipolar neurons suggest that diamond electrodes are not toxic to retinal neurons. This study confirms the considerable benefits of the diamond as an attractive electrode material applied in the biomedical field. Additionally, diamond is favorable material for biochemical sensors due to it has biocompatibility, chemical inertness, resistance to biofouling, extremely wide potential window, and low double-layer capacitance. Fig. 12.4B shows flexible, diamond-based microelectrodes for neural sensing, which



(Continued)

consist of multichannel boron-doped polycrystalline diamond (BDD) microelectrodes on a soft Parylene C substrate (Fan et al., 2020). The dopamine (DA) sensing capability of the BDD microelectrodes is validated in a 1.0 mM dopamine solution. The BDD microelectrodes exhibit a featureless background current and wider water potential windows compared to the standard gold electrode, which permits the detection of chemical analytes in an expanded potential range of operation with reduced interference from the non-Faradaic background current of the electrolyte.

Despite its unique features, the wide application of diamond in the biomedical field is limited by processing technologies and difficulties in its integration with heterogeneous devices and substrates. Xie et al. report a facile process to form large-area, free-standing diamond thin films and combine them with optoelectronic devices on flexible substrates. By transferring printing, diamond thin films released from original substrates can be heterogeneously integrated onto any foreign substrates of interest. As shown in Fig. 12.4C left photo, diamond thin films are transferred onto a polyethylene terephthalate (PET) substrate (Xie et al., 2021). Diamond films are heterogeneously integrated with micro-LEDs to facilitate heat dissipation during operation (shown in Fig. 12.4C right photo). Experimental and calculation results suggest that the temperature rises during operation for micro-LEDs can be reduced by approximately 20% by using diamond films as heat sinks. These materials and device strategies provide promising paths to the broad applications of thin-film diamonds in the biomedical field.

As the representatives of the wide band gap semiconductor materials, GaN has been widely studied due to their excellent characteristics and plays an important role in solid-state lighting, flat panel displays, solar energy, electronic power, and other

←

Figure 12.4 Wide bandgap materials. (A) Three-dimensional (3D) diamond-based electrodes for flexible retinal neuroprostheses (*Upper*: SEM image of 3D diamond-based electrodes; *Bottom*: eye fundus of rat with implanted diamond-based electrodes). (B) Flexible diamond-based microelectrodes for neural sensing (*Left*: SEM images of a fabricated implantable neural probe; *Right*: setup of in vivo neural recording in a male rat). (C) Biocompatible diamond thin films integrated with flexible substrates (*Upper*: the free-standing diamond films on PET-based flexible substrates; *Bottom*: the schematics and corresponding images of diamond films integrated with blue micro-LEDs). (D) The wireless e-skin based on freestanding ultrathin single crystalline GaN film (*Upper*: SEM images of GaN e-skins with 200-nm-thick GaN attached to skin replica samples; *Bottom*: the wireless pulse measurements using GaN e-skin strain sensors). (E) The freestanding SiC for implantable and stretchable bioelectronics (*Upper*: SEM images of the SiC spring/PDMS membrane under mechanical deformation; *Bottom*: SEM images of the free-standing SiC micro-spring structures). (A) *Reproduced with permission; Copyright © 2015 Published by Elsevier Ltd.*; (B) *Reproduced with permission; Copyright © 2020 The Author (s).*; (C) *Reproduced with permission; Copyright © 2020 Wiley-VCH GmbH.* (D) *Reproduced with permission; Copyright © 2022 The American Association for the Advancement of Science.*; (E) *Reproduced with permission; Copyright © 2021 IOP Publishing Ltd Printed in the UK.*

fields. GaN also has great potential applications in bioelectronics. Kim et al. report a chipless wireless e-skin based on surface acoustic wave sensors made of freestanding ultrathin single-crystalline piezoelectric GaN membranes. The ultrathin GaN epitaxial layers (200 nm) are grown on graphene (GP)-coated GaN substrates and are easily released from the weak GP-GaN interface. Then ultrathin GaN films are transferred on a flexible patch as the material for passive wireless sensing. The excellent piezoelectricity and perfect single-crystallinity of GaN film enable wireless communication without chips. As shown in Fig. 12.4D upper photo, ultrathin GaN films can conformal coverage on the skin replica made of Ecoflex silicone (Kim et al., 2022). The chipless wireless e-skin allows the continuous measurement of arterial pulse waves on the wrist with highly sensitive over 7 days (as shown in Fig. 12.4D bottom photo). This presents routes to inexpensive, high-sensitivity platforms for wireless health monitoring devices.

SiC is an attractive candidate for bioelectronic devices among various wide band-gap semiconductor materials due to its chemical inertness and stable mechanical and electrical properties and is suitable for integration in reliable implantable, and stretchable sensing devices. Pham et al. report a versatile transfer printing process that employs a thin aluminum film as a sacrificial layer to facilitate the release and transfer diverse SiC films from rigid Si wafers onto flexible PDMS substrates (shown in Fig. 12.4E) (Pham et al., 2020). The transferred SiC films exhibit a high degree of structural perfection without cracks or tears and good semiconducting functionality. The SiC surface is an inert, nontoxic contact site that allows cells to firmly attach, proliferate, and then eventually spread to establish cell-cell contact. The physiological and morphological features of the human dermal fibroblast on the SiC surface are investigated. The results indicate the cytological compatibility of SiC and demonstrate the potential of flexible SiC electronics for implantable applications.

12.2.5 Two-dimensional materials

2D materials are emerging material candidates for electronic and photoelectric devices, energy storage, conversion devices, and bioelectronics. The most fascinating feature of 2D materials is their ultrathin vertically layered nanostructure that provides high optical transparency, extraordinary softness, and inherent flexibility to the devices. The quantum confinement effect in atomically thin layered nanostructure also introduces interesting optoelectronic characteristics and superb photodetection capabilities. The large-area continuous planar structure of 2D materials allows efficient carrier transport within the 2D plane. Benefiting from the unique 2D layered structure and outstanding properties, 2D materials have proven to be good candidates for flexible bioelectronic devices. These interesting properties of the 2D materials enable unconventional device functions in biological and optical sensing, as well as superb performance in electrical and biochemical therapeutic (Choi et al., 2019) (Fig. 12.5).

Among various 2D materials, GP stands out in the flexible electronics field due to its combination of high carrier mobility, high thermal conductivity, high specific surface area, high optical transparency, excellent mechanical flexibility, and environmental stability. GP is an ideal material for wearable and implantable electronics. Lim et al. report a transparent and stretchable interactive human–machine interface (iHMI) system composed of wearable motion sensors which consist of piezoelectric polymer (PLA)/SWNT composite thin film sandwiched between GP electrodes and insulating layers (shown in Fig. 12.5A upper photo) (Lim et al., 2015). The GP is grown through a chemical vapor deposition (CVD) process using copper as the catalyst and transferred onto the top and bottom surfaces of PLA/SWNT composite thin film respectively to form sandwich structures. The bending tests confirm that GP heterostructures maintain their high electrical conductivity even after being subjected to extreme bending. The iHMI system can be conformally laminated onto human skin (shown in Fig. 12.5A bottom photo) and have a natural appearance, comfort, and high SNR, which benefits from the high conductivity of GP and the ultrathin and lightweight design.

GP is an emerging ideal transparent electrode material due to high optical transparency and high electrical conductivity. GP biocompatibility increases its potential use in implantable biomedical applications. Fig. 12.5B shows a transparent and flexible low-noise GP electrode, which enables simultaneous optical imaging and electrophysiological recording (Kuzum et al., 2014). CVD-grown GP on Cu substrate is transferred onto the desired areas of the polyimide substrate using the poly(methyl methacrylate) (PMMA)/PDMS stamping method and is patterned using photolithography and oxygen plasma etching. In vivo experiments confirm that transparent GP electrodes can simultaneously record neural activity during calcium imaging with confocal or multiphoton microscopy without any light-induced artifacts in the electrical recordings. GP transparent electrodes offer a solution for high spatial-temporal resolution electro-optic mapping of the dynamic neuronal activity.

GP as a promising electrode material has tremendous potential for electrochemical sensing and biosensing due to excellent properties including chemical inertness, high conductivity and electron mobility at room temperature, large surface-to-volume ratio, and robust mechanical and flexibility. Mannoor et al. establish an approach to integrate GP electrochemical electrodes with biomaterials. The CVD-grown GP thin films are released from donor substrate and transferred onto the silk films. Planar inductive and capacitive elements are then incorporated onto the GP/silk samples to enable wireless interrogation (shown in Fig. 12.5C left photo) (Mannoor et al., 2012). GP-based sensing element with wireless readout coil is then transferred onto biomaterials via dissolution of the supporting silk film (shown in Fig. 12.5C right photo). The sensor is integrated onto the surface of a bovine tooth for investigating the performance (shown in Fig. 12.5C right photo). The results exhibit the capability of remote monitoring of pathogenic bacteria.

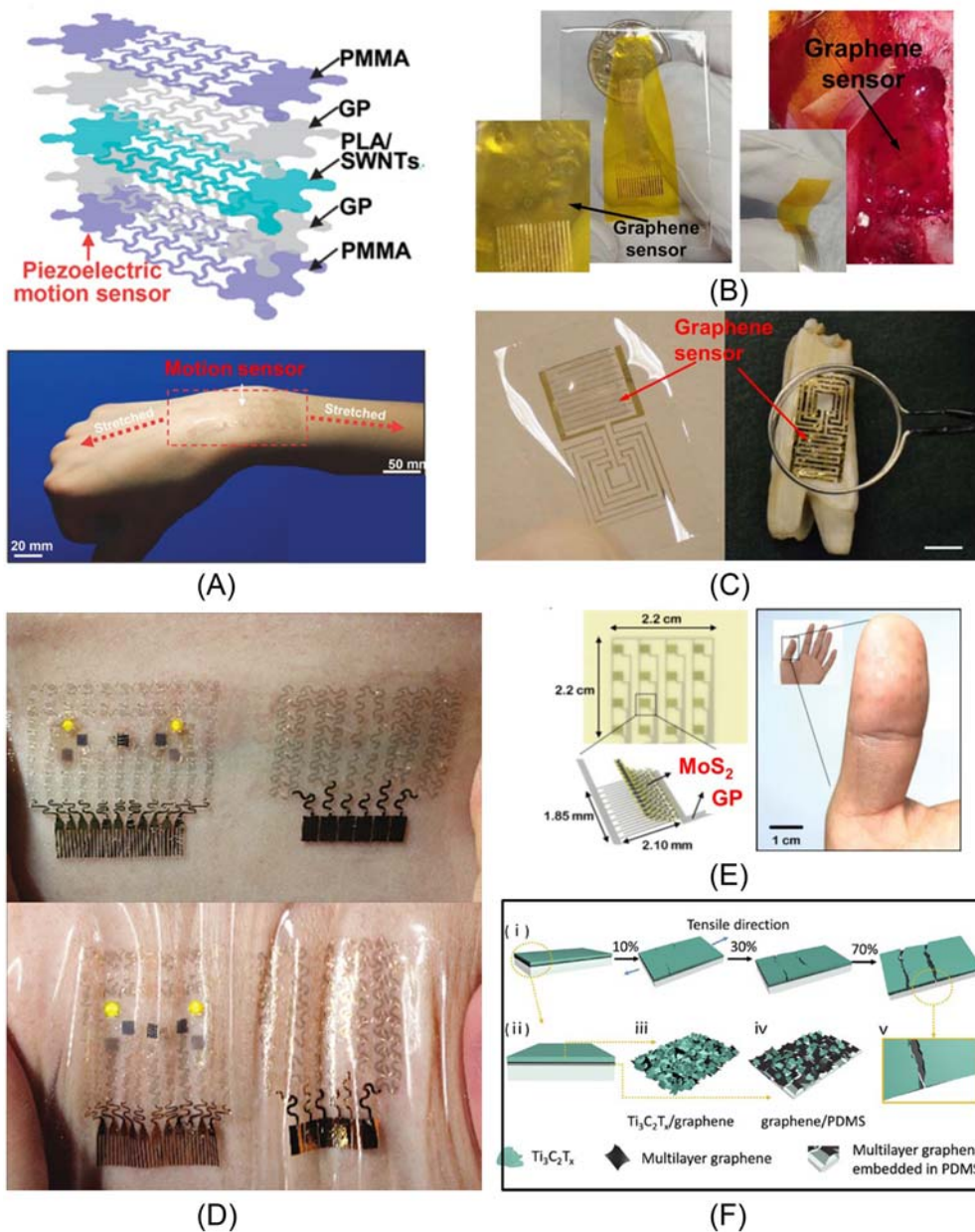


Figure 12.5 Two-dimensional (2D) materials. (A) Transparent and stretchable interactive human-machine interface based on transferred graphene (*Upper*: the exploded schematics of the transferred graphene used in the motion sensor; *Bottom*: the image of the motion sensor on the human wrist). (B) Graphene electrodes for simultaneous electrophysiology and neuroimaging (*Left*: the
(Continued)

However, the low defect density of CVD-grown GP results in poor electrochemical activity, which limits its application in biosensing. To overcome this limitation, gold-doped GP is used to replace GP for electrochemical sensing. Lee et al. report that GP doped with gold and combined with a gold mesh has improved electrochemical activity over bare GP and fabricate a stretchable patch for sweat-based diabetes monitoring (Lee et al., 2016). The gold mesh and gold-doped GP form an efficient electrochemical interface for the stable transfer of electrical signals. The patch with stretchable designs shows extremely conformal contacts to the human skin under deformation (shown in Fig. 12.5D). This conformal and intimate interfacing enables stable sensing.

MoS₂ materials have recently attracted attention due to their outstanding mechanical and optical transmittance, high gage factor, and tunable band gap. Fig. 12.5E shows an ultrathin conformal, MoS₂-based tactile sensing array (Park et al., 2016). Bilayer MoS₂ (1.4 nm) used as a strain-sensing layer is transferred on SU-8 substrate (32 nm). Transferred GP (0.9 nm) is used as an electrode. The total thickness of the sensor is less than 75 nm. The ultrathin tactile sensor shows high sensitivity, good uniformity, and linearity. In addition, it provides excellent mechanical flexibility, good optical transparency, and stable performance even on a human fingertip (shown in Fig. 12.5E right photo).

Laser-induced graphene (LIG) is a 3D porous material prepared by direct laser writing with a CO₂ laser on carbon materials in ambient atmosphere (Ye et al., 2019). This technique combines 3D GP preparation and patterning into a single step without the need for high-temperature reaction conditions, solvent, or subsequent treatments. Since its discovery in 2014, LIG has attracted broad research interest (Lin et al., 2014; Ye et al., 2018). Using transfer printing technology, LIG could integrate with various substrates and obtain exciting performance. He et al. report a self-healable, flexible, and multimodal sweat sensor based on LIG electrodes for healthcare monitoring

← photograph of a 16-electrode array; *Right*: the photograph of the graphene electrode placed on the cortical surface of the left hemisphere of rat). (C) Graphene-based wireless bacteria detection platform. (D) Graphene-based electrochemical device for glucose monitoring (*Upper*: the optical image of the electrochemical sensor array; *Bottom*: the optical images of electrochemical sensor array on human skin). (E) MoS₂-based tactile sensor for electronic skin applications (*Left*: the fabrication steps for the strain gage sensor based on the MoS₂; *Right*: the photographs of the MoS₂ tactile sensor on a fingertip). (F) Wearable strain sensors based on transferred MXene-graphene composite materials. (A) *Reproduced with permission; Copyright © 2014 WILEY-VCH Verlag GmbH & Co. KGaA, Weinheim*; (B) *Reproduced with permission; Copyright © 2014, Nature Publishing Group, a division of Macmillan Publishers Limited. All Rights Reserved*; (C) *Reproduced with permission; Copyright © 2016, Nature Publishing Group*; (D) *Reproduced with permission; Copyright © 2012, Nature Publishing Group, a division of Macmillan Publishers Limited. All Rights Reserved*; (E) *Reproduced with permission; © 2016 WILEY-VCH Verlag GmbH & Co. KGaA, Weinheim* *Reproduced with permission; Copyright © 2019 Elsevier Ltd. All rights reserved.*

applications, which can conduct simultaneous detections of pH, UA, and Tyrosine in sweat (He et al., 2021). The LIG on the donor substrate is pressed onto the self-healing substrate. Due to the strong adhesive force provided by the hydrogen bonds in the self-healing elastomer, the patterned LIG is thus transferred from the donor substrate onto the self-healing substrate. Due to the highly porous structure and high electron mobility of LIG, the sensor has outperformed commercial glassy carbon electrodes in terms of sensitivity to the targeted uric acid and tyrosine molecules. In addition, the sensor can recover from catastrophic through-cut damage by a razor blade, which benefits from the self-healable substrate.

Due to high metallic conductivity, good oxidation resistance, and excellent mechanical properties, MXenes have been integrated with various flexible substrates for bioelectronic applications (Li et al., 2019; Yang et al., 2019; Zhan et al., 2020). Sun et al. report a wearable strain sensor based on a spontaneously formed $\text{Ti}_3\text{C}_2\text{T}_x$ /graphene/PDMS layered structure, which requires no complicated manufacturing process (Yang et al., 2019). As shown in Fig. 12.5F, a $\text{Ti}_3\text{C}_2\text{T}_x$ suspension prepared by a chemical liquid etching method and a multilayer GP suspension prepared by an electrochemical exfoliation method is mixed and filtrated into a conductive film. Then the $\text{Ti}_3\text{C}_2\text{T}_x$ /GP films are transferred to prepolymerized PDMS substrates to form flexible and stretchable strain sensors. The strain sensor can be divided into two layers when being stretched: a $\text{Ti}_3\text{C}_2\text{T}_x$ dominated brittle upper layer and a flexible GP/PDMS composite bottom layer. The upper layer is brittle and tended to generate cracks to dissipate stresses when being stretched, while the bottom layer kept contact to maintain the conductive pathways. The synergetic motion of the upper and bottom layers rendered the film with highly sensitive and linear responses to strains in a wide strain range.

12.2.6 Biomaterials

Applications in biotechnology demand the ability to pattern relevant bioorganic materials, ranging from small molecule drug candidates to living cells (Carlson et al., 2012). The transfer printing technique is available for such purposes. It has been verified that various biomaterials can be patterned using the transfer printing method, such as DNA, proteins, Viruses, and cell. DNA patterned has become one of the essential tools to investigate the expression or mutation of thousands of genes simultaneously. Fig. 12.6A shows a simple and cost-effective transfer scheme for patterning DNA with high submicron resolution (Thibault et al., 2005), which is named namely microcontact printing. The patterned stamps are made of elastomeric poly (dimethylsiloxane) (PDMS) which has a strong hydrophobic surface and does not require any surface modification to be able to adsorb oligonucleotides or PCR products. The adsorbed DNA molecules are subsequently printed efficiently on a target surface. Experiments confirm

that this scheme can pattern DNA microarrays at a relatively high speed, high resolution, and high reproducibility (Thibault et al., 2005). DNA patterns can also be replicated at large-scale high resolution by other forms of printing, such as supramolecular nanostamping (SuNS) (Yu et al., 2005; Yu & Stellacci, 2006) and liquid supramolecular nanostamping (LiSuNS) (Yu & Stellacci, 2007). Supramolecular nanostamping encompasses a class of protocols that form high-resolution patterns of single-stranded DNA molecules. Additionally, LiSuNS and SuNS have a common advantage: the ability of printing features made of different DNA sequences in a single printing cycle while preserving their chemical differences (shown in Fig. 12.6B) (Yu & Stellacci, 2007) (Fig. 12.6).

Microcontact printing technology can also be used for patterning proteins. As shown in Fig. 12.6C. Renault et al. propose modified microcontact printing: patterning stamp surfaces with ensembles of biomolecules where the pattern on the affinity stamp is determined by the position of various proteins covalently linked to a planar stamp (Renault et al., 2002). After the capture process, target protein molecules are patterned on the stamp, and can be microcontact-printed onto a substrate in one step. This method enables the simultaneous capture of different target proteins from a complex solution (shown in Fig. 12.6C). Wigenius et al. report a simple method based on PDMS stamps can be used to pattern proteins: hydrophobic patterns achieved by transfer printing silicone oligomers from a PDMS stamp onto a hydrophilic substrate can selective adsorption of proteins from solution (shown in Fig. 12.6D) (Wigenius et al., 2008).

Additionally, the subtractive printing technique has been developed as a versatile method for the patterned transfer of proteins and viruses from solution to substrate through a series of step-wise reductions in nonspecific hydrophobic interactions. This method can be used to generate patterns with sub-100 nm resolution (Coyer et al., 2007; Solis et al., 2010). Fig. 12.6E shows the nanometer-scale patterning of viruses (M13 bacteriophages) by subtractive printing (Solis et al., 2010). A planar, hydrophobic elastomer (PDMS) using the spontaneous adsorption of viruses from solution onto hydrophobic surfaces, to subtract viruses from the elastomer using a nanotemplate during a brief contact step, and to print the remaining viruses pattern from the elastomer onto the target substrate. The key in this method is that the nano-template and final substrate have a higher work of adhesion for water than the elastomer.

Cell patterning in two and three dimensions provides great opportunities for basic science investigations, tissue engineering, and regenerative medicine applications (Schiele et al., 2010). Transfer printing technology can enable precise cell placement on 2D and even 3D surfaces. Stevens et al. report a simple potentially generic methodology for generating patterns of mammalian cells on porous scaffolds (Stevens et al., 2005). The hydrogel stamps are used in this method, which provided a “wet,” biocompatible surface and maintained the viability of cells adsorbed on stamps during the patterning process.

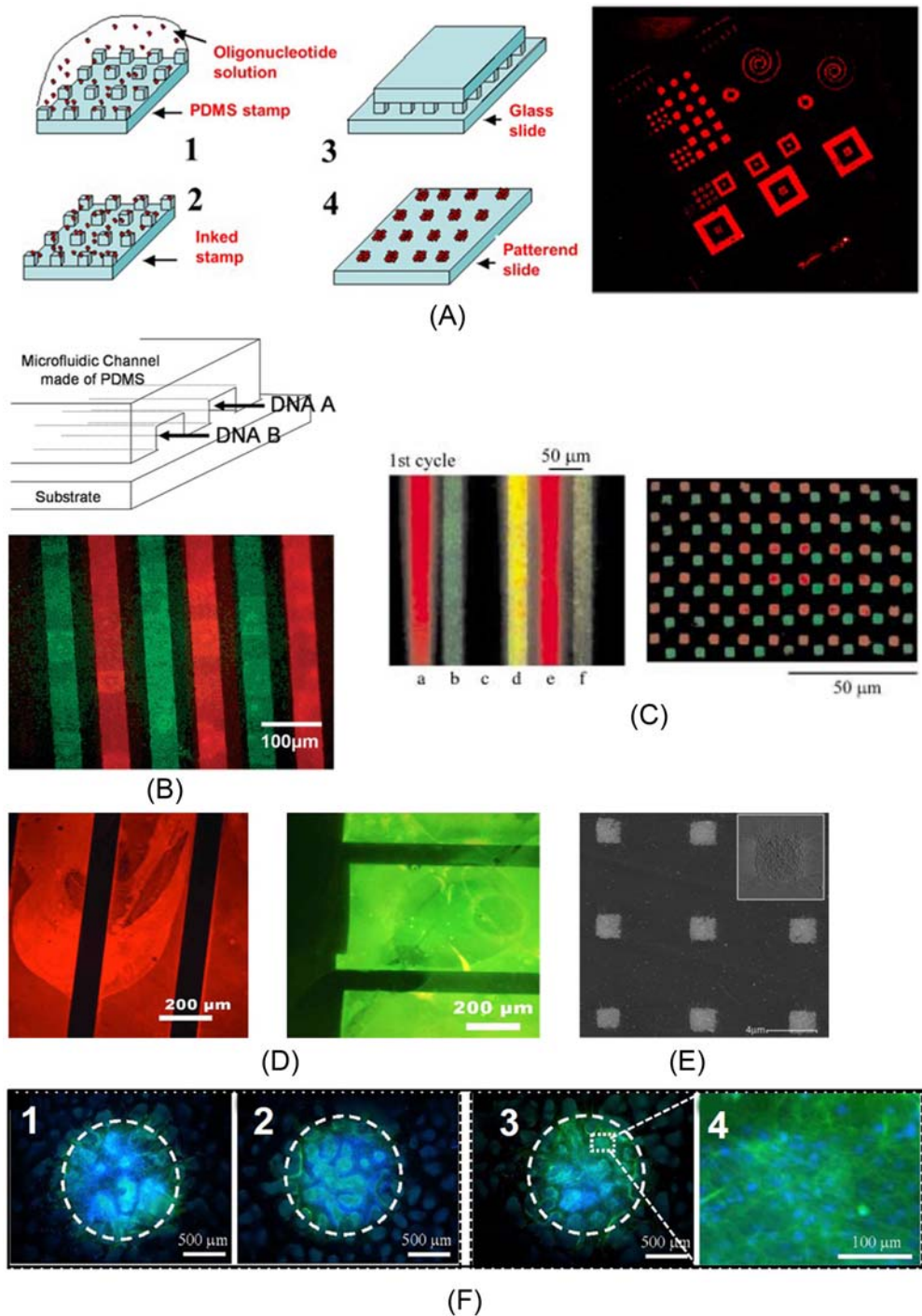


Figure 12.6 Biomaterials. (A) Transfer printing of oligonucleotides for biochip applications (*Left*: the principle of microcontact printing of DNA molecules; *Right*: the fluorescence images of printed micronic patterns). (B) Large-area transfer printing DNA via liquid supramolecular nanostramping (*Continued*)

The technique transferred material to the surface of the substrate in parallel, making it possible to pattern multiple spots of cells simultaneously. Fig. 12.6F shows three spots of cells patterned on the surface of hydroxyapatite at the same time and illustrates the reproducibility of the pattern transfer.

12.3 Functional devices

12.3.1 Light emitting diodes

LEDs have received considerable attention as a new light source in biomedical fields due to their high efficiency, long life, low power consumption, excellent portability, and easy integration with other electronic devices (Corbett et al., 2017; Zhang, Peng, et al., 2022). In addition to common phototherapy, their applications have been expanded to optical neural modulation, photodynamic therapy, and optical sourcing (Gutruf & Rogers, 2018; Lee et al., 2012; Lee et al., 2022). With the rapid development of optogenetics, micro-LEDs as implantable optical sources for controlling neurons have attracted intensive research interest in recent years. The implantable LED optical sources can provide precision optical stimulation, effective photon treatment, and other benefits. By integrating the micro-LEDs with flexible substrates, biocompatibility at the chemistry and mechanics level can be obtained, which are critical specifications for the long-term integration of implants with a biological host (Fallegger et al., 1903). Li et al. report a heterogeneous integration strategy, which enables the integration of tri-color (red, green, and blue) microscale, thin-film LEDs with the heterogeneous substrate (Li, Tang, et al., 2021). The first and key step

←

(Upper: the schematic illustrating the approach used for master preparation; Bottom: a false-color overlay of printed result). (C) Fabricating high-resolution arrays of proteins via affinity contact printing (Left: the captured molecules on the stamp are chicken IgGs (lines a and e), goat IgGs (lines b and f), protein A (line d), and mouse IgGs (line c); Right: the fluorescence microscope image showing the placement of the TRITC-anti-chicken and FITC-anti-goat antibodies from a stamp onto a glass substrate). (D) Protein biochips patterned by microcontact printing [the fluorescence microscopy pictures of algG-Alexa μ CP onto glass substrates followed by incubation with IgG-TxR illuminated at 546 nm (left) and followed by incubation with streptavidin-FITC illuminated at 470 nm (right)]. (E) The patterned transfer of viruses from solution to the substrate. (F) Mammalian cells are transferred onto porous tissue engineering substrates by hydrogel stamps (images 1–3 show different regions of a hydroxyapatite scaffold patterned with osteoblasts using a single agarose stamp; 4 is the higher magnification of the area within the white box in 3). (A) Reproduced with permission; Copyright © 2005, Thibault et al.; licensee BioMed Central Ltd.; (B) Reproduced with permission; Copyright © 2007 WILEY-VCH Verlag GmbH & Co. KGaA, Weinheim; (C) Reproduced with permission; Copyright © 2002 WILEY-VCH Verlag GmbH, Weinheim, Fed. Rep. of Germany; (D) Reproduced with permission; Rights managed by AIP Publishing; (E) Reproduced with permission; Copyright © 2010 WILEY-VCH Verlag GmbH & Co. KGaA, Weinheim; (F) Reproduced with permission; Copyright © 2005 Elsevier Ltd. All rights reserved.

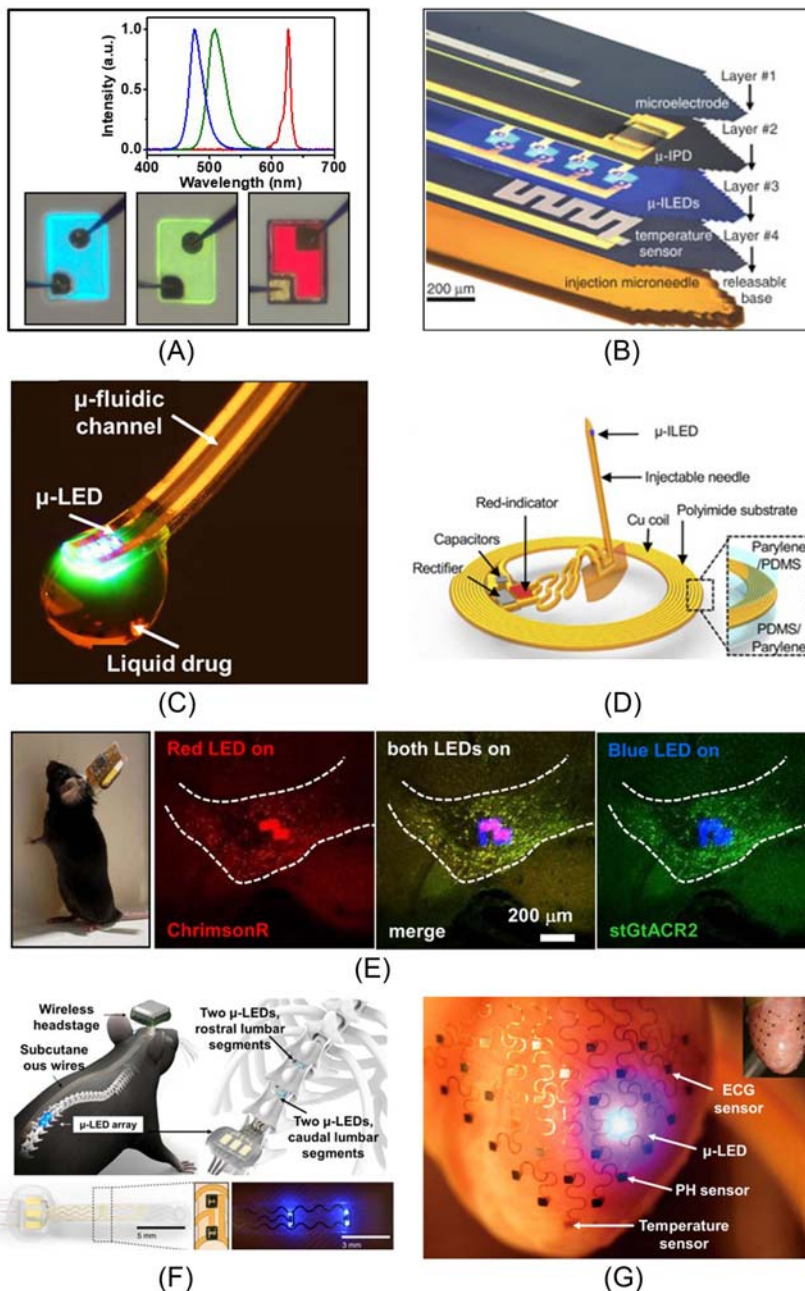


Figure 12.7 Microlight emitting diodes (LEDs) for implantable light sources. (A) Microscope images and electroluminescence spectra of multicolor micro-LEDs after transfer printing. (B) GaN μ -LEDs are transferred onto thin plastic strips for optogenetics. (C) Optofluidic neural probes that combine
(Continued)

in this integration strategy is forming free-standing thin-film LEDs. Thin-film, freestanding red LEDs based on gallium arsenide (GaAs) are formed by selective sacrificial etching: a lattice-matched $\text{Al}_{0.95}\text{Ga}_{0.05}\text{As}$ sacrificial layer is incorporated beneath the epitaxial layer during the growth of functional structure, and then thin-film LEDs can be released from the grown substrate by highly selective etching of sacrificial layer. Thin-film GaN-based blue/green LEDs are released from sapphire by a laser lift-off (LLO) technique. Free-standing LEDs can be integrated with various foreign substrates, such as flexible, stretchable, and even biodegradable substrates. Fig. 12.7A shows the Microscope images and spectrum of tri-color (red, green, and blue) thin-film LEDs integrated with the flexible substrate. This integration strategy enables a wide range of new opportunities for fabricating a multifunctional flexible optogenetic platform with good biocompatibility and conformability (Li et al., 2021). Fig. 12.7B shows a multifunctional optogenetic probe consisting of micro-LEDs to enable optical stimulation, precision temperature sensors to monitor thermal load, platinum microelectrodes to perform electrical recording, and a micro-scale PD to allow for photometry (Kim et al., 2013). Despite its multilayer structure, the multifunctional optoelectronic systems have a total thickness of approximately $\sim 20 \mu\text{m}$, high mechanical flexibility, and minimally invasive stimulation. Another example is Fig. 12.7C shows optofluidic neural probes consisting of soft microfluidic drug delivery with micro-LED arrays, which enable programmed spatiotemporal control of fluid delivery and photostimulation (Jeong et al., 2015). The microfluidic channel is fabricated by bonding two transparent thin elastomers (PDMS), which enable high flexibility and transmittance after incorporation with $\mu\text{-LED}$ arrays. Experiments in freely moving animals demonstrate that the dopaminergic system is activated by micro-LED, and then blocked by dopamine receptor antagonists delivered through the microfluidic channel in a temporally precise programmable manner. Conventional hardware for optogenetic stimulation physically tethers the experimental animal to an external power supply equipment

← soft microfluidic drug delivery with micro-LED arrays. (D) Flexible near-field wireless optogenetic probe. (E) Dual-color optogenetic probe for simultaneous neural activation and inhibition in the same brain region (*Left*: the photograph of a behaving mouse after intracranial implantation of a probe; *Right*: micrographs of a dual-color micro-LED probe embedded into the tissue). (F) Closed-loop optogenetic probe across the entire dorsoventral spinal cord (Upper: the schematic overview of the optoelectronic; Bottom: photographs of the micro-LED array). (G) Micro-LEDs are served as local light sources in a 3D multifunctional integumentary membrane integrated on a rabbit heart (Inset: the electronics can cover both anterior and posterior surfaces of the heart). (A and B) Reproduced with permission; Copyright © 2013, The American Association for the Advancement of Science; (C) Reproduced with permission; Copyright © 2015 Elsevier Inc. All rights reserved; (D) Reproduced with permission; Copyright © 2016 Elsevier Inc; € Reproduced with permission; Copyright © 2022, The Author (s); (F) Reproduced with permission; Copyright © 2021, The Author (s), under exclusive license to Springer Nature America, Inc.; (G) Reproduced with permission; Copyright © 2014, Nature Publishing Group, a division of Macmillan Publishers Limited. All Rights Reserved.

and imposes constraints on the animal's movement. Emerging wireless options offer important capabilities to solve this problem. Fig. 12.7D shows a thin, flexible, and fully implantable wireless optogenetic system, which combines subdermal magnetic coil antennas connected to micro-LEDs (Shin et al., 2017). This wireless system can operate at wavelengths ranging from UV to blue, green-yellow, and red. This wireless power transfer technology has a low operating frequency (13.56 MHz), which reduces the absorption in biological tissues, provides greater penetration depth, and minimizes adverse biological effects (Fig. 12.7).

To control neural activities more precisely, bidirectional neural modulations are required. Li et al. report a wireless dual-color optogenetic probe, which comprises vertically integrated microscale thin-film red and blue LEDs and exhibits superior biocompatibility for long-term light stimulation in vivo (Li, Lu, et al., 2022). Cooperating with the coexpression of two spectrally distinct excitatory and inhibitory channelrhodopsins (ChrimsonR and stGtACR2), bidirectional optogenetic activation and inhibition are achieved in behaving mice. In vivo experiment results demonstrate that wireless dual-color optogenetic probes enable efficient, bidirectional control of neuronal activity in the ventral tegmental area and dopamine release of the nucleus accumbens (shown in Fig. 12.7E). These technologies provide numerous opportunities and implications for neuroscience research.

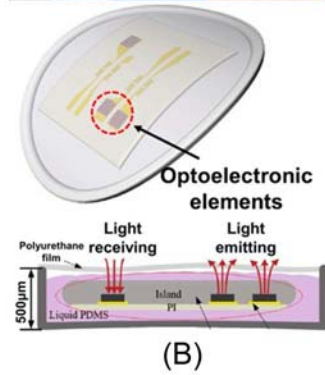
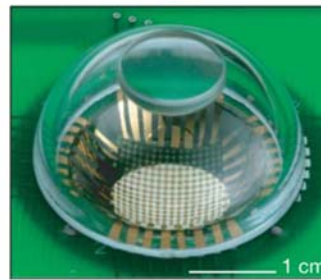
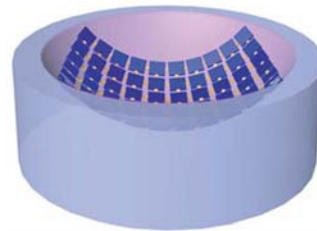
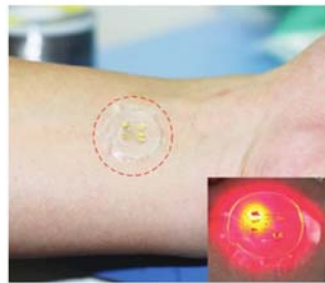
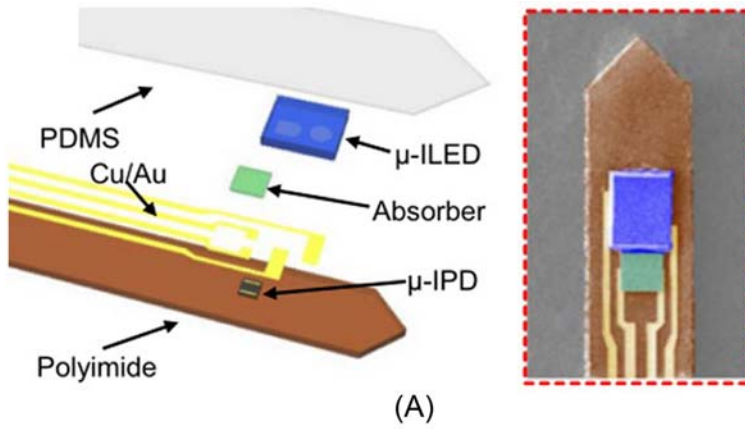
Photogenetic, as an efficient neural modulation technology, enables millisecond-scale optical control of neural activity in defined cell types during animal behavior, which allows scientists to pursue closed-loop optogenetic control (Grosenick et al., 2015; Lee et al., 2022). In the field of neuroscience, the closed-loop control system used for optogenetic modulation has been reported, where the input is a time-varying light stimulus and the output may be physiological parameters, such as electrophysiological, behavioral, pH, blood oxygen or glucose levels, or neurochemical changes associated with neurotransmitter release (Armstrong et al., 2013; Grosenick et al., 2015; Zaaimi et al., 2022). For example, Fig. 12.7F shows a wireless closed-loop optogenetic system inserted between the spinal cord and vertebrae to modulate muscle responses, which enables ultrafast, wireless, closed-loop manipulation of targeted neurons and pathways across the entire dorsoventral spinal cord in untethered mice (Kathe et al., 2022). This system is comprised of dual-color LEDs (red and blue), used for light activation and inhibition (input), and electrophysiological electrode, used for collecting electromyographic (EMG) signals. In vivo experiment results confirm that the system enables closed-loop control of optogenetic stimulation using real-time processing of physiological signals.

Conventional electronic devices can only be fabricated on a planar surface, which is mismatched with the shape of 3D biotissues, such as the heart, and brain. It is necessary to develop curvy electronics that can be assembled into devices on 3D surfaces without losing performance in some applications. Stretchable electronics create an

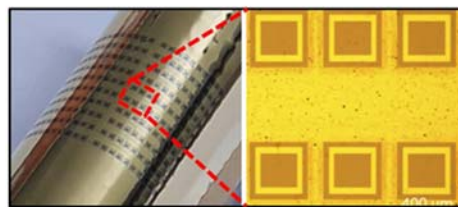
opportunity to meet this challenge. As shown in Fig. 12.7G, full 3D integration of electronics with the epicardial surface (Xu et al., 2014). Micro-LEDs and other several sensors are transferred onto 3D elastic membranes shaped precisely to match the epicardium of the heart. The electronic system completely envelops the heart, and possesses inherent elasticity, providing a mechanically stable biotic/abiotic interface during normal cardiac cycles. This integration scheme presents a promising opportunity to design and implement bioelectronics with complex structures.

12.3.2 Photodetectors

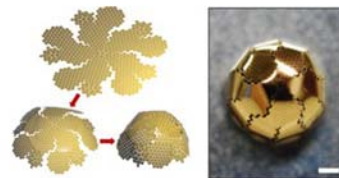
PDs are indispensable components for the light sensor, which are found in a variety of applications such as optical telecommunications, imaging, and biomedical sensing. In recent years, new flexible PD applications, such as e-eyes, oximeters, and flexible cameras, have attracted a great deal of research interest. Fig. 12.8A shows a wireless, injectable fluorescence photometer that integrates a LED and a PD on a flexible, needle-shaped polymer substrate (Lu, Gutruf, et al., 2018). The ultrathin geometry and compliant mechanics of these probes allow minimally invasive implantation. The fluorescence photometer can record neuronal activity using genes expressing calcium indicators, which is a standard fluorescent technique that detects Ca^{2+} changes associated with cell activity. In vivo studies in freely moving animals shows that the photometry can capture transient calcium fluorescence from active neurons in the deep brain (basolateral amygdala), demonstrating the capability to monitor neural activity in freely moving animals. The technology scheme that excitation light sources based on micro-LED, in collaboration with a PD for measuring transmission, reflection, and emission can also be used to fabricate the oximetry sensors. As shown in Fig. 12.8B, an epidermal optoelectronic device with the integration of red and infrared LEDs and a Si-based PD is fabricated for blood oxygen measurement based on Beer–Lambert law (Li et al., 2017). The reflected light is analyzed by a PD to determine the blood oxygen level in real-time. The epidermal optoelectronic device is attached to the wrist for demonstrating the practical application of the epidermal optoelectronic device. Similar photoelectric systems can also be used to monitor blood oxygen in biological tissues. Zhang et al. report a pair of micro-LEDs and a PD are integrated on a needle-shaped polymer substrate to form an implantable probe for measuring tissue oxygen saturation (Zhang, Gutruf, et al., 2019). The implantable oximeter enables monitoring regional tissue oxygen saturation levels in vivo, including deep brain regions, on freely moving animal models. Hong et al. report a low-cost, high-throughput flexible GaAs PD arrays fabrication scheme. GaAs PD arrays are grown on a Si substrate and transferred to a polyimide film via metal wafer bonding and epitaxial lift-off (Hong et al., 2020). 100% transfer yield of a 20×10 GaAs PD array is achieved. PD arrays that are highly uniform and thermal crack-free after the transfer process. The optical and



(C)



(D)



(E)

(Continued)

electrical properties of the GaAs PD array are almost the same before and after the transfer process. Fig. 12.8D shows a flexible GaAs PD array in a bent configuration. One thousand bending cycles of the flexible PD array confirm excellent durability. This technology offers an opportunity for large-scale optoelectronic device integration (Fig. 12.8).

The human eye is a remarkable imaging device, which has photoreceptors that capture and transduce photons into electrochemical signals. The eye-inspired optoelectronic systems have always attracted the attention of researchers due to their many unique features. Eyes enable a wide field of view and low aberrations with few-component imaging optics benefiting from a hemispherical detector geometry (Ko et al., 2008). Inspired by the eye, Ko et al. report a hemispherical electronic eye camera based on single-crystalline silicon PDs (shown in Fig. 12.8C) (Ko et al., 2008). The hemispherical PDMS substrate formed by casting PDMS in the gap between opposing convex and concave lenses with matching radii of curvature transform into the planar shape of a “drumhead” at sufficiently large radial tension. The focal plane PD array is fabricated on the silicon-on-insulator wafer and then peeled off from the wafer by etching the oxide layer and further transferred on the tensioned, planar drumhead shape PDMS substrate. Finally, the PDMS substrate with PD array returns to its initial hemispherical shape by releasing the radial tension. Fig. 12.8E illustrates a simple origami approach for fabricating Si-based focal plane arrays and artificial compound eyes that have hemisphere-like structures (Zhang, Jung, et al., 2017). The silicon-based devices are fabricated on the silicon-on-insulator wafer and shaped into maps of a truncated icosahedron, then transferred onto the PI substrate with a matching shape and further folded either into a concave or convex hemisphere. Those technologies provide practical routes for integrating planar devices onto complex curved surfaces.

←

Figure 12.8 Photodetectors (PD). (A) Implantable fluorescence photometer that combines light sources and PDs (*Left*: the schematic exploded-view illustration of photometry probe; *Right*: SEM image of the probe tip). (B) Wearable blood oxygen detection device that integrates LED and Si-based PD (*Upper*: the device integrated onto human wrist; *Bottom*: the illustration of blood oxygen detection device). (C) Eye-like optical imaging system based on compressible silicon optoelectronics (the schematic illustrating (*upper*) and optical image (*bottom*) of eye-like optical imaging system). (D) Flexible GaAs PD arrays for wearable photonics platform (*Left*: the image of the flexible PD mounted on a curved surface; *Right*: the optical microscope image of PD array). (E) The hemispherical electronic eye systems based on origami silicon nanomembrane-based photodiode (*Left*: the schematic illustration of the net of half truncated icosahedron being folded into a hemisphere; *Right*: a photograph of the half truncated icosahedron). (A) Reproduced with permission from. Copyright © 2018. Published under the PNAS license; (B) Reproduced with permission from. Copyright © 2017 WILEY-VCH Verlag GmbH & Co. KGaA, Weinheim; (C) Reproduced with permission from. Copyright © 2008, Macmillan Publishers Limited; (D) Reproduced with permission from. Copyright © 2020 Optical Society of America; (E) Reproduced with permission from. Copyright © 2017, The Author (s).

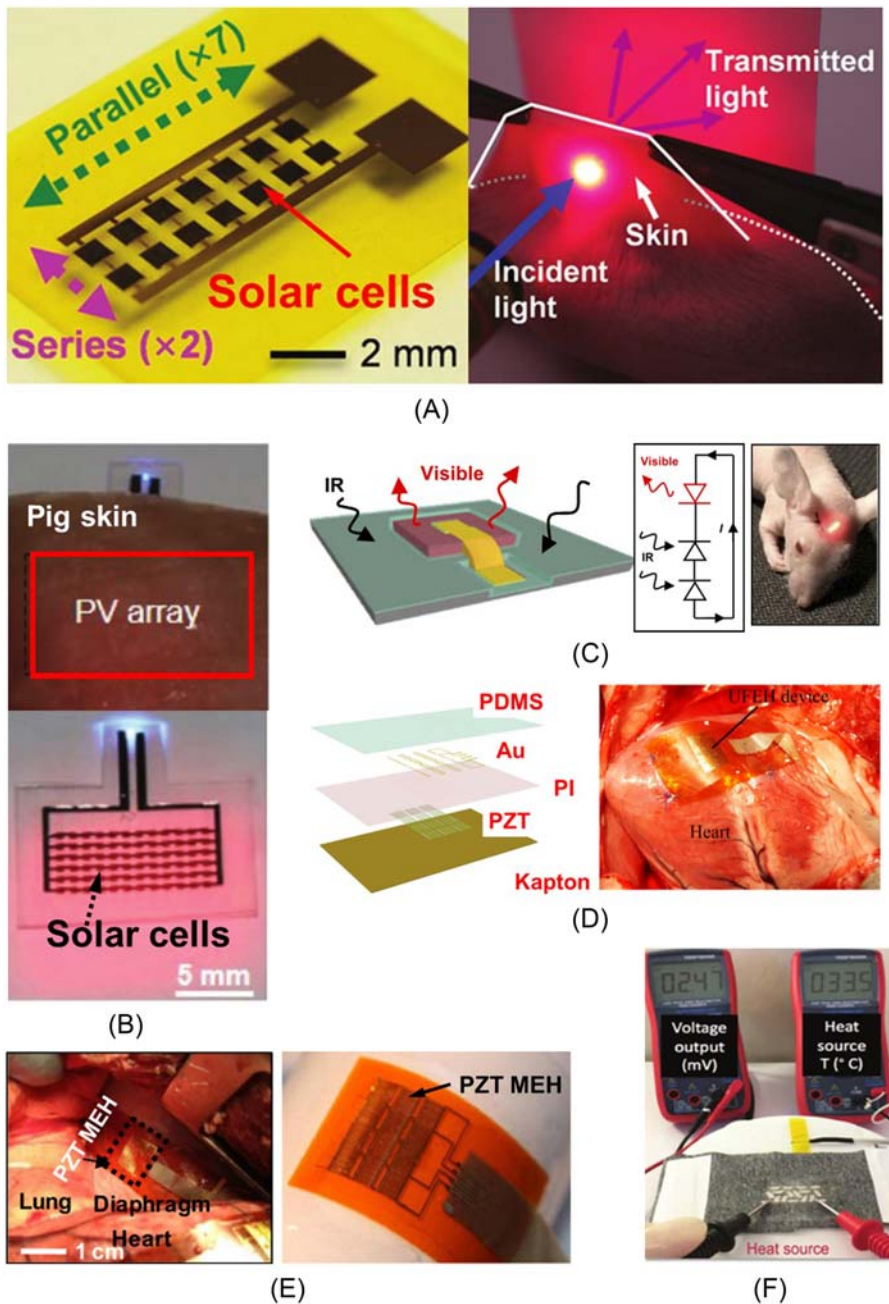


Figure 12.9 Energy-harvesting devices. (A) Implantable solar cell arrays for powering medical electronics (Left: the optical image of solar cell arrays; Right: the schematic illustration of a potential (Continued)

12.3.3 Energy-harvesting devices

Despite significant advances in the area, the power supply is a critical challenge for flexible bioelectronic devices, which require stable operation without behavioral or environmental restrictions. Conventional devices usually use external batteries to provide sufficient and stable power, whose electrical capacities, size, and weight is barriers to further minimization. Various innovative approaches are being proposed for power in bioelectronic devices, using mechanical movement, photovoltaic (PV) conversion, thermoelectric effect, and others. Flexible solar cells have been actively developed as attractive power sources for bioelectronic devices. Song et al. report a flexible solar cell array for powering medical electronics. The schematic illustration of a solar cell is shown in Fig. 12.9A left photo (Song et al., 2016). The dual junction (GaInP: bandgap ≈ 1.8 eV, GaAs: bandgap ≈ 1.4 eV) solar microcells are fabricated and released from the original wafer with an elastomeric stamp (PDMS) and further transferred onto a PI film. To demonstrate the in vivo electrical performances, a solar cell array is implanted into live mouse models. The subdermally solar cell array generates approximately $647 \mu\text{W}$ of direct current power, which can power a custom-built flexible pacemaker. Based on bioresorbable materials, including Si, Mo, and PLGA. As shown in Fig. 12.9B, Lu et al. develop a fully biodegradable, monocrystalline silicon PV platform (Lu, Yang, et al., 2018). Si-solar cells are fabricated on SOI substrate with Mo interconnections and poly (lactic-co-glycolic acid) (PLGA) as an encapsulation layer and released from the silicon wafer by back-side etching. The remaining buried oxide layer underneath the microcells serves as a back biofluid barrier for the array. The Si-solar cell array (including 72 solar cells) can generate $\approx 60 \mu\text{W}$ of electrical power under 4 mm of porcine skin. The solar

application of solar cell arrays that power implantable electronics). (B) Monocrystalline silicon photovoltaic microcells as power supplies for biomedical implants (*Upper*: Si PV array under pig skin and fat; *Bottom*: Si PV array after immersion in PBS solution). (C) The infrared-to-visible upconversion devices as injectable light sources (*Left*: The schematic illustration of the fabricated upconversion device; *Middle*: the operational principle of the upconversion device design; *Right*: the image of a mouse with devices implanted). (D) The ultra-flexible energy harvester (UFEH) based on piezoelectric devices for harvesting the biomechanical energy (*Left*: the schematic illustration of UFEH; *Right*: the image of UFEH mounted between left ventricular apex and right ventricle). (E) The piezoelectric energy harvester integrated with heart, lung, and diaphragm. (F) The thermoelectric generator for body heat harvesting (*Left*: the photograph of a PZT energy harvester on the bovine diaphragm; *Right*: the photograph of the PZT energy harvester). (A) Reproduced with permission from. Copyright © 2016 WILEY-VCH Verlag GmbH & Co. KGaA, Weinheim; (B) Reproduced with permission from. Copyright © 2018 WILEY-VCH Verlag GmbH & Co. KGaA, Weinheim; (C) Reproduced with permission from. Copyright © 2018. Published under the PNAS license; (D) Reproduced with permission from. Copyright © 2015, The Author (s); (E) Reproduced with permission from. Copyright © 2014. Published under the PNAS license; (F) Reproduced with permission from. Copyright © 2019 WILEY-VCH Verlag GmbH & Co. KGaA, Weinheim.

cell array fully dissolves in biofluids after 4 months, and the degradation process introduces no inflammatory responses in the surrounding tissues. These characteristics illustrate the potential for using silicon solar cells as bioresorbable power supplies for various transient biomedical implants (Fig. 12.9).

As shown in Fig. 12.9C, an infrared-to-visible upconversion microscale device is achieved based on the full integration of solar cells and LED (Ding et al., 2018). The upconversion device includes a connected double junction gallium arsenide (GaAs) solar cell and an aluminum gallium indium phosphide (AlGaInP)-based visible LED. GaAs-based solar cell captures low-energy near-infrared photons, providing photogenerated currents and voltages that drive the visible LED. The device is fabricated on GaAs substrates and released by etching sacrificial layer and further can be integrated with various heterogeneous substrates via transfer printing. The encapsulated microscale device can be implanted in the subcutaneous tissue and provides stable, long-term implantable light sources in behavioral animals. This approach provides a feasible route for developing passive wireless implantable light sources.

Mechanical energy is an important source of energy for powering bioelectronics. The human body produces abundant kinetic energy, such as the motion of the heart, and the contraction/relaxation of the diaphragm and lungs. For instance, the cardiac output power is about 1.4 W, which is enough to power many bioelectronic devices. Piezoelectric materials are capable of mechanical-to-electrical energy conversion, which offer practical routes to energy harvesting in vivo. As a common piezoelectric material, lead zirconate titanate (PZT) has already been used to collect biomechanical energy from the motion of the heart, lung, and diaphragm. Dagdeviren et al. report a flexible PZT mechanical energy harvester (Fig. 12.9E) (Dagdeviren et al., 2014). The key functional elements of the energy harvester consist of 12 groups of 10 PZT ribbons transferred onto the PI substrate. In vivo studies demonstrated that PZT energy harvesters enable high-efficiency mechanical-to-electrical energy conversion from the natural contractile and relaxation motions of the heart, lung, and diaphragm. The devices exhibit excellent mechanical and electrical stability. There is no noticeable degradation in the properties after over 20 million bending/releasing cycles in moist environments. Fig. 12.9D shows an ultra-flexible PZT energy harvester used to harvest biomechanical energy from heart motions (Lu et al., 2015). The brittle piezoelectric film with high piezoelectric coefficients is integrated onto the extremely soft PI substrate via transfer printing technology. The PZT energy harvester is implanted in pigs under different conditions, such as with an open or closed chest, or awake or under anesthesia. The output voltage can be up to 3 V, which is approximately the same as the required value for biomedical implants.

Body heat can be an inexhaustible source of energy during the lifespan of a person because the core body temperature is regulated at 37°C. The total heat dissipated from the whole human body is approximately 60–180 W depending on body activity (Riemer & Shapiro, 2011), which is a very attractive energy source.

Thus, thermoelectric generators have attracted the attention of academic researchers. Elmoughni et al. report a textile-integrated thermoelectric generator for body heat harvesting to power wearable electronics (Elmoughni et al., 2019). A 32-leg device with a modest fill factor ($\approx 30\%$) is fabricated on a commercial sports fabric substrate via stencil and transfer printing techniques (shown in Fig. 12.9F). The textile-integrated thermoelectric generator yields an open circuit voltage of ≈ 3 mV at $\Delta T = 3$ K (Elmoughni et al., 2019). The fabrication technology offers new opportunities for advancing thermoelectric material integration into clothing.

12.3.4 Bioresorbable materials and devices

Biodegradable electronics that can partially or completely decompose, dissolve, degrade, resorb or physically disappear into physiological or environmental solutions in a well-regulated way, after the desired lifetime, thereby eliminating the costs, complications, and risks associated with secondary surgical procedures for device retrieval (Choi et al., 2020; Li et al., 2018; Rajaram et al., 2022; Singh et al., 2000). This chapter focus on inorganic bioresorbable electronic systems in biomedicine fabricated by transferring printing technology. Compared to organic materials, inorganics offer excellent electrical performance. Inorganic biodegradable materials include monocrystalline silicon (mono-Si), polycrystalline silicon (poly-Si), amorphous silicon (a-Si), germanium (Ge), silicon germanium alloy (SiGe), indium–gallium–zinc oxide (a-IGZO), and zinc oxide (ZnO) for semiconductors; magnesium (Mg), molybdenum (Mo), tungsten (W), iron (Fe), and zinc (Zn) for conductive materials; and magnesium oxide (MgO), silicon dioxide (SiO₂), and silicon nitride (SiN_x) for dielectric materials (Li et al., 2018). Biodegradable electronics have been made for a variety of biomedical applications, such as biomedical sensors, stimulators, and photonic devices. Fig. 12.10A shows the representative flexible biodegradable circuit based on dissolvable inorganic silicon-based CMOS, including transistors made by Si/MgO/Mg, diodes made by Si, and inductors and capacitors made by Mg/MgO, as well as resistor and connection wires made by Mg. Si-based COMS is the key component of the electronics, which is fabricated on an SOI wafer and transferred onto a silk substrate (Hwang et al., 2012). All of the components, including inductors, capacitors, resistors, diodes, transistors, interconnects, substrates, and encapsulation layers, disintegrate and dissolve over controlled periods when immersed in deionized (DI) water (Fig. 12.10).

Various transient sensors fabricated by inorganic biodegradable materials are proposed. As shown in Fig. 12.10B (Hwang et al., 2015), The transient stretchable pH sensors are built using doped Si nanoribbons via transfer printing technology. Mg serves as the electrodes and interconnects, and SiO₂ serves as the interlayer dielectrics and encapsulants. Studies show that dissolve kinetics depend strongly on temperature, pH, and ionic content/concentration of solutions, as well as the morphologies of the materials. Kang et al. report a biodegradable pressure sensor based on the piezoresistive

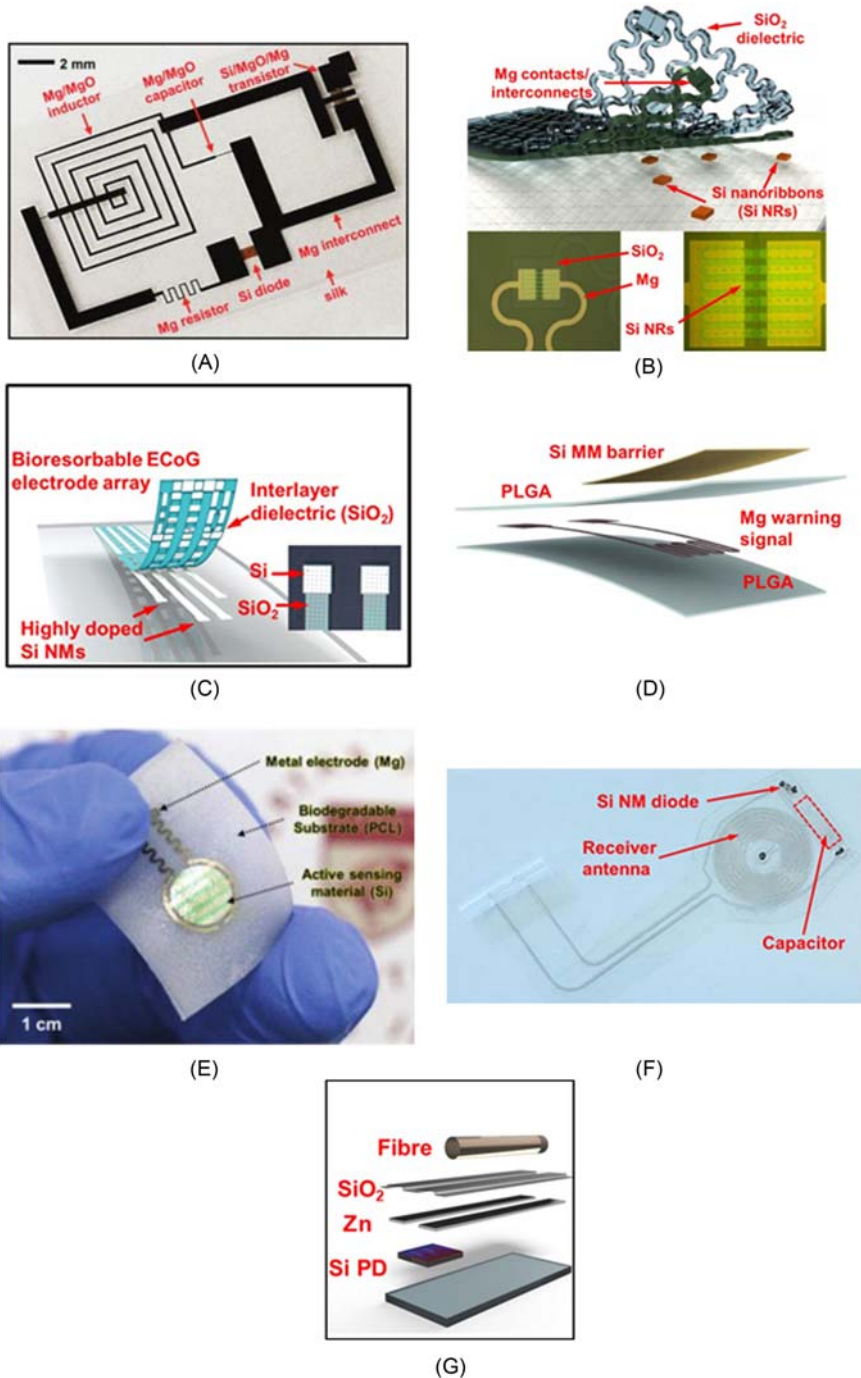


Figure 12.10 Bioreabsorbable materials and devices. (A) The transient electronics platform: includes transistors, diodes, capacitors, and resistors. (B) The transient electronics and biosensors based on (Continued)

Si nanomembrane (Kang et al., 2016). Si nanomembrane is formed on SOI wafer and then transferred onto poly (lactic-*co*-glycolic acid) (PLGA) substrate. The resistance of this sensing element increases monotonically in a linear fashion across the full range of pressures that are relevant to intracranial monitoring (that is, 0–70 mmHg). Monocrystalline silicon nanomembrane array can also be used to fabricate ECoG electrodes, as shown in Fig. 12.10C (Yu et al., 2016). In vivo studies confirm the capability for recording electrophysiological signals from the cortical surface and the subgaleal space. The devices detect normal physiologic and epileptiform activity, both in acute and chronic recordings. Yang et al. report a sensor for the onset of water penetration. The failure of implanted electronic devices mostly starts from water penetration. Evaluating water penetration can be extremely useful in cases where the encapsulation unexpectedly fails for implantable electronics. A schematic illustration of water penetration is shown in Fig. 12.10D (Yang et al., 2020). the addition of an Mg resistor at the middle position of the PLGA layer underneath the Si micromembranes (MMs) can serve as a sensor for water penetration. Si MM is fabricated on SOI substrate and transferred onto PLGA as an encapsulation layer. The studies show that the sudden increase in Mg resistance can reflect water penetration. A transient electrochemical sensor is shown in Fig. 12.10E (Kim et al., 2018). Ultrathin monocrystalline silicon nanomembranes coated with iron (Fe)-containing nanoparticles (NPs) as a catalyst serve as active sensing elements for continuous, real-time monitoring of dopamine secretion, which is integrated with biodegradable polycaprolactone substrate via transfer printing. All of the materials are gradually hydrolyzed or dissolved in the PBS (pH 11, 37°C) via reactive diffusion, and most of the components disappear in ≈ 15 hours. Dissolution rates can be adjusted by pH, temperature, and ionic contents and concentrations of solutions.

← biodegradable silicon nanomembranes; *Upper*: the exploded view schematic illustration of the device; *Bottom*: the optical microscope image of an individual pH sensor (*left*) and its magnified view. (C) The bioresorbable neural electrode array for ECoG and subdermal EEG measurements based on silicon electronics. (D) The bioresorbable sensor for the onset of water penetration in the intracranial space. (E) The transient electrochemical sensor based on silicon nanomembranes. (F) The bioresorbable electronic neuro regenerative medical device. (G) The transient photonic platform for the continuous monitoring of cerebral temperature, oxygenation and neural activity in freely moving mice. (A) Reproduced with permission from. Copyright © 2012, American Association for the Advancement of Science; (B) Reproduced with permission from. Copyright © 2015 American Chemical Society; (C) Reproduced with permission from. Copyright © 2016, Nature Publishing Group; (D) Reproduced with permission from. Copyright © 2020 WILEY-VCH Verlag GmbH & Co. KGaA, Weinheim; (E) Reproduced with permission from. Copyright © 2018 WILEY-VCH Verlag GmbH & Co. KGaA, Weinheim; (F) Reproduced with permission from. Copyright © 2018, The Author (s), under exclusive licence to Springer Nature America, Inc; (G) Reproduced with permission from. Copyright © 2019, The Author (s), under exclusive licence to Springer Nature Limited.

Koo et al. report a bioresorbable, wireless electrical stimulator used as an electronic neuro-regenerative medical device (shown in Fig. 12.10F) (Koo et al., 2018). The stimulator includes a loop antenna made of Mg, a RF diode made of silicon nano-membrane with electrodes of Mg, a parallel plate capacitor made of Mg/SiO₂/Mg, and a stimulation electrode made of Mg or Mo strip. In vivo experiments demonstrate that electrical stimulation enables enhances and accelerates neuron functional recovery.

Implantable biodegradable photonic devices are composed for the spectroscopic characterization of targeted tissues and biofluids. As shown in Fig. 12.10G (Bai et al., 2019), the devices incorporate a collection of bioresorbable optical components which are heterogeneously integrated into PLGA fiber via the transfer printing method, including single-junction PDs based on Si nanomembranes; foundry-produced tri-color PDs based on tri-layer stacks of Si P–N junctions; optical multilayer filters of SiO_x and SiN_y. The devices are implanted into deep brain regions of freely moving mice for continuous absorption spectroscopic analysis of biochemical and physiological status.

12.4 Conclusion

This chapter provides an overview of heterogeneously integrated inorganic materials and devices for biomedical applications. Diverse and disparate classes of materials and functional devices, including metals, oxides, semiconductors, 2D materials, biomaterials, optoelectronics, energy-harvesting devices, and bioresorbable materials and devices, can be assembled into single and multifunctional systems. Such materials and functional devices can serve a variety of roles in bioelectronic devices, such as electrodes, antennae, heat sinkers, sensors, stimulators, and energy harvesters. Transfer printing is a highly versatile technique for the heterogeneous integration of bioelectronic devices with other components and circuits in 2D and 3D layouts. This technology enables the cointegration of a broad spectrum of materials regardless of conditions for their growth, deposition, or patterning, and thereby maximizes their performance and cost-effectiveness or imparts novel hybrid functionalities. More and more multifunctional bioelectronic devices will be developed via transfer printing technology. These multifunctional bioelectronic devices can provide unprecedented advantages in healthcare applications.

References

- Armstrong, C., Krook-Magnuson, E., Oijala, M., & Soltesz, I. (2013). Closed-loop optogenetic intervention in mice. *Nature Protocols*, 8(8), 1475–1493. Available from <https://doi.org/10.1038/nprot.2013.080>.
- Bai, W., Shin, J., Fu, R., Kandela, I., Lu, D., Ni, X., Park, Y., Liu, Z., Hang, T., Wu, D., Liu, Y., Haney, C. R., Stepien, I., Yang, Q., Zhao, J., Nandoliya, K. R., Zhang, H., Sheng, X., Yin, L., . . . Rogers, J. A. (2019). Bioresorbable photonic devices for the spectroscopic characterization of physiological status and neural activity. *Nature Biomedical Engineering*, 3(8), 644–654. Available from <https://doi.org/10.1038/s41551-019-0435-y>, <http://www.nature.com/natbiomedeng/>.

- Behl, M., & Lendlein, A. (2007). Shape-memory polymers. *Materials Today*, 10(4), 20–28. Available from [https://doi.org/10.1016/S1369-7021\(07\)70047-0](https://doi.org/10.1016/S1369-7021(07)70047-0).
- Bendali, A., Rousseau, L., Lissorgues, G., Scorsone, E., Djilas, M., Dégardin, J., Dubus, E., Fouquet, S., Benosman, R., Bergonzo, P., Sahel, J. A., & Picaud, S. (2015). Synthetic 3D diamond-based electrodes for flexible retinal neuroprostheses: Model, production and in vivo biocompatibility. *Biomaterials*, 67, 73–83. Available from <https://doi.org/10.1016/j.biomaterials.2015.07.018>, <http://www.journals.elsevier.com/biomaterials/>.
- Cao, Y., Wang, S., Lv, J., Li, F., Liang, Q., Yang, M., Ma, X., Wang, H., & Hao, Y. (2022). Fully physically transient volatile memristor based on Mg/magnesium oxide for biodegradable neuromorphic electronics. *IEEE Transactions on Electron Devices*, 69(6), 3118–3123. Available from <https://doi.org/10.1109/TED.2022.3166868>, <https://ieeexplore.ieee.org/xpl/mostRecentIssue.jsp?punumber=16>.
- Carlson, A., Bowen, A. M., Huang, Y., Nuzzo, R. G., & Rogers, J. A. (2012). Transfer printing techniques for materials assembly and micro/nanodevice fabrication. *Advanced Materials*, 24(39), 5284–5318. Available from <https://doi.org/10.1002/adma.201201386>.
- Chen, Y., Zhang, Y., Liang, Z., Cao, Y., Han, Z., & Feng, X. (2020). Flexible inorganic bioelectronics. *Npj Flexible Electronics*.
- Choi, Y., Koo, J., & Rogers, J. A. (2020). Inorganic materials for transient electronics in biomedical applications. *MRS Bulletin*, 45(2), 103–112. Available from <https://doi.org/10.1557/mrs.2020.25>, <http://journals.cambridge.org/MRS>.
- Choi, C., Lee, Y., Cho, K. W., Koo, J. H., & Kim, D. H. (2019). Wearable and implantable soft bioelectronics using two-dimensional materials. *Accounts of Chemical Research*, 52(1), 73–81. Available from <https://doi.org/10.1021/acs.accounts.8b00491>, <https://doi.org/10.1021/acs.accounts.8b00491>.
- Corbett, B., Loi, R., Zhou, W., Liu, D., & Ma, Z. (2017). Transfer print techniques for heterogeneous integration of photonic components. *Progress in Quantum Electronics*, 52, 1–17. Available from <https://doi.org/10.1016/j.pquantelec.2017.01.001>.
- Coyer, S. R., García, A. J., & Delamarche, E. (2007). Facile preparation of complex protein architectures with sub-100-nm resolution on surfaces. *Angewandte Chemie - International Edition*, 46(36), 6837–6840. Available from <https://doi.org/10.1002/anie.200700989>.
- Dagdeviren, C., Yang, B. D., Su, Y., Tran, P. L., Joe, P., Anderson, E., Xia, J., Doraiswamy, V., Dehdashti, B., Feng, X., Lu, B., Poston, R., Khalpey, Z., Ghaffari, R., Huang, Y., Slepian, M. J., & Rogers, J. A. (2014). Conformal piezoelectric energy harvesting and storage from motions of the heart, lung, and diaphragm. *Proceedings of the National Academy of Sciences*, 111(5), 1927–1932. Available from <https://doi.org/10.1073/pnas.1317233111>.
- Ding, H., Lu, L., Shi, Z., Wang, D., Li, L., Li, X., Ren, Y., Liu, C., Cheng, D., Kim, H., Giebink, N. C., Wang, X., Yin, L., Zhao, L., Luo, M., & Sheng, X. (2018). Microscale optoelectronic infrared-to-visible upconversion devices and their use as injectable light sources. *Proceedings of the National Academy of Sciences*, 115(26), 6632–6637. Available from <https://doi.org/10.1073/pnas.1802064115>.
- Elmoughni, H. M., Menon, A. K., Wolfe, R. M., & Yee, S. K. (2019). A textile-integrated polymer thermoelectric generator for body heat harvesting. *Advanced Materials Technologies*, 2019(7).
- Fallegger, F., Schiavone, G., & Lacour, S. P. (1903). Conformable hybrid systems for implantable bioelectronic interfaces. *Advanced Materials*, 2020(15).
- Fang, H., Zhao, J., Yu, K. J., Song, E., Farimani, A. B., Chiang, C. H., Jin, X., Xue, Y., Xu, D., Du, W., Seo, K. J., Zhong, Y., Yang, Z., Won, S. M., Fang, G., Choi, S. W., Chaudhuri, S., Huang, Y., Alam, M. A., . . . Rogers, J. A. (2016). Ultrathin, transferred layers of thermally grown silicon dioxide as biofluid barriers for biointegrated flexible electronic systems. *Proceedings of the National Academy of Sciences of the United States of America*, 113(42), 11682–11687. Available from <https://doi.org/10.1073/pnas.1605269113>, <http://www.pnas.org/content/113/42/11682.full.pdf>.
- Fan, B., Rusinek, C. A., Thompson, C. H., Setien, M., Guo, Y., Rechenberg, R., Gong, Y., Weber, A. J., Becker, M. F., & Purcell, E. (2020). Flexible, diamond-based microelectrodes fabricated using the diamond growth side for neural sensing. *Microsystems & Nanoengineering*, 2020(1), 1–12.
- Feron, K., Lim, R., Sherwood, C., Keynes, A., Brichta, A., & Dastoor, P. C. (2018). Organic bioelectronics: Materials and biocompatibility. *International Journal of Molecular Sciences*, 19(8). Available from <https://doi.org/10.3390/ijms19082382>, <http://www.mdpi.com/journal/ijms>.

- Grosenick, L., Marshel, J. H., & Deisseroth, K. (2015). Closed-loop and activity-guided optogenetic control. *Neuron*, *86*(1), 106–139. Available from <https://doi.org/10.1016/j.neuron.2015.03.034>, <http://www.cell.com/neuron/home>.
- Gutruf, P., & Rogers, J. A. (2018). Implantable, wireless device platforms for neuroscience research. *Current Opinion in Neurobiology*, *50*, 42–49. Available from <https://doi.org/10.1016/j.conb.2017.12.007>, <http://www.elsevier.com/locate/conb>.
- Hess, A. E., Sabens, D. M., Martin, H. B., & Zorman, C. A. (2011). Diamond-on-polymer microelectrode arrays fabricated using a chemical release transfer process. *Journal of Microelectromechanical Systems*, *20*(4), 867–875. Available from <https://doi.org/10.1109/JMEMS.2011.2159099>.
- He, P., Peng, Y., & Lin, L. (2021). A multimodal self-healing flexible sensor for healthcare monitoring. In *Proceedings of the IEEE international conference on micro electro mechanical systems (MEMS)*. Institute of Electrical and Electronics Engineers Inc., United States, pp. 517–520. 9781665419123. 10.1109/MEMS51782.2021.9375234.
- Hong, N., Chu, R. J., Kang, S. S., Ryu, G., Han, J.-H., Yu, K. J., Jung, D., & Choi, W. J. (2020). Flexible GaAs photodetector arrays hetero-epitaxially grown on GaP/Si for a low-cost III-V wearable photonics platform. *Optics Express*, *2020*(24), 36559–36567.
- Hwang, S. W., Lee, C. H., Cheng, H., Jeong, J. W., Kang, S. K., Kim, J. H., Shin, J., Yang, J., Liu, Z., Ameer, G. A., Huang, Y., & Rogers, J. A. (2015). Biodegradable elastomers and silicon nanomembranes/nanoribbons for stretchable, transient electronics, and biosensors. *Nano Letters*, *15*(5), 2801–2808. Available from <https://doi.org/10.1021/nl503997m>, <http://pubs.acs.org/journal/nalefd>.
- Hwang, S. W., Tao, H., Kim, D. H., Cheng, H., Song, J. K., Rill, E., Brenckle, M. A., Panilaitis, B., Won, S. M., Kim, Y. S., Song, Y. M., Yu, K. J., Ameen, A. A., Li, R., Su, Y., Yang, M., Kaplan, D. L., Zakin, M. R., Slepian, M. J., . . . Rogers, J. A. (2012). A physically transient form of silicon electronics. *Science (New York, N.Y.)*, *337*(6102), 1640–1644. Available from <https://doi.org/10.1126/science.1226325>, <http://www.sciencemag.org/content/337/6102/1640.full.pdf>.
- Jeong, J. W., McCall, J. G., Shin, G., Zhang, Y., Al-Hasani, R., Kim, M., Li, S., Sim, J. Y., Jang, K. I., Shi, Y., Hong, D. Y., Liu, Y., Schmitz, G. P., Xia, L., He, Z., Gamble, P., Ray, W. Z., Huang, Y., Bruchas, M. R., & Rogers, J. A. (2015). Wireless optofluidic systems for programmable in vivo pharmacology and optogenetics. *Cell*, *162*(3), 662–674. Available from <https://doi.org/10.1016/j.cell.2015.06.058>, <https://www.sciencedirect.com/journal/cell>.
- Jin, S. H., Kang, S. K., Cho, I. T., Han, S. Y., Chung, H. U., Lee, D. J., Shin, J., Baek, G. W., Kim, T. I., Lee, J. H., & Rogers, J. A. (2015). Water-soluble thin film transistors and circuits based on amorphous indium-gallium-zinc oxide. *ACS Applied Materials and Interfaces*, *7*(15), 8268–8274. Available from <https://doi.org/10.1021/acsami.5b00086>, <http://pubs.acs.org/journal/aamick>.
- Kang, S. K., Murphy, R. K. J., Hwang, S. W., Lee, S. M., Harburg, D. V., Krueger, N. A., Shin, J., Gamble, P., Cheng, H., Yu, S., Liu, Z., McCall, J. G., Stephen, M., Ying, H., Kim, J., Park, G., Webb, R. C., Lee, C. H., Chung, S., . . . Rogers, J. A. (2016). Bioresorbable silicon electronic sensors for the brain. *Nature*, *530*(7588), 71–76. Available from <https://doi.org/10.1038/nature16492>, <http://www.nature.com/nature/index.html>.
- Kathe, C., Michoud, F., Schönle, P., Rowald, A., Brun, N., Ravier, J., Furfaro, I., Paggi, V., Kim, K., Soloukey, S., Asboth, L., Hutson, T. H., Jelescu, I., Philippides, A., Alwahab, N., Gandar, J., Huber, D., De Zeeuw, C. I., Barraud, Q., . . . Courtine, G. (2022). Wireless closed-loop optogenetics across the entire dorsoventral spinal cord in mice. *Nature Biotechnology*, *40*(2), 198–208. Available from <https://doi.org/10.1038/s41587-021-01019-x>, <http://www.nature.com/nbt/index.html>.
- Khang, D. Y., Jiang, H., Huang, Y., & Rogers, J. A. (2006). A stretchable form of single-crystal silicon for high-performance electronics on rubber substrates. *Science (New York, N.Y.)*, *311*(5758), 208–212. Available from <https://doi.org/10.1126/science.1121401>.
- Kim, Y. S., Basir, A., Herbert, R., Kim, J., Yoo, H., & Yeo, W. H. (2020). Soft materials, stretchable mechanics, and optimized designs for body-wearable compliant antennas. *ACS Applied Materials and Interfaces*, *12*(2), 3059–3067. Available from <https://doi.org/10.1021/acsami.9b20233>, <http://pubs.acs.org/journal/aamick>.
- Kim, D. H., Lu, N., Ma, R., Kim, Y. S., Kim, R. H., Wang, S., Wu, J., Won, S. M., Tao, H., Islam, A., Yu, K. J., Kim, T. I., Chowdhury, R., Ying, M., Xu, L., Li, M., Chung, H. J., Keum, H.,

- McCormick, M., ... Rogers, J. A. (2011). Epidermal electronics. *Science (New York, N.Y.)*, 333(6044), 838–843. Available from <https://doi.org/10.1126/science.1206157>, <http://www.sciencemag.org/content/333/6044/838.full.pdf>, United States.
- Kim, T. I., McCall, J. G., Jung, Y. H., Huang, X., Siuda, E. R., Li, Y., Song, J., Song, Y. M., Pao, H. A., Kim, R. H., Lu, C., Lee, S. D., Song, I. S., Shin, G., Al-Hasani, R., Kim, S., Tan, M. P., Huang, Y., Omenetto, F. G., ... Bruchas, M. R. (2013). Injectable, cellular-scale optoelectronics with applications for wireless optogenetics. *Science (New York, N.Y.)*, 340(6129), 211–216. Available from <https://doi.org/10.1126/science.1232437>, <http://www.sciencemag.org/content/340/6129/211.full.pdf>.
- Kim, Y., Suh, J. M., Shin, J., Liu, Y., Yeon, H., Qiao, K., Kum, H. S., Kim, C., Lee, H. E., Choi, C., Kim, H., Lee, D., Lee, J., Kang, J. H., Park, B. I., Kang, S., Kim, J., Kim, S., Perozek, J. A., ... Kim, J. (2022). Chip-less wireless electronic skins by remote epitaxial freestanding compound semiconductors. *Science (New York, N.Y.)*, 377(6608), 859–864. Available from <https://doi.org/10.1126/science.abn7325>, <https://www.science.org/doi/10.1126/science.abn7325>.
- Kim, H. S., Yang, S. M., Jang, T. M., Oh, N., Kim, H. S., & Hwang, S. W. (2018). Bioresorbable silicon nanomembranes and iron catalyst nanoparticles for flexible, transient electrochemical dopamine monitors. *Advanced Healthcare Materials*, 7(24). Available from <https://doi.org/10.1002/adhm.201801071>, [https://onlinelibrary.wiley.com/journal/10.1002/\(ISSN\)2192-2659](https://onlinelibrary.wiley.com/journal/10.1002/(ISSN)2192-2659).
- Koo, J., MacEwan, M. R., Kang, S. K., Won, S. M., Stephen, M., Gamble, P., Xie, Z., Yan, Y., Chen, Y. Y., Shin, J., Birenbaum, N., Chung, S., Kim, S. B., Khalifeh, J., Harburg, D. V., Bean, K., Paskett, M., Kim, J., Zohny, Z. S., ... Rogers, J. A. (2018). Wireless bioresorbable electronic system enables sustained nonpharmacological neuroregenerative therapy. *Nature Medicine*, 24(12), 1830–1836. Available from <https://doi.org/10.1038/s41591-018-0196-2>, <http://www.nature.com/nm/index.html>.
- Ko, H. C., Stoykovich, M. P., Song, J., Malyarchuk, V., Choi, W. M., Yu, C. J., Geddes, J. B., Xiao, J., Wang, S., Huang, Y., & Rogers, J. A. (2008). A hemispherical electronic eye camera based on compressible silicon optoelectronics. *Nature*, 454(7205), 748–753. Available from <https://doi.org/10.1038/nature07113>, <http://www.nature.com/nature/index.html>.
- Kuzum, D., Takano, H., Shim, E., Reed, J. C., Juul, H., Richardson, A. G., De Vries, J., Bink, H., Dichter, M. A., Lucas, T. H., Coulter, D. A., Cubukcu, E., & Litt, B. (2014). Transparent and flexible low noise graphene electrodes for simultaneous electrophysiology and neuroimaging. *Nature Communications*, 5. Available from <https://doi.org/10.1038/ncomms6259>, <http://www.nature.com/ncomms/index.html>.
- Lee, H., Choi, T. K., Lee, Y. B., Cho, H. R., Ghaffari, R., Wang, L., Choi, H. J., Chung, T. D., Lu, N., Hyeon, T., Choi, S. H., & Kim, D. H. (2016). A graphene-based electrochemical device with thermoresponsive microneedles for diabetes monitoring and therapy. *Nature Nanotechnology*, 11(6), 566–572. Available from <https://doi.org/10.1038/nnano.2016.38>, <http://www.nature.com/nnano/index.html>.
- Lee, K. J., Koo, J., & Park. (2012). Biointegrated flexible inorganic light emitting diodes. *Nanobiosensors in Disease Diagnosis*, 5. Available from <https://doi.org/10.2147/NDD.S26593>.
- Lee, H., Lee, J., Kim, S., & Lee, D. (2022). Implantable micro-light-emitting diode (μ LED)-based optogenetic interfaces toward human applications. *Advanced Drug Delivery Reviews*, 187.
- Lee, W. S., Sunkara, V., Han, J. R., Park, Y. S., & Cho, Y. K. (2015). Electrospun TiO₂ nanofiber integrated lab-on-a-disc for ultrasensitive protein detection from whole blood. *Lab on a Chip*, 15(2), 478–485. Available from <https://doi.org/10.1039/c4lc00900b>, <http://pubs.rsc.org/en/journals/journal/lc>.
- Liao, F., Zhu, Z., Yan, Z., Yao, G., Huang, Z., Gao, M., Pan, T., Zhang, Y., Li, Q., & Feng, X. (2017). Ultrafast response flexible breath sensor based on vanadium dioxide. *Journal of Breath Research*, 2017(3).
- Lim, S., Son, D., Kim, J., Lee, Y. B., Song, J. K., Choi, S., Lee, D. J., Kim, J. H., Lee, M., Hyeon, T., & Kim, D. H. (2015). Transparent and stretchable interactive human machine interface based on patterned graphene heterostructures. *Advanced Functional Materials*, 25(3), 375–383. Available from <https://doi.org/10.1002/adfm.201402987>, [http://onlinelibrary.wiley.com/journal/10.1002/\(ISSN\)1616-3028](http://onlinelibrary.wiley.com/journal/10.1002/(ISSN)1616-3028).
- Lin, J., Peng, Z., Liu, Y., Ruiz-Zepeda, F., Ye, R., Samuel, E. L. G., Yacaman, M. J., Yakobson, B. I., & Tour, J. M. (2014). Laser-induced porous graphene films from commercial polymers. *Nature Communications*, 5. Available from <https://doi.org/10.1038/ncomms6714>, <http://www.nature.com/ncomms/index.html>.

- Li, K., Chang, T. H., Li, Z., Yang, H., Fu, F., Li, T., Ho, J. S., & Chen, P. Y. (2019). Biomimetic MXene textures with enhanced light-to-heat conversion for solar steam generation and wearable thermal management. *Advanced Energy Materials*, 2019(34), 1901.
- Li, L., Lu, L., Ren, Y., Tang, G., Zhao, Y., Cai, X., Shi, Z., Ding, H., Liu, C., & Cheng, D. (2022). Colocalized, bidirectional optogenetic modulations in freely behaving mice with a wireless dual-color optoelectronic probe. *Nature Communications*, 2022(1), 1–14.
- Li, L., Tang, G., Shi, Z., Ding, H., Liu, C., Cheng, D., Zhang, Q., Yin, L., Yao, Z., & Duan, L. (2021). Transfer-printed, tandem microscale light-emitting diodes for full-color displays. *Proceedings of the National Academy of Sciences*, 2021(18).
- Li, R., Wang, L., & Yin, L. (2018). Materials and devices for biodegradable and soft biomedical electronics. *Materials*, 2018(11).
- Li, H., Xu, Y., Li, X., Chen, Y., Jiang, Y., Zhang, C., Lu, B., Wang, J., Ma, Y., Chen, Y., Huang, Y., Ding, M., Su, H., Song, G., Luo, Y., & Feng, X. (2017). Epidermal inorganic optoelectronics for blood oxygen measurement. *Advanced Healthcare Materials*, 6(9), 1601013. Available from <https://doi.org/10.1002/adhm.201601013>.
- Lu, B., Chen, Y., Ou, D., Chen, H., Diao, L., Zhang, W., Zheng, J., Ma, W., Sun, L., & Feng, X. (2015). Ultra-flexible piezoelectric devices integrated with heart to harvest the biomechanical energy. *Scientific Reports*, 2015(1), 1–9.
- Lu, L., Gutruf, P., Xia, L., Bhatti, D. L., Wang, X., Vazquez-Guardado, A., Ning, X., Shen, X., Sang, T., Ma, R., Pakeltis, G., Sobczak, G., Zhang, H., Seo, Do, Xue, M., Yin, L., Chanda, D., Sheng, X., Bruchas, M. R., & Rogers, J. A. (2018). Wireless optoelectronic photometers for monitoring neuronal dynamics in the deep brain. *Proceedings of the National Academy of Sciences of the United States of America*, 115(7), E1374–E1383. Available from <https://doi.org/10.1073/pnas.1718721115>, <http://www.pnas.org/content/pnas/115/7/E1374.full.pdf>.
- Lu, L., Yang, Z., Meacham, K., Cvetkovic, C., Corbin, E. A., Vázquez-Guardado, A., Xue, M., Yin, L., Boroumand, J., Pakeltis, G., Sang, T., Yu, K. J., Chanda, D., Bashir, R., Gereau, R. W., Sheng, X., & Rogers, J. A. (2018). Biodegradable monocrystalline silicon photovoltaic microcells as power supplies for transient biomedical implants. *Advanced Energy Materials*, 8(16), 1703035, Article 201703035. Available from <https://doi.org/10.1002/aenm.201703035>.
- Mannoor, M. S., Tao, H., Clayton, J. D., Sengupta, A., Kaplan, D. L., Naik, R. R., Verma, N., Omenetto, F. G., & McAlpine, M. C. (2012). Graphene-based wireless bacteria detection on tooth enamel. *Nature Communications*, 2012(1), 1–9.
- Moreno, S., Keshkar, J., Rodriguez-Davila, R. A., Bazaid, A., Ibrahim, H., Rodriguez, B. J., Quevedo-Lopez, M. A., & Minary-Jolandan, M. (2020). Bioelectronics on mammalian collagen. *Advanced Electronic Materials*, 6(8), Article 202000391. Available from <https://doi.org/10.1002/aelm.202000391>.
- Mostafalu, P., Nezhad, A. S., Nikkhah, M., & Akbari, M. (2016). *Flexible electronic devices for biomedical applications* (pp. 341–366). Springer Science and Business Media LLC. Available from 10.1007/978-3-319-32180-6_16.
- Park, M., Park, Y. J., Chen, X., Park, Y. K., Kim, M. S., & Ahn, J. H. (2016). MoS₂-based tactile sensor for electronic skin applications. *Advanced Materials*, 28(13), 2556–2562. Available from <https://doi.org/10.1002/adma.201505124>, <http://www3.interscience.wiley.com/journal/119030556/issue>.
- Pham, T. A., Nguyen, T. K., Vadivelu, R. K., Dinh, T., Qamar, A., Yadav, S., Yamauchi, Y., Rogers, J. A., Nguyen, N. T., & Phan, H. P. (2020). A versatile sacrificial layer for transfer printing of wide bandgap materials for implantable and stretchable bioelectronics. *Advanced Functional Materials*, 30(43), Article 202004655. Available from <https://doi.org/10.1002/adfm.202004655>.
- Rajaram, K., Yang, S. M., & Hwang, S.-W. (2022). Transient, biodegradable energy systems as a promising power solution for ecofriendly and implantable electronics. *Advanced Energy and Sustainability Research*, 2022, 2100.
- Renault, J. P., Bernard, A., Juncker, D., Michel, B., Bosshard, H. R., & Delamarque, E. (2002). Fabricating microarrays of functional proteins using affinity contact printing. *Angewandte Chemie - International Edition*, 41(13), 2320–2323. Available from [https://doi.org/10.1002/1521-3773\(20020703\)41:13 < 2320::AID-ANIE2320 > 3.0.CO;2-Z](https://doi.org/10.1002/1521-3773(20020703)41:13 < 2320::AID-ANIE2320 > 3.0.CO;2-Z).

- Riemer, R., & Shapiro, A. (2011). Biomechanical energy harvesting from human motion: theory, state of the art, design guidelines, and future directions. *Journal of Neuroengineering and Rehabilitation*, 8(1), 22. Available from <https://doi.org/10.1186/1743-0003-8-22>.
- Rogers, J. A., Ghaffari, R., & Kim, D. H. (2016). *Stretchable bioelectronics for medical devices and systems microsystems and nanosystems*. Springer International Publishing. Available from 10.1007/978-3-319-28694-5.
- Schiele, N. R., Corr, D. T., Huang, Y., Raof, N. A., Xie, Y., & Chrisey, D. B. (2010). Laser-based direct-write techniques for cell printing. *Biofabrication*, 2(1), 012001.
- Shin, G., Gomez, A. M., Al-Hasani, R., Jeong, Y. R., Kim, J., Xie, Z., Banks, A., Lee, S. M., Han, S. Y., & Yoo, C. J. (2017). Flexible near-field wireless optoelectronics as subdermal implants for broad applications in optogenetics. *Neuron*, 94(3), 509–521.
- Shin, J., Liu, Z., Bai, W., Liu, Y., Yan, Y., Xue, Y., Kandela, I., Pezhouh, M., MacEwan, M. R., & Huang, Y. (2019). Bioresorbable optical sensor systems for monitoring of intracranial pressure and temperature. *Science Advances*, 5(11), eaar1111.
- Sim, K., Rao, Z., Li, Y., Yang, D., & Yu, C. (2018). Curvy surface conformal ultra-thin transfer printed Si optoelectronic penetrating microprobe arrays. *NPJ Flexible Electronics*, 2(1), 1–6.
- Singh, R., Bathaei, M. J., Istif, E., & Beker, L. (2000). A review of bioresorbable implantable medical devices: materials, fabrication, and implementation. *Advanced Healthcare Materials*, 1(18), 1811–1822.
- Solis, D. J., Coyer, S. R., García, A. J., & Delamarche, E. (2010). Large-scale arrays of aligned single viruses. *Advanced Materials*, 22(1), 111–114. Available from <https://doi.org/10.1002/adma.200902086Switzerland>, <http://www3.interscience.wiley.com/cgi-bin/fulltext/122589009/PDFSTART>.
- Song, E., Chiang, C. H., Li, R., Jin, X., Zhao, J., Hill, M., Xia, Y., Li, L., Huang, Y., Won, S. M., Yu, K. J., Sheng, X., Fang, H., Alam, M. A., Huang, Y., Viventi, J., Chang, J. K., & Rogers, J. A. (2019). Flexible electronic/optoelectronic microsystems with scalable designs for chronic biointegration. *Proceedings of the National Academy of Sciences*, 116(31), 15398–15406. Available from <https://doi.org/10.1073/pnas.1907697116>.
- Song, K., Han, J. H., Lim, T., Kim, N., Shin, S., Kim, J., Choo, H., Jeong, S., Kim, Y. C., Wang, Z. L., & Lee, J. (2016). Subdermal flexible solar cell arrays for powering medical electronic implants. *Advanced Healthcare Materials*, 5(13), 1572–1580. Available from <https://doi.org/10.1002/adhm.201600222>, [http://onlinelibrary.wiley.com/journal/10.1002/\(ISSN\)2192-2659](http://onlinelibrary.wiley.com/journal/10.1002/(ISSN)2192-2659).
- Stevens, M. M., Mayer, M., Anderson, D. G., Weibel, D. B., Whitesides, G. M., & Langer, R. (2005). Direct patterning of mammalian cells onto porous tissue engineering substrates using agarose stamps. *Biomaterials*, 26(36), 7636–7641. Available from <https://doi.org/10.1016/j.biomaterials.2005.05.001>.
- Thibault, C., Le Berre, V., Casimirius, S., Trévisiol, E., François, J., & Vieu, C. (2005). Direct microcontact printing of oligonucleotides for biochip applications. *Journal of Nanobiotechnology*, 3(1). Available from <https://doi.org/10.1186/1477-3155-3-7>.
- Viventi, J., Kim, D.-H., Moss, J. D., Kim, Y.-S., Blanco, J. A., Annetta, N., Hicks, A., Xiao, J., Huang, Y., & Callans, D. J. (2010). A conformal, bio-interfaced class of silicon electronics for mapping cardiac electrophysiology. *Science Translational Medicine*, 2(4), 24.
- Viventi, J., Kim, D. H., Vigeland, L., Frechette, E. S., Blanco, J. A., Kim, Y. S., Avrin, A. E., Tiruvadi, V. R., Hwang, S. W., Vanleer, A. C., Wulsin, D. F., Davis, K., Gelber, C. E., Palmer, L., Van Der Spiegel, J., Wu, J., Xiao, J., Huang, Y., Contreras, D., ... Litt, B. (2011). Flexible, foldable, actively multiplexed, high-density electrode array for mapping brain activity in vivo. *Nature Neuroscience*, 14(12), 1599–1605. Available from <https://doi.org/10.1038/nn.2973>.
- Wang, Y., Qiu, Y., Ameri, S. K., Jang, H., Dai, Z., Huang, Y. A., & Lu, N. (2018). Low-cost, μm -thick, tape-free electronic tattoo sensors with minimized motion and sweat artifacts. *NPJ Flexible Electronics*, 2(1), 6. Available from <https://doi.org/10.1038/s41528-017-0019-4>.
- Wigenius, J. A., Fransson, S., von Post, F., & Inganäs, O. (2008). Protein biochips patterned by microcontact printing or by adsorption-soft lithography in two modes. *Biointerphases*, 3(3), 75–82. Available from <https://doi.org/10.1116/1.2988771>, <http://scitation.aip.org/getpdf/servlet/GetPDFServlet?filetype=pdf&cid=BJIOBN000003000003000075000001&cidtype=cvips&prog=normal&doi=10.1116/1.2988771>.

- Xie, Y., Wang, H., Cheng, D., Ding, H., Kong, D., Li, L., Yin, L., Zhao, G., Liu, L., & Zou, G. (2021). Diamond thin films integrated with flexible substrates and their physical, chemical and biological characteristics. *Journal of Physics D: Applied Physics*, 2021(38).
- Xu, L., Gutbrod, S. R., Bonifas, A. P., Su, Y., Sulkin, M. S., Lu, N., Chung, H. J., Jang, K. I., Liu, Z., Ying, M., Lu, C., Webb, R. C., Kim, J. S., Laughner, J. I., Cheng, H., Liu, Y., Ameen, A., Jeong, J. W., Kim, G. T., . . . Rogers, J. A. (2014). 3D multifunctional integumentary membranes for spatio-temporal cardiac measurements and stimulation across the entire epicardium. *Nature Communications*, 5. Available from <https://doi.org/10.1038/ncomms4329>.
- Yang, Y., Cao, Z., He, P., Shi, L., Ding, G., Wang, R., & Sun, J. (2019). Ti3C2Tx MXene-graphene composite films for wearable strain sensors featured with high sensitivity and large range of linear response. *Nano Energy*, 66, 104134. Available from <https://doi.org/10.1016/j.nanoen.2019.104134>.
- Yang, Q., Lee, S., Xue, Y., Yan, Y., Liu, T. L., Kang, S. K., Lee, Y. J., Lee, S. H., Seo, M. H., & Lu, D. (2020). Materials, mechanics designs, and bioresorbable multisensor platforms for pressure monitoring in the intracranial space. *Advanced Functional Materials*, 2020(17), 1910.
- Yan, Z., Pan, T., Xue, M., Chen, C., Cui, Y., Yao, G., Huang, L., Liao, F., Jing, W., & Zhang, H. (2017). Thermal release transfer printing for stretchable conformal bioelectronics. *Advanced Science*, 2017(11).
- Yeo, W. H., Kim, Y. S., Lee, J., Ameen, A., Shi, L., Li, M., Wang, S., Ma, R., Jin, S. H., Kang, Z., Huang, Y., & Rogers, J. A. (2013). Multifunctional epidermal electronics printed directly onto the skin. *Advanced Materials*, 25(20), 2773–2778. Available from <https://doi.org/10.1002/adma.201204426>.
- Ye, R., James, D. K., & Tour, J. M. (2019). Laser-induced graphene: From discovery to translation. *Advanced Materials*, 31(1). Available from <https://doi.org/10.1002/adma.201803621>, [http://onlinelibrary.wiley.com/journal/10.1002/\(ISSN\)1521-4095](http://onlinelibrary.wiley.com/journal/10.1002/(ISSN)1521-4095).
- Ye, R., James, D. K., & Tour, J. M. (2018). Laser-induced graphene. *Accounts of Chemical Research*, 51(7), 1609–1620. Available from <https://doi.org/10.1021/acs.accounts.8b00084>, <http://pubs.acs.org/journal/achre4>.
- Yoon, J., Lee, S. M., Kang, D., Meitl, M. A., Bower, C. A., & Rogers, J. A. (2015). Heterogeneously integrated optoelectronic devices enabled by micro-transfer printing. *Advanced Optical Materials*, 3(10), 1313–1335. Available from <https://doi.org/10.1002/adom.201500365>, [http://onlinelibrary.wiley.com/journal/10.1002/\(ISSN\)2195-1071](http://onlinelibrary.wiley.com/journal/10.1002/(ISSN)2195-1071).
- Yu, K. J., Kuzum, D., Hwang, S. W., Kim, B. H., Juul, H., Kim, N. H., Won, S. M., Chiang, K., Trumpis, M., Richardson, A. G., Cheng, H., Fang, H., Thompson, M., Bink, H., Talos, D., Seo, K. J., Lee, H. N., Kang, S. K., Kim, J. H., . . . Rogers, J. A. (2016). Bioresorbable silicon electronics for transient spatiotemporal mapping of electrical activity from the cerebral cortex. *Nature Materials*, 15(7), 782–791. Available from <https://doi.org/10.1038/nmat4624>, <http://www.nature.com/nmat/>.
- Yu, J., Ling, W., Li, Y., Ma, N., Wu, Z., Liang, R., Pan, H., Liu, W., Fu, B., & Wang, K. (2021). A multichannel flexible optoelectronic fiber device for distributed implantable neurological stimulation and monitoring. *Small*, 17(4), Article 2005925. Available from <https://doi.org/10.1002/smll.202005925>.
- Yu, A. A., Savas, T. A., Taylor, G. S., Guiseppe-Elie, A., Smith, H. I., & Stellacci, F. (2005). Supramolecular nanostamping: Using DNA as movable type. *Nano Letters*, 5(6), 1061–1064. Available from <https://doi.org/10.1021/nl050495w>.
- Yu, A. A., & Stellacci, F. (2007). Contact printing beyond surface roughness: Liquid supramolecular nanostamping. *Advanced Materials*, 19(24), 4338–4342. Available from <https://doi.org/10.1002/adma.200701068>.
- Yu, A. A., & Stellacci, F. (2006). Stamping with high information density. *Journal of Materials Chemistry*, 16(28), 2868–2870. Available from <https://doi.org/10.1039/b602552h>.
- Zaaimi, B., Turnbull, M., Hazra, A., Wang, Y., Gandara, C., McLeod, F., McDermott, E., Escobedo-Cousin, E., Idil, A. S., & Bailey, R. (2022). Closed-loop optogenetic control of the dynamics of neural activity in non-human primates. *Nature Biomedical Engineering*, 2022, 1–17.
- Zhang, H., Gutruf, P., Meacham, K., Montana, M. C., Zhao, X., Chiarelli, A. M., Vázquez-Guardado, A., Norris, A., Lu, L., & Guo, Q. (2019). Wireless, battery-free optoelectronic systems as subdermal implants for local tissue oximetry. *Science Advances*, 2019(3).

- Zhang, Y., Zheng, N., Cao, Y., Wang, F., Wang, P., Ma, Y., Lu, B., Hou, G., Fang, Z., & Liang, Z. (2019). Climbing-inspired twining electrodes using shape memory for peripheral nerve stimulation and recording. *Science Advances*, 2019(4).
- Zhang, K., Jung, Y. H., Mikael, S., Seo, J.-H., Kim, M., Mi, H., Zhou, H., Xia, Z., Zhou, W., & Gong, S. (2017). Origami silicon optoelectronics for hemispherical electronic eye systems. *Nature Communications*, 2017(1), 1–8.
- Zhang, H., Peng, Y., Zhang, N., Yang, J., Wang, Y., & Ding, H. (2022). Emerging optoelectronic devices based on microscale LEDs and their use as. Implantable biomedical applications. *Micromachines*, 2022(7).
- Zhang, M., Wang, X., Huang, Z., & Rao, W. (2020). Liquid metal based flexible and implantable biosensors. *Biosensors*, 2020(11).
- Zhan, X., Si, C., Zhou, J., & Sun, Z. (2020). MXene and MXene-based composites: Synthesis, properties and environment-related applications. *Nanoscale Horizons*, 5(2), 235–258. Available from <https://doi.org/10.1039/c9nh00571d>, <http://www.rsc.org/journals-books-databases/about-journals/nanoscale-horizons/?id=8277>.
- Zhao, R., Guo, R., Xu, X., & Liu, J. (2020). A fast and cost-effective transfer printing of liquid metal inks for three-dimensional wiring in flexible electronics. *ACS Applied Materials & Interfaces*, 12(32), 36723–36730. Available from <https://doi.org/10.1021/acsami.0c08931>.

This page intentionally left blank

CHAPTER 13

Laser-driven transfer printing techniques for micro-LED display

Hongyu Luo¹, Chengjun Wang², Shun Zhang² and Jizhou Song^{1,3,4}

¹Department of Engineering Mechanics, Soft Matter Research Center, and Key Laboratory of Soft Machines and Smart Devices of Zhejiang Province, Zhejiang University, Hangzhou, P.R. China

²International Research Center for Information Science and Electronic Engineering, Zhejiang University, Haining, P.R. China

³Department of Rehabilitation Medicine, The First Affiliated Hospital, Zhejiang University, Hangzhou, P.R. China

⁴The State Key Lab of Brain-Machine Intelligence, Zhejiang University, Hangzhou, P.R. China

13.1 Introduction to micro-light-emitting diode display

The display technique has been developed continuously in the past few decades. Nowadays, relatively mature display techniques include liquid crystal display (LCD) and organic light-emitting diode (OLED). As shown in Fig. 13.1, the display unit of LCD consists of a backlight source, anode, liquid crystal, cathode, and RGB (red, green, and blue) filters. The display panel emits white light, which can be converted into RGB light through RGB filter (Chen et al., 2018; Zhdanov et al., 2014). The brightness of red, green, and blue light can be controlled, respectively, by changing the light transmittance of liquid crystal via the applied voltage between the anode and the cathode. Although LCD display technique is very mature with low cost, the performance of

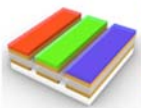





Category	Structure	Light Source	Contrast	Color Saturation	Lifespan	Cost
LCD	 	backlight	low	low	long	low
OLED	 	self-emissive	high	medium	medium	medium
microLED	 	self-emissive	high	high	long	high

Figure 13.1 Working principles and performance comparison of different types of displays.

LCD display is still not as good as desired [such as low contrast and low color saturation (Lee et al., 2019; Parbrook et al., 2021; Schadt, 2009)] due to its complex layouts and inherent working principles. To improve the display performance, OLED was introduced in the 1990s (Tang & Vanslyke, 1987). The display unit of OLED consists of anode, cathode and RGB OLED pixels, which does not involve the backlight source (Fig. 13.1). The brightness of red, green and blue light can be controlled by the voltage applied on the RGB OLED. This simple construct makes OLED thinner with higher contrast and better color saturation (Geffroy et al., 2006). However, the lifespan of OLED is shorter compared to LCD since the light-emitting materials are based on organic materials whose stability is weak. A new display technique to provide better display performance and a longer lifetime is highly desired.

Micro-LED display technique has been regarded as one of the most promising candidates for the next-generation display technique since its appearance in the 2000s (Ding et al., 2019; Jin et al., 2000; Liu et al., 2020; Meng et al., 2021). The display unit of micro-LED is only made of RGB micro-LED pixels and electrodes with the brightness controlled by applying voltage on the RGB micro-LEDs directly. Compared to LCD and OLED, the micro-LED display offers much better display performance, such as longer lifetime (> 10 years for micro-LED, ~ 8 years for LCD, ~ 4 years for OLED) (Parbrook et al., 2021), lower power consumption ($\sim 1\%$ of LCD and 40% of OLED) (Kim et al., 2012), and the wider view angle (max. 140 degrees for micro-LED, max. 100 degrees for LCD and max. 140 degrees for OLED) (Lee et al., 2019). However, the commercialization of micro-LED displays has been discouraged by the great challenges and high cost during the massive transfer of RGB micro-LED pixels from the fabrication wafers onto the display panels, as illustrated in Fig. 13.2. For example, a 4K TV display demands the transfer of approximately 25 millions RGB micro-LED pixels. To increase the cost effectiveness, the massive transfer should be highly efficient (\sim tens of millions/hour) (Chen et al., 2022) with the high yield ($\geq 99.9999\%$) (Virey et al., 2019) and the high accuracy ($\leq 5\%$ micro-LED chip size) (Li et al., 2021; Liu et al., 2019). Several promising mass transfer techniques, such as pick-and-place transfer (Kahler et al., 2012; Virey & Baron, 2018), magnetic transfer (Ashdown et al., 2011; Wu et al., 2017, 2020), fluid transfer (Kaltwasser et al., 2018; Rupp et al., 2019; Sasaki et al., 2017), electrostatic transfer (Biedermann et al., 2010; Chaji et al., 2018; Kim et al., 2019), laser transfer (Bian et al., 2019; Chu et al., 2004; Kim et al., 2012; Ueda et al., 2011) and transfer printing (Carlson et al., 2011; Carlson, Wang, et al., 2012; Kim et al., 2010; Meitl et al., 2006), have been developed to address the above challenges. Despite the notable advances, significant efforts are still needed to meet the stringent requirements on efficiency, yield and accuracy of mass transfer.

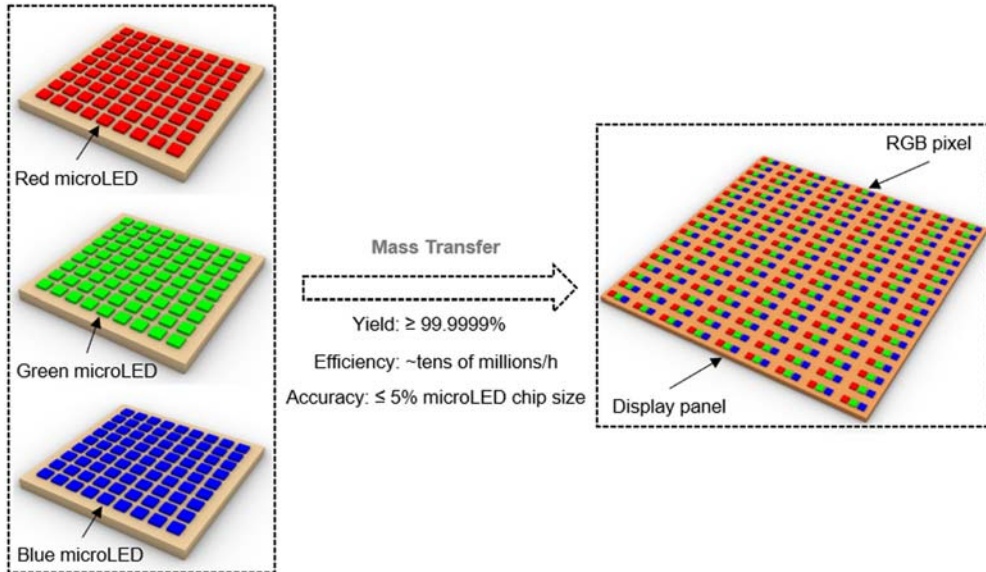


Figure 13.2 Challenges of the mass transfer process.

13.2 Laser-driven transfer printing techniques for micro-light-emitting diode display

Among the existing mass transfer techniques, the transfer printing technique represents a set of transfer methods where an elastomeric stamp is used to pick up the micro-LEDs from the fabrication substrate and print them onto the receiver substrate. This method is versatile in its good compatibility with different micro-LEDs at different scales and provides a promising mass transfer route for micro-LED display, which has earned immense focus and fast development from academia and industry. Typical transfer printing techniques include kinetically controlled transfer printing technique (Feng et al., 2007; Jiang et al., 2012; Meitl et al., 2006) based on the rate effect of the stamp, gecko-inspired transfer printing technique (Jeong et al., 2014; Mengüç et al., 2012) based on the fibrillary surface microstructures assisted by specific manipulation such as lateral movement or retraction angle, aphid-inspired transfer printing technique (Carlson, Wang et al., 2012; Linghu, Wang, et al., 2019; Linghu, Zhu, et al., 2019; Zhang, Linghu et al., 2019) based on the interfacial contact area change, and laser-driven transfer printing technique (Al-Okaily & Ferreira, 2015; Gao et al., 2017; Li, Li, Lü, Song, Saeidpouraza, et al., 2012; Li, Li, Lü, Song, Saeidpourazar, et al., 2012; Saeidpourazar, Li, et al., 2012; Saeidpourazar, Sangid, et al., 2012) based on the change of adhesion state driven by a laser pulse. The principles of these transfer printing techniques with applications in flexible inorganic electronics have been reviewed

in the recent literature (Bian et al., 2019; Carlson, Bowen, et al., 2012; Linghu et al., 2018; Ravikumar et al., 2017). In the scenario of micro-LED display, laser-driven transfer printing techniques offer the unique advantage of selectivity in a high-throughput way and are more suitable for mass transfer of micro-LEDs.

Fig. 13.3 shows the integration procedure of micro-LEDs with the display panel through the laser-driven transfer printing technique. At first, the red, green and blue micro-LEDs are fabricated on their growth substrate such as sapphire (Fig. 13.3I), and then stamps are used to pick up these micro-LEDs due to the strong interfacial adhesion between the stamp and micro-LED (Fig. 13.3II), then a laser beam is applied on the selected micro-LEDs to weaken the interfacial adhesion and print them onto the display panel (Fig. 13.3III for red micro-LEDs, Fig. 13.3IV for green micro-LEDs, and Fig. 13.3V for green micro-LEDs; the transfer sequence of red, green and blue micro-LEDs can be different) to assemble the micro-LED display. The display panel is also called the receiver substrate. The laser-driven transfer printing technique consists of two steps: pick-up and printing. To enable a reliable pick-up of micro-LEDs from the growth substrate, the adhesion between the stamp and micro-LED should be strong. To enable an easy release of micro-LEDs from the stamp onto the receiver substrate

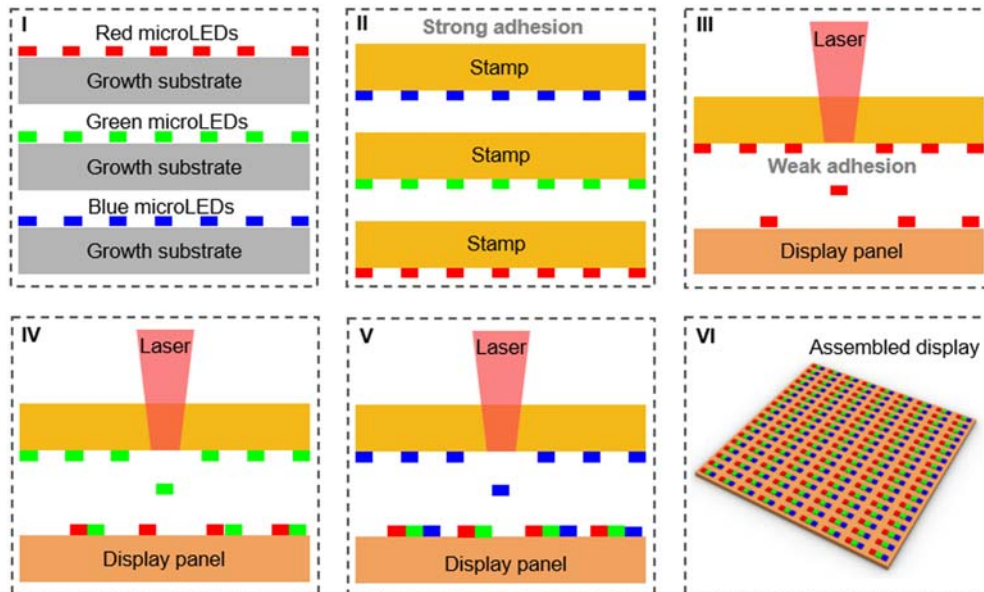


Figure 13.3 Technical procedure of the integration of micro-LEDs through the laser-driven transfer printing technique. (I) The micro-LED chips are fabricated on the growth substrate. (II) The micro-LED chips are picked up by the stamp because of the strong adhesion. (III–V) The red, green, and blue micro-LED chips are printed onto the display panel through a laser beam. (VI) The display panel is integrated with red, green and blue micro-LED chips.

(i.e., the display panel), the adhesion between the stamp and micro-LED should be weak. Thus, the success of transfer printing of micro-LED critically relies on the adhesion switch from a strong state to a weak state.

Based on whether the stamp contacts the receiver substrate, the laser-driven transfer printing techniques can be classified into two categories: contact laser-driven transfer printing techniques (Eisenhaure & Kim, 2016; Eisenhaure et al., 2013; Guo, 2022; Huang et al., 2016; Linghu et al., 2020; Marinov et al., 2013; Marinov, 2018; Pan et al., 2020; Tan et al., 2019; Wang et al., 2020; Xue et al., 2015; Yan et al., 2017; Zhang et al., 2021; Zhang, Lu et al., 2019) and noncontact laser-driven transfer printing techniques (Gao et al., 2017; Hu et al., 2022; Li, Li, Lü, Song, Saeidpouraza, et al., 2012; Luo et al., 2020; Luo et al., 2021; Saeidpourazar, Li, et al., 2012; Saeidpourazar, Sangid, et al., 2012) (Fig. 13.4). The contact mode requires the aid of receiver substrate to complete the printing process with its performance depending on the geometry and material properties of the receiver substrate. The noncontact mode can eliminate the limitation of the receiver substrate and enable the printing of inks onto any receiver substrates (i.e., the curved, nonstick and liquid surface). In the next

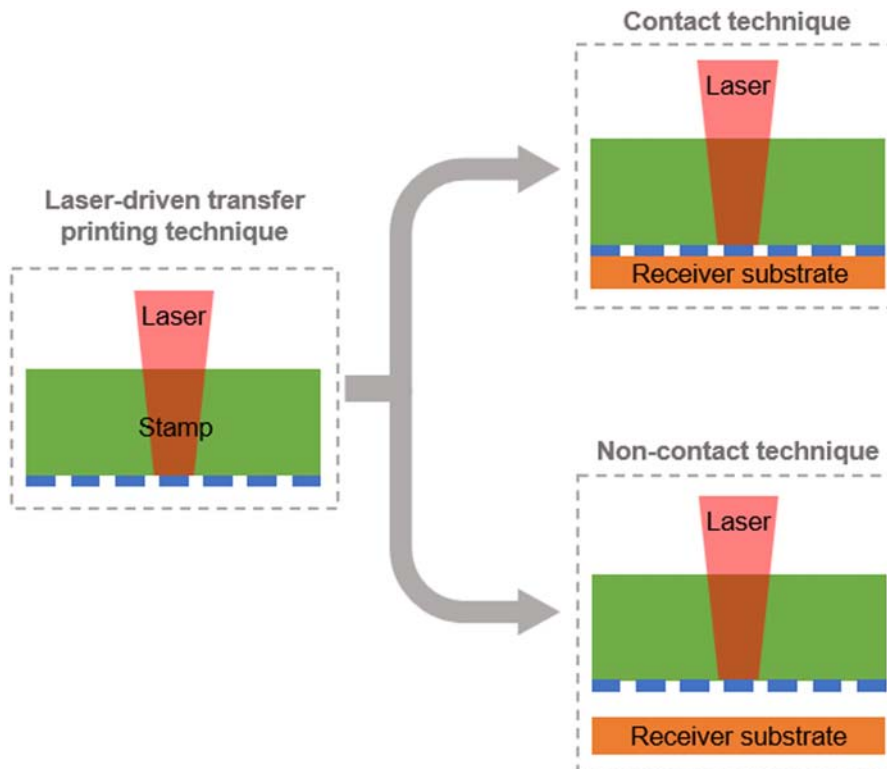


Figure 13.4 The classification of laser-driven transfer printing technique.

two sections, the latest development of contact laser-driven transfer printing techniques and noncontact laser-driven transfer printing techniques will be overviewed, respectively.

13.3 Contact laser-driven transfer printing techniques

13.3.1 Contact laser-driven transfer printing based on a smart tape

Smart tapes refer to adhesives that can switch the adhesion state from strong and weak at one time and have been widely used for developing contact-laser-driven transfer printing techniques. Based on the interfacial adhesion regulation mechanisms, smart tapes have different types: thermal release tape (Wang et al., 2020; Yan et al., 2017), ultraviolet (UV) rays release tape (Guo, 2022; Pan et al., 2020; Zhang et al., 2019), and dynamic release tape (Marinov, 2018; Marinov et al., 2013). Recently, Wang et al. (Wang et al., 2020) reported a cost-effective yet robust transfer printing technique via a thermal release tape with actively actuated surface microstructures for programmable and scalable transfer printing with high reliability and efficiency, as illustrated in Fig. 13.5. The thermal release tape consists of two layers, namely the polymeric backing layer and the commercially available adhesive layer with embedded expandable microspheres. Fig. 13.5A schematically illustrates the novel concept of the thermal release tape with large adhesion switchability. Initially, the tape has a flat topography due to the small size of expandable microspheres, which provides a strong adhesion. Upon external thermal stimuli, the expandable microspheres expand extremely to introduce hierarchical microstructures, which change the flat topography to rough topography and decrease the adhesion strength remarkably. This large adhesion switchability due to thermal stimuli establishes the basis to develop the contact laser-driven transfer printing technique with high yields in a programmable fashion.

To illustrate the working mechanism of thermal release tape, the randomly distributed thermally expandable microspheres (TEMs) with hydrocarbons encapsulated inside thermoplastic polymer shells in the adhesive layer are chosen as an example. The temperature when the microspheres start to expand due to the liquid-vapor transition of inner hydrocarbons and softening of the thermoplastic polymer shell is referred as the transition temperature, which is about 80°C–90°C. The microsphere can have a large volume expansion from 10 to 45 mm in diameter. As illustrated in Fig. 13.5B, the change of surface roughness caused by the expansion of microspheres can be clearly observed when the stimuli temperature is over the transition temperature. This change in surface roughness results in an abrupt drop in energy release rate (Fig. 13.5C). It should be noted that the adhesion switchability of the thermal release tape with actively controllable microstructures surpasses most of previous stamp designs with predefined surface release microstructures (Jeong et al., 2014; Kim et al., 2010; Mengüç et al., 2012; Yang et al., 2012). A programmable and scalable transfer printing

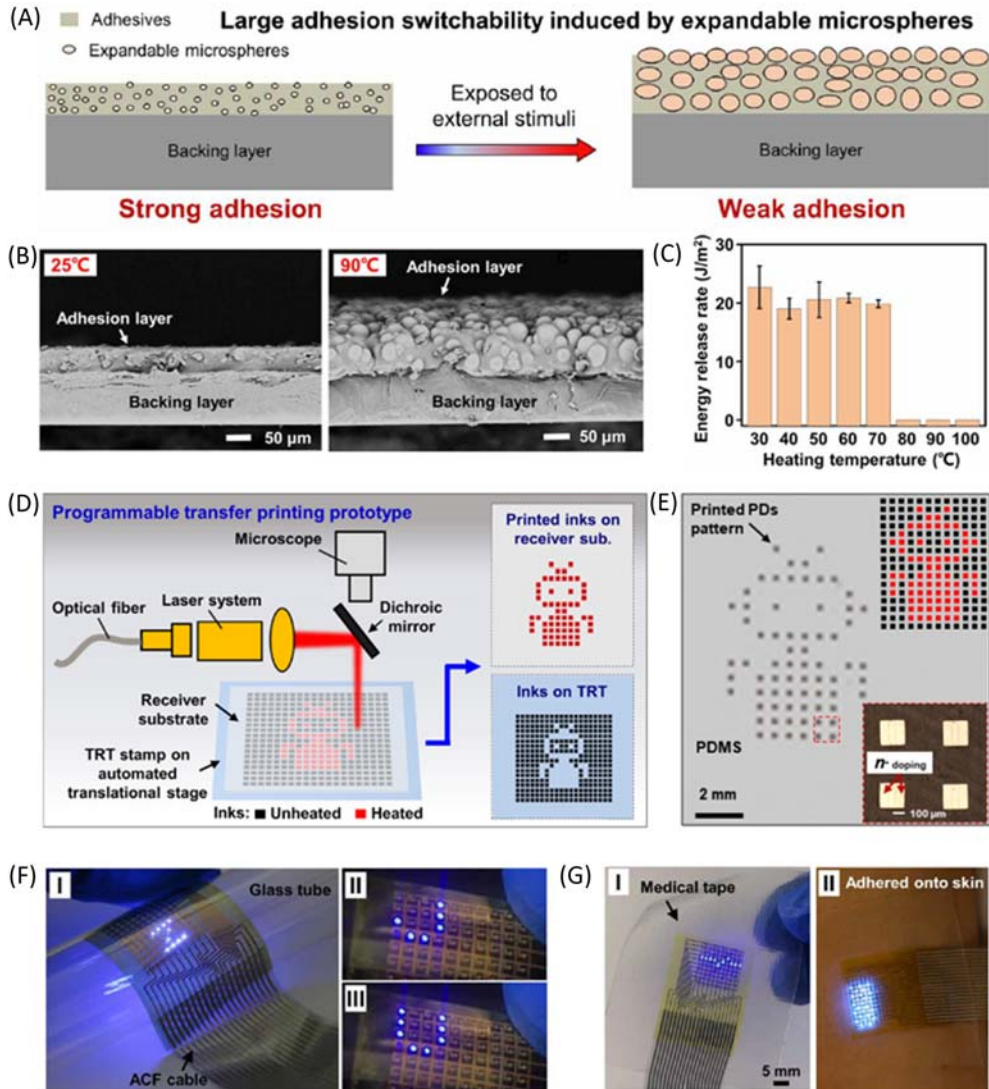


Figure 13.5 Contact laser-driven transfer printing technique based on a smart tape. (A) The smart tape changes from a flat state (strong adhesion) to a rough state (weak adhesion) under external thermal stimulus. (B) The scanning electron microscope images of the smart tape under 25°C and 90°C, respectively. (C) The energy release rate of the smart tape/glass interface under different heating temperatures. (D) the schematic prototype of the laser-driven programmable transfer printing system via the automated translational stage. (E) Selectively printed Si nanomembrane-based photodetectors with a robot-like pattern on PDMS substrate. (F) The optical image of micro-LED array-based flexible display wrapped around a glass tube with displayed letters of ZJU. (G) The optical image of the flexible display is attached to the medical tape and mounted onto the skin for phototherapy. From Wang, C., Linghu, C., Nie, S., Li, C., Lei, Q., Tao, X., Zeng, Y., Du, Y., Zhang, S., Yu, K., Jin, H., Chen, W. & Song, J. (2020). Programmable and scalable transfer printing with high reliability and efficiency for flexible inorganic electronics. *Science Advances*, 6(25). <https://doi.org/10.1126/sciadv.abb2393>

technique can be easily developed by combining the benefits of extraordinary adhesion switchability of the thermal release tape and the merits of a digitally controllable and highly localized laser heating system. Fig. 13.5D schematically shows the prototype of the laser-driven programmable transfer printing system. Fig. 13.5E shows the programmable control capability of this technique by transfer printing the Si nanomembrane-based photodetectors onto the PDMS (polydimethylsiloxane) substrate to form a robot pattern. A micro-LED array-based flexible display can be fabricated via this transfer printing technique. Fig. 13.5F shows the optical image of the micro-LED array-based flexible display wrapped around a glass tube with displayed letters of ZJU. Fig. 13.5G shows the optical image of the flexible display attached to the medical tape and mounted onto the skin for phototherapy.

13.3.2 Universal contact laser-driven transfer printing based on a shape memory polymer block

Shape memory polymer (SMP) is an intelligent material that can change the initial shape at high temperature, memorize the temporary shape at low temperature and restore the initial shape at high temperature, which has been used broadly for developing contact laser-driven transfer printing techniques (Eisenhaure et al., 2013; Eisenhaure & Kim, 2016; Huang et al., 2016; Linghu et al., 2020; Tan et al., 2019; Xue et al., 2015; Zhang et al., 2021). Most SMP-based transfer printing techniques are only suitable for flat objects. Recently, Linghu et al. (2020) reported a universal solution to transfer print multiscaled, arbitrarily shaped objects by utilizing a simple SMP block as the stamp. The embedding of objects into the SMP at the soft state enables the pick-up while the shape recovery at the stiff state upon stimulation facilitates the printing. Fig. 13.6A schematically shows the typical process of the universal transfer printing technique based on a heat-responsive SMP stamp. At first, the SMP stamp is brought to approach and contact the objects on the original substrate, then the SMP is transformed to the soft state via external thermal stimulus and pressed against the objects, then the SMP is transformed back to the stiff state by removing the external thermal stimulus to lock the objects, then the objects are picked up with them embedded in the SMP, then the SMP embedded with the objects is moved to the target receiver substrate, and then the SMP is heated again via external thermal stimulus after the alignment to recover its initial shape, which facilitates the release of the objects onto the target receiver substrate.

Systematic experiments have been conducted to investigate the adhesion performance of the SMP stamp by focusing on the grip force (i.e., strong adhesion) and residual force (i.e., weak adhesion) during the transfer printing of objects. A steel sphere with a diameter of 5 mm is taken as the object to measure the grip force and residual force. The grip force is obtained by pushing the sphere into the SMP at a fixed embedding depth of 3 mm at 120°C followed by pulling out the sphere at a

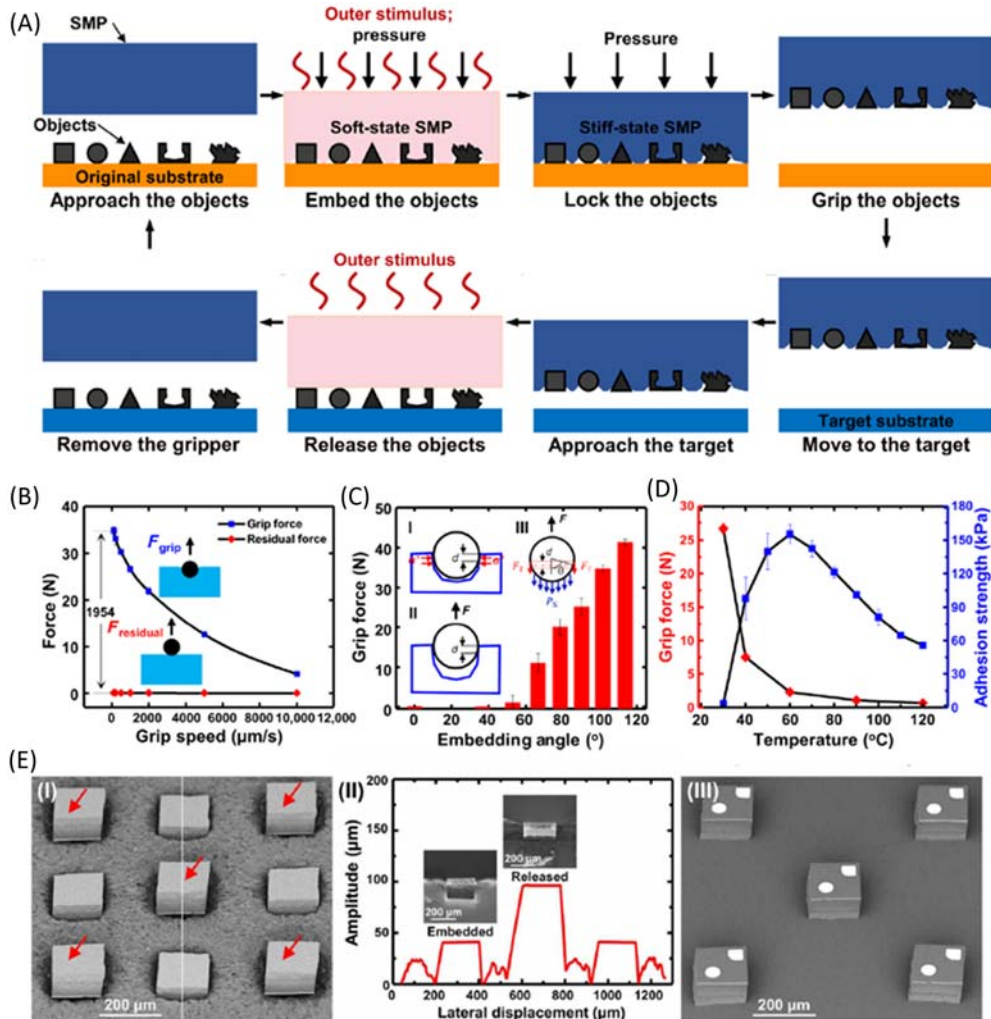


Figure 13.6 Universal contact laser-driven transfer printing technique based on a shape memory polymer (SMP) block. (A) The schematic illustration of the transfer printing process. (B) Comparison of the grip and residual forces as functions of the grip speed. (C) Influence of the embedding angle on the grip force. (D) Influence of the temperature on the grip force. (E) Selective printing of micro-LED chips by local laser heating: (I) Scanning electron microscope images of the SMP with selectively released micro-LED chips with the arrows indicating the released chips, (II) Cross-sectional profile along the white line in (I) with insets for the sectional view of the embedded and released micro-LED chips, and (III) The selectively released micro-LED chips printed onto the PDMS substrate. From Linghu, C., Zhang, S., Wang, C., Yu, K., Li, C., Zeng, Y., Zhu, H., Jin, X., You, Z. & Song, J. (2020). Universal SMP gripper with massive and selective capabilities for multiscaled, arbitrarily shaped objects. *Science Advances*, 6(7). <https://doi.org/10.1126/sciadv.aay5120>

given retraction speed at 30°C. The residual force is obtained by gently placing the sphere on the SMP with the embedding depth close to zero at 120°C followed by pulling out the sphere at a given speed at 30°C. Fig. 13.6B shows the grip force and residual force as functions of pulling speed. The huge difference (~ 1954 times) between the grip force and the residual force reveals that the main contributor to the large grip force is not the van der Waals force since the adhesion between the SMP and the sphere is quite low under the stiff state. To explore the mechanism of large grip force, the grip forces are measured under different embedding angles in Fig. 13.6C, which indicates that the grip force mainly comes from the friction force at the contact interface, the suction force generated when pulling and geometric interlocking (when the embedding angle is above $\pi/2$). The larger the embedding angle is, the larger the grip force will be. The influences of temperature on the grip force and adhesion strength are shown in Fig. 13.6D. The grip force decreases with the increasing temperature mainly due to the softening effect, while the adhesion strength increases at first and then drops as the pulling temperature increases due to the competition between the softening effect and true interfacial contact area. Fig. 13.6E shows the programmable transfer printing of micro-LEDs ($167 \mu\text{m} \times 167 \mu\text{m} \times 95 \mu\text{m}$) by following the embedding-pushing out strategy enabled by the SMP stamp and laser heating. Fig. 13.6E(I) shows the scanning electron microscopy (SEM) image of the selective release of five micro-LEDs out of 3×3 array. The cross-sectional profile of the white line denoted in Fig. 13.6E(I) is shown in Fig. 13.6E(II), and the amplitude difference indicates the change from the embedded state to the released state. The embedded SMP stamp is pressed on a PDMS substrate and the released micro-LEDs will be printed onto the PDMS substrate leaving other micro-LEDs still embedded in the SMP stamp [Fig. 13.6E(III)]. The above demonstration illustrates the extraordinary capability of the universal transfer printing technique for mass transfer of micro-LEDs in the development of micro-LED display.

13.3.3 Contact laser-driven transfer printing based on a microstructured shape memory polymer stamp

The universal transfer printing technique based on an SMP block is suitable to transfer objects with complex shapes, but not suitable for thin objects especially with a thickness on the order of hundreds of nanometers or even smaller due to the relatively large residual force between the stamp and thin objects. Surface microstructures have been introduced to further weaken the residual force to enable the successful printing of thin objects (Eisenhaure & Kim, 2016; Huang et al., 2016). A typical example is the pyramid microstructure. Huang et al. (2016) presented a programmable contact laser-driven transfer printing technique based on an SMP stamp with pyramid microstructures, which can transfer hundreds nanometer thick objects (Fig. 13.7). The programmable transfer printing process via automated laser-writing is illustrated in Fig. 13.7A. The adhesion control

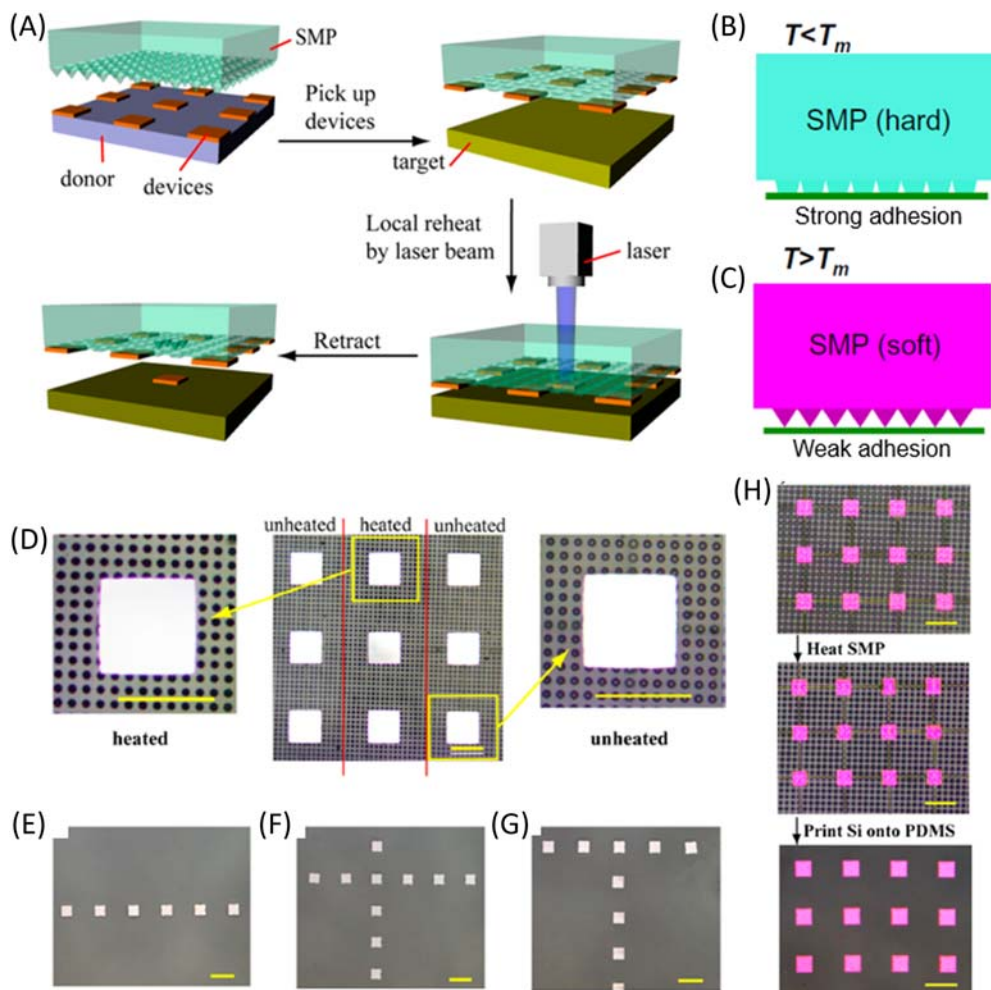


Figure 13.7 Contact laser-driven transfer printing technique based on a pyramid microstructured shape memory polymer (SMP) stamp. (A) Schematic illustration of the transfer printing process via automated laser writing. (B) The strong adhesion state of the SMP stamp with collapsed pyramid microstructures. (C) The weak adhesion state of the SMP stamp with recovered pyramid microstructures. (D) Selective heating silicon platelets via laser scanning. (E)–(G) Printed patterns on PDMS in line, cross, and T-shape, respectively. (H) Global transfer printing of silicon platelets to a PDMS substrate. (Scale bars: 100 μm .) From Xue, Y., Zhang, Y., Feng, X., Kim, S., Rogers, J. A. & Huang, Y. (2015). *A theoretical model of reversible adhesion in shape memory surface relief structures and its application in transfer printing*. *Journal of the Mechanics and Physics of Solids*, 77, 27–42. <https://doi.org/10.1016/j.jmps.2015.01.001> From Huang, Y., Zheng, N., Cheng, Z., Chen, Y., Lu, B., Xie, T. & Feng, X. (2016). *Direct laser writing-based programmable transfer printing via bioinspired shape memory reversible adhesive*. *ACS Applied Materials and Interfaces*, 8(51), 35628–35633. <https://doi.org/10.1021/acsami.6b11696>.

comes from the changes in the modulus of SMP and interfacial contact area. At first, the SMP stamp is heated to the soft state, and then press the SMP stamp on the donor substrate and keep the pressure unchanged till cooling the SMP stamp below T_m (the glass transition temperature of SMP). The SMP becomes hard with a large interfacial contact area due to the fixed and collapsed pyramid microstructures, which provide strong adhesion to ensure a successful pick-up (Fig. 13.7B). The inked SMP stamp is then moved to contact with the receiver substrate followed by selective laser heating, which recovers the shape of pyramid microstructures and softens the SMP, yielding a quite small interfacial contact area and thus providing a weak adhesion to enable a successful printing (Fig. 13.7C). The retraction of the stamp completes the transfer printing process with heated inks printed onto the receiver substrate while the others remain on the stamp.

Fig. 13.7D shows the experimental images of Si platelets on the microstructured SMP stamp with partial region heated by laser scanning. The heated region is between the red lines with the pyramid microstructures (dark-colored) recovering back to their original shape, which indicates a weak adhesion state. The unheated region is located outside the red lines with the pyramid microstructures (light-colored) remaining deformed flat topography, which indicates a strong adhesion state. Fig. 13.6E–G illustrate the extraordinary selective transfer printing ability of this technique. Microscale Si platelets can be printed onto a PDMS substrate to form a line shape (Fig. 13.7E), a cross shape (Fig. 13.7F), and a T shape (Fig. 13.7G). Furthermore, this technique has not only selective capability but also a massive capability of transfer printing. As illustrated in Fig. 13.7H, a large scale of Si platelets can be successfully transfer printed onto a PDMS substrate after global heating and contact printing procedures.

The heat is absorbed by the ink (e.g., functional component, micro-LED) during the process of the above-mentioned transfer technique based on a pyramid microstructured SMP stamp, which may cause thermal damage to the ink. To minimize the possible thermal damage, heat absorption should occur within the stamp. Eisenhaure and Kim (Eisenhaure & Kim, 2016) introduced carbon black/SMP (CBSMP) microstructures to enhance the heat absorption capability of SMP stamp. The microstructure features an SMP core and a CBSMP surface, which enables the stamp to absorb most of the laser power and convert it to heat. When the laser passes through the CBSMP stamp, the total attenuation of the laser energy is 61%, which is much higher than the flat SMP (only 1%). This extraordinary heat absorption ability protects electronic components from possible thermal damage due to laser heating.

13.3.4 Contact laser-driven transfer printing based on an elastomer/shape memory polymer composite stamp

Microstructures offer better adhesion control capability when regulating interfacial adhesion. However, the fabrication of microstructure usually involves complex operations such

as lithography, etching, etc. To bypass these undesired operations, Zhang et al. (2021) developed a contact laser-driven transfer printing technique based on an elastomer/SMP composite stamp. The composite stamp features a stiff sphere embedded in a thermal-responsive SMP substrate and encapsulated by an elastomeric membrane, as illustrated in Fig. 13.8A. The embedding of the stiff sphere can be achieved by pressing it into the heated SMP followed by cooling to fix the temporary flat shape, maximizing the interfacial contact area and the corresponding adhesive force. This construct bypasses unfavorable micro- and nanofabrication processes via molding and pressing processes and yields an attractive level of switchable adhesion through the combination of the peel-rate dependent effect of the elastomeric membrane and the thermal actuation of a subsurface embedded stiff sphere. Fig. 13.8A schematically shows the transfer printing process enabled by the composite stamp. At first, the composite stamp is moved above a donor substrate. The stamp is then brought into contact with the ink. After the quick retraction, the ink is picked up by the composite stamp because of the strong adhesion between the stamp and ink. The inked stamp is then brought into contact with the receiver substrate. After the stamp is heated, the SMP recovers to its original bulged shape and pushes the stiff sphere out, creating a bulge on the stamp surface. The stamp is then slowly retracted from the receiver substrate by leaving the ink onto the receiver substrate because of the weak adhesion between the stamp and ink. Finally, the stamp is heated, pressed to a flat state and cooled to maintain the strong adhesion for the next transfer printing cycle.

The adhesion characteristics of the composite stamp have been studied systematically. Fig. 13.8B shows the measured adhesion strengths of the stamp/glass interface as functions of preload at a fixed retraction speed of 100 $\mu\text{m}/\text{second}$. The adhesion switchability (i.e., the maximum adhesion strength over the minimum adhesion strength) increased with the preload and reached above 300 in experiments under a fixed retraction speed of 100 $\mu\text{m}/\text{second}$. Fig. 13.8C shows the measured adhesion strengths of the stamp/glass interface as functions of retraction speed at a fixed preload of 1 N. The maximum adhesion switchability can reach 1000, which is superior to most existing stamp designs. Fig. 13.8D shows the reversibility and repeatability of the thermal actuated adhesive under a preload of 10 N and a retraction speed of 100 $\mu\text{m}/\text{second}$. Due to the high shape fixation ratio (greater than 99.8%) of SMP, the strong adhesion and weak adhesion remain stable. When combined with a laser beam and an automated displacement platform, a contact laser-driven transfer printing process can be realized, as shown in Fig. 13.8E. Micro-LEDs can be selectively printed onto a microstructured PDMS substrate with quite weak adhesion to form a triangular pattern (Fig. 13.8F). What's more, the voltage–current curves of micro-LEDs before and after transfer printing remain almost the same, which indicates that the laser-driven transfer printing process does no thermal damage to micro-LEDs (Fig. 13.8G).

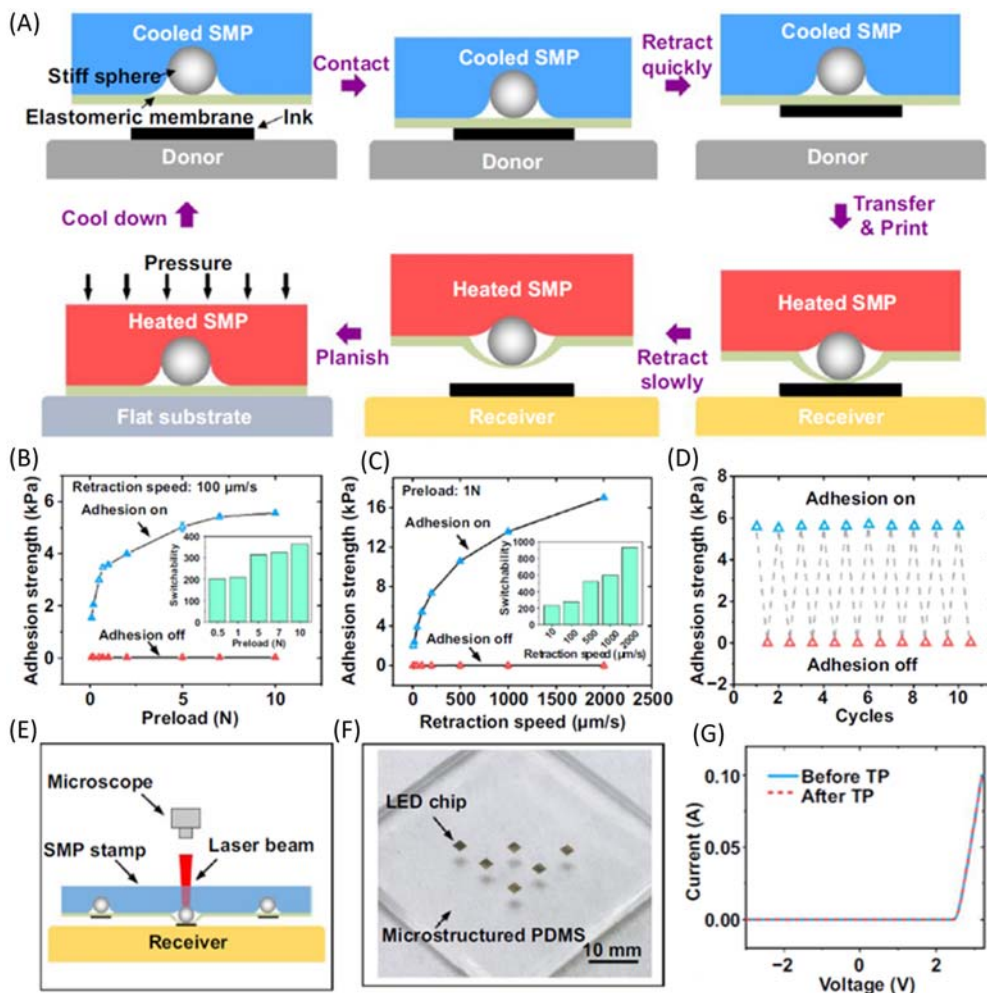


Figure 13.8 Contact laser-driven transfer printing technique based on an elastomer/shape memory polymer (SMP) composite stamp. (A) Schematic illustration of the transfer printing process enabled by a composite stamp. (B) Measured adhesion strengths of the stamp/glass interface as functions of preload. Inset: adhesion switchability. (C) Measured adhesion strengths of the stamp/glass interface as functions of retraction speed. Inset: adhesion switchability. (D) Reversibility and repeatability tests of adhesion measurements of the composite stamp. (E) Schematic illustration of programmable transfer printing platform. (F) Programmable printing of light-emitting diode (LED) chips with a triangular pattern onto a microstructured PDMS substrate. (G) Voltage–current curves of the LED chip before and after transfer printing. From Zhang, S., Luo, H., Wang, S., Chen, Z., Nie, S., Liu, C. & Song, J. (2021). A thermal actuated switchable dry adhesive with high reversibility for transfer printing. *International Journal of Extreme Manufacturing*, 3(3), 035103. <https://doi.org/10.1088/2631-7990/abff69>.

13.4 Noncontact laser-driven transfer printing techniques

13.4.1 Noncontact laser-driven transfer printing based on the interfacial thermal mismatch

Compared with contact laser-driven transfer printing techniques, noncontact laser-driven transfer printing techniques (Gao et al., 2017; Hu et al., 2022; Li, Li, Lü, Song, Saeidpouraza, et al., 2012; Luo et al., 2020; Luo et al., 2021; Saeidpourazar, Li, et al., 2012; Saeidpourazar, Sangid, et al., 2012) eliminate constraints on the shape and materials of the receiver substrate and can print inks onto any substrates (i.e., the curved, nonstick and liquid surface). The earliest version of noncontact laser-driven transfer printing is based on the thermal mismatch of the interface due to laser heating with the process schematically illustrated in Fig. 13.9A. At first, move the elastomeric

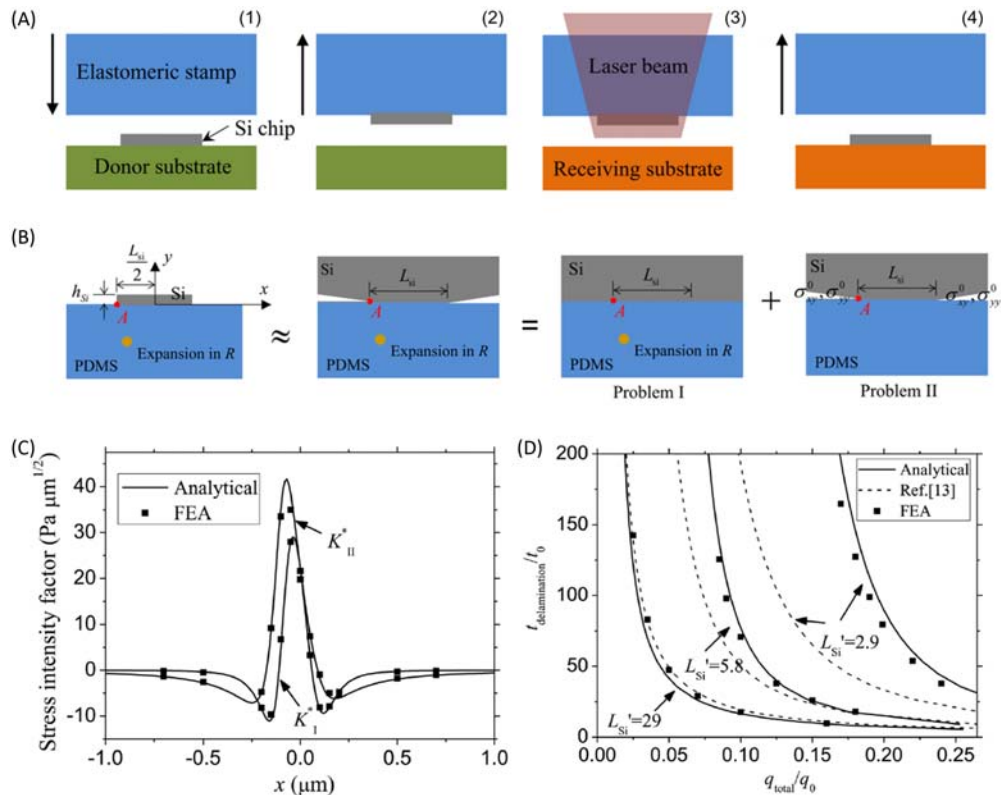


Figure 13.9 Noncontact laser-driven transfer printing technique based on the interfacial thermal mismatch. (A) The typical laser-driven transfer printing cycle. (B) The mechanics model to obtain the stress intensity factor at the crack tip A between PDMS and Si chip. (C) The stress intensity factor at the interfacial crack tip A. (D) The scaling law for the delamination time at the PDMS/Si chip interface. From Gao, Y., Li, Y., Li, R. & Song, J. (2017). An accurate thermomechanical model for laser-driven microtransfer printing. *Journal of Applied Mechanics*, 84(6). <https://doi.org/10.1115/1.4036257>.

(PDMS) stamp above the donor substrate where the ink (Si chip) is fabricated. The stamp is then brought into contact with the donor substrate to pick up the Si chip. After the inked stamp is positioned close to the receiving substrate, a pulsed laser beam is introduced to heat the Si chip. The temperature increase at the interface due to laser heating induces a thermal mismatch due to the large difference in thermal expansion coefficients of the stamp and ink. Once the thermal mismatch reaches some critical value, the interfacial delamination occurs to release the Si chip from the stamp onto the receiving substrate.

Analytical thermomechanical models and finite element models are established to reveal the weakening mechanism of interfacial adhesion caused by laser heating and predict the interface delamination time. Fig. 13.9B schematically shows the analytically modeled system with a uniform transformation strain spot embedded in PDMS. To develop the interfacial fracture mechanics model accounting for the Si chip width effect, the complex stress intensity factor at the crack tip A is derived at first, and then energy release rate G at the crack tip due to the pulsed laser heating is obtained. Since the modulus of Si chip is 5 orders of magnitude larger than that of PDMS, it is reasonable to approximate the Si chip by a large Si solid, which can be solved by superposing the solutions of the following two problems: (I) A uniform transformation strain spot embedded in PDMS bonded well with Si and (II) Interfacial crack with prescribed tractions to negate those from problem I on the faces. Fig. 13.9C shows the stress intensity factor subjected to a transformation strain corresponding to a temperature rise of 1°C within a circular region of radius $0.03\ \mu\text{m}$ at different locations with varying x and y as $-0.2\ \mu\text{m}$. The analytical predictions for the stress intensity factor agree well with finite element analysis. The good agreement validates the accuracy of the analytical model for the stress intensity factor due to the uniform transformation strain spot, which provides the basic solution for integrating over the thermal expansion in PDMS to obtain the stress intensity factor due to laser heating, thus the interfacial crack tip energy release rate. When the interfacial crack energy release rate reaches the work of adhesion of the interface, interfacial delamination occurs. Fig. 13.9D shows the normalized delamination time versus the normalized total heat flux into the system. These results may serve as the design basis for system optimization, especially for determining the optimal condition in laser-driven noncontact transfer printing.

13.4.2 Noncontact laser-driven transfer printing based on an active elastomeric microstructured stamp

Although the transfer printing technique based on thermal mismatch can print inks onto any substrate, it has an intrinsic limitation of requiring a high temperature of 200°C – 300°C to reach the sufficient thermal mismatch for the ink release (Saeidpourazar, Li, et al., 2012). This unfavorably high-temperature increase may

damage the stamp/ink interface and thus reduce the reliability of the process significantly. To overcome this limitation, Luo et al. (2020) developed a noncontact laser-driven transfer printing technique based on an active elastomeric microstructured stamp. The stamp has circular cavities filled with air and encapsulated by micro-patterned surface membranes, which can be inflated dynamically to control the interfacial adhesion by heating the air in cavities through the laser-absorbing metal layer on the inner-cavity surfaces. Fig. 13.10A schematically illustrates the typical process of the laser-driven programmable noncontact transfer printing via the active elastomeric microstructured stamp. At first, the stamp is moved above the donor followed by intimate contact with the inks to be transferred. Without heating, the stamp membrane remains flat with the microtips collapsed, enabling conformal contact between the stamp and the inks to yield a relatively strong adhesion. Rapid retraction of the stamp maximizes the adhesion due to the viscoelastic effect and ensures the retrieval of inks from the donor. The inked stamp is then moved above the receiver by leaving a small gap between the stamp surface and the receiver. After the laser alignment, the air in the cavities is heated quickly for inflation to induce pressure on the stamp membrane and form a bulge, which ensures weak adhesion and facilitates the ejection of selected inks from the stamp to the receiver. The retraction of the stamp completes the transfer printing process with the bulged membrane recovering back to a flat one.

The adhesion performance of the active elastomeric microstructured stamp was systematically investigated. Fig. 13.10B shows the measured pull-off force under various temperature increases. Below 40°C, the pull-off force decreases almost linearly and dramatically, while above 40°C, the pull-off force decreases slowly due to the negligible difference in the change of contact area at a high-temperature increase. Fig. 13.10C shows the adhesion switchability, defined as the maximum adhesion strength over the minimum adhesion strength, as the function of the temperature increase for the active stamp and flat stamp. Compared to the flat stamp, whose adhesion switchability is up to two orders of magnitude, the adhesion switchability of the active stamp can reach as high as three orders of magnitude with a temperature increase of below 100°C. The microstructures on the stamp membrane, as shown in Fig. 13.10D, play a key role in the noncontact printing process. The cavity has the dimensions of 160 μm in diameter and 350 μm in depth. The spacing between the centers of neighboring cavities is 240 μm. The stamp membrane (25 μm thick) is duplicated from a cheap sandpaper (2000 mesh). Microscale inks can be transferred to various substrates programmatically without thermal damage via this transfer printing technique. Fig. 13.10E shows microscale Si platelets printed onto a PDMS substrate to form a “ZJU” pattern. Fig. 13.10F shows microscale LED chips printed onto a postcard with a triangle pattern. These demonstrations illustrate the great potential of the active elastomeric microstructured stamp for the mass transfer of micro-LEDs.

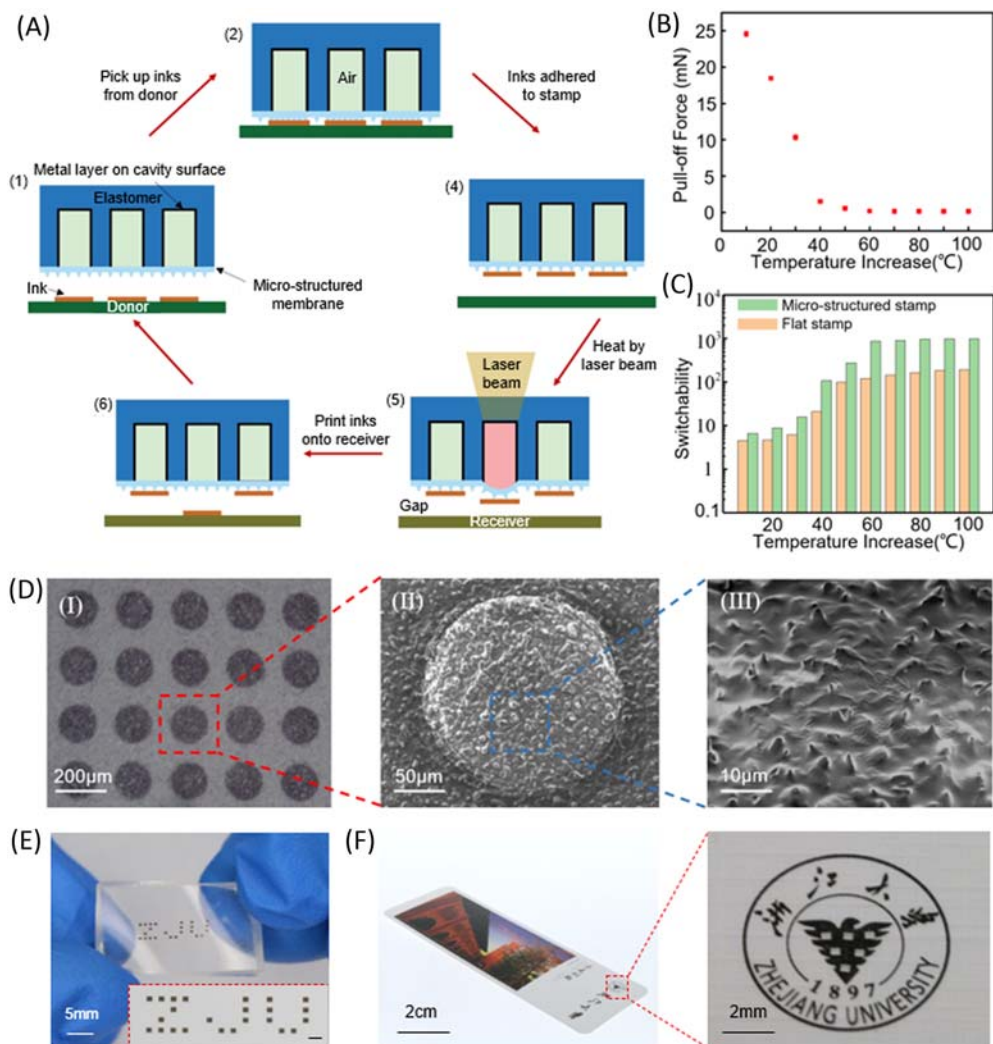


Figure 13.10 Noncontact laser-driven transfer printing technique based on an active elastomeric microstructured stamp. (A) Schematic illustration of the laser-driven programmable noncontact transfer printing process via an active elastomeric microstructured stamp. (B) The pull-off force of the microstructured stamp as the function of the temperature increase. (C) The adhesion switchability versus the temperature increase. (D) Microscopy images of the microstructured stamp surface (stamp height: 2 mm; stamp width: 16 mm; cavity diameter: 160 μm; membrane thickness: 25 μm): (I) Optical and (II, III) scanning electron microscope (SEM) images of the microstructured stamp surface. (E) Si platelets printed onto a PDMS substrate to form a "ZJU" pattern. (F) Microscale LED chips printed onto a postcard with a triangle pattern. From Luo, H., Wang, C., Linghu, C., Yu, K., Wang, C. & Song, J. (2020). Laser-driven programmable noncontact transfer printing of objects onto arbitrary receivers via an active elastomeric microstructured stamp. *National Science Review*, 7(2), 296–304. <https://doi.org/10.1093/nsr/nwz109>.

13.4.3 Noncontact laser-driven transfer printing based on an octopus-inspired thermal controlled stamp

Most transfer printing techniques increase the interfacial adhesion switchability by weakening the interfacial adhesion during printing but do not provide a means to enhance the interfacial adhesion during pick-up, which is not conducive to pick up devices from a sticky donor substrate. To enhance the adhesion for pick-up, Luo et al. (Luo et al., 2021) developed a noncontact laser-driven transfer printing technique based on an octopus-inspired thermal controlled stamp. The design of the stamp is inspired by the octopus suction cup but controlled by external temperature, as illustrated in Fig. 13.10A–C. The biomimetic thermal controlled stamp consists of a circular cavity filled with air on an elastomer surface. Prior to attachment, the adhesive is heated to a temperature T_1 higher than the ambient temperature T_{ambient} and the air pressure in the cavity is the same as the atmospheric pressure (Fig. 13.11A). When pressing the adhesive on the target substrate and cooling the stamp to ambient temperature (Fig. 13.11B), the negative pressure caused by the temperature drop of air in the cavity will yield a strong suction ΔP_1 . When reheating the adhesive to a temperature T_2 higher than temperature T_1 (Fig. 13.11C), the positive pressure caused by the temperature increase of air in the cavity will yield a strong thrust ΔP_2 . The “suction ON” state and “thrust ON” states not only provide strategies to enhance the interfacial adhesion but also to eliminate the interfacial adhesion, which makes deterministic assembly possible by transfer printing.

Theoretical and experimental investigations reveal the relationships between the suction/thrust and the temperature change of air in the cavity, which are important to provide guidelines on controlling temperatures to achieve the desired interfacial adhesion. Fig. 13.11D shows the suction pressure ΔP_1 as the function of temperature drop ΔT_1 . Fig. 13.11E shows the thrust pressure ΔP_2 as the function of temperature increase ΔT_2 . The higher the temperature drop (or temperature increase), the higher the suction pressure (or thrust pressure). Fig. 13.11F shows the optical image of the microscale stamp with the cavity dimension of $20\ \mu\text{m}$ in diameter, $20\ \mu\text{m}$ in depth, and $30\ \mu\text{m}$ in cavity spacing. To explore the underlying delamination mechanism of the laser printing process and obtain the critical delamination condition, an axisymmetric finite element model is established with the geometry characteristics shown in Fig. 13.11G. Fig. 13.11H presents the temperature distributions from FEA, which indicates that the temperature reaches a maximum within the ink region and decreases significantly out of the ink region. Despite the nonuniform temperature distribution of air in the cavity, the temperature increase will induce a pressure increase, which facilitates the delamination of ink from the stamp. The delamination temperature and delamination time as the functions of the absorbed laser power can be further determined (Fig. 13.11I). The delamination time does not exceed 10 Ms and the delamination temperature is below 165°C , which

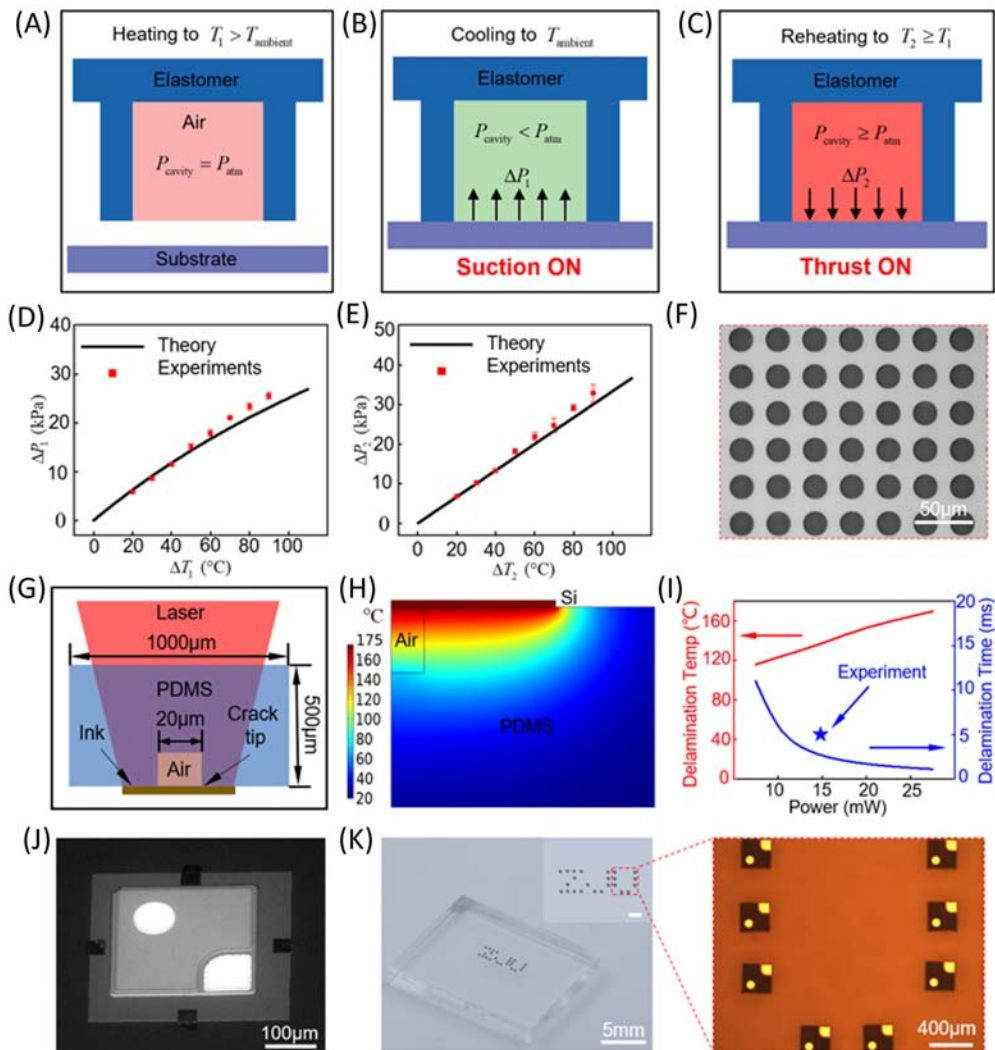


Figure 13.11 Noncontact laser-driven transfer printing technique based on an octopus-inspired thermal controlled stamp. (A) Heat the adhesive to T_1 higher than the ambient temperature T_{ambient} before contacting the target substrate. (B) Press the adhesive on the target substrate and then cool the adhesive to ambient temperature. (C) Reheat the adhesive to T_2 higher than T_1 . (D) The suction pressure ΔP_1 as the function of temperature drop ΔT_1 . (E) The thrust ΔP_2 as the function of temperature increase ΔT_2 . (F) Optical images of the microscale stamp with cylindrical cavities. (G) The geometry of finite element model. (H) The temperature distribution from FEA. (I) The delamination temperature and delamination time as the functions of the absorbed laser power. (J) Printing a $\mu\text{-LED}$ chip onto the center of a Si ink. (K) Programmable printing of $\mu\text{-LED}$ s onto a flat PDMS substrate to form a "ZJU" pattern. From Luo, H., Wang, S., Wang, C., Linghu, C. & Song, J. (2021). Thermal controlled tunable adhesive for deterministic assembly by transfer printing. *Advanced Functional Materials*, 31(16), 2010297. <https://doi.org/10.1002/adfm.202010297>.

enables a rapid printing process without inducing any thermal damage to the interface. Three-dimensional stacking and programmable transfer printing of microscale devices can be realized via this technique. Demonstrations of printing a μ -LED chip printed onto the center of a Si chip (Fig. 13.11J) and programmable printing of μ -LEDs onto a flat PDMS substrate to form a “ZJU” pattern (Fig. 13.11K) illustrate the great potential of this technique in mass transfer for micro-LED display.

13.4.4 Noncontact laser-driven transfer printing based on a dynamic release stamp

Recently, Hu et al. (2022) developed a noncontact laser-driven transfer printing technique based on a dynamic release stamp by combining the dynamic release strategy in laser transfer and the adhesion switch strategy in transfer printing. The stamp consists of three components: a composite adhesive layer with embedded (TEMs, a dynamic release layer (DRL), e.g., polyimide), and a transparent substrate (e.g., sapphire). Fig. 13.12A schematically shows the laser-driven transfer printing process based on the dynamic release stamp. Initially, the TEMs do not affect the flatness of the stamp, which ensures enough contact and adhesion between the stamp and the chip. Once the stamp is heated, the TEMs expand dramatically, resulting in numerous microstructures at the interface between the stamp and the chips. As a result, the contact area and adhesion strength of the stamp/chip interface are reduced by the expanded TEMs, and the thickness of the adhesive layer is increased by the expansion of the internal TEMs, which brings the chip closer to the receiver substrate. To facilitate the selective transfer of chips, the DRL is irradiated by a low-energy laser to generate a blister accompanied by shock waves. The blister further reduces the chip/stamp interfacial adhesion and the transfer distance, resulting in the successful transfer of the chip onto the receiver. With the increase in the thickness of the adhesive layer and the blister height of DRL, the noncontact mode evolves to contact mode, which is very helpful to enhance the placement accuracy.

Fig. 13.12B shows the morphological changes of the stamp before and after heating. The height of the heated one is higher than the unheated one, which indicates that the expansion of the internal TEMs increases the thickness of the stamp. The increased roughness change from heating reduces the adhesion of the stamp (Fig. 13.12C and D). From 80°C to 120°C, the adhesion strength of the stamp gradually decreases with increasing temperature and then drops rapidly (20 times) after TEMs are fully foamed. These results show that the expansion of TEMs can dramatically reduce the contact area of the chip/stamp interface, which facilitates the subsequent transfer printing process. Fig. 13.12E demonstrates the transfer printing of Si chip array onto a curved surface (i.e., egg substrate) in a noncontact and contact mode, respectively. It is shown that the distance between the stamp and the receiver substrate must be accurately controlled in order to ensure good transfer accuracy.

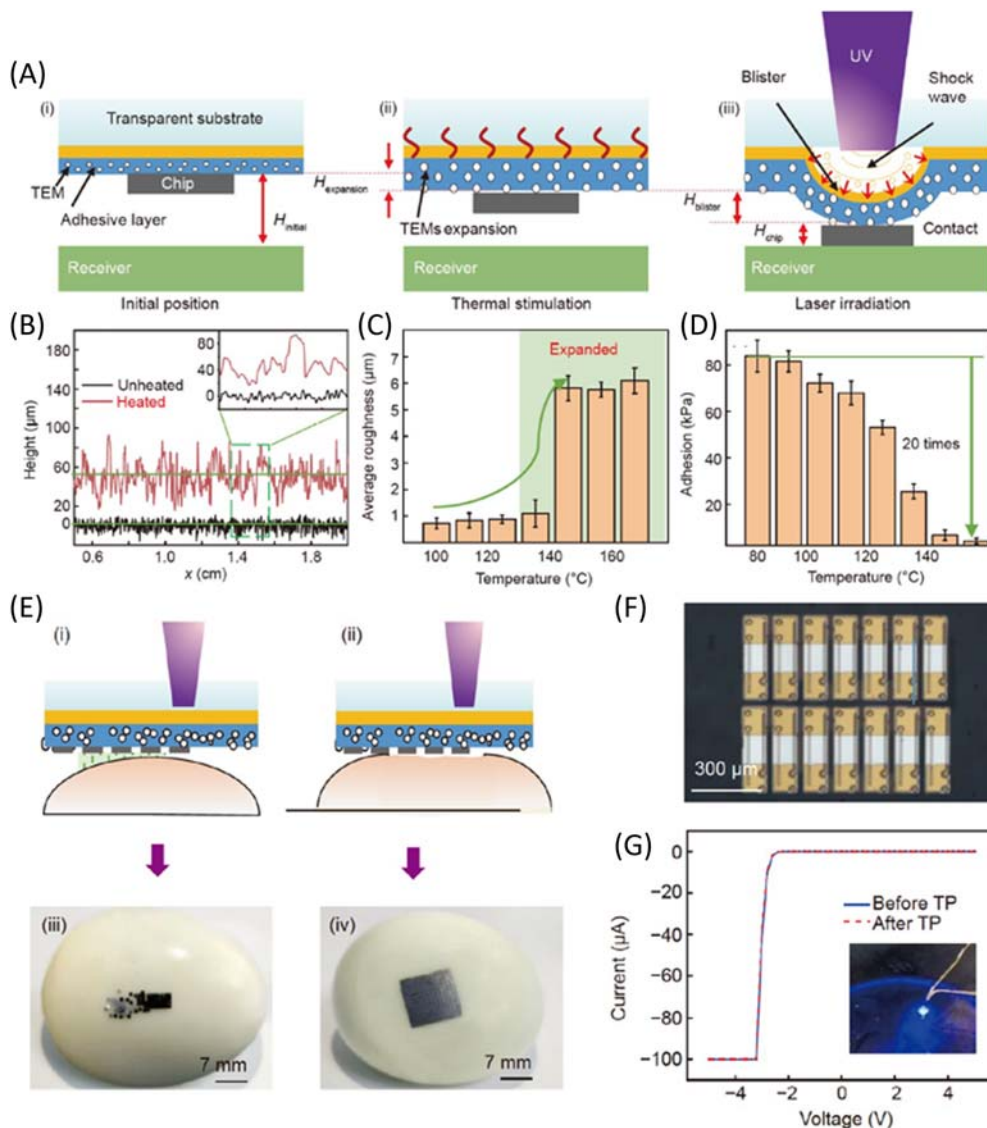


Figure 13.12 Noncontact laser-driven transfer printing technique based on a dynamic release stamp. (A) Schematic illustration of the laser-driven transfer printing process based on the dynamic release stamp. (B) Morphological changes of the stamp before and after heating. (C) Measured average roughness of the stamp surface at different temperatures. (D) Measured adhesion strength of the stamp surface at different temperatures. (E) Transfer results on a curved surface: (i) and (ii) schematic diagram of noncontact transfer and contact transfer; (iii) and (iv) a silicon chip array is transferred to an egg substrate. (F) Micro-LED chips transferred via the dynamic release stamp. (G) Electrical properties of micro-LED chips before and after transfer printing. From Hu, J. L., Chen, F. R., Bian, J., Sun, N. N., Wang, K. X., Ling, H., Yu, H. Y., Gai, M. X., Xu, L. Z. & Huang, Y. A. (2022). Laser projection proximity transfer for deterministic assembly of microchip arrays at scale. *Science China Technological Sciences*, 65(9), 2205–2214. <https://doi.org/10.1007/s11431-022-2138-x>.

Fig. 13.12F shows the example of printing 2×7 micro-LED chips enabled by the dynamic release stamp. Fig. 13.12G shows the electrical properties of micro-LED chips before and after transfer printing. The consistency of these two curves shows that the performance of the device is not influenced by the gripping and manipulation. These demonstrations illustrate the great potential of the dynamic release stamp for deterministic assembly, especially for mass transfer of micro-LEDs with high yield and accuracy.

13.5 Conclusion

In this chapter, we reviewed the laser-driven transfer printing techniques for micro-LED display. The mass transfer of micro-LEDs with high efficiency, high yield and high accuracy has delayed the commercialization process of micro-LED display. Laser-driven transfer printing techniques may provide an alternate solution for mass transfer of micro-LEDs and have been developing quickly. The basic principles, typical protocols, and performance of the recently developed laser-driven transfer printing techniques are overviewed in this chapter including the contact laser-driven transfer printing techniques (such as transfer printing based on a smart tape, universal transfer printing based on an SMP block, transfer printing based on a microstructured SMP stamp, and transfer printing based on an elastomer/SMP composite stamp) and noncontact laser-driven transfer printing techniques (such as transfer printing based on the interfacial thermal mismatch, transfer printing based on an active elastomeric microstructured stamp, transfer printing based on an octopus-inspired thermal controlled stamp, and transfer printing based on a dynamic release stamp).

References

- Al-Okaily, A. M., & Ferreira, P. M. (2015). Multi-physics modeling for laser micro-transfer printing delamination. *Journal of Manufacturing Processes*, 20, 414–424. Available from <https://doi.org/10.1016/j.jmapro.2014.07.006>, http://www.elsevier.com/wps/find/journaldescription.cws_home/620379/description#description.
- Ashdown, I., Speier, I., Sheen, C.W., & Schick, P.M. (2011) Method and magnetic transfer stamp for transferring semiconductor dice using magnetic transfer printing techniques.
- Bian, J., Zhou, L., Wan, X., Zhu, C., Yang, B., & Huang, Y. A. (2019). Laser transfer, printing, and assembly techniques for flexible electronics. *Advanced Electronic Materials*, 5(7). Available from <https://doi.org/10.1002/aelm.201800900>, [http://onlinelibrary.wiley.com/journal/10.1002/\(ISSN\)2199-160X](http://onlinelibrary.wiley.com/journal/10.1002/(ISSN)2199-160X).
- Biedermann, L. B., Beechem, T. E., Ross, A. J., Ohta, T., & Howell, S. W. (2010). Electrostatic transfer of patterned epitaxial graphene from SiC (0001) to glass. *New Journal of Physics*, 12. Available from <https://doi.org/10.1088/1367-2630/12/12/125016>, http://iopscience.iop.org/1367-2630/12/12/125016/pdf/1367-2630_12_12_125016.pdf, United States.
- Carlson, A., Bowen, A. M., Huang, Y., Nuzzo, R. G., & Rogers, J. A. (2012). Transfer printing techniques for materials assembly and micro/nanodevice fabrication. *Advanced Materials*, 24(39), 5284–5318. Available from <https://doi.org/10.1002/adma.201201386>.
- Carlson, A., Kim-Lee, H. J., Wu, J., Elvikis, P., Cheng, H., Kovalsky, A., Elgan, S., Yu, Q., Ferreira, P. M., Huang, Y., Turner, K. T., & Rogers, J. A. (2011). Shear-enhanced adhesiveless transfer printing for use in deterministic materials assembly. *Applied Physics Letters*, 98(26)264104. Available from <https://doi.org/10.1063/1.3605558>.

- Carlson, A., Wang, S., Elvikis, P., Ferreira, P. M., Huang, Y., & Rogers, J. A. (2012). Active, programmable elastomeric surfaces with tunable adhesion for deterministic assembly by transfer printing. *Advanced Functional Materials*, 22(21), 4476–4484. Available from <https://doi.org/10.1002/adfm.201201023>.
- Chaji, G.W., & Fathi, E. (2018). Integration of micro-devices into system substrate.
- Chen, F., Bian, J., Hu, J., Sun, N., Yang, B., Ling, H., Yu, H., Wang, K., Gai, M., Ma, Y., & Huang, Y. (2022). Mass transfer techniques for large-scale and high-density microLED arrays. *International Journal of Extreme Manufacturing*, 4(4)042005. Available from <https://doi.org/10.1088/2631-7990/ac92ee>.
- Chen, H. W., Lee, J. H., Lin, B. Y., Chen, S., & Wu, S. T. (2018). Liquid crystal display and organic light-emitting diode display: present status and future perspectives. *Light: Science and Applications*, 7(3), 17168. Available from <https://doi.org/10.1038/lsa.2017.168>, <http://www.nature.com/lsa/>.
- Chu, C. F., Lai, F. I., Chu, J. T., Yu, C. C., Lin, C. F., Kuo, H. C., & Wang, S. C. (2004). Study of GaN light-emitting diodes fabricated by laser lift-off technique. *Journal of Applied Physics*, 95(8), 3916–3922. Available from <https://doi.org/10.1063/1.1651338>.
- Ding, K., Avrutin, V., Izyumskaya, N., Özgür, Ü., & Morkoç, H. (2019). Micro-LEDs, a manufacturability perspective. *Applied Sciences*.
- Eisenhaure, J., & Kim, S. (2016). Laser-driven shape memory effect for transfer printing combining parallelism with individual object control. *Advanced Materials Technologies*, 1(7)1600098. Available from <https://doi.org/10.1002/admt.201600098>.
- Eisenhaure, J. D., Xie, T., Varghese, S., & Kim, S. (2013). Microstructured shape memory polymer surfaces with reversible dry adhesion. *ACS Applied Materials and Interfaces*, 5(16), 7714–7717. Available from <https://doi.org/10.1021/am402479f>.
- Feng, X., Meitl, M. A., Bowen, A. M., Huang, Y., Nuzzo, R. G., & Rogers, J. A. (2007). Competing fracture in kinetically controlled transfer printing. *Langmuir: the ACS Journal of Surfaces and Colloids*, 23(25), 12555–12560. Available from <https://doi.org/10.1021/la701555n>.
- Gao, Y., Li, Y., Li, R., & Song, J. (2017). An accurate thermomechanical model for laser-driven micro-transfer printing. *Journal of Applied Mechanics*, 84(6). Available from <https://doi.org/10.1115/1.4036257>.
- Geffroy, B., le Roy, P., & Prat, C. (2006). Organic light-emitting diode (OLED) technology: Materials, devices and display technologies. *Polymer International*, 55(6), 572–582. Available from <https://doi.org/10.1002/pi.1974>.
- Guo, C. (2022). Large-scale programmable assembly of functional micro-components for advanced electronics via light-regulated adhesion and polymer growth. *NPJ Flexible Electronics*, 6. Available from <https://doi.org/10.1038/s41528-022-00180-w>.
- Huang, Y., Zheng, N., Cheng, Z., Chen, Y., Lu, B., Xie, T., & Feng, X. (2016). Direct laser writing-based programmable transfer printing via bioinspired shape memory reversible adhesive. *ACS Applied Materials and Interfaces*, 8(51), 35628–35633. Available from <http://pubs.acs.org/journal/aamick>, 10.1021/acsami.6b11696.
- Hu, J. L., Chen, F. R., Bian, J., Sun, N. N., Wang, K. X., Ling, H., Yu, H. Y., Gai, M. X., Xu, L. Z., & Huang, Y. A. (2022). Laser projection proximity transfer for deterministic assembly of microchip arrays at scale. *Science China Technological Sciences*, 24(9), 2205–2214. Available from <https://doi.org/10.1007/s11431-022-2138-x>, <http://link.springer.com/journal/11431>.
- Jeong, J., Kim, J., Song, K., Autumn, K., & Lee, J. (2014). Geckoprinting: Assembly of microelectronic devices on unconventional surfaces by transfer printing with isolated gecko setal arrays. *Journal of The Royal Society Interface*, 11(99). Available from <https://doi.org/10.1098/rsif.2014.0627>, 20140627.
- Jiang, D., Feng, X., Qu, B., Wang, Y., & Fang, D. (2012). Rate-dependent interaction between thin films and interfaces during micro/nanoscale transfer printing. *Soft Matter*, 2, 418–423. Available from <https://doi.org/10.1039/c1sm06483e>.
- Jin, S. X., Li, J., Li, J. Z., Lin, J. Y., & Jiang, H. X. (2000). GaN microdisk light emitting diodes. *Applied Physics Letters*, 76(5), 631–633. Available from <https://doi.org/10.1063/1.125841>, <http://scitation.aip.org/content/aip/journal/apl>.
- Kahler, J., Heuck, N., Stranz, A., Waag, A., & Peiner, E. (2012). Pick-and-place silver sintering die attach of small-area chips. *IEEE Transactions on Components, Packaging and Manufacturing Technology*, 2(2), 199–207. Available from <https://doi.org/10.1109/tcpmt.2011.2170571>.

- Kaltwasser, M., Schmidt, U., Biswas, S., Reiprich, J., Schlag, L., Isaac, N. A., Stauden, T., & Jacobs, H. O. (2018). Core-shell transformation-imprinted solder bumps enabling low-temperature fluidic self-assembly and self-alignment of chips and high melting point interconnects. *ACS Applied Materials and Interfaces*, *10*(47), 40608–40613. Available from <https://doi.org/10.1021/acsami.8b12390>, <http://pubs.acs.org/journal/aamick>.
- Kim, S., Jiang, Y., Towell, K. L. T., Boutilier, M. S. H., Nayakanti, N., Cao, C., Chen, C., Jacob, C., Zhao, H., Turner, K. T., & Hart, A. J. (2019). Soft nanocomposite electroadhesives for digital micro- and nanotransfer printing. *Science Advances*, *5*(10). Available from <https://doi.org/10.1126/sciadv.aax4790>, <https://advances.sciencemag.org/content/5/10/eaax4790/tab-pdf>.
- Kim, T. I., Jung, Y. H., Song, J., Kim, D., Li, Y., Kim, H. S., Song, I. S., Wierer, J. J., Pao, H. A., Huang, Y., & Rogers, J. A. (2012). High-efficiency, microscale GaN light-emitting diodes and their thermal properties on unusual substrates. *Small (Weinheim an der Bergstrasse, Germany)*, *8*(11), 1643–1649. Available from <https://doi.org/10.1002/smll.201200382>.
- Kim, S., Wu, J., Carlson, A., Jin, S. H., Kovalsky, A., Glass, P., Liu, Z., Ahmed, N., Elgan, S. L., Chen, W., Ferreira, P. M., Sitti, M., Huang, Y., & Rogers, J. A. (2010). Microstructured elastomeric surfaces with reversible adhesion and examples of their use in deterministic assembly by transfer printing. *Proceedings of the National Academy of Sciences*, *107*(40), 17095–17100. Available from <https://doi.org/10.1073/pnas.1005828107>.
- Lee, H. E., Shin, J. H., Park, J. H., Hong, S. K., Park, S. H., Lee, S. H., Lee, J. H., Kang, I. -S., & Lee, K. J. (2019). Micro light-emitting diodes for display and flexible biomedical applications. *Advanced Functional Materials*, *29*(24)1808075. Available from <https://doi.org/10.1002/adfm.201808075>.
- Linghu, C., Wang, C., Cen, N., Wu, J., Lai, Z., & Song, J. (2019). Rapidly tunable and highly reversible bio-inspired dry adhesion for transfer printing in air and a vacuum. *Soft Matter*, *15*(1), 30–37. Available from <https://doi.org/10.1039/C8SM01996G>, <http://pubs.rsc.org/en/journals/journal/sm>.
- Linghu, C., Zhang, S., Wang, C., & Song, J. (2018). Transfer printing techniques for flexible and stretchable inorganic electronics. *NPJ Flexible Electronics*, *2*(1). Available from <https://doi.org/10.1038/s41528-018-0037-x>, <http://nature.com/npjflexelectron/>.
- Linghu, C., Zhang, S., Wang, C., Yu, K., Li, C., Zeng, Y., Zhu, H., Jin, X., You, Z., & Song, J. (2020). Universal SMP gripper with massive and selective capabilities for multiscaled, arbitrarily shaped objects. *Science Advances*, *6*(7). Available from <https://doi.org/10.1126/sciadv.aay5120>, <https://advances.sciencemag.org/content/6/7/eaay5120/tab-pdf>.
- Linghu, C., Zhu, H., Zhu, J., Li, C., & Song, J. (2019). Mechanics of magnet-controlled transfer printing. *Extreme Mechanics Letters*, 76–82. Available from <https://doi.org/10.1016/j.eml.2019.01.006>, <http://www.journals.elsevier.com/extreme-mechanics-letters/>.
- Liu, Z., Lin, C. H., Hyun, B. R., Sher, C. W., Lv, Z., Luo, B., Jiang, F., Wu, T., Ho, C. H., Kuo, H. C., & He, J. H. (2020). Micro-light-emitting diodes with quantum dots in display technology. *Light: Science and Applications*, *9*(1). Available from <https://doi.org/10.1038/s41377-020-0268-1>, <http://www.nature.com/lsa/>.
- Liu, X., Tong, C., Luo, X., Li, W., & Liu, Z. (2019). P-6.8: Study of mass transfer for micro-LED manufacturing. *SID Symposium Digest of Technical Papers*, *5*(S1), 775–778. Available from <https://doi.org/10.1002/sdtp.13644>.
- Li, R., Li, Y., Lü, C., Song, J., Saeidpourazar, R., Fang, B., Zhong, Y., Ferreira, P. M., Rogers, J. A., & Huang, Y. (2012). Axisymmetric thermo-mechanical analysis of laser-driven non-contact transfer printing. *International Journal of Fracture*, *176*(2), 189–194. Available from <https://doi.org/10.1007/s10704-012-9744-9>.
- Li, R., Li, Y., Lü, C., Song, J., Saeidpouraza, R., Fang, B., Zhong, Y., Ferreira, P. M., Rogers, J. A., & Huang, Y. (2012). Thermo-mechanical modeling of laser-driven non-contact transfer printing: Two-dimensional analysis. *Soft Matter*, *8*(27), 7122–7127. Available from <https://doi.org/10.1039/c2sm25339a>, <http://pubs.rsc.org/en/journals/journal/sm>.
- Li, L., Tang, G., Shi, Z., Ding, H., Liu, C., Cheng, D., Zhang, Q., Yin, L., Yao, Z., Duan, L., Zhang, D., Wang, C., Feng, M., Sun, Q., Wang, Q., Han, Y., Wang, L., Luo, Y., & Sheng, X. (2021). Transfer-printed, tandem microscale light-emitting diodes for full-color displays. *Proceedings of the National Academy of Sciences*, *118*(18). Available from <https://doi.org/10.1073/pnas.2023436118>.

- Luo, H., Wang, C., Linghu, C., Yu, K., Wang, C., & Song, J. (2020). Laser-driven programmable non-contact transfer printing of objects onto arbitrary receivers via an active elastomeric microstructured stamp. *National Science Review*, 7(2), 296–304. Available from <https://doi.org/10.1093/nsr/nwz109>, <http://nsr.oxfordjournals.org/>.
- Luo, H., Wang, S., Wang, C., Linghu, C., & Song, J. (2021). Thermal controlled tunable adhesive for deterministic assembly by transfer printing. *Advanced Functional Materials*, 31(16)2010297. Available from <https://doi.org/10.1002/adfm.202010297>.
- Marinov, V. R. (2018). 52-4: Laser-enabled extremely-high rate technology for μ LED assembly. *SID Symposium Digest of Technical Papers*, 49(1), 692–695. Available from <https://doi.org/10.1002/sdtp.12352>.
- Marinov, V. R., Swenson, O., Atanasov, Y., & Schneck, N. (2013). Laser-assisted ultrathin die packaging: Insights from a process study. *Microelectronic Engineering*, 101, 23–30. Available from <https://doi.org/10.1016/j.mee.2012.08.016>.
- Meitl, M. A., Zhu, Z. T., Kumar, V., Lee, K. J., Feng, X., Huang, Y. Y., Adesida, I., Nuzzo, R. G., & Rogers, J. A. (2006). Transfer printing by kinetic control of adhesion to an elastomeric stamp. *Nature Materials*, 5(1), 33–38. Available from <https://doi.org/10.1038/nmat1532>, <http://www.nature.com/nmat/>.
- Meng, W., Xu, F., Yu, Z., Tao, T., Shao, L., Liu, L., Li, T., Wen, K., Wang, J., He, L., Sun, L., Li, W., Ning, H., Dai, N., Qin, F., Tu, X., Pan, D., He, S., Li, D., . . . Wang, X. (2021). Three-dimensional monolithic micro-LED display driven by atomically thin transistor matrix. *Nature Nanotechnology*, 16(11), 1231–1236. Available from <https://doi.org/10.1038/s41565-021-00966-5>, <http://www.nature.com/nnano/index.html>.
- Mengüç, Y., Yang, S. Y., Kim, S., Rogers, J. A., & Sitti, M. (2012). Gecko-inspired controllable adhesive structures applied to micromanipulation. *Advanced Functional Materials*, 22(6), 1246–1254. Available from <https://doi.org/10.1002/adfm.201101783>.
- Pan, Z., Guo, C., Wang, X., Liu, J., Cao, R., Gong, Y., Wang, J., Liu, N., Chen, Z., Wang, L., Ishikawa, M., & Gong, Z. (2020). Wafer-scale micro-LEDs transferred onto an adhesive film for planar and flexible displays. *Advanced Materials Technologies*, 5(12)2000549. Available from <https://doi.org/10.1002/admt.202000549>.
- Parbrook, P. J., Corbett, B., Han, J., Seong, T. -Y., & Amano, H. (2021). Micro-light emitting diode: From chips to applications. *Laser & Photonics Reviews*, 15(5)2000133. Available from <https://doi.org/10.1002/lpor.202000133>.
- Ravikumar, V., Yi, N., Vepachedu, V., & Cheng, H. (2017). *Industrial internet of things: cybermanufacturing systems* (pp. 671–690). Springer International Publishing.
- Rupp, B.B., Plochowitz, A., Crawford, L.S., Shreve, M., Raychaudhuri, S., Butylkov, S., Wang, Y., Mei, P., Wang, Q., Kalb, J., Wang, Y., Chow, E.M., & LuJ. (2019). *IEEE 69th electronic components and technology conference (ECTC)*, pp. 2377–5726 1312–1315. Chiplet Micro-Assembly Printer <https://doi.org/10.1109/ECTC.2019.00203>.
- Saeidpourazar, R., Li, R., Li, Y., Sangid, M. D., Lu, C., Huang, Y., Rogers, J. A., & Ferreira, P. M. (2012). Laser-driven micro transfer placement of prefabricated microstructures. *Journal of Microelectromechanical Systems*, 21(5), 1049–1058. Available from <https://doi.org/10.1109/JMEMS.2012.2203097>.
- Saeidpourazar, R., Sangid, M. D., Rogers, J. A., & Ferreira, P. M. (2012). A prototype printer for laser driven micro-transfer printing. *Journal of Manufacturing Processes*, 14(4), 416–424. Available from <https://doi.org/10.1016/j.jmapro.2012.09.014>, United States.
- Sasaki, K., Schuele, P.J., Washougal, W.A., Ulmer, K., & Lee, J.J. (2017). System and method for the fluidic assembly of emissive displays.
- Schadt, M. (2009). Milestone in the history of field-effect liquid crystal displays and materials. *Japanese Journal of Applied Physics*, 48(3), 03B001. Available from <https://doi.org/10.1143/jjap.48.03b001>.
- Tang, C. W., & Vanslyke, S. A. (1987). Organic electroluminescent diodes. *Applied Physics Letters*, 51(12), 913–915. Available from <https://doi.org/10.1063/1.98799>.
- Tan, D., Wang, X., Liu, Q., Shi, K., Yang, B., Liu, S., Wu, Z. -S., & Xue, L. (2019). Switchable adhesion of micropillar adhesive on rough surfaces. *Small (Weinheim an der Bergstrasse, Germany)*, 15(50) 1904248. Available from <https://doi.org/10.1002/sml.201904248>.

- Ueda, T., Ishida, M., & Yuri, M. (2011). Separation of thin GaN from sapphire by laser lift-off technique. *Japanese Journal of Applied Physics*, 50(4). Available from <https://doi.org/10.1143/JJAP.50.041001>Japan, <http://jjap.jsap.jp/link?JJAP/50/041001/pdf>.
- Virey, E. H., & Baron, N. (2018). 45-1: Status and prospects of microLED displays. *SID Symposium Digest of Technical Papers*, 49(1), 593–596. Available from <https://doi.org/10.1002/sdtp.12415>.
- Virey, E. H., Baron, N., & Bouhamri, Z. (2019). 11-3: Overlooked challenges for microLED displays. *SID Symposium Digest of Technical Papers*, 50(1), 129–132. Available from <https://doi.org/10.1002/sdtp.12872>.
- Wang, C., Linghu, C., Nie, S., Li, C., Lei, Q., Tao, X., Zeng, Y., Du, Y., Zhang, S., Yu, K., Jin, H., Chen, W., & Song, J. (2020). Programmable and scalable transfer printing with high reliability and efficiency for flexible inorganic electronics. *Science Advances*, 6(25). Available from <https://doi.org/10.1126/sciadv.abb2393>, <https://advances.sciencemag.org/content/advances/6/25/EABB2393.full.pdf>.
- Wu, M.H., Fang, Y.H., & Chao, C.H. (2020). Magnetic transfer module and method for transferring electronic element.
- Wu, M.H., Fang, Y.H., & Chao, C.H. (2017). Electric-programmable magnetic module and picking-up and placement process for electronic devices.
- Xue, Y., Zhang, Y., Feng, X., Kim, S., Rogers, J. A., & Huang, Y. (2015). A theoretical model of reversible adhesion in shape memory surface relief structures and its application in transfer printing. *Journal of the Mechanics and Physics of Solids*, 77, 27–42. Available from <https://doi.org/10.1016/j.jmps.2015.01.001>.
- Yang, S. Y., Carlson, A., Cheng, H., Yu, Q., Ahmed, N., Wu, J., Kim, S., Sitti, M., Ferreira, P. M., Huang, Y., & Rogers, J. A. (2012). Elastomer surfaces with directionally dependent adhesion strength and their use in transfer printing with continuous roll-to-roll applications. *Advanced Materials*, 24(16), 2117–2122. Available from <https://doi.org/10.1002/adma.201104975>.
- Yan, Z., Pan, T., Xue, M., Chen, C., Cui, Y., Yao, G., Huang, L., Liao, F., Jing, W., Zhang, H., Gao, M., Guo, D., Xia, Y., & Lin, Y. (2017). Thermal release transfer printing for stretchable conformal bioelectronics. *Advanced Science*, 4(11)1700251. Available from <https://doi.org/10.1002/adv.201700251>.
- Zhang, X., Linghu, C., & Song, J. (2019). Three-dimensional mechanical modeling of magnet-controlled transfer printing. *International Journal of Applied Mechanics*, 11(05)1950042. Available from <https://doi.org/10.1142/s175882511950042x>.
- Zhang, S., Luo, H., Wang, S., Chen, Z., Nie, S., Liu, C., & Song, J. (2021). A thermal actuated switchable dry adhesive with high reversibility for transfer printing. *International Journal of Extreme Manufacturing*, 3(3)035103. Available from <https://doi.org/10.1088/2631-7990/abff69>.
- Zhang, Y., Lu, B., Wang, T., Feng, X., & Xu, H. (2019). A photochemical approach toward high-fidelity programmable transfer printing. *Advanced Materials Technologies*, 91900163. Available from <https://doi.org/10.1002/admt.201900163>.
- Zhdanov, D. D., Sokolov, V. G., Potemin, I. S., Voloboy, A. G., Galaktionov, V. A., & Kirilov, N. (2014). Modeling and computer design of liquid crystal display backlight with light polarization film. *Optical Review*, 21(5), 642–650. Available from <https://doi.org/10.1007/s10043-014-0103-0>, <http://www.springeronline.com/sgw/cda/frontpage/0,11855,5-40109-70-1126859-0,00.html>.

This page intentionally left blank

CHAPTER 14

Energy systems fabricated by transfer printing technologies

Yijia Wang and Yang Zhao

Department of Mechanical and Materials Engineering, Western University, London, ON, Canada

14.1 Introduction

Transfer printing offers great potential for the heterogeneous integration of materials arranged in two-dimensional and three-dimensional layouts. The typical transfer printing methods consist of two steps: (1) prefabricated ink (device) on the donor substrate is picked up by a stamp, and (2) the inked stamp is brought into contact with the receiver substrate and print the device onto the receiver substrate. Since the fabrication of the ink sometimes requires harsh chemical environments and high processing temperatures, transfer printing enables the ink transfer from the fabrication substrate to the receiver substrate and allows the device to be utilized on expanded substrate materials, including flexible substrates with limited thermal, mechanical, and chemical stability (Carlson et al., 2012; Lawes et al., 2015; Linghu et al., 2018; Zhou et al., 2019).

This chapter mainly focuses on the application of the transfer printing method in different energy systems, including rechargeable batteries, supercapacitors, fuel cells, water splitting, and solar cells. For each category, we will focus on the role of transfer printing in addressing the challenges in the energy system and the performance of the resultant devices.

14.2 Rechargeable batteries

Rechargeable batteries that offer requisite energy and power density are promising for next-generation energy storage systems. The electronics industry projects a demand for flexible electronics, which entails the demand for performant and flexible energy storage in varied cell configurations (Zhao & Guo, 2020). The performance of the batteries is highly dependent on the properties of the electrode-electrolyte interphase, which needs to be rationally designed. Transfer printing not only enables the fabrication of patterned electrodes that fulfill the purpose of the assembled device on a flexible substrate but also allows the incorporation of the artificial solid-electrolyte interphase, which cannot be directly formed on the electrodes due to the incompatibility of the processing

conditions. Over the years, transfer printing has been gradually employed in artificial interface and battery electrode fabrication to realize flexible battery and resolve the contacting issues between the solid-state electrolyte and battery electrode. In 2013, Xu et al. reported a stretchable lithium-ion battery, in which the cathode LiCoO_2 and the anode $\text{Li}_4\text{Ti}_5\text{O}_{12}$ were transfer printed onto the segmented current collectors. The resulting battery offers biaxial stretchability up to strains of 300% and delivers an areal capacity of 1.1 mAh/cm^2 at a charge/discharge rate of $C/2$ (Xu et al., 1543). One of the key advantages of the transfer printing method is that it allows the tuning of film properties without affecting the underlying substrate. In 2017, the polyaniline (PANI) was first spin-coated and tape-casted onto the stainless-steel foil, then annealed at 180°C for 1 hour, before being printed on the graphene oxide (GO)-sulfur (S) electrodes using a roll press. The process is depicted in Fig. 14.1. The resulting PANI film effectively suppressed the dissolution of sulfur in Li-S battery using a liquid electrolyte. Compared with a conventional sulfur electrode that has a poor capacity retention of only 41% after 200 cycles, the $1 \mu\text{m}$ printed conductive polymer layer enhances the cycling performance: 96.4% of the initial capacity was retained and an average Coulombic efficiency of 99.6% was achieved after 200 cycles. The uniform, transfer-printed PANI film with tunable thickness provides the robust protection of the GO-S electrodes by effectively suppressing the dissolution of polysulfides and enhancing electronic conductivity (Moon et al., 2017).

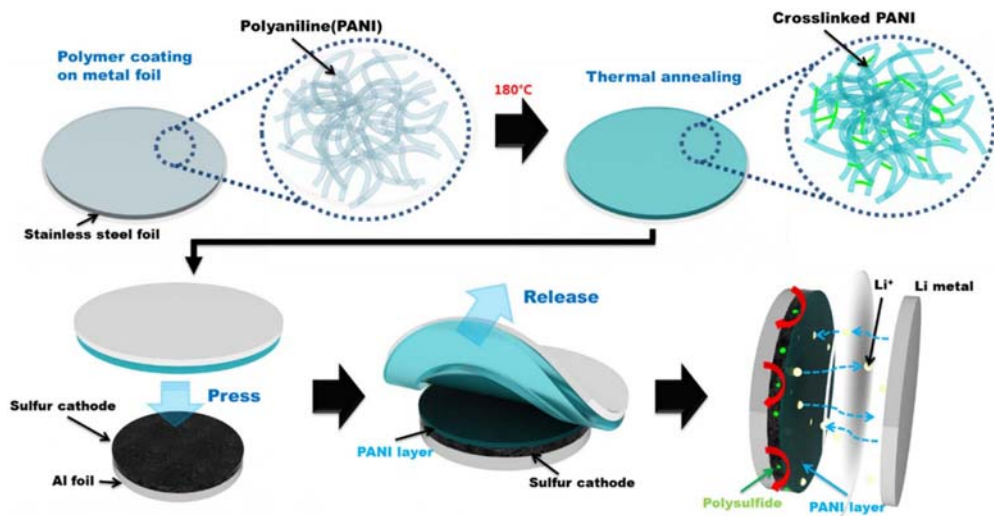


Figure 14.1 Schematic illustration of the polyaniline-layer coated by a printing method. From Moon, S., Yoo, J.-K., Jung, Y. H., Kim, J.-H., Jung, Y. S. & Kim, D. K. (2017). Journal of The Electrochemical Society. 164. (Original work published 2017).

In solid-state batteries, the poor contact between the cathode and the solid-state electrolyte usually leads to large transfer resistance and compromised electrochemical performance. To this end, Liu et al. optimized the contact between the cathode and SSE using transfer printing technology. In this study, the LiFePO_4 (LFP) cathode was transfer-printed on $\text{La}_2\text{Sn}_2\text{O}_7$ ceramic layer coated $\text{Li}_{6.4}\text{La}_3\text{Zr}_{1.4}\text{Ta}_{0.6}\text{O}_{12}$ (LLZTO@LSO-CSE). It is found that the AC impedances of the interface between the transfer-printed LFP cathode and the LLZTO@LSO-CSE before and after 100 cycles are 213 and 379 Ω , respectively, which are considerably lower than that of the interface formed between the LFP cathode assembled using ordinary assembly method. The ameliorated interfacial contact leads to the enhanced rate capability and cycling performance of the transfer-printed LFP cathodes, which exhibit capacities of 141.4 and 128.1 mAh/g at 1°C and 2°C, respectively, and demonstrate a high capacity retention of 72% after 400 cycles (Liu et al., 2021).

Although vertically aligned carbon nanotube (VACNT) offers unique templates for constructing hierarchical structures with controlled morphology at different length scales, the fragile structure limits the surface modification and decoration to gas phase processes. Herein, Jessl et al. secured the VACNTs firmly to the substrate through transfer printing and decorated the VACNTs with metal oxide nanoparticles using microwave-assisted hydrothermal synthesis. Compared with the conventional battery electrode, the open honeycomb architectures enhance the electron and ion transport, increase the areal loading, and promote the interface contact between the active materials and the VACNTs (Fig. 14.2A). The VACNTs were first grown on patterned catalyst using chemical vapor deposition (CVD) on Si wafer, and then transfer printed on a conductive PCP film covered glass substrate. The $\alpha\text{-Fe}_2\text{O}_3$ nanoplatelets were introduced to the VACNTs forest via hydrothermal synthesis. The process is illustrated in Fig. 14.2B. The resulting decorated electrodes deliver a high initial discharge capacity above 1500 mAh/g at 0.05°C (Fig. 14.2C), with a well-defined voltage plateau at 0.75 V (Fig. 14.2C and D). The transfer-printed VACNTs with hydrothermal decorated $\alpha\text{-Fe}_2\text{O}_3$ nanoparticles demonstrate a stable cycling capacity at 912 mAh/g after 20 cycles, while the capacities of conventional CNT- Fe_2O_3 electrode and CNT honeycomb with drop-casted Fe_2O_3 drop below 400 mAh/g after 20 cycles (Fig. 14.2E). The corresponding scanning electron microscopy (SEM) images of the cycled electrodes are shown in Fig. 14.2F, respectively. The improved electrochemical performance of the structured electrodes is attributed to the synergistic effects of the transfer-printed VACNTs forest, which prevent the delamination during the hydrothermal process, and the good interfacial contact resulting from the hydrothermal synthesis of nanoparticles on the VACNTs (Jessel et al., 2019).

Very recently, Li et al. fabricated a freestanding submicrometer-thick electrochromic cathode composed of Prussian blue (PB) nanoparticles, silver nanowires (AgNW), and poly(3,4-ethylenedioxythiophene):poly(styrenesulfonate) (PEDOT:PSS) and transferred the

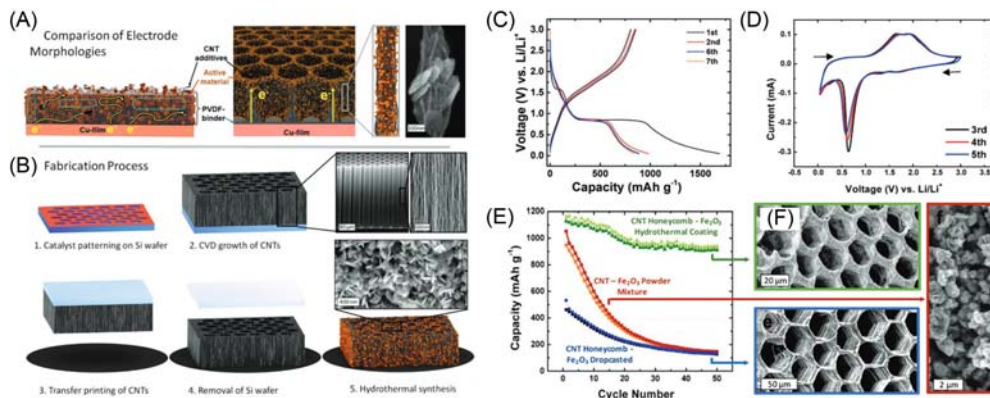


Figure 14.2 (A) Comparison of the morphologies of a standard battery electrode (*left*) and our suggested electrode structure (*right*), which allows for better Li-ion and electron transport. (B) Fabrication process of the electrodes using chemical vapor deposition (CVD) growth of carbon nanotubes (CNTs) and hydrothermal synthesis of α - Fe_2O_3 nanoplatelets. (C) Charge–discharge curves and (D) cyclic voltammetry of the hydrothermally synthesized CNT- Fe_2O_3 honeycomb electrode. (E) Cycling performance at 0.2°C of the new electrode architecture (green), the same CNT honeycomb architecture with drop-casted active material (blue), and a CNT-active material film casted at $100\ \mu\text{m}$ (red). From Jessl, S., Copic, D., Engelke, S., Ahmad, S. & Volder, M. De. (2019). Small. (Original work published 2019).

composite cathode onto a hydrogel electrolyte using water-assisted transfer printing (Fig. 14.3A). Coupled with zinc metal anode, the resulted ultrathin battery with thickness of $33.5\ \mu\text{m}$ exhibits high flexibility, high optical modulation, and a capacity of $63.2\ \text{mAh/g}$ (Fig. 14.3B). Owing to the appealing mechanical stability and flexibility, these energy devices demonstrate excellent conformability with irregular surface (Fig. 14.3C). The simple and scalable electrode fabrication using water-assisted transfer printing developed opened up avenues for development of smart power sources (Li et al., 2023).

14.3 Supercapacitors

Flexible supercapacitors that utilize carbonaceous materials such as carbon nanotubes and high-quality graphene are promising for wearable electronics. However, the synthesis of these materials is usually carried out at high temperatures, which limits the choices of substrate materials (Lawes et al., 2015). To this end, transfer printing enables the adoption of these materials for flexible supercapacitors and facilitates the controlled fabrication of ultrathin film with high precision and good reproducibility. In 2013, Niu et al. reported a fast and effective strategy for fabricating ultrathin single-walled carbon nanotubes (SWCNTs) transparent and conductive films from directly grown SWCNTs via transfer printing. The directly grown SWCNTs film was first spread out on a flat silicon substrate and then transferred to the poly(ethylene terephthalate) (PET) substrate with

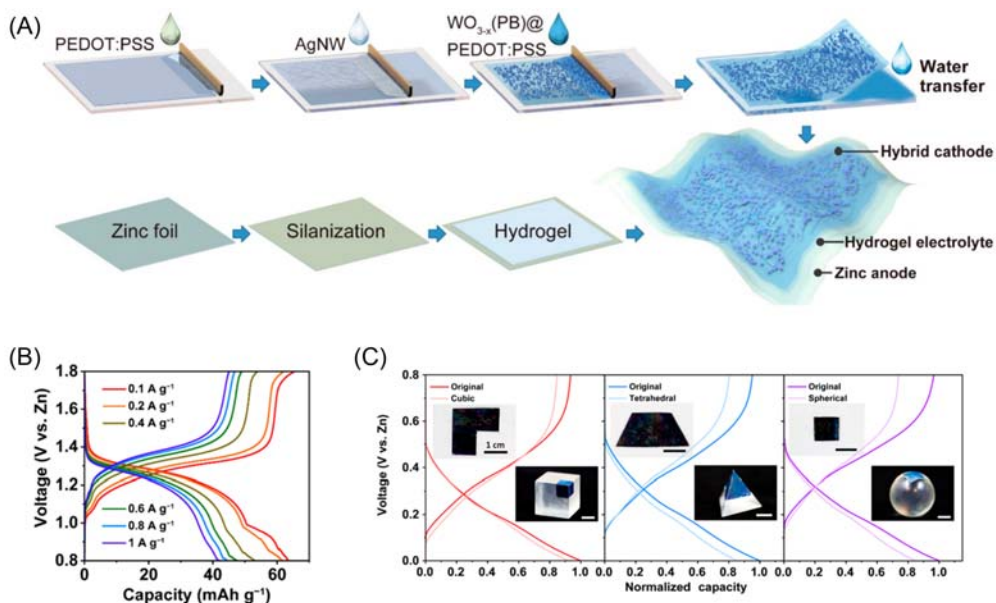


Figure 14.3 (A) Schematic of the transfer printing process and device assembly. (B) Galvanostatic charging and discharging curves of the Zn-PB battery. (C) Capacity retention of the capacitive device on various curved surfaces. Insets show the original and attached states. *From Li, J., Yang, P., Li, X., Jiang, C., Yun, J., Yan, W., Liu, K., Fan, H. J. & Lee, S. W. (2023). ACS Energy Letters, 8(1), 1–8. <https://doi.org/10.1021/acsenergylett.2c02029>.*

electrostatic charges. Through transferring the SWCNTs film between two PET substrates, the thickness of the film was halved by each transfer, and the continuous ultrathin film with uniform thickness can be obtained. For SWCNTs transparent electrodes with a thickness of 50 nm, a specific capacitance of $146 \mu\text{F}/\text{cm}^2$ can be attained (Niu et al., 2013). In 2017, Song et al. realized high-resolution transfer printing of graphene lines with $<5 \mu\text{m}$ width and spacing. The quasi-three-dimensional graphene lines with a high aspect ratio pattern lead to increased surface area for a given projected area, which are highly desirable for miniaturized graphene microsupercapacitors with high areal capacitance (Song et al., 2017). Later in 2018, Song et al. demonstrated the use of transfer-printed graphene electrodes in microsupercapacitors. The transfer printing process is illustrated in Fig. 14.4A. Specifically, graphene ink was first introduced to the hydrophobic silicon mold to fill the trenches. After the ink dried, NOA73 UV-curable adhesive was spread on the mold, and the PET substrate was pressed from the top. The PET-NOA73-graphene stack was then obtained, after curing with UV light. The graphene electrodes were cured by a two-step annealing process, before and after the ion gel deposition, for microsupercapacitors assembly. The microsupercapacitors exhibit a capacitance of $6.63 \text{ mF}/\text{cm}^2$ and superior longitudinal and transverse flexibility (Fig. 14.4B) (Song et al., 2018).

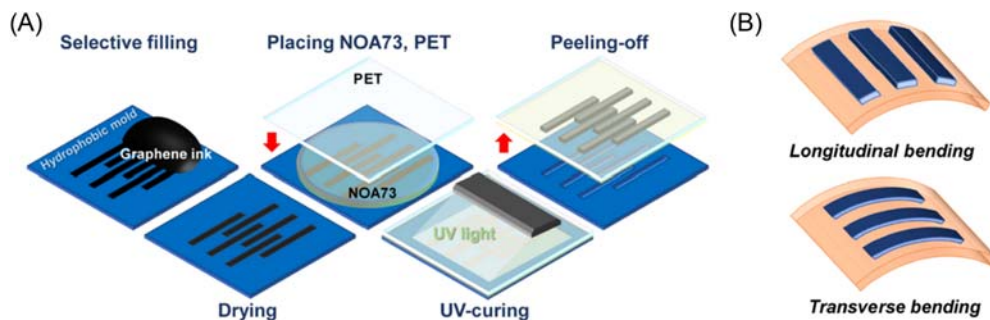


Figure 14.4 (A) Transfer printing steps using selective filling method for high-resolution graphene lines. (B) Schematics of directional bending, showing bending axis with respect to graphene lines. From Song, D., Secor, E.B., Wang, Y., Hersam, M.C. & Daniel Frisbie, C. (2018). Transfer printing of sub-5 μm graphene electrodes for flexible microsupercapacitors. *ACS Applied Materials and Interfaces*, 10(26), 22303–22310. <https://doi.org/10.1021/acsami.8b06235>.

In 2018, a cotton fabric-sandwiched ultra-flexible supercapacitor was demonstrated by Zhou et al. The silver film, carbon paste, and the active material (activated carbon ink) were screen printed successively onto the polydimethylsiloxane (PDMS) substrate to produce the electrodes. The as-prepared electrodes were then transfer printed on both sides of the poly(vinyl alcohol)/ H_3PO_4 -soaked cotton fabric solid-state electrolyte. After solidification at room temperature for 1 hour, the PDMS substrates were peeled off and the symmetric flexible supercapacitors were obtained. The device exhibits a specific gravimetric capacitance of 63.7 F/g at a current density of 1 A/g, with a capacity retention of 85% after 2000 cycles. Even after 100 times of bending or twisting, 93.3% of the capacitance at original level was retained (Zhou et al., 2018). Chen et al. designed a three-dimensional nanotube-structured Ni@MnO_2 electrode for planar supercapacitors in 2019. The patterned Ni was achieved on fluorine-doped tin oxide (FTO) glass, and then transfer printed onto a flexible Kapton tape. The Ni nanotubes were grown onto the substrate through electrochemically alloying-dealloying Ni–Cu alloy. After that, the MnO_2 nanoflakes were electrodeposited onto the Ni nanotubes. The supercapacitor employing the three-dimensional nanotube-structured Ni@MnO_2 electrode delivers a remarkably enhanced areal capacitance of 10.75 mF/cm^2 , which is 2.4 times of the pristine supercapacitors and maintains stable cycling performance under different bending conditions (Chen et al., 2019). Qiu et al. developed flexible asymmetric microsupercapacitors (AMSCs), in which the interdigital indium tin oxide (ITO)/PET substrate was realized by transfer printing. The AMSC comprised of NiCoP@NiOOH positive electrode and zeolite imidazolid framework derived carbon (ZIF-C) negative electrode, achieves a high specific areal capacitance of 54.7 mF/cm^2 at 0.5 mA/cm^2 and an excellent energy density of 13.9 $\mu\text{Wh}/\text{cm}^2$ at the power density of 270.5 $\mu\text{W}/\text{cm}^2$ (Qiu et al., 2019).

In 2020, Giannakou demonstrated a novel approach to transfer print three-dimensional objects. Silver nanoparticles were first inkjet-printed onto a water-soluble PVA substrate, and then the NiO nanoparticles were inkjet-printed on top of the silver current collector. The three-dimensional object is placed inside a plastic container fulfilled with water. The PVA substrate with the printed device was then placed on the water surface to allow the dissolution of the PVA substrate. Once the PVA substrate dissolved, the water-assisted transfer printing process would start by lowering the water level inside the container with a syringe, until the printed device conformed on the three-dimensional object. Unlike conventional water transfer printing, this approach avoids the printed device from contacting with water, which enables a variety of design flexibility. The conformal supercapacitors showed a maximum specific areal capacitance of 87.2 mF/cm^2 within $0 - 1.5 \text{ V}$ (Giannakou et al., 2020).

In 2021, Lu et al. presented a cost-effective, green, and scalable process for fabricating activated carbon electrodes for planar microsupercapacitors using transfer printing techniques. The process renders the resulting microsupercapacitors a tunable voltage output, shape diversity, remarkable mechanical flexibility, and modularization on various substrates (Lu et al., 2021). Xu et al. transfer printed the laser-scribed graphene (LSG) from the polyimide substrate to the stretchable PDMS substrate. The LSG/PDMS electrodes are then used in constructing the in-plane stretchable supercapacitors, which can achieve a capacitance of 18 mF/cm^2 at a current density of 0.02 mA/cm^2 and demonstrates stable cycling for up to 1000 cycles (Xu et al., 2021).

14.4 Fuel cells

Fuel cells have been regarded as one of the most promising power systems in the 21st century (Chiang et al., 2022). The performance of the fuel cell is closely related to the amount, thickness, and type of catalyst used. Conventional coating method such as roll press fails to achieve a thin catalyst layer, hence transfer printing combined with hot pressing method are developed to address this issue (Pettersson et al., 2006). Transfer printing is also an effective technique to enhance the efficiency of the catalyst by controlling the morphology of the resulting catalyst layer. The employment of transfer printing to construct the thin catalyst layer provides pathways for the fundamental study of catalysts and practical applications. In 2019, Zhou et al. developed a one-step impressing process to prepare the patterned cathode catalyst layer, in which Nylon sieves of different sizes were used as transfer printing templates (Fig. 14.5). The optimized patterned catalyst leads to a superior performance of 705 mW/cm^2 , which is 10% higher than that of the plain one (Zhou et al., 2022). In 2022, Chiang et al. fabricated the catalyst layer using heat transfer printing. The authors proposed to increase the hydrophilicity of the anode and reduce the platinum (Pt) catalyst by replacing organic dispersants with inorganic dispersant montmorillonite. The dispersed carbon black with inorganic dispersants

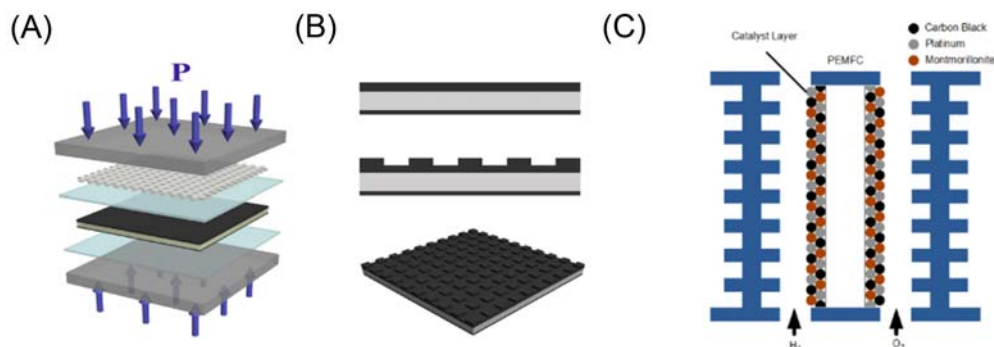


Figure 14.5 (A) Schematic diagram of the impressing process. (B) Side view and perspective views of the plain and patterned catalyst-coated membrane. (C) Proton exchange membrane fuel cells with a catalyst layer fabricated using an inorganic dispersant. From Zhou, Y., Zhang, W., Yu, S., Jiang, H. & Li, C. (2022). *Patterned catalyst layer boosts the performance of proton exchange membrane fuel cells by optimizing water management*. Chinese Journal of Chemical Engineering, 44, 246–252. <https://doi.org/10.1016/j.cjche.2021.06.001>

was coated with platinum through thermal chemical recovery. The Pt/C catalyst prepared with ultrasonic mixing was coated on a polytetrafluoroethylene (PTFE) membrane. The catalyst layer was heat-transfer printed onto both sides of DuPont Nafion 212 membrane at a temperature of 125°C and a pressure of 120 psi. After that, the PTFE films were peeled off from the Nafion membrane, and then the Nafion membranes were incorporated in PEMFC. At room temperature and a hydrogen gas flow rate of 15 sccm. PEMFC with the catalyst prepared using inorganic dispersants deliver an impressive power density of 4.49 mW/cm² (Chiang et al., 2022).

14.5 Water splitting

Photoelectrochemical (PEC) water splitting device utilizes a photoelectrode to absorb sunlight, after which the photogenerated electrons and holes would react with water to produce hydrogen and oxygen. Compared with the flat substrate, a textured substrate with large surface area would effectively enhance the light absorption. However, the deposition conditions of the photoelectrodes limit the choices of the viable surface-textured substrate. Transfer printing facilitates the integration of photoelectrodes and ensures conformal coatings onto these textured substrates. Photoanodes made using BiVO₄ is particularly promising given the favorable features of BiVO₄, such as moderate bandgap, visible light activity, chemical stability, and cost-effective synthesis methods (Choi et al., 2020; Gaikwad et al., 2022; Zhao et al., 2016) In 2016, Zhao et al. fabricated ultrathin BiVO₄ photoanode film on textured PDMS substrates using a modified water-assisted transfer printing method (Fig. 14.6A). Briefly, the patterned PDMS substrate was prepared by pouring the PDMS solution into the

silicon molds with varied microstructures, including rods, squares, and pillars, fabricated by photolithography and deep reactive ion etching. After the PDMS substrate was cured, the patterned PDMS substrate was peeled off from the mold and used as the textured substrate. To prepare the photoanode film, 300 nm Au film was first deposited on SiO₂/Si wafer by electron beam evaporation. Next, 10 nm SnO₂ thin film and 80 nm BiVO₄ thin film were spin-coated on top of the Au film. A thin layer of water-soluble poly(vinyl alcohol) (PVA) was spin-coated on top of BiVO₄. A thermal release tape (TRT) was attached to the top of the stack and served as a temporary transfer holder. At room temperature, the stacking (TRT/PVA/BiVO₄/SnO₂/Au) was peeled off from the SiO₂/Si wafer in a water bath. The patterned PDMS substrate was then used to fish out the stacking, and the stacking is attached to the PDMS substrate due to the capillary force induced by water drying. The resulting BiVO₄ photoanode of only 80 nm thick shows a photocurrent density of 1.37 mA/cm² at 1.23 V versus reversible hydrogen electrode (RHE) on patterned PDMS substrates, which is 60% higher than that of the BiVO₄/SnO₂/Au on flat Si. The photocurrent density further increases to approximately 2.0 mA/cm² at 1.23 V_{RHE}, when FeOOH oxygen evolution catalyst is introduced (Zhao et al., 2016). In 2020, Choi et al. demonstrated a two-dimensional arranged globular Au nanosphere monolayer array with a highly ordered hexagonal hole pattern, which was transfer printed onto the surface of photoanodes comprised of metal oxide films (α -Fe₂O₃ and Mo:BiVO₄) to enhance the PEC water oxidation through plasmon-induced resonance energy transfer (PRT) effect (Fig. 14.6B). The rationally designed Au array simultaneously promotes the light

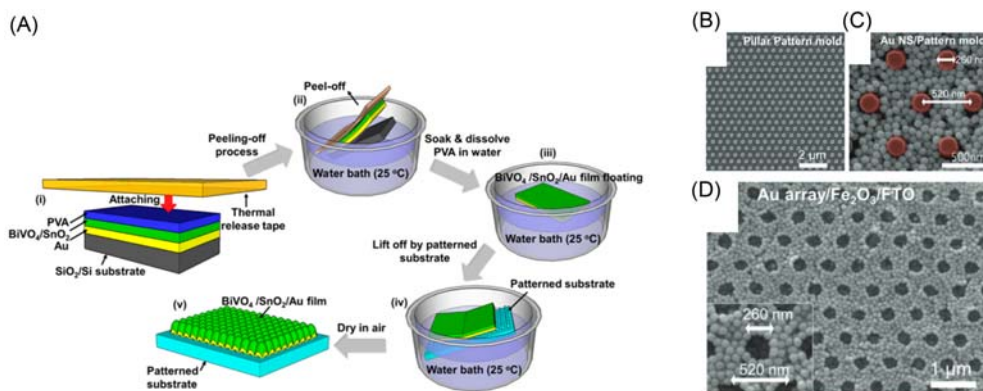


Figure 14.6 (A) Schematic illustration of the transfer process for integrating BiVO₄ onto patterned PDMS substrates. The scanning electron microscopy images of (B) the pillar pattern mold with a hexagonal arrangement, (C) the assembled Au NSs on the pillar pattern mold, and (D) the transfer-printed AuNS patterned array (Au array) on Fe₂O₃ film. From Zhao, J., Guo, Y., Cai, L., Li, H., Wang, K. X., Cho, I.S., Lee, C.H., Fan, S. & Zheng, X. (2016). High-performance ultrathin BiVO₄ photoanode on textured polydimethylsiloxane substrates for solar water splitting. *ACS Energy Letters*, 1(1), 68–75. <https://doi.org/10.1021/acsenergylett.6b00032>.

absorptance, charge transport, and charge transfer efficiency. As a result, the Au array-incorporated α -Fe₂O₃ film exhibits an over 3.3-fold higher photocurrent density at 1.23 V versus RHE, while the Au array-incorporated BiVO₄ film demonstrates around 1.5-fold (2.76 mA/cm²) of that of the bare photoanode at 1.23 V versus RHE. Transfer-printed Au array amplifies the PRT effect, therefore ameliorating the recombination of photogenerated holes and significantly improving the efficiency of PEC water oxidation (Choi et al., 2020).

14.6 Solar cells

Flexible thin film solar cells (TFSCs) not only broaden the applications of solar cells, but also plays a vital role in reducing the materials cost and the installation cost (Lee et al., 2014). The major challenge for fabricating flexible TFSCs arises from the incompatibility between the TFSCs fabrication condition and the thermal, mechanical, and chemical properties of the substrate (Lee et al., 2014). To this end, the transfer printing method enables the integration of high-temperature processed TFSCs onto the low-temperature tolerant flexible receiver substrate. Based on their fundamental working principle, three major transfer printing methods for TFSCs fabrication can be categorized: (1) transfer printing by sacrificial layer (Lumb et al., 2019; Nam et al., 2016), (2) transfer printing by controlled crack (Adrian et al., 2020; Bronstein et al., 2014; Cheng et al., 2021; Fan et al., 2016, 2019; Gai et al., 2019; Gong et al., 2022; Hu et al., 2021; Kang et al., 2010; Lumb et al., 2016; Mohapatra et al., 2019; Obaid & Lu, 2019; Schmieder et al., 2019; Srivastava et al., 1467; Sun et al., 2020; Wang et al., 2021; Wei et al., 2022; Yi et al., 2019; Yu et al., 2022; Yüce et al., 2019), and (3) transfer printing by water-assisted thin film delamination (Sun et al., 2019; Wang et al., 2020; Wang et al., 2022; Xie et al., 2022; Yu et al., 2021).

Transfer printing of inorganic thin film semiconductors had been challenging, due to the lack of a suitable sacrificial layer that can be etched away using mild etchant. In 2016, Nam et al. developed a water-soluble germanium oxide sacrificial layer and fabricated stretchable amorphous Si TFSCs using transfer printing. The transfer printing process is illustrated in Fig. 14.7. The authors compare the performance of the solar cells on the growth substrate and that on the flexible substrate and show that the performance was well-preserved after the transfer printing process. Furthermore, stretchable solar cells can withstand a stretching up to 50% without any decay in performance. The germanium oxide sacrificial layer has multiple advantages, including mild etching conditions, compatibility with high process temperature, and mechanical stability during the fabrication process (Nam et al., 2016).

Transparent conductive electrode suffers from either low conductivity or high surface roughness, which leads to reduced fill factor (FF) and power conversion efficiency (PCE). To address this issue, Kang et al. fabricated a transparent Cu nanowire mesh

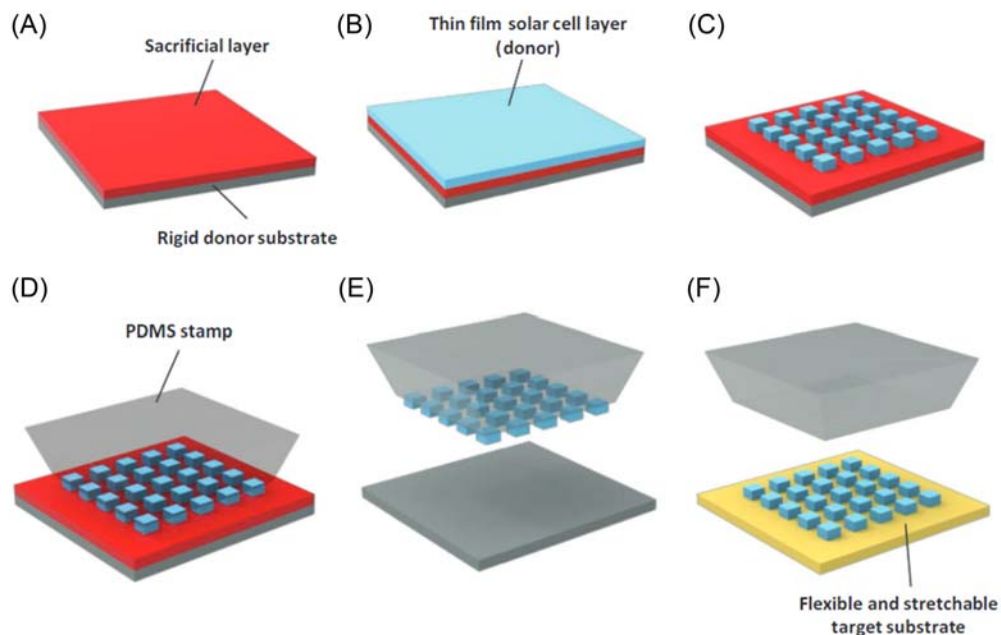


Figure 14.7 Schematic diagram of the transfer printing process for thin film solar cells (TFSCs) using a sacrificial layer. (A) Deposition of germanium oxide sacrificial layer on rigid donor substrate. (B) Deposition of TFSC layers on the sacrificial layer. (C) Patterning of TFSC through photolithography and etching. (D) Attachment of PDMS stamp to top of solar cell layers to hold patterned solar cells during sacrificial layer etching. (E) Release of TFSCs from donor substrate by etching sacrificial layer. (F) Transfer printing of TFSCs on the target substrate. *From Nam, J., Lee, Y., Choi, W., Kim, C. S., Kim, H., Kim, J., Kim, D. H. & Jo, S. (2016). Advanced Energy Materials. (Original work published 2016).*

electrode on PET substrate by a simple transfer printing method in 2010. The resulting transparent Cu electrode offers comparable optical transmittance and reduced sheet resistance with that of the conventional ITO electrode (Kang et al., 2010). In 2014, Bronstein et al. employed transfer-printed, ultrathin, crystalline Si solar cells to study the performance of luminescent solar concentrator (Bronstein et al., 2014). In 2016, Fan et al. designed a PEDOT:PSS flexible transparent electrodes by transfer printing using mild acid. The fabricated electrodes exhibit a significantly improved stability, conductivity, transparency, and mechanical stability on a plastic substrate (Fan et al., 2016). In 2020, Sun et al. demonstrated an efficient all-solution-processed nonfullerene (NF) organic solar cells. The group introduced hydrogen molybdenum bronze (H_xMoO_3) between the NF active layer and the PEDOT:PSS to (1) effectively extract holes from the NF active layer and (2) resolve the contact issues between the NF active layer and PEDOT:PSS. During the fabrication of the organic solar cells, the PEDOT:PSS films were transfer printed on top of the H_xMoO_3 film. The assembled organic solar cells exhibit an efficiency of 11.9% for small-area devices [0.04 cm

(Lawes et al., 2015)] and 10.3% for large-area [1 cm (Lawes et al., 2015)] devices (Sun et al., 2020). In 2021, Wang et al. introduced a low amount of PDMS additive, and the intrinsic stretchability of PTB7-Th:IEICO-4F bulk heterojunction film is greatly improved from 5% to 20% strain without sacrificing the photovoltaic performance. During the organic solar cell assembly, the multilayer stacking was realized through transfer printing with the assistance of electrical adhesive D-Sorbitol. The resultant devices display an excellent PCE of 10.1% with an electrode transmittance of 84%. The ultra-flexible and mechanically robust stretchable organic solar cells maintain the same PCE even after bending at small radius of 2 mm for 300 times and retain a PCE of 86.7% with 70% electrode transmittance under the tensile strain of 20%.

Water-assisted transfer printing enables the transfer of devices onto various unconventional substrates (Lee et al., 2011). Interactions between the printable electrode and the active layer are critical to the performance of the device. Printable polymer PEDOT:PSS is one main electrode material for organic solar cells, owing to its high conductivity, high work function, and processing orthogonality with an active layer. The widely used additive 1,8-diiodooctane (DIO) in the active layer, was found to induce the reduction of PEDOT:PSS, which led to a decrease in work function and poor hole transport and collection. To address this issue, Wang et al. developed a 15 nm ultrathin active layer film without DIO between the PEDOT:PSS electrode and the active layer using water transfer printing. The cell with the ultrathin film without DIO exhibits improved performance compared with the cell without the film: V_{OC} of 0.84 V, short-circuit current density (J_{SC}) of 17.8 mA/cm², FF of 67%, and PCE of 10.1% (Wang et al., 2020). In 2022, a stable bilayer organic solar cell was demonstrated by Wang et al. using spread transfer printing. The spread transfer printing combined with solvent additives effectively controls the domain formation and the molecular orientation at the donor-acceptor interface (Wang et al., 2022). Xie et al. achieved silver nanowires (AgNWs) transparent film by water transfer printing. The authors demonstrated a large-area flexible organic solar modules containing 10 subcells with a PCE of 12.3% (Xie et al., 2022).

14.7 Conclusion

This chapter covers the working principle of transfer printing and the application of transfer printing in the field of energy storage and conversion. Remarkable progress has been made in utilizing transfer printing to address the challenges faced in energy storage and energy conversion device. Transfer printing endows energy systems with desirable properties, such as conformality, flexibility, and transparency, thereby opening up a wide range of possibilities in the field of energy storage and conversion.

Continuing efforts are necessary to achieve high resolution, low cost, scalable transfer printing process for fabricating performant energy systems. It is highly desirable to

optimize the electrochemical performance of the assembled devices and explore the scalability of the employed transfer printing process. To date, limited ink recipes, materials for donor substrates, and materials for receiver substrates were examined, and materials that fulfill the needs of different energy systems need to be extensively studied. The growing interest in developing devices with complex geometries also requires a thorough investigation of transfer printing on three-dimensional objects. These considerations suggest that there exists ample opportunity in both fundamental study and applied research in the field of transfer printing techniques.

References

- Adrian, A., Rudolph, D., Willenbacher, N., & Lossen, J. (2020). Finger metallization using pattern transfer printing technology for c-si solar cell. *IEEE Journal of Photovoltaics*, 10(5), 1290–1298. Available from <https://doi.org/10.1109/JPHOTOV.2020.3007001>, <https://ieeexplore.ieee.org/xpl/RecentIssue.jsp?punumber=5503869>.
- Bronstein, N. D., Li, L., Xu, L., Yao, Y., Ferry, V. E., Alivisatos, A. P., & Nuzzo, R. G. (2014). Luminescent solar concentration with semiconductor nanorods and transfer-printed micro-silicon solar cells. *ACS Nano*, 8(1), 44–53. Available from <https://doi.org/10.1021/nn404418h>.
- Carlson, A., Bowen, A. M., Huang, Y., Nuzzo, R. G., & Rogers, J. A. (2012). Transfer printing techniques for materials assembly and micro/nanodevice fabrication. *Advanced Materials*, 24(39), 5284–5318. Available from <https://doi.org/10.1002/adma.201201386>.
- Cheng, H. W., Mohapatra, A., Chang, Y. M., Liao, C. Y., Hsiao, Y. T., Chen, C. H., Lin, Y. C., Huang, S. Y., Chang, B., Yang, Y., Chu, C. W., & Wei, K. H. (2021). High-performance organic solar cells featuring double bulk heterojunction structures with vertical-gradient selenium heterocyclic nonfullerene acceptor concentrations. *ACS Applied Materials and Interfaces*, 13(23), 27227–27236. Available from <https://doi.org/10.1021/acsami.1c06762>, <http://pubs.acs.org/journal/aamick>.
- Chen, Y., Xie, S., Li, G., Jia, S., Gao, X., & Li, X. (2019). 3D nanotube-structured Ni@MnO₂ electrodes: Toward enhanced areal capacitance of planar supercapacitors. *Applied Surface Science*, 494, 29–36. Available from <https://doi.org/10.1016/j.apsusc.2019.07.063>, <http://www.journals.elsevier.com/applied-surface-science/>.
- Chiang, W. H., Lin, S. J., & Wu, J. S. (2022). On the performance of proton exchange membrane fuel cells with a catalyst layer fabricated using an inorganic dispersant with various ultrasonic mixing. *ACS Omega*, 7(25), 21370–21377. Available from <https://doi.org/10.1021/acsomega.1c05777>, pubs.acs.org/journal/acsodf.
- Choi, Y. M., Lee, B. W., Jung, M. S., Han, H. S., Kim, S. H., Chen, K., Kim, D. H., Heinz, T. F., Fan, S., & Lee, J. (2020). *Advanced energy materials*.
- Fan, X., Song, W., Lei, T., Xu, B., Yan, F., Wang, N., Cui, H., & Ge, Z. (2019). High-efficiency robust organic solar cells using transfer-printed PEDOT:PSS electrodes through interface bonding engineering. *Materials Chemistry Frontiers*, 3(5), 901–908. Available from <https://doi.org/10.1039/c8qm00614h>, rsc.li/frontiers-materials.
- Fan, X., Xu, B., Liu, S., Cui, C., Wang, J., & Yan, F. (2016). Transfer-printed PEDOT:PSS electrodes using mild acids for high conductivity and improved stability with application to flexible organic solar cells. *ACS Applied Materials and Interfaces*, 8(22), 14029–14036. Available from <https://doi.org/10.1021/acsami.6b01389>, <http://pubs.acs.org/journal/aamick>.
- Gaikwad, M. A., Suryawanshi, U. P., Ghorpade, U. V., Jang, J. S., Suryawanshi, M. P., Kim, J. H. (2022).
- Gai, B., Geisz, J. F., Friedman, D. J., Chen, H., & Yoon, J. (2019). Printed assemblies of microscale triple-junction inverted metamorphic GaInP/GaAs/InGaAs solar cells. *Progress in Photovoltaics: Research and Applications*, 27(6), 520–527. Available from <https://doi.org/10.1002/pip.3127>, [http://onlinelibrary.wiley.com/journal/10.1002/\(ISSN\)1099-159X](http://onlinelibrary.wiley.com/journal/10.1002/(ISSN)1099-159X).

- Giannakou, P., Tas, M. O., Le Borgne, B., & Shkunov, M. (2020). Water-transferred, inkjet-printed supercapacitors toward conformal and epidermal energy storage. *ACS Applied Materials and Interfaces*, *12*(7), 8456–8465. Available from <https://doi.org/10.1021/acsami.9b21283>, <http://pubs.acs.org/journal/aamick>.
- Gong, O.Y., Seo, M.K., Choi, J.H., Kim, S.-Y., Kim, D.H., Cho, I.S., Park, N.-G., Han, G.S., & Jung, H.S. (2022). *Applied surface science*.
- Hu, L., You, W., Sun, L., Yu, S., Yang, M., Wang, H., Li, Z., & Zhou, Y. (2021). Surface doping of non-fullerene photoactive layer by soluble polyoxometalate for printable organic solar cells. *Chemical Communications*, *57*(21), 2689–2692. Available from <https://doi.org/10.1039/d1cc00032b>, <http://pubs.rsc.org/en/journals/journal/cc>.
- S. Jessl, D. Copic, S. Engelke, S. Ahmad, M.De Volder, Small. (2019).
- Kang, M. G., Joon Park, H., Hyun Ahn, S., & Jay Guo, L. (2010). Transparent Cu nanowire mesh electrode on flexible substrates fabricated by transfer printing and its application in organic solar cells. *Solar Energy Materials and Solar Cells*, *94*(6), 1179–1184. Available from <https://doi.org/10.1016/j.solmat.2010.02.039>.
- Lawes, S., Riese, A., Sun, Q., Cheng, N., & Sun, X. (2015). Printing nanostructured carbon for energy storage and conversion applications. *Carbon*, *92*, 150–176. Available from <https://doi.org/10.1016/j.carbon.2015.04.008>, <http://www.journals.elsevier.com/carbon/>.
- Lee, C. H., Kim, D. R., & Zheng, X. (2014). Transfer printing methods for flexible thin film solar cells: Basic concepts and working principles. *ACS Nano.*, *8*(9), 8746–8756. Available from <https://doi.org/10.1021/nn5037587>, <http://pubs.acs.org/journal/ancac3>.
- Lee, C. H., Kim, D. R., & Zheng, X. (2011). Fabrication of nanowire electronics on nonconventional substrates by water-assisted transfer printing method. *Nano Letters*, *11*(8), 3435–3439. Available from <https://doi.org/10.1021/nl201901z>.
- Linghu, C., Zhang, S., Wang, C., & Song, J. (2018). *NPJ Flexible Electronics*.
- Liu, H., Li, J., Feng, W., & Kang, F. (2021). Interface improvement of $\text{Li}_{6.4}\text{La}_3\text{Zr}_{1.6}\text{Ta}_{0.6}\text{O}_{12}@ \text{La}_2\text{Sn}_2\text{O}_7$ and cathode transfer printing technology with splendid electrochemical performance for solid-state lithium batteries. *ACS Applied Materials and Interfaces*, *13*(33), 39414–39423. Available from <https://doi.org/10.1021/acsami.1c09692>, <http://pubs.acs.org/journal/aamick>.
- Li, J., Yang, P., Li, X., Jiang, C., Yun, J., Yan, W., Liu, K., Fan, H. J., & Lee, S. W. (2023). Ultrathin smart energy-storage devices for skin-interfaced wearable electronics. *ACS Energy Letters.*, *8*(1), 1–8. Available from <https://doi.org/10.1021/acsenerylett.2c02029>, <https://doi.org/10.1021/acsenerylett.2c02029>.
- Lumb, M. P., Meitl, M., Schmieder, K. J., Gonzalez, M., Mack, S., Yakes, M. K., Bennett, M. F., Frantz, J., Steiner, M.A., & Geisz, J.F. (2016).
- Lumb, M. P., Schmieder, K. J., Mood, T. C., Bennett, M. F., Taploo, A., Moore, J. E., Scheiman, D., Armour, E., Fisher, B., & Meitl, M. (2019).
- Lu, Y., Li, L., Wang, X., & Chen, D. (2021). *Materials Today Communications*.
- Mohapatra, A., Singh, A., Abbas, S. A., Lu, Y.-J., Boopathi, K. M., Hanmandlu, C., Kaiser, N., Lee, C.-H., Chu, C.-W. (2019). *Nano Energy*.
- Moon, S., Yoo, J.-K., Jung, Y. H., Kim, J.-H., Jung, Y. S., & Kim, D. K. (2017). *Journal of The Electrochemical Society*.
- Nam, J., Lee, Y., Choi, W., Kim, C. S., Kim, H., Kim, J., Kim, D. H., & Jo, S. (2016). *Advanced Energy Materials*.
- Niu, Z., Zhou, W., Chen, J., Feng, G., Li, H., Hu, Y., Ma, W., Dong, H., Li, J., & Xie, S. (2013). A repeated halving approach to fabricate ultrathin single-walled carbon nanotube films for transparent supercapacitors. *Small.*, *9*(4), 518–524. Available from <https://doi.org/10.1002/sml.201201587>.
- Obaid, S., & Lu, L. (2019). Highly efficient microscale gallium arsenide solar cell arrays as optogenetic power options. *IEEE Photonics Journal.*, *11*(1), 1–8. Available from <https://doi.org/10.1109/jphot.2019.2896005>.
- Petterson, J., Ramsey, B., & Harrison, D. (2006). A review of the latest developments in electrodes for unitised regenerative polymer electrolyte fuel cells. *Journal of Power Sources*, *157*(1), 28–34. Available from <https://doi.org/10.1016/j.jpowsour.2006.01.059>.

- Qiu, M., Sun, P., Cui, G., Tong, Y., & Mai, W. (2019). A flexible microsupercapacitor with integral photocatalytic fuel cell for self-charging. *ACS Nano*, 7, 8246–8255. Available from <https://doi.org/10.1021/acsnano.9b03603>.
- Schmieder, K. J., Mood, T. C., Meitl, M. A., Fisher, B., Carter, J., Bennett, M. F., Armour, E. A., Diaz, M., Kotulak, N. A., Ruppalt, L. (2019).
- Song, D., Mahajan, A., Secor, E. B., Hersam, M. C., Francis, L. F., & Frisbie, C. D. (2017). High-resolution transfer printing of graphene lines for fully printed, flexible electronics. *ACS Nano*, 11(7), 7431–7439. Available from <https://doi.org/10.1021/acsnano.7b03795>, <http://pubs.acs.org/journal/ancac3>.
- Song, D., Secor, E. B., Wang, Y., Hersam, M. C., & Daniel Frisbie, C. (2018). Transfer printing of sub-5 μm graphene electrodes for flexible microsupercapacitors. *ACS Applied Materials and Interfaces*, 10(26), 22303–22310. Available from <https://doi.org/10.1021/acsnano.7b03795>, <http://pubs.acs.org/journal/aamick>.
- Srivastava, R. P., Jung, H.-S., & Khang, D.-Y. (1467).
- Sun, L., Jiang, X., & Zhou, Y. (2019). Efficient nonfullerene organic solar cells with active layers fabricated by water transfer printing. *Journal of Energy Chemistry*, 37, 220–224. Available from <https://doi.org/10.1016/j.jechem.2019.04.001>, elsevier.com/journals/journal-of-energy-chemistry/2095-4956.
- Sun, L., Zeng, W., Xie, C., Hu, L., Dong, X., Qin, F., Wang, W., Liu, T., Jiang, X., & Jiang, Y. (2020). *Advanced Materials*.
- Wang, R., Jiang, Y., Gruber, W., He, Y., Wu, M., Weitz, P., Zhang, K., Lüer, L., Forberich, K., & Unruh, T. (2022). *Advanced Materials Interfaces*.
- Wang, W., Qin, F., Zhu, X., Liu, Y., Jiang, X., Sun, L., Xie, C., & Zhou, Y. (2020). Exploring the chemical interaction between diiodooctane and PEDOT-PSS electrode for metal electrode-free non-fullerene organic solar cells. *ACS Applied Materials and Interfaces*, 12(3), 3800–3805. Available from <https://doi.org/10.1021/acsnano.7b03795>, <http://pubs.acs.org/journal/aamick>.
- Wang, Z., Xu, M., Li, Z., Gao, Y., Yang, L., Zhang, D., & Shao, M. (2021). *Advanced Functional Materials*.
- Wei, W., Dong, X., Zhou, X., Lu, X., Liu, Y., Chen, J., Xie, C., & Zhou, Y. (2022). *Advanced Materials Interfaces*.
- Xie, C., Liu, Y., Wei, W., Zhou, Y. (2022). *Advanced Functional Materials*.
- Xu, G., Chen, Y., Chen, F., Meng, Y., Ma, Y., & Feng, X. (2021).
- Xu, S., Zhang, Y., Cho, J., Lee, J., Huang, X., Jia, L., Fan, J. A., Su, Y., Su, J., & Zhang, H. (1543). *Nature Communications*.
- Yi, M., Jang, W., Cho, J. S., & Wang, D. H. (2019). Enhanced interface of polyurethane acrylate via per-fluoropolyether for efficient transfer printing and stable operation of PEDOT:PSS in perovskite photovoltaic cells. *Applied Surface Science*, 467–468, 168–177. Available from <https://doi.org/10.1016/j.apsusc.2018.10.066>, <http://www.journals.elsevier.com/applied-surface-science/>.
- Yu, S., Qin, F., Dong, X., Xie, C., Xiong, S., Lu, X., Jiang, X., & Zhou, Y. (2021). *Organic Electronics*.
- Yu, R., Wei, X., & Wu Tan, G. (2022).
- Yüce, C., Okamoto, K., Karpowich, L., Adrian, A., & Willenbacher, N. (2019). *Solar Energy Materials and Solar Cells*.
- Zhao, J., Guo, Y., Cai, L., Li, H., Wang, K. X., Cho, I. S., Lee, C. H., Fan, S., & Zheng, X. (2016). High-performance ultrathin BiVO₄ photoanode on textured polydimethylsiloxane substrates for solar water splitting. *ACS Energy Letters*, 1(1), 68–75. Available from <https://doi.org/10.1021/acsnano.7b03795>, <http://pubs.acs.org/journal/aelccp>.
- Zhao, Y., & Guo, J. (2020). Development of flexible Li-ion batteries for flexible electronics. *InfoMat.*, 2(5), 866–878. Available from <https://doi.org/10.1002/inf2.12117>, onlinelibrary.wiley.com/journal/25673165.
- Zhou, H., Qin, W., Yu, Q., Cheng, H., Yu, X., & Wu, H. (2019). *Nanomaterials*.
- Zhou, M., Zhang, H., Qiao, Y., Li, C. M., & Lu, Z. (2018). A flexible sandwich-structured supercapacitor with poly(vinyl alcohol)/H₃PO₄-soaked cotton fabric as solid electrolyte, separator and supporting layer. *Cellulose*, 25(6), 3459–3469. Available from <https://doi.org/10.1007/s10570-018-1786-3>.
- Zhou, Y., Zhang, W., Yu, S., Jiang, H., & Li, C. (2022). Patterned catalyst layer boosts the performance of proton exchange membrane fuel cells by optimizing water management. *Chinese Journal of Chemical Engineering*, 44, 246–252. Available from <https://doi.org/10.1016/j.cjche.2021.06.001>, <https://www.journals.elsevier.com/chinese-journal-of-chemical-engineering>.

This page intentionally left blank

CHAPTER 15

Transfer printing of metal films

Kaihao Zhang

Smart Manufacturing Thrust, Systems Hub, The Hong Kong University of Science and Technology, Guangzhou, P.R. China

15.1 Preparation of metal films

This section provides an overview of commonly used deposition techniques and processes for fabricating a thin metal film onto a substrate, especially on a squashable and stretchable elastomeric substrate for applications such as organic electronics, and flexible and wearable devices. Metallization provides the metal materials to be transferred from a stamp onto other desired substrates for transfer printing. The morphology and microstructures of the deposited metal layer are essential for high-quality transfer printing and are decisive in the final functionality of the transferred features.

15.1.1 Physical vapor deposition of thin metal films

Physical vapor deposition (PVD) involves physical processes, such as evaporation, sublimation, or ionic impingement towards a source material, which facilitate the transfer of atoms from a solid or molten source onto a target substrate. PVD represents a variety of versatile material coating techniques applicable to an almost unlimited combination of coating substances and substrate materials. In practice, the technique is mainly used to deposit metallic materials. Possible substrates include metals, semiconductors, ceramics, and polymers. Evaporation and sputtering are the two widely used PVD techniques for thin metal film deposition. Fig. 15.1 sketches four typical PVD processes and illustrates the key features involved. In general, these PVD processes consist of the following elementary steps: (1) generation of the coating vapor from the source material, (2) transport of the vapor towards the

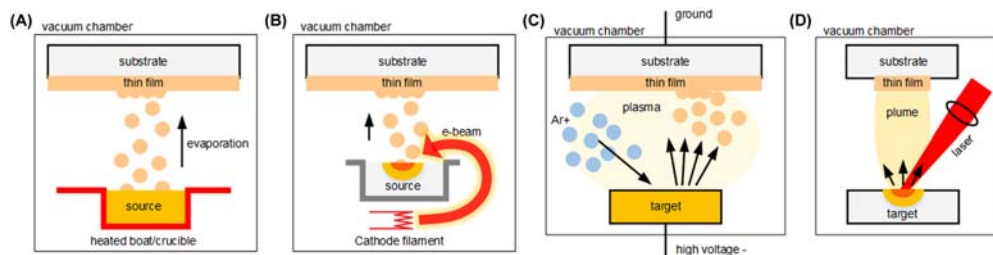


Figure 15.1 Schematics of typical physical vapor deposition processes of thin metal films: (A) thermal evaporation; (B) e-beam evaporation (EBPVD); (C) sputtering; (D) pulsed laser deposition (PLD).

target substrate, and (3) condensation of vapors onto the target surface. Notably, these steps are carried out in a vacuum chamber to reduce the evaporation of atom collisions and prevent oxidation of the source material at the heating temperatures. The target substrates are typically held upside down to minimize particulate contamination (Madou, 2012).

In evaporation deposition, the source material can be heated by several methods. For example, passing a high current through a highly refractory metal boat or crucible (e.g., a W or Mo boat or filament), as shown in Fig. 15.1A. The resistively heated crucible then heats or melts the source material in contact with it. Evaporation is based on the boiling off or sublimating of the heated source material in a vacuum. This method is called thermal evaporation deposition. The evaporated atoms travel through reduced background pressure in the vacuum chamber and condense on the surface of the target substrate. This resistive heating method is one of the oldest and simplest thin film deposition PVD techniques. Large volumes of source material can be heated to achieve a high deposition rate (e.g., thousands of atomic layers per second). One drawback with the resistive heating method is possible alloying between the crucible and the source material, as a result, the deposited film is easily contaminated with the metal of the container (Madou, 2012). Alternatively, a high-intensity electron beam (e.g., 3–20 keV) can be generated and magnetically directed onto the target material, which is placed in a water-cooled hearth, as shown in Fig. 15.1B, this method is called e-beam evaporation (EBPVD). In this method, the source material is heated and melted locally, and the container-source cross-contamination can be circumvented. EBPVD can result in higher-quality thin film deposition. However, compared with thermal evaporation, EBPVD usually requires a high vacuum, and e-beam generation and guidance increase the equipment complexity and cost, and it might induce X-ray damage and even some ion damage to the target substrate. There are other PVD techniques, for example, pulsed laser deposition (PLD) that replace the e-beam with intense laser radiation to erode a target material, so that avoids the X-ray issues associated with EBPVD, as illustrated in Fig. 15.1D. More related features of these PVD techniques are summarized in Table 15.1.

In sputter deposition, as illustrated in Fig. 15.1C, a plasma is created between the target material and substrate where positive gas ions (e.g., Ar, Xe) bombard the cathode target at high speed. The neutral atoms of the target material are dislodged to form the vapor in the chamber and condense onto the surface of the substrate. Table 15.1 compares the critical features of sputtering over other deposition techniques. Notably, sputtering can work with a wide range of source materials, exhibits better uniformity in terms of thin film topography and stoichiometry over large areas, and results in better film/substrate adhesion. However, sputtering is a relatively slow process with a deposition rate of around one atomic layer per second; and the substrate heating effect is also substantial due to ions striking.

For transfer printing which is the main focus of this chapter, an ultrathin metal film needs to be firstly patterned and deposited onto a soft (e.g., elastomer) or a hard (e.g., Si) stamp. Fig. 15.2 shows a typical as-metallized stamp surface via thermal evaporation. When the deposited metal layer exhibits poor adhesion to the substrate,

Table 15.1 Typical metal deposition methods, materials, and key features.

Deposition technique	Deposition rate	Advantages	Disadvantages
Thermal evaporation	High (10^3 atomic layers per second)	<ul style="list-style-type: none"> • Low substrate heating • Large grain size with fewer orientations • No radiation issues 	<ul style="list-style-type: none"> • Coating adhesion is not as good as for other PVD methods • Large shadowing effect • Only for some simple compounds • Low uniformity over large areas • Induces contaminations
E-beam evaporation	High (50–500 nm/min)	<ul style="list-style-type: none"> • Low contaminations • Less source decomposition when depositing alloys 	<ul style="list-style-type: none"> • May induce radiation damage • Substrate heating and surface damage • High vacuum required
Sputtering	Slow (one atomic layer per second)	<ul style="list-style-type: none"> • Almost unlimited material selection • Good coating adhesion • Compounds deposition is available, and stoichiometry retains as the original target composition • Good uniformity over large areas • Small shadowing effect 	<ul style="list-style-type: none"> • Substantial substrate heating • Smaller grain size with many grain orientations
Pulsed laser deposition	Variable growth rate by varying laser parameters	<ul style="list-style-type: none"> • Suitable for complex compounds or desired stoichiometry, e.g., YBCO • Growth in various environment • Good control of growth rate • Low-temperature epitaxy 	<ul style="list-style-type: none"> • Expensive • Splashing due to subsurface boiling and exfoliation • High defect density • Low uniformity over large areas

(Continued)

Table 15.1 (Continued)

Deposition technique	Deposition rate	Advantages	Disadvantages
Molecular beam epitaxy	Very slow (0.1–10 $\mu\text{m}/\text{h}$)	<ul style="list-style-type: none"> • High-purity deposition with good crystal structures control • Relatively low growth temperature • High uniformity (<1% deviation) 	<ul style="list-style-type: none"> • Expensive • Ultrahigh vacuum required • Not suitable for large-area metallization
CVD	Low (varies with growth conditions and recipes)	<ul style="list-style-type: none"> • A wide range of materials including refractory metals • Good coating adhesion • Fabricate net or near-net complex shapes • Good conformity and step coverage • Can be carried out at atmospheric pressure 	<ul style="list-style-type: none"> • Expensive (mainly in terms of high-purity gases and chemicals consumption) • Low material utilization • Safety issues due to corrosive, toxic, and flammable gases involved • Highly recipe-dependent and low repeatability • Not suitable for polymer substrates due to high synthesis temperatures
Electrochemical deposition	Variable growth rate by varying plating parameters	<ul style="list-style-type: none"> • Conformal coating on irregular substrates, including the inner and hidden surfaces • Compatible with a variety of metals • Cost-effective • Results in customizable surface finish 	<ul style="list-style-type: none"> • Low density of the deposited films and high tendency to cracking • Environmental issues due to acidic, heavy metal, and toxic pollutants emissions

(Continued)

Table 15.1 (Continued)

Deposition technique	Deposition rate	Advantages	Disadvantages
Gilding	It is a lamination process with no atomic scale deposition or growth involved	<ul style="list-style-type: none"> • Cost-effective • Limited metals having high ductility, e.g., Au, Ag, Cu, Pd, Pt • Room temperature and atmospheric pressure operations • Large grain size (e.g., > 10 μm grains for 100–300 nm thick films) • Good mechanical properties 	<ul style="list-style-type: none"> • High density of dislocations • Film thickness depends on metal leaf fabrication (e.g., 100 nm to 1 μm) • Poor conformity on complex surfaces

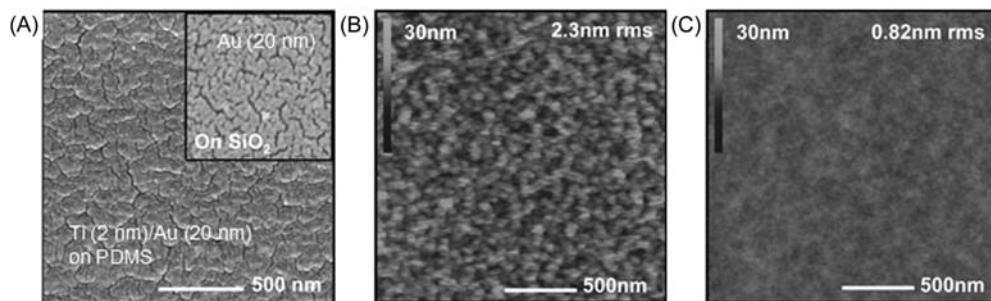


Figure 15.2 Surface morphologies of a thermal evaporated Ti/Au layer on the surface of a PDMS stamp. (A) SEM image of a stamp coated with Ti/Au (2 nm/20 nm). SiO_2 wafer surface coated with Au (20 nm) in the inset. AFM images of (B) Ti (2 nm)/Au (20 nm) deposited directly onto the untreated surface of PDMS, and (C) the stamp is exposed to a short (13 s) oxygen plasma treatment before metal deposition. Adapted from Menard, E., Bilhaut, L., Zaumseil, J. & Rogers, J. A. (2004). *Langmuir*, 20(16), 6871–6878. <https://doi.org/10.1021/la048827k>.

nanoscale cracking in the metal could occur (Menard et al., 2004). Necessary treatments to the stamp are required prior to or during deposition. Fig. 15.2B presents a smooth Au surface that is free of nanocrack by exposing the stamp to an oxygen plasma before thermal evaporation. More details will be discussed in later sections.

Notably, the microstructure of the deposited metal film shows dependence on the film thickness, which can then be controlled by the deposition time. Fig. 15.3A shows typical evolutions of grain size and orientation of sputtered Cu films with increasing deposition time and thus film thickness (Lu et al., 2010). Generally, as-sputtered metal

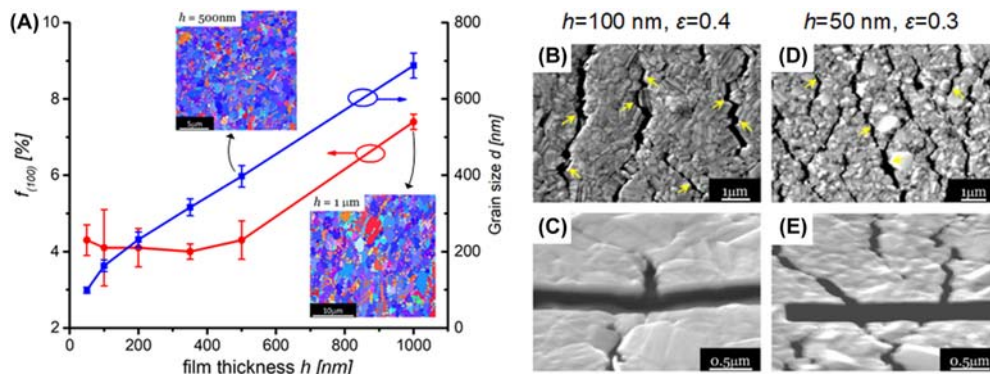


Figure 15.3 Thickness-dependent microstructures and nanocracking in sputtered Cu films on Kapton substrates. (A) Grain size and (100) texture fracture as a function of deposited film thickness. The insets are electron backscattering diffraction (EBSD) maps for the 500 nm and 1000 nm Cu films; (B–E) surface and cross-sectional SEM images of the 100 nm (B, C) and 50 nm (D, E) Cu films upon uniaxial strains (along the horizontal direction) of 40% and 30%, respectively. Yellow arrows highlight the nanoscale intergranular cracks in Cu films. Adapted from Lu, N., Suo, Z. & Vlassak, J. J. (2010). *Acta Materialia*, 58(5), 1679–1687. <https://doi.org/10.1016/j.actamat.2009.11.010>.

films show nanoscale grain size but a strong (111) texture. With increasing the film thickness, grains grow gradually, and more (100) grains appear. Similar to the evaporated metal films shown in Fig. 15.2A, nanocracking occurs in as-sputtered metal films and will result in intergranular fracture when external strains are applied, see Fig. 15.3B–E. We will discuss this in detail in the later section.

15.1.2 Chemical vapor deposition of thin metal films

Chemical vapor deposition (CVD) of metal films involves the thermally induced reaction of a metal-containing molecule on the surface of a heated substrate. Fig. 15.4 illustrates the elementary subprocesses involved in a CVD process (Boyd et al., 1997; Hampden-Smith & Kodas, 1995). A vapor phase precursor consisting of a metal core and ligands is added to the reaction chamber, where it can adsorb to the surface of a substrate and reacts at particular conditions (e.g., elevated temperatures, specific precursor concentration) to release the supporting ligands, which are subsequently evacuated out of the chamber as byproducts. The decomposed metal atoms diffuse on the substrate surface to form stable nuclei and grow into a continuous metal film. Compared with PVD processes, the CVD method is versatile and can work over a wide range of temperatures and pressures, even in an atmospheric environment. Table 15.1 also lists the detailed advantages cited for the CVD of thin metal films. Notably, it is possible to conformally deposit refractory metals onto a substrate with good film/substrate adhesion via the CVD method. To ensure the desired microstructures and quality of deposited metal films via the CVD method, many cross-length scale factors such as surface chemical reactions, vapor phase

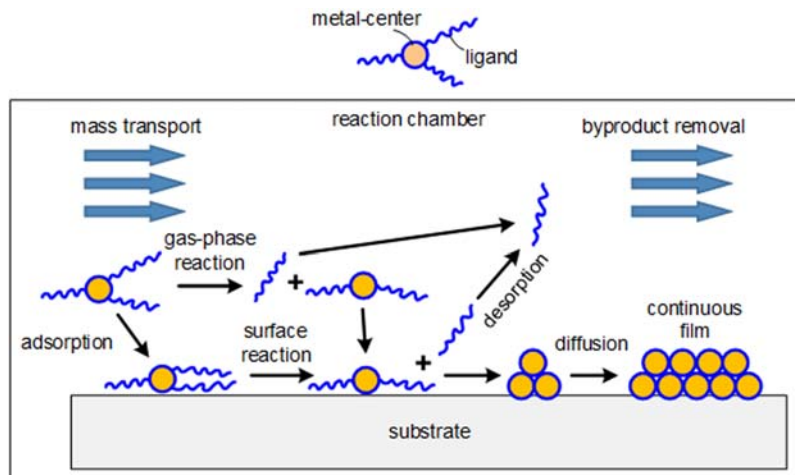


Figure 15.4 Schematics of key steps involved in chemical vapor deposition of metal films. *Modified from Hampden-Smith, M. J. & Kodas, T. T. (1995). Chemical Vapor Deposition, 1(1), 8–23. <https://doi.org/10.1002/cvde.19950010103>.*

transportation, radical diffusion, and segregation, as well as metal precursor materials need to be carefully designed and controlled. For example, low gas supersaturation and high substrate temperatures promote metal film growth with highly aligned grain orientations on substrates (Madou, 2012). Hampden-Smith and Kodas (1995) broadly classified the precursors for CVD of metals into three types: (1) inorganic precursors without carbon; (2) metal–organic precursors containing organic ligands but without metal–carbon bonds; and (3) organometallic precursors with organic ligands and metal–carbon bonds.

In previous studies, uniform and mirror-like thin metal—including Co, Fe, Ru, Os, and their alloys or multilayer—films have been prepared on a heated glass slide using the metal–carbonyls precursors via a low-pressure CVD (LPCVD) method (Boyd et al., 1997). Fig. 15.5 displays the CVD-grown a Co (200 nm)/Ru (300 nm)/Co (200 nm) layered film.

Given that the thermally induced chemical reaction is one of the critical steps involved in CVD, a substrate is usually heated to an elevated temperature (below the metal’s melting point but higher than most polymers’ glass transition points) to promote the precursor decomposition and metal atoms diffusion. This might limit the use of substrate materials in transfer printing, for example, an elastomer substrate is hardly used for the CVD process.

15.1.3 Other thin metal film deposition techniques

Besides the abovementioned PVD and CVD techniques for metal film deposition, there are several relatively simple and inexpensive ways for fabricating ultrathin metal films on various substrates. Electrochemical deposition is a process whereby the

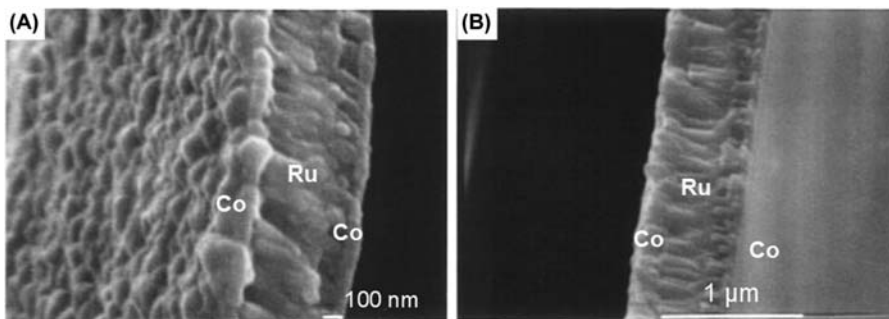


Figure 15.5 SEM images of chemical vapor deposition deposited Co/Ru/Co layered film, (A) showing edge and surface features; (B) showing thickness of each layer. Adapted from Boyd, E. P., Ketchum, D. R., Deng, H. & Shore, S. G. (1997). *Chemical Materials*, 9(5), 1154–1158. <https://doi.org/10.1021/cm9605330>.

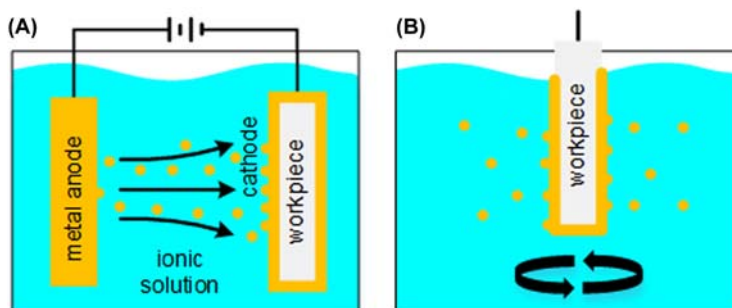


Figure 15.6 Schematics of electrochemical deposition. Schematics of electroplating (A) and electroless plating (B) for metallization on a workpiece.

metallic ions deposit onto the surface of a workpiece with or without a sufficient amount of electric current passing through the electrolyte solution, which contains charged ions of the source material (Bhattacharyya, 2015). In general, electrochemical deposition of metallic materials is widely used in the plating and finishing processes to protect, improve the appearance, or increase the corrosion protection and conductivity of the substrate materials. These processes can be classified into two primary categories: electroplating and electroless plating, as illustrated in Fig. 15.6.

In electroplating, as shown in Fig. 15.6A, an electrical current passes through an electrolyte solution containing metal ions and causes the ions to migrate from a positive electrode (anode and the source material) to a negative one (cathode and the target substrate). While electroplating is typically viewed as a metal-to-metal manufacturing process, it is also possible to deposit metals onto a nonmetallic substrate. The first commercial metal plating on the plastic process was developed in the early 1960s, primarily for applications in the automotive industry, and is still frequently used for metallization in many industries

today. Different from metal workpiece electroplating, plating on plastic requires an initial metallization on the nonconductive plastic surface in an electroless plating solution. Fig. 15.6B illustrates the basic electroless metal deposition process, which, as the name implies, involves the production of coatings from a solution of metal ions without using an external source of electrical energy. The ionic solution, also called an electroless bath, is in a metastable state where redox reactions will not spontaneously take place but will in the presence of a catalytic surface. Ni and Cu are preferably deposited by electroless plating as their electroless baths can easily be stabilized, while the Ag electroless baths are known to lack stability (Bhattacharyya, 2015; Ryspayeva et al., 2019).

There are extensive studies on the electrochemical deposition of ultrathin metal patterns onto polymer substrates for fabricating flexible microelectronic systems (Li et al., 2019; Li et al., 2021; Sahasrabudhe et al., 2018). Fig. 15.7A gives an example

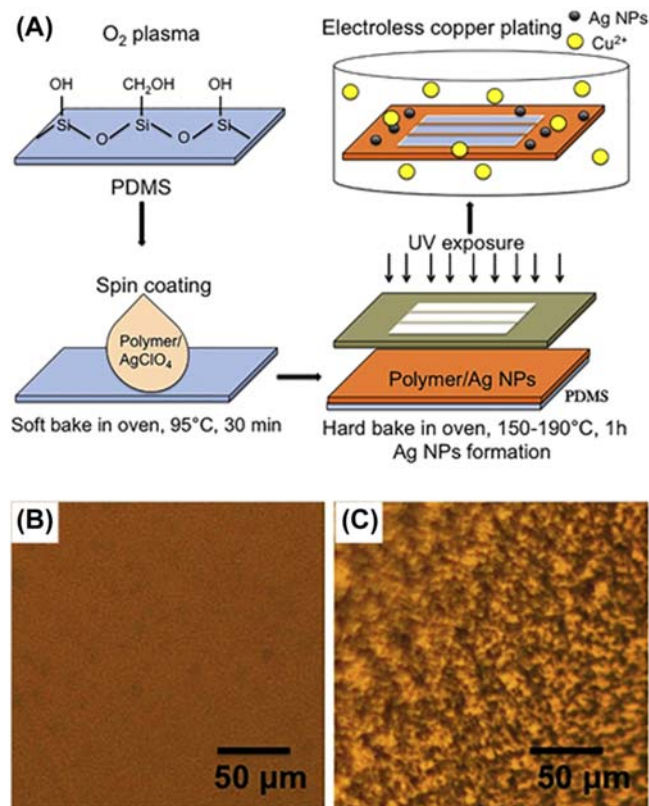


Figure 15.7 Direct metallization of polymer substrates. (A) Schematic steps of photolithography and electroless copper plating for metal patterning on a PDMS substrate; Optical micrographs of (B) polymer/Ag NPs film baked at 150°C; (C) electroless plated copper film. Adapted from Ryspayeva, A., Jones, T. D. A., Esfahani, M. N., Shuttleworth, M. P., Harris, R. A., Kay, R. W., Desmulliez, M. P. Y. & Marques-Hueso, J. (2019). *Microelectronic Engineering*, 209, 35–40. <https://doi.org/10.1016/j.mee.2019.03.001>.

of direct and selective metallization on a polydimethylsiloxane (PDMS) substrate by combining photo-patterning and electroless plating (Ryspayeva et al., 2019). Modified DNQ-novolac photoresist was first mixed with silver perchlorate (AgClO_3) salt and spin-coated on a PDMS substrate for photolithography patterning. The patterned polymer- AgClO_3 layer was then hard-baked and thermally reduced to a conductive layer consisting of Ag nanoparticles (NPs) inside the polymer. The patterned Ag NPs layer can serve as the electroless plating sites for further Cu circuit fabrication on the PDMS. These processes led to relatively high interfacial adhesion between the deposited metal layer and the underlying PDMS backplane. As a result, crack-free thin Cu patterns on the PDMS surface can be obtained, as shown in Fig. 15.7B and C.

Beating pure metals into ultrathin films, called metal leaves, down to 100–150 nm thick, was developed in the second millennium B.C. and was extensively used for surface coating and finishing, also known as “gilding,” for example, on temple walls, precious furniture, and sculptures. This gilding process is ubiquitously seen in artifacts that it enriches them with tiny amounts of precious metals and protects the artwork from corrosion and wear (Oddy, 1991; Thomsen & Thomsen, 1978). Further, these ultrathin metal leaves and gilding processes can also be utilized in fabricating micro/nano-scale electronic devices (Zhang & John Hart, 2022; Zhang et al., 2018; Zhang et al., 2020). Fig. 15.8A highlights the critical steps in fabricating freestanding metal films with <200 nm thickness via repeated annealing, oil-paper separation, and hammer forging processes. Metal foils are downsized in thickness while expanding in lateral

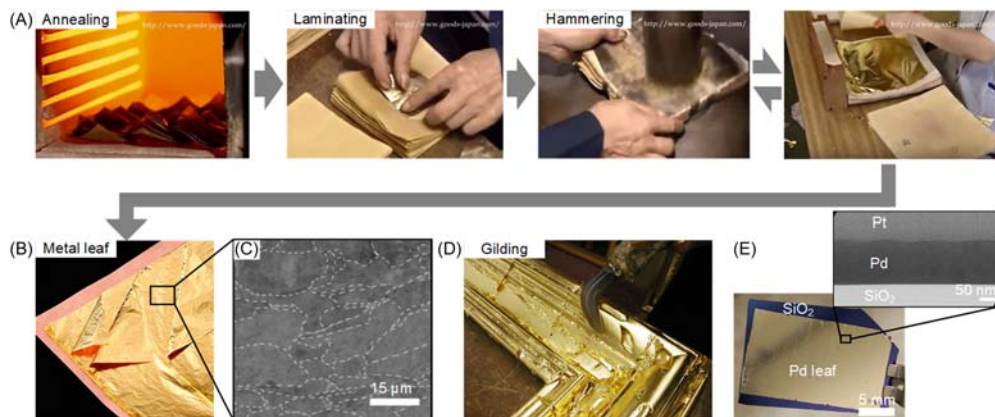


Figure 15.8 Generation of ultrathin metal leaves and gilding process for metal leaf lamination. (A and B) repeated annealing-forging steps for fabricating freestanding metal leaves with thickness down to ~ 150 nm; (C) SEM image of a Pd leaf; (D) metal leaf gilded wooden frame; (E) laminated a Pd leaf on a SiO_2/Si substrate. Inset: cross-sectional TEM image of Pd/ SiO_2 interface. Adapted from Zhang, K., Androulidakis, C., Chen, M. & Tawfick, S. (2018). *Advanced Functional Materials*, 28(48), 1804068. <https://doi.org/10.1002/adfm.201804068>; <https://en.wikipedia.org/wiki/Gilding>; Zhang, K. & John Hart, A. (2022). *Applied Surface Science*, 602, 154367. <https://doi.org/10.1016/j.apsusc.2022.154367>.

dimensions, as shown in Fig. 15.8B. Fig. 15.8C gives an example of such freestanding Pd leaf having relatively large grain sizes up to 10–20 μm (compared with those nano-scale grains from PVD and CVD processes shown in Figs. 15.2 and 15.5). With the help of the low bending stiffness of those ultrathin metal leaves and high ductility due to large grain structures, metal leaves can be easily laminated on various substrates conformally, for example, coating a wooden frame (Fig. 15.8D) (Gilding, 2023) and metallization of a SiO_2 surface (Zhang & John Hart, 2022). The inset of Fig. 15.8E shows the highly intimate and uniform metal leaf-substrate interface, which enables postfabrication processes such as photo-patterning, wet etching, and transfer printing.

15.2 Metal transfer principles

Before detailed metal film transfer printing techniques are introduced, this section revisits some basic principles of thin film mechanics, especially the metal/substrate interface separation behaviors.

15.2.1 Driving force for the film/substrate interface separation

Considering the detailed transfer printing process of an ultrathin metal film from a donor to a receiver surface, debonding or delamination of predeposited metal films from the substrate is one essential step that is decisive to the actual “peeling” process, integrity, and quality of the metal patterns. A model system to analyze such film/substrate separation or delamination process can be created as a two-material system containing a crack at the interface. Consider a thin metal film with a characteristic surface energy density γ_f and a semi-infinite substrate with γ_s are joined together along an interface, then the interface has a characteristic adhesion energy of W_{fs} . If these two adjoined solids are separate without any inelastic deformation or strain energy dissipation in either of the materials, the work that is required to achieve this separation, namely the work of fracture, was described by Dupré as:

$$\Gamma_0 = \gamma_f + \gamma_s - W_{fs} \quad (15.1)$$

Note that the interfacial adhesion energy $W_{fs} = 2\sqrt{\gamma_f^D \gamma_s^D} + 2\sqrt{\gamma_f^P \gamma_s^P}$, where γ^D and γ^P are the dispersive and polar components of the surface energies of the metal film and the substrate, respectively (Kinloch, 1980). Table 15.2 summarizes surface energies of some commonly used metal/polymer materials. Fig. 15.9 compares the interfacial adhesion energies of Au and Al, which are typical thin film materials used in printed electronics on polymer substrates listed in Table 15.2.

As illustrated in Fig. 15.10A, we can consider this interface separation model in a way that is analogous to the Griffith criterion for crack advancing, in which the stress applied to the material tends to cause the preexisting crack to extend while the

Table 15.2 Surface energies of typical film/substrate pairs and their adhesion energies used for metal transfer printing.

Surface energy (mJ/m ²)	SU-8 (Saravanan et al., 2014)	DPVA (Aldakov et al., 2011)	PMMA (Aldakov et al., 2011)	PET (Song et al., 2019)	Polyimide (PI) (Cen-Puc et al., 2021; Hur et al., 2004)	PDMS (Hur et al., 2004)	Au (Grosse, 1964; Vitos et al., 1998)	Ag (Vitos et al., 1998)	Al (Vitos et al., 1998)	Cu (Vitos et al., 1998)
γ^D	21.2	21.4	29.6	27.2	22.7	19	130	n/a	76	n/a
γ^P	11.4	21.4	11.5	1.3	14.8	0.8	1000	n/a	1060	n/a
γ	32.6	42.8	41.1	28.5	37.6	19.8	1130	1250	1136	1825

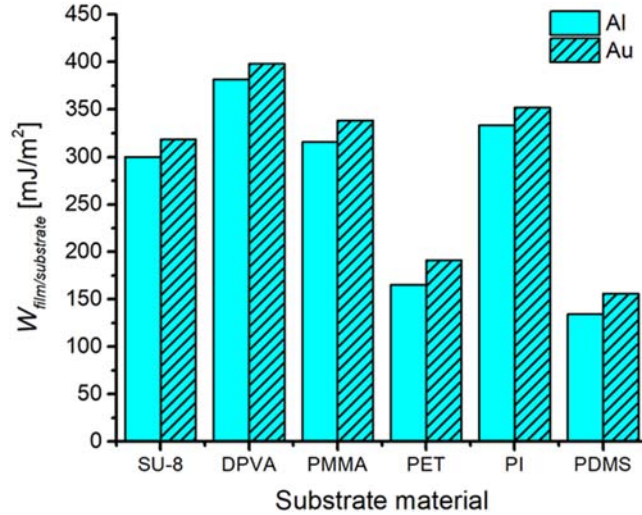


Figure 15.9 Interfacial adhesion energies for Al and Au films on typical polymer substrates.

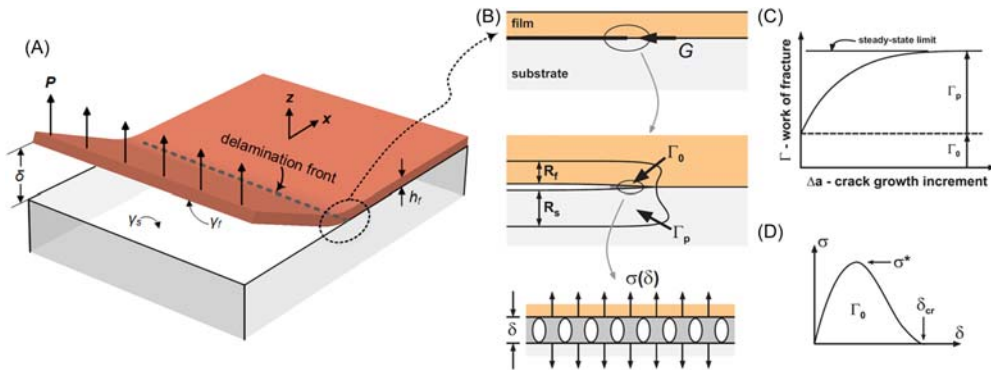


Figure 15.10 Schematics of fracture at the interface of two adjoining solids. (A) Schematic of the delamination front between a metal film and a substrate and it is advancing as a line in the x direction upon applied peeling force; (B) a zoomed-in view of details of the elastic–plastic deformation and ductile fracture mechanism as a metal film is delaminated from a substrate; (C) conceptual dependence of work of interfacial fracture as a function crack growth; (D) a cohesive traction–two plane separation relationship for a mode I separation. Adapted from Freund, L. B. & Suresh, S. (2004). *Thin film materials: stress, defect formation and surface evolution*. Cambridge University Press. <https://doi.org/10.1017/CBO9780511754715>; Hutchinson, J. W. & Evans, A. G. (2000). *Acta Materialia*, 48(1), 125–135. [https://doi.org/10.1016/S1359-6454\(99\)00291-8](https://doi.org/10.1016/S1359-6454(99)00291-8).

strength of the material tends to resist the crack growth (Griffith, 1921). The schematics in Fig. 15.10B magnify the details at the crack front or the film delamination front. The driving force of separation or the continuum potential energy reduction per unit delamination area G is compared to the interfacial adhesion energy Γ to assess

the tendency of crack advancing. For example, $G = \Gamma$ is a necessary condition for the onset of interfacial delamination. It should be noted that the Griffith criterion is based on the elastic deformation in a homogeneous material. However, for the peeling of a metal film, which is originally bonded onto a substrate of another material, the process inevitably accompanied by some inelastic deformation in either of the materials adjacent to the delamination front (Orowan, 1944; Irwin, 1957). As depicted in Fig. 15.10B, the size of the plastic zone can be described by R_f in the film and R_s in the substrate, which are determined by the material's strain hardening property and the yield stress (σ_Y) compared to the maximum cohesive traction σ^* . The plastic zone size increases with increasing the ratio of σ^*/σ_Y and with decreasing the strain hardening rate. As a result, there is an amount of work done for the interfacial crack advancing to dissipate through plastic flow in the plastically deforming zones. This energy reduction per unit area of the fracture surface is denoted by Γ_p . Then the total amount of work per unit cracking area to sustain crack advancing is the sum of $\Gamma_0 + \Gamma_p$. If R_f and R_s are small compared to metal film thickness and overall thickness of the specimen, the $\Gamma_0 + \Gamma_p = \Gamma$ serves as a material parameter in the Griffith criterion. However, if the size of either of the plastic zones is comparable to the materials' thicknesses, then Γ_p will depend on sample dimensions (Freund & Suresh, 2004). Hutchinson and Evans (2000) implemented detailed analyses on the total adhesion energy evolution with the interfacial crack advancing, as conceptually presented in Fig. 15.10C. Once the film/substrate delamination front extends a distance on the order of the plastic zones, the plastic deformation will approach a steady state.

One interesting phenomenon according to the above-discussed adjoining solid separation model is the spontaneous peeling of a strained film from the substrate. Consider a film with a thickness h_f is bonded to a semiinfinite thick substrate. Both materials deform linearly and elastically. The stress far behind the delamination front is σ_a and the biaxial stress in the bonded region of the film is $\sigma_m - \sigma_a$. Therefore, the state of stress near the delamination front depends on the difference. This yields the energy release rate:

$$G = \frac{1 - \nu_f^2}{2E_f} (\sigma_m - \sigma_a)^2 h_f \quad (15.2)$$

According to the Griffith criterion, the film/substrate delamination continues or ceases based on competition between G and Γ . For a straight delamination front ($\sigma_a = 0$):

$$G = \frac{1 - \nu_f^2}{2E_f} \sigma_m^2 h_f = \Gamma \quad (15.3)$$

here σ_m can come from the mismatch strain ε_m at the film/substrate interface, for example, the residual thermal stress caused by different thermal expansion coefficients

of the film and the substrate. Therefore, we can estimate a critical film thickness at which it is possible to drive spontaneous delamination due to the mismatch strain:

$$h_f|_{\text{crit}} = 2 \frac{E_f \Gamma}{(1 - \nu_f^2) \sigma_m^2} = 2 \frac{(1 - \nu_f) \Gamma}{(1 - \nu_f) E_f \varepsilon_m^2} \quad (15.4)$$

Such spontaneous peeling can usually be observed when depositing ultrathin metal films on a substrate with low adhesion and high thermal expansion mismatch (Freund & Suresh, 2004; Yu & Hutchinson, 2003). For example, Fig. 15.11 presents the residual stress engineering in a Ni film to facilitate its delamination from a SiO₂ surface (McNerny et al., 2014). ε_m was caused and controlled by the Ni film microstructure evolution and CVD synthesis processes of graphene layers on the Ni surface as functions of the thermal history of the Ni film.

15.2.2 Edge effects in thin film delamination

In thin film delamination from its substrate, the original configuration of the film/substrate laminate, especially the edge zones plays a significant role (Yu et al., 2001). According to the discussion in Fig. 15.10C, the energy release rate near the film edge is less than that for the steadily advancing delamination. Yu et al. considered two film/substrate configurations: (a) the film edge lies in the interior of the substrate, as shown in the inset of Fig. 15.12A and usually the case of patterned thin film features on a substrate, and (b) the film edge is aligned with the edge of the substrate, see the inset of Fig. 15.12B or usually a metal film fully covered a substrate (Yu et al., 2001). When the delamination front is sufficiently far away from the substrate edge, namely the scenario (a) and large crack extension in Fig. 15.10C, the energy release rate is independent of crack growth length a , as shown in Fig. 15.12A, where $G_{ss} = \frac{1 - \nu_f^2}{2E_f} \sigma_m^2 h_f$ is the steady-state limit expressed in Eq. (15.4). For the crack length approaches the order of the film thickness, say $a/h_f > 1$, G becomes the steady-state value and exhibits no dependence on the elastic mismatch parameter α . Note that α is a Dundurs parameter $\alpha = (\bar{E}_f - \bar{E}_s) / (E_f + E_s)$, where $\bar{E} = E / (1 - \nu^2)$. On the other hand, when the film edge is at the corner of the substrate edge, see Fig. 15.12B, the situation becomes substantially different. In this case, the energy release rate slowly approaches the steady-state value as the crack advances. For a thin metal film bonded on a substrate of the same material ($\alpha = 0$) or on a relatively stiff substrate ($\alpha < 0$), approaches when exceeds 10 times the film thickness. As for a compliant substrate ($\alpha > 0$), it takes longer crack extension for G to approach the steady-state limit. Overall, a thin film with an interior edge is inherently more susceptible to delamination than that with a corner edge, while the film/substrate elastic mismatch exhibits a more significant effect on the energy release rate.

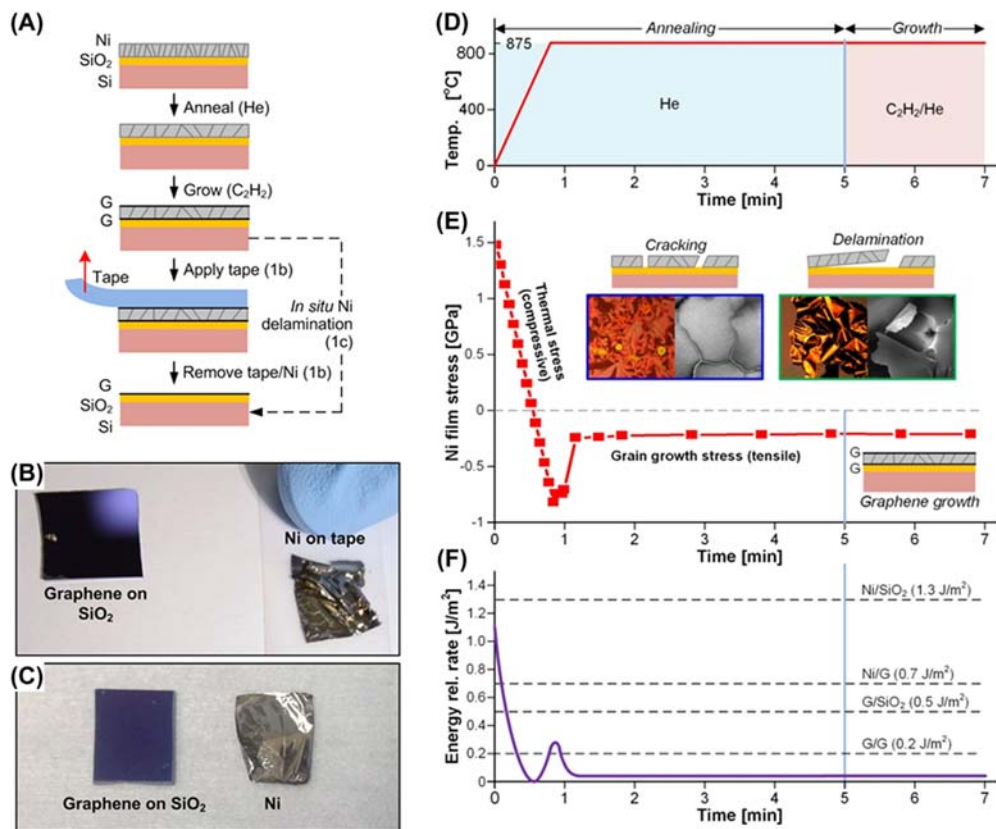


Figure 15.11 Thin metal film delamination from a substrate via stress engineering. (A) Schematic procedures of an interfacial graphene layer growth via chemical vapor deposition (CVD) synthesis, and accompanied Ni film grain growth and delamination after graphene growth; (B and C) optical photos of substrates and delaminated Ni films in case of (B) tape delamination after graphene growth, and (C) in situ delamination during the graphene growth; (D) conceptual temperature profile for annealing and CVD growth; (E) calculated Ni film stress evolution. The insets are optical and SEM images of Ni film cracking and delamination at different times; (F) the corresponding strain energy release rate evolution with comparisons with interfacial energies of Ni/SiO₂, Ni/graphene, graphene/SiO₂, graphene/graphene. A steady-state energy release rate is far below the adhesion energies marked indicating that the delamination at these interfaces is unfavorable. Additional mechanical energy is required to trigger G/G interface fracture. *Republished with permission from McNerny, D. Q., Viswanath, B., Copic, D., Laye, F. R., Prohoda, C., Brieland-Shoultz, A. C., Polsen, E. S., Dee, N. T., Veerasamy, V. S. & Hart, A. J. (2014). Direct fabrication of graphene on SiO₂ enabled by thin film stress engineering. Scientific Reports, 4(1), 5049. <https://doi.org/10.1038/srep05049>.*

15.3 Transfer printing processes for metal films

In this section, detailed transfer printing techniques will be introduced, and essential considerations will be discussed to achieve high throughput metal feature transferring with high fidelity and micro/nanoscale resolution. Fig. 15.13 summarizes the

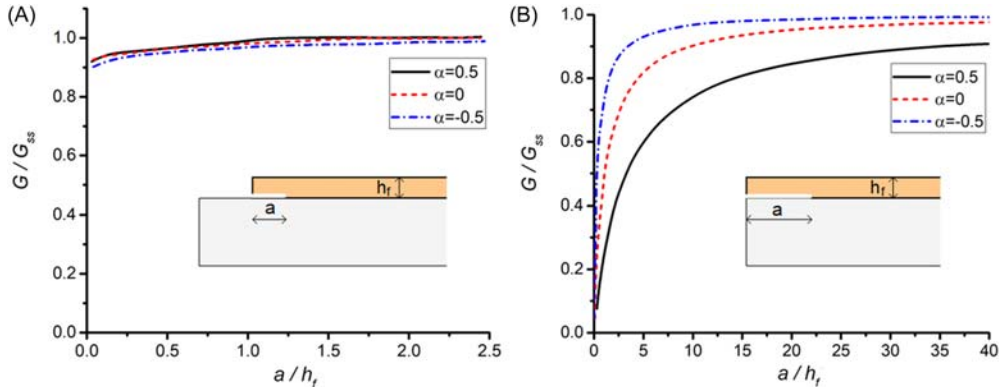


Figure 15.12 Normalized energy release rate as a function of crack length for (A) a crack emerging at an interior edge; (B) a crack emerging at the corner edge. Modified from Yu, H.-H., He, M. Y. & Hutchinson, J. W. (2001). *Acta Materialia*, 49(1), 93–107. [https://doi.org/10.1016/S1359-6454\(00\)00293-7](https://doi.org/10.1016/S1359-6454(00)00293-7).

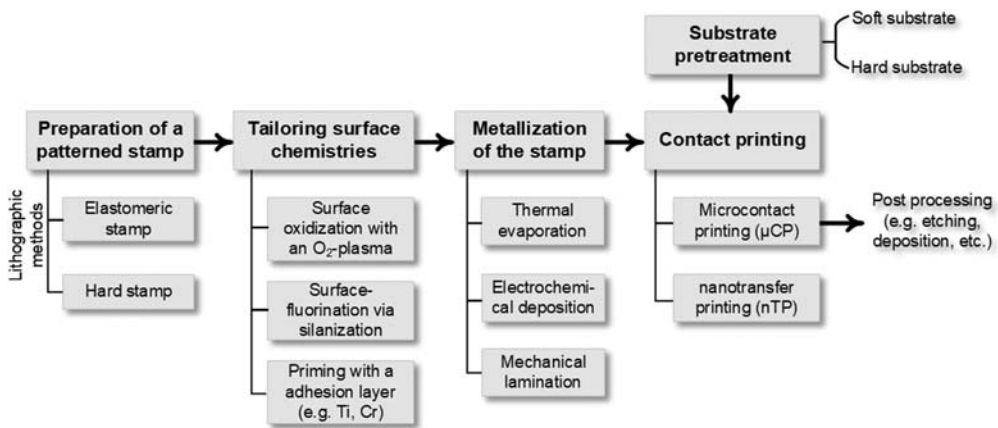


Figure 15.13 General metal transfer printing process flow.

elementary components involved in metal transfer printing (mTP) processes. In principle, mTP originates from soft lithography. It employs relief features on a stamp and specially tailored surface chemistries to pick ultrathin metal patterns from one surface and place them onto another. In order to successfully implement this, plenty of issues regarding material properties, surface chemistries, thin film mechanics, manufacturing, etc., need to be carefully considered. We have overviewed the metallization step for metal film preparation and some fundamental mechanics involved in contact printing. In the following context, we discuss other crucial steps while introducing representative research on microcontact printing (μ CP) and nanotransfer printing (nTP) of ultrathin metal films.

15.3.1 Microcontact printing of metal films

μ CP is a key element of the soft lithographic method that uses a high-resolution elastomeric stamp with a chemical ink to form self-assembled monolayer (SAM) patterns on the surface of a target substrate by contact (Rogers & Nuzzo, 2005; Xia & Whitesides, 1998). The transferred SAM layer can further function as the mask for material removal by etching or material deposition so that the stamp patterns can be transferred to the substrate materials with remarkably high fidelity. Fig. 15.14A depicts a general μ CP process flow for fabricating metal features having μm to cm scale dimensions (Kumar & Whitesides, 1993). Since initially invented by the Whitesides group at Harvard University about three decades ago, μ CP techniques have been widely used for applications ranging from photonics and microfluidics to plastic and flexible electronics.

Although the original μ CP does not a technique that directly transfers a metal film from one donor surface to another receiver surface, it is worth understanding the key steps involved since it shares many elementary features with later metal film transfer printing methods. In Fig. 15.14A, there are two main parts in μ CP processes: (a) fabrication of the elastomeric stamps and (b) SAM pattern transfer by contact between a stamp and the surface of a target substrate. The μ CP stamps are commonly fabricated from the elastomer PDMS via the established photolithographic techniques.

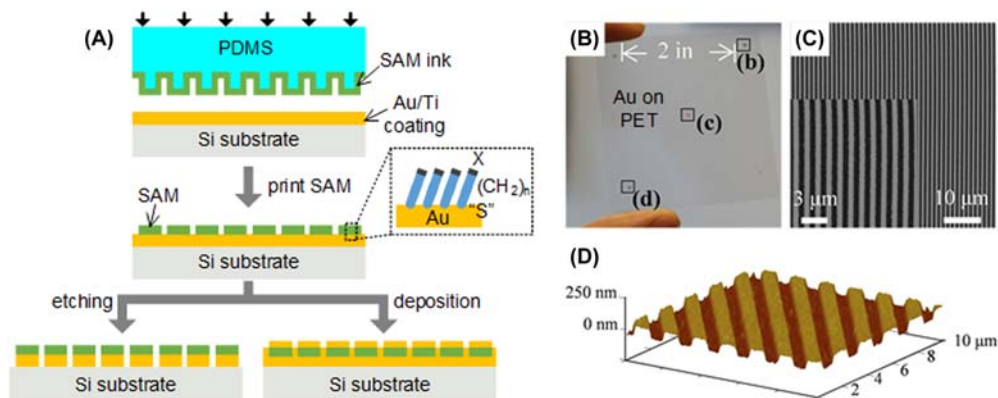


Figure 15.14 Microcontact printing (μ CP) for thin metal film patterning. (A) Schematic procedures for μ CP of self-assembled monolayers on the surface of a gold film and postwet etching or metal deposition processes; (B) photo of the gold-nanograting arrays transfer printed onto a PET substrate; (C) SEM image of the gold nanograting with 600 nm line width and 600 nm spacing; (D) AFM topography of 600 nm line width gratings. Adapted from Xia, Y. & Whitesides, G. M. (1998). *Annual Review of Material Science*, 28(1), 153–184. <https://doi.org/10.1146/annurev.matsci.28.1.153>; Zhou, X., Xu, H., Cheng, J., Zhao, N. & Chen, S.-C. (2015). *Flexure-based roll-to-roll platform: A practical solution for realizing large-area microcontact printing*. *Scientific Reports*, 5(1), 10402. <https://doi.org/10.1038/srep10402>.

Table 15.3 summarizes some commonly used SAM-metal pairs that result in low densities of defects in the transferred features. This might be of substantial significance in adjusting the interfacial adhesion energy between the metal film and the surface of another material, for example, using the chemical interaction between the thiol and Au or Ag for debonding and bonding purposes (Loo et al., 2002).

μ CP of SAMs on thin films of Au or Ag appears to be the most reproducible process. For example, using similar processes depicted in Fig. 15.14A, Au and Ag gratings of 300, 400, and 600 nm line width on a 4-inch plastic substrate (e.g., a PET sheet) can be fabricated at a speed of 60 cm/min, as shown in Fig. 15.14B (Zhou et al., 2015). The high yield with submicrometer resolution stems from the roll-to-roll μ CP process, which will be discussed in the later section. Here, it gives a good example that μ CP can be versatile and implemented in various configurations towards high-resolution, high-throughput micro/nanomanufacturing.

Furthermore, μ CP is also capable of producing SAMs with submicrometer patterns on a curved substrate. Curved surface μ CP takes advantage of a compliant elastomeric stamp, which can conform to a nonplanar surface with minimal pattern distortion on the surface. Fig. 15.15 presents a typical μ CP process flow and experimental results of 50 nm thick Au patterns onto the surface of a glass capillary having a diameter down to approximately 500 μ m (Jackman et al., 1995; Xia & Whitesides, 1998). What should be noted here is that the conformal transfer of micro/nanopatterns adds valuable functionalities, and this is also one of the salient issues in flexible or wearable electronics design and fabrication (Han et al., 2020; Hong et al., 2016; Kim et al., 2011; Ko et al., 2008; Linghu et al., 2018). Although micro/nanoscale metal patterns can be

Table 15.3 Typical self-assembled monolayer (SAM)/metal or SAM/substrate pairs used for metal transfer printing.

SAM material	Metal or substrate materials	References
Alkanethiolates	Au, Ag, Cu, GaAs, Pt	Fenter et al. (1991), Delamarche et al. (1996), Sheen et al. (1992), Schlenoff et al. (1995), and Lee et al. (1991)
Alkylsiloxanes	SiO ₂ /Si, Al ₂ O ₃ /Al, glass, mica, polymers (treated by plasma)	Ulman (1991), Allara et al. (1995), and Wirth et al. (1997)
Alkyl group	Si	Linford et al. (1995)
Alkanesulfonates	Au	Chadwick et al. (1993)
Alkylphosphines	Au	Uvdal et al. (1995)
Octadecylsiloxanes	Al, Al ₂ O ₃ /Al	Lee et al. (2007)
Alkylisocyanides	Pt, Au	Hickman et al. (1992)
Carboxylic	Metal oxides	Tao et al. (1993)

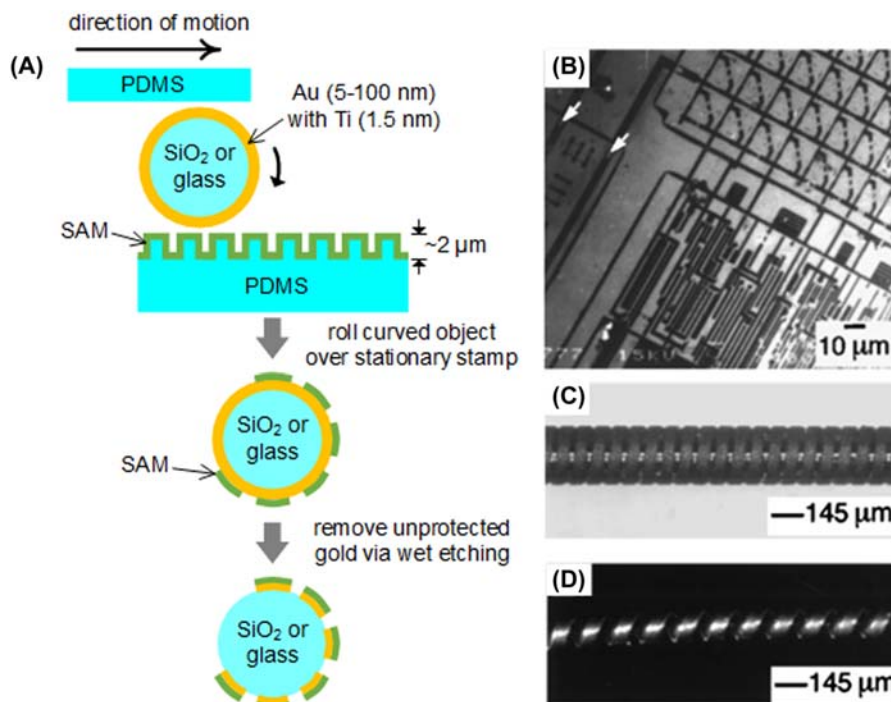


Figure 15.15 Microcontact printing (μ CP) for metal film patterning on curved surfaces. (A) Schematic procedures of SAM imprint onto the surface of a capillary. The transferred self-assembled monolayer was used as the mask for selective etching; (B) SEM image of patterned Au on a SiO_2 capillary; (C and D) optical micrographs of a Ni/Ag microtransformer and a Cu/Ag microspring fabricated by μ CP, selective etching, and electroplating. Adapted from Xia, Y. & Whitesides, G. M. (1998). *Annual Review of Material Science*, 28(1), 153–184. <https://doi.org/10.1146/annurev.matsci.28.1.153>; Jackman, R. J., Wilbur, J. L. & Whitesides, G. M. (1995). *Science*, 269(5224), 664–666. <https://doi.org/10.1126/science.7624795>.

well transferred onto a simple cylindrical surface by μ CP, existing processes accommodate only limited curvatures and even types of nonplanar surface. A number of variants including stamp stiffness, geometry, metal pattern dimensions, and contact printing process, as well as the dynamic deformations of the pattern and the stamp as the stamp approaches the target surfaces need to be specifically designed and locally controlled to obtain intimate contact and bonding between the patterns and a substrate with a particular curvature.

15.3.2 Nanotransfer printing of metal films

nTP is similar to μ CP processes, while in nTP, a pattern of the thin metal film is deposited onto the surface of a stamp or “peeling off” from a “donor” substrate using a stamp and directly printed onto a target substrate by controlling the film/substrate

interfacial adhesion energies (Gamota et al., 2004; Rogers & Nuzzo, 2005). In this regard, nTP is a purely additive printing process, and it can pattern the micro/nano-scale features discussed for μ CP in a single process step. Fig. 15.16 highlights the critical steps involved in the nTP process. A patterned elastomeric (e.g., PDMS, PFFE) or hard (e.g., Si, glass) stamp is firstly fabricated by lithographic and subsequent etching methods, and the raised stamp patterns are selectively coated with a thin layer of SAM, and the desired metal film. The coated stamp is then brought into contact with the target substrate, which is also pretreated with an adhesion layer to “capture” the metal features. In some instances, external pressure and/or heat are needed to minimize the gaps and improve the interfacial adhesion between the metal film on the raised stamp patterns and the receiver substrate. By controlling the adhesion interplay between the different layers in the SAM/metal/adhesion stack, as we discussed previously, the thin metal patterns can delaminate from the raised surface of the stamp and bond to the substrate. Fig. 15.16 also gives an example of e-beam evaporated Al thin

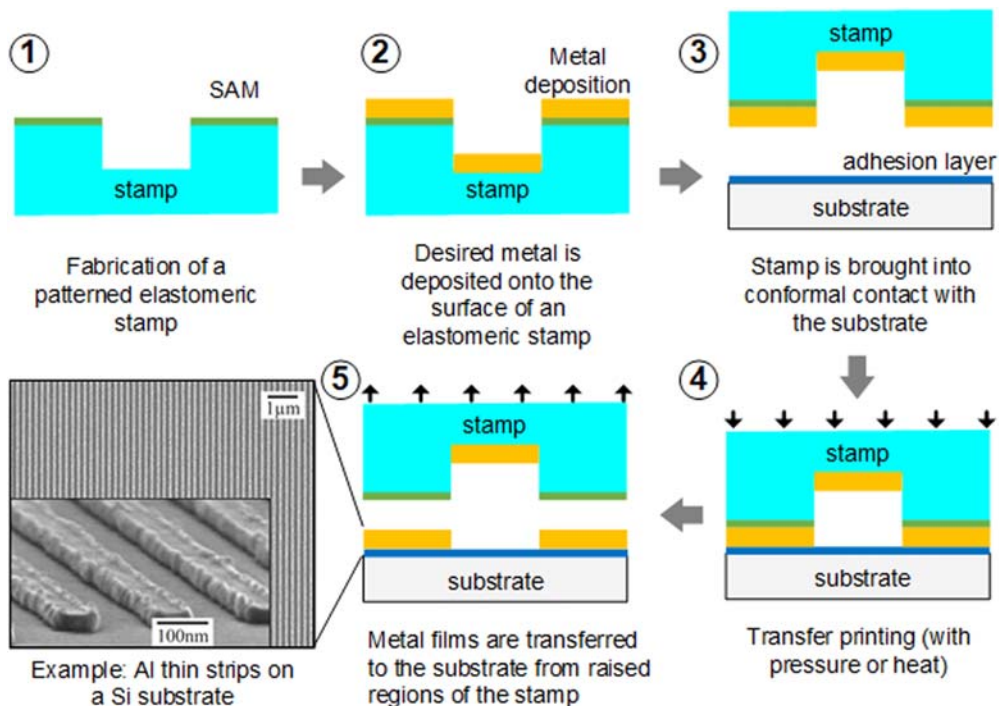


Figure 15.16 Schematic procedures for fabricating patterned metal films using micro/nanoscale transfer printing with a prepatterned stamp. The inset SEM image shows an example of transfer printed Al strips with a width of 61 nm onto a Si substrate. Adapted from Lee, B. H., Cho, Y. H., Lee, H., Lee, K.-D., Kim, S. H. & Sung, M. M. (2007). *Advanced Materials*, 19(13), 1714–1718. <https://doi.org/10.1002/adma.200601884>.

strips with a width of 61 nm on a Si substrate using nTP (Lee et al., 2007). In this and the following sections, we will discuss some determining elements during nTP processes, including different nTP procedures, pretreatment of the stamp, environmentally assisted bonding and debonding three-dimensional nanostructures transfer, and roll-to-roll nTP for high productivity.

The nTP method depicted in Fig. 15.16 is in general simple and straightforward, but relatively slow and not efficient enough from the manufacturing perspective since after each transfer printing cycle, we need to repeat the stamp surface pretreatment and metal deposition steps that are usually time-consuming and require vacuum. Alternatively, another metal film-picking process can replace the above recoating step, as depicted in Fig. 15.17A. A patterned stamp picks the desired metal patterns from a thin metal film deposited on a flat glass inkpad and places them onto the target substrate (Oh et al., 2009). In this case, the stamp can be used repeatedly without treatment or recoating, and continuous nTP is possible over large areas. Fig. 15.17B shows the experimental results based on this pick-and-place nTP process, indicating that both the transferred metal patterns and the residual metal patterns remaining on the inkpad very closely match the dimensions of the stamp structures, and the metal residual patterns have clean fracture edges. This is important for nTP with high fidelity.

Further, nTP can be added as a subsequent step after conventional lithographic procedures. For example, metal films can be photolithographically patterned onto a Si wafer, which is precoated with a layer of parylene C, as shown in Fig. 15.18. Here, positive metal patterns bulged up from the donor substrate. The patterned wafer was then brought into contact with the receiver substrates, such as polyethylene naphthalene (PEN), polycarbonate (PC), or Kapton, and released the metal features onto these

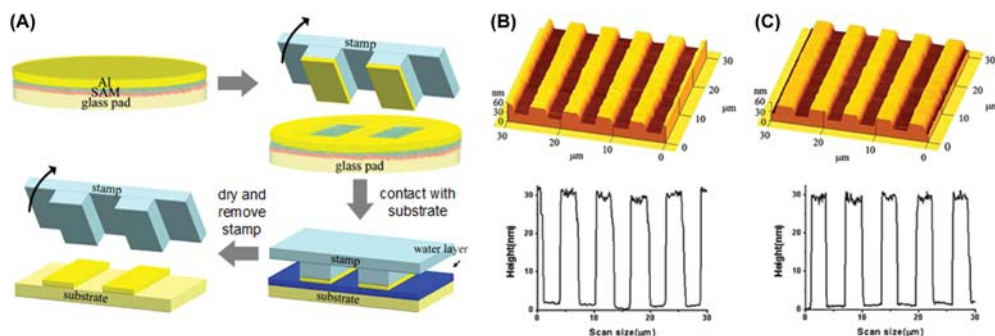


Figure 15.17 Transfer printing procedures using an Al thin film predeposited on a flat glass inkpad. (A) Schematic outline of the procedure for fabricating patterned Al thin films using water-mediated metal transfer printing with contact inking; (B and C) AFM images and topography profiles of (B) Al residual thin films on a glass inkpad after peeling off the stamp, and (C) transfer printed Al thin films on a Si substrate. Adapted from Oh, K., Lee, B. H., Hwang, J. K., Lee, H., Im, S. & Sung, M. M. (2009). *Small*, 5(5), 558–561. <https://doi.org/10.1002/sml.200801108>.

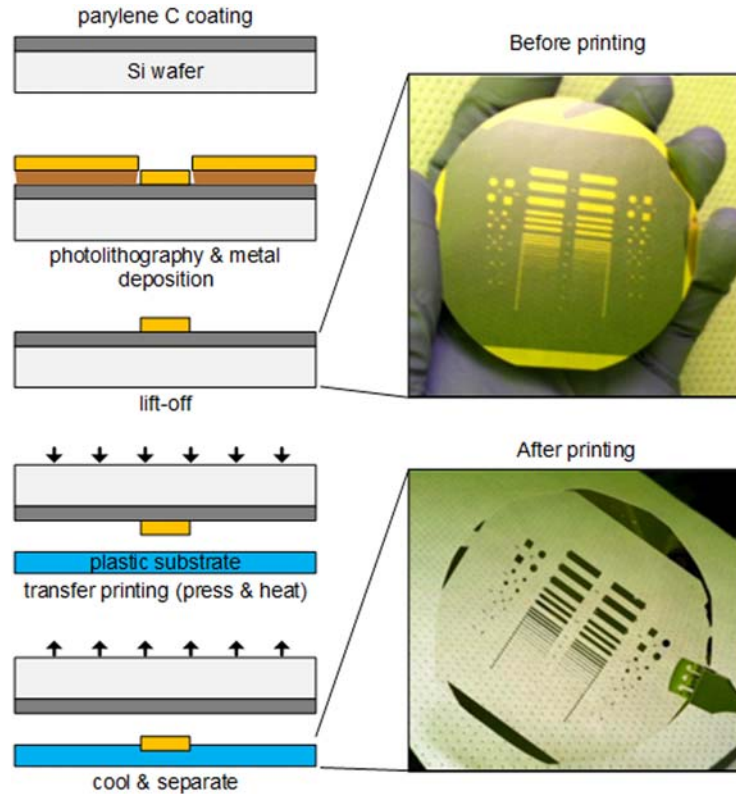


Figure 15.18 Transfer printing of patterned metal films using perylene C coated surfaces. Schematic procedures of steps involved in fabricating patterned metal films using traditional lithography methods and the transfer printing onto a plastic substrate. The optical images show the fabricated thin metal patterns before and after transfer printing. Adapted from Bavier, J., Cumings, J. & Hines, D. R. (2013). *Microelectronic Engineering*, 104, 18–21. <https://doi.org/10.1016/j.mee.2012.10.020>.

substrates (Bavier et al., 2013). In this case, no stamp is needed. Metal patterns and the Si backplane are used directly for nTP, while plastic substrates are usually suitable for receiving the metal patterns in this method.

Using the nTP methods, complex thin metal patterns with thicknesses down to several nanometers and lateral dimensions of a half to several hundreds of micrometers can be readily printed on various substrates including metals, semiconductors, and polymers in a scalable manner. Figs. 15.19 and 15.20 present some examples of such transferred metal patterns with multifunctionality (Lee et al., 2007; Loo et al., 2002; Oh et al., 2009; Park et al., 2020; Rogers, 2001).

Recall the discussion in Section 15.1.1 on thin metal film deposition, especially for PVD of metal films onto an elastomeric surface, multiple types of defects in the

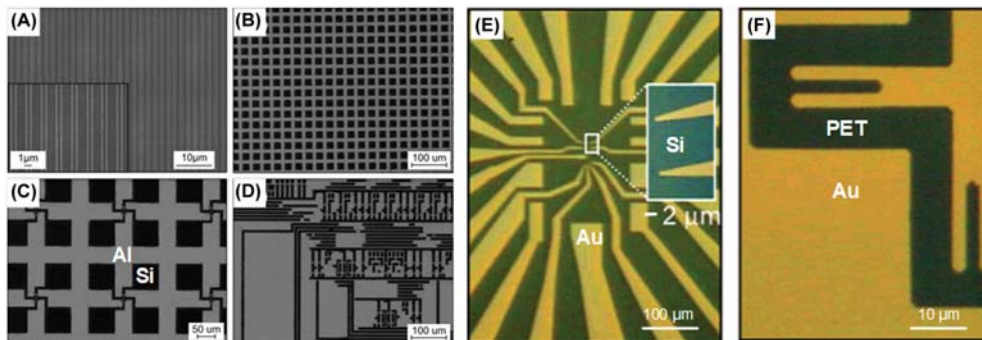


Figure 15.19 Examples of nanotransfer printing (nTP) ultrathin metal patterns. Example SEM images of nTP ultrathin metal patterns with a feature size of (A) 500 nm, (B) 20 μm , (C) 50 μm , and (D) 10 μm ; (E and F) optical micrographs of nTP Au patterns on (E) a Si wafer and (F) a PET sheet. Adapted from Lee, B. H., Cho, Y. H., Lee, H., Lee, K.-D., Kim, S. H. & Sung, M. M. (2007). *Advanced Materials*, 19(13), 1714–1718. <https://doi.org/10.1002/adma.200601884>; Loo, Y.-L., Willett, R. L., Baldwin, K. W. & Rogers, J. A. (2002). *Journal of American Chemical Society*, 124(26), 7654–7655. <https://doi.org/10.1021/ja026355v>.

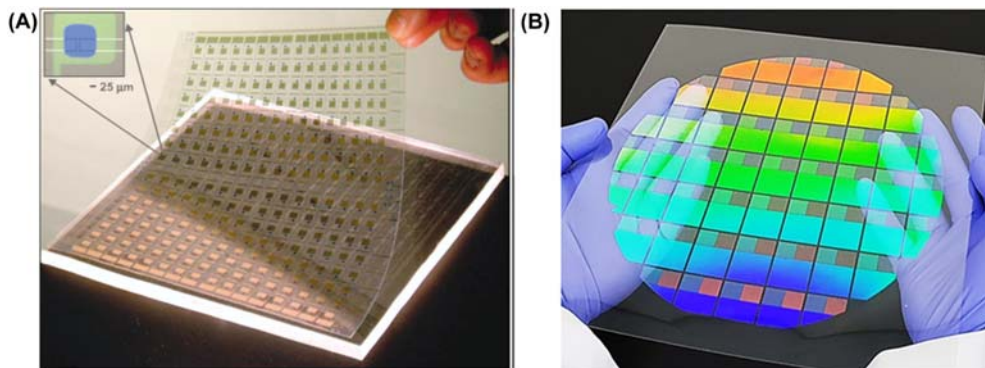


Figure 15.20 Examples of nanotransfer printing (nTP) metallic patterns for flexible electronics. (A) Photo of a 256-element plastic active-matrix backplane circuit and the planar stamp that was used for nTP. The inset shows a micrograph of one of the transistors (blue: the organic semiconductor; green: the gate electrode; gold: the source/drain electrodes and related interconnects); (B) transfer printed Pt nanowires with a width of 250 nm on a transparent and flexible PET substrate by nTP by using an 8-inch PMMA stamp. Adapted from Rogers, J. A. (2001). *Rubber Stamping for Plastic Electronics and Fiber Optics*. *MRS Bulletin*, 26(7), 530–534. <https://doi.org/10.1557/Mrs2001.125>; Park, T. W., Byun, M., Jung, H., Lee, G. R., Park, J. H., Jang, H.-I., Lee, J. W., Kwon, S. H., Hong, S., Lee, J.-H., Jung, Y. S., Kim, K. H. & Park, W. I. (2020). *Science Advances*, 6(31), eabb6462. <https://doi.org/10.1126/sciadv.abb6462>.

deposited metal film may occur. Firstly, for sputtering or e-beam evaporation deposition on the surface of a PDMS, the metal ions heat and expand the PDMS surface before and during the deposition. This local heating-induced surface straining depends on the material properties and dimensions of the metal and the substrate, and it may

cause various wrinkling, folding, and even cracking patterns on the metal film. These are frequently observed in other studies, as shown in Fig. 15.21A and B (Bowden et al., 1998; Cai et al., 2011; Yu et al., 2015; Yu et al., 2016). Therefore stamp design and its surface morphology and chemistries control are of great significance in metal transfer printing processes. Further, for an ultrathin metal film with a thickness <50 nm, it becomes relatively brittle than its bulk counterparts (Meyers & Chawla, 2008), plus the inherently poor wettability of metals on a PDMS, nanoscale cracking in the metal film can occur. Fig. 15.21C and D show examples of 20 nm thick Au on the surface of PDMS, while a high density of nanocracks is present even with an adhesion layer of 2 nm Ti between the Au and PDMS (Menard et al., 2004). Smooth PVD thin metal films on PDMS can be obtained by pretreating the PDMS surface with a short oxygen plasma exposure to remove the hydrocarbon groups and activate hydrophilic –OH groups on the surface, as shown in Fig. 15.21E and F (Duffy et al., 1998; Menard et al., 2004; Tan et al., 2010). Fig. 15.2 also compares the surface roughnesses for the samples with and without plasma treatment of the stamp.

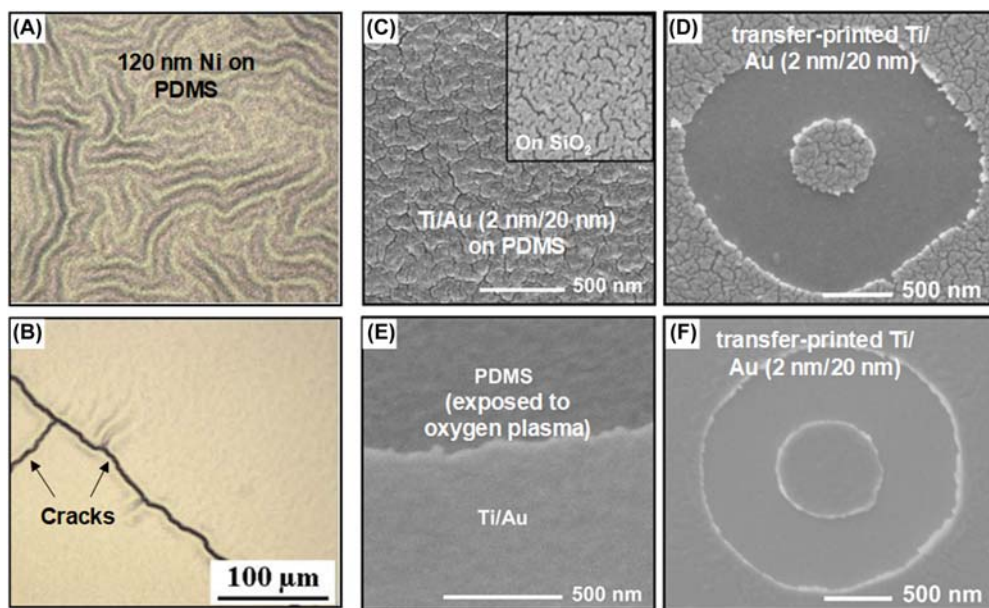


Figure 15.21 Defects of deposited (on stamps) and transfer printed metal films (onto substrates). (A and B) Optical micrographs of typical surface morphologies of a sputtered Ni film (120 nm thick) on PDMS; (C) a PDMS stamp coated with Ti/Au. The inset: SiO₂ surface coated with Au (20 nm); (D) nTP Ti/Au onto a Si substrate; (E) the Ti/Au film was deposited onto a pretreated PDMS stamp (13 s exposure to oxygen plasma); (F) nTP Ti/Au onto a Si substrate with optimized nTP conditions. Adapted from Menard, E., Bilhaut, L., Zaumseil, J. & Rogers, J. A. (2004). *Langmuir*, 20(16), 6871–6878. <https://doi.org/10.1021/la048827k>; Yu, S., Sun, Y., Ni, Y., Zhang, X. & Zhou, H. (2016). *ACS Applied Material Interfaces*, 8(8), 5706–5714. <https://doi.org/10.1021/acsami.5b12369>.

Elastomeric stamp sagging is another flaw that usually happens during nTP, as illustrated in Fig. 15.22. The recessed surfaces on the stamp sag down and come into contact with the substrate, as a result, unwanted metal patterns may also bond to the substrate, see the example in Fig. 15.22. This flaw can be caused by several factors such as unwanted deformation of the stamp or a strong suction effect when using a water layer as an adhesion layer in Figs. 15.16 and 15.17. Using liquids like water, ethanol, etc., can promote robust bonding between the metal and substrates like Si (Aldakov et al., 2011; Lee et al., 2007; Oh et al., 2009). We will introduce this liquid-assisted bonding effect in a later section. However, the high surface energy of water ($\gamma_{\text{H}_2\text{O}} = 72\text{mJ/m}^2$) applies a strong capillary force pulling the stamp down when water is drying. This stiction issue is a common problem in micro/nanofabrication and contact printing (Madou, 2012; Xia & Whitesides, 1998). Low surface energy liquid like ethanol ($\gamma_{\text{Ethanol}} = 23\text{mJ/m}^2$) was used to circumvent this problem (Aldakov et al., 2011).

15.3.3 Advanced transfer printing procedures for metal films

All the abovementioned transfer printing methods are to fabricate thin metal patterns on a planar surface or a simple curved surface with relatively low curvatures. This section will introduce other transfer printing methods capable of fabricating ultrathin metal films out of the plane for additional functionalities. Firstly, the sidewalls of the patterned stamp (Fig. 15.16) can also be used as the carrier of metal so that the transferred patterns are not only from the raised discrete flat surfaces but also the

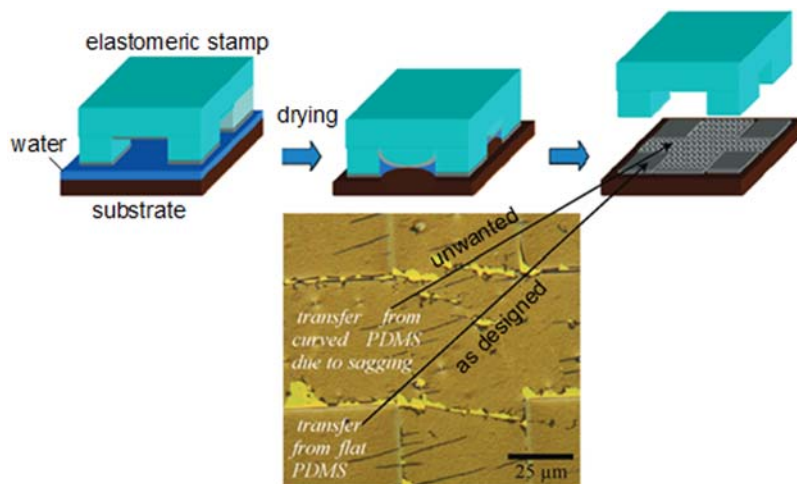


Figure 15.22 Stamp sagging issue in nanotransfer printing. Schematics of stamp sagging and a typical result of water-mediated metal transfer printing onto a polymer substrate. Adapted from Aldakov, D., Tondelier, D., Palacin, S. & Bonnassieux, Y. (2011). ACS Applied Material Interfaces, 3(3), 740–745. <https://doi.org/10.1021/am101085k>.

continuous micro/nanostructured three-dimensional surfaces. Figs. 15.23 and 15.24 show two examples based on this idea.

Using the three-dimensional nTP method described in Fig. 15.24, arrays of Au nanocapsules and “L-shaped” nanostructures with high mechanical integrity and low density of defects can be formed, see Fig. 15.25A and B (Menard et al., 2004). What should be aware of is meticulous control of bonding between the metal film and the contacted substrate areas, as well as debonding at the continuous metal/stamp interface is critical for high-quality three-dimensional nTP. In this case, a thiol-terminated SAM on the substrate enhanced the metal/substrate adhesion (Loo et al., 2002; Menard et al., 2004). Such three-dimensional nTP can be repeated multiple times for fabricating more complex multilayer three-dimensional metal structures with nanoscale channels, as shown in Fig. 15.25E and F (Zaumseil et al., 2003).

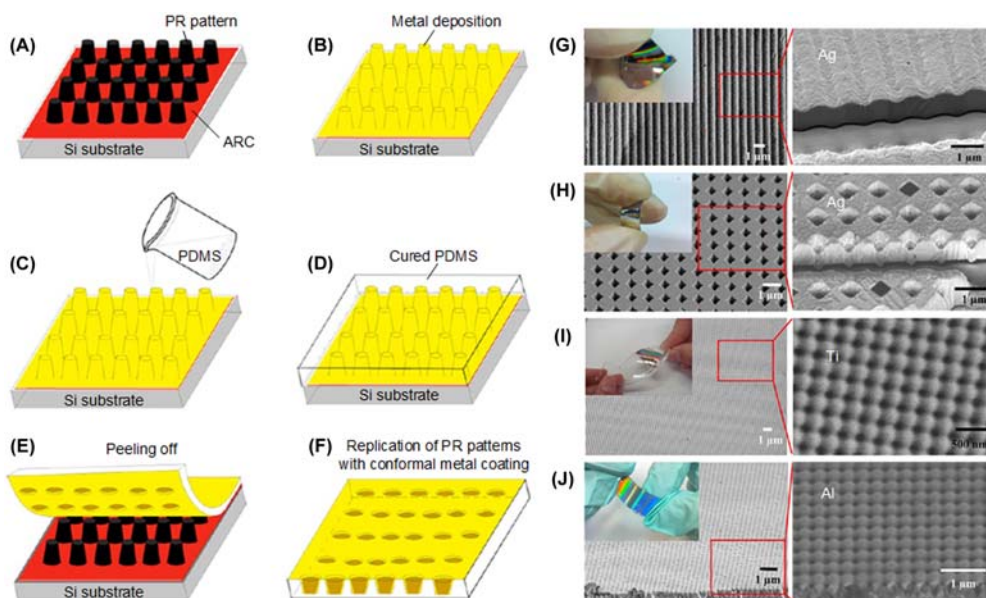


Figure 15.23 Transfer printing of three-dimensional metal nanostructures via holographic nanopatterns. Schematic illustrations of pattern transfer processes of metal nanostructures onto a PDMS substrate, including (A) photoresist nanopatterns fabricated on a Si substrate by using laser interference lithography. An antireflective coating (ARC) layer is coated between the PR and the Si substrate; (B) E-beam evaporation of a metal film on the PR layer; (C) molding of PDMS elastomer on the metal layer; (D) curing of the PDMS layer to form a planar substrate; (E) mechanical peeling of the PDMS/metal layer from the PR surface; (F) the metal nanostructures transferred onto the PDMS substrate; (G–J) SEM images of Ag, Ti, and Al films transferred onto the PDMS substrate. The inset of each image in a left column shows the nanostructured PDMS substrate bent by hands. Adapted from Du, K., Wathuthantri, I., Liu, Y., Xu, W. & Choi, C.-H. (2012). ACS Applied Material Interfaces, 4 (10), 5505–5514. <https://doi.org/10.1021/am301423s>.

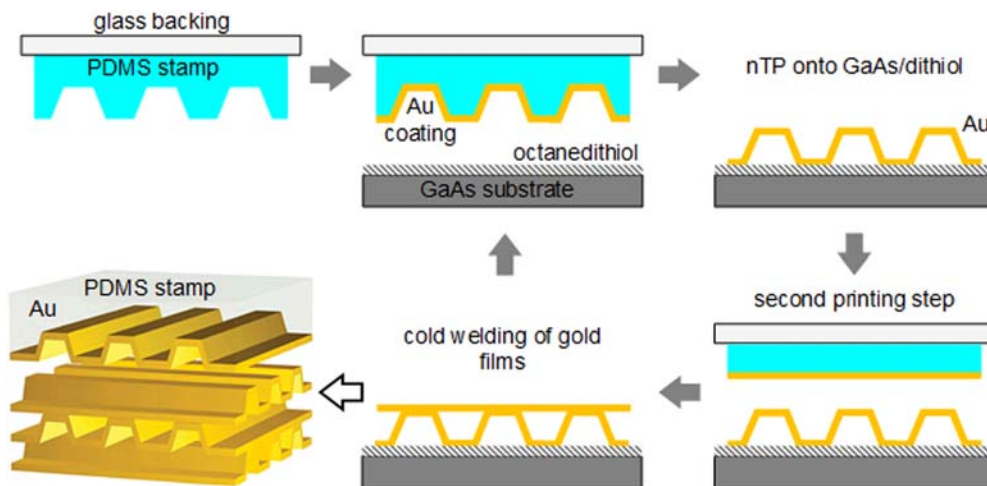


Figure 15.24 Schematic procedures for nanotransfer printing of three-dimensional and multilayer metal structures. A PDMS stamp with sloping sidewalls leads to a continuous metal layer when Au is deposited onto the stamp surface. The three-dimensional metal coatings can be transferred in a single step onto a GaAs substrate. Adapted from reference (Zaumsei et al., 2003). From Zaumseil, J., Meitl, M. A., Hsu, J. W. P., Acharya, B. R., Baldwin, K. W., Loo, Y.-L. & Rogers, J. A. (2003). *Nano Lett.*, 3 (9), 1223–1227. <https://doi.org/10.1021/nl0344007>.

Given that there are various transfer printing methods, which are different in the process flow, material selection, and surface chemistries, almost all μ CP and nTP techniques we have discussed previously fall in the general framework as shown in Fig. 15.13. As the first and essential step, solid stamps facilitate the macroscopic handling of micro/nanoscale metal features and accurate pick and place. Nevertheless, the solid nature of stamps and the corresponding solid–solid delamination and replacement processes also impede metal film transfer printing in some conditions, for example, freestanding nanostructures having large overhanging areas (i.e., insufficient metal/substrate contact surfaces and consequent bonding for nTP) or complex nonplanar surfaces with high local curvatures.

Fig. 15.26 depicts a wet transfer process analogous to wedging transfer of thin films widely used in transferring two-dimensional materials and fabricating flexible electronics (Aghajamali et al., 2018; Schneider et al., 2010; Song et al., 2013; Suk et al., 2011; Zhang et al., 2020). In this case, no solid stamps are required, instead, a liquid phase resist [e.g., polymethylmethacrylate (PMMA) or polyvinylalcohol (PVA)] is spin-coated on the patterned metal structures and forms a polymer supporting layer/metal/donor substrate stack after resist curing. Delamination occurs at the metal/donor substrate interface in a solution (e.g., acidic solution) releasing the polymer/metal film floating on the surface of the solution. Then wedging transfer can be applied with a slotted substrate, thus polymer/metal film can be transferred overhanging the slot.

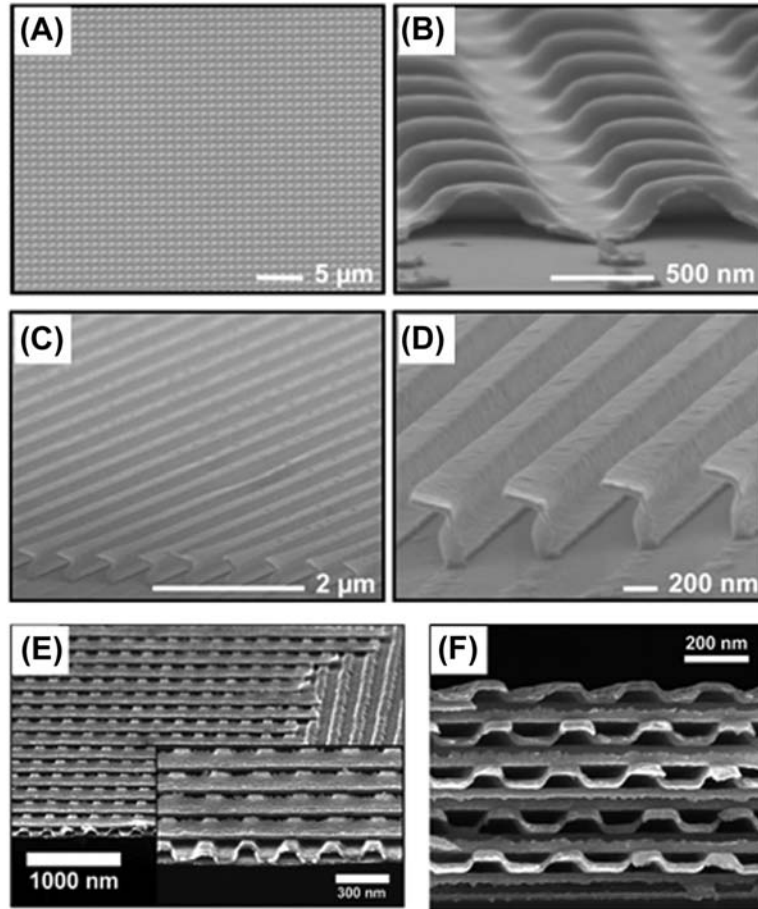


Figure 15.25 SEM images of three-dimensional Au nanostructures and multilayer stacks transfer printed by a PDMS stamp with sloping sidewalls. (A–D) reprinted with permission from Menard, E., Bilhaut, L., Zaumseil, J. & Rogers, J. A. (2004). *Langmuir*, 20(16), 6871–6878. <https://doi.org/10.1021/la048827k>. (E and F) Reprinted with permission From Zaumseil, J., Meitl, M. A., Hsu, J. W. P., Acharya, B. R., Baldwin, K. W., Loo, Y.-L. & Rogers, J. A. (2003). *Nano Letters*, 3(9), 1223–1227. <https://doi.org/10.1021/nl0344007>.

Supporting by the relatively stiff polymer layer, ultrathin metal structures can suspend without sagging. Lastly, the polymer supporting layer can be removed by reactive ion etching (RIE), leaving the suspended metal structures.

As for nonplanar surfaces with high curvatures, either compliant monolithic stamps or thin polymer supporting carriers can hardly contact the substrate conformally without notable mechanical deformations in thin metal films (Hong et al., 2016; Xiao et al., 2018). One solution to this issue is designing advanced stamp structures or applying desirable stamp materials. For instance, richer modes of stamp deformation and more curved stamp/substrate

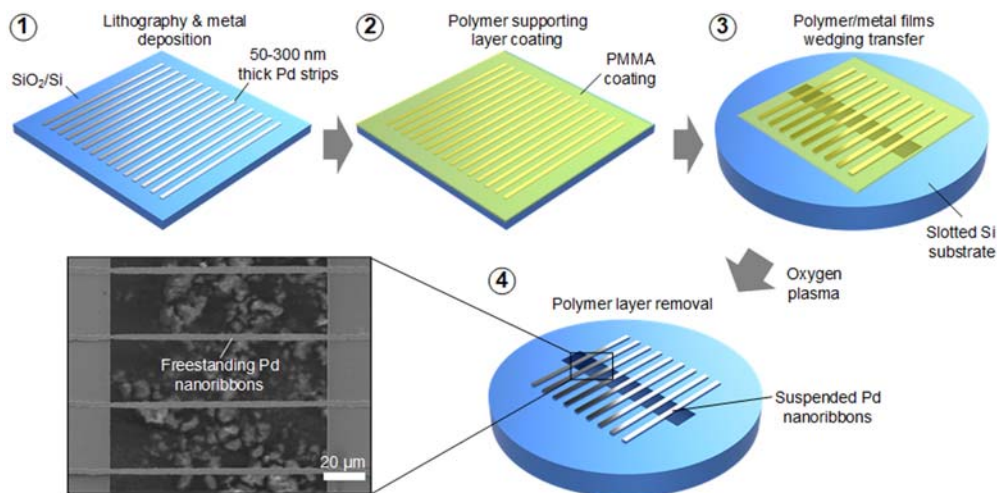


Figure 15.26 Fabrication of freestanding ultrathin metal ribbons. Schematic procedures for fabricating freestanding ultrathin metal ribbons and a typical SEM image of as-transferred freestanding Pd nanoribbons on a slotted SiO₂/Si substrate. Adapted from Zhang, K., Surana, M., Haasch, R. & Tawfik, S. (2020). *Elastic modulus scaling in graphene-metal composite nanoribbons*. *Journal of Physics D: Applied Physics*, 53(18), 185305. <https://doi.org/10.1088/1361-6463/ab7329>.

interfaces were achieved by using an elastomeric stamp with hierarchical structures, as depicted in Fig. 15.27A (Park et al., 2014). Alternatively, a reflowable stamp made from a sugar and corn syrup mixture that transforms between solid and liquid on demand can freely stretch to achieve micro/nanoscale patterns transfer printing that is naturally conformal to arbitrarily complex surfaces having nanoscale radii of curvature, as presented in Fig. 15.27B–E (Zabow, 2022). Notably, the flow direction of the reflowable stamp guides the lamination of ultrathin metal films resulting in suspended or conformal placement on demand (Fig. 15.27D).

Harnessing the functionality and potential applications of transfer printed micro/nanoscale metal features in various practical fields such as wearable devices, bioscience and engineering, and plasmonics requires the scalable manufacturing capability of producing large-area metal/substrate laminates with high fidelity and nanoscale printing resolution. During the decades of exploration and development in metal transfer printing processes, elastomeric stamps have been widely used to complete the crucial steps of transfer printing. In light of these advances, roll-to-roll processing, also known as R2R, is probably one of the most suitable processes to implement μ CP or nTP that enables high-throughput and high-quality micro/nanoscale metal patterning on various substrates. To be specific, R2R processing refers to applying processes such as coating and printing starting with a roll of a flexible material and re-reeling to create desired patterns or structures on an output roll (Roll-to-roll processing, 2023). R2R

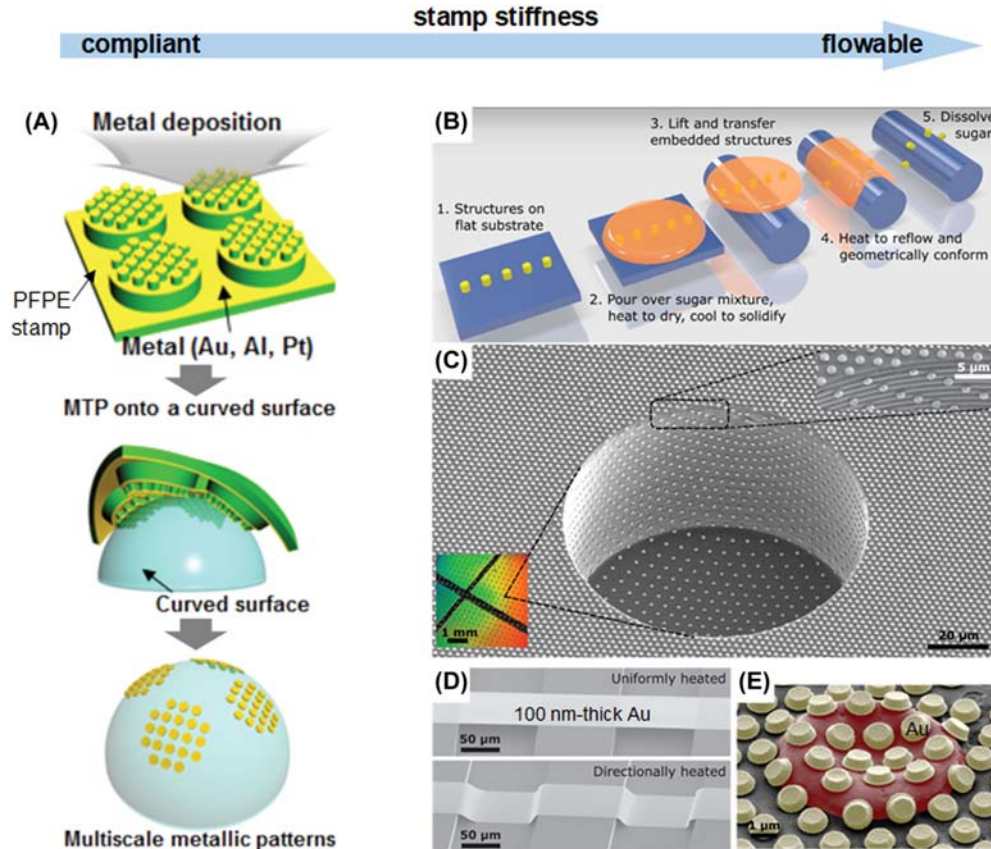


Figure 15.27 Stamp stiffness control for conformal three-dimensional transfer printing. (A) Schematics of nonplanar surface microcontact printing of metal patterns using a hierarchical PFPE stamp; (B) schematic illustration of key steps for microstructure transfer using reflowable materials that “melt” on the receiving substrate; (C) SEM of an array of $1\ \mu\text{m}$ Au disks transfer printed onto a surface with $100\ \mu\text{m}$ diameter, $50\ \mu\text{m}$ deep holes. Upper inset shows transfer pattern conformation over hole edge; (D) SEM images of $100\ \text{nm}$ thick metal strips printed across trenches, showing suspended or conforming placement, determined by controlling the reflow direction; (E) false-colored SEM image showing $0.5\ \mu\text{m}$ thick, $1\ \mu\text{m}$ diameter Au disks transfer printed over a red blood cell surface. Adapted from Park, H., Cho, H., Kim, J., Bang, J. W., Seo, S., Rahmawan, Y., Lee, D. Y. & Suh, K.-Y. (2014). Multiscale transfer printing into recessed microwells and on curved surfaces via hierarchical perfluoropolyether stamps. *Small*, 10, 52–59. <https://doi.org/10.1002/sml.201300772>; Zabow, G. (2022). *Science*, 378(6622), 894–898. <https://doi.org/10.1126/science.add7023>.

techniques are quite prevalent mainly in achieving scalable production of advanced nanomaterials and flexible devices, like graphene (Bae et al., 2010; Kobayashi et al., 2013; Polsen et al., 2015), flexible solar cells (Kim et al., 2020), and printed electronics (Jung et al., 2017; Lin et al., 2017; Montbach & Davis, 2018). Here, two example

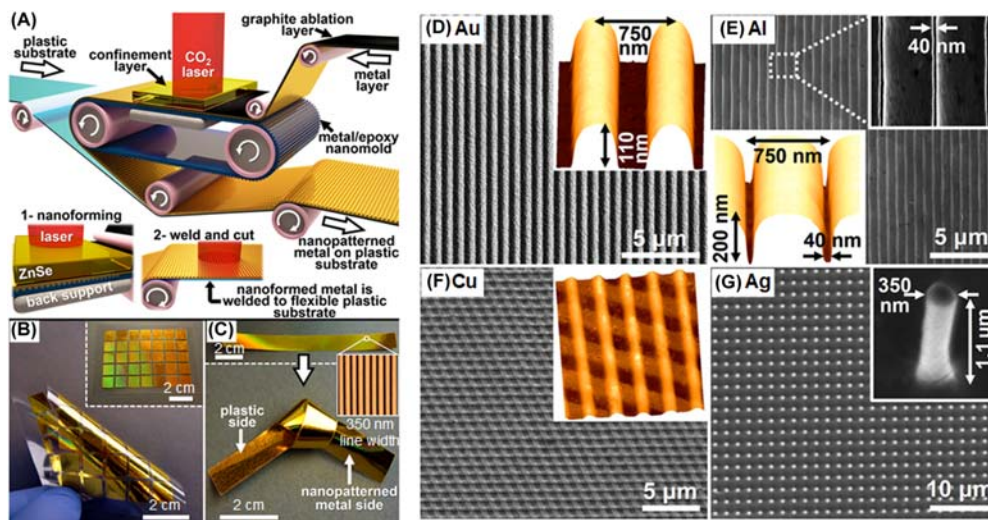


Figure 15.28 Roll-to-roll laser-induced superplasticity setup and examples of continuous nanoforming of metal films. (A) Schematic illustration of (1) the nanoforming of the metal film by superplastic deformation on a nanomold upon laser irradiation; (2) the nanoformed metal film is welded to the supporting plastic film by a second laser scan; (B) a 1 cm² nanoformed Au films welded to a flexible PET sheet; (C) photos of nanoformed Au/PET film with enough flexibility and interfacial adhesion to accommodate external strains, for example, bending and being tied into a knot. The inset shows an AFM image of the nanoformed Au gratings with a line width of 350 nm. (D–G) SEM and AFM images of three-dimensional metal nanostructures fabricated by a laser-induced superplasticity (R2RLIS) method. *Adapted from Goswami, D., Munera, J. C., Pal, A., Sadri, B., Scarpetti, C. L. P. G. & Martinez, R. V. (2018). Nano Letters, 18(6), 3616–3622. <https://doi.org/10.1021/acs.nanolett.8b00714>.*

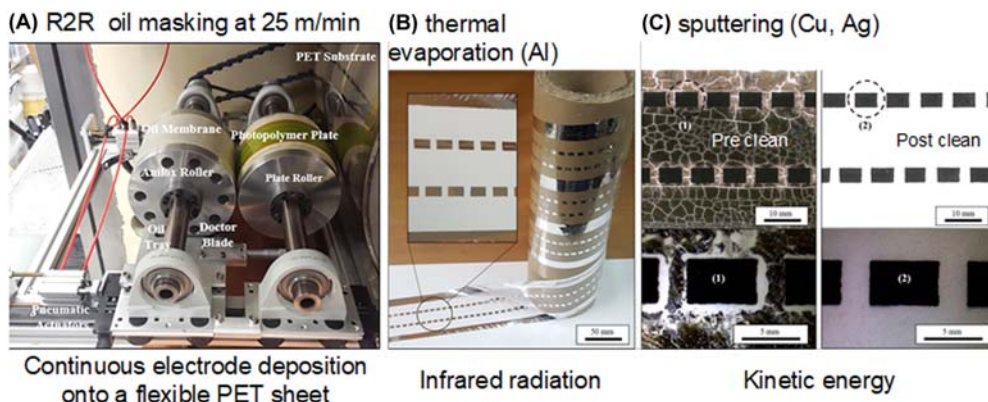


Figure 15.29 Roll-to-roll transfer printing of ultrathin metal electrodes on flexible PET films by oil masking. (A) Photo of a retrofitted flexography system with printing force and anilox to plate forces applied by pneumatic actuators; (B) as-deposited Al patterns by single-step electrode patterning and thermal evaporation; (C) pre and postwash deposited Cu electrodes (same for Ag) by inline patterning on a PET sheet. *Adapted from Stuart, B. W., Tao, X., Gregory, D. & Assender, H. E. (2020). Applied Surface Science, 505, 144294. <https://doi.org/10.1016/j.apsusc.2019.144294>.*

studies related to nTP are gathered for our discussion, as shown in Figs. 15.28 and 15.29.

Fig. 15.28A–C present an R2R, laser-induced superplasticity (R2RLIS) method that uses a laser shock to induce high-strain-rate superplastic deformation on a thin metal layer so that the nanoscale patterns on an epoxy mold can be replicated onto the metal surface. The patterned metal film is then laminated onto a plastic backplane for postdevice fabrication (Goswami et al., 2018). Using this R2RLIS method, Au nanograting, V-grooves, Cu film with fishnet surface, and Ag nanopillars were produced rapidly, and the minimum feature size down to 40 nm was obtained, see Fig. 15.28D–G. This so-called “metal nanoforming” R2R method can represent a group of potential continuous μ CP or nTP processes that use a flexible or even hard patterned mold or stamp to reshape the surface of the metal films that are transported by rollers or to pick up desired metal patterns from a roll of metallized flexible inkpads then transfer to another roll of receiver substrate.

In addition, R2R metal transfer printing can be implemented by combining flexography printing and metal deposition techniques. Flexography is a widely used “letterpress” process that employs a flexible raised relief plate to collect ink or oil and then transfer it to other flexible substrates including plastic, metallic films, and paper (Khan et al., 2015). By using flexography printing, ink or oil patterns with feature sizes down to 1 μ m with 200 nm edge roughnesses can be produced scalable and rapidly (Kim et al., 2016). Subsequently, ink or oil patterns can serve as a flexible thin mask for selective metallization via evaporation or sputtering. Fig. 15.29 gives an example that employs such R2R flexography plus metallization method to create ultrathin Al, Cu, and Ag microelectrodes on flexible PET sheets at a speed of 25 m/min (Stuart et al., 2020).

15.4 Environmentally-assisted bonding and debonding of the metal/substrate interfaces

The chemical and moisture content of the surrounding environment at the metal/substrate interface can significantly affect interfacial stoichiometry, adhesive strength, and subsequent interface fracture behaviors. One straightforward example, as mentioned previously, is that water can be used as the adhesion layer to form a uniform and intimate Al/Si interface (Figs. 15.16 and 15.17). In more detail here, covalent bonds between the Al and the Si surfaces are claimed to form during the water layer drying process even though each surface possesses a thin native oxide layer, as presented in Fig. 15.30, strong EDX peaks for Al, Si, and O show up in the interfacial layer (Lee et al., 2007). This phenomenon has been termed “solid bonds,” usually resulting in strong adhesion between two smooth surfaces (Takakuwa et al., 2021).

More insights into environmental effects are for metal/substrate interfacial debonding, which can facilitate the thin film delamination process. The critical interfacial fracture energy G_c is almost insensitive to the environment. However, for the driving

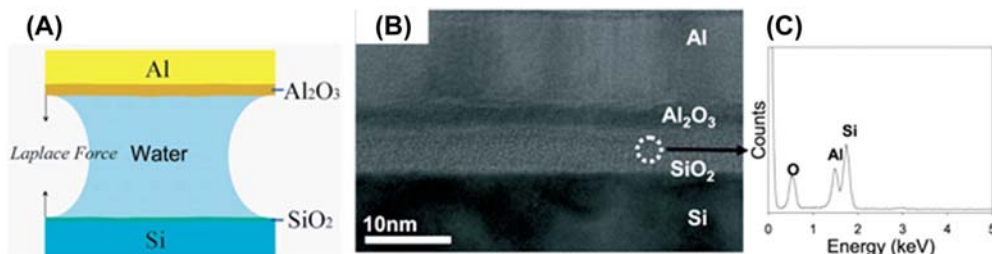


Figure 15.30 Water-assisted metal-substrate bonding. (A) Schematic illustration of a liquid bridge formed by a thin water layer between a thin Al film and a Si substrate; (B) TEM image of a transfer printed Al layer bonded onto a Si substrate. Thin native oxide layers grew naturally on the Al and the Si surfaces before nanotransfer printing; (C) energy-dispersive X-ray spectrum (EDX) taken from the middle (white dashed circle) of the interfacial layer between the Al and the Si surfaces, indicating that two surfaces are covalently bonded. Adapted from Lee, B. H., Cho, Y. H., Lee, H., Lee, K.-D., Kim, S. H. & Sung, M. M. (2007). *Advanced Materials*, 19(13), 1714–1718. <https://doi.org/10.1002/adma.200601884>.

force below G_c , environmentally assisted debonding generally occurs and it is a time-dependent process controlled by several rate-limiting processes at the delamination front (Birringer et al., 2012). Fig. 15.31A presents a general debonding curve, in which two extremes should be first noted: (a) G_{th} is the threshold fracture energy below which crack advancing can be arrested due to energetically unfavorable chemical reactions or steric hindrance effects at the delamination front (Lane et al., 2001); (b) G_c at which the film/substrate separation driving force becomes independent of the chemical environment. Two rate-limiting steps control the debonding curve shape between G_{th} and G_c . In region 1, a chemical reaction-controlled region, changes in the slope indicate a change in the chemical reaction rate-controlled step for delamination front extension. While in region 2, a transport-controlled region, the debond growth rate is found to depend on the chemical environment but only slightly on the applied crack driving force. This is because the chemical reaction rate at the delamination front is higher than the rate at which the reactive species can transport to the delamination front. Notably, an atomistic bond rupture model can be used when describing the kinetics of environmentally assisted debond growth (Lawn, 1975; Lawn, 1993), the net debond velocity at the delamination front can be defined as the sum of the rate of bond rupture and bond healing:

$$\begin{aligned}
 v_c &= v_0 a_x \left\{ \exp \left[-\frac{U_+(G)}{kT} \right] - \exp \left[-\frac{U_-(G)}{kT} \right] \right\} \\
 &= v_0 a_x \exp \left(-\frac{2\gamma'_{tz}}{\pi N_B kT} \right) \exp \left[\frac{G - N_B (\mu_{B*} - \mu_B - \eta \mu_A^S - \eta kT \ln(a_A))}{2N_B kT} \right]
 \end{aligned} \tag{15.5}$$

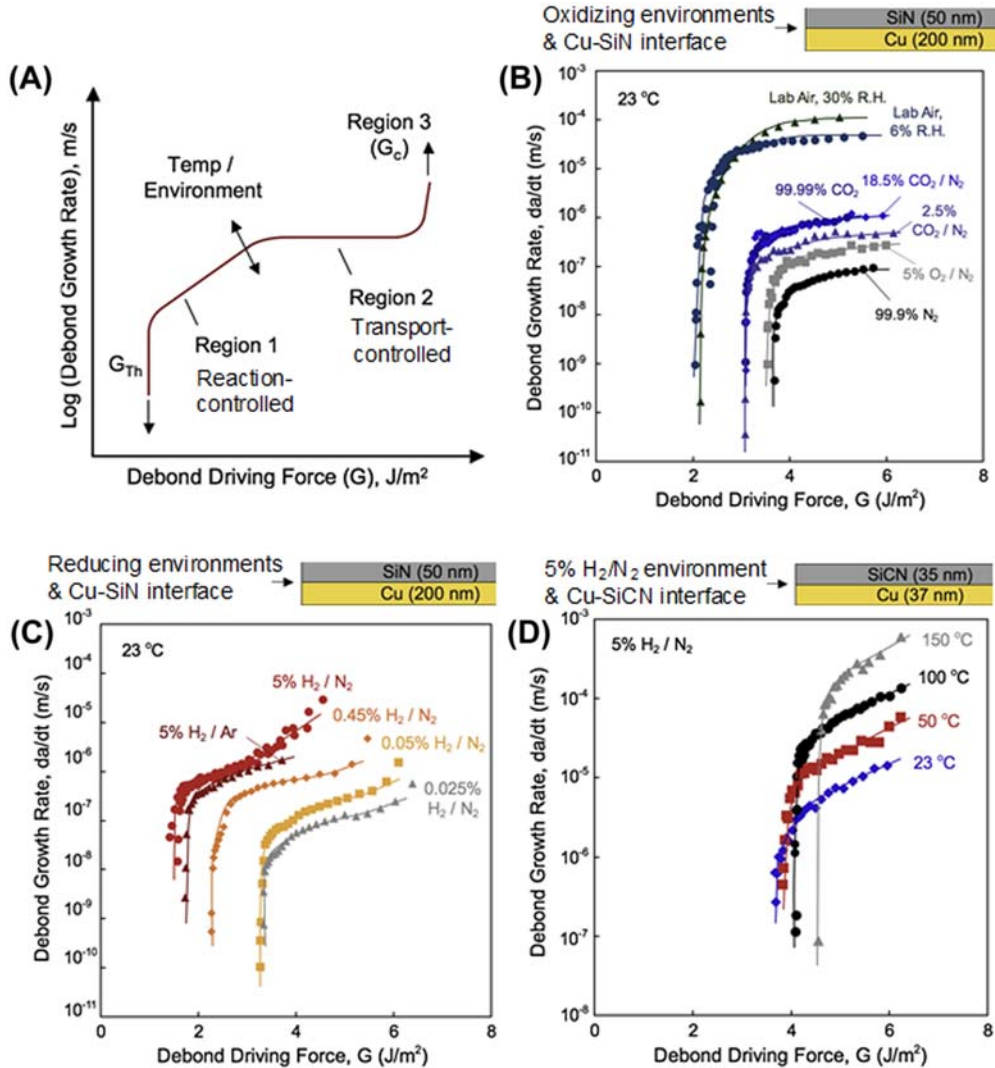


Figure 15.31 Environmentally assisted debonding of Cu-substrate interfaces. (A) A schematic of an environmentally assisted debonding curve indicating the lower bound or threshold G_{Th} , the critical interfacial fracture energy G_c , and the reaction and transport controlled regions; (B) the debond growth rate measured in oxidizing environments as a function of the applied driving force G for the Cu–SiN interface; (C) the debonding curve for the Cu–SiN interface in reducing environments; (D) the debonding curve for the Cu–SiCN interface in reducing environments at various temperatures. Adapted from Birringer, R. P., Shaviv, R., Besser, P. R. & Dauskardt, R. H. (2012). *Acta Materialia*, 60(5), 2219–2228. <https://doi.org/10.1016/j.actamat.2012.01.007>.

where ν_0 is the lattice vibration frequency, a_x is the crack advancing distance, T is the temperature, k is Boltzmann's constant, and $U_+(G)$ and $U_-(G)$ are the activation energy for kink advancement and healing. γ'_{tz} is an energy term associated with the lattice trapping range. N_B is the areal density of bonds along the metal/substrate interface, μ_{B^*} and μ_B correspond to the chemical potentials of the broken and unbroken bonds, η corresponds to the number of reactive species A associated with the bond rupture process, μ_A^S is the chemical potential of A, a_A is the activity of A. For $G = G_{th}$, cracking is arrested thus $U_+(G) = U_-(G)$ giving:

$$G_{th} = N_B(\mu_{B^*} - \mu_B - \eta\mu_A^S - \eta kT \ln(a_A)) \quad (15.6)$$

This means the threshold delamination driving force is largely in a linear relationship with $\ln(a_A)$. Fig. 15.31B–D show some measured debonding curves for the Cu–SiN and the Cu–SiCN interfaces. For the Cu–SiN interface in oxidizing environments, in general, an inverse relationship between oxygen concentration and adhesion energy exists, and the type of oxidizing species shows stronger influences in shifting the curve than differences in activity of the same species (Birringer et al., 2012; Liniger & Dziobkowski, 2006). While for the Cu–SiN and the Cu–SiCN interfaces in reducing environments, like H_2 , an acceleration of the interface debonding is observed with increasing H_2 activity, which can be captured by Eq. (15.6).

One important observation here is the presence of moisture significantly accelerates metal/substrate delamination and reduces compared with dry conditions, as shown in Fig. 15.31B. This may be related to the metal surface oxidation at the delamination front in humid oxidizing environments and implies that metal film/substrate delamination or peeling may be energetically favorable with the aid of moisture or inside of the water. This phenomenon is further observed and studied in later works (Lee et al., 2013). Fig. 15.32 shows a water-assisted peeling of thin metal films like Ni, Cu, Ag from a SiO_2/Si substrate. From molecular dynamic (MD) simulation results, the Ni– SiO_2 system potential energy is lowest with a high level of moisture, which matches well with the trend in Fig. 15.31B. It is believed that H_2O reacts at the Ni– SiO_2 interface and forms Ni–O–H and Si–O–H groups, which opens new hydrophilic surfaces and drags more H_2O species to the delamination front for crack advance (Lee et al., 2013).

15.5 Electromechanical behaviors of ultrathin metal films bonded on a substrate

Mechanical behaviors of an ultrathin metal film on a substrate are of significant importance for metal transfer printing due for many reasons, for example: (1) during transfer printing, it is inevitable that the metal films are mechanically deformed when they are

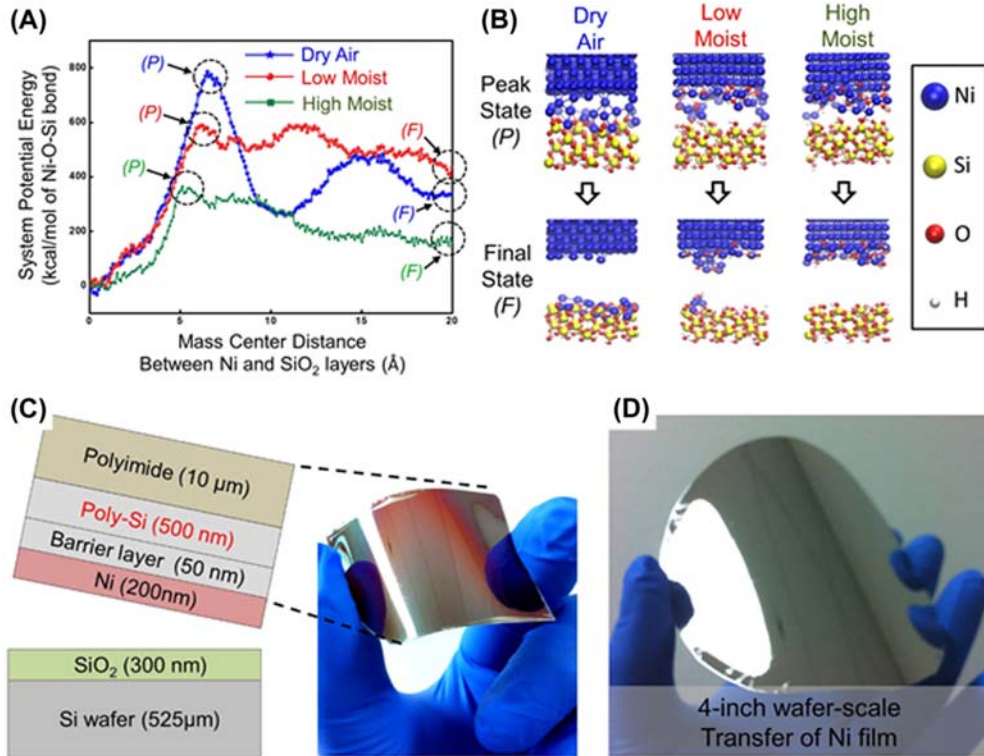


Figure 15.32 Water-assisted transfer printing of thin metal films from a SiO₂/Si wafer to various non-Si-based substrates. (A) Molecular dynamics (MD) simulation results compare the Ni–SiO₂ system potential energy as increasing the mass center distance between the Ni layer and the SiO₂ in dry-air, low-moist, and high-moist environments; (B) snapshots corresponding to the peak state (P) and final state (F) in (A); (C) poly-Si film transfer printed onto a flexible polyimide substrate, *left*: a schematic of the peel-and-stick process, *right*: an optical image of the transferred poly-Si/polyimide stack; (D) an optical image of a transfer printed Ni film from a SiO₂/Si wafer onto a flexible 4-inch plastic substrate. Adapted from Lee, C. H., Kim, J.-H., Zou, C., Cho, I. S., Weisse, J. M., Nemeth, W., Wang, Q., van Duin, A. C. T., Kim, T.-S. & Zheng, X. (2013). *Peel-and-stick: Mechanism study for efficient fabrication of flexible/transparent thin-film electronics*. *Scientific Reports*, 3(1), 2917. <https://doi.org/10.1038/srep02917>.

transferred from an elastomeric stamp to a hard substrate or from a hard stamp to a plastic substrate. It is necessary to control the thin film structure integrity and morphology; (2) after being transferred onto a substrate, especially a compliant substrate, metal film's physical properties, and functionalities become extremely sensitive to the external loads applied to the metal/substrate laminate.

Fig. 15.33 shows a typical example of deformation, especially the cracking evolution of approximately 20 nm thick Au films bonded on a PDMS substrate under different levels of uniaxial tension (Baëtens et al., 2018). What is interesting here is that

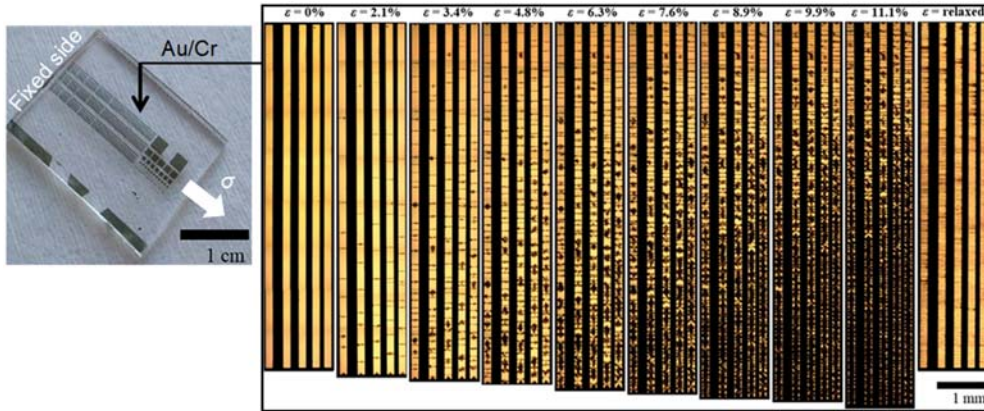


Figure 15.33 Cracking evolution in an ultrathin Au film on a PDMS substrate. Cracking evolution in an ultrathin Cr/Au (0.9 nm/21.6 nm) film bonded on a PDMS substrate upon the uniaxial strains. The image on the very right shows the sample in a relaxed state at zero strain after stretching. Adapted from Baëtens, T., Pallecchi, E., Thomy, V. & Arscott, S. (2018). Cracking effects in squashable and stretchable thin metal films on PDMS for flexible microsystems and electronics. *Scientific Reports*, 8(1), 9492. <https://doi.org/10.1038/s41598-018-27798-z>.

for a freestanding Au thin film subjected to a tensile load, the film ruptures by strain localization and forms a neck within a narrow region of a size comparable to the film thickness. The plastic zone is limited by the dimension of the film, as a result, the metal film fails at very small elongations like $<1\%$, which is far below the ultimate tensile strength of its bulk counterpart (Espinosa et al., 2003; Huang & Spaepen, 2000; Kim et al., 2013; Xiang et al., 2006; Zhang, 2019). However, for a metal film well bonded on a polymer substrate, cracking occurs at a much higher elongation, even beyond a strain of 50% (Lu et al., 2007). It has been claimed in previous extensive studies that strain localization in an ultrathin metal film can be retarded by the supporting substrate so that polymer-supported metal films can deform without rupture up to very large strains than freestanding ones (Lu et al., 2007; Li & Suo, 2006; 2007; Xiang et al., 2005).

Assuming a rectangular film upon uniaxial tensile and the film shape retains during deformation, the electrical resistance of the unstained film can be expressed as $R_0 = \rho L_0/A_0$ and the resistance of the strained film is $R = \rho L/A$, where L_0, A_0 and L, A correspond to the length and cross-sectional area of the pristine and strained films, respectively. Consequently, the normalized electrical resistance evolution of a strained metal film can be described as (Lu et al., 2007):

$$R/R_0 = \left(\frac{L}{L_0}\right)^2 \quad (15.7)$$

Eq. (15.7) looks simple but is helpful in guiding us to detect the discrepancy between the experimental measurements and this theoretically predicted deforming behavior. For example, Fig. 15.34A compares the normalized electrical resistance evolution with the normalized specimen length from previous studies (Lu et al., 2007, 2010). There are several interesting observations: remarkable deviations in the resistance–elongation curves from Eq. (15.7) for the thinner metal films' deformations on Kapton substrates. This is because of the local fracture and crack propagation in the metal films, as shown in Fig. 15.3B–E. The metal film becomes interconnected thus the resistance surges significantly, like curves for 50 and 100 nm Cu in Fig. 15.34A. Previous studies have suggested that stain localization and film/substrate debonding work together toward metal film rupture (Li & Suo, 2007; Li et al., 2004, 2005). Suppose the metal film is less well bonded on the polymer surface, in that case, strain localization can easily occur as that happens to the freestanding thin films and induces local metal/substrate delamination. Two processes facilitate each other (Lu et al., 2007). Therefore, strong metal/substrate bonding is necessary for the laminate to accommodate large deformation without fracture. This guides us to another interesting observation in Fig. 15.34A that the Cu/Cr/Kapton specimen exhibits an excellent match to Eq. (15.7) since the Cr is known as an adhesion layer to strengthen the metal/substrate interfacial energy. Fig. 15.34B and C confirm the above speculations and show an isolated short through-the-thickness crack identified for the Cu/Cr/Kapton laminate strained to 50% (Lu et al., 2007).

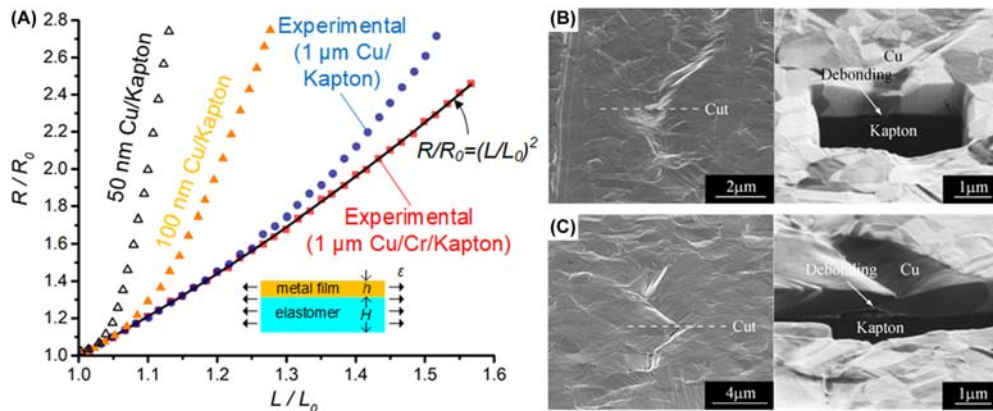


Figure 15.34 Stretching of thin Cu films on a Kapton substrate. (A) The normalized electrical resistance R/R_0 increases with the relative elongation L/L_0 of the specimen. The dots are the experimental data and the solid line is the theoretical relation of $R/R_0 = (L/L_0)^2$; (B and C) SEM images of the Cu/Cr/Kapton laminates after elongation of (B) 30% and (C) 50%, indicating simultaneous local thinning and debonding. Adapted from Lu, N., Wang, X., Suo, Z. & Vlassak, J. (2007). Applied Physics Letters, 91(22), 221909. <https://doi.org/10.1063/1.2817234>; Lu, N., Suo, Z. & Vlassak, J. J. (2010). Acta Materialia, 58(5), 1679–1687. <https://doi.org/10.1016/j.actamat.2009.11.010>.

Notably, the supporting polymer substrate's effect on the critical elongation of the metal film just discussed above applies under certain conditions. For metal films with ultrathin thickness and grain structures too small to allow abundant dislocation activity in the metal, the metal/polymer laminate shows nonuniform deformation and ruptures at tiny strains without local debonding, see 50 nm Cu/Kapton in Fig. 15.34A and corresponding SEM images in Fig. 15.3B and D (Lu et al., 2010). Taking one step further, this uniform deformation (at small strains) to nonuniform deformation (at large strains) bifurcation problem has been extensively studied (Bigoni et al., 1997; Dorris & Nemat-Nasser, 1980; Hill & Hutchinson, 1975). Consider a sinusoidal perturbation with the wavenumber of k , for the long wave limit, $kh \rightarrow 0$, the perturbation wavelength is larger compared with the metal film thickness, the uniform deformation is unstable when the strain reaches the material's hardening index (e.g., $N \sim 0.02$ for metals, $N \sim 0.5$ for polymer), see Fig. 15.35A. This is the case we discussed above, the polymer substrate significantly elevates the critical elongation of the metal well bonded on a polymer substrate. However, for the short wave limit, $kh \rightarrow \infty$, when the perturbation wavelength is much smaller than the metal film thickness, the critical elongation of the metal/polymer laminate corresponds to that of the surface mode for the freestanding metal films, as shown in Fig. 15.35B (Li et al., 2005). In this case, the polymer substrate supporting is unimportant and will not alter the brittle fracture in the metal film.

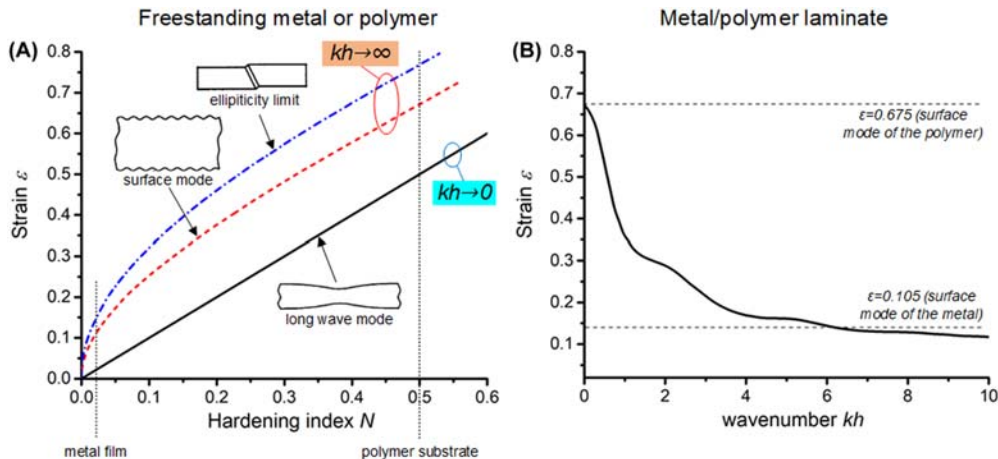


Figure 15.35 The mechanical behaviors of metal film/substrate laminate upon external uniaxial tensile stretching. (A) The stress–strain curves for a weakly hardening metal and a steeply hardening polymer; (B) three kinds of force–strain relations of a metal film/substrate laminate when deforming uniformly. Adapted from Li, T., Huang, Z. Y., Xi, Z. C., Lacour, S. P., Wagner, S. & Suo, Z. (2005). *New directions in mechanics and selected articles in micromechanics of materials*, 37(2), 261–273. <https://doi.org/10.1016/j.mechmat.2004.02.002>; Li, T. & Suo, Z. (2006). *International Journal of Solids and Structures*, 43(7), 2351–2363. <https://doi.org/10.1016/j.ijsolstr.2005.04.034>.

Although an ultrathin metal film may not fully rupture upon reasonable external stretching when it is well-bonded onto a polymer substrate, the local thinning and isolated short through-the-thickness cracks affect the metal/polymer laminate's functionalities and eventually lead to electrical failure, especially under cyclic loading. Fig. 15.36A and B (bare Au curve) depict the interconnected thin metal film on a stretchable substrate and present a typical change in resistance as a function of applied strain. For a bare Au/PDMS

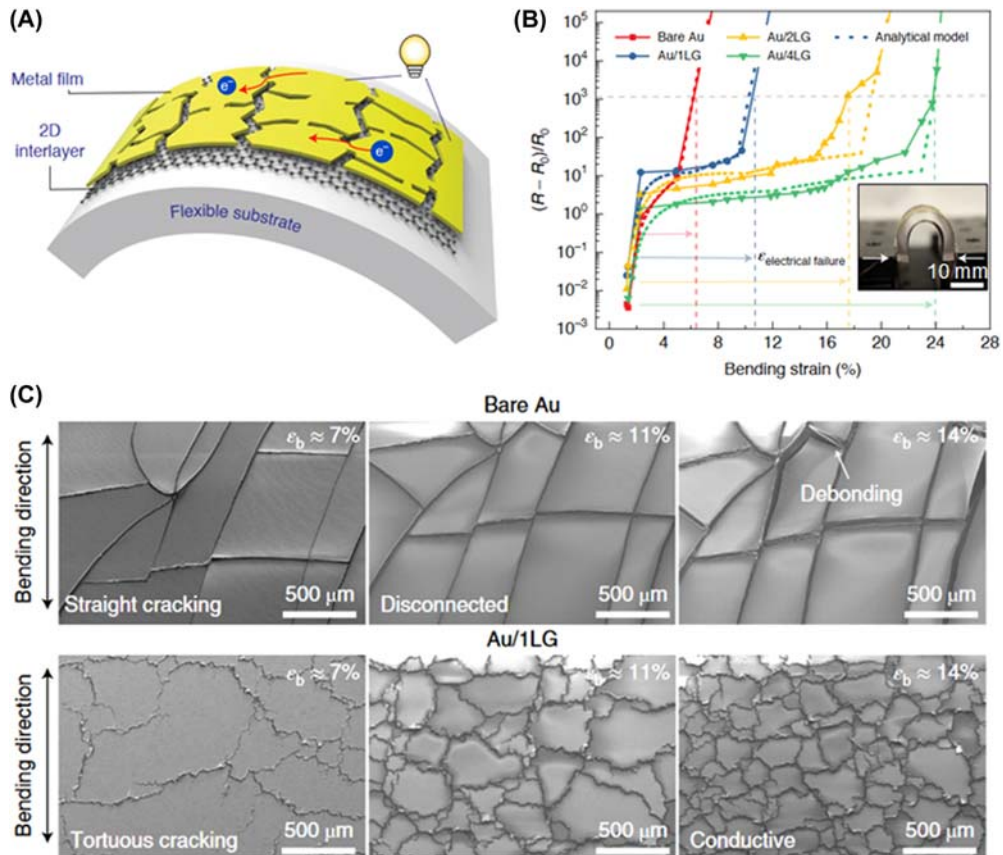


Figure 15.36 The flexible metal electrode on a compliant substrate with a two-dimensional material interlayer. (A) Schematic of a flexible metal electrode with an atomically thin two-dimensional material inserted between the metal film and the substrate; (B) electrically ductile behaviors (both experimental and analytical) of the Au/graphene/PDMS laminates in response to bending deformation. R_0 is initial electrical resistance; R is electrical resistance with bending; (C) crack progression at various bending strains in a bare Au electrode and a Au/graphene electrode. *Republished with permission from Cho, C., Kang, P., Taqieddin, A., Jing, Y., Yong, K., Kim, J. M., Haque, M. F., Aluru, N. R. & Nam, S. (2021). Strain-resilient electrical functionality in thin-film metal electrodes using two-dimensional interlayers. Nature Electronics, 4(2), 126–133. <https://doi.org/10.1038/s41928-021-00538-4>.*

laminate upon bending, it behaves like the thin Cu/Kapton cases shown in Fig. 15.34A. Alternatively, recent research found that adding another thin interlayer (e.g., atomically thin two-dimensional materials like graphene, molybdenum disulfide, or hexagonal boron nitride) between the metal film and the polymer substrate induces continuous in-plane crack deflection in the metal film, instead of the through cracks that directly cleave the film. This results in strain-resilient electrical performance of the thin metal electrodes, as shown in Fig. 15.36B and C. Compared with the bare Au/PDMS, Au/Graphene/PDMS laminates exhibit notable “resistance locking” plateaus in the resistance-strain curves, suggesting high electrical ductility upon external loading (Cho et al., 2021).

Lastly, let us check the fatigue behaviors of a metal film/polymer laminate. There have been extensive studies of polymer-supported thin metal films’ resistance to repeated stretching, bending, or twisting due to the increasing interest in flexible electronics, and also due to the difficulties in testing a freestanding ultrathin metal film’s mechanical properties (Luo et al., 2019; Schwaiger & Kraft, 2003; Sun et al., 2008; Zhang et al., 2006; Zhang et al., 2008). This section collects some useful results to analyze the failure of a metal/polymer laminate when strained repetitively. Typically, two failure modes are observed in a metal film during cyclic loading: type I: cracks through the metal thickness following extrusion (on the metal surface) and intrusion (at the metal/polymer interface) paths, as shown in Fig. 15.37A yellow circle regions,

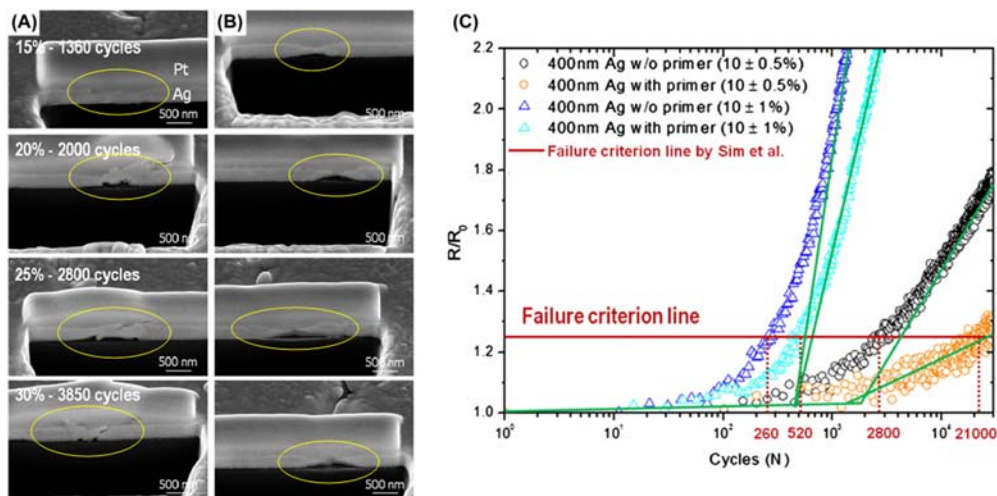


Figure 15.37 Fatigue of thin Ag film bonded on a PET substrate. (A and B) Typical cross-sectional SEM images for (A) type I failure and (B) type II failure (400 nm Au/PET tested at a total strain range of 1.0%); (C) comparison of the fatigue behaviors between the Ag/PET and Ag/acrylic-primer/PET specimens. $R/R_0 = 1.25$ is used as the failure criterion. Adapted from Sim, G.-D., Hwangbo, Y., Kim, H.-H., Lee, S.-B. & Vlassak, J. J. (2012). Viewpoint set no. 49: Strengthening effect of nano-scale twins, 66(11), 915–918. <https://doi.org/10.1016/j.scriptamat.2012.02.030>.

and type II: through-the-thickness strain location or necking, as shown in Fig. 15.37B (Sim et al., 2012, 2013). Previous research suggests that type I failure is associated with local debonding of the metal film from the substrate, see the voids at the Ag/PET interface in Fig. 15.37A. It is claimed that the shift between different fracture mechanisms depends on the metal film thickness and strain range of cyclic loading. When the cyclic strain is small, cyclic dislocation motions occur in the metal resulting in repetitive slips on individual glide planes and the consequent extrusions and intrusions, these are what happen in type I failure. What is worth noting is that intergranular cracks appear in a metal film with a thickness smaller than the plastic zone, then dimensional constraints on dislocation activity make it difficult to deform the film plastically (Meyers et al., 2006). This brittle failure mechanism is referred to as type III failure in previous studies (Sim et al., 2013). When a considerable cyclic strain is applied, more extensive dislocation activities get involved in each loading cycle. Such large plastic deformation results in the coevolution of local debonding and necking. These are what happens in type II failure. In practice, electrical resistance measurements are used to quantify the fatigue life of a metal/polymer laminate. Fig. 15.37C shows some typical fatigue test results under cyclic tension. These experimental results suggest that fatigue life increases by using the acrylic primer to improve adhesion between the metal film and the substrate (Sim et al., 2012).

References

- Aghajamali, M., Cheong, I. T., & Veinot, J. G. C. (2018). Water-assisted transfer patterning of nanomaterials. *Langmuir*, 34(32), 9418–9423. Available from <https://doi.org/10.1021/acs.langmuir.8b00694>.
- Aldakov, D., Tondelier, D., Palacin, S., & Bonnasieux, Y. (2011). Ethanol-mediated metal transfer printing on organic films. *ACS Applied Material Interfaces*, 3(3), 740–745. Available from <https://doi.org/10.1021/am101085k>.
- Allara, D. L., Parikh, A. N., & Rondelez, F. (1995). Evidence for a unique chain organization in long chain silane monolayers deposited on two widely different solid substrates. *Langmuir*, 11(7), 2357–2360. Available from <https://doi.org/10.1021/la00007a007>.
- Bae, S., Kim, H., Lee, Y., Xu, X., Park, J.-S., Zheng, Y., Balakrishnan, J., Lei, T., Kim, H. R., Song, Yo. I., Kim, Y.-J., Kim, K. S., Özyilmaz, B., Ahn, J.-H., Hong, B. H., & Iijima, S. (2010). Roll-to-roll production of 30-inch graphene films for transparent electrodes. *Nature Nanotechnology*, 5(8), 574–578. Available from <https://doi.org/10.1038/nnano.2010.132>.
- Baëtens, T., Pallecchi, E., Thomy, V., & Arscott, S. (2018). Cracking effects in squashable and stretchable thin metal films on PDMS for flexible microsystems and electronics. *Scientific Reports*, 8(1), 9492. Available from <https://doi.org/10.1038/s41598-018-27798-z>.
- Bavier, J., Cumings, J., & Hines, D. R. (2013). Transfer printing of patterned metal films using parylene C coated surfaces. *Microelectronic Engineering*, 104, 18–21. Available from <https://doi.org/10.1016/j.mee.2012.10.020>; <https://www.sciencedirect.com/science/article/pii/S0167931712005722>.
- Bhattacharyya, B. (2015). *Electrochemical micromachining for nanofabrication*. MEMS and nanotechnology. William Andrew. Available from <http://doi.org/10.1016/C2014-0-00027-5>.
- Bigoni, D., Ortiz, M., & Needleman, A. (1997). Effect of interfacial compliance on bifurcation of a layer bonded to a substrate. *International Journal of Solids and Structures*, 34(33), 4305–4326. Available from [https://doi.org/10.1016/S0020-7683\(97\)00025-5](https://doi.org/10.1016/S0020-7683(97)00025-5); <https://www.sciencedirect.com/science/article/pii/S0020768397000255>.

- Biringer, R. P., Shaviv, R., Besser, P. R., & Dauskardt, R. H. (2012). Environmentally assisted debonding of copper/barrier interfaces. *Acta Materialia*, *60*(5), 2219–2228. Available from <https://doi.org/10.1016/j.actamat.2012.01.007>; <https://www.sciencedirect.com/science/article/pii/S1359645412000341>.
- Bowden, N., Brittain, S., Evans, A. G., Hutchinson, J. W., & Whitesides, G. M. (1998). Spontaneous formation of ordered structures in thin films of metals supported on an elastomeric polymer. *Nature*, *393*(6681), 146–149. Available from <https://doi.org/10.1038/30193>.
- Boyd, E. P., Ketchum, D. R., Deng, H., & Shore, S. G. (1997). Chemical vapor deposition of metallic thin films using homonuclear and heteronuclear metal carbonyls. *Chemical Material*, *9*(5), 1154–1158. Available from <https://doi.org/10.1021/cm9605330>.
- Cai, S., Breid, D., Crosby, A. J., Suo, Z., & Hutchinson, J. W. (2011). Periodic patterns and energy states of buckled films on compliant substrates. *Journal of the Mechanics and Physics of Solids*, *59*(5), 1094–1114. Available from <https://doi.org/10.1016/j.jmps.2011.02.001>; <https://www.sciencedirect.com/science/article/pii/S0022509611000299>.
- Can-Puc, M., Schander, A., Vargas, G. M. G., & Lang, W. (2021). An assessment of surface treatments for adhesion of polyimide thin films. *Polymers*, *13*(12). Available from <https://doi.org/10.3390/polym13121955>.
- Chadwick, J. E., Myles, D. C., & Garrell, R. L. (1993). Self-assembly of sulfinate monolayers on gold: new membrane mimetics. *Journal of American Chemical Society*, *115*(22), 10364–10365. Available from <https://doi.org/10.1021/ja00075a064>.
- Cho, C., Kang, P., Taqieddin, A., Jing, Y., Yong, K., Kim, J. M., Haque, M. F., Aluru, N. R., & Nam, S. W. (2021). Strain-resilient electrical functionality in thin-film metal electrodes using two-dimensional interlayers. *Nature Electronics*, *4*(2), 126–133. Available from <https://doi.org/10.1038/s41928-021-00538-4>.
- Delamarche, E., Michel, B., Biebuyck, H. A., & Gerber, C. (1996). Golden interfaces: The surface of self-assembled monolayers. *Advanced Materials*, *8*(9), 719–729. Available from <https://doi.org/10.1002/adma.19960080903>.
- Dorris, J. F., & Nemat-Nasser, S. (1980). Instability of a layer on a half space. *Journal of Applied Mechanics*, *47*(2), 304–312. Available from <https://doi.org/10.1115/1.3153660>.
- Duffy, D. C., McDonald, J. C., Schueller, O. J. A., & Whitesides, G. M. (1998). Rapid prototyping of microfluidic systems in poly(dimethylsiloxane). *Analytical Chemistry*, *70*(23), 4974–4984. Available from <https://doi.org/10.1021/ac980656z>.
- Espinosa, H. D., Prorok, B. C., & Fischer, M. (2003). A methodology for determining mechanical properties of freestanding thin films and MEMS materials. *Journal of the Mechanics and Physics of Solids*, *51*(1), 47–67. Available from [https://doi.org/10.1016/S0022-5096\(02\)00062-5](https://doi.org/10.1016/S0022-5096(02)00062-5); <https://www.sciencedirect.com/science/article/pii/S0022509602000625>.
- Fenter, P., Eisenberger, P., Li, J., Camillone, N. I. I., Bernasek, S., Scoles, G., Ramanarayanan, T. A., & Liang, K. S. (1991). Structure of octadecyl thiol self-assembled on the silver(111) surface: An incommensurate monolayer. *Langmuir*, *7*(10), 2013–2016. Available from <https://doi.org/10.1021/la00058a008>.
- Freund, L. B., & Suresh, S. (2004). *Thin film materials: Stress, defect formation and surface evolution*. Cambridge: Cambridge University Press. Available from <https://www.cambridge.org/core/books/thin-film-materials/9DC3055061A07C92A6A9D83CBF804029>; <http://doi.org/10.1017/CBO9780511754715>.
- Gilding, 2023 1 26 <https://en.wikipedia.org/wiki/Gilding>.
- Gamota, D. R., Brazis, P., Kalyanasundaram, K., & Zhang, J. (2004). *Printed organic and molecular electronics* (1st). Springer.
- Goswami, D., Munera, J. C., Pal, A., Sadri, B., Scarpetti, C. L. P. G., & Martinez, Ra. V. (2018). Roll-to-roll nanofarming of metals using laser-induced superplasticity. *Nano Letters*, *18*(6), 3616–3622. Available from <https://doi.org/10.1021/acs.nanolett.8b00714>.
- Griffith, A. A. (1921). The phenomena of rupture and flow in solids. *Philosophical Transactions of the Royal Society of London. Series A, Containing Papers of a Mathematical or Physical Character*, *221*, 163–198. Available from <http://www.jstor.org/stable/91192>.
- Grosse, A. A. V. (1964). The relationship between surface tension and energy of liquid metals and their heat of vaporization at the melting point. *Journal of Inorganic and Nuclear Chemistry*, *26*(8), 1349–1361.

- Available from [https://doi.org/10.1016/0022-1902\(64\)80114-7](https://doi.org/10.1016/0022-1902(64)80114-7); <https://www.sciencedirect.com/science/article/pii/S0022190264801147>.
- Hampden-Smith, M. J., & Kodas, T. T. (1995). Chemical vapor deposition of metals: Part 1. An overview of CVD processes. *Chemical Vapor Deposition.*, 1(1), 8–23. Available from <https://doi.org/10.1002/cvde.19950010103>.
- Han, M., Chen, L., Aras, K., Liang, C., Chen, X., Zhao, H., Li, K., Faye, N. R., Sun, B., Kim, J.-H., Bai, W., Yang, Q., Ma, Y., Lu, W., Song, E., Baek, J. M., Lee, Y., Liu, C., Model, J. B., ... Rogers, J. A. (2020). Catheter-integrated soft multilayer electronic arrays for multiplexed sensing and actuation during cardiac surgery. *Nature Biomedical Engineering*, 4(10), 997–1009. Available from <https://doi.org/10.1038/s41551-020-00604-w>.
- Hickman, J. J., Laibinis, P. E., Auerbach, D. I., Zou, C., Gardner, T. J., Whitesides, G. M., & Wrighton, Mark S. (1992). Toward orthogonal self-assembly of redox active molecules on platinum and gold: selective reaction of disulfide with gold and isocyanide with platinum. *Langmuir*, 8(2), 357–359. Available from <https://doi.org/10.1021/la00038a005>.
- Hill, R., & Hutchinson, J. W. (1975). Bifurcation phenomena in the plane tension test. *Journal of the Mechanics and Physics of Solids*, 23(4), 239–264. Available from [https://doi.org/10.1016/0022-5096\(75\)90027-7](https://doi.org/10.1016/0022-5096(75)90027-7); <https://www.sciencedirect.com/science/article/pii/S0022509675900277>.
- Hong, J.-Y., Shin, Y. C., Zubair, A., Mao, Y., Palacios, T., Dresselhaus, M. S., Kim, S. H., & Kong, J. (2016). A rational strategy for graphene transfer on substrates with rough features. *Advanced Materials*, 28(12), 2382–2392. Available from <https://doi.org/10.1002/adma.201505527>.
- Huang, H., & Spaepen, F. (2000). Tensile testing of free-standing Cu, Ag and Al thin films and Ag/Cu multilayers. *Acta Materialia*, 48(12), 3261–3269. Available from [https://doi.org/10.1016/S1359-6454\(00\)00128-2](https://doi.org/10.1016/S1359-6454(00)00128-2); <https://www.sciencedirect.com/science/article/pii/S1359645400001282>.
- Hur, S.-H., Khang, D.-Y., Kocabas, C., & Rogers, J. A. (2004). Nanotransfer printing by use of noncovalent surface forces: Applications to thin-film transistors that use single-walled carbon nanotube networks and semiconducting polymers. *Applied Physics Letters*, 85(23), 5730–5732. Available from <https://doi.org/10.1063/1.1829774>.
- Hutchinson, J. W., & Evans, A. G. (2000). Mechanics of materials: top-down approaches to fracture. *Acta Materialia*, 48(1), 125–135. Available from [https://doi.org/10.1016/S1359-6454\(99\)00291-8](https://doi.org/10.1016/S1359-6454(99)00291-8); <https://www.sciencedirect.com/science/article/pii/S1359645499002918>.
- Irwin, G. R. (1957). Analysis of stresses and strains near the end of a crack traversing a plate. *Journal of Applied Mechanics*, 24(3), 361–364. Available from <https://doi.org/10.1115/1.4011547>.
- Jackman, R. J., Wilbur, J. L., & Whitesides, G. M. (1995). Fabrication of submicrometer features on curved substrates by microcontact printing. *Science*, 269(5224), 664–666. Available from <https://doi.org/10.1126/science.7624795>.
- Jung, E., Kim, C., Kim, M., Chae, H., Cho, J. H., & Cho, S. M. (2017). Roll-to-roll preparation of silver-nanowire transparent electrode and its application to large-area organic light-emitting diodes. *Organic Electronics*, 41, 190–197. Available from <https://doi.org/10.1016/j.orgel.2016.11.003>; <https://www.sciencedirect.com/science/article/pii/S1566119916304761>.
- Khan, S., Lorenzelli, L., & Dahiya, R. S. (2015). Technologies for printing sensors and electronics over large flexible substrates: A review. *IEEE Sensors Journal*, 15(6), 3164–3185. Available from <https://doi.org/10.1109/JSEN.2014.2375203>.
- Kim, D.-H., Lu, N., Ghaffari, R., Kim, Y.-S., Lee, S. P., Xu, L., Wu, J., Kim, R.-H., Song, J., Liu, Z., Viventi, J., de Graff, B., Elolampi, B., Mansour, M., Slepian, M. J., Hwang, S., Moss, J. D., Won, S.-M., Huang, Y., ... Rogers, J. A. (2011). Materials for multifunctional balloon catheters with capabilities in cardiac electrophysiological mapping and ablation therapy. *Nature Materials*, 10(4), 316–323. Available from <https://doi.org/10.1038/nmat2971>.
- Kim, J.-H., Nizami, A., Hwangbo, Y., Jang, B., Lee, H.-J., Woo, C.-S., Hyun, S., & Kim, T.-S. (2013). Tensile testing of ultra-thin films on water surface. *Nature Communications*, 4(1), 2520. Available from <https://doi.org/10.1038/ncomms3520>.
- Kim, S., Sojoudi, H., Zhao, H., Mariappan, D., McKinley, G. H., Gleason, K. K., & Hart, A. J. (2016). Ultrathin high-resolution flexographic printing using nanoporous stamps. *Science Advances*, 2(12), e1601660. Available from <https://doi.org/10.1126/sciadv.1601660>.

- Kim, Y. Y., Yang, T.-Y., Suhonen, R., Kemppainen, A., Hwang, K., Jeon, N. J., & Seo, J. (2020). Roll-to-roll gravure-printed flexible perovskite solar cells using eco-friendly antisolvent bathing with wide processing window. *Nature Communications*, *11*(1), 5146. Available from <https://doi.org/10.1038/s41467-020-18940-5>.
- Kinloch, A. J. (1980). The science of adhesion. *Journal of Materials Science*, *15*(9), 2141–2166. Available from <https://doi.org/10.1007/BF00552302>.
- Ko, H. C., Stoykovich, M. P., Song, J., Malyarchuk, V., Choi, W. M., Yu, C.-J., Geddes, J. B., III, Xiao, J., Wang, S., Huang, Y., & Rogers, J. A. (2008). A hemispherical electronic eye camera based on compressible silicon optoelectronics. *Nature*, *454*(7205), 748–753. Available from <https://doi.org/10.1038/nature07113>.
- Kobayashi, T., Bando, M., Kimura, N., Shimizu, K., Kadono, K., Umezu, N., Miyahara, K., Hayazaki, S., Nagai, S., Mizuguchi, Y., Murakami, Y., & Hobara, D. (2013). Production of a 100-m-long high-quality graphene transparent conductive film by roll-to-roll chemical vapor deposition and transfer process. *Applied Physics Letters*, *102*(2), 023112. Available from <https://doi.org/10.1063/1.4776707>.
- Kumar, A., & Whitesides, G. M. (1993). Features of gold having micrometer to centimeter dimensions can be formed through a combination of stamping with an elastomeric stamp and an alkanethiol “ink” followed by chemical etching. *Applied Physic Letters*, *63*(14), 2002–2004. Available from <https://doi.org/10.1063/1.110628>.
- Lane, M. W., Snodgrass, J. M., & Dauskardt, R. H. (2001). Environmental effects on interfacial adhesion. *Microelectronics Reliability*, *41*(9), 1615–1624. Available from [https://doi.org/10.1016/S0026-2714\(01\)00150-0](https://doi.org/10.1016/S0026-2714(01)00150-0); <https://www.sciencedirect.com/science/article/pii/S0026271401001500>.
- Lawn, B. (1993). *Fracture of brittle solids Cambridge solid state science series* (2). Cambridge: Cambridge University Press. Available from <https://www.cambridge.org/core/books/fracture-of-brittle-solids/B1EC1413BDBA1DCF49E1665D4B0A20F3>; <http://doi.org/10.1017/CBO9780511623127>.
- Lawn, B. R. (1975). An atomistic model of kinetic crack growth in brittle solids. *Journal of Materials Science*, *10*(3), 469–480. Available from <https://doi.org/10.1007/BF00543692>.
- Lee, B. H., Cho, Y. H., Lee, H., Lee, K.-D., Kim, S. H., & Sung, M. M. (2007). High-resolution patterning of aluminum thin films with a water-mediated transfer process. *Advanced Materials*, *19*(13), 1714–1718. Available from <https://doi.org/10.1002/adma.200601884>.
- Lee, C. H., Kim, J.-H., Zou, C., Cho, I. S., Weisse, J. M., Nemeth, W., Wang, Q., van Duin, A. C. T., Kim, T.-S., & Zheng, X. (2013). Peel-and-stick: Mechanism study for efficient fabrication of flexible/transparent thin-film electronics. *Scientific Reports*, *3*(1), 2917. Available from <https://doi.org/10.1038/srep02917>.
- Lee, T. R., Laibinis, P. E., Folkers, J. P., & Whitesides, G. M. (1991). Heterogeneous catalysis on platinum and self-assembled monolayers on metal and metal oxide surfaces. Available from: <https://doi.org/10.1351/pac199163060821>.
- Li, P., Zhang, Y., & Zheng, Z. (2019). Polymer-assisted metal deposition (PAMD) for flexible and wearable electronics: Principle, Materials, printing, and devices. *Advanced Materials*, *31*, 1902987. Available from <https://doi.org/10.1002/adma.201902987>.
- Li, T., Huang, Z., Suo, Z., Lacour, S. P., & Wagner, S. (2004). Stretchability of thin metal films on elastomer substrates. *Applied Physics Letters*, *85*(16), 3435–3437. Available from <https://doi.org/10.1063/1.1806275>.
- Li, T., Huang, Z. Y., Xi, Z. C., Lacour, S. P., Wagner, S., & Suo, Z. (2005). Delocalizing strain in a thin metal film on a polymer substrate. *New Directions in Mechanics and Selected Articles in Micromechanics of Materials*, *37*(2), 261–273. Available from <https://doi.org/10.1016/j.mechmat.2004.02.002>; <https://www.sciencedirect.com/science/article/pii/S0167663604000821>.
- Li, T., & Suo, Z. (2006). Deformability of thin metal films on elastomer substrates. *International Journal of Solids and Structures*, *43*(7), 2351–2363. Available from <https://doi.org/10.1016/j.ijsolstr.2005.04.034>; <https://www.sciencedirect.com/science/article/pii/S0020768305002064>.
- Li, T., & Suo, Z. (2007). Ductility of thin metal films on polymer substrates modulated by interfacial adhesion. *Physics and Mechanics of Advanced Materials*, *44*(6), 1696–1705. Available from <https://doi.org/10.1016/j.ijsolstr.2006.07.022>; <https://www.sciencedirect.com/science/article/pii/S0020768306002964>.

- Li, W., Li, L., Sun, Q., Liu, X., Kanehara, M., Nakayama, T., Jiu, J., Sakamoto, K., & Minari, T. (2021). Direct fabrication of high-resolution and high-performance flexible electronics via surface-activation-localized electroless plating. *Chemical Engineering Journal*, 416(15), 127644. Available from <https://doi.org/10.1016/j.cej.2020.127644>.
- Lin, S., Bai, X., Wang, H., Wang, H., Song, J., Huang, K., Wang, C., Wang, N., Li, B., Lei, M., & Wu, H. (2017). Roll-to-roll production of transparent silver-nanofiber-network electrodes for flexible electrochromic smart windows. *Advanced Materials*, 29(41), 1703238. Available from <https://doi.org/10.1002/adma.201703238>.
- Linford, M. R., Fenter, P., Eisenberger, P. M., & Chidsey, C. E. D. (1995). Alkyl monolayers on silicon prepared from 1-alkenes and hydrogen-terminated silicon. *Journal of American Chemical Society*, 117(11), 3145–3155. Available from <https://doi.org/10.1021/ja00116a019>.
- Linghu, C., Zhang, S., Wang, C., & Song, J. (2018). Transfer printing techniques for flexible and stretchable inorganic electronics. *NPJ Flexible Electronics*, 2(1), 26. Available from <https://doi.org/10.1038/s41528-018-0037-x>.
- Liniger, E. G., & Dziobkowski, C. (2006). Effect of oxygen at the Cu–SiC_xN_y interface on electromigration performance of interconnect structures. *Thin Solid Films*, 513(1), 295–299. Available from <https://doi.org/10.1016/j.tsf.2006.01.075>; <https://www.sciencedirect.com/science/article/pii/S0040609006002793>.
- Loo, Y.-L., Willett, R. L., Baldwin, K. W., & Rogers, J. A. (2002). Interfacial chemistries for nanoscale transfer printing. *Journal of American Chemical Society*, 124(26), 7654–7655. Available from <https://doi.org/10.1021/ja026355v>.
- Lu, N., Suo, Z., & Vlassak, J. J. (2010). The effect of film thickness on the failure strain of polymer-supported metal films. *Acta Materialia*, 58(5), 1679–1687. Available from <https://doi.org/10.1016/j.actamat.2009.11.010>; <https://www.sciencedirect.com/science/article/pii/S135964540900785X>.
- Lu, N., Wang, X., Suo, Z., & Vlassak, J. (2007). Metal films on polymer substrates stretched beyond 50%. *Applied Physics Letters*, 91(22), 221909. Available from <https://doi.org/10.1063/1.2817234>.
- Luo, X. M., Zhang, B., & Zhang, G. P. (2019). Fatigue of metals at nanoscale: Metal thin films and conductive interconnects for flexible device application. *Nano Materials Science*, 1(3), 198–207. Available from <https://doi.org/10.1016/j.nanoms.2019.02.003>; <https://www.sciencedirect.com/science/article/pii/S2589965119300030>.
- Madou, M. J. (2012). *Fundamentals of microfabrication and nanotechnology*. Taylor & Francis. Available from <http://doi.org/10.1201/9781315274164>.
- McNerny, D. Q., Viswanath, B., Copic, D., Laye, F. R., Prohoda, C., Brieland-Shoultz, A. C., Polsen, E. S., Dee, N. T., Veerasamy, V. S., & Hart, A. J. (2014). Direct fabrication of graphene on SiO₂ enabled by thin film stress engineering. *Scientific Reports*, 4(1), 5049. Available from <https://doi.org/10.1038/srep05049>.
- Menard, E., Bilhaut, L., Zaumseil, J., & Rogers, J. A. (2004). Improved surface chemistries, thin film deposition techniques, and stamp designs for nanotransfer printing. *Langmuir*, 20(16), 6871–6878. Available from <https://doi.org/10.1021/la048827k>.
- Meyers, M. A., & Chawla, K. K. (2008). *Mechanical behavior of materials* (2). Cambridge: Cambridge University Press. Available from <https://www.cambridge.org/core/books/mechanical-behavior-of-materials/48AD6E15E989D76D5DAF9926123137CF>; <http://doi.org/10.1017/CBO9780511810947>.
- Meyers, M. A., Mishra, A., & Benson, D. J. (2006). Mechanical properties of nanocrystalline materials. *Progress in Materials Science*, 51(4), 427–556. Available from <https://doi.org/10.1016/j.pmatsci.2005.08.003>; <https://www.sciencedirect.com/science/article/pii/S0079642505000447>.
- Montbach, E., & Davis, D. (2018). *Roll-to-roll manufacturing of flexible displays roll-to-roll manufacturing*, 285–323. Available from <https://doi.org/10.1002/9781119163824.ch10>.
- Oddy, W. A. (1991). Gilding: An outline of the technological history of the plating of gold on to silver or copper in the Old World. *A Modern Approach to the Protection of the Environment*, 15(1), 29–33. Available from [https://doi.org/10.1016/0160-9327\(91\)90085-P](https://doi.org/10.1016/0160-9327(91)90085-P); <https://www.sciencedirect.com/science/article/pii/016093279190085P>.
- Oh, K., Lee, B. H., Hwang, J. K., Lee, H., Im, S., & Sung, M. M. (2009). Water-mediated Al metal transfer printing with contact inking for fabrication of thin-film transistors. *Small*, 5(5), 558–561. Available from <https://doi.org/10.1002/smll.200801108>.

- Orowan, E. (1944). The fatigue of glass under stress. *Nature*, 154(3906), 341–343. Available from <https://doi.org/10.1038/154341a0>.
- Park, H., Cho, H., Kim, J., Bang, J. W., Seo, S., Rahmawan, Y., Lee, D. Y., & Suh, K.-Y. (2014). Multiscale transfer printing into recessed microwells and on curved surfaces via hierarchical perfluoropolyether stamps. *Small*, 10, 52–59. Available from <https://doi.org/10.1002/sml.201300772>.
- Park, T. W., Byun, M., Jung, H., Lee, G. R., Park, J. H., Jang, H.-I., Lee, J. W., Kwon, S. H., Hong, S., Lee, J.-H., Jung, Y. S., Kim, K. H., & Park, W. I. (2020). Thermally assisted nanotransfer printing with sub–20-nm resolution and 8-inch wafer scalability. *Science Advances*, 6(31), eabb6462. Available from <https://doi.org/10.1126/sciadv.abb6462>.
- Polson, E. S., McNerny, D. Q., Viswanath, B., Pattinson, S. W., & Hart, A. J. (2015). High-speed roll-to-roll manufacturing of graphene using a concentric tube CVD reactor. *Scientific Reports*, 5(1), 10257. Available from <https://doi.org/10.1038/srep10257>.
- Rogers, J. A., & Nuzzo, R. G. (2005). Recent progress in soft lithography. *Materials Today*, 8(2), 50–56. Available from [https://doi.org/10.1016/S1369-7021\(05\)00702-9](https://doi.org/10.1016/S1369-7021(05)00702-9); <https://www.sciencedirect.com/science/article/pii/S1369702105007029>.
- Rogers, J. A. (2001). Rubber stamping for plastic electronics and fiber optics. *MRS Bulletin*, 26(7), 530–534. Available from <https://doi.org/10.1557/mrs2001.125>; <https://www.cambridge.org/core/article/rubber-stamping-for-plastic-electronics-and-fiber-optics/BBBDD6676E492CDE5F43BAE2C1DBD13D>.
- Roll-to-roll processing 2023 1 30 https://en.wikipedia.org/wiki/Roll-to-roll_processing.
- Ryspayeva, A., Jones, T. D. A., Esfahani, M. N., Shuttleworth, M. P., Harris, R. A., Kay, R. W., Desmulliez, M. P. Y., & Marques-Hueso, J. (2019). A rapid technique for the direct metallization of PDMS substrates for flexible and stretchable electronics applications. *Microelectronic Engineering*, 209, 35–40. Available from <https://doi.org/10.1016/j.mee.2019.03.001>; <https://www.sciencedirect.com/science/article/pii/S0167931719300462>.
- Sahasrabudhe, A., Dixit, H., Majee, R., & Bhattacharyya, S. (2018). Value added transformation of ubiquitous substrates into highly efficient and flexible electrodes for water splitting. *Nature Communications*, 9, 2014. Available from <https://doi.org/10.1038/s41467-018-04358-7>.
- Saravanan, P., Satyanarayana, N., & Sinha, S. K. (2014). SU-8 composite based “lube-tape” for a wide range of tribological applications. *Micromachines*, 5(2), 263–274. Available from <https://doi.org/10.3390/mi5020263>.
- Schlenoff, J. B., Li, M., & Ly, H. (1995). Stability and self-exchange in alkanethiol monolayers. *Journal of American Chemical Society*, 117(50), 12528–12536. Available from <https://doi.org/10.1021/ja00155a016>.
- Schneider, G. F., Calado, V. E., Zandbergen, H., Vandersypen, L. M. K., & Dekker, C. (2010). Wedging transfer of nanostructures. *Nano Letters*, 10(5), 1912–1916. Available from <https://doi.org/10.1021/nl1008037>.
- Schwaiger, R., & Kraft, O. (2003). Size effects in the fatigue behavior of thin Ag films. *Acta Materialia*, 51(1), 195–206. Available from [https://doi.org/10.1016/S1359-6454\(02\)00391-9](https://doi.org/10.1016/S1359-6454(02)00391-9); <https://www.sciencedirect.com/science/article/pii/S1359645402003919>.
- Sheen, C. W., Shi, J. X., Maartensson, J., Parikh, A. N., & Allara, D. L. (1992). A new class of organized self-assembled monolayers: Alkane thiols on gallium arsenide(100). *Journal of American Chemical Society*, 114(4), 1514–1515. Available from <https://doi.org/10.1021/ja00030a076>.
- Sim, G.-D., Hwangbo, Y., Kim, H.-H., Lee, S.-B., & Vlassak, J. J. (2012). Fatigue of polymer-supported Ag thin films. *Viewpoint set no. 49: Strengthening effect of nano-scale twins*, 66(11), 915–918. Available from <https://doi.org/10.1016/j.scriptamat.2012.02.030>; <https://www.sciencedirect.com/science/article/pii/S1359646212001327>.
- Sim, G.-D., Lee, Y.-S., Lee, S.-B., & Vlassak, J. J. (2013). Effects of stretching and cycling on the fatigue behavior of polymer-supported Ag thin films. *Materials Science and Engineering: A*, 575, 86–93. Available from <https://doi.org/10.1016/j.msea.2013.03.043>; <https://www.sciencedirect.com/science/article/pii/S0921509313003134>.
- Song, J., Kam, F.-Y., Png, R.-Q., Seah, W. L., Zhuo, J.-M., Lim, G.-K., Ho, P. K. H., & Chua, L.-L. (2013). A general method for transferring graphene onto soft surfaces. *Nature Nanotechnology*, 8(5), 356–362. Available from <https://doi.org/10.1038/nnano.2013.63>.

- Song, K., Lee, J., Choi, S.-O., & Kim, J. (2019). Interaction of surface energy components between solid and liquid on wettability, and its application to textile anti-wetting finish. *Polymers*, 11(3). Available from <https://doi.org/10.3390/polym11030498>.
- Stuart, B. W., Tao, X., Gregory, D., & Assender, H. E. (2020). Roll-to-roll patterning of Al/Cu/Ag electrodes on flexible poly(ethylene terephthalate) by oil masking: a comparison of thermal evaporation and magnetron sputtering. *Applied Surface Science*, 505, 144294. Available from <https://doi.org/10.1016/j.apsusc.2019.144294>; <https://www.sciencedirect.com/science/article/pii/S0169433219331101>.
- Suk, J. W., Kitt, A., Magnuson, C. W., Hao, Y., Ahmed, S., An, J., Swan, A. K., Goldberg, B. B., & Ruoff, R. S. (2011). Transfer of CVD-grown monolayer graphene onto arbitrary substrates. *ACS Nano*, 5(9), 6916–6924. Available from <https://doi.org/10.1021/nn201207c>.
- Sun, X. J., Wang, C. C., Zhang, J., Liu, G., Zhang, G. J., Ding, X. D., Zhang, G. P., & Sun, J. (2008). Thickness dependent fatigue life at microcrack nucleation for metal thin films on flexible substrates. *Journal of Physics D: Applied Physics*, 41(19), 195404. Available from <https://doi.org/10.1088/0022-3727/41/19/195404>.
- Takakuwa, M., Fukuda, K., Yokota, T., Inoue, D., Hashizume, D., Umezue, S., & Someya, T. (2021). Direct gold bonding for flexible integrated electronics. *Science Advances*, 7(52), eabl6228. Available from <https://doi.org/10.1126/sciadv.abl6228>.
- Tan, S. H., Nguyen, N.-T., Chua, Y. C., & Kang, T. G. (2010). Oxygen plasma treatment for reducing hydrophobicity of a sealed polydimethylsiloxane microchannel. *Biomicrofluidics*, 4(3), 032204. Available from <https://doi.org/10.1063/1.3466882>.
- Tao, Y. T., Lee, M. T., & Chang, S. C. (1993). Effect of biphenyl and naphthyl groups on the structure of self-assembled monolayers: packing, orientation, and wetting properties. *Journal of American Chemical Society*, 115(21), 9547–9555. Available from <https://doi.org/10.1021/ja00074a020>.
- Thomsen, E. G., & Thomsen, H. H. (1978). Hammer forging of thin sections in antiquity. *Journal of Applied Metalworking*, 1(1), 50–58. Available from <https://doi.org/10.1007/BF02833959>.
- Ulman, A. (1991). *An introduction to ultrathin organic films from Langmuir–Blodgett to self-assembly*. Academic Press. Available from <http://doi.org/10.1016/C2009-0-22306-3>.
- Uvdal, K., Persson, I., & Liedberg, B. (1995). Tricyclohexylphosphine adsorbed on gold. *Langmuir*, 11(4), 1252–1256. Available from <https://doi.org/10.1021/la00004a034>.
- Vitos, L., Ruban, A. V., Skriver, H. L., & Kollár, J. (1998). The surface energy of metals. *Surface Science*, 411(1), 186–202. Available from [https://doi.org/10.1016/S0039-6028\(98\)00363-X](https://doi.org/10.1016/S0039-6028(98)00363-X); <https://www.sciencedirect.com/science/article/pii/S003960289800363X>.
- Wirth, M. J., Fairbank, R. W., & Fatunmbi, H. O. (1997). Mixed self-assembled monolayers in chemical separations. *Science*, 275(5296), 44–47. Available from <https://doi.org/10.1126/science.275.5296.44>.
- Xia, Y., & Whitesides, G. M. (1998). Soft lithography. *Annual Review of Material Science*, 28(1), 153–184. Available from <https://doi.org/10.1146/annurev.matsci.28.1.153>.
- Xiang, Y., Li, T., Suo, Z., & Vlassak, J. J. (2005). High ductility of a metal film adherent on a polymer substrate. *Applied Physics Letters*, 87(16), 161910. Available from <https://doi.org/10.1063/1.2108110>.
- Xiang, Y., Tsui, T. Y., & Vlassak, J. J. (2006). The mechanical properties of freestanding electroplated Cu thin films. *Journal of Materials Research*, 21(6), 1607–1618. Available from <https://doi.org/10.1557/jmr.2006.0195>.
- Xiao, L., Zhu, C., Xiong, W., Huang, Y. A., & Yin, Z. (2018). The conformal design of an island-bridge structure on a non-developable surface for stretchable electronics. *Micromachines*, 9(8). Available from <https://doi.org/10.3390/mi9080392>.
- Yu, H.-H., He, M. Y., & Hutchinson, J. W. (2001). Edge effects in thin film delamination. *Acta Materialia*, 49(1), 93–107. Available from [https://doi.org/10.1016/S1359-6454\(00\)00293-7](https://doi.org/10.1016/S1359-6454(00)00293-7); <https://www.sciencedirect.com/science/article/pii/S1359645400002937>.
- Yu, H.-h., & Hutchinson, J. W. (2003). Delamination of thin film strips. *Thin Solid Films*, 423(1), 54–63. Available from [https://doi.org/10.1016/S0040-6090\(02\)00973-2](https://doi.org/10.1016/S0040-6090(02)00973-2).
- Yu, S., Ni, Y., He, L., & Ye, Q.-L. (2015). Tunable formation of ordered wrinkles in metal films with controlled thickness gradients deposited on soft elastic substrates. *ACS Applied Material Interfaces*, 7(9), 5160–5167. Available from <https://doi.org/10.1021/am507450x>.

- Yu, S., Sun, Y., Ni, Y., Zhang, X., & Zhou, H. (2016). Controlled formation of surface patterns in metal films deposited on elasticity-gradient PDMS substrates. *ACS Applied Material Interfaces*, 8(8), 5706–5714. Available from <https://doi.org/10.1021/acsami.5b12369>.
- Zabow, G. (2022). Reflow transfer for conformal three-dimensional microprinting. *Science*, 378(6622), 894–898. Available from <https://doi.org/10.1126/science.add7023>.
- Zaumseil, J., Meidl, M. A., Hsu, J. W. P., Acharya, B. R., Baldwin, K. W., Loo, Y.-L., & Rogers, J. A. (2003). Three-dimensional and multilayer nanostructures formed by nanotransfer printing. *Nano Letters*, 3(9), 1223–1227. Available from <https://doi.org/10.1021/nl0344007>.
- Zhang, G. P., Sun, K. H., Zhang, B., Gong, J., Sun, C., & Wang, Z. G. (2008). Tensile and fatigue strength of ultrathin copper films. *14th international conference on the strength of materials*, 483–484, 387–390. Available from <https://doi.org/10.1016/j.msea.2007.02.132>; <https://www.sciencedirect.com/science/article/pii/S0921509307008192>.
- Zhang, G. P., Volkert, C. A., Schwaiger, R., Wellner, P., Arzt, E., & Kraft, O. (2006). Length-scale-controlled fatigue mechanisms in thin copper films. *Acta Materialia*, 54(11), 3127–3139. Available from <https://doi.org/10.1016/j.actamat.2006.03.013>; <https://www.sciencedirect.com/science/article/pii/S1359645406002023>.
- Zhang, K. (2019). Strengthening of metals using a graphene monolayer. Ph.D. thesis. Available from: <https://hdl.handle.net/2142/105683>.
- Zhang, K., Androulidakis, C., Chen, M., & Tawfick, S. (2018). Gilding with graphene: Rapid chemical vapor deposition synthesis of graphene on thin metal leaves. *Advanced Functional Materials*, 28(48), 1804068. Available from <https://doi.org/10.1002/adfm.201804068>.
- Zhang, K., & John, H. A. (2022). Interfacial chemical vapor deposition of wrinkle-free bilayer graphene on dielectric substrates. *Applied Surface Science*, 602, 154367. Available from <https://doi.org/10.1016/j.apsusc.2022.154367>; <https://www.sciencedirect.com/science/article/pii/S0169433222019006>.
- Zhang, K., Surana, M., Haasch, R., & Tawfick, S. (2020). Elastic modulus scaling in graphene-metal composite nanoribbons. *Journal of Physics D: Applied Physics*, 53(18), 185305. Available from <https://doi.org/10.1088/1361-6463/ab7329>.
- Zhou, X., Xu, H., Cheng, J., Zhao, N., & Chen, S.-C. (2015). Flexure-based roll-to-roll platform: A practical solution for realizing large-area microcontact printing. *Scientific Reports*, 5(1), 10402. Available from <https://doi.org/10.1038/srep10402>.

CHAPTER 16

Stacking of two-dimensional materials

Wenhao Li, Jichuang Shen, Huaze Zhu, Han Chen and Wei Kong

School of Engineering, Westlake University, Hangzhou, P.R. China

16.1 Introduction

Two-dimensional (2D) materials with atomic thickness typically exhibit behavior that is markedly different from their bulk counterparts. The van der Waals interactions between 2D layers hold greater significance as they enable the integration of various 2D materials without the constraints of crystal lattice matching. As a result, 2D layers can be employed as building blocks, akin to “Lego,” to construct a diverse array of artificial 2D crystals. The properties of these structures can be tailored by adjusting the types of 2D materials, sequence order, and interlayer twist angle, providing a versatile platform for designing materials with desired properties for specific technological applications (Liu, 2016; Novoselov et al., 2016).

Since the successful isolation of graphene from graphite, monolayer graphene has been the subject of intensive research due to its remarkable properties. In the last decade, researchers further have extended their focus to other 2D materials, such as hexagonal boron nitride (h-BN), molybdenum disulfide (MoS_2), other dichalcogenides, and layered oxides. The rapidly expanding family of 2D materials encompasses various types, including semimetal, conductor, semiconductor, insulator, and superconductor. Initial studies primarily investigated their individual structures and properties. The exploration of new types of 2D materials and their intrinsic properties has paved the way for an emerging research field focused on heterostructures and devices created by stacking different 2D crystals together. The interaction of 2D materials in heterostructures can give rise to novel functionalities, enabling a wide range of applications in electronics, optics, sensors, and more (Abbas, 2020; Duong et al., 2017; Pham et al., 2022).

A wide variety of electronic and optoelectronic devices based on 2D materials and their heterostructures have emerged, including transistors, photodetectors, solar cells, sensors, and memory devices (Pham et al., 2022). Transistors utilizing graphene and MoS_2 have gained attention due to their high mobility (Wang et al., 2013) and on-off ratios (Radisavljevic et al., 2011). As stacking technology advances, more complex 2D heterostructures have been explored for various applications. For example, photodetectors using graphene/transition-metal dichalcogenide(TMDC)/graphene heterostructures have demonstrated outstanding performance, with external quantum efficiencies reaching up to

55% (Furchi et al., 2014). Additionally, tunable light-emitting diodes based on 2D heterostructures have achieved extrinsic quantum efficiencies of nearly 10% (Withers et al., 2015). Large-area 2D heterostructures have also allowed for 90% narrowband absorption in less than 4 nm of active layer excitonic absorber medium at room temperature (Kumar, 2021). Furthermore, diverse 2D memory and sensor devices have been developed (Bag & Lee, 2019). Beyond functional devices, 2D heterostructures serve as an excellent platform for study of physics. For instance, flat bands and many-body correlated states have been discovered in twisted 2D stacks (Cao, Fatemi, Demir, et al., 2018; Cao, Fatemi, Fang, et al., 2018; Wang, Shih, et al., 2020), while superlattice Dirac points (Yankowitz et al., 2012) and fractal quantum Hall effects (Dean et al., 2013) have been observed in graphene/BN stacks.

In this chapter, we will discuss the techniques involved in creating heterostructures, controlling twist angles, and exploring their typical performance characteristics and applications.

16.2 Process

16.2.1 Bottom-up fabrication of two-dimensional stack (direct growth)

16.2.1.1 Growth methods

Bottom-up approaches are a widely used way to synthesize 2D materials with high crystal quality. These methods include both physical methods such as physical vapor transport (PVT) (Hu et al., 2017; Muratore et al., 2019) and chemical methods such as chemical vapor deposition (CVD) (Cai et al., 2018; Sun, 2021a; Tang et al., 2021).

PVT is a method for obtaining high-quality single-crystal multilayer 2D materials (Muratore et al., 2019). As shown in Fig. 16.1A, PVT generally occurs in a quartz tube sealed after vacuum pumping, with powdered raw materials placed at the high-temperature end and the growth substrate placed at the low-temperature end. After thermal evaporation and transport, the raw materials crystallize on the substrate to obtain multilayer 2D materials, even reaching bulk thickness. Although high crystal quality can be obtained through the PVT method, the number of layers is uncontrollable, and it is not suitable for obtaining heterogeneous structures.

Molecular-beam epitaxy (MBE) (Cheng et al., 2019; Kum et al., 2019) is a highly controllable thin film growth technique that can satisfy the aforementioned requirements Fig. 16.1B. When growing multilayer 2D materials such as TMDs, in an ultra-high vacuum environment, the transition metals and chalcogenides are evaporated and the beam is sprayed onto the crystal substrate in a controlled flow, where slow epitaxial growth occurs on the substrate surface. MBE allows for control of single-layer growth, and when different raw materials are selected for each layer, it can produce multilayer 2D heterostructures (Vishwanath et al., 2016).

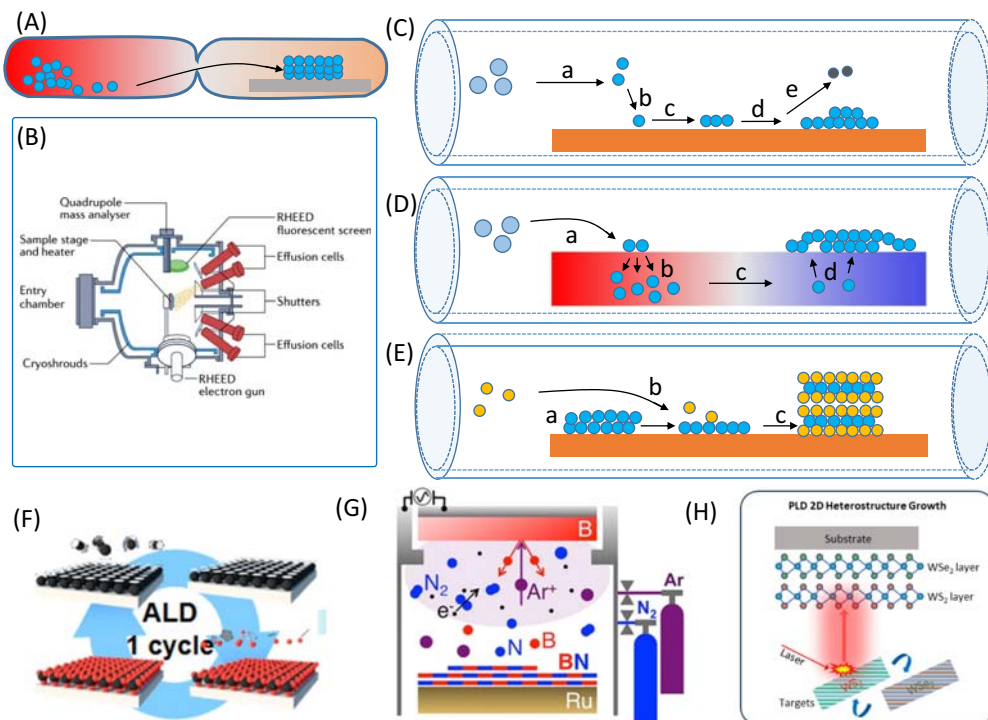


Figure 16.1 Bottom-up synthesis strategy for multilayer two-dimensional (2D) materials. (A) physical vapor transport (PVT). (B) Molecular beam epitaxy (MBE). (C)–(E) Three main mechanisms for 2D multilayer materials growth by chemical vapor depositions (CVD). (F) Atomic layer deposition (ALD). (G) Magnetron sputtering physical vapor deposition (PVD). (H) Pulsed laser deposition (PLD). (B) Kum, H., Lee, D., Kong, W., Kim, H., Park, Y., Kim, Y., Baek, Y., Bae, S.-H., Lee, K., & Kim, J. (2019). Epitaxial growth and layer-transfer techniques for heterogeneous integration of materials for electronic and photonic devices. *Nature Electronics*, 2(10), 439–450. <https://doi.org/10.1038/s41928-019-0314-2>; (F) Kim, H. G., & Lee, H. B. R. (2017). Atomic Layer Deposition on 2D Materials. *Chemistry of Materials*, 29(9), 3809–3826. <https://doi.org/10.1021/acs.chemmater.6b05103>; (G) Sutter, P., Lahiri, J., Zahl, P., Wang, B., & Sutter, E. (2013). Scalable synthesis of uniform few-layer hexagonal boron nitride dielectric films. *Nano Letters*, 13(1), 276–281. <https://doi.org/10.1021/nl304080y>.

However, MBE is not suitable for thick film growth and large-scale production for its low growth rate. As a bottom-up method of chemical growth, CVD provides a scalable and controllable way to grow high-quality 2D materials at a reasonable cost (see Fig. 16.1C–E). (Sun, 2021a) CVD is not only widely used to grow large-area single-layer 2D materials (Chen et al., 2020; Li, Zhang, et al., 2021; Wang et al., 2021; Wang, Li, et al., 2020; Ye et al., 2016; Yu et al., 2017), but also to obtain multilayer 2D materials and their heterostructures by adjusting growth parameters such as substrate engineering, precursor, growth temperature, and growth time (Feng et al., 2014;

Uchida et al., 2018; Zheng et al., 2017). Generally, as shown in Fig. 16.1C, the CVD process includes several steps:

1. precursor molecules enter the chamber with the carrier gas dissociates into active species,
2. adsorbs on the substrate surface,
3. migrates and collides on the substrate surface to form nuclei,
4. further grow laterally to form a thin film.

In the CVD process, achieving the nucleation and growth of the second layer is crucial to obtain multilayer 2D materials. In addition, when the substrate has a certain solubility for the constituent atoms of the 2D material, a temperature-controlled dissolution-precipitation growth mechanism (Ma et al., 2022; Nakajima et al., 2018; Uchida et al., 2018; Vaněk et al., 2020), as shown in Fig. 16.1D, can be achieved. In this process, the atoms are partially dissolved in the substrate metal at high temperatures, and then precipitate and grow into the target multilayer 2D material as the temperature decreases. Another CVD growth method that directly sulfurization of the precursors to quickly synthesize large-area multilayer TMD materials (Lin et al., 2012; Lu et al., 2017; Zhan et al., 2012). In this process, the metal source is introduced onto the substrate by metal deposition or spin coating, and then subjected to high-temperature sulfurization to obtain a multilayer TMD film. The thickness of the 2D material is directly determined by the thickness of the prefabricated metal source film, and the prefabricated metal heterostructure can also be converted into a TMD heterostructure by this method (Seok et al., 2021).

In addition to the above methods, there are other methods used to synthesize multilayer 2D materials (Fig. 16.1F–H), such as atomic layer deposition (ALD) (Kim & Lee, 2017; Nieken, 2022), magnetron sputtering physical vapor deposition (PVD) (Song et al., 2016; Sutter et al., 2013) and pulsed laser deposition (PLD). The principles of these methods involve using high-energy plasma or pulsed laser to bombard the target material, causing the 2D material target to evaporate or decompose, and subsequently depositing it onto the substrate, to obtain multilayer 2D materials.

In a word, there are many bottom-up synthesis methods for obtaining multilayer 2D materials. During the growth process, different materials and properties lead to different mechanisms for multilayer growth, appropriate synthesis methods should be chosen. Additionally, the construction of heterostructures presents higher requirements for controllable growth of multilayers compared to homojunctions, such as the controllability of layer number and interlayer twist angle. In particular, the twist angle introduces Moiré patterns to the 2D material system, bringing new electronic states and physical properties, and becoming an important research direction in the field of multilayer 2D materials (Andrei & MacDonald, 2020; Andrei et al., 2021; Mak & Shan, 2022; Xiao et al., 2020). Based on this, in the following section, we will analyze

the mechanisms of homogenous and heterogenous epitaxial growth of multilayer 2D materials, and then discuss appropriate bottom-up growth methods to obtain multilayer 2D structures with controllable layer numbers and twist angles.

16.2.1.2 Homostructures

16.2.1.2.1 Multilayer graphene

There are generally two mechanisms for the growth of graphene: metal surface catalyzed growth (Fig. 16.1C) and dissolution and precipitation growth (Fig. 16.1D) (Dong et al., 2019). In the surface catalysis process, the substrate, such as Cu, has a very small solubility for carbon atoms, and gas molecules such as CH₄ are catalytically cracked by the metal substrate to nucleate and grow into graphene. In the dissolution and precipitation growth process, at high temperatures, the substrate, such as Ni, not only has a catalytic cracking effect on CH₄, but also has a certain solubility for carbon (Yankowitz et al., 2012). As the temperature decreases, carbon atoms precipitate and crystallize from the substrate to obtain graphene.

Due to the passivation effect of the initial layer of graphene on the Cu substrate, it is difficult to effectively crack the carbon precursor to supply the growth of the second layer of graphene. To solve this problem, in 2011, Yan et al. proposed a two-step growth scheme to obtain bilayer graphene (Yan et al., 2011). As shown in Fig. 16.2A, pregrown single-layer graphene on a copper foil is placed downstream in the furnace, and fresh copper foil is placed upstream. In this way, CH₄ can be decomposed on the surface of the upstream copper foil, and carbon radicals or fragments can be transported to the surface of the second copper foil to provide nutrients for the growth of the second layer of graphene. In 2012, Sun et al. demonstrated that the number of graphene layers grown on Cu substrates is controlled by the H₂:CH₄ ratio and CH₄ partial pressure (Fig. 16.2B) (Jorio & Cançado, 2013). They proposed that the growth of multilayer graphene is achieved by nucleation and growth of two layers simultaneously (Fig. 16.2C).

As mentioned above, growing multilayer graphene on a Cu substrate requires precise control of experimental conditions or complex strategies. Therefore, some researchers have proposed using Cu–Ni alloys as substrates to grow multilayer graphene, as Ni is more reactive than Cu and has a much higher carbon solubility (Huang & Ruoff, 2020). Takesaki et al. studied the growth of bilayer graphene on Cu–Ni alloy substrates and found that alloy composition, growth temperature, and cooling rate are important factors affecting the formation of bilayer graphene (Takesaki et al., 2016). In particular, the authors proposed that the first layer of graphene is formed by the aggregation of carbon atoms on the catalyst surface, while the second layer is separated from the alloy body by carbon (Fig. 16.2D). In 2020 Nguyen et al. reported that Cu–Si alloys can be used as substrates to synthesize large-scale single-crystal graphene with controllable layer numbers (Fig. 16.2E) (Nguyen et al.,

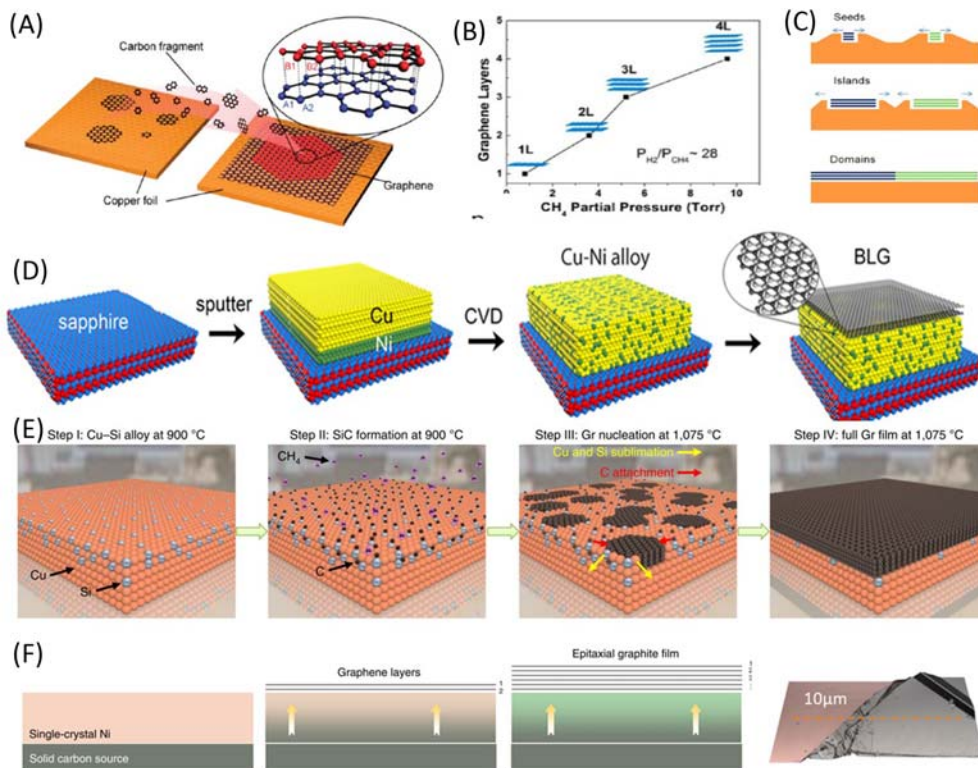


Figure 16.2 Bottom-up growth of multilayer graphene. (A) Two steps growth of bilayer graphene on Cu. (B) Growth of multilayer graphene controlled by the $\text{H}_2:\text{CH}_4$ ratio and CH_4 partial pressure. (C) Simultaneous nucleation and growth of bilayer graphene on Cu. (D) Growth of bilayer graphene on Cu–Ni alloy substrate. (E) Single crystal graphene grown on Cu–Si alloy substrate with controllable layer numbers. (F) Growth of large area high-quality graphite on Ni. (A) From Zatko, V., Dubois, S. M. M., Godel, F., Carretero, C., Sander, A., Collin, S., Galbiati, M., Peiro, J., Panciera, F., Patriarche, G., Brus, P., Servet, B., Charlier, J. C., Martin, M. B., Dlubak, B., & Seneor, P. (2021). Formation of bilayer bernal graphene: Layer-by-layer epitaxy via chemical vapor deposition. *Nano Letters*, 11(3), 1106–1110. <https://doi.org/10.1021/nl104000b>; (B and C) Jorio, A., & Cancado, L. G. (2013). Raman spectroscopy of twisted bilayer graphene. *Solid State Communications*, 175–176, 3–12. <https://doi.org/10.1016/j.ssc.2013.08.008>; (D) Takesaki, Y., Kawahara, K., Hibino, H., Okada, S., Tsuji, M., & Ago, H. (2016). Highly uniform bilayer graphene on epitaxial Cu–Ni (111) alloy. *Chemistry of Materials*, 28(13), 4583–4592. <https://doi.org/10.1021/acs.chemmater.6b01137>; (E) Nguyen, V. L., Duong, D. L., Lee, S. H., Avila, J., Han, G., Kim, Y. M., Asensio, M. C., Jeong, S. Y., & Lee, Y. H. (2020). Layer-controlled single-crystalline graphene film with stacking order via Cu–Si alloy formation. *Nature Nanotechnology*, 15(10), 861–867. <https://doi.org/10.1038/s41565-020-0743-0>; (F) Zhan, Y., Liu, Z., Najmaei, S., Ajayan, P. M., & Lou, J. (2012). Large-area vapor-phase growth and characterization of MoS_2 atomic layers on a SiO_2 substrate. *Small*, 8(7), 966–971. <https://doi.org/10.1002/smll.201102654>.

2020). In their study, diluted CH_4 was introduced into a CVD furnace and decomposed on a Cu–Si substrate to form SiC, followed by stopping the supply of CH_4 and raising the temperature to 1075°C . Si atoms sublimated from SiC and formed multilayer graphene islands. In addition, it was found that the carbon supply in the CVD furnace can effectively control the number of layers.

Although the solubility of carbon in Cu–Ni substrate is significantly increased compared to the situation of the pure copper substrate, the number of layers of graphene obtained by Cu–Ni alloy is still less than five layers, and the scale range is limited to the nanometer range. It has become a challenge to grow thicker graphene or even single-crystal graphene. Since the solubility of C in pure nickel will be further improved, the use of nickel substrates usually produces thicker multilayer graphene by dissolution and precipitation mode. Nakajima et al. used amorphous carbon as a carbon source to study the process of penetrating into nickel metal to form multilayer graphene, and obtained a graphene layer with a thickness of 100 nm (Murata et al., 2019; Nakajima et al., 2018). The authors call this process the “layer exchange” of metals and systematically study the effect of transition metal species on the interaction between metals and a-C in the temperature. It is found that the metal with layer exchange is Co, Ni, Cr, Mn, Fe, Ru, Ir, and Pt in addition to Ni, which provides a broader prospect for the synthesis of multilayer graphene. Recently, Zhang et al. reported a new growth mechanism of isothermal dissolution–diffusion–precipitation, which realized the preparation of centimeter-level high-quality single-crystal graphite (Fig. 16.2F). The resulting graphene layer is $10\mu\text{m}$ in thickness and has hundreds of thousands of layers (Zhang, 2022).

16.2.1.2.2 Multilayer hexagonal boron nitride

Due to the extremely low solubility of boron and/or nitrogen in most transition metals, the growth of h-BN is self-limiting, and it is challenging to synthesize multilayer h-BN by codeposition of boron and nitrogen. h-BN samples grown on Cu foil typically consist of only one atomic layer, mainly due to the low solubility of boron and nitrogen in Cu. The precursors commonly used for h-BN growth are borazine or ammonia borane (Li, Zhang, et al., 2021). Based on experimental observations, Kidambi et al. proposed a growth model for h-BN on Cu foil (Kidambi et al., 2014), as shown in Fig. 16.3A. At growth temperatures of 950°C – 1000°C , boron–nitrogen molecules dissociate on the Cu surface, and boron atoms first dissolve into the Cu foil. The supply of nitrogen must be achieved through surface-catalyzed processes during h-BN growth, while the supply of boron can be achieved through surface diffusion or precipitation from the bulk. It should be noted that by increasing the supply of h-BN precursors or extending the growth time, multilayer h-BN can be formed on Cu substrates.

Similar to the CVD growth of graphene, besides Cu, h-BN can also be grown on many transition metals and their alloy substrates such as Ni, Pt, Ru, and Rh. However, the

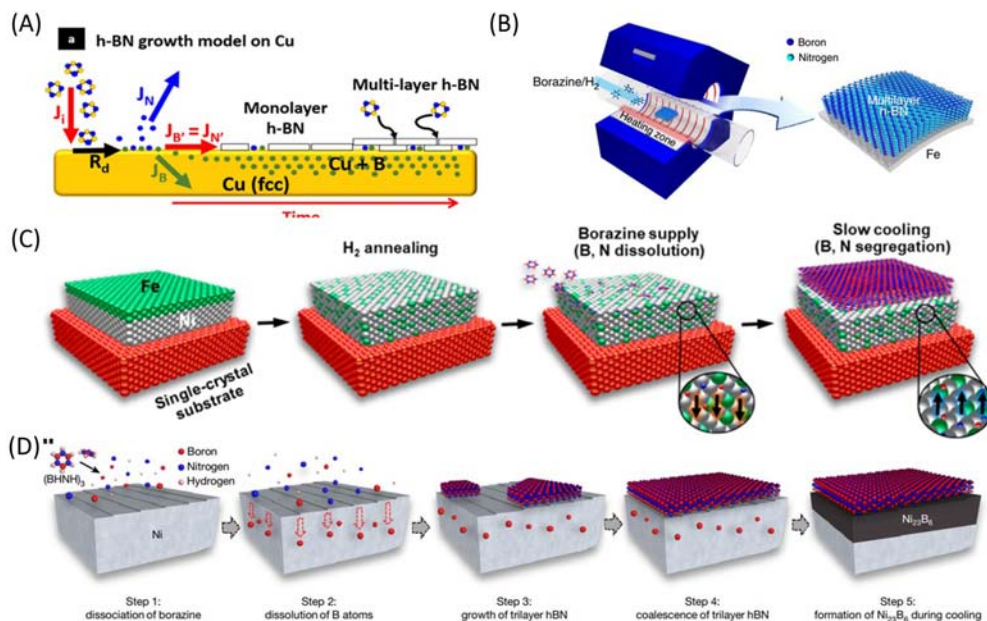


Figure 16.3 Bottom-up growth of multilayer hexagonal boron nitride (h-BN). (A) Multilayer h-BN growth model on Cu. (B) Growth of multilayer h-BN on Fe substrate. (C) Growth of multilayer h-BN on Fe–Ni alloy substrate. (D) Growth of single crystal h-BN on Ni. (A) From Kidambi, P. R., Blume, R., Kling, J., Wagner, J. B., Baehtz, C., Weatherup, R. S., Schloegl, R., Bayer, B. C., & Hofmann, S. (2014). *In situ observations during chemical vapor deposition of hexagonal boron nitride on polycrystalline copper*. *Chemistry of Materials*, 26(22), 6380–6392. <https://doi.org/10.1021/cm502603n>; (B and C) Kim, S. M. (2015). *Synthesis of large-area multilayer hexagonal boron nitride for high material performance*. *Nature Communications*, 6(1); (D) Ma, K. Y., Zhang, L., Jin, S., Wang, Y., Yoon, S. I., Hwang, H., Oh, J., Jeong, D. S., Wang, M., Chatterjee, S., Kim, G., Jang, A. R., Yang, J., Ryu, S., Jeong, H. Y., Ruoff, R. S., Chowalla, M., Ding, F., & Shin, H. S. (2022). *Epitaxial single-crystal hexagonal boron nitride multilayers on Ni (111)*. *Nature*, 606(7912), 88–93. <https://doi.org/10.1038/s41586-022-04745-7>.

low solubility of boron and/or nitrogen in the metal substrates (Cu, Ni, Pt, etc.) severely hinders the synthesis of multilayer h-BN and limits the growth mechanism (Uchida et al., 2018). Therefore, selecting a substrate with high boron–nitrogen solubility is advantageous for growing multilayer h-BN. Kim et al. reported the growth of multilayer h-BN on Fe substrate using low-pressure CVD and boron–nitrogen as precursors at 1100°C (Fig. 16.3B) (Kim, 2015). They found that the thickness of h-BN films can be controlled by the cooling rate of the CVD system, indicating that the growth of multilayer h-BN is mainly dominated by the separation of boron and nitrogen in the Fe substrate.

In recent years, to address the issue of low solubility of boron and/or nitrogen in transition metal substrates, alloy substrates (or metal borides) have been used to synthesize multilayer h-BN (Fukamachi et al., 2023). Uchida et al. reported the synthesis of

uniform multilayer h-BN on a Fe–Ni alloy substrate (Fig. 16.3C) (Kim, 2015). The authors found that low grain boundary density is crucial for the uniformity of the synthesized multilayer h-BN, as boron and nitrogen tend to separate from the substrate grain boundary rather than the crystal face. Furthermore, by changing the concentration of Ni, the solubility of boron and nitrogen in the Fe–Ni alloy can be effectively adjusted to ensure the equilibrium segregation of boron and nitrogen from the Fe–Ni alloy matrix, thereby improving the uniformity of the multilayer h-BN film.

It should be noted that due to the fourfold symmetry (100) or twofold symmetry (110) of the Fe–Ni alloy substrate surface, the obtained multilayer h-BN is also polycrystalline. However, the development of growth techniques for large-area single-crystal multilayer h-BN has important significance in the field of high-performance electronic devices. Ma et al. reported the epitaxial growth of wafer-scale single-crystal three-layer h-BN using CVD (Ma et al., 2022). The dissociation of boron–nitrogen precursor on the Ni surface at 1220°C provided B and N species for the h-BN film. Due to the high solubility under growth conditions, B dissolved in Ni in the form of a solid solution. Uniformly arranged h-BN islands nucleated and grew epitaxially on a single-crystal Ni (111) substrate, eventually merging into a continuous three-layer single-crystal h-BN film (Fig. 16.3D).

16.2.1.2.3 Multilayer TMDs

The synthesis of TMDCs does not require a metallic substrate as a catalyst for the precursor is highly active and easy to decompose. Instead, commonly used substrates are inorganic SiO₂ and sapphire. In 2017, Zheng et al. reported the synthesis of multilayer MoS₂ islands using S vapor and MoO_x vapor as precursors on SiO₂/Si substrates (Fig. 16.4A) (Zheng et al., 2017). It was found that the number of MoS₂ layers synthesized could be effectively adjusted by changing the degree of oxidation of the Mo foil (Fig. 16.4B).

In addition, TMD materials can also be obtained by depositing a metal source thin film on the substrate and then subjecting it to high-temperature sulfidation. In 2012, Lin et al. used the sputtered MoO₃ film as the starting material and performed two-step heating to obtain a three-layer wafer-level MoS₂ film by reducing it in H₂ at 500°C and sulfurizing it in S at 1000°C (Fig. 16.4C) (Lin et al., 2012).

Large-area multilayer single-crystal TMD materials have significant demand in the field of high-performance electronic devices, but their synthesis has been a major challenge. Although discrete multilayer single-crystal islands can be obtained on SiO₂ substrates through binary gas-phase deposition, their longitudinal dimensions are limited to within a few tens of microns, making it difficult to meet the requirements of large-scale device integration. Although metal source films with controllable thickness can be quickly obtained by sulfidation of precursors, it is difficult to obtain single crystal

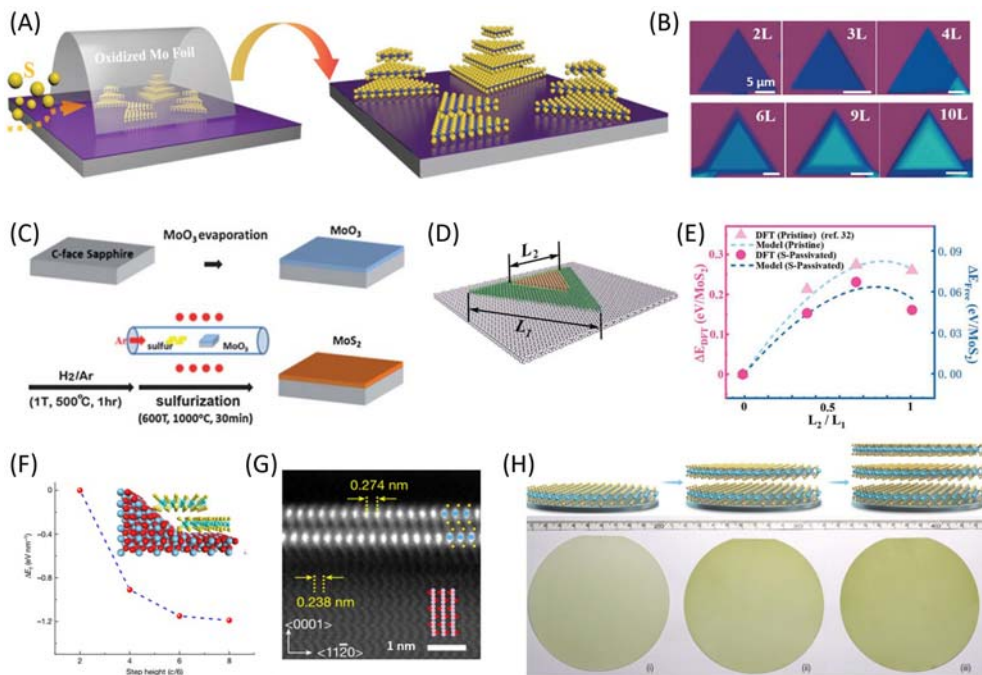


Figure 16.4 Bottom-up growth of multilayer TMDs. (A) Multilayer MoS₂ synthesized from MoO_x and S. (B) Optical images of multilayer MoS₂ on SiO₂/Si; (C) Multilayer MoS₂ by sulfurization of MoO₃ Film. (D) Simulation of bilayer MoS₂ on sapphire. (E) DFT calculated energy differences for the layer-by-layer transition from monolayer to bilayer MoS₂ domains. (F) The calculated step-height-dependent formation energy of MoS₂ bilayers. (G) Cross-sectional HAADF-STEM image. (H), Layer-by-layer epitaxy of three-layer MoS₂ wafers. (A and B) From Zhan, Y., Liu, Z., Najmaei, S., Ajayan, P. M., & Lou, J. (2012). Large-area vapor-phase growth and characterization of MoS₂ atomic layers on a SiO₂ substrate. *Small*, 8(7), 966–971. <https://doi.org/10.1002/smll.201102654>; (C) Lin, Y. C., Zhang, W., Huang, J. K., Liu, K. K., Lee, Y. H., Liang, C. T., Chu, C. W., & Li, L. J. (2012). Wafer-scale MoS₂ thin layers prepared by MoO₃ sulfurization. *Nanoscale*, 4(20), 6637–6641. <https://doi.org/10.1039/c2nr31833d>; (D and E) Dong, R. (2022). The intrinsic thermodynamic difficulty and a step-guided mechanism for the epitaxial growth of uniform multilayer MoS₂ with controllable thickness. *Advanced Material*, 34; (F and G) Liu, L., Li, T., Ma, L., Li, W., Gao, S., Sun, W., Dong, R., Zou, X., Fan, D., Shao, L., Gu, C., Dai, N., Yu, Z., Chen, X., Tu, X., Nie, Y., Wang, P., Wang, J., Shi, Y., & Wang, X. (2022). Uniform nucleation and epitaxy of bilayer molybdenum disulfide on sapphire. *Nature*, 605(7908), 69–75. <https://doi.org/10.1038/s41586-022-04523-5>; (H) Wang, Q. (2022). Layer-by-layer epitaxy of multi-layer MoS₂ wafers. *National Science Review*, 9(6).

2D materials by this method. Selecting suitable epitaxial single crystal substrates and establishing new epitaxial modes are both critical to solving this problem.

Ding et al. showed through calculations that on an epitaxial Al₂O₃ substrate, single-layer MoS₂ domains are thermodynamically more favorable than multilayer MoS₂ domains due to the competition between surface interactions and edge formation (Fig. 16.4D and E) (Dong, 2022). They proposed a step-guided mechanism for

the growth of uniformly multilayer MoS₂ on an epitaxial substrate. Step heights on the sapphire surface can guide the simultaneous nucleation of neatly edged and uniformly thick multilayer MoS₂, promoting the continuous growth of multilayer MoS₂ films. Calculations showed that a step angle of 42.3 degrees is the most stable structure. The step heights for the nucleation and growth of uniform bilayer, trilayer, and quadrilayer MoS₂ are 1.3, 1.75, and 2.2 nm, respectively. Based on this, Liu et al. first realized this substrate-induced bilayer nucleation and a new “race-to-the-top” growth mechanism and reported the epitaxial growth of large-area uniform bilayer MoS₂ films (Fig. 16.4F) (Liu, Li, Ma, et al., 2022). The authors used high-temperature annealing to obtain a uniformly distributed high-atomic-step plateau on the sapphire surface, successfully obtaining over 99% bilayer nucleation and achieving centimeter-scale continuous bilayer films. Furthermore, it was shown that bilayer MoS₂ has a specific epitaxial relationship with the sapphire substrate (Fig. 16.4G). In addition, Wang et al. reported the growth of high-quality multilayer MoS₂ 4-inch wafers through layer-by-layer epitaxy (Wang, 2022). Epitaxy results in well-defined stacking sequences between adjacent epitaxial layers and provides precise layer control, with up to six layers (Fig. 16.4H).

16.2.1.3 Heterostructures

Based on the above discussions, people can obtain multilayered homogeneous 2D materials such as graphene, h-BN, and TMDs through different CVD methods. Furthermore, synthesizing directly grown multilayered heterostructures (vertical heterostructures) becomes a new challenge, as it requires consideration of lattice matching between different materials and the compatibility of growth processes for different materials. Many studies have reported CVD growth methods for bilayer or multilayered heterostructures based on graphene, h-BN, or TMDs systems. These methods can be categorized into three types: (1) one-pot growth, (2) two-step growth, and (3) prefabricated multilayered metal superlattices followed by sulfidation.

One-pot synthesis is commonly used to fabricate heterostructures of TMDs. In the CVD process, all metal precursors undergo sublimation, transportation, and deposition reactions, resulting in multilayer heterostructures directly on the substrate. Ajayan et al. used S, W, and MoO₃ powders as precursors, and added Te powder to accelerate the melting of W powder during growth (Fig. 16.5A) (Gong et al., 2014). At low temperature (650°C), nucleation and growth of WS₂ were extremely difficult and slow, tending to occur at the edges of MoS₂, which resulted in in-plane heterostructures. At high temperatures (850°C), the environment provides enough energy to overcome the nucleation barrier, and the thermodynamically more stable vertical heterostructure product becomes preferred (Fig. 16.5B). It can be seen that the competition reaction of lateral heterostructures is a key issue in one-pot synthesis, and high temperature favors the growth of vertical heterostructures.

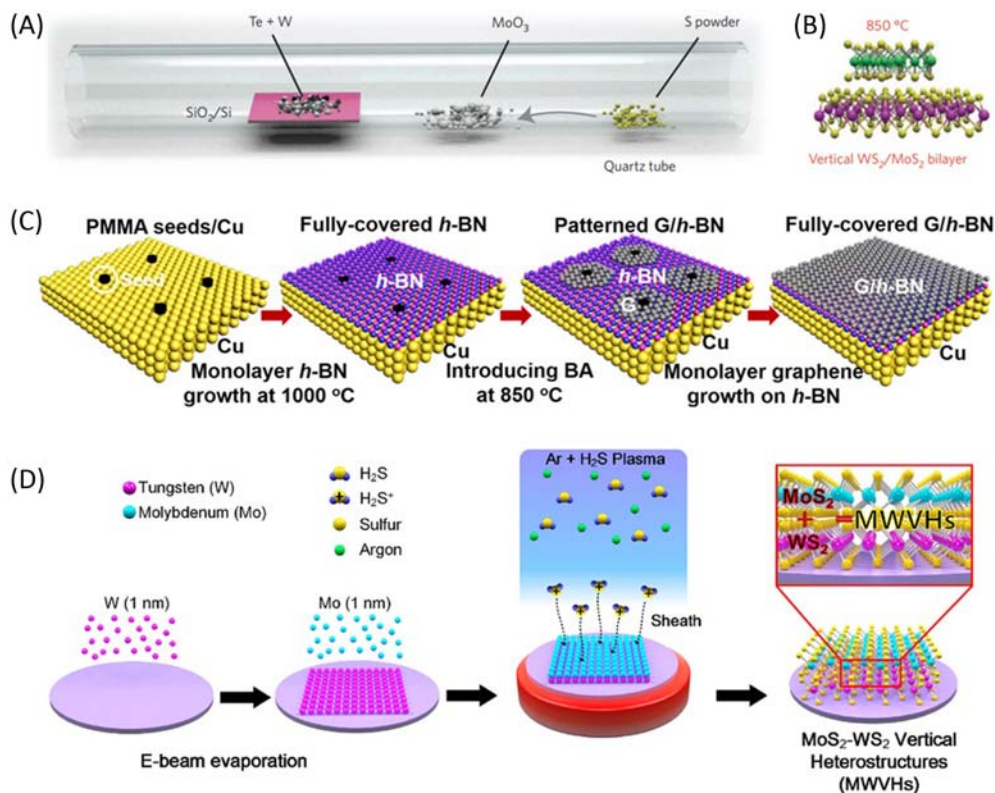


Figure 16.5 *Bottom-up growth of two-dimensional heterostructures.* (A) One-pot synthesis of vertical WS_2/MoS_2 heterostructure. (B) Schematic diagram of vertical WS_2/MoS_2 heterostructure. (C) Two-steps growth of h-BN/graphene heterostructure. (D) MoS_2/WS_2 heterostructure by sulfuration of predeposited W-Mo film. (C) From Song, X., Gao, T., Nie, Y., Zhuang, J., Sun, J., Ma, D., Shi, J., Lin, Y., Ding, F., Zhang, Y., & Liu, Z. (2016). Seed-assisted growth of single-crystalline patterned graphene domains on hexagonal boron nitride by chemical vapor deposition. *Nano Letters*, 16(10), 6109–6116. <https://doi.org/10.1021/acs.nanolett.6b02279>; (D) Seok, H., Megra, Y. T., Kanade, C. K., Cho, J., Kanade, V. K., Kim, M., Lee, I., Yoo, P. J., Kim, H. U., Suk, J. W., & Kim, T. (2021). Low-temperature synthesis of wafer-scale MoS_2-WS_2 vertical heterostructures by single-step penetrative plasma sulfuration. *ACS Nano*, 15(1), 707–718. <https://doi.org/10.1021/acsnano.0c06989>.

The two-step method is easy to understand, which means obtaining the first 2D material by CVD first, then replacing the raw materials and growth conditions to grow the second 2D material on the surface of the obtained 2D material. This method is widely used for the synthesis of most heterostructures based on graphene, h-BN, or TMDs (Jianping Shi et al., 2015; Tian, 2022; Gong et al., 2015). However, because the surface of the first layer of 2D material has no dangling bonds, it is not conducive to the nucleation of the second layer of 2D material, which is also a problem in this method. To address this issue, Song et al. developed a two-step method for growing graphene/h-BN heterostructures (Fig. 16.5C)

(Song et al., 2016). First, they used PMMA seeds on Cu substrate as nucleation points, which is conducive to the nucleation of graphene on the surface of h-BN due to the presence of PMMA seeds. Both graphene and h-BN are suitable for the further growth of TMDs. For the synthesis of multilayer heterostructures of TMDs, MBE, MOCVD, and ALD are all highly controllable and effective methods, generally resulting in multilayer heterostructures with controllable layer numbers and high crystal quality, but the drawback is slow growth rate (Jin et al., 2021; Kanazawa et al., 2017; Kang et al., 2015; Mattinen et al., 2019). PLD can rapidly obtain multilayer TMD heterostructures (Hussain et al., 2016; Zatko et al., 2021).

For the growth of multilayer TMD heterostructures, the presynthesized metal film and subsequent sulfurization method shown in Fig. 16.1E are also applicable. In this method, the multilayer metal superlattice is predeposited on the substrate, and then sulfur is introduced under high-temperature conditions to achieve sulfurization and obtain the multilayer TMDs (Chiappe et al., 2016). For example, Seok et al. used plasma-enhanced chemical vapor deposition (PE-CVD) and time-dependent analysis to develop a single-step penetrating sulfidation process, synthesizing wafer-scale MoS₂-WS₂ vertical heterostructures at a low temperature (Fig. 16.5D) (Seok et al., 2021).

16.2.1.4 Twisting of two-dimensional materials

When two layers of 2D materials are stacked with a certain twist angle, a Moiré pattern is generated, also known as a Moiré superlattice. The Moiré periodicity of the stacked system is modulated under different twist angles, and the interlayer interaction is changed, leading to differences in electronic states and physical properties (Andrei & MacDonald, 2020; Andrei et al., 2021; Mak & Shan, 2022; Xiao et al., 2020). The precise and controllable synthesis of bilayer 2D materials with specific twist angles is of great significance for observing novel electronic states and physical phenomena.

CVD can be used to grow bilayer 2D structures with twist angles. For the growth of bilayer graphene, bilayer h-BN and bilayer TMDs, the symmetry of the two layers is highly consistent because of the homonuclear growth mechanism, resulting in thermodynamically stable bilayer graphene with 0 degree or 30 degrees twist angles. This makes it difficult to obtain other twisted bilayers with arbitrary twist angles. To solve this problem, it is crucial to break the high symmetry of the graphene bilayer caused by single-point nucleation. Sun developed an ectopic nucleation strategy by controlling the airflow perturbation during graphene formation, which provides a new method for preparing tBLG with arbitrary twist angles within 0–30 degrees by one-pot process (Fig. 16.6A) (Sun, 2021b). Liu et al. proposed a “prestacked substrate-angle replication” single-crystal growth strategy for the controlled growth of large-area bilayer single-crystal graphene with arbitrary angles (Fig. 16.6B) (Liu, Li, Qiao, et al., 2022). In this strategy, given that graphene can be epitaxially grown at a fixed angle on the surface of single-crystal Cu (111), the authors designed the angle by folding the

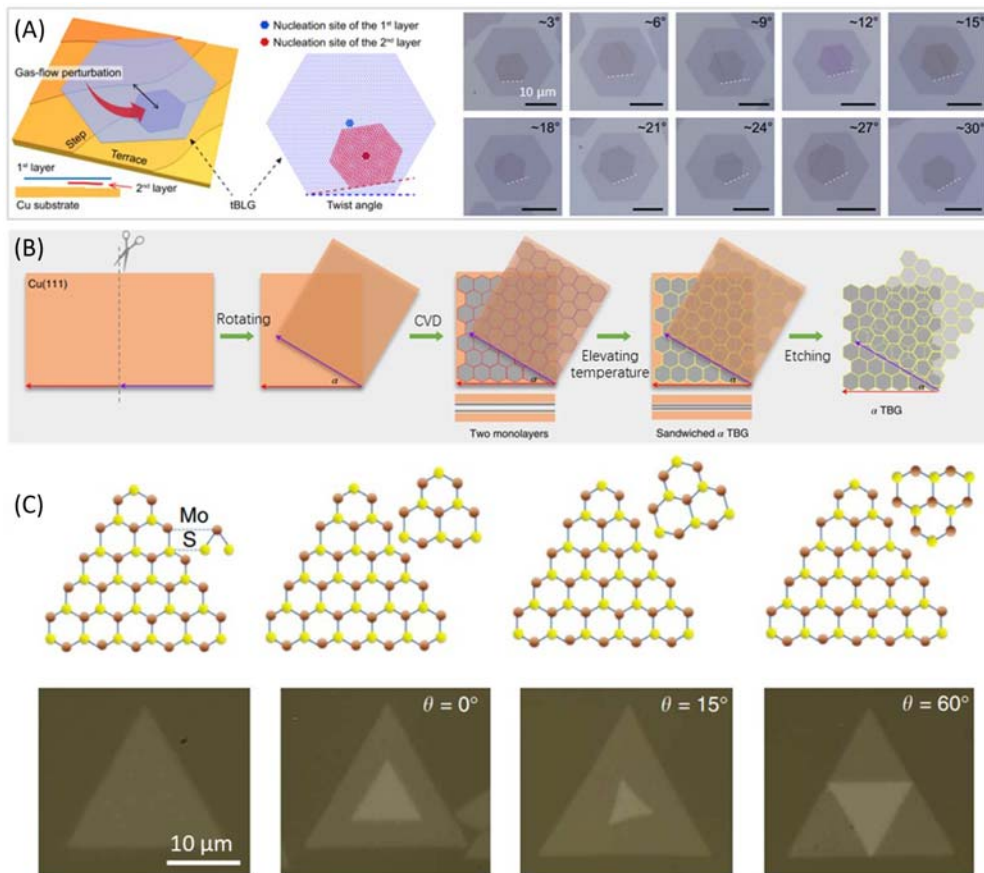


Figure 16.6 Twisting of stacked two-dimensional materials. (A) Growth of arbitrary twist angle *t*BLG by ectopic nucleation strategy. (B) Growth of twist angle designable *t*BLG by prestacked substrate-angle replication strategy. (C) Twisted bilayer MoS₂ with different twist angles. (A) From Sun, L. (2021b). Hetero-site nucleation for growing twisted bilayer graphene with a wide range of twist angles. *Nature Communications*, 12(1); (B) Liu, C., Li, Z., Qiao, R., Wang, Q., Zhang, Z., Liu, F., Zhou, Z., Shang, N., Fang, H., Wang, M., Liu, Z., Feng, Z., Cheng, Y., Wu, H., Gong, D., Liu, S., Zhang, Z., Zou, D., Fu, Y., . . . , & Liu, K. (2022). Designed growth of large bilayer graphene with arbitrary twist angles. *Nature Materials*, 21(11), 1263–1268. <https://doi.org/10.1038/s41563-022-01361-8>; (C) Liu, K., Zhang, L., Cao, T., Jin, C., Qiu, D., Zhou, Q., Zettl, A., Yang, P., Louie, S. G., & Wang, F. (2014). Evolution of inter-layer coupling in twisted molybdenum disulfide bilayers. *Nature Communications*, 5. <https://doi.org/10.1038/ncomms5966>.

single-crystal copper foil in advance. During the growth process, the two layers of graphene grown between the two copper foils strictly replicate the folding angle of the copper foil, and the subsequent high-temperature fusion and wet transfer can yield *t*BGs with customizable twist angles. This strategy provides a new perspective for the precise preparation of twisted 2D materials by CVD. In the case of the growth of

TMDs and h-BN, both parallel (0 degree) and antiparallel (60 degrees) triangular TMD crystal domains were revealed (Ago et al., 2015; Gong et al., 2015; Ji et al., 2017). Fig. 16.6C show that three twist angles of 0, 15, and 60 degrees generally exist for CVD-grown bilayer MoS₂ (Liu et al., 2014).

16.2.2 Top-down fabrication of two-dimensional stack (mechanically assembly)

Although direct growth can create heterostructures with ultra-clean interfaces, this strategy is constrained by the lattice mismatch between different layers in heterostructures and the distinct growth parameters for every 2D system further limits the application of this method. Besides, it is extremely challenging to consecutively control the interlayer twist angle. A more widely used strategy is to create 2D heterostructures through mechanical stacking, which involves isolating 2D materials as building blocks and vertically integrating them with predefined angles.

16.2.2.1 Wet process

The stacking method can be categorized into wet process, semidry process, and dry process based on the use of polymer and etchant. Initially, the wet process was developed to transfer graphene grown on metal substrates, involving the use of polymer and etchant. The wet process has been widely applied to the isolation and stacking of different 2D materials for its universality. Based on this technology, large-area graphene has been transferred from Cu foil to arbitrary substrate (Chen, Gong, et al., 2016; Lee et al., 2010; Li et al., 2009). In the wet process (see Fig. 16.7), after the deposition of

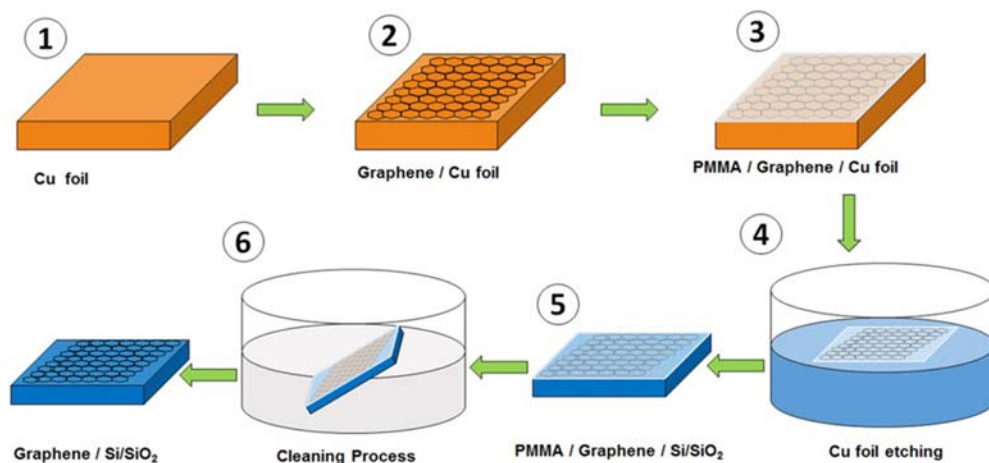


Figure 16.7 Scheme of conventional wet process. From Kashyap, P. K., Sharma, I., & Gupta, B. K. (2019). Continuous growth of highly reproducible single-layer graphene deposition on Cu foil by indigenously developed LPCVD setup. ACS Omega, 4(2), 2893–2901. <https://doi.org/10.1021/acsomega.8b03432>.

polymethyl methacrylate (PMMA) and etching of the substrate, PMMA/2D stack is picked up by the target substrate (Kashyap et al., 2019). A stack with multilayers can be got by repeating previous procedures. The strength of these traditional wet processes lies in their universality. One can transfer and stack any kind of 2D materials if only the appropriate etchant and polymer are selected. There is a little limitation for the size of 2D materials, which makes it a potential method to be adopted in mass production in industry. For instance, on the basis of it, Roll-to-Roll technology has realized mass production of graphene (Bae et al., 2010).

For TMDs grown on a sapphire substrate, a modified wet process was developed. Utilizing different wettability between TMDs and sapphire to make distilled water permeate into the TMDs/substrate interface, leading to the separation of the layers (Kim, 2019). Wafer-scale MoS₂ has been stacked by this method with the help of polymers such as polydimethylsiloxane (PDMS) and PMMA (Liao, 2020). Compared with the conventional wet process, the modified wet process avoids contamination and doping effect from harsh etchant but still uses polymer as a support layer.

The use of polymers and etchants in wet processes can lead to contamination, doping, and other defects (Kim et al., 2015). Consequently, numerous research efforts are centered on adjusting polymer and etchant types to minimize defects throughout the process. For example, a modified “Radio Corporation of America clean” was employed to eliminate Cu residue from transferred graphene (Lupina et al., 2015). Alternatives such as PDMS, polyvinyl alcohol (Whelan et al., 2017; Yang et al., 2015), and polystyrene (PS) were utilized in place of PMMA to achieve a cleaner surface. ultraviolet/ozone treatment was discovered to effectively diminish residue on PDMS stamps (Jain et al., 2018). However, these methods can only reduce residue to a certain degree, and the complete elimination of contaminations from polymers and etchants remains unattainable.

Compared with other stacking methods, it is relatively harder for the wet process to achieve a clean interface and gain control over the twist angle. To control the twist angle in the wet process, a probe needle is used to move the carrier and position the top material along the water/air interface. After being aligned, the top materials are placed on the bottom materials by pumping the water out and lowering the water level using a syringe pump (Schneider et al., 2010). The alignment for the wet process acquires complex and high-skilled operation, the position of the top layer must be continuously tuned until the top layer and bottom layer are brought into contact. Twist angles can also be controlled by pretreatment of the substrates. For instance, twisted bilayer graphene was fabricated by adjusting the hydrophilicity of the substrates (Wang et al., 2017). The process also acquires complex operation and its application is limited in bilayer homostructures.

16.2.2.2 Semidry transfer

The semidry process is an emerging method for efficiently stacking 2D materials. It typically involves the use of etchant but without any polymer at the 2D–2D interface. Metal can provide strong adhesion and peel off 2D materials from their bulk or growth substrate. In a typical procedure, metal is deposited on 2D materials and isolated and transferred to a target substrate. Etching metal and repeating the above procedures can realize the stack process. For instance, a bilayer film of palladium/polyimide was reported to successfully stack graphene grown on SiC substrate layer by layer. The process is compatible with bulk and CVD samples. The adhesion energy provided by the metal layer is sufficient for isolating various 2D materials. Like the wet process, the size of the stack is only constrained by the raw materials used. The isolation and stacking of wafer-scale graphene, MoS₂ and WS₂ grown by CVD were successfully demonstrated using Ni (see Fig. 16.8) (Shim et al., 2018).

For TMDs, gold can provide high adhesion energy due to the strong interaction of gold and sulfur atoms, making it suitable for use in the semidry process (Desai et al., 2016). The use of “gold tape” has been reported to isolate large-area MoS₂ from its bulk material, with a size much larger than flakes produced by conventional mechanical exfoliation (see Fig. 16.9). With “gold tape,” multilayers of MoS₂ were stacked,

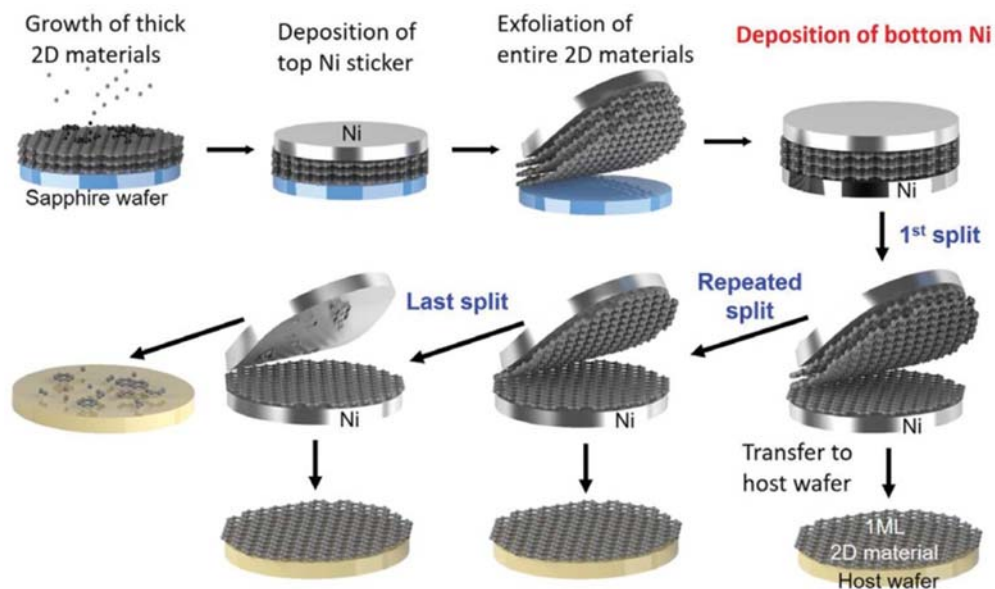


Figure 16.8 Scheme of semidry process with the assist of Ni. From Shim, J., Bae, S. H., Kong, W., Lee, D., Qiao, K., Nezhich, D., Park, Y. J., Zhao, R., Sundaram, S., Li, X., Yeon, H., Choi, C., Kum, H., Yue, R., Zhou, G., Ou, Y., Lee, K., Moodera, J., Zhao, X., . . . & Kim, J. (2018). Controlled crack propagation for atomic precision handling of wafer-scale two-dimensional materials. *Science*, 362(6415), 665–670. <https://doi.org/10.1126/science.aat8126>.

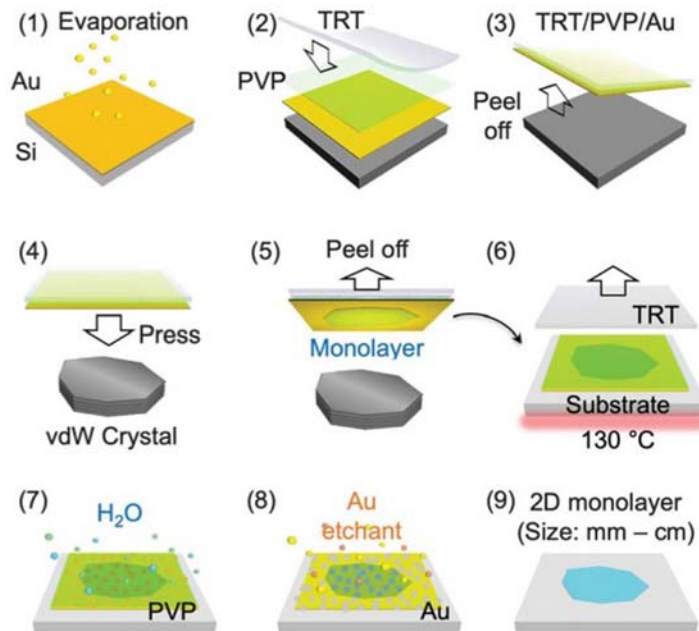


Figure 16.9 Scheme of semidry process with assist of Au. From Liu, F., Wu, W., Bai, Y., Chae, S. H., Li, Q., Wang, J., Hone, J., & Zhu, X. Y. (2020). *Disassembling 2D van der Waals crystals into macroscopic monolayers and reassembling into artificial lattices*. *Science*, 367(6480), 903–906. <https://doi.org/10.1126/science.aba1416>.

and the enhancement of second harmonic generation (SHG) was achieved by modifying the crystal orientation of the flakes (Liu et al., 2020). It has been shown that “gold tape” is compatible with various TMDs. The technology also has its shortcomings. While it avoids contamination from polymers, it still involves the use of an etchant solution, and the transfer process requires careful handling to avoid cracking, which can affect the production efficiency of multilayer stacks.

In contrast to the wet process, the semidry process can achieve water-scale alignment using a manipulator, three-axis micrometer stages, and a rotary table under a microscope. This makes it compatible with various alignment processes, such as “tear and stack” and mark alignment, which will be discussed in the following sections.

16.2.2.3 Dry process

In contrast to the wet and semidry processes, the dry process is able to avoid neither polymer nor etchant. For the 2D flakes produced by mechanical exfoliation, the hot pick-up technology (Pizzocchero et al., 2016; Purdie, 2018) is one of the most popular methods to create 2D stacks, which is described in detail in Fig. 16.10.

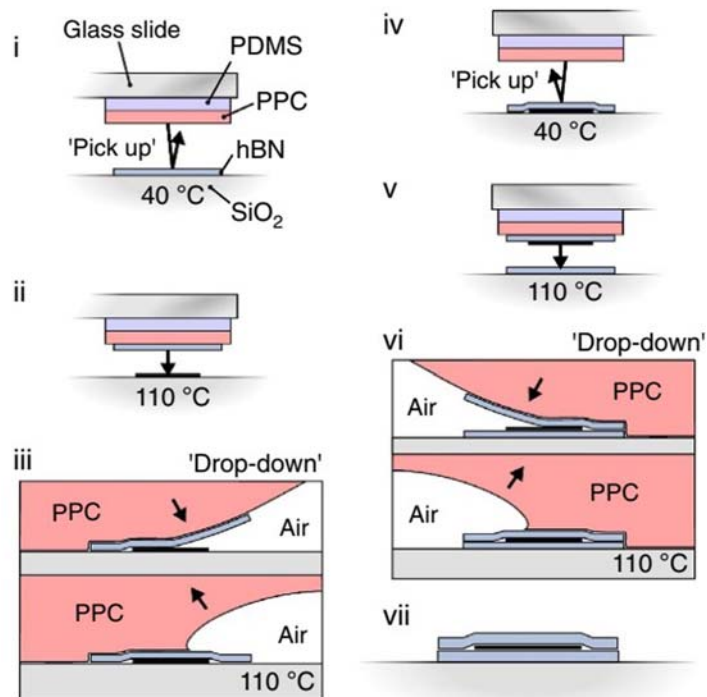


Figure 16.10 Scheme of dry process with PDMS/PPC stamp. From Pizzocchero, F., Gammelgaard, L., Jessen, B. S., Caridad, J. M., Wang, L., Hone, J., Bøggild, P., & Booth, T. J. (2016). The hot pick-up technique for batch assembly of van der Waals heterostructures. *Nature Communications*, 7. <https://doi.org/10.1038/ncomms11894>.

The key to this process lies in leveraging the adhesion between the 2D–2D interface. A PDMS/PPC/h-BN stamp, which can form conformal contact with 2D materials, is employed to pick up exfoliated 2D flakes. A 2D stack with a clean interface can be achieved by repetitive pick-up procedures and finally, release them on the target substrate. The polymer residue is removed by acetone or vacuum annealing. It should be noted that although the polymer stamp is used, it only contacts the first-layer BN. Typically, another BN flake would be selected as the last layer to encapsulate the entire stack. Thereby avoiding contamination from polymer and solution to the greatest extent possible and maintaining a clean 2D interface. This method has been used to observe monolayer graphene’s room-temperature mobility, which is comparable to the theoretical phonon-scattering limit (Wang et al., 2013), as well as other novel properties such as Mott insulator and superconductor phases (Cao, Fatemi, Demir, et al., 2018; Cao, Fatemi, Fang, et al., 2018). There are some limitations to this method: (1) the 2D materials to be integrated are usually flakes produced by mechanical exfoliation from bulk materials. (The method is not suitable for CVD samples. Grown 2D materials cannot be

picked up by h-BN for their strong adhesion with substrates). (2) The size of the stack is typically limited to less than $25 \times 25 \mu\text{m}$, which hinders its potential for industrial adoption.

Another promising dry process is the vacuum bonding process, which addresses the shortcomings of the hot pick-up process by being compatible with wafer-scale CVD samples. Similar to the hot pick-up method, it relies on 2D–2D adhesion and avoids polymer or etchant through encapsulation. Layer-by-layer assembly of 2D materials into wafer-scale heterostructures has been achieved using this process (Kang et al., 2017). In the process, 2D materials grown on SiO_2 were selected as building blocks for the stack. The first layer was isolated by coating of PMMA and the resulting PMMA/2D stack is used to peel off other 2D materials by vacuum bonding which is proved to enhance the 2D–2D adhesion, as shown in Fig. 16.11.

Modified bonding processes have also been explored, such as the development of a freestanding viscoelastic polymer to substitute PMMA. Its low glass transition temperature enables intimate contact between 2D materials, ensuring strong van der Waals forces between them (Boandoh et al., 2019). The nature of 2D–2D adhesion is van der Waals force which is relatively weaker than other chemical bonds. Therefore, the application of this technology is limited to systems with weak adhesion, such as CVD films grown on SiO_2 .

Aside from vertically stacking separate layers of 2D materials, the folding of single-layer 2D materials is a promising dry process. In the folding process, a high vacuum can be induced to improve cleanliness. AFM-tip manipulation is a popular way to create bilayer 2D materials by folding. By using contact mode, the monolayer can be scratched and exfoliated from the substrate and then stacked onto other parts of the monolayer (Carozo et al., 2013; Ni, 2009). A similar process can also be achieved in the STM system. The edge of the graphene flake is lifted by an STM probe and dragged along a predefined path, resulting in a bilayer (Chen et al., 2019). Neither polymer nor etchant is induced, but the method requires costly equipment and complicated operation. Except for the folding process, the dry process mentioned above also has high compatibility over different alignment processes.

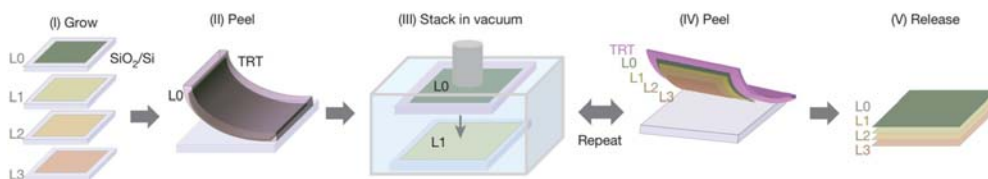


Figure 16.11 Scheme of dry process with vacuum bonding. From Kang, K., Lee, K. H., Han, Y., Gao, H., Xie, S., Muller, D. A., & Park, J. (2017). Layer-by-layer assembly of two-dimensional materials into wafer-scale heterostructures. *Nature*, 550(7675), 229–233. <https://doi.org/10.1038/nature23905>.

In summary, the wet process is a widely used stacking technology. However, it leaves polymer residue on 2D materials and its alignment is limited. The semidry process can avoid polymer residue but involves the use of etchants. On the other hand, the dry process can achieve a 2D interface without contamination from polymer or etchant. Both the semidry and dry processes are compatible with various alignment methods. A universal process for stacking and alignment of 2D materials still needs to be explored.

16.2.2.4 Mechanical twisting

Interlayer twist angle causes the formation of Moiré patterns and provides a new degree of freedom to modulate properties of 2D materials, leading to various intriguing phenomena (Gao et al., 2020; He et al., 2021). To create Moiré pattern in 2D materials, technologies to control twist angle is essential. There are roughly four types of alignment methods: “tear and stack” (Kim et al., 2016; Kim, 2017), mark alignment (Chen, Xin, et al., 2016), predetermination of crystal orientation (Jin et al., 2019), and dynamically alignment (Ribeiro-Palau et al., 2018).

The “tear and stack” method is widely employed for creating Moiré patterns with two layers of 2D materials and does not require additional alignment procedures. For a single crystalline 2D flake, crystal orientation remains consistent throughout. As Fig. 16.12A and B shows, half of the 2D flake is picked up by a sticky stamp and rotated to a certain angle θ . The rotated section is then released onto the surface of the remaining half, resulting in a twisted angle of θ (Kim, 2017). To improve the success rate of this method, the AFM tip can be used to divide 2D flakes into two sections before the stack process. This method offers high accuracy and the error is only induced by the transfer stage. However, the method is not suitable for stack alignment beyond two layers.

Armchair (zigzag) direction of TMD materials can be determined through polarization-resolved SHG for its intensity varies according to the angle between the incident laser polarization and the armchair direction, as illustrated in Fig. 16.13A–C (Hsu et al., 2014; Wang & Qian, 2017). Armchair (zigzag) direction can be labeled on

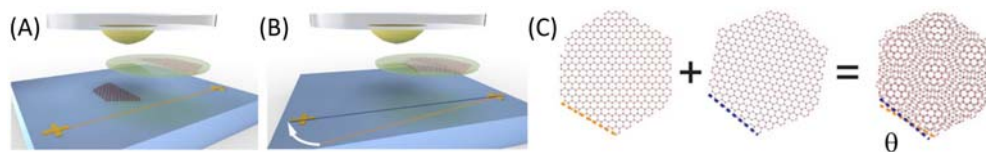


Figure 16.12 Scheme of “tear and stack” process. (A) and (B) Pick-up of a graphene segment using a hemispherical transfer stamp and pick-up of the other segment after substrate rotation. (C) Schematic illustration of the Moiré pattern formation as a result of the twist angle between the two layers. From Kim, K. (2017). *Tunable moire bands and strong correlations in small-twist-angle bilayer graphene*. Proceedings of the National Academy of Sciences USA, 114, 3364–3369.

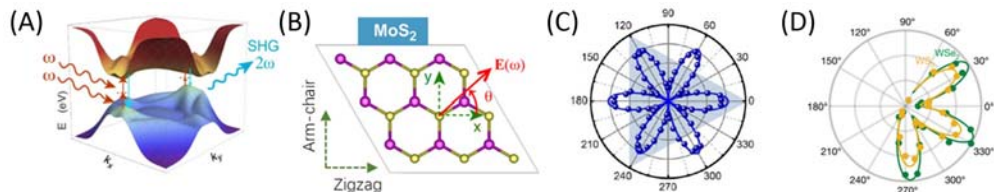


Figure 16.13 Alignment with second-harmonic generation (SHG). (A) Scheme of the generation of SHG. (B) MoS_2 crystal with armchair and zigzag edges. (C) The polarization-dependent SHG signal measured on the monolayer MoS_2 . (D) The polarization-dependent SHG signal measured on the monolayer WSe_2 and WS_2 . (A and B) From Wang, H., & Qian, X. (2017). Giant optical second harmonic generation in two-dimensional multiferroics. *Nano Letters*, 17(8), 5027–5034. <https://doi.org/10.1021/acs.nanolett.7b02268>; (C) Hsu, W. T., Zhao, Z. A., Li, L. J., Chen, C. H., Chiu, M. H., Chang, P. S., Chou, Y. C., & Chang, W. H. (2014). Second harmonic generation from artificially stacked transition metal dichalcogenide twisted bilayers. *ACS Nano*, 8(3), 2951–2958. <https://doi.org/10.1021/nn500228r>; (D) Jin, C., Regan, E. C., Yan, A., Iqbal Bakti Utama, M., Wang, D., Zhao, S., Qin, Y., Yang, S., Zheng, Z., Shi, S., Watanabe, K., Taniguchi, T., Tongay, S., Zettl, A., & Wang, F. (2019). Observation of Moiré excitons in WSe_2/WS_2 heterostructure superlattices. *Nature*, 567(7746), 76–80. <https://doi.org/10.1038/s41586-019-0976-y>.

the photograph under a microscope and used to control the twist angle. Experimental observation of Moiré excitons has been successfully achieved in WSe_2/WS_2 heterostructures with controllable twist angles by polarization-dependent SHG generation measurements, as demonstrated in Fig. 16.13D (Jin et al., 2019).

Mark can be used to facilitate the alignment. During the alignment process, the angle between interlayer marks determines the twist angle. For instance, a single crystalline MoS_2 grown on a sapphire wafer was cut into rectangular slides by a linear guided wafer scribe. As the entire MoS_2 film is oriented, the edges of the slides can serve as line marks to determinate the interlayer twist angle (Liao, 2020). Contrary to the “tear and stack,” this method provides a simple way to realize alignment for large-area multilayer-stacking, which can be easily applied in real industry. The error in twist angle mainly depends on the alignment process under the telescope and the cut procedure (i.e., whether the edges of slices are linear enough). It should be noted that the cut procedure can damage 2D materials. In addition, some CVD samples exhibit regular triangle-shaped domains on the substrate. The edges of the triangle can also be used to achieve alignment (Rosenberger et al., 2020).

To improve the accuracy of the alignment process, femtosecond laser machining precision was used to cut 2D materials and the “cutting line” can serve as a mark. As Fig. 16.14A describes, single-crystal graphene is cut into two pieces by femtosecond laser, with a pair of straight and parallel edges. And these parallel “cutting lines” were used as marks to control twist angles (Chen, Xin, et al., 2016). Fig. 16.14B exhibits the bilayer graphene with a twist angle of 13 degrees by the method. Notably, even though it took an extra step to create a line mark and involves the use of expensive

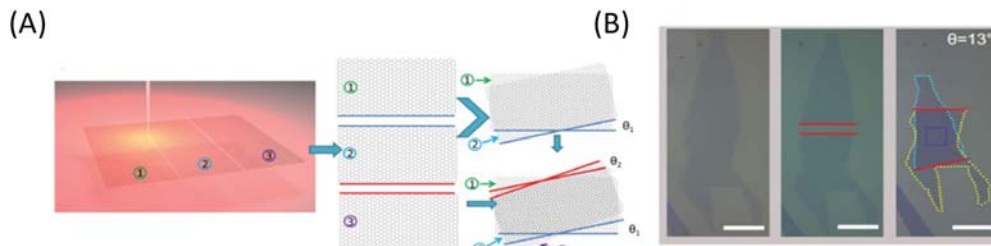


Figure 16.14 Alignment with mark. (A) Schematic of alignment method by laser. (B) Optical images of the laser process. From Chen, X. D., Xin, W., Jiang, W. S., Liu, Z. B., Chen, Y. S., & Tian, J. G. (2016). *High-precision twist-controlled bilayer and trilayer graphene*. *Advanced Materials*, 28(13), 2563–2570. <https://doi.org/10.1002/adma.201505129>.

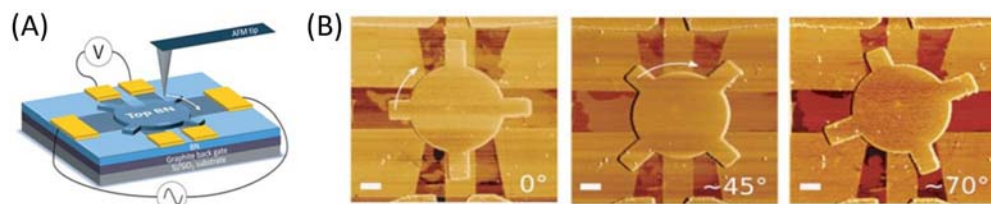


Figure 16.15 Dynamical alignment. (A) Scheme of atomic force microscopy (AFM)-tip manipulation process for dramatically modifying twist angle between lower graphene and upper BN. (B) AFM images of BN/graphene stack at different twist angles. From Ribeiro-Palau, R., Zhang, C., Watanabe, K., Taniguchi, T., Hone, J., & Dean, C. R. (2018). *Twistable electronics with dynamically rotatable heterostructures*. *Science*, 361(6403), 690–693. <https://doi.org/10.1126/science.aat6981>.

equipment, the laser-cutting approach features contamination-free operation. The deviations of the determined angles from the designated twist angles are claimed to be less than 0.1 degree.

Dynamically alignment provides a way to fabricate a Moiré pattern in which the period can be dynamically tuned. The approach can be achieved through AFM-tip manipulation. As Fig. 16.15A shows (Ribeiro-Palau et al., 2018), a BN flake etched into a Hall bar shape is placed on graphene. The Twist angle between them can be dynamically controlled using the AFM tip. A range of twist angles has been successfully achieved within a single heterostructure device, as depicted in Fig. 16.15B. This approach enables the optical, mechanical, and electronic properties of the twisted system to be dynamically tuned. The shortcoming is that it acquires costly equipment, labor-intensive operation and extra lithography process which can induce contamination and defects to 2D materials.

In summary, the “tear and stack” method is widely used for fabricating twisted bilayer 2D materials from a single crystalline 2D flake. However, this method is not suitable for creating bilayer heterostructures and multilayer twisted stacks.

SHG measurement is a contamination-free method that can be used to determine the armchair (zigzag) direction of TMD flakes, which can aid in achieving alignment. Mark alignment holds the potential for industrial adoption as it is suitable for large-area 2D films grown on a wafer. Dynamically aligning 2D stacks serves as an excellent research platform, although it involves a complicated fabrication process. However, achieving a contamination-free interface and precise alignment remains a challenge to be addressed.

16.3 Characterization

2D materials can be utilized to form homojunctions or heterojunctions by twisting and stacking them. In particular, parameters such as composition, layer number, and twisting angle of the two-dimensional materials will significantly impact the electrical and optical properties of the homojunction or heterojunction. Additionally, the quality, surface roughness, and presence of residue or damage in homojunctions and heterojunctions are influenced by different preparation methods. Therefore, it is essential to investigate the characteristics and features of two-dimensional homojunctions and heterojunctions using various technical means, in order to elucidate the structure-activity relationship between them.

16.3.1 X-ray diffraction

In essence, X-ray diffraction (XRD) is based on the concept that when a beam of X-rays with a single wavelength is directed towards a crystal, the atoms within the crystal will scatter the X-rays in various directions. This scattering creates a pattern of interference that is dependent on the spatial arrangement of the atoms in the crystal. When the interference is particularly strong in certain directions, it results in a phenomenon known as XRD. The distribution, orientation, and intensity of this diffraction are closely linked to the crystal's structure. Therefore, XRD is a useful tool for identifying crystal phases, determining lattice parameters, measuring microscopic stresses, and assessing crystallinity.

Mikhail Chubarov et al. (2018) pointed out that in the measurement of 2D thin film materials using XRD, the thin film cannot be evaluated by pole map measurement along the [000] direction due to lack of continuity. However, periodicity is still present in the (0001) plane, which allows the use of diffraction techniques to determine the epitaxial relationship between the film and the substrate in the (hkl0) plane. For in-plane diffraction, the incident X-ray plane needs to be adjusted to nearly coincide with the sample surface plane, typically at an angle of less than 1° from the surface to the beam. This diffraction technique can be applied to the study of 2D materials for the determination of their structure and epitaxial relationship. Fig. 16.16A shows the

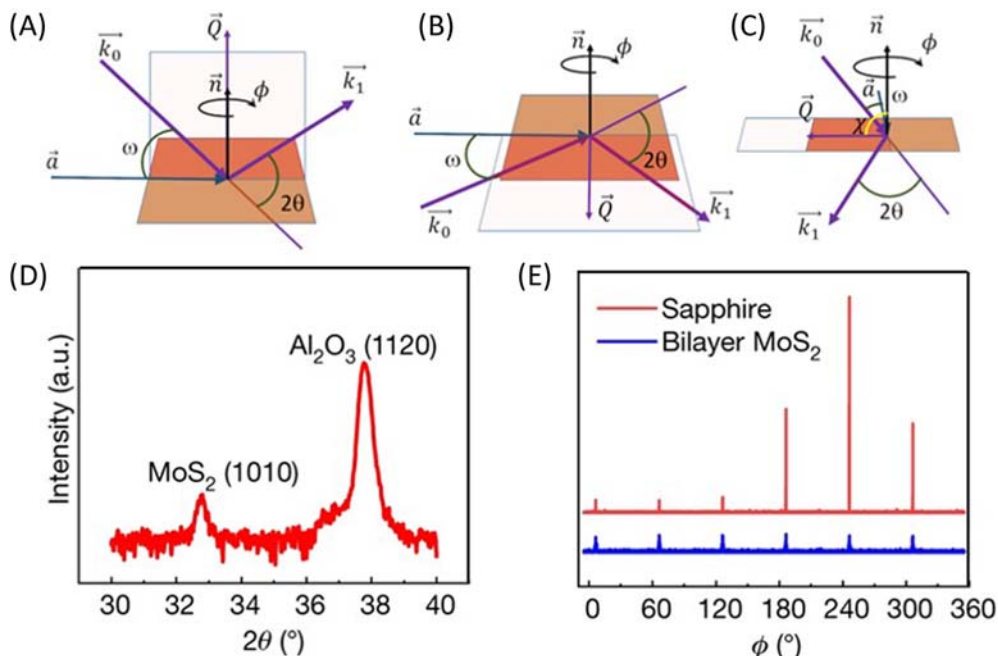


Figure 16.16 Applications of X-ray diffraction (XRD) in two-dimensional materials. (A) Bragg–Brentano measurement geometry. (B) and (C), In-plane measurement geometry from two perspectives. (D) In-plane XRD θ – 2θ diffractogram. (E) In-plane XRD φ scan of the (100) planes of MoS₂ and the (110) planes of α -Al₂O₃. (A and B) From Duong, D. L., Yun, S. J., & Lee, Y. H. (2017). *Van der Waals layered materials: Opportunities and challenges*. ACS Nano, 11(12), 11803–11830. <https://doi.org/10.1021/acsnano.7b07436>; (C and D) Liu, L., Li, T., Ma, L., Li, W., Gao, S., Sun, W., Dong, R., Zou, X., Fan, D., Shao, L., Gu, C., Dai, N., Yu, Z., Chen, X., Tu, X., Nie, Y., Wang, P., Wang, J., Shi, Y., & Wang, X. (2022). *Uniform nucleation and epitaxy of bilayer molybdenum disulfide on sapphire*. Nature, 605(7908), 69–75. <https://doi.org/10.1038/s41586-022-04523-5>; (E) Kang, K., Lee, K. H., Han, Y., Gao, H., Xie, S., Muller, D. A., & Park, J. (2017). *Layer-by-layer assembly of two-dimensional materials into wafer-scale heterostructures*. Nature, 550(7675), 229–233. <https://doi.org/10.1038/nature23905>.

schematic representation of the Bragg–Brentano measurement geometry, while Fig. 16.16B and c illustrate the principle of in-plane diffraction.

Liu, Li, Ma, et al. (2022) used in-plane XRD to investigate MoS₂ grown on the surface of an α -Al₂O₃ substrate. They observed the diffraction peaks of MoS₂(100) and α -Al₂O₃(110) at the same φ angle, which indicated an epitaxial relationship between MoS₂(100) and α -Al₂O₃(110), as shown in Fig. 16.16C and D. Additionally, they observed sixfold symmetry for both bilayer MoS₂ and sapphire via φ -scanning around the surface normal, leading to the confirmation of a clear R30 degrees epitaxial relationship between bilayer MoS₂ and c-plane sapphire. Kibum Kang et al. (2017) concluded that the relative signal intensity of XRD can be used to assess the coherence and interfacial cleanliness of 2D materials. This technique can be employed to

evaluate the structure and quality of 2D materials under different conditions, providing valuable guidance for the preparation and application of these materials.

16.3.2 Raman effect

The Raman effect is observed when a sample is irradiated with monochromatic light that has a wavelength much smaller than the particle size of the sample, as shown in Fig. 16.17A. In this effect, several weak Raman spectral lines appear, shifted in frequency relative to the incident light, as shown in Fig. 16.17B. The number of these lines, the size of the shift, and the length of the spectrum are all related to the molecular vibration or rotation energy level of the sample. Raman spectroscopy can be used to analyze various properties of the sample, such as its chemical structure, the structure

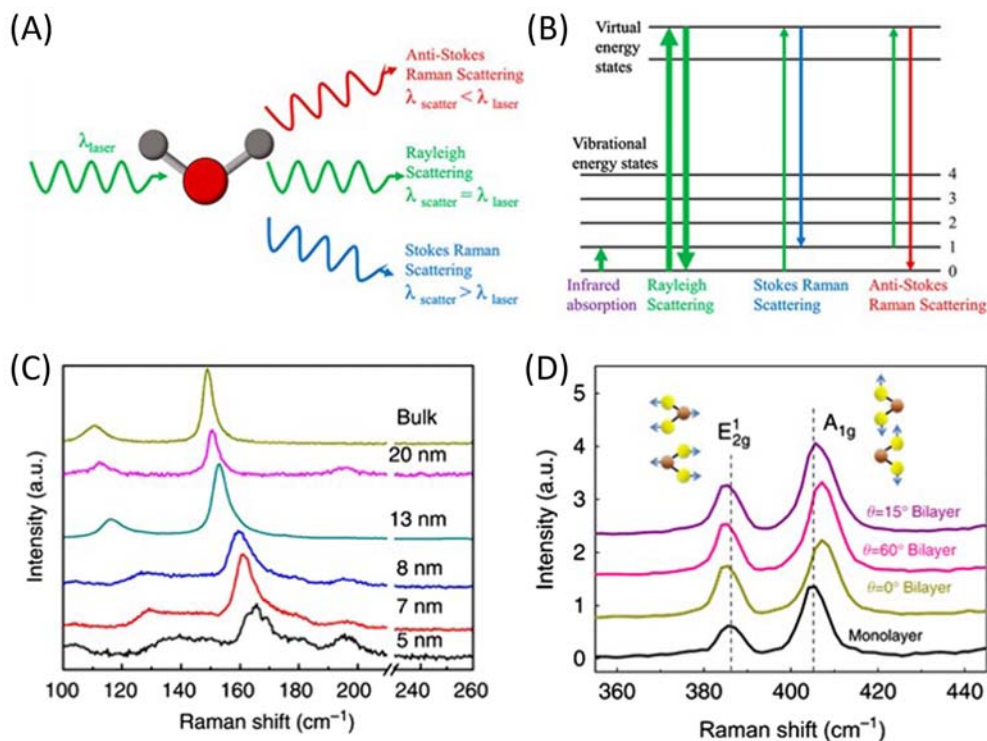


Figure 16.17 Applications of Raman in twisted two-dimensional homojunction/heterojunction. (A) Raman scattering and Rayleigh scattering. (B) Energy level diagram of Raman scattering, Rayleigh scattering and infrared absorption. (C) Raman spectra of antimonene polygons with thicknesses varying from 5 nm to bulk. (D) Raman spectra of a MoS_2 monolayer and bilayers with twist angles of $\theta = 0, 15,$ and 60 degrees. (C) From Ji, J. (2016). Two-dimensional antimonene single crystals grown by van der Waals epitaxy. *Nature Communications*, 7(1); (D) Liu, K., Zhang, L., Cao, T., Jin, C., Qiu, D., Zhou, Q., Zettl, A., Yang, P., Louie, S. G., & Wang, F. (2014). Evolution of interlayer coupling in twisted molybdenum disulfide bilayers. *Nature Communications*, 5. <https://doi.org/10.1038/ncomms5966>.

of aggregated states, crystallographic changes, defects, surface composition distribution, depth composition distribution, and stress relaxation, among others.

Liu et al. (2014) found that the effective interlayer mechanical coupling strength of MoS₂ bilayers can be characterized by the difference ($\omega_A - \omega_E$) between the two peaks of the in-plane E_{2g1} and out-of-plane A_{1g} phonon modes, as shown in Fig. 16.17D. The greater the separation, the stronger the coupling strength. By analyzing the Raman peak separation versus twist angle in 44 MoS₂ bilayers, they observed that AA or AB stacks have the strongest coupling, whereas other twist angles have weaker but constant couplings.

Quan et al. (2021) demonstrated that the Raman spectra show little variation with the twist angle in both the relaxed ($0^\circ \leq \theta < 2^\circ$) and rigid ($\theta \geq 6^\circ$) states. However, in the transition region ($2^\circ \leq \theta < 6^\circ$), the low-frequency interlayer shear (S) and layer breathing (LB) modes exhibit rapid evolution with the twist angle. This evolution is caused by the lattice reconstruction and the ultra-strong coupling of different phonon modes. TBL Raman spectroscopy can be used to infer the twist angle and supercell size, providing a powerful and straightforward spectroscopic technique to characterize Moiré crystals. Jianping Ji (2016) discovered that the E_g and A_{1g} peak frequencies of few-layered antimonene were higher than those of bulk antimony, as shown in Fig. 16.17C. This shift in frequency was caused by a reduction in the number of layers or a weakening of the long-range Coulomb interaction between layers, resulting in a smaller lattice constant. As the thickness of the sample decreased, the frequency difference decreased in a monotonic manner. This finding suggests that the frequency difference can be used as a straightforward method to estimate the thickness of antimonene.

16.3.3 Photoluminescence

The underlying mechanism of photoluminescence (PL) involves the absorption of photons by a substance, which causes it to transit to a higher energy level or excited state, as shown in Fig. 16.18A. Subsequently, the substance returns to its lower energy state and releases photons. PL is a noninvasive and highly responsive analytical technique that can offer insights into the structure, composition, and atomic arrangement of materials by analyzing their band gap, luminescence wavelength, and other properties.

Liu et al. (2014) employed PL spectroscopy to investigate the changes in electronic coupling in MoS₂ bilayers with varying degrees of twisting, as shown in Fig. 16.18B. Their findings suggest that the energy level of the indirect band gap (peak II) directly reflects the strength of the interlayer electronic coupling, with a lower energy level indicating stronger coupling. The bilayers with AA and AB stacking exhibit the lowest peak II energies, indicating the strongest coupling, whereas all other twist angles show

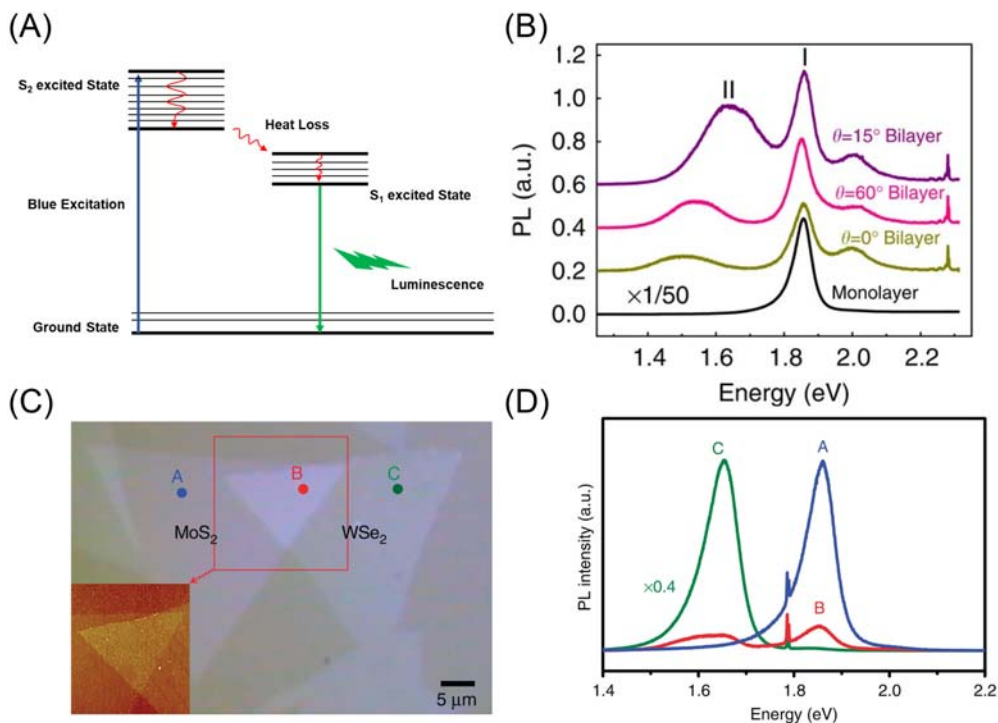


Figure 16.18 Hotoluminescence of TMD two-dimensional materials. (A) Typical photoluminescence (PL), where blue photons are absorbed and red photons are emitted. (B) PL spectra of MoS₂ monolayer and bilayers with twist angles of $\theta = 0, 15$ and 60 degrees. (C) Optical micrograph and atomic force microscopy images of WSe₂/MoS₂ heterostructure. (D) PL spectra for the selected sites including MoS₂, WSe₂, and WSe₂/MoS₂ stacked areas. (B) From Liu, K., Zhang, L., Cao, T., Jin, C., Qiu, D., Zhou, Q., Zettl, A., Yang, P., Louie, S. G., & Wang, F. (2014). Evolution of interlayer coupling in twisted molybdenum disulfide bilayers. *Nature Communications*, 5. <https://doi.org/10.1038/ncomms5966>; (C and D) Chiu, M.-H. (2015). Determination of band alignment in the single-layer MoS₂/WSe₂ hetero-junction. *Nature Communications*, 6(1).

higher but relatively constant values. These results suggest that interlayer electronic coupling is significant for all twist angles but most pronounced in AA or AB stacked MoS₂ bilayers. Xiumei Zhang et al. demonstrated that the interlayer interactions in AA-stacked materials are significantly weaker than in AB-stacked materials. Meanwhile, Ming-Hui Chiu (2015) used PL to study the WSe₂/MoS₂ heterostructure and observed that the PL intensity of both MoS₂ and WSe₂ in the overlapping region is notably lower than that of individual WSe₂ or MoS₂, as shown in Fig. 16.18C and D. These findings suggest that photoexcited carriers take other pathways instead of being emitted from the edges of individual WSe₂ or MoS₂ bands.

16.3.4 Second-harmonic generation

SHG is a nonlinear optical effect that results from the interaction between matter and intense light, as shown in Fig. 16.19A. SHG is highly sensitive to the symmetry of few-layer 2D materials. Noncentrosymmetric materials inherently exhibit SHG signals, while the SHG signals of centrosymmetric materials change with the number of atomic layers. Generally, the SHG signal of odd-layered materials is enhanced, whereas the SHG signal of even-layered materials disappears, resulting in fluctuating changes in the wave signal. Thus, different stacking methods, layer numbers, and interlayer stacking angles of materials can be characterized using SHG, with the signals displaying varying relative intensities.

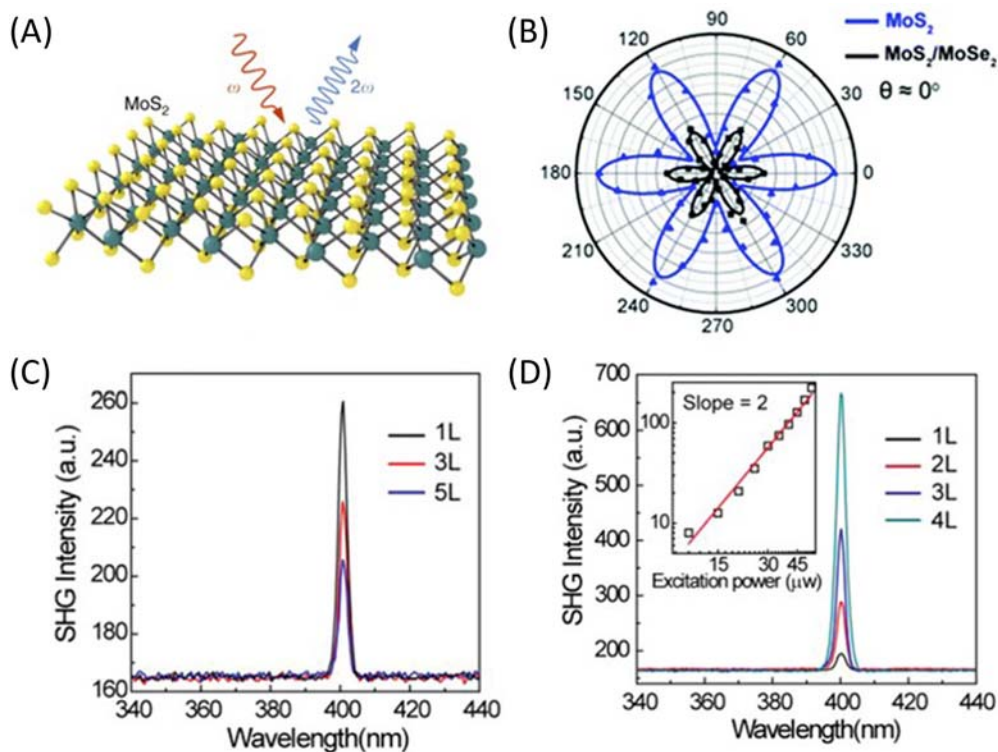


Figure 16.19 *Second harmonic generation two-dimensional homojunction/heterojunction.* (A) Schematic illustration of the second-harmonic generation (SHG) process. (B) SHG of the MoS₂ monolayer region and MoS₂/MoSe₂ bilayer region, respectively. (C) and (D), Layer number-dependent SHG spectra of 3R and 2H phase WS₂. (B) From Cai, Q., Ju, Q., Hong, W., Jian, C., Wang, T., & Liu, W. (2022). Water assisted growth of two-dimensional MoS₂/MoSe₂ vertical heterostructures on molten glass. *Nanoscale*, 14(5), 1990–1996. <https://doi.org/10.1039/d1nr08095d>; (C) and (D) Zeng, Z. (2019). Controlled vapor growth and nonlinear optical applications of large-area 3R phase WS₂ and WSe₂ atomic layers. *Advanced Functional Material*, 29(11).

Cai et al. (2022) utilized SHG to assess the MoS₂/MoSe₂ double-layer heterojunction, and identified an interlayer twist angle of approximately 0 degree, as shown in Fig. 16.19B. The SHG intensity of this 2H stacking configuration did not completely vanish, potentially due to the presence of small crystals arising from periodic lattice repetition between MoSe₂ and MoS₂ despite lattice mismatch. Similarly, Sandhya and colleagues employed SHG to determine the twist angle of WS₂/WSe₂ nanosheet heterojunction, which was found to be 0.09 ± 0.23 degrees.

Zeng (2019) conducted a study on the SHG signal intensity of the 3R phase and 2H phase of WS₂ with different numbers of layers, as shown in Fig. 16.19C and D. They discovered an exponential relationship between the SHG signal intensity of the 3R phase and the number of layers due to the noncentrosymmetric structure of the 3R phase. In contrast, the signals in the even-numbered layers of the 2H phase vanished, and the signal strength of the odd-numbered layers gradually weakened with an increase in the number of layers. This occurs because the offset causes the signal to disappear in the even-numbered layers. In the case of odd layers, since the signal of the N-1 layer disappears, the SHG signal from 2H phase WS₂ tends to weaken the oscillations, with single-layer maxima and disappearance occurring in even-numbered layers. Shi (2017) and Liu et al. (2020) have conducted studies that also confirm the rule that SHG can rapidly identify the number of stacked layers and twist angles of 2D materials. The unique characteristics of SHG make it a valuable tool in advancing research on the structure and physical properties of two-dimensional materials.

16.3.5 Scanning electron microscope—back-scattered electron channeling contrast imaging

Electron channeling contrast imaging (ECCI) is a technique that utilizes the difference in backscattered electron intensity resulting from the relative orientation between the crystal lattice and incident electron beam. This method generates images with varying gray levels depending on the orientation, as illustrated in Fig. 16.20A. ECCI is a powerful tool for examining crystal defects such as dislocations, stacking layer dislocations, and twin boundaries.

Andersen et al., 2021 used scanning electron microscopy to investigate the Moiré pattern of bilayer graphene and found that the intensity of secondary electrons displayed a 120 degrees periodic oscillation with the rotation of the platform azimuth angle, with a 60 degrees phase shift between the two domain types, as shown in Fig. 16.20B. The authors attribute the observed domains to different levels of electron conduction through the AB layer and BA layer graphene domains. They explain that when the incoming electron beam is parallel to open cavities, or “channels,” within the atomic lattice, these channels occur at the specific polarity and azimuthal angles (θ), which allow electrons to travel through the material with minimal scattering.

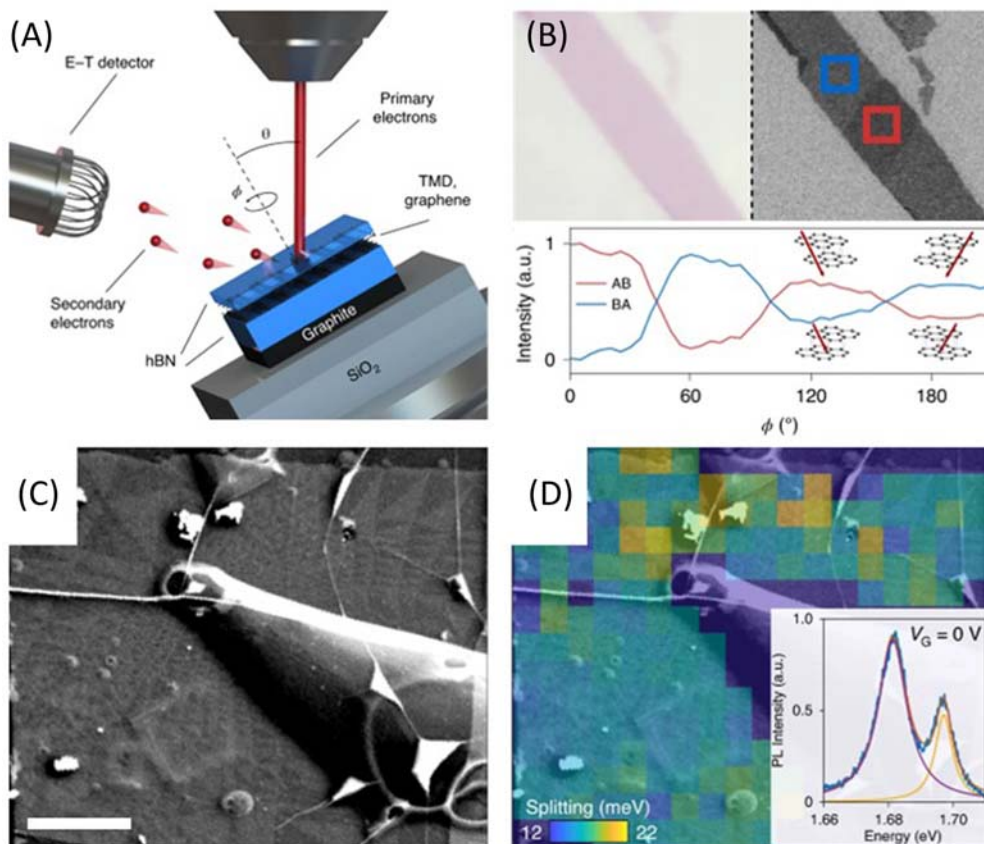


Figure 16.20 Scanning electron microscopy (SEM)-based imaging of stacking order in twisted two-dimensional homojunction/heterojunction. (A) Schematic of operating principle. (B) Optical and SEM images of a natural bilayer graphene, Dependence of the SEM signal on ϕ in the boxed locations in SEM. (C) SEM image of reconstructed Moiré domains in the entire twisted bilayer region, scale bars, 1 μm . (D) Map of extracted exciton-peak splitting overlaid with the SEM image from (C). From Andersen, T. I., Scuri, G., Sushko, A., De Greve, K., Sung, J., Zhou, Y., Wild, D. S., Gelly, R. J., Heo, H., Berube, D., Joe, A. Y., Jauregui, L. A., Watanabe, K., Taniguchi, T., Kim, P., Park, H. & Lukin, M. D. (2021). Excitons in a reconstructed Moiré potential in twisted WSe₂/WSe₂ homobilayers. *Nature Materials*, 20(4), 480–487. <https://doi.org/10.1038/s41563-020-00873-5>.

The optimal channel conditions arise when j is aligned with one of the three in-plane displacement vectors between the top and bottom layers, resulting in the observed 120 degrees of periodicity and 60 degrees relative angle between the AB and BA domains. In addition, SEM was combined with PL to explore the dependence between the size of the Moiré domain and the exciton multiplets in the twisted homojunction. Weston et al. also used scanning electron microscopy to achieve large molar period imaging of graphene/MoS₂, with a measurement accuracy of less than 0.1 degree.

The electron channel contrast imaging technique does not require the sample to be electron transparent, which is different from transmission electron microscopy (TEM). This means that a larger area of the sample can be imaged and analyzed using electron channel contrast imaging, making the results more statistically significant. However, the optimal test parameters for electron channel contrast imaging can vary depending on the material being analyzed, as well as the electron beam energy, working distance, convergence angle, and detector position. These variables can significantly affect the accuracy and reliability of the detection results.

16.3.6 Transmission electron microscope

Selected area electron diffraction (SAED) is a technique that employs an aperture to select a specific area of a sample for imaging. The selected-area aperture blocks the electron beam outside the selected area, allowing only the imaging electron beam from the micro-region of the sample within the aperture hole to pass through. The resulting electron diffraction patterns observed on the fluorescent screen only correspond to the crystal structure within the selected area. This technique can be used to determine the twist angle of two or more layers of 2D stacks based on the diffraction pattern obtained.

Liu, Li, Qiao, et al. (2022) utilized SAED to determine the twist angle of graphene grown on bilayer Cu and confirmed the results by high-resolution TEM (HR-TEM), as shown in Fig. 16.21A–C. SAED has limitations due to the addition of double symmetry, making specific twist angles uncertain, and thus necessitating confirmation through complementary means. HR-TEM operates on the principle that when the transmission beam and at least one diffraction beam pass through the objective aperture simultaneously and interfere with each other, a streak image and a structural image that reflects the period of the crystal lattice are formed. However, this means that only nanometer-sized regions can be imaged. Rouviere (2007) proposed that HR-TEM can measure stresses in materials, which is essential for studying the interaction forces between layers of 2D materials.

The process of SAED involves using an objective aperture to select a beam of diffracted light for imaging, resulting in a dark field image. This type of image is particularly sensitive to electron diffraction angles and crystal orientation alignment. Yoo et al. (2019) were able to use SAED to achieve imaging of the Moiré period of double-layer TBG, combining it with dark-field imaging, as shown in Fig. 16.21D–F. This revealed a relationship between twist angle and period, whereby a large period corresponds to a small twist angle. Butz et al. (2014) also discovered that the shape of the Moiré patterns varies depending on which diffraction spots are chosen for dark-field imaging, and tilting the sample rod can affect both the shape and contrast of the Moiré pattern. The period of the dark field image plays a crucial role in determining

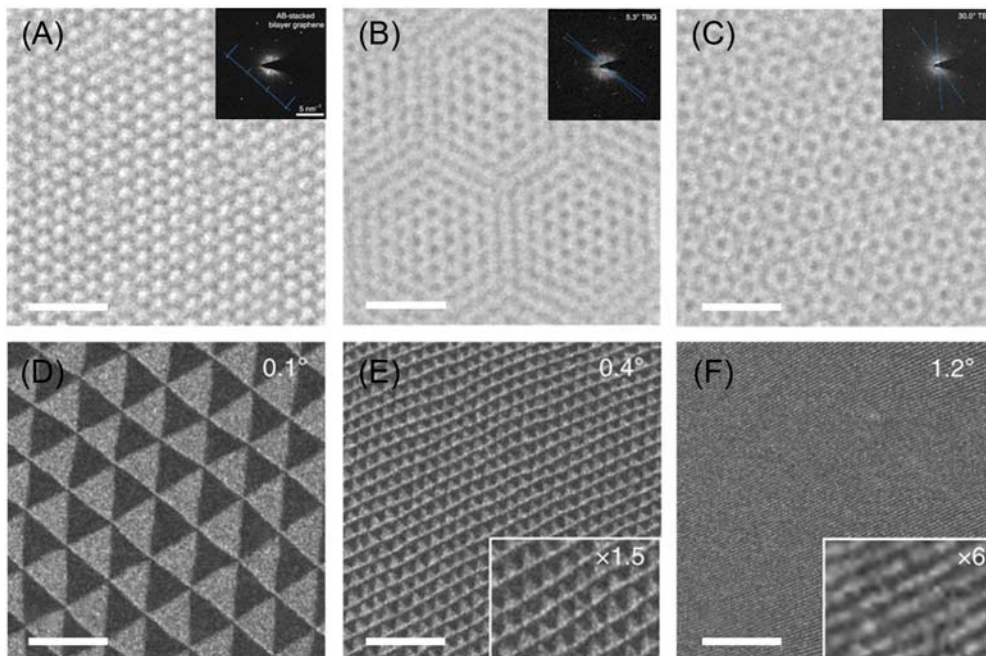


Figure 16.21 Transmission electron microscopy (TEM)-based imaging of stacking order in twisted two-dimensional homojunction/heterojunction. (A)–(C) HRTEM images and SAED patterns of TBG with the designed twist angles α of 0, 5, and 30 degrees, respectively, scale bars, 1 nm. (D)–(F) TEM dark-field images obtained by selecting the graphene diffraction peak ($g = 1010$) in TBG with the designed twist angles α of 0.1, 0.4, and 1.2 degrees, respectively, scale bars, 200 nm. From Liu, C., Li, Z., Qiao, R., Wang, Q., Zhang, Z., Liu, F., Zhou, Z., Shang, N., Fang, H., Wang, M., Liu, Z., Feng, Z., Cheng, Y., Wu, H., Gong, D., Liu, S., Zhang, Z., Zou, D., Fu, Y., . . . , & Liu, K. (2022). Designed growth of large bilayer graphene with arbitrary twist angles. *Nature Materials*, 21(11), 1263–1268. <https://doi.org/10.1038/s41563-022-01361-8>.

the twist angle using SAED, and while large periods can be imaged with good contrast, there are challenges in imaging small periods of just a few nanometers.

16.3.7 Scanning transmission electron microscopy

The scanning transmission electron microscope (STEM) can produce different types of images depending on the angle of electron distribution collected, as shown in Fig. 16.22A. These include bright field (BF)-STEM images, annular dark field (ADF)-STEM images, and high-angle annular dark field (HAADF)-STEM images. ADF-STEM imaging mainly involves scattered electrons and some Bragg electrons, resulting in an image similar to that produced by dark field (DF)-TEM. However, ADF-STEM uses an annular receiver, which allows it to accept more diffraction beams, making it more efficient in selecting a diffraction beam for imaging than DF-TEM. In contrast,

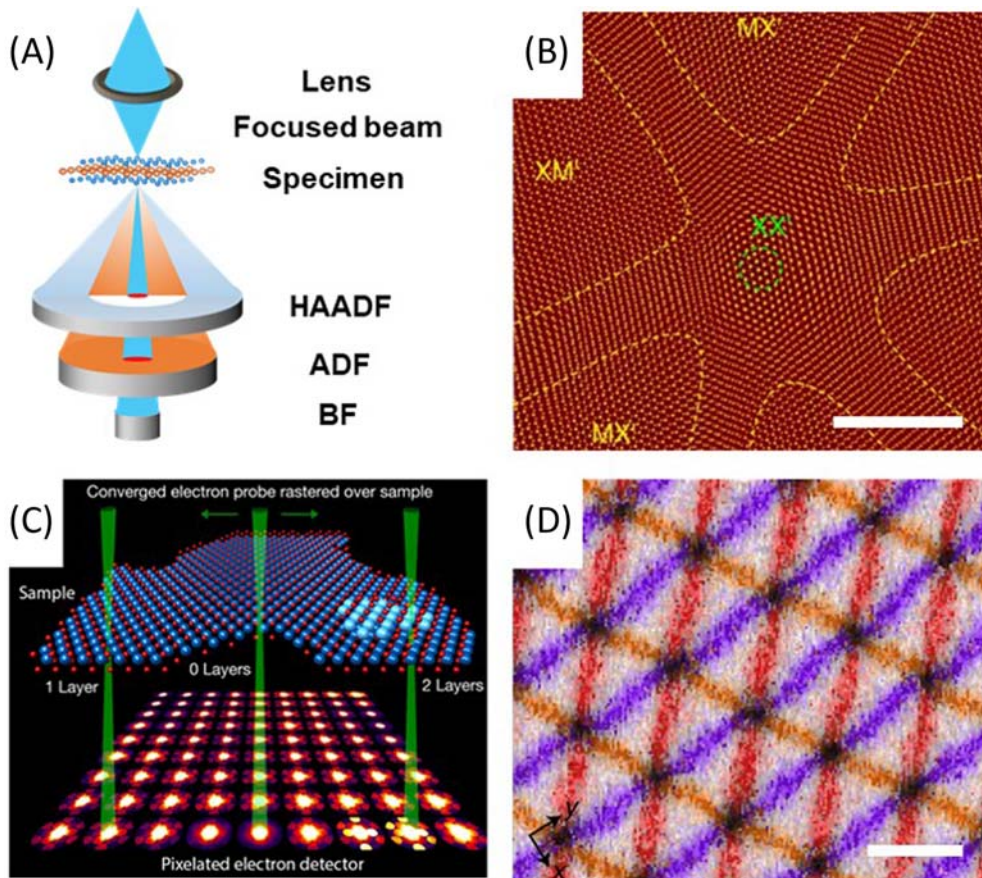


Figure 16.22 *Scanning transmission electron microscopy (STEM)-based imaging of stacking order in twisted two-dimensional (2D) homojunction/heterojunction.* (A) Schematic diagram of STEM signal collection. (B) The lattice reconstruction in P-WSe₂ for a twist angle of $\theta = 1.29$ degrees, scale bar, 5 nm. (C) Schematic diagram of 4D-STEM signal generation. (D) Displacement field maps for TBG at $\theta = 0.63$ degrees, scale bars, 20 nm. (B) From Weston, A., Zou, Y., Enaldiev, V., Summerfield, A., Clark, N., Zolyomi, V., Graham, A., Yelgel, C., Magorrian, S., Zhou, M., Zultak, J., Hopkinson, D., Barinov, A., Bointon, T. H., Kretinin, A., Wilson, N. R., Beton, P. H., Fal'ko, V. I., Haigh, S. J., & Gorbachev, R. (2020). Atomic reconstruction in twisted bilayers of transition metal dichalcogenides. *Nature Nanotechnology*, 15(7), 592–597; (D) Kazmierczak, N. P., Van Winkle, M., Ophus, C., Bustillo, K. C., Carr, S., Brown, H. G., Ciston, J., Taniguchi, T., Watanabe, K., & Bediako, D. K. (2021). Strain fields in twisted bilayer graphene. *Nature Materials*, 20(7), 956–963. <https://doi.org/10.1038/s41563-021-00973-w>.

HAADF-STEM collects mainly inelastically scattered electrons, making it useful for imaging elements with large atomic numbers in materials. It has been shown that the image contrast in HAADF-STEM is positively correlated with the square of the atomic number, ranging from 1.4 to 2.

Weston et al. (2020) utilized ADF-STEM to examine the Moiré period of stacked WS_2/WS_2 and $\text{MoS}_2/\text{MoS}_2$ structures at various angles. Their research revealed that the atoms were arranged differently in AA and AB stacks, as shown in Fig. 16.22B. Furthermore, they observed significant differences in Moiré patterns between centrosymmetric and noncentrosymmetric stacking. Compared to TEM, ADF-STEM allows for continuous adjustment from a micron to an atomic field of view and offers greater versatility. Both ADF-STEM and HAADF-STEM can be used for atomic imaging, which is crucial in studying the structural changes of 2D materials during stacking at the atomic scale. Different research groups, such as Li, Song, et al. (2021) and Weston et al. (2020), have conducted extensive studies on this technology and found that different elemental materials require exploring the appropriate collection angle independently.

STEM can also be equipped with spectroscopic detectors such as energy dispersive X-ray spectroscopy and electron energy loss spectroscopy (EELS) to identify elemental species and analyze chemical valence states, which are important for establishing physical property relationships. Susarla et al. (2022) employed a combination of ADF-STEM and EELS to investigate intralayer excitons in WS_2/WSe_2 molar superlattices. By integrating spectroscopy and ab initio calculations, they determined that the exciton center-of-mass wave function was confined to a radius of approximately 2 nm around the highest energy stacking position in the molar cell. This indicates that atomic reconfiguration leads to a strongly confined molar potential, which implies that novel excitonic lattices could potentially be prepared by engineering strain at the nanoscale.

In contrast to conventional STEM detection methods, 4D-STEM records all BF, ABF, ADF, HAADF, and differential phase contrast (DPC) signals instead of only specific scattering angles, as shown in Fig. 16.22C. This allows for more sample information to be obtained as a “virtual” detector is used for image analysis. By adding a virtual detector to the convergent beam diffraction pattern to capture the appropriate range of data, more information such as the structure of the material, orientation of the crystal, stress or strain distribution, electric or magnetic field distribution and integrated DPC (iDPC) images can be obtained. Even the spatial resolution can be further improved by the method of stacked diffraction imaging (ptychography). Kazmierczak et al. (2021) used 4D-STEM to achieve stress detection in bilayer graphene with a twist angle of 0.63 degrees molar period, as shown in Fig. 16.22D. The large-area stress detection analysis is not possible with conventional HR-TEM, ADF-STEM and HAADF-STEM techniques. Nathanael P. Kazmierczak et al. (2021) used 4D-STEM to measure the local pm-scale in-plane lattice distortion as well as the distortion direction and the average interlayer spacing in the bilayer and trilayer graphene. Compared with several other (S)TEM modes, 4D-STEM has significant advantages, but there are problems with higher performance detectors and excessive experimental data, which make the use cost higher.

16.3.8 Atomic probing technique

16.3.8.1 Scanning tunneling microscope

The basic principle of the scanning tunneling microscope (STM) is illustrated in Fig. 3.8C, in which the fine probe and the surface of the substance serve as the two electrodes, and electrons flow to another electrode under the electric field. The quantum tunneling effect in the nano-gap between the tip of the needle and the sample surface is produced by the exponential relationship between the tunnel current and the gap size. In Fig. 3.8G (Nieken, 2022), a 12 nm Moiré pattern in an H-type device of the $\text{WSe}_2/\text{MoSe}_2$ heterostructure is shown, consistent with prior results and calculations (Carr et al., 2018; Huang et al., 2021; Lv, 2022). Tilak et al. (2023) also employed STM and PFM simultaneously to study Moiré patterns and obtained similar results. In recent years, several studies have reported similar findings (Pan et al., 2018; Wong et al., 2015; Zhang et al., 2020). STM provides atomic resolution, allowing scientists to visualize and study surface structures at the atomic scale. However, unlike CAFM and PFM, STM measurements must be carried out under vacuum and low-temperature conditions. Despite this limitation, STM has opened new avenues for characterizing 2D materials.

16.3.8.2 Atomic force microscope

The piezoelectric and conductive atomic force microscope (AFM) have become an essential tool for characterizing Moiré pattern in twisted 2D stack. Fig. 3.8A schematically illustrates the piezoelectric AFM (PFM), which enables the detection of local electromechanical responses, such as the electro-induced deformation variable and deformation direction of the sample under the influence of an applied voltage. The PFM technique is capable of detecting both out-of-plane displacement and in-plane displacement, which can be detected by a photodetector referred to as the vertical mode (Fig. 16.23A red line) and the lateral mode (Fig. 16.23A blue line) respectively. In recent years, researchers have employed this technology to study Moiré patterns of van der Waal heterostructures, particularly those with small twist angles. Irrespective of the Moiré pattern's origin, McGilly et al. (2020) have clearly demonstrated the existence of an alternating triangle Moiré pattern in multiple systems, such as the graphene-h-BN heterostructure (Fig. 16.23D red line) and the twisted bilayer WSe_2 (Fig. 16.23D blue line). This result confirms the PFM technology's universality and high resolution (<5 nm) in imaging. Similar observations have been made in twisted double bilayer grapheme (Li, 2021). The application of PFM technology enables the piezoelectric effects in materials to be characterized at a small scale, such as the observation of Moiré patterns in superlattices. Overall, piezoelectric AFMs offer high resolution, versatility, stability, and sensitivity, but they may be more complex, expensive, and fragile than some other types of AFMs. Therefore, the PFM technology has been

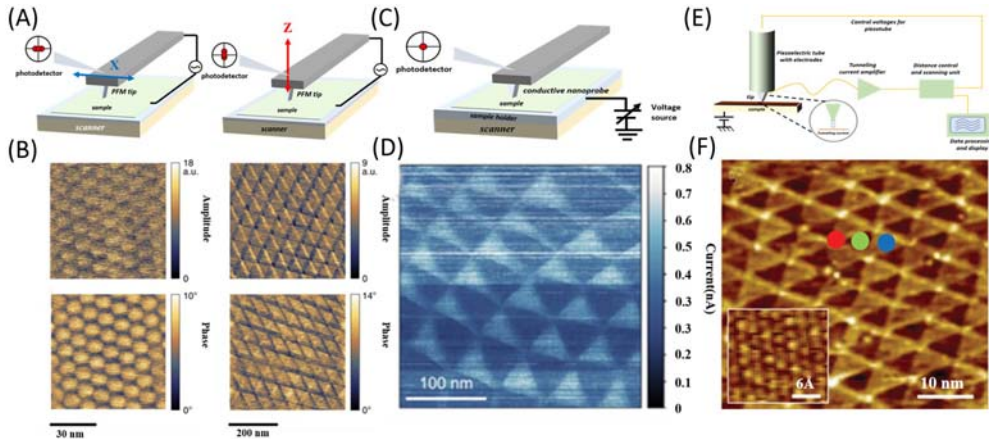


Figure 16.23 Atomic force microscopy (AFM)-based characterization. (A) Schematic of PFM measurement: (blue line) lateral mode (red line) vertical mode. (B) Schematic of CAFM measurement. (C) Schematic of scanning tunneling microscope (STM) measurement. (D) (red line) PFM amplitude (top view), and phase (bottom view) of monolayer graphene on hexagonal boron nitride. (E) (blue line) Twisted bilayer WSe_2 . (F) CAFM image of 0.4° R-type heterostructure showing alternating triangle domains of different conductivity. (G) STM topography image of an H-type heterostructure with a 12 nm Moiré, which agrees with (F). From McGilly, L. J., Kerelsky, A., Finney, N. R., Shapovalov, K., Shih, E. M., Ghiotto, A., Zeng, Y., Moore, S. L., Wu, W., Bai, Y., Watanabe, K., Taniguchi, T., Stengel, M., Zhou, L., Hone, J., Zhu, X., Basov, D. N., Dean, C., Dreyer, C. E., & Pasupathy, A. N. (2020). Visualization of Moiré superlattices. *Nature Nanotechnology*, 15(7), 580–584. <https://doi.org/10.1038/s41565-020-0708-3>.

extensively used in the research and development of piezoelectric materials in various fields, including materials science (Pillai et al., 2018), electronics (Lu et al., 2020), energy technology (Chen et al., 2017), and nanoscience (Tanaka et al., 2008).

The conductive AFM (CAFM) is another effective method for mapping the Moiré pattern of 2D materials, as shown schematically in Fig. 16.23B. In contrast to the PFM, the CAFM technique employs a sharp conductive probe to map the local changes in sample conductivity at the nanometer scale. It is used to investigate the conductivity and electrical characteristics of the sample, such as nanoscale charge transfer and charge distribution. It has been previously demonstrated that large-scale domain formation is anticipated if the lattices are aligned closely to a commensurate angle. These domains are separated by domain walls with different conductivity, resulting in a strikingly different pattern for the 0 degree alignment in the case of MoSe_2 (Rosenberger et al., 2020), as depicted in the CAFM image in Fig. 16.23F. Comparable results have been obtained in previous research, supporting the feasibility of using CAFM to characterize Moiré patterns. These technologies based on AFM offer a simple and undamaged method to characterize Moiré pattern of the 2D stack. But the technology requires a clean 2D surface and high-skilled operation.

16.4 Performance

16.4.1 Properties

Many new phenomena emerge from 2D–2D interface, therefore, various types of heterostructures were developed for novel properties and applications. The intrinsic nature of 2D materials, sequence, number of layers and interlayer twist angle are the four decisive factors to design and modulate 2D heterostructures' properties.

16.4.1.1 Modulation of band structure

The graphene/BN stack is one of the simplest heterostructures. The periodical Moiré pattern results in a change in DOS, as seen in STM images (Fig. 16.24A). It is known that the massless Dirac fermions lead to the zero-band gap in graphene. The periodical potential will open the band gap in graphene and lead to the emergence of a new set of Dirac points at energies dependent on the period of the Moiré pattern. As Fig. 16.24B shows, new dips in the density of states indicate the emergence of new Dirac points, and the energies where they occur depend on the period of the Moiré pattern (Yankowitz et al., 2012). These emerging Dirac points have the potential to control the transport properties of electrons in graphene as it induces anisotropic velocities for the charge carriers.

16.4.1.2 Correlated phase in twisted two-dimensional stack

A novel flat band will emerge from twisted bilayer graphene when the twist angle is around 1.01 degrees. The flat band has weak dispersion in momentum space, with the

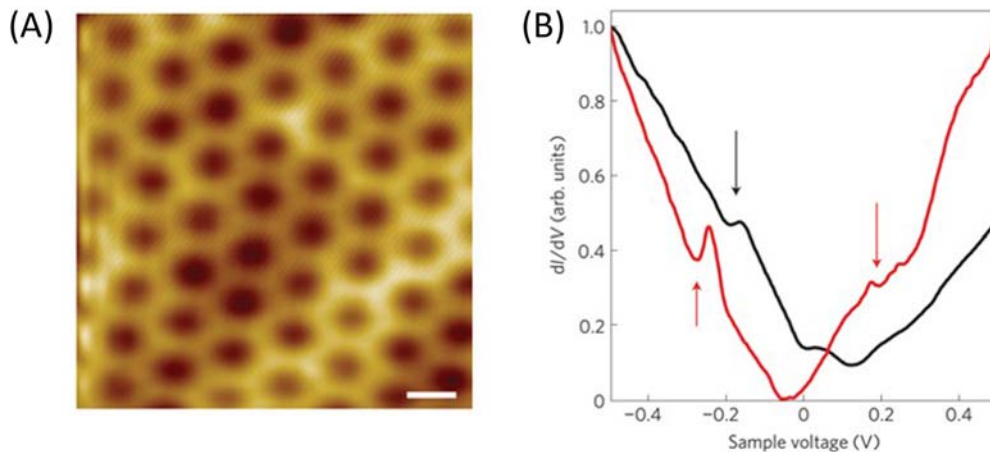


Figure 16.24 Density of states of graphene on hexagonal boron nitride showing new superlattice Dirac points. (A) Scanning tunneling microscope topography images showing Moiré patterns. (B) Experimental dI/dV curves for two different Moiré wavelengths, 9.0 nm (black) and 13.4 nm (red). The dips in the dI/dV curves are marked by arrows. From Yankowitz, M., Xue, J., Cormode, D., Sanchez-Yamagishi, J. D., Watanabe, K., Taniguchi, T., Jarillo-Herrero, P., Jacquod, P., & Leroy, B. J. (2012). Emergence of superlattice Dirac points in graphene on hexagonal boron nitride. *Nature Physics*, 8(5), 382–386. <https://doi.org/10.1038/nphys2272>.

kinetic energy of the electron set by the bandwidth. When the Fermi level lies within the flat bands, Coulomb interactions can greatly exceed the kinetic energy of the electrons and drive the system into various strongly correlated phases. The generation of correlated phases, such as Mott insulator (Cao, Fatemi, Demir, et al., 2018) and superconductor (Cao, Fatemi, Fang, et al., 2018), has been observed experimentally. Similarly, the flat band also exist in twisted TMD materials, research found that the electron correlation state could be observed at angles between 4 and 5.1 degrees (Wang, Shih, et al., 2020).

16.4.1.3 Lattice reconstruction

When the twist angle is small enough (<2 degrees) in twisted bilayer graphene, a unique reconstruction phenomenon occurs. Periodically arranged triangles can be observed using TEM, SEM, and AFM, indicating reconstruction caused by atomic interactions between the upper and lower layers (Halbertal, 2021; Rosenberger et al., 2020; Weston et al., 2020).

Due to the twist angle, a Moiré pattern (superlattice) with a specific period forms in bilayer graphene, resulting in three periodic stacking modes: AA, AB, and BA (see Fig. 16.25A). Due to the relatively lower free energy of AB and BA, atoms in the upper

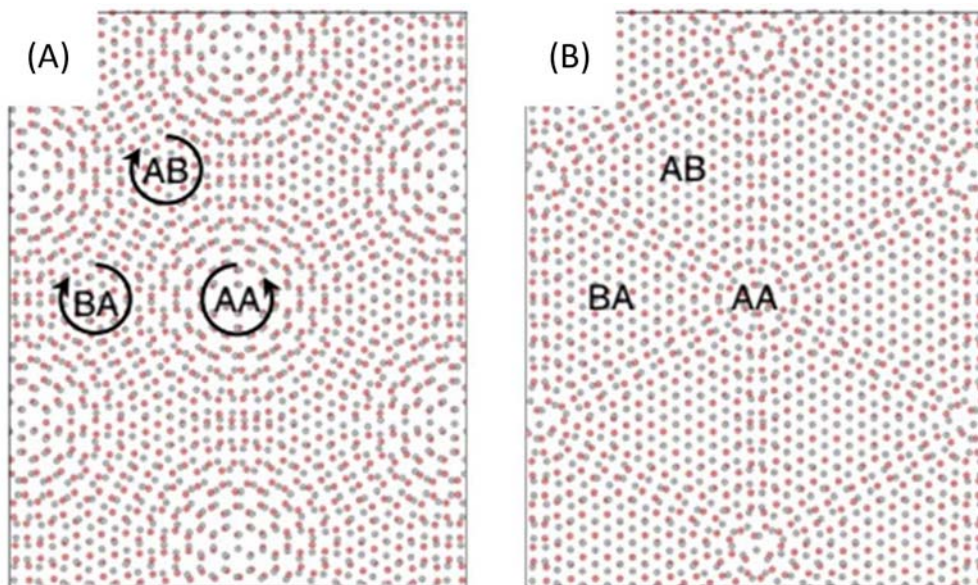


Figure 16.25 Atomic reconstruction in bilayer graphene. (A) and (B) Schematic diagrams of TBG before (A) and after (B) the atomic reconstruction. From Yoo, H., Engelke, R., Carr, S., Fang, S., Zhang, K., Cazeaux, P., Sung, S. H., Hovden, R., Tsen, A. W., Taniguchi, T., Watanabe, K., Yi, G. C., Kim, M., Lusk, M., Tadmor, E. B., Kaxiras, E., & Kim, P. (2019). Atomic and electronic reconstruction at the van der Waals interface in twisted bilayer graphene. *Nature Materials*, 18(5), 448–453. <https://doi.org/10.1038/s41563-019-0346-z>.

and lower layers shift to favor the formation of AB and BA stacking, leading to the expansion of AB and BA stacking areas and the contraction of the AA stacking area. Eventually, a distinct pattern with periodic regular triangles forms (see Fig. 4.2, 16.25B and 16.21D–E) (Yoo et al., 2019). Similar triangular patterns can also be found in TMDs and h-BN materials when the twist angle is close to 0 degrees (Rosenberger et al., 2020; Woods, 2021). Since monolayer TMD materials have a noncentrosymmetric structure, meaning that 0 and 180 degrees angles are not equivalent, a hexagonal reconstruction pattern emerges when the twist angle is close to 180 degrees (Rosenberger et al., 2020; Weston et al., 2020), differing from the previous situation.

The examples mentioned above are cases of twisted homostructures. In fact, similar atomic reconfiguration can also occur in heterostructures. Due to lattice mismatch between dissimilar TMD materials, Moiré patterns can be generated even if the twist angle is exactly 0 degrees, resulting in a similar reconstruction phenomenon. When the twist angle is large (Moiré pattern period is small), the superlattice is divided into smaller domains (AA, AB, and BA), where domain walls are difficult to migrate, hindering the emergence of reconstruction. Researchers suggest that such reconstruction is a result of interlayer interaction. With a small twist angle, interlayer interaction is strong, and reconstruction occurs. As the twist angle increases, the boundaries become blurry, indicating the weakening of interlayer interaction.

16.4.1.4 Optics

The nonlinear optical effect in 2D materials can be modified by the twist angle. Multilayer MoS₂ stacks with strong SHG response were fabricated by stacking each layer of MoS₂ in parallel direction (twist angle = 0 degrees), in which the central symmetry was broken. When MoS₂ was stacked in an antiparallel direction (twist angle = 180 degrees), the SHG response vanished completely (Hsu et al., 2014). By controlling the twist angle, SHG response can emerge from twisted bilayer graphene, whose Bernal AB stacking cannot produce any SHG response (Yang et al., 2020).

Long-lived interlayer excitons have been observed and tuned in 2D heterostructures. For TMD-based heterostructures with type-II band alignment, some bound electrons and holes are localized in individual monolayers, resulting in interlayer excitons. It has been reported that new PL peaks arise in MoSe₂–WSe₂ heterostructures, which are signals of interlayer excitons and differ from intralayer excitons in monolayer MoSe₂ or WSe₂ (Cheng et al., 2014). These interlayer excitons are highly tunable by the gate voltage, providing a new path for designing functional optoelectronic devices.

16.4.2 Application

16.4.2.1 Transistors

As candidates for the next generation of transistors, various types of 2D heterostructure-based transistors have been developed, including field-effect transistor

(FET), high-speed transistor, MOSFET, tunnel-field-effect transistor, negative capacitance FET, and barristors (Iannaccone et al., 2018). Mobility of 140,000 cm²/Vs, comparable to the theoretical phonon-scattering limit in graphene, has been observed in h-BN/graphene/h-BN stacks, as indicated in Fig. 16.26 (Wang et al., 2013). On the one hand, the encapsulation of h-BN prevents polymer contaminations from the stacking process. On the other hand, the 2D interface without dangling bonds avoids electron scattering at the interface. The heterostructure ensures a pristine interface and achieves ultra-high carrier mobilities.

Vertical field-effect transistors based on BN/graphene/WS₂/graphene heterostructures have been reported to exhibit high on/off ratios exceeding 10⁶ at room temperature with very high ON currents (Georgiou et al., 2013). Fig. 16.27 shows the structure and band diagram. With 0 bias, as described in Fig. 16.27B, the Fermi levels of the two graphene sheets are located near the bottom of the WS₂ conduction band. After applying a negative gate voltage, the Fermi level of graphene drops down and increases the tunneling barrier height, leading to the “OFF” state of the device (see Fig. 16.27C). Given a positive gate voltage, the Fermi level of graphene is shifted into the conduction band, reducing the tunneling barrier height, which results in an over-barrier thermionic current and the “ON” state (see Fig. 16.27D).

16.4.2.2 Light-emitting diodes

TMDs such as MoS₂, MoSe₂, WS₂, and WSe₂ exhibit a transformation of band gap from indirect in bulk to direct in monolayer (typically in the range of 1–2 eV).

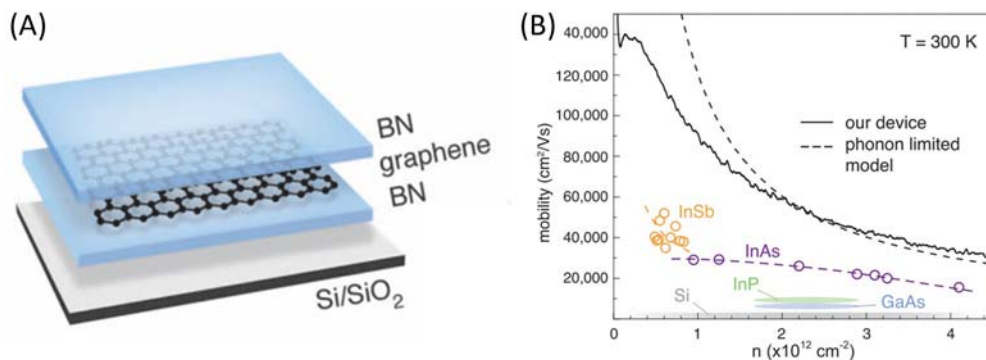


Figure 16.26 Graphene-based field-effect transistor (FET). (A) Scheme of the h-BN/graphene/h-BN heterostructure. (B) Room-temperature mobility versus density (*solid black curve*). Dashed black curve indicates the theoretical mobility limit due to acoustic-phonon scattering. Remaining data points label the range of mobilities reported in the literature for high-performance two-dimensional semiconductor FETs. From Wang, L., Meric, I., Huang, P. Y., Gao, Q., Gao, Y., Tran, H., Taniguchi, T., Watanabe, K., Campos, L. M., Muller, D. A., Guo, J., Kim, P., Hone, J., Shepard, K. L. & Dean, C. R. (2013). One-dimensional electrical contact to a two-dimensional material. *Science*, 342(6158), 614–617. <https://doi.org/10.1126/science.1244358>.

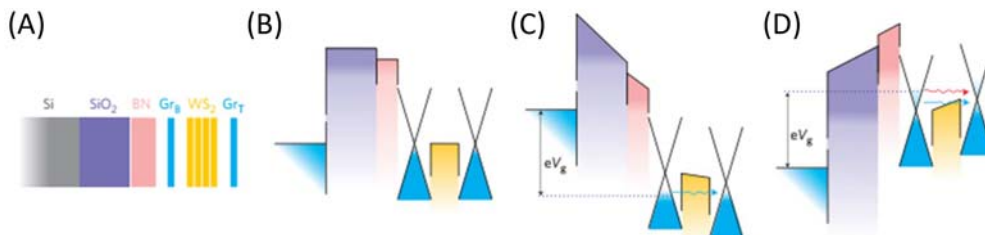


Figure 16.27 Graphene- WS_2 heterotransistor. (A) Schematic of vertical architecture of transistor. (B) Band diagram corresponding to no bias, V_g . (C) Negative V_g shifts the Fermi level of the two graphene layers down from the neutrality point, increasing the potential barrier and switching the transistor OFF. (D) Applying positive V_g results in an increased current between graphene due to both thermionic (red arrow) and tunneling (blue arrow) contributions. From Georgiou, T., Jalil, R., Belle, B. D., Britnell, L., Gorbachev, R. V., Morozov, S. V., Kim, Y. J., Gholinia, A., Haigh, S. J., Makarovskiy, O., Eaves, L., Ponomarenko, L. A., Geim, A. K., Novoselov, K. S. & Mishchenko, A. (2013). Vertical field-effect transistor based on graphene- WS_2 heterostructures for flexible and transparent electronics. *Nature Nanotechnology*, 8(2), 100–103. <https://doi.org/10.1038/nnano.2012.224>.

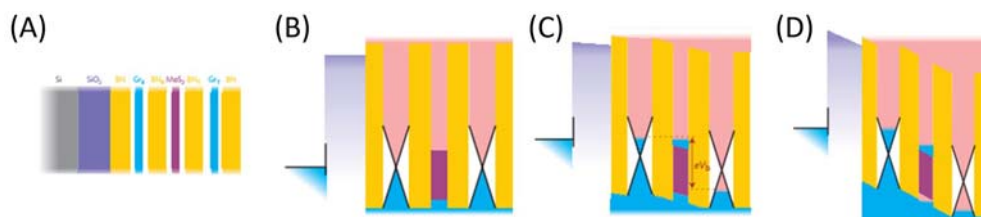


Figure 16.28 Heterostructure devices with a quantum well. (A) Schematic of the heterostructure consisting of Si/SiO₂/h-BN/graphene/h-BN/MoS₂/h-BN/graphene/h-BN. (B)–(D) Band diagrams for the case of zero applied bias (B), intermediate applied bias (C) and high bias (D) for the heterostructure presented in (A). From Withers, F., Del Pozo-Zamudio, O., Mishchenko, A., Rooney, A. P., Gholinia, A., Watanabe, K., Taniguchi, T., Haigh, S. J., Geim, A. K., Tartakovskii, A. I. & Novoselov, K. S. (2015). Light-emitting diodes by band-structure engineering in van der Waals heterostructures. *Nature Materials*, 14(3), 301–306. <https://doi.org/10.1038/nmat4205>.

The strong light-matter interaction (strong absorption of up to 30% and high quantum yield in PL up to a factor of 10^{-4}), tunable optical characteristic, and potential to integrate into conventional optoelectronic systems render them for optoelectronic devices such as photodiodes, photovoltaic cells and light-emitting devices.

Heterostructure with TMDs switched by multilayer h-BN and graphene is a typical light-emitting diode (Withers et al., 2015), as shown in Fig. 16.28A. Insulation h-BN layers avoid quenching of light by separating light-emitting 2D layers from the metallic graphene layers while improving the electrical performance of the graphene electrodes. Band diagrams for the case of zero applied bias are described in Fig. 16.28B. With the intermediate applied bias, the fermi level of graphene rises

above the conduction band of MoS₂, causing the injection of electrons in MoS₂. The accumulation of electrons forms negatively charged excitons (see Fig. 16.28C). In the situation of high bias, the fermi level of top graphene is brought below the valence band of MoS₂. Therefore, not only electrons but also holes are injected in MoS₂, leading to the formation of exciton formation and their radiative recombination (see Fig. 16.28D). The QE (quantum efficiency) is around 1% which is ten times higher than that of the planar p–n diode. Furthermore, the QE can be enhanced by multiple quantum wells stacked in series. Owing to the development of CVD growth and stacking technology, large-area multiquantum wells comprising alternating layers of 2D excitonic chalcogenides and dielectric insulators have been realized. Near-unity absorption was achieved while maintaining the enhanced PL emission and optoelectronic properties of monolayer TMDs.

The valley of the monolayer TMDs provides a new degree of freedom to modulate its optical properties. Specifically, electronic transitions near the *K* and *K'* points couple only to right or left-handed CP light, respectively. Based on it, current-driven or electroluminescent light emission can be realized with the p–n junction structure.

A WSe₂-based ambipolar transistor was developed to emit circularly polarized electroluminescence from p–i–n junctions electrostatically formed in transistor channels (Zhang et al., 2014). And the net handedness of this polarized light can be modified by reversing the applied bias, demonstrating the ability to modulate optical properties by valley degree of freedom.

16.4.2.3 Light-harvesting and detection devices

Considering that radiative recombination is the only loss mechanism, there is a maximum theoretical efficiency in conventional photocells described by the Shockley–Queisser (SQ) limit. 2D heterostructure offers a new strategy to exceed the fundamental limit. Spatial confinement of 2D heterostructures slows down the hot carrier cooling by restricting various carrier relaxation channels, and thus large quantum efficiencies beyond the SQ limit are expected. A type II van der Waals heterojunction (described in Fig. 16.29A) made of MoS₂ and WSe₂ monolayers was fabricated to demonstrate its potential as a new photovoltaic solar technology. The band structure of the junction was shown in Fig. 16.29B (Furchi et al., 2014). Photons are absorbed in WSe₂ and MoS₂, resulting in electron–hole pairs (excitons) in both monolayers. Relaxation of the photogenerated carriers then occurs, driven by the type II band offsets ΔE_C and ΔE_V . As the lowest energy electron and hole states are spatially separated, charge transfer occurs across the heterojunction. The relaxed carriers then diffuse laterally to the contacts, resulting in a photocurrent. The photovoltaic response of the heterostructure is demonstrated by *J–V* traces in Fig. 16.29C. Similar light-harvesting devices are also realized in other TMD heterostructure, such as

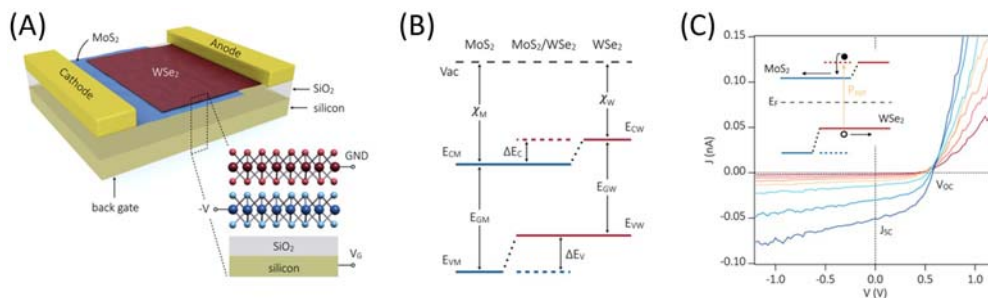


Figure 16.29 Device based on $\text{MoS}_2/\text{WSe}_2$. (A) Scheme of the device structure. (B) Schematic energy band diagrams of MoS_2 (left; blue lines) and WSe_2 (right; red lines) in the vicinity of the K-point. The $\text{MoS}_2/\text{WSe}_2$ heterostructure bands (center) are a superposition of the monolayer bands. The lowest energy electron states (solid blue line) are spatially located in the MoS_2 layer and the highest energy hole states (solid red line) lie in the WSe_2 . The excited states are shown as dashed lines. EC, conduction band edge; EV, valence band edge; Vac, vacuum level. (C) $J - V$ characteristics of the device under optical illumination with incident optical power of 180, 400, 670, 1100, 1800, 4000, and 6400 W/m^2 . (Inset) Schematic illustration of the photovoltaic effect: electron – hole pairs are generated in the heterostructure, relax to the bottom of the conduction and valence bands, and eventually diffuse to the contacts. From Furchi, M. M., Pospischil, A., Libisch, F., Burgdorfer, J. & Mueller, T. (2014). Photovoltaic effect in an electrically tunable van der Waals heterojunction. *Nano Letters*, 14(8), 4785–4791. <https://doi.org/10.1021/nl501962c>.

WS_2/MoS_2 (Zhang et al., 2023), WSe_2/WS_2 (Lin & Yang, 2020), and $\text{WSe}_2/\text{MoSe}_2$ (Flöry et al., 2015).

16.4.2.4 Sensors

2D heterostructures have the potential to serve as sensitive sensors in various areas. Sensors for DNA, gas, strain, and pH have been reported. For instance, a graphene/ MoS_2 stack was developed to detect DNA concentrations, with a detection limit reaching the level of aM (Loan et al., 2014). In the heterostructure, graphene acts as a protection layer, preventing ambient environmental influences on MoS_2 . Due to the linear relationship between the PL intensity of the stack and the DNA concentration, DNA concentrations can be detected with high sensitivity. In gas sensor applications, graphene/ MoS_2 for NO_2 gas detection (Tabata et al., 2018) and graphene/ WS_2 /graphene/h-BN (Choi et al., 2017) for NO_2 and NH_3 gas detection have been reported, demonstrating the potential of 2D heterostructures as sensors.

Apart from the above examples, the application of 2D heterostructures has expanded into many other fields. Due to the electronic/optical performance and mechanical flexibility of 2D materials, functional 2D heterostructures have great potential for use in future flexible electronics and wearable devices (Gao, 2017). 2D heterostructures also play an important role in memories, with various types of memory devices based on 2D heterostructures demonstrated. In the area of energy harvesting, research is ongoing in

piezoelectric nanogenerators (Wu & Wang, 2016), optical catalysts (Kumar & Xu, 2018), water splitting (Faraji et al., 2019), fuel cells, thermoelectric power generation (Zhao, 2020), and low-grade heat harvesting (Yu et al., 2020).

16.5 Conclusion

2D heterostructures provide an unprecedented opportunity to design and fabricate functional devices for specific purposes. The band structures and properties can be tuned by modifying the types of 2D materials, sequence, number of layers, and twist angles. A clean 2D interface is essential for realizing these novel properties. Two primary methods of fabricating 2D heterostructures are direct growth and mechanical assembly. The in situ growth method can produce ultra-clean interfaces but is limited by complex growth parameters. In contrast, mechanical assembly is more versatile, with three main types of stacking technologies developed: dry, wet, and semidry processes, each suitable for different 2D systems. However, completely avoiding contamination and achieving large-area stacks with ultra-clean 2D interfaces remains a challenge.

Various applications of 2D stacks have been reported, particularly in electronics and optoelectronics. Devices such as photodetectors, light-emitting diodes, solar cells, sensors, and transistors have been demonstrated. Furthermore, 2D heterostructures serve as an important platform for studying new physics. Overall, 2D heterostructures pave the way for innovative functional devices and the study of novel physics.

References

- Abbas, G. (2020). Recent advances in twisted structures of flatland materials and crafting Moiré superlattices. *Advanced Functional Materials.*, 30(36), 1–23.
- Ago, H., Endo, H., Solís-Fernández, P., Takizawa, R., Ohta, Y., Fujita, Y., Yamamoto, K., & Tsuji, M. (2015). Controlled van der Waals epitaxy of monolayer MoS₂ triangular domains on graphene. *ACS Applied Materials and Interfaces*, 7(9), 5265–5273. Available from <https://doi.org/10.1021/am508569m>, <http://pubs.acs.org/journal/aamick>.
- Andersen, T. I., Scuri, G., Sushko, A., De Greve, K., Sung, J., Zhou, Y., Wild, D. S., Gelly, R. J., Heo, H., Bérubé, D., Joe, A. Y., Jauregui, L. A., Watanabe, K., Taniguchi, T., Kim, P., Park, H., & Lukin, M. D. (2021). Excitons in a reconstructed Moiré potential in twisted WSe₂/WSe₂ homobilayers. *Nature Materials*, 20(4), 480–487. Available from <https://doi.org/10.1038/s41563-020-00873-5>, <http://www.nature.com/nmat/>.
- Andrei, E. Y., Efetov, D. K., Jarillo-Herrero, P., MacDonald, A. H., Mak, K. F., Senthil, T., Tutuc, E., Yazdani, A., & Young, A. F. (2021). The marvels of Moiré materials. *Nature Reviews Materials*, 6(3), 201–206. Available from <https://doi.org/10.1038/s41578-021-00284-1>, <http://www.nature.com/natrevmats/>.
- Andrei, E. Y., & MacDonald, A. H. (2020). Graphene bilayers with a twist. *Nature Materials*, 19(12), 1265–1275. Available from <https://doi.org/10.1038/s41563-020-00840-0>, <http://www.nature.com/nmat/>.
- Bae, S., Kim, H., Lee, Y., Xu, X., Park, J. S., Zheng, Y., Balakrishnan, J., Lei, T., Ri Kim, H., Song, Y. I., Kim, Y. J., Kim, K. S., Özyilmaz, B., Ahn, J. H., Hong, B. H., & Iijima, S. (2010). Roll-to-

- roll production of 30-inch graphene films for transparent electrodes. *Nature Nanotechnology*, 5(8), 574–578. Available from <https://doi.org/10.1038/nnano.2010.132>.
- Bag, A., & Lee, N. E. (2019). Gas sensing with heterostructures based on two-dimensional nanostructured materials: A review. *Journal of Materials Chemistry C*, 7(43), 13367–13383. Available from <https://doi.org/10.1039/c9tc04132j>, <http://pubs.rsc.org/en/journals/journal/tc>.
- Boandoh, S., Agyapong-Fordjour, F. O. T., Choi, S. H., Lee, J. S., Park, J. H., Ko, H., Han, G., Yun, S. J., Park, S., Kim, Y. M., Yang, W., Lee, Y. H., Kim, S. M., & Kim, K. K. (2019). Wafer-scale van der Waals heterostructures with ultraclean interfaces via the aid of viscoelastic polymer. *ACS Applied Materials and Interfaces*, 11(1), 1579–1586. Available from <https://doi.org/10.1021/acsaami.8b16261>, <http://pubs.acs.org/journal/aamick>.
- Butz, B., Dolle, C., Niekietel, F., Weber, K., Waldmann, D., Weber, H. B., Meyer, B., & Spiecker, E. (2014). Dislocations in bilayer graphene. *Nature*, 505(7484), 533–537. Available from <https://doi.org/10.1038/nature12780>.
- Cai, Q., Ju, Q., Hong, W., Jian, C., Wang, T., & Liu, W. (2022). Water assisted growth of two-dimensional MoS₂/MoSe₂ vertical heterostructures on molten glass. *Nanoscale*, 14(5), 1990–1996. Available from <https://doi.org/10.1039/d1nr08095d>, <http://pubs.rsc.org/en/journals/journal/nr>.
- Cai, Z., Liu, B., Zou, X., & Cheng, H. M. (2018). Chemical vapor deposition growth and applications of two-dimensional materials and their heterostructures. *Chemical Reviews*, 118(13), 6091–6133. Available from <https://doi.org/10.1021/acs.chemrev.7b00536>, <http://pubs.acs.org/journal/chreay>.
- Cao, Y., Fatemi, V., Demir, A., Fang, S., Tomarken, S. L., Luo, J. Y., Sanchez-Yamagishi, J. D., Watanabe, K., Taniguchi, T., Kaxiras, E., Ashoori, R. C., & Jarillo-Herrero, P. (2018). Correlated insulator behaviour at half-filling in magic-angle graphene superlattices. *Nature*, 556(7699), 80–84. Available from <https://doi.org/10.1038/nature26154>, <http://www.nature.com/nature/index.html>.
- Cao, Y., Fatemi, V., Fang, S., Watanabe, K., Taniguchi, T., Kaxiras, E., & Jarillo-Herrero, P. (2018). Unconventional superconductivity in magic-angle graphene superlattices. *Nature*, 556(7699), 43–50. Available from <https://doi.org/10.1038/nature26160>, <http://www.nature.com/nature/index.html>.
- Carozo, V., Almeida, C. M., Fragneaud, B., Bedê, P. M., Moutinho, M. V. O., Ribeiro-Soares, J., Andrade, N. F., Souza Filho, A. G., Matos, M. J. S., Wang, B., Terrones, M., Capaz, R. B., Jorio, A., Achete, C. A., & Cançado, L. G. (2013). Resonance effects on the Raman spectra of graphene superlattices. *Physical Review B - Condensed Matter and Materials Physics*, 88(8). Available from <https://doi.org/10.1103/PhysRevB.88.085401>Brazil, <http://oai.aps.org/filefetch?identifier=10.1103/PhysRevB.88.085401&component=fulltext&description=markup&format=xml>.
- Carr, S., Massatt, D., Torrisi, S. B., Cazeaux, P., Luskin, M., & Kaxiras, E. (2018). Relaxation and domain formation in incommensurate two-dimensional heterostructures. *Physical Review B*, 98(22). Available from <https://doi.org/10.1103/PhysRevB.98.224102>, <http://harvest.aps.org/bagit/articles/10.1103/PhysRevB.98.224102/apsxml>.
- Chen, H., Zhang, X. L., Zhang, Y. Y., Wang, D., Bao, D. L., Que, Y., Xiao, W., Du, S., Ouyang, M., Pantelides, S. T., & Gao, H. J. (2019). Atomically precise, custom-design origami graphene nanostructures. *Science (New York, N.Y.)*, 365(6457), 1036–1040. Available from <https://doi.org/10.1126/science.aax7864>, <https://science.sciencemag.org/content/365/6457/1036/tab-pdf>.
- Chen, H. M., Huang, H.-C., Jheng, S.-H., Huang, H.-T., & Huang, Y.-S. (2017). High-efficiency PFM boost converter with an accurate zero current detector. *IEEE Transactions on Circuits and Systems II: Express Briefs*, 65(11), 1644–1648. Available from <https://doi.org/10.1109/TCSII.2017.2754514>, <https://ieeexplore.ieee.org/abstract/document/8047321>.
- Chen, T. A., Chuu, C. P., Tseng, C. C., Wen, C. K., Wong, H. S. P., Pan, S., Li, R., Chao, T. A., Chueh, W. C., Zhang, Y., Fu, Q., Yakobson, B. I., Chang, W. H., & Li, L. J. (2020). Wafer-scale single-crystal hexagonal boron nitride monolayers on Cu (111). *Nature*, 579(7798), 219–223. Available from <https://doi.org/10.1038/s41586-020-2009-2>, <http://www.nature.com/nature/index.html>.
- Chen, X. D., Xin, W., Jiang, W. S., Liu, Z. B., Chen, Y. S., & Tian, J. G. (2016). High-precision twist-controlled bilayer and trilayer graphene. *Advanced Materials*, 28(13), 2563–2570. Available from <https://doi.org/10.1002/adma.201505129>, <http://www3.interscience.wiley.com/journal/119030556/issue>.

- Chen, Y., Gong, X. L., & Gai, J. G. (2016). Progress and challenges in transfer of large-area graphene films. *Advancement of Science*, 3(8).
- Cheng, P., Zhang, W., Zhang, L., Gou, J., Wong, P. K. J., & Chen, L. (2019). *Molecular beam epitaxy fabrication of two-dimensional materials. 2D semiconductor materials and devices* (pp. 103–134). China: Elsevier. Available from <http://www.sciencedirect.com/science/book/9780128161876>, 10.1016/B978-0-12-816187-6.00004-2.
- Cheng, R., Li, D., Zhou, H., Wang, C., Yin, A., Jiang, S., Liu, Y., Chen, Y., Huang, Y., & Duan, X. (2014). Electroluminescence and photocurrent generation from atomically sharp WSe₂/MoS₂ heterojunction p–n diodes. *Nano Letters*, 14(10), 5590–5597. Available from <https://doi.org/10.1021/nl502075n>.
- Chiappe, D., Asselberghs, I., Sutar, S., Iacovo, S., Afanas'ev, V., Stesmans, A., Balaji, Y., Peters, L., Heyne, M., Mannarino, M., Vandervorst, W., Sayan, S., Huyghebaert, C., Caymax, M., Heyns, M., De Gendt, S., Radu, I., & Thean, A. (2016). Controlled sulfurization process for the synthesis of large area MoS₂ films and MoS₂/WS₂ heterostructures. *Advanced Materials Interfaces*, 3(4), 1500635. Available from <https://doi.org/10.1002/admi.201500635>.
- Chiu, M.-H. (2015). Determination of band alignment in the single-layer MoS₂/WSe₂ heterojunction. *Nature Communication*, 6(1).
- Choi, H. K., Park, J., Myoung, N., Kim, H. J., Choi, J. S., Choi, Y. K., Hwang, C. Y., Kim, J. T., Park, S., Yi, Y., Chang, S. K., Park, H. C., Hwang, C., Choi, C. G., & Yu, Y. J. (2017). Gas molecule sensing of van der Waals tunnel field effect transistors. *Nanoscale*, 9(47), 18644–18650. Available from <https://doi.org/10.1039/c7nr05712a>, <http://www.rsc.org/publishing/journals/NR/Index.asp>.
- Chubarov, M., Choudhury, T. H., Zhang, X., & Redwing, J. M. (2018). In-plane x-ray diffraction for characterization of monolayer and few-layer transition metal dichalcogenide films. *Nanotechnology*, 29(5), 1–8. Available from <https://doi.org/10.1088/1361-6528/aaa1bd>.
- Dean, C. R., Wang, L., Maher, P., Forsythe, C., Ghahari, F., Gao, Y., Katoch, J., Ishigami, M., Moon, P., Koshino, M., Taniguchi, T., Watanabe, K., Shepard, K. L., Hone, J., & Kim, P. (2013). Hofstadter's butterfly and the fractal quantum Hall effect in Moiré superlattices. *Nature*, 497(7451), 598–602. Available from <https://doi.org/10.1038/nature12186>.
- Desai, S. B., Madhupathy, S. R., Amani, M., Kiriya, D., Hettick, M., Tosun, M., Zhou, Y., Dubey, M., Ager, J. W., Chrzan, D., & Javey, A. (2016). Gold-mediated exfoliation of ultralarge optoelectronically-perfect monolayers. *Advanced Materials*, 28(21), 4053–4058. Available from <https://doi.org/10.1002/adma.201506171>, <http://www3.interscience.wiley.com/journal/119030556/issue>.
- Dong, R. (2022). The intrinsic thermodynamic difficulty and a step-guided mechanism for the epitaxial growth of uniform multilayer MoS₂ with controllable thickness. *Advanced Materials*, 34.
- Dong, J., Zhang, L., & Ding, F. (2019). Kinetics of graphene and 2D materials growth. *Advanced Materials*, 31(9).
- Duong, D. L., Yun, S. J., & Lee, Y. H. (2017). Van der Waals layered materials: Opportunities and challenges. *ACS Nano*, 11(12), 11803–11830. Available from <https://doi.org/10.1021/acsnano.7b07436>, <http://pubs.acs.org/journal/ancac3>.
- Faraji, M., Yousefi, M., Yousefzadeh, S., Zirak, M., Naseri, N., Jeon, T. H., Choi, W., & Moshfegh, A. Z. (2019). Two-dimensional materials in semiconductor photoelectrocatalytic systems for water splitting. *Energy and Environmental Science*, 12(1), 59–95. Available from <https://doi.org/10.1039/c8ee00886h>, <http://pubs.rsc.org/en/journals/journal/ee>.
- Feng, W., Zheng, W., Cao, W., & Hu, P. A. (2014). Back gated multilayer InSe transistors with enhanced carrier mobilities via the suppression of carrier scattering from a dielectric interface. *Advanced Materials*, 26(38), 6587–6593. Available from <https://doi.org/10.1002/adma.201402427>.
- Flöry, N., Jain, A., Bharadwaj, P., Parzefall, M., Taniguchi, T., Watanabe, K., & Novotny, L. (2015). A WSe₂/MoSe₂ heterostructure photovoltaic device. *Applied Physics Letters*, 107(12). Available from <https://doi.org/10.1063/1.4931621>, <http://scitation.aip.org/content/aip/journal/apl>.
- Fukamachi, S., Solís-Fernández, P., Kawahara, K., Tanaka, D., Otake, T., Lin, Y. C., Suenaga, K., & Ago, H. (2023). Large-area synthesis and transfer of multilayer hexagonal boron nitride for enhanced graphene device arrays. *Nature Electronics*, 6(2), 126–136. Available from <https://doi.org/10.1038/s41928-022-00911-x>, <https://www.nature.com/natelectron/>.

- Furchi, M. M., Pospischil, A., Libisch, F., Burgdörfer, J., & Mueller, T. (2014). Photovoltaic effect in an electrically tunable Van der Waals heterojunction. *Nano Letters*, *14*(8), 4785–4791. Available from <https://doi.org/10.1021/nl501962c>, <http://pubs.acs.org/journal/nalefd>.
- Gao, L. (2017). Flexible device applications of 2D semiconductors. *Small (Weinheim an der Bergstrasse, Germany)*, *13*(35), 1603994. Available from <https://doi.org/10.1002/smll.201603994>.
- Gao, X. G., Li, X. K., Xin, W., Chen, X. D., Liu, Z. B., & Tian, J. G. (2020). Fabrication, optical properties, and applications of twisted two-dimensional materials. *Nanophotonics*, *9*(7), 1717–1742. Available from <https://doi.org/10.1515/nanoph-2020-0024>, <http://www.degruyter.com/view/j/nanoph?rskey=PZEKdQ&result=1&q=Nanophotonics>.
- Georgiou, T., Jalil, R., Belle, B. D., Britnell, L., Gorbachev, R. V., Morozov, S. V., Kim, Y. J., Gholinia, A., Haigh, S. J., Makarovskiy, O., Eaves, L., Ponomarenko, L. A., Geim, A. K., Novoselov, K. S., & Mishchenko, A. (2013). Vertical field-effect transistor based on graphene-WS₂ heterostructures for flexible and transparent electronics. *Nature Nanotechnology*, *8*(2), 100–103. Available from <https://doi.org/10.1038/nnano.2012.224>, <http://www.nature.com/nnano/index.html>.
- Gong, Y., Lin, J., Wang, X., Shi, G., Lei, S., Lin, Z., Zou, X., Ye, G., Vajtai, R., Yakobson, B. I., Terrones, H., Terrones, M., Tay, B. K., Lou, J., Pantelides, S. T., Liu, Z., Zhou, W., & Ajayan, P. M. (2014). Vertical and in-plane heterostructures from WS₂/MoS₂ monolayers. *Nature Materials*, *13*(12), 1135–1142. Available from <https://doi.org/10.1038/nmat4091>, <http://www.nature.com/nmat/>.
- Gong, Y., Lei, S., Ye, G., Li, B., He, Y., Keyshar, K., Zhang, X., Wang, Q., Lou, J., Liu, Z., Vajtai, R., Zhou, W., & Ajayan, P. M. (2015). Two-step growth of two-dimensional WSe₂/MoSe₂ heterostructures. *Nano Letters*, *15*(9), 6135–6141. Available from <https://doi.org/10.1021/acs.nanolett.5b02423>.
- Halbatal, D. (2021). Moire metrology of energy landscapes in van der Waals heterostructures. *Nature Communications*, *12*(1).
- He, F., Zhou, Y., Ye, Z., Cho, S. H., Jeong, J., Meng, X., & Wang, Y. (2021). Moiré patterns in 2D materials: A review. *ACS Nano*, *15*(4), 5944–5958. Available from <https://doi.org/10.1021/acsnano.0c10435>, <http://pubs.acs.org/journal/ancac3>.
- Hsu, W. T., Zhao, Z. A., Li, L. J., Chen, C. H., Chiu, M. H., Chang, P. S., Chou, Y. C., & Chang, W. H. (2014). Second harmonic generation from artificially stacked transition metal dichalcogenide twisted bilayers. *ACS Nano*, *8*(3), 2951–2958. Available from <https://doi.org/10.1021/nl500228r>.
- Hu, D., Xu, G., Xing, L., Yan, X., Wang, J., Zheng, J., Lu, Z., Wang, P., Pan, X., & Jiao, L. (2017). Two-dimensional semiconductors grown by chemical vapor transport. *Angewandte Chemie - International Edition*, *56*(13), 3611–3615. Available from <https://doi.org/10.1002/anie.201700439>, [http://onlinelibrary.wiley.com/journal/10.1002/\(ISSN\)1521-3773](http://onlinelibrary.wiley.com/journal/10.1002/(ISSN)1521-3773).
- Huang, M., & Ruoff, R. S. (2020). Growth of single-layer and multilayer graphene on Cu/Ni alloy substrates. *Accounts of Chemical Research*, *53*(4), 800–811. Available from <https://doi.org/10.1021/acs.accounts.9b00643>, <http://pubs.acs.org/journal/achre4>.
- Huang, X., Chen, L., Tang, S., Jiang, C., Chen, C., Wang, H., Shen, Z. X., Wang, H., & Cui, Y. T. (2021). Imaging dual-Moiré lattices in twisted bilayer graphene aligned on hexagonal boron nitride using microwave impedance microscopy. *Nano Letters*, *21*(10), 4292–4298. Available from <https://doi.org/10.1021/acs.nanolett.1c00601>, <http://pubs.acs.org/journal/nalefd>.
- Hussain, S., Shehzad, M. A., Vikraman, D., Khan, M. F., Singh, J., Choi, D. C., Seo, Y., Eom, J., Lee, W. G., & Jung, J. (2016). Synthesis and characterization of large-area and continuous MoS₂ atomic layers by RF magnetron sputtering. *Nanoscale*, *8*(7), 4340–4347. Available from <https://doi.org/10.1039/c5nr09032f>, <http://www.rsc.org/publishing/journals/NR/Index.asp>.
- Iannaccone, G., Bonaccorso, F., Colombo, L., & Fiori, G. (2018). Quantum engineering of transistors based on 2D materials heterostructures. *Nature Nanotechnology*, *13*(3), 183–191. Available from <https://doi.org/10.1038/s41565-018-0082-6>, <http://www.nature.com/nnano/index.html>.
- Jain, A., Bharadwaj, P., Heeg, S., Parzefall, M., Taniguchi, T., Watanabe, K., & Novotny, L. (2018). Minimizing residues and strain in 2D materials transferred from PDMS. *Nanotechnology*, *29*(26), 265203. Available from <https://doi.org/10.1088/1361-6528/aabd90>.
- Ji, J. (2016). Two-dimensional antimonene single crystals grown by van der Waals epitaxy. *Nature Communications*, *7*(1).

- Ji, Y., Calderon, B., Han, Y., Cueva, P., Jungwirth, N. R., Alsalman, H. A., Hwang, J., Fuchs, G. D., Muller, D. A., & Spencer, M. G. (2017). Chemical vapor deposition growth of large single-crystal mono-, bi-, tri-layer hexagonal boron nitride and their interlayer stacking. *ACS Nano*, *11*(12), 12057–12066. Available from <https://doi.org/10.1021/acsnano.7b04841>, <http://pubs.acs.org/journal/ancac3>.
- Jin, C., Regan, E. C., Yan, A., Iqbal Bakti Utama, M., Wang, D., Zhao, S., Qin, Y., Yang, S., Zheng, Z., Shi, S., Watanabe, K., Taniguchi, T., Tongay, S., Zettl, A., & Wang, F. (2019). Observation of Moiré excitons in WSe₂/WS₂ heterostructure superlattices. *Nature*, *567*(7746), 76–80. Available from <https://doi.org/10.1038/s41586-019-0976-y>, <http://www.nature.com/nature/index.html>.
- Jin, G., Lee, C. S., Okello, O. F. N., Lee, S. H., Park, M. Y., Cha, S., Seo, S. Y., Moon, G., Min, S. Y., Yang, D. H., Han, C., Ahn, H., Lee, J., Choi, H., Kim, J., Choi, S. Y., & Jo, M. H. (2021). Heteroepitaxial van der Waals semiconductor superlattices. *Nature Nanotechnology*, *16*(10), 1092–1098. Available from <https://doi.org/10.1038/s41565-021-00942-z>, <http://www.nature.com/nnano/index.html>.
- Jorio, A., & Cançado, L. G. (2013). Raman spectroscopy of twisted bilayer graphene. *Solid State Communications*, *175*–, 176, 3–12. Available from <https://doi.org/10.1016/j.ssc.2013.08.008>.
- Kanazawa, T., Amemiya, T., Upadhyaya, V., Ishikawa, A., Tsuruta, K., Tanaka, T., & Miyamoto, Y. (2017). Performance improvement of HfS₂ transistors by atomic layer deposition of HfO₂. *IEEE Transactions on Nanotechnology*, *16*(4), 582–587. Available from <https://doi.org/10.1109/TNANO.2017.2661403>, <http://ieeexplore.ieee.org/xpl/RecentIssue.jsp?puNumber=7729>.
- Kang, K., Lee, K. H., Han, Y., Gao, H., Xie, S., Muller, D. A., & Park, J. (2017). Layer-by-layer assembly of two-dimensional materials into wafer-scale heterostructures. *Nature*, *550*(7675), 229–233. Available from <https://doi.org/10.1038/nature23905>, <http://www.nature.com/nature/index.html>.
- Kang, K., Xie, S., Huang, L., Han, Y., Huang, P. Y., Mak, K. F., Kim, C. J., Muller, D., & Park, J. (2015). High-mobility three-atom-thick semiconducting films with wafer-scale homogeneity. *Nature*, *520*(7549), 656–660. Available from <https://doi.org/10.1038/nature14417>, <http://www.nature.com/nature/index.html>.
- Kashyap, P. K., Sharma, I., & Gupta, B. K. (2019). Continuous growth of highly reproducible single-layer graphene deposition on Cu foil by indigenously developed LPCVD setup. *ACS Omega*, *4*(2), 2893–2901. Available from <https://doi.org/10.1021/acsomega.0b03432>, <http://pubs.acs.org/journal/acsofd>.
- Kazmierczak, N. P., Van Winkle, M., Ophus, C., Bustillo, K. C., Carr, S., Brown, H. G., Ciston, J., Taniguchi, T., Watanabe, K., & Bediako, D. K. (2021). Strain fields in twisted bilayer graphene. *Nature Materials*, *20*(7), 956–963. Available from <https://doi.org/10.1038/s41563-021-00973-w>, <http://www.nature.com/nmat/>.
- Kidambi, P. R., Blume, R., Kling, J., Wagner, J. B., Baetz, C., Weatherup, R. S., Schloegl, R., Bayer, B. C., & Hofmann, S. (2014). In situ observations during chemical vapor deposition of hexagonal boron nitride on polycrystalline copper. *Chemistry of Materials*, *26*(22), 6380–6392. Available from <https://doi.org/10.1021/cm502603n>, <http://pubs.acs.org/journal/cmatex>.
- Kim, H. G., & Lee, H. B. R. (2017). Atomic layer deposition on 2D materials. *Chemistry of Materials*, *29*(9), 3809–3826. Available from <https://doi.org/10.1021/acs.chemmater.6b05103>, <http://pubs.acs.org/journal/cmatex>.
- Kim, J. H. (2019). Centimeter-scale green integration of layer-by-layer 2D TMD vdW heterostructures on arbitrary substrates by water-assisted layer transfer. *Scientific Reports.*, *9*(1).
- Kim, K. (2017). Tunable moiré bands and strong correlations in small-twist-angle bilayer graphene. *Proceedings of the National Academy of Science USA*, *114*, 3364–3369.
- Kim, K., Yankowitz, M., Fallahzad, B., Kang, S., Movva, H. C. P., Huang, S., Larentis, S., Corbet, C. M., Taniguchi, T., Watanabe, K., Banerjee, S. K., Leroy, B. J., & Tutuc, E. (2016). Van der Waals heterostructures with high accuracy rotational alignment. *Nano Letters*, *16*(3), 1989–1995. Available from <https://doi.org/10.1021/acs.nanolett.5b05263>, <http://pubs.acs.org/journal/nalefd>.
- Kim, S. M. (2015). Synthesis of large-area multilayer hexagonal boron nitride for high material performance. *Nature Communication.*, *6*(1).
- Kim, Y., Kim, H., Kim, T. Y., Rhyu, S. H., Choi, D. S., Park, W. K., Yang, C. M., Yoon, D. H., & Yang, W. S. (2015). Influence of the transfer and chemical treatment of monolayer graphene grown

- for flexible transparent electrodes. *Carbon*, 81(1), 458–464. Available from <https://doi.org/10.1016/j.carbon.2014.09.078>, <http://www.journals.elsevier.com/carbon/>.
- Kum, H., Lee, D., Kong, W., Kim, H., Park, Y., Kim, Y., Baek, Y., Bae, S.-H., Lee, K., & Kim, J. (2019). Epitaxial growth and layer-transfer techniques for heterogeneous integration of materials for electronic and photonic devices. *Nature Electronics*, 2(10), 439–450. Available from <https://doi.org/10.1038/s41928-019-0314-2>.
- Kumar. (2021). Light-matter coupling in large-area van der Waals superlattices. *Nature Nanotechnology*, 17(2), 182–189.
- Kumar, A., & Xu, Q. (2018). Two-dimensional layered materials as catalyst supports. *ChemNanoMat*, 4(1), 28–40. Available from <https://doi.org/10.1002/cnma.201700139>, [http://onlinelibrary.wiley.com/journal/10.1002/\(ISSN\)2199-692X](http://onlinelibrary.wiley.com/journal/10.1002/(ISSN)2199-692X).
- Lee, Y., Bae, S., Jang, H., Jang, S., Zhu, S. E., Sim, S. H., Song, Y. I., Hong, B. H., & Ahn, J. H. (2010). Wafer-scale synthesis and transfer of graphene films. *Nano Letters*, 10(2), 490–493. Available from <https://doi.org/10.1021/nl903272n>.
- Li, J., Song, P., Zhao, J., Vaklinova, K., Zhao, X., Li, Z., Qiu, Z., Wang, Z., Lin, L., Zhao, M., Herng, T. S., Zuo, Y., Jonhson, W., Yu, W., Hai, X., Lyu, P., Xu, H., Yang, H., Chen, C., ... Lu, J. (2021). Printable two-dimensional superconducting monolayers. *Nature Materials*, 20(2), 181–187. Available from <https://doi.org/10.1038/s41563-020-00831-1>, <http://www.nature.com/nmat/>.
- Li, L., Zhang, Y., Zhang, R., Han, Z., Dong, H., Yu, G., Geng, D., & Yang, H. Y. (2021). A minireview on chemical vapor deposition growth of wafer-scale monolayer: H-BN single crystals. *Nanoscale*, 13(41), 17310–17317. Available from <https://doi.org/10.1039/d1nr04034k>, <http://pubs.rsc.org/en/journals/journal/nr>.
- Li, X., Cai, W., An, J., Kim, S., Nah, J., Yang, D., Piner, R., Velamakanni, A., Jung, I., Tutuc, E., Banerjee, S. K., Colombo, L., & Ruoff, R. S. (2009). Large-area synthesis of high-quality and uniform graphene films on copper foils. *Science (New York, N.Y.)*, 324(5932), 1312–1314. Available from <https://doi.org/10.1126/science.1171245>.
- Li, Y. (2021). Unraveling strain gradient induced electromechanical coupling in twisted double bilayer graphene Moiré superlattices. *Advanced Materials*, 33(51).
- Liao, M. (2020). Precise control of the interlayer twist angle in large scale MoS₂ homostructures. *Nature Communication*, 11(1).
- Lin, P., & Yang, J. (2020). Tunable WSe₂/WS₂ van der Waals heterojunction for self-powered photodetector and photovoltaics. *Journal of Alloys and Compounds*, 842, 155890. Available from <https://doi.org/10.1016/j.jallcom.2020.155890>.
- Lin, Y. C., Zhang, W., Huang, J. K., Liu, K. K., Lee, Y. H., Liang, C. T., Chu, C. W., & Li, L. J. (2012). Wafer-scale MoS₂ thin layers prepared by MoO₃ sulfurization. *Nanoscale*, 4(20), 6637–6641. Available from <https://doi.org/10.1039/c2nr31833d>, <http://pubs.rsc.org/en/journals/journal/nr>.
- Liu, C., Li, Z., Qiao, R., Wang, Q., Zhang, Z., Liu, F., Zhou, Z., Shang, N., Fang, H., Wang, M., Liu, Z., Feng, Z., Cheng, Y., Wu, H., Gong, D., Liu, S., Zhang, Z., Zou, D., Fu, Y., ... Liu, K. (2022). Designed growth of large bilayer graphene with arbitrary twist angles. *Nature Materials*, 21(11), 1263–1268. Available from <https://doi.org/10.1038/s41563-022-01361-8>, <https://www.nature.com/nmat/>.
- Liu, F., Wu, W., Bai, Y., Chae, S. H., Li, Q., Wang, J., Hone, J., & Zhu, X. Y. (2020). Disassembling 2D van der Waals crystals into macroscopic monolayers and reassembling into artificial lattices. *Science (New York, N.Y.)*, 367(6480), 903–906. Available from <https://doi.org/10.1126/science.aba1416>, <https://science.sciencemag.org/content/367/6480/903/tab-pdf>.
- Liu, K., Zhang, L., Cao, T., Jin, C., Qiu, D., Zhou, Q., Zettl, A., Yang, P., Louie, S. G., & Wang, F. (2014). Evolution of interlayer coupling in twisted molybdenum disulfide bilayers. *Nature Communications*, 5. Available from <https://doi.org/10.1038/ncomms5966>, <http://www.nature.com/ncomms/index.html>.
- Liu, L., Li, T., Ma, L., Li, W., Gao, S., Sun, W., Dong, R., Zou, X., Fan, D., Shao, L., Gu, C., Dai, N., Yu, Z., Chen, X., Tu, X., Nie, Y., Wang, P., Wang, J., Shi, Y., & Wang, X. (2022). Uniform nucleation and epitaxy of bilayer molybdenum disulfide on sapphire. *Nature*, 605(7908), 69–75.

- Available from <https://doi.org/10.1038/s41586-022-04523-5>, <http://www.nature.com/nature/index.html>.
- Liu, Y. (2016). Van der Waals heterostructures and devices. *Nature Review Materials*, 1(9), 1–17.
- Loan, P. T. K., Zhang, W., Lin, C. T., Wei, K. H., Li, L. J., & Chen, C. H. (2014). Graphene/MoS₂ heterostructures for ultrasensitive detection of DNA hybridisation. *Advanced Materials*, 26(28), 4838–4844. Available from <https://doi.org/10.1002/adma.201401084>, <http://www3.interscience.wiley.com/journal/119030556/issue>.
- Lu, A.-Y., Zhu, H., Xiao, J., Chuu, C.-P., Han, Y., Chiu, M.-H., Cheng, C.-C., Yang, C.-W., Wei, K.-H., Yang, Y., Wang, Y., Sokaras, D., Nordlund, D., Yang, P., Muller, D. A., Chou, M.-Y., Zhang, X., & Li, L.-J. (2017). Janus monolayers of transition metal dichalcogenides. *Nature Nanotechnology*, 12(8), 744–749. Available from <https://doi.org/10.1038/nnano.2017.100>.
- Lu, Y., Huang, X., Huang, Y., & Liu, D. (2020). Sigmoid function model for a PFM power electronic converter. *IEEE Transactions on Power Electronics*, 35(4), 4233–4241. Available from <https://doi.org/10.1109/TPEL.2019.2935632>, <https://ieeexplore.ieee.org/xpl/mostRecentIssue.jsp?punumber=63>.
- Lupina, G., Kitzmann, J., Costina, I., Lukosius, M., Wenger, C., Wolff, A., Vaziri, S., Östling, M., Pasternak, I., Krajewska, A., Strupinski, W., Kataria, S., Gahoi, A., Lemme, M. C., Ruhl, G., Zoth, G., Luxenhofer, O., & Mehr, W. (2015). Residual metallic contamination of transferred chemical vapor deposited graphene. *ACS Nano*, 9(5), 4776–4785. Available from <https://doi.org/10.1021/acsnano.5b01261>, <http://pubs.acs.org/journal/ancac3>.
- Lv, M. (2022). Spatially resolved polarization manipulation of ferroelectricity in twisted hBN. *Advanced Materials*.
- Ma, K. Y., Zhang, L., Jin, S., Wang, Y., Yoon, S. I., Hwang, H., Oh, J., Jeong, D. S., Wang, M., Chatterjee, S., Kim, G., Jang, A. R., Yang, J., Ryu, S., Jeong, H. Y., Ruoff, R. S., Chhowalla, M., Ding, F., & Shin, H. S. (2022). Epitaxial single-crystal hexagonal boron nitride multilayers on Ni (111). *Nature*, 606(7912), 88–93. Available from <https://doi.org/10.1038/s41586-022-04745-7>, <http://www.nature.com/nature/index.html>.
- Mak, K. F., & Shan, J. (2022). Semiconductor moire materials. *Nature Nanotechnology*, 17(7), 686–695.
- Mattinen, M., Popov, G., Vehkamäki, M., King, P. J., Mizohata, K., Jalkanen, P., Räisänen, J., Leskelä, M., & Ritala, M. (2019). Atomic layer deposition of emerging 2D semiconductors, HfS₂ and ZrS₂, for optoelectronics. *Chemistry of Materials*, 31(15), 5713–5724. Available from <https://doi.org/10.1021/acs.chemmater.9b01688>.
- McGilly, L. J., Kerelsky, A., Finney, N. R., Shapovalov, K., Shih, E. M., Ghiotto, A., Zeng, Y., Moore, S. L., Wu, W., Bai, Y., Watanabe, K., Taniguchi, T., Stengel, M., Zhou, L., Hone, J., Zhu, X., Basov, D. N., Dean, C., Dreyer, C. E., & Pasupathy, A. N. (2020). Visualization of Moiré superlattices. *Nature Nanotechnology*, 15(7), 580–584. Available from <https://doi.org/10.1038/s41565-020-0708-3>, <http://www.nature.com/nnano/index.html>.
- Murata, H., Saitoh, N., Yoshizawa, N., Suemasu, T., & Toko, K. (2019). Impact of amorphous-C/Ni multilayers on Ni-induced layer exchange for multilayer graphene on insulators. *ACS Omega*, 4(10), 14251–14254. Available from <https://doi.org/10.1021/acsomega.9b01708>, <http://pubs.acs.org/journal/acsodf>.
- Muratore, C., Voevodin, A. A., & Glavin, N. R. (2019). Physical vapor deposition of 2D van der Waals materials: A review. *Thin Solid Films*, 688. Available from <https://doi.org/10.1016/j.tsf.2019.137500>, <http://www.journals.elsevier.com/journal-of-the-energy-institute>.
- Nakajima, Y., Murata, H., Saitoh, N., Yoshizawa, N., Suemasu, T., & Toko, K. (2018). Metal catalysts for layer-exchange growth of multilayer graphene. *ACS Applied Materials and Interfaces*, 10(48), 41664–41669. Available from <https://doi.org/10.1021/acsami.8b14960>, <http://pubs.acs.org/journal/aamick>.
- Nguyen, V. L., Duong, D. L., Lee, S. H., Avila, J., Han, G., Kim, Y. M., Asensio, M. C., Jeong, S. Y., & Lee, Y. H. (2020). Layer-controlled single-crystalline graphene film with stacking order via Cu–Si alloy formation. *Nature Nanotechnology*, 15(10), 861–867. Available from <https://doi.org/10.1038/s41565-020-0743-0>, <http://www.nature.com/nnano/index.html>.
- Ni, Z. (2009). G-band Raman double resonance in twisted bilayer graphene: Evidence of band splitting and folding. *Physics Review B*, 80(12).
- Nieken, R. (2022). Direct STM measurements of R-type and H-type twisted MoSe₂/WSe₂. *APL Material*, 10(3).

- Novoselov, K. S., Mishchenko, A., Carvalho, A., & Neto, A. H. C. (2016). 2D materials and van der Waals heterostructures. *Science (New York, N.Y.)*, 353(6298). Available from <https://doi.org/10.1126/science.aac9439>, <http://science.sciencemag.org/content/sci/353/6298/aac9439.full.pdf>.
- Pan, Y., Fölsch, S., Nie, Y., Waters, D., Lin, Y.-C., Jariwala, B., Zhang, K., Cho, K., Robinson, J. A., & Feenstra, R. M. (2018). Quantum-confined electronic states arising from the Moiré pattern of MoS₂-Se₂ heterobilayers. *Nano Letters*, 18(3), 1849–1855. Available from <https://doi.org/10.1021/acs.nanolett.7b05125>.
- Pham, P. V., Bodepudi, S. C., Shehzad, K., Liu, Y., Xu, Y., Yu, B., & Duan, X. (2022). 2D heterostructures for ubiquitous electronics and optoelectronics: Principles, opportunities, and challenges. *Chemical Reviews*, 122(6), 6514–6613. Available from <https://doi.org/10.1021/acs.chemrev.1c00735>, <http://pubs.acs.org/journal/chreay>.
- Pillai, U., Heider, Y., & Markert, B. (2018). A diffusive dynamic brittle fracture model for heterogeneous solids and porous materials with implementation using a user-element subroutine. *Computational Materials Science*, 153, 36–47. Available from <https://doi.org/10.1016/j.commatsci.2018.06.024>.
- Pizzocchero, F., Gammelgaard, L., Jessen, B. S., Caridad, J. M., Wang, L., Hone, J., Bøggild, P., & Booth, T. J. (2016). The hot pick-up technique for batch assembly of van der Waals heterostructures. *Nature Communications*, 7. Available from <https://doi.org/10.1038/ncomms11894>, <http://www.nature.com/ncomms/index.html>.
- Purdie, D. G. (2018). Cleaning interfaces in layered materials heterostructures. *Nature Communications*, 9(1).
- Quan, J., Linhart, L., Lin, M. L., Lee, D., Zhu, J., Wang, C. Y., Hsu, W. T., Choi, J., Embley, J., Young, C., Taniguchi, T., Watanabe, K., Shih, C. K., Lai, K., MacDonald, A. H., Tan, P. H., Libisch, F., & Li, X. (2021). Phonon renormalization in reconstructed MoS₂ Moiré superlattices. *Nature Materials*, 20(8), 1100–1105. Available from <https://doi.org/10.1038/s41563-021-00960-1>, <http://www.nature.com/nmat/>.
- Radisavljevic, B., Radenovic, A., Brivio, J., Giacometti, V., & Kis, A. (2011). Single-layer MoS₂ transistors. *Nature Nanotechnology*, 6(3), 147–150. Available from <https://doi.org/10.1038/nnano.2010.279>, <http://www.nature.com/nnano/index.html>.
- Ribeiro-Palau, R., Zhang, C., Watanabe, K., Taniguchi, T., Hone, J., & Dean, C. R. (2018). Twistable electronics with dynamically rotatable heterostructures. *Science (New York, N.Y.)*, 361(6403), 690–693. Available from <https://doi.org/10.1126/science.aat6981>, <http://science.sciencemag.org/content/361/6403/690/tab-pdf>.
- Rosenberger, M. R., Chuang, H. J., Phillips, M., Oleshko, V. P., McCreary, K. M., Sivaram, S. V., Hellberg, C. S., & Jonker, B. T. (2020). Twist angle-dependent atomic reconstruction and Moiré patterns in transition metal dichalcogenide heterostructures. *ACS Nano*, 14(4), 4550–4558. Available from <https://doi.org/10.1021/acs.nano.0c00088>, <http://pubs.acs.org/journal/ancac3>.
- Rouviere, J. (2007). *The use of the geometrical phase analysis to measure strain in nearly periodic images. Microscopy of semiconducting materials*. Springer.
- Schneider, G. F., Calado, V. E., Zandbergen, H., Vandersypen, L. M. K., & Dekker, C. (2010). Wedging transfer of nanostructures. *Nano Letters*, 10(5), 1912–1916. Available from <https://doi.org/10.1021/nl1008037>.
- Seok, H., Megra, Y. T., Kanade, C. K., Cho, J., Kanade, V. K., Kim, M., Lee, I., Yoo, P. J., Kim, H. U., Suk, J. W., & Kim, T. (2021). Low-temperature synthesis of wafer-scale MoS₂-WS₂ vertical heterostructures by single-step penetrative plasma sulfurization. *ACS Nano*, 15(1), 707–718. Available from <https://doi.org/10.1021/acs.nano.0c06989>, <http://pubs.acs.org/journal/ancac3>.
- Shi, J. (2017). 3R MoS₂ with broken inversion symmetry: A promising ultrathin nonlinear optical device. *Advanced Materials*, 29(30).
- Shi, J., Liu, M., Wen, J., Ren, X., Zhou, X., Ji, Q., Ma, D., Zhang, Y., Jin, C., Chen, H., Deng, S., Xu, N., Liu, Z., & Zhang, Y. (2015). All chemical vapor deposition synthesis and intrinsic bandgap observation of MoS₂/graphene heterostructures. *Advanced Materials*, 27(44), 7086–7092. Available from <https://doi.org/10.1002/adma.201503342>.
- Shim, J., Bae, S. H., Kong, W., Lee, D., Qiao, K., Nezich, D., Park, Y. J., Zhao, R., Sundaram, S., Li, X., Yeon, H., Choi, C., Kum, H., Yue, R., Zhou, G., Ou, Y., Lee, K., Moodera, J., Zhao, X., ... Kim, J. (2018). Controlled crack propagation for atomic precision handling of wafer-scale

- two-dimensional materials. *Science (New York, N.Y.)*, 362(6415), 665–670. Available from <https://doi.org/10.1126/science.aat8126>, <http://science.sciencemag.org/content/362/6415/665>.
- Song, X., Gao, T., Nie, Y., Zhuang, J., Sun, J., Ma, D., Shi, J., Lin, Y., Ding, F., Zhang, Y., & Liu, Z. (2016). Seed-assisted growth of single-crystalline patterned graphene domains on hexagonal boron nitride by chemical vapor deposition. *Nano Letters*, 16(10), 6109–6116. Available from <https://doi.org/10.1021/acs.nanolett.6b02279>, <http://pubs.acs.org/journal/nalefd>.
- Sun, L. (2021a). Chemical vapour deposition. *Nature Review Methods Primers.*, 1, 1–20.
- Sun, L. (2021b). Hetero-site nucleation for growing twisted bilayer graphene with a wide range of twist angles. *Nature Communications*, 12(1).
- Susarla, S., Naik, M. H., Blach, D. D., Zipfel, J., Taniguchi, T., Watanabe, K., Huang, L., Ramesh, R., da Jornada, F. H., Louie, S. G., Ercius, P., & Raja, A. (2022). Hyperspectral imaging of exciton confinement within a Moiré unit cell with a subnanometer electron probe. *Science (New York, N.Y.)*, 378(6625), 1235–1239. Available from <https://doi.org/10.1126/science.add9294>, <https://www.science.org/doi/10.1126/science.add9294>.
- Sutter, P., Lahiri, J., Zahl, P., Wang, B., & Sutter, E. (2013). Scalable synthesis of uniform few-layer hexagonal boron nitride dielectric films. *Nano Letters*, 13(1), 276–281. Available from <https://doi.org/10.1021/nl304080y>.
- Tabata, H., Sato, Y., Oi, K., Kubo, O., & Katayama, M. (2018). Bias- and gate-tunable gas sensor response originating from modulation in the Schottky barrier height of a graphene/MoS₂ van der Waals heterojunction. *ACS Applied Materials and Interfaces*, 10(44), 38387–38393. Available from <https://doi.org/10.1021/acsami.8b14667>, <http://pubs.acs.org/journal/aamick>.
- Takesaki, Y., Kawahara, K., Hibino, H., Okada, S., Tsuji, M., & Ago, H. (2016). Highly uniform bilayer graphene on epitaxial Cu–Ni (111) alloy. *Chemistry of Materials*, 28(13), 4583–4592. Available from <https://doi.org/10.1021/acs.chemmater.6b01137>, <http://pubs.acs.org/journal/cmater>.
- Tanaka, K., Kurihashi, Y., Uda, T., Daimon, Y., Odagawa, N., Hirose, R., Hiranaga, Y., & Cho, Y. (2008). Scanning nonlinear dielectric microscopy nano-science and technology for next generation high density ferroelectric data storage. *Japanese Journal of Applied Physics*, 47(5), 3311–3325. Available from <https://doi.org/10.1143/JJAP.47.3311Japan>, <http://jjap.ipap.jp/link?JJAP/47/3311/pdf>.
- Tang, L., Tan, J., Nong, H., Liu, B., & Cheng, H. M. (2021). Chemical vapor deposition growth of two-dimensional compound materials: Controllability, material quality, and growth mechanism. *Accounts of Materials Research*, 2(1), 36–47. Available from <https://doi.org/10.1021/accountsmr.0c00063>, <http://pubs.acs.org/journal/amrcda>.
- Tian, B. (2022). Synthesis of AAB-stacked single-crystal graphene/hBN/graphene trilayer van der Waals heterostructures by in situ CVD. *Advancement of Science*, 9(21).
- Tilak, N., Li, G., Taniguchi, T., Watanabe, K., & Andrei, E. Y. (2023). Moiré potential, lattice relaxation, and layer polarization in marginally twisted MoS₂ bilayers. *Nano Letters*, 23(1), 73–81. Available from <https://doi.org/10.1021/acs.nanolett.2c03676>.
- Uchida, Y., Nakandakari, S., Kawahara, K., Yamasaki, S., Mitsuhashi, M., & Ago, H. (2018). Controlled growth of large-area uniform multilayer hexagonal boron nitride as an effective 2D substrate. *ACS Nano*, 12(6), 6236–6244. Available from <https://doi.org/10.1021/acsnano.8b03055>, <http://pubs.acs.org/journal/ancac3>.
- Vaněk, F., Jati, G. N. P., Okada, K., Xie, Y., Zhu, W., Macháč, P., Marin, E., & Pezzotti, G. (2020). Transfer-free layered graphene on silica via segregation through a nickel film for electronic applications. *ACS Applied Nano Materials*, 3(10), 9984–9992. Available from <https://doi.org/10.1021/acsnm.0c01938>.
- Vishwanath, S., Liu, X., Rouvimov, S., Basile, L., Lu, N., Azcatl, A., Magno, K., Wallace, R. M., Kim, M., Idrobo, J. C., Furdyna, J. K., Jena, D., & Xing, H. G. (2016). Controllable growth of layered selenide and telluride heterostructures and superlattices using molecular beam epitaxy. *Journal of Materials Research*, 31(7), 900–910. Available from <https://doi.org/10.1557/jmr.2015.374>, <http://journals.cambridge.org/action/displayJournal?jid=JMR>.
- Wang, B., Huang, M., Kim, N. Y., Cunnings, B. V., Huang, Y., Qu, D., Chen, X., Jin, S., Biswal, M., Zhang, X., Lee, S. H., Lim, H., Yoo, W. J., Lee, Z., & Ruoff, R. S. (2017). Controlled folding of

- single crystal graphene. *Nano Letters*, 17(3), 1467–1473. Available from <https://doi.org/10.1021/acs.nanolett.6b04459>, <http://pubs.acs.org/journal/nalefd>.
- Wang, H., & Qian, X. (2017). Giant optical second harmonic generation in two-dimensional multiferroics. *Nano Letters*, 17(8), 5027–5034. Available from <https://doi.org/10.1021/acs.nanolett.7b02268>, <http://pubs.acs.org/journal/nalefd>.
- Wang, L., Shih, E. M., Ghiotto, A., Xian, L., Rhodes, D. A., Tan, C., Claassen, M., Kennes, D. M., Bai, Y., Kim, B., Watanabe, K., Taniguchi, T., Zhu, X., Hone, J., Rubio, A., Pasupathy, A. N., & Dean, C. R. (2020). Correlated electronic phases in twisted bilayer transition metal dichalcogenides. *Nature Materials*, 19(8), 861–866. Available from <https://doi.org/10.1038/s41563-020-0708-6>, <http://www.nature.com/nmat/>.
- Wang, L., Meric, I., Huang, P. Y., Gao, Q., Gao, Y., Tran, H., Taniguchi, T., Watanabe, K., Campos, L. M., Muller, D. A., Guo, J., Kim, P., Hone, J., Shepard, K. L., & Dean, C. R. (2013). One-dimensional electrical contact to a two-dimensional material. *Science (New York, N.Y.)*, 342(6158), 614–617. Available from <https://doi.org/10.1126/science.1244358>, <http://www.sciencemag.org/content/342/6158/614.full.pdf>.
- Wang, M., Huang, M., Luo, D., Li, Y., Choe, M., Seong, W. K., Kim, M., Jin, S., Wang, M., Chatterjee, S., Kwon, Y., Lee, Z., & Ruoff, R. S. (2021). Single-crystal, large-area, fold-free monolayer graphene. *Nature*, 596(7873), 519–524. Available from <https://doi.org/10.1038/s41586-021-03753-3>, <http://www.nature.com/nature/index.html>.
- Wang, Q. (2022). Layer-by-layer epitaxy of multi-layer MoS₂ wafers. *National Science Review*, 9(6).
- Wang, Q., Li, N., Tang, J., Zhu, J., Zhang, Q., Jia, Q., Lu, Y., Wei, Z., Yu, H., Zhao, Y., Guo, Y., Gu, L., Sun, G., Yang, W., Yang, R., Shi, D., & Zhang, G. (2020). Wafer-scale highly oriented monolayer MoS₂ with large domain sizes. *Nano Letters*, 20(10), 7193–7199. Available from <https://doi.org/10.1021/acs.nanolett.0c02531>.
- Weston, A., Zou, Y., Enaldiev, V., Summerfield, A., Clark, N., Zólyomi, V., Graham, A., Yelgel, C., Magorrian, S., Zhou, M., Zultak, J., Hopkinson, D., Barinov, A., Bointon, T. H., Kretinin, A., Wilson, N. R., Beton, P. H., Fal'ko, V. I., Haigh, S. J., & Gorbachev, R. (2020). Atomic reconstruction in twisted bilayers of transition metal dichalcogenides. *Nature Nanotechnology*, 15(7), 592–597. Available from <https://doi.org/10.1038/s41565-020-0682-9>, <http://www.nature.com/nnano/index.html>.
- Whelan, P. R., Jessen, B. S., Wang, R., Luo, B., Stoot, A. C., Mackenzie, D. M. A., Braeuninger-Weimer, P., Jouvray, A., Prager, L., Camilli, L., Hofmann, S., Bøggild, P., & Booth, T. J. (2017). Raman spectral indicators of catalyst decoupling for transfer of CVD grown 2D materials. *Carbon*, 117, 75–81. Available from <https://doi.org/10.1016/j.carbon.2017.02.028>, <http://www.journals.elsevier.com/carbon/>.
- Withers, F., Del Pozo-Zamudio, O., Mishchenko, A., Rooney, A. P., Gholinia, A., Watanabe, K., Taniguchi, T., Haigh, S. J., Geim, A. K., Tartakovskii, A. I., & Novoselov, K. S. (2015). Light-emitting diodes by band-structure engineering in van der Waals heterostructures. *Nature Materials*, 14(3), 301–306. Available from <https://doi.org/10.1038/nmat4205>, <http://www.nature.com/nmat/>.
- Wong, D., Wang, Y., Jung, J., Pezzini, S., Dasilva, A. M., Tsai, H. Z., Jung, H. S., Khajeh, R., Kim, Y., Lee, J., Kahn, S., Tollabimazraehno, S., Rasool, H., Watanabe, K., Taniguchi, T., Zettl, A., Adam, S., Macdonald, A. H., & Crommie, M. F. (2015). Local spectroscopy of moiré-induced electronic structure in gate-tunable twisted bilayer graphene. *Physical Review B - Condensed Matter and Materials Physics*, 92(15). Available from <https://doi.org/10.1103/PhysRevB.92.155409>, <http://harvest.aps.org/bagit/articles/10.1103/PhysRevB.92.155409/apsxml>.
- Woods, C. R. (2021). Charge-polarized interfacial superlattices in marginally twisted hexagonal boron nitride. *Nature Communications*, 12(1).
- Wu, W., & Wang, Z. L. (2016). Piezotronics and piezo-phototronics for adaptive electronics and optoelectronics. *Nature Review Materials*, 1(7), 1–17.
- Xiao, Y., Liu, J., & Fu, L. (2020). Moiré is more: Access to new properties of two-dimensional layered materials. *Matter*, 3(4), 1142–1161. Available from <https://doi.org/10.1016/j.matt.2020.07.001>, <http://www.cell.com/matter>.

- Yan, K., Peng, H., Zhou, Y., Li, H., & Liu, Z. (2011). Formation of bilayer bernal graphene: Layer-by-layer epitaxy via chemical vapor deposition. *Nano Letters*, *11*(3), 1106–1110. Available from <https://doi.org/10.1021/nl104000b>.
- Yang, F., Song, W., Meng, F., Luo, F., Lou, S., Lin, S., Gong, Z., Cao, J., Barnard, E. S., Chan, E., Yang, L., & Yao, J. (2020). Tunable second harmonic generation in twisted bilayer graphene. *Matter*, *3*(4), 1361–1376. Available from <https://doi.org/10.1016/j.matt.2020.08.018>, <http://www.cell.com/matter>.
- Yang, S. Y., Oh, J. G., Jung, D. Y., Choi, H. K., Yu, C. H., Shin, J., Choi, C. G., Cho, B. J., & Choi, S. Y. (2015). Metal-etching-free direct delamination and transfer of single-layer graphene with a high degree of freedom. *Small (Weinheim an der Bergstrasse, Germany)*, *11*(2), 175–181. Available from <https://doi.org/10.1002/smll.201401196>, [http://onlinelibrary.wiley.com/journal/10.1002/\(ISSN\)1613-6829](http://onlinelibrary.wiley.com/journal/10.1002/(ISSN)1613-6829).
- Yankowitz, M., Xue, J., Cormode, D., Sanchez-Yamagishi, J. D., Watanabe, K., Taniguchi, T., Jarillo-Herrero, P., Jacquod, P., & Leroy, B. J. (2012). Emergence of superlattice Dirac points in graphene on hexagonal boron nitride. *Nature Physics*, *8*(5), 382–386. Available from <https://doi.org/10.1038/nphys2272>.
- Ye, Z., Lum, G. Z., Song, S., Rich, S., & Sitti, M. (2016). Phase change of gallium enables highly reversible and switchable adhesion. *Advanced Materials*, *28*(25), 5088–5092. Available from <https://doi.org/10.1002/adma.201505754>, <http://www3.interscience.wiley.com/journal/119030556/issue>.
- Yoo, H., Engelke, R., Carr, S., Fang, S., Zhang, K., Cazeaux, P., Sung, S. H., Hovden, R., Tsen, A. W., Taniguchi, T., Watanabe, K., Yi, G. C., Kim, M., Luskin, M., Tadmor, E. B., Kaxiras, E., & Kim, P. (2019). Atomic and electronic reconstruction at the van der Waals interface in twisted bilayer graphene. *Nature Materials*, *18*(5), 448–453. Available from <https://doi.org/10.1038/s41563-019-0346-z>, <http://www.nature.com/nmat/>.
- Yu, B., Duan, J., Cong, H., Xie, W., Liu, R., Zhuang, X., Wang, H., Qi, B., Xu, M., Wang, Z. L., & Zhou, J. (2020). Thermosensitive crystallization-boosted liquid thermocells for low-grade heat harvesting. *Science (New York, N.Y.)*, *370*(6514), 342–346. Available from <https://doi.org/10.1126/science.abd6749>, <https://science.sciencemag.org/content/370/6514/342>.
- Yu, H., Liao, M., Zhao, W., Liu, G., Zhou, X. J., Wei, Z., Xu, X., Liu, K., Hu, Z., Deng, K., Zhou, S., Shi, J. A., Gu, L., Shen, C., Zhang, T., Du, L., Xie, L., Zhu, J., Chen, W., . . . Zhang, G. (2017). Wafer-scale growth and transfer of highly-oriented monolayer MoS₂ continuous films. *ACS Nano*, *11*(12), 12001–12007. Available from <https://doi.org/10.1021/acsnano.7b03819>, <http://pubs.acs.org/journal/acsnano>.
- Zatko, V., Dubois, S. M. M., Godel, F., Carrétéro, C., Sander, A., Collin, S., Galbiati, M., Peiro, J., Panciera, F., Patriarche, G., Brus, P., Servet, B., Charlier, J. C., Martin, M. B., Dlubak, B., & Seneor, P. (2021). Band-gap landscape engineering in large-scale 2D semiconductor van der Waals heterostructures. *ACS Nano*, *15*(4), 7279–7289. Available from <https://doi.org/10.1021/acsnano.1c00544>, <http://pubs.acs.org/journal/acsnano>.
- Zeng, Z. (2019). Controlled vapor growth and nonlinear optical applications of large-area 3R phase WS₂ and WSe₂ atomic layers. *Advanced Functional Materials*, *29*(11).
- Zhan, Y., Liu, Z., Najmaei, S., Ajayan, P. M., & Lou, J. (2012). Large-area vapor-phase growth and characterization of MoS₂ atomic layers on a SiO₂ substrate. *Small (Weinheim an der Bergstrasse, Germany)*, *8*(7), 966–971. Available from <https://doi.org/10.1002/smll.201102654>.
- Zhang, S., Maruyama, M., Okada, S., Xue, M., Watanabe, K., Taniguchi, T., Hashimoto, K., Miyata, Y., Canton-Vitoria, R., & Kitaura, R. (2023). Observation of the photovoltaic effect in a van der Waals heterostructure. *Nanoscale*, *15*(12), 5948–5953. Available from <https://doi.org/10.1039/d2nr06616e>, <http://pubs.rsc.org/en/journals/journal/nr>.
- Zhang, Y. J., Oka, T., Suzuki, R., Ye, J. T., & Iwasa, Y. (2014). Electrically switchable chiral light-emitting transistor. *Science (New York, N.Y.)*, *344*(6185), 725–728. Available from <https://doi.org/10.1126/science.1251329>, <http://www.sciencemag.org/content/344/6185/725.full.pdf>.
- Zhang, Z. (2022). Continuous epitaxy of single-crystal graphite films by isothermal carbon diffusion through nickel. *Nature Nanotechnology*, *17*(12), 1–7.
- Zhang, Z., Wang, Y., Watanabe, K., Taniguchi, T., Ueno, K., Tutuc, E., & LeRoy, B. J. (2020). Flat bands in twisted bilayer transition metal dichalcogenides. *Nature Physics*, *16*(11), 1093–1096.

Available from <https://doi.org/10.1038/s41567-020-0958-x>, <http://www.nature.com/nphys/index.html>.

Zhao, Y. (2020). Thermal transport in 2D semiconductors—Considerations for device applications. *Advanced Functional Materials*, 30(8).

Zheng, J., Yan, X., Lu, Z., Qiu, H., Xu, G., Zhou, X., Wang, P., Pan, X., Liu, K., & Jiao, L. (2017). High-mobility multilayered MoS₂ flakes with low contact resistance grown by chemical vapor deposition. *Advanced Materials*, 29(13). Available from <https://doi.org/10.1002/adma.201604540>, <http://www3.interscience.wiley.com/journal/119030556/issue>.

CHAPTER 17

2D materials—based electronics enabled by transfer printing technologies

Sangmoon Han¹, Zhihao Xu^{1,2}, Yuan Meng^{1,2} and Sang-Hoon Bae^{1,2}

¹Department of Mechanical Engineering & Materials Science, Washington University in St. Louis, Saint Louis, MO, United States

²The Institution of Materials Science and Engineering, Washington University in St. Louis, Saint Louis, MO, United States

17.1 Overview

Over the past decade, two-dimensional (2D) layered materials have established themselves as a new paradigm for advanced electronics applications. Graphene was the first 2D substance to be thoroughly researched. It has been intensively studied as a channel material for field-effect transistors (FETs), thanks to its high mobility above $15,000 \text{ cm}^2/\text{V} \cdot \text{s}$ (Chen et al., 2008; Schwierz, 2010). Also, many different applications have been explored, thanks to their outstanding properties. Inspired by graphene, intensive research interests are devoted to exploring semiconducting, insulating, and metallic 2D materials such as transition metal dichalcogenides (TMD), triggering a huge amount of research results for the materials applications (Long et al., 2019; Miao et al., 2015). Distinctive from conventional three-dimensional (3D) bulk materials, the absence of dangling bonds on the surface of 2D materials enables handy heterointegration at the van der Waals (vdW) interface, which has the potential to overcome the physical limitations of conventional heteroepitaxy-based heterostructures. This chapter describes several interesting electronic applications based on 2D materials, such as advanced transistors, optoelectronics, and memory devices, fabricated by transfer printing technology.

17.2 2D layer—based logic devices

The FET is one of the foundational components of an electronic device as it can realize logic cells as well as circuit amplification. Early FETs apply bottom-gate and top-gate structures. To date, as the integration density of FETs in circuits increases, researchers have been dedicated to reducing the channel length of FETs to below a few nanometers (Chau et al., 2007; Wu et al., 2022). However, these attempts are blocked by a huge barrier called the short-channel effect. The short-channel effect is the charge tunneling by

the scale-down of metal–oxide–semiconductor FET (MOSFET) channel length, and eventually, the channel is not closed (Liu, Duan, et al., 2021). To overcome this problem, many researchers have led to various technological adaptations in MOSFET design, ranging from high- κ dielectrics with metal gates in 45-nm node processors in 2007 to making 3D Fin FET (Fin-FETs) in 2012 (Mistry et al., 2007). Recently a gate-all-around FET structure reportedly addresses the short-channel effect (Ferain et al., 2011). However, conventional semiconductors such as Silicon (Si) still suffer from rich dangling bonds, leading to the scattering of charge carriers and severe degradation in carrier mobility because of undesirable coupling with phonons and the creation of interface states.

Meanwhile, 2D materials hold the promise to further advance complementary metal–oxide–semiconductor (CMOS) technology, thanks to their smooth surface and being free of dangling bonds (Bediako et al., 2018; Kang et al., 2017; Lee et al., 2014). Another important advantage of 2D materials is that they are immune to short-channel effects, thanks to their atomically thin thickness (Akinwande et al., 2019; Si et al., 2018). Nevertheless, controlling short-channel effects for sustained dimensional scaling still remains a critical challenge. The main issue is the damage to the 2D layer during the deposition of the electrode and oxide layer. Difficulty in the high- k dielectric layer includes one of the main problems. In this chapter, we discuss the history from 2D back-gate FET to GAAFET (see Fig. 17.1) and deliberate on their evolution and emerging opportunities.

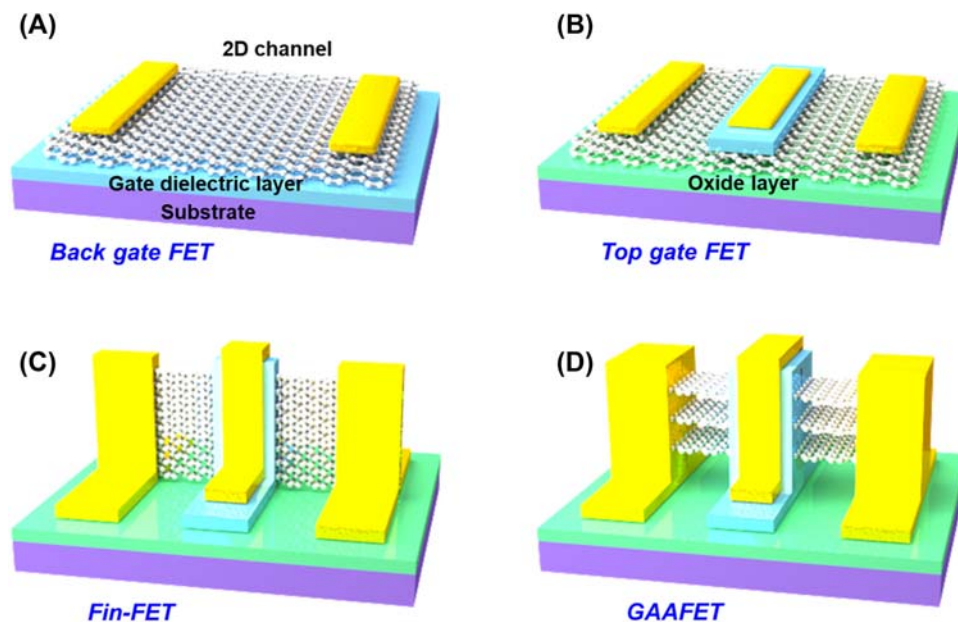


Figure 17.1 2D material–based FETs. (A) Back-gated FET, (B) top-gated FET, (C) Fin-FET, and (D) GAAFET structures.

17.2.1 Homogeneous 2D field-effect transistors

Graphene was first studied as a channel in 2D FETs. Graphene has a hexagonal lattice spacing with two equivalent sublattices in each unit cell and the band structure is different from conventional bulk semiconductors as follows: First, 2D graphene has zero bandgap characteristics with degenerate conduction and valence bands at the six corners of the Brillouin zone (Yazyev & Louie, 2010). Second, near the edge of the Brillouin zone, the energy dispersion relationship is nearly linear rather than quadratic, which can be described by the massless Dirac equation (like harmonic oscillation), analogous to relativistic particles (Pesin & MacDonald, 2012). Third, the density of states (DOS) at the Dirac point is zero, making 2D graphene a semimetallic material with a tunable Fermi level. Graphene transistors have a bipolar electric field effect, which means that graphene's carriers can be continuously tuned between holes and electrons (Gomes et al., 2012; Ponomarenko et al., 2010). However, the no-bandgap nature of graphene does not allow for making a switching device.

A new 2D materials system expected to solve this problem is a group of TMDs. Molybdenum disulfide (MoS_2) is a representative TMD material for 2D FETs because of its relatively large band gap (≤ 1.8 eV) and high mobility ($50\text{--}200$ $\text{cm}^2/\text{V}\cdot\text{s}$) (Kim et al., 2012). Recently the vertically structured 2D FETs with the MoS_2 channel were reported that only have a sub-1 nm gate length (see Fig. 17.2) (Wu et al., 2022). MoS_2 and the edge of graphene act as the channel and the gate, respectively, which enabled the achievement of 0.34 nm gate-length sidewall transistors. The sidewall structure effectively uses the natural ultrathin thickness of graphene and shows wafer-scale production. The on/off ratio and subthreshold swing (SS) value were measured to be 1.02×10^5 and 117 mV/dec, respectively (see Fig. 17.2B and C).

Larger on-currents can be implemented using a material with a narrow bandgap and high mobility, such as black phosphorus (BP) (Li et al., 2014). It is also important to recognize that using 2D channel materials is compatible with other performance-enhancing techniques. These include using negative capacitance to improve gate-channel coupling and channel materials to improve local current drive (Li et al., 2019; Liu, Zhou, et al., 2016). The 2D FETs can be fabricated at low temperatures, a key requirement for the next-generation computing performance and monolithic 3D integration of energy-efficient logic and memory (Conti et al., 2020; Jiang et al., 2019; Wang et al., 2018).

17.2.2 Back-gate field-effect transistors

A SiO_2 layer underneath the 2D material was a dielectric layer, and a highly doped silicon substrate acted as the back-gate electrode (Novoselov et al., 2004). Early 2D-based FETs were also fabricated with a back-gate structure. Fig. 17.3 shows the single-layer MoS_2 FET, where the channel length and on-off ratio are 1.5 μm and 10^6 , respectively (Radisavljevic et al., 2011). Such back-gate devices have been particularly useful for

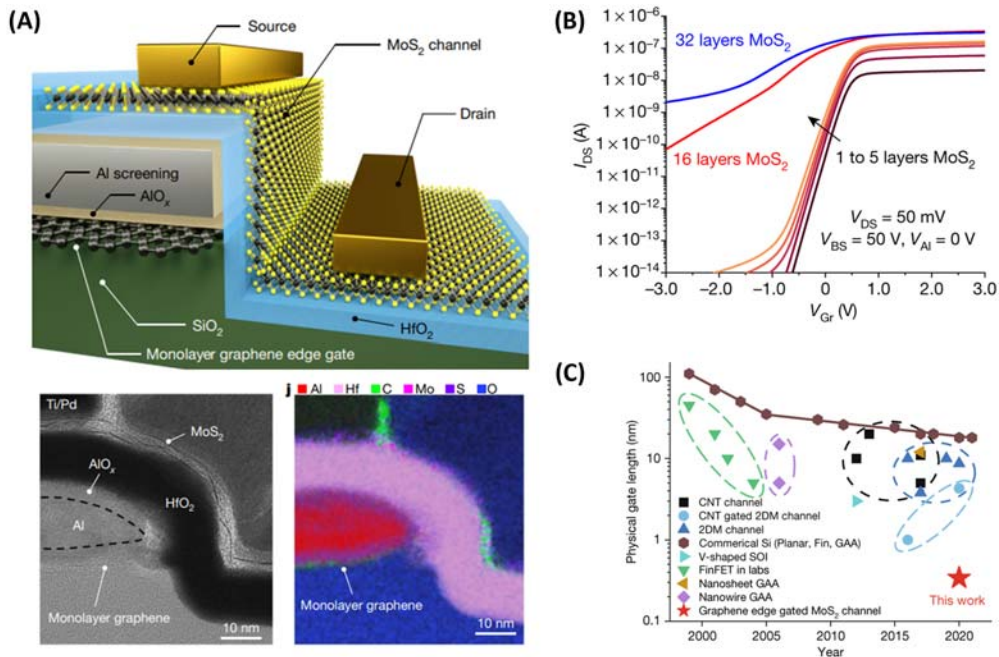


Figure 17.2 Homogeneous 2D FET. (A) Schematic illustration, transmission electron microscopy, and energy dispersion spectroscopy image of the vertical MoS₂ FETs. (B) The MoS₂ layer dependent I_D - V_G curve and (C) the time scale evolution of the gate length. From Wu et al. (2022). Vertical MoS₂ transistors with sub-1-nm gate lengths. *Nature*, 603(7900), 259–264. <https://doi.org/10.1038/s41586-021-04323-3>.

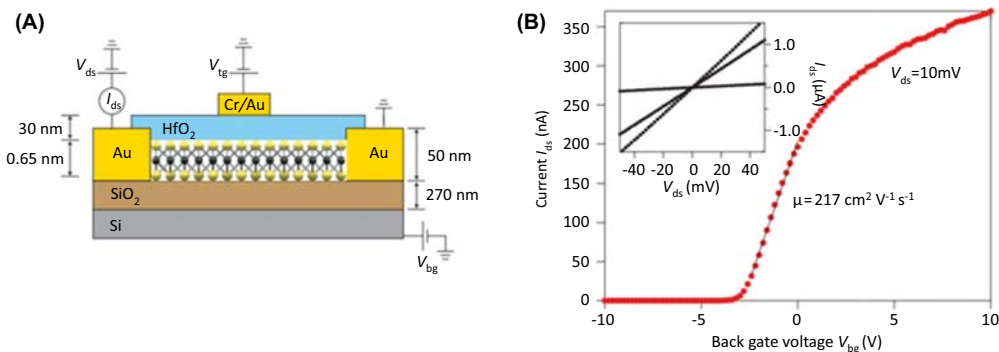


Figure 17.3 Back-gate FET. (A) Schematic illustration and (B) electrical characterization of top-gated monolayer MoS₂ FET. From Radisavljevic et al. (2011). Single-layer MoS₂ transistors. *Nature Nanotechnology*, 6(3), 147–150. <https://doi.org/10.1038/nnano.2010.279>.

proof-of-concept purposes, but they suffer from unacceptably large parasitic capacitances and cannot be integrated with other components on the same chip due to the presence of the global back gate, which is typically a degenerately doped Si substrate.

17.2.3 Novel hetero-integrated 2D field-effect transistors

Given that any passivated dangling-bond-free surface will interact with another through vdW forces, the vdW heterostructure concept can be extended to include the integration of 2D materials with nD materials ($n = 0, 1, \text{ or } 3$) that are assembled primarily through noncovalent interactions (Han et al., 2021; Nian et al., 2017). The emergence of both structural and electronic variety in vdW-bonded layered materials has opened new avenues for fundamental scientific studies and applied device designs; several combinations of 2D-layered materials have been assembled to produce vdW heterostructures with varying functionalities. These 2D vdW heterostructures exhibit unique properties such as gate tunability, enabling new functionalities compared with conventional devices. 2D-nD integration is fabricated by growing nD materials on a 2D surface. For example, depositing metal electrodes and a dielectric layer on a 2D channel layer to fabricate a top-gate FET provides higher gate controllability than back-gate counterparts. However, the large kinetic energy of adatom during growth causes defects, dislocation, and interdiffusion at the 2D interface will degrade the performance of the device. However, this approach induces defects, dislocations, and interdiffusions at the 2D interface due to the large kinetic energy of adatom during growth. Moreover, it is difficult to grow high-crystalline high- k materials due to unstable nucleation sites. These results dramatically decrease the device's performance. As an alternative to direct growth, layer transition-based nD/3D heterointegration-based FETs are attractive. As an example, high- k complex oxide, which acts as a gate dielectric layer, was integrated into a 2D channel as shown in Fig. 17.4. The SS swing of 71.5 mV/dec and mobility of $39.7 \text{ cm}^2/\text{V} \cdot \text{s}$ were observed (Huang et al., 2022).

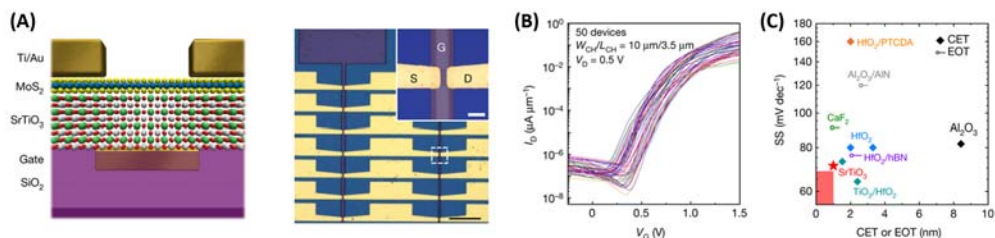


Figure 17.4 2D/3D FETs. (A) Schematic and optical micrograph of the FETs. (B) I_D – V_G curves of 50 SrTiO₃/MoS₂ FETs. (C) Comparison of SS values achieved by state-of-the-art CVD-prepared MoS₂ FETs with the sub-10-nm CET or EOT technologies. From Huang et al. (2022). High- κ perovskite membranes as insulators for two-dimensional transistors. *Nature*, 605(7909), 262–267. <https://doi.org/10.1038/s41586-022-04588-2>.

17.3 2D layer–based optoelectronics

2D materials have tremendous potential for novel optoelectronic and photonic applications, thanks to their unique physical phenomena such as tunable band gaps, spin-polarized valleys, and large excitonic binding energies. Various 2D material candidates exist covering the entire visible range and their optical bandgap can also be controlled by applied strain and/or electric field (Huang et al., 2015; Maiti et al., 2020). The thin thickness of the 2D layer enables heterogeneous integration with diverse materials for vdW heterostructures, opening up various opportunities for high-performance optoelectronics with tailored optical properties. In this chapter, we discuss various optoelectronic devices such as photodetectors, photovoltaic cells, and LEDs based on 2D materials.

17.3.1 Photodetectors

2D material–based photodetectors have been widely studied. The photodetectors began to be studied in a 2D photoconductive layer, as shown in Fig. 17.5A (Lopez-Sanchez et al., 2013). Since monolayer MoS₂ has a direct bandgap, thanks to its quantum-mechanical confinement, it is a suitable material for optoelectronics, where the direct bandgap would allow a high absorption coefficient and efficient electron–hole pair generation under photoexcitation. A p–n junction with homogeneous or heterogeneous materials was also commonly reported to fabricate high-performance photodetection with the help of the in-built electric field for enhanced photogenerated carrier separation. A p–n photodetector with low dark current and high response time can be achieved simultaneously due to efficient carrier separation and extraction at the junction interface (Luo et al., 2019). Moreover, the carrier separation and extraction efficiencies are improved as there is no depletion area due to the thin thickness of the 2D material and the vdW interface (Chen et al., 2021; Lukman et al., 2020). Recently, bioinspired devices, including optical memory and neuromorphic devices, have been widely studied using an optical sensor array, as shown in Fig. 17.5C and d (Jayachandran et al., 2020; Shastri et al., 2021). The easy heterointegration of 2D materials will open the way for new systems synergized with photodetectors.

17.3.2 Photovoltaics

Photovoltaics is a rapidly growing field driven by the search for more efficient and scalable solar cells for clean and renewable energy. Currently, silicon solar cells hold approximately 95% of the global photovoltaic market (Dias et al., 2022; Yu et al., 2021). 2D materials–based photovoltaic devices with good performance have been demonstrated but significant improvements are needed for pushing these devices to reach efficiencies comparable to other non-Si alternatives. For this reason, early 2D-based photovoltaics has been integrated and developed with Si solar cells (Das et al., 2019). Thanks to the high

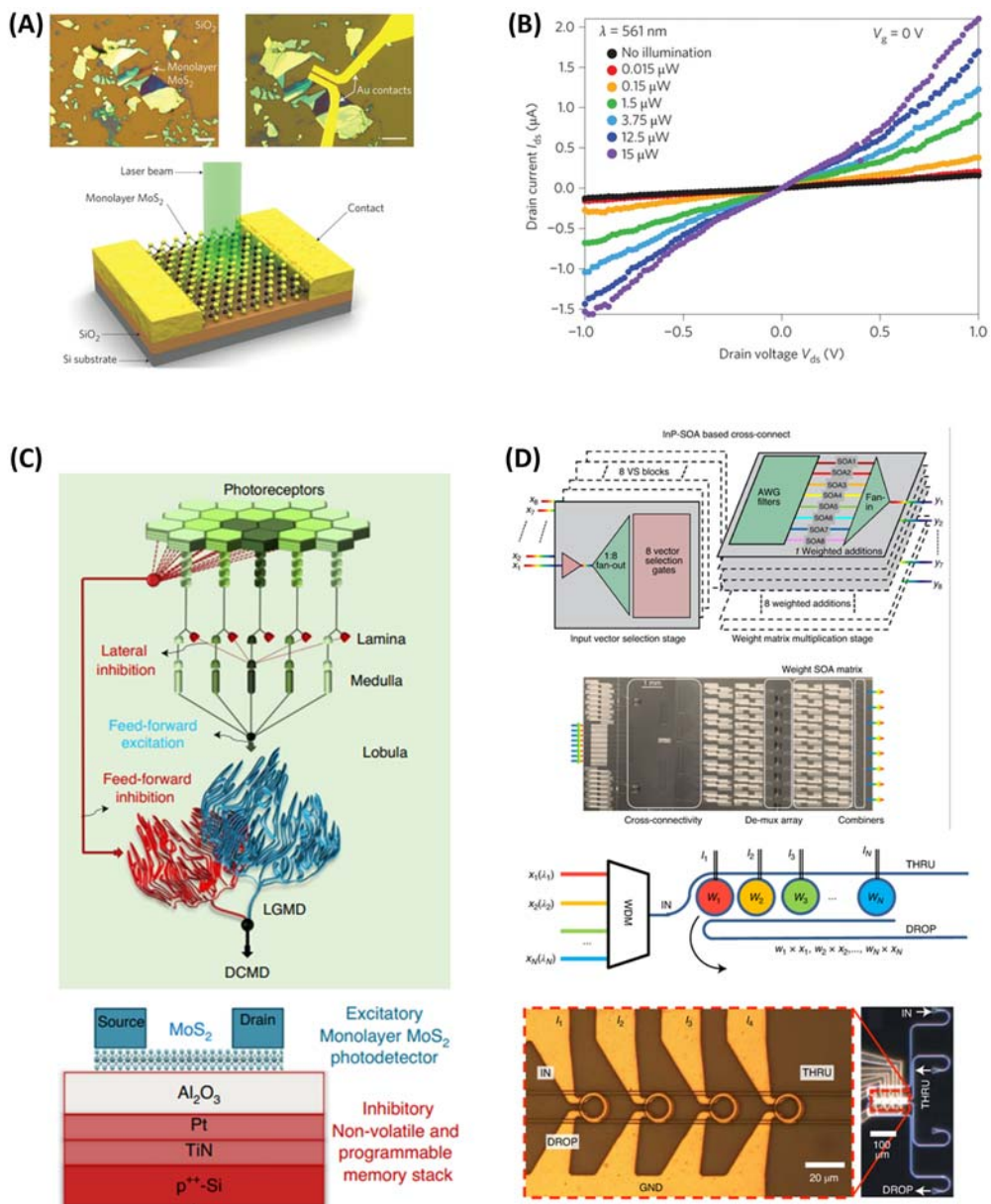


Figure 17.5 2D material-based photodetectors. (A) Optical image and schematic illustration of the single-layer MoS₂ flake serving as the conductive channel. (B) I_d - V_d characteristic of the device in the dark and under different illumination intensities. (C) Anatomical drawing of a locust's vision pathway elucidating the neurobiological architecture for collision avoidance and schematic of a biomimetic collision detector consisting of a monolayer MoS₂-based photodetector. (D) Parallel weighting of wavelength-division multiplexing signals with microring resonators weight banks as tunable filters and balanced photodetector sums these signals and allows for positive and negative weights. (A and B) From Lopez-Sanchez et al. (2013). *Ultrasensitive photodetectors based on monolayer MoS₂*. *Nature Nanotechnology*, 8 (7), 497–501. <https://doi.org/10.1038/nnano.2013.100>. (C) From Jayachandran et al. (2020). *A low-power biomimetic collision detector based on an in-memory molybdenum disulfide photodetector*. *Nature Electronics*, 3(10), 646–655. <https://doi.org/10.1038/s41928-020-00466-9>. (D) From Shastri et al. (2021). *Photonics for artificial intelligence and neuromorphic computing*. *Nature Photonics*, 15(2), 102–114. <https://doi.org/10.1038/s41566-020-00754-y>.

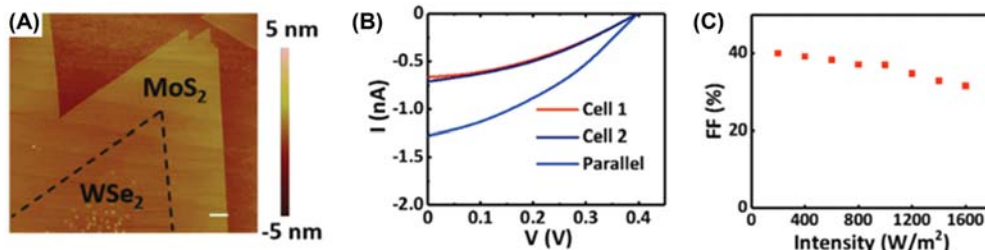


Figure 17.6 2D material–based solar cells. (A) Atomic force microscopy image of monolayer MoS₂/WSe₂ heterostructure. (B) I - V characteristic curve and (C) light intensity dependent FF of the device under AM 1.5 G light illumination. From Tsai et al. (2017). Single atomically sharp lateral monolayer p - n heterojunction solar cells with extraordinarily high power conversion efficiency. *Advanced Materials*. 29, 2017.

optical transparency and fast carrier extraction efficiency, 2D materials can contribute to improving device performance and efficiencies of 3D solar cells. Then, 2D p - n junction-based vertical photovoltaic devices were reported, demonstrating the high carrier extraction efficiency and short electrical paths for photogenerated carriers (Buscema et al., 2014; Pospischil et al., 2014). As aforementioned, 2D heterointerfaces with vdW interfaces can expand the light absorption spectrum regions through an appropriate heterointegration of the 2D materials. Fig. 17.6A shows a solar cell with a monolayer MoS₂/WSe₂ interface, with a power conversion efficiency of 2.56% under AM 1.5 G illumination (Tsai et al., 2017). The V_{oc} , I_{sc} , and fill factor (FF) were measured to be 0.39 V, 0.71 nA, and 37.01%, respectively (see Fig. 17.6B and C). The benefit of this structure lies in the exposure of the full depletion area to light, with excellent omnidirectional light-harvesting characteristics.

Although a high V_{oc} can be achieved relatively easily by a reasonable choice of material properties, low FF and power conversion efficiency (PCE) reduce the output power. This is a common observation in 2D materials–based solar cells due to various reasons, including but not limited to (1) inefficient absorption across the entire solar spectrum, (2) lack of reliable, controlled, and selective means of doping, (3) poor control over minority carrier diffusion lengths/lifetimes, and (4) unoptimized contact interfaces to reduce carrier collection losses. These aspects also highlight the areas for future research for 2D materials–based photovoltaic cells. Although TMDCs have high theoretically projected PCE values, lower external quantum efficiency (EQE) values at reduced thicknesses and inefficient device designs hinder the output performance. EQE can be improved via proper device design, whereas the careful choice of materials and interface properties engineering are crucial to improving PCE. Despite such efforts, the fundamental limitation in the light-matter interaction of 2D materials may still restrain the potential of 2D material–based photovoltaic cells.

17.3.3 Light-emitting devices

Even though 2D materials possess ultrathin thickness and a small DOS for electron–photon confinement, TMDs-based electroluminescence (EL) and lasing action are still attractive research fields, thanks to their direct bandgap at monolayer thickness.

A p–n junction is widely required to inject electrons and holes for efficient photon generation in ELs. For 2D TMDs, lateral junctions or vertically stacked structures can be fabricated for electron or hole injection for EL. The EL emission from the lateral junctions made from mono-/few-layer TMDs has been recently reported (Li et al., 2015). However, the local area EL emission was observed across the one-dimensional junction interface (Li et al., 2020; Zhang et al., 2020). For large area EL emission, vertically stacked structures with 2D junction interfaces are suggested (Nikam et al., 2017). However, fast carrier leakage through monolayer TMDs in vertical junctions due to their atomically thin thickness can prevent efficient recombination of injected carriers and limit EL efficiency in vertically stacked electrically driven light-emitting devices. Multilayer TMDs can be advantageous for this, but they are usually indirect bandgap semiconductors and optically inactive. Recently, broadband EL emission on the junction area of vertically stacked heterostructures of multilayer MoS₂ has been reported (Li et al., 2015) achieving unique EL property fundamentally stems from the unique electronic band structure of multilayer MoS₂ that is not readily achievable in other traditional indirect semiconductors (e.g., Si). Such a feature is also observed in other TMD materials.

TMDs can be used as a gain medium in micro–nano lasers. Fig. 17.7 shows the strong optical confinement and high modal gain achieved by embedding the monolayer WS₂ between Si₃N₄ and hydrogen silsesquioxane (Ye et al., 2015). The emission spectrum is observed at a wavelength of 612.2 nm. The microring- or microdisk-shaped cavity can offer the possibility of an ultralow threshold laser. Moreover, stimulated emission accumulates

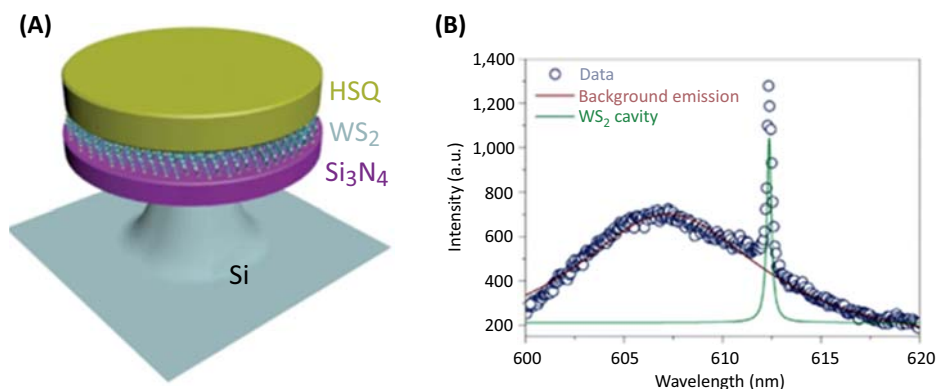


Figure 17.7 2D material–based laser. (A) Schematic image of a monolayer WS₂ microdisk laser. (B) Photoluminescence spectrum for a pump intensity of 65.7 MW/cm². From Ye et al. (2015). *Monolayer excitonic laser. Nature Photonics*. 9(11), 733–737. <https://doi.org/10.1038/nphoton.2015.197>.

beyond the lasing threshold by integrating 2D materials, enabling a high laser gain. Such advances could result in devices that fully integrate 2D materials for quantum optoelectronics (Kianinia et al., 2017; Peyskens et al., 2019).

17.4 2D layer–based memory devices

To address the ever-increasing demand for data processing load and density in a modern information society, memory devices are evolving toward miniaturization in size and high density in integration. 2D materials as an emerging material platform can address the device integration issue due to their atomically thin nature (Geim & Novoselov, 2007). In addition, no dangling bonds generally exist at the surface of 2D materials, and vertical heterogeneous integration can be made handy and possible, providing highly efficient integration devices. For instance, h-BN can be used as a dielectric layer (Britnell et al., 2012), graphene is a good interconnector, and TMDs and BP play an important role in channel material (Wu et al., 2020). Recently, researchers have been exploring 2D material–based memory devices such as floating gate memories and ferroelectric FETs, which will be described in this chapter.

17.4.1 Floating gate memories

The universal floating gate memory based on 2D materials consists of a channel layer, dielectric layer, tunneling layer, and charge trapping layer, as shown in Fig. 17.8A. According to different charge trapping layers, floating gate memory devices can be divided into different types, such as traditional floating gate memory, silicon–oxide–nitride–oxide memory, and nano floating gate memory (Bachhofer et al., 2001; Wang et al., 2015). Floating gate memory devices work by injecting (charging) and releasing (discharging) charges in the floating gate. When electrons are injected into the floating gate, the memory is in the program state, and there is a small source–drain current in the channel under a specific read voltage. On the contrary, when the electrons are released in the floating gate, the memory is in the erase state, and the source–drain current increases under the same read voltage. Compared with the program state, in the erase state, the threshold

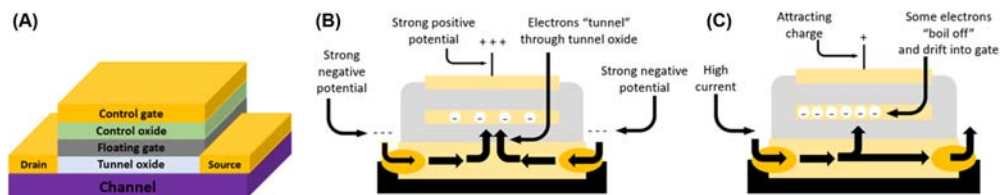


Figure 17.8 2D material–based floating gate memory. (A) Schematic of a floating gate memory. (B,C) Charging and discharging mechanisms: Fowler–Nordheim tunneling and channel hot electron injection.

voltage decreases. It is generally believed that charging and discharging occur through two mechanisms, Fowler–Nordheim tunneling and channel hot electron injection (CHE), namely, as shown in Fig. 17.8B and C. Fowler–Nordheim tunneling often occurs when there is a large electric potential difference between the control gate and the source. When a large positive voltage is applied to the control gate under the electric field, the carriers in the channel material tunnel to the floating gate and are trapped inside. Channel hot electron injection, also known as hot carrier injection, requires the large current in the channel to provide electrons enough energy to “boil” out of the channel and break through the tunnel oxide layer. Then the threshold voltage of the floating gate is changed. The positive charge in the control gate attracts electrons from the channel to the floating gate, where they are trapped. The erase process is a behavior of removing the electrons from the floating gate. This process can be realized by applying a large negative voltage or exposing the memory to ultraviolet light.

Various attempts have been carried out for 2D material–based floating gate memory. Zhan et al. fabricated a floating gate memory based on the Graphene/HfO₂/Ni nanocrystal structure and realized a memory window of 23.1 V by back-gate sweep in 2011 (Zhan et al., 2011), as shown in Fig. 17.9A. One can also conclude that the on-off ratio of this memory is very low based on Fig. 17.9A, which is caused by the semimetallic properties of graphene. However, this experiment provides a novel idea: 2D materials are compatible with memory devices. Unlike graphene, TMDs tend to have tunable band gaps based on the layer difference and are highly sensitive to the charges, which makes them more suitable as channel materials for memory devices. The graphene/h-BN/MoS₂ heterojunction memory devices were developed in 2013, resulting in a factor of 10⁴ difference between the memory program and erase states (Bertolazzi et al., 2013), as shown in Fig. 17.9B. In this structure, the h-BN layer acts as the tunneling layer and the MoS₂ layer is the channel layer, respectively. It is worth noting that in this device structure, graphene is not only used as a charge trapping layer but also used as an electrode material to improve the contact behavior. Wang et al. used nanoparticles instead of graphene as the charge trapping material to realize a floating gate memory with MoS₂ as the channel material. This device exhibited an excellent on/off ratio over 10⁶, a large memory window of 10 V, a stable program/erase ratio, and good retention time (Wang et al., 2015), as shown in Fig. 17.9C. However, the traditional floating gate memory device shows a limitation in writing speed. Liu et al. reported a quasi-nonvolatile semifloating gate structure that greatly enhances the writing operation performance, as shown in Fig. 17.9C. Here, WSe₂ works as the channel material, and MoS₂ and h-BN serve as the semitunneling layer with HfS₂ as the floating gate (Liu et al., 2018). The MoS₂/WSe₂ heterostructures enable extremely swift carrier transportation. In addition, bandgap engineering improved the refresh time by up to 10 s, solving the power consumption problem of conventional volatile memory devices.

dipoles tend to align with the direction of the electric field. Due to the small movement of atoms in the ferroelectric materials, the centers of positive and negative charges no longer coincide. The separation of positive and negative charge centers makes the dipoles retain their polarization state. Binary “0”s and “1”s are stored as one of two possible electrical polarizations in each data storage cell. For example, a “1” is encoded using a negative remanent polarization “-Pr,” while a “0” is encoded using a positive remanent polarization “+ Pr,” as shown in Fig. 17.10. For the ferroelectric memory, the writing process is similar to the floating gate memory. By charging the plates on both sides of the ferroelectric layer, an electric field is then applied across the ferroelectric layer, forcing the atoms inside to an “up” or “down” state, thereby storing a “1” or a “0” in the memory. However, the reading process is a bit different from floating gate memory. The 1T structure is required, which forces the memory into a specific state, such as “0.” Nothing happens in the output lines if the cell already contains “0.” If the cell stays “1,” the atoms in the film will orient again bringing pulses of current in the output as they push electrons out of the metal on the “down” side. The presence of this pulse means that the cell holds a “1” state. However, the read-out process in the traditional 1T1C structure is destructive and requires a rewrite after each reading operation. Those drawbacks hinder the miniaturization and commercialization of 1T1C-based ferroelectric memory.

Ferroelectric field-effect transistors (Fe-FET) were designed to solve the data-destructive problem during the data reading operation by building a one-transistor nonvolatile memory. Fe-FETs generally employ the same architecture as conventional FETs, but the conductance of the channel is controlled by the polarization of the ferroelectric material. The principle of Fe-FET is similar to one of the traditional FETs. Taking depletion n-type FET as an example, the channel is switched off due to carrier depletion between the source and the drain. By applying a voltage on the gate to change the energy band at the interface between the insulator and the semiconductor, electrons can move in the channel region to turn on the device. However, due to the ferroelectricity and remnant polarization “Pr” mentioned earlier, the state in Fe-FET will be maintained even though the applied voltage is removed, leading to nonvolatility (Liu, Wang, et al., 2021; Kim et al., 2021). The retained state disappears only when the applied voltage exceeds the

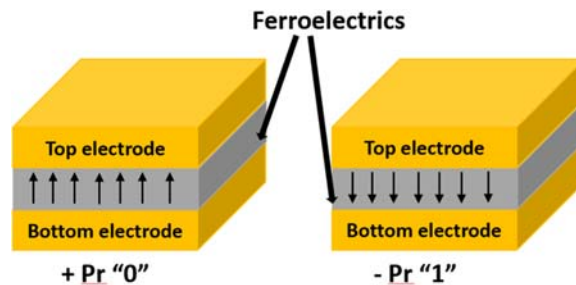


Figure 17.10 Operation mechanism. Schematic for the storage mode of a ferroelectric memory device.

coercive field (E_c) and is large enough to cause a change in the ferroelectric polarization direction (Kim et al., 2021). Even if the concept of Fe-FET structure was first proposed in 1957, several persistent challenges have prevented the creation of scalable and durable Fe-FETs. One of the biggest obstacles is the poor retention of Fe-FET (Ma & Han, 2002). The two main causes of this obstacle are the depolarization field and gate leakage current.

Recently, new materials and structures were suggested. Liu et al. demonstrated a high-performance FE-FET with high retention that integrates an atomically thin, 2D MoS_2 channel on top of an AlScN dielectric (Liu, Wang, et al., 2021), which is shown in Fig. 17.11A. The on-off ratio of the different states (“0” and “1”) reached 10^6 , as shown in Fig. 17.11B. It is worth noting that the remanent polarization of aluminum scandium nitride (AlScN) can become very large by adjusting the composition of Sc

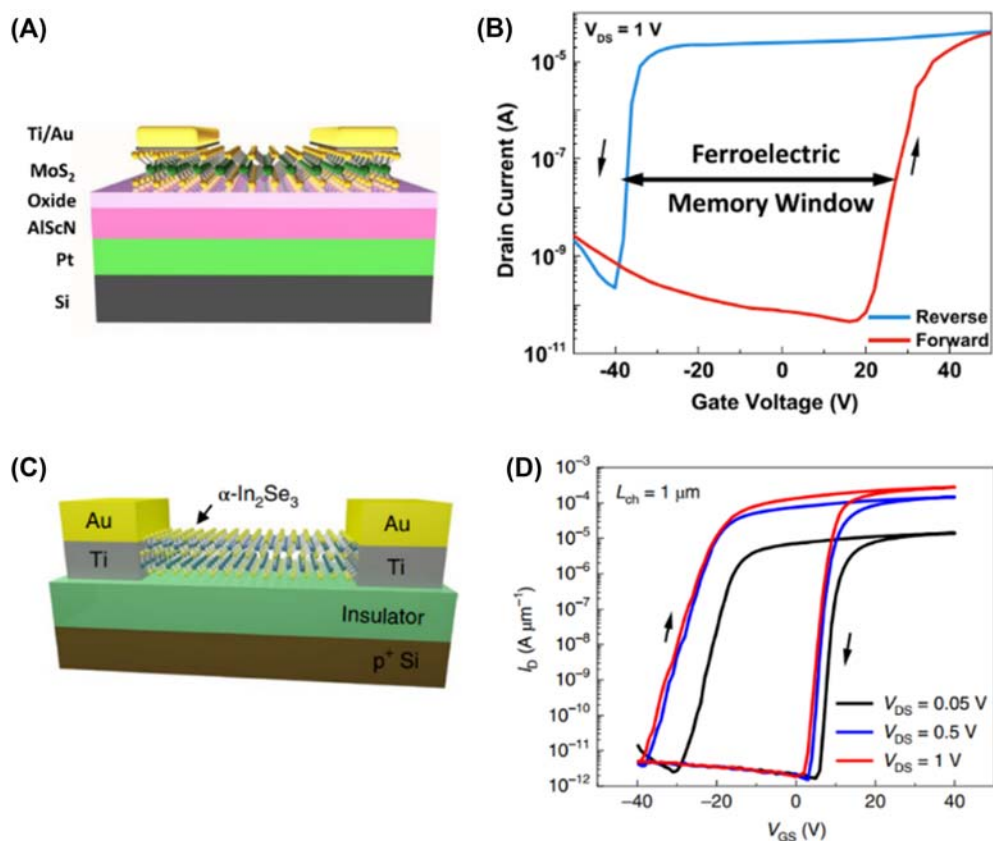


Figure 17.11 FE-FETs. (A) Device structure of an $\text{AlScN}/\text{MoS}_2$ FE-FET. (B) Transfer characteristics during both forward and backward sweeps for $\text{AlScN}/\text{MoS}_2$ FE-FET. (C) Schematic view of In_2Se_3 FeS-FET. (D) I_D - V_{GS} characteristics of a representative $\alpha\text{-In}_2\text{Se}_3$ FeS-FET. (C and D) From Si et al. (2019). A ferroelectric semiconductor field-effect transistor. *Nature Electronics*. 2(12), 580–586. <https://doi.org/10.1038/s41928-019-0338-7>.

(Fichtner et al., 2019). The key advantage of high remnant polarization is that charge trapping through the ferroelectric insulator and instability induced by leakage currents do not significantly affect FE-FET device performance. Also, the higher coercive field exhibited by AlScN is effectively immune to the depolarizing field for a given polarization (Fichtner et al., 2019). This is also why AlScN-based FE-FET can achieve very large retention.

Another strategy to solve the low retention of FE-FET is implementing a new structure, a ferroelectric semiconductor field-effect transistor (FeS-FET). Si et al. used a ferroelectric semiconductor (In_2Se_3) as the channel material, while the insulator is the high-quality amorphous gate insulator (HfO_2 or SiO_2) instead of the polycrystalline ferroelectric insulators found in common Fe-FETs, as shown in Fig. 17.11C. In the FeS-FET structure, mobile charges in a semiconductor can shield the depolarization field. Thus, the charge trapping and leakage currents can be eliminated through ferroelectric insulators found in the conventional Fe-FETs (Si et al., 2019). As a result, the high on-off ratio and retention time were realized, as shown in Fig. 17.11D.

17.5 Conclusion and outlook

From these sections and discussions, we cataloged the complete flow chart for producing electronic devices based on 2D materials fabricated with transfer printing technology. Recent advances in hetero-integrated applications of 2D materials are also comprehensively discussed, highlighting the unique advantages and device structures enabled by the various 2D layers.

Meanwhile, despite the wide applications and unique advantages, 2D layer-based approaches still encounter some challenges. It is quite hard to fabricate the devices on a wafer scale through large area transfer printing technology of 2D layer, which means a major obstacle to application in industry. In terms of crystallinity, it is difficult to grow monolayers and single-domain 2D layers that cover an entire 4-inch substrate. Controlling the kinetics of atoms at the level of a few angstroms requires lots of research as well as novel approaches.

Nevertheless, the unique materialistic properties of 2D materials open up new avenues toward diverse exotic heterostructures, and highly flexible, stretchable, and biointegrated applications. Thus, 2D electronics formed by transfer printing technology have provided a new world in the electronic era by showing new artificial heterointegrations.

References

- Akinwande, D., Huyghebaert, C., Wang, C. H., Serna, M. I., Goossens, S., Li, L. J., Wong, H. S. P., & Koppens, F. H. L. (2019). Graphene and two-dimensional materials for silicon technology. *Nature*, 573(7775), 507–518. Available from <https://doi.org/10.1038/s41586-019-1573-9>, <http://www.nature.com/nature/index.html>.

- Bachhofer, H., Reisinger, H., Bertagnolli, E., & Von Philipsborn, H. (2001). Transient conduction in multilayered silicon-oxide-nitride-oxide semiconductor structures. *Journal of Applied Physics*, 89(5), 2791–2800. Available from <https://doi.org/10.1063/1.1343892>.
- Bediako, D. K., Rezaee, M., Yoo, H., Larson, D. T., Zhao, S. Y. F., Taniguchi, T., Watanabe, K., Brower-Thomas, T. L., Kaxiras, E., & Kim, P. (2018). Heterointerface effects in the electrointercalation of van der Waals heterostructures. *Nature*, 558(7710), 425–429. Available from <https://doi.org/10.1038/s41586-018-0205-0>, <http://www.nature.com/nature/index.html>.
- Bertolazzi, S., Krasnozhan, D., & Kis, A. (2013). Nonvolatile memory cells based on MoS₂/graphene heterostructures. *ACS Nano*, 7(4), 3246–3252. Available from <https://doi.org/10.1021/nn3059136>.
- Britnell, L., Gorbachev, R. V., Jalil, R., Belle, B. D., Schedin, F., Katsnelson, M. I., Eaves, L., Morozov, S. V., Mayorov, A. S., Peres, N. M. R., Castro Neto, A. H., Leist, J., Geim, A. K., Ponomarenko, L. A., & Novoselov, K. S. (2012). Electron tunneling through ultrathin boron nitride crystalline barriers. *Nano Letters*, 12(3), 1707–1710. Available from <https://doi.org/10.1021/nl3002205>.
- Buscema, M., Groenendijk, D. J., Steele, G. A., Van Der Zant, H. S. J., & Castellanos-Gomez, A. (2014). Photovoltaic effect in few-layer black phosphorus PN junctions defined by local electrostatic gating. *Nature Communications*, 5. Available from <https://doi.org/10.1038/ncomms5651>, <http://www.nature.com/ncomms/index.html>.
- Chau, R., Doyle, B., Datta, S., Kavalieros, J., & Zhang, K. (2007). Integrated nanoelectronics for the future. *Nature Materials*, 6(11), 810–812. Available from <https://doi.org/10.1038/nmat2014>, <http://www.nature.com/nmat/>.
- Chen, J. H., Jang, C., Xiao, S., Ishigami, M., & Fuhrer, M. S. (2008). Intrinsic and extrinsic performance limits of graphene devices on SiO₂. *Nature Nanotechnology*, 3(4), 206–209. Available from <https://doi.org/10.1038/nnano.2008.58>, <http://www.nature.com/nnano/index.html>.
- Chen, Y., Wang, Y., Wang, Z., Gu, Y., Ye, Y., Chai, X., Ye, J., Chen, Y., Xie, R., Zhou, Y., Hu, Z., Li, Q., Zhang, L., Wang, F., Wang, P., Miao, J., Wang, J., Chen, X., Lu, W., . . . Hu, W. (2021). Unipolar barrier photodetectors based on van der Waals heterostructures. *Nature Electronics*, 4(5), 357–363. Available from <https://doi.org/10.1038/s41928-021-00586-w>, <https://www.nature.com/natelectron/>.
- Conti, S., Pimpolari, L., Calabrese, G., Worsley, R., Majee, S., Polyushkin, D. K., Paur, M., Pace, S., Keum, D. H., Fabbri, F., Iannaccone, G., Macucci, M., Coletti, C., Mueller, T., Casiraghi, C., & Fiori, G. (2020). Low-voltage 2D materials-based printed field-effect transistors for integrated digital and analog electronics on paper. *Nature Communications*, 11(1). Available from <https://doi.org/10.1038/s41467-020-17297-z>, <http://www.nature.com/ncomms/index.html>.
- Das, S., Pandey, D., Thomas, J., & Roy, T. (2019). The role of graphene and other 2D materials in solar photovoltaics. *Advanced Materials*, 31(1). Available from <https://doi.org/10.1002/adma.201802722>, [http://onlinelibrary.wiley.com/journal/10.1002/\(ISSN\)1521-4095](http://onlinelibrary.wiley.com/journal/10.1002/(ISSN)1521-4095).
- Dias, P. R., Schmidt, L., Chang, N. L., Lunardi, M. M., Deng, R., Trigger, B., Gomes, L. B., Egan, R., Veit, H. J. R., & Reviews, S. E. (2022). High yield, low cost, environmentally friendly process to recycle silicon solar panels: technical, economic and environmental feasibility assessment. *Renewable and Sustainable Energy Reviews*, 169.
- Ferain, I., Colinge, C. A., & Colinge, J. P. (2011). Multigate transistors as the future of classical metal-oxide-semiconductor field-effect transistors. *Nature*, 479(7373), 310–316. Available from <https://doi.org/10.1038/nature10676>.
- Fichtner, S., Wolff, N., Lofink, F., Kienle, L., & Wagner, B. (2019). AlScN: a III-V semiconductor based ferroelectric. *Journal of Applied Physics*, 125(11), 114103. Available from <https://doi.org/10.1063/1.5084945>.
- Geim, A. K., & Novoselov, K. S. (2007). The rise of graphene. *Nature Materials*, 6(3), 183–191. Available from <https://doi.org/10.1038/nmat1849>.
- Gomes, K. K., Mar, W., Ko, W., Guinea, F., & Manoharan, H. C. (2012). Designer Dirac fermions and topological phases in molecular graphene. *Nature*, 483(7389), 306–310. Available from <https://doi.org/10.1038/nature10941>.
- Han, S., Noh, S., Kim, J. W., Lee, C. R., Lee, S. K., & Kim, J. S. (2021). Stretchable inorganic GaN-nanowire photosensor with high photocurrent and photoresponsivity. *ACS Applied Materials and Interfaces*, 13(19), 22728–22737. Available from <https://doi.org/10.1021/acsami.1c03023>, <http://pubs.acs.org/journal/aamick>.

- Huang, J. K., Wan, Y., Shi, J., Zhang, J., Wang, Z., Wang, W., Yang, N., Liu, Y., Lin, C. H., Guan, X., Hu, L., Yang, Z. L., Huang, B. C., Chiu, Y. P., Yang, J., Tung, V., Wang, D., Kalantar-Zadeh, K., Wu, T., ... Li, S. (2022). High- κ perovskite membranes as insulators for two-dimensional transistors. *Nature*, *605*(7909), 262–267. Available from <https://doi.org/10.1038/s41586-022-04588-2>, <http://www.nature.com/nature/index.html>.
- Huang, L., Li, Y., Wei, Z., & Li, J. (2015). Strain induced piezoelectric effect in black phosphorus and MoS₂ van der Waals heterostructure. *Scientific Reports*, *5*(1). Available from <https://doi.org/10.1038/srep16448>.
- Jayachandran, D., Oberoi, A., Sebastian, A., Choudhury, T. H., Shankar, B., Redwing, J. M., & Das, S. (2020). A low-power biomimetic collision detector based on an in-memory molybdenum disulfide photodetector. *Nature Electronics*, *3*(10), 646–655. Available from <https://doi.org/10.1038/s41928-020-00466-9>, <https://www.nature.com/natelectron/>.
- Jiang, S., Li, L., Wang, Z., Shan, J., & Mak, K. F. (2019). Spin tunnel field-effect transistors based on two-dimensional van der Waals heterostructures. *Nature Electronics*, *2*(4), 159–163. Available from <https://doi.org/10.1038/s41928-019-0232-3>, <https://www.nature.com/natelectron/>.
- Kang, K., Lee, K. H., Han, Y., Gao, H., Xie, S., Muller, D. A., & Park, J. (2017). Layer-by-layer assembly of two-dimensional materials into wafer-scale heterostructures. *Nature*, *550*(7675), 229–233. Available from <https://doi.org/10.1038/nature23905>, <http://www.nature.com/nature/index.html>.
- Kianinia, M., Tawfik, S. A., Regan, B., Tran, T. T., Ford, M. J., Aharonovich, I., & Toth, M. (2017). *Robust Solid State Quantum System Operating at 800 K*. Optica Publishing Group.
- Kim, J. Y., Choi, M.-J., & Jang, H. W. (2021). Ferroelectric field effect transistors: progress and perspective. *APL Materials*, *9*(2), 021102. Available from <https://doi.org/10.1063/5.0035515>.
- Kim, S., Konar, A., Hwang, W. S., Lee, J. H., Lee, J., Yang, J., Jung, C., Kim, H., Yoo, J. B., Choi, J. Y., Jin, Y. W., Lee, S. Y., Jena, D., Choi, W., & Kim, K. (2012). High-mobility and low-power thin-film transistors based on multilayer MoS₂ crystals. *Nature Communications*, *3*. Available from <https://doi.org/10.1038/ncomms2018>, <http://www.nature.com/ncomms/index.html>.
- Lee, C. H., Lee, G. H., Van Der Zande, A. M., Chen, W., Li, Y., Han, M., Cui, X., Arefe, G., Nuckolls, C., Heinz, T. F., Guo, J., Hone, J., & Kim, P. (2014). Atomically thin p-n junctions with van der Waals heterointerfaces. *Nature Nanotechnology*, *9*(9), 676–681. Available from <https://doi.org/10.1038/nnano.2014.150>, <http://www.nature.com/nnano/index.html>.
- Li, D., Cheng, R., Zhou, H., Wang, C., Yin, A., Chen, Y., Weiss, N. O., Huang, Y., & Duan, X. (2015). Electric-field-induced strong enhancement of electroluminescence in multilayer molybdenum disulfide. *Nature Communications*, *6*. Available from <https://doi.org/10.1038/ncomms8509>, <http://www.nature.com/ncomms/index.html>.
- Li, L., Yu, Y., Ye, G. J., Ge, Q., Ou, X., Wu, H., Feng, D., Chen, X. H., & Zhang, Y. (2014). Black phosphorus field-effect transistors. *Nature Nanotechnology*, *9*(5), 372–377. Available from <https://doi.org/10.1038/nnano.2014.35>, <http://www.nature.com/nnano/index.html>.
- Li, X., Yu, Z., Xiong, X., Li, T., Gao, T., Wang, R., Huang, R., & Wu, Y. (2019). High-speed black phosphorus field-effect transistors approaching ballistic limit. *Science Advances*, *5*(6). Available from <https://doi.org/10.1126/sciadv.aau3194>, <https://advances.sciencemag.org/content/5/6/eaau3194/tab-pdf>.
- Li, Y., Sun, H., Gan, L., Zhang, J., Feng, J., Zhang, D., & Ning, C. Z. (2020). Optical properties and light-emission device applications of 2-D layered semiconductors. *Proceedings of the IEEE*, *108*(5), 676–703. Available from <https://doi.org/10.1109/JPROC.2019.2936424>, <http://ieeexplore.ieee.org/xpl/RecentIssue.jsp?punumber=5>.
- Liu, C., Yan, X., Song, X., Ding, S., Zhang, D. W., & Zhou, P. (2018). A semi-floating gate memory based on van der Waals heterostructures for quasi-non-volatile applications. *Nature Nanotechnology*, *13*(5), 404–410. Available from <https://doi.org/10.1038/s41565-018-0102-6>, <http://www.nature.com/nnano/index.html>.
- Liu, F., Zhou, Y., Wang, Y., Liu, X., Wang, J., & Guo, H. (2016). Negative capacitance transistors with monolayer black phosphorus. *npj Quantum Materials*, *1*. Available from <https://doi.org/10.1038/npjquantmats.2016.4>, <http://www.nature.com/npjquantmats/>.
- Liu, X., Wang, D., Kim, K.-H., Katti, K., Zheng, J., Musavigharavi, P., Miao, J., Stach, E. A., Olsson, R. H., & Jariwala, D. (2021). Post-CMOS compatible aluminum scandium nitride/2D channel ferroelectric field-effect-transistor memory. *Nano Letters*, *21*(9), 3753–3761. Available from <https://doi.org/10.1021/acs.nanolett.0c05051>.

- Liu, Y., Duan, X., Shin, H. J., Park, S., Huang, Y., & Duan, X. (2021). Promises and prospects of two-dimensional transistors. *Nature*, 591(7848), 43–53. Available from <https://doi.org/10.1038/s41586-021-03339-z>, <http://www.nature.com/nature/index.html>.
- Long, M., Wang, P., Fang, H., & Hu, W. (2019). Progress, challenges, and opportunities for 2D material based photodetectors. *Advanced Functional Materials*, 29(19), 1803807. Available from <https://doi.org/10.1002/adfm.201803807>.
- Lopez-Sanchez, O., Lembke, D., Kayci, M., Radenovic, A., & Kis, A. (2013). Ultrasensitive photodetectors based on monolayer MoS₂. *Nature Nanotechnology*, 8(7), 497–501. Available from <https://doi.org/10.1038/nnano.2013.100>, <http://www.nature.com/nnano/index.html>.
- Lukman, S., Ding, L., Xu, L., Tao, Y., Riis-Jensen, A. C., Zhang, G., Wu, Q. Y. S., Yang, M., Luo, S., Hsu, C., Yao, L., Liang, G., Lin, H., Zhang, Y. W., Thygesen, K. S., Wang, Q. J., Feng, Y., & Teng, J. (2020). High oscillator strength interlayer excitons in two-dimensional heterostructures for mid-infrared photodetection. *Nature Nanotechnology*, 15(8), 675–682. Available from <https://doi.org/10.1038/s41565-020-0717-2>, <http://www.nature.com/nnano/index.html>.
- Luo, M., Chen, X., Wu, P., Wang, H., Chen, Y., Chen, F., Zhang, L., & Chen, X. (2019). Gate-tunable ReS₂/MoTe₂ heterostructure with high-performance photodetection. *Optical and Quantum Electronics*, 51(5). Available from <https://doi.org/10.1007/s11082-019-1839-3>, <https://rd.springer.com/journal/11082>.
- Ma, T. P., & Han, J. P. (2002). Why is nonvolatile ferroelectric memory field-effect transistor still elusive? *IEEE Electron Device Letters*, 23(7), 386–388. Available from <https://doi.org/10.1109/LED.2002.1015207>.
- Maiti, R., Patil, C., Saadi, M. A. S. R., Xie, T., Azadani, J. G., Uluutku, B., Amin, R., Briggs, A. F., Miscuglio, M., Van Thourhout, D., Solares, S. D., Low, T., Agarwal, R., Bank, S. R., & Sorger, V. J. (2020). Strain-engineered high-responsivity MoTe₂ photodetector for silicon photonic integrated circuits. *Nature Photonics*, 14(9), 578–584. Available from <https://doi.org/10.1038/s41566-020-0647-4>, <http://www.nature.com/nphoton/index.html>.
- Miao, J., Hu, W., Guo, N., Lu, Z., Liu, X., Liao, L., Chen, P., Jiang, T., Wu, S., Ho, J. C., Wang, L., Chen, X., & Lu, W. (2015). High-responsivity graphene/InAs nanowire heterojunction near-infrared photodetectors with distinct photocurrent on/off ratios. *Small (Weinheim an der Bergstrasse, Germany)*, 11(8), 936–942. Available from <https://doi.org/10.1002/smll.201402312>, [http://onlinelibrary.wiley.com/journal/10.1002/\(ISSN\)1613-6829](http://onlinelibrary.wiley.com/journal/10.1002/(ISSN)1613-6829).
- Mistry K., Allen C., Auth C., Beattie B., Bergstrom D., Bost M., Brazier M., Buehler M., Cappellani A., Chau R., Choi C.H., Ding G., Fischer K., Ghani T., Grover R., Han W., Hanken D., Hattendorf M., He J., ... Zawadzki K. (2007) A 45nm logic technology with high-k + metal gate transistors, strained silicon, 9 Cu interconnect layers, 193nm dry patterning, and 100% Pb-free packaging. Technical Digest - International Electron Devices Meeting, IEDM. Available from <https://doi.org/10.1109/IEDM.2007.4418914>.
- Nian, Q., Gao, L., Hu, Y., Deng, B., Tang, J., & Cheng, G. J. (2017). Graphene/PbS-quantum dots/graphene sandwich structures enabled by laser shock imprinting for high performance photodetectors. *ACS Applied Materials and Interfaces*, 9(51), 44715–44723. Available from <https://doi.org/10.1021/acsami.7b14468>, <http://pubs.acs.org/journal/aamick>.
- Nikam, R. D., Sonawane, P. A., Sankar, R., & Chen, Y. T. (2017). Epitaxial growth of vertically stacked p-MoS₂/n-MoS₂ heterostructures by chemical vapor deposition for light emitting devices. *Nano Energy*, 32, 454–462. Available from <https://doi.org/10.1016/j.nanoen.2017.01.006>, <http://www.journals.elsevier.com/nano-energy/>.
- Novoselov, K. S., Geim, A. K., Morozov, S. V., Jiang, D., Zhang, Y., Dubonos, S. V., Grigorieva, I. V., & Firsov, A. A. (2004). Electric field effect in atomically thin carbon films. *Science (New York, N.Y.)*, 306(5696), 666–669. Available from <https://doi.org/10.1126/science.1102896>.
- Pesin, D., & MacDonald, A. H. (2012). Spintronics and pseudospintronics in graphene and topological insulators. *Nature Materials*, 11(5), 409–416. Available from <https://doi.org/10.1038/nmat3305>, <http://www.nature.com/nmat/>.
- Peyskens, F., Chakraborty, C., Muneeb, M., Van Thourhout, D., & Englund, D. (2019). Integration of single photon emitters in 2D layered materials with a silicon nitride photonic chip. *Nature Communications*, 10(1). Available from <https://doi.org/10.1038/s41467-019-12421-0>, <http://www.nature.com/ncomms/index.html>.
- Ponomarenko, L. A., Yang, R., Gorbachev, R. V., Blake, P., Mayorov, A. S., Novoselov, K. S., Katsnelson, M. I., & Geim, A. K. (2010). Density of states and zero Landau level probed through

- capacitance of graphene. *Physical Review Letters*, 105(13). Available from <https://doi.org/10.1103/physrevlett.105.136801>.
- Pospischil, A., Furchi, M. M., & Mueller, T. (2014). Solar-energy conversion and light emission in an atomic monolayer p–n diode. *Nature Nanotechnology*, 9(4), 257–261. Available from <https://doi.org/10.1038/nnano.2014.14>, <http://www.nature.com/nnano/index.html>.
- Radisavljevic, B., Radenovic, A., Brivio, J., Giacometti, V., & Kis, A. (2011). Single-layer MoS₂ transistors. *Nature Nanotechnology*, 6(3), 147–150. Available from <https://doi.org/10.1038/nnano.2010.279>, <http://www.nature.com/nnano/index.html>.
- Schwierz, F. (2010). Graphene transistors. *Nature Nanotechnology*, 5(7), 487–496. Available from <https://doi.org/10.1038/nnano.2010.89>, <http://www.nature.com/nnano/index.html>.
- Shastri, B. J., Tait, A. N., Ferreira de Lima, T., Pernice, W. H. P., Bhaskaran, H., Wright, C. D., & Prucnal, P. R. (2021). Photonics for artificial intelligence and neuromorphic computing. *Nature Photonics*, 15(2), 102–114. Available from <https://doi.org/10.1038/s41566-020-00754-y>, <http://www.nature.com/nphoton/index.html>.
- Si, M., Saha, A. K., Gao, S., Qiu, G., Qin, J., Duan, Y., Jian, J., Niu, C., Wang, H., Wu, W., Gupta, S. K., & Ye, P. D. (2019). A ferroelectric semiconductor field-effect transistor. *Nature Electronics*, 2(12), 580–586. Available from <https://doi.org/10.1038/s41928-019-0338-7>.
- Si, M., Su, C. J., Jiang, C., Conrad, N. J., Zhou, H., Maize, K. D., Qiu, G., Wu, C. T., Shakouri, A., Alam, M. A., & Ye, P. D. (2018). Steep-slope hysteresis-free negative capacitance MoS₂ transistors. *Nature Nanotechnology*, 13(1), 24–28. Available from <https://doi.org/10.1038/s41565-017-0010-1>, <http://www.nature.com/nnano/index.html>.
- Tsai, M. L., Li, M. Y., Retamal, J. R. D., Lam, K. T., Lin, Y. C., Suenaga, K., Chen, L. J., Liang, G., Li, L. J., & He, J. H. (2017). Single atomically sharp lateral monolayer p–n heterojunction solar cells with extraordinarily high power conversion efficiency. *Advanced Materials*, 29.
- Wang, J., Zou, X., Xiao, X., Xu, L., Wang, C., Jiang, C., Ho, J. C., Wang, T., Li, J., & Liao, L. (2015). Floating gate memory-based monolayer MoS₂ transistor with metal nanocrystals embedded in the gate dielectrics. *Small (Weinheim an der Bergstrasse, Germany)*, 11(2), 208–213. Available from <https://doi.org/10.1002/smll.201401872>, [http://onlinelibrary.wiley.com/journal/10.1002/\(ISSN\)1613-6829](http://onlinelibrary.wiley.com/journal/10.1002/(ISSN)1613-6829).
- Wang, Y., Qiu, G., Wang, R., Huang, S., Wang, Q., Liu, Y., Du, Y., Goddard, W. A., Kim, M. J., Xu, X., Ye, P. D., & Wu, W. (2018). Field-effect transistors made from solution-grown two-dimensional tellurene. *Nature Electronics*, 1(4), 228–236. Available from <https://doi.org/10.1038/s41928-018-0058-4>, <https://www.nature.com/natelectron/>.
- Wu, F., Tian, H., Shen, Y., Hou, Z., Ren, J., Gou, G., Sun, Y., Yang, Y., & Ren, T. L. (2022). Vertical MoS₂ transistors with sub-1-nm gate lengths. *Nature*, 603(7900), 259–264. Available from <https://doi.org/10.1038/s41586-021-04323-3>, <http://www.nature.com/nature/index.html>.
- Wu, G., Wang, X., Chen, Y., Wu, S., Wu, B., Jiang, Y., Shen, H., Lin, T., Liu, Q., & Wang, X. J. A. M. (2020). MoTe₂ p–n homojunctions defined by ferroelectric polarization. *Adv. Mater.*, 32.
- Yazyev, O. V., & Louie, S. G. (2010). Electronic transport in polycrystalline graphene. *Nature Materials*, 9(10), 806–809. Available from <https://doi.org/10.1038/nmat2830>, <http://www.nature.com/nmat/>.
- Ye, Y., Wong, Z. J., Lu, X., Ni, X., Zhu, H., Chen, X., Wang, Y., & Zhang, X. (2015). Monolayer excitonic laser. *Nature Photonics*, 9(11), 733–737. Available from <https://doi.org/10.1038/nphoton.2015.197>, <http://www.nature.com/nphoton/index.html>.
- Yu, J., Li, J., Zhao, Y., Lambert, A., Chen, T., Duan, W., Liu, W., Yang, X., Huang, Y., & Ding, K. (2021). Copper metallization of electrodes for silicon heterojunction solar cells: process, reliability and challenges. *Solar Energy Materials and Solar Cells*, 224, 110993. Available from <https://doi.org/10.1016/j.solmat.2021.110993>.
- Zhan, N., Olmedo, M., Wang, G., & Liu, J. (2011). Graphene based nickel nanocrystal flash memory. *Applied Physics Letters*, 99(11), 113112. Available from <https://doi.org/10.1063/1.3640210>.
- Zhang, D., Gan, L., Zhang, J., Zhang, R., Wang, Z., Feng, J., Sun, H., & Ning, C. Z. (2020). Reconstructing local profile of exciton-emission wavelengths across a WS₂ bubble beyond the diffraction limit. *ACS Nano*, 14(6), 6931–6937. Available from <https://doi.org/10.1021/acsnano.0c01337>, <http://pubs.acs.org/journal/ancac3>.

This page intentionally left blank

CHAPTER 18

Outlooks

Changyong (Chase) Cao^{1,2,3}

¹Department of Mechanical and Aerospace Engineering, Case Western Reserve University, Cleveland, OH, United States

²Department of Electrical, Computer, and Systems Engineering, Case Western Reserve University, Cleveland, OH, United States

³Advanced Platform Technology (APT) Center, Louis Stokes Cleveland VA Medical Center, Cleveland, OH, United States

18.1 Introduction

Transfer printing is a versatile and scalable approach for fabricating electronic devices with a wide range of applications (Hines et al., 2007; Zhou et al., 2019). In recent years, there have been significant developments in various transfer printing technologies for fabricating flexible electronics and energy devices with different materials and architectures (Bian et al., 2019; Li et al., 2021; Linghu et al., 2020; Park et al., 2020; Wang et al., 2020; Zhang et al., 2021a, 2021b). These advances enable the creation of flexible devices that can conform to different surfaces and shapes, making them suitable for applications such as wearable electronics and biomedical devices. Moreover, transfer printing offers a cost-effective and scalable approach for fabricating large-area electronics with high throughput (Zhou et al., 2019). The precise placement of electronic components, such as sensors and transistors, onto flexible substrates allows for complex circuits with high precision and reliability. The method is also compatible with various materials, including organic and inorganic semiconductors, metals, and insulators, enabling the integration of different materials to create multifunctional devices. In addition, it can be used to integrate electronic components onto a broad range of substrates, including glass, plastic, and biological tissues, enabling the creation of hybrid devices that can interface with biological systems (Dahiya et al., 2022; Park et al., 2020).

18.2 Major challenges

Despite the potential of transfer printing in fabricating flexible electronics, several significant challenges need to be addressed to fully realize its potential. These challenges include the following:

- Limited material compatibility: The current transfer printing process has limited compatibility with a wide range of materials, making it challenging to apply transfer printing to nonplanar or rough surfaces (Meitl et al., 2006). The adhesion between the materials and the substrates needs to be improved to address this limitation.

- **Reliability and durability:** The reliability and durability of flexible electronic devices created using transfer printing can be limited due to issues such as delamination, cracking, and material degradation (Carlson et al., 2012). Improvements in the adhesion and mechanical properties of the materials used in transfer printing are needed to improve the reliability and durability of flexible devices. In addition, the transfer printing yield and resolution need to be improved, particularly for large-scale production and high-performance components.
- **Limited scalability:** The current transfer printing process is limited in scalability, making it difficult to produce large quantities of flexible electronics at a low cost (Huang & Lin, 2022). Improvements in the scalability of the process are needed to enable the mass production of flexible electronics for commercial production.
- **High manufacturing costs:** The specialized equipment, materials, and processing steps needed for transfer printing can make the manufacturing process expensive and time-consuming. The cost of transfer printing needs to be reduced, particularly for high-performance and high-volume applications, to make transfer printing more accessible and competitive.
- **Environmental impacts:** The manufacturing process for transfer printing of flexible electronics can generate a significant amount of electronic waste, which can have a negative effect on the environment. Developing more sustainable and environmentally friendly manufacturing processes is essential in reducing the environmental impacts of transfer printing.

18.3 Future research directions

To fully realize the potential of transfer printing for flexible electronics, to be focused on in the future. A multidisciplinary approach that combines materials science, manufacturing engineering, design, and sustainability will be necessary to overcome the obstacles currently faced by this technology and enable the creation of novel advanced electronic devices with new functionalities and applications. Specifically, in the future development of transfer printing, a few critical research areas should be focused on:

- **Materials development:** The development of new materials with improved properties, such as mechanical flexibility, electrical conductivity, and biocompatibility, is a crucial area in future research (Zhou et al., 2019). This could involve the synthesis of new materials, as well as the modification of existing ones, to enable the fabrication of more advanced and versatile electronic devices. In addition, the durability and the environmental impacts of the materials should also be studied.
- **Process optimization:** The optimization of transfer printing processes is an important area for future research, particularly in terms of improving the efficiency, precision, and scalability of the technique. This could involve the development of

new printing methods, such as aerosol jet printing (Andrews et al., 2017; Cao et al., 2017; Zhou et al., 2021) and roll-to-roll printing (Lee et al., 2020; Søndergaard et al., 2012), as well as the integration of other manufacturing processes, such as 3D printing and photolithography. The development of green printing technology to reduce energy consumption and waste production will be an essential topic in this field (Zi et al., 2018).

- **Device integration:** Integrating different electronic components, such as sensors, actuators, and energy harvesting devices, into a single flexible device is an important area for future research. This could enable the development of multifunctional devices with enhanced capabilities, such as sensing and actuation or energy harvesting and storage.
- **System-level design:** The development of system-level design approaches for transfer-printed flexible electronics is an important area for future research (McPhillimy et al., 2020). This could involve using simulation tools and optimization algorithms to design complex electronic systems with improved performance and reliability. In addition, automated transfer printing systems and software are likely to be developed to improve the speed, efficiency, and consistency of the transfer printing process.
- **Applications:** The development of new applications for transfer-printed flexible electronics is an important area for future research, particularly in areas such as biomedical devices (Wu et al., 2015), energy harvesting (Kim et al., 2019), and wearable electronics (Choi et al., 2015a). This could involve the exploration of new use cases and the development of new device architectures and materials to enable the creation of novel electronic devices.

18.3.1 Materials development

The future research and development of transfer printing of flexible electronics will require a focus on several critical areas related to materials, including the following:

- **New materials for flexible substrates:** Developing flexible substrates with improved mechanical, electrical, and thermal properties will be crucial for advancing flexible electronics. There is a growing demand for environmentally friendly electronics made from biodegradable or recycled materials. Therefore the synthesis of new polymers, such as biodegradable and biocompatible materials, or the development of new composites and nanomaterials will be an essential area for future research.
- **New materials for electronic components:** To improve the performance and durability of the electronic components such as semiconductors, conductors, and insulators, the synthesis of new organic and inorganic materials and the modification of existing ones to improve their properties, such as mobility and stability, will be necessary.

- Hybrid materials for multifunctional devices: Hybrid materials that combine different functionalities, such as sensing, actuation, and energy harvesting, will be highly desirable for future flexible electronics. This could involve integrating electronic components with biological materials such as proteins and DNA, or creating new composites that combine different properties.
- High-throughput and scalable synthesis of materials: Developing techniques, such as inkjet printing, roll-to-roll processing, and continuous flow synthesis, will be essential for the mass production of materials with high quality and uniformity.
- Multiscale characterization of materials: The development of multiscale characterization techniques will be critical for advancing the transfer printing of flexible electronics. This could involve using advanced imaging and spectroscopy techniques to characterize materials at different length scales, from atomic to macroscopic, enabling a deeper understanding of their properties and behavior. This information can be used to inform the development of new materials and the optimization of transfer printing processes for improved device performance and reliability.

18.3.2 Process/manufacturing optimization

To optimize manufacturing and processing, future research on transfer printing could focus on integrating advanced automation and control technologies, developing new printing techniques, and implementing sustainable manufacturing processes. Critical areas for future research could include the following:

- Automation and scalability: Developing automated transfer printing systems that can handle large-scale production of flexible electronics will improve the speed, accuracy, and consistency of the transfer printing process. The research may involve the integration of robotic arms, computer vision systems, and other automation technologies to improve the efficiency and throughput of the manufacturing process.
- Integration with other manufacturing processes: Integrating transfer printing with other manufacturing processes, such as 3D printing and photolithography, could enable the creation of more complex and versatile electronic devices that can be fabricated in a single process.
- Printing techniques: The development of new printing techniques, such as aerosol jet printing and roll-to-roll printing, could enable the mass production of flexible electronics with high resolution and accuracy. The ability to customize transfer printing is expected to be improved, allowing for personalized and unique designs on a variety of surfaces and materials.
- In situ monitoring and control: The development of in situ monitoring and control systems that can monitor the quality of the transfer printing process in real time and adjust as necessary could help improve the reliability and consistency of the manufacturing process.

- **Sustainability:** The development of sustainable manufacturing processes for transfer printing of flexible electronics could involve the use of renewable materials and energy sources, as well as the development of recycling and waste reduction strategies. Research on new transfer printing methods that reduce the cost of materials, energy, and labor will be essential to make it a more attractive option for manufacturers.

These advances could enable the mass production of flexible electronics with high quality and consistency and allow the creation of new applications and markets for this technology.

18.3.3 Device and system integration

Transfer printing has the potential to create highly integrated and efficient electronic devices and systems for various applications, including smart agriculture systems, personalized health-monitoring systems, and biointegrated or biomedical devices. One of the promising advances and future directions is to develop a roll-to-roll manufacturing process to integrate sensors, energy harvesting devices, wireless communication modules, and data processing units onto a single flexible substrate, creating a self-powered smart and connected device. In addition, it will be desirable to investigate new technical routes with high-level automation processes and control for ease of recycling of electronic devices, allowing for the repair and upgrade of individual components rather than the disposal of the entire device. This approach has the potential to reduce electronic waste and increase manufacturing/recycling throughput.

18.3.4 Novel applications

Transfer printing of flexible electronics is a highly versatile technique with great potential for a broad range of applications, including wearable electronics, biomedical devices, and environmental monitoring. In the future, there are exciting opportunities to expand the applications of this technology in numerous ways, such as the following:

- **Internet of Things (IoT):** Integrating transfer printing with IoT technologies could create new opportunities for developing smart devices and systems. For example, transfer printing could be used to create sensors and actuators that can be integrated into a range of IoT applications, such as smart homes, smart cities, and Industry 4.0 (Roges & Malik, 2021).
- **Biomedical devices:** Transfer printing could enable the creation of highly functional biomedical devices, such as implantable sensors, drug delivery systems, and prosthetic devices (Herbert et al., 2021). These devices could improve patient care and treatment outcomes and enable new forms of personalized medicine.

- Environmental monitoring: Transfer printing could create low-cost and portable sensors for environmental monitoring applications, such as air and water quality monitoring, pollution detection, and climate monitoring (Liao et al., 2020).
- Flexible and transparent electronics: Transfer printing could be used to create flexible and transparent electronics for a wide range of applications, such as wearable electronics, displays, and touchscreens (Choi et al., 2015b).
- Energy harvesting: Transfer printing could be used to create energy harvesting devices that can convert ambient energy, such as motion, light, and heat, into electrical energy (Pang et al. 2020, 2022). For example, flexible solar cells (Zi et al., 2018) can be integrated into clothing, backpacks, and other portable devices to power low-power electronic devices, without the need of batteries or external power sources.
- Smart agriculture: Transfer printing can be used to create sensors that can be integrated into farming equipment, such as tractors and harvesters. These sensors can be used to monitor soil conditions, crop growth, and other environmental factors, enabling farmers to optimize their farming practices (Yin et al., 2021).
- Sports: Transfer printing of flexible electronics can be used to create wearable devices that can monitor an athlete's performance, track biometric data, and provide real-time feedbacks. This technology can help athletes to optimize their training and improve their performance (Yamashita & Kobayashi, 2021).
- 3D-Printed electronics: Transfer printing can be used to produce 3D-printed electronics, such as sensors, actuators, and microfluidic devices, by combining transfer printing with 3D printing technology (Tan et al., 2022).

18.3.5 Combination with other fabrication technologies

Transfer printing is a highly versatile technology that can combine with other manufacturing methods, such as 3D printing, photolithography, aerosol jet printing, and roll-to-roll process, to create hybrid manufacturing methods that offer improved performance, functionality, and versatility. For instance, by integrating transfer printing with roll-to-roll processing, which uses flexible substrates on large-scale rolls, it is possible to produce electronic devices such as flexible displays and solar panels on a large scale. Transfer printing can also be combined with 3D printing to create complex 3D-printed electronic devices, such as sensors, actuators, and microfluidic devices (Tan et al., 2022). Combining transfer printing with microfabrication techniques such as photolithography and etching will enable the manufacturing of high-performance electronic devices such as microelectromechanical systems (MEMS) and integrated circuits (ICs).

The combination process requires the identification of material and process compatibility. It is also necessary to design the transfer printing process to ensure accurate and undamaged material transfer. More importantly, the performance of combined

technology needs to be tested to ensure that it meets the desired requirements. It is expected that the future innovative use of transfer printing will be driven by advances in materials science, engineering, and other related fields and will offer the potential for exciting new applications in areas such as flexible and wearable electronics, printed and organic electronics, and 3D-printed electronics.

18.4 Possible breakthroughs in future transfer printing

As discussed earlier, we can expect several possible breakthroughs in the future development of transfer printing technology. One of them is the integration of transfer printing with 3D printing, which will enable the creation of complex and customizable electronic devices with high resolution and accuracy. This could lead to the development of new applications and markets for flexible electronics, including personalized medical devices, flexible displays, and wearable electronics. Another possible breakthrough could be the development of printable electronics with high performance, including high-speed data transfer, low-power consumption, and increased durability. This could open new opportunities for flexible electronics, including high-speed communication systems, intelligent wearables, and advanced sensors.

A third breakthrough is the development of self-powered flexible electronics, which could harvest energy from ambient sources such as light, motion, and heat to drive wearable devices, environmental sensors, and other electronic systems that do not require external power sources. Moreover, multimaterial transfer printing that can handle multiple materials and substrates will fabricate complex and integrated electronic systems for broad applications, including smart packaging, IoT devices, and biomedical implants.

Finally, the development of sustainable and environmentally friendly manufacturing processes would reduce the environmental impact of electronic waste and enable the creation of more sustainable electronic devices. These breakthroughs offer exciting opportunities for the future of transfer printing technology, and their realization could transform the electronics industry that we have today.

18.5 Conclusion

Transfer printing technology is expected to undergo significant development in the next 5–10 years. The precision and resolution of the technology will be improved, enabling the production of high-quality and high-performance electronic devices with enhanced functionality and versatility. Intensive research on material properties and compatibility will further advance the performance, sustainability, and affordability of flexible electronics. The scalable process of this technology will enable the production of large-scale electronic devices, such as flexible displays and solar panels, with improved efficiency and cost-effectiveness. Integration with other technologies, such as 3D printing, roll-to-roll

processing, and microfabrication, will bring about hybrid manufacturing methods that enhance the devices' performance, functionality, and versatility. This will ultimately accelerate the development of new applications, such as printed and organic electronics, flexible and wearable electronics, and 3D-printed electronics, offering exciting new opportunities for innovation and growth. Overall, transfer printing technology has a promising future and is poised to revolutionize the electronics industry.

References

- Andrews, J. B., et al. (2017). Noninvasive material thickness detection by aerosol jet printed sensors enhanced through metallic carbon nanotube ink. *IEEE Sensors Journal*, 17(14), 4612–4618.
- Bian, J., et al. (2019). Laser transfer, printing, and assembly techniques for flexible electronics. *Advanced Electronic Materials*, 5(7), 1800900.
- Cao, C., Andrews, J. B., & Franklin, A. D. (2017). Completely printed, flexible, stable, and hysteresis-free carbon nanotube thin-film transistors via aerosol jet printing. *Advanced Electronic Materials*, 3(5), 1700057.
- Carlson, A., et al. (2012). Transfer printing techniques for materials assembly and micro/nanodevice fabrication. *Advanced Materials*, 24(39), 5284–5318.
- Choi, M. K., et al. (2015a). Thermally controlled, patterned graphene transfer printing for transparent and wearable electronic/optoelectronic system. *Advanced Functional Materials*, 25(46), 7109–7118.
- Choi, Y.-M., et al. (2015b). Fabrication of a single-layer metal-mesh touchscreen sensor using reverse-offset printing. *Journal of Information Display*, 16(1), 37–41.
- Dahiya, A. S., et al. (2022). In tandem contact-transfer printing for high-performance transient electronics. *Advanced Electronic Materials*, 8(9), 2200170.
- Herbert, R., et al. (2021). Recent advances in printing technologies of nanomaterials for implantable wireless systems in health monitoring and diagnosis. *Advanced Healthcare Materials*, 10(17), 2100158.
- Hines, D., et al. (2007). Transfer printing methods for the fabrication of flexible organic electronics. *Journal of Applied Physics*, 101(2), 024503.
- Huang, Z., & Lin, Y. (2022). Transfer printing technologies for soft electronics. *Nanoscale*, 14(45), 16749–16760.
- Kim, S., Tentzeris, M. M., & Georgiadis, A. (2019). Hybrid printed energy harvesting technology for self-sustainable autonomous sensor application. *Sensors*, 19(3), 728.
- Lee, J., Byeon, J., & Lee, C. (2020). Theories and control technologies for web handling in the roll-to-roll manufacturing process. *International Journal of Precision Engineering and Manufacturing-Green Technology*, 7, 525–544.
- Li, C., Luo, H., & Song, J. (2021). Magnetically driven non-contact transfer printing based on a bi-stable elastomeric stamp. *Advanced Materials Technologies*, 6(11), 2100335.
- Liao, J., et al. (2020). Wireless water quality monitoring and spatial mapping with disposable whole-copper electrochemical sensors and a smartphone. *Sensors and Actuators B: Chemical*, 306, 127557.
- Linghu, C., et al. (2020). Universal SMP gripper with massive and selective capabilities for multiscaled, arbitrarily shaped objects. *Science advances*, 6(7), eaay5120.
- McPhillimy, J., et al. (2020). Automated nanoscale absolute accuracy alignment system for transfer printing. *ACS applied nano materials*, 3(10), 10326–10332.
- Meitl, M. A., et al. (2006). Transfer printing by kinetic control of adhesion to an elastomeric stamp. *Nature Materials*, 5(1), 33–38.
- Pang, Y., et al. (2020). Additive manufacturing of batteries. *Advanced Functional Materials*, 30(1), 1906244.
- Pang, Y., et al. (2022). Self-powered multifunctional human-machine interfaces for respiratory monitoring and smart system control. *Advanced Materials Interfaces*, 2201202.
- Park, J., et al. (2020). Transfer printing of electronic functions on arbitrary complex surfaces. *ACS nano*, 14(1), 12–20.

- Roges, R., & Malik, P. K. (2021). Planar and printed antennas for Internet of Things-enabled environment: opportunities and challenges. *International Journal of Communication Systems*, 34(15), e4940.
- Søndergaard, R., et al. (2012). Roll-to-roll fabrication of polymer solar cells. *Materials today*, 15(1-2), 36–49.
- Tan, H. W., et al. (2022). 3D printed electronics: processes, materials and future trends. *Progress in Materials Science*, 100945.
- Wang, C., et al. (2020). Programmable and scalable transfer printing with high reliability and efficiency for flexible inorganic electronics. *Science advances*, 6(25), eabb2393.
- Wu, H., et al. (2015). Transfer printing of metallic microstructures on adhesion-promoting hydrogel substrates. *Advanced Materials*, 27(22), 3398–3404.
- Yamashita, T., & Kobayashi, T. (2021). Smart table tennis racket using a rubber mounted ultrathin piezoelectric sensor array. *Sensors and Materials*, 33(3), 1081–1089.
- Yin, H., et al. (2021). Soil sensors and plant wearables for smart and precision agriculture. *Advanced Materials*, 33(20), 2007764.
- Zhang, S., et al. (2021a). A thermal actuated switchable dry adhesive with high reversibility for transfer printing. *International Journal of Extreme Manufacturing*, 3(3), 035103.
- Zhang, X., et al. (2021b). Mechanics of active elastomeric surfaces with tunable adhesion for non-contact pick-up and printing. *International Journal of Solids and Structures*, 219-220, 166–176.
- Zhou, H., et al. (2019). Transfer printing and its applications in flexible electronic devices. *Nanomaterials*, 9(2), 283.
- Zhou, Y., et al. (2021). 4D Printing of stretchable supercapacitors via hybrid composite materials. *Advanced Materials Technologies*, 6(1), 2001055.
- Zi, W., et al. (2018). Flexible perovskite solar cells based on green, continuous roll-to-roll printing technology. *Journal of energy chemistry*, 27(4), 971–989.

This page intentionally left blank

Index

Note: Page numbers followed by “*f*” and “*t*” refer to figures and tables, respectively.

A

Active-matrix (AM), 235
Adhesion data, 157–158
Adhesion-free transfer method, 254
Adhesion strength, 99–100
Adhesive layer, 67–68
Aerosol jet printing, 210–211, 498
Ag microelectrodes, 401
AgNWs. *See* Silver nanowires (AgNWs)
a-IGZO. *See* Amorphous indium-gallium-zinc oxide (a-IGZO)
ALD. *See* Atomic layer deposition (ALD)
Aluminum gallium indium phosphide (AlGaInP), 312
Ambient temperature, 83
AMLCD. *See* AM liquid crystal display (AMLCD)
AM liquid crystal display (AMLCD), 235
Amorphous indium-gallium-zinc oxide (a-IGZO), 249–251, 287–288
Amorphous silica adhesion layer, 289–291
Amorphous silicon (a-Si), 287–288, 313
AMSCs. *See* Asymmetric microsupercapacitors (AMSCs)
Analytical thermomechanical models, 340
Angled microflap stamp, 18–20
Aphid-inspired stamp, 99–100, 100*f*
Aphid-inspired transfer printing technique, 327–328
Arc discharge method, 124–126
Artificial solid-electrolyte interphase, 353–354
a-Si. *See* Amorphous silicon (a-Si)
Asymmetric microsupercapacitors (AMSCs), 358
Atomic force microscopy (AFM), 120–123, 441*f*, 454–455, 455*f*
Atomic layer deposition (ALD), 128–129, 422, 430–431
Atomic probing technique, 454–455
 atomic force microscope, 454–455, 455*f*
 scanning tunneling microscope, 454
Au conductive layer, 281–283
Au pyramids, 190

Axisymmetric finite element model, 104

Axisymmetric model, 157

B

Back-gate field-effect transistors, 477–479, 478*f*
Backing layer, 67–68
Ball milling methods, 124–125
Balloon catheter-based systems, 225
Battery electrode, 353–354
BDD. *See* Boron-doped polycrystalline diamond (BDD)
Beer–Lambert law, 307–309
Biaxially buckled 3D strain sensor, 212–214
Binocular parallax-induced stereoscopy, 188
Biodegradable electronics, 313
Bio-inspired transfer printing method, 181
Bio-integrated electronics, 63
Biomaterials, 300–303, 302*f*
Biomedical applications
 functional devices, 303–316
 bioresorbable materials and devices, 313–316
 energy-harvesting devices, 311–313
 light emitting diodes, 303–307, 304*f*
 photodetectors, 307–310, 309*f*
 materials, 281–303
 biomaterials, 300–303, 302*f*
 metals, 281–285
 oxides, 285–288
 silicon, 289–292
 two-dimensional materials, 296–300, 298*f*
 wide bandgap semiconductors, 292–296
Biomedical devices, 499
Biomedical field, 284
Biosensors, 177–178
Bismuth vanadate (BiVO₄), 149–150, 150*f*
Bi-stable stamp, 105–107, 106*f*
Black phosphorus (BP), 477
Blanket transfer (BT), 164
Blister/bulging test, 50–51
Boltzmann’s constant, 118, 401–404

- Boron-doped polycrystalline diamond (BDD), 293–295
- Bottom-up approaches, 420
- Bottom-up fabrication methods, 207–208
- Bottom-up growth methods, 422–423
- Bottom-up synthesis methods, 422–423
- BP. *See* Black phosphorus (BP)
- Bragg-Brentano measurement geometry, 442–443
- ## C
- Cantilever-shaped stamp, 101–102, 101*f*
- Capillary forces, 118–119
- Carbon, 123–124
- Carbon-based materials, 217, 244–245
- Carbon black (CB), 154
- Carbon black/SMP (CBSMP), 162, 336
- Carbon nanotubes (CNTs), 118, 123–124, 123*f*, 210–211, 244–245, 356–357
conformal surface coating methods for, 130*t*
synthesis methods for, 125*f*
- Carbonyl iron particles (CIPs), 104
- Cartesian coordinate system, 82–83
- CAS. *See* Conformal additive stamp (CAS)
- Catalyst layer, 359–360
- CB. *See* Carbon black (CB)
- Cell patterning, 301–303
- Cellulose nanofibril (CNF), 242
- Ceramics, 130*t*
- Channel hot electron injection (CHE), 484–485
- Charged-driven force, 119–120
- CHE. *See* Channel hot electron injection (CHE)
- Chemical etching techniques, 168–169
- Chemical sensors, 226–230
biosensors, 227
electrochemical sensors, 226
gas sensors, 227
mass-based sensors, 227
optical sensors, 226
- Chemical transfer printing, 183–187
chemo-mechanical transfer printing technique, 185–187, 186*f*
thermo-mechanical transfer printing technique, 184–185, 184*f*
- Chemical vapor deposition (CVD), 51, 120, 244–245, 297, 355, 356*f*, 371*t*, 420, 422, 431–433
- Chemo-mechanical transfer method, 196
- Chemo-mechanical transfer printing techniques, 185–187, 186*f*, 197–198
- CIPs. *See* Carbonyl iron particles (CIPs)
- CMOS. *See* Complementary metal-oxide-semiconductor (CMOS)
- CNTs. *See* Carbon nanotubes (CNTs)
- Coefficient of the thermal expansion (CTE), 85
- Collagen, 287–288
- Colloidal quantum dot (c-QD), 166
- Colloids, 163
- Complementary inverter, 237
- Complementary metal-oxide-semiconductor (CMOS), 238, 280, 476
- Composite materials, 163
- Conductive AFM (CAFM), 455
- Conductive materials, 119–120
- Conductive nanomaterials, 210
- Conductive polymers, 207–208, 217
- Conformal additive stamp (CAS), 220
- Contact laser-driven transfer printing techniques, 329–338, 331*f*
based on elastomer/shape memory polymer composite stamp, 336–338, 338*f*
based on microstructured shape memory polymer stamp, 334–336
based on pyramid microstructured shape memory polymer, 335*f*
based on shape memory polymer block, 332–334, 333*f*
based on smart tape, 330–332
- Contact printing, 384–385
- Controlled interface delamination, 24
- Conventional Si-based TFTs, 291–292
- Cost-effective approach, 145
- Coulomb interactions, 456–457
- Crack-driven transfer printing, 182–183, 182*f*
- Critical dimension (CD), 164
- Crust layer, 132–133
- CTE. *See* Coefficient of the thermal expansion (CTE)
- Cu/Cr/Kapton specimen, 407
- Cu–Ni alloy, 425
- Curvy electronics, 70–71
- Cu–Si alloys, 423–425
- CVD. *See* Chemical vapor deposition (CVD)
- ## D
- DCB. *See* Double cantilever beam (DCB)
- Defect-free interfacial debonding, 187
- Deionized (DI) water, 313
- Density of states (DOS), 477

- Deposition process, 166
- Derjaguin, Muller, and Toporov (DMT) theory, 133–134
- Detachment lithography (DL), 164
- Detachment transfer (DT), 164
- Device/receiver interface, 3–5
- Dichalcogenides, 419
- Differential phase contrast (DPC), 453
- Dilemma, 162
- 1,8-diiodooctane (DIO), 364
- Dipole moment, 118
- Dirac equation, 477
- Directional peeling, 48
- DMT theory. *See* Derjaguin, Muller, and Toporov (DMT) theory
- DNA, 300–301
- Dodecylbenzene sulfonic acid (DBSA), 27–29
- Dopamine (DA), 293–295
- DOS. *See* Density of states (DOS)
- Double cantilever beam (DCB), 50–51
force–displacement responses of, 52*f*
- Double-transfer printing method, 261–262
- Dry printing technique, 246–247
- Dry process, 433–434, 436–439, 437*f*
- Dry/wet etching process, 68–69
- Dundurs parameter, 383
- Dynamic release layer (DRL), 345
- E**
- E-beam evaporation (EBPVD), 369*f*, 370, 371*t*
- EBPVD. *See* E-beam evaporation (EBPVD)
- EBSD. *See* Electron backscattering diffraction (EBSD)
- ECCI. *See* Electron channeling contrast imaging (ECCI)
- ECG. *See* Electrocardiography (ECG)
- Ecoflex substrate, 212–214
- EEG. *See* Electroencephalography (EEG)
- EELS. *See* Electron energy loss spectroscopy (EELS)
- EESs. *See* Epidermal electronic systems (EESs)
- EL. *See* Electroluminescence (EL)
- Elastic deformation, 379–382
- Elastic membrane, 109
- Elastomeric membrane pattern transfer technique, 169–170
- Elastomeric stamp sagging, 327–328, 394
- Electric-assisted transfer printing techniques, 97
- Electric vehicles, 240–241
- Electroadhesive mechanism, 119–123
- Electrocardiogram (ECG), 151
- Electrocardiography (ECG), 221
- Electrochemical deposition, 371*t*, 375–376, 376*f*
- Electrochemical devices, 229
- Electrochemical sensors, 228, 230
- Electrocorticography (ECoG), 221, 281–283
- Electrode–electrolyte interphase, 353–354
- Electrode materials, 228
- Electrodes, 221
- Electroencephalography (EEG), 221
- Electrohydrodynamic (EHD) printing, 252
- Electroless bath, 376–377
- Electroluminescence (EL), 483
- Electrolysis, 124–125
- Electrolyte-gated TFT (EGT), 246–247
- Electromagnet, 109–111
- Electromagnetic waves, 177–178
- Electromyography (EMG), 221
- Electron backscattering diffraction (EBSD), 374*f*
- Electron channeling contrast imaging (ECCI), 448, 450
- Electron energy loss spectroscopy (EELS), 453
- Electrooculography (EOG), 221
- Electrophysiology sensors, 221–226
- Electroplating, 376–377
- Electrostatic forces, 119–120
- Electrostatic nanoporous stamp, 130
- Electrowetting process, 118–119
- Encapsulation materials, 288
- Energy harvesting, 500
- Energy-harvesting devices, 280, 310*f*, 311–313
- Energy systems fabricated by transfer printing technologies
fuel cells, 359–360
rechargeable batteries, 353–356
solar cells, 362–364
supercapacitors, 356–359
water splitting, 360–362
- Environmentally-assisted bonding and debonding
of metal/substrate interfaces, 401–404
- Environmental monitoring, 500
- Enzymatic biofuel cells function, 227–228
- EOG. *See* Electrooculography (EOG)
- Epidermal electronic systems (EESs), 281–283, 282*f*
- Epidermal optoelectronic device, 307–309

Epoxy-based subtractive transfer printing, 170
 pattern generation through epoxy stamp with temperature control, 170
 EQE. *See* External quantum efficiency (EQE)
 Ethyl-3-methylimidazolium *bis*(trifluoromethyl sulfonyl)amide (EMI), 246–247
 Ethylene (C₂H₄), 125–126
 Ethylene-vinyl acetate, 67–68
 Euler's beam theory, 132
 Evaporation, 370
 External quantum efficiency (EQE), 249–251
 Extraordinary optical transmission (EOT), 190

F

Fabrication processes, 210–211
 Fabry-Pérot interferometer (FPI) design, 289–291
 FEA. *See* Finite element analysis (FEA)
 Fe-FET. *See* Ferroelectric field-effect transistors (Fe-FET)
 FEM. *See* Finite element method (FEM)
 Ferroelectric field-effect transistors (Fe-FET), 487–488
 Ferroelectric memory devices, 486–489, 487*f*
 Ferroelectric semiconductor field-effect transistor (FeS-FET), 489
 FeS-FET. *See* Ferroelectric semiconductor field-effect transistor (FeS-FET)
 FETs. *See* Field-effect transistors (FETs)
 Field-effect transistors (FETs), 235, 287–288, 458–459, 475–476
 Film/substrate interface, 382–383
 Finite deformation effect, 42–43
 Finite-difference time-domain simulations, 188
 Finite element analysis (FEA), 8–10, 90, 157, 157*f*
 Finite element method (FEM), 242–244
 Finite element models, 44–45, 111–113, 340
 First-order instability stress, 132
 5G communication networks, 240–241
 Flexible and transparent electronics, 500
 Flexible electrodes, 281–283
 Flexible inorganic electronics, 280
 Flexible metal-semiconductor FET (MESFET), 241–242
 Flexible microwave integrated circuits (f-MIC), 242
 Flexible organic thin film field effect transistor (f-OTFT), 236–237
 Flexible Si-based TFTs, 291–292
 Flexible solar cells, 311–312

Flexible strain sensors, 208–210
 Flexible transistors
 with carbon materials, 244–246
 compound semiconductor-based flexible transistors, 240–244
 flexible oxide transistors, 249–252, 250*f*
 flexible Si thin-film transistors, 238–240
 flexible Si transistors with novel transfer methods, 255–260
 ion gel-based flexible transistors, 246–249, 248*f*
 with other materials, 252–255
 on various flexible substrates, 260–262
 Flexography, 401
 Floating gate memories, 484–485, 484*f*
 Fluorine-doped tin oxide (FTO), 358
 f-OTFT. *See* Flexible organic thin film field effect transistor (f-OTFT)
 Fourier transform method, 84
 Fowler-Nordheim tunneling, 484–485
 FTO. *See* Fluorine-doped tin oxide (FTO)
 Fuel cells, 359–360, 462
 Functional membrane, 64–65

G

GaAs. *See* Gallium arsenide (GaAs)
 Gallium arsenide (GaAs), 303–306, 312
 Gallium nitride (GaN), 37–38, 292–293
 GaN. *See* Gallium nitride (GaN)
 Gas injection, 118–119
 Gas-phase hydrocarbon source, 125–126
 Gecko-inspired transfer printing technique, 327–328
 Germanium (Ge), 313
 Gilding, 371*t*, 378–379
 Glucono-1,5-lactone, 254–255
 Glucose sensor, 237
 GO. *See* Graphene oxide (GO)
 Graphene, 71–73, 244–245, 477
 rate-dependent mechanical transfer of, 50–56
 Graphene oxide (GO), 353–354
 Graphite, 244–245
 Griffith criterion, 379–383
 Griffith theory, 39–41
 Growth methods, 420–423

H

HA. *See* Hyaluronic acid (HA)
 Hall bar shape, 441
 h-BN. *See* Hexagonal boron nitride (h-BN)

- Heat-assisted transfer printing techniques, 97
- HEMT. *See* High electron mobility transistor (HEMT)
- Herman's orientation factor, 125–126
- Heterogeneously-integrated monolithic f-MIC (f-MMIC), 242
- Hexagonal boron nitride (h-BN), 71–73, 419
- High electron mobility transistor (HEMT), 241–242
- High-performance sensing materials, 212–214
- High-resolution TEM (HR-TEM), 450, 453
- High-speed transistor, 458–459
- Homogeneous 2D field-effect transistors, 477, 478*f*
- Homogeneous material, 379–382
- Homostructures, 423–429
 - multilayer graphene, 423–425, 424*f*
 - multilayer hexagonal boron nitride, 425–427, 426*f*
 - multilayer TMDs, 427–429, 428*f*
- Hot carrier injection, 484–485
- Hot pick-up method, 438
- HSQ. *See* Hydrogen silsequioxane (HSQ)
- Human-computer interface, 196–197
- Human eye, 309
- Human-machine interactions (HMIs), 63, 212–214, 255
- Human-machine interfaces, 289–291
- Hyaluronic acid (HA), 188
- Hybrid materials, 498
- Hybrid photodiode, 194–196
- Hydrogen peroxide (H₂O₂), 254–255
- Hydrogen silsequioxane (HSQ), 254
- Hydrophilic material, 27–30
- Hydrothermal process, 355
- Hydro-thermal synthesis, 124–125
- I**
- ICs. *See* Integrated circuits (ICs)
- Implantable biodegradable photonic devices, 316
- Indentation test, 50–51
- Indium-gallium-zinc oxide (a-IGZO), 313
- Indium tin oxide (ITO), 154, 358
- Inductively coupled plasma CVD (ICP-CVD), 255–257
- Infrared (IR), 68–69, 188
- Infundibulum groove, 113
- Initiated CVD (iCVD), 128–129
- Inkjet-printed process, 359
- Inorganic materials, 63
- In situ growth method, 463
- In situ mechanical testing, 131–132
- Intaglio transfer printing method, 181–182, 196–197
- Integrated circuits (ICs), 235, 500
- Integrated DPC (iDPC), 453
- Interactive human-machine interface (iHMI) system, 297
- Interface adhesion strength, 17
- Interface separation model, 379–382
- Interfacial adhesion energy, 379
- Interfacial adhesion strength, 118
- Interfacial delamination, 85–89
- Interfacial energy, 164
- Interlayer electronic coupling, 445–446
- Intermolecular distance, 118
- Intermolecular interactions, 120–123
- Internet of Things (IoT), 236–237, 499
- Intracranial pressure (ICP), 289–291
- Intracranial temperature (ICT), 289–291
- Ion gel-based flexible transistors, 246–249, 248*f*
- Ionization energy, 118
- IoT. *See* Internet of Things (IoT)
- Iridium oxide (IrO_x), 221
- Iron (Fe), 313
- Isothermal dissolution-diffusion-precipitation, 425
- ITO. *See* Indium tin oxide (ITO)
- J**
- J-integral method, 157
- Johnson, Kendall, and Roberts (JKR) theory, 133–134
- Johnson-Kendall-Roberts (JKR) contact mechanics model, 39
- K**
- Kapton, 390–391
- Kinetically controlled transfer printing method, 5–6
- L**
- Large deformation pillars (LDPs), 107
- Lase-driven transfer printing method, 20
- Laser beam, 20
- Laser-driven noncontact transfer printing (LNTP) technique, 8–11, 9*f*, 79, 80*f*, 81*f*
- interfacial delamination, 85–89

- Laser-driven noncontact transfer printing (LNTP) technique (*Continued*)
 size effect of the ink, 89–90
 stamp modification design, 91–93
 transient heat conduction model, 82–85, 83*f*
- Laser-driven transfer printing techniques
 classification of, 329*f*
 contact laser-driven transfer printing techniques, 330–338
 based on elastomer/shape memory polymer composite stamp, 336–338, 338*f*
 based on microstructured shape memory polymer stamp, 334–336
 based on pyramid microstructured shape memory polymer, 335*f*
 based on shape memory polymer block, 332–334, 333*f*
 based on smart tape, 330–332
 micro-light-emitting diode display, 327–330
 noncontact laser-driven transfer printing techniques, 339–347
 based on active elastomeric microstructured stamp, 340–342, 342*f*
 based on an octopus-inspired thermal controlled stamp, 343–345, 344*f*
 based on dynamic release stamp, 345–347, 346*f*
 based on interfacial thermal mismatch, 339–340, 339*f*
- Laser-induced forward transfer (LIFT) technique, 79
- Laser-induced graphene (LIG), 299–300
- Laser-induced superplasticity (R2RLIS) method, 401
- Laser-induced thin-film lift-off (ILLO), 251–252
- Laser interference lithography, 145–147
- Laser lift-off (LLO) technique, 303–306
- Laser-scribed graphene (LSG), 359
- Layer-by-layer assembly, 438
- Layer-by-layer spin-coating method, 208–210
- LCD. *See* Liquid crystal display (LCD)
- LDPs. *See* Large deformation pillars (LDPs)
- Lead zirconate titanate (PZT), 208–210, 312
- LEDs. *See* Light-emitting diodes (LEDs)
- Letterpress process, 401
- LIG. *See* Laser-induced graphene (LIG)
- Light-assisted transfer printing techniques, 97
- Light-emitting devices, 483–484
- Light-emitting diodes (LEDs), 177, 244–245, 280, 303–307, 304*f*, 459–461
- Light-emitting materials, 325–326
- Light-harvesting and detection devices, 461–462
- Light scattering, 192–193
- Linear elastic fracture theory, 155
- Liquid crystal display (LCD), 325–326
- Liquid metal, 284–285
- Liquid–metal honeycomb circuit, 284–285
- Liquid supramolecular nanostamping (LiSuNS), 300–301
- Liquid–vapor transition, 30–31, 67–68
- LiSuNS. *See* Liquid supramolecular nanostamping (LiSuNS)
- Lithium-ion battery, 353–354
- LNTP technique. *See* Laser-driven noncontact transfer printing (LNTP) technique
- Localized surface plasmon resonance (LSPR), 187–188, 190
- Low-pressure CVD (LPCVD) method, 375
- Low-temperature poly-silicon (LTPS), 236
- LSG. *See* Laser-scribed graphene (LSG)
- LSPR. *See* Localized surface plasmon resonance (LSPR)
- ## M
- Magnesium (Mg), 313
- Magnesium oxide (MgO), 313
- Magnet-controlled transfer printing process, 14–17, 15*f*
- Magnetic-assisted transfer printing method, 11–13
- Magnetic-assisted transfer printing techniques, 97–113, 98*f*
 based on van der Waals force control, 99–108
 based on air pressure-controlled stamp, 112*f*
 based on a micropillar-shaped stamp, 107–108, 108*f*
 based on aphid-inspired stamp, 99–100, 100*f*
 based on bi-stable stamp, 105–107, 106*f*
 based on cantilever-shaped stamp, 101–102, 101*f*
 based on gas pressure control, 108–113
 based on mechanical property changing stamp, 102–105, 103*f*
 based on octopus-inspired stamp, 110*f*
- Magnetic field, 14–16, 98
- Magnetic force, 118–119
- Magnetic nanoparticles, 107

- Magnetorheological elastomer (MRE), 105
 Magnetorheological material, 105
 Magnetorheological polymer gel (MRPG), 102–104
 Material assembly technique, 97
 MBE. *See* Molecular-beam epitaxy (MBE)
 Mechanical energy, 312
 Mechanical property changing stamp, 102–105, 103*f*
 Mechanical transfer printing, 180–183
 crack-driven transfer printing, 182–183, 182*f*
 pick and place, 180–182, 181*f*
 Mechanical twisting, 439–442
 Membrane devices, 13
 Memristors, 287
 MEMS. *See* Microelectromechanical systems (MEMS)
 Metal deposition techniques, 401, 422
 Metal films
 electromechanical behaviors of ultrathin metal films bonded on substrate, 404–411
 environmentally-assisted bonding and debonding of metal/substrate interfaces, 401–404
 preparation of, 369–379
 chemical vapor deposition of thin metal films, 373*f*, 374–375
 other thin metal film deposition techniques, 375–379
 physical vapor deposition of thin metal films, 369–374, 369*f*
 transfer principles, 379–383
 driving force for the film/substrate interface separation, 379–383
 edge effects in thin film delamination, 383
 transfer printing processes for, 384–401
 advanced transfer printing procedures, 394–401
 microcontact printing, 386–388, 386*f*
 nanotransfer printing, 388–394
 Metal-free phthalocyanine (H₂Pc), 170
 Metal layers, 20, 147
 Metal leaves, 378–379
 Metallic electrodes, 119–120
 Metallic materials, 375–376
 Metallic nanoparticles, 188
 Metal materials, 281, 284
 Metal nanodots, 118
 Metal nanoforming R2R method, 401
 Metal oxide nanoparticles, 355
 Metal–oxide–semiconductor FET (MOSFET), 458–459, 475–476
 Metals, 281–285
 Metal-to-metal manufacturing process, 376–377
 Metal transfer printing (mTP) processes, 384–385
 MgO. *See* Magnesium oxide (MgO)
 Micro acetabulum, 113
 μ CP. *See* Microcontact printing (μ CP)
 Microcontact printing (μ CP), 164, 301, 384–388, 386*f*, 388*f*
 Microelectromechanical systems (MEMS), 500
 Microfabrication techniques, 63
 Micro-light-emitting diode display technique, 326–330
 Micromanufacturing technique, 164
 Micromembranes (MMs), 313–315
 Micro/nanoelectromechanical systems, 57–58
 Micro/nanometer scale, 117
 Micropillars, 107
 Micropillar-shaped stamp, 107–108, 108*f*
 Micro-structured semiconductors (μ s-Sc), 241
 Microtransfer printing techniques
 optical applications, 187–197
 optical filters, 187–194
 optoelectronics, 194–197
 transfer printing techniques, 180–187
 chemical transfer printing, 183–187
 mechanical transfer printing, 180–183
 Microwave-assisted hydrothermal synthesis, 355
 Mo. *See* Molybdenum (Mo)
 MOCVD, 430–431
 Mode-I stress intensity factor, 155
 Moiré superlattice, 431
 Molecular-beam epitaxy (MBE), 371*t*, 420–422, 421*f*, 430–431
 Molecular dynamic (MD) simulation, 127, 404, 405*f*
 Molybdenum (Mo), 313
 Molybdenum disulfide (MoS₂), 409–410, 419, 477
 Monocrystalline silicon (mono-Si), 313
 Monolayer graphene, 419
 Monolithic fabrication methods, 177–178
 Mott insulator, 456–457
 Multichannel flexible optoelectronic fiber, 284
 Multifunctional optoelectronic systems, 303–306

Multilayer single-crystal TMD materials, 427–428
 Multilayer TMDs, 483
 Multi-walled CNT (MWCNT), 123–124, 123*f*
 MXenes, 300

N

Nafion membrane, 359–360
 Nanocomposite electrodes, 223
 Nanofabrication techniques, 63
 Nanofiber (NF), 252
 Nanoimprinting lithography (NIL), 238–240
 Nanoimprinting method, 192
 Nanomaterials, 207–208
 Nanomembranes (NMs), 238–240
 Nanoparticles (NPs), 377–378
 Nanopatterned polymer, 118
 Nanoporous materials, 135–136
 Nanoscale transfer printing, 137
 Nanoscopic contacts, 132–133
 Nanostructured materials, 118
 Nanotransfer printing (nTP), 384–385, 388–394, 392*f*
 Nanowires (NWs), 30, 148–149
 Natural fibers, 210
 n-channel metal oxide semiconductors (NMOS), 240
 Near-infrared (NIR), 68–69, 93, 162
 Negative bias-temperature-illumination stress (NBTIS) test, 251–252
 Negative bias-temperature stress (NBTS) test, 251–252
 Next-generation display technique, 326
 Next-generation energy storage systems, 353–354
 Nickel-based sacrificial layer, 148–149, 148*f*
 NIR. *See* Near-infrared (NIR)
 NMOS. *See* n-channel metal oxide semiconductors (NMOS)
 N,N'-di(naphthalen-1-yl)-N,N'-diphenylbenzidine (NPB), 170
 N,N'-diphenyl-N,N'-bis(3-methylphenyl)-1_1'-biphenyl-4,4'-diamine (TPD), 169
 NOA73 UV-curable adhesive, 356–357
 Noncentrosymmetric materials, 447
 Noncontact laser-driven transfer printing techniques, 329–330, 339–347
 based on active elastomeric microstructured stamp, 340–342, 342*f*

 based on an octopus-inspired thermal controlled stamp, 343–345, 344*f*
 based on dynamic release stamp, 345–347, 346*f*
 based on interfacial thermal mismatch, 339–340, 339*f*

Nonplanar surfaces, 397–398
 Novel hetero-integrated 2D field-effect transistors, 479
 Novel state-of-the-art materials, 135–136
 nTP. *See* Nanotransfer printing (nTP)

O

Octadecyltrichlorosilane (ODTS), 167
 Octopus-inspired stamp, 22–24
 ODTS. *See* Octadecyltrichlorosilane (ODTS)
 OEECTs. *See* Organic electrochemical transistors (OEECTs)
 OLED. *See* Organic light-emitting diode (OLED)
 One-pot synthesis, 429
 Open circuit voltage, 312–313
 Optical applications, 187–197
 optical filters, 187–194
 optoelectronics, 194–197
 Optical catalysts, 462
 Optical fibers, 289–291
 Optical filters, 187–194
 metamaterials tailored for plasmonic color filters, 192–194
 three-dimensional metamaterials for tuning optical properties, 190–192
 two-dimensional metamaterials for tuning optical properties, 188–190
 Optical microscopy, 55
 Optical sensing techniques, 227
 Optics, 458
 Optoelectronic devices, 178
 Optoelectronics, 194–197
 displays, 196–197
 photodetector, 194–196, 195*f*
 Optogenetics, 292
 Organic electrochemical transistors (OEECTs), 254–255
 Organic light-emitting diode (OLED), 325–326
 Organic materials, 63, 130*t*
 Organic semiconductor (OSC), 252
 Organic solar cell assembly, 362–364
 Ostwald ripening, 126
 Oxides, 285–288

P

- PANI. *See* Polyaniline (PANI)
- Parallel transfer printing, 161–162
- Pareto Frontier chart, 53–54
- Patterned layer, 192
- PBS. *See* Phosphate-buffered saline (PBS)
- PC. *See* Polycarbonate (PC)
- PCE. *See* Power conversion efficiency (PCE)
- PCFs. *See* Plasmonic color filters (PCFs)
- PDMS. *See* Polydimethylsiloxane (PDMS)
- PDs. *See* Photodetectors (PDs)
- PE-CVD. *See* Plasma-enhanced chemical vapor deposition (PE-CVD)
- PEDOT. *See* Poly(3,4-ethylenedioxythiophene) (PEDOT)
- Peeling process, 379
- Peeling velocity, 13, 14*f*
- PEN. *See* Polyethylene naphthalene (PEN)
- 1 H,1 H,2 H,2H-perfluorodecyltrichlorosilane (FDTS), 166
- PET. *See* Polyethylene terephthalate (PET)
- PET-NOA73-graphene stack, 356–357
- Phosphate-buffered saline (PBS), 240
- Phosphorene, 71–73
- Photoconductive devices, 178
- Photodetector array, 196
- Photodetectors (PDs), 70–71, 194–196, 195*f*, 237, 280, 307–310, 309*f*, 419–420, 480, 481*f*
- Photoelectrochemical (PEC) devices, 149–150
- Photoelectrochemical (PEC) water splitting device, 360–362
- Photolithography, 68–69, 158, 164
- Photoluminescence (PL), 169, 445–446, 446*f*
- Photonic crystals, 192–193
- Photo-patterning, 378–379
- Photoresist (PR), 241
- Photovoltaic cells, 480
- Photovoltaics, 480–482
- Physical vapor deposition (PVD), 422
- Physical vapor transport (PVT), 420, 421*f*
- PI. *See* Polyimide (PI)
- Pick-and-place transfer printing technique, 188
- Picking process, 145
- Piezoelectric AFM (PFM), 454–455
- Piezoelectric materials, 312
- Piezoresistive stress sensor, 284–285
- Placing process, 145
- Plasma-enhanced chemical vapor deposition (PE-CVD), 235–236, 431
- Plasmonic color filters (PCFs), 192–193, 193*f*
- Plasmonic metamaterials, 187, 192–193
- Plasmonics, 187
- Plasmon-induced resonance energy transfer (PRT) effect, 360–362
- Plasmon modes, 187–188
- Platinum (Pt) catalyst, 359–360
- PLGA. *See* Poly (lactic-*co*-glycolic acid) (PLGA)
- Pneumatic force, 118–119
- p-n junction, 483
- Poisson's ratio, 47, 85, 91–92
- Polarizability, 118
- Polarization charge, 486–487
- Polarization-driven force, 119–120
- Poly(3,4-ethylenedioxythiophene) (PEDOT), 221
- Poly(acrylic acid) (PAA), 192
- Poly(ethylene terephthalate) (PET), 356–357
- Poly (lactic-*co*-glycolic acid) (PLGA), 311–315
- Poly(styrene sulfonate) (PSS), 221
- Poly(styrene-*b*-ethylene oxide-*b*-styrene) (SOS), 246–247
- Poly(vinyl alcohol) (PVA), 67–68, 147, 208–210, 252–253, 360–362, 396–397, 434
- Poly(vinylidene fluoride) (PVDF), 249
- Polyaniline (PANI), 353–354
- Polycarbonate (PC), 245–246, 390–391
- Poly-crystalline silicon (poly-Si), 236, 313
- Polydimethylsiloxane (PDMS), 38, 79, 93*f*, 99–100, 145–147, 154, 163, 208–210, 218, 240, 281–283, 300–301, 358, 377–378, 393*f*, 434
- rate-dependent adhesion of, 39
- viscoelastic response of, 38–39
- Polyethylene (PE), 208–210
- Polyethylene naphthalene (PEN), 390–391
- Polyethylene terephthalate (PET), 208–210, 238–240, 295
- Polyimide (PI), 70–71, 148–149, 154, 208–210, 245–246
- Polymeric layer, 54–55
- Polymeric viscoelasticity, 157–158
- Polymer materials, 208–210
- Polymer programming, 153
- Polymers, 130*t*
- Polymer thin films, 207–208

- Polymethyl methacrylate (PMMA), 163, 245–246, 396–397, 433–434
- Poly(3,4-ethylenedioxythiophene) polystyrene sulfonate (PEDOT:PSS), 27–29, 29*f*, 355–356
- Polystyrene (PS), 434
- Polytetrafluoroethylene (PTFE), 359–360
- Polythiophene, 236–237
- Polyurethane (PU), 67–68, 104, 218, 241–242
- Polyvinyl acetate, 67–68
- Polyvinyl alcohol-based sacrificial layer, 149–151, 150*f*
- Positive bias-temperature stress (PBTS) test, 251–252
- Power conversion efficiency (PCE), 362–364
- Pressure-modulated switchable adhesion, 46–47
- Pressure sensors, 214–217, 216*f*
- Prestacked substrate-angle replication, 431–433
- Probability density function, 133–134
- Programmable elastomeric stamps, 197–198
- Programmable transfer printing method, 30–32, 64
- Proteins, 300–301
- Prussian blue (PB) nanoparticles, 355–356
- PS. *See* Polystyrene (PS)
- PTFE. *See* Polytetrafluoroethylene (PTFE)
- PU. *See* Polyurethane (PU)
- Pull-off tests, 99–100
- Pulsed laser deposition (PLD), 369*f*, 370, 371*t*, 422
- PVA. *See* Poly(vinyl alcohol) (PVA)
- PVDF. *See* Poly(vinylidene fluoride) (PVDF)
- PVT. *See* Physical vapor transport (PVT)
- Q**
- QD. *See* Quantum dot (QD)
- QE. *See* Quantum efficiency (QE)
- QLED. *See* Quantum dot light emitting diode (QLED)
- Qualitative description, 132
- Quantitative analysis, 120–123
- Quantum dot (QD), 163, 181–182
- Quantum dot light emitting diode (QLED), 181–182
- Quantum efficiency (QE), 460–461
- Quasi-3D plasmonic nanostructures, 191–192
- R**
- R2R metal transfer printing, 401
- Rabbit animal model, 223
- Race-to-the-top growth mechanism, 428–429
- Radio Corporation of America clean, 434
- Radio frequency (RF), 238–240, 289–291
- Raman effect, 444–445
- Raman scattering, 444*f*
- Raman spectroscopy, 444–445
- Rayleigh scattering, 444*f*
- Reactive ion etching (RIE), 168–169, 251, 396–397
- Receiver substrate, 328–329
- Rechargeable batteries, 353–356
- Red, green and blue (RGB), 169, 181–182
- Reference peeling velocity, 66–67
- Refractive index, 189–190
- Relative permittivity, 134
- Renewable energy, 240–241
- Resistance-force curve, 284–285
- Resistance-strain curves, 409–410
- Resistance temperature detectors (RTDs), 217
- Resistive heating method, 370
- Reversible hydrogen electrode (RHE), 360–362
- RHE. *See* Reversible hydrogen electrode (RHE)
- RIE. *See* Reactive ion etching (RIE)
- Roll-to-roll printing, 498
- Roll-to-roll (R2R) processing, 71–73
- Root-mean-square roughness (rms), 247
- RTDs. *See* Resistance temperature detectors (RTDs)
- Rubbers, 210
- S**
- Sacrificial layer, 147
- SAED. *See* Selected area electron diffraction (SAED)
- SAM. *See* Self-assembled monolayer (SAM)
- Scanning electron microscopy (SEM), 160, 244–245, 332–334, 355, 448–449, 449*f*
- Scanning transmission electron microscope (STEM), 451–453, 452*f*
- Scanning tunneling microscope (STM), 454
- Schottky-type photodetectors, 196
- SDPs. *See* Small deformation pillars (SDPs)
- Second-harmonic generation (SHG), 435–436, 440*f*, 447–448, 447*f*
- Seebeck effect, 217
- Selected area electron diffraction (SAED), 450
- Self-assembled monolayer (SAM), 145, 160–161, 386, 387*t*

- Self-assembled monolayer-based release layer, 145–147, 146*f*
- Self-delamination-based pattern transfer, 183–187, 183*f*
- SEM. *See* Scanning electron microscopy (SEM)
- Semiconductor circuits, 177
- Semiconductor industries, 119–120
- Semidry process, 433–434
- Sensing arrays, 177, 280
- Sensors, 462–463
- Serial transfer printing mode, 161–162
- Shape memory polymer (SMP), 24–27, 26*f*, 57, 92–93, 153, 221, 283, 332
 - background of, 153–154
 - for deterministic transfer printing, 158–159
 - mechanics of shape memory polymer for deterministic transfer printing, 155–158
 - microassembly of unusual three-dimensional microstructures using, 159–160
 - multilayered thin film contact printing with, 160–161
 - for subtractive transfer printing of colloids, 163–164
- Shape memory polymer composite (SMPC), 154
- Shear-enhanced transfer printing, 6–8, 7*f*
- SHG. *See* Second-harmonic generation (SHG)
- Shockley–Queisser (SQ) limit, 461–462
- Short-channel effect, 475–476
- Signal-to-noise ratio (SNR), 279–280
- Silicon (Si), 289–292, 475–476
- Silicon carbide (SiC), 292–293
- Silicon dioxide (SiO₂), 166, 313
- Silicone elastomers, 210
- Silicon germanium alloy (SiGe), 313
- Silicon MOSFET, 289–291
- Silicon nanomembranes (Si NMs), 289–291
- Silicon nanowire (SiNW), 71–73
- Silicon nitride (SiN), 148–149, 241–242, 313
- Silicon-on-insulator (SOI), 238–240
- Silver nanoparticles, 359
- Silver nanowires (AgNWs), 210–211, 355–356, 364
- SiN. *See* Silicon nitride (SiN)
- Single-crystal graphene, 440–441
- Single crystal silicon (sc-Si), 235
- Single-crystal Si semiconductors, 238
- Single-layer arrays, 189–190
- Single-walled carbon nanotubes (SWCNTs), 123–124, 244–246, 356–357
- Sketch and peel lithography (SPL), 254
- Small deformation pillars (SDPs), 107
- Smart agriculture, 500
- SMPC. *See* Shape memory polymer composite (SMPC)
- Soft electronics, 63
- Soft robotics, 212–214
- Solar cells, 177, 280, 362–364
- Sol–gel process, 168–169
- Solid-state batteries, 355
- Solid-state electrolyte, 353–354
- Spin-coating, 246–247, 422
- Spiral patterns, 212–214
- Spontaneous peeling, 383
- SPPs. *See* Surface plasmon polaritons (SPPs)
- Spray pyrolysis deposition, 229–230
- Sputter deposition, 370
- Sputtering, 369*f*, 371*t*
- SSVEPs. *See* Steady-state visual evoked potentials (SSVEPs)
- Stamp, 26–27, 336–337
 - device adhesion, 3–5
 - functional membrane interface, 64–65
 - ink interfacial adhesion strength, 98
 - modification design, 91–93
- Steady-state visual evoked potentials (SSVEPs), 281–283
- STEM. *See* Scanning transmission electron microscope (STEM)
- Stencil-printed electrodes, 229
- STM. *See* Scanning tunneling microscope (STM)
- Strain sensors, 207–214, 209*f*
- Stress intensity factor, 11
- Stress-strain curves, 104
- Structural engineering, 192–193
- Subthreshold swing (SS), 240
- Subtractive transfer printing, 163
- Supercapacitors, 356–359
- Supramolecular nanostamping (SuNS), 300–301
- Surface adhesion, 117–120
 - low surface adhesion via nanoscale porosity, 117–118
 - strong adhesion and reversible adhesion modulation via electrostatic force, 118–120
- Surface catalysis process, 423

- Surface chemical reactions, 374–375
 Surface modification approaches, 127–128
 Surface plasmon (SP), 187
 Surface plasmon polaritons (SPPs), 187
 Surface plasmon resonance (SPR), 190
 System-level design, 497
- T**
- Tear and stack method, 441–442
 Temperature coefficient of resistance (TCR), 217
 Temperature distribution, 225
 Temperature sensors, 218
 TEMs. *See* Thermally expandable microspheres (TEMs)
 Textile industries, 119–120
 TFSCs. *See* Thin film solar cells (TFSCs)
 TFTs. *See* Thin-film transistors (TFTs)
 Thermal conductivity, 124
 Thermal evaporation deposition, 370, 371*t*
 Thermal expansion coefficient (CTE), 185, 382–383
 Thermally expandable microspheres (TEMs), 330–332
 Thermally grown silicon dioxide (t-SiO₂), 289–291
 Thermal release-assisted transfer printing processes, 223
 Thermal release tape (TRT), 13, 63, 73*f*, 148–149, 257–258, 360–362
 shape-conformal thermal release tape stamp for curve electronics, 70–71
 stamp-enabled roll-to-roll processing for large-scale transfer printing, 71–73
 thermally expandable microspheres-based thermal release tape stamp for large adhesion switchability, 67–68
 thermal release transfer printing, 64–67, 66*f*
 thermal treatment with laser for programmable transfer printing, 68–70
 Thermal release transfer printing, 13, 14*f*, 64–67
 Thermal sensors, 217–220
 Thermistors, 217
 Thermocouples, 217
 Thermo-mechanical axisymmetric model, 10
 Thermomechanical model, 81–82
 Thermo-mechanical transfer printing techniques, 184–185, 184*f*, 197–198
 Thermoplastic polymers, 30–32, 210
 Thin film delamination process, 401–404
 Thin-film/multilayer interference, 192–193
 Thin film solar cells (TFSCs), 362, 363*f*
 Thin-film transistors (TFTs), 235, 280, 287–288
 3D Fin FET (Fin-FETs), 475–476
 Three-dimensional integration, 252–253
 Three-dimensional mechanics models, 18
 Three-dimensional metamaterials for tuning optical properties, 190–192
 Three-dimensional nTP method, 395
 3D penetrating microprobe array, 292
 3D-printed electronics, 500
 Three-dimensional printing technology, 57, 70–71
 Three-dimensional stacking, 343–345
 Three-dimensional transfer printing, 399*f*
 Threshold delamination driving force, 404
 Tissue engineering, 301–303
 Titanium dioxide (TiO₂), 285
 Top-down fabrication methods, 207–208
 Top-down method, 238
 Top-down process, 241–242
 Transfer printing, 3–5, 63, 177, 180–187, 196–197, 495
 chemical sensors, 226–230
 biosensors, 227
 electrochemical sensors, 226
 gas sensors, 227
 mass-based sensors, 227
 optical sensors, 226
 chemical transfer printing, 183–187
 combination with other fabrication technologies, 500–501
 device and system integration, 499
 of elastic membrane for pattern generation, 168–170
 transfer of elastomeric membrane for lift-off mask, 168–169
 transfer of elastomeric membrane to pattern photoluminescent material, 169–170
 electrophysiology sensors, 221–226
 epoxy-based subtractive transfer printing, 170
 involving photoresist thin film, 164–168
 detachment lithography—photoresist thin film patterning, 164–166
 quantum dot patterning via photoresist transfer printing, 166–168
 major challenges, 495–496

- environmental impacts, 496
- high manufacturing costs, 496
- limited material compatibility, 495
- limited scalability, 496
- reliability and durability, 496
- materials development, 497–498
- materials science of, 24–32
 - hydrophilic material, 27–30
 - shape memory polymer, 24–27, 26*f*
 - thermoplastic polymer, 30–32
- mechanical transfer printing, 180–183
- mechanics of, 5–17
 - kinetically controlled transfer printing, 5–6
 - laser-driven noncontact transfer printing, 8–11, 9*f*
 - magnet-controlled transfer printing, 14–17, 15*f*
 - magnetic-assisted transfer printing, 11–13
 - shear-enhanced transfer printing, 6–8, 7*f*
 - thermal release transfer printing, 13, 14*f*
- mechanics theory, 39–42
- modulation strategy, 42–50
 - stamp stiffness, 42–43
 - stamp thickness, 44–46
 - surface patterning, 46–48
 - temperature, 49–50
- novel applications, 499–500
- possible breakthroughs in future transfer printing, 501
- pressure sensors, 214–217, 216*f*
- process/manufacturing optimization, 498–499
- process physics, 123–134
 - carbon nanotubes, 123–124
 - contact mechanics of vertically aligned carbon nanotubes, 130–134
 - electrostatic adhesion of vertically aligned carbon nanotubes, 134
 - surface modification of vertically aligned carbon nanotubes, 127–129
 - synthesis of vertically aligned carbon nanotubes, 124–127
- rate-dependent mechanical transfer of graphene, 50–56
- selective printing combined cooperatively with parallelism in, 161–163
- strain sensors, 207–214, 209*f*
- structure for, 17–24
 - biomimetic structures, 20–21, 23*f*
 - bulging structures, 20–21, 21*f*
 - surface relief structures, 18–20, 19*f*
- thermal sensors, 217–220
- using Al₂O₃-coated vertically aligned carbon nanotubes, 121*f*
- using unusual manipulator—shape memory polymer, 153–164
- working principle, 38–39
- working principles, 117–123
 - large contrast in surface adhesion, 117–120
 - vertically-aligned carbon nanotube for soft nanocomposite electrodes, 120–123
- Transient heat conduction equation, 10
- Transient heat conduction model, 82–85, 83*f*
- Transistors, 291–292, 458–459
- Transition metal dichalcogenides (TMD), 71–73, 430–431, 434, 475, 483–484
- Transition temperature, 64–65
- Transmission electron microscopy (TEM), 450–451, 451*f*
- Tris(8-quinolinolato)aluminum (AlQ₃), 170
- TRT. *See* Thermal release tape (TRT)
- Tungsten (W), 313
- Tunnel-field-effect transistor, 458–459
- 2D heterostructures, 462
- Two-dimensional (2D) layered materials, 475
 - based logic devices, 475–479
 - back-gate field-effect transistors, 477–479, 478*f*
 - homogeneous 2D field-effect transistors, 477, 478*f*
 - novel hetero-integrated 2D field-effect transistors, 479
 - based memory devices, 484–489
 - ferroelectric memory devices, 486–489, 487*f*
 - floating gate memories, 484–485, 484*f*
 - based optoelectronics, 480–484
 - light-emitting devices, 483–484
 - photodetectors, 480, 481*f*
 - photovoltaics, 480–482
 - based solar cells, 482*f*
- Two-dimensional (2D) materials, 37–38, 51, 57–58, 71–73, 280, 296–300, 298*f*, 419
 - application, 458–463
 - light-emitting diodes, 459–461
 - light-harvesting and detection devices, 461–462
 - sensors, 462–463

- Two-dimensional (2D) materials (*Continued*)
- transistors, 458–459
 - bottom-up fabrication of two-dimensional stack, 420–433
 - growth methods, 420–423
 - heterostructures, 429–431, 430*f*
 - homostructures, 423–429
 - twisting of, 431–433, 432*f*
 - characterization, 442–455
 - atomic probing technique, 454–455
 - photoluminescence, 445–446, 446*f*
 - Raman effect, 444–445
 - scanning electron microscope—back-scattered electron channeling contrast imaging, 448–450
 - scanning transmission electron microscopy, 451–453, 452*f*
 - second-harmonic generation, 447–448, 447*f*
 - transmission electron microscope, 450–451
 - X-ray diffraction, 442–444, 443*f*
 - electronic and optoelectronic devices based on, 419–420
 - properties, 456–458
 - correlated phase in twisted two-dimensional stack, 456–457
 - lattice reconstruction, 457–458
 - modulation of band structure, 456
 - optics, 458
 - top-down fabrication of two-dimensional stack, 433–442
 - dry process, 436–439, 437*f*
 - mechanical twisting, 439–442
 - semidry transfer, 435–436, 435*f*
 - wet process, 433–434, 433*f*
- Two-dimensional mechanics models, 18
- Two-dimensional metamaterials, 188
 - for tuning optical properties, 188–190
- 2D precursors, 211–212
- U**
- Ultraviolet (UV), 208–210
- V**
- VACNT. *See* Vertically-aligned carbon nanotube (VACNT)
- Vacuum bonding process, 438
- Vacuum permittivity, 118, 134
- Vanadium dioxide (VO₂), 285, 286*f*
- Van der Waals (vdW) force control, 99–108
 - based on air pressure-controlled stamp, 112*f*
 - based on a micropillar-shaped stamp, 107–108, 108*f*
 - based on aphid-inspired stamp, 99–100, 100*f*
 - based on bi-stable stamp, 105–107, 106*f*
 - based on cantilever-shaped stamp, 101–102, 101*f*
 - based on gas pressure control, 108–113
 - based on mechanical property changing stamp, 102–105, 103*f*
 - based on octopus-inspired stamp, 110*f*
- Vapor–liquid–solid (VLS) mechanism, 125–126
- Vapor phase transportation, 374–375
- Vertical field-effect transistors, 459
- Vertically-aligned carbon nanotube (VACNT), 120, 210–211, 355
 - contact mechanics of, 130–134, 131*f*
 - electrostatic adhesion of, 134
 - mechanical behavior of, 130
 - surface modification of, 127–129, 128*f*
 - synthesis of, 124–127
- Virtual detector, 453
- Viruses, 300–301
- Volumetric effects, 153–154
- W**
- Water-assisted transfer printing (WTP) techniques, 30, 145
 - with nickel-based sacrificial layer, 148–149, 148*f*
 - with polyvinyl alcohol-based sacrificial layer, 149–151, 150*f*
 - with self-assembled monolayer-based release layer, 145–147, 146*f*
- Water-soluble tape (WST), 257–258
- Water splitting, 360–362, 462
- Wax transfer printing, 229
- Wearable electronics, 280
- Web processing, 71–73
- Wet-chemical etching, 168–169
- Wet-etching process, 238, 378–379
- Wet process, 433–434, 433*f*
- Wide bandgap semiconductors, 292–296
- Working electrode, 229
- WTP techniques. *See* Water-assisted transfer printing (WTP) techniques

X

Xenes, 71–73

X-ray diffraction (XRD), 442–444, 443f

X-ray spectroscopy, 453

XRD. *See* X-ray diffraction (XRD)

Y

Young's modulus, 6–8, 91–92, 128–129

Z

Zeolite imidazolide framework derived carbon (ZIF-C), 358

Zero-band gap, 456

Zero-gap metals, 124

ZIF-C. *See* Zeolite imidazolide framework derived carbon (ZIF-C)

Zinc (Zn), 313

Zinc oxide (ZnO), 184–185, 313

ZnO. *See* Zinc oxide (ZnO)

Transfer Printing Technologies and Applications

Edited by Changhong Cao and Yu Sun

Transfer printing (TP) is a class of techniques for the deterministic assembly of disparate micro/nanomaterials into functional devices and has become an emerging suite of technologies for micro/nanofabrication. Systems enabled by TP range from complex molecular-scale materials, to high-performance hard materials, to fully integrated devices. A variety of subtechniques for different purposes have grown significantly in the past decade, leading to nonconventional electronics, optoelectronics, photovoltaics, and photonics and enabling the development of nonplanar and flexible electronics.

Transfer Printing Technologies and Applications is a complete guide to TP techniques and their cutting-edge applications. The first section of the book provides a solid grounding in TP methods and the fundamentals behind these technologies. The second part of the book focuses on state-of-the-art applications enabled by TP techniques, including areas such as flexible sensors, flexible transistors, optical devices, energy systems, micro-LED-based displays, biomedical devices, 2D materials/electronics, and among others. A concluding chapter addresses current challenges and future opportunities in this innovative field.

This book is of interest to researchers and advanced students across nanotechnology, materials science, electrical engineering, mechanical engineering, chemistry, and biomedicine, as well as scientists, engineers, and R&D professionals involved with nanomaterials, micro- or nano-fabrication, wearable electronics, microelectromechanical systems, display technology, biotechnology, and devices.

Key Features

- Examines a range of TP technologies and their specific features for different applications
- Highlights breakthrough results and systems enabled by novel TP techniques
- Offers an insightful outlook on trends and future directions in each subarea of TP

About the Editors

Changhong Cao is the director of the McGill NanoFactory and an assistant professor in the Department of Mechanical Engineering, at the McGill University, Canada.

Yu Sun is a professor in the Department of Mechanical and Industrial Engineering, with joint appointments in the Institute of Biomaterials and Biomedical Engineering, the Department of Electrical and Computer Engineering, and the Department of Computer Science at the University of Toronto (UofT), in Canada. He is a Tier I Canada Research Chair and the founding director of the UofT Robotics Institute.



ELSEVIER

elsevier.com/books-and-journals

materialstoday
Connecting the materials community

ISBN 978-0-443-18845-9



9 780443 188459